Additive Manufacturing Materials and Technologies

FUNDAMENTALS OF LASER POWDER BED FUSION OF METALS

Edited by

Igor Yadroitsev, Ina Yadroitsava,
Anton Du Plessis, and Eric MacDonald

ELSEVIER

Additive Manufacturing Materials and Technologies Series Edited by Ma Qian

Published titles

- *Science, Technology and Applications of Metals in Additive Manufacturing,* Datta, Babu & Jared, 9780128166345
- *Design for Additive Manufacturing,* Martin Leary, 9780128167212
- *Multiscale Modeling of Additively Manufactured Meta*ls, Zhang, Jung and Zhang, 9780128196007

Additive Manufacturing Materials and Technologies

Fundamentals of Laser Powder Bed Fusion of Metals

Edited by

Igor Yadroitsev

Department of Mechanical and Mechatronic Engineering, Central University of Technology, Bloemfontein, Free State, South Africa

Ina Yadroitsava

Department of Mechanical and Mechatronic Engineering, Central University of Technology, Bloemfontein, Free State, South Africa

Anton Du Plessis

Department of Mechanical Engineering, Nelson Mandela University, Port Elizabeth, Eastern Cape, South Africa; Research Group 3D Innovation, Stellenbosch University, Stellenbosch, Western Cape, South Africa

Eric MacDonald

W. M. Keck Center for 3D Innovation, University of Texas at El Paso, El Paso, TX, United States

ELSEVIER

Elsevier
Radarweg 29, PO Box 211, 1000 AE Amsterdam, Netherlands
The Boulevard, Langford Lane, Kidlington, Oxford OX5 1GB, United Kingdom
50 Hampshire Street, 5th Floor, Cambridge, MA 02139, United States

Copyright © 2021 Elsevier Inc. All rights reserved.

No part of this publication may be reproduced or transmitted in any form or by any means, electronic or mechanical, including photocopying, recording, or any information storage and retrieval system, without permission in writing from the publisher. Details on how to seek permission, further information about the Publisher's permissions policies and our arrangements with organizations such as the Copyright Clearance Center and the Copyright Licensing Agency, can be found at our website: www.elsevier.com/permissions.

This book and the individual contributions contained in it are protected under copyright by the Publisher (other than as may be noted herein).

Notices
Knowledge and best practice in this field are constantly changing. As new research and experience broaden our understanding, changes in research methods, professional practices, or medical treatment may become necessary.

Practitioners and researchers must always rely on their own experience and knowledge in evaluating and using any information, methods, compounds, or experiments described herein. In using such information or methods they should be mindful of their own safety and the safety of others, including parties for whom they have a professional responsibility.

To the fullest extent of the law, neither the Publisher nor the authors, contributors, or editors, assume any liability for any injury and/or damage to persons or property as a matter of products liability, negligence or otherwise, or from any use or operation of any methods, products, instructions, or ideas contained in the material herein.

Library of Congress Cataloging-in-Publication Data
A catalog record for this book is available from the Library of Congress

British Library Cataloguing-in-Publication Data
A catalogue record for this book is available from the British Library

ISBN: 978-0-12-824090-8

For information on all Elsevier publications visit our website at https://www.elsevier.com/books-and-journals

Publisher: Matthew Deans
Acquisitions Editor: Christina Gifford
Editorial Project Manager: Chiara Giglio
Production Project Manager: Prasanna Kalyanaraman
Cover Designer: Christian J. Bilbow
Cover Image: A design demonstrator for an additively manufactured aerospike nozzle with a height of 200 mm by Fraunhofer IWS and ILR, TU Dresden - see Chapter 21 for more details.

ELSEVIER Book Aid International
Working together
to grow libraries in
developing countries
www.elsevier.com • www.bookaid.org

Typeset by TNQ Technologies

Contributors

Daniel Anderson 3DX Research Group, The Polytechnic School, Arizona State University, Mesa, AZ, United States

Moataz M. Attallah School of Metallurgy and Materials, University of Birmingham, Birmingham, United Kingdom

Bonnie Attard School of Metallurgy and Materials, University of Birmingham, Birmingham, United Kingdom; Department of Metallurgy and Materials Engineering, Faculty of Engineering, University of Malta, Msida, Malta

Abolfazl Azarniya Department of Mechanical Engineering, National University of Singapore, Singapore, Singapore

Sara Bagherifard Department of Mechanical Engineering, Polytechnic University of Milan, Milan, Italy

Joseph J. Beaman University of Texas, Austin, TX, United States

Filippo Berto Department of Mechanical and Industrial Engineering, Norwegian University of Science and Technology (NTNU), Trondheim, Norway

Dhruv Bhate 3DX Research Group, The Polytechnic School, Arizona State University, Mesa, AZ, United States

Dermot Brabazon School of Mechanical Engineering, Dublin City University, Dublin, Ireland; I-Form, Advanced Manufacturing Research Centre, Dublin City University, Dublin, Ireland

Milan Brandt Centre for Additive Manufacturing, School of Engineering, RMIT University, Melbourne, VIC, Australia

Frank Brueckner Fraunhofer IWS, Dresden, Germany

Bianca Maria Colosimo Department of Mechanical Engineering, Polytechnic University of Milan, Milan, Italy

David Downing Centre for Additive Manufacturing, School of Engineering, RMIT University, Melbourne, VIC, Australia

Anton Du Plessis Research Group 3D Innovation, Stellenbosch University, Stellenbosch, Western Cape, South Africa; Department of Mechanical Engineering, Nelson Mandela University, Port Elizabeth, Eastern Cape, South Africa

Johan Els Centre for Rapid Prototyping and Manufacturing, Central University of Technology, Bloemfontein, Free State, South Africa

Kate Fox Centre for Additive Manufacturing, School of Engineering, RMIT University, Melbourne, VIC, Australia

Marco Grasso Department of Mechanical Engineering, Polytechnic University of Milan, Milan, Italy

Robert Groarke School of Mechanical Engineering, Dublin City University, Dublin, Ireland; I-Form, Advanced Manufacturing Research Centre, Dublin City University, Dublin, Ireland

Samira Gruber Fraunhofer IWS, Dresden, Germany

Mario Guagliano Department of Mechanical Engineering, Polytechnic University of Milan, Milan, Italy

Johannes Gumpinger ESA/ESTEC, European Space Research and Technology Center, Noordwijk, the Netherlands

Andrey V. Gusarov Moscow State University of Technology STANKIN, Moscow, Russia

Jonathan Harris nTopology, New York, NY, United States

Nataliya Kazantseva Institute of Metal Physics of the Ural Branch of the Russian Academy of Sciences (IMP UB RAS), Ekaterinburg, Russia

Mahyar Khorasani School of Engineering, Deakin University, Waurn Ponds, VIC, Australia

Alex Kingsbury Centre for Additive Manufacturing, School of Engineering, RMIT University, Melbourne, VIC, Australia

Pavel Krakhmalev Karlstad University, Department of Engineering and Physics, Karlstad, Sweden

Martin Leary Centre for Additive Manufacturing, School of Engineering, RMIT University, Melbourne, VIC, Australia

Elena Lopez Fraunhofer IWS, Dresden, Germany

Bill Lozanovski Centre for Additive Manufacturing, School of Engineering, RMIT University, Melbourne, VIC, Australia

Eric MacDonald W. M. Keck Center for 3D Innovation, University of Texas at El Paso, El Paso, TX, United States

Mauro Madia Federal Institute for Materials Research and Testing (BAM), Berlin, Germany

Nkutwane Washington Makoana Department of Mechanical and Mechatronic Engineering, Central University of Technology, Bloemfontein, Free State, South Africa; Council for Scientific and Industrial Research, National Laser Centre, Pretoria, South Africa

Mohammad J. Mirzaali Department of Biomechanical Engineering, Faculty of Mechanical, Maritime, and Materials Engineering, Delft University of Technology (TU Delft), Delft, the Netherlands

Yash Mistry 3DX Research Group, The Polytechnic School, Arizona State University, Mesa, AZ, United States

Abd El-Moez A. Mohamed School of Metallurgy and Materials, University of Birmingham, Birmingham, United Kingdom

Andrey Molotnikov Centre for Additive Manufacturing, School of Engineering, RMIT University, Melbourne, VIC, Australia

Lameck Mugwagwa Department of Mechanical and Mechatronic Engineering, Central University of Technology, Bloemfontein, Free State, South Africa

Daniel Powell Centre for Defense Engineering, Cranfield University, Shrivenham, United Kingdom; Engineering Department, Lancaster University, Lancaster, United Kingdom

Seyed Mohammad Javad Razavi Department of Mechanical and Industrial Engineering, Norwegian University of Science and Technology (NTNU), Trondheim, Norway

Allan Rennie Engineering Department, Lancaster University, Lancaster, United Kingdom

Richard W. Russell NASA Engineering and Safety Center (NESC), Langley Research Center, Hampton, VA, United States

Avik Sarker Centre for Additive Manufacturing, School of Engineering, RMIT University, Melbourne, VIC, Australia

Christian Seidel Munich University of Applied Sciences Munich, Germany; Fraunhofer IGCV, Augsburg, Germany

Mohsen Seifi ASTM International, Washington, DC, United States; Case Western Reserve University, Cleveland, OH, United States

Nima Shamsaei National Center for Additive Manufacturing Excellence (NCAME), Auburn University, Auburn, AL, United States; Department of Mechanical Engineering, Auburn University, Auburn, AL, United States

Kevin Slattery The Barnes Global Advisors, Pittsburgh, PA, United States

Saeed Sovizi Independent Researcher, Tehran, Iran

Naoki Takata Department of Materials Process Engineering, Graduate School of Engineering, Nagoya University, Nagoya, Aich, Japan

Johnathan Tran Centre for Additive Manufacturing, School of Engineering, RMIT University, Melbourne, VIC, Australia

Rajani K. Vijayaraghavan I-Form, Advanced Manufacturing Research Centre, Dublin City University, Dublin, Ireland; School of Electronic Engineering, Dublin City University, Dublin, Ireland

Anna Martin Vilardell Department of Materials Process Engineering, Graduate School of Engineering, Nagoya University, Nagoya, Aich, Japan

Jess M. Waller NASA-Johnson Space Center White Sands Test Facility, Las Cruces, NM, United States

Igor Yadroitsev Department of Mechanical and Mechatronic Engineering, Central University of Technology, Bloemfontein, Free State, South Africa

Ina Yadroitsava Department of Mechanical and Mechatronic Engineering, Central University of Technology, Bloemfontein, Free State, South Africa

Amir A. Zadpoor Department of Biomechanical Engineering, Faculty of Mechanical, Maritime, and Materials Engineering, Delft University of Technology (TU Delft), Delft, the Netherlands

Uwe Zerbst Federal Institute for Materials Research and Testing (BAM), Berlin, Germany

Jie Zhou Department of Biomechanical Engineering, Faculty of Mechanical, Maritime, and Materials Engineering, Delft University of Technology (TU Delft), Delft, the Netherlands

Editors' bios

Prof. Igor Yadroitsev is a Research Chair in Medical Product Development through Additive Manufacturing at the Central University of Technology launched by the National Research Foundation of South Africa in 2015. He has been involved in additive manufacturing with emphasis on laser powder bed fusion at the Vitebsk Institution of Technical Acoustics (Belarus) since 1995, when this technology was in its infancy. He continued his research in the field at the National School of Engineering (Saint-Étienne, France) and published a book on selective laser melting in 2009. His research interests include applied optics and laser technologies: additive manufacturing, laser powder bed fusion of metals and plastics, laser processing, materials science, and optics. He has authored over 100 articles in the field of laser powder bed fusion.

Dr. Ina Yadroitsava, PhD, has been involved in additive manufacturing since 2007 when she started to work in the Laboratory of Diagnostics and Engineering of Industrial Processes at the National School of Engineering (Saint-Étienne, France). At present, she is working as Senior Researcher at the Department of Mechanical and Mechatronic Engineering, Faculty of Engineering, Built Environment and Information Technology at the Central University of Technology, Free State. In 2019, she was recognized by the South Africa National Research Foundation as an established researcher in such areas as laser metal additive manufacturing, advanced materials, and numerical modeling. Her research interests include laser powder bed fusion, material characterization, bio-medical applications, and properties of advanced additively manufactured materials.

Prof. Anton Du Plessis is an Associate Professor at Stellenbosch University, South Africa, and is also affiliated with Nelson Mandela University, South Africa. He is an experienced scholar in the field of additive manufacturing, with specific interests in quality control and process optimization, X-ray tomography, and biomimicry applied to additive manufacturing. His interests and expertise range across several disciplines in the sector, and he is an Associate Editor of Elsevier's leading journal *Additive Manufacturing*.

Prof. Eric MacDonald, PhD, is a Professor of Mechanical Engineering and the Murchison Chair at the University of Texas at El Paso, as well as Deputy Editor of the Elsevier journal *Additive Manufacturing*. Dr. MacDonald received his PhD degree in Electrical Engineering from the University of Texas at Austin and has worked in industry for 12 years at IBM and Motorola, and subsequently co-founded a start-up—Pleiades, Inc., which was acquired by Magma Inc. (San Jose, CA) in 2003. Dr. MacDonald has held faculty fellowships at NASA's Jet Propulsion Laboratory, SPAWAR Navy Research (San Diego), and a State Department Fulbright Fellowship in South America. His research interests include 3D-printed multifunctional applications and advanced process monitoring in additive manufacturing.

Foreword

Powder bed fusion is now widely used in aerospace, medical, automotive, and other industries because it can make a wide variety of customized parts that are difficult to produce by conventional manufacturing[1]. It is a fascinating innovation[2] that can produce intricate parts with fine features by melting thin layers of metal powder, often thinner than a human hair, layer upon layer using a heat source such as a laser beam. However, it is a new and complex process and faces several scientific, technological, and commercial problems,[3] whose solutions require a comprehensive scientific understanding of the technology. It has empowered[3] engineers to dream big, but the complexity of the process, the high costs of equipment and feedstock have challenged them to adopt solutions based on knowledge and reject or at least minimize the traditional trial-and-error search for solutions. It is not surprising that only the large corporations that can assemble interdisciplinary teams of engineers to solve complex problems of powder bed fusion dominate the business landscape. This book is a valuable and timely comprehensive resource for knowledge, data, analysis, and ideas for addressing these problems.

My students and I have benefited from the valuable research contributions of the four editors. The entire additive manufacturing community has also benefited from the professional services of the senior editors who also serve as Editors of *Additive Manufacturing*, the leading journal of 3D printing or additive manufacturing. The editorial team has a dominating presence in the additive manufacturing field and is a perfect group of accomplished researchers to assemble this volume.

The depth of coverage of the important topics is remarkable and the twenty-four chapters are contributed by an impressive list of active researchers. Because of the diversity of topics, it is an excellent introductory book for senior undergraduates, and its depth of coverage makes it appropriate for graduate students. This book will enable practicing engineers to acquire valuable knowledge, solve problems, get creative thoughts, and serve as a much-appreciated reference book. I expect satisfied readers to recommend it to everyone in the field.

T. DebRoy

Professor of Materials Science and Engineering, The Pennsylvania State University,
University Park, PA, United States

---

[1] MacDonald, E., Wicker, R., 2016. Multiprocess 3D printing for increasing component functionality. Science 353, 6073.

[2] DebRoy, T., Bhadeshia, H.K.D.H., 2020. Innovations in Everyday Engineering Materials. https://www.springer.com/gp/book/9783030576110

[3] DebRoy, T., et al., 2019. Scientific, technological and economic issues in metal printing and their solutions. Nat. Mater. 18 (10), 1026−1032.

Preface

Laser powder bed fusion (L-PBF)[1] of metals is now the most mature additive manufacturing technology, being widely used today in real-world commercial applications in medical, aerospace, and other industries. The wider adoption of this technology in industry is inevitable due to specific advantages when compared to traditional manufacturing methods. These advantages include relatively short manufacturing times, cost and efficiency benefits for high-complexity parts, mass customization, the combination of functions, consolidation of manifold parts, and distributed manufacturing capabilities.

The huge growth in the field in recent years (in academia and industry) is a testament to the substantial interest in leveraging these advantages, to provide benefits and add real value. While these advantages are being capitalized on by various stake holders, a need exists on a fundamental level to support and advance the entire field. This involves people at various levels, from students, researchers, and technical staff to application scientists, engineers, and managers, with varying levels of experience from beginners to experts in L-PBF. In addition, due to the manufacturing process being a complex and interdisciplinary topic, often specialists from a diversity of expertise are involved—metallurgists; chemical, mechanical, electronic, industrial, and design engineers; physicists; applied mathematicians (recently machine learning for example), etc.

This book is a reference text suitable for all of these levels of abstraction, providing a comprehensive conceptual understanding of all of the important aspects and issues to fully utilize L-PBF. The text serves to provide an overview covering all of the fundamentals, while also clearly demonstrating the current state of the art. It includes references to up-to-date literature on each topic, as well as tables and figures which are suitable for quick reference. The book was written by a selection of the world's leading experts in their fields: a total of 59 authors from 14 countries contributed to comprehensively cover all aspects. The diversity of authors and the wide-ranging coverage of the field ensure there is "something for everyone" and that even experts will benefit.

The aim and expected impact of this book is twofold. First, a comprehensive overview of all important topics is provided which will lead to improved utilization of the technology. A deeper understanding of L-PBF is paramount for all users, who will improve the success of the utilization of the technology. In this aspect, the book is also well suited to accompany student teaching and for coursework. On the other hand, it can be useful to managers or new industry users, to grasp the potential challenges for their applications, leading to a shorter learning curve when using L-PBF. Second, the text provides a shared terminology and language among all the diverse users from many fields and with varying levels of expertise in accordance to the ISO/ASTM 52900 standards. This shared language and conceptual basis for the technology is crucial for further successful discussion, research, and applications moving forward. The next 10 years of L-PBF are set to be exciting, and the authors truly hope this book contributes to the advancements and look forward to learning of the diversity of applications that emerge.

---

[1] Also called Selective Laser Melting (SLM), Direct Laser Metal Sintering (DMLS), Direct Laser Melting (DLM), etc. The terminology adopted by ISO/ASTM 52911-1:2019 is Powder Bed Fusion by Laser Beam or PBF-LB in technical documentation. We use here term "Laser Powder Bed Fusion (L-PBF)," which is widespread in scientific literature.

We hope you enjoy the book!

The editors: Igor Yadroitsev, Ina Yadroitsava, Anton du Plessis, Eric MacDonald

Historical background

1

Joseph J. Beaman
University of Texas, Austin, TX, United States

Chapter outline

1.1 Introduction 1
1.2 Conception of L-PBF 4
  1.2.1 Description of manufacturing problem to be solved 4
  1.2.2 Early L-PBF system 5
  1.2.3 Early L-PBF system with roller and heat 5
1.3 Early commercialization 6
  1.3.1 Second-generation laboratory equipment 6
  1.3.2 L-PBF startup company DTM 8
  1.3.3 First commercial system DTM 125 10
  1.3.4 First commercial system for sale 11
1.4 L-PBF metal parts 11
1.5 Conclusion 13
References 14

1.1 Introduction

First, the author of this chapter would like to acknowledge the important work of Carl Deckard, who was an initial developer of Laser Power Bed Fusion (L-PBF). Carl unexpectedly passed away in December 2019. He will be missed.

L-PBF is a one of a class of Additive Manufacturing (AM) methodologies that includes directed energy deposition, material extrusion, and vat polymerization among others. This is discussed in more detail in Chapter 2; also see ASTM (2009) and Beaman et al. (2020). In this chapter, a short description of layered processes and the unique features of L-PBF will be presented. This chapter will present early research systems and some of the early polymer and metal parts made on these systems. In addition, the early commercial development of L-PBF polymer systems is presented.

Additive Manufacturing was defined in an ASTM standard in 2009 (ASTM, 2009) as **Additive Manufacturing (AM),** *n*—a process of joining materials to make objects from 3D model data, usually layer upon layer, as opposed to subtractive manufacturing methodologies. Synonyms: additive fabrication, additive processes, additive techniques, additive layer manufacturing, layer manufacturing, and freeform fabrication.

Fundamentals of Laser Powder Bed Fusion of Metals. https://doi.org/10.1016/B978-0-12-824090-8.00002-0
Copyright © 2021 Elsevier Inc. All rights reserved.

Solid Freeform Fabrication was defined in Beaman et al. (1997) as **Solid Freeform Fabrication (SFF)**—Production of complex freeform solid objects from a computer model of an object without part-specific tooling or knowledge.

AM in this chapter will be taken as a combination of the ASTM Standard and the SFF definition. L-PBF is a layer-by-layer AM process that can produce complex objects from a computer geometric model without part-specific tooling. An early 1990 example of this concept was presented at the Solid Freeform Conference as shown in Fig. 1.1. This figure depicts the concept of a computer geometric object created on computer[1] being 3D-printed. The object was generated from a mathematical three-dimensional equation in x, y, and z. This computer-based geometric object was subsequently virtually sliced into $2\frac{1}{2}$ dimensional layers by the computer and fabricated on an L-PBF system with polymeric material. Although objects of this complexity are somewhat commonplace today, this was quite novel in early 1990.

Shown below in Fig. 1.2 is a schematic of the first commercial L-PBF machine that was sold to the public. This machine was manufactured by DTM Corp., which merged with 3D Systems Corp. in 2001. The term "Laser Powder Bed Fusion" was not used at this time. Rather the technology was named "Selective Laser Sintering" (SLS). In retrospect, L-PBF is a better term for the technology. This is primarily because sintering is usually too slow a fusion process for AM since fusion is desired in milliseconds and sintering relies on diffusion times, which can be hours. The laser beam in SLS or L-PBF actually melts the material whether it is polymer or metal. Another common name for the technology is Selective Laser Melting (SLM), which is a better description of the process. Unfortunately, SLM is commonly just used for metal L-PBF.

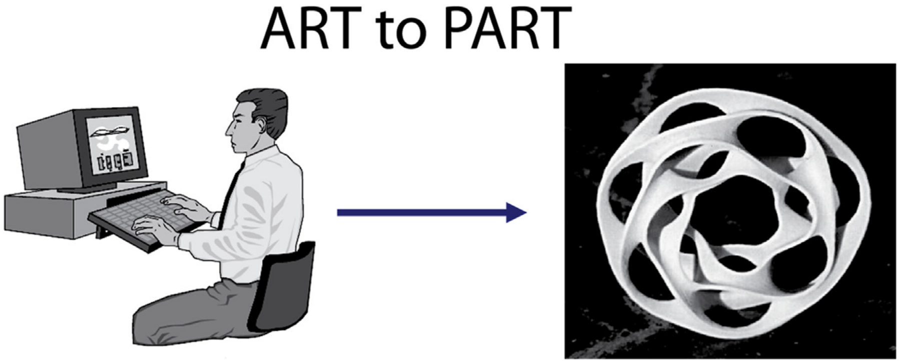

Figure 1.1 Early 1990 depiction of Additive Manufacturing (AM).
Computer reprinted by permission of Elsevier. Beaman, J., et al., 1997. Solid Freeform Fabrication: A New Direction in Manufacturing. Kluwer Academic Publishers, Norwell, MA.

---

[1] This is what computers looked like in early 1990.

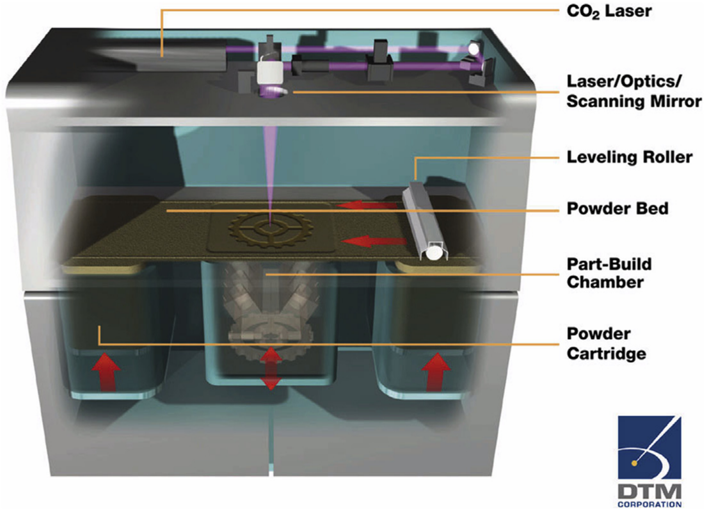

Figure 1.2 Schematic of first commercial L-PBF system sold to the public. Courtesy of DTM Corporation.

Fig. 1.2 depicts many of the features of L-PBF systems. Shown on the two sides of the system are two powder cartridges. The material, as indicated by the name of the process, uses powder as its material input form. A leveling roller (or a recoating and leveling blade in some L-PBF systems) rotates in a counter-rotating fashion to deliver powder alternately from one of the two powder cartridges. The powder in the cartridges is raised by a cartridge piston to enable sufficient powder to coat the part-build chamber surface. The powder surface of the part-build chamber is dropped in exact amount by a piston to ensure accurate dimensions of the part in the vertical direction. The leveling roller essentially “mills” the top of the powder to ensure this accuracy. Once the powder has been accurately delivered to the part-build chamber, a laser scans the top surface of the powder with a cross-section of the part to be made at this layer. The thickness of the layer can be adjusted by the piston drop, but often is 100 μm or less. When scanned with the laser, the powder melts and then solidifies into a solid. The laser melt pool is deeper than a powder layer and therefore the layers are bonded together by melting the top layer into previous layers. The critical control of this melting and remelting process is discussed in later chapters of this book. When the laser melt region of the part-build chamber surface solidifies, it ideally approaches a 100% density for desired part strength. Since the powder material is at a lower apparent density (approximately 50% of full density), there is a deviation in the part-build chamber surface with laser scanned regions deeper than unscanned regions. The powder delivery system described above inherently compensates for this deviation by automatically delivering more powder to the scanned regions than the unscanned regions. This process creates a level powder surface for the next laser scanning pattern.

L-PBF is a thermal process and thermal stresses are developed during fabrication of L-PBF parts. For polymers, these stresses are relieved by heating the top surface of the part-build chamber and also preheating the powder in the powder delivery cartridges. These heating elements are not shown in Fig. 1.2. For metal systems which do not typically have heating elements, the thermal stresses are controlled by fabricating support structures that are fabricated into a bottom platform and built into the part to restrain warpage of the part. These supports have to be removed, typically after annealing the part in a furnace and/or Hot Isostatic Pressing (HIP) of the part. Polymer parts typically do not have these support structures.

Of course, layered additive structures have been around for many years. Layered additive structures include the pyramids. The oldest pyramid known is the Step Pyramid of King Zoser at Saqqara. It was built around 2800 BCE. What is unique about AM is the ability to do this automatically without part-specific tooling. It is not too surprising that many new AM processes came about in the 1980s and early 1990s. At least, two technology advancements enabled this in the 1980s. One was the development of computer geometric modeling. This advancement allowed three-dimensional parts to be designed and viewed on a computer screen. More importantly for AM, it allowed these three-dimensional parts to be sliced into $2\frac{1}{2}$ dimensional layers for subsequent fabrication on an AM system. The other important technology was the personal computer, which allowed economic and local computation of these layer operations and other aspects of AM.

1.2 Conception of L-PBF

1.2.1 Description of manufacturing problem to be solved

L-PBF was initially developed and commercialized by Carl Deckard, who was Dr. Beaman's graduate student at the time, and Joe Beaman at the University of Texas at Austin. The basic problem they were trying to solve in 1986 was "why does it take so long to make a new part for the first time." In order to make a new part (a prototype) of any complexity at this time could often take months. The reason for this was partly technical and partly scheduling. Prototypes, at this time, were typically made in machine shops with machining, joining, casting, and other capabilities. It always takes some time to get scheduled into a machine shop with skilled machinists that can make accurate and reliable parts. Even after the part is scheduled, the part can take considerable time. Assuming the part is to be machined, it is not the machining time that takes so long; it is the time to obtain the fixtures to hold the part and the path planning required for tool clearance that are often the determining factors that delay part production.[2] These issues can take considerable part-specific knowledge. Deckard and Beaman wanted to greatly reduce or eliminate this time. This is the reason that they pursued powder systems that implicitly produce their own supporting fixtures and layered $2\frac{1}{2}$ dimensional methods that require a minimum of tool path planning.

---

[2] Other processes such as casting and welding have similar issues.

1.2.2 Early L-PBF system

The early stages of the first L-PBF system that would later be called Betsy by the research team at the University of Texas at Austin was a simple small box that was filled with polymer powder with a device similar to a salt shaker while a laser scanned a square pattern across the surface of the powder. There were no distinct layers and no real discernible parts with geometry. In a later version of Betsy, a blower powder delivery system that mimicked the salt shaker device was implemented and more importantly the scan patterns were improved. Fig. 1.3 shows the part and the system. The part was somewhat interesting as it was a block inside of a block, which would be difficult to make with traditional manufacturing methods, but the accuracy was poor. It was supposed to be a square block inside of a hollow square block. The reason for the inaccuracy was lack of vertical precision due to the powder blower approach.

1.2.3 Early L-PBF system with roller and heat

In 1988, Betsy was upgraded to include a counter-rotating leveling roller and a feed hopper that deposited powder for the roller to deliver this powder across the build surface. It also included a part heater via a heat lamp. These modifications greatly improved the quality of the parts as seen in Fig. 1.4. There was still no part-build piston, which means the part accuracy in the vertical direction was still not comparable to later systems.

The parts were still not spectacular, but they were good enough to capture the attention of the national press. An article entitled "Device Quickly Builds Models of a Computer's Designs" in the *NY Times* was published on March 16, 1988, that was based on the Betsy system (Lewis, 1988). The schematic in the *NY Times* of the Betsy L-PBF system was accurate. In the text of the article it stated, "[t]he immediate commercial application of the system, once it is refined, would be to significantly cut the time and cost of making prototypes of parts for a variety of industrial purposes, a process that can now take weeks or months." This statement was also accurate. The only

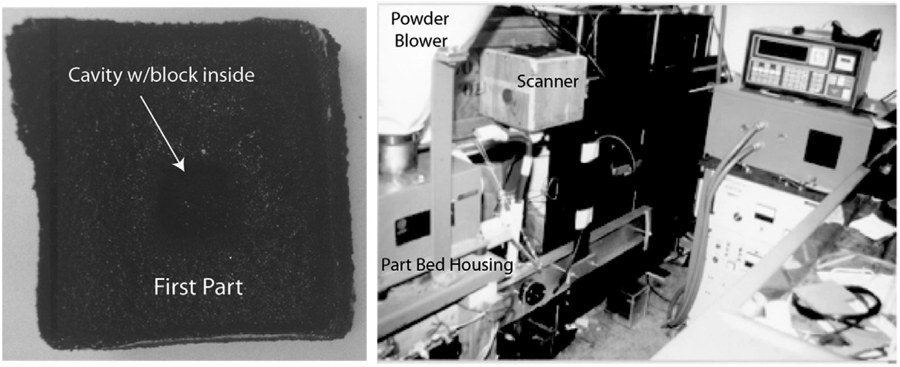

Figure 1.3 Earliest L-PBF part and system.

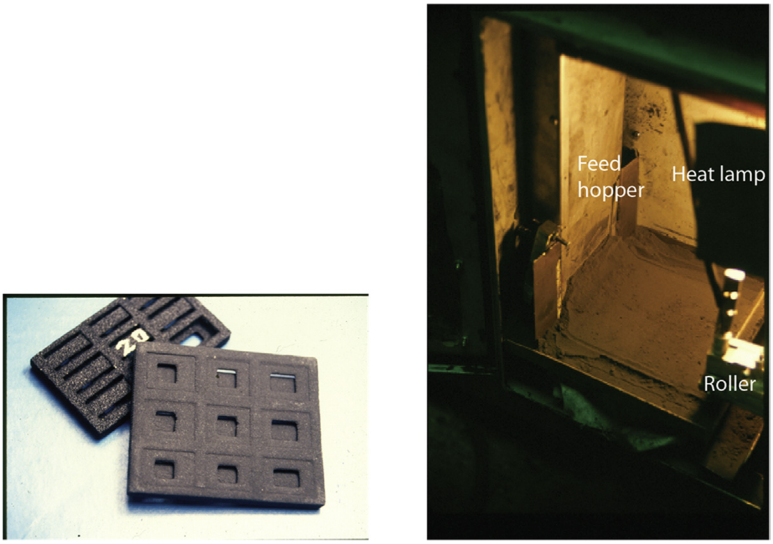

Figure 1.4 Betsy L-PBF system with roller and heat and parts that were produced.

problem with the article was the implied immediate time frame for having reliable full-strength prototypes. It was not until approximately 5 years later in 1993 that L-PBF systems were consistently producing high-quality prototypes.

1.3 Early commercialization

1.3.1 Second-generation laboratory equipment

Due in part to the attention received from the *NY Times* and other media outlets, the research team at the University of Texas at Austin was able to procure research funding to construct a second-generation research L-PBF machine that produced much better parts in 1989. This machine was called Bambi by the research team at the University of Texas at Austin. Bambi had many of the aspects of a present-day commercial L-PBF system. This system had only a single powder cartridge with a powder cartridge piston to accurately meter out the amount of powder for a powder leveling and delivery roller. The exterior of Bambi is shown in Fig. 1.5.

As seen in Fig. 1.6A, Bambi deposited an amount of powder in front of the roller from a slightly raised circular powder cartridge. This was done by an actuated powder delivery blade. A counter-rotating powder delivery and leveling roller delivered the powder to the surface of the part-build chamber that had a piston to control layer thickness. In addition to the powder delivery components, Bambi also had a ring heater for uniformly heating the powder surface of the part-build chamber. The large glow from the window shown in Fig. 1.5 was due to this heater. This window is shown better in

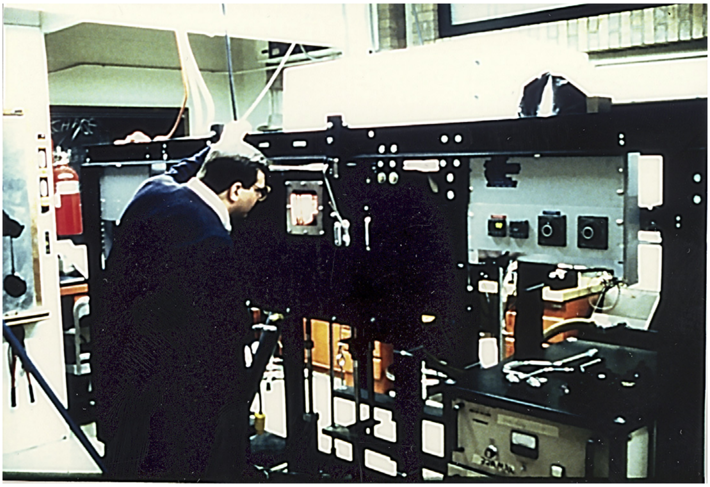

Figure 1.5 Bambi—second-generation L-PBF system.

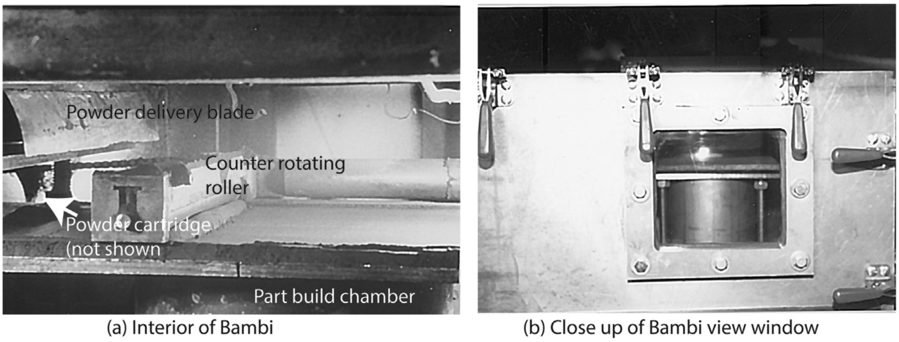

(a) Interior of Bambi
(b) Close up of Bambi view window

Figure 1.6 Details of Bambi.

Fig. 1.6B. The glow shown through this window in Fig. 1.6B was due to the laser interacting with the surface of the powder bed as the heater is off. This figure also shows latches for easily removing the door. Once the door was removed, the part chamber was also removeable in order to efficiently remove the powder from the parts in the chamber. This removable door in Fig. 1.6B postdated the picture in Fig. 1.5.

Although Bambi was a laboratory system, it often produced parts that approached commercial quality. Shown in Fig. 1.7 is a picture of polymer parts produced on Bambi in 1989. The metal part in the lower-right corner of the figure was fabricated by using a casting pattern made by Bambi. This photograph is from DTM's booth at Autofact in 1989. DTM was the startup company that spun out of the University of Texas at Austin to commercialize SLS (L-PBF). Autofact was a major annual trade show in Detroit that included manufacturing equipment and included AM hardware. DTM's commercial

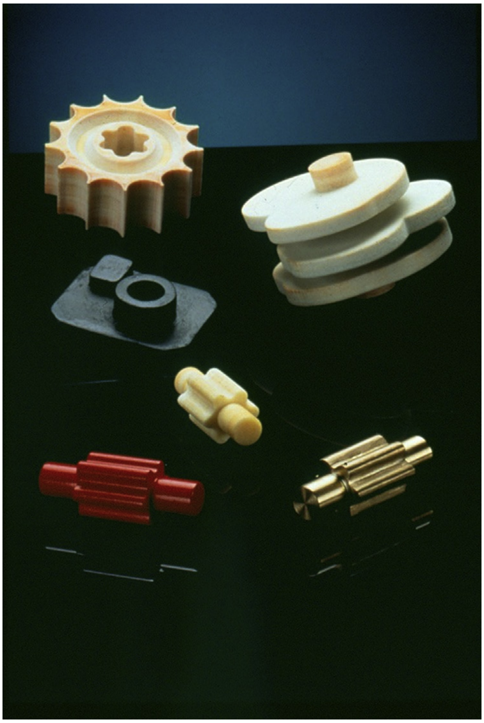

Figure 1.7 Bambi parts displayed at Autofact in 1989.

system was not finished in time to make parts for display at Autofact, so Bambi parts were utilized instead for display. The commercial system (a DTM 125) was delivered directly to Autofact and made its first parts on the floor of the convention center.

Besides polymer parts, Bambi also made direct metal parts. The first direct metal part on an L-PBF system was built in 1990 on Bambi. The material was an elemental blend of copper and solder (70 Pb-30 Sn). The part was made by Professor Dave Bourell of the University of Texas and his student Manriquez-Frayer (Manriquez-Frayre and Bourell, 1990) and is shown below in Fig. 1.8a. A later more detailed copper Bambi part is shown in Fig. 1.8b. Bambi was also capable of building intricate geometric parts as shown in Fig. 1.8c (Barlow and Vail, 1994) (Barlow et al., 1997). Bambi stayed in use for many years at the University of Texas as a valuable research and production machine.

1.3.2 L-PBF startup company DTM

In 1986, nascent attempts at forming a company to commercialize L-PBF began. The first company was called Nova Automation, which was named after Nova Graphics. Nova Graphics was owned by Harold Blair, an Austin business owner. Nova Automation was an unfunded startup company. The principals in this company were Harold

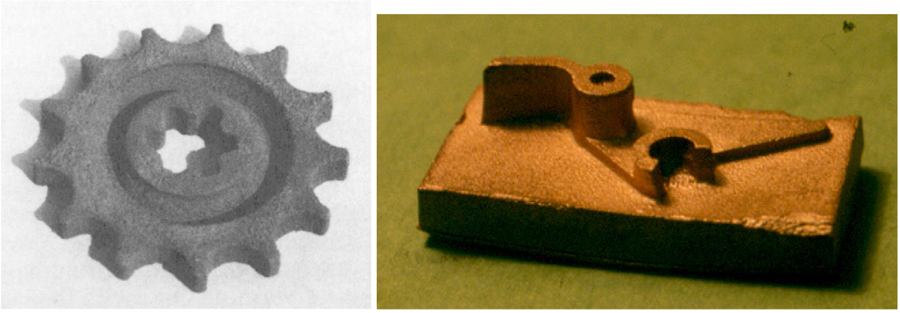

(a) First L-PBF metal part (b) Later Copper part built on Bambi

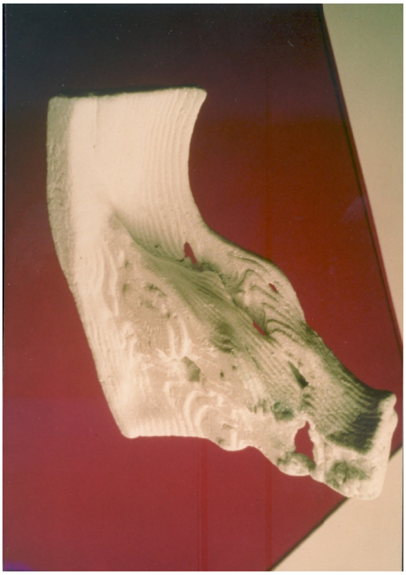

(c) Intricate artificial bone part made on Bambi with polymer binders

Figure 1.8 Parts built on Bambi. (a) First L-PBF metal part, (b) Later copper part built on Bambi, (c) Intricate artificial bone part made on Bambi with polymer binders.

Blair, Paul McClure, who worked as an assistant to the Dean of Engineering at the University of Texas, Carl Deckard, and eventually Joseph Beaman. At the time of the formation of Nova Automation, it was not legal for University of Texas faculty to be major equity holders in a private startup company. In order to become an equity holder, Dr. Beaman had to receive permission from the University of Texas System Board of Regents. This happened with the support of Dr. Hans Mark, who was Chancellor of the University of Texas System and also a faculty of the College of Engineering of the University of Texas at Austin.

Nova Automation signed a license agreement with the University of Texas, which required Nova Automation to raise $300,000 by the end of 1988. By the end of 1988, Nova Automation had formed a tentative funding arrangement for the required

$300,000 with chemicals and aerospace giant, Goodrich Corporation. After obtaining a 3-month extension of the licensing agreement with the University of Texas, Goodrich provided funding to Nova Automation in early 1989. Around this same time, Paul McClure became president of the company, Dr. Beaman became the CTO, and the company changed its name to DTM Corporation, a reference to desktop manufacturing, which came from desktop printing. Desktop printing was a term used to describe processes at the time that allowed customers to create their own printed literature with a computer, software, and a color printer. Goodrich eventually ended up owning controlling interest in DTM and invested millions of dollars in the technology. DTM grew to approximately 100 employees and reached $25 million in annual sales. DTM was acquired by 3D Systems Corporation in 2001.

1.3.3 First commercial system DTM 125

The first commercial system from DTM was called a 125. There were only four of these machines built and they were never sold. Internally, they closely mirrored Bambi. They had two cylinders, a feed cylinder and a part cylinder. It did not have a powder delivery blade. Rather a counter-rotating roller reached across the entire width of the DTM 125 chamber to gather powder from the feed cylinder after the powder was raised by a feed piston. The powder was then accurately deposited on the surface of the part bed after a part-bed piston was dropped by one-layer depth. One innovation was the use of an infrared temperature sensor to measure one spot on the part cylinder and use this to control the temperature of the part-bed surface. Shown in Fig. 1.9 are two of the DTM 125's. Although the DTM 125's were never sold, the parts fabricated on the DTM 125's were sold. In fact, they were used in a DTM service bureau business to sell parts to customers. This parts-on-demand service

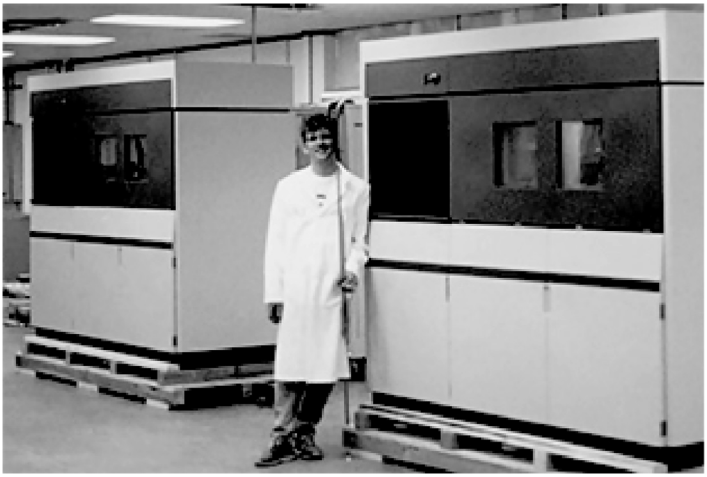

Figure 1.9 DTM 125 systems.

bureau was quite profitable. The parts made from these systems were accurate and strong. They were made from nylon and other materials. They had the strength and accuracy to test the form, fit, and function of commercial parts. These systems helped usher in what is known as the Rapid Prototyping industry.

1.3.4 First commercial system for sale

The first commercial system for sale was called a SinterStation 2000 and was described above and a schematic was shown in Fig. 1.2. Fig. 1.10 shows the actual SinterStation 2000. The SinterStation 2000 was first made in 1992, with the first sale to Sandia National Laboratory. This was the first modern L-PBF system with a 13 inches cylindrical build area. Three models of the SinterStation followed the SinterStation 2000:

- SinterStation 2500: Featuring a square 13 × 13″ fabrication area (rather than the previous cylindrical fabrication area).
- SinterStation 2500+: A cost-reduced machine with fewer options and a square 13 × 13″ fabrication area.
- SinterStation Pro (released by 3D Systems): Featuring a square 24 × 24″ fabrication area.

1.4 L-PBF metal parts

In 1991, Dr. Suman Das, who was a PhD student of Dr. Joseph Beaman at the time, started design of and eventually built a high-temperature powder bed fusion system capable of using high performance metals such as titanium and nickel-based super alloys. The chamber could be heated to as high as 1000°C, and a 1.1 kW CO_2 laser was used (Das et al., 1991). Through the 1990s, this system was used to process a number of metal feedstocks. As part of Suman Das' research on combining L-PBF with a subsequent Hot Isostatic Press (HIP) (Das et al., 1998) in 1998, he was able to produce a Military Specification Ti6Al4V fully dense miniature missile part with excellent microstructure without the subsequent HIP step (Das et al., 1999). This meant that Das had made a fully dense L-PBF part directly from the high-temperature powder bed fusion system. Shown below in Fig. 1.11 is the high-temperature powder bed

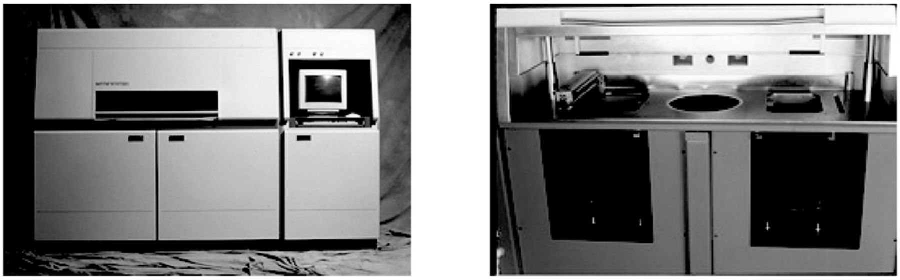
(a) Exterior of SinterStation 2000
(b) Interior of SinterStation 2000

Figure 1.10 DTM SinterStation 2000

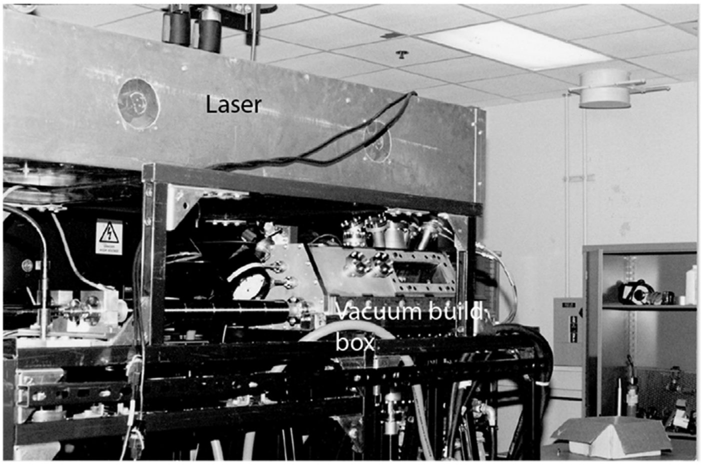

(a) High temperature L-PBF system

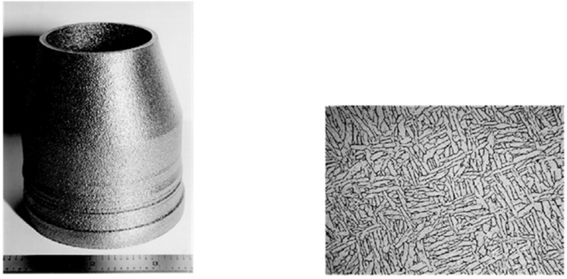

(b) Fully dense Ti-6Al-4V part (Courtesy Elsevier)

(c) Microstructure (Courtesy Elsevier)

Figure 1.11 High temperature L-PBF system and parts.

fusion system Fig. 1.11(A), which includes a vacuum capable build box, the fully dense miniature missile part that it built Fig. 1.11(B), and a microstructure of the part Fig. 1.11(C).

In 1996, Olli Nyrhilä at Electrolux, collaborating with EOS GmbH, developed a direct metal process called direct metal laser sintering (Nyrhila, 1996; Nyrhila et al., 1998). The material was a bronze-nickel elemental powder mixture in an L-PBF apparatus. A unique feature of the alloy was that it sintered without shrinking and thus normal part warpage was reduced. The mechanism was a counterbalance of normal densification with pore removal and Kirkendall porosity which formed as the bronze and nickel particles mixed via diffusion (Agarwala et al., 1993). This Kirkendall porosity limited the strength of the parts made from this material.

Electron-beam powder bed fusion of metals was invented by Ralf Larson in 1994 (Larson, 1998). In collaboration with Chalmers University of Technology in Gothenburg, the process was commercialized with the founding of Arcam in 1997.

1.5 Conclusion

This chapter provides a brief history of L-PBF from its inception in a university laboratory to its earliest commercial systems. This activity occurred in roughly a decade from the mid-1980s to the mid-1990s. During this time frame, L-PBF went from a curiosity in a laboratory to a successful and valuable method for making functional prototypes. This was given the name Rapid Prototyping. These prototypes had both the accuracy and strength to test form, fit, and function of industrial grade applications. In the decades that followed this early period, L-PBF has grown into a technology that can now be used for end-use parts. This is sometimes called Rapid Manufacturing. Special historical note is given to Harvest Technologies founded by David Leigh, which was the commercial AM service bureau that partnered with Boeing to manufacture some of the earliest L-PBF end-use parts. These polymer parts were flight certified and are used today. Very recently, note is also made of Greg Morris, Dave Abbott, and Todd Rockstroh of GE aviation, who helped successfully qualify a geometrical complex fuel-saving metal jet engine nozzle for L-PBF production. In closing, shown below in Fig. 1.12 is a listing of early inventors and companies that developed

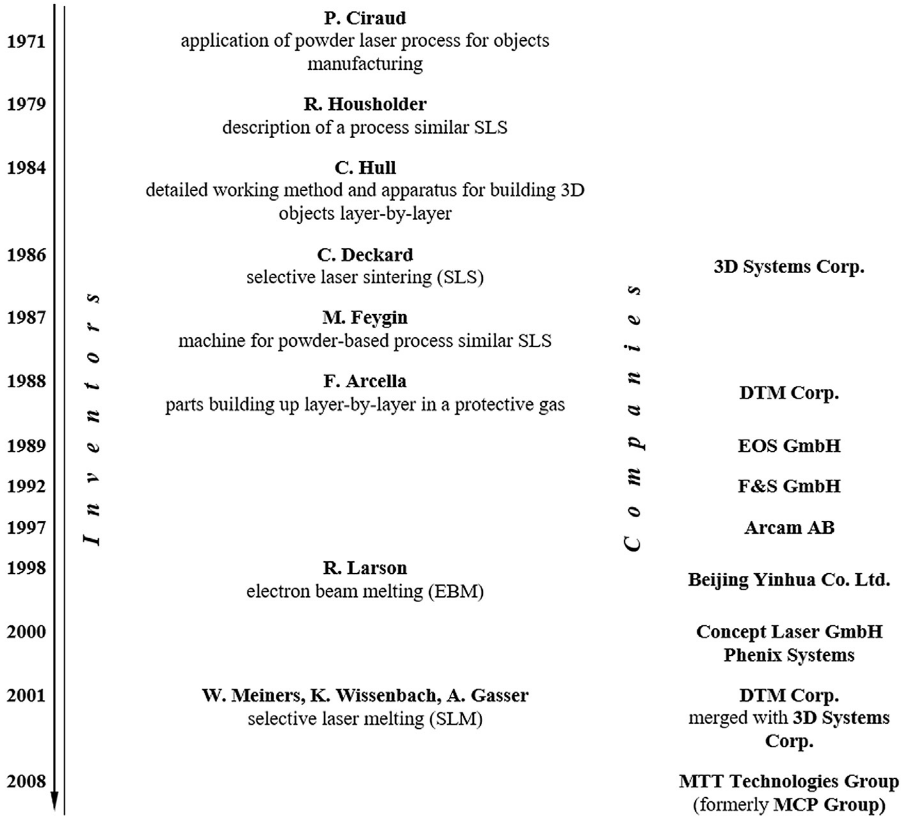
1971
P. Ciraud
application of powder laser process for objects manufacturing
1979
R. Housholder
description of a process similar SLS
1984
C. Hull
detailed working method and apparatus for building 3D objects layer-by-layer
1986
C. Deckard
selective laser sintering (SLS)
3D Systems Corp.
1987
M. Feygin
machine for powder-based process similar SLS
1988
F. Arcella
parts building up layer-by-layer in a protective gas
DTM Corp.
1989
EOS GmbH
1992
F&S GmbH
1997
Arcam AB
1998
R. Larson
electron beam melting (EBM)
Beijing Yinhua Co. Ltd.
2000
Concept Laser GmbH
Phenix Systems
2001
W. Meiners, K. Wissenbach, A. Gasser
selective laser melting (SLM)
DTM Corp.
merged with 3D Systems Corp.
2008
MTT Technologies Group
(formerly MCP Group)
Inventors
Companies

Figure 1.12 Schematic of selected patent history and founding years of selected additive manufacturing and direct metal sintering companies.

L-PBF and related AM processes. Also, if the readers of this chapter would like to know more about the history of AM processes beyond L-PBF they can refer to the following recent articles by Bourell and Wohlers (2020) and Beaman et al. (2020).

References

Agarwala, M., Bourell, D., Wu, B., Beaman, J., 1993. An evaluation of the mechanical behavior of bronze nickel composites produced by selective laser sintering. In: The University at Austin, Solid Freeform Fabrication Conference.

ASTM, 2009. Standard F2792-09, Standard Terminology for Additive Manufacturing Technologies, Superseded, 2009. ASTM, US.

Barlow, J., et al., 1997. Method for Fabricating Artificial Bone Implant Green Parts. United States of America, Patent No. 5,639,402.

Barlow, J., Vail, N., 1994. Method of Producing High-Temperature Parts by Way of Low-Temperature Sintering. United States, Patent No. 5,284,695.

Beaman, J., et al., 1997. Solid Freeform Fabrication: A New Direction in Manufacturing. Kluwer Academic Publishers, Norwell, MA.

Beaman, J., Bourell, D., Seepersad, C., Kovar, D., 2020. Additive manufacturing review − early past to current practice. J. Manf. Sci. 142 (11).

Bourell, D., Wohlers, T., 2020. Introduction to additive manufacturing. In: Additive Manufacturing, vol. 24. ASM, Materials Park, OH.

Das, S., Beaman, J., Wohlert, M., Bourell, D., 1998. Direct laser freeform fabrication of high performance metal components. Rapid Prototyp. J. 4 (3), 112−117.

Das, S., McWIlliams, J., Wu, B., Beaman, J., 1991. Design of a high temperature workstation for the selective laser sintering process. In: University of Texas at Austin, Solid Freeform Fabrication Conference.

Das, S., Wohlert, M., Beaman, J., Bourell, D., 1999. Processing of titanium net shapes by SLS/HIP. Mater. Des. 20, 115−121.

Larson, R., 1998. Method and Device for Producing Three-Dimensional Bodies. US, Patent No. 5,786,562.

Lewis, P., March 16, 1988. Device quickly builds models of a computer's designs. N. Y. Times.

Manriquez-Frayre, J., Bourell, D., 1990. Selective laser sintering of binary metallic powder. In: The University of Texas at Austin, Solid Freeform Fabrication Conference.

Nyrhila, O., 1996. Direct laser sintering of injection moulds. In: University of Nottingham, 5th European Conference on Rapid Prototyping and Manufacturing.

Nyrhila, O., Kotila, J., Lind, J., Syvänen, T., 1998. Industrial use of direct metal laser sintering. In: University of Texas at Austin, Solid Freeform Fabrication Conference.

Basics of laser powder bed fusion

2

Igor Yadroitsev[1], *Ina Yadroitsava*[1], *Anton Du Plessis*[2,3]
[1]Department of Mechanical and Mechatronic Engineering, Central University of Technology, Bloemfontein, Free State, South Africa; [2]Research Group 3D Innovation, Stellenbosch University, Stellenbosch, Western Cape, South Africa; [3]Department of Mechanical Engineering, Nelson Mandela University, Port Elizabeth, Eastern Cape, South Africa

Chapter outline

2.1 Introduction 15
2.2 The L-PBF process 18
2.3 L-PBF hardware 21
  2.3.1 L-PBF systems 21
  2.3.2 Lasers 23
  2.3.3 Scanning systems 25
  2.3.4 Powder delivery system 26
  2.3.5 Powder deposition system 26
  2.3.6 Build platform and base plate 28
  2.3.7 Powder removal, gas supply, and filtration systems 29
2.4 Powder material 30
2.5 L-PBF software 30
2.6 Post-processing 33
2.7 Safety aspects 35
2.8 Conclusion 35
2.9 Questions 35
Acknowledgments 36
References 36

2.1 Introduction

The new industrial paradigm of Additive Manufacturing (AM) comprises of a class of technologies that allows the creation of three-dimensional (3D) objects by sequentially adding material, usually layer by layer, as opposed to subtractive and formative manufacturing methodologies (casting, forging, rolling, stamping). AM technologies are unique in many ways and radically change the entire supply chain of production and consumption from product design to the implementation of the finished product (Beaman et al., 2020). The complexity and variety of shapes of parts, reducing the

Fundamentals of Laser Powder Bed Fusion of Metals. https://doi.org/10.1016/B978-0-12-824090-8.00024-X
Copyright © 2021 Elsevier Inc. All rights reserved.

time from prototype development to the final component, the ability to use different materials in one production cycle, the prompt production of "product on demand," and customization are the principle advantages of additive manufacturing. The ISO/ ASTM 52900:2015 standard categorizes all AM processes into seven broad subclasses (Fig. 2.1):

- Powder bed fusion, PBF: "an AM process in which thermal energy selectively fuses regions of a powder bed." This category contains the laser-based powder bed fusion process (L-PBF), and according to the ISO/ASTM standard, the process should be described as using a laser beam (LB) with the acronym PBF-LB in technical documentation. However, the terminology L-PBF is widely in use and is acceptable. This category also contains electron beam powder bed fusion (PBF-EB).
- Directed energy deposition (DED): an AM process "in which focused thermal energy is used to fuse materials by melting as they are being deposited. Focused thermal energy means that an energy source (e.g., laser, electron beam, or plasma arc) is focused to melt the materials being deposited." This process uses powder (entrained in a gas flow) or wire as a deposited material and allows to create large-sized industrial engineering parts with high speed but has limitations in resolution.
- Binder jetting: "an AM process in which a liquid bonding agent is selectively deposited to join powder materials." Various materials can be manufactured by binder jetting (metals, ceramics, sand, etc.). This technology allows manufacturing directly, with high complexity and high-resolution capabilities. Binder jetted parts are "green parts" and require a secondary process after printing (sintering and/or infiltration). Limitations of binder jetting metal parts are

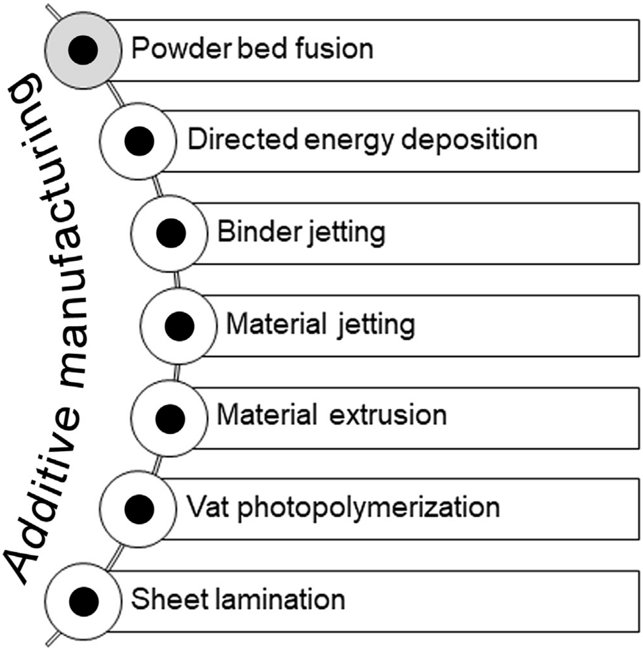

Figure 2.1 Additive manufacturing process categories according ISO/ASTM 52900:2015.

porosity, impurities from solvent material, mechanical properties, and limited size, but this technology shows great progress in overcoming these limitations, developing new materials, and improving systems and processes (Jurisch et al., 2015; Ziaee and Crane, 2019).

- Material jetting: "an AM process in which droplets of build material are selectively deposited, materials include photopolymers, resins and waxes." Material jetting allows achievement of good resolution. Multiple materials and color options can be combined by material jetting, typically used to create anatomical models for surgical planning and high-end colorized prototypes. The recent introduction of metal and ceramic materials in material jetting process is highly promising.
- Material extrusion: "an AM process in which material is selectively dispensed through a nozzle or orifice." Material extrusion is the lowest-cost additive manufacturing technology and is widely known as 3D printing when referring to entry-level desktop polymer extrusion printers—also known by the terms Fused Deposition Modeling (FDM) and Fused Filament Fabrication (FFF). Some recent developments with fiber reinforcement are promising to extend the capabilities toward structural applications. Bioprinting by microextrusion falls in this category and refers to extrusion and manufacturing of artificial biological soft tissue materials, bones, and organs. Another extrusion-based additive manufacturing technology that has grown in recent years is concrete printing —from small lab scale "brick" size parts up to full houses or even larger-scale structures. Recently Markforged Inc. (2020) developed the Metal X 3D printer allowing to print metal parts by a material extrusion method.
- Vat photopolymerization: "an AM process in which liquid photopolymer in a vat is selectively cured by light-activated polymerization." The method allows high resolution and good surface finish but is limited to photo-sensitive polymers and resins. Nevertheless, high-quality parts can be produced in these materials with high complexity.
- Sheet lamination: "an AM process in which sheets of material are bonded to form an object." This technique is less widely available but holds some promise for structural applications due to the ability to change materials or fiber composite orientations per layer. As a relatively fast technique, growth is expected in this category for industrial applications.

It is also necessary to mention hybrid systems equipped with both additive and subtractive manufacturing capabilities within the same machine, which can significantly complement each other and open up a range of possibilities for improved versatile manufacturing. Hybrid systems take advantage of the most valuable capabilities of both technologies: complexity and variety of additive manufacturing and high precision of subtractive manufacturing methodologies. In metal AM, the following combinations are used in such hybrid solutions: direct energy deposition (DED) combined with computer numerical control (CNC) high-speed milling, laser powder bed fusion can also be coupled with CNC machining, resulting in a hybrid powder bed process (Esmaeilian et al., 2016; Le et al., 2017; Yi et al., 2019). This allows parts to be produced without subsequent finishing and to achieve better surface quality and tighter tolerances.

The laser powder bed fusion technology, as we know it today, has evolved over more than 30 years—and is still continuously improving and advancing. As with all 3D printing process categories, the original use was relegated to prototyping and model manufacturing only. In the last decade, its use has strongly moved toward functional and structural final products, and even serial production is being realized in various industry sectors (Seibold, 2019), see Chapter 21 "Industrial applications."

Currently, intensive research is being implemented in various areas (Chapter 23): design for additive manufacturing, details and intricacies of the L-PBF process, numerical simulation and process optimization, development of new materials, investigation of the properties of the manufactured materials and components, post-processing, new equipment, applications, environmental and economic justification of this technology (Chapter 22) as well as development of training courses for specialists in these areas.

2.2 The L-PBF process

The high degree of freedom offered by L-PBF technology allows the creation of objects with unique geometries and complex internal structures and associated with this the ability to implement topological optimization (see Chapters 5, 16, and 17). L-PBF can combine many components into one functional part (part consolidation), can create complex and tailored gradient structures both in terms of volumetric structural design and also spatially varying material composition (see Chapters 19 and 21). These advantages are highly beneficial and motivate the strong growth in this technology and promote the wide adoption in various industries in recent years (Tofail et al., 2018).

It should be noted that both the scientific and popular literature use different names for the L-PBF process. The most well-known terms used are: selective laser melting (SLM), direct metal laser sintering (DMLS), LaserCusing, direct metal laser melting (DMLM), and laser metal fusion (LMF). However, one must clearly understand that these are only different commercial names for the same process.

On the one hand, L-PBF is an elegant and simple concept—adding material layer by layer according to a 3D design. However, on the other hand, it is quite complicated to implement due to many practical issues. The L-PBF technology involves many different fields of science: condensed matter physics, thermodynamics, materials science, quantum physics, fluid mechanics, computational physics, electrical engineering, programming, design, mechanical engineering, industrial engineering, etc. The L-PBF process can be interpreted as the result of the superposition and interaction of many subprocesses, including the absorption and reflection of laser radiation by a dispersed medium, heat and mass transfer, phase transformations, a moving interface between phases, gas and fluid dynamics, chemical reactions, solidification and evaporation, shrinkage, deformation, etc. (Yadroitsev, 2009; DebRoy et al., 2018; Meier et al., 2018; Rubenchik et al., 2018), Chapter 4. Fig. 2.2 presents a schematic of an L-PBF machine, the laser-material interaction process in L-PBF, and a flowchart showing the workflow for producing an L-PBF part from CAD.

Rehme and Emmelmann (2005) indicated that more than 130 input parameters generally may affect the L-PBF process. Predefined parameters are the properties of the material used: density, melting point, thermal conductivity, particle size distribution, absorption coefficient of laser radiation, etc.; build environment parameters (for example, shield gas properties); and laser beam properties (mode, wavelength, etc.). Variable or controlled system parameters are laser power, focal spot diameter, scanning speed, powder layer thickness, oxygen level in the surrounding atmosphere,

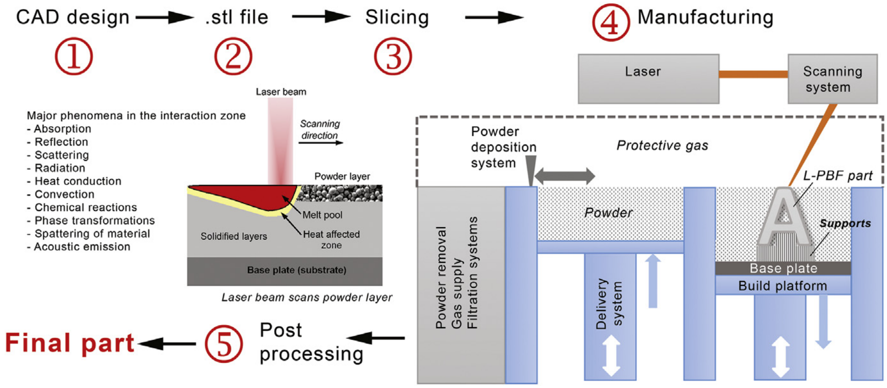
CAD design
①
.stl file
②
Slicing
③
④ Manufacturing
Laser
Scanning system
Laser beam
Major phenomena in the interaction zone
- Absorption
- Reflection
- Scattering
- Radiation
- Heat conduction
- Convection
- Chemical reactions
- Phase transformations
- Spattering of material
- Acoustic emission
Scanning direction
Powder layer
Melt pool
Heat affected zone
Solidified layers
Base plate (substrate)
Laser beam scans powder layer
Powder deposition system
Protective gas
L-PBF part
Powder
Supports
Powder removal
Gas supply
Filtration systems
Delivery system
Base plate
Build platform
Final part
⑤
Post processing

Figure 2.2 A workflow of part creation from CAD design, schematic of L-PBF machine and process of laser-material interaction in L-PBF.

protective gas flow rate, etc. (O'Regan et al., 2016). The parameters that have the greatest impact on the L-PBF component and its quality can be divided into four large groups: "Machine-based," "Material-based," "Process-parameters," and "Post-treatment parameters" (Fig. 2.3). Their mutual interaction is not always clear but is highly important, and although much progress has already been made, there is still no comprehensive "unified" theory of the L-PBF process. Understanding the effect of changing some parameters on the process as a whole is not yet available. This is because, firstly, the L-PBF process is nonlinear, i.e., a change in one parameter does not necessarily mean a linear increase in an output value and, secondly, often a change in one of the parameters leads to a change in several other parameters, which can lead to unpredictable results (Klocke et al., 2003; Rehme and Emmelmann, 2005; O'Regan et al., 2016; Schmidt et al., 2017; Moges et al., 2019; Vock et al., 2019). Nevertheless, despite this complexity, some general guidelines are being developed: the most important parameters controlling the process have been identified, for some materials and systems the optimal process parameters and good practice procedures are known to ensure high quality.

The manufacturing process starts with the formation of a single track. As a result of the interaction of the laser beam with a predeposited layer of metal powder on the base plate (substrate), a single track is formed by melting and solidification (Fig. 2.2). The single track is the fundamental structural unit of 3D L-PBF objects: numerous single tracks together form a single layer, and the layers form a three-dimensional object. Choosing patterns for the laser beam scanning path, scanning directions, scanning sequence, etc. (described in more detail in Chapter 3), is crucial for the quality and performance of L-PBF components. To manufacture complex objects, various scanning strategies and process parameters can be used for different areas of the part and for supports. The L-PBF part during manufacturing has to be fixed on the substrate directly and/or by support structures. Supports serve for fixation of the part to the base plate, to prevent deformation, and for heat dissipation. The design of the component, its orientation on the base plate, the type and placement of supports, the scanning strategy,

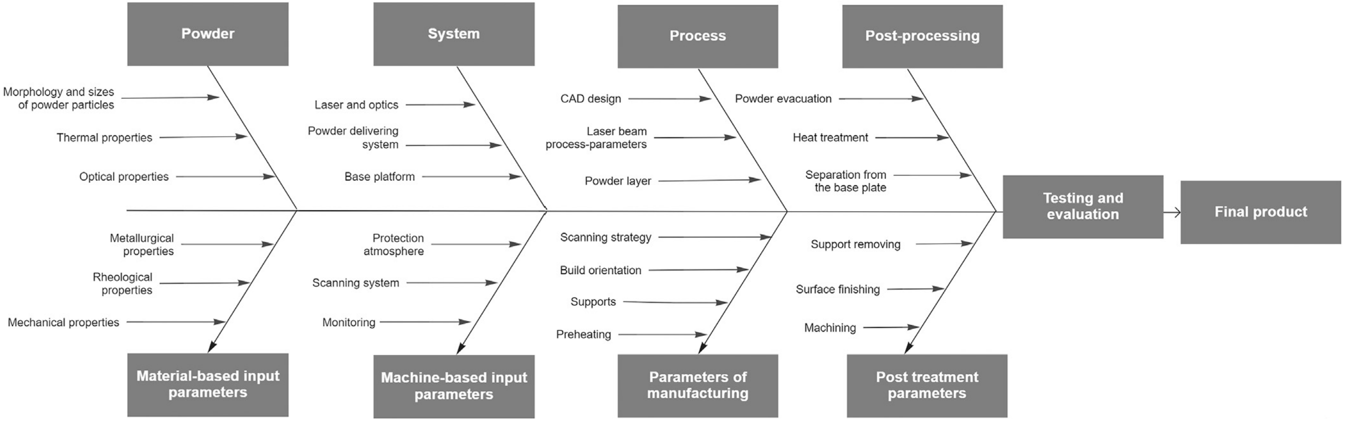
Powder
System
Process
Post-processing
Morphology and sizes of powder particles
Thermal properties
Optical properties
Laser and optics
Powder delivering system
Base platform
CAD design
Laser beam process-parameters
Powder layer
Powder evacuation
Heat treatment
Separation from the base plate
Testing and evaluation
Final product
Metallurgical properties
Rheological properties
Mechanical properties
Protection atmosphere
Scanning system
Monitoring
Scanning strategy
Build orientation
Supports
Preheating
Support removing
Surface finishing
Machining
Material-based input parameters
Machine-based input parameters
Parameters of manufacturing
Post treatment parameters

Figure 2.3 Main parameters influencing the quality of L-PBF components.

etc., all need to be taken into account to ensure the high density, surface quality, and accuracy of the part.

All of these operations and interactions with the L-PBF system, the correct handling with powder, choice of parameters, and building strategies require certain skills and knowledge of the L-PBF machine user, technician, or engineer. This requires constant training and practical experience, as well as coordinated work with designers and end-users.

2.3 L-PBF hardware

2.3.1 L-PBF systems

Laser powder bed fusion is being implemented in the automotive, aerospace, medical, and other high-tech industries (Chapter 21). Global manufacturing industries are increasingly aware of the benefits of manufacturing metal parts through additive manufacturing; therefore, sales of such systems are growing every year. The main and largest manufacturers of L-PBF systems are: EOS GmbH (Germany); Concept Laser (GE Additive, Germany); SLM Solutions Group AG (Germany); 3D Systems, Inc. (USA); Renishaw plc. (Great Britain); TRUMPF GmbH + Co. KG (Germany), and recently VELO3D (USA), among a growing number of others. In the period 2013−15, the key patents for L-PBF expired, so every year more companies offer their solutions in this area of technology (Fig. 2.4). The most comprehensive information about all companies producing L-PBF equipment, the prices for this equipment, the materials used, applications, new trends and research directions globally can be found in the Wohlers Report (Wohlers Associates), the industry's leading additive manufacturing review. This annual report highlights the development and future of

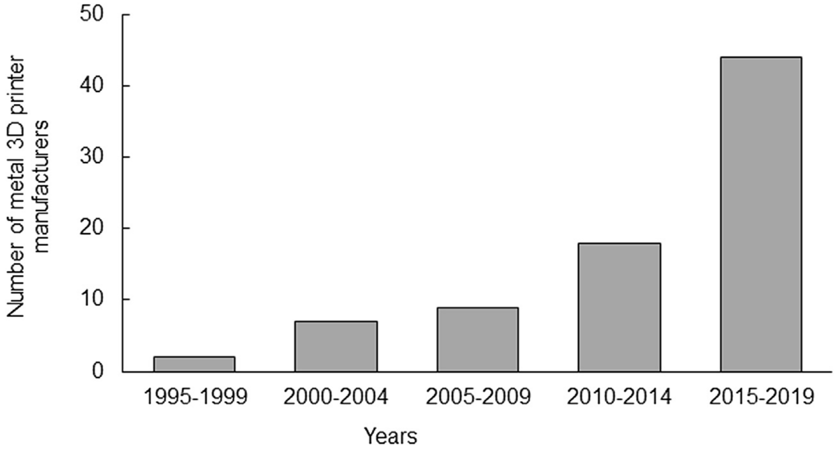

Figure 2.4 Number of manufacturers offering metal 3D printing systems (The Additive Manufacturing Landscape, 2019).

AM, new AM materials and systems, applications, services, design, software, as well as patents, standards, investments, and much more.

Active research in the field of L-PBF has been conducted since the early 2000s, when equipment of this type began to be massively supplied to universities and industrial enterprises (Chapter 1). Advances in high-power fiber lasers have contributed to the transition from partial melting to the complete melting of the powder. The advantage of this approach is that the L-PBF system produces a practically finished functional part that requires only "insignificant" post-processing. L-PBF brought the opportunity to work with a wide range of metal powder materials and significantly improved the mechanical properties of the final parts.

Over the past 20 years of development, metal AM technology has advanced significantly with great year on year increases in commercial systems manufacturers (Fig. 2.4). Modern L-PBF systems include one to four laser sources; the maximum size of the manufactured part can reach 800 × 400 × 500 mm^3 (Table 2.1). The increase in the number of laser sources and the working volume can significantly increase the productivity of the process and produce large-size critical parts with high resolution and with the highest quality, suitable for the aerospace and automotive industries.

L-PBF systems are complex and require in-depth knowledge of both the design and parameters of the machine, as well as the physical principles underlying the L-PBF

Table 2.1 Commercially available L-PBF systems having the largest number of laser sources and the largest working volumes.

Manufacturers	L-PBF system	Laser source: fiber laser	Working volume (X, Y, Z)
EOS GmbH (Germany)	EOS M 300-4	4 × 400 W	300 × 300 × 400 mm^3
	EOS M 400-4	4 × 400 W	400 × 400 × 400 mm^3
Concept Laser (GE Additive, Germany)	M Line factory	4 × 400 W or 4 × 1000 W	500 × 500 × 400 mm^3
	X Line 2000R	2 × 1000 W	800 × 400 × 500 mm^3
SLM Solutions Group AG (Germany)	SLM® 500	4 × 400 W or 4 × 700 W	500 × 280 × 365 mm^3
	SLM® 800	4 × 400 W or 4 × 700 W	500 × 280 × 850 mm^3
3D Systems, Inc. (USA)	DMP factory 500 Solution	3 × 500 W	500 × 500 × 500 mm^3
Renishaw plc. (Great Britain);	RenAM 500Q	4 × 500 W	250 × 250 × 350 mm^3
TRUMPF GmbH + Co. KG (Germany)	TruPrint 5000	3 × 500 W	∅300 mm × 400 mm
VELO3D (USA)	Sapphire XC	8 × 1000 W	∅600 mm × 550 mm

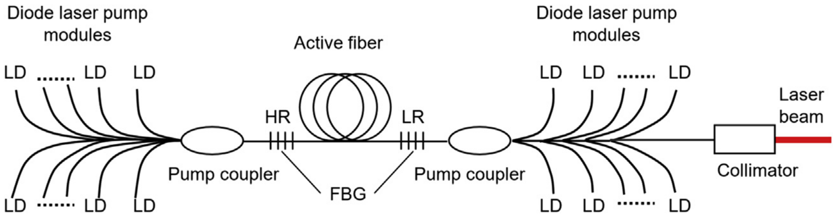

Figure 2.5 Schematic of a typical single-mode fiber laser utilizing single-emitter diodes. LD—a laser diode, HR-FBG is a high reflective fiber Bragg grating, LR-FBG is a low reflective fiber Bragg grating.

process, to be further improved. The basic scheme of an L-PBF system is shown in Fig. 2.2. The main structural components of the L-PBF system are: laser, scanning system, powder delivery system, powder deposition system, build platform, powder removal, gas supply, and filtration systems, which are each described separately in the sections that follow.

2.3.2 Lasers

In most cases, modern L-PBF systems use a continuous wave (CW) Yb-fiber laser (Ytterbium-doped fiber laser) with wavelength 1070 ± 10 nm as a source of thermal energy that selectively melts regions of a powder bed. The operation principle of the fiber laser is similar to an amplification unit used in fiber-optic systems. In the fiber laser, a doped silica fiber is excited by a diode source (Fig. 2.5). Two Bragg gratings (high reflective—HR and low reflective—LR) which are written into the Fiber Bragg Grating (FBR) act as the mirrors of a linear laser cavity to generate the laser emission. The diode pump energy is delivered to the active medium through multimode fibers spliced to the multiclad coil. The laser cavity is therefore created directly in the active fiber. The laser emission leaves the fiber laser through a passive single-mode fiber, typically with a core diameter of only a few micrometers (5—12 μm, as indicated in Shiner (2015)), and can propagate only in a single spatial mode, the profile of which in most cases has an approximately Gaussian shape (also called the TEM_{00} mode). Changing the launch conditions of the input diode pump energy only affects the power launched into the guided mode, whereas the spatial distribution of the light exiting the fiber is fixed. Fiber laser output power is controlled by changing the applied current (typically 0—10 A) and usually has a linear dependence. By using a collimator, the beam can be transformed into a high-quality collimated beam. This results in an efficient, compact laser source with high beam quality. The design also has the advantages of high reliability and long life. The use of a distributed single-emitter pump architecture makes the expected lifetime of such lasers more than 100,000 working hours (IPG Photonics Corp.). One of the main advantages of fiber lasers is the ability to produce a single-mode TEM_{00} beam at high power. A quality factor or beam propagation factor M^2 determines the degree of variation of a beam from an ideal Gaussian beam. M^2 is equal to 1 for a Gaussian beam, closer values of M^2 to 1 indicate better beam quality.

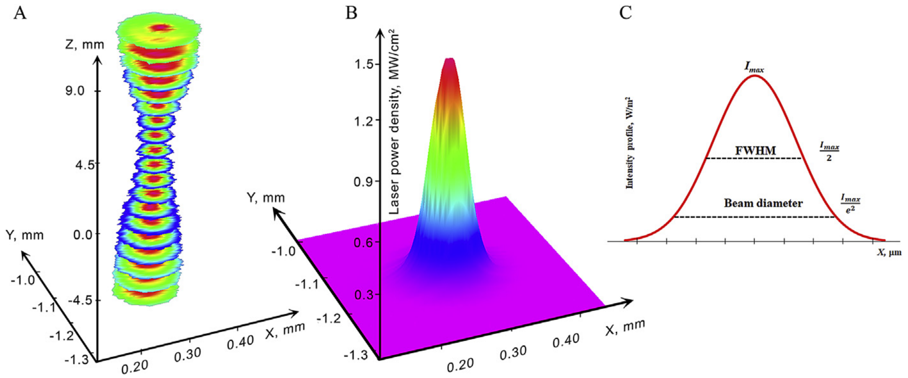

Figure 2.6 Laser beam spatial profile at different locations along the beam axis (A); power density distribution of CW Yb-fiber laser (focal spot diameter of 80 µm, $M^2 = 1.14$) (B); and Gaussian beam diameter definition (C).

Basic principles of laser physics, laser-matter interaction, mechanisms of laser processing, and using lasers in engineering and manufacturing can be found in Steen and Mazumder (2010) and Gladush and Smurov (2011).

In Fig. 2.6A and B the entire range of power density distribution in contour sections, indicated by the color maps, and three-dimensional visualization of the power density at the focus of the laser beam are shown. The diameter of the focal spot usually refers to a beam's diameter as its Gaussian diameter, the diameter of the beam at which its intensity equals $1/e^2 \times I_{\max}$ where: e is a mathematical constant (approx. 2.7183) and the base of the natural logarithm; $I_{\max}$ is the maximum intensity of the laser beam (Fig. 2.6C). There is a second approach to determining the beam diameter—the beam width at the half-intensity points or FWHM. This is a more general definition that can be applied to any beam intensity profile, not just Gaussian profiles. The Gaussian diameter is about 1.7 times the FWHM (full width at half maximum). In L-PBF, it is also important to know exactly how much power is in a given area. A circular Gaussian beam profile integrated down to $1/e^2$ of its peak value $I_{\max}$ (i.e., focal spot diameter) contains 86% of its total power.

The absorption of laser radiation in metals occurs in a very thin layer at the surface by free electrons also known as an "electron gas." The radiation is able to penetrate to a depth of only one to two atomic diameters, therefore metals are opaque and shiny. The reflectivity of metals is very high across a wide wavelength range (Fig. 2.7, using data from Paquin, 1994). According to Fig. 2.7, the reflectivity decreases and absorption increases as the wavelength becomes shorter (and photon energy increases) (Steen and Mazumder, 2010). The infrared (IR) absorption (wavelengths from ~0.7 to 1000 µm) of metals largely depends on the conductive absorption by free electrons. The absorptivity of polished surfaces of metals (for perpendicular incidence to a plane) is proportional to the square root of the electrical resistivity (Arata and Miyamoto, 1978). The absorption depends also on beam polarization, temperature, roughness,

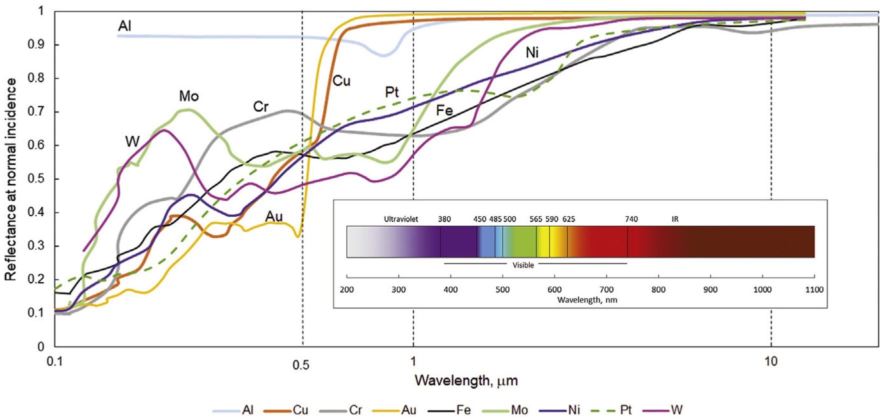

Figure 2.7 Normal-incidence reflectivity of selected metals as function of wavelength.
On the basis of data from Paquin, R.A., 1994. Properties of metals. In: Bass, M. (Ed.), Handbook of Optics, Devices, Measurements, and Properties, vol. II, second ed. McGraw-Hill, New York, pp. 35.1–35.78.

and the presence of an oxide layer that increases absorption (Mazumder, 1983; Indhu et al., 2018).

The absorption coefficient of many highly reflective metals (e.g., the platinum-group metals (PGMs), copper, gold, etc.) is higher at the wavelength near 0.5 μm than in the IR range; therefore, the use of a green laser with wavelength of 500–565 nm is much more effective for these metals. In addition, the green laser beam can be focused into a smaller spot (compared to Yb-fiber IR laser), so that the L-PBF process can be used to produce much more fine components, which is especially important for the jewelry and medical industries. In 2017, Fraunhofer ILT (Fraunhofer ILT) demonstrated L-PBF copper materials manufactured with a green laser. Currently, the market offers green fiber lasers (with the wavelength of ~532 nm) that provide maximum average powers between 100 and 1000 W in a single-mode output beam.

2.3.3 Scanning systems

After the collimated output and the laser beam expander (usually with a magnifying power of 2x–3x), the expanded beam enters the scanning system. Typically, one of two types of scanning systems can be used: with "passive" or "active" optics. The deflection of the laser beam is carried out by two mirrors of the orthogonal scanner.

In the first case ("passive" optics), after a galvanometer scanner, the laser beam enters the F-theta lens (Fig. 2.8A). A typical spherical lens can focus only along a circular plane; therefore, at the edges of the processing field there are large distortions due to the defocusing of the laser beam in these areas. To avoid this distortion, the position of the focused spot should linearly depend on the product of the focal length (F) and the tangent of the deflection angle (θ, *Greek letter* "theta"). F-theta lenses are designed

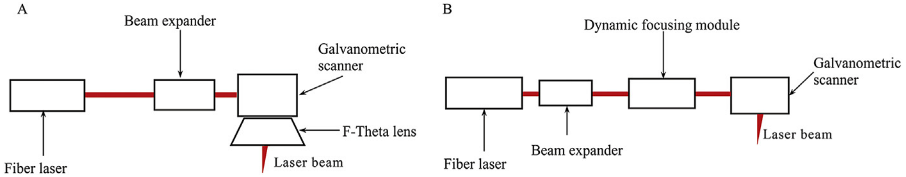

Figure 2.8 Scanning systems with “passive” (A) and “active” optics (B).

with built-in barrel distortion, which results in a displacement that is linear with θ, thereby simplifying positioning algorithms and allows for a fast, relatively inexpensive, and compact scanning system (Dickey, 2018). When using F-theta lenses, small laser spots practically do not change size over the entire scanning plane within the working field that maximize laser scanning performance and quality. For aerospace, automotive, and other high-tech applications, the requirements for the size of the working field of L-PBF systems are constantly growing. F-theta lenses for large working fields will be big, costly, and unpractical, since maintaining a small focused spot size requires conformity with numerical aperture, which in turn demands larger laser beam diameters and scan mirrors. For this reason, alternative 3-axis scanning systems with “active” optics are gaining acceptance in the L-PBF (Fig. 2.8B). In a 3-axis scanning system, a dynamic focusing module (DFM) is located before the galvanometer scanner, and in order to achieve a flat field, a third axis (Z-axis) of motion is introduced in the form of a linear lens translator. DFM provides a motorized focus optic, which manages not only focal z-adjustment, but also flat-field correction, working distance, and spot size.

2.3.4 Powder delivery system

In modern L-PBF systems, two main methods are used for powder delivery:

- Preloading powder into the reservoir with the subsequent supply by moving the piston from the bottom in an upward direction as shown in Fig. 2.2. Many commercial L-PBF systems use this method including, for example, EOS GmbH (Germany).
- The second method is that the powder from the reservoir from above is supplied in portions into the hopper, which is located above the plane of the working field and which combines the functions of powder delivery and powder deposition. Such a system is used by SLM Solutions Group AG (Germany).

Velo3D uses a different method, a “non-contact” deposition system, to avoid obstructions if there is deformation of the underlying structure, but up to now this invention is not disclosed.

2.3.5 Powder deposition system

The main task of the powder deposition system is to apply a uniform layer of powder (homogeneous and of equal thickness) to the base plate (substrate) mounted on a build platform. Usually, the powder deposition system performs linear reciprocating movements, but there are some exceptions, as in the Creator 3D system from Coherent, Inc. (USA) where a radial rotating mechanism is used.

The recoating systems have various types of recoaters: soft blade recoaters with rubber or carbon fiber brush, hard blade recoater from hard tool steel and roller from hard tool steel.

A soft recoater is a silicon or rubber blade or a carbon fiber brush that distributes powder in a thin layer over a substrate. Soft recoaters are flexible, so in a case of collision with L-PBF metal parts during manufacturing (for example, deformation of the part during processing or other defects), the soft recoater does not damage the part and does not require stopping of the process. However, this can also lead to further problems, since a defect growing for several layers can lead to collision with the solid part of the recoating system. The metal part will be completely defective and serious damage to the entire deposition system can take place. In addition, soft recoaters require frequent replacement as they are easily damaged. This type of recoater is useful for manufacturing delicate and cellular structures, which are easily deformed and can be damaged during the deposition of the subsequent layer of powder.

Hard blade recoaters are produced from tool steel or ceramic, which does not allow even slight deformation of the metal part during the manufacturing process; when the hard recoater collides with the part, the process stops. In this case, the defective part will not be manufactured, thereby saving money and time, since by eliminating this defective component from the manufacturing process, it is possible to continue manufacturing other parts on the base plate.

The powder deposition system by roller is used by 3D Systems, Inc. Spreading by roller is the best for deposition of a well-leveled powder layer, as it has two degrees of freedom: the roller moves both translationally and rotates in the opposite direction of translational motion. By choosing certain ratios between translational and rotational movements, a homogeneous powder deposition can be achieved for different materials and for different particle size distributions (PSDs) (Wang et al., 2020). However, due to the considerable size of the roller, this method can only be used for small or medium-sized working fields. Detailed review on existing powder delivering systems can be found in Nagarajan et al. (2019).

It is necessary to provide some practical recommendations on the optimal positioning of parts on the build platform in order to avoid the probability of damage to them as well as to the whole system. Firstly, the contact area of the recoater with the surface of the part should be minimized (see Chapter 5 “Design principles”). It is preferable to place parts unparallel to the blade of the recoater (Fig. 2.9A). The rotation of the part around the axis OZ and OX helps to significantly improve the redistribution of the recoater force and eases passing over the surface in case of deformation of the part. The rotation angle can be from several degrees to several tens of degrees around the Z-axis and several degrees around the X- or Y-axis. Before positioning a part on the build platform, it is imperative to carefully study the geometry of the part, since the correct placement will reduce the probability of a failure and help maintain high quality of the part as a whole. Secondly, the placement of parts directly one after another should be avoided (Fig. 2.9B) because during the manufacturing process one of the parts can be damaged due to a collision with the recoater, then some of the

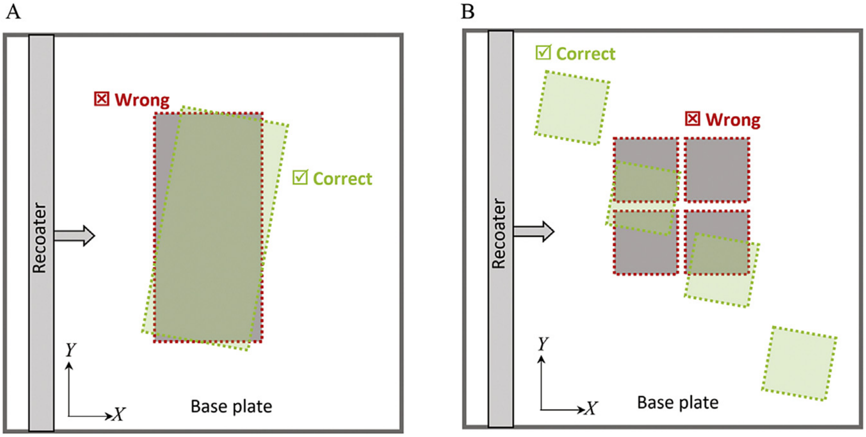

Figure 2.9 Positioning of the part on the base plate in relation to the recoater (A) and positioning of several parts (B).

broken parts will pass through the entire working field and, thus, may damage parts located directly behind the collision zone in the recoating direction.

2.3.6 Build platform and base plate

The base plate (or the substrate) on which the L-PBF objects are manufactured is attached directly to the build platform. The substrate material must ideally correspond to the powder material: to be the closest in chemical composition or match each other in weldability. It is necessary to avoid situations when, as a result of melting of the powder and the substrate, brittle intermetallic compounds are formed, or the metal components are mutually insoluble. This can lead to detachment of the part from the substrate during the manufacturing process, since the L-PBF parts have high residual stresses (Chapter 9). To reduce residual stress, platforms with a preheating system are sometimes used. This is particularly necessary for brittle materials and materials prone to cracking, for example, aluminum alloys, for which the preheating temperature reaches more than 200°C. For high-temperature materials, customized build platforms are being developed with the ability to heat up to 1000°C. These are complex engineering solutions, since it is necessary to maintain such high temperatures in the working chamber and at the same time isolate the influence of temperature on other components of the L-PBF system. Also, for especially expensive materials or research projects, special inserts can be used that are attached to the build platform and reduce the size of the manufacturing area, for example, to reduce the build area from $200 \times 200\ \text{mm}^2$ to $50 \times 50\ \text{mm}^2$. Most build platforms are rectangular in shape and are less often round. As seen from Table 2.1, the maximum platform size is currently $800 \times 400\ \text{mm}^2$ ($0.32\ \text{m}^2$) and ∅600 mm ($0.28\ \text{m}^2$).

2.3.7 Powder removal, gas supply, and filtration systems

After completion of manufacturing, the L-PBF parts require cool-down time, especially if preheating was used. It is then necessary to clean them from unused powder and to remove the base plate with parts from the chamber for further post-processing. An extraction of powder remaining in the working chamber under the build platform and in a special bunker, where excess powder is collected during the powder deposition process, is also required. It should be noted that in the process of forming a powder layer, an excess amount of powder is always used, so that it is guaranteed to be sufficient for the entire working surface.

There are several ways to remove powder: manually by the operator for L-PBF systems with small working areas; a semi-automatic system, when the powder is manually vacuumed to a container with a special vacuum technology, and a fully automatic system. The collected powder is then sieved to remove large particles or debris. The entire powder handling process from loading the powder into the L-PBF machine to extracting, sieving, and storing is best done in a closed system under an inert gas atmosphere, which will maximally preserve the quality of the powder for reuse and minimize operator contact with the powder for safety.

Since the powder has a large specific surface area, to prevent the metal material from intense oxidation, the L-PBF process takes place in an inert gas atmosphere. For more inert (resistant to oxidation) metal alloys (Ni-based, Co-based, Fe-based, etc.), nitrogen is used, and for more active metal alloys (Al-based, Ti-based, etc.), argon is used.

As a result of the interaction of laser radiation with metal powder, intensive evaporation and ejection of the material occurs. Powder particles entrained by evaporation-driven protection gas flow are pulled into the melt pool or are ejected away. The spatter ejection depends on protective gas flows, laser plume, and dynamics of the melt pool. To prevent contamination of the surface of the powder layer, which can further negatively affect the quality of the manufactured parts, and the L-PBF machine as a whole, a filtration system is used. When changing protective gases, it is imperative to change filters: firstly, nitrogen and argon have different physical properties and different gas permeability, and secondly, various metals deposited on the filters can react chemically, which can cause the filters to ignite and destroy the L-PBF system.

A directional flow of shielding inert gas, which uniformly flows directly over the surface of the powder layer, removes byproducts of the process (metal condensate and spatter particles) from the laser-powder interaction zone. While the metal condensate is sucked out of the chamber and removed from the process by filters, a certain amount of spatter particles (depending on the density of the powder material and the location on the working plane) will remain on the processed powder layer in the downstream direction, which can lead to defects in L-PBF parts. On the one hand, insufficient shielding gas flow can cause such defects in the L-PBF process, and on the other hand, an excessively strong gas flow will blow off the powder from the powder bed in the process of deposition, which will also lead to defects. Thus, the uniformity and stability of the gas flow is an important L-PBF process parameter (Ferrar et al., 2012; Ladewig et al., 2016; Schniedenharn et al., 2018).

2.4 Powder material

One of the most important components of the L-PBF process is the powder material (see Chapter 18). The powder material properties affect the further selection of all other process parameters. The chemical composition, thermal, optical, metallurgical, mechanical, and rheological characteristics of the material play a key role in L-PBF. Typically, L-PBF systems use metal powders ranging in size from 5 to 60 μm. Granulo-morphometric properties, such as the particle size, particle shape, elongation, roundness, specific surface area, particle size distribution (PSD), etc., affect the delivery of the powder layer, its homogeneity, and the absorption coefficient of laser radiation. An analysis of the relationships between the properties of the powder, bulk powder behavior, in-process performance, and their mutual correlations, as well as their influence on the quality of the final L-PBF part shows that special procedures for the evaluation of powder properties has to be developed in future (Vock et al., 2019). In order to expand the choice of materials used in the L-PBF process, it is necessary to evaluate the behavior of the material throughout the entire process chain, from a single track to a three-dimensional part, to determine possible ranges of process parameters, and analyze the quality of the final part for different L-PBF systems. Such evaluation (and ideally, qualification) of L-PBF material (Yadroitsev et al., 2015) is useful for all participants in the additive manufacturing industry:

- powder manufacturers will be able to develop powders of optimal quality for the L-PBF process and gain access to a wider market;
- manufacturers of L-PBF systems will benefit from the wider use of their equipment;
- end users will receive an improvement in the quality and consumer properties of manufactured products.

The most suitable powders for L-PBF are those with spherical particle morphology that has a high packing density, good flowability, and are evenly deposited to the substrate. Powders containing a significant fraction of small particles of ~1−2 μm in size are easily agglomerated and cannot be properly deposited to the substrate or to the previous layer processed by a laser beam in the working field. Coarse powders, with a particle size of more than 60 μm, are not used, since in this case the application of sufficiently thick layers and use a larger focal spot will be required, which will lead to a loss in manufacturing accuracy and significantly increase the risk of porosity growth, followed by a deterioration in mechanical properties of the L-PBF parts. Table 2.2 lists some commercial materials widely used in L-PBF technology.

2.5 L-PBF software

The implementation of a product idea begins with the creation of a 3D model. Computer Aided Design (CAD) software that can be used to design products for 3D printing are Solidworks, AutoCAD, Fusion 360, CATIA, Rhino, Creo, Sculptris, OpenSCAD, FreeCAD, SketchUp, etc. CAD software is commonly used to design

Table 2.2 Commercial materials (powders) used in L-PBF technology.

Al-based alloys	**AlSi10Mg, AlSi7Mg0.6, AlSi9Cu3**
Ni-based alloys	Nickel alloy HX, IN625, IN718, IN939
Ti-based alloys	TiAl6V4, TiAl6V4 ELI, TA15, CP (commercially pure) Ti
Co-based alloys	CoCr28Mo6, CoCr28W9
Fe-based alloys	304L, 316L, 15-5PH, 17-4PH, Maraging Steel 1.2709, Maraging Steel M300, H13, Invar 36, 20MnCr5 steel, Stainless Steel CX
Cu-based alloys	CuNi2SiCr, CuSn10, CP Cu, CuCr1Zr
Precious metals	Gold (Au), Silver (Ag), Platinum (Pt), Palladium (Pd)
Refractory metals	Tungsten (W), Molybdenum (Mo)

industrial products. On the other hand, some CAD software provide more freedom and a wider range of tools, because the design does not only have to be industrial and functional, but also can carry out aesthetic and artistic functions. The increased complexity available to additive manufacturing allows new design approaches such as biomimetic design for AM, including the use of freeform organic design, topology optimization, lattice structures, and more (Du Plessis et al., 2019). In a broader sense, the designer must also incorporate knowledge of additive manufacturing processes to optimize the design for additive manufacturing (DfAM) (Gibson et al., 2015; Diegel et al., 2019; Leary, 2019).

The CAD model, in addition to basic information about dimensions and tolerances, may also contain complementary data, such as material properties and information about the manufacturing process. Modern CAD software have advanced rendering and animation capabilities, which allow bringing product design visualization to a new level.

Generally, after creating a 3D model using CAD, it is necessary to make a polygonal model of object and to save the model in a stereolithography (STL) file format. STL is the first file format developed for 3D printing in 1987 and is still the most common file format for additive manufacturing. The acronym STL refers to either standard tessellation language or standard triangle language, both of which refer to the same format. The STL file saves information about the 3D model as surfaces of geometrical shapes and turns them into a triangular mesh. Currently, there are other file formats that contain additional information such as color, texture, materials, lattices, and constellations (e.g., AMF, 3MF), see Chapter 5 and Xiao et al. (2018), where data formats are presented in more detail.

At the next stage of working with a three-dimensional model in STL format, software is used to correct errors made at the design stage, create supports where necessary, and slice the model into thin layers. Information about each layer is translated into machine codes and transferred to the L-PBF machine, where the 3D object manufacturing process takes place. Examples of 3D printing software incorporating aspects from design to additive manufacturing in the same package are Materialise Magics, Autodesk Netfabb, and Altair Inspire Print3D.

Materialise Magics, allows conversion and editing of files to STL format, correction of design errors, and preparation of data and the build platform for the manufacturing process. Materialise Build Processor is a technology that provides communication between software and 3D printing machines.

Netfabb software includes build preparation capabilities as well as design optimization tools, simulation of the laser powder bed fusion process and planning subsequent post-processes (e.g., CNC processing).

Altair Inspire Print3D provides a set of tools to design and simulate the manufacturing process of parts by L-PBF. Inspire Print3D helps identify and correct potential problems with deformation, delamination, and excessive heat before the start of the manufacturing process, and the workflow can be represented as follows: model setup, thermo-mechanical analysis, manufacturability optimization.

It is also worth noting that the leaders of the L-PBF market are developing their own software. 3D systems, for example, developed 3DXpert specialized software that includes the entire chain from design to manufacturing and post-processing (3DXpert 3D Additive Manufacturing Software):

- importing data from different CAD formats to .STL file,
- positioning of the components on the base plate, taking into account gas flow, recoating mechanism movement, geometry and design of the component, etc.,
- optimizing the structure of the part with introducing different lattice structures, tools for improving accuracy, etc.,
- designing of supports,
- simulating the build layer-by-layer,
- optimizing building strategies through selection of special patterns with optimal process parameters for different areas of the component to speed up production time without compromising in quality and repeatability,
- optimizing the arrangement of many different components on the build platform and identification of each part,
- post-processing operations to remove supports, to improve surface quality and accuracy.

The manufacture of parts of complex shape and relatively large size can require a long build time, several days or even more. Therefore, information on the progress of the L-PBF process, operational monitoring of process parameters and quality control, are some of the most urgent tasks to prevent unforeseen situations during this build time. For L-PBF technology, continuous monitoring, measurement, and documentation of the main parameters of the process (for example, the laser power, the focal spot size, the spatial distribution of the radiation intensity, the scanning speed), powder layer quality (for example, optical observation of the layer), and powder properties (flowability, particle size distribution, particle morphology) are crucial.

Although the L-PBF process can be quite stable, deviation of the process parameters beyond certain limits can lead to process instability and deterioration of the quality of the manufactured parts (porosity, surface roughness, mechanical properties), Chapters 6, 7, and 13−15 in this book. Online monitoring methods in the L-PBF process are a significant aspect of the implementation of modern additive technologies in the industry (Chapter 11). It is necessary to develop additional monitoring solutions in order to control not only the process parameters but also evaluate the quality of the consolidated material in each layer. The system should ideally create reports in real time and at the output present a "quality certificate" of the produced L-PBF parts indicating the location of possible defects. Online monitoring is also the basis for developing in future feedback control systems to optimize the quality of manufactured products, so as not only to register defects, but also to dynamically correct problem areas during the L-PBF process, smartly and promptly changing process parameters. These types of online monitoring should subsequently be correlated with nondestructive testing data such as computed tomography (CT). The CT data obtained from the manufactured L-PBF parts are needed for the interpretation of monitoring data, and to develop rules for the limits of intervention and acceptability for different types and sizes of defects.

Currently, certain types of monitoring solutions are starting to be successfully implemented in the hardware and software packages of L-PBF systems by all the leading manufacturers of this equipment. Concept Laser GmbH (Germany) developed quality assurance modules for system status monitoring: QM Live View, QM Atmosphere, QM Fibre Powder, QM Cusing power, etc., for remote monitoring entire build platform, protective atmosphere and laser system, as well as QM Coating and QMmeltpool 3D for inline process monitoring. EOS GmbH (Germany) has developed EOSTATE monitoring software that is a modular solution consisting of four blocks: EOSTATE Base, EOSTATE PowderBed, EOSTATE MeltPool, and EOSTATE Exposure OT designed to monitor the entire production chain of the L-PBF process. Similar in functionality monitoring, Additive.Quality was developed and implemented by SLM Solutions Group AG (Germany) in which melt pool monitoring, laser power, and layer control systems are realized.

Modern software systems for computer simulation of additive processes such as MSC Simufact Additive, Ansys Additive Print, Siemens NX, Autodesk Netfabb, Materialise Magics Simulation, Altair Inspire Print3D, and many others permit to simulate processes at various parameters, to predict deviations of the part shape from the digital model, evaluate predicted residual stresses, etc. Thus, modern L-PBF equipment and software allow not only to produce parts of the highest quality but also to fully control the process itself and obtain a quality assurance certificate. Reliability and repeatability are vital to this innovative technology.

2.6 Post-processing

The quality of the final L-PBF product is determined by key characteristics: microstructure, porosity, residual stresses, surface roughness, and dimensional accuracy.

The necessary stages of the subsequent processing should be taken into account already at the stage of product design, considering the properties of the material used. The parts manufactured using the L-PBF process may not meet all product requirements directly in the "as-built" state; therefore, post-processing is often required to achieve the appropriate standards (Chapter 20).

One of the disadvantages of the L-PBF technology is the relatively high surface roughness of the parts (Chapter 7). To improve the surface roughness and dimensional accuracy of the product, mechanical post-processing is widely used (Chapter 12). The challenge is to identify the methods of subsequent processing considering the features of L-PBF process and get the best possible result from the point of view of surface roughness. In order to achieve the desired microstructure, relieve residual stresses, and reduce porosity, an appropriate heat treatment is required (Chapters 8, 9, 12). Post-processing may include the following steps: heat treatment to relieve residual

Table 2.3 Main hazards for PBF machines.

Type or group	Origin	Details of the powder bed fusion/sintering
Mechanical	Moving elements	Powder leveling device, transmissions
	Sharp edged parts, corners, rough surfaces	Elements of the machine made in sheet metal
	Fall or projection of objects	Base plate, gas equipment devices, powder cases
Electrical	Electromagnetic phenomena	Emitted by the machine electrical circuits or devices
	Electrostatic phenomena	Produced by powder flowing, charge accumulation within plastic bags or cases, devices for sweeping
	Electrified parts	Internal circuits accessed during maintenance
	Parts becoming conductive in case of machine failure	Accidental contact with broken cables
Thermal	Hot surfaces	Part of the machine heat during the manufacturing process, surrounding the finished part before its extraction from the machine
Radiation	Optical radiations	Laser beams
	Ionizing	Electron beam on a metallic target
Material /substance	Powder	Micro-powders, flammable and reactive materials, inert gases

Modified from Ferraro, A., et al., 2020. Powder bed fusion/sintering machines: safety at workplaces. In: Procedia Manufacturing. Elsevier B.V. pp. 370–374. https://doi.org/10.1016/j.promfg.2020.02.061.

stress; base plate removal; support removal; ultrasonic cleaning; annealing (argon atmosphere or vacuum furnace) or hot isostatic pressing; grit blasting; machining and polishing (for whole parts or only in selected areas as necessary). Thus, it is clearly seen that post-processing should be an integral part of the L-PBF technology. Included at this stage is nondestructive testing (NDT) of final parts for quality assurance (Chapter 10).

2.7 Safety aspects

Working with lasers, complex mechanical systems, and powder material requires special attention from the staff involved in the L-PBF process. The main hazards connected with PBF machines are indicated in Table 2.3 (Ferraro et al., 2020). Complex L-PBF equipment requires highly qualified personnel who understand how the equipment works and the risks associated with it. Compliance with safety measures when working with equipment and powders is an important aspect of L-PBF technology.

2.8 Conclusion

The L-PBF process can be described in the following steps (Fig. 2.2): an idea for special application; material choice; creation of product design; creating CAD model considering the features of the L-PBF process and material properties; converting CAD model to .STL format; virtual placement (software) of 3D model on the build platform taking into account design features; creation of supports for the 3D model where necessary; slicing 3D model into layers; transferring data to L-PBF machine; machine setup, manufacturing process; removal of parts from the build platform; post-processing chain; application of the finished part.

Factors that influence the quality, repeatability, and performance of L-PBF components involve machine parameters that define the system, such as laser type and wavelength, build volume, the range of operational temperature in the internal chamber, accuracy of build platform motion, etc. Additionally, this includes many variable parameters such as laser power, focal spot diameter, scanning speed, powder layer thickness, oxygen level in the surrounding atmosphere, protective gas flow rate, material and surface roughness of the substrate, and much more. All this variety of processes and parameters make L-PBF technology incredibly flexible and able to manufacture parts with incredibly complex shape and functionality.

2.9 Questions

- What is additive manufacturing?
- What are the main categories of additive manufacturing?

- What is laser powder bed fusion? What other terms are used for L-PBF?
- What are main hardware components of the L-PBF system?
- Describe the working principle of a fiber laser.
- What is the Gaussian diameter?
- How is the absorption of laser radiation related to the wavelength for different metals?
- What is the preferred wavelength for copper? And for molybdenum? Use Fig. 2.7 to support your explanations.
- Describe the principle of the scanning system with active optics.
- What is an F-theta lens? Where it is used?
- How does a powder deposition system work?
- What types of recoaters are used in L-PBF?
- What is a build platform?
- What shape and size of powders are more preferable in L-PBF? Why?
- What does "CAD" and "STL" mean?
- Why is monitoring important in L-PBF?
- What is post-processing? What processes it can include? Why is it needed?
- Explain safety issues when working with L-PBF systems and powders.

Acknowledgments

Igor Yadroitsev and Ina Yadroitsava are supported by the South African Research Chairs Initiative of the Department of Science and Technology and National Research Foundation of South Africa (Grant No. 97994). The authors acknowledge the Collaborative Program in Additive Manufacturing. We appreciate Stellenbosch Institute for Advanced Study (STIAS) that supported the development of this book.

References

Arata, Y., Miyamoto, I., 1978. Laser welding. Technocrat 11, 33–42.

Beaman, J.J., et al., 2020. Additive manufacturing review: early past to current practice. J. Manufact. Sci. Eng. ASME Int. 142 (11). https://doi.org/10.1115/1.4048193.

DebRoy, T., et al., 2018. Additive manufacturing of metallic components – process, structure and properties. Prog. Mater. Sci. 92, 112–224. https://doi.org/10.1016/j.pmatsci.2017.10.001. Elsevier Ltd.

Dickey, F.M., 2018. Laser Beam Shaping. In: Dickey, F.M. (Ed.). CRC Press. https://doi.org/10.1201/b17140.

Diegel, O., Nordin, A., Motte, D., 2019. A Practical Guide to Design for Additive Manufacturing. Springer Singapore (Springer Series in Advanced Manufacturing), Singapore. https://doi.org/10.1007/978-981-13-8281-9.

Du Plessis, A., et al., 2019. Beautiful and functional: a review of biomimetic design in additive manufacturing. Addit. Manufact. 27 https://doi.org/10.1016/j.addma.2019.03.033.

Esmaeilian, B., Behdad, S., Wang, B., 2016. The evolution and future of manufacturing: a review. J. Manuf. Syst. 79–100. https://doi.org/10.1016/j.jmsy.2016.03.001. Elsevier B.V.

Ferrar, B., et al., 2012. Gas flow effects on selective laser melting (SLM) manufacturing performance. J. Mater. Process. Technol. 212 (2), 355–364. https://doi.org/10.1016/j.jmatprotec.2011.09.020. Elsevier.

Ferraro, A., et al., 2020. Powder bed fusion/sintering machines: safety at workplaces. In: Procedia Manufacturing. Elsevier B.V., pp. 370−374. https://doi.org/10.1016/j.promfg.2020.02.061

Gibson, I., Rosen, D., Stucker, B., 2015. Design for additive manufacturing. In: Additive Manufacturing Technologies. Springer New York, New York, NY, pp. 399−435. https://doi.org/10.1007/978-1-4939-2113-3_17.

Gladush, G.G., Smurov, I., 2011. Physics of laser materials processing: theory and experiment. Springer Mater. Sci. 146 (1) https://doi.org/10.1007/978-3-642-19831-1.

Indhu, R., et al., 2018. Overview of laser absorptivity measurement techniques for material processing. Lasers Manufactur. Mater. Process. 458−481. https://doi.org/10.1007/s40516-018-0075-1. Springer.

Jurisch, M., et al., 2015. 3D screen printing for the fabrication of small intricate Ti-6Al-4V parts. Powder Metall. 58 (5), 339−343. https://doi.org/10.1179/0032589915Z.000000000255. Maney Publishing.

Klocke, F., Wagner, C., Ader, C., 2003. Development of an integrated model for selective metal laser sintering - PDF free download. In: 36th CIRP International Seminar on Manufacturing Systems. Saarbrucken, Germany, pp. 387−392. Available at: http://docplayer.net/18693330-Development-of-an-integrated-model-for-selective-metal-laser-sintering.html.

Ladewig, A., et al., 2016. Influence of the shielding gas flow on the removal of process by-products in the selective laser melting process. Addit. Manufact. 10, 1−9. https://doi.org/10.1016/j.addma.2016.01.004. Elsevier B.V.

Le, V.T., Paris, H., Mandil, G., 2017. Process planning for combined additive and subtractive manufacturing technologies in a remanufacturing context. J. Manuf. Syst. 44, 243−254. https://doi.org/10.1016/j.jmsy.2017.06.003. Elsevier B.V.

Leary, M., 2019. In: Design for Additive Manufacturing, first ed. Elsevier. Available at: https://www.elsevier.com/books/design-for-additive-manufacturing/leary/978-0-12-816721-2.

Markforged Inc, 2020. Markforged Metal 3D Printer. The Metal X 3D Printing Solution. Available at: https://markforged.com/metal-x/.

Mazumder, J., 1983. Laser welding. In: Bass, M. (Ed.), Materials Processing: Theory and Practices. Elsevier, pp. 113−200. https://doi.org/10.1016/B978-0-444-86396-6.50009-X.

Meier, C., et al., 2018. Thermophysical phenomena in metal additive manufacturing by selective laser melting: fundamentals, modeling, simulation, and experimentation. Ann. Rev. Heat Trans. 20 (1), 241−316. https://doi.org/10.1615/annualrevheattransfer.2018019042. Begell House.

Moges, T., Ameta, G., Witherell, P., 2019. A review of model inaccuracy and parameter uncertainty in laser powder bed fusion models and simulations. J. Manufactur. Sci. Eng. Trans. ASME. https://doi.org/10.1115/1.4042789. American Society of Mechanical Engineers (ASME).

Nagarajan, B., et al., 2019. Development of micro selective laser melting: the state of the art and future perspectives. Engineering 702−720. https://doi.org/10.1016/j.eng.2019.07.002. Elsevier Ltd.

O'Regan, P., et al., 2016. Metal based additive layer manufacturing: variations, correlations and process control. Proc. Comp. Sci. 216−224. https://doi.org/10.1016/j.procs.2016.08.134. Elsevier B.V.

Paquin, R.A., 1994. Properties of metals. In: Bass, M. (Ed.), Handbook of Optics, Devices, Measurements, and Properties, second ed., vol. II. McGraw-Hill, New York, pp. 35.1−35.78.

Rehme, O., Emmelmann, C., 2005. Reproducibility for properties of selective laser melting products. In: Beyer, E. (Ed.), Lasers in Manufacturing 2005 : Proceedings of the Third International WLT-Conference on Lasers in Manufacturing. AT-Verlag, Munich, Germany, pp. 227−232.

Rubenchik, A.M., King, W.E., Wu, S.S., 2018. Scaling laws for the additive manufacturing. J. Mater. Process. Technol. 257, 234−243. https://doi.org/10.1016/j.jmatprotec.2018.02.034. Elsevier Ltd.

Schmidt, M., et al., 2017. Laser based additive manufacturing in industry and academia. CIRP Ann. 66 (2), 561−583. https://doi.org/10.1016/j.cirp.2017.05.011. Elsevier USA.

Schniedenharn, M., Wiedemann, F., Schleifenbaum, J.H., 2018. Visualization of the shielding gas flow in SLM machines by space-resolved thermal anemometry. Rapid Prototyp. J. 24 (8), 1296−1304. https://doi.org/10.1108/RPJ-07-2017-0149. Emerald Group Publishing Ltd.

Seibold, M., 2019. Additive manufacturing for serial production of high-performance metal parts. Mech. Eng. 141 (5), 49−50. https://doi.org/10.1115/1.2019-MAY5. American Society of Mechanical Engineers (ASME).

Shiner, B., 2015. Fiber Lasers: New Types and Features Expand Applications. Photonics Buyers' Guide, Photonics Handbook. In: Lasers | Photonics Handbook. IPG Photonics Corp. Available at: https://www.photonics.com/Articles/Fiber_Lasers_New_Types_and_Features_Expand/a25158.

Steen, W.M., Mazumder, J., 2010. In: Laser Material Processing, fourth ed. Springer, London. https://doi.org/10.1007/978-1-84996-062-5.

The Additive Manufacturing Landscape, 2019. Available at: https://amfg.ai/wp-content/uploads/2019/08/The-Additive-Manufacturing-Landscape-2019_Whitepaper.pdf.

Tofail, S.A.M., et al., 2018. Additive manufacturing: scientific and technological challenges, market uptake and opportunities. Mater. Today 22−37. https://doi.org/10.1016/j.mattod.2017.07.001. Elsevier B.V.

Vock, S., et al., 2019. Powders for powder bed fusion: a review. Prog. Addit. Manufactur. 383−397. https://doi.org/10.1007/s40964-019-00078-6. Springer.

Wang, L., et al., 2020. Adhesion effects on spreading of metal powders in selective laser melting. Powder Technol. 363, 602−610. https://doi.org/10.1016/j.powtec.2019.12.048. Elsevier B.V.

Wohlers Associates (no date). Available at: https://wohlersassociates.com/2020report.htm (Accessed: August 10, 2020).

Xiao, J., et al., 2018. Information exchange standards for design, tolerancing and additive manufacturing: a research review. Int. J. Interact. Design Manufactur. 12 (2), 495−504. https://doi.org/10.1007/s12008-017-0401-4. Springer-Verlag France.

Yadroitsev, I., 2009. Selective Laser Melting : Direct Manufacturing of 3D-Objects by Selective Laser Melting of Metal Powders (Book, 2009) [WorldCat.org]. Lambert Academic Publishing, Saarbrücken.

Yadroitsev, I., Krakhmalev, P., Yadroitsava, I., 2015. Hierarchical design principles of selective laser melting for high quality metallic objects. Addit. Manufact. 7, 45−56. https://doi.org/10.1016/j.addma.2014.12.007. Elsevier B.V.

Yi, L., Gläßner, C., Aurich, J.C., 2019. How to integrate additive manufacturing technologies into manufacturing systems successfully: a perspective from the commercial vehicle industry. J. Manuf. Syst. 53, 195−211. https://doi.org/10.1016/j.jmsy.2019.09.007. Elsevier B.V.

Ziaee, M., Crane, N.B., 2019. Binder jetting: a review of process, materials, and methods. Addit. Manufact. 781−801. https://doi.org/10.1016/j.addma.2019.05.031. Elsevier B.V.

A step-by-step guide to the L-PBF process

3

Igor Yadroitsev, Ina Yadroitsava
Department of Mechanical and Mechatronic Engineering, Central University of Technology, Bloemfontein, Free State, South Africa

Chapter outline

3.1 Introduction 39
3.2 Single track formation 40
  3.2.1 Melt-pool dynamics and track formation 40
  3.2.2 Process stability 42
  3.2.3 Influence of process parameters on single track characteristics 45
    3.2.3.1 Delivery of powder layer 45
    3.2.3.2 Geometry of single tracks 47
3.3 Single layer formation 50
  3.3.1 Morphology of a single layer: Scanning strategies and hatching 50
  3.3.2 Contouring, offset, and skywriting 51
  3.3.3 Characterization of a single layer 51
3.4 Thin wall formation 54
3.5 L-PBF object formation 55
3.6 Optimization of L-PBF process parameters 58
  3.6.1 Where to begin? 58
  3.6.2 Numerical simulations of single tracks 58
  3.6.3 Optimal process parameters for single tracks 61
  3.6.4 Optimal process parameters for single layers 62
  3.6.5 Optimal process parameters for 3D parts 64
3.7 Conclusions 67
3.8 Questions 68
Acknowledgements 68
References 68

3.1 Introduction

Further development of additive manufacturing (AM) and wide applications of laser powder bed fusion (L-PBF) in high-performance industries require quality assurance of manufactured objects. According to the ISO 9000 standard, "*quality is the degree*

Fundamentals of Laser Powder Bed Fusion of Metals. https://doi.org/10.1016/B978-0-12-824090-8.00026-3
Copyright © 2021 Elsevier Inc. All rights reserved.

to which a set of inherent characteristics fulfil requirements." Customer requirements serve as the engine of progress for all technologies and for AM in particular. The term "quality" in L-PBF includes high relative density (up to 100%), dimensional tolerance, special surface features that minimize post-treatment (for example, low waviness and roughness, lack of oxidation, etc.), original chemical composition without contamination and inclusions, appropriate microstructure, and mechanical properties, as well as high repeatability of fabricated parts. The L-PBF system, material, and process parameters determine the quality of as-built products and their properties.

Process parameters are "*a set of operating parameters and system settings used during a single build cycle*" (ISO/ASTM 52900:2015). These factors are interconnected, for example, parameters of the system affect the range of possible materials, maximum part size, the size of the powders, layer thickness, etc. Different materials, in turn, require different energy inputs that influence the range of laser powers and scanning speeds of the system, the special protective atmosphere required, etc. Thus, system parameters can impose restrictions on the choice of powder materials, scanning parameters, and size of objects. In turn, the powder characteristics govern the acceptable thickness of the layers. Layer thicknesses affect manufacturing dimensional accuracy, surface morphology and roughness, etc. Track-by-track, layer-by-layer manufacturing of parts from powder by laser beam leads to a specific as-built tolerance for accuracy, density, surface topology, and roughness. Anisotropy in microstructure and mechanical properties relate to building and scanning strategies, since the 3D L-PBF parts are a kind of "construction" consisting of tracks and layers.

Single tracks are the fundamental units for L-PBF components; their combination creates a single layer, and a 3D object is built from the sequence of layers. To produce fully dense objects from the employed powder material, optimal process parameters and a specific strategy of manufacturing should be used. Using post-processing enables to reduce porosity, improve surface roughness, and change other properties, but it increases the cost of production and cannot always eliminate defects in as-built L-PBF parts.

3.2 Single track formation

3.2.1 Melt-pool dynamics and track formation

When the laser beam scans over the surface of a thin powder layer deposited on a substrate or on the previously processed layer, energy absorbed from the laser beam heats the underlying material. Molten powder particles and the substrate create a joint melt pool. Heating, time-evolution of the melt pool, and the solidification process depend on powder material properties, process parameters, and the build environment. The process parameters affect the phases, recoil pressure, surface tension and Marangoni effect, and hydrodynamics that in turn define the evolution of the melt pool, its size, and shape (Khairallah et al., 2016; Zhang et al., 2019). When the laser beam leaves the melt area, the melt pool starts to cool down and solidifies. To create a stable melt pool with a regular shape and geometrical characteristics, several factors have to be consistent with each other: these are discussed below. Sufficient energy is needed to melt both the powder and the substrate under the laser beam and the interaction time has to be optimized to create a joint stable melt pool.

The energy absorbed by material is strictly dependent on laser characteristics such as wavelength, pulse width and frequency (if a pulsed laser is used), average and maximum power, intensity profile, laser mode, spot size, irradiation time, etc. The key energy parameters of L-PBF are laser power and focused beam diameter (spot size). In Fig. 3.1A, typical Ti powder is shown in comparison with the size of the laser spot. The smaller the spot size, the fewer powder particles interact directly with the laser beam. A single track (Fig. 3.1B) is formed not only from powder placed directly under the laser spot; adjacent particles are involved in the process and a denudation zone forms (Yadroitsev, 2009). The powder denudation zone defines the volume of powder involved in the track formation and spattering process. Matthews et al. (2016) showed that the dynamics of denudation depend on the geometry of the melt pool, the metal vapor flow that is induced by heating under the laser beam, and ambient gas pressure. At a typical pressure of about 1 atm in the L-PBF processing chamber, the dominant factor for the denudation is gas flow caused by pressure drops inside the evaporated jet (Bernoulli effect) that entrain powder particles surrounding the melt pool into the process. Powder particles from the denudation zone are pulled into the melt pool or ejected away. Powder particles, or their agglomerates that were

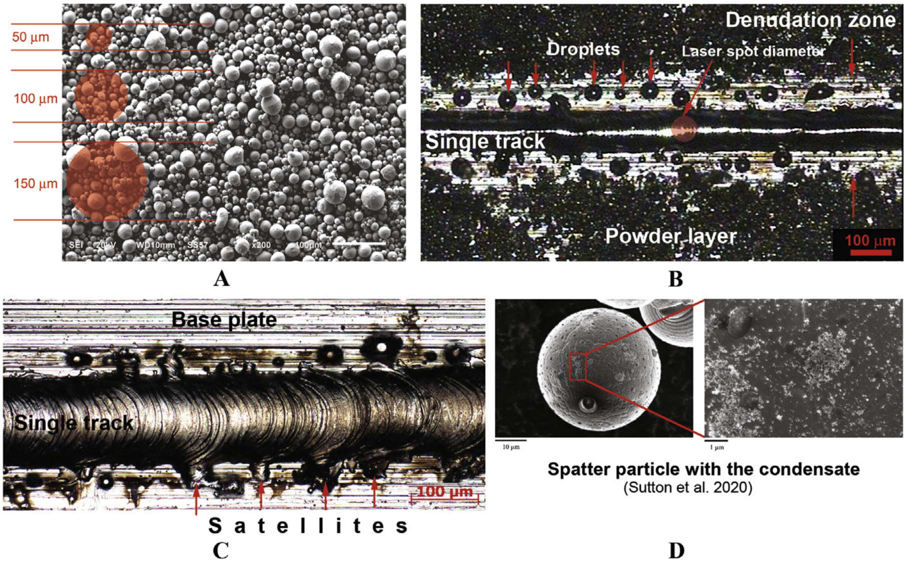

A

B

C

D

Spatter particle with the condensate
(Sutton et al. 2020)

Figure 3.1 Ti grade 2 powder (−45 µm) in comparison with the laser beam spots (*red circle*) (A); single track on the substrate with powder showing denudation zone, droplets, and laser spot (B); single track with satellites (C); SEM micrographs showing a spatter particle and its surface with the condensate (Sutton et al., 2020) (D).

partially melted, can create "satellites" at the edges of the track (Fig. 3.1C). Satellites can also occur from the spattering effect, when powder particles and melt droplets are ejected during the L-PBF process.

Spattering from the laser beam−matter interaction zone refers to the ejection of powder particles, as well as molten material, from the melt pool. Spatter ejection depends on protective gas flows, process parameters, dynamics of the melt pool, and powder material (Ly et al., 2017; Wang et al., 2017; Gunenthiram et al., 2018).

Bidare et al. (2018) studied powder spattering by high-speed *Schlieren* imaging. They showed that at low laser power (50 W), the laser-generated plume direction is established forwards in the scanning direction. Induced flow of ambient gas captures powder particles, entraining them into the melt pool from all directions. These powder particles predominantly melt and consolidate into the track and some of them are ejected forwards in the scanning direction (50 W, 0.1 m/s). With increasing laser power and scanning speed (100 W and 0.5 m/s), the laser plume and spatter are directed predominantly vertically upwards. Further increases in laser power (200 W) and scanning speed (1 m/s) lead to intensive blowing backwards of powder particles, thus expanding the denudation zone. Since laser beam parameters are responsible for the generation of spatters and overheating of the melt pool, it has been suggested to decrease the laser power density or to use laser beam shaping (e.g., top-hat beam profile) (Simonelli et al., 2015).

Spatter particles can be divided into three main classes: particles that travel toward the vapor jet and (1) miss the laser beam, or "cold" spatters, (2) "hot" particles that cross the laser beam; and (3) ejections from the melt pool due to melt dynamics and recoil pressure (Ly et al., 2017). Energy input affects the size and dynamics of spattering: the general trend is that a higher laser power leads to more intense spatter behavior (Liu et al., 2015). Hot spatters and melt droplets are visible as bright sparks around the track when the laser beam scans the powder bed. Molten/partially molten particles can coalesce creating agglomerates, attaching to the substrate forming droplets near the L-PBF track, or create satellites at the sides of tracks (Fig. 3.1C). The diameters of the melt droplets can be bigger than the original powder particles, thus changing the effective particle size distribution of the feedstock powder.

When energy from the laser beam is enough to intensively evaporate underlying material, vaporized material solidifies rapidly in the protective gas; this is visible as a "fume" during the laser melting process and creates dark spots on the processed layer. By SEM imaging, these condensates look like a fluffy coating consisting of nano-sized particles. In Fig. 3.1D a spatter particle covered by condensed material is shown.

3.2.2 Process stability

The morphology of single tracks has a complex dependence on process parameters. The mechanisms of distortions and irregularities in single tracks are associated with thermophysical properties of materials, granulomorphometric characteristics of the powder, and inhomogeneity in powder layer thickness; energy input parameters such as laser power, spot size, and scanning speed; build environmental parameters, etc. (Yadroitsev et al., 2010; Yuan et al., 2020). Analysis of the formation of single tracks from metal powders by L-PBF showed that the process has a threshold character: there are continuous tracks with regular sizes and ripples (Fig. 3.2A and B), continuous tracks having periodic humps and valleys (humping effect, Fig. 3.2C), tracks with irregular flow front with many satellites (Fig. 3.2D), and irregular tracks with highly varying widths and heights (Fig. 3.2E and F) up to a chain of beads—the so-called "balling effect." The evolution of a single track from a regular shape to a chain of beads with increasing scanning speed is shown in Fig. 3.2G.

The balling effect, or "balling phenomenon" was first described in investigations on selective laser sintering (SLS), causing "*laser molten material to ball up upon solidification instead of forming a flat surface*" (Manriquez-Frayre and Bourell, 1991). The segmentation of a molten region of cylindrical shape (a scan track) was associated with liquid cylinder instability, described by Rayleigh and called Plateau-Raleigh capillary instability: this causes a tendency to reduce the surface area—a sufficiently long melt pool breaks up into a row of beads. Kinetics of the balling effect for thick powder layers was described in detail by Tolochko et al. (2004). Niu and Chang (1998, 1999) found that the balling effect depends on laser power, scanning speed, and layer thickness and has a detrimental effect on the density of SLS parts. Morgan et al. (2004) suggested that spherical shaping of the melt may also be amplified by Marangoni flow inside the melt pool.

Fig. 3.2G shows the development of the balling effect on a thick powder layer (~100 μm) with increasing scanning speed: the tracks change from continuous (0.12 m/s) to transition state (0.14–0.16 m/s), the track is continuous, but there are places of narrowing (necking) and expansion (swelling) and finally, up to a chain of beads with metallurgical contact with the substrate (0.18–0.20 m/s) and rare single beads that remained after the powder layer was swept away during the cleaning

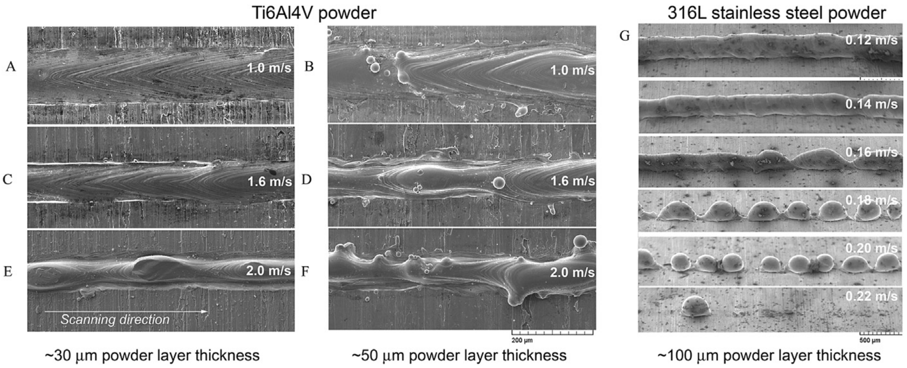

Figure 3.2 Different morphology of L-PBF Ti6Al4V ELI single tracks manufactured at 170 W laser power, 80 μm spot size, scanning speed of 1.0, 1.6, and 2.0 m/s. Powder layer thickness was about 30 μm (A, C, E) and about 50 μm (B, D, F); (G) 316L stainless steel single tracks manufactured at 50 W laser power, 70 μm spot size, scanning speed of 0.12–0.22 m/s. Powder layer thickness was about 100 μm. The chemical compositions of substrates and powders were similar.

procedure. The penetration into the substrate provides an additional stabilizing effect for the formation of continuous tracks: the segmental cylinders are more stable than the free circular ones (Yadroitsev et al., 2010). At low laser power (low energy input), Plateau-Rayleigh instability might be suppressed by the wetting behavior between the substrate and molten powder, as was proven by C. Tang et al. (2020b).

Similar to welding (Yinglei and Jiguo, 2020), the humping effect was found in the L-PBF process and results in continuous tracks which can have periodic waviness of the profile and undercuts. It was found that in L-PBF, the humping effect is very pronounced at high laser power and high scanning speed (Makoana et al., 2018; Tang et al., 2020). The mechanisms and implications of the humping effect on L-PBF require further study. Tang et al. (2020a) showed recently that low surface tension and positive surface tension gradient, recoil pressure, and viscous shear stress contribute to the humping effect. DebRoy et al. (2018) indicated that Kelvin Helmholtz hydrodynamic instability can be one of the main reasons of humping.

The morphology of the L-PBF Ti6Al4V track with expressed humping effect is shown in Fig. 3.3A. It can be seen that the depth of penetration is sufficiently high, and the single track is continuous. It is necessary to clearly distinguish the balling and humping effects since they have different origins and both influence the final

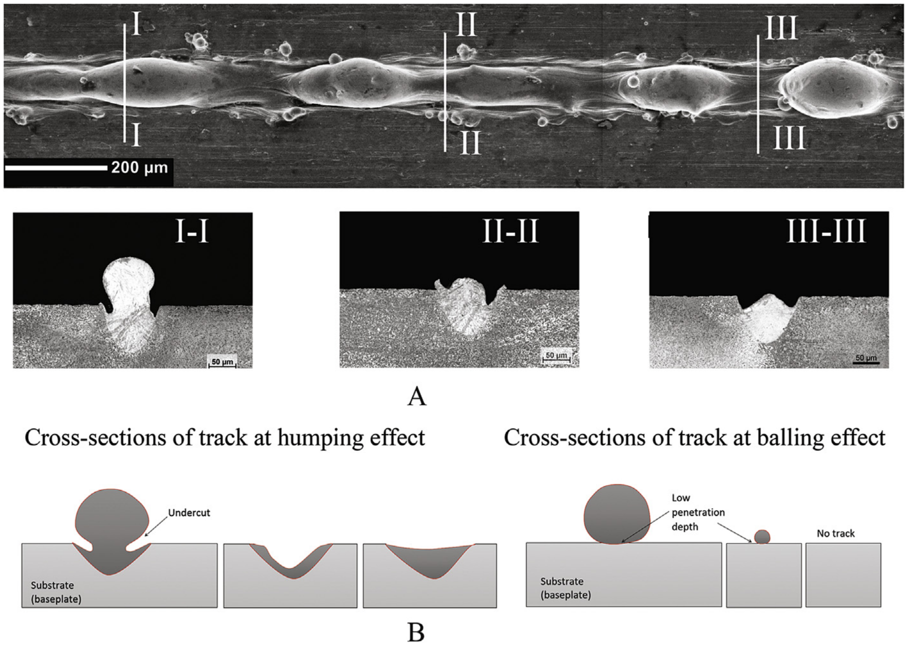
I
II
III
I
II
III
200 µm
I-I
II-II
III-III
50 µm
50 µm
50 µm
A
Cross-sections of track at humping effect
Cross-sections of track at balling effect
Undercut
Substrate (baseplate)
Low penetration depth
No track
Substrate (baseplate)
B

Figure 3.3 Humping effect in single tracks. Ti6Al4V ELI single track manufactured at 350 W laser power, 80 μm spot size, and scanning speed of 2.4 m/s. Powder layer thickness is 50 μm, the substrate is Ti6Al4V grade 5. I-I, II-II and III-III show 2D cross-sections of the sample at corresponding locations along the single track (A); Comparison of cross-sections of tracks at humping and balling effects (B).

part quality. From the point of view of building parts with low porosity, the deep penetration of the melt pool into the substrate observed during the humping effect can make it possible to build nonporous parts from irregular (humping) tracks by reducing the hatch distance (shift between center of tracks). With the balling effect, when the penetration depth is very small (Fig. 3.3B), lack of fusion porosity will be very pronounced in 3D objects. Humping as well as balling effects are undesirable processes in L-PBF, since they can lead to inhomogeneity of the following powder layer or to collision with the recoater/roller that deposits the powder layer. An impact can deform the L-PBF part, recoater, or even the whole system.

Most L-PBF systems use a velocity profile to control the movement of the laser beam to improve the spatial and temporal accuracy, because it is impossible to instantly achieve a certain scanning speed (Yeung et al., 2018). Since the geometry of the melt pool depends on laser beam—material interaction time (sometimes called "dwell time" (Trapp et al., 2017)), if the scanning speed is gradually increased/decreased at the start and end of the scanning, geometrical characteristics of the single track at these points will differ from scanning with constant speed (main part of the track). This phenomenon can be called the "beginning-end effect" in track formation (Fig. 3.4). Furthermore, some researchers use a term "vectors" instead of "single track," rather focusing on the fact that scanning direction matters (Kruth et al., 2004; Yadroitsev et al., 2007; Oliveira et al., 2020).

3.2.3 Influence of process parameters on single track characteristics

3.2.3.1 Delivery of powder layer

Different materials show different and sometimes peculiar behavior in the process of single track formation. In most cases, experiments with single tracks are carried out on a substrate of the same material or a similar material to simulate the formation of layers of the 3D object, since each solidified layer is the substrate for a next layer in a 3D L-PBF part. A high content of oxides on the surface of the substrate is undesirable — oxides change the absorption coefficient of laser radiation and increase the melting temperature of the scanned material. This affects the wettability of the substrate by molten material, and can lead to the balling effect. Oxides also contribute to the formation of cracks (Bergström, 2008; Hruška et al., 2018; Abedi and Gollo, 2019). It is obvious that with high roughness it is impossible to deliver a thin homogeneous powder layer, and inversely, particles on top of a mirror-polished

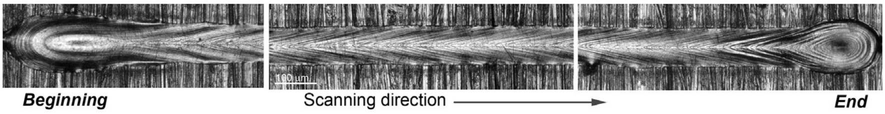

Figure 3.4 Differences in the beginning, middle, and end of a single track on Ti6Al4V substrate.

substrate surface can roll easily and move during deposition leading to an apparently low powder density. The roughness of the substrate surface therefore influences the morphology and geometry of single tracks (Mishra and Kumar, 2020).

For single track experiments, it is recommended to use machined substrates with an average roughness and wavelength (distance between peaks) of the same order of magnitude as the powder particle size (see Chapter 7 for more about roughness). In Fig. 3.5, a stainless steel substrate is presented, the arithmetic mean deviation of the roughness profile is $R_a \sim 2$ µm, the total height of roughness profile is $R_t \sim 18$ µm. The first powder layer delivered to the substrate with a prescribed thickness of 40 µm shows R_t of 40 ± 4 µm when evaluated with a confocal microscope (Fig. 3.5). To date, standards for the condition of the substrate and its roughness have not yet been developed.

A powder layer for single track experiments needs to be delivered very carefully; skewing the substrate or its irregularities can lead to the track not only having different geometric characteristics but also different behavior, up to the balling effect on a thick layer or irregular shape on an inhomogeneous layer. Powder quality, environmental

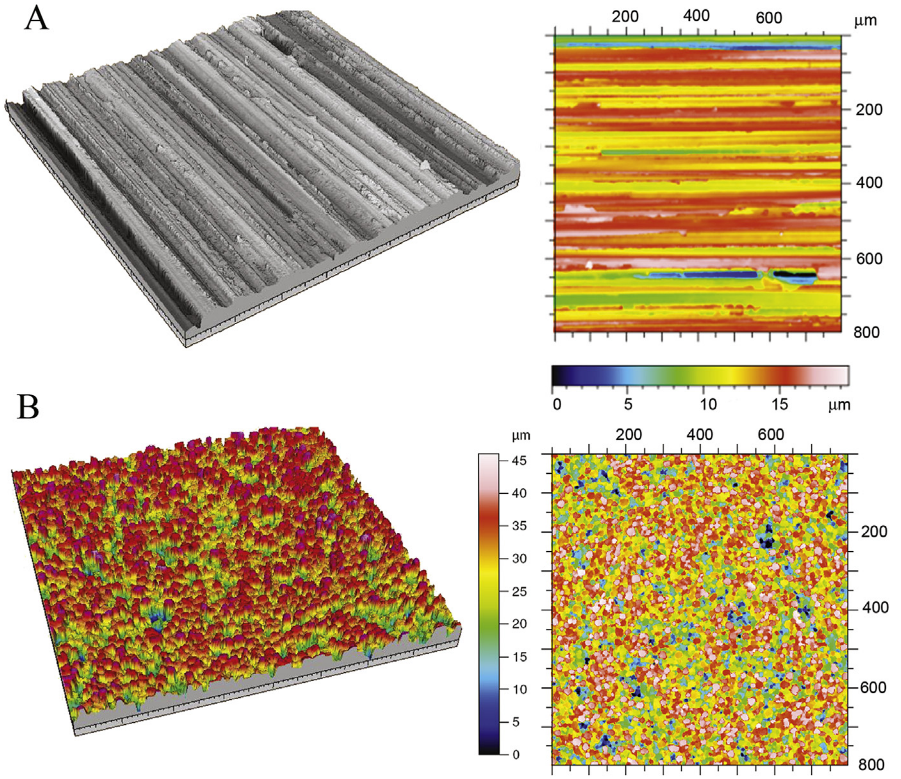

Figure 3.5 3D image and morphology of the substrate from stainless steel grade 304L (A), and powder layer deposited to the substrate with prescribed thickness of 40 µm (B); images made by the µsurf confocal microscope (NanoFocus AG).

conditions, such as humidity and temperature, static charge, the type of recoater (blade/roller/brush), the deposition rate, etc., all influence the powder deposition process (Clayton and Deffley, 2014; Slotwinski and Garboczi, 2015; Snow et al., 2019).

3.2.3.2 Geometry of single tracks

The formation of a single track proceeds along the scanning direction of the laser beam. The set of process parameters for the employed powder defines the morphology of the single track. Key features that are used for single tracks' characterization are the shape of the tracks and their geometric dimensions. From the top view without cross-sectioning, tracks can be evaluated as having one or more of the following characteristics: (a) continuous and uniform, (b) transitional (continuous but with necking or irregularities), (c) having expressed swelling and depression zones (humping effect), (d) consisting of a chain of beads (balling effect), (e) cracks, (f) satellites, and (g) droplets near the sintered track.

The main geometrical characteristics of single tracks are width, remelted depth (or penetration depth), and height (Fig. 3.6A). The total remelted area, contact angle, and width of contact zone are also used to describe the specific features of a single track formation at different process parameters. The width of the track is strongly correlated with laser power, diameter of laser spot and scanning speed that governs the interaction time (ratio of laser spot diameter to the scanning speed). At high laser power and interaction time, the track is usually much wider than the spot size (Fig. 3.6B).

Factor analysis showed that the most influencing factors on the remelted depth of single tracks are laser power density and interaction time (Yadroitsev et al., 2012). In cases where powder layer thickness was kept constant, penetration depth increased with laser power density. In the conduction mode of L-PBF, the penetration depth is a linear function of interaction time for similar spatially averaged laser power density, i.e., the ratio of laser power to the focused laser spot area (Fig. 3.6C). Typically, in L-PBF systems, lasers with a Gaussian intensity distribution are used, where the maximum intensity is in the center. Thus, the intensity profile and hence temperature gradient will have an influence on the laser melting process. Similar to laser welding, in the L-PBF conduction mode, energy from the laser beam is enough to melt material and the penetration depth is a result of heat conduction. The melt pool has a semi-spherical shape in the cross-section and aspect ratio of depth to width of the melt pool does not exceed 1:2. With increasing laser power and interaction time (decreasing scanning speed), the melt pool starts to deepen and the transition mode of L-PBF is achieved (Fig. 3.7). At higher laser power density and low scanning speed, the temperature of the melt pool reaches boiling point and intense metal evaporation and plasma formation can occur. High energy input under the laser spot causes a vapor-filled depression zone in the processed material that leads to keyhole mode melting. A keyhole forms at a certain threshold of laser power input, which in combination with the scanning speed and melt-pool conditions leads to an unstable vapor cavity which collapses. At transition and keyhole modes, a deeper melt pool forms (Fig. 3.7). Metal evaporation controls the depth of the melt pool and its variability (Gong et al., 2014; King et al., 2014; Bayat et al., 2019; Cunningham et al., 2019).

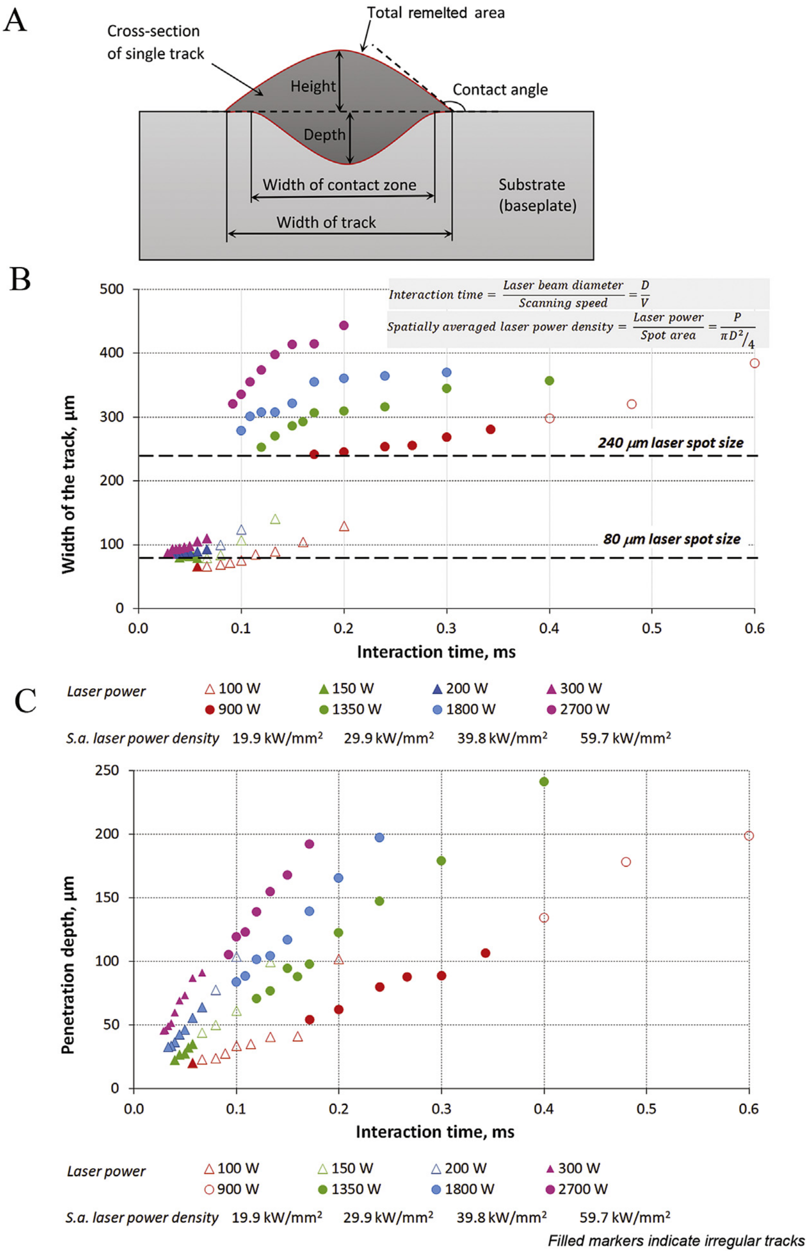

Figure 3.6 General schema of cross-section of single track (A); width (B); and penetration depth (C) of the tracks versus interaction time at different laser power density for 17-4 PH steel powder. Powder layer thickness is 50 μm. A spatially averaged laser power density is used for simplicity. *Filled markers* indicate cases with irregular tracks.
Based on data published by Makoana, N. et al., 2018. Characterization of 17-4PH single tracks produced at different parametric conditions towards increased productivity of LPBF systems—the effect of laser power and spot size upscaling. Metals 8 (7), 475. (MDPI AG). https://doi.org/10.3390/met8070475.

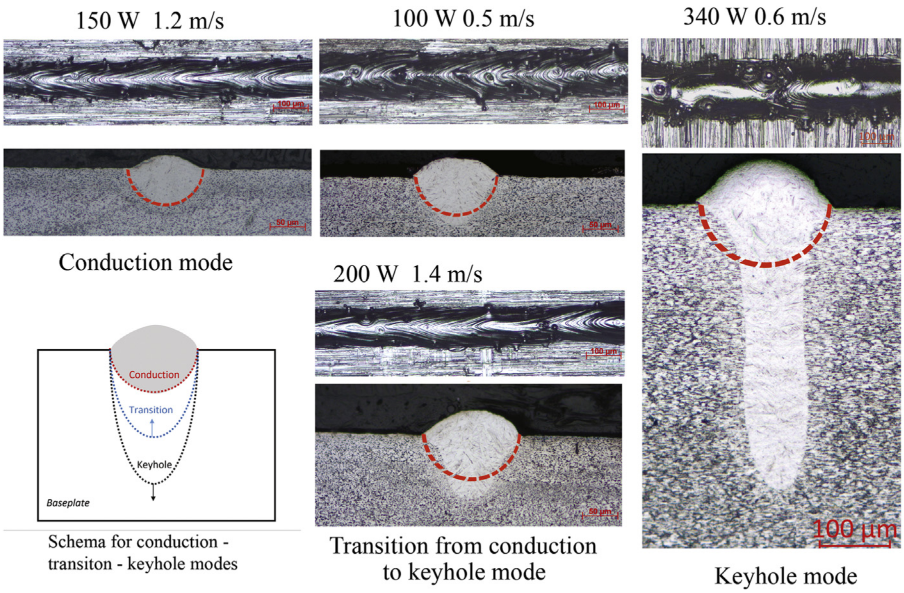
150 W 1.2 m/s
100 µm
50 µm
Conduction mode
100 W 0.5 m/s
100 µm
50 µm
340 W 0.6 m/s
100 µm
200 W 1.4 m/s
100 µm
50 µm
Conduction
Transition
Keyhole
Baseplate
Schema for conduction - transiton - keyhole modes
Transition from conduction to keyhole mode
100 µm
Keyhole mode

Figure 3.7 Top view and cross-sections of single tracks in different modes of L-PBF Ti6Al4V alloy. Powder layer thickness is ~60 µm. The *red semicircular line* shows the melt pool in a conduction mode.

The keyhole mode in L-PBF provokes extensive porosity; therefore, keyhole mode is undesirable for manufacturing 3D parts by using this technology (King et al., 2014; Gong et al., 2014; Cunningham et al., 2019; Bayat et al., 2019).

Argon and nitrogen are used as a protective atmosphere in L-PBF. They serve to protect against oxidation and to remove byproducts from the process. Ladewig et al. (2016) showed that optimization of gas flow rate can improve the removal process of spatters and condensates, thus decreasing porosity in 3D parts. Careful selection of process parameters, protection gas purity, and accurate flow regimes and pressure are required for manufacturing high-quality L-PBF parts. Special attention must be given to reused powder since its particle size distribution, morphology, chemical composition, and microstructure may be changed during the L-PBF process (Pauzon et al., 2019; Santecchia et al., 2020). In 316L and AlSi10Mg spatter particles, Simonelli et al. (2015) found oxide layers because these alloys have chemical elements with high affinity to oxygen.

Zhao et al. (2020) studied the role of base plate preheating and ambient pressure on the melt-pool behavior and single track morphology during L-PBF. It was found that these factors affect the mode of the process (conduction, transition, or keyhole) and resulting porosity formation. Preheating of the base plate is used to reduce residual stress and eliminate cracks and deformations as well as to change microstructure and mechanical properties in as-built 3D L-PBF objects, but this strongly depends on the particular material (Iveković et al., 2018; Mertens et al., 2018).

3.3 Single layer formation

3.3.1 Morphology of a single layer: Scanning strategies and hatching

Each solidified L-PBF layer is a superposition of single tracks. Its surface morphology depends on the morphology and the geometrical characteristics of individual single tracks, the scanning strategy, and the hatch distance, which is the shift between tracks in the plane of the laser beam scanning (Fig. 3.8A). The start-and-stop effect in the hatched area leads to a specific shape of the edge; the attached powder particles and irregularities deteriorate accuracy and surface quality and so contouring is often used (Fig. 3.8A and B). Different laser power and scanning speeds can be used for hatching and contour areas. Scanning strategies represent the manner of scanning of a cross-section. In a layer, different hatching patterns can be realized; the more frequently used methods are scanning by stripes, islands (chess-board) (Fig. 3.8C), or the whole cross-section is scanned without partitioning by elementary hatching patterns. In-layer patterns can vary in size as well, and can be done in a different order—randomly, or sequentially, stripe-by-stripe or island-by-island, for example. Hatching patterns always overlap to avoid porosity (Fig. 3.8B). Laser beam scanning inside each pattern can be done in one direction, zigzag (back-and-forth), spiral, or other programmed laser beam movements. Recently, fractal scanning was tested in

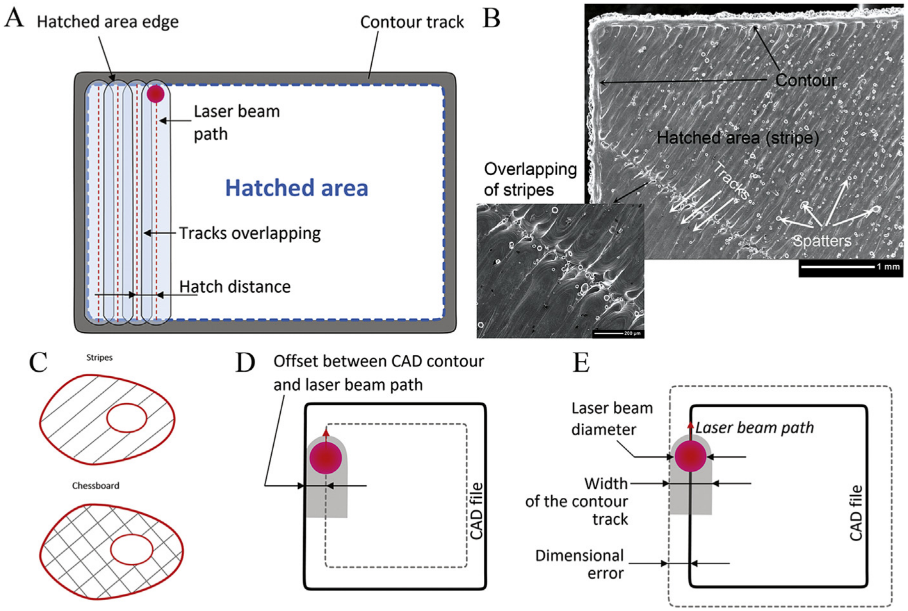
A
Hatched area edge
Contour track
Laser beam path
Hatched area
Tracks overlapping
Hatch distance
B
Contour
Hatched area (stripe)
Overlapping of stripes
Tracks
Spatters
1 mm
200 µm
C
Stripes
Chessboard
D
Offset between CAD contour and laser beam path
CAD file
E
Laser beam diameter
Laser beam path
Width of the contour track
Dimensional error
CAD file

Figure 3.8 Single layer scanning strategies: schematic of hatched area and contouring (A); top view of hatched areas with contour (B); example of scanning patterns: stripes and chessboard (C); contouring with offset (D); contouring without offset (E).

an attempt to reduced thermal gradients in L-PBF for "unweldable" nickel superalloys (Catchpole-Smith et al., 2017). Cross-sections can also be rescanned numerous times in different directions to improve the morphology of the layer. Various scanning strategies for different areas of the cross-section of the part can also be implemented depending on the design, size, and functional properties of the manufactured part. In practice, scanning strategies entail much more than just the pattern or path followed by a laser beam, as it scans the powder bed. For example, the implementation of a specific scanning pattern may include varying lengths of scan tracks, changing the exposure strategy with regards to the number of times the laser passes over one layer, changing the orientation of the scan tracks between layers, etc. Scanning strategy is important in terms of reducing temperature gradients, distortions, residual stress, porosity, and improving accuracy (Dong et al., 2018; Zhou et al., 2020).

3.3.2 Contouring, offset, and skywriting

The beginning-end effect of single tracks and the changing direction of the laser beam or path (when the laser beam accelerates/decelerates and turns around) has an influence on the melt-pool size and morphology of single tracks. In single layers and 3D parts this leads to edge and corner effects where rough and irregular surfaces may occur. To decrease edge ridges and corner effects, Matache et al. (2020) recommend to optimize laser power and scanning speed, as well as to scan top layers several times with lower linear energy input.

In a mirror-based laser scanning system for L-PBF, mirrors accelerate and decelerate in turning points which can be one possible reason for overheating and keyhole porosity. A skywriting option, incorporated in L-PBF EOS systems, shuts off the laser beam when the scanner is positioning the beam for scanning so that powder material does not melt during positioning.

An important feature of the layer scanning strategy which deserves special attention is contour scanning of the edges of the L-PBF component. Pre-contouring (scanning the contour of the part before hatching) or post-contouring (after hatching) can be used to improve in-plane (XY) accuracy and surface roughness. Different scanning parameters can be used for contouring (Fig. 3.8D and E). Since the melt pool is bigger than the laser spot size, the laser beam has to be offset from the edges of the scanned cross-section to compensate for this difference and to provide accurate dimensions of the part to be manufactured. A special "power profile strategy" that adjusts the laser power depending on the position of the laser scanning was proposed by Martin et al. (2019) to mitigate keyhole defects near the edges.

Skywriting, contour, and hatch offset options, as well as special strategies that can be realized in modern L-PBF equipment, significantly improve component manufacturing accuracy and can avoid defects (Tang et al., 2004; Yeung et al., 2017).

3.3.3 Characterization of a single layer

The powder layer thickness for the first and further layers in L-PBF is different and is defined as a combination of the distance moved by the build platform in the

Z-direction (nominal “set value” layer thickness) and the thickness of the previously processed layer. Considering the apparent density of a loose powder layer (about 50%) (Yadroitsev, 2009; Wischeropp et al., 2019), and Z movement of the build platform, the actual powder layer thickness after deposition of several layers during the L-PBF process will be higher than the Z distance of the movement of the build platform (Fig. 3.9). Thus, if the 3D sample is to be manufactured at 30 μm Z movement of the build platform, experiments with single tracks and layers are frequently conducted at 50−60 μm powder layer thickness in order to have similar actual powder layer thickness as in the manufacturing process of a 3D object (Vilardell et al., 2020).

The hatch distance is often associated with the size of the focal spot of the laser beam since the spot size and laser power play a decisive role in the shape and size of the melt pool and, accordingly, in the geometric characteristics of the single tracks. In practice, the track shape, its width, and penetration depth must be considered to find the optimum hatch distance.

During scanning of the powder, the amount of powder material involved in the track’s formation process varies from scan to scan. As was mentioned in the previous section, the denudation zone of powder is broader than the solidified track (Fig. 3.10A and B). As in shown in Fig. 3.10C and D, the denudation zone diminishes with the scanning of the second track, since the powder volume involved in the laser melting process is reduced. In laser scanning with overlapping, one part of the melt pool is solidified in contact with the previous solidified track, and the other part of the melt pool only has contact with the bare substrate and a small amount of powder. Therefore, the first track is always larger than the subsequent tracks during the sequential scanning process. The geometrical characteristics (height, width, even remelted depth, Fig. 3.10E and F) of the next tracks are different from each other and the layer has a regular repetitive morphology. The shape of single tracks and their geometrical features vary with processing of a single layer, thus defining the morphology of the single layer.

Nonuniform thickness of the deposited powder layer can also influence the morphology of single tracks and single layers (Fig. 3.11). It could be critical for the density of the 3D object: if there is insufficient laser energy to remelt the thickest powder layer, the balling effect starts, which provokes porosity formation.

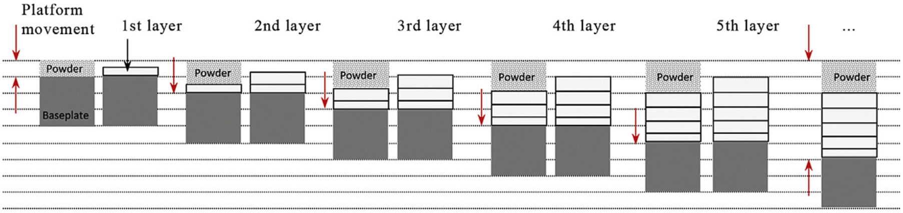

Figure 3.9 The relationship between the build platform movement, powder layer thickness delivered, and solid layer thickness considering the “shrinkage” of powder material during L-PBF process.

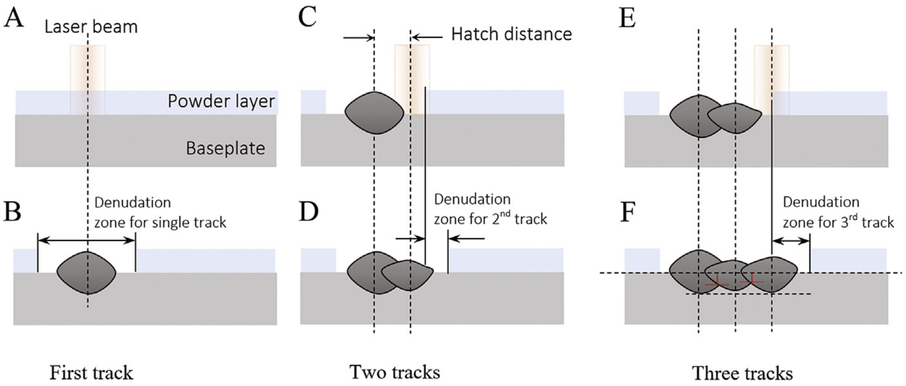
A
Laser beam
Powder layer
Baseplate
B
Denudation zone for single track
C
Hatch distance
D
Denudation zone for 2nd track
E
F
Denudation zone for 3rd track
First track
Two tracks
Three tracks

Figure 3.10 Scheme of track-by track manufacturing of single layer: laser beam scans first track (A); solidified single track and its denudation zone (B); scanning of second track and reduction of denudation zone (C, D); third track is scanned by laser beam (E) and denudation zone increases (F).

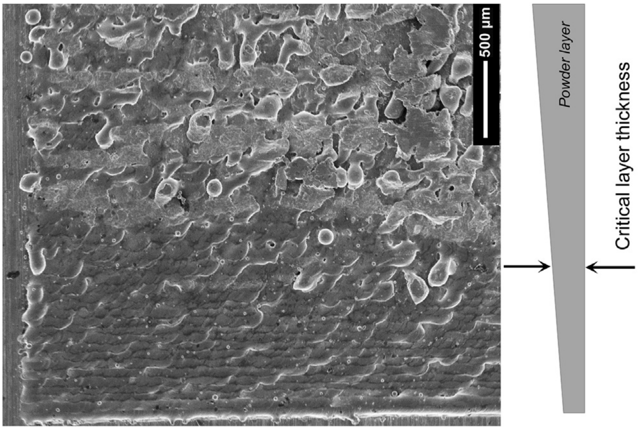
500 μm
Powder layer
Critical layer thickness

Figure 3.11 Increasing layer thickness (wedge-shaped, from 50 to 400 μm) has resulted in significant balling effect and irregular layer with open cavities.

The surface morphology after laser melting includes peaks and valleys, attached powder particles and droplets, i.e., spatters (Fig. 3.8B). For the characterization of L-PBF parts, the surface roughness, waviness, deviation from prescribed dimensions, presence of spatters and surface pores have to be analyzed. If a single layer was built with nonregular tracks or with nonoptimal hatch distance, the surface has irregular morphology. For characterization of a single layer, SEM images, optical 3D measurement techniques, and CT scans are often used. The balling effect, cracks, and overlapping can be identified on the top view; CT scans and cross-sections help to find internal porosity and other defects.

When a rescanning strategy is used, the thermophysical conditions of the process are different during the second laser pass: the laser beam interacts with only solid material. In solid material, the absorptivity, reflectivity, thermal conductivity, and heat transfer are not the same as for the powder material and the geometrical characteristics of the tracks differ. In the formation of a single layer, multiple interconnected physical phenomena take place and changes in process parameters or scanning strategy can trigger other morphology of the sintered layer and formation of defects such as porosity, high roughness, etc.

3.4 Thin wall formation

A thin wall can be defined as an object consisting of single tracks superimposed on each other in the vertical direction (Z-axis). Thus, a thin wall can be considered as a single layer manufactured in the vertical direction. Supports that are widely used in the manufacture of L-PBF parts or lattice structures for light-weight and unique applications often have dimensions at this scale. Thin walls may also act as indicators of the manufacturing quality for fine features, for a given set of process parameters. Therefore, a discussion of the peculiarities of the formation of thin walls is useful.

Fig. 3.12 shows the surface of single-pass thin walls fabricated at a laser power of 50 W and a spot size of 70 μm, with a gradual increase in the layer thickness from 40 to 80 μm with a step of 10 μm for each of 20 layers (Yadroitsev and Smurov, 2011). This experiment was done for understanding how layer thickness influences the morphology and defects in thin walls. Over the whole range of layer thicknesses there are many powder particles and droplets attached to the surfaces of the walls. The thin walls have no pores up to a scanning speed of 0.12 m/s for the selected range of layer thicknesses. At 0.14 m/s and layer thickness of >70 μm, small irregular pores appeared because the balling effect had started. With an increase in the scanning speed, pores became regular and larger, and they appeared at a lower layer thickness. The pores are elongated in the vertical (building) direction. On a smaller layer thickness (40–50 μm), the surface of the wall is less wavy (Fig. 3.12I and J), since the structure of the solidified track is thinner (the height of the track is smaller and the remelted depth into the underlying track is bigger). In the top view (Fig. 3.12K), a significant balling effect is visible starting at a scanning speed of 0.14 m/s.

Miranda et al. (2019) showed that powder particles attached to the surface of thin walls are highly influential on surface roughness and dimensions of the walls. Z. Li et al. (2018) found that scan length has an influence on the accuracy of thin-wall production. If the thin wall consists of more than one pass, its orientation relative to the scan tracks has an influence on the topology of the thin walls (Calignano et al., 2018).

When a complex specimen consists of thin walls, the surface topology is quite different: there are smooth areas and extremely rough regions. Boegelein et al. (2016) suggested that the protective gas flow and turbulence can be responsible for these phenomena. It needs to be noted that when a part has a rough surface, the recoating blade can start to make contact with the specimen that increases the risk of

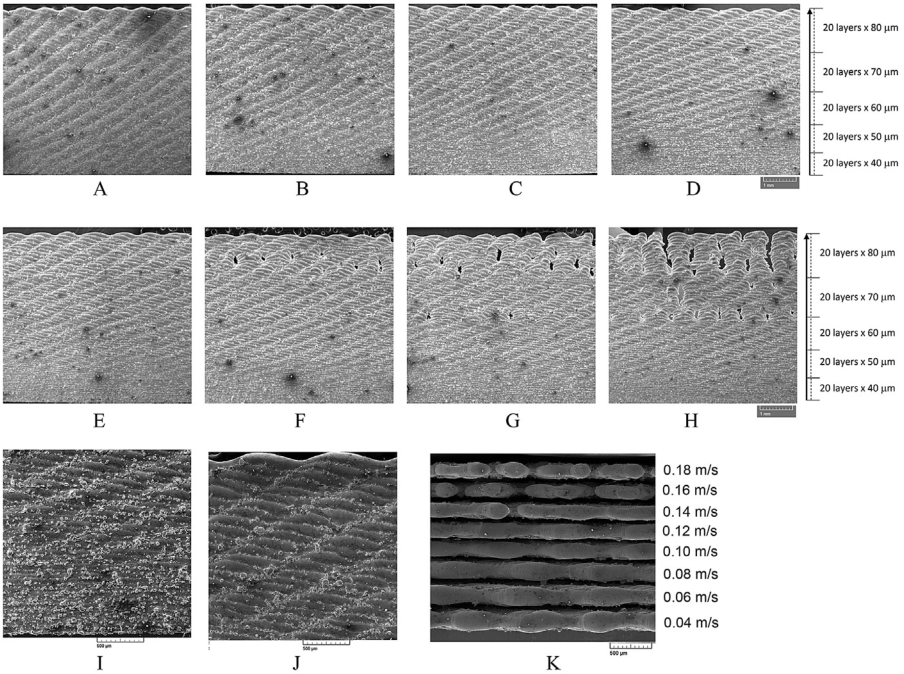

Figure 3.12 Lateral view (A—J) on SS grade 316L powder one-pass vertical thin walls manufactured at 50 W laser power and 70 µm spot size with scanning speeds of 0.04 m/s (A), 0.06 m/s (B), 0.08 m/s (C), 0.1 m/s (D), 0.12 m/s (E), 0.14 m/s (F), 0.16 m/s (G) and 0.18 m/s (H); higher magnification of thin wall at 0.12 m/s: bottom (I) and top part (J) of the specimen and top view on all thin walls (K).

distortion of the specimen, delamination is possible, and this can lead to damage of the powder deposition system. There are limitations in accuracy and surface roughness when fine components are produced such as thin walls. This has been demonstrated in numerous studies on lattice structures, where fine micro-walls and struts are decisive factors in perfecting L-PBF structures (Du Plessis et al., 2019; Lin et al., 2019; Vilardell et al., 2019; Benedetti et al. 2021).

3.5 L-PBF object formation

L-PBF provides freedom of design and allows the manufacturing of complex structures such as lattice structures, topology optimized parts, graded structures, and parts with integrated functions. However, there are some limitations and specific features typical of the powder bed fusion process, for example, the dimensional accuracy and surface finishing of the parts. Fine structures and minimum feature sizes are limited by powder material and process parameters, such as spot size, laser power, scanning speed, layer thickness, scanning strategy, etc.

A 3D component can be divided into three parts: the core part, upskin, and downskin regions. Areas that have no upper layers are called upskin; conversely, downskin has no underlying solidified layer. The inner region of the component is called the core part. For all these areas, the scanning strategy needs to be optimized. There are many possible ways of scanning: scanning the whole component with similar process parameters or scan by stripes or islands; scanning with different patterns, such as in one direction, zigzag, spiral, etc.; rescanning of the solidified layer; rescanning only specific areas; changing the scanning direction for each subsequent layer, etc. Each of the scanning strategies can be applied to achieve specific goals: to improve density, surface quality, and manufacturing accuracy; to decrease residual stress; to achieve a specific microstructure, etc. (Parry et al., 2016; Bhardwaj and Shukla, 2018; Mugwagwa et al., 2019; Valente et al., 2019). Special scanning procedures can be devised even for particular local thermal conditions, similar to a heat-treatment processing, in order to change the microstructure and hence the material properties in certain areas of the manufactured part. Modern multi-beam L-PBF systems (Table 2.1, Chapter 2) can significantly expand the range of applied scanning strategies and thereby improve the mechanical properties of parts, achieve unique microstructures, and reduce the residual stresses. As will be shown in detail in Chapter 9, during L-PBF, internal stresses are high, which can cause cracks, deformation, and warping of parts; the contact area between the L-PBF part and the base plate has a high concentration of residual stress that can lead to separation of the part from the substrate and deformation during processing (van Zyl et al., 2016).

Side surfaces of L-PBF parts always make contact with powder material, so these surfaces often show many attached powder particles and pronounced layered structure. The layer-by-layer L-PBF process results in the surface quality being different in the vertical (between layers, Z-direction) and horizontal directions (in-layer, XY direction). The powder material and the track-by-track, layerwise nature of L-PBF govern the surface topology of L-PBF parts (Strano et al., 2013b; Charles et al., 2019). In Fig. 3.13, an L-PBF semi-sphere is shown with expressed stair-step effect (see Chapter 7); higher magnification with SEM shows hatched areas and contours, as well as attached powder particles.

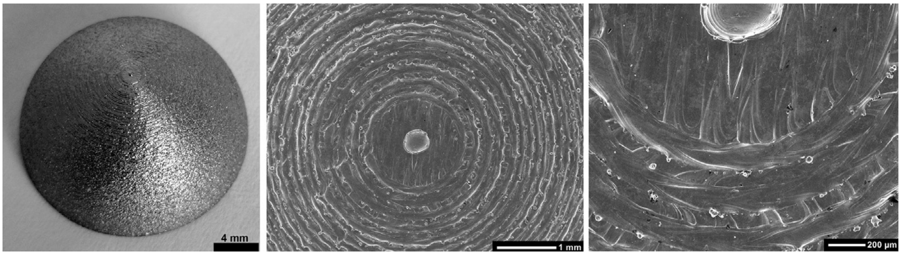

Figure 3.13 L-PBF semi-sphere at different magnifications.

Upward (upskin) and downward (downskin) surfaces are different in L-PBF, and frequently downskin is rougher and has poorer surface quality in comparison with upskin: tracks manufactured on loose powder differ in morphology and size from tracks that have contact with solid surface (previously solidified layer). To improve surface quality, upward surfaces can be rescanned several times with a special pattern similar to laser polishing, while side and internal surfaces require special post-processing surface finishing (see Chapter 12 on post-processing).

Powder from external surfaces of a 3D object can be removed with compressed air, ultrasonic bathing, mechanically, with chemical reagents, plasma and electrochemical methods, etc. However, for lattice structures and parts with small channels with complex shape, powder cleaning presents a real problem that limits applications of powder bed fusion manufacturing. Recently, Hunter et al. (2020) tested a vacuum-boiling powder removal process and found that this method is suitable for cleaning U-shaped L-PBF channels.

The manufacturing of overhang components and bridges require special methods and optimization because distortions and dross formation can occur (Fox et al., 2016; Chen et al., 2017; Han et al., 2018). Strictly speaking, the use of the term “dross” in L-PBF is not entirely correct because by definition in metal processing, a dross is a metal contamination, i.e., mixture of solid impurities, most often oxides and nitrides, rather than pure alloy. On the other hand, the term *dross* is also used in the sense of unwanted material forms on the surface of processed metal. The dross looks like a “coat” thus resembling a highly irregular L-PBF overhanging surface with irregularly solidified melt pool and agglomeration of partially melted powder; so this phenomenon is often called the dross formation in L-PBF.

Taking into account that objects of complex shapes can contain elements that are at an angle to the base plate, when the critical angle of the surface to vertical axis exceeds 45 degrees, it is obvious that supports or special self-support strategies of manufacturing should be used. It is also worth noting that during manufacturing, supported overhanging parts have different cooling rates compared with unsupported components; this influences the microstructure and mechanical properties, as shown by Kajima et al. (2018). Bobbio et al. (2017) noted that areas with high residual stress can be determined by thermomechanical simulations of the process and an optimal support type with sufficient strength can be chosen for further manufacturing. Optimization and minimization of support structures improve process efficiency, reduce deformation, and improve quality of L-PBF components. Supports in L-PBF is a system of thin walls, pins, and cellular structures that serve several purposes: for heat dissipation, to fix the part, to stiffen the structure, and to resist deformation and bending of the parts during the manufacturing process, and should also provide a convenient and simple separation of the finished part from the base plate. L-PBF makes use of specialized software tools that can generate different types of supports and allows for the selection of certain configurations to change the type of supports and size of their contact zone with the part. Comprehensive analysis of design for L-PBF, supports and orientation of the overhanging components were done by Calignano (2014); Strano et al. (2013a); D. Wang et al. (2013); Schnabel et al. (2017).

3.6 Optimization of L-PBF process parameters

3.6.1 Where to begin?

In practice, most commercial L-PBF systems have preset optimized process parameters for specific materials and powder sizes. However, ideally optimization or refinement of the parameters should be performed for every new material used.

Optimization of process parameters can start from numerical simulations. Basic physical processes in the area of the interaction of a laser beam with a powder material, as described in Chapter 4 “Physics and modeling,” shows the complexity of the L-PBF process. Theoretically, an advanced numerical model can be created that takes into account the existing L-PBF system with certain spot size, the range of laser power, and scanning speed as well as the powder material that has a specific particle size distribution, protection atmosphere parameters and flows, etc. An advanced model, which includes absorption, reflection, conduction and convection, evaporation and emission of material, chemical reactions, radiation phenomena, fluid flows, solidification, etc., would be most accurate for calculating temperature fields and the solidification process during L-PBF. However, this would require large computing resources and unique calculation methods, which are currently not implemented even in leading scientific institutions dealing with L-PBF. Currently, there are multiscale approaches to simulation of the L-PBF process: particle-scale or mesoscopic-scale simulations that simulate single track/single layer manufacturing and part-scale or macroscale modeling (King et al., 2015; Zhang et al., 2018).

3.6.2 Numerical simulations of single tracks

The first step in optimization of process parameters can be numerical simulations of single tracks on the substrate without powder material, as suggested by Yadroitsev et al. (2015), Fig. 3.14. This approach makes it possible to roughly estimate what laser power and scanning speed for a given diameter of the laser beam can be used to melt the material. A simple conduction model can be useful to preliminarily establish the relationship between input process parameters and geometry of the melt pool. Based on numerical simulation, the size of the melt pool and heat-affected zones can be estimated at different laser powers, spot sizes, and scanning speeds. These parameters ideally correspond to the range of capabilities of the L-PBF system that is selected for experiments.

DebRoy et al. (2018) recommend using nondimensional numbers, such as Peclet, Marangoni, Fourier numbers, and nondimensional heat input, for a comprehensive understanding of the AM process stability, structure, defects, and properties of the AM parts.

Yadroitsev (2009), Guo et al. (2019), and D. Wang et al. (2012) suggested using linear energy input (the ratio of laser power to scanning speed, P/V), spatially averaged laser power density ($P/\pi d^2$), and energy input per unit time ($P/\pi d^2 V$) to predict the status of keyhole or conduction mode in the process of laser melting, or to predict the different types of morphology of single tracks.

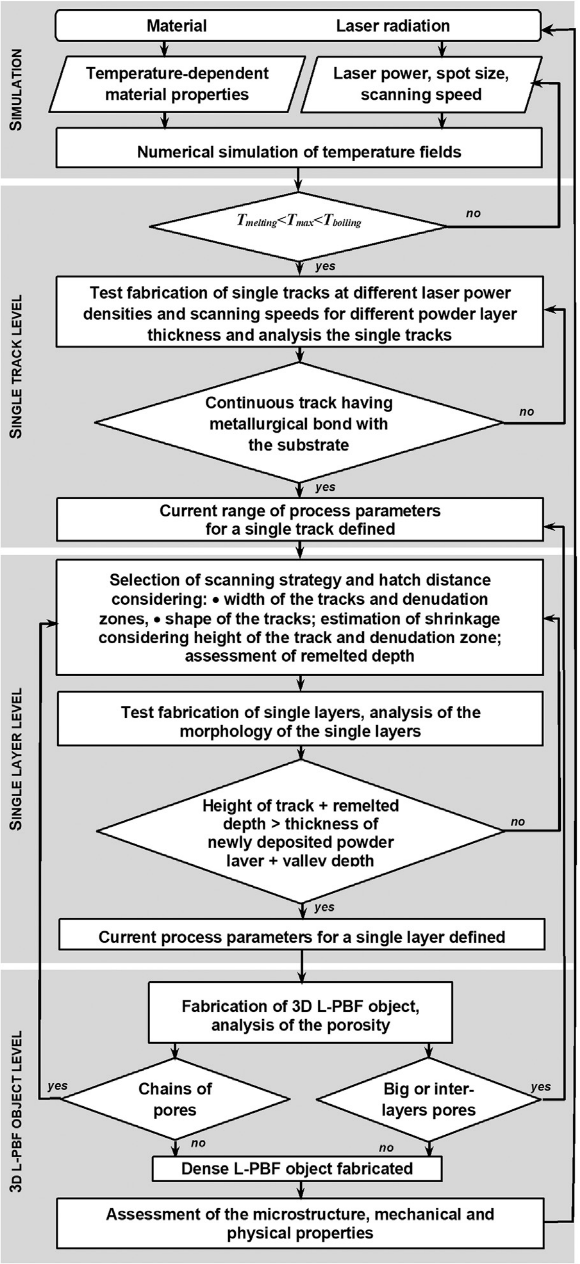
SIMULATION
Material
Laser radiation
Temperature-dependent material properties
Laser power, spot size, scanning speed
Numerical simulation of temperature fields
SINGLE TRACK LEVEL
$T_{melting} < T_{max} < T_{boiling}$
no
yes
Test fabrication of single tracks at different laser power densities and scanning speeds for different powder layer thickness and analysis the single tracks
Continuous track having metallurgical bond with the substrate
no
yes
Current range of process parameters for a single track defined
SINGLE LAYER LEVEL
Selection of scanning strategy and hatch distance considering: • width of the tracks and denudation zones, • shape of the tracks; estimation of shrinkage considering height of the track and denudation zone; assessment of remelted depth
Test fabrication of single layers, analysis of the morphology of the single layers
Height of track + remelted depth > thickness of newly deposited powder layer + valley depth
no
yes
Current process parameters for a single layer defined
3D L-PBF OBJECT LEVEL
Fabrication of 3D L-PBF object, analysis of the porosity
yes
Chains of pores
Big or inter-layers pores
yes
no
no
Dense L-PBF object fabricated
Assessment of the microstructure, mechanical and physical properties

Figure 3.14 Hierarchical approach for optimization of L-PBF process parameters.
Modified version from Yadroitsev, I., Krakhmalev, P., Yadroitsava, I., 2015. Hierarchical design principles of selective laser melting for high quality metallic objects. Addit. Manuf. 7, 45–56. (Elsevier B.V.) https://doi.org/10.1016/j.addma.2014.12.007

An empirical methodology with nondimensional numbers was used by Hann et al. (2011) for predicting laser-weld quality based on material properties and laser parameters taking into account surface enthalpy ΔH and ratio of $\frac{\Delta H}{h_s}$ (i.e., normalized enthalpy):

$$\Delta H = \frac{A \times P \times C}{\rho \sqrt{r^3 \times \alpha \times V}}$$

where A is the absorptivity of the surface, P is laser power, C is a dimensionless constant, r is half-width of Gaussian beam at surface, V is speed of weld (laser scanning speed), ρ, α, and h_s are material density, thermal diffusivity, and the enthalpy at melting temperature, correspondingly. This approach was used recently by Martin et al. (2019) for description of the dynamics of pore formation during the L-PBF process. Based on numerical simulations, analytical approach, and experimental results it was found there was a linear dependence between the local normalized enthalpy at the material surface and vapor depression depth. Keeping normalized enthalpy below transition point, a pore formation mitigation strategy was proposed. A similar approach with threshold values of normalized enthalpy to detect conduction-to-keyhole transition was recently done by Forien et al. (2020). It was shown that increased normalized enthalpy corresponded with an increase "in the number of pores, likely caused by keyhole instability."

To simulate the L-PBF process with a powder material, the equivalent properties of material (density, specific heat capacity, thermal conductivity) are frequently used (Gusarov and Smurov, 2009). But numerical simulations of balling or humping effects, for example, require complex models with powder material and involvement of radiation transfer, thermal processes in a dispersed system, coalescent models for the formation of a melt pool from a powder, i.e., particle-scale simulations, or mesoscopic scale simulations (Körner et al., 2011; Liu et al., 2016, 2020). Models with fluid flows in the melt pool, evaporation, and the effects of the recoil pressure are more precise, since they permit simulated spatter generation, keyhole mode, denudation effect, etc. (Ly et al., 2017; Wu et al., 2018; Yuan et al., 2020).

Simulations of temperature fields and final solidified L-PBF track morphologies were recently performed by Cao (2019) where the adopted normal distribution of powder particles was used. Q. Tang et al. (2020b) introduced a high-fidelity powder scale model to simulate the formation mechanisms of irregularities and porosity inside the tracks. It was shown that the wetting behavior of the melt pool influences the single track's discontinuity and irregularities. Powder-level numerical simulation is a powerful instrument for understanding phenomena in L-PBF and influencing parameters. These parameters are used directly to estimate the threshold thickness of the powder layer, possible formation of pores due to metal evaporation, and for prediction of phase transformation in the heat-affected zone. In addition, the possibility of preheating the substrate, the substrate material itself, the properties and parameters of the protective atmosphere (Masoomi et al., 2018), the size of the powder, and much more must be considered.

3.6.3 Optimal process parameters for single tracks

Different designs of experiments can be performed to find optimal process parameters for single tracks such as full factor analysis or orthogonal designs (Yadroitsev et al., 2012; Ciurana et al., 2013; Aversa et al., 2018). For this, critical factors have to be chosen such as laser power, spot size, scanning speed, powder layer thickness, etc. A targeted response is a morphology of single tracks and their geometric characteristics.

First, it is highly recommended to conduct a pilot study even without powder if similar material is used as the substrate. This helps with choosing the range of laser power and scanning speeds and to evaluate numerical simulations. The next step is to experiment with powder material. Powder layer thickness has to be based on the particle size distribution of the employed powder. A well-levelled base plate as well as a homogenous powder layer will provide stable results. Special attention should also be paid to the range of values of the influencing factors. A choice of a very wide or, on the contrary, a very narrow range of values for one or several parameters may lead to incorrect conclusions about the influence of factors. For example, when choosing a scanning speed of 0.1−3 m/s (wide range) and laser power 100−120 W (narrow range), of course the most influencing factor will be scanning speed, thus, appropriate values have to be chosen.

In pilot experiments there is no need to vary everything at once: a layer thickness and laser power can be fixed, and only vary the scanning speed, as was done by Yadroitsev et al. (2015). To investigate the influence of laser scanning speed on a single track's quality made of AISI 420 steel, the single tracks were fabricated by the laser beam with 50 W power at scanning speeds ranging from 0.08 to 0.16 m/s and a deposited powder layer thickness of 50 μm. At the selected scanning speed range, all single tracks had good metallurgical bond with the substrate. With these parameters, single track width decreased with increasing scanning speed from 150 to 125 μm. The remelted depth also diminished with scanning speed. The scanning speeds of 0.1 and 0.12 m/s were found optimal since with these energy inputs, tracks had more stable geometrical characteristics and remelted depth into the substrate was 40−60 μm, i.e., close to the value of the deposited powder layer thickness. The following experiment can be performed with two or more factors, if needed.

Statistical factor analysis ANOVA of L-PBF process parameters has shown that geometric characteristics of continuous tracks, such as track width and remelted depth, are determined mainly by the laser power density and irradiation time (Yadroitsev et al., 2012). The height of the track is basically determined by the powder layer thickness. Scanning speed is the most flexible and easily changeable parameter in laser melting. Therefore, by fixing the laser power density, ensuring the correct layer thickness for the employed powder, and optimizing the scanning speed, stability of the tracks can be ensured. A similar approach with analysis of the tracks' morphology and geometrical features was successfully used to produce high-density components (Shi et al., 2016, 2017; Wei et al., 2017; Makoana et al., 2018; Ramirez-Cedillo et al., 2018; Gao et al., 2019; Jing et al., 2020). For each powder material there are sets of optimal process parameters. An example of a processing map for single tracks

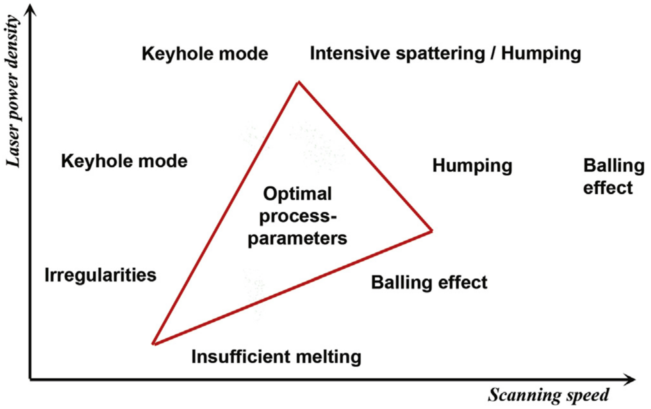

Figure 3.15 Example of processing map for single tracks.

is shown in Fig. 3.15. Usually, conductive or transition modes are used for further optimization of single layers. Higher L-PBF productivity requires maximum scanning speed with appropriate track width as well as the penetration depth providing full remelting of the previous layer.

3.6.4 Optimal process parameters for single layers

Knowledge of the geometric characteristics of single tracks determines the hatch distance, which together with the selected scanning strategy governs the quality of a single L-PBF layer. Analysis of the morphology of a single layer, in turn, is crucial for the selection of the optimal strategy for manufacturing 3D pore-free objects. Parameter optimization to produce fully dense material starts with the questions: “What scanning strategy is optimal? What hatch distance and penetration depth are optimal?” A single layer forms from single tracks and their geometrical characteristics vary when a sequence of tracks is manufactured. The scanning strategy determines the topology of a single layer; however, in some cases, it is difficult to change the scanning strategy on a specific type of equipment, since the manufacturers of L-PBF equipment have already chosen the scanning strategy that is optimal from their point of view, and to which the user can make changes only within certain limits. For example, if a “stripes” scanning strategy is chosen, then it is no longer possible to apply islands or spiral scanning strategy on this equipment.

Too large a hatch distance results in lack of fusion porosity and high roughness, since gaps between tracks are created. Too small a hatch distance can lead to low efficiency of the process; it is nonoptimal from an energy consumption point of view, it also can lead to overheating, increased number of thermal cycles, and creation of undesirable phases in the processed material that can influence the mechanical properties. Strictly speaking, the optimal hatch distance depends on the amount of overlapping of the tracks and penetration into the previous layer. So, the width and penetration depth of a single track regulate hatch distance and overlapping parameters (Yadroitsev, 2009; Shi et al., 2016; Xia et al., 2016; Mutua et al., 2018; Du Plessis, 2019). There are different approaches to the definition of the "overlapping rate" term. Dong et al. (2018) defined the overlapping rate as a percent of the remelting area of the previous track (Fig. 3.16A) and found that ~50% overlapping rate was optimal to produce dense 316L stainless steel samples with appropriate surface roughness. D. Wang et al. (2012) considered overlapping rate as the ratio of the difference between the width of a single track (w) and a hatch distance (h) to the width of the track and indicated that $(w\text{-}h)/w$ overlapping rate of 30% was optimal taking into account fabrication efficiency and stability. (Majeed et al., 2019) used a similar approach and suggested 35% overlapping rate for AlSi10Mg alloy for the best surface quality in as-built components.

In Fig. 3.16C single layer of L-PBF maraging steel powder manufactured with overlapping rates $(w - h)/w = 50\%$ and a joint remelted area of about 25%–30% is shown. This overlapping was optimal to produce 99.9% dense samples from MS1 powder material.

For full melting in the powder layer and to avoid lack of fusion porosity, a "lack of fusion index" can be used, which is the ratio of melt pool depth to layer thickness. Other criteria are based on coupled parameters—hatch distance and layer thickness,

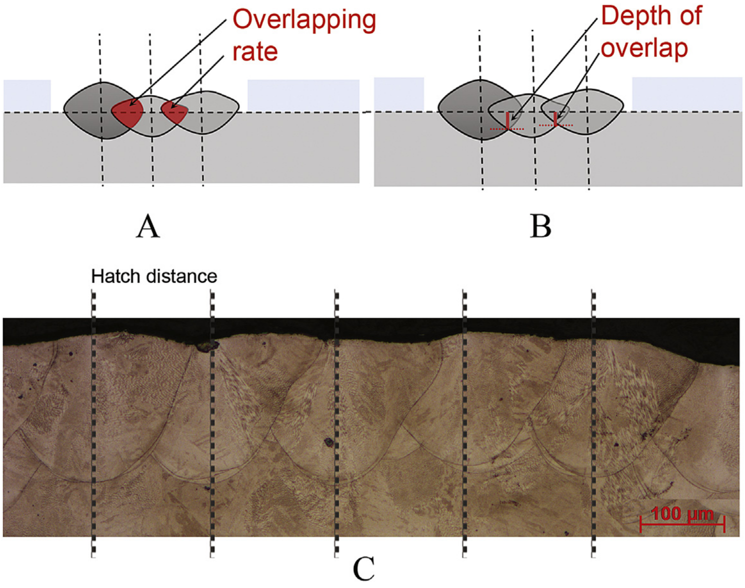

Figure 3.16 Overlapping rate based on area of joint melt pool (A); depth of overlap indicated with *red lines* (B); cross-section of single layer from maraging steel powder (C). Dashed *vertical lines* show a hatch distance.

which is called “minimum depth of overlap” (Oliveira et al., 2020). This value is the penetration depth for two shifted tracks (Fig. 3.16B). The minimal value of the depth of overlap has to be higher than the layer thickness to prevent lack of fusion porosity.

Numerous single tracks together form single layers, and multiple layers form a 3D object. It is, therefore, understandable that, due to a large number of tracks used to form a part, the quality and homogeneity of these tracks are critical in order to produce a good quality final part. When forming a single track, it is always very important to maintain a balance between the values of the different process parameters to ensure a stable and continuous track is formed. Analysis of the surfaces of single layers will assist with the identification of lack of fusion and other irregularities. For example, too many spatters attached to the surface can indicate excessive energy input, while well-melted, regularly overlapped tracks forming the surface make it possible to safely assume that the 3D sample will be completely dense and have a minimum number of pores.

Layer-by-layer manufacturing of a 3D sample by L-PBF has some peculiarities when compared with the production of a first single layer. The first layer is manufactured on the substrate with predetermined low roughness. The first solidified layer has a certain regular morphology with higher roughness than the base plate. Surface irregularities in the solidified layer lead to uneven thickness of the following powder layer. In order to decrease repetitive accumulation of these kinds of faults, the scanning direction in each single layer can be turned (rotated) relative to the previous layer, or rescanning of each layer can be done. Another approach is to use a thinner powder layer or to choose optimal process parameters for single layers found for higher laser power. This approach is shown in detail in Yadroitsev et al. (2015). It should also be noted that there may be several possible optimal sets of parameters for different combinations of laser power, powder layer thickness, and scanning speed, which ensure a high quality of single tracks, layers, and, finally, L-PBF parts.

3.6.5 Optimal process parameters for 3D parts

The primary challenges for L-PBF parts are porosity, residual stress, roughness, and the specific microstructure of as-built components, inherited from rapid cooling and layer-by-layer manufacturing from powder material. Therefore, optimization of 3D L-PBF parts includes different aspects: dimensional optimization of whole parts and specific fine features; optimization of surface quality, microstructure, and mechanical properties; manufacturing fully dense objects, i.e., maximizing density.

Many authors use an “integral” parameter, such as volumetric energy density, to optimize process parameters. This parameter is defined as follows: the ratio of laser power to the product of scanning speed, layer thickness, and laser spot diameter, or ratio of laser power to the product of scanning speed, hatch distance, and powder layer thickness (Ciurana et al., 2013; Carter et al., 2016; Arısoy et al., 2017; Caiazzo et al., 2020; Kuo et al., 2020; Zhou et al., 2020). This value per se is in reality not an appropriate metric to quantify the morphology and behavior of single tracks and layers, porosity, microstructure, and mechanical properties of 3D L-PBF components as was clearly shown by Scipioni Bertoli et al. (2017), Prashanth et al. (2017), Salman et al. (2019), Shipley et al. (2018), and Calignano et al. (2018) on different materials. It is necessary to clearly understand that it is impossible to simply indicate the value of the energy density; it is also necessary to indicate the values of the constituent parameters and how and within what range they changed. Often one or more parameters are fixed and the effect of laser power, scanning speed, layer thickness, hatch distance, and their multifactor relationships with properties of 3D parts are studied separately. The range of factors and their limits also influence the results. The same volumetric energy density values can be obtained, for example, by reducing/doubling the layer thickness or reducing/doubling the scanning speed. Since the parameters “layer thickness” and “scanning speed” have different effects on the process formation of tracks during L-PBF, the results at the same energy density will be different. Also, the same volumetric energy density value can be obtained using a laser spot size of 50 microns or 500 microns (by changing the laser powder for example to match the spot size), but the melting conditions in terms of penetration depth, melt-pool size, etc., and resulting properties of the parts produced under these different process parameters will be entirely different. Therefore, volumetric energy density should be used with caution when referring to process optimization.

One of the ways to optimize parameters is a hierarchical approach: optimization of single tracks—layers—3D parts, as recommended by Yadroitsev et al. (2015). Other researchers start directly from manufacturing 3D samples omitting the analysis of single tracks and layers at different process-parameters: some parameters are kept constant, while others change. For example, hatch distances and powder layer thickness are kept constant, and the 3D samples are built at different laser power settings and scanning speeds. Following from this, nondestructive testing and cross-sectioning estimate the porosity in the manufactured samples; thus, the sets of laser power and appropriate ranges for scanning speeds for production of solid, nonporous samples can be selected.

Experimental design, such as factorial design, Taguchi method, and response surface methodology and their combinations are used to find correlations between input process parameters or strategies and output part parameters such as density, accuracy, surface roughness, mechanical properties, etc. G. Wang et al. (2020) used Taguchi-response surface methodology to optimize the process parameters of L-PBF nickel-based superalloy. Bai et al. (2018) used a central composite design of experiment with a response surface method to evaluate density, microstructure, and mechanical properties of Al alloy. Input parameters were laser power, scanning speed, and hatch distance. A multiple linear regression model for density was done and it was shown that the most influential factor on the resulting density is laser power, and interaction of scanning speed and hatch distance. On the basis of these data, optimal process parameters were found and solid samples were manufactured. A response surface methodology was also used by Terner et al. (2019) for optimizing the process parameters for manufacturing solid samples by varying scanning speed and laser power. Full factor ANOVA analysis and regression models were used by Majeed et al. (2019) to improve the surface quality of AlSi10Mg samples. The processes of optimization for surface roughness and for nonporous 3D samples are essentially similar, but there are some minor differences. For example, a solid, nonporous sample can be made from thick layers of powder, but the resulting surface roughness will be much higher compared to using a thin layer of powder. In-layer roughness can be eliminated by using a rescanning strategy with smaller hatch distance.

Nguyen et al. (2020) successfully used a deep neural network not only to build fully dense samples but also to maximize productivity, defined as material volume created over time, that is, the product of scanning speed, hatch distance, and layer thickness. Brika et al. (2017) proposed an integrated approach by developing software to determine optimal build orientation, mechanical properties, surface roughness, support structure, build time, and total cost.

While optimization is often performed with simple geometries such as cubes, it should not be forgotten that L-PBF allows the production of complex parts. Therefore, optimization of design and build strategy, including positioning and orientation of parts on the base plate, optimization of supports, and reduction of residual stresses require careful research. The multifactor optimization algorithms realized in the Genetic Algorithm, Genetic Programming, Evolutionary Programming, Simulated Annealing, and Particle Swarm Optimization and Ant Colony Optimization are used for AM at the present time. A comprehensive discussion on evolutionary algorithms in AM was presented by Leirmo and Martinsen (2019).

L-PBF process parameters and scanning strategy have an influence on values, distribution, and direction of residual stresses, as shown in Buchbinder et al. (2014), Yadroitsev and Yadroitsava (2015), Robinson et al. (2019), Robinson et al. (2018), Zaeh and Branner (2010), and Song et al. (2018). Peter et al. (2020) used various software available commercially and compared numerical simulations with experimental results on distortions of L-PBF specimens caused by residual stress. It was shown that different software types have advantages and disadvantages, and currently there is no comprehensive software to simulate prediction of distortion during L-PBF, but software capabilities develop rapidly. It was also noted that results were received for a specific material and system, so it should not be generalized for other materials or other additive manufacturing process. Residual stresses in L-PBF require special investigation and will be described in detail in Chapter 9 “Residual stress in laser powder bed fusion”.

It was shown that preheating of the base plate is efficient for crack prevention, phase transformations, and changing microstructure of L-PBF parts, but each material showed its own specific behavior (Li et al., 2016; Mertens et al., 2018). It should be noted that there is a whole class of alloys, for example, intermetallic alloys or tungsten, which are prone to cracking in the L-PBF process from high thermal gradients. These alloys have remarkable mechanical properties when produced carefully crack-free. To reduce thermal gradients, heating of the substrate or surface of the powder layer is used up to 1000°C (Müller et al., 2019; Polozov et al., 2020). Heating helps to avoid or minimize the process of cracking; however, it imposes restrictions on the complexity of the internal structure of the part, since the powder begins to sinter due to the high preheating temperature and long production time; it will be impossible to evacuate it from the internal cavities and channels. For this class of materials, heating is an important parameter that also needs to be optimized.

Build orientation on the base plate, type, and quantity of support structures and preheating of the powder bed during manufacturing determine the build strategy—exactly how the sample is manufactured. Properties of components, even those produced from similar powder material, depend on the process parameters, scanning and build strategies, as was shown by Olakanmi et al. (2015), Schmidt et al. (2017), Salman et al. (2019), Higashi and Ozaki (2020), Pal et al. (2020), and Balbaa et al. (2020). Vertical, horizontal, and inclined channels inside L-PBF parts can have different diameters and dimensional deviations when using the same process parameters (Hassanin et al., 2018). Special approaches are used for manufacturing internal cavities: they can be produced with supports or with a special shape (tear-shape) to avoid requirement for supports. Leutenecker-Twelsiek et al. (2016) recommend a special procedure to determine optimal part orientation on the base plate by early stage design: decomposition of complex parts to elements, analysis of each element taking into account the best orientation, then consider the relevance of elements for part orientation and finally, adapt elemental designs to the whole part.

3.7 Conclusions

In this chapter, the processes of forming single tracks, single layers, and 3D L-PBF objects were discussed in detail, as well as different approaches for optimizing the process parameters. To obtain a stable and continuous single track it is necessary to find the optimal laser power, laser spot size, and scanning speed. Moreover, for different materials and different thicknesses of the powder layer, an individual set of parameters with different values is required. The initial thickness of the powder layer corresponds to the particle size distribution. However, it should be remembered that the actual thickness of the powder layer after deposition of several layers is approximately double the distance of the movement of the build platform in the Z-axis. This is due to the fact that the thickness of the powder layer in L-PBF for subsequent layers (after the first layer) depends both on the distance moved by the build platform in the Z-direction (nominal layer thickness) and on the thickness and morphology of the previously processed layer, which is subject to the effect of solidification shrinkage and depends on the uniformity of the powder deposition and powder packing density.

The geometric characteristics of the single tracks influence the subsequent selection of hatch distances and scanning strategies. The choice of hatch distance and scanning strategy determines the morphology of the layer, which in turn affects the thickness, regularity, and continuity of the subsequent layers. The high quality of the single layer should guarantee that the thickness of the next deposited powder layer does not vary greatly, preventing further irregularity and balling effect. Thus, it has been convincingly shown that for powders with a certain particle size distribution there is correlation between the energy input parameters and the selected layer thickness.

Both numerical simulation of the temperature fields of parts and analysis of the resulting porosity and pore shapes in manufactured parts can provide comprehensive information for determining the optimal process parameters to produce nonporous 3D L-PBF objects. Since the temperature distribution and the cooling rate determine the microstructure of the material obtained in the L-PBF process, numerical simulation also allows the estimation of the optimal conditions for manufacturing L-PBF objects with the desired microstructure and mechanical properties.

3.8 Questions

- What are process parameters in L-PBF?
- How is a single track formed?
- What is the denudation zone? What factors influence its formation?
- What is spattering in L-PBF? What kinds of spatter particles exist?
- What are satellites?
- What are balling and humping effects in L-PBF? Give reasons for these phenomena.
- How does powder layer thickness and scanning speed influence the stability of single tracks?
- What is the difference between keyhole, transition, and conduction modes in L-PBF?
- Why does keyhole mode and balling provoke porosity in 3D parts?
- Why is a homogenous layer important for track stability?
- What is a hatch distance? How is it connected to the geometry of single tracks? What is overlapping rate?
- How does layer thickness link with build platform movement and shrinkage of powder material?
- What is scanning pattern? What is contouring, offsets, and skywriting?
- Explain why geometrical characteristics of tracks vary when a single layer is formed.
- What is core part, upskin, and downskin?
- What are support structures? Why are they needed?
- Why is numerical simulation important in L-PBF? What approaches exist?
- What is a hierarchical approach to optimization of 3D L-PBF objects?
- How does energy density influence the process and quality of L-PBF parts?
- What are the main concerns in L-PBF?

Acknowledgements

The authors would like to thank the South African Research Chairs Initiative of the Department of Science and Technology and National Research Foundation of South Africa (Grant No. 97994).

References

Abedi, H.R., Gollo, H.M., 2019. An experimental study of the effects of surface roughness and coating of Cr_2O_3 layer on the laser-forming process. Optic Laser. Technol. 109, 336−347. https://doi.org/10.1016/j.optlastec.2018.07.064. Elsevier Ltd.

Arısoy, Y.M., et al., 2017. Influence of scan strategy and process parameters on microstructure and its optimization in additively manufactured nickel alloy 625 via laser powder bed fusion. Int. J. Adv. Manuf. Technol. 90 (5–8), 1393–1417. https://doi.org/10.1007/s00170-016-9429-z. Springer London.

Aversa, A., et al., 2018. Single scan track analyses on aluminium based powders. J. Mater. Process. Technol. 255, 17–25. https://doi.org/10.1016/j.jmatprotec.2017.11.055. Elsevier Ltd.

Bai, Y., et al., 2018. Process optimization and mechanical property evolution of AlSiMg0.75 by selective laser melting. Mater. Des. 140, 257–266. https://doi.org/10.1016/j.matdes.2017.11.045. Elsevier Ltd.

Balbaa, M., et al., 2020. On selective laser melting of Inconel 718: densification, surface roughness, and residual stresses. Mater. Des. 193, 108818. https://doi.org/10.1016/j.matdes.2020.108818. Elsevier Ltd.

Bayat, M., et al., 2019. Keyhole-induced porosities in laser-based powder bed fusion (L-PBF) of Ti6Al4V: high-fidelity modelling and experimental validation. Addit. Manuf. 30, 100835. https://doi.org/10.1016/j.addma.2019.100835. Elsevier B.V.

Benedetti, M., du Plessis, A., Ritchie, R.O., Dallago, M., Razavi, S.M.J., Berto, F., 2021. Architected cellular materials: a review on their mechanical properties towards fatigue-tolerant design and fabrication. Mater. Sci. Eng. R Rep. 144 (100606).

Bergström, D., 2008. The Absorption of Laser Light by Rough Metal Surfaces. Luleå University of Technology.

Bhardwaj, T., Shukla, M., 2018. Effect of laser scanning strategies on texture, physical and mechanical properties of laser sintered maraging steel. Mater. Sci. Eng. A 734, 102–109. https://doi.org/10.1016/j.msea.2018.07.089. Elsevier Ltd.

Bidare, P., et al., 2018. Fluid and particle dynamics in laser powder bed fusion. Acta Mater. 142, 107–120. https://doi.org/10.1016/j.actamat.2017.09.051. Acta Materialia Inc.

Bobbio, L.D., et al., 2017. Characterization of the strength of support structures used in powder bed fusion additive manufacturing of Ti-6Al-4V. Addit. Manuf. 14, 60–68. https://doi.org/10.1016/j.addma.2017.01.002. Elsevier B.V.

Boegelein, T., et al., 2016. Characterisation of a complex thin walled structure fabricated by selective laser melting using a ferritic oxide dispersion strengthened steel. Mater. Char. 112, 30–40. https://doi.org/10.1016/j.matchar.2015.11.021. Elsevier Inc.

Brika, S.E., et al., 2017. Multi-objective build orientation optimization for powder bed fusion by laser. Ind. Eng. Manag. 6, 236. https://doi.org/10.4172/2169-0316.1000236.

Buchbinder, D., et al., 2014. Investigation on reducing distortion by preheating during manufacture of aluminum components using selective laser melting. J. Laser Appl. 26 (1), 012004. https://doi.org/10.2351/1.4828755. Laser Institute of America.

Caiazzo, F., Alfieri, V., Casalino, G., 2020. On the Relevance of volumetric energy density in the investigation of inconel 718 laser powder bed fusion. Materials 13 (3). https://doi.org/10.3390/ma13030538. MDPI AG.

Calignano, F., 2014. Design optimization of supports for overhanging structures in aluminum and titanium alloys by selective laser melting. Mater. Des. 64, 203–213. https://doi.org/10.1016/j.matdes.2014.07.043. Elsevier Ltd.

Calignano, F., Cattano, G., Manfredi, D., 2018. Manufacturing of thin wall structures in AlSi10Mg alloy by laser powder bed fusion through process parameters. J. Mater. Process. Technol. 255, 773–783. https://doi.org/10.1016/j.jmatprotec.2018.01.029. Elsevier Ltd.

Cao, L., 2019. Numerical simulation of the impact of laying powder on selective laser melting single-pass formation. Int. J. Heat Mass Tran. 141, 1036–1048. https://doi.org/10.1016/j.ijheatmasstransfer.2019.07.053. Elsevier Ltd.

Carter, L.N., et al., 2016. Process optimisation of selective laser melting using energy density model for nickel based superalloys. Mater. Sci. Technol. 32 (7), 657–661. https://doi.org/10.1179/1743284715Y.0000000108. Taylor and Francis Ltd.

Catchpole-Smith, S., et al., 2017. Fractal scan strategies for selective laser melting of ‘unweldable’ nickel superalloys. Addit. Manuf. 15, 113−122. https://doi.org/10.1016/j.addma.2017.02.002. Elsevier B.V.

Charles, A., et al., 2019. Effect of process parameters on the generated surface roughness of down-facing surfaces in selective laser melting. Appl. Sci. 9 (6), 1256. https://doi.org/10.3390/app9061256. MDPI AG.

Chen, H., et al., 2017. Improving additive manufacturing processability of hard-to-process overhanging structure by selective laser melting. J. Mater. Process. Technol. 250, 99−108. https://doi.org/10.1016/j.jmatprotec.2017.06.044. Elsevier Ltd.

Ciurana, J., Hernandez, L., Delgado, J., 2013. Energy density analysis on single tracks formed by selective laser melting with CoCrMo powder material. Int. J. Adv. Manuf. Technol. 68 (5−8), 1103−1110. https://doi.org/10.1007/s00170-013-4902-4. Springer.

Clayton, J., Deffley, R., 2014. Optimising metal powders for additive manufacturing. Met. Powder Rep. 69 (5), 14−17. https://doi.org/10.1016/S0026-0657(14)70223-1. Elsevier Ltd.

Cunningham, R., et al., 2019. Keyhole threshold and morphology in laser melting revealed by ultrahigh-speed x-ray imaging. Science 363 (6429), 849−852. https://doi.org/10.1126/science.aav4687. American Association for the Advancement of Science.

DebRoy, T., et al., 2018. “Additive manufacturing of metallic components − process, structure and properties. Prog. Mater. Sci. 92, 112−224. https://doi.org/10.1016/j.pmatsci.2017.10.001. Elsevier Ltd.

Dong, Z., et al., 2018. Effect of hatch spacing on melt pool and as-built quality during selective laser melting of stainless steel: modeling and experimental approaches. Materials 12 (1). https://doi.org/10.3390/ma12010050. MDPI AG.

Forien, J.B., et al., 2020. Detecting keyhole pore defects and monitoring process signatures during laser powder bed fusion: a correlation between in situ pyrometry and ex situ X-ray radiography. Addit. Manuf. 35, 101336. https://doi.org/10.1016/j.addma.2020.101336. Elsevier B.V.

Fox, J.C., Moylan, S.P., Lane, B.M., 2016. Effect of process parameters on the surface roughness of overhanging structures in laser powder bed fusion additive manufacturing. Procedia CIRP 131−134. https://doi.org/10.1016/j.procir.2016.02.347. Elsevier B.V.

Gao, P., Wang, Z., Zeng, X., 2019. Effect of process parameters on morphology, sectional characteristics and crack sensitivity of Ti-40Al-9V-0.5Y alloy single tracks produced by selective laser melting. Int. J. Lightweight Mater. Manuf. 2 (4), 355−361. https://doi.org/10.1016/j.ijlmm.2019.04.001. KeAi Publishing Communications Ltd.

Gong, H., et al., 2014. Analysis of defect generation in Ti-6Al-4V parts made using powder bed fusion additive manufacturing processes. Addit. Manuf. https://doi.org/10.1016/j.addma.2014.08.002.

Gunenthiram, V., et al., 2018. Experimental analysis of spatter generation and melt-pool behavior during the powder bed laser beam melting process. J. Mater. Process. Technol. 251, 376−386. https://doi.org/10.1016/j.jmatprotec.2017.08.012. Elsevier Ltd.

Guo, M., et al., 2019. Formation of scanning tracks during Selective Laser Melting (SLM) of pure tungsten powder: morphology, geometric features and forming mechanisms. Int. J. Refract. Metals Hard Mater. 79, 37−46. https://doi.org/10.1016/j.ijrmhm.2018.11.003. Elsevier Ltd.

Gusarov, A.V., Smurov, I., 2009. Two-dimensional numerical modelling of radiation transfer in powder beds at selective laser melting. Appl. Surf. Sci. 255 (10), 5595−5599. https://doi.org/10.1016/j.apsusc.2008.07.202. Elsevier.

Han, Q., et al., 2018. Manufacturability of AlSi10Mg overhang structures fabricated by laser powder bed fusion. Mater. Des. 160, 1080−1095. https://doi.org/10.1016/j.matdes.2018.10.043. Elsevier Ltd.

Hann, D.B., Iammi, J., Folkes, J., 2011. A simple methodology for predicting laser-weld properties from material and laser parameters. J. Phys. D Appl. Phys. 44 (44), 445401. https://doi.org/10.1088/0022-3727/44/44/445401.

Hassanin, H., et al., 2018. Tailoring selective laser melting process for titanium drug-delivering implants with releasing micro-channels. Addit. Manuf. 20, 144−155. https://doi.org/10.1016/j.addma.2018.01.005. Elsevier B.V.

Higashi, M., Ozaki, T., 2020. Selective laser melting of pure molybdenum: evolution of defect and crystallographic texture with process parameters. Mater. Des. 191, 108588. https://doi.org/10.1016/j.matdes.2020.108588. Elsevier Ltd.

Hruška, M., et al., 2018. The effect of the material surface oxidation on laser light absorption - IOPscience. In: IOP Conference Series: Materials Science and Engineering, Volume 179, 4th International Conference Recent Trends in Structural Materials 9−11 November 2016, vol. 179. Pilsen, Czech Republic, p. 012029. https://doi.org/10.1088/1757-899X/179/1/012029. Available at: (Accessed 5 June 2020).

Hunter, L.W., et al., 2020. Assessment of trapped powder removal and inspection strategies for powder bed fusion techniques. Int. J. Adv. Manuf. Technol. 106 (9−10), 4521−4532. https://doi.org/10.1007/s00170-020-04930-w. Springer.

Iveković, A., et al., 2018. Selective laser melting of tungsten and tungsten alloys. Int. J. Refract. Metals Hard Mater. 72, 27−32. https://doi.org/10.1016/j.ijrmhm.2017.12.005. Elsevier Ltd.

Jing, G., et al., 2020. Formability, microstructure and mechanical properties of 300M steel single tracks fabricated by high power selective laser melting. Optic Laser. Technol. 131, 106434. https://doi.org/10.1016/j.optlastec.2020.106434. Elsevier Ltd.

Kajima, Y., et al., 2018. Effect of adding support structures for overhanging part on fatigue strength in selective laser melting. J. Mech. Behav. Biomed. Mater. 78, 1−9. https://doi.org/10.1016/j.jmbbm.2017.11.009. Elsevier Ltd.

Khairallah, S.A., et al., 2016. Laser powder-bed fusion additive manufacturing: physics of complex melt flow and formation mechanisms of pores, spatter, and denudation zones. Acta Mater. 108, 36−45. https://doi.org/10.1016/j.actamat.2016.02.014. Elsevier Ltd.

King, W., et al., 2015. Overview of modelling and simulation of metal powder bed fusion process at Lawrence Livermore National Laboratory. Mater. Sci. Technol. 957−968. https://doi.org/10.1179/1743284714Y.0000000728. Maney Publishing.

King, W.E., et al., 2014. Observation of keyhole-mode laser melting in laser powder-bed fusion additive manufacturing. J. Mater. Process. Technol. 214 (12), 2915−2925. https://doi.org/10.1016/j.jmatprotec.2014.06.005.

Körner, C., Attar, E., Heinl, P., 2011. Mesoscopic simulation of selective beam melting processes. J. Mater. Process. Technol. 211 (6), 978−987. https://doi.org/10.1016/j.jmatprotec.2010.12.016.

Kruth, J.P., et al., 2004. Selective laser melting of iron-based powder. J. Mater. Process. Technol. 616−622. https://doi.org/10.1016/j.jmatprotec.2003.11.051. Elsevier.

Kuo, C.N., et al., 2020. “Microstructure evolution and mechanical property response via 3D printing parameter development of Al−Sc alloy. Virtual Phys. Prototyp. 15 (1), 120−129. https://doi.org/10.1080/17452759.2019.1698967. Taylor and Francis Ltd.

Ladewig, A., et al., 2016. Influence of the shielding gas flow on the removal of process by-products in the selective laser melting process. Addit. Manuf. 10, 1−9. https://doi.org/10.1016/j.addma.2016.01.004. Elsevier B.V.

Leirmo, T.S., Martinsen, K., 2019. Evolutionary algorithms in additive manufacturing systems: discussion of future prospects. Procedia CIRP 671−676. https://doi.org/10.1016/j.procir.2019.03.174. Elsevier B.V.

Leutenecker-Twelsiek, B., Klahn, C., Meboldt, M., 2016. Considering Part Orientation in design for additive manufacturing. Procedia CIRP 408−413. https://doi.org/10.1016/j.procir.2016.05.016. Elsevier B.V.

Li, W., et al., 2016. Effect of substrate preheating on the texture, phase and nanohardness of a Ti-45Al-2Cr-5Nb alloy processed by selective laser melting. Scripta Mater. 118, 13−18. https://doi.org/10.1016/j.scriptamat.2016.02.022. Elsevier Ltd.

Li, Z., et al., 2018. The influence of scan length on fabricating thin-walled components in selective laser melting. Int. J. Mach. Tool Manufact. 126, 1−12. https://doi.org/10.1016/j.ijmachtools.2017.11.012. Elsevier Ltd.

Lin, K., Yuan, L., Gu, D., 2019. Influence of laser parameters and complex structural features on the bio-inspired complex thin-wall structures fabricated by selective laser melting. J. Mater. Process. Technol. 267, 34−43. https://doi.org/10.1016/j.jmatprotec.2018.12.004. Elsevier Ltd.

Liu, B., et al., 2020. A new ray tracing heat source model for mesoscale CFD simulation of selective laser melting (SLM). Appl. Math. Model. 79, 506−520. https://doi.org/10.1016/j.apm.2019.10.049. Elsevier Inc.

Liu, X., et al., 2016. Numerical simulation of balling phenomenon in metallic laser melting process. In: ASME 2016 Heat Transfer Summer Conference, HT 2016, Collocated with the ASME 2016 Fluids Engineering Division Summer Meeting and the ASME 2016 14th International Conference on Nanochannels, Microchannels, and Minichannels. American Society of Mechanical Engineers. https://doi.org/10.1115/HT2016-1070.

Liu, Y., et al., 2015. Investigation into spatter behavior during selective laser melting of AISI 316L stainless steel powder. Mater. Des. 87, 797−806. https://doi.org/10.1016/j.matdes.2015.08.086. Elsevier Ltd.

Ly, S., et al., 2017. Metal vapor micro-jet controls material redistribution in laser powder bed fusion additive manufacturing. Sci. Rep. 7 (1), 1−12. https://doi.org/10.1038/s41598-017-04237-z. Nature Publishing Group.

Majeed, A., et al., 2019. Surface quality improvement by parameters analysis, optimization and heat treatment of AlSi10Mg parts manufactured by SLM additive manufacturing. Int. J. Lightweight Mater. Manuf. 2 (4), 288−295. https://doi.org/10.1016/j.ijlmm.2019.08.001. KeAi Publishing Communications Ltd.

Makoana, N., et al., 2018. "Characterization of 17-4PH single tracks produced at different parametric conditions towards increased productivity of LPBF systems—the effect of laser power and spot size upscaling. Metals 8 (7), 475. https://doi.org/10.3390/met8070475. MDPI AG.

Manriquez-Frayre, J.A., Bourell, D.L., 1991. Selective laser sintering of Cu-Pb/Sn solder powders. In: International Solid Freeform Fabrication Symposium. Austin, pp. 236−244. Available at: http://utw10945.utweb.utexas.edu/Manuscripts/1991/1991-27-Frayre.pdf. (Accessed 14 May 2020).

Martin, A.A., et al., 2019. Dynamics of pore formation during laser powder bed fusion additive manufacturing. Nat. Commun. 10 (1), 1−10. https://doi.org/10.1038/s41467-019-10009-2. Nature Publishing Group.

Masoomi, M., et al., 2018. A numerical and experimental investigation of convective heat transfer during laser-powder bed fusion. Addit. Manuf. 22, 729−745. https://doi.org/10.1016/j.addma.2018.06.021. Elsevier B.V.

Matache, G., et al., 2020. Edge and corner effects in selective laser melting of IN 625 alloy. Manuf. Rev. 7, 8. https://doi.org/10.1051/mfreview/2020008. EDP Sciences.

Matthews, M.J., et al., 2016. Denudation of metal powder layers in laser powder bed fusion processes. Acta Mater. 114, 33−42. https://doi.org/10.1016/j.actamat.2016.05.017. Elsevier Ltd.

Mertens, R., et al., 2018. Application of base plate preheating during selective laser melting. Procedia CIRP 5−11. https://doi.org/10.1016/j.procir.2018.08.002. Elsevier B.V.

Miranda, G., et al., 2019. A study on the production of thin-walled Ti6Al4V parts by selective laser melting. J. Manuf. Process. 39, 346−355. https://doi.org/10.1016/j.jmapro.2018.12.036. Elsevier Ltd.

Mishra, A.K., Kumar, A., 2020. Effect of surface morphology on the melt pool geometry in single track selective laser melting. Mater. Today Proceed. 27, 816−823. https://doi.org/10.1016/j.matpr.2019.12.357. Elsevier BV.

Morgan, R., Sutcliffe, C.J., O'Neill, W., 2004. Density analysis of direct metal laser re-melted 316L stainless steel cubic primitives. J. Mater. Sci. 39 (4), 1195−1205. https://doi.org/10.1023/B:JMSC.0000013875.62536.fa.

Mugwagwa, L., et al., 2019. Evaluation of the impact of scanning strategies on residual stresses in selective laser melting. Int. J. Adv. Manuf. Technol. 102 (5−8), 2441−2450. https://doi.org/10.1007/s00170-019-03396-9. Springer London.

Müller, A.V., et al., 2019. Additive manufacturing of pure tungsten by means of selective laser beam melting with substrate preheating temperatures up to 1000°C. Nucl. Mater. Energy 19, 184−188. https://doi.org/10.1016/j.nme.2019.02.034. Elsevier Ltd.

Mutua, J., et al., 2018. Optimization of selective laser melting parameters and influence of post heat treatment on microstructure and mechanical properties of maraging steel. Mater. Des. 139, 486−497. https://doi.org/10.1016/j.matdes.2017.11.042.

Nguyen, D.S., Park, H.S., Lee, C.M., 2020. Optimization of selective laser melting process parameters for Ti-6Al-4V alloy manufacturing using deep learning. J. Manuf. Process. 55, 230−235. https://doi.org/10.1016/j.jmapro.2020.04.014. Elsevier Ltd.

Niu, H.J., Chang, I.T.H., 1998. Liquid phase sintering of M3/2 high speed steel by selective laser sintering. Scripta Mater. 39 (1), 67−72. https://doi.org/10.1016/S1359-6462(98)00126-2. Elsevier Ltd.

Niu, H.J., Chang, I.T.H., 1999. Instability of scan tracks of selective laser sintering of high speed steel powder. Scripta Mater. 41 (11), 1229−1234. https://doi.org/10.1016/S1359-6462(99)00276-6. Elsevier Science Ltd.

Olakanmi, E.O., Cochrane, R.F., Dalgarno, K.W., 2015. A review on selective laser sintering/melting (SLS/SLM) of aluminium alloy powders: processing, microstructure, and properties. Prog. Mater. Sci. 401−477. https://doi.org/10.1016/j.pmatsci.2015.03.002. Elsevier Ltd.

Oliveira, J.P., LaLonde, A.D., Ma, J., 2020. Processing parameters in laser powder bed fusion metal additive manufacturing. Mater. Des. 193, 108762. https://doi.org/10.1016/j.matdes.2020.108762. Elsevier Ltd.

Pal, S., et al., 2020. Evolution of the metallurgical properties of Ti-6Al-4V, produced with different laser processing parameters, at constant energy density in selective laser melting. Results Phys. 17, 103186. https://doi.org/10.1016/j.rinp.2020.103186. Elsevier B.V.

Parry, L., Ashcroft, I.A., Wildman, R.D., 2016. Understanding the effect of laser scan strategy on residual stress in selective laser melting through thermo-mechanical simulation. Addit. Manuf. 12, 1−15. https://doi.org/10.1016/j.addma.2016.05.014. Elsevier B.V.

Pauzon, C., et al., 2019. Effect of argon and nitrogen atmospheres on the properties of stainless steel 316 L parts produced by laser-powder bed fusion. Mater. Des. 179, 107873. https://doi.org/10.1016/j.matdes.2019.107873. Elsevier Ltd.

Peter, N., et al., 2020. Benchmarking build simulation software for laser powder bed fusion of metals. Addit. Manuf. 36, 101531. https://doi.org/10.1016/j.addma.2020.101531. Elsevier BV.

Du Plessis, A., et al., 2019. Beautiful and functional: a review of biomimetic design in additive manufacturing. Addit. Manuf. 408−427. https://doi.org/10.1016/j.addma.2019.03.033. Elsevier B.V.

Du Plessis, A., 2019. Effects of process parameters on porosity in laser powder bed fusion revealed by X-ray tomography. Addit. Manuf. 30, 100871.

Polozov, I., et al., 2020. Microstructure, densification, and mechanical properties of titanium intermetallic alloy manufactured by laser powder bed fusion additive manufacturing with high-temperature preheating using gas atomized and mechanically alloyed plasma spheroidized powders. Addit. Manuf. 34, 101374. https://doi.org/10.1016/j.addma.2020.101374. Elsevier B.V.

Prashanth, K.G., et al., 2017. Is the energy density a reliable parameter for materials synthesis by selective laser melting? Mater. Res. Lett. 5 (6), 386−390. https://doi.org/10.1080/21663831.2017.1299808. Taylor and Francis Ltd.

Ramirez-Cedillo, E., et al., 2018. Process planning guidelines in selective laser melting for the manufacturing of stainless steel parts. Procedia Manuf. 973−982. https://doi.org/10.1016/j.promfg.2018.07.125. Elsevier B.V.

Robinson, J., et al., 2018. Determination of the effect of scan strategy on residual stress in laser powder bed fusion additive manufacturing. Addit. Manuf. 23, 13−24. https://doi.org/10.1016/j.addma.2018.07.001. Elsevier B.V.

Robinson, J.H., et al., 2019. The effect of hatch angle rotation on parts manufactured using selective laser melting. Rapid Prototyp. J. 25 (2), 289−298. https://doi.org/10.1108/RPJ-06-2017-0111. Emerald Group Publishing Ltd.

Salman, O.O., et al., 2019. Impact of the scanning strategy on the mechanical behavior of 316L steel synthesized by selective laser melting. J. Manuf. Process. 45, 255−261. https://doi.org/10.1016/j.jmapro.2019.07.010. Elsevier Ltd.

Santecchia, E., Spigarelli, S., Cabibbo, M., 2020. Material reuse in laser powder bed fusion: side effects of the laser—metal powder interaction. Metals 10 (3), 341. https://doi.org/10.3390/met10030341. MDPI AG.

Schmidt, M., et al., 2017. Laser based additive manufacturing in industry and academia. CIRP Ann. 66 (2), 561−583. https://doi.org/10.1016/j.cirp.2017.05.011. Elsevier USA.

Schnabel, T., Oettel, M., Mueller, B., 2017. Design for Additive Manufacturing Guidelines and Case Studies for Metal Applications Prepared for Industry Canada-Manufacturing & Life Sciences Branch (MLSB).

Scipioni Bertoli, U., et al., 2017. On the limitations of volumetric energy density as a design parameter for selective laser melting. Mater. Des. 113, 331−340. https://doi.org/10.1016/j.matdes.2016.10.037. Elsevier Ltd.

Shi, X., et al., 2016. Performance of high layer thickness in selective laser melting of Ti6Al4V. Materials 9 (12), 975. https://doi.org/10.3390/ma9120975. MDPI AG.

Shi, X., et al., 2017. Parameter optimization for Ti-47Al-2Cr-2Nb in selective laser melting based on geometric characteristics of single scan tracks. Optic Laser. Technol. 90, 71−79. https://doi.org/10.1016/j.optlastec.2016.11.002. Elsevier Ltd.

Shipley, H., et al., 2018. Optimisation of process parameters to address fundamental challenges during selective laser melting of Ti-6Al-4V: a review. Int. J. Mach. Tool Manufact. 1−20. https://doi.org/10.1016/j.ijmachtools.2018.01.003. Elsevier Ltd.

Simonelli, M., et al., 2015. A study on the laser spatter and the oxidation reactions during selective laser melting of 316L stainless steel, Al-Si10-Mg, and Ti-6Al-4V. Metall. Mater.

Trans. A Phys. Metall. Mater. Sci. 46 (9), 3842–3851. https://doi.org/10.1007/s11661-015-2882-8. Springer Boston.

Slotwinski, J.A., Garboczi, E.J., 2015. Metrology needs for metal additive manufacturing powders. JOM 67 (3), 538–543. https://doi.org/10.1007/s11837-014-1290-7. Minerals, Metals and Materials Society.

Snow, Z., Martukanitz, R., Joshi, S., 2019. On the development of powder spreadability metrics and feedstock requirements for powder bed fusion additive manufacturing. Addit. Manuf. 28, 78–86. https://doi.org/10.1016/j.addma.2019.04.017. Elsevier B.V.

Song, J., et al., 2018. Role of scanning strategy on residual stress distribution in Ti-6Al-4V alloy prepared by selective laser melting. Optik 170, 342–352. https://doi.org/10.1016/j.ijleo.2018.05.128. Elsevier GmbH.

Strano, G., Hao, L., Everson, R.M., Evans, K.E., 2013a. A new approach to the design and optimisation of support structures in additive manufacturing. Int. J. Adv. Manuf. Technol. 66 (9–12), 1247–1254. https://doi.org/10.1007/s00170-012-4403-x.

Strano, G., Hao, L., Everson, R.M., Evans, K.E., 2013b. Surface roughness analysis, modelling and prediction in selective laser melting. J. Mater. Process. Technol. 213 (4), 589–597. https://doi.org/10.1016/j.jmatprotec.2012.11.011. Elsevier Ltd.

Sutton, A.T., et al., 2020. Characterization of laser spatter and condensate generated during the selective laser melting of 304L stainless steel powder. Addit. Manuf. 31, 100904. https://doi.org/10.1016/j.addma.2019.100904. Elsevier B.V.

Tang, C., Le, K.Q., Wong, C.H., 2020a. Physics of humping formation in laser powder bed fusion. Int. J. Heat Mass Tran. 149, 119172. https://doi.org/10.1016/j.ijheatmasstransfer.2019.119172. Elsevier Ltd.

Tang, Q., et al., 2020b. Numerical simulation of selective laser melting temperature conduction behavior of H13 steel in different models. Optik 163336. https://doi.org/10.1016/j.ijleo.2019.163336. Elsevier GmbH, 201.

Tang, Y., et al., 2004. Accuracy Analysis and Improvement for Direct Laser Sintering. Available at: https://dspace.mit.edu/handle/1721.1/3898. (Accessed 31 July 2020).

Terner, M., et al., 2019. The response surface methodology for optimizing the process parameters of selective laser melting. J. Weldi. Join. 37 (1), 27–39. https://doi.org/10.5781/jwj.2019.37.1.4. The Korean Welding and Joining Society.

Tolochko, N., et al., 2004. Balling processes during selective laser treatment of powders. Rapid Prototyp. J. 10 (2), 78–87. https://doi.org/10.1108/13552540410526953. Emerald Group Publishing Ltd.

Trapp, J., et al., 2017. In situ absorptivity measurements of metallic powders during laser powder-bed fusion additive manufacturing. Appl. Mater. Today 9, 341–349. https://doi.org/10.1016/j.apmt.2017.08.006. Elsevier Ltd.

Valente, E.H., et al., 2019. Effect of scanning strategy during selective laser melting on surface topography, porosity, and microstructure of additively manufactured Ti-6Al-4V. Appl. Sci. 9 (24), 5554. https://doi.org/10.3390/app9245554. MDPI AG.

Vilardell, A.M., et al., 2019. Topology optimization and characterization of Ti6Al4V ELI cellular lattice structures by laser powder bed fusion for biomedical applications. Mater. Sci. Eng. A 766, 138330. https://doi.org/10.1016/j.msea.2019.138330. Elsevier Ltd.

Vilardell, A.M., et al., 2020. Manufacturing and characterization of in-situ alloyed Ti6Al4V(ELI)-3 at.% Cu by laser powder bed fusion. Addit. Manuf. 36, 101436. https://doi.org/10.1016/j.addma.2020.101436. Elsevier.

Wang, D., et al., 2012. Study on energy input and its influences on single-track,multi-track, and multi-layer in SLM. Int. J. Adv. Manuf. Technol. 58 (9–12), 1189–1199. https://doi.org/10.1007/s00170-011-3443-y. Springer.

Wang, D., et al., 2013. Research on the fabricating quality optimization of the overhanging surface in SLM process. Int. J. Adv. Manuf. Technol. 65 (9−12), 1471−1484. https://doi.org/10.1007/s00170-012-4271-4. Springer.

Wang, D., et al., 2017. Mechanisms and characteristics of spatter generation in SLM processing and its effect on the properties. Mater. Des. 117, 121−130. https://doi.org/10.1016/j.matdes.2016.12.060. Elsevier Ltd.

Wang, G., et al., 2020. Process optimization and mechanical properties of oxide dispersion strengthened nickel-based superalloy by selective laser melting. Mater. Des. 188, 108418. https://doi.org/10.1016/j.matdes.2019.108418. Elsevier Ltd.

Wei, K., Wang, Z., Zeng, X., 2017. Preliminary investigation on selective laser melting of Ti-5Al-2.5Sn α-Ti alloy: from single tracks to bulk 3D components. J. Mater. Process. Technol. 244, 73−85. https://doi.org/10.1016/j.jmatprotec.2017.01.032. Elsevier Ltd.

Wischeropp, T.M., et al., 2019. Measurement of actual powder layer height and packing density in a single layer in selective laser melting. Addit. Manuf. 176−183. https://doi.org/10.1016/j.addma.2019.04.019. Elsevier B.V.

Wu, Y.C., et al., 2018. Numerical modeling of melt-pool behavior in selective laser melting with random powder distribution and experimental validation. J. Mater. Process. Technol. 254, 72−78. https://doi.org/10.1016/j.jmatprotec.2017.11.032. Elsevier Ltd.

Xia, M., et al., 2016. Influence of hatch spacing on heat and mass transfer, thermodynamics and laser processability during additive manufacturing of Inconel 718 alloy. Int. J. Mach. Tool Manufact. 109, 147−157. https://doi.org/10.1016/j.ijmachtools.2016.07.010. Elsevier Ltd.

Yadroitsev, I., et al., 2007. Strategy of manufacturing components with designed internal structure by selective laser melting of metallic powder. Appl. Surf. Sci. 254 (4), 980−983. https://doi.org/10.1016/j.apsusc.2007.08.046. Elsevier.

Yadroitsev, I., 2009. Selective Laser Melting: Direct Manufacturing of 3D-Objects by Selective Laser Melting of Metal Powders. LAP Lambert Academic Publ, Saarbrücken (Book, 2009) [WorldCat.org].

Yadroitsev, I., et al., 2010. Single track formation in selective laser melting of metal powders. J. Mater. Process. Technol. 210 (12), 1624−1631. https://doi.org/10.1016/j.jmatprotec.2010.05.010.

Yadroitsev, I., et al., 2012. Factor analysis of selective laser melting process parameters and geometrical characteristics of synthesized single tracks. Rapid Prototyp. J. 18 (3), 201−208. https://doi.org/10.1108/13552541211218117.

Yadroitsev, I., Krakhmalev, P., Yadroitsava, I., 2015. Hierarchical design principles of selective laser melting for high quality metallic objects. Addit. Manuf. 7, 45−56. https://doi.org/10.1016/j.addma.2014.12.007. Elsevier B.V.

Yadroitsev, I., Smurov, I., 2011. Surface morphology in selective laser melting of metal powders. Phys. Procedia 264−270. https://doi.org/10.1016/j.phpro.2011.03.034. Elsevier.

Yadroitsev, I., Yadroitsava, I., 2015. Evaluation of residual stress in stainless steel 316L and Ti6Al4V samples produced by selective laser melting. Virtual Phys. Prototyp. 10 (2), 67−76. https://doi.org/10.1080/17452759.2015.1026045. Taylor and Francis Ltd.

Yeung, H., et al., 2017. Continuous laser scan strategy for faster build speeds in laser powder bed fusion system. Solid Freeform Fabr. 1423−1431. Austin.

Yeung, H., et al., 2018. Implementation of advanced laser control strategies for powder bed fusion systems. Procedia Manuf. 871−879. https://doi.org/10.1016/j.promfg.2018.07.112. Elsevier B.V.

Yinglei, P., Jiguo, S., 2020. Understanding humping formation based on keyhole and molten pool behaviour during high speed laser welding of thin sheets. Eng. Res. Expr. 2 (2), 025031. https://doi.org/10.1088/2631-8695/ab93aa. IOP Publishing Ltd.

Yuan, W., et al., 2020. Effects of laser scanning speeds on different states of the molten pool during selective laser melting: simulation and experiment. Mater. Des. 189, 108542. https://doi.org/10.1016/j.matdes.2020.108542. Elsevier Ltd.

Zaeh, M.F., Branner, G., 2010. Investigations on residual stresses and deformations in selective laser melting. J. Inst. Eng. Prod. 4 (1), 35−45. https://doi.org/10.1007/s11740-009-0192-y.

Zhang, T., et al., 2019. Evolution of molten pool during selective laser melting of Ti−6Al−4V. J. Phys. D Appl. Phys. 52 (5), 055302. https://doi.org/10.1088/1361-6463/AAEE04. IOP Publishing.

Zhang, Y., et al., 2018. Numerical modelling of fluid and solid thermomechanics in additive manufacturing by powder-bed fusion: continuum and level set formulation applied to track- and part-scale simulations. Compt. Rendus Mec. 1055−1071. https://doi.org/10.1016/j.crme.2018.08.008. Elsevier Masson SAS.

Zhao, Y., et al., 2020. Role of operating and environmental conditions in determining molten pool dynamics during electron beam melting and selective laser melting. Addit. Manuf. 101559. https://doi.org/10.1016/j.addma.2020.101559. Elsevier.

Zhou, Y.H., et al., 2020. “Selective laser melting of Ti−22Al−25Nb intermetallic: significant effects of hatch distance on microstructural features and mechanical properties. J. Mater. Process. Technol. 276, 116398. https://doi.org/10.1016/j.jmatprotec.2019.116398. Elsevier Ltd.

van Zyl, I., Yadroitsava, I., Yadroitsev, I., 2016. Residual stress in TI6AL4V objects produced by direct metal laser sintering. S. Afr. J. Ind. Eng. 27 (4), 134−141. https://doi.org/10.7166/27-4-1468. South African Institute of Industrial Engineering.

Physics and modeling

4

Andrey V. Gusarov
Moscow State University of Technology STANKIN, Moscow, Russia

Chapter outline

4.1 Introduction 79
4.2 Energy transfers 83
4.3 Gas phase flow 89
4.4 Melt pool dynamics 95
4.5 Heat transfer in the condensed phase 100
4.6 Process stability 106
4.7 Thermomechanics 109
4.8 Nomenclature 113
4.9 Questions 115
References 115

4.1 Introduction

In laser powder bed fusion (L-PBF), powder consolidates in a high-temperature zone where the laser beam strikes the powder bed. The size of this zone can be several diameters of the laser beam. Below, this is referred to as the laser interaction zone. Various interrelated physical processes in the laser-interaction zone determine the formation of defects, specific microstructures, and residual stresses, which crucially affect the quality of the obtained part. To control and optimize the whole L-PBF process, one should control the basic physical processes in the laser-interaction zone. This chapter is concerned with the physical processes in the laser interaction zone. Currently, the typical laser beam applied for L-PBF has a diameter somewhat below 100 μm and a power of the order of 100 W to 1 kW. The beam scans the powder bed with a speed of few centimeters to few meters per second. The size of powder particles can vary from approximately 15−60 μm. The typical powder layer thickness is around a few particle diameters.

Process parameters of L-PBF may be intentionally varied over a wide range. The optimal process parameters can also vary significantly for different materials. Therefore, the full picture of the laser-matter interaction can vary significantly too. However, one can recognize the following frequently observed features of the laser-interaction zone: a jet-like flow in the gas phase, the melt pool, and the heat-affected zone

Fundamentals of Laser Powder Bed Fusion of Metals. https://doi.org/10.1016/B978-0-12-824090-8.00008-1
Copyright © 2021 Elsevier Inc. All rights reserved.

(HAZ) in the solid phase. Below, the principal experimental facts are presented about the processes in the gas, liquid, and solid phases of the laser interaction zone.

Bidare et al. (2018a–c) and Zhirnov et al. (2018) observed an intensive jet-like flow in the gas phase at different conditions. Fig. 4.1A shows schlieren images of the jet

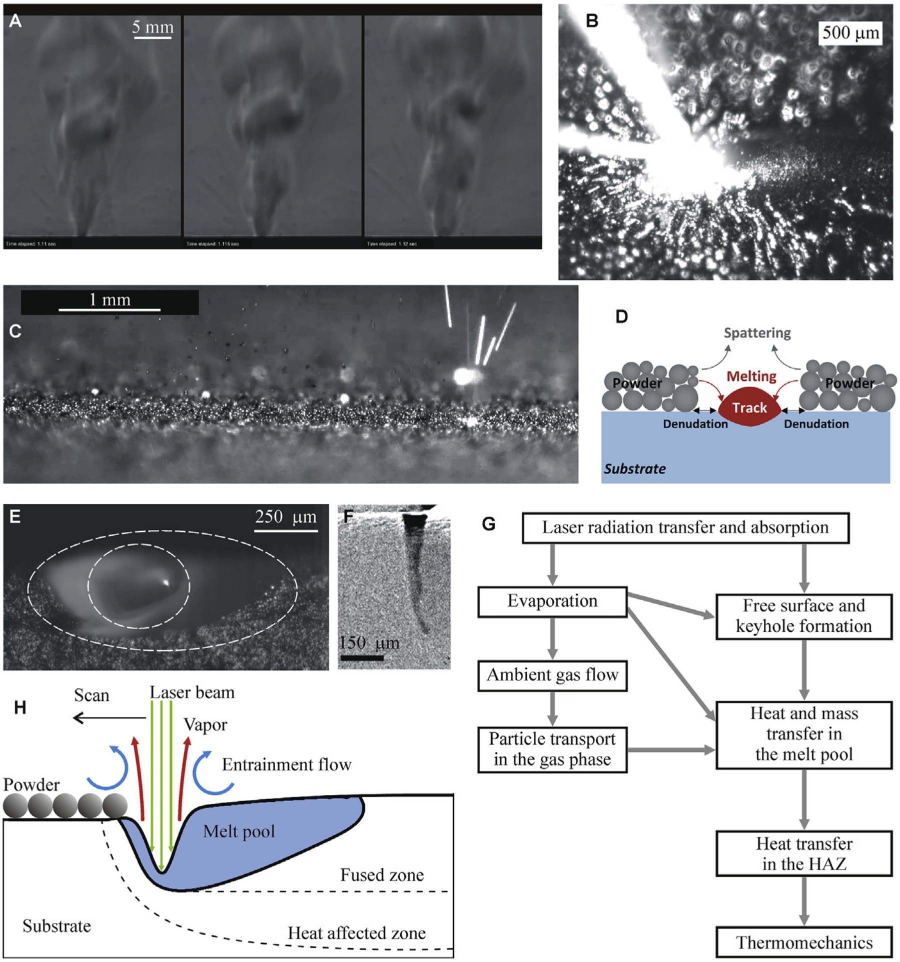
A
5 mm
Time elapsed: 1.11 sec
Time elapsed: 1.115 sec
Time elapsed: 1.12 sec
B
500 µm
1 mm
C
D
Spattering
Powder
Melting
Powder
Track
Denudation
Denudation
Substrate
E
250 µm
F
150 µm
G
Laser radiation transfer and absorption
Evaporation
Free surface and keyhole formation
Ambient gas flow
Heat and mass transfer in the melt pool
Particle transport in the gas phase
Heat transfer in the HAZ
Thermomechanics
H
Scan
Laser beam
Vapor
Entrainment flow
Powder
Melt pool
Fused zone
Substrate
Heat affected zone

Figure 4.1 Interaction of the laser beam with powder bed. (A) Evaporation-induced vapor jet in the gas phase: series of three schlieren images with the interval of 5 ms and (C) ejected particles in a profile view (scanning from left to right, Bidare et al., 2018a). (B) Melt pool, single track, powder particles, and the traces of moving particles in a superposition of 16 consecutive frames taken with the interval of 0.1 ms and the exposure of 0.1 ms (scanning from right to left, Zhirnov et al., 2018). (D) Schematic transversal cross-section of an interaction zone consisting of a single track and a denudation zone. (E) Side view of a melt pool on the top of a thin metal plate (scanning from right to left, Egorov et al., 2020). (F) In situ X-ray imaging of a keyhole in the middle of the melt pool (scanning from right to left, Calta et al., 2020). (G) Flowchart of physical processes. (H) Schematic longitudinal cross-section of the laser interaction zone at L-PBF.

where the contrast is due to the variation of the refractive index. The refractive index of the gas depends on parameters such as chemical composition, temperature, and pressure. The jet moves with the scanning laser beam. Comparison of the three images taken at different instances (see Fig. 4.1A) indicates that the contour of the jet is relatively steady while its internal structure is turbulent. Laser energy can overheat the material to the point of boiling, and consequently, intensive evaporation is expected. The vapor jet can also entrain the surrounding ambient gas according to Matthews et al. (2016) and Ly et al. (2017), who reasonably hypothesized the gas flow formation. Also, a contribution of the natural convection driven by buoyancy forces applied to heated gas cannot be excluded (Bidare et al., 2018a).

Another common feature of L-PBF is the transport of particles through the gas phase, which can be entrainment of powder particles by the gas flow (Bidare et al., 2018a) or spattering of molten material (Liu et al., 2015; Gunenthiram et al., 2018). Fig. 4.1C shows the two kinds of possible particles. The several bright radial dashes each emanate from the bright spot on the surface of the powder bed on the right of this figure (the melt pool). The bright spot on the surface illuminates because of intensive thermal emission from the domain heated by the laser beam. The laser radiation is not visible because a bandstop filter was used. This spot indicates the position of the laser beam and is referred to as the laser spot. The bright dashes are identified as fast and hot spatters ejected from the laser spot. The length of the emanating dash is the distance traveled by the spatter during the exposure time of the camera. Dark small particles suspended in the gas to the left of the laser spot (see Fig. 4.1C) are most likely powder particles entrained by the gas jet (Bidare et al., 2018a−c). According to this image, the entrained particles are considerably colder and slower than the bright spatters. The entrained cold particles appear motionless in the time scale of the exposure. It is also possible that some of the bright dashes are not spatters but the entrained powder particles exposed to laser radiation and accelerated by the gas jet (Bidare et al., 2018a−c).

Fig. 3.1B in Chapter 3 shows the single track formed by the scanning laser beam. The single track consists of fused powder and remelted substrate. A bright band on either side of the single track (Fig. 3.1B) means that the substrate becomes visible, i.e., not only the powder located directly under the beam but also powder particles at a significant distance from the beam become involved in the process. This phenomenon is called the denudation of the substrate, and the zones free from powder are called the “denudation zone.” A significant part of the powder involved in the process is spent on the formation of the single track, and part of the material is jetted away from the interacted area (spattering effect). Thus, the powder entrained by the gas flow significantly contributes to the mass transfer in the laser-interaction zone (Ly et al., 2017). The denudation effect was first described by Yadroitsev et al. (2007). However, a clear explanation was proposed only in 2016 when Matthews et al. (2016) observed a collective motion of powder particles toward the laser spot and supposed that it is the gas flow which moves the particles. Further works of Bidare et al. (2018a−c), Ly et al. (2017), and Zhirnov et al. (2018) confirmed the gas-driven mechanism of the denudation.

A high-resolution image of the zone around the laser spot is shown on the top of Fig. 4.1B, where powder particles are visible. A diffuse dash on the top can be a trace of spatter particles. A large cylindrical body on the right of the laser spot is the single track. The single track is clearly visible at the middle of the denudation zone in Fig. 3.1B in Chapter 3. The rough surface of the track in Fig. 4.1B indicates that it is in the solid state. The left part of the track around the laser spot is considered to be in the liquid state. However, the boundary of the melt pool is not resolved in this figure. Fig. 4.1B presents a superposition of 16 consecutive frames. Therefore, moving particles trace dashes here. The radial thin dashes around the melt pool indicate that the powder particles move toward the melt pool. The thick dashes on the top of the image show that spatters are ejected from the melt pool. Transport of powder particles toward the melt pool provides the material necessary for formation of the single track, which is the elementary addition unit or "building block" of the additive manufacturing process in L-PBF.

Fig. 4.1D shows the scheme of powder transfer in the laser interaction zone outlined according to the above observations. The entrainment gas flow moves some particles from the powder layer to the melt pool. These particles contribute to the single track formation. Some particles are entrained by the gas flow and can be identified as spatter. The region near the single track, from which the particles are removed, is the denudation zone.

The important domain of the laser-interaction zone is the melt pool where separate powder particles are fused together to form the single track. Fig. 4.1E shows an in situ image of the melt pool in a thin plate obtained by a high-speed camera (Egorov et al., 2020). A laser beam scans the plate along the top edge and forms a melt pool occupying the whole width of the plate. Small bright points in the image are likely the reflections of light from crystals in the solid state. There are no crystals in the melt pool. Therefore, melt pool identifies it as the uniformly bright domain in the center of the image (surrounded with the outer white dashed line) The disturbed zone in the center of the melt pool (see Fig. 4.1E, surrounded with the inner white dashed line) seems to indicate the place where the beam strikes the pool.

Fig. 4.1F shows a deep cavity observed in the middle of the melt pool at higher laser powers (Calta et al., 2020), a so-called keyhole forms due to the recoil pressure of vapor. In the keyhole regime, energy transfer changes considerably in the melt pool. The principal peculiarities of the keyhole mode are: (1) laser energy penetrates deeper through the keyhole, see Fig. 4.1H, which substantially increases the depth of the melt pool; (2) multiple reflections of laser radiation by the keyhole walls increase the effective absorptance; (3) the keyhole can be a source of undesirable pores (Calta et al., 2020).

The quality of the material structure obtained in the L-PBF process depends on the metallurgical bond formed between the single track and the substrate and between adjacent tracks and on the quality of the tracks themselves including their shape, internal defects, and microstructure. The mentioned factors strongly depend on the dynamics of the melt pool, convective and conductive heat transfer in the melt pool, conductive heat transfer in the heat affected zone (HAZ) in the surrounding solid phase, and the thermomechanical processes in the HAZ resulting in residual stresses, which can induce microcracking and deformation of the manufactured part. Fig. 4.1H shows the typical longitudinal cross-section of laser-interaction zone for L-PBF. The numerous physical processes in the laser-interaction zone are interdependent. Some processes induce others, so that the interdependence can be approximately reduced to the flowchart in Fig. 4.1G. All these phenomena will be considered in detail in this chapter.

Absorption of laser radiation and further transformations of energy are analyzed in Section 4.2. Section 4.3 considers the influence of the parameters of the gas atmosphere and the laser beam on gas-phase flow and the transport of powder particles. Section 4.4 is dedicated to the melt flow and its influence on heat and mass transfer. Section 4.5 studies energy balance and heat transfer in the HAZ and the corresponding possible influence on the metallurgical bonding and microstructure. Section 4.6 studies the capillary stability of the melt pool related to the stability of L-PBF. Section 4.7 considers local thermomechanical stresses around the track.

4.2 Energy transfers

The electromagnetic energy of the laser beam is partly absorbed by the object being processed and partly reflected by it, see Fig. 4.2A. The absorbed radiative energy is transformed into thermal energy. The maximum temperature is attained inside the laser spot, the surface domain where the beam strikes the object. The temperature gradually decreases with increasing distance from the laser spot. The thermal energy is transferred from the hotter central domain to the colder periphery of the laser-interaction zone according to the second law of thermodynamics. Due to the high concentration of the energy in the laser spot, the temperature T can locally overcome the melting point T_m and the boiling point T_b. One can generally distinguish the domains of solid, $T < T_m$, liquid, $T > T_m$, and overheated liquid, $T > T_b$, phases as shown schematically in Fig. 4.2A. This scheme is applicable to a powder bed as well as to a compact material undergoing the similar transport processes and phase transformations. Heat is transferred by conduction in the solid and liquid phases and by convection in the liquid phase. In addition, it is transferred to the ambient atmosphere due the thermal radiation from the hot surface domain, by ambient gas convection, and by evaporation of the overheated liquid.

The absorbed fraction of the laser beam energy, the absorptance a, can be theoretically estimated by solving the Maxwell equations (Born and Wolf, 1970). A plane electromagnetic wave propagating in an isotropic medium 1, with the complex refractive index n_1, falls on a plane interface with isotropic medium 2 with the complex refractive index n_2. Fig. 4.2B shows the direction of the incident wave propagation, the normal to the interface, and the plane of incidence containing both directions. The electromagnetic wave is a transverse wave where the electric vector $\mathbf{E}$ is perpendicular to the propagation direction. One can distinguish a component of $\mathbf{E}$ parallel to the plane of incidence $\mathbf{E}_p$ and a perpendicular component $\mathbf{E}_s$. Thus, the electric vector is the sum $\mathbf{E} = \mathbf{E}_p + \mathbf{E}_s$ while the considered electromagnetic wave is a superposition of the p-polarized wave with electric vector $\mathbf{E}_p$ and the s-polarized wave with electric vector $\mathbf{E}_s$.

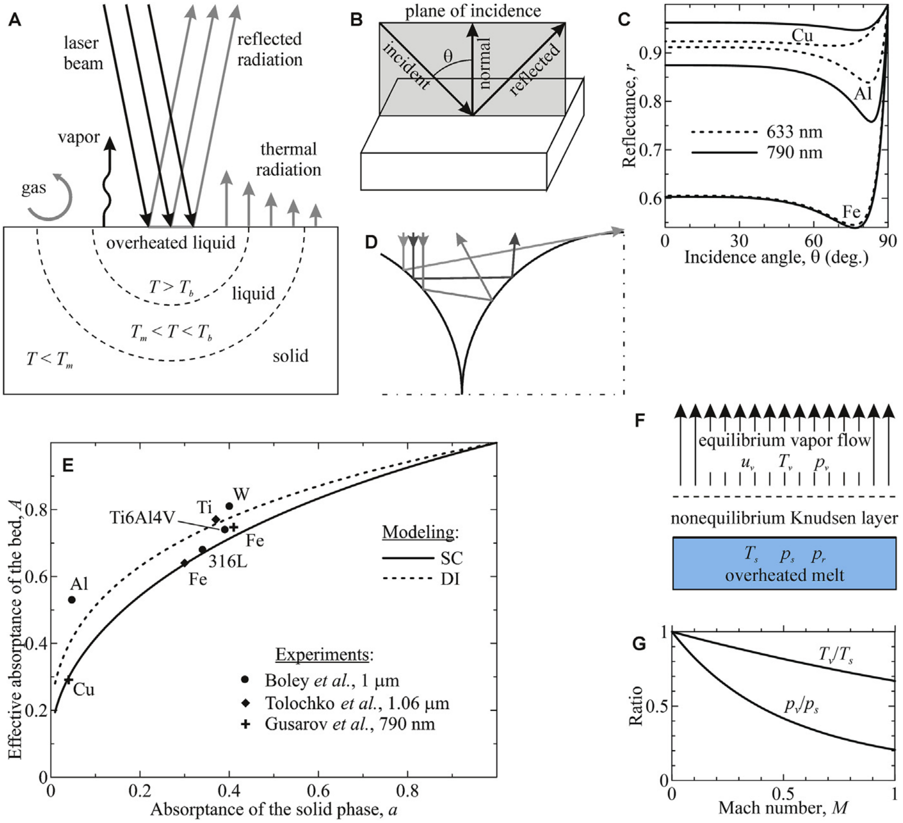

Figure 4.2 (A) Energy transformations due to the interaction of the laser beam with a solid object. (B) Reflection of an electromagnetic wave by a surface. (C) Typical angular reflectance of metal surface for nonpolarized radiation estimated by the Fresnel equations. (D) Double reflections in a cavity between two spherical particles. (E) Effective absorptance of the powder bed: comparison of ray-tracing modeling by Gusarov (2020c) with experiments of Boley et al. (2016), Gusarov et al. (2006), and Tolochko et al. (2000). (F) Formation of the Knudsen layer[1] at evaporation. (G) Temperature and pressure ratios at strong evaporation.

In the considered interface problem for the Maxwell equations, an incident wave induces one reflected wave and one refracted wave. The reflected wave (specular reflection) propagates in the plane of incidence and the angle between its direction and the normal is equal to the angle between the incident direction and the normal, the incidence angle θ, see Fig. 4.2B. The ratio of the energy of the reflected wave to that of the incident wave is referred to as the reflectance of the interface r. The reflectance depends on polarization: for the p- and s-polarizations of the incident wave, it is r_p and r_s,

---

[1] The Knudsen layer (or evaporation layer) is the layer of a vapor near an evaporating surface. It is named after Danish physicist Martin Knudsen.

$$
\begin{aligned}
r_p &= \left| \frac{n_1 \sqrt{1 - \left(\frac{n_1}{n_2} \sin\theta \right)^2} - n_2 \cos\theta}{n_1 \sqrt{1 - \left(\frac{n_1}{n_2} \sin\theta \right)^2} + n_2 \cos\theta} \right|^2, \\
r_s &= \left| \frac{n_1 \cos\theta - n_2 \sqrt{1 - \left(\frac{n_1}{n_2} \sin\theta \right)^2}}{n_1 \cos\theta + n_2 \sqrt{1 - \left(\frac{n_1}{n_2} \sin\theta \right)^2}} \right|^2,
\end{aligned}
\tag{4.1}
$$

respectively (Born and Wolf, 1970). Eqs. (4.1) are known as the Fresnel equations. If radiation consists of a great number of randomly polarized waves, it is nonpolarized. In this case the reflectance is $r = (r_p + r_s)/2$ (Born and Wolf, 1970).

Consider a nonpolarized radiation propagating in a medium with $n_1 = 1$ incident on metal. Metals are highly absorbing for electromagnetic waves. The energy of the refracted wave propagating inside metal dissipates within the distance of about the wavelength (Born and Wolf, 1970). Therefore, the energy of the refracted wave is completely absorbed by metal near the surface. In such conditions, the absorptance and the reflectance are complementary values, $r + a = 1$.

The reflectance r and absorptance a of laser radiation by metals essentially depend on the complex refractive index n_2 and the angle of incidence θ. Databases of refractive index are available for many materials in a wide range of wavelengths, see for example at, RefractiveIndex.INFO (2020). Fig. 4.2C shows typical angular dependences of the reflectance for selected metals calculated by the Fresnel Eq. (4.1) (Gusarov et al., 2006). A significant variation of the reflectance with θ is observed at grazing incidence only. Therefore, specular reflection independent of angle can be an acceptable approximation. The constant reflectance is estimated at the normal incidence, $\theta = 0$, from Eq. (4.1),

$$
r = r_p = r_s = \left| \frac{n_1 - n_2}{n_1 + n_2} \right|^2 . \tag{4.2}
$$

A deviation of the reflecting surface from a plane can result in a deviation from the specular reflection law. At very rough surface, the angular distribution of the reflected radiation approaches the uniform one in the backward hemisphere of directions at any incident angle, the so-called diffuse reflection law (Howell et al., 2015).

If the laser-processed surface contains deep cavities, multiple reflections by the cavity walls are possible, which can considerably decrease the effective reflectance R and increase the effective absorptance A. That is the case of L-PBF because the laser beam can strike the powder bed and the spaces between particles act as deep cavities with walls at sharp angles to the incident beam. Fig. 4.2D shows rays reflected two times in a cavity between particles of a powder bed to illustrate this concept. Gusarov (2020c) modeled the powder bed as regular arrays of equal spheres packed in simple cubic (SC) and diamond-like (DI) structures with the solid fraction (relative density) of 0.524 and 0.34, respectively, and simulated the reflectance of these structures by ray tracing, taking into account multiple reflections. The calculation results shown by lines in Fig. 4.2E indicate that the effective absorptance of the powder bed A is considerably greater than the absorptance of a plane surface a and that A increases with a decrease in the solid fraction in the powder bed. In this plot, the points show experimental measurements of A (Boley et al., 2016; Gusarov et al., 2006; Tolochko et al., 2000). One can see that the experimental data for Cu, Fe, stainless steel 316L, and titanium alloy Ti6Al4V agree with the calculations of Gusarov (2020c) for the SC structure. This is expected because the solid fraction of the studied powders of spherical particles typically lies in the range from 0.5 to 0.6 (Gusarov et al., 2006), which corresponds better to the SC packing. However, the experimental absorptance of Al, Ti, and W powders is significantly greater than the ray-tracing calculations, see Fig. 4.2E. This can be explained by surface oxidation of powder particles in the experimental works (Boley et al., 2016; Gusarov et al., 2006).

Ye et al. (2019) modeled multiple reflections at the interaction of a laser beam with the keyhole and found that the effective absorptance A correlates with the aspect ratio of the keyhole. They also analyzed experimental data for various materials and process parameters and proposed a universal scaling law to predict A in the conditions of L-PBF with the keyhole formation. This law roughly reduces to a function of A versus the ratio of the keyhole depth to the laser beam diameter. The effective absorptance tends to a constant value as the depth increases. This asymptotic value is approximately equal to $A = 0.7$ for the metals and alloys studied by Ye et al. (2019).

In addition to the reflected radiation with the wavelength equal to that of the laser, a high-temperature surface irradiates in a wide spectral range corresponding to the Planck distribution at the given temperature T. The wavelength of the maximum thermal radiation is estimated by Wien's displacement law (Howell et al., 2015), $\lambda_{\max} = b/T$, where $b \approx 2898\ \mu\text{m} \cdot \text{K}$ is Wien's displacement constant. The energy flux of the thermal radiation is easily calculated for the so-called gray body having optical properties independent of the wavelength, at least in the relevant spectral interval. The thermal radiative energy flux per unit surface is equal to $\varepsilon\sigma T^4$ (Howell et al., 2015), where ε is the emissivity and σ the Stefan-Boltzmann constant. According to Kirchhoff's law, the emissivity is equal to the absorptance (Howell et al., 2015). However, this does not mean that the emissivity is equal to the absorptance of the laser radiation because the laser wavelength can be far from the spectral interval of the thermal radiation. Often, the energy flux of thermal emission is much less than the energy flux of the laser beam at laser processing. One can neglect the thermal radiation in this case. However, estimates by the gray body model can be useful in particular conditions.

The most important energy loss from the surface in L-PBF is generally associated with evaporation. Evaporation starts when the saturated vapor pressure p_s becomes greater than the ambient pressure. The function of p_s versus the temperature of the melt surface T_s obeys the thermodynamic Clausius-Clapeyron relation (Callen, 1985),

$$\frac{\mathrm{d}p_s}{\mathrm{d}T_s} = \frac{L_b}{T_s \Delta V}, \tag{4.3}$$

where L_b is the latent heat of evaporation and ΔV the volume change. The latter can be estimated assuming the ideal gas equation of state for the vapor and neglecting the volume of the condensed phase, $\Delta V = kT_s/p_s$ per one vapor molecule, where k is the Boltzmann constant. Suppose that L_b is a constant. Then, integration of Eq. (4.3) with the initial condition $p_s(T_b) = p_0$ results in the following function:

$$p_s = p_0 \exp\left[\frac{L_b}{kT_b}\left(1 - \frac{T_b}{T_s}\right)\right], \tag{4.4}$$

where p_0 is the atmospheric pressure, T_b the boiling point at the atmospheric pressure, and L_b is taken per one vapor molecule. Eq. (4.4) can be used at the temperatures T_s around T_b (Zel'dovich and Raiser, 1967).

At the very beginning of laser evaporation, the vapor temperature and pressure are equal to their equilibrium values T_b and p_s, respectively. However, the deviation from the thermodynamic equilibrium increases with the intensity of evaporation. A significant nonequilibrium appears when the vapor flow velocity u_v becomes comparable with the sound speed in the vapor S. It is the so-called case of strong evaporation. The useful measure of nonequilibrium is the Mach number $M = u_v/S$. It is known that the vapor velocity cannot be greater than the sound speed, see Gusarov and Smurov (2002). Therefore, the Mach number varies from zero at the thermodynamic equilibrium to one at the maximum possible nonequilibrium. The nonequilibrium manifests itself as the deviation from the Maxwell velocity distribution of vapor molecules, the translational nonequilibrium in the vapor. Translational nonequilibrium holds in a narrow layer within several mean free paths from the surface, the Knudsen layer. Above the Knudsen layer, the velocity distribution becomes Maxwellian. However, the vapor temperature T_v and pressure p_v may considerably differ from T_s and p_s, respectively. Fig. 4.2F schematically shows evaporation with formation of the nonequilibrium Knudsen layer. It has to be noted that the vapor velocity vector is perpendicular to the evaporating surface.

The equilibrium vapor parameters above the Knudsen layer are theoretically estimated by the half-space problem for the Boltzmann equation. Knight (1979) found the following approximate analytical solution by a moment method:

$$\left(\frac{T_v}{T_s}\right)^{1/2} = \left(1 + \frac{\pi\psi^2}{64}\right)^{1/2} - \frac{\pi^{1/2}}{8}\psi, \tag{4.5}$$

$$\begin{aligned}\frac{p_v}{p_s} = \left(\frac{T_v}{T_s}\right)^{1/2}\left[\left(\psi^2 + \frac{1}{2}\right)\operatorname{erfc}(\psi)\ \exp\left(\psi^2\right) - \frac{\psi}{\pi^{1/2}}\right] \\ + \frac{1}{2}\left[1 - \pi^{1/2}\psi\ \operatorname{erfc}(\psi)\ \exp\left(\psi^2\right)\right],\end{aligned} \tag{4.6}$$

where $\psi = u_v/(2kT_v/m_v)^{1/2}$ is the speed ratio and m_v the vapor molecular mass. Gusarov and Smurov (2002) reviewed various analytical and numerical approaches to strong evaporation and concluded that Eqs. (4.5) and (4.6) are a reasonable approximation. In assumption that vapor is a monatomic gas with a constant specific heat, the sound speed is $S = [5kT_v/(3m_v)]^{1/2}$, and the Mach number becomes proportional to the speed ratio, $M = (6/5)^{1/2}\psi$. Therefore, the temperature T_v/T_s and pressure p_v/p_s ratios can be plotted versus the Mach number as shown in Fig. 4.2G. Both ratios are not greater than 1 and decrease with M. Gusarov and Smurov (2005) reported the following minimum values of the ratios at $M = 1$: $T_v/T_s = 0.644$ and $p_v/p_s = 0.207$. Vapor pressure p_v is not lower than the ambient pressure p_0. Taking into account that $p_v/p_s < 1$, one can obtain that the saturated vapor pressure p_s is greater than p_0 at strong evaporation. This inequality is compatible with Eq. (4.4) only if $T_s > T_b$. Thus, the melt is always overheated at strong evaporation.

The fluxes of mass, momentum, and energy through the melt/vapor interface can be evaluated by the gas-dynamic parameters of the vapor. In particular, the momentum flux per unit surface is $m_v n_v u_v^2 + p_v$, where n_v is the number of vapor molecules per unit volume. The momentum flux transferred by vapor per unit surface is balanced by the melt pressure and referred to as the recoil pressure, see Fig. 4.2F. Suppose that vapor is an ideal monatomic gas with a constant specific heat. Then, $n_v = p_v/(kT_v)$ and $u_v = M[5kT_v/(3m_v)]^{1/2}$. Substitution of these expressions reduces the recoil pressure to

$$p_r = p_v\left(1 + \frac{5}{3}M^2\right) \tag{4.7}$$

This equation is useful at $M < 1$ where p_v is approximately equal to the ambient pressure. In the important case of sonic evaporation with $M = 1$, one can substitute the reported above pressure ratio into Eq. (4.7) to obtain

$$p_r = \frac{8}{3}p_v = 0.553p_s, \tag{4.8}$$

indicating that the recoil pressure is a fraction of the saturated vapor pressure.

4.3 Gas phase flow

Intensive evaporation of the melt by the laser beam (see Fig. 4.2F) results in formation of a vapor jet. Fig. 4.3A shows computational fluid dynamics (CFD) results for a vapor flow ejected from a flat surface of a metal into ambient gas reported by Bidare et al. (2018a). The simulations were made in the conditions typical for L-PBF with the laser

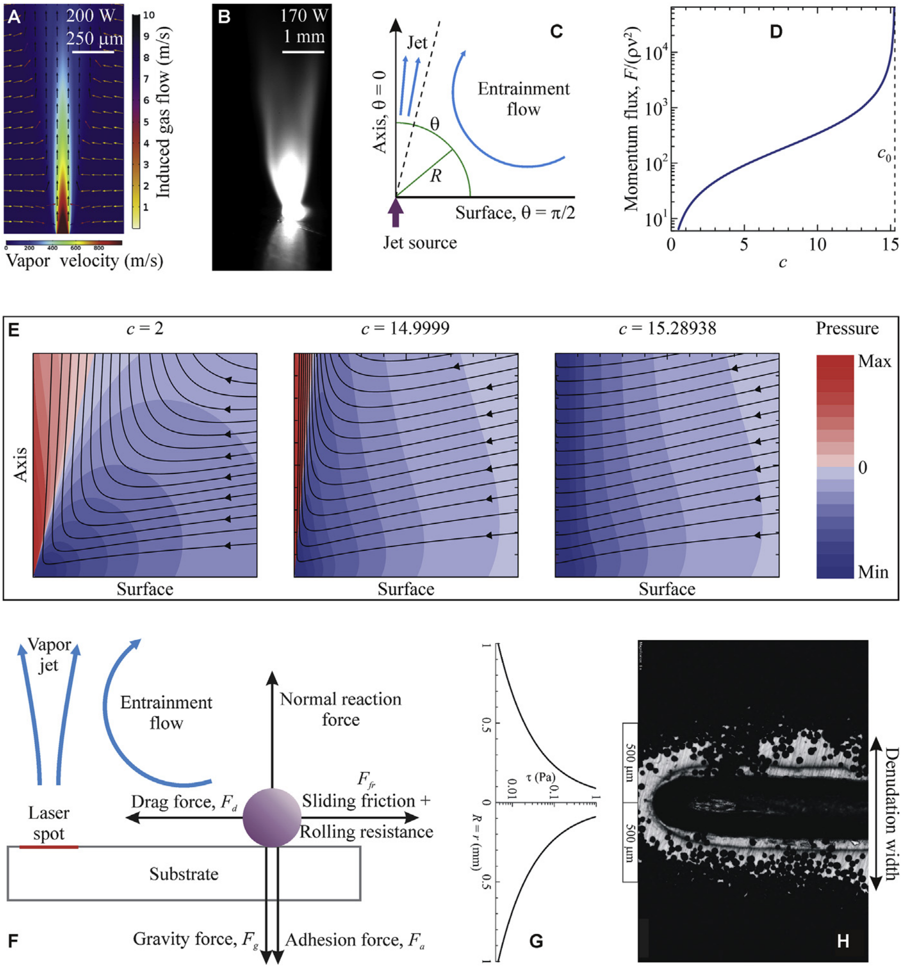
A
200 W
250 µm
10
9
8
7
6
5
4
3
2
1
Induced gas flow (m/s)
0
200
400
600
800
Vapor velocity (m/s)
B
170 W
1 mm
C
Jet
Axis, θ = 0
θ
R
Entrainment flow
Surface, θ = π/2
Jet source
D
Momentum flux, $F/(\rho\nu^2)$
10^4
10^3
10^2
10^1
c_0
0
5
10
15
c
E
c = 2
c = 14.9999
c = 15.28938
Pressure
Max
0
Min
Axis
Surface
Surface
Surface
Vapor jet
Entrainment flow
Laser spot
Normal reaction force
Drag force, F_d
F_{fr}
Sliding friction +
Rolling resistance
Substrate
Gravity force, F_g
Adhesion force, F_a
F
1
0.5
0
0.5
1
R = r (mm)
τ (Pa)
0.01
0.1
1
G
500 µm
500 µm
Denudation width
H

Figure 4.3 (A) Calculated velocity field of the vapor jet and the induced gas flow at 200 W laser power, Bidare et al. (2018a). (B) Experimental image of laser plume at 170 W laser power and 100 µm spot diameter. (C) Axisymmetric entrainment flow in spherical coordinates (R, θ). (D) Momentum flux F transferred by the jet. (E) Self-similar pressure fields and streamlines. (F) Forces applied to a powder particle (Khmyrov et al., 2020). (G) Calculated distribution of the shear stress on the surface τ around the evaporation spot (Gusarov, 2020b). (H) Denudation zone around a single track (Gusarov, 2020b).

power of 200 W and 50 μm spot size. The vapor flow velocity is around several hundred meters per second and hence is comparable with the sound speed. The calculated vapor jet approximately corresponds to the bright laser plume formed at laser processing of a steel substrate observed by Zhirnov et al. (2018) shown in Fig. 4.3B. The vapor is hot and emits thermal radiation which makes it visible. The CFD reveals an ambient gas flow toward the vapor jet with the velocity of several meters per second, see Fig. 4.3A. The jet entrains the ambient gas due to the Bernoulli effect: an increase in the speed of a fluid in the jet results in a decrease in the pressure; therefore, the ambient gas tends to move toward the jet region. The ambient gas is cold and invisible in experiments. However, the movement of powder particles toward the melt pool indirectly proves the existence of such an entrainment flow, see Fig. 4.1C, Matthews et al. (2016), Zhirnov et al. (2018).

The entrainment flow of ambient gas induced by evaporation appears responsible for the transport of powder particles in L-PBF presented in Fig. 4.1B–D. Experimental work of Zauner (1985) and theoretical analysis of Schneider (1981, 1985) indicated that the entrainment flow is a laminar one with the Reynolds number of the order of one even if the jet itself is a turbulent flow with a high Reynolds number. Therefore, it can be described in the framework of the Navier-Stokes approach to viscous flows. Below, we do not consider complicated thermal and kinetic processes around the laser spot. The aim is to evaluate the entrainment flow as a whole. The temperature and pressure variations are assumed negligible in the ambient gas. Therefore, it is treated as an incompressible viscous fluid described by the following mass and momentum conservation laws in a steady state:

$$\begin{aligned} \nabla\cdot\mathbf{u} = 0, \quad \nabla\cdot\mathbf{\Pi} = 0, \\ \mathbf{\Pi} = p\mathbf{I} + \rho\mathbf{uu} - \rho\nu\left[\nabla\mathbf{u} + (\nabla\mathbf{u})^{\mathrm{T}}\right], \end{aligned} \tag{4.9}$$

where $\mathbf{u}$ is the flow velocity vector, $\mathbf{\Pi}$ the momentum flow tensor, p the pressure, $\mathbf{I}$ the identity tensor,[2] ρ the density, and ν the kinematic viscosity.

The ambient gas domain is bounded by the surface of the L-PBF object. The characteristic scale of interest is greater than the diameter of a powder particle or that of a laser spot but lower that the size of the object. Therefore, a flat surface is a reasonable approximation for the model gas-phase flow. The other boundaries are far from the vapor jet. That is why fluid flow is considered in a half space with the no-slip condition $\mathbf{u} = 0$ on the bounding plane. Gusarov (2020a) found an analytical similarity solution to the no-slip half-space problem for Eq. 4.9 under the assumption that the jet and the entrainment flow are axially symmetric. In spherical coordinates (R,θ) shown in Fig. 4.3C,

$$u_R = \frac{\varphi(\theta)}{R}, \quad u_\theta = \frac{f(\theta)}{R}, \quad \frac{p}{\rho} = \frac{g(\theta)}{R^2}, \qquad \frac{\mathbf{\Pi}}{\rho} = \frac{\boldsymbol{\pi}(\theta)}{R^2}, \tag{4.10}$$

---

[2] The identity tensor is a linear transformation which transforms any vector into itself.

with angular factors specified by functions φ, f, and p and matrix of functions $\boldsymbol{\pi}$. The angular factor of the angular velocity component is (Gusarov, 2020a)

$$
\begin{aligned}
\frac{f}{\nu} = & \left\{ 2\frac{\alpha\beta}{\gamma}\left(\cos\frac{\theta}{2}\right)^{\gamma+1}\sin^2\frac{\theta}{2}\mathrm{F}\left(\alpha+1,\beta+1;\gamma+1;\cos^2\frac{\theta}{2}\right)\right. \\
& -\left(\cos\frac{\theta}{2}\right)^{\gamma-1}\left[2-(2+\gamma)\sin^2\frac{\theta}{2}\right]\mathrm{F}\left(\alpha,\beta;\gamma;\cos^2\frac{\theta}{2}\right) \\
& +2\frac{c_2}{c_1}\frac{(2-\alpha)(2-\beta)}{2-\gamma}\left(\cos\frac{\theta}{2}\right)^{3-\gamma}\sin^2\frac{\theta}{2}\mathrm{F}\left(3-\alpha,3-\beta;3-\gamma;\cos^2\frac{\theta}{2}\right) \\
& \left.-\frac{c_2}{c_1}\left(\cos\frac{\theta}{2}\right)^{1-\gamma}\left[2-(4-\gamma)\sin^2\frac{\theta}{2}\right]\mathrm{F}\left(2-\alpha,2-\beta;2-\gamma;\cos^2\frac{\theta}{2}\right)\right\} \Big/ \\
& \left\{\left(\cos\frac{\theta}{2}\right)^{\gamma}\sin\frac{\theta}{2}\mathrm{F}\left(\alpha,\beta;\gamma;\cos^2\frac{\theta}{2}\right)\right. \\
& \left.+\frac{c_2}{c_1}\left(\cos\frac{\theta}{2}\right)^{2-\gamma}\sin\frac{\theta}{2}\mathrm{F}\left(2-\alpha,2-\beta;2-\gamma;\cos^2\frac{\theta}{2}\right)\right\},
\end{aligned}
\tag{4.11}
$$

where

$$
\begin{gathered}
2\alpha = 2-\sqrt{1+c}+\sqrt{1+2c}, \quad 2\beta = 2-\sqrt{1+c}-\sqrt{1+2c}, \\
\gamma = 1-\sqrt{1+c},
\end{gathered}
\tag{4.12}
$$

and $\mathrm{F}(\alpha,\beta;\gamma;\theta)$ is the hypergeometric function. Angular factor f given by Eqs. (4.11) and (4.12) depends on constant c and ratio of constants c_2/c_1. The other angular factors are (Gusarov, 2020a)

$$\varphi = -\frac{1}{2\nu}f^2 - 2f\cot\theta - c\nu\left(\frac{\cos\theta-1}{\sin^2\theta}+1\right), \tag{4.13}$$

$$g = \nu\varphi - \frac{1}{2}f^2 - \nu^2 c, \tag{4.14}$$

$$\pi_{RR} = g + \varphi^2 + 2\nu\varphi, \tag{4.15}$$

$$\pi_{\theta\theta} = -c\nu^2\left(\frac{\cos\theta-1}{\sin^2\theta}+2\right), \tag{4.16}$$

$$\pi_{\varphi\varphi} = cv^2 \frac{\cos\,\theta - 1}{\sin^2\,\theta}, \tag{4.17}$$

$$\pi_{R\theta} = cv^2 \frac{2\,\cos\,\theta - 1}{\sin\,\theta}. \tag{4.18}$$

Physically meaningful similarity solutions were found for jets emerging into a half space for the values of constant c in the interval $0 < c < c_0$ where $c_0 \approx 15.2894$, and the values of ratio c_2/c_1 as a function of c were reported by Gusarov (2020a).

It turns out that the momentum flux F transferred by the jet is a function of constant c. Fig. 4.3D shows this function calculated by Gusarov (2020a). Gusarov (2020b) has shown that the normalized momentum flux is related to the laser evaporation characteristics,

$$\frac{F}{\rho v^2} = \frac{\pi}{3} Re^2, \tag{4.19}$$

where the jet Reynolds number is defined through the evaporation spot diameter D and the mean vapor velocity over the evaporation spot $\langle u_v \rangle$,

$$Re = \frac{\langle u_v \rangle D}{v}. \tag{4.20}$$

Fig. 4.3E shows examples of flow fields and pressure distributions at various values of c. One can see that the jet becomes narrower with increasing c. When c approaches its maximum value c_0 (see the right diagram in Fig. 4.3E), the streamlines meet the axis. Thus, a slender jet forms that behaves like a linear mass sink. The described similarity solution is a point-source solution where the evaporation spot size is neglected. Therefore, it is not applicable in the domain around the evaporation spot. The mass flux associated with the similarity solution is equal to zero (Gusarov, 2020a), while a realistic flow induced by evaporation transfers both mass and momentum. Thus, the similarity solution neglects the mass flux. Gusarov (2020b) found that the error due to neglecting the mass flux decreases with Re and the similarity solution is essentially applicable to laser evaporation at $Re \geq 30$.

Matthews et al. (2016) estimated that the jet Reynolds number in L-PBF is of the order of 10^3. Then, Eq. (4.19) gives the normalized momentum flux $F/(\rho v^2)$ of the order of 10^6. Finally, the tendency shown by Fig. 4.3D indicates that the corresponding value of constant c is very close to its limit value c_0. Constant c determines fluid dynamic fields given by Eqs. (4.10)–(4.18). Therefore, one can conclude that the entrainment flow is essentially independent of the evaporation intensity in the conditions of L-PBF. Indeed, the known entrainment-flow manifestations saturate with the laser power. For example, Matthews et al. (2016) have shown that the denudation effect is principally independent of the power above 100 W in the conditions of L-PBF with the spot diameter around 100 μm and the scan speed of 2 m/s.

Fig. 4.3F considers forces applied to a spherical powder particle on a substrate. This idealized sketch neglects the interactions of a particle with other particles of the powder bed. Such interactions are similar to the interaction of a particle with the substrate. Therefore, this approach is useful to understand the force balance. The gravity force is

$$F_g = g\rho_p \frac{\pi d^3}{6}, \tag{4.21}$$

where g is the gravity acceleration, ρ_p the mass density of particle material, and d the particle diameter. The adhesion force is (Leite et al., 2012)

$$F_a = \frac{Ad}{12\varepsilon^2}, \tag{4.22}$$

where A is the Hamaker constant and ε the gap between the sphere and the substrate. Both the gravity and the adhesion forces are directed downward, see Fig. 4.3F. The normal reaction force balances their sum.

The drag force arises due to the entrainment flow of the gas toward the evaporation spot. It is estimated as the projected area of the particle $\pi d^2/4$ multiplied by the shear stress τ on the substrate surface due to the gas flow,

$$F_d = \tau \frac{\pi d^2}{4}. \tag{4.23}$$

The drag force is directed toward the evaporation spot and balances the friction force, see Fig. 4.3F. The shear stress on the surface is given by the similarity solution (Gusarov, 2020a) as

$$\tau = c\frac{\rho \nu^2}{R^2}. \tag{4.24}$$

Gusarov (2020b) compared Eq. (4.24) with a CFD modeling and found that it underestimates the stress around the evaporation spot of finite diameter D, and proposed the following correction:

$$\tau = c\frac{\rho \nu^2}{(R-s)^2}, \tag{4.25}$$

where shift s is a fraction of D depending on constant c. He proposed the value of $s/D = 0.22$ for the case of L-PBF, $c \approx c_0$, and calculated the stress profile shown in Fig. 4.3G for Ar ambient gas and $D = 100$ µm. This profile corresponds to the experimental image of Fig. 4.3H.

For the saturated entrainment flow, combining Eqs. (4.23) and (4.25) gives the drag force independent of the process parameters,

$$F_d = c_0 \frac{\rho v^2}{(R-s)^2} \frac{\pi d^2}{4}. \tag{4.26}$$

This equation shows that the drag force sharply increases when approaching the evaporation spot. At a certain distance R, the drag force becomes greater than the combined friction and rolling resistance force F_{fr} that holds the particle in its place. The gas flow removes all particles within this critical distance, which determines the denudation width.

The considerable redistribution of coarse powder particles over the denudation zone shown in Fig. 4.3H suggests that they can roll under the convective forces. In the combined translational/rotational motion, one should account for both the sliding friction and the rolling resistance. The components are both proportional to the normal force while the rolling resistance coefficient can be much less than the sliding friction coefficient (Hibbeler, 2016). The maximum force holding the particle in its place is a fraction of the normal force,

$$F_{fr} = \mu(F_g + F_a), \tag{4.27}$$

where μ is the effective coefficient taking a value somewhere between the rolling resistance and sliding friction coefficients. Therefore, the balance equation $F_d = F_{fr}$ to find the critical value of R becomes

$$F_d = \mu(F_g + F_a). \tag{4.28}$$

It has to be noted that the adhesion force F_a, Eq. (4.22), is proportional to the particle diameter d, the drag force F_d, Eq. (4.26), is proportional to the particle diameter squared, d^2, and the gravity force F_g, Eq. (4.21), is proportional to the particle diameter cubed, d^3. Therefore, in the limit of small d, the gravity force becomes negligible in Eq. (4.28), and the critical distance R is essentially determined by the balance between the drag force and the adhesive force. In the limit of great d, the adhesive force becomes negligible in Eq. (4.28), and the critical distance R is essentially determined by the balance between the drag force and the gravity force.

One can obtain from Eq. (4.28) that in the limit of small d, the critical distance in the denudation zone R is

$$(R-s)^2 = 3\pi \frac{c_0}{\mu} \frac{\rho v^2 \varepsilon^2}{A} d. \tag{4.29}$$

Similarly, in the limit of great d,

$$(R-s)^2 = \frac{3}{2}\frac{c_0}{\mu}\frac{\rho\nu^2}{g\rho_p}\frac{1}{d}. \tag{4.30}$$

Thus, the critical distance R increases as $d^{1/2}$ at small d and decreases as $d^{-1/2}$ at large d. The largest critical distance is found at an intermediate value of d where the adhesive force is comparable with the gravity force. The critical distance R is the distance from the evaporation spot center to the boundary of nonremoved powder layer. The full denudation width measured from a boundary to the opposite one over the fused layer (see Fig. 4.3H) is equal to $2R$. Khmyrov et al. (2020) measured the denudation width for several powders applied in L-PBF and concluded that the gravity and adhesive forces applied to powder particles are comparable at the layer thickness comparable with the maximum particle diameter.

Experiments on L-PBF at various pressures indicated that the denudation zone widens with decreasing pressure, see Bidare et al. (2018b) and Matthews et al. (2016). Both Eqs. (4.29) and (4.30) explain this result. It is known that the dynamic viscosity $\rho\nu$ of gases is approximately independent of pressure while kinematic viscosity ν is proportional to the mean free path which is inversely proportional to pressure (Ferziger and Kaper, 1972). Thus, according to Eqs. (4.29) and (4.30) the increase of the kinematic viscosity with decreasing pressure determines the widening of the denudation zone.

4.4 Melt pool dynamics

Radiative laser energy is focused on a small domain where the beam strikes the processed layer, and transfers into thermal energy. Therefore, intensive heat fluxes are formed in the laser interaction zone. They are directed from the center to the periphery. According to the second law of thermodynamics, the heat fluxes are related to temperature gradients. Surface tension on the interface between the condensed and gas phases depends on temperature. The general tendency is that the surface tension decreases with temperature. That is why considerable gradients of surface tension are formed along with the temperature gradients. The surface tension gradient gives rise to the so-called thermocapillary or Marangoni force applied to the surface of the condensed phase. The thermocapillary force vector is tangent to the interface and directed toward increasing the surface tension, see Fig. 4.4A. It becomes the principal force driving convection in the melt pool formed in the center of the laser interaction zone. The thermocapillary convection can considerably intensify heat transfer.

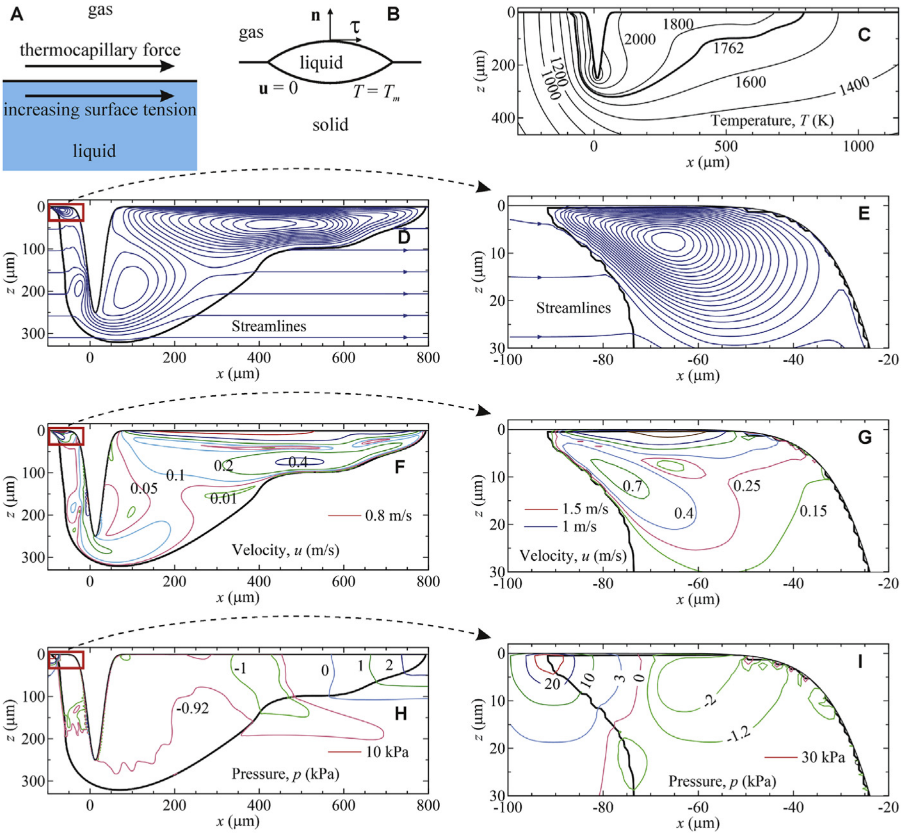

Figure 4.4 Modeling of coupled heat transfer and thermocapillary convection in a melt pool with a keyhole in a steel: (A) thermocapillary force; (B) boundary conditions. Calculated fluid-dynamic fields in the melt pool: (C) temperature; (D), (E) streamlines; (F), (G) absolute value of flow velocity; (H), (I) pressure (Egorov et al., 2020).

The melt pool can be treated as incompressible viscous fluid. The following transient equations of continuity, momentum, and energy describe melt dynamics:

$$\begin{gathered} \rho_t + \nabla\cdot(\rho\mathbf{u}) = 0, \quad (\rho\mathbf{u})_t + \nabla\cdot\mathbf{\Pi} = 0, \\ E_t + \nabla\cdot\mathbf{Q} = 0, \end{gathered} \tag{4.31}$$

where ρ is the melt density, $\mathbf{u}$ its flow velocity, E the energy per unit volume, and index t designates the time derivative. In a viscous thermal-conductive medium, the momentum flow tensor $\mathbf{\Pi}$ and energy flow vector $\mathbf{Q}$ are

$$\begin{gathered} \mathbf{\Pi} = p\mathbf{I} + \rho\mathbf{u}\mathbf{u} - \eta\left[\nabla\mathbf{u} + (\nabla\mathbf{u})^{\mathrm{T}}\right], \\ \mathbf{Q} = E\mathbf{u} + \mathbf{\Pi}\cdot\mathbf{u} - \lambda\nabla T, \end{gathered} \tag{4.32}$$

where p is the pressure, $\mathbf{I}$ the identity tensor, η the dynamic viscosity, λ the thermal conductivity, and T the temperature. The mass and momentum equations are similar to Eq. (4.9) applied to the gas phase. The thermal equation of state $U(T)$ closes the system of Eqs. (4.31)–(4.32), where $U = E - \rho u^2/2$ is the internal energy per unit volume. Specific heat capacity C is defined as derivative $\mathrm{d}U/\mathrm{d}T$. Therefore, the thermal equation of state can be obtained by integration of the known function $C(T)$. In a model medium with constant specific heat capacities C_s in the solid and C_l in the liquid phases, the inverse function $T(U)$ becomes

$$T = \begin{cases} \dfrac{U}{C_s} & , \quad U \le T_m C_s \\ T_m & , \quad T_m C_s < U \le T_m C_s + L_m \, , \\ \dfrac{U - L_m - T_m C_s}{C_l} + T_m & , \quad U > T_m C_s + L_m \end{cases} \tag{4.33}$$

where L_m is the latent heat of melting. More complicated models can account for variation of C with temperature and release of the latent heat in the interval between the solidus and liquidus temperatures.

Fig. 4.4B shows that the melt pool is bounded by a liquid/solid and a liquid/gas interfaces. The boundary conditions on these interfaces determine both the internal flow in the pool and the exchange of mass, momentum, and energy between the pool and the ambient atmosphere. Conservation of mass, momentum, and energy should be assured on the interfaces. This means that the fluxes of these quantities transferred by liquid to any part of the interface are equal to the corresponding fluxes transferred by gas or solid from the other side of this part of the interface. Besides, the boundary conditions should be compatible with the additional conditions imposed by the kinetics of evaporation and melting/solidification.

In the quasi-equilibrium approach to melting/solidification, the liquid/solid interface is isothermal, $T = T_m$. One can neglect the difference in density ρ between the solid and the liquid phases. Then, the conservation of mass means the continuity of flow velocity $\mathbf{u}$ on the liquid/solid interface. Flow velocity is equal to zero in the solid phase. Therefore, the no-slip boundary condition $\mathbf{u} = 0$ for the melt on the liquid/solid interface is equivalent to mass conservation in the assumption of no density change at melting/solidification. Currently, the modeling approach without tracking the liquid/solid interface is the most useful one. Eqs. (4.31)–(4.32) are applied to the both liquid and solid phases. This assures conservation of mass, momentum, and energy on the interface. An external force field can be applied at $T < T_m$ to stop convection in the solid phase. In these conditions, the solid phase is essentially described by the energy equation that reduces to the heat diffusion one,

$$U_t = \nabla \cdot (\lambda \nabla T). \tag{4.34}$$

In contrast, the uniform description of the liquid and gas phases by the same equations is rarely used because of a considerable difference in characteristics, for example, the density. On the part of the interface with $T < T_b$, there are no mass flux through the interface. The interface moves with the melt. The momentum transfer through the interface is defined by the momentum flow tensor $\mathbf{\Pi}'$ in the frame moving with the interface, namely the normal Π'_{nn} and shear $\Pi'_{n\tau}$ components defined in accordance with the unit normal vector $\mathbf{n}$ and a unit tangent vector $\boldsymbol{\tau}$ shown in Fig. 4.4B. The normal component

$$\Pi'_{nn} = p_g + \alpha\kappa, \tag{4.35}$$

is the sum of gas pressure p_g and surface tension pressure $\alpha\kappa$, where α is the surface tension coefficient and κ the interface curvature taken with sign "+" for the convex case as shown in Fig. 4.4B, and with sign "−" for a concave melt surface. The shear momentum flow component is due to the thermocapillary force.

$$\mathit{\Pi}'_{n\tau} = -\beta\boldsymbol{\tau}\cdot\nabla T, \tag{4.36}$$

where $\beta = \mathrm{d}\alpha/\mathrm{d}T$ is the derivative of the surface tension coefficient with respect to temperature. Energy flux through the liquid/gas interface is controlled by convection and thermal conduction in the gas and thermal radiation from the melt pool surface. The three components are often much lower than the energy fluxes in the liquid phase. Therefore, the adiabatic boundary condition with no energy flux through the liquid/gas interface is applicable in the absence of evaporation.

On the part of the liquid/gas interface with $T > T_b$, strong evaporation may considerably change the boundary conditions. A mass flux through the interface arises. It can be evaluated as the mass flow in the frame moving with the interface,

$$\rho_v u_v \mathbf{n}, \tag{4.37}$$

directed along the external normal $\mathbf{n}$, see Fig. 4.4B, with the vapor parameters defined in Section 4.2. The normal component of momentum flow through the liquid/gas interface in the frame moving with the interface should be corrected to account for the recoil pressure of vapor p_r,

$$\mathit{\Pi}'_{nn} = p_r + \alpha\kappa. \tag{4.38}$$

Latent heat of evaporation is often much greater that the thermal and kinetic energy of vapor. In such conditions, the energy flow through the liquid/gas interface in the frame moving with the interface is approximately

$$\mathbf{Q}' = L_b \frac{p_v u_v}{kT_v}\mathbf{n} + A\mathbf{Q_R}, \tag{4.39}$$

where L_b is the latent heat of evaporation per one vapor molecule and the vapor parameters are defined in Section 4.2. Eq. (4.39) accounts for the flow of laser radiative energy $\mathbf{Q_R}$ usually localized in the zone of evaporation. It is multiplied by the effective absorptance A of the liquid/gas interface.

The recoil pressure term in Eq. (4.38) can considerably increase at intensive evaporation. If the recoil pressure overcomes the pressures of the melt and the surface tension, a deep channel, the keyhole, is formed in the melt. Fig. 4.1F shows a visualized keyhole in the conditions of L-PBF. A perturbation observed in the middle of the melt pool shown in Fig. 4.1E may also indicate the formation of a keyhole. Direct experiments on measuring the flow velocity in the melt pool in L-PBF are hardly possible because the small scale, high temperature, and intensive energy fluxes make observation extremely difficult. Currently, the only confident experimental data concerning the shape of the pool and keyhole can be found in Bobel et al. (2019) and Calta et al. (2020).

Egorov et al. (2020) tried to estimate the melt flow field corresponding to the experimentally observed melt pool shown in Fig. 4.1E by numerical modeling. The model equations and boundary conditions essentially corresponded to the above approach. The momentum balance on the liquid/gas interface was not considered. Instead, the shape of the keyhole was predefined. The keyhole diameter was taken approximately equal to the laser beam diameter in accord to the experimental results, see Fig. 4.1F. The keyhole depth was a fit parameter. Fig. 4.4C–I show the modeling results for the keyhole depth of 250 μm providing with the best agreement between the modeling and the experiment in the melt pool shape. Fig. 4.4C shows the calculated temperature field. The temperature attains its maximum near the bottom of the keyhole. The melting isotherm $T = T_m$ (bold line) is the boundary of the melt pool. The calculated dimensions of the melt pool estimated by this isotherm are 900 ± 20 μm length and 320 ± 20 μm depth. Considerable temperature variation over the surface induces a thermocapillary convection in the melt pool. The frame chosen for the modeling moves with the scanning laser beam. Therefore, streamlines (Fig. 4.4D) enter from the left and exit to the right through the solid phase, which moves uniformly from left to right. They form four vortices in the melt pool. Two vortices are upstream of the keyhole and two of them are downstream of the keyhole. Two vortices are on the top of the melt pool and two of them are near the bottom of the keyhole. One can distinguish two shear flow domains between the front-bottom boundaries of the melt pool and the keyhole. The first shear flow domain is between the top-upstream and bottom-upstream vortices and the second one is between the bottom-upstream and bottom-downstream vortices. The top-upstream vortex is very small. Fig. 4.4E,G and I zoom the region of this vortex. Fig. 4.4F shows the flow velocity absolute value. The smallest top-upstream vortex is the strongest one because the flow velocity attains its absolute maximum around 2 m/s on the free surface adjacent to this vortex, see Fig. 4.4G. The maximum flow velocity in the top-downstream vortex is around 1 m/s, see Fig. 4.4G. The bottom-upstream and bottom-downstream vortices are considerably weaker. The melt pressure, Fig. 4.4H–I, considerably increases when approaching to the top-left and top-right corners of the melt pool. The top-left pressure peak attains $\approx 40\,\text{kPa}$ and the top-right one attains $\approx 3\,\text{kPa}$. The sharp pressure peaks near the corners are consistent with the drastic change in the flow direction occurred in these regions (see the streamlines).

The calculation results for a steel presented in Fig. 4.4 indicate formation of four vortices. The same number of vortices was reported for a pool in massive substrate by Kovalev and Gurin (2014). The number of vortices can depend on the melt pool shape and the Reynolds number of the flow. In the considered conditions, one can estimate the Reynolds number from the melt depth $H = 300\ \mu\text{m}$ and the maximum velocity $u_{\max} = 2$ m/s as

$$Re = \frac{\rho_0 H u_{\max}}{\eta} = 780, \tag{4.40}$$

The thermal Peclet number

$$Pe = \frac{C H u_{\max}}{\lambda} = 110, \tag{4.41}$$

gives the ratio of the convective heat transfer to the conductive one. The obtained value indicates that the convective heat transfer is much more important than the conductive one even in such a small melt pool typical for L-PBF. Khariallah et al. (2020) developed a more complicated high-fidelity model of the melt pool in L-PBF including dynamics of the liquid/gas interface with formation of the keyhole and the possibility to simulate fusion of powder particles and formation of defects. Such models help to understand the mechanisms of defect formation and to optimize the process parameters for given materials and conditions.

4.5 Heat transfer in the condensed phase

Energy transfer in the condensed phase reduces to conductive heat transfer described by the heat diffusion Eq. (4.34). It can be numerically solved for an arbitrary thermal equation of state and a temperature dependence of the thermal conductivity, see Gusarov et al. (2009). Important results can be obtained in the assumption of constant heat capacity per unit volume C and conductivity λ, where Eq. (4.34) reduces to the following linear equation:

$$T_t = \alpha \Delta T, \tag{4.42}$$

where $\alpha = \lambda / C$ is the thermal diffusivity and Δ the Laplace operator. Suppose that the heat affected zone (HAZ) with the elevated temperature around the laser beam is small relative to the L-PBF object and the curvature radius of the surface. Then, the size and the shape of the object are irrelevant and the HAZ can be considered in a half space bounded by the laser-processed surface as shown in Fig. 4.5A.

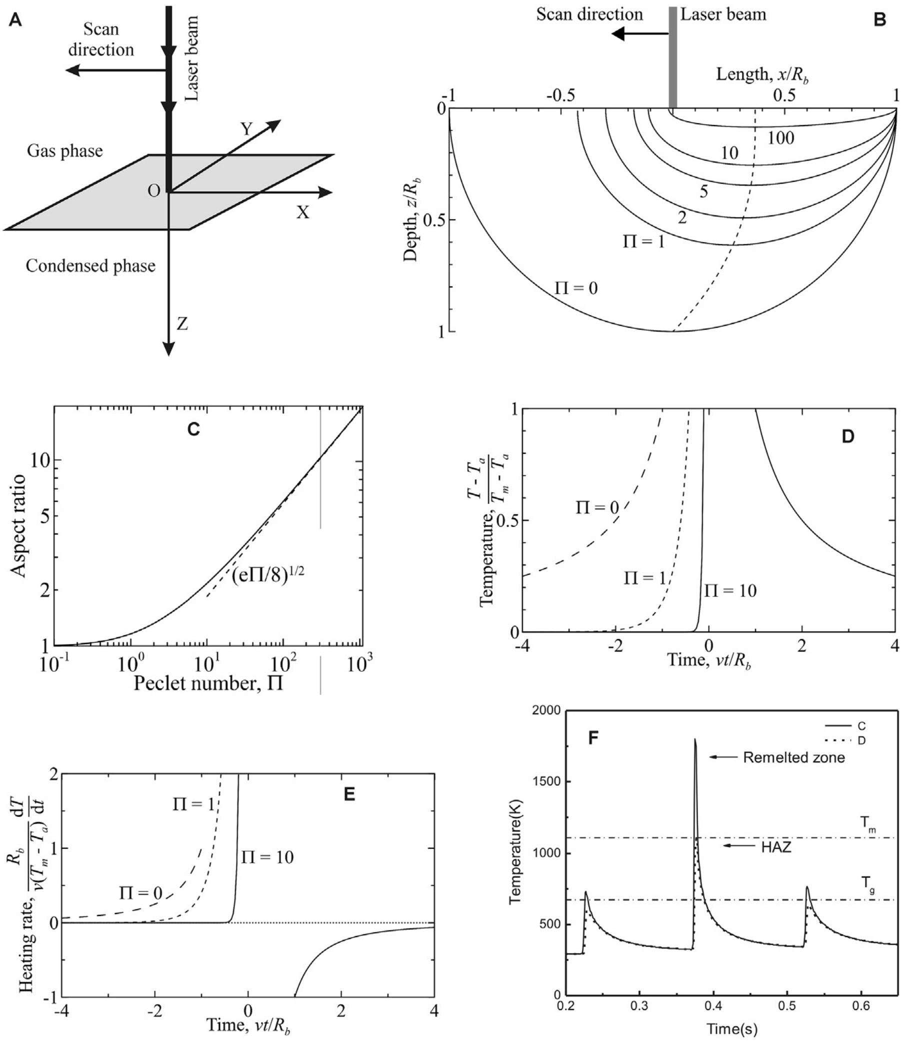

Figure 4.5 (A) Half-space problem for the heat diffusion equation. (B) Estimated melt pool profiles. (C) Aspect ratio of the melt pool. (D) Dimensionless thermal cycle at a point on the scan axis (OX). (E) Dimensionless heating (positive) and cooling (negative) rate. (F) Numerical modeling of the thermal cycle ($Zr_{55}Cu_{30}Al_{10}Ni_5$; C, point in the remelted zone; D point in the HAZ; Zhang et al., 2015).

Let the laser beam scan from right to left (negative x direction) with a constant scan speed v, see Fig. 4.5A. Consider Eq. (4.42) in a frame moving with the beam. In this frame, the time derivative transforms to $T_t - vT_x$, where index x means $\partial T/\partial x$. In the moving frame, the temperature field attains a steady state where the time derivative vanishes. Therefore, the steady solution satisfies the following equation:

$$vT_x + \alpha\Delta T = 0, \tag{4.43}$$

where the first term is responsible for advection due to displacement of the medium relative to the frame. Below, this equation is studied in a frame shown in Fig. 4.5A with the origin O placed at the intersection of the beam axis and the surface, axis (OY) parallel to the surface and perpendicular to the scan direction and axis (OZ) perpendicular to the surface and directed downward.

The laser beam provides a localized heat source on the surface. The heat flux through the surface outside the laser spot can be neglected. Thus, the adiabatic boundary condition of zero heat flow component in z-direction is imposed on the boundary plane $z = 0$. In a conductive medium, the heat flow is proportional to the temperature gradient. Therefore, the adiabatic boundary condition is written for the partial derivative with respect to z, $T_z = 0$. Far from the laser spot, the temperature approaches the ambient temperature T_a. Carslaw and Jaeger (1959) reported the following point-source analytical solution of the above heat-transfer problem:

$$T - T_a = \frac{P}{2\pi\lambda R}\exp\left(\frac{vx}{2\alpha} - \frac{vR}{2\alpha}\right), \tag{4.44}$$

where P is the power of the point source and R the distance from the point source, $R^2 = x^2 + y^2 + z^2$. This solution has a singularity at the origin, $R = 0$. It approaches realistic temperature distributions in the HAZ at distances R much greater than the laser spot size.

The example of melt pool considered in Section 4.4 shows that the melt pool dimensions are considerably greater than the laser spot size in L-PBF. Therefore, Eq. (4.44) should be a satisfactory approximation for the temperature distribution outside the melt pool. It is not applicable inside the melt pool because it does not account for the convective heat transfer which is dominant there, as shown in Section 4.4. However, heat transfer from the melt pool is controlled by conduction in the solid phase. Therefore, in the regime without keyhole formation, the melt pool shape can be estimated from the model temperature distribution, Eq. (4.44), as solution of equation $T = T_m$. It has to be noted that the temperature distribution along the positive part of axis (OX) is independent of the scan speed. Indeed, $y = z = 0$ there. Therefore $R = x$ and the argument of the exponent function in Eq. (4.44) becomes zero. The positive part of axis (OX) corresponds to the line traced by the laser beam axis on the surface. Then, the distance from the origin to the intersection of the melt pool boundary with axis (OX) behind the laser spot is obtained from Eq. (4.44) as

$$R_b = \frac{P}{2\pi\lambda(T_m - T_a)}. \tag{4.45}$$

This value is convenient to use as the characteristic size of the melt pool. The value of R_b is between a half length and the length of the melt pool.

One can define the thermal Peclet number with the scan speed v and the characteristic size R_b,

$$\Pi = \frac{vR_b}{2\alpha}, \tag{4.46}$$

and dimensionless coordinates $(x', y', z', R') = (x, y, z, R)/R_b$. In these coordinates, the melt pool boundary equation $T = T_m$ becomes

$$R' = \exp(\Pi x' - \Pi R'). \tag{4.47}$$

If the scan speed equals zero, $\Pi = 0$ and Eq. (4.47) indicates that the melt pool is half sphere $R' = 1$. At arbitrary Π, one can solve Eq. (4.47) relative to x',

$$x' = R' + \frac{\ln R'}{\Pi}. \tag{4.48}$$

Consider the profile of the melt pool $z'(x')$ in the vertical symmetry plane $y = 0$. In this plane,

$$z' = \sqrt{R'^2 - x'^2}. \tag{4.49}$$

Eqs. (4.48) and (4.49) define this profile parametrically, where R' is regarded as the parameter. Fig. 4.5B plots the melt pool profiles for various values of the Peclet number Π. This plot shows that the melt pool volume decreases with Π while the aspect ratio increases.

Parameter R' varies in the interval from R'_f to 1. The maximum distance from the origin to the melt pool boundary $R' = 1$ is attained on the axis (OX) behind the laser spot. Indeed, the substitution of value $R' = 1$ into Eqs. (4.48) and (4.49) gives point $(x', z') = (1, 0)$. As mentioned above, this distance does not depend on the scan speed. The minimum distance from the origin to the melt pool boundary $R' = R'_f$ is attained on the axis (OX) in front of the laser spot in point $(x', z') = \left(-R'_f, 0\right)$. Substitution of these coordinates into Eq. (4.47) or (4.48) results in the following transcendental equation:

$$R'_f = \exp\left(-2\Pi R'_f\right), \tag{4.50}$$

indicating that $R'_f = 1$ at $\Pi = 0$ and $R'_f \to 0$ when Π tends to infinity, which is in line with Fig. 4.5B.

The maximum melt depth is attained in a point where $\mathrm{d}z'/\mathrm{d}x' = 0$. Differentiation of the parametric function $z'(x')$ specified by Eqs. (4.48) and (4.49) results in the following condition:

$$x' = \frac{\Pi R'^2}{1 + \Pi R'}. \tag{4.51}$$

Parameter Π is excluded from Eqs. (4.51) and (4.48) to obtain that

$$x' = -R' \ln R', \tag{4.52}$$

in the point of the maximum melt depth. The parametric curve specified by Eqs. (4.52) and (4.49) gives the positions of the maxima in plane (x', z'). The dashed line shows this curve in Fig. 4.5B. One can see that it does connect the extremum points of the full-line profiles. Eq. (4.51) indicates that the maximum melt depth is attained at $x' = 0$ if $\Pi = 0$ and at $x' = R'$ if $\Pi \to \infty$. Substitution of the latter equation into Eq. (4.52) gives that

$$x' \to e^{-1} \text{ at } \Pi \to \infty. \tag{4.53}$$

It is the x-coordinate of the point where the dashed curve intersects the surface in Fig. 4.5B.

To find the maximum melt depth z'_m as function of Π, one can exclude x' from Eqs. (4.51) and (4.52) resulting in the following transcendental equation,

$$\ln R' + \frac{\Pi R'}{1 + \Pi R'} = 0. \tag{4.54}$$

The exclusion of x' from Eqs. (4.49) and (4.52) expresses the maximum melt depth through the solution of Eq. (4.54),

$$z'_m = R' \sqrt{1 - \ln^2 R'}. \tag{4.55}$$

Variables y and z are interchangeable in Eq. (4.44). In particular, this means that the found depth profile $z(x)$ in vertical plane $y = 0$ is similar to the width profile $y(x)$ in the horizontal surface plane $z = 0$. The only difference is that there are two symmetric branches, $y_+(x)$ and $y_-(x) = -y_+(x)$. Thus, the maximum width of the melt pool D is twice the maximum depth,

$$D/R_b = 2z'_m. \tag{4.56}$$

The length of the melt pool L is the sum of the forward R_f and backward R_b radii,

$$L/R_b = 1 + R'_f. \tag{4.57}$$

The aspect ratio of the melt pool is estimated as

$$\frac{L}{D} = \frac{1 + R'_f}{2z'_m}. \tag{4.58}$$

This equation results in a universal relation between dimensionless parameters L/D and Π applicable to any materials and laser parameters. Fig. 4.5C plots L/D versus the thermal Peclet number Π calculated by Eq. (4.58). The value of R'_f is calculated by numerical solution of Eq. (4.50). The value of z'_m is obtained from Eq. (4.55) where the value of R' is the numerical solution of Eq. (4.54). Fig. 4.5C indicates that the aspect ratio tends to 1 at $\Pi = 0$ and infinitely increases with Π. One can use Eq. (4.47) to find an asymptotic expression for the aspect ratio at high Π. At high Π, z' coordinate of the melt profile extremum becomes much lower than x' coordinate, which approaches e^{-1} according to Eq. (4.53). Therefore, the left hand side of Eq. (4.47) $R' = \left(x'^2 + z'^2\right)^{1/2}$ approaches e^{-1} too and difference $x' - R'$ from the right hand side is expanded as

$$x' - R' \approx -\frac{z'^2}{2x'}. \tag{4.59}$$

Substitution of Eq. (4.59) and expression $R' \approx e^{-1}$ into Eq. (4.47) results

$$z'_m \approx \sqrt{\frac{2}{e\Pi}}. \tag{4.60}$$

Besides, R'_f tends to 0 at high Π. Therefore, Eq. (4.58) reduces to

$$\frac{L}{D} \approx \sqrt{\frac{e\Pi}{8}}. \tag{4.61}$$

This function is shown by a dashed line in Fig. 4.5C. One can see that it does approach the full line with increasing Π.

Materials obtained by L-PBF frequently have a rather fine microstructure indicating a high cooling rate. Varying the cooling rate offers the possibility to control the microstructure. The thermal cycle in a given point can be estimated using the point-source solution Eq. (4.44). The steady temperature field given by Eq. (4.44) is applicable in a frame moving with the laser beam. Consider the transient temperature distribution in a laboratory frame attached to the laser-processed object with the same directions of axes as shown in Fig. 4.5A. In order to pass to the laboratory frame, expression $x + vt$ should be substituted instead of x in Eq. (4.44). Consider the thermal cycle in a point on the scan axis (OX) with $y = z = 0$. Let $t = 0$ is the instant when the laser spot attains the point. Then, Eq. (4.44) reduces to

$$\frac{T - T_a}{T_m - T_a} = \frac{1}{|t'|}\exp\left(\Pi t' - \Pi|t'|\right), \tag{4.62}$$

where dimensionless time $t' = vt/R_b$. This equation can be used in the solid phase where $T < T_m$. Fig. 4.5D shows that in the chosen dimensionless form, the heating branch of the thermal cycle depends on the Peclet number Π while the cooling branch is independent of Π.

Differentiation of Eq. (4.62) results in the heating rate

$$\frac{R_b}{v(T_m - T_a)}\frac{\mathrm{d}T}{\mathrm{d}t} = \begin{cases} \dfrac{1 - 2\Pi t'}{t'^2}\exp(2\Pi t') & , \quad t < 0 \\ & , \\ -1/t'^2 & , \quad t > 0 \end{cases} \tag{4.63}$$

Fig. 4.5E shows the dimensionless function with the positive branch describing heating rate at $t < 0$ and the negative branch concerning cooling at $t > 0$. The cooling rate is only important for the microstructure formation. The dimensionless cooling rate is a universal function independent on the thermal Peclet number. The scaling factor $v(T_m - T_a)/R_b$ gives the essential dependence of the cooling rate on the process parameters and material properties,

$$\frac{\mathrm{d}T}{\mathrm{d}t} \approx \frac{v(T_m - T_a)}{R_b} = 2\pi\lambda(T_m - T_a)^2\frac{v}{P}. \tag{4.64}$$

It should be noted that the cooling rate is proportional to the scan velocity v and inversely proportional to the laser power P. Fig. 4.5F shows an example of the thermal cycle numerically calculated by a model of nonlinear heat diffusion (Zhang et al., 2015). One can see that the typical thermal cycle in L-PBF consists of several peaks corresponding to different laser scans. Each peak takes a few milliseconds. The cooling rate can be as high as 10^8 K/s (Zhang et al., 2015).

4.6 Process stability

The objective of L-PBF is obtaining parts of uniform low-defect structure and corresponding to their digital models. The part is built of tracks of fused powder formed at laser scanning over powder layers. Therefore, it is important to assure the constant width of the track. The necessary condition is the uniformity of the powder layer in depth and density. However, experiments on single track formation indicated that the track can be irregular or discontinuous even if the powder layer is uniform, see Fig. 3.2G, see Chapter 3. The formation of separated melt droplets shown on the bottom of Fig. 3.2G, Chapter 3, is referred to as the balling effect. The nonuniformity of the single track in length indicates that some nonsteady processes arise in the laser interaction zone.

Yadroitsev et al. (2007) have shown that the single track becomes irregular or discontinuous at insufficient energy input that can be evaluated by the linear energy density *P*/*v*, where *P* is the laser power and *v* the scan speed. Yadroitsev and Smurov (2010) found that the stability of the process decreases with increasing the thickness of the powder layer *H*. The domain of stable process parameters can be experimentally obtained in the parametric space of *P*, *v*, and *H* for the given material. Fig. 4.6A shows a section of this space at constant *P*. Experimental parametric analysis to estimate the stability domain in the parametric space is a labor-consuming task. To find optimal process parameters, a theoretical concept can be useful along with experiments.

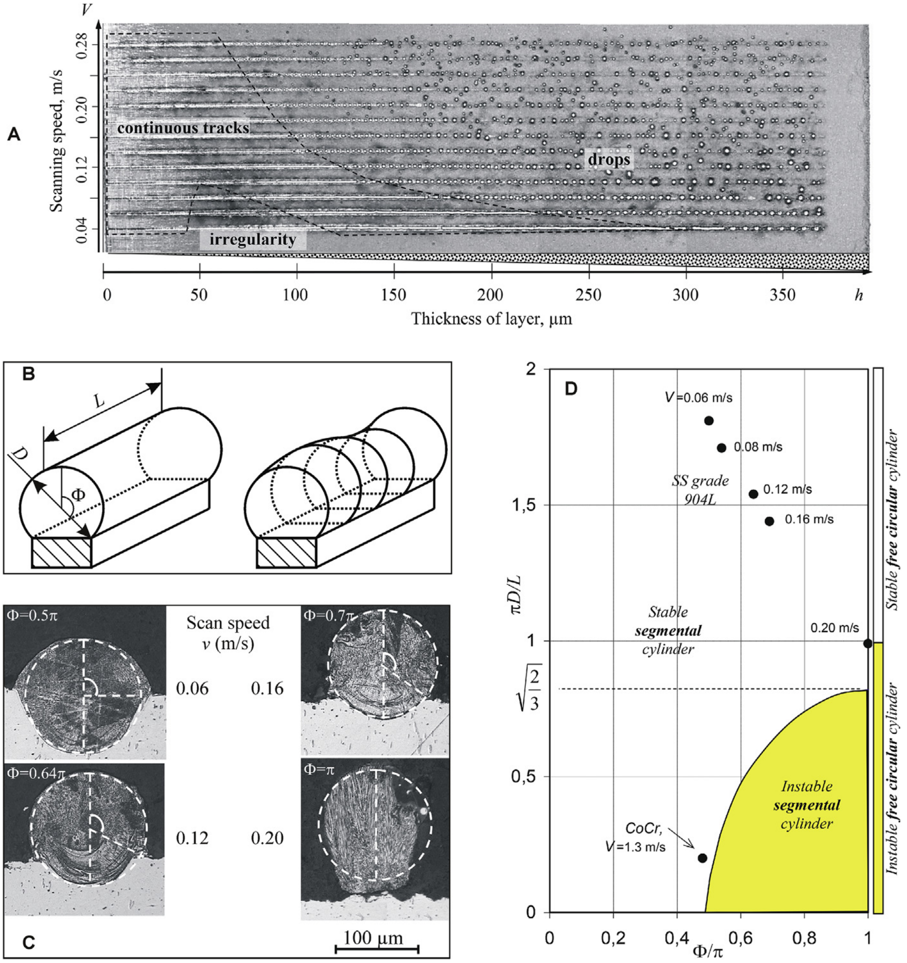

Figure 4.6 (A) Domain of continuous tracks below the top dashed curve in parameter space *v*-*H* at $P = 50$ W (Yadroitsev and Smurov, 2010). (B) Segmental cylinder of fluid adjacent to a solid substrate: initial state (left) and disturbance due to the capillary instability (right). (C) Cross-sections of continuous single tracks at the indicated values of the scan speed *v* (steel AISI 904L, laser power 50 W) and (D) Stability map for the segmental and free circular cylinders. The points correspond to single track experiments, Yadroitsev et al. (2010).

On the top-right of Fig. 4.6A, the discontinuous fused material looks like droplets. Yadroitsev et al. (2010) supposed that such droplets are formed as the result of melt pool disintegration because of a capillary instability. A long cylinder of liquid tends to break up into drops with the same volume but smaller surface. This effect is known as the Plateau-Rayleigh instability. One can model the melt pool as a circular cylinder of diameter D and length L. Such a cylinder is stable if its aspect ratio $L/D < \pi$ and unstable otherwise (Chandrasekhar, 1981). Section 4.5 demonstrated that the aspect ratio of the melt pool increases with the scan speed. Thus, the Plateau-Rayleigh instability of a circular cylinder explains the loss of stability with increasing the scan speed. However, such a model cannot describe the observed influence of the laser power and the layer thickness.

The laser beam melts not only powder but the adjacent domain of the substrate. Thus, a metallurgical bond is formed between the fused powder and the substrate. The above model of free circular cylinder does not account for the influence of the solid substrate on the melt pool. A more complicated geometry of segmental cylinder is shown in Fig. 4.6B that describes the experimentally observed single tracks with the cross-sections shown in Fig. 4.6C. The half-angle Φ of the segmental cylinder characterizes the width of the bond with the substrate. Fig. 4.5C shows that the bond diminishes with increasing the scan speed. It corresponds to increasing Φ. Angle $\Phi = 0$ corresponds to a substrate without powder. Angle $\Phi = \pi$ corresponds to a single track not bonded to the substrate. A disturbance of the segmental cylinder (on the right of Fig. 4.6B) at the constant width of the bond and concluded that the segmental cylinder is stable if

$$\frac{\pi D}{L} > \sqrt{2}\sqrt{\frac{\Phi(1+\cos 2\,\Phi) - \sin 2\,\Phi}{2\Phi(2+\cos 2\,\Phi) - 3\sin 2\,\Phi}}, \tag{4.65}$$

at $\Phi > \pi/2$ and it is stable at $\Phi < \pi/2$ independently on the aspect ratio L/D. Fig. 4.6D shows the domains of stability and instability of the segmental cylinder in the two-dimensional parameter space of angle Φ and inverse aspect ratio D/L. It has to be noted that a half-cylinder or less with $\Phi < \pi/2$ is unconditionally stable, which is favorable for L-PBF. To attain such a shape of the cross-section, one should ensure melting of the substrate and decrease the thickness of the powder layer. If the thickness of the powder layer increases at the constant laser power, the bond does not widen while the tracks diameter increases. This means that angle Φ increases, see Fig. 4.6C. Thus, the capillary stability decreases. If the laser power increases at the constant powder thickness, the bond widens and angle Φ decreases. Thus, the capillary stability increases. Both trends are in line with the experiments, see Yadroitsev et al. (2010) and Ciurana et al. (2013).

At $\Phi = \pi$, the segmental cylinder reduces to a circular one and condition Eq. (4.65) reduces to

$$\frac{\pi D}{L} > \sqrt{\frac{2}{3}}, \tag{4.66}$$

which is weaker than the stability condition for the free circular cylinder because the segmental cylinder is still attached to the substrate by a line at $\Phi = \pi$. Comparison of the stability maps for the free circular cylinder and the segmental cylinder attached to the substrate in Fig. 4.6D indicates that a bond with a substrate generally increases the capillary stability.

To validate the stability map of Fig. 4.6D, the experiments shown in Fig. 4.5C can be applied. The track diameter D and the half angle Φ are measured on the cross-sections while the length of the melt pool L is estimated by numerical modeling. The resulting points in the parameter space are shown in Fig. 4.6D. All the points for steel AISI 904L lie in the stability domain for the segmental cylinder, which agrees with the experimentally observed continuous uniform single tracks. The point corresponding to $v = 0.2$ m/s falls on the boundary of the stability domain for the free circular cylinder, see Fig. 4.6D. The corresponding single track is continuous but the bond with the substrate is very weak, see Fig. 4.6C. Indeed, experiments of Yadroitsev et al. (2007) revealed balling at further increase of the scan speed. In Fig. 4.6C, the experimental point for CoCr alloy corresponds to a considerably greater scan speed of 1.3 m/s. The melt pool is estimated to be significantly elongated, with the aspect ratio $L/D \approx 15$. However, this point falls on the stability domain of the segmental cylinder because a wide bond formed between the single track and the substrate. The measured value of angle Φ was around $\pi/2$, which corresponds to a half cylinder (Fig. 4.6D).

In summary, undesirable irregular and discontinuous single tracks are observed at insufficient energy input. Experiments indicate that melting of the substrate and formation of a wide metallurgical bond with the substrate is favorable for obtaining continuous and uniform tracks. The formation of irregular and discontinuous tracks can be explained by a capillary instability of the melt pool. The stability map for the segmental cylinder may help to find the optimal L-PBF process parameters.

4.7 Thermomechanics

During L-PBF, the laser beam locally heats the manufactured object. The materials not resistant to thermal shocks may crack at laser processing. Microcracks are often observed after L-PBF of brittle materials. Fig. 4.7A shows typical cracks in a single track of a hard metal. The origin of the cracking is the thermomechanical stresses arising due to a nonuniform thermal expansion. Fig. 4.7B schematically considers a heating-cooling thermal cycle experienced by a portion of a medium at laser processing. After the laser beam strikes the considered region (left), the temperature rises locally and compressive stresses are formed in the heat affected zone (HAZ) of the solid phase due to thermal expansion. Then, the central part of the HAZ melts (middle). The stresses relax in the melt pool. When the laser beam goes out (right) and the temperature is decreasing down to the initial value, the HAZ region around the remelted domain would tend to the initial nonstressed state. However, it interacts

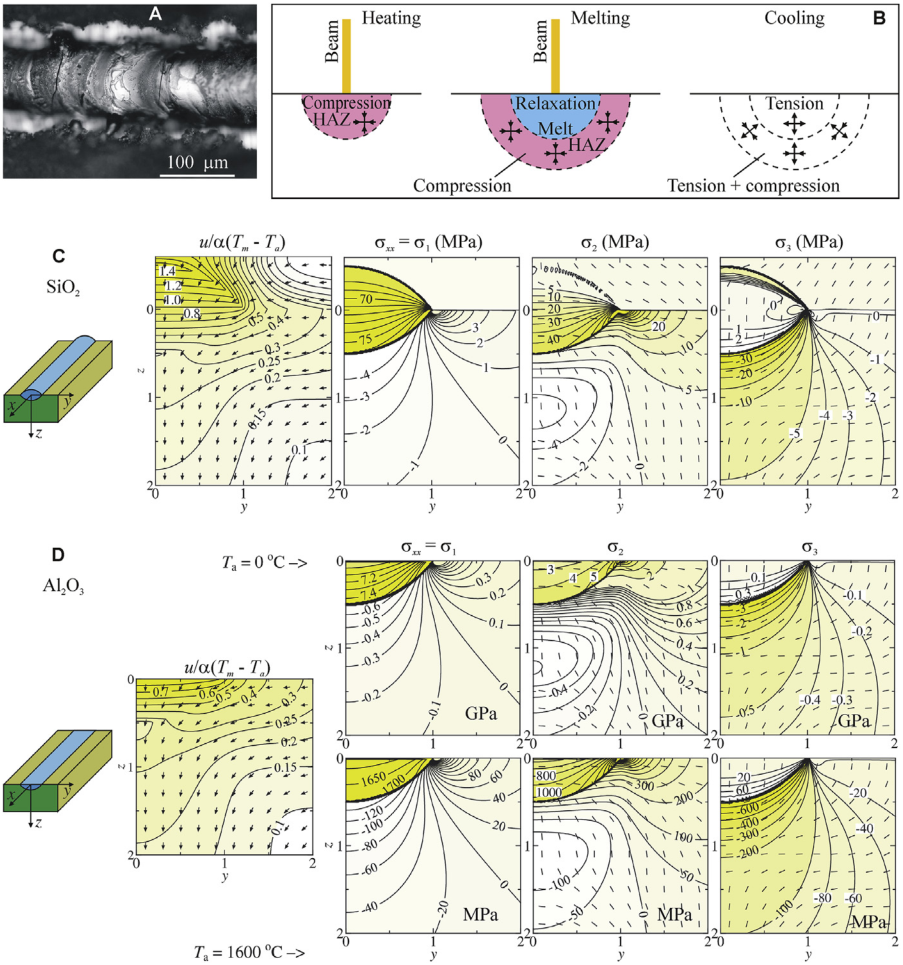

Figure 4.7 (A) Single track with transverse cracks (WC-Co, laser power of 50 W, scan speed of 0.03 m/s). (B) Formation of residual stresses in a laser processing cycle due to consecutive expansion in a heat affected zone (HAZ), left, stress relaxation in a melt pool, middle, and contraction at cooling, right. Calculated distributions of residual deformations are specified by the contours of the absolute value *u* and the arrows indicate the direction, and the residual stresses are specified by the principal values σ_1, σ_2, and σ_3 and the dashes indicate the directions of the principal axes, Gusarov et al. (2011): (C) Silica at the room temperature; (D) Alumina at the room temperature (top) and 1600°C preheat (bottom).

with the remelted domain that is being cooled from a nonstressed state at the melting point. Tensile stresses arise in the remelted domain due to a thermal contraction. This domain pulls the surrounding medium. That is why tensile stresses are formed in the radial direction and compressive stresses in the tangential direction around the remelted domain; see the right diagram in Fig. 4.7B.

This diagram gives a typical distribution of residual stresses after local laser processing. They can partly relax due to a plastic flow or cracking. Tension in all the three axes is expected in the remelted domain. It is in this domain that cracking occurs as shown in Fig. 4.7A. In the L-PBF process, thermomechanical stresses and deformations of the multiple laser scans are superposed giving rise to a stress distribution and a deformation of the whole part being manufactured. Chapter 9 considers the residual stresses and deformations in the scale of the part. This section studies local stresses around a single fused track.

It is difficult to deduce general conclusions applicable to a wide range of materials with variable rheology. That is why, the linear isotropic thermoelastic medium is investigated below. While the spectrum of realistic materials quantitatively matching this model is restricted, it may predict right tendencies. Gusarov et al. (2011) proposed the following formulation of the problem. Let the laser beam scan parallel to axis X. When the residual stresses are formed after complete cooling, their distribution becomes uniform in this direction. The deformation state in plane (YZ) is specified by the vector field of displacement $\mathbf{u} = (u_y, u_z)$. The strain tensor with components $\varepsilon_{\beta\gamma}$ is

$$\begin{gathered}\varepsilon_{xx} = \varepsilon_{xy} = \varepsilon_{xz} = 0, \quad \varepsilon_{yy} = \frac{\partial u_y}{\partial y}, \quad \varepsilon_{zz} = \frac{\partial u_z}{\partial z}, \\ \varepsilon_{yz} = \frac{1}{2}\left(\frac{\partial u_y}{\partial z} + \frac{\partial u_z}{\partial y}\right).\end{gathered} \tag{4.67}$$

In the calculation domain distributions of solid, remelted, and gas phases are specified by the phase indicator functions ϕ_s, ϕ_r, and ϕ_g, respectively, which are equal to 1 in the corresponding phase and 0 otherwise. The generalized Hooke's law for the components of the stress tensor $\sigma_{\beta\gamma}$ is written as

$$\begin{gathered}\sigma_{\beta\beta} = \left(1 - \phi_g\right)\left[\lambda\theta + 2\mu\varepsilon_{\beta\beta} + \phi_r 3\alpha K(T_m - T_a)\right], \\ \sigma_{xy} = \sigma_{xz} = 0, \quad \sigma_{yz} = \left(1 - \phi_g\right)2\mu\varepsilon_{yz},\end{gathered} \tag{4.68}$$

where $\beta = x,\ y,\ z$, λ is Lame's first parameter, μ the shear modulus, K the bulk modulus, α the linear thermal expansion coefficient, T_a the ambient temperature, T_m the melting point, and $\theta = \varepsilon_{yy} + \varepsilon_{zz}$. The system of force balance equations is (Gusarov et al., 2011)

$$\frac{\partial \sigma_{yy}}{\partial y} + \frac{\partial \sigma_{yz}}{\partial z} = 0, \quad \frac{\partial \sigma_{zz}}{\partial z} + \frac{\partial \sigma_{yz}}{\partial y} = 0. \tag{4.69}$$

Fig. 4.7C and D show the results obtained by numerical solution of Eqs. (4.67)–(4.69). There, the displacement field is normalized by $\alpha(T_m - T_a)$ and the stress field is given by the principal values σ_1, σ_2, and σ_3 and the direction of the principal axes (dashes). According to the symmetry, axis X is a principal axis. The directions of the other two principal axes in plane (YZ) are variable.

The calculation results indicate that inside the remelted domain, the second principal axis is approximately axis Y and the third principal axis is approximately axis Z. The maximum tensile stress is attained in the remelted domain in the longitudinal direction, axis X. See, for example, the distribution of σ_{xx} in Fig. 4.7C with the maximum of around 75 MPa attained at the bottom of the remelted domain. The tensile stress in the transverse direction, axis Y, is significantly lower, see the distribution of σ_2 in Fig. 4.7C with the maximum of around 40 MPa attained at the bottom of the remelted domain. The tensile stress in the vertical direction, axis Z, inside the remelted domain is much lower than the longitudinal and transverse stresses, see the distribution of σ_3 in Fig. 4.7C with the maximum of around 2 MPa. The maximum compressive stress around -30 MPa is attained outside the remelted domain near its bottom boundary, see the distribution of σ_3 in Fig. 4.7C. The compression direction is parallel to the boundary in agreement with the right diagram in Fig. 4.7B.

The tensile stresses in the remelted domain explain cracking frequently observed at L-PBF. One can expect cracking if a stress becomes greater than the tensile strength of the material. Maintaining the L-PBF-machine working chamber at an elevated temperature referred to as the preheating is the best known method to reduce residual stresses, and thus to avoid or reduce cracking. It can be explained in the framework of the thermoelastic model. Indeed, the residual stresses are proportional to the inhomogeneous term $\sim\alpha K(T_m - T_a)$ in the first Eq. (4.68). The ambient temperature T_a in this term is the temperature in the working chamber. The preheating decreases the difference $(T_m - T_a)$ to which the residual stresses are proportional. The model also indicates that the residual stresses are proportional to the thermal expansion coefficient α and the bulk modulus K. Thus, choosing materials with low α and K is favorable to avoid cracking. The lower row of diagrams in Fig. 4.7D shows that preheating of alumina up to $T_a = 1600°\text{C}$ reduces the maximum stress from ~ 7 to ~ 1.7 GPa. Thus, the calculations confirm that the preheating is useful to reduce the residual stresses.

All the three examples shown in Fig. 4.7C and D indicate that in the remelted domain, the longitudinal tensile stresses are greater than the transverse ones by a factor of approximately 2. It is consistent with the image of cracks in a fused track in Fig. 4.7A. There are only transverse cracks in the image. The transverse cracks are due to the longitudinal tensile stress. Thus, one can conclude that the longitudinal stress attains the tensile strength while the transverse stress is lower than the tensile stress. Gusarov et al. (2013) applied the thermoelastic model to metals and alloys prone to plastic flow. The model calculations without preheating indicated that the stresses easily attain the yield strength. The model does not account for plastic flow, so that it is not applicable when the stresses become greater than the yield strength. However, the qualitative stress distribution is still valid, which is shown by the right diagram in Fig. 4.7B. The maximum stresses in the remelted domain should be around the yield strength.

4.8 Nomenclature

A	effective absorptance
C	specific heat capacity
c	constant
D	diameter, depth
d	diameter
E	energy per unit volume
e	Euler's number
$\mathbf{E}$	electric vector
F	hypergeometric function
F	momentum flux, force
f	angular factor of angular velocity
g	angular factor of pressure, gravity acceleration
H	melt depth, layer thickness
$\mathbf{I}$	identity tensor
K	bulk modulus
k	Boltzmann constant
L	latent heat, length
M	Mach number
m	molecular mass
n	refractive index, number density
$\mathbf{n}$	unit normal vector
P	power
p	pressure
Pe	thermal Peclet number
$\mathbf{Q}$	energy flow
R	effective reflectance, radius
r	reflectance
Re	Reynolds number
S	sound speed
s	shift
T	temperature
t	time
U	internal energy per unit volume
$\mathbf{u}$	flow velocity, displacement
v	scanning speed
x	coordinate in the direction of laser scanning
y	coordinate
z	coordinate in the direction perpendicular to the surface

Greek symbols

α	absorption coefficient, parameter, thermal diffusivity, surface tension coefficient, linear thermal expansion coefficient
β	extinction coefficient, parameter, derivative of the surface tension coefficient with respect to temperature
γ	parameter
Δ	Laplace operator

ε	gap
η	dynamic viscosity
θ	incidence angle, polar angle, variable
κ	curvature
λ	thermal conductivity, Lame's first parameter
μ	friction coefficient, shear modulus
ν	kinematic viscosity
Π	thermal Peclet number
ρ	density
τ	shear stress
Φ	angle
ϕ	phase indicator
φ	angular factor of radial velocity
ψ	speed ratio
$\boldsymbol{\varepsilon}$	strain tensor
$\boldsymbol{\Pi}$	momentum flow tensor
$\boldsymbol{\pi}$	angular factor of momentum flow tensor
$\boldsymbol{\sigma}$	stress tensor
$\boldsymbol{\tau}$	unit tangent vector
ΔV	volume change

Subscripts

a	adhesion, ambient
b	boiling, behind
d	drag
f	forward
fr	friction
g	gravity, gas
g	glass transition
l	liquid
m	melting
max	maximum
n	normal
p	parallel, particle
R	radiative
r	recoil, remelted
s	perpendicular, saturated vapor, solid
t	time derivative
v	vapor
x	directional derivative in the direction of laser scanning
τ	tangential

Superscript

T	transpose

Other

∇	nabla operator

4.9 Questions

- What is the difference between the laser beam and the laser spot?
- Why is the effective absorptance of a powder bed greater than the absorptance of the same material in a compact state?
- Can the vapor pressure be greater than the saturated vapor pressure at laser evaporation?
- What are the typical values of the Reynolds number in the entrainment flow of ambient gas induced by the evaporation jet?
- Why can the keyhole arise in the melt pool?
- What is the thermal Peclet number in a fluid flow?
- How does the melt pool volume vary with the scan speed?
- What are the typical values of the cooling rate in L-PBF?
- What is the balling effect?
- What is the difference between the heat affected zone and the remelted domain?
- Why does the preheating reduce residual stresses?

References

Bidare, P., Bitharas, I., Ward, R.M., Attallah, M.M., Moore, A.J., 2018a. Fluid and particle dynamics in laser powder bed fusion. Acta Mater. 142, 107−120.

Bidare, P., Bitharas, I., Ward, R.M., Attallah, M.M., Moore, A.J., 2018b. Laser powder bed fusion at sub-atmospheric pressures. Int. J. Mach. Tool Manufact. 130−131, 65−72.

Bidare, P., Bitharas, I., Ward, R.M., Attallah, M.M., Moore, A.J., 2018c. Laser powder bed fusion in high-pressure atmospheres. Int. J. Adv. Manuf. Technol. 99, 543−555.

Bobel, A., Hector Jr., L.G., Chelladurai, I., Sachdev, A.K., Brown, T., Poling, W.A., Kubic, R., Gould, B., Zhao, C., Parab, N., Greco, A., Sun, T., 2019. In situ synchrotron X-ray imaging of 4140 steel laser powder bed fusion. Materialia 6, 100306.

Boley, C.D., Mitchell, S.C., Rubenchik, A.M., Wu, S.S.Q., 2016. Metal powder absorptivity: modeling and experiment. Appl. Optic. 55, 6496−6500.

Born, M., Wolf, E., 1970. Principles of Optics. Pergamon Press, Oxford.

Callen, H.B., 1985. Thermodynamics and An Introduction to Thermostatistics. Wiley, New York.

Calta, N.P., Martin, A.A., Hammons, J.A., Nielsen, M.H., Roehling, T.T., Fezzaab, K., Matthews, M.J., Jeffries, J.R., Willey, T.M., Lee, J.R.I., 2020. Pressure dependence of the laser-metal interaction under laser powder bed fusion conditions probed by in situ X-ray imaging. Addit. Manufact. 32, 101084.

Carslaw, H.S., Jaeger, J.C., 1959. Conduction of Heat in Solids. Clarendon Press, Oxford.

Chandrasekhar, S., 1981. Hydrodynamic and Hydromagnetic Stability. Dover Publications, New York.

Ciurana, J., Hernandez, L., Delgado, J., 2013. Energy density analysis on single tracks formed by selective laser melting with CoCrMo produced by selective laser melting. Int. J. Adv. Manuf. Technol. 68, 1103−1110.

Egorov, S.A., Khmyrov, R.S., Korotkov, A.D., Gusarov, A.V., 2020. Experimental study and modeling of melt pool in laser powder-bed fusion of thin walls. Procedia CIRP 94, 372−377.

Ferziger, J.H., Kaper, H.G., 1972. Mathematical Theory of Transport Processes in Gases. North−Holland.

Gunenthiram, V., Peyre, P., Schneider, M., Dal, M., Coste, F., Koutiri, I., Fabbro, R., 2018. Experimental analysis of spatter generation and melt-pool behavior during the powder bed laser beam melting process. J. Mater. Process. Technol. 251, 376−386.

Gusarov, A.V., Smurov, I., 2002. Gas-dynamic boundary conditions of evaporation and condensation: numerical analysis of the Knudsen layer. Phys. Fluids 14, 4242−4255.

Gusarov, A.V., Smurov, I., 2005. Thermal model of nanosecond pulsed laser ablation: analysis of energy and mass transfer. J. Appl. Phys. 97, 014307.

Gusarov, A.V., Bentefour, E.H., Rombouts, M., Froyen, L., Glorieux, C., Kruth, J.-P., 2006. Normal-directional and normal-hemispherical reflectances of micron- and submicron-sized powder beds at 633 and 790 nm. J. Appl. Phys. 99, 113528.

Gusarov, A.V., Yadroitsev, I., Bertrand, P., Smurov, I., 2009. Model of radiation and heat transfer in laser-powder interaction zone at selective laser melting. J. Heat Tran. 131, 072101.

Gusarov, A.V., Pavlov, M., Smurov, I., 2011. Residual stresses at laser surface remelting and additive manufacturing. Phys. Procedia 12, 248−254.

Gusarov, A.V., Malakhova-Ziablova, I.S., Pavlov, M.D., 2013. Thermoelastic residual stresses and deformations at laser treatment. Phys. Procedia 41, 889−896.

Gusarov, A.V., 2020a. Analytic similarity solutions of the Navier-Stokes equations for a jet in a half space with the no-slip boundary condition. Phys. Fluids 32, 053104.

Gusarov, A.V., 2020b. Entrainment flow of a jet emerging into a half-space with the no-slip boundary condition. Phys. Fluids 32, 083107.

Gusarov, A.V., 2020c. Radiative transfer, absorption, and reflection by metal powder beds in laser powder-bed processing. J. Quant. Spectrosc. Radiat. Transf. 257, 107366.

Hibbeler, R.C., 2016. Engineering Mechanics: Statics and Dynamics. Pearson, New York.

Howell, J.R., Menguc, M.P., Siegel, R., 2015. Thermal Radiation Heat Transfer. Taylor & Francis, Boca Raton.

Khairallah, S.A., Martin, A.A., Lee, J.R.I., Guss, G., Calta, N.P., Hammons, J.A., Nielsen, M.H., Chaput, K., Schwalbach, E., Shah, M.N., Chapman, M.G., Willey, T.M., Rubenchik, A.M., Anderson, A.T., Wang, Y.M., Matthews, M.J., King, W.E., 2020. Controlling interdependent meso-nanosecond dynamics and defect generation in metal 3D printing. Science 368, 660−665.

Khmyrov, R.S., Ableeva, R.R., Gusarov, A.V., 2020. Metallographic study of denudation in laser powder-bed fusion. Procedia CIRP 94, 194−199.

Knight, C.J., 1979. Theoretical modeling of rapid surface vaporization with back pressure. AIAA J. 17, 519−523.

Kovalev, O.B., Gurin, A.M., 2014. Multivortex convection of metal in molten pool with dispersed impurity induced by laser radiation. Int. J. Heat Mass Tran. 68, 269−277.

Leite, F.L., Bueno, C.C., Da Róz, A.L., Ervino Ziemath, E.C., Oliveira Jr., O.N., 2012. Theoretical models for surface forces and adhesion and their measurement using atomic force microscopy. Int. J. Mol. Sci. 13, 12773−12856.

Liu, Y., Yang, Y., Mai, A., Wang, D., Song, C., 2015. Investigation into spatter behavior during selective laser melting of AISI 316L stainless steel powder. Mater. Des. 87, 797−806.

Ly, S., Rubenchik, A.M., Khairallah, S.A., Guss, G., Matthews, M.J., 2017. Metal vapor micro-jet controls material redistribution in laser powder bed fusion additive manufacturing. Sci. Rep. 7, 4085.

Matthews, M.J., Guss, G., Khairallah, S.A., Rubenchik, A., Anderson, A.T., Depond, P.J., King, W.E., 2016. Denudation of metal powder layers in laser powder bed fusion processes. Acta Mater. 114, 33−42.

Refractive Index.INFO, 2020. https://refractiveindex.info/.

Schneider, W., 1981. Flow induced by jets and plumes. J. Fluid Mech. 108, 55−65.

Schneider, W., 1985. Decay of momentum flux in submerged jets. J. Fluid Mech. 154, 91−110.

Tolochko, N.K., Laoui, T., Khlopkov, Y.V., Mozzharov, S.E., Titov, V.I., Ignatiev, M.B., 2000. Absorptance of powder materials suitable for laser sintering. Rapid Prototyp. J. 6, 155−160.

Yadroitsev, I., Bertrand, P., Smurov, I., 2007. Parametric analysis of the selective laser melting process. Appl. Surf. Sci. 253, 8064−8069.

Yadroitsev, I., Smurov, I., 2010. Selective laser melting technology: from the single laser melted track stability to 3D parts of complex shape. Phys. Procedia 5, 551−560.

Yadroitsev, I., Gusarov, A., Yadroitsava, I., Smurov, I., 2010. Single track formation in selective laser melting of metal powders. J. Mater. Process. Technol. 210, 1624−1631.

Ye, J., Khairallah, S.A., Rubenchik, A.M., Crumb, M.F., Guss, G., Belak, J., Matthews, M.J., 2019. Energy coupling mechanisms and scaling behavior associated with laser powder bed fusion additive manufacturing. Adv. Eng. Mater. 21, 1900185.

Zauner, E., 1985. Visualization of the viscous flow induced by a round jet. J. Fluid Mech. 154, 111−119.

Zel'dovich, Y.B., Raiser, Y.P., 1967. Physics of Shock Waves and High-Temperature Hydrodynamic Phenomena. Acad. Press, New York.

Zhang, Y., Lin, X., Wang, L., Wei, L., Liu, F., Huang, W., 2015. Microstructural analysis of $Zr_{55}Cu_{30}Al_{10}Ni_5$ bulk metallic glasses by laser surface remelting and laser solid forming. Intermetallics 66, 22−30.

Zhirnov, I., Kotoban, D.V., Gusarov, A.V., 2018. Evaporation-induced gas-phase flows at selective laser melting. Appl. Phys. A 124, 157.

Design principles

5

Martin Leary[1], *David Downing*[1], *Bill Lozanovski*[1], *Jonathan Harris*[2]
[1]Centre for Additive Manufacturing, School of Engineering, RMIT University, Melbourne, VIC, Australia; [2]nTopology, New York, NY, United States

Chapter outline

5.1 Introduction 120
5.2 The laser powder bed fusion process 120
5.3 L-PBF design challenges 121
5.4 L-PBF design strategies 123
  5.4.1 Implications of layerwise manufacture 123
  5.4.2 Positioning of specimens on a base plate and recoater trajectory 124
  5.4.3 Thermal systems 125
  5.4.4 Support structures 125
  5.4.5 Digital dataflow 127
  5.4.6 Optimization for material addition 128
5.5 Case study: L-PBF manufacture of high-value product 128
5.6 L-PBF design opportunities 130
5.7 Digital data optimization 130
  5.7.1 Metadata analysis—doing more with less 132
  5.7.2 Resolution restriction—how much data is enough? 132
5.8 Digital geometry formats 134
  5.8.1 Boundary representation (meshes and B-Rep CAD) 134
  5.8.2 Volumetric representation (voxel and implicit) 136
5.9 Generative design 137
5.10 Simulation-driven design 137
  5.10.1 Topology optimization 138
  5.10.2 Parametric optimization 140
5.11 Uncertainty quantification for L-PBF design 142
  5.11.1 Numerical prediction 142
  5.11.2 Experimental methods 143
  5.11.3 Uncertainty quantification methods 143
  5.11.4 Lattice simulation—component level 144
  5.11.5 Lattice simulation—strut level 144
  5.11.6 Lattice simulation—node level 147
5.12 Emerging opportunities for L-PBF design outcomes 147
5.13 Concluding comments 148
5.14 Questions 150
Acknowledgments 150
References 150

Fundamentals of Laser Powder Bed Fusion of Metals. https://doi.org/10.1016/B978-0-12-824090-8.00013-5
Copyright © 2021 Elsevier Inc. All rights reserved.

5.1 Introduction

Additive Manufacturing (AM) is a unique and emerging manufacturing philosophy. Although AM inherently enables commercial and technical opportunities, it is fundamentally complex in both technical and economic domains. These complexities are often poorly understood, potentially leading to suboptimal design decisions. This possibility for commercial failure can be offset by reference to established Design for Additive Manufacturing (DFAM) tools and methodologies.

DFAM methods may be classified as either generalized contributions that are relevant to the overarching theme of AM or specifically within a particular subbranch of AM (Frazier, 2014). DFAM tools and methodologies engage with the unique attributes of AM, specifically that AM is inherently (ISO/ASTM, 2015):

- associated with a digital workflow
- implemented by a common source material
- enabled by the sequential addition of input material.

DFAM guidance is increasingly available as formal design guidelines and associated case studies; the following summarizes the research contributions and commercial best-practice applications of relevance to L-PBF.

5.2 The laser powder bed fusion process

Powder Bed Fusion (PBF) processes within the ISO/ASTM classification of PBF technologies are defined as an AM process "in which thermal energy selectively fuses regions of a powder bed" (ISO/ASTM, 2015). Laser energy is a robust and precise energy source and is applied in the commercially valuable classification of Laser PBF (L-PBF). The technical and economic attributes of this important AM technology classification are characterized in detail in Chapters 2 and 22, respectively; but in summary, they include the following aspects (and associated design challenges) (Fig. 5.1):

- Sequential addition of tracks and layers (potential source of defects).
- Galvanometer guided laser beam (defects due to trajectory planning).
- Local melting and solidification by a laser-induced melt pool (source of thermal defects, challenges for various materials, emerging opportunities of in-situ control).
- Digitally defined data input (potentially high data complexity).
- Common source material (challenge for net-shape design that may require multiple materials).
- Variable process parameters (challenging for process optimization, including layer thickness, laser energy density, hatch spacing, scan strategy).

Specific L-PBF design challenges are defined in the following section, allowing opportunities for enhanced L-PBF design to be presented in the following sections.

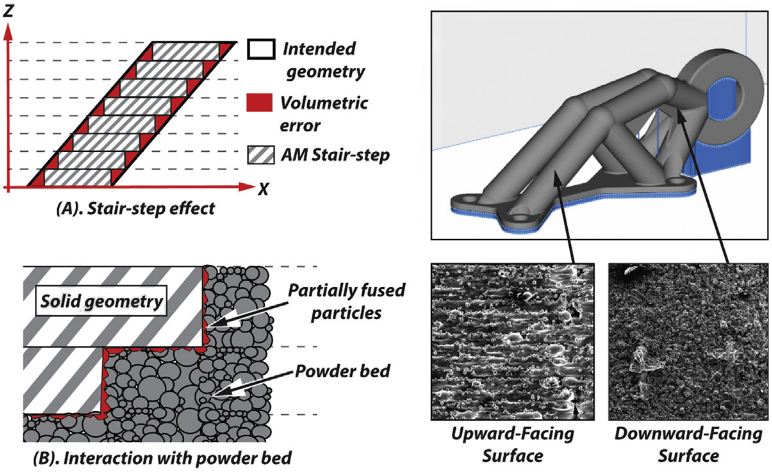

Figure 5.1 Potential defects of relevance to L-PBF design include: (A) effect of stair-step geometry due to layerwise manufacture and (B) surface roughness due to thermal effects and interaction with powder bed.

5.3 L-PBF design challenges

The fundamental L-PBF process involves the temporal and spatially transient interaction between the laser beam, particulate powder bed, and shielding atmosphere, and is therefore a highly complex interaction of physical, chemical, and thermal processes. These complex interactions are directly influenced by material parameters (powder sizes, shapes, and packing density), process parameters (laser power, hatch spacing, layer thickness), scanning strategy, and design of the input geometry (including support structure selection). The functionally relevant outcomes of the complex interactions of the L-PBF manufacturing process must be accommodated for by robust design principles. The properties of L-PBF fabricated components differ from those fabricated using traditional subtractive manufacturing methods. For example, the rapidly solidifying melt pool in a stochastic distribution of metallic powder produces uncertainties in the as-manufactured geometry and material properties.

The following summary attempts to briefly quantify these challenges as relevant to L-PBF design (Fig. 5.2):

- ***Stair-step effects:*** The AM process is inherently associated with the sequential addition of material. Commercial L-PBF systems are implemented as a Cartesian kinematic system thereby resulting in a layerwise discretization of the intended component geometry (Strano et al., 2013). This intrinsic loss of geometric resolution results in a periodic interruption to the intended geometry; this defect tends to become exacerbated for acute inclination between a surface and the build plate, as well as for increasing layer-thickness (Han et al., 2018).

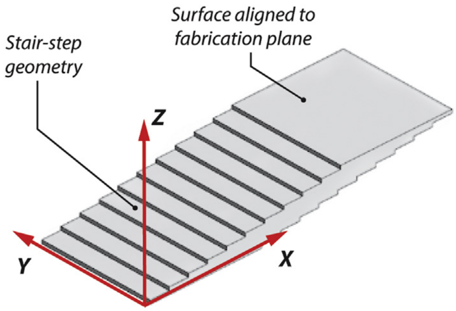

Figure 5.2 Stair-step effects are visible on geometry that is not either vertical or parallel to the fabrication plane.

- ***Particle attachment:*** L-PBF uses particulate metallic material as both input to the melt pool and to provide a supporting structure for the overhanging material. This scenario leads to spattering of particles ejected from the melt pool on upward-facing surfaces; and partial melting of particles on downward-facing surfaces (especially for acute inclinations), as the powder-bed provides support to the solidifying melt pool (Sarker et al., 2018). Powder attachment behavior during energy deposition and melt pool evolution depends on material parameters (such as thermal diffusivity and contact resistance) and powder bed attributes (such as powder morphology and packing density), which determine whether a particle is absorbed by the melt pool, partially melts to the bulk geometry, or remains solid and unattached (Khorasani et al., 2019).
- ***Digital data overload:*** L-PBF scanning strategies are generated via processing of digital geometry representations (Section 5.6). The magnitude of this data can be very large causing processing bottlenecks if the machine's capability to accommodate the data is overloaded.
- ***Geometry optimization:*** The selection of component geometry for L-PBF is an engineered compromise between as-manufactured outcomes and fundamental structural requirements. This compromise can be challenging and can benefit from formal methods of topology and parametric optimization (Section 5.7).
- ***Melt pool solidification:*** Melt pool solidification is a complex transient thermal-fluid event, which dictates the behavior of the melted metallic powder particles during the build process as well as the fabricated geometry. Other factors which also impact melt pool dynamics and associated defects are processing parameters, such as scan speed and laser energy density, as well as neighboring temperature fields and previously fused geometry. Inconsistencies in melt pool solidification can occur resulting in a series of identifiable L-PBF defects (McMillan et al., 2017):
  - *Slumping* describes the spread of the melt pool resulting in both lateral and vertical distortion of the solidified geometry. It also causes undesired contact with powder particles below the melt pool, therefore increasing the melt pool size (Leary, 2018; Sampson et al., 2020).
  - *Balling* occurs due to poor wetting of the substrate by the melt pool, resulting in the molten track or pool to separate and form a sphere due to surface tension. The balling effect leads to high surface roughness and can induce porosity, causing a discrepancy between the as-designed and as-manufactured geometry (Li et al., 2012; Sun et al., 2017), see also Chapter 3.
  - *Porosity* defects are highly relevant to the functional performance of L-PBF structures and can occur due to several factors as detailed in Chapter 6. *Gas porosity* occurs due to the

entrapment of shielding gas during melt-pool solidification or entrained gas from the original powder feedstock manufacture (Aboulkhair et al., 2014; Gong et al., 2015; Martin et al., 2019). *Keyhole porosity* occurs when excess energy is delivered to the laser melt pool (especially during changes in laser velocity as occurs at scan turning points), resulting in melt-pool evaporation that initiates a keyhole depression that upon collapse can trap shielding gasses. *Lack of fusion porosity* can occur between layers due to insufficient laser power density and is characterized by an irregular or elongated pore shape. *Intra-layer porosity* occurs due to nonoptimized overlap between neighboring laser scan trajectories within a layer. For more information on porosity, please refer to Chapter 6.

5.4 L-PBF design strategies

L-PBF enables the fabrication of high-complexity structures with low material waste and without the need for custom tooling. These capabilities enable commercially valuable production outcomes *if* the design challenges identified above are addressed. A series of designs for AM (DFAM) rules are emerging that provide generalizable insight for commercial best-practice L-PBF design, and are summarized below, and then applied in the context of a commercial application (Section 5.5).

5.4.1 Implications of layerwise manufacture

The L-PBF technology is implemented in a layerwise manner that directly influences the as-manufactured geometry due to stair-step effects and interaction with the powder bed. The following design considerations are of relevance and should be considered when orienting an L-PBF component such that surface geometry is acceptable for the intended function (Fig. 5.2):

- For geometry that is inclined to the fabrication plane, a stair-step error is introduced due to the layerwise architecture of the L-PBF technology. This stair-step error increases as the inclination becomes more acute, resulting in increased geometric error.
- For geometry that is either vertical or parallel to the fabrication plane, stair-step error is nil, and the geometric accuracy is maximized. Consequently, geometry that is critical to component function should be preferentially aligned to the fabrication plane, although downward-facing surfaces are potentially problematic.
- Downward-facing surfaces are supported by contact with the powder bed during melt-pool solidification. This powder bed support enables L-PBF manufacture, but does compromise surface quality due to partially adhered powder.
- As the inclination becomes more acute, local temperatures increase, increasing geometric error and eventually resulting in catastrophic failure to manufacture the intended geometry (see Fig. 5.4). Although the specific allowable inclination depends on the particular L-PBF application, 45° is often cited as a conservative design rule for allowable L-PBF inclination.
- For geometry that is excessively acute, active support structures can be used; these structures are valuable in enhancing manufacturability, but these supports can introduce geometric defects when removed from the as-manufactured L-PBF component.

5.4.2 Positioning of specimens on a base plate and recoater trajectory

The L-PBF technology utilizes a recoater to screed the powder bed and ensure a consistent layer thickness (Fig. 5.3). This recoater is typically a flexible wiper that is periodically replaced. The wiper can be prematurely damaged by sharp edges associated with large prismatic structures; these structures should therefore be inclined to the recoater trajectory to avoid wiper damage which can then compromise consistency in layer thickness. Similarly, lattice structures should be inclined such that successive strut cross-sections are not on the same wiper trajectory.

(A). *Orientation of prismatic structures*

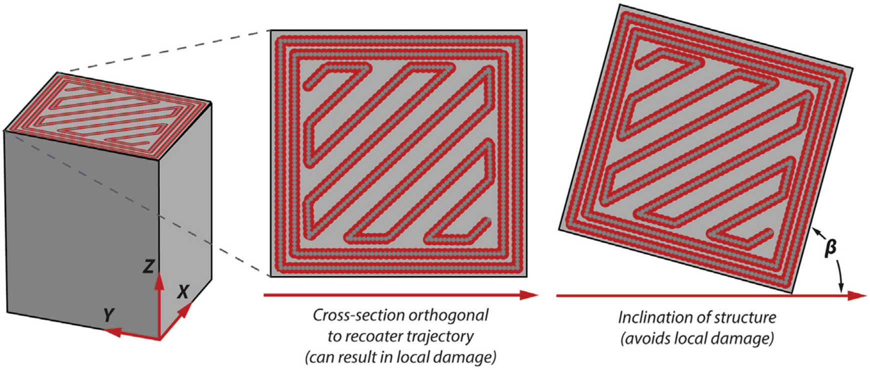
Z
X
Y
β
Cross-section orthogonal to recoater trajectory (can result in local damage)
Inclination of structure (avoids local damage)

(B). *Orientation of lattice structures*

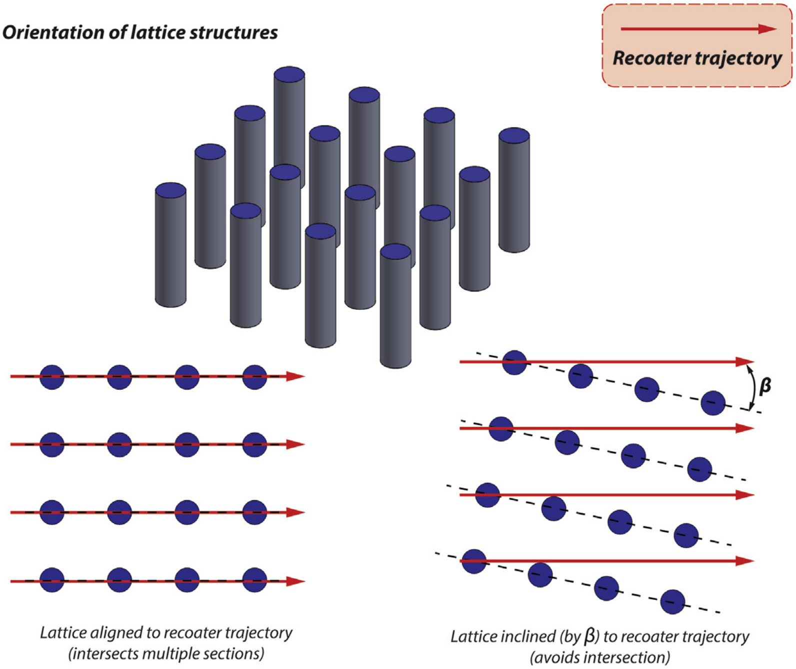
Recoater trajectory
β
Lattice aligned to recoater trajectory (intersects multiple sections)
Lattice inclined (by β) to recoater trajectory (avoids intersection)

Figure 5.3 Influence of recoater and preferred orientation of (A) prismatic structures and (B) lattice structures (Leary, 2019).

5.4.3 Thermal systems

L-PBF methods fundamentally enable material addition by the local melting and solidification of powdered input material. Transient thermal energy must be systematically managed to avoid thermal defects including bulk failure of structures due to thermal overload and excessive residual stresses on cooling. Thermal energy is managed by controlling laser toolpath, energy density, plate heating, component orientation, and support structure deployment. Established L-PBF DFAM rules for managing these thermal effects include (Fig. 5.4):

- The component orientation is of direct influence on the transient thermal field. In general, orientations that increase the conductive cross-sectional area while reducing the area exposed to laser heating result in cooler thermal fields.
- Structures with acute inclination to the build plate are typically associated with elevated thermal fields. Orientations that avoid these acute angles are preferred; however active support structures can be used to reduce thermal overloads for structures with acute inclination.
- L-PBF is a layerwise fabrication method, and thermal paths therefore vary with time. Awareness of these temporarily variable conduction paths can avoid excessive local temperatures. Component orientation and the use of supporting structures can assist in avoiding thermal overload.
- Laser scanning paths can be selected to avoid thermal overloads and component cross-sections can be optimized to reduce input heat loads.
- Build plate preheating provides an opportunity to reduce the temperature variation within the thermal field. This preheating can then be used to minimize distortion in the as-manufactured component.

5.4.4 Support structures

The use of support structures can significantly enhance L-PBF manufacturability; however, the additional material associated with support structure use increases material consumption and adds to production costs by requiring removal post-manufacture. The following L-PBF DFAM rules are useful for optimizing support structure deployment (Fig. 5.5):

- Functional surfaces may be geometrically compromised by frangible support structures. Near-net manufacture is enhanced by component design and orientations that avoid the need for support structures on functional surfaces.
- Part orientation and support structure design should be implemented such that overall support material required is minimized.
- L-PBF enables the fabrication of high complexity lattice structures that provide enhanced function and reduce manufacturing costs (by their associated reduction in part volume). These lattice structures can potentially be designed to provide both supporting structure and functional value to the manufactured product.

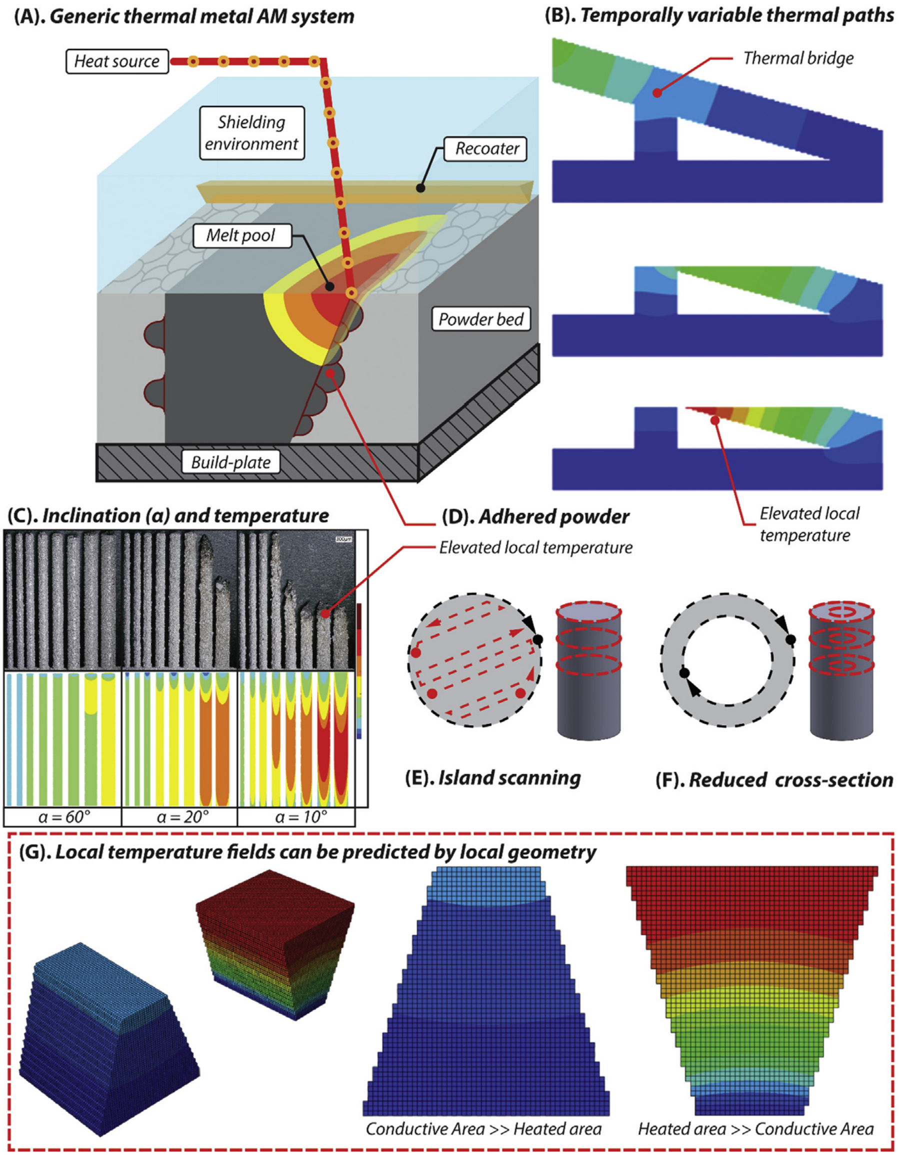
(A). Generic thermal metal AM system
Heat source
Shielding environment
Recoater
Melt pool
Powder bed
Build-plate
(B). Temporally variable thermal paths
Thermal bridge
Elevated local temperature
(C). Inclination (a) and temperature
a = 60°
a = 20°
a = 10°
(D). Adhered powder
Elevated local temperature
(E). Island scanning
(F). Reduced cross-section
(G). Local temperature fields can be predicted by local geometry
Conductive Area >> Heated area
Heated area >> Conductive Area

Figure 5.4 Thermal aspects of L-PBF design, including: (A) generic representation of L-PBF system, (B) effect of temporally variable conduction paths, (C) effect of inclination on thermal field, (D) adhered powder especially on downward-facing surfaces, (E) island scanning strategies, (F) reduced cross-section to reduce local thermal intensity, and (G) effect of orientation on temperature field (Leary, 2019).

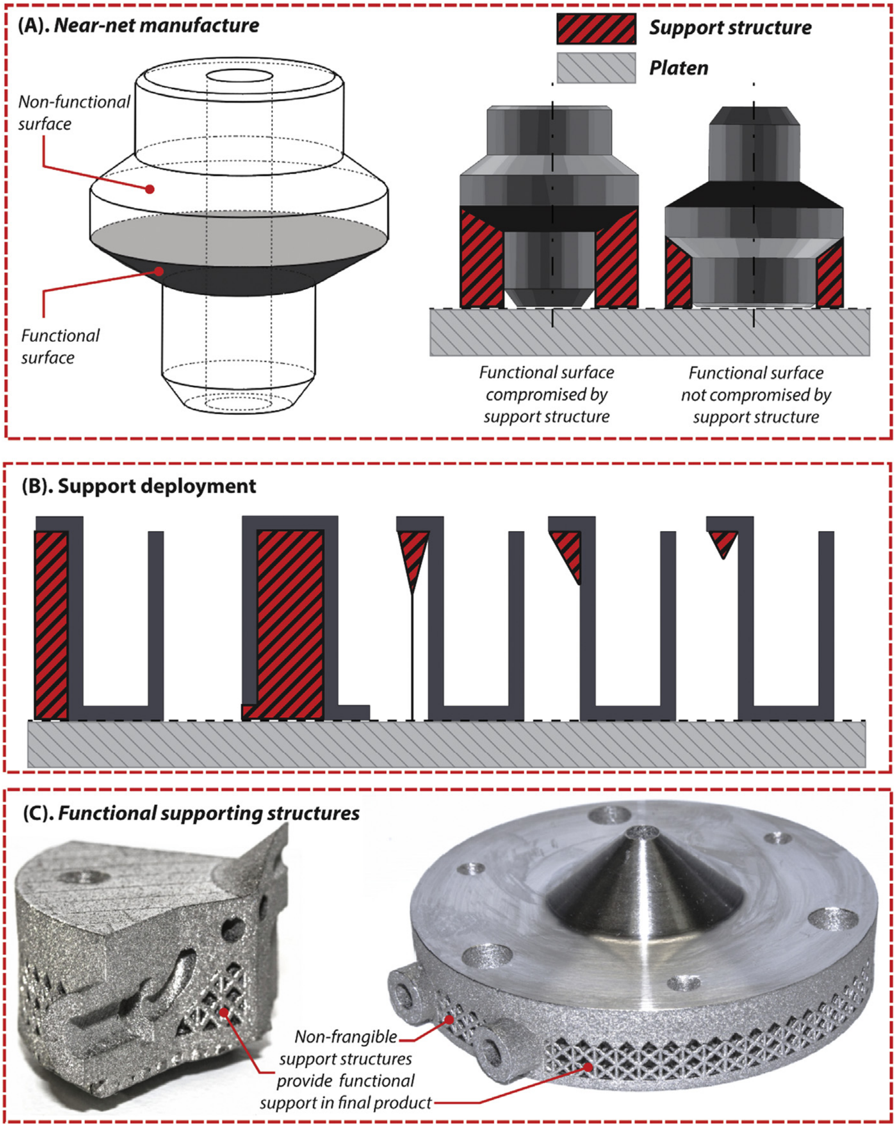
(A). Near-net manufacture
Support structure
Platen
Non-functional surface
Functional surface
Functional surface compromised by support structure
Functional surface not compromised by support structure
(B). Support deployment
(C). Functional supporting structures
Non-frangible support structures provide functional support in final product

Figure 5.5 Support structures to enhance L-PBF manufacturability. (A) enabling near-net manufacture by avoiding support use on functional surfaces, (B) effective component orientation to minimize support use, and (C) the design of supporting structures that are functional in the as-manufactured product (Leary, 2019).

5.4.5 Digital dataflow

L-PBF design workflow is inherently digital, from the digital representation associated with the intended component geometry to the digital data used as input for the L-PBF process and the digital representation of individual laser scanning paths. Optimization of these digital aspects enables best-practice design as is required for commercially successful L-PBF applications. These aspects have received less research attention than have practical design for manufacturability rules, and in response are presented in detail in Section 5.7, including design considerations for effective data representations and algorithmic methods for generative design.

5.4.6 Optimization for material addition

Traditional manufacturing methods such as casting, machining, and forging are typically designed to achieve their technical function by the definition of the external component surface. L-PBF enables a shift of this design focus from the external surface to any surface that is of benefit to the design. This *inside-out* design approach allows a focus on high-efficiency geometry such as lattice structures and hollow column sections. These structures can be specified to minimize the need for external support structures. Topology optimization provides a useful design tool for optimization of L-PBF structures; these simulation-driven design strategies are introduced in detail in Section 5.10.

5.5 Case study: L-PBF manufacture of high-value product

L-PBF technologies are especially suited to the manufacture of high-value componentry, especially for scenarios with high complexity or low-volume production that are not compatible with traditional manufacturing methods. The application of associated DFAM is combined with the economic considerations of Chapter 22 to illustrate commercial best-practices for the design of a high-value L-PBF aircraft structure (Fig. 5.6):

- ***Optimization for material addition.*** Topology optimization provides unambiguous and systematic insight into the optimal material distribution for a required loading condition. For example, these insights suggest a column network structure where the column elements are specified as closed sections to optimize buckling resistance; stiffening structures are utilized to avoid local buckling.
- ***Laser scanning path optimization.*** Logical deployment of laser scanning paths can avoid local overheating or failure to correctly melt a specific region. Where possible, component cross-sections should be optimized to enable laser scanning paths that conform to the local cross-section and can be traversed without unnecessary intersections.
- ***Net-shape manufacture.*** The economic value of a proposed L-PBF design is enhanced by reducing the number of post-processing operations required to implement the design. In this design, net-shape manufacture is achieved by accommodating access for fastener clearance, including drainage holes such that powder drainage is automated and by specifying frangible support structures that can be readily separated from the as-manufactured component.
- ***Component orientation.*** By considering the limits of inclination of self-supporting structures the topologically optimal geometry can be modified such that structural elements are self-supporting (especially relevant for internal volumes that are not accessible

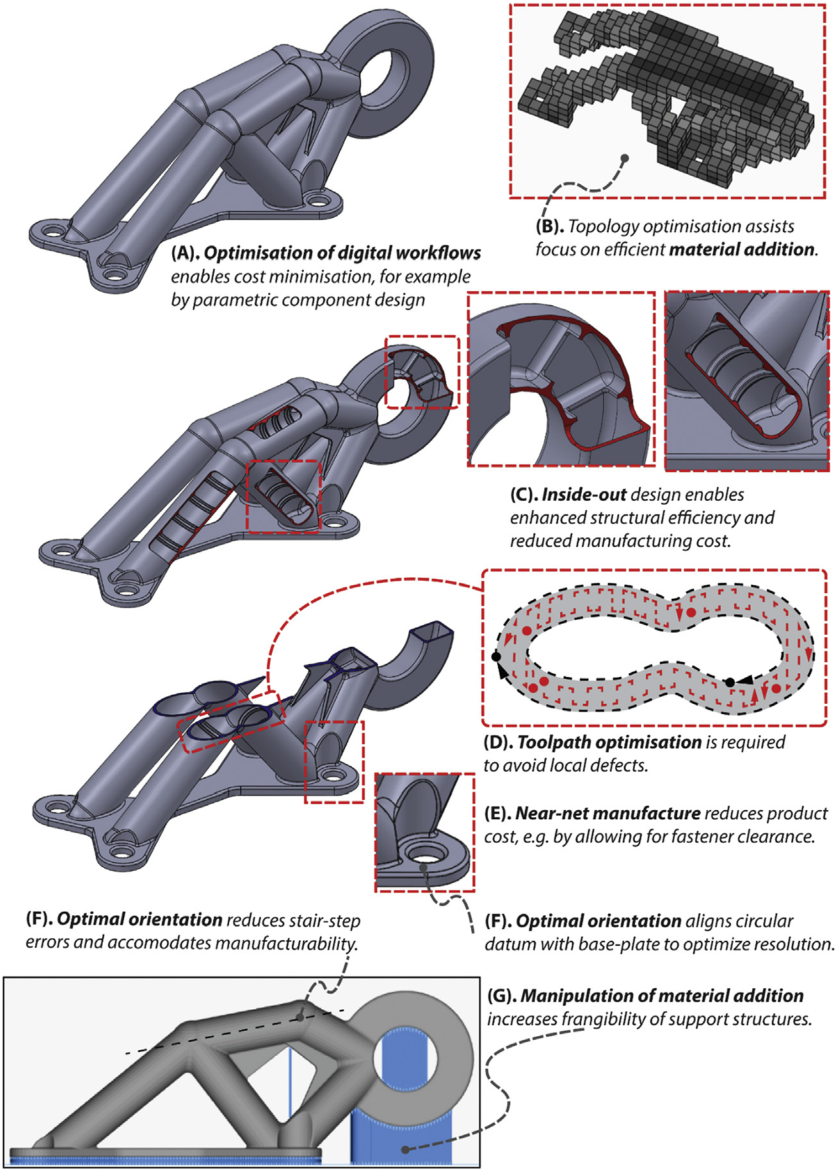
(A). Optimisation of digital workflows enables cost minimisation, for example by parametric component design
(B). Topology optimisation assists focus on efficient **material addition**.
(C). Inside-out design enables enhanced structural efficiency and reduced manufacturing cost.
(D). Toolpath optimisation is required to avoid local defects.
(E). Near-net manufacture reduces product cost, e.g. by allowing for fastener clearance.
(F). Optimal orientation reduces stair-step errors and accomodates manufacturability.
(F). Optimal orientation aligns circular datum with base-plate to optimize resolution.
(G). Manipulation of material addition increases frangibility of support structures.

Figure 5.6 Application of generalizable DFAM strategies to high-value aerospace bracket fabricated with Powder Bed Fusion (PBF): (A) Optimization of digital workflows to allow minimum manual effort in production and promote generative design methods. (B) Focus on material addition, especially enabled by topology optimization. (C) Inside-out design to maximize structural efficiency while reducing manufacturing cost. (D) Toolpath optimization to avoid local defects. (E) Near-net manufacture focus to reduce holistic component cost. (F) Orientation design to improve manufacturability and product function. (G) Manipulation of material addition to enhance support structure removal (Leary, 2019).

post-manufacture). Functional geometry is preferably oriented to be parallel to the fabrication plane to minimize stair-step effects.

- ***Thermal management.*** Structurally efficient topologies such as lattice structures and tubular sections are preferred, as they introduce lower thermal loads during manufacture. Relative orientation of these structures allows thermal conduction paths to be optimized.

5.6 L-PBF design opportunities

The L-PBF technology implementation inherently enables the fabrication of high-value structures with high geometric complexity and fundamentally robust mechanical properties. L-PBF production is highly automated and compatible with methods of generative design, thereby enabling cost-effective fabrication even for complex design outcomes. In response to these favorable techno-economic attributes, the commercial offerings in the L-PBF space are relatively mature turnkey industrial machines.

Despite L-PBF being a commercial technology, there exist quantifiable failure modes that if not addressed can lead to sub-optimal design outcomes, including functional failure or failure to satisfy economic constraints:

- ***Digital data management:*** L-PBF processes are inherently digital and if not effectively managed can result in data overload (conversely, effective data management enables batch processing and generative design).
- ***Functional optimization:*** formal methods of structural optimization (including parametric and topological optimization) provide an opportunity to systematically implement optimal L-PBF design.
- ***Management of stochastic uncertainties:*** the stochastic uncertainties inherent to L-PBF processes must be quantified and effectively managed for high-value product design.

These potential failure modes are defined in general terms below and are then considered in detail in terms of commercial best-practice in the following sections.

5.7 Digital data optimization

AM systems are inherently digital: digital geometry data is generated to represent the intended production geometry; this data is then digitally preprocessed to generate a series of laser scanning paths; and digital process data is then acquired during production and for certification of the manufactured component. Digital data provides a distinct advantage over manually processed data in that it allows high-efficiency data processing such that high complexity design can be implemented algorithmically. Algorithmic workflows also enable opportunities for generative design and in-situ documentation; for example, to demonstrate that certification protocols are satisfied. Digital AM workflows can be represented by various classifications; in this work, the classifications proposed by Leary (2019) are used, whereby nodes are defined to occur when the design data changes form (Fig. 5.7):

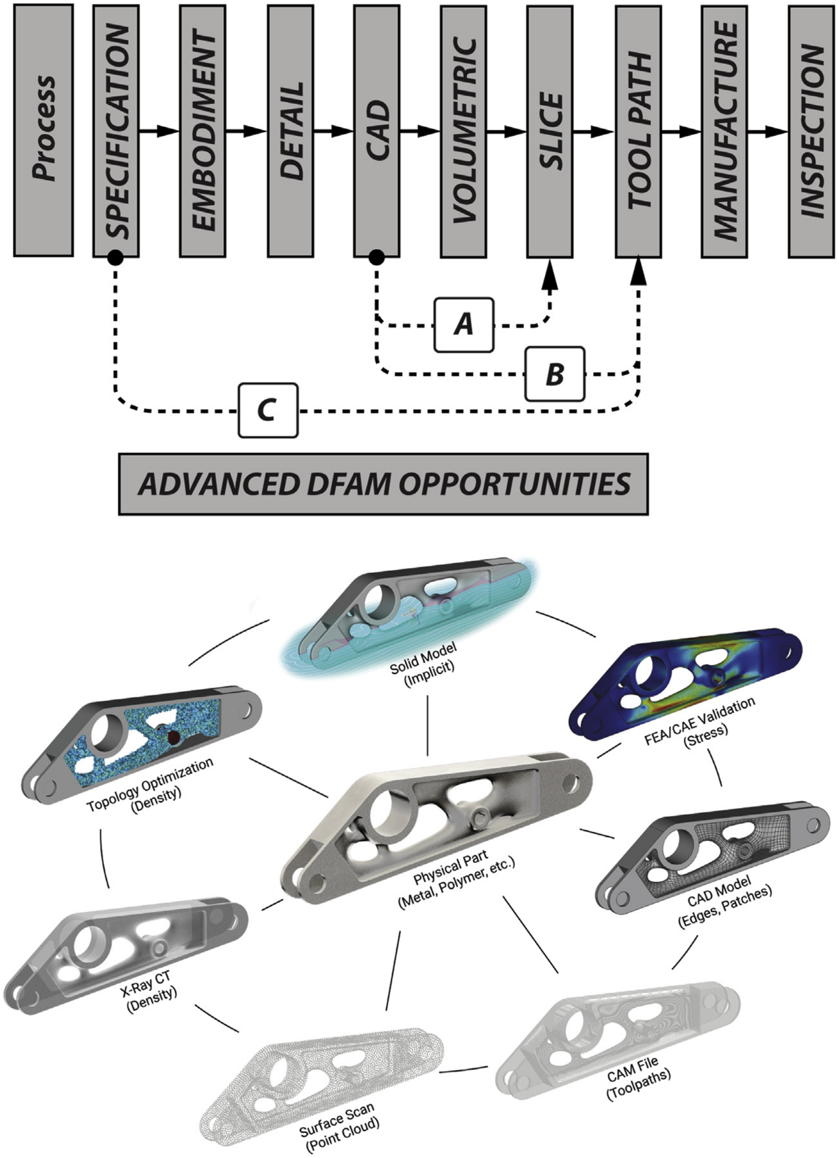
Process
SPECIFICATION
EMBODIMENT
DETAIL
CAD
VOLUMETRIC
SLICE
TOOL PATH
MANUFACTURE
INSPECTION
A
B
C
ADVANCED DFAM OPPORTUNITIES
Solid Model
(Implicit)
FEA/CAE Validation
(Stress)
Topology Optimization
(Density)
Physical Part
(Metal, Polymer, etc.)
CAD Model
(Edges, Patches)
X-Ray CT
(Density)
Surface Scan
(Point Cloud)
CAM File
(Toolpaths)

Figure 5.7 Schematic representation (upper) and practical implementation (lower) of the digital L-PBF workflow, indicating advanced DFAM outcomes: (A) direct CAD to slice, (B) direct CAD to tool path, and (C) generative design.

- ***Specification:*** constraints, objectives, and boundary conditions formalized.
- ***Embodiment:*** initial geometric specification, often aided by topology optimization, the data format may be a voxel field.
- ***Detail:*** geometry refinement, data typically in parametric format, including CSG (Constructive Solid Geometry), Boolean, implicit or vector field.

- ***CAD:*** formal definition of as-manufactured geometry. File format typically nonparametric solid.
- ***Volumetric:*** specification of the volume to be manufactured, formats include stereolithographic (STL), Additive Manufacturing Format (AMF), and 3D Manufacturing Format (3MF).
- ***Slice:*** discrete layerwise representation of the layers associated with the volume to be manufactured; this representation is often proprietary.
- ***Laser scanning path:*** algorithmically generated representation of the laser scanning path. This is a function of specific L-PBF process parameters and is typically represented by a cryptographically restricted proprietary format.
- ***Manufacture:*** in-situ generated data including process data such as ambient oxygen content, as well as thermal camera imagery—this data is large and is possibly reported as metadata.
- ***Inspection:*** includes various post-manufacture inspection data such as coordinate measurement machine (CMM) and μCT spatial fields, data format varies.

Inherently digital processes are a mixed blessing for commercially successful design. Digital processes can generate substantial volumes of data (which must then be interpreted, stored, and acted on); and this data may be embedded within formats that are incompatible, encrypted, or proprietary. Conversely, for design teams that can engage with the challenges of inherently digital design, digital data provides an opportunity for highly effective design outcomes; these opportunities include: meta-data analysis, resolution restriction, and generative design.

5.7.1 Metadata analysis—doing more with less

Digital data can readily overwhelm available computational resources. Relevant examples include in-situ thermal data and μCT data, which can readily generate terabytes of digital data for a single, nontrivial specimen. To avoid data overload, statistical analysis can be applied to represent large datasets by a metadata summary (Fig. 5.8). For example, thermal sensor data can be acquired at full resolution initially and then statistically analyzed in terms of the observed temperature distribution rather than the explicit temperature field. Although metadata analysis may impose challenges in data processing, it can allow data storage size to be dramatically reduced and can provide highly valuable data for certification, for example, explicit locations and durations where the temperature field exceeded allowable thresholds.

5.7.2 Resolution restriction—how much data is enough?

Data resolution is pertinent to the successful management of digital data for L-PBF. This challenge is relevant at all stages of the digital workflow (Fig. 5.7), especially for scenarios associated with large datasets, for example:

- curvilinear to discrete geometry conversion, e.g., in topology optimization or in preparation of volumetric data representation;
- continuous to discrete thermal fields as acquired by thermal nondestructive testing (NDT);
- continuous NDT data such as μCT converted to a discrete representation.

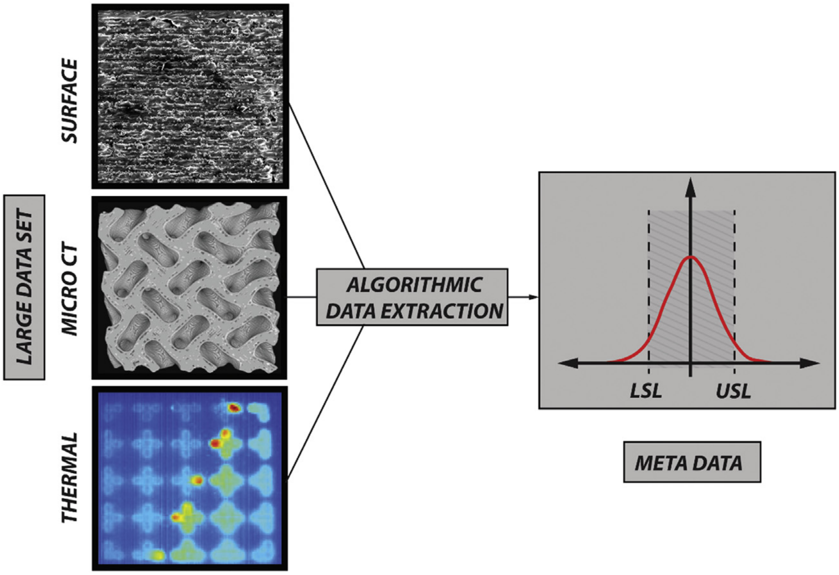

Figure 5.8 Metadata analysis provides an opportunity for large datasets to be algorithmically represented in a manner that mitigates data storage challenges while allowing clear engineering decision making, for example, by the definition of allowable upper and lower specification limits (USL, LSL).

In these scenarios, a conscientious design team may suffer from a tendency to increase resolution to upper achievable limits. This outcome is analogous to the potentially high cost of quality control where costs increase when designers specify an unnecessarily high tolerance on manufacturing outcomes; conversely, where data resolution is insufficient, product function is compromised, and associated costs increase. To counter the tendency to either excessive or insufficient data resolution, it is useful for the L-PBF design team to specify a functional limit on the required data resolution such that an appropriate resolution can be identified systematically rather than intuitively.

For example, topology optimization routines must be completed within a limited available time budget with the available computational resource. This data compromise may then be specified in terms of the allowable voxel resolution for a proposed optimization routine. Similarly, design engineers may be tempted to increase the facet resolution used to represent curvilinear geometry; resulting in a significant increase in file size and associated data management challenges. In this scenario, a systematic resolution limit may be unambiguously defined by comparing the facet resolution of as-manufactured struts with the intended geometric objective, allowing an upper limit of the appropriate file size to be systematically defined. Additionally, design engineers can also utilize advanced digital geometry formats that are emerging to efficiently represent AM geometry.

5.8 Digital geometry formats

There are a variety of digital formats available to represent a 3D solid model of interest, each with associated advantages and disadvantages (Foley et al., 1996). These digital formats can be classified as either surface boundary models (e.g., meshes and boundary representation CAD files) or direct volumetric models (e.g., voxels and implicit representation). Surface boundary formats are well established in engineering practice but are subject to some limitations, as is to be expected of legacy technology. Relevant digital geometry formats (Fig. 5.9) and associated challenges and opportunities for L-PBF are discussed below.

5.8.1 Boundary representation (meshes and B-Rep CAD)

A common strategy for the representation of a 3D solid is the formal definition of the exterior surface. Although many such boundary representation methods exist, the principal representations in commercial use are the mesh and Boundary Representation CAD (B-Rep) methods. An unfortunate naming confusion arises here, as both meshes and CAD models are subcategories of Boundary Representations, though the CAD variant is sometimes used synonymously. These data formats are well represented in engineering design practice but are fundamentally more suited to relatively low complexity geometry and are potentially limited in their ability to accommodate the geometric complexity often associated with L-PBF products as described below.

Mesh models represent the intended surface with a collection of triangular or quadrilateral facets and are widely adopted for a range of applications from numerical simulation to graphical rendering. Mesh representations are appealing in their simplicity of

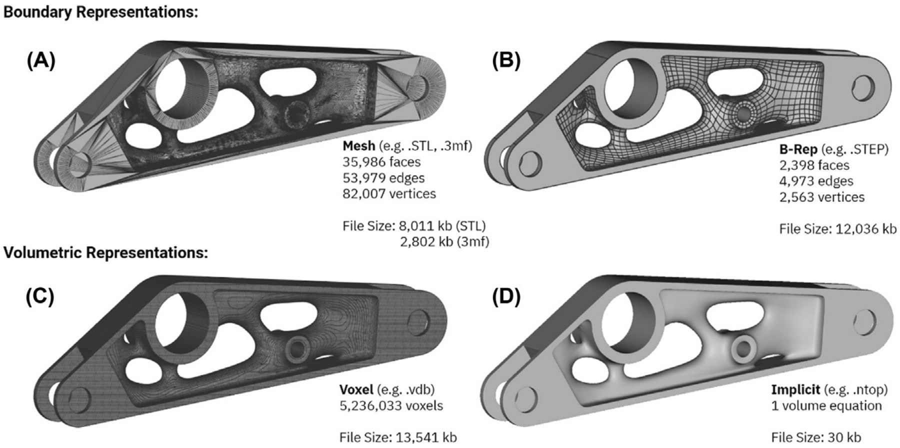
Boundary Representations:
(A)
Mesh (e.g. .STL, .3mf)
35,986 faces
53,979 edges
82,007 vertices
File Size: 8,011 kb (STL)
2,802 kb (3mf)
(B)
B-Rep (e.g. .STEP)
2,398 faces
4,973 edges
2,563 vertices
File Size: 12,036 kb
Volumetric Representations:
(C)
Voxel (e.g. .vdb)
5,236,033 voxels
File Size: 13,541 kb
(D)
Implicit (e.g. .ntop)
1 volume equation
File Size: 30 kb

Figure 5.9 Digital geometry formats for 3D model representation. (A, B) boundary representation models, including meshes and CAD; (C, D) volumetric representations, including voxels and implicit representations. An approximate indication of file size is also given, though this is only one metric for the choice of format.

geometric representation, but often scale poorly in representing the geometric complexity achievable by L-PBF systems; and consequently, can induce challenges in computational data management. For example, the stereolithographic (STL) representation is based on the explicit representation of the constituent facets and has been applied to represent AM geometry since the 1980s. To overcome the data inefficiency inherent to the STL format, alternate mesh representations have been proposed that reduce mesh file size by efficient storage and geometry representations as well as providing support for colors, textures, and multi-material definitions (Fig. 5.10). These formats include the 3D Manufacturing Format (3MF) and Additive Manufacturing Format (AMF). In the example shown below, simply switching from STL to 3MF for this lattice part results in a drastic reduction in file size. The reason is primarily that each lattice strut in the 3MF file is now stored as a single line and its thickness profile, rather than a collection of dozens (or hundreds) of triangles for each strut. Furthermore, 3MF represents each of the triangle mesh vertices uniquely, and shares them across neighboring triangles; STL has many duplicate vertices, as it stores no connectivity information of neighboring triangles. In a full-scale build, this difference can quickly overwhelm computational resources with gigabytes of redundant data.

Boundary representation (B-Rep) CAD models represent a volume via the formal definition of its surface boundary. This representation is commonly applied in parametric CAD formats including the STEP format (Bhandarkar et al., 2000). The B-Rep protocol applies a quilt of surface patches to enclose the volume of interest. These surface patches are more sophisticated than the facet mesh representation but remain limited in terms of the achievable geometric complexity and scale poorly with complex geometry. Consequently, B-Rep modeling operations can be slow and fragile for complex geometry, especially the organic topology optimized structures feasible with L-PBF. Furthermore, meshing is often required behind the scenes for rendering or for export to manufacture, so most of the aforementioned challenges inherent to mesh representations still apply. Meshes and B-Rep CAD are inherently linked in this manner.

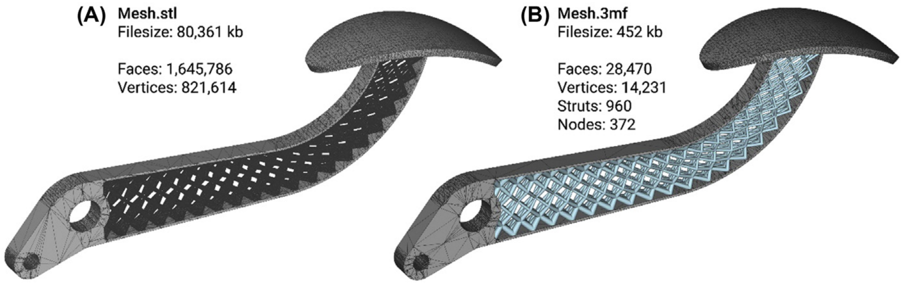

Figure 5.10 Equivalent lattice geometry characterized by (A) stereolithographic (STL) and (B) 3D Manufacturing Format (3MF).

5.8.2 Volumetric representation (voxel and implicit)

A model of a 3D object may also be stored in digital format as a 3D solid directly (as opposed to its bounding surface as above). With volumetric representations, concepts such as watertightness (a term which instils fear into mesh modelers) do not apply as we represent the body of water directly, not the water's container. As a consequence, volumetric modeling operations can be more stable than for equivalent boundary representations. These volumetric representations are a more modern approach and take full advantage of computing architectures including GPUs and high core-count CPUs, whereas most boundary representation methods are fundamentally difficult to parallelize.

The volume of a 3D object may be represented by a collection of 3D cubes, known as voxels. When compared to surface model representations, these discrete representations enable technically stable 3D modeling operations such as offsets, shells, and Boolean operations. The primary challenge to the application of voxel models for L-PBF is their difficulty in capturing exact geometries smoothly thereby requiring substantial file size to adequately represent the intended L-PBF geometry.

Implicit models, also known as signed-distance functions (SDF), are an inherently volumetric representation of a 3D component whereby the geometry is represented by continuous volumetric equations (Malladi et al., 1995). The tangible surface of the part exists where the implicit function equals zero; the inside is negative, and the outside is positive (Fig. 5.11). In comparison with boundary representations and voxel arrays, implicit models are computationally efficient and enable operations like shelling, Boolean operations, and offsets by simple manipulation of the volumetric equation. Due to their inherent computational efficiency, implicit models are well established

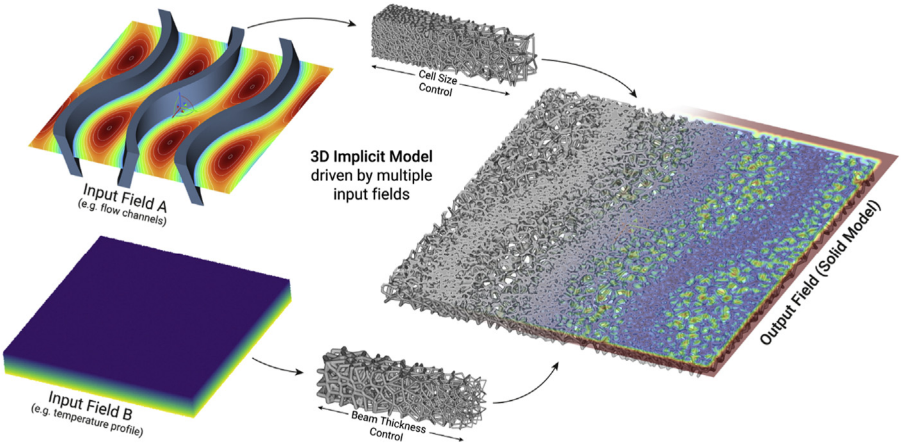
Cell Size Control
3D Implicit Model driven by multiple input fields
Input Field A (e.g. flow channels)
Output Field (Solid Model)
Input Field B (e.g. temperature profile)
Beam Thickness Control

Figure 5.11 An implicit solid model driven by multiple input fields (left), combined algorithmically to generate a solid model (right). In this example, cell size is a function of flow channel geometry (input field A); while strut thickness is a function of temperature profile (input field B).

in computer graphics applications; their application in mechanical design is emerging, especially for computationally challenging design applications such as for high-complexity L-PBF design. For these implicit models, geometric parameters are represented as gradients of the volumetric equations. For example, this representation enables modeling with stress fields and thermal data such that the component geometry is optimized directly for the underlying functional objectives (Fig. 5.11).

5.9 Generative design

Generative design refers to goal-driven computational methods of engineering design that generate and optimize product geometry based on a set of algorithmic operations made with reference to a user-defined expert system. Generative design methods can be considered as “the rules for generating form, rather than the forms themselves” (Frazer, 2002). Generative design implementations vary in complexity and range from highly customized implementations of machine learning and artificial intelligence to pragmatic implementations of confirmed manufacturable geometry. For either extreme, it is important that the inner workings of these algorithms are exposed to the L-PBF designer so that all assumptions of the model are transparent.

Much of the overall cost associated with the manufacture of high-complexity products lies in the associated design and certification effort; effort that incurs the high cost of experienced engineers who invest time and experience to implement the design and certify its accordance with associated standards. L-PBF is particularly suited to the design of high-complexity components including (for example) patient-specific medical devices. For these high-value applications, generative design provides an opportunity to significantly reduce the cost of design and certification thereby enabling mass customization of high-value products—an outcome infeasible with either traditional design or traditional manufacturing methods (Plocher and Panesar, 2019). These opportunities for high-complexity design can exceed the technical capability of a human engineer implemented via manual modeling, as demonstrated by the examples below (Fig. 5.12), in which manual modeling of the roughness texture or lattice structure would be extremely time consuming and compounded for each part variant or new product. Instead, an algorithmic approach enables that design effort to be deployed to any number of parts or part configurations.

5.10 Simulation-driven design

Technically and commercially successful designs are a result of effective product function. To meet commercial timelines and associated budgets, it is critical that simulation-driven design techniques be implemented efficiently and precisely. Simulation-driven design, in the context of AM, refers to the use of numerical simulations to generate more optimal design configurations given performance criteria (Du Plessis et al., 2019a). In response to this requirement, systematic methods of

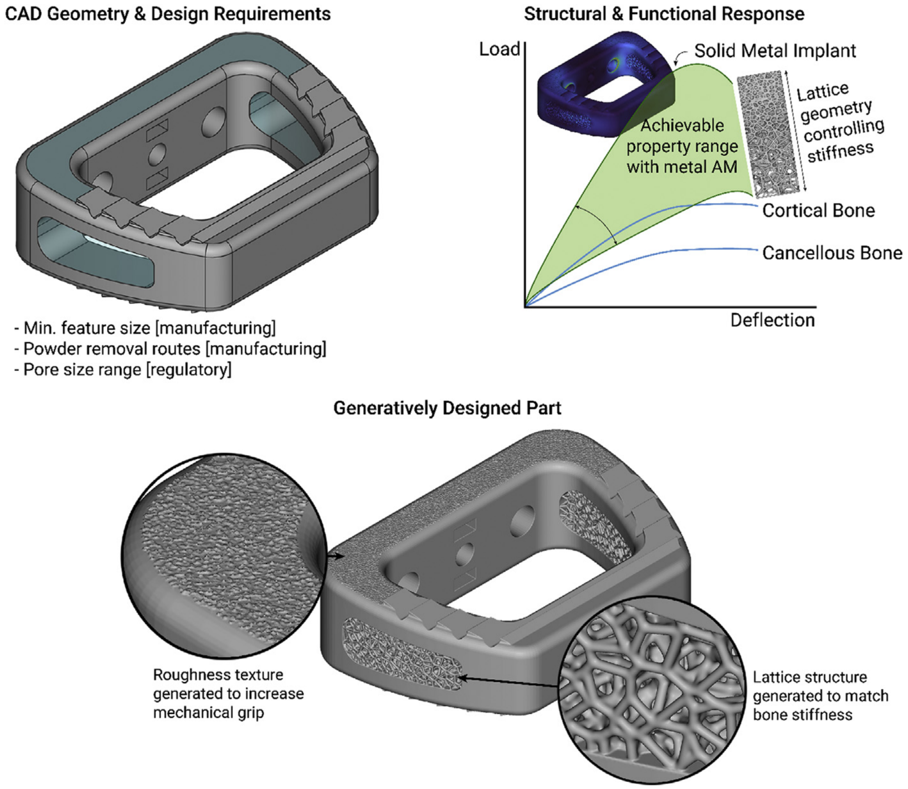
CAD Geometry & Design Requirements
- Min. feature size [manufacturing]
- Powder removal routes [manufacturing]
- Pore size range [regulatory]
Structural & Functional Response
Load
Solid Metal Implant
Achievable property range with metal AM
Lattice geometry controlling stiffness
Cortical Bone
Cancellous Bone
Deflection
Generatively Designed Part
Roughness texture generated to increase mechanical grip
Lattice structure generated to match bone stiffness

Figure 5.12 Generative methods enable algorithmic design of patient-specific spinal implant to satisfy L-PBF manufacturability requirements with patient-specific geometry and mechanical response.

topological and parametric optimization have been developed, each with a unique set of design relevant attributes. The former, topology optimization, refers specifically to the use of simulation to acquire design embodiments. Whereas the latter, parametric optimization, generally refers to the optimization of parameters associated with a determined design. These methods are presented in the following sections with reference to their effective application in L-PBF component design at the design embodiment and refinement phases.

5.10.1 Topology optimization

Topology optimization is a computational technique for the systematic optimization of the material distribution within an available design space. This objective is technically challenging as the search for topologically optimized geometry can be computationally overwhelming and intuitive solutions are often suboptimal. In response, algorithmic methods of topological optimization are an active research focus, and many commercially successful strategies have been presented, including: *ground structures* where a predetermined grid is constructed and inefficient elements are iteratively deleted (Wang et al., 2018b); *Solid-Isotropic Material with Penalization (SIMP)* where the discretized design space of interest is iteratively assigned a reduced material density according to a specified penalization function (Krishna et al., 2017); *Bidirectional Evolutionary Structural Optimization (BESO)* where a voxel solution space is numerically analyzed to define and optimize the voxel distribution for the required functional objective (Tang et al., 2015); and *level-set method* where the effect of local geometry is characterized in terms of its influence on the objective function of relevance, allowing the optimal boundary to be defined by the intersection of this influence with a reference surface (Wang et al., 2018a).

Irrespective of the specific algorithm selected, the topology optimization process is applied to pursue a user-defined objective through simulation and is subject to boundary conditions and constraints imposed by the user. Objectives relevant to L-PBF typically include structural compliance or thermal conductivity, while constraints generally include the allowable volume fraction and allowable stress and deflections (Fig. 5.13).

The relative merit and applicability of these distinct topology optimization strategies should be reviewed for each particular design scenario. However, it is worthwhile to note potential design challenges inherent to these methods, including poor scaling with increased design resolution, and failure to accommodate all relevant failure modes. To mitigate the risk of overwhelming the available computational resources, the design team should develop an awareness of the influence of geometric resolution on the required computational effort (Section 5.7). Potential simulation idealizations of relevance to L-PBF optimization include: assumptions of linear material response and accommodation of nonlinear failure modes such as the buckling failure and fatigue. As with all engineering design tools, it is imperative that the designer be aware of any limitations introduced by simulation idealizations such that technically robust design outcomes are achieved.

Structural lightweighting is the most common application of topology optimization in L-PBF components, as it can enhance performance measures, such as aircraft endurance, spacecraft payloads, and fuel economy of ground vehicles. In addition to enhanced function, topology optimized structures also provide an opportunity to enhance commercial aspects of L-PBF by the reduction of powder consumption and

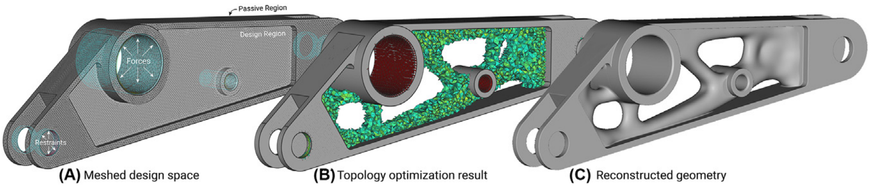

(A) Meshed design space **(B)** Topology optimization result **(C)** Reconstructed geometry

Figure 5.13 (A) Meshed design space subject to loads and constraints (*blue*), (B) Topology optimization processes, and (C) Reconstructed geometry for manufacture.

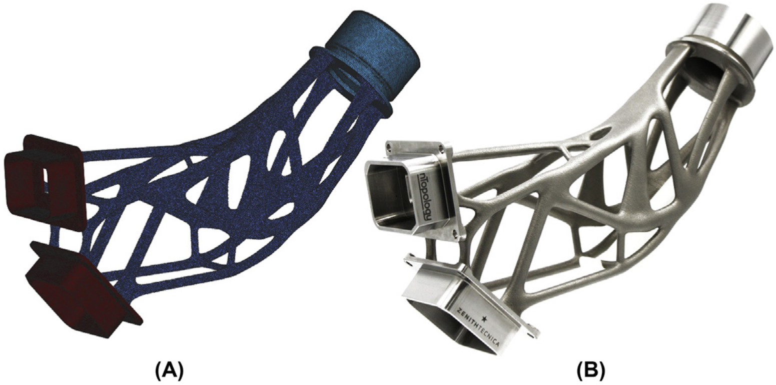

Figure 5.14 Ti6Al4V spacecraft bracket designed through topology optimization (A) and implemented via L-PBF. (B) This high stiffness-to-weight ratio would be challenging to engineer without topology optimization tools and infeasible without L-PBF technologies. Final component was manufactured by Zenith Tecnica.

manufacturing time. For example, the organic freeform geometry enabled by topology optimization applied to L-PBF is evident in the spacecraft bracket of Fig. 5.14. This commercial structure would be technically and commercially infeasible with conventional methods but is readily implemented in the L-PBF process.

Topology optimization provides a valuable design tool for embodiment design, but is computationally inefficient for the optimization of specific geometric details; parametric optimization methods enable the systematic optimization of functionally critical design variables as required.

5.10.2 Parametric optimization

As the detail design specification evolves, the final component geometry can be represented parametrically in terms of the functionally critical variables. This parametric model provides an opportunity to systematically optimize functionally critical variables and to accommodate functional compromise, for example, between component mass and strength or stiffness.

Parametric optimization provides a useful complement to topology optimization, and enables a series of advantages that are highly relevant for commercially focused L-PBF design, including:

1. Refinement of topologically optimized structures.
2. Parallelization of simulation (multiple parametric permutations can be concurrently assessed).
3. The generative design of optimal topologies for specific scenarios.
4. Point certification (as required for medical device manufacture).

Parametric optimization is typically implemented with iterative optimization techniques that make use of the local gradient of the objective function to inform the direction toward an improved result, with repeated iterations leading to the local optimum. These techniques generally require a convex objective function that is continuous and differentiable in the region of interest. Examples of iterative optimization techniques include: *gradient descent*, which evaluates the local gradient of the objective function across all parameters with each iteration and follows the direction of steepest descent; *coordinate descent*, which sequentially evaluates gradient and minimizes for each parameter one at a time, while fixing the other parameters; and *Newton's method*, which builds a Taylor series expansion of the objective function to seek a local optima (Lange, 2013).

The local optima found through the gradient methods are dependent on the initial selection of design parameters. To improve the chances of identifying the global optima, or the best of several local optima, it is useful to run the gradient method from multiple initial solutions. Optimization through Design of Experiments (DoE) methods involve the evaluation of multiple combinations of parameter values according to a predetermined selection of parameters. The optimization can then proceed through use of simplex method or in combination with a response surface model to approximate the system response in polynomial form (Lundstedt et al., 1998). These brute-force methods lack the mathematical elegance of iterative optimization techniques but provide several distinct opportunities for commercial L-PBF optimization over iterative optimization methods, specifically they can (Leary, 2019) be applied to scenarios where the objective function is not differentiable as no gradient is required; accommodate models that are not robust for all combinations of parameters without suspending the optimization process; and be evaluated for multiple combinations of parameters in parallel.

Heuristic optimization methods can also be applied to the outcome of DoE methods in an attempt to enhance the parameters selection in the successive simulation round. Heuristic methods include:

- *Genetic algorithms*, which use concepts of natural selection including concepts of crossover and mutation to identify parameter values of interest (Kramer, 2017).
- *Swarm optimization*, where a population of candidate solutions traverses the search-space and is guided by their solutions as well as those of the other candidates (Kiranyaz et al., 2014; Kaipa and Ghose, 2017).
- *Simulated annealing*, a probabilistic technique inspired by metal annealing, with successive results tending toward a lower energy state (Otten and van Ginneken, 2012).

Shape optimization and size optimization are subcategories of parametric optimization. Shape optimization allows rearrangement of the geometric shape while retaining the fundamental topology. Size optimization allows discrete structural elements (such as plates and beams) to vary geometrically while retaining their initial connection locations. Appropriate selection of either shape or size optimization (or a combination of methods) will enable effective optimization for L-PBF design. For example, size optimization is effective in the enhancement of a surface-based structure (Yang et al., 2019), where each shell element thickness is locally optimized to minimize compliance under a vertical compressive load; enabling material to be distributed preferentially at regions that are aligned to efficiently transmit the load (Fig. 5.15).

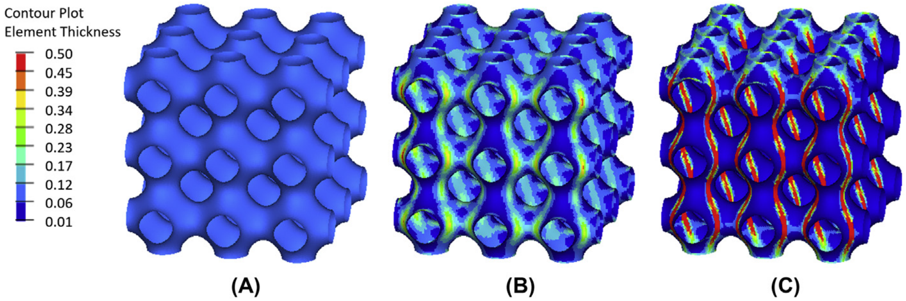

Figure 5.15 Gradient-based size optimization of the Triply Periodic P-surface under vertical compressive loading (using a minimum compliance objective and a fixed volume constraint). The initial uniform wall thickness (A) changes to a spatially varying distribution that best resists the load case (B) and (C), colored contours represent the varying surface thickness The thickened regions provide the most direct load path for the compressive forces.

5.11 Uncertainty quantification for L-PBF design

Defects and dimensional inaccuracies in metal additively manufactured parts inherently cause discrepancies between the as-designed and as-manufactured component geometry. These geometric uncertainties may introduce variability in the functional response of as-manufactured L-PBF structures. Prediction of the geometric variabilities for a specific L-PBF build, and the effect of these variabilities on functional response, is necessary for cost-effective design. These uncertainties may be quantified by numerical prediction or experimental methods.

5.11.1 Numerical prediction

Numerical simulation of AM processing enables prediction of defects and distortion in manufactured parts, it also allows for selection of optimal part build orientation for the minimization of residual stresses and excessively heated zones (Biegler et al., 2020; McMillan et al., 2017). L-PBF involves localized laser melting and rapid solidification on a temporal and spatial scale many orders of magnitude below the fabrication time and bulk dimensions of the as-built component. Multiscale numerical simulation of complex physical interactions is computationally impractical using direct approaches. A reduction in model complexity is required to provide computationally feasible prediction of the as-manufactured structure's response; for example, including the effect of L-PBF thermal gradients on part distortion, as is required for commercial L-PBF design. These process simulations may be categorized according to the geometric scale being analyzed (Downing et al., 2020).

- *Melt-pool simulations:* physical phenomena at the melt-pool scale, including individual particle heating and the thermal fluid dynamics of the melt pool.
- *Single-layer simulations:* behavior of single- or multi-scan tracks, as are typically applied for comparison of candidate laser scan strategies.

- *Layer-by-layer simulations:* dynamic interactions between the thermal heat source and the individual (or previous) deposition layers.

These representations provide geometric simplifications associated with the spatial domain. Furthermore, *reduced-order models* utilize idealized physical processes to reduce simulation complexity and can be applied at any scale. For example, layer-by-layer simulations typically simplify thermal processes to ensure the numerical model is computationally feasible. Of these simulation classifications, layer-by-layer simulations implemented with reduced order models are computationally feasible for the prediction of thermal defects and dimensional inaccuracies in component-scale structures as is required for L-PBF design (McMillan et al., 2017; Biegler et al., 2020). These emerging modeling solutions provide an opportunity for commercial design outcomes.

5.11.2 Experimental methods

An alternative approach to the numerical prediction of variability in L-PBF structures is the empirical investigation of an experimentally fabricated part. In this case, geometric defects and dimensional inaccuracies are characterized by image-based measuring techniques, in particular, micro-computed tomography (μCT), as discussed in (Du Plessis et al., 2018) and Chapter 10 of this book. CT image data can be used as inputs to image-based simulations, incorporating the pores, actual surface geometry and imperfections. Such simulations can provide insight into the performance as compared to the design, especially in regards to the effect-of-defects (Du Plessis et al., 2019b). Experimental measurements are especially suited to stable L-PBF processes where representative specimens can be reliably used to predict the response of the larger as-manufactured structure. The use of μCT reconstructed geometry poses two challenges. First this data is deterministic, as it characterizes the representative specimen only, and not the full range of possible build outcomes. Second, simulation of this data typically requires the use of solid elements, where, especially for slender lattice structures, requires very high mesh resolution and introduces computational challenges. Methods exist for reducing the computational cost associated with μCT-based FE models. These methods include geometric approximation with reduced-density mesh and the use of beam or shell-based representations. These methods can reduce solution complexity, but potentially at the cost of predictive capability.

5.11.3 Uncertainty quantification methods

Even if the challenges associated with modeling complexity are resolved, the aforementioned numerical methods are deterministic and do not inherently accommodate the randomness of the L-PBF system. Formal methods of Uncertainty Quantification (UQ) are required to provide a probabilistic approach to L-PBF component design and allow the a priori prediction of the feasible range of physical properties of an L-PBF component. UQ itself can be defined as the “end-to-end study of the reliability incientific inferences,” covering both *aleatory* and *epistemic* sources of uncertainty;

where the former refers to the intrinsic uncertainties in the model's predictive capability, the latter refers to a lack of fundamental knowledge which cannot be improved by the acquisition of additional data (Eiermann et al., 2007).

The Stochastic Finite Element Method (SFEM) is an extension of FEM to UQ and is used to model uncertainties that arise in material properties, geometries, and boundary conditions (Schuëller, 2001). Nonintrusive SFEM utilizes the deterministic FEM to quantify or predict the influence of uncertainties or randomness in the modeled system. There are multiple SFEM approaches including the (Aldosary et al., 2018; Arregui-Mena et al., 2016) *direct Monte Carlo methods*, where deterministic models are iteratively evaluated to generate an estimate of the parameter of interest; *perturbation methods*, an intrusive approach that introduces randomness in the model via Taylor series expansions; and *Polynomial Chaos Expansions*, where selected orthogonal polynomial series represent the statistical distribution of model outputs with respect to probability density functions of input uncertainties. UQ methods offer a robust approach to quantifying the variability and uncertainty in the physical response of L-PBF components. The following sections present SFEM-based approaches for the accommodation of defects in L-PBF lattice structures.

5.11.4 Lattice simulation—component level

Components with highly complex geometric features are readily manufacturable by L-PBF, an example being cellular lattice structures, which consist of a network of intersecting strut and node elements (Gibson and Ashby, 1999). L-PBF lattice structures have garnered interest in a range of applications, including in the aerospace, medical, and automotive industries (Maconachie et al., 2019). Despite the commercial opportunities for high-value L-PBF lattice structures, their application is hindered by uncertainties associated with dimensional variation in each node and strut element of the lattice structure (manufacturing errors). The as-manufactured lattice deviates geometrically from its digital geometry input (Fig. 5.16, left); and micro-computed tomography (μCT) derived representations can display this (Fig. 5.16, center). To fully realize the potential of L-PBF manufactured lattice structures, these uncertainties must be quantified for both strut and node elements.

5.11.5 Lattice simulation—strut level

As-manufactured strut elements within an L-PBF lattice exhibit a varying cross-section, as well as a cross-section centroid that also deviates from the idealized longitudinal, resulting in roughness and waviness in the as-manufactured strut. These struts may also contain internal defects such as porosity and microstructural variability (Lozanovski et al., 2019a; Echeta et al., 2019). Numerous design methods have been proposed to more accurately characterize geometric uncertainties of strut-level defects in numerical models, including:

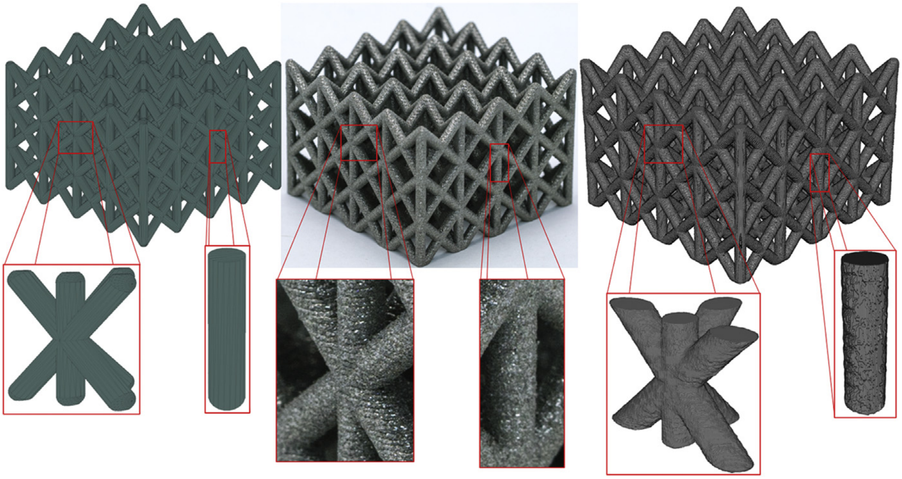

Figure 5.16 Lattice structure digital geometry input (left), as-manufactured (center), and digital μCT reconstruction (right).

- The merging of spheres via Boolean operations, in which each sphere represents the as-manufactured centroid deviation and cross-sectional diameter along the length of the strut (Ravari et al., 2016; Karamooz Ravari and Kadkhodaei, 2014).
- The use of a wavy spline that represents a lengthwise varying cross-sectional diameter, which is swept around an idealized longitudinal axis to generate the solid AM representative strut geometry (Ravari et al., 2014).
- A series of ellipses that mimic the μCT-derived strut cross-sectional area properties, in which each cross-sectional slice has an equivalent elliptical cross-section (Fig. 5.17). The solid model is then generated by CAD loft operations (Lozanovski et al., 2019b).
- Voxel-mesh-based methods that mimic the layer-by-layer manufacturing process and account for the variation in cross-sectional radii along the length of the strut (Park et al., 2014), as well as lengthwise variation in diameter, strut-build angle, and porosity (Gorguluarslan et al., 2017).

The most direct and general approach to the prediction of random geometric defects on the mechanical properties of manufactured struts is the Monte Carlo method (Cunha et al., 2014). Statistical analysis of the geometric properties can then be randomly sampled to create realizations of AM strut geometry. The physical properties of interest can then be obtained numerically for each realization (Figs. 5.17 and 5.18). High-resolution methods to include manufacturing defects, such as the elliptical cross-section method which matches the μCT scan resolution, require more advanced methods to generate random geometric properties. Methods that have been proposed to simulate properties for each strut realization include the use of Markov-Chains in which transition probabilities are derived directly from the sequential CT slice datasets (Lozanovski et al., 2020b). Fig. 5.17 displays five example output stress distributions and deformed shapes from a Monte Carlo investigation into the effect of geometric defects on the mechanical response of AM struts.

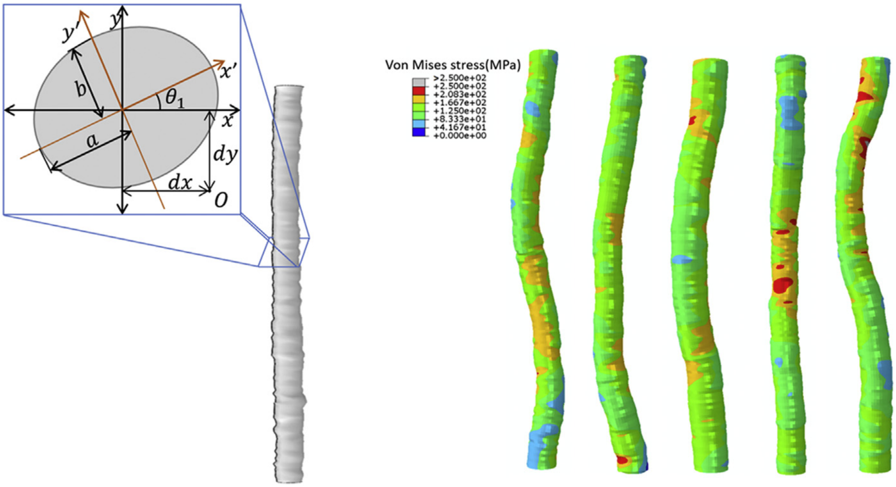

Figure 5.17 Method to generate digital realizations of AM struts (left) and their simulation for inferring distributions of mechanical properties (right).

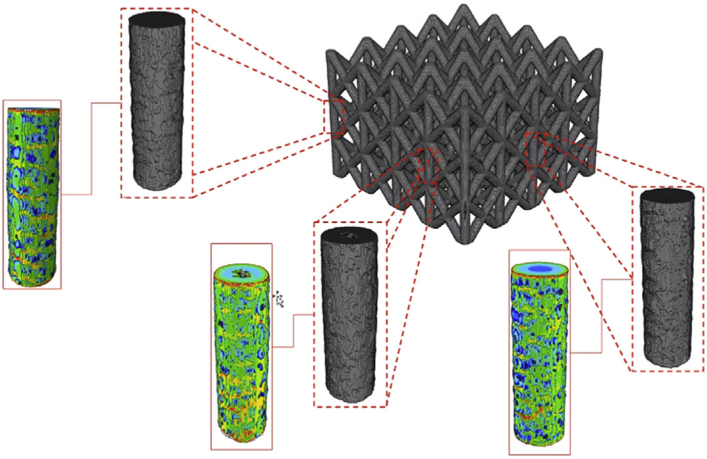

Figure 5.18 Methods of studying the influence of AM defects on the mechanical response of lattice strut elements, as well as their intralattice variability and difference between their CAD idealizations.

UQ can also be utilized in reduced order approaches, such as the specification of random beam element parameters along the length of the strut (Campoli et al., 2013). An approach to this is the random specification of diameters in the struts of the lattice-scale models; the random beam parameters are drawn from probability distributions from strut level UQ studies. Multiple realizations of the lattice-scale beam element model can be solved to easily obtain low-order statistics (i.e., means and variances) of the mechanical properties of interest (Liu et al., 2017; Lei et al., 2019). A UQ approach to multiscale modeling of lattices has also been proposed in which uncertainties at the strut-level are propagated through to the unit-cell level and finally the lattice-level (Gorguluarslan et al., 2017). Multiscale modeling methods can drastically reduce the computational cost of lattice FE models, the aim of the process is the replacement of heterogeneous material at the microscale with a developed homogenous material that has a macroscopic response equal or average to that of the heterogeneous material (Liu and McVeigh, 2008). Homogenization enables the development of equivalent continua and the properties of the developed material are generally referred to as effective or homogenized properties (Bishop et al., 2015).

5.11.6 Lattice simulation—node level

The effect of variability in lattice node elements is less frequently investigated than for strut elements. However, there is a requirement for node element simulation for optimized L-PBF design, especially for lattices with bending-dominated deformation behavior—that is, those which deform via generated bending moments at nodes (de Galarreta et al., 2020; Lozanovski et al., 2020b; Mines, 2019; Smith et al., 2013). The accommodation of nodal defects in numerical simulation is typically achieved heuristically, for example, by the local thickening of the strut diameter in the region of the node element. This simplification is often necessary due to a lack of experimental data to quantify the geometrical and mechanical differences between the as-designed and as-fabricated nodes.

Emerging methods assist in quantifying the geometrical and mechanical difference between the as-designed and as-manufactured node elements, for example, automated methods to isolate and classify individual node elements from μCT data based on observed location and number of intersecting strut elements (Lozanovski et al., 2020a). These tools enable novel insights into the intra-lattice variation in strut and node geometries, as well as its deviation from the idealized design (Figs. 5.18 and 5.19, respectively). These isolated struts and nodes can then be assessed for mechanical response, and these uncertainties propagated to lattice level to provide detailed insight into the effect of strut and node variability on L-PBF lattice performance. The accuracy of this method is dependent on the quality and resolution of the μCT scan.

5.12 Emerging opportunities for L-PBF design outcomes

Commercial opportunities for L-PBF applications especially exist for innovative design teams who embrace emerging design opportunities. These opportunities include:

- *AM aware topology optimization*, where the topology optimization tool accommodates L-PBF design requirements such as thermal field constraints and allowable inclination angle (Mirzendehdel and Suresh, 2016).

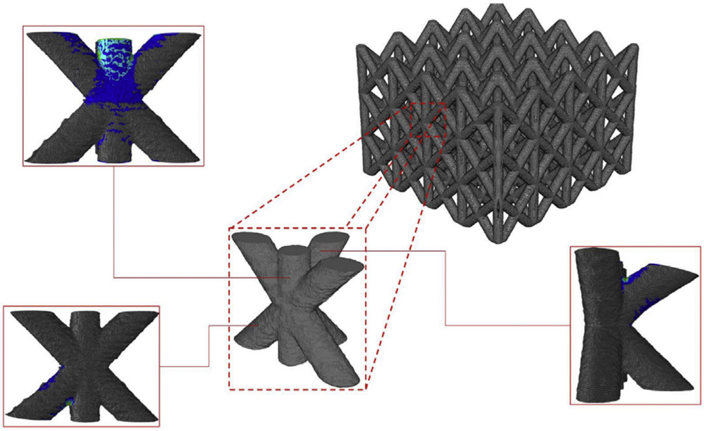

Figure 5.19 Methods of studying the influence of AM defects on the mechanical response of lattice node elements, as well as their intra-lattice variability and difference between their actual and CAD idealizations.

- *Three-dimensional part nesting,* where a detailed understanding of L-PBF process constraints is algorithmically applied to increase production rates by 3D nesting while avoiding compromise in component quality (Araújo et al., 2019).
- *Enhanced support structures*, where support structures are actively designed to achieve repeatable mechanical response (Brackett et al., 2011).
- *Optimal component orientation during manufacture*, especially accommodating the thermal interaction between neighboring objects to ensure dimensional accuracy (Abele et al., 2015; Byun and Lee, 2005).
- *Quantification and prediction of surface morphology*, with understanding of L-PBF process influence on surface roughness to qualify parts with surface finish or bio-interface requirements (Cabanettes et al., 2018).
- *Simulation driven design,* where topology optimization and generative design are applied to distribute and orient lattice structures that are optimal at multiple scales while accommodating the physics associated with L-PBF manufacture. This inherently results in highly complex geometry (suitable only for AM, and requiring advanced digital methods) but offers previously inaccessible levels of performance (Bendsoe and Kikuchi, 1988; Groen and Sigmund, 2018).
- *Automated mass-customization* using stable and scalable generative design algorithms. These generative design algorithms utilize stable simulation methods to simulate component function and AM process to enable the automated design of functionally optimized structures that are compatible with the L-PBF process. Commercial opportunities range from customized vehicle interior components to patient-specific medical applications.

5.13 Concluding comments

Laser Powder Bed Fusion (L-PBF) is a commercially mature technology that allows the manufacture of high-value products with distinct technical and economic advantages. Despite the fundamental opportunities enabled by L-PBF, there remain design challenges to their successful commercial implementation. These challenges can be addressed by formal methods of Design for Additive Manufacture (DFAM), whereby the technical and economic challenges associated with L-PBF are characterized and resolved. This chapter has identified the technical basis for these challenges and identified practically applicable DFAM tools of relevance to L-PBF design.

Commercial L-PBF systems are turnkey industrial machines with relatively well-developed process parameters for specific powders. These systems are supported by well-developed algorithmic methods of support structure and toolpath generation methods and can consistently generate high-density structures. In contrast to these robust design attributes, aspects of the L-PBF design process remain uncertain and therefore introduce risk of design failure, including challenges associated with digital data management, functional optimization, and management of stochastic uncertainties. Design teams that actively engage with these design challenges can more confidently develop innovative and commercially valuable L-PBF products.

The inherently digital nature of AM processes provides both a design challenge and a commercial opportunity. L-PBF products are especially relevant in this context, where the effective management of digital data is vital to commercial production. The management of excessive digital data can be achieved by systematically managing data resolution such that excessive data is avoided, and the representation of excess data is managed by statistically defined metadata. Of critical importance to effective data management is the selection and implementation of appropriate digital geometry format; where multiple formats exist, each with inherent advantages and disadvantages.

Functional optimization is critical to effective L-PBF design. For commercial applications it is imperative that this optimization be achieved consistently and with computational efficiency. Formal methods of design optimization can be applied to enable effective optimization while avoiding the pitfalls of intuitive manual design methods. Topological and parametric optimizations provide complementary optimization methods for identifying and refining effective geometry. When well understood, these methods enable significant design opportunities by enabling generative design methods that allow computationally efficient mass-customization of L-PBF products.

The high-value products enabled by L-PBF production is compromised for commercial production if the associated geometric and microstructural variation is not understood and quantified. To enable deployment of highly optimized L-PBF structures requires the application of formal methods of uncertainty quantification; these DFAM tools are emerging and should be applied by L-PBF design teams that seek to deploy optimized structures with confidence.

Despite the turnkey nature of commercial L-PBF systems, the L-PBF design process involves substantial complexities that must be effectively managed for robust L-PBF design. These challenges are increasingly matched by formal DFAM tools and methodologies, which enable confident application of L-PBF technologies for commercial applications.

5.14 Questions

The following questions are provided to assist in review of the fundamental concepts associated with L-PBF design principles:

- Explain in simple terms the implications of layerwise manufacture on the quality of L-PBF components. What design considerations are relevant to the orientation of an L-PBF component such that surface geometry is acceptable for the intended function (Section 5.4.1).
- Explain how the orientation of prismatic components and lattice structures on the build-plate can assist in avoiding wiper damage and avoid compromise to the build quality of the L-PBF component (Fig. 5.3).
- In simple terms explain why the local temperature fields tend to increase when the heater area is greater than the conductive area (as in Fig. 5.4).
- How can support structures be functionally integrated with the structure of the as-manufactured product (as in Fig. 5.5)? Brainstorm a list of commercial L-PBF applications for which functional supports may be useful.
- Digital data provides an opportunity for deep technical understanding, but can result in a volume of data that is overwhelming to manage. Explain in simple terms how meta-data analysis can be used to provide valuable data for certification while reducing the required data storage size.
- L-PBF components are often geometrically complex and optimized for the technical function. These curvilinear structures are often challenging to represent without excessive file size. What options does the L-PBF designer have to reduce digital geometry file size without unduly compromising the resolution of the manufactured component?
- What digital data formats exist to represent 3D geometric data? What relative advantages and disadvantages do these data formats present for L-PBF design?
- In simple terms describe the process of topology optimization. Why are topological optimization outcome more suitable to L-PBF than traditional manufacturing technologies?
- Lattice structures enable high efficiency L-PBF structures that are not feasible with traditional manufacturing. What emerging methods of uncertainty quantification can be applied to understand the performance of these systems at the component, strut and node level?

Acknowledgments

The authors acknowledge support from the facilities and technical staff of RMIT's Advanced Manufacturing Precinct; the Australian Research Council Industrial Transformation Training Centre in Additive Biomanufacturing (IC160100026) www.additivebiomanufacturing.org; nTopology for use of their software to generate figures; and Zenith Tecnica for the manufacture of demonstration components.

References

Abele, E., Stoffregen, H.A., Klimkeit, K., Hoche, H., Oechsner, M., 2015. Optimisation of process parameters for lattice structures. Rapid Prototyping J. 21, 117–127.

Aboulkhair, N.T., Everitt, N.M., Ashcroft, I., Tuck, C., 2014. Reducing porosity in AlSi10Mg parts processed by selective laser melting. Addit. Manuf. 1–4, 77–86.

Aldosary, M., Wang, J., Li, C., 2018. Structural reliability and stochastic finite element methods: state-of-the-art review and evidence-based comparison. Eng. Comput. 35 (4).

Araújo, L.J., Özcan, E., Atkin, J.A., Baumers, M., 2019. Analysis of irregular three-dimensional packing problems in additive manufacturing: a new taxonomy and dataset. Int. J. Prod. Res. 57, 5920−5934.

Arregui-Mena, J.D., Margetts, L., Mummery, P.M., 2016. Practical application of the stochastic finite element method. Arch. Comput. Methods Eng. 23, 171−190.

Bendsoe, M.P., Kikuchi, N., 1988. Generating Optimal Topologies in Structural Design Using a Homogenization Method.

Bhandarkar, M.P., Downie, B., Hardwick, M., Nagi, R., 2000. Migrating from IGES to STEP: one to one translation of IGES drawing to STEP drafting data. Comput. Ind. 41, 261−277.

Biegler, M., Elsner, B.A., Graf, B., Rethmeier, M., 2020. Geometric distortion-compensation via transient numerical simulation for directed energy deposition additive manufacturing. Sci. Technol. Weld. Join. 1−8.

Bishop, J.E., Emery, J.M., Field, R.V., Weinberger, C.R., Littlewood, D.J., 2015. Direct numerical simulations in solid mechanics for understanding the macroscale effects of microscale material variability. Comput. Methods Appl. Mech. Eng. 287, 262−289.

Brackett, D., Ashcroft, I., Hague, R., 2011. Topology optimization for additive manufacturing. In: Proceedings of the Solid Freeform Fabrication Symposium, Austin, TX, pp. 348−362.

Byun, H.-S., Lee, K.H., 2005. Determination of the optimal part orientation in layered manufacturing using a genetic algorithm. Int. J. Prod. Res. 43, 2709−2724.

Cabanettes, F., Joubert, A., Chardon, G., Dumas, V., Rech, J., Grosjean, C., Dimkovski, Z., 2018. Topography of as built surfaces generated in metal additive manufacturing: a multi scale analysis from form to roughness. Precis. Eng. 52, 249−265.

Campoli, G., Borleffs, M.S., Yavari, S.A., Wauthle, R., Weinans, H., Zadpoor, A.A., 2013. Mechanical properties of open-cell metallic biomaterials manufactured using additive manufacturing. Mater. Des. 49, 957−965.

Cunha Jr., A., Nasser, R., Sampaio, R., Lopes, H., Breitman, K., 2014. Uncertainty quantification through the Monte Carlo method in a cloud computing setting. Comput. Phys. Commun. 185, 1355−1363.

De Galarreta, S.R., Jeffers, J.R., Ghouse, S., 2020. A validated finite element analysis procedure for porous structures. Mater. Des. 189, 108546.

Downing, D., Leary, M., Mcmillan, M., Alghamdi, A., Brandt, M., 2020. Heat transfer in lattice structures during metal additive manufacturing: numerical exploration of temperature field evolution. Rapid Prototyp. J. 26 (5).

Du Plessis, A., Broeckhoven, C., Yadroitsava, I., Yadroitsev, I., Hands, C.H., Kunju, R., Bhate, D., 2019a. Beautiful and functional: a review of biomimetic design in additive manufacturing. Addit. Manuf. 27, 408−427.

Du Plessis, A., Yadroitsava, I., Yadroitsev, I., 2019b. Effects of defects on mechanical properties in metal additive manufacturing: a review focusing on x-ray tomography insights. Mater. Des. 108385.

Du Plessis, A., Yadroitsev, I., Yadroitsava, I., Le Roux, S.G., 2018. X-ray microcomputed tomography in additive manufacturing: a review of the current technology and applications. 3D Print. Addit. Manuf. 5, 227−247.

Echeta, I., Feng, X., Dutton, B., Leach, R., Piano, S., 2019. Review of defects in lattice structures manufactured by powder bed fusion. Int. J. Adv. Manuf. Technol. 1−20.

Eiermann, M., Ernst, O.G., Ullmann, E., 2007. Computational aspects of the stochastic finite element method. Comput. Visual Sci. 10, 3−15.

Foley, J.D., Van, F.D., Van Dam, A., Feiner, S.K., Hughes, J.F., Angel, E., Hughes, J., 1996. Computer Graphics: Principles and Practice. Addison-Wesley Professional.

Frazer, J., 2002. Chapter 9. Creative design and the generative evolutionary paradigm. In: Bentley, P.J., Corne, D.W. (Eds.), Creative Evolutionary Systems. Morgan Kaufmann, San Francisco.

Frazier, W.E., 2014. Metal additive manufacturing: a review. J. Mater. Eng. Perform. 23, 1917−1928.

Gibson, L.J., Ashby, M.F., 1999. Cellular Solids: Structure and Properties. Cambridge University Press.

Gong, H., Rafi, K., Gu, H., Janaki Ram, G.D., Starr, T., Stucker, B., 2015. Influence of defects on mechanical properties of Ti-6Al-4V components produced by selective laser melting and electron beam melting. Mater. Des. 86, 545−554.

Gorguluarslan, R.M., Choi, S.-K., Saldana, C.J., 2017. Uncertainty quantification and validation of 3D lattice scaffolds for computer-aided biomedical applications. J. Mech. Behav. Biomed. Mater. 71, 428−440.

Groen, J.P., Sigmund, O., 2018. Homogenization-based topology optimization for high-resolution manufacturable microstructures. Int. J. Numer. Methods Eng. 113, 1148−1163.

Han, X., Zhu, H., Nie, X., Wang, G., Zeng, X., 2018. Investigation on selective laser melting AlSi10Mg cellular lattice strut: molten pool morphology, surface roughness and dimensional accuracy. Materials 11, 392.

ISO/ASTM, 2015. ISO/ASTM 52900:2015(E): Standard Terminology for Additive Manufacturing − General Principles − Terminology 1,2.

Kaipa, K.N., Ghose, D., 2017. Glowworm Swarm Optimization: Theory, Algorithms, and Applications. Springer International Publishing.

Karamooz Ravari, M.R., Kadkhodaei, M., 2014. A computationally efficient modeling approach for predicting mechanical behavior of cellular lattice structures. J. Mater. Eng. Perform. 24, 245−252.

Khorasani, A.M., Gibson, I., Ghaderi, A., Mohammed, M.I., 2019. Investigation on the effect of heat treatment and process parameters on the tensile behaviour of SLM Ti-6Al-4V parts. Int. J. Adv. Manuf. Technol. 101, 3183−3197.

Kiranyaz, S., Ince, T., Gabbouj, M., 2014. Multidimensional Particle Swarm Optimization for Machine Learning and Pattern Recognition. Springer-Verlag Berlin, Heidelberg.

Kramer, O., 2017. Genetic Algorithm Essentials. Springer International Publishing, Cham.

Krishna, L.S.R., Mahesh, N., Sateesh, N., 2017. Topology optimization using solid isotropic material with penalization technique for additive manufacturing. Mater. Today Proc. 4, 1414−1422.

Lange, K., 2013. Optimization. Springer New York, New York, NY.

Leary, M., 2018. Design of titanium implants for additive manufacturing. In: Froes, F.H., Qian, M. (Eds.), Titanium in Medical and Dental Applications. Woodhead Publishing.

Leary, M., 2019. Design for Additive Manufacturing. Elsevier.

Lei, H., Li, C., Meng, J., Zhou, H., Liu, Y., Zhang, X., Wang, P., Fang, D., 2019. Evaluation of compressive properties of SLM-fabricated multi-layer lattice structures by experimental test and μ-CT-based finite element analysis. Mater. Des. 169, 107685.

Li, R., Liu, J., Shi, Y., Wang, L., Jiang, W., 2012. Balling behavior of stainless steel and nickel powder during selective laser melting process. Int. J. Adv. Manuf. Technol. 59, 1025−1035.

Liu, L., Kamm, P., García-Moreno, F., Banhart, J., Pasini, D., 2017. Elastic and failure response of imperfect three-dimensional metallic lattices: the role of geometric defects induced by Selective Laser Melting. J. Mech. Phys. Solid. 107, 160−184.

Liu, W.K., Mcveigh, C., 2008. Predictive multiscale theory for design of heterogeneous materials. Comput. Mech. 42, 147–170.

Lozanovski, B., Downing, D., Tino, R., Du Plessis, A., Tran, P., Jakeman, J., Shidid, D., Emmelmann, C., Qian, M., Choong, P., 2020a. Non-destructive simulation of node defects in additively manufactured lattice structures. Addit. Manuf. 101593.

Lozanovski, B., Downing, D., Tran, P., Shidid, D., Qian, M., Choong, P., Brandt, M., Leary, M., 2020b. A Monte Carlo simulation-based approach to realistic modelling of additively manufactured lattice structures. Addit. Manuf. 32, 1–21.

Lozanovski, B., Leary, M., Tran, P., Shidid, D., Qian, M., Choong, P., Brandt, M., 2019a. Computational modelling of strut defects in SLM manufactured lattice structures. Mater. Des. 107671.

Lozanovski, B., Leary, M., Tran, P., Shidid, D., Qian, M., Choong, P., Brandt, M., 2019b. Computational modelling of strut defects in SLM manufactured lattice structures. Mater. Des. 171.

Lundstedt, T., Seifert, E., Abramo, L., Thelin, B., Nyström, Å., Pettersen, J., Bergman, R., 1998. Experimental design and optimization. Chemometr. Intell. Lab. Syst. 42, 3–40.

Maconachie, T., Leary, M., Lozanovski, B., Zhang, X., Qian, M., Faruque, O., Brandt, M., 2019. SLM lattice structures: properties, performance, applications and challenges. Mater. Des. 108137.

Malladi, R., Sethian, J.A., Vemuri, B.C., 1995. Shape modeling with front propagation: a level set approach. IEEE Trans. Pattern Anal. Mach. Intell. 17, 158–175.

Martin, A.A., Calta, N.P., Khairallah, S.A., Wang, J., Depond, P.J., Fong, A.Y., Thampy, V., Guss, G.M., Kiss, A.M., Stone, K.H., 2019. Dynamics of pore formation during laser powder bed fusion additive manufacturing. Nat. Commun. 10, 1–10.

Mcmillan, M., Leary, M., Brandt, M., 2017. Computationally efficient finite difference method for metal additive manufacturing: a reduced-order DFAM tool applied to SLM. Mater. Des. 132, 226–243.

Mcmillan, M., Leary, M., Emmelmann, C., Brandt, M., 2018. SLM Lattice Thermal Fields Acquired by Wide-Field Thermal Camera. In: 10th Conference on Photonic Technologies – LANE 2018.

Mines, R., 2019. Metallic Microlattice Structures. Springer.

Mirzendehdel, A.M., Suresh, K., 2016. Support structure constrained topology optimization for additive manufacturing. Comput. Aided Des. 81, 1–13.

Otten, R.H., Van Ginneken, L.P., 2012. The Annealing Algorithm. Springer Science & Business Media, p. 72.

Park, S.-I., Rosen, D.W., Choi, S.-K., Duty, C.E., 2014. Effective mechanical properties of lattice material fabricated by material extrusion additive manufacturing. Addit. Manuf. 1, 12–23.

Plocher, J., Panesar, A., 2019. Review on design and structural optimisation in additive manufacturing: towards next-generation lightweight structures. Mater. Des. 183, 108164.

Ravari, M.K., Esfahani, S.N., Andani, M.T., Kadkhodaei, M., Ghaei, A., Karaca, H., Elahinia, M., 2016. On the effects of geometry, defects, and material asymmetry on the mechanical response of shape memory alloy cellular lattice structures. Smart Mater. Struct. 25, 025008.

Ravari, M.K., Kadkhodaei, M., Badrossamay, M., Rezaei, R., 2014. Numerical investigation on mechanical properties of cellular lattice structures fabricated by fused deposition modeling. Int. J. Mech. Sci. 88, 154–161.

Sampson, R., Lancaster, R., Sutcliffe, M., Carswell, D., Hauser, C., Barras, J., 2020. An improved methodology of melt pool monitoring of direct energy deposition processes. Optic Laser. Technol. 127, 106194.

Sarker, A., Tran, N., Rifai, A., Elambasseril, J., Brandt, M., Williams, R., Leary, M., Fox, K., 2018. Angle defines attachment: switching the biological response to titanium interfaces by modifying the inclination angle during selective laser melting. Mater. Des. 154, 326−339.

Schuëller, G.I., 2001. Computational stochastic mechanics−recent advances. Comput. Struct. 79, 2225−2234.

Sigmund, O., 2001. A 99 line topology optimization code written in Matlab. Struct. Multidiscip. Optim. 21, 120−127.

Smith, M., Guan, Z., Cantwell, W., 2013. Finite element modelling of the compressive response of lattice structures manufactured using the selective laser melting technique. Int. J. Mech. Sci. 67, 28−41.

Strano, G., Hao, L., Everson, R.M., Evans, K.E., 2013. Surface roughness analysis, modelling and prediction in selective laser melting. J. Mater. Process. Technol. 213, 589−597.

Sun, S., Brandt, M., Easton, M., 2017. Powder Bed Fusion Processes: An Overview. In: Laser Additive Manufacturing. Elsevier.

Tang, Y., Kurtz, A., Zhao, Y.F., 2015. Bidirectional Evolutionary Structural Optimization (BESO) based design method for lattice structure to be fabricated by additive manufacturing. Comput. Aided Des. 69, 91−101.

Wang, Y., Gao, J., Kang, Z., 2018a. Level set-based topology optimization with overhang constraint: towards support-free additive manufacturing. Comput. Methods Appl. Mech. Eng. 339, 591−614.

Wang, Y., Zhang, L., Daynes, S., Zhang, H., Feih, S., Wang, M.Y., 2018b. Design of graded lattice structure with optimized mesostructures for additive manufacturing. Mater. Des. 142, 114−123.

Yang, E., Leary, M., Lozanovski, B., Downing, D., Mazur, M., Sarker, A., Khorasani, A., Jones, A., Maconachie, T., Bateman, S., Easton, M., Qian, M., Choong, P., Brandt, M., 2019. Effect of geometry on the mechanical properties of Ti-6Al-4V Gyroid structures fabricated via SLM: a numerical study. Mater. Des. 108165.

Porosity in laser powder bed fusion

6

Anton Du Plessis[1,2]
[1]Research Group 3D Innovation, Stellenbosch University, Stellenbosch, Western Cape, South Africa; [2]Department of Mechanical Engineering, Nelson Mandela University, Port Elizabeth, Eastern Cape, South Africa

Chapter outline

6.1 Introduction 156
6.2 Porosity in cast metals 157
6.3 Overview of porosity in L-PBF 158
6.4 Pore formation mechanisms and porosity types 160
    6.4.1 Single track without powder 160
    6.4.2 Single track with powder 160
    6.4.3 Single layers 162
    6.4.4 Multiple layers 163
    6.4.5 Summary of pore types 165
6.5 Porosity measurement 169
    6.5.1 Archimedes method 169
    6.5.2 Optical microscopy 170
    6.5.3 Computed tomography 170
6.6 Effect of defects 170
    6.6.1 Mechanical properties 171
    6.6.2 Corrosion 171
6.7 Pore closure and mitigation 172
    6.7.1 Porosity minimization 172
    6.7.2 Remelting 173
    6.7.3 Hot isostatic pressing 173
    6.7.4 Peening and surface processing 173
6.8 Conclusion 174
6.9 Questions 175
Acknowledgements 175
References 175

Fundamentals of Laser Powder Bed Fusion of Metals. https://doi.org/10.1016/B978-0-12-824090-8.00007-X
Copyright © 2021 Elsevier Inc. All rights reserved.

6.1 Introduction

Porosity in Additive Manufacturing (AM) is a widespread concern. Pores are often found to negatively influence the mechanical properties, especially fatigue performance, of additively manufactured parts. Laser Powder Bed Fusion (L-PBF) is arguably the AM technology that is best suited to produce complex end-use components for critical applications. For this reason the porosity in L-PBF requires special attention to understand the mechanisms behind the formation of the pores, to devise methods to reduce or even eliminate them in the process, to understand their effects on part properties, and to develop post-processing methods to mitigate or remove them entirely. This chapter addresses all the above points and thereby provides an overview of the current understanding of porosity in L-PBF and how best to address it.

Porosity is defined as the ratio of the volume of pores to the volume of bulk material. Pores here refer to spaces inside solid material, typically produced during the manufacturing process (any manufacturing process, not only L-PBF). The terms "pores" and "defects" are often used interchangeably but in reality the term "defects" has a wider meaning and refers to all forms of imperfections including pores, cracks, surface roughness, microstructural discontinuities, or inclusions, among others. This chapter only discusses pores, and only "unexpected" or unwanted pores in otherwise designed solid material. Cellular or lattice structures provide a way to introduce known interconnected pore spaces or porosity to parts, but this is not relevant to the current discussion.

Porosity could be considered the Achilles heel of AM. It occurs widely in almost all types of additively manufactured materials, in different sizes, shapes, and distributions. It typically has a negative influence on the mechanical properties of produced parts, rendering it difficult to qualify processes and obtain reliable part properties. However, all is not lost. First, porosity content varies considerably and low levels of porosity have been found to be acceptable in many applications. Secondly, the mechanisms behind porosity formation in AM processes are increasingly being revealed and better understood. This makes it possible to devise efficient porosity mitigation and minimization approaches, or apply pore closure methods.

This chapter provides an overview of the current understanding of porosity in L-PBF. The next section introduces the basic concepts of porosity in metals, using the example of porosity in cast metals. This illustrates the fact that the differences in porosity type, shapes, and distributions originate from the differences in the manufacturing processes and mechanisms involved. The next section discusses the specific mechanisms of pore formation in L-PBF in some detail including a summary table of the most widely known forms of porosity, for easy reference. This is followed by a section describing the measurement of porosity. The next section provides a brief overview of the "effect of defect"—which involves understanding the influence of pores on mechanical and other properties. This is followed by a section in which pore minimization and mitigation is discussed, as well as post-processing to close porosity.

6.2 Porosity in cast metals

Porosity occurs in all kinds of materials; it is not a problem exclusively of AM. It is known to occur often in cast metals, for example, in the form of shrinkage porosity or gas porosity. These two types of casting porosity have different formation mechanisms resulting in different morphologies and extents in the cast parts (Fig. 6.1). Large casting pores can have a negative influence on mechanical properties of parts. However, the casting pores are often found in the middle of the part, due to the pore formation mechanisms of the casting and solidification processes. Near-surface pores can be expected to have a stronger effect on fatigue and corrosion properties. This depends on the geometry, wall thickness, actual pore size relative to distance from surface, and the loading conditions, but overall pores are typically quite large (>1 mm in diameter) and yet have minimal influence on the strength properties of the parts. In a study of castings subjected to CT scans before and after static tensile

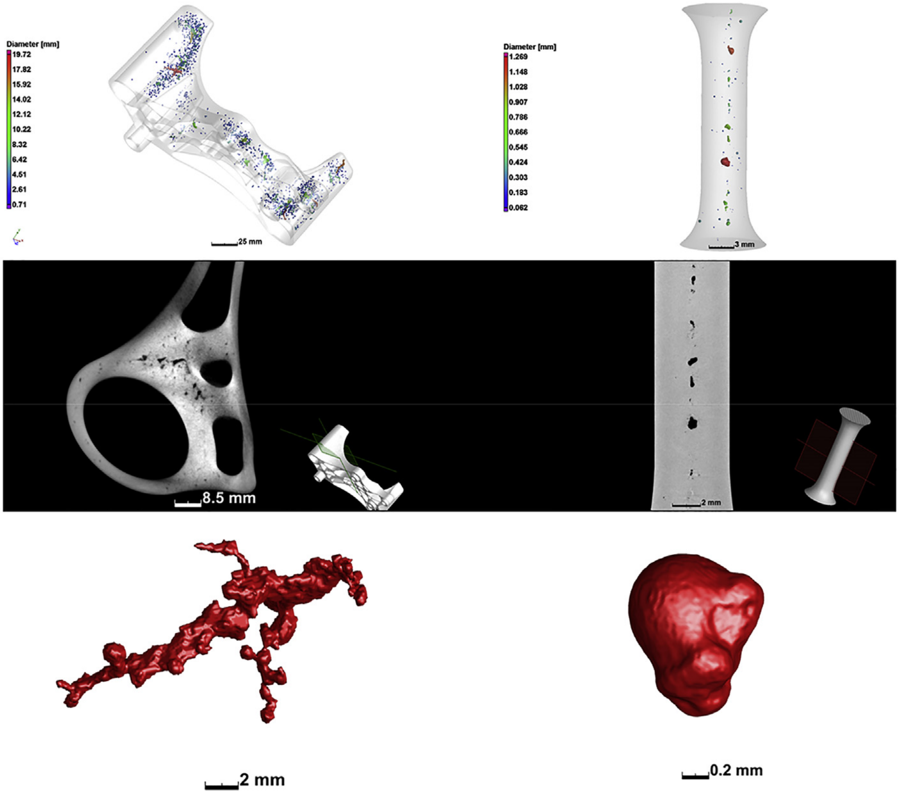
Diameter [mm]
19.72
17.82
15.92
14.02
12.12
10.22
8.32
6.42
4.51
2.61
0.71
25 mm
Diameter [mm]
1.269
1.148
1.028
0.907
0.786
0.666
0.545
0.424
0.303
0.183
0.062
3 mm
8.5 mm
2 mm
2 mm
0.2 mm

Figure 6.1 Examples of two types of casting porosity: shrinkage porosity (left, aluminum alloy) and gas porosity (right, titanium alloy). Shrinkage porosity is irregular shaped and elongated while gas porosity is rounded in shape.
Images taken from microCT scans (Stellenbosch University).

tests, it was confirmed that most failures occurred at the largest casting pores, but the yield strength was not strongly affected (Du Plessis et al., 2017) despite the pore sizes of around 5 mm in diameter. Ductility was affected—reduced ductility was found with increased porosity content and pore size despite the strength remaining unaffected. Due to the potential negative effects of porosity, nondestructive testing of castings—typically using radiographic inspection—is widely used to ensure pore sizes are limited to some maximum value (e.g., nothing larger than 1 mm). As seen in Fig. 6.1, the casting pores can be large—in this case up to 20 mm in their longest axis for shrinkage porosity (aluminum alloy) and 1.2 mm for gas porosity in an experimental tensile bar (Ti6Al4V).

6.3 Overview of porosity in L-PBF

Similar to cast metals, porosity in AM occurs in specific forms and these are related to specific mechanisms of the additive process used. In L-PBF there are numerous pore formation mechanisms which will be described in more detail in the next section. The presence of porosity in L-PBF is widely attributed to process parameters as, for example, explained in Gong et al. (2014). In this work, process parameter maps were constructed and zones of keyhole porosity and lack of fusion porosity were demonstrated, which are still the two most well-known and widely occurring forms of porosity in L-PBF. Examples of keyhole and lack of fusion porosity are shown in physical cross-sections in Fig. 6.2 and explained in some more detail below.

Lack of fusion (LoF) porosity occurs when insufficient melting occurs, either due to too high scan speed or too low laser power for the selected powder layer thickness. This type of porosity is irregular in shape as shown in Fig. 6.2 and may contain unmelted powder particles. These pores may occur in different sizes and, due to the irregular shape, typically have sharp edges. These sharp edges act as stress concentrators under load, causing a significant effect on mechanical properties (Gong et al., 2015; Du Plessis et al., 2020).

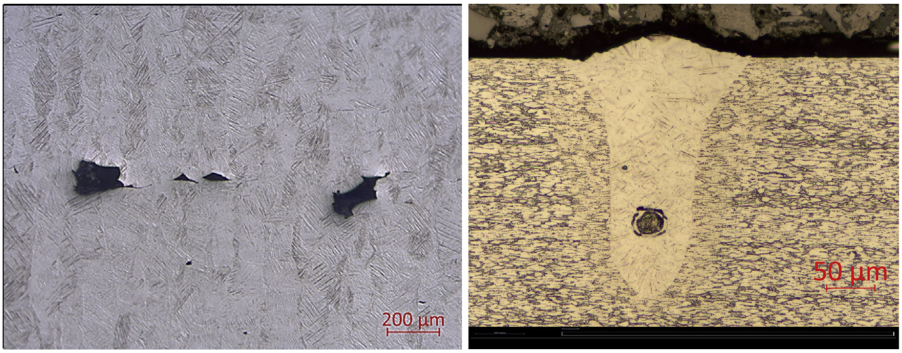

Figure 6.2 Examples of lack of fusion porosity (left) and keyhole porosity (right) shown in metallurgical cross-sections of L-PBF Ti alloys.

Another well-known type of porosity in L-PBF is keyhole porosity—this occurs when the laser power is high and scan speed is low. Keyhole mode melting occurs when the laser causes sufficient material vaporization to create a vapor cavity which creates a depression in the surface. This depression or keyhole cavity may penetrate deeply into the melt pool, and may become unstable and collapse as the melt pool moves, leaving a trapped vapor cavity (or keyhole pore) in the track as it solidifies. This porosity type is more rounded in shape and has a lower influence on mechanical properties if its presence is in low quantities or in small size (Gong et al., 2015; Du Plessis et al., 2020). These two types are shown in CT images in 3D in Fig. 6.3, taken from 5 mm cubes of Ti6Al4V.

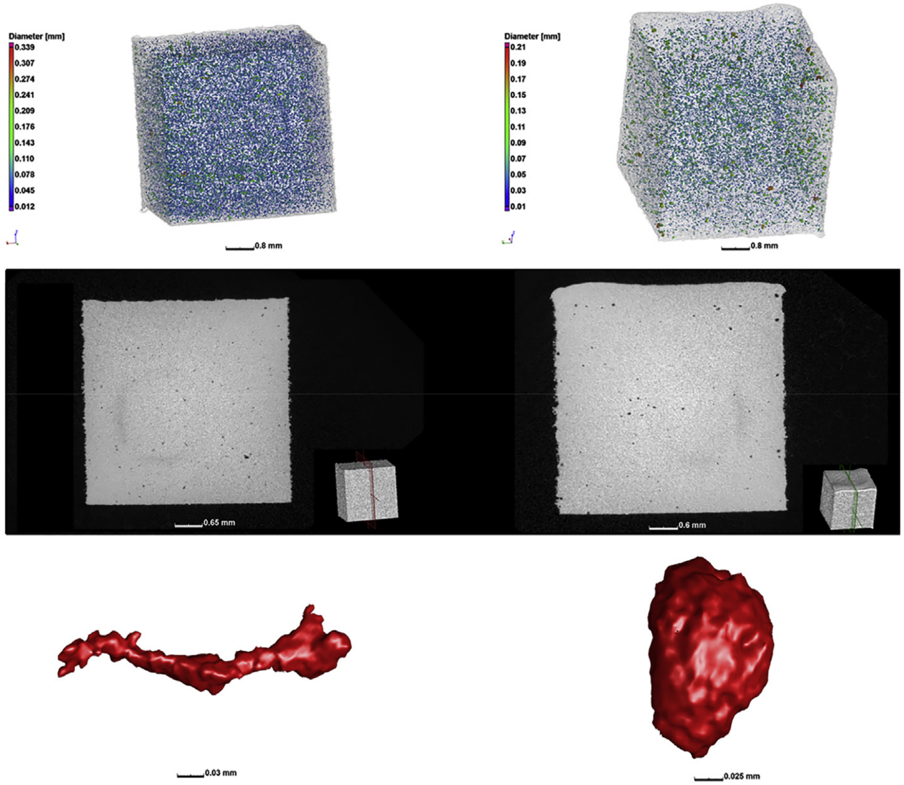
Diameter [mm]
0.339
0.307
0.274
0.241
0.209
0.176
0.143
0.110
0.078
0.045
0.012
0.8 mm
Diameter [mm]
0.21
0.19
0.17
0.15
0.13
0.11
0.09
0.07
0.05
0.03
0.01
0.8 mm
0.65 mm
0.6 mm
0.03 mm
0.025 mm

Figure 6.3 Examples of lack of fusion porosity (left) and keyhole porosity (right) in a typical L-PBF system for Ti6Al4V—5 mm cubes. The LoF porosity was induced by using 1.2 m/s and 120 W laser power, resulting in a total porosity of 0.47% of the volume with 0.34 mm maximum pore diameter. By changing only the laser power up to 360 W, keyhole mode porosity was induced resulting in porosity values of 0.37% total and maximum pore diameter of 0.21 mm.
New images taken from data reported Du Plessis (2019).

6.4 Pore formation mechanisms and porosity types

The L-PBF process has many variables which can cause different types of porosity and many peculiarities and instabilities which can result in porosity formation. This may result in a variety of pore morphologies (as seen in previous section for LoF and keyhole porosity), unique 3D distributions, or clustering of pores in specific regions, varied sizes and total number of pores (Sanaei et al., 2019).

A hierarchical approach is taken here to the discussion of porosity formation and types of porosity found in L-PBF. This involves a process of starting the discussion with a single laser-melted track on a solid substrate without powder, then discussing a single track of melted powder on a solid substrate, followed by single layers (multiple tracks alongside one another) and finally full 3D parts (multiple layers) with increasing complexity. In this way, all (the most important) pore formation mechanisms currently known are discussed and a summary is provided for easy reference in Table 6.1.

6.4.1 Single track without powder

A melted track on a solid substrate without powder can contain significant amounts of porosity or can be pore-free depending on the process parameters and material involved. This is already well known from laser welding, and especially keyhole mode porosity is prevalent at low scan speed and high laser power for a given laser spot size and material. In laser welding, the conduction mode melting is preferred, which is a stable continuous welding mode with appropriate matching laser power and scan speed, lacking keyhole pores. In between these two melting modes (conduction and keyhole mode melting) is what is termed the transition mode melting regime, which combines some aspects of conduction and keyhole mode, and there is no clear threshold between these modes. This is described in detail in a recent review highlighting the similarities between laser welding and L-PBF (Oliveira et al., 2020).

Besides keyhole porosity in the melt pool on a substrate without powder, shielding gas flow can create conditions for entrapment of gas porosity into the melt pool; the entrapped pore is then subjected to turbulent Marangoni flow and often remains after solidification. In other words, the trapped pore does not have time to escape the melt pool due to the fast solidification taking place, combined with melt-pool flow preventing it from simply rising to the surface. The direct formation of pores in a solid substrate without powder was imaged by high speed X-ray imaging experiments recently (Hojjatzadeh et al., 2020), revealing various pore formation mechanisms such as entrapped pores from melt-pool surface fluctuations, vapor cavity depression zone instability during transition zone melting, and pore formation from pre-existing cracks during melting. All of these may occur without any powder present (but also can occur with powder present of course).

6.4.2 Single track with powder

When powder is melted and solidified in a single track, which is the basic building block of the L-PBF process, additional pore formation mechanisms may occur than those described above (Chapter 3). In simple terms, the single track melted using powder can contain (i) keyhole and other pores as explained above, (ii) trapped pores from inside powder particles, (iii) pores from inclusions and oxidation associated with powder particles, which alter the melt-pool dynamics (Leung et al., 2019), and (iv) entrapped gas porosity, either from shielding gas (as explained above) or from between particles in the powder bed. Some of these conditions have been elucidated by modeling approaches where the spatter, denudation zones, keyhole porosity, and melt-pool dynamics were shown to be all related to fast changing thermal conditions, which all affect the pore formation dynamics (Khairallah et al., 2016).

High speed X-ray imaging experiments at synchrotron sources in recent years have been exceptionally useful for confirming and revealing in detail these pore formation mechanisms and their dynamics. These experiments typically use a small "powder bed," and a single track of melting is imaged in real time to visualize the pore formation mechanisms as shown in Fig. 6.4 (Hojjatzadeh et al., 2020). This X-ray image sequence shows the powder bed on a solid substrate, with the vapor cavity inside the substrate and the vapor cavity instability creating a keyhole pore. This work also demonstrates different types of keyhole pores, for example, from instability-induced collapse of vapor cavity, creation of a ledge on the rear wall of the vapor cavity, and from laser stopping at the end of a track which causes the keyhole cavity to collapse rapidly.

In the above-mentioned high speed imaging study, and in other similar works described below, videos are often included which are very useful to visualize the real-time formation and movement of pores and even powder particles. Other studies of this type include the visualization of the entrapment of powder porosity (pores inside powder particles) into the melt pool (Bobel et al., 2019; Hojjatzadeh et al., 2020), dynamics of pore formation at the turning point of a track (Martin et al., 2019), spatter of particles and their dynamics (Guo et al., 2018), movement of pores entrained into the melt pool (Martin et al., 2019), pore dynamics inside the melt pool, and elimination mechanisms by thermocapillary forces (Hojjatzadeh et al., 2019) and keyhole formation (Zhao et al., 2017). One particularly interesting result was revealed in the work studying the threshold for keyhole formation across a wide range of laser power and scan speeds (Cunningham et al., 2019)—it was found that the vapor depression exists across a wide range of conditions and is almost always present at the typical laser power and scan speeds used in commercial L-PBF systems. It is only in some of these high power and slow scan speed conditions that the keyhole becomes suddenly very deep and unstable, resulting in most (and largest) keyhole pore formation. The direct imaging of the dynamics of various fast events in the L-PBF process is continuously revealing more useful information such as this and is valuable in supporting modeling efforts (Khairallah et al., 2020).

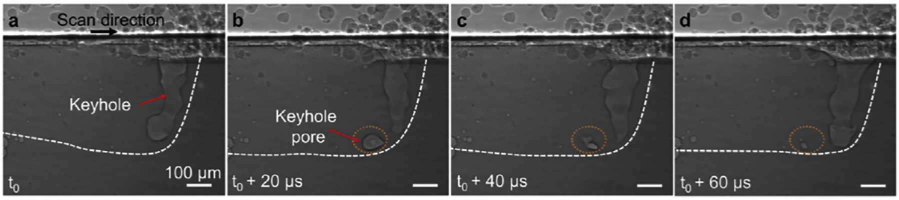

Figure 6.4 Example of fast synchrotron X-ray imaging of keyhole pore formation. Reproduced with approval from Hojjatzadeh et al. (2020).

Besides the direct pore formation mechanisms already mentioned, some mechanisms indirectly create conditions for porosity formation. Powder spattering and denudation of surrounding powder can create irregular tracks (Khairallah et al., 2016) and instability of the melt pool. Similarly, balling and humping effects (Yadroitsev et al., 2013) are extreme cases of irregular track formation with variations in track height, width, and penetration depth. These irregular tracks create instability in the melt pool which can lead to porosity formation by various mechanisms. Additionally, the irregular shaped tracks can also lead to lack of fusion porosity—either between adjacent tracks or by insufficient penetration of the next layer (poor overlap of tracks and layers). The stability of the single track melting process may be monitored by various in-process monitoring tools (see Chapter 11: Process monitoring of laser powder bed fusion).

Clearly there are multiple requirements for creating a pore-free single melted track of powder, and many fast processes may occur in the melt pool which may create conditions for porosity formation. For this reason process optimization and refinement is required for any specific set of process parameters, L-PBF system and powder used. The ideal situation is to create a smooth continuous track without pores and without irregularities. A stable track sets the foundation for good overlap of adjacent tracks and subsequent layers, minimizing porosity formation.

6.4.3 Single layers

The next level of complexity is the melting of a single layer according to the area required in the design. The scan strategy used is therefore important and may affect the pore formation characteristics of the process. The interior of the part in a single layer is scanned in different patterns with adjacent tracks partially overlapped. This overlap is dictated by the hatch spacing—a value set in the process parameters. It can be understood that insufficient overlap will lead to regions containing insufficient melting—a form of lack of fusion. Therefore it is clear that if the single track varies in width along the length of the track (for example, due to balling effect, denudation, or other instability), this might lead to regions of insufficient overlap and LoF between adjacent tracks. In addition to variations in track width, a stable track might simply be spaced too far apart from the next adjacent track—too large set hatch spacing. This seems like an obvious error, but easily happens if the actual melted track width is too narrow, as this depends on the powder size, morphology and material type used, the laser power, beam spot size, and scanning speed. On the other hand, too much overlap causes long manufacturing times and may lead to higher temperatures and related thermally induced problems.

The hatch scanning of the core of the part is usually followed by contour scanning (see Chapter 3). Contour scanning may make use of different process parameters than the hatch scan and due to the continuous scanning along the perimeter, it has been found to result in improved (smoother) surface properties (Tian et al., 2017). Again, the overlap between the hatch core tracks and contour tracks needs to be sufficient, as this region may be particularly prone to porosity formation. In this region near the contour of the part, there are multiple possible reasons for porosity formation.

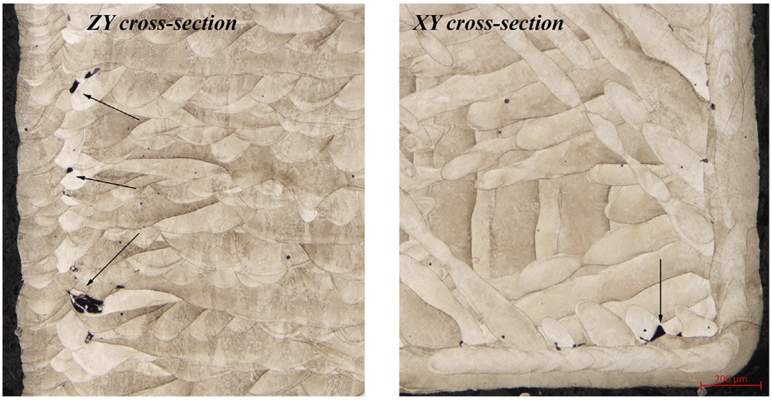

Figure 6.5 Examples of pores at the boundary of contour and hatch tracks.

Insufficient overlap creates a form of lack of fusion between hatch and contour tracks as explained. However, there are also other possible causes for pores in this region. Keyhole pores or pores entrapped in the melt pool as the laser moves toward the end of the hatch track, may be deposited at the end of the track when the laser is switched off momentarily. Depending on the system used, the laser might not switch off (or shutter off) at the end of scan tracks and may slow down creating higher local power density creating conditions more conducive to keyhole pore formation, specifically at the end of the hatch scan track, as the laser turns around. In the case of switch-off, the keyhole cavity can suddenly collapse due to lack of laser power, causing trapped keyhole pores. These mechanisms all create pores near the start or end of hatch core tracks (Thijs et al., 2013), which are always near the surface of the part. In addition, under some conditions, denudation of powder around the track may create regions at the end or sides of tracks with less powder, resulting in insufficient melting of subsequent contours despite good overlap values.

All the above described pore formation mechanisms may occur in scan strategies using stripes or islands, between the stripe or island regions (see Chapter 3). For example, in the case of powder denudation, the first solidified region (island or stripe) creates an area around it affected by denudation leaving too little powder for the next region which must be melted later, causing possible porosity in this region despite good overlap between the stripes or islands. Therefore the edges between different stripes, islands, or between hatch tracks and contour tracks are possible locations of porosity. Examples of pores at the interface of the hatch and contour tracks are shown in Fig. 6.5 in cross-sections.

6.4.4 Multiple layers

The next level of complexity involves multiple layers on top of one another. Here it is clear why the stability of the process is important. Balling, humping, large denudation zones or instability of the track height and width due to various reasons will lead to areas with more or less powder than the ideal case. Too thin powder layers (areas with too little powder compared to surrounding regions) create too thick powder layers on the next layer to be melted. Too thick powder layers result in insufficient melting resulting in a type of lack of fusion porosity. In the previous section the lack of fusion was described between adjacent tracks, in this case it is between subsequent layers. Both of these forms of lack of fusion were investigated, and in particular their 3D morphologies studied in Du Plessis (2019).

Besides the requirement for stable tracks and layers, the layer height itself may be set too high—causing lack of fusion porosity. As multiple layers are built, some systems use rotation of hatch tracks by 90 or 67 degrees for subsequent layers to experience different track directions. When porosity is formed between tracks or between layers, in the form of continuous horizontal pore trails, the rotation of the tracks on the next layer leads to remelting (and hence pore closure) of some areas. This remelting process results in interesting 3D distributions of the remaining pores in different types of checkerboard patterns of porosity such as that shown in Fig. 6.6 (du Plessis and Yadroitsev, 2018).

As with hatch overlap, the layer height selection also affects the total processing speed (for smaller layer height more layers are needed for the same part) and therefore the local thermal history and hence the microstructure are affected too. The different local temperatures may affect the formation of keyhole pores since the higher temperature may lead to excessive energy input. This may lead to differences in porosity between the first layers of a build (when relatively cold) compared to higher on the part when the process has stabilized in temperature.

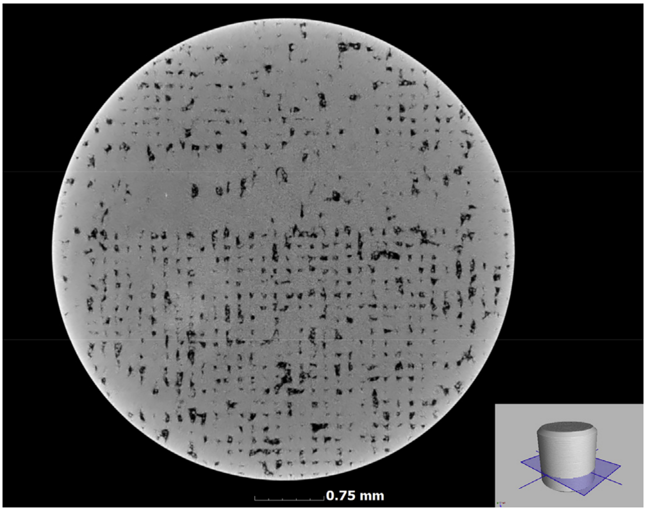

Figure 6.6 Example of a checkerboard pattern resulting from LoF tracks remelted at 90 degrees layer rotations—these LoF regions are between tracks.
New image from data used in Du Plessis et al. (2018).

Overhang regions are particularly problematic, as the local temperature may increase due to the lack of underlying solid material for heat dissipation, since the underlying powder has very low thermal conductivity relative to solid material. This local increased temperature leads to different melt-pool dynamics, leading to keyhole porosity or entrapment of pores. Overhang regions may create such high thermal stress that it causes warping of the part. This warping upwards may lead to irregular spreading of subsequent powder layers by shielding some areas of powder, or even by damaging the powder scraper which leads to nonuniform powder deposition. Overhang regions may also have support structures which are typically thin pillars—powders may get trapped or may not spread properly in or around these structures, leading to an irregular powder bed, which can then lead to forms of lack of fusion porosity. The discussion above is also relevant to complex structures such as lattices and fine features, where heat builds up leading to direct or indirect pore formation.

The powder deposition on each layer is important to ensure lack of porosity formation as explained above. The powder morphology and size distribution affect flowability, which is required to ensure good and evenly spread powder on each layer. Lack of flowability may lead to clumping of powder (see Chapter 18), which leads to regions of high or low powder thickness which leads to insufficient melting. In addition, gas can be entrapped from between powder particles into the melt pool. Therefore larger powder particles which inherently have larger spaces between them, potentially lead to larger pore entrapment. Used (recycled) powders may have attached satellites or irregular powder morphology reducing the flowability and creating lower packing density with larger pore spaces leading to possible porosity formation. In addition, used powders or powders handled incorrectly may have oxidized surfaces, which can lead to pore formation (Leung et al., 2019).

6.4.5 Summary of pore types

As is clear from the above descriptions, many forms of porosity may occur in the L-PBF process. A few years ago, this description was limited to only major porosity present in levels of the order of >1%. A good summary of early work is found in Gong et al. (2014). In recent times however, commercial systems have improved to the point where it is common to obtain parts with porosity <0.1% as evidenced by the results of a round robin study in (Du Plessis and le Roux, 2018). Despite the low levels of porosity from different industry and R&D laboratories, there are differences in the porosity distributions, as expected. This is because each system uses different process parameters and slightly different powders, shielding gas flows, etc. Many different mechanisms of porosity formation have been identified in recent years, and variations and combinations of these may exist. Table 6.1 provides an overview of most of the different mechanisms in L-PBF of metals, with their characteristics.

Table 6.1 Porosity formation mechanisms and their characteristics.

Porosity name	Mechanism	Shape, distribution, and size
Low energy lack of fusion (LoF)	Insufficient melting, can be due to various reasons: - Low energy causing insufficient penetration to previous layer - Low energy causing insufficient overlap between tracks (or too large hatch spacing) - Insufficient track overlap between hatch and contours near surfaces of material	Irregular shaped pores with sharp edges, can be aligned perpendicular to or parallel to the build direction, depending on the LoF with previous layers or between tracks. Large LoF pores may contain unmelted powder.
Keyhole	Excessive energy creating rounded pores inside the solidified tracks, can occur: - All along the track - Only at turnaround points where laser slows down to turn around or switches off leaving keyhole to collapse - Size of pores depends on keyhole size which scales with laser power and spot size	Rounded pores all along tracks or at end of scan tracks. At intermediate powers this also occurs, the pores are simply smaller.
Track instability LoF	Instability and uneven tracks lead to variations in powder layer thickness on the next layer, and in critical cases balling or humping occurs, creating special forms of LoF on the next layer due to varying thickness of the powder layer	Irregular and sometimes large LoF pores.
Turbulent melt-pool induced LoF	Conditions of melt-pool turbulence creating entrapment of pores, particle and spatter ejection, denudation, and combinations of pore formation mechanisms	Large irregular LoF pores.
Powder porosity	Pores inside powders trapped inside melt pool and do not get time to escape as the solidification is too fast	Rounded and small (smaller than powder particles which are generally about 30 μm).

Gas entrapment	Powder packing density or shielding gas related. Pores are entrained into the melt pool and move inside the melt pool but cannot escape before solidification. Entrapment depends on melt-pool conditions as well as shielding gas and powder packing density	Small pores trapped into melt pool, found randomly all over part—typically much smaller than melt pool (also in region of 30 μm).
Uneven powder bed LoF	Uneven powder bed due to scraper damage, local powder clumping, or irregular powders (e.g., re-used powder). Uneven powder bed affects melt-pool stability and indirectly causes pores. In extreme cases, for example, a large particle will not melt sufficiently creating lack of fusion under the region	Elongated pores in build plane (pore tracks), or similar to layered LoF.
Local heating induced keyhole porosity	Local heating creates different melt-pool dynamics creating conditions for pore formation and trapping in solidified material; this can be due to lack of solid material under it (overhang regions) for thermal dissipation - At supported areas but between supports - At solid areas where thermal dissipation is lower, e.g., in corners of parts	Small pores at down-skin regions and at narrow features.
Stop-start pores	When system stops and restarts, part cooling and shrinkage creates a thicker powder layer and insufficient melting of new layer	Layered pores in build plane.
Checkerboard pores	When LoF occurs with some scan strategies, remelting on subsequent layers closes some pores. May occur between tracks or between islands or stripes—regions where porosity often occurs	Small pores in regular grid-patterns.

Continued

Table 6.1 Porosity formation mechanisms and their characteristics.—cont'd

Porosity name	Mechanism	Shape, distribution, and size
Upskin keyhole pores	When surface finishing is used—different laser power for upskin parameters. Higher laser power provides a smooth surface finish, but this may cause subsurface keyhole pores	Rounded pores under top surfaces.
Contour pores	May occur due to different reasons - Keyhole pores trapped when laser is switched off at turnaround end of scan track - Slowing of laser at the turn point increases energy creating keyhole pore formation conditions - Entrained pores (e.g., from shielding gas) trapped in Marangoni flow in melt pool and carried along track, then left at end of scan track - Lack of fusion between contour and hatch tracks	Pores under surface at vertical side walls, next to contour tracks. The morphology may vary depending on the mechanism involved in its formation.
Spatter on powder bed	Irregular melting in some areas due to previous spatter particles	Large LOF pores.
Denudation-zone-induced pores	When powder is lacking in areas at the end and sides of hatch tracks, LOF porosity is induced in subsequent layers as powder layers are too thick. This might be a specialized form of LOF occurring in short hatch tracks, e.g., in lattice structures	Specialized form of LoF pores.
Tree-like pores connected in build direction	In cases of excessively large porosity, overlap and accumulation of pores may lead to building up of pore networks resembling a tree-like structure in the build direction	Tree-like large porous structures following build direction.
Oxides on powder and oxygen contamination	Oxides on powder or oxygen in shielding gas leads to vaporization differences and/or different melt-pool dynamics that may be conducive to pore entrapment	Pore entrapment into melt pool— large roundish pores (Leung et al., 2019).
Small randomly distributed spherical porosity	In conduction mode, small random porosity is still found in very low levels, despite optimal process parameters and scanning strategy	Small (<30 μm) spherical pores randomly distributed and very low levels (<0.01%).

6.5 Porosity measurement

Porosity measurement is necessary and a wide variety of methods are available for this purpose. A popular method in the AM community is the Archimedes method. Another popular method is cross-sectioning of the sample and optical microscopy, in combination with image analysis methods. An emerging method is laboratory X-ray tomography—using 3D data for a similar image analysis process as for 2D optical microscopy. However, the 3D data also includes local 3D distribution information and information on pore morphology, potentially useful information considering the pore diversity explained in the previous section.

Other methods which can be used are mercury porosimetry, helium pycnometry, and variations of the optical microscopy (or electron microscopy) and Archimedes methods. An important concept is to understand the difference between open and closed porosity—referring to the connection of the pore to the surface. In L-PBF parts, especially with rough as-built surfaces and potentially with large lack of fusion porosity present, some internal pores may be connected to the surface through narrow pore throats. These may be included or excluded from porosity measurement depending on the method and specific method variation used, and depending on the pore throat size. X-ray tomography is the only method that provides the opportunity to quantify both open and closed porosity.

Nondestructive pore detection methods other than X-ray tomography also exist but are typically less quantitative, and are meant more for indicating the presence of porosity rather than for quantification. For example, X-ray radiography, ultrasound, and other methods are described in more detail in Chapter 10.

6.5.1 Archimedes method

This is a widely used method which has some limitations but is relatively fast and inexpensive. The method leverages an accurate scale, and measures the part mass in air and in a fluid, which is typically water, but sometimes acetone is also used. The following equation is used:

$$\rho_p = \frac{m_a}{m_a - m_{fl}} \cdot \rho_{fl} \tag{6.1}$$

where m_a is the mass in air, m_{fl} is the mass in fluid, ρ_p is the density of the part, ρ_{fl} is the density of the fluid.

The obtained density can be compared to the theoretical density of the material to calculate effective porosity (porosity in % = 100 − density in %). For more information the reader is referred to Spierings et al. (2011). The disadvantages of the method are the assumption of material reference density, which leads to problems in measuring small porosity values. In addition, open cavities may be penetrated by the fluid leading to “false high” readings of density. It is also possible for air bubbles to attach to the rough surfaces which may affect the mass measurement in the fluid.

Other variations of the Archimedes principle exist, such as measurement of the object volume by water displacement and mass of object measured in air, and a similar method using microCT data to measure the volume accurately and make use of scale mass (Du Plessis et al., 2018b).

6.5.2 Optical microscopy

Sectioning and optical microscopy is widely used, as it provides a relatively simple method to evaluate porosity. The process of sectioning, polishing, and etching parts is already in wide use for microstructural analysis; therefore, the analysis of porosity is often done in tandem. However, quantitative evaluation may depend on magnification and on specific image analysis procedures used. The field of view is typically small and pores may be evaluated incorrectly in terms of their 3D shape or connectivity. It is only good in cases when pores are evenly distributed; otherwise many cross-sections are required. The cost and time investment is also often underestimated as the entire process is labor-intensive. The cross-sectioning and/or polishing process may also modify the inspected surface in the case of some materials, e.g., soft aluminum alloys may smear over small pores.

6.5.3 Computed tomography

X-ray micro-computed tomography is a powerful technique, but not as widely used as other methods yet, largely due to lack of widespread availability thus far. Its advantages are its ability to visualize 3D distributions of pores, pore morphologies, and also quantification using prescribed image analysis workflows similar as for optical microscopy. Some prescribed methods for coupon samples have been developed and are presented in Du Plessis et al. (2018a). As with optical microscopy, the field of view affects the measured smallest pore sizes. This means that the CT inspection of a large part will miss many small pores. For porosity evaluation therefore, it is suggested to use 5–10 mm coupon samples for high-quality porosity quantification. This method is described in more detail in Chapter 10.

6.6 Effect of defects

It is clear that porosity in L-PBF is widely present in different forms and in different extents. But at what point is this a problem? Is there a threshold value that can be defined as being "acceptable"? Is there a critical pore size? How does porosity affect the properties of the parts? These questions require further research but some rules have started to emerge in recent years, as the types of porosity are increasingly being recognized in metal AM, and as careful studies of the "effect of defects" are made (Gong et al., 2015; Malekipour and El-Mounayri, 2018; Du Plessis et al., 2020; Sanaei and Fatemi, 2020). This section briefly provides an overview of this topic. Something that assists greatly in understanding the "effect of defects" is the creation of artificial porosity through designed cavities or modified process parameters and thereby learning (for specific materials and parts) what the direct consequence of a specific porosity type is. In addition to creating artificial pores, the use of X-ray tomography to make time-lapse analysis of crack initiation (either in-situ or ex-situ tomography during mechanical tests) is particularly promising to learn more about the specific effects of defects and their “safe zones”.

6.6.1 Mechanical properties

Porosity may influence static mechanical properties by reducing the effective area which carries a load. Pores may also act as crack initiation locations, with largest pores often being the failure location. However, it has been found that the small porosity found in L-PBF does not strongly influence the static strength of parts, despite widespread porosity in parts up to about 1% (Du Plessis et al., 2020). Other factors are often the overriding factors in these cases, such as residual stress or surface roughness. It has been found that ductility is strongly influenced by the presence of porosity, with increased porosity acting to reduce ductility sharply. These effects are however difficult to predict and may work in competition with other influencing factors such as the surface roughness, residual stress, and microstructure which also changes with process parameters. It has been shown that during tensile testing, small pores coalesce to form larger pores which lead to failure (Krakhmalev et al., 2016). Generally therefore porosity should be minimized to at least below 1% for reasonable static properties for bulk parts. This limit may become more stringent in narrow sections or complex parts such as in struts of lattice structures, where the pore size in relation to the local material thickness is very high compared to bulk parts.

Fatigue properties are strongly influenced by porosity and even small pores are found to be crack initiation locations in fatigue failures. Porosity results in low fatigue strength while contributing to a wide scatter in fatigue life (Sanaei and Fatemi, 2020). It is widely accepted that pores near the surface are most critical (Masuo et al., 2017; Murakami et al., 2019a; Zerbst et al., 2019), while those on the interior of bulk parts are less important and may play minimal roles in most fatigue failures.

In both static and fatigue tests, the amount of porosity, its location or its size are not the only important factors. The pore morphology strongly influences the properties, as lack of fusion pores with irregular and sharp edges are much more detrimental to mechanical properties than the rounded keyhole pores or small entrapped gas pores (Gong et al., 2015; Carlton et al., 2016; Debroy et al., 2018).

6.6.2 Corrosion

Corrosion resistance is important for many end-use applications, and in general this is a metallurgy issue, but the presence of porosity has been shown to strongly influence the corrosion resistance (Kong et al., 2019). Large quantities of porosity lead to higher corrosion rates as the pores act as corrosion sites. It is clear that this effect would be most detrimental near the surfaces exposed to corrosion, and the near-surface porosity is therefore paramount. Rough surfaces typical of the as-built state may also be particularly conducive to corrosion, which combines with near-surface porosity to degrade corrosion performance. Further work in this topic is ongoing, and it is expected that surface quality improvements lead to improved corrosion resistance.

6.7 Pore closure and mitigation

Having discussed the formation of pores, this section focuses on practical solutions to this problem, and the relative advantages and disadvantages of these solutions.

6.7.1 Porosity minimization

The obvious first step in minimizing porosity is to find optimal process parameters. This involves careful testing to find for the particular process, powder, gas flow and other conditions of the system used, the optimal parameters which lead to stable, continuous tracks with sufficient width and depth of penetration. A careful optimization process is needed to find not only the optimal value between high and low energy density, but also to find the optimal melt-pool dynamics, which ideally eliminates entrained porosity through thermocapillary forces (Hojjatzadeh et al., 2019). This "holy grail" of conditions may be more difficult to find for some materials and systems.

It is not only the process that needs optimization, but quality control is needed on all levels, starting with powder used which requires: (a) minimal internal porosity (since these can be trapped in the solidification process); (b) spherical morphology and appropriate size distribution to allow good flowability and packing density; and (c) careful handling to prevent water absorption or oxidation. Water in the powder causes clumping as well as excess vaporization, and can cause hydrogen embrittlement in some metals. Both oxygen and hydrogen (from water vapor)—impurities in the gas flow of the chamber—can easily lead to the same problems, and therefore a clean environment is necessary and this needs to be continuously monitored.

Once tracks and coupon samples are manufactured with proven high density and lack of porosity, the scan strategies might require further optimization, as explained in the previous sections of this chapter. When optimal parameters are found and validated, the process is "good to go." However, even with a perfectly optimized process, unexpected errors may occur when a complex part is produced. For this purpose, various in-process monitoring tools are available and are being developed to ensure the stability of the process and to highlight potential problematic areas.

Despite the best intentions to minimize porosity, pores may occur and may be interrelated to other effects—there will be some compromise between optimal density (lack of porosity), residual stress, optimized microstructure, surface quality, low build time, and other factors. Specific geometries may induce porosities unexpectedly such as in struts of lattice structures or in narrow sections of topology optimized parts. These require further investigation and may be optimized retrospectively once the cause is identified or removed by post-processing. Some small forms of porosity might be acceptable and will be left in place, or the design might be adjusted to compensate for this local porous region (e.g., redesign the problematic part to be thicker).

6.7.2 Remelting

To some extent, good process parameters lead to sufficient penetration into the previous layer to cause some form of remelting. The depth of this penetration depends on the laser power, scan speed, and material used. Remelting by a complete cycle of laser melting of the same layer of previously solidified material allows to close pores. A full remelting prior to new powder deposition has been investigated in Yasa and Kruth (2011) and was shown to significantly reduce porosity while increasing scan (manufacturing) times. A similar concept was used by Aboulkhair et al. (2014) to minimize porosity. A full layer was “pre-sintered” at half the full melting power, with the subsequent full-power melt being very successful to minimize porosity. The drawback of these methods is the additional laser scanning time. Another strategy that can be used is to entirely remelt selected layers which are highlighted as potentially containing defects in combination with in-process monitoring tools. For example, when a process instability or error is detected during melting of a layer, this entire layer can be remelted, but only on the erroneous layer, therefore not adding much time to the total build. Remelting is a good solution to close unexpected pores but is not efficient when the melt tracks are inherently creating keyhole pores or are unstable, for example.

6.7.3 Hot isostatic pressing

One post-processing technique often used, especially for aerospace parts, is hot isostatic pressing (HIPing). This high temperature and high pressure process consolidates pores entirely and has been shown to effectively close all forms of pores in L-PBF except those very near the surface in isolated cases (Du Plessis and Macdonald, 2020). As shown in this work, internal pores are easily closed but near-surface pores connected to the surface make the HIP process ineffective and are not closed. This highlights the need for ensuring pore-free parts in the first place in the L-PBF process as far as possible, and then additional HIP may close those few which remain. It should be kept in mind that HIP is performed not only for pore closure but it also coarsens the microstructure removing anisotropy and improving the ductility of the material. This typically improves the fatigue strength, and a partial role is played by the closure of pores in this improvement. The work reported in Du Plessis and Macdonald (2020) shows near-surface pores may remain problematic which also highlights the need for surface processing when possible, or strategies to improve the surface finish in the L-PBF process itself. Fig. 6.7 shows an example of keyhole porosity closed by HIP (CT scans before and after HIP shown for the same sample). It is seen that the porosity is strikingly closed, and in the cross-section near the top one surface-connected pore remains unchanged. The problem is that such open pores may act as notches in cyclic loading applications (Murakami et al., 2019b; Du Plessis and Beretta, 2020; Molaei et al., 2020).

6.7.4 Peening and surface processing

Shot peening and laser shock peening are discussed in another chapter of this book in more detail (Chapter 12). The focus of shot peening and similar processes is usually on

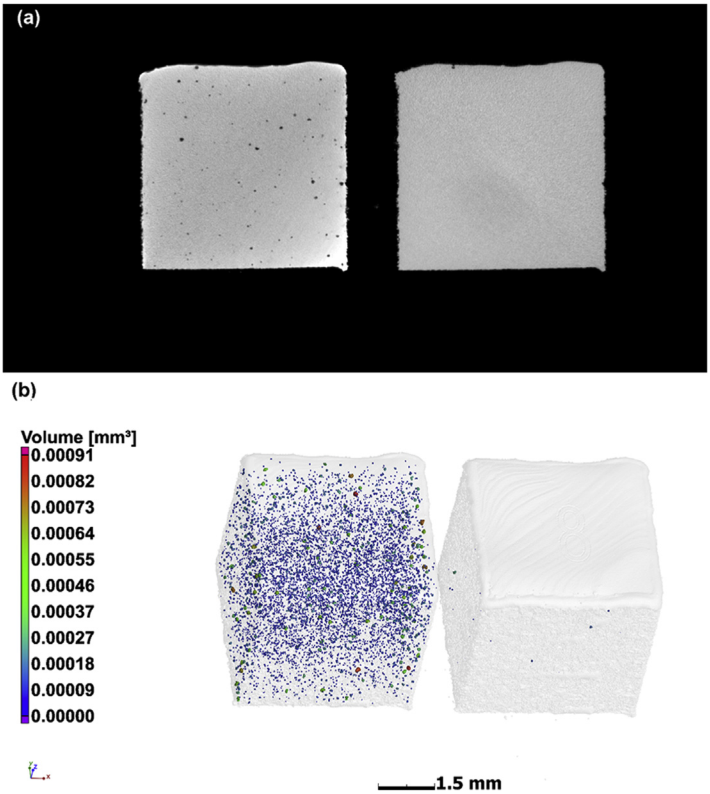

Figure 6.7 Pore closure by HIP for L-PBF cubes with keyhole mode porosity of 0.33% (left) reduced to less than 0.001% (right).
From Du Plessis and Macdonald (2020).

surface processing, improving the roughness, and imparting a local compressive residual stress, which help to improve the fatigue performance of parts. Additionally to this, peening was also recently shown to affect pores near surface (which are highly critical). These pores can be either partially closed by the laser shock peening process (Damon et al., 2018) or fully closed (Du Plessis et al., 2019). This is therefore an additional promising tool for improving the near-surface porosity. However, it requires simple surface access to the shock peening laser; therefore, this is not applicable to complex geometries or lattice structures.

6.8 Conclusion

Porosity in L-PBF is an area of great importance, and the mechanisms behind the pore formation is now well understood. This makes it possible to achieve (routinely) parts with <0.01% porosity of well-distributed small porosity below 30 μm. In these cases mechanical and other properties are highly reliable and suitable for critical applications. However, it can be understood from this chapter that the presence and extent of porosity can increase significantly due to any number of parameter or system errors. Quality control of feedstock and machine maintenance is crucial, as is the optimization of process parameters for each powder type. A well-optimized process with process monitoring to ensure a stable process is the best solution to minimize porosity. Post-process quality control of final parts (e.g., by X-ray CT scans) is beneficial to identify potential unexpected porosity or other defects. Various post-processing options exist to improve the part quality— these are being developed continuously. The realization of fully dense metal parts in L-PBF is exciting and will contribute to the continued success and further uptake of this technology in highly critical applications.

6.9 Questions

- What are the main forms of porosity in L-PBF?
- What level of porosity is typical for today's commercial L-PBF systems?
- Name three possible causes for near-surface pores.
- Name three methods for porosity measurement.
- What effect does porosity have on mechanical properties?
- How can porosity be reduced?

Acknowledgements

A. Du Plessis thanks the Collaborative Program for Additive Manufacturing for financial support.

References

Aboulkhair, N.T., et al., 2014. Reducing porosity in AlSi10Mg parts processed by selective laser melting. Addit. Manuf. 1–4, 77–86. https://doi.org/10.1016/J.ADDMA.2014.08.001. Elsevier.

Bobel, A., et al., 2019. In situ synchrotron X-ray imaging of 4140 steel laser powder bed fusion. Materialia 6, 100306. https://doi.org/10.1016/j.mtla.2019.100306. Elsevier B.V.

Carlton, H.D., et al., 2016. Damage evolution and failure mechanisms in additively manufactured stainless steel. Mater. Sci. Eng. A 651, 406–414. https://doi.org/10.1016/j.msea.2015.10.073. Elsevier.

Cunningham, R., et al., 2019. Keyhole threshold and morphology in laser melting revealed by ultrahigh-speed x-ray imaging. Science 363 (6429), 849–852. https://doi.org/10.1126/science.aav4687.

Damon, J., et al., 2018. Process dependent porosity and the influence of shot peening on porosity morphology regarding selective laser melted AlSi10Mg parts. Addit.Manuf. 20 (January), 77–89. https://doi.org/10.1016/j.addma.2018.01.001. Elsevier.

Debroy, T., et al., 2018. Additive manufacturing of metallic components − process, structure and properties. Prog. Mater. Sci. 92, 112−224. https://doi.org/10.1016/j.pmatsci.2017.10.001.

Du Plessis, A., et al., 2017. Prediction of mechanical performance of Ti6Al4V cast alloy based on microCT-based load simulation. J. Alloys Compd. 724, 267−274. https://doi.org/10.1016/J.JALLCOM.2017.06.320. Elsevier.

Du Plessis, A., Sperling, P., et al., 2018a. MethodsX Standard method for microCT-based additive manufacturing quality control 1 : porosity analysis. MethodsX 5 (September), 1102−1110. https://doi.org/10.1016/j.mex.2018.09.005. Elsevier B.V.

Du Plessis, A., Sperling, P., et al., 2018b. 'MethodsX Standard method for microCT-based additive manufacturing quality control 2: density measurement. MethodsX 5 (September), 1117−1123. https://doi.org/10.1016/j.mex.2018.09.006. Elsevier B.V.

Du Plessis, A., 2019. Effects of process parameters on porosity in laser powder bed fusion revealed by X-ray tomography. Addit. Manuf. 30 (June), 100871. https://doi.org/10.1016/j.addma.2019.100871. Elsevier.

Du Plessis, A., et al., 2019. Pore closure effect of laser shock peening of additively manufactured AlSi10Mg. 3D Print. Addit. Manuf. 6 (5) https://doi.org/10.1089/3dp.2019.0064. Mary Ann Liebert Inc.

Du Plessis, A., Beretta, S., 2020. Killer notches: the effect of as-built surface roughness on fatigue failure in AlSi10Mg produced by laser powder bed fusion. Addit. Manuf. 35 (March), 101424. https://doi.org/10.1016/j.addma.2020.101424. Elsevier.

Du Plessis, A., Macdonald, E., 2020. Hot isostatic pressing in metal additive manufacturing: X-ray tomography reveals details of pore closure. Addit. Manuf. 34 (April), 101191. https://doi.org/10.1016/j.addma.2020.101191. Elsevier.

Du Plessis, A., le Roux, S.G., 2018. Standardized X-ray tomography testing of additively manufactured parts: a round robin test. Addit. Manuf. 24, 125−136. https://doi.org/10.1016/j.addma.2018.09.014. Elsevier.

Du Plessis, A., Yadroitsava, I., Yadroitsev, I., 2020. Effects of defects on mechanical properties in metal additive manufacturing: a review focusing on X-ray tomography insights. Mater. Des. https://doi.org/10.1016/j.matdes.2019.108385. Elsevier Ltd.

Du Plessis, A., Yadroitsev, I., et al., 2018c. X-Ray microcomputed tomography in additive manufacturing: a review of the current technology and applications. 3D Print. Addit. Manuf. 5 (3), 227−247. https://doi.org/10.1089/3dp.2018.0060. Mary Ann Liebert Inc.

Gong, H., et al., 2014. Analysis of defect generation in Ti-6Al-4V parts made using powder bed fusion additive manufacturing processes. Addit. Manuf. 1, 87−98. https://doi.org/10.1016/j.addma.2014.08.002. Elsevier B.V.

Gong, H., et al., 2015. Influence of defects on mechanical properties of Ti−6Al−4 V components produced by selective laser melting and electron beam melting. Mater. Des. 86, 545−554. https://doi.org/10.1016/J.MATDES.2015.07.147. Elsevier.

Guo, Q., et al., 2018. Transient dynamics of powder spattering in laser powder bed fusion additive manufacturing process revealed by in-situ high-speed high-energy x-ray imaging. Acta Mater. 151, 169−180. https://doi.org/10.1016/j.actamat.2018.03.036. Acta Materialia Inc.

Hojjatzadeh, S.M.H., et al., 2019. Pore elimination mechanisms during 3D printing of metals. Nat. Commun. 10 (1), 1−8. https://doi.org/10.1038/s41467-019-10973-9. Nature Publishing Group.

Hojjatzadeh, S.M.H., et al., 2020. Direct observation of pore formation mechanisms during LPBF additive manufacturing process and high energy density laser welding. Int. J. Mach. Tools Manuf. 153 (April), 103555. https://doi.org/10.1016/j.ijmachtools.2020.103555. Elsevier Ltd.

Khairallah, S.A., et al., 2016. Laser powder-bed fusion additive manufacturing: physics of complex melt flow and formation mechanisms of pores, spatter, and denudation zones. Acta Mater. 108, 36−45. https://doi.org/10.1016/J.ACTAMAT.2016.02.014. Pergamon.

Khairallah, S.A., et al., 2020. Controlling interdependent meso-nanosecond dynamics and defect generation in metal 3D printing. Science 368 (6491), 660−665. https://doi.org/10.1126/science.aay7830. American Association for the Advancement of Science.

Kong, D., et al., 2019. Corrosion of metallic materials fabricated by selective laser melting. npj Mater. Degrad. 3 (1) https://doi.org/10.1038/s41529-019-0086-1.

Krakhmalev, P., et al., 2016. Deformation behavior and microstructure of Ti6Al4V manufactured by SLM. Phys. Proced. 83, 778−788. https://doi.org/10.1016/J.PHPRO.2016.08.080. Elsevier.

Leung, C.L.A., et al., 2019. The effect of powder oxidation on defect formation in laser additive manufacturing. Acta Mater. 166, 294−305. https://doi.org/10.1016/j.actamat.2018.12.027. Acta Materialia Inc.

Malekipour, E., El-Mounayri, H., 2018. Common defects and contributing parameters in powder bed fusion AM process and their classification for online monitoring and control: a review. Int. J. Adv. Manuf. Technol. 95 (1−4), 527−550. https://doi.org/10.1007/s00170-017-1172-6.

Martin, A.A., Calta, N.P., Khairallah, S.A., et al., 2019a. Dynamics of pore formation during laser powder bed fusion additive manufacturing. Nat. Commun. 10 (1), 1−10. https://doi.org/10.1038/s41467-019-10009-2. Springer US.

Martin, A.A., Calta, N.P., Hammons, J.A., et al., 2019b. Ultrafast dynamics of laser-metal interactions in additive manufacturing alloys captured by in situ X-ray imaging. Mater. Today Adv. 1, 100002. https://doi.org/10.1016/j.mtadv.2019.01.001. Elsevier Ltd.

Masuo, H., et al., 2017. Effects of defects, surface roughness and HIP on fatigue strength of Ti-6Al-4V manufactured by additive manufacturing. Proced. Struct. Integr. 7, 19−26. https://doi.org/10.1016/j.prostr.2017.11.055.

Molaei, R., et al., 2020. Fatigue of additive manufactured Ti-6Al-4V, Part II: the relationship between microstructure, material cyclic properties, and component performance. Int. J. Fatigue 132, 105363. https://doi.org/10.1016/j.ijfatigue.2019.105363. Elsevier Ltd.

Murakami, Y., et al., 2019a. Defect analysis for additively manufactured materials in fatigue from the viewpoint of quality control and statistics of extremes. Proced. Struct. Integr. 19, 113−122. https://doi.org/10.1016/j.prostr.2019.12.014. Elsevier BV.

Murakami, Y., et al., 2019b. Defects as a root cause of fatigue failure of metallic components. III: cavities, dents, corrosion pits, scratches. Eng. Fail. Anal. 97 (June 2018), 759−776. https://doi.org/10.1016/j.engfailanal.2019.01.034.

Oliveira, J.P., LaLonde, A., Ma, J., 2020. Processing parameters in laser powder bed fusion metal additive manufacturing. Mater. Des. 108762. https://doi.org/10.1016/j.matdes.2020.108762. Elsevier.

Sanaei, N., Fatemi, A., 2020. Defects in additive manufactured metals and their effect on fatigue performance: a state-of-the-Art review. Prog. Mater. Sci. 100724. https://doi.org/10.1016/j.pmatsci.2020.100724. Pergamon.

Sanaei, N., Fatemi, A., Phan, N., 2019. Defect characteristics and analysis of their variability in metal L-PBF additive manufacturing. Mater. Des. 182, 108091. https://doi.org/10.1016/j.matdes.2019.108091. Elsevier BV.

Spierings, A.B., Schneider, M., Eggenberger, R., 2011. Comparison of density measurement techniques for additive manufactured metallic parts. Rapid Prototyp. J. 17 (5), 380−386. https://doi.org/10.1108/13552541111156504. Emerald Group Publishing Limited.

Thijs, L., et al., 2013. Fine-structured aluminium products with controllable texture by selective laser melting of pre-alloyed AlSi10Mg powder. Acta Mater. 61 (5), 1809−1819. https://doi.org/10.1016/j.actamat.2012.11.052. Pergamon.

Tian, Y., et al., 2017. Influences of processing parameters on surface roughness of Hastelloy X produced by selective laser melting. Addit. Manuf. 13, 103−112. https://doi.org/10.1016/j.addma.2016.10.010. Elsevier.

Yadroitsev, I., et al., 2013. Energy input effect on morphology and microstructure of selective laser melting single track from metallic powder. J. Mater. Process. Technol. 213 (4), 606−613. https://doi.org/10.1016/j.jmatprotec.2012.11.014. Elsevier.

Yasa, E., Kruth, J.P., 2011. Microstructural investigation of selective laser melting 316L stainless steel parts exposed to laser re-melting. Proced. Eng. 389−395. https://doi.org/10.1016/j.proeng.2011.11.130. Elsevier Ltd.

Zerbst, U., et al., 2019. Defects as a root cause of fatigue failure of metallic components. I: basic aspects. Eng. Fail. Anal. 97 (June 2018), 777−792. https://doi.org/10.1016/j.engfailanal.2019.01.055.

Zhao, C., et al., 2017. Real-time monitoring of laser powder bed fusion process using high-speed X-ray imaging and diffraction. Sci. Rep. 7 (1), 1−11. https://doi.org/10.1038/s41598-017-03761-2. Springer US.

Surface roughness

7

Martin Leary[1], *Mahyar Khorasani*[2], *Avik Sarker*[1], *Johnathan Tran*[1], *Kate Fox*[1], *David Downing*[1], *Anton Du Plessis*[3,4]

[1]Centre for Additive Manufacturing, School of Engineering, RMIT University, Melbourne, VIC, Australia; [2]School of Engineering, Deakin University, Waurn Ponds, VIC, Australia; [3]Research Group 3D Innovation, Stellenbosch University, Stellenbosch, Western Cape, South Africa; [4]Department of Mechanical Engineering, Nelson Mandela University, Port Elizabeth, Eastern Cape, South Africa

Chapter outline

7.1 Introduction 180
7.2 The underlying reasons for L-PBF surface roughness 180
  7.2.1 Surface morphology—stair-step phenomena 182
  7.2.2 Surface morphology—spattering and satellite particles 183
  7.2.3 Surface morphology— melt-pool stability and track uniformity 183
  7.2.4 Surface morphology—influence of recoil pressure 183
  7.2.5 Surface morphology— influence of surface orientation on residual attached particles 185
  7.2.6 Surface morphology—variation in roughness with solidified tracks and track overlap 187
  7.2.7 Models of surface roughness 188
7.3 Surface roughness characterization 190
  7.3.1 Surface roughness characterization objective 190
  7.3.2 Surface roughness characterization methods 191
  7.3.3 Innovation in surface roughness modeling for L-PBF lattice structures 192
7.4 Surface roughness management 194
7.5 Surface roughness and texture parameters 195
  7.5.1 Profile roughness parameters 197
  7.5.2 Areal roughness parameters 198
  7.5.3 Virtual stylus methods 199
7.6 Implications of surface roughness for technical applications 201
  7.6.1 Medical L-PBF applications 201
  7.6.2 Dynamically loaded L-PBF applications 203
  7.6.3 Hydraulic and thermofluidic L-PBF applications 204
7.7 Conclusion 205
7.8 Questions 207
Acknowledgements 208
References 208

Fundamentals of Laser Powder Bed Fusion of Metals. https://doi.org/10.1016/B978-0-12-824090-8.00023-8
Copyright © 2021 Elsevier Inc. All rights reserved.

7.1 Introduction

Laser Powder Bed Fusion (L-PBF) technology is increasingly important for the fabrication of innovative engineering systems, including high-value products such as bespoke medical implants, mass-optimized structural components, and thermofluidic systems, to name a few. The mechanical performance and manufacturability of L-PBF components are increasingly understood; however, an unresolved challenge of significance to L-PBF application is associated with the as-manufactured surface roughness. This is because the surface roughness induced in L-PBF may be higher than for traditional manufacturing processes, and varies with inclination angle and other local conditions in the manufacturing process.

A phenomenological understanding of the roughness of as-manufactured L-PBF products is required to recognize the possible influences of surface roughness on performance. Some important considerations are, for example, fatigue failure of dynamically loaded systems; osseointegration of bone implants; and form and fit of net-shape products. This chapter compiles the current state of knowledge of surface roughness induced by L-PBF technologies. Methods for the quantification and prediction of L-PBF roughness are provided, as are emerging methods for roughness post-processing. The challenges and opportunities associated with the as-built L-PBF surface roughness are then addressed from the perspective of the relevant performance issues for: metal-fatigue, osseointegration, and net-shape manufacture.

7.2 The underlying reasons for L-PBF surface roughness

The fundamental technology implementation of L-PBF processes inherently generates surface roughness with unique texture, properties, and size ranges. The observed L-PBF surface roughness occurs at various scales and occurs due to various phenomena, ranging from implications of layerwise manufacture and the chosen layer thickness, size of powder, influence of the supporting powder bed, and thermofluidic interactions within the transient melt pool. These phenomena include (Figs. 7.1 and 7.2):

- **Stair-step effects** associated with layerwise manufacturing and influenced directly by layer thickness and component inclination angle (Section 7.2.1).
- Ejection of particles from the melt pool and neighboring regions, resulting in the **spattering** of satellite particles, which attach to upward facing surfaces (Section 7.2.2).
- Stability of the melt pool and associated **morphology of the solidified laser track**, potentially leading to nonuniform track geometry (Section 7.2.3).
- **Melt-pool phenomena**, including interactions of vapor pressure, internal convection currents and surface tension (Section 7.2.4).

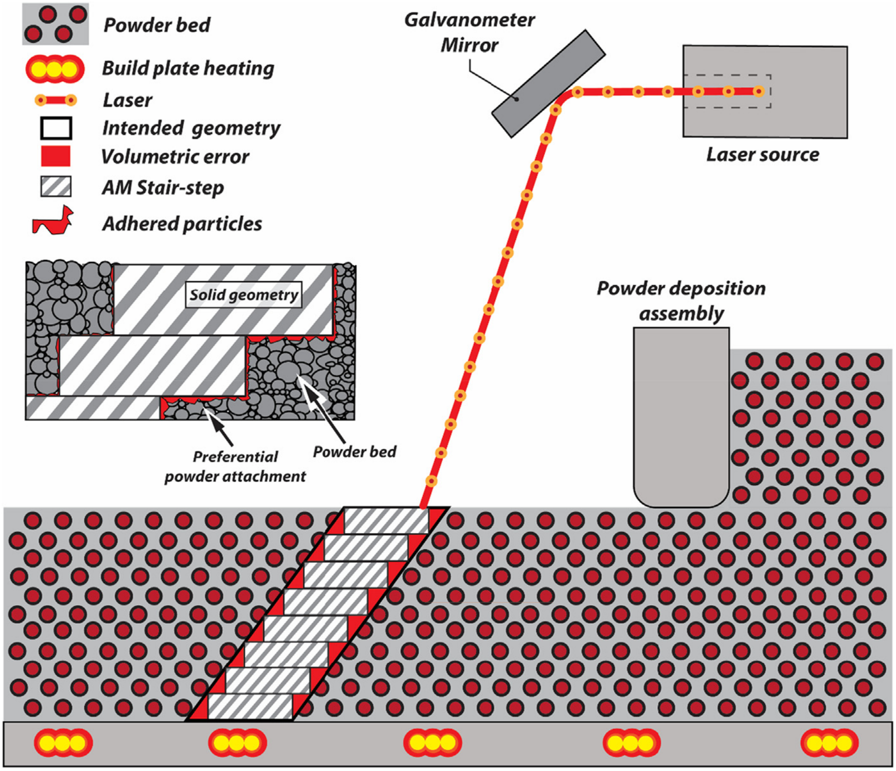
Powder bed
Build plate heating
Laser
Intended geometry
Volumetric error
AM Stair-step
Adhered particles
Galvanometer Mirror
Laser source
Solid geometry
Preferential powder attachment
Powder bed
Powder deposition assembly

Figure 7.1 Schematic representation of L-PBF process indicating stair-step effect and preferential powder attachment at downward-facing surfaces.

- Surfaces that are not upward-facing are in intimate contact with the powder bed during melt-pool solidification. This contact results in **attachment of residual particles**, especially for acutely inclined surfaces, which are typically associated with elevated local temperature (Section 7.2.5).
- **Neighboring tracks interact** to form complex local geometry, especially in the overlap region that is formed by the sequential action of melting and remelting of neighboring and overlapping tracks (Section 7.2.6).

These roughness phenomena are influenced by a range of L-PBF design variables, including (Bourell et al., 2011): ***pre-process parameters*** such as powder size, particle distribution, build-plate preheating, and L-PBF chamber environment; ***process parameters*** such as scanning speed, laser power, hatch spacing, layer thickness, and scanning strategy; and ***post-process*** parameters such as heat treatment and material removal processes. Opportunities to manage, predict, and quantify L-PBF surface roughness by the control of these design variables are presented in the following sections.

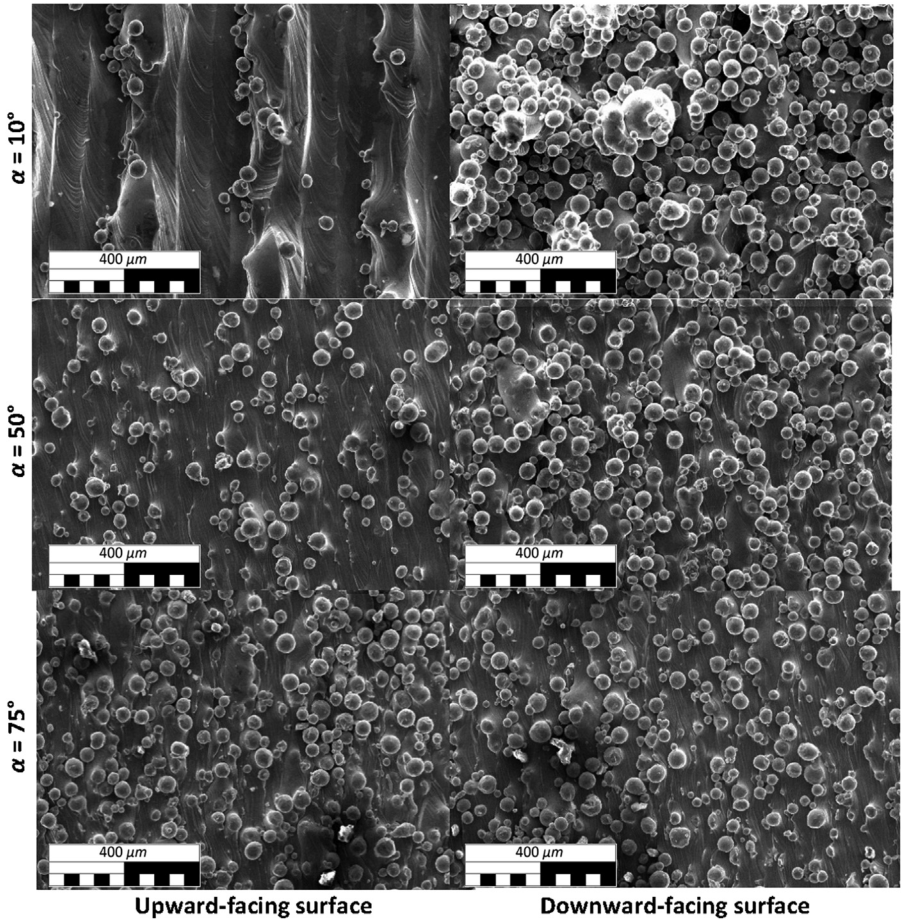

Figure 7.2 Electron microscopy of typical surface features of L-PBF Ti6Al4V specimens for upward- and downward-facing surfaces at various inclinations to the build plate (α). Attached particles are observed for all inclination angles but are prevalent on downward-facing surfaces.

7.2.1 Surface morphology—stair-step phenomena

L-PBF is inherently a layerwise AM technology, where the full-scale component geometry is fabricated by successive layer-by-layer addition. These layers are typically in the order of 30—90 μm in thickness, where larger layer thickness results in higher production rates, but results in a larger disruption to the intended geometry of the as-manufactured L-PBF component (Fig. 7.1). The factors affecting the stair-step phenomena and its influence on roughness are primarily:

- The layer thickness—where a larger layer thickness results in a larger stair-step feature. Note that in general there is an inverse relationship between layer thickness and overall processing time. In response, adaptive layering may be considered where the core is processed with large layers to reduce manufacturing time and the skin is processed with fractionally smaller layers to enhance the stair-step surface condition.

- The inclination angle relative to the build plate—this affects the frequency of the stair-step events, which in turn affects the observed roughness.

In addition to the discrete stair-step effect typically idealized (for example) in predictive models of surface roughness (Section 7.2.7), the stair-step geometry results in adhered powder on lateral faces of the geometric stair-step (Fig. 7.3).

7.2.2 Surface morphology—spattering and satellite particles

In the L-PBF process, the ejection of particles from the melt pool and neighboring regions of the powder bed leads to spattering (Chapter 3, "A step-by-step guide to the L-PBF process"). This spattering results in *satellite* particles adhered to the component's upward facing surfaces (Aboulkhair et al., 2016) (Fig. 7.3).

7.2.3 Surface morphology— melt-pool stability and track uniformity

In L-PBF, the continuity of the solidified track is affected by the laser spot size and associated energy input, with various surface morphologies reported according to the associated melt-pool stability; each with distinct surface morphology and associated roughness (Yuan et al., 2020). For relatively low energy input for a given laser spot size (corresponding to high laser scan speed), melt-pool instability is observed, leading to a series of discontinuous solidified regions. This undesirable phenomenon is known as ***balling***, and results in high surface roughness and structural discontinuities within the manufactured specimen (Fig. 7.4). Increasing the energy input results in a stable melt pool with an associated deposition track that is uniform and ***continuous***, as is required for commercial L-PBF production. For energy input between the stable melt pool and balling regimes, a transition state is also observed where the deposition track is continuous but is nonuniform with substantial changes in track width known as ***necking***. These observations of melt-pool stability and the influence on deposition track uniformity are also dependent on dynamic variables such as the neighboring temperature field. The following discussions assume that process variables are sufficiently well understood and controlled such that a uniform and continuous deposition track is obtained.

7.2.4 Surface morphology—influence of recoil pressure

In surface metrology, the upward-facing surface is often a reference for the roughness measurement. In L-PBF, due to recoil pressure of the laser or vapor plume and scan movement, an asymmetric surface is formed which has a different value of roughness in different measurement directions (Fig. 7.5).

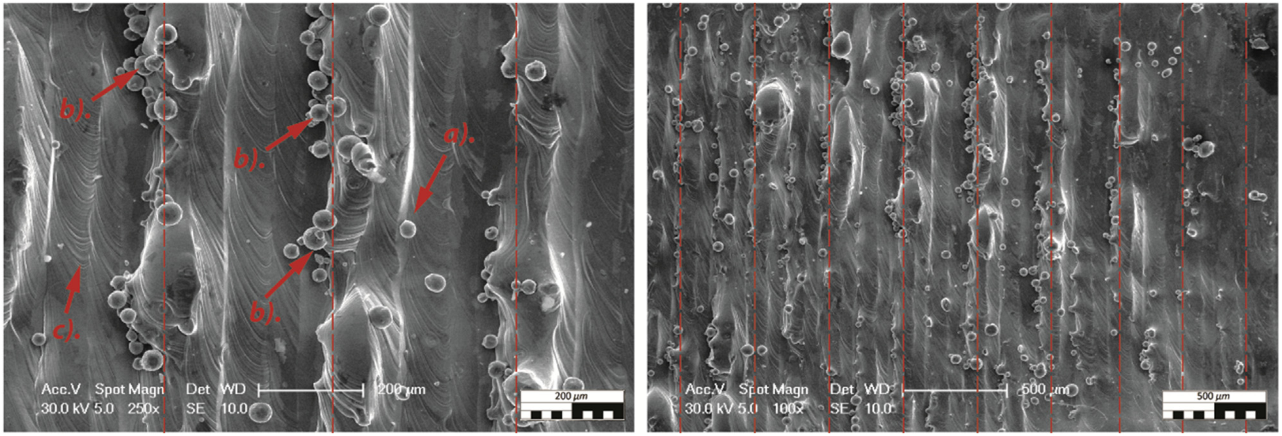
b).
b).
a).
b).
c).
Acc.V Spot Magn Det WD 200 µm
30.0 kV 5.0 250x SE 10.0
200 µm
Acc.V Spot Magn Det WD 500 µm
30.0 kV 5.0 100x SE 10.0
500 µm

Figure 7.3 Upward-facing surface of Ti6Al4V with inclination of $\alpha = 10$ degrees at high (left) and low (right) magnification. Observable phenomena of relevance to surface roughness include a) satellite particles, b) powder bed particles adhered to layerwise edge features (*red-dashed line*), and c) chevron features of solidified track with neighboring track overlap.

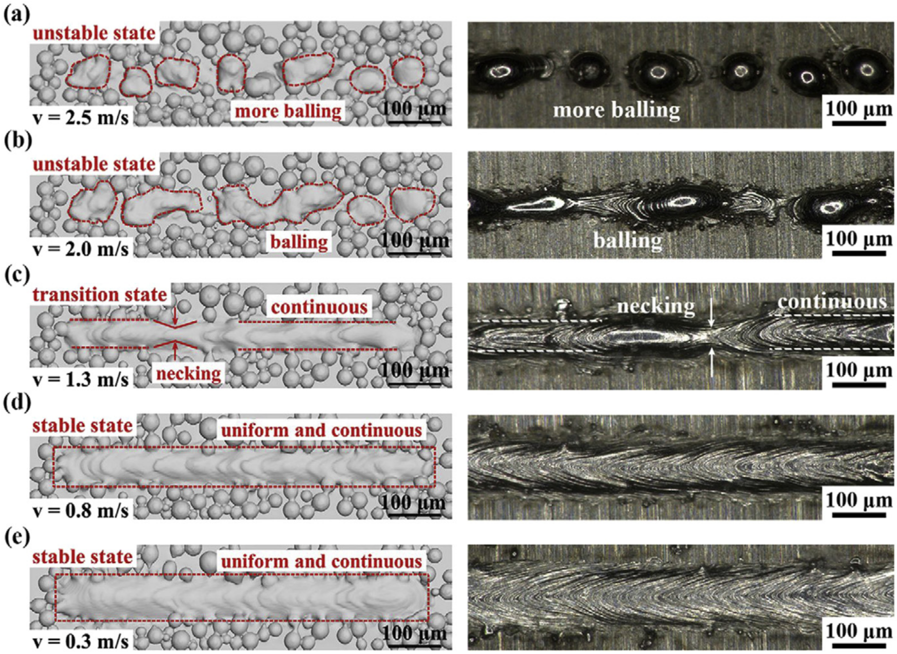
(a)
unstable state
more balling
v = 2.5 m/s
100 μm
more balling
100 μm
(b)
unstable state
balling
v = 2.0 m/s
100 μm
balling
100 μm
(c)
transition state
continuous
necking
v = 1.3 m/s
100 μm
necking
continuous
100 μm
(d)
stable state
uniform and continuous
v = 0.8 m/s
100 μm
100 μm
(e)
stable state
uniform and continuous
v = 0.3 m/s
100 μm
100 μm

Figure 7.4 Distinct surface morphologies (balling, necking, and continuous) observed in simulation (left) and experimental (right) observations due to variation of melt-pool stability (Yuan et al., 2020).

High melt-pool temperature can result in metallic vaporization, resulting in a jet of ejected metal vapor that is equilibrated by a ***recoil pressure*** on the melt-pool surface (Gladush and Smurov, 2011). This recoil pressure forms a ripple effect on this surface that influences surface morphology and associated roughness. Therefore, the value of surface parameters such as R_a, R_q, and R_z (Section 7.5.1) vary when measured parallel, angled, or perpendicular to the scan trajectory (Fig. 7.5).

7.2.5 Surface morphology— influence of surface orientation on residual attached particles

In L-PBF coupons, surfaces with a lateral orientation within the powder bed are typically observed to display higher roughness than equivalent upward-facing surfaces. This observation is partly related to the preferential attachment of residual particles to these lateral surfaces, due to their intimate contact with the powder bed during melt-pool solidification. The phenomenon is especially evident for downward-facing surfaces with acute inclination angle, as these surfaces are associated with substantially increased heat transfer into the supporting powder bed (Calignano, 2018).

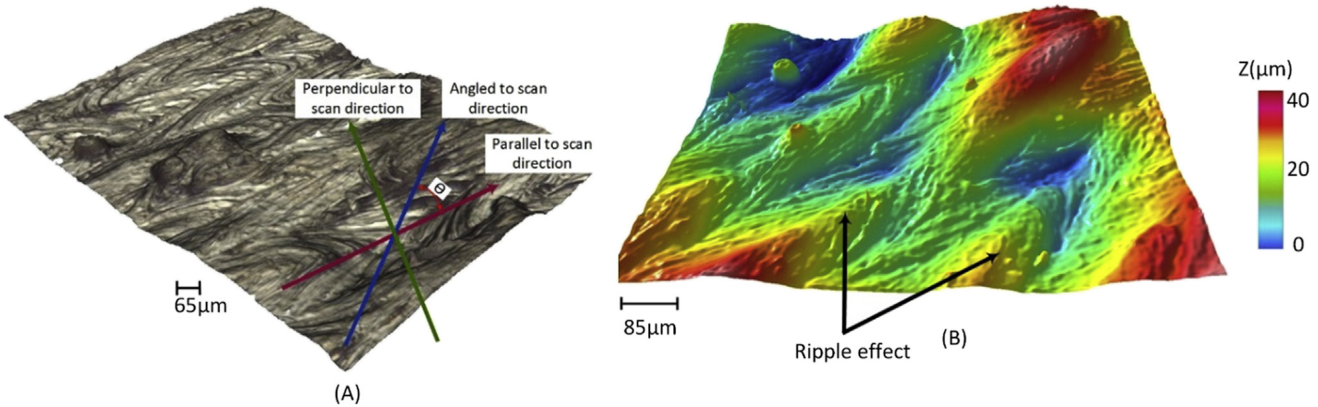
Perpendicular to scan direction
Angled to scan direction
Parallel to scan direction
θ
65µm
(A)
85µm
Ripple effect
(B)
Z(µm)
40
20
0

Figure 7.5 (A) Measurement directions relative to scan trajectory. (B) Ripple marks on the surface of L-PBF. Sample acquired for Ti6Al4V material manufactured with L-PBF.

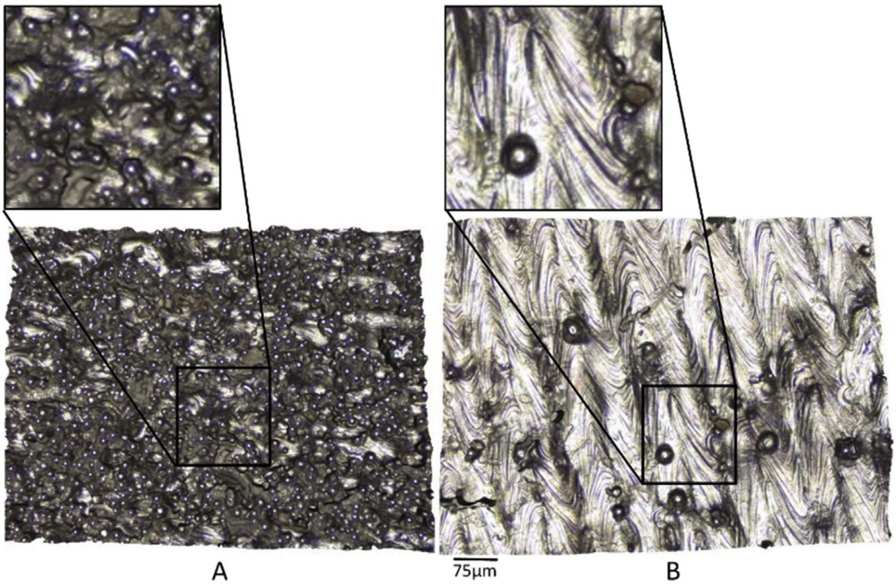

Figure 7.6 Residual attached particles on (A) downward-facing surface and (B) upward-facing surface. Sample of Ti6Al4V material manufactured with L-PBF.

For example, Fig. 7.6 shows the residual particles on the horizontal surfaces that compromise surface quality (typically measured by arithmetic mean roughness, R_a), which is considered poor for many technical applications. In the lateral surfaces due to the number of layers, a large amount of powder is observed to collect at layer boundaries. This level of surface quality cannot satisfy the roughness specification for many high-value applications, therefore post-processing operations may be required (Section 7.4). Where possible, surfaces with functional requirement for surface roughness should be preferably oriented to avoid acute downward facing orientations (Leary, 2017).

7.2.6 Surface morphology—variation in roughness with solidified tracks and track overlap

The layerwise solidification in L-PBF occurs by the action of sequential laser tracks that are aligned with some specified overlap distance. The observed variation of average roughness in the overlap of neighboring tracks can be significantly higher than is observed on the track centerline. Therefore, when measured with linear profile techniques (Section 7.3), the upward-facing horizontal surfaces are asymmetric and substantial variation is observed in the value of R_a when measured in different directions with respect to the laser trajectory. To provide consistency in the reported roughness measurement, areal roughness parameters (Section 7.5) such as the average areal surface roughness, S_a, can provide a useful solution. An optimal overlap value exists for minimizing roughness—too little overlap creates larger peaks and valleys between tracks and too much overlap increases processing time and causes higher temperature buildup, likely increasing the number of attached particles.

Surface quality is also a complex function of melt-pool size, laser power, and scan speed, in combination with the track overlap. For example, for scenarios with higher laser power and higher energy density, partial melting, Marangoni convection, and liquid flow occur over a wider area which influence local roughness. Higher melt-pool temperatures also result in a decrease in surface tension, potentially resulting in a smoother surface (Sing et al., 2016; Martinez et al., 2019).

The surface quality of L-PBF specimens is also affected by defects such as lack of fusion and keyhole porosity (see Chapter 6. "Porosity in Laser Powder Bed Fusion"). With high laser power and low scan speed, keyhole mode melting occurs. In this mode, if the interaction of surface tension and hydrostatic force versus vapor pressure is not balanced, keyholes appear that affect the surface quality (King et al., 2015). When the temperature of the melt pool increases, stronger Marangoni's convection and fluid flow occur, potentially leading to an unstable melt pool creating keyhole pores intermittently. This may also result in stronger movement of unmelted powders toward the melt pool, resulting in increased roughness (Ahn et al., 2017). At low laser power and high scan speed, lack of fusion porosity occurs due to insufficient melting of some areas between tracks and between layers, which leads to irregular surface morphology and increased roughness.

7.2.7 Models of surface roughness

Various models have been proposed to provide a priori predictions of surface roughness for layerwise AM technologies such as L-PBF. These models are applied as Design for Additive Manufacturing (DFAM) tools for the prediction of roughness as a function of design variables and are based on a combination of first principles analysis and empirical observation.

These models presented below consider the local inclination of geometry to build plate and the layer thickness. Early roughness models were based solely on the stair-step effect, for example, as proposed for stereolithographic systems by Reeves and Cobb (1996, 1997). These roughness models enable prediction of stair-step edge distance, h (Eq. 7.1), and estimated average profile roughness, $R_{a,est}$ (Section 7.5) (Eq. 7.2), based on an idealized representation of solidified layers for a specific layer thickness, L_t, and inclination, α (Fig. 7.7).

$$\text{Estimated edge distance} \quad h = \frac{L_t}{\sin(\alpha)} \tag{7.1}$$

$$\text{Estimated roughness} \quad R_{a,\,est} = \frac{1}{l}\int_0^l |z(x)|dx = \frac{1}{4}L_t\cos(\alpha) \tag{7.2}$$

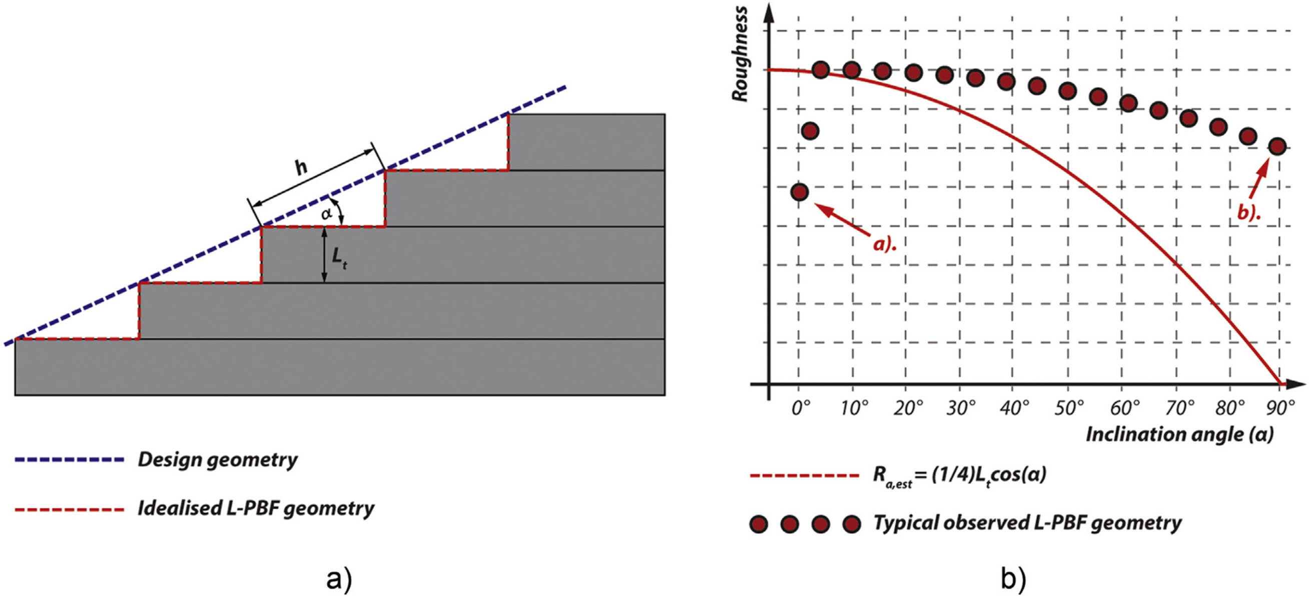
h
α
L_t
Design geometry
Idealised L-PBF geometry
a)
Roughness
a).
b).
0°
10°
20°
30°
40°
50°
60°
70°
80°
90°
Inclination angle (α)
$R_{a,est} = (1/4)L_t\cos(\alpha)$
Typical observed L-PBF geometry
b)

Figure 7.7 (a) Schematic representation of idealized solidified layers and associated edge distance, h, and estimated roughness $R_{a,est}$, for a given layer thickness, L_t, and inclination α. (b) The idealized roughness model, $R_{a,est}$, fails to represent typically observed roughness in a) the region of $\alpha = 0$ degree due to the relatively low roughness on upward-facing horizontal surfaces and b) due to the relatively high roughness on lateral-facing surfaces as $\alpha \rightarrow 90$ degrees.

These roughness models have evolved to accommodate the typical surface roughness observed for as-built L-PBF geometry (Fig. 7.7). For example, the models proposed by Strano et al. (2013) and Boschetto et al. (2017) accommodate the observed surface roughness on upward-facing horizontal and lateral-facing surfaces (these surfaces display roughness, but are not subject to stair-step effects), as well as the effect of surface orientation (either upward-facing or downward-facing). These enhanced roughness models require calibration to accommodate the influence of specific L-PBF powder properties and associated laser processing parameters.

7.3 Surface roughness characterization

Many techniques exist to measure and quantify surface roughness. These techniques range from traditional stylus methods based on physical measurement, to the statistical analysis of Micro-Computed Tomography data and areal roughness measures. The applicability of these methods to the design and certification of L-PBF structures is presented, especially associated with costs and applicability for pre-production and production validation. Although the science of metrology is well documented and standardized, AM methods such as L-PBF provide specific technical and economic challenges, including (Leach et al., 2019):

- Potential complexity of as-manufactured AM specimens in comparison with traditionally manufactured specimens.
- Complex surface texture with high roughness at multiple scales.
- Locally occluded features and challenging access to features of interest.
- Range of candidate materials with corresponding range of optical and surface properties.

7.3.1 Surface roughness characterization objective

The geometric complexity enabled by L-PBF production systems is high and enables the fabrication of complex topologies that would be inconceivable for traditional manufacturing methods. Concurrently, these L-PBF technologies induce local geometric artifacts and defects[1] that superimpose local geometric variation on these complex topologies.

Consequently, considerations of surface roughness should be made with reference to the intended functional objective. Once this objective is understood, an appropriate surface roughness characterization objective can be defined, for example:

- *Biological applications*, such as medical implants may require that the specific nature of the attached particles be characterized to confirm appropriateness for cell attachment and to confirm the effectiveness of particle removal processes.

---

[1] Where artifacts are defined to be inherent attributes of the L-PBF process, such as stair-step effects, whereas defects are avoidable attributes such as excessive surface roughness due to unsupported overhang features.

- *Fluid-flow applications*, including heat exchange devices require confirmation that the intended flow attributes will be achieved.
- *Geometric dimensioning and tolerancing applications* require that the effect of roughness over the as-manufactured surface be characterized such that the ability to meet production tolerances can be quantified.
- *Structural applications*, especially dynamically loaded structures, require that the effect of local roughness on fatigue response be understood.

Further to these domain-specific objectives, the surface characterization will be achieved for either certification of the concept or for ongoing production validation—both of which may have inherently different objectives—for example, the potential damage to the specimen and allowable cost and time of data acquisition. Once an appropriate surface roughness objective has been determined, the appropriate method of surface roughness characterization may be selected.

7.3.2 Surface roughness characterization methods

Various methods of surface roughness characterization exist, each with specific attributes associated with their ability to acquire data on internal and external surfaces, compatibility with Non-Destructive Testing (NDT), acquisition speed, and relative cost (Table 7.1, Fig. 7.8). In summary:

- Tactile methods require direct physical contact between the probe and specimen. These methods allow rapid and inexpensive data acquisition, although the probe may be unable to acquire data on undercut features and requires direct access and nominally flat surfaces that may not be available for complex L-PBF structures. Tactile methods may be used to generate areal roughness parameters (Section 7.5.2) but are typically applied to acquire linear profile roughness data (Section 7.5.1).
- Optical methods such as confocal microscopy and focus variation microscopy provide an inexpensive and relatively fast mechanism for acquiring surface topography data (Leach, 2011). These methods are especially suited to areal roughness measurement (although profile data can also be extracted). These methods require line-of-sight access, and data acquisition for nonplanar specimens may be challenging.
- Scanning electron microscopy and atomic force microscopy provide finer resolution (Sato, and O-hori, 1987), but these too are limited by line of sight to external surfaces.

Table 7.1 Summary of roughness characterization methods.

Method	NDT	External features	Internal features	Relative speed	Relative cost
Tactile	✓	✓	×	Very high	Low
Optical	✓	✓	×	High	Moderate
microCT	✓	✓	✓	Low	Very high

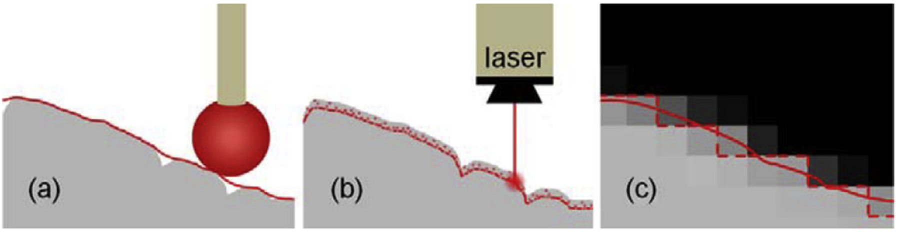

Figure 7.8 Schematic representation of the technical basis for surface characterization methods (a) tactile probe, (b) optical (showing point cloud converted to estimated profile), and (c) CT scanning (showing discrete voxel thresholding and estimated surface representation) of surface roughness characterization (Carmignato and Savio, 2011).

- Computed Tomography (CT) or microCT is an indirect measurement technique based on the reconstruction of multiple X-ray images to generate tomographic (cross-sectional) views of the specimen of interest. The capability to measure internal structures is valuable for high-complexity topologies that are enabled by L-PBF, including, for example, medical implants and thermal fluidic systems. Challenges and opportunities for CT methods presented in more detail can be found in Du Plessis et al. (2018a,b).

These surface roughness characterization methods provide a range of complementary technologies for the characterization and certification of L-PBF components. To aid in formalizing the application of these methods for L-PBF component certification, formal methods of benchmarking test piece geometries are emerging, for example, the “ISO/ASTM Standard guideline for geometric capability assessment of additive manufacturing systems” (ISO/ASTM 52902, 2018).

7.3.3 Innovation in surface roughness modeling for L-PBF lattice structures

L-PBF enables the production of complex lattice structures for automotive, aerospace, and biomedical applications. These applications often benefit from the lattice structures’ capability to reduce weight, tune mechanical properties, or provide increased surface area. Surface roughness of these lattice structures is a technically relevant attribute for critical applications, as it influences crack initiation and fatigue, resistance to fluid flow, and biological cell attachment.

The ability to characterize the roughness of surfaces within the lattice is hampered by limited accessibility and line-of-sight access as is required by contact stylus or optical methods. The microcomputed tomography techniques discussed in Section 7.5.3 and in Chapter 10 “Non-Destructive Testing of Parts Produced by Laser Powder Bed Fusion” provide access to the internal surfaces of a lattice without limitations of accessibility (Table 7.1). For example, Fig. 7.9 shows a lattice structure design, photograph, and micro-CT images with differences of roughness in different locations. For medical applications, surface roughness and the existence of attached particles must be quantified; however, limited access exists for measurement using contact stylus or optical methods. A micro-CT reconstruction of the scanned lattice

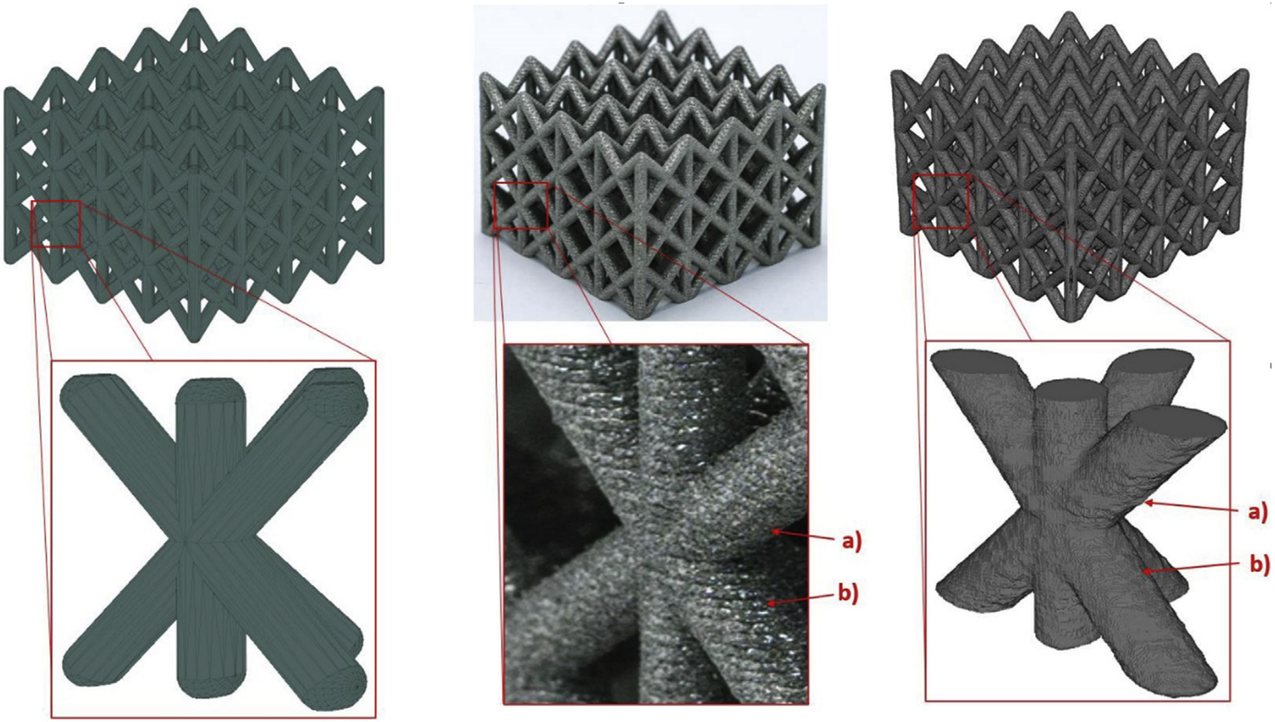

Figure 7.9 Surface details of an L-PBF lattice structure fabricated with 60 μm layer thickness in Ti6Al4V, showing (left) CAD data (center), high resolution photographic images and (right) micro-CT reconstruction of the fabricated lattice at 35 μm resolution. a) downward-facing surface, b) upward-facing surface.

provides an opportunity to acquire roughness data from any strut element within the L-PBF lattice structure, thereby providing a mechanism for the certification of these complex structures.

Despite the opportunities for NDT roughness characterization of lattice structures enabled by micro-CT methods, there remain technical challenges to the acquisition of robust roughness data. The high resolution photographic images of Fig. 7.9 qualitatively demonstrate the potential challenges in using micro-CT reconstruction data, including resolution effects of imaging large lattice structures and the direct effect on the detectability of small structures. For example, Pyka et al. (2014), investigating the effect of surface treatment upon the size range of detectable structures within lattices, performed micro-CT scans before and after surface treatment, both at different micro-CT resolutions—it was found that higher resolution was needed to fully characterize the roughness features of interest.

7.4 Surface roughness management

In response to the criticality of surface roughness for many industrial applications, numerous technical processes are proposed for surface roughness management. These processes may be categorized as either passive or active. Passive processes include modification of design inputs (including build orientation, layer thickness, process parameters, and scan strategy) such that surface roughness is managed as required. Active processes include methods of acid etching, machining, ball milling, and electropolishing to actively modify the as-manufactured surface finish as required.

Passive methods of surface roughness management can be manually or algorithmically implemented. These methods are typically achieved with reference to the predicted influence of inclination and process parameters on local roughness. Manual implementation is achieved based on the designer's intuition and experience, such that an acceptable compromise is achieved between technical and aesthetic requirements for specific roughness values at individual locations of importance. This compromise will also include consideration of the influence of support structures on the associated surface finish. Algorithmic methods of surface roughness management apply some formal optimization algorithm to identify optimal input variables, typically including orientation within the build envelope but also may refer to optimal selection of process parameters (Leary, 2017). This algorithm may include weighting factors to accommodate the relative importance of identified surfaces and allowable surface finish. Both manual and algebraic methods of surface roughness management should be interactively applied with consideration of options for redesign and postprocessing—for example, the relocation of critical features to enhance surface features or to allow appropriate postprocessing is valuable for the industrial application of L-PBF.

Active methods of surface roughness management refer to postprocessing techniques (see Chapter 12 "Post Processing" for more details) that modify the as-manufactured surface finish. This modification is traditionally achieved by machining surfaces that do not satisfy the associated design requirements. This approach may be limiting for L-PBF structures that include complex local geometry (such as patient-specific medical implants) as well as for L-PBF structures that accommodate internal conduits or other features that are inaccessible with traditional machining operations. In response to these challenges for surface finish optimization, a range of innovative methods of active surface roughness management have been proposed for L-PBF, including:

- ***Surface etch*** by the action of corrosive fluids, whereby the L-PBF component is immersed in a corrosive fluid for a controlled time period. Fluid etching allows refinement of surfaces that are not accessible with traditional manufacturing methods and therefore is valuable for L-PBF applications (Sun et al., 2016).
- ***Surface erosion*** by local electro-discharge machining, also known as anodic polishing or electrochemical polishing, whereby a fluid electrolyte allows erosion of the anodic L-PBF material. This erosion occurs preferentially at surface peaks and valleys, thereby resulting in local surface smoothing (Ali et al., 2020).
- ***Mass finishing*** refers to surface finishing methods based on an abrasive media (Boschetto et al., 2013) such as Abrasive Centrifugal Barrel Finishing (ACBF) and Wet Abrasive Centrifugal Barrel Finishing (WACBF). These methods are compatible with the geometric complexity of L-PBF specimens. These processes are economically valuable as hardware is relatively inexpensive and high-throughput production can be achieved without compromising finishing quality (Khorasani et al., 2020).
- ***Controlled wear*** by abrasive fluids, whereby a slurry of abrasive material is reciprocated under high pressure to erode contacting surfaces by the action of shearing stresses. This method, termed Abrasive Flow Machining (AFM) is highly suitable to the controlled machining of internal conduits that are otherwise inaccessible; and has an established precedent of industrial application in the precise machining of orifice diameters such as for fuel injector applications (Peng et al., 2018; Wang et al., 2016a,b).

A combination of chemical etching, to remove the attached particles that often dominate the downward facing surfaces, and then electrochemical polishing, to further reduce surface roughness was found to produce a more even roughness on all surfaces (Pyka et al., 2012). If required, an increased roughness can then be reintroduced in a controllable fashion by a second round of chemical etching causing pitting. These active management techniques increase lattice porosity and reduces strut thickness, so these changes need to be factored into the designed strut thickness for lattice structures (Pyka et al., 2013).

7.5 Surface roughness and texture parameters

An as-manufactured surface can have many levels of deviation from the ideal designed surface as shown in Fig. 7.10. The surface ***roughness*** is a measure of the minute surface irregularities that are generally at the scale of microns. ***Waviness*** is a measure of

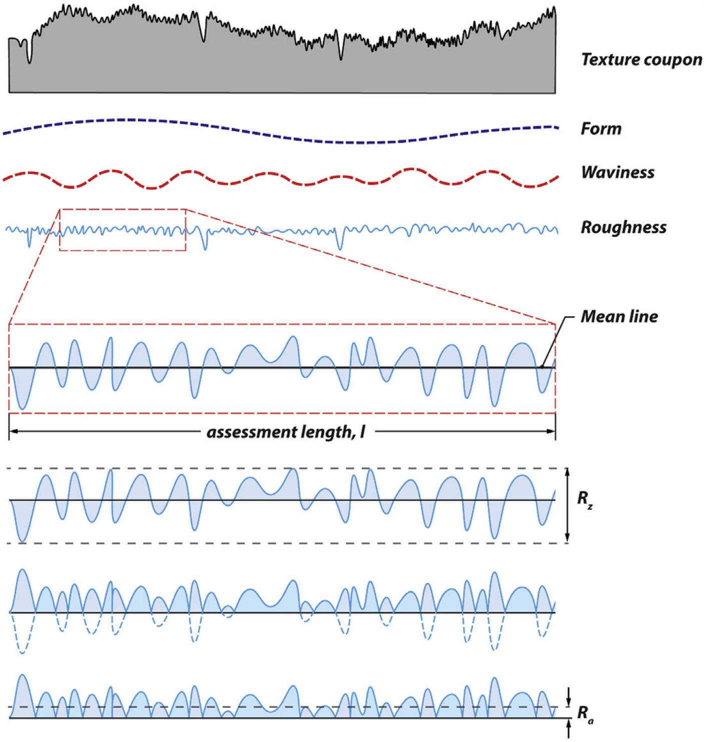

Figure 7.10 Surface texture can be separated into variation at different scales, such as short wavelength ***roughness***, ***waviness*** and ***form*** at intermediate and longer wavelengths (Whitehouse, 2002). Methodology for extraction of maximum peak to valley height, R_z, and arithmetical mean deviation, R_a, are shown for a given assessment length, l.

the secondary irregularities upon which the roughness is superimposed. The waviness is measured at longer wavelengths than the roughness. At even larger wavelengths, the surface variability may be described as a ***form error*** (Cabanettes et al., 2018).

For specimens fabricated with L-PBF, form errors may be considered to occur due to bulk deviation from the intended specimen geometry, for example, as can occur due to thermally induced residual stresses. Waviness errors occur at a local resolution, for example, due to stair-step errors. Roughness is associated with the contributions of individual partially adhered particles and irregularities on the micron scale due to L-PBF parameters, as described in previous sections.

To separate the surface roughness from the longer wavelength components of the surface irregularities of waviness and form, a means of filtering the wavelengths is required, where Gaussian and spline filters are recommended (ISO 16610, 2015a,b). After filtering, the waviness and form are represented by the mean line, while the roughness is represented as the deviation from the mean line (Fig. 7.11).

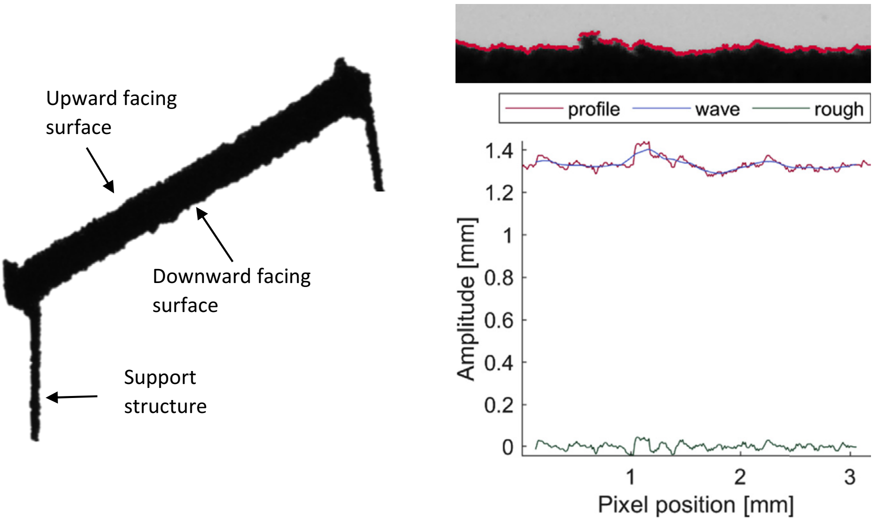

a) *b)*

Figure 7.11 Silhouette of an additively manufactured Ti6Al4V strut allowing profile surface roughness measurements. (a) indicates the upward-facing and downward-facing surfaces. (b) shows an example of the profile, waviness, and roughness extracted from a silhouette edge.

To compare surface texture across samples and to specifications, standardized surface roughness parameters have been developed (ISO 4287, 1998; ISO 25178-2, 2012). These parameters represent the measured roughness data with a single statistical value. Some roughness parameters are highly sensitive to the influence of large peaks or valleys, while other parameters tend to reduce the influence of these outliers.

There are two general categories of surface roughness measurement: profile and areal. Profile measurements are performed along a contour of the surface, typically in a plane perpendicular to the surface, providing length averaged results or identifying the dominant peak height or valley depth within a measurement length. Areal measurements consider a region of the surface and provide area-averaged results.

7.5.1 Profile roughness parameters

Given a profile along a surface contour, represented by the vertical deviation from the mean line, $z(x)$, measured within a sampling length, l, the most common profile roughness parameters are (Whitehouse, 2002; ISO 4287, 1998):

$$\text{Arithmetical mean deviation} \quad R_a = \frac{1}{l}\int_0^l |z(x)|\,dx \tag{7.3}$$

$$\text{Root mean squared deviation} \quad R_q = \sqrt{\frac{1}{l}\int_0^l z(x)^2 dx} \tag{7.4}$$

$$\text{Maximum peak height above mean line} \quad R_{p_i} = \max(z(x));\ R_p = \frac{\sum_{i=1}^{n} R_{p_i}}{n} \tag{7.5}$$

$$\text{Maximum valley depth below mean line} \quad R_{v_i} = |\min(z(x))|;\ R_v = \frac{\sum_{i=1}^{n} R_{v_i}}{n} \tag{7.6}$$

$$\text{Maximum peak to valley height} \quad R_{z_i} = R_{p_i} + R_{v_i}\ ; R_z = \frac{\sum_{i=1}^{n} Rz_i}{n} \tag{7.7}$$

where R_p, R_v, and R_z, are typically averaged across five sampling lengths, $n = 5$. Recommended sampling lengths are dependent on whether the roughness is periodic or nonperiodic, and on the estimated magnitude of the roughness parameter (ISO 4288, 1996). For instance, a sampling length of 8 mm is recommended for roughness measurements $10\ \mu m < R_a \leq 80\ \mu m$ or $50\ \mu m < R_z \leq 200\ \mu m$ on nonperiodic profiles (Table 7.2). After measurement, sampling length should be revised if the measured roughness exceeds the bounds of the estimated roughness.

7.5.2 Areal roughness parameters

Many of the profile roughness parameters determined along a single trajectory have an analogous parameter for evaluating the roughness of a surface region. For a surface with height $z(x, y)$ at point (x, y), within a sample region with extent l_1 and l_2, measured from a reference surface, such as a plane, cylinder, or sphere. Some common areal roughness parameters are (Whitehouse, 2002; ISO 25178-2, 2012):

$$\text{Arithmetical mean deviation} \quad S_a = \frac{1}{l_1 l_2} \int_0^{l_2} \int_0^{l_1} |z(x, y)|\ dxdy \tag{7.8}$$

Table 7.2 Summary of roughness sampling lengths and associated evaluation length (for $n = 5$) for nonperiodic profiles, appropriate for L-PBF technologies from (ISO 4288, 1996).

R_a (μm)	R_z (μm)	Roughness sampling length, l (mm)	Roughness evaluation length (mm)
$0.1 < R_a \leq 2$	$0.5 < R_z \leq 10$	0.8	4
$2 < R_a \leq 10$	$10 < R_z \leq 50$	2.5	12.5
$10 < R_a \leq 80$	$50 < R_z \leq 200$	8	40

Root mean squared deviation $$S_q = \sqrt{\frac{1}{l_1 l_2}\int_0^{l_2}\int_0^{l_1} (z(x,y))^2\, dxdy} \tag{7.9}$$

Maximum peak height $$S_p = \max(z(x,y)) \tag{7.10}$$

Maximum valley depth $$S_v = |\min(z(x,y))| \tag{7.11}$$

Maximum height $$S_z = S_p + S_v \tag{7.12}$$

Additional areal roughness parameters include: skewness and kurtosis of the height distribution; spatial parameters for aspect ratio and texture direction; and parameters relating to distribution of the material such as the surface bearing area ratio. Areal measurements may be obtained by a set of parallel profile measurements or through various areal topography methods based on optical and X-ray technologies, each with its own performance attributes to consider (Senin et al., 2017).

7.5.3 Virtual stylus methods

Many L-PBF components, such as lattice structures, are not compatible with roughness measurement using a contact profilometer or optical methods that require uninterrupted access to the surface. A noncontact method of surface roughness measurement has been developed using backlit images of cylindrical struts, used to capture the silhouette of the strut element with external surface features visible in shadow profile. From these backlit images, silhouette edges and associated profile roughness data may be extracted from both the upward-facing and downward-facing surfaces (Fig. 7.11). To minimize detection of material from adjacent profiles, the technique requires surfaces that are highly convex about the direction of the acquired profile, such as a profile along a cylinder (Alghamdi et al., 2019).

An extension of this virtual stylus method is to utilize micro-computed tomography (microCT) data of the lattice structure. Following scanning and 3D model reconstruction, internal or otherwise inaccessible surfaces can be isolated and sectioned at any orientation to perform virtual linear profile roughness measurements, without the requirement for line-of-sight access. Fig. 7.12 shows multiple cross-sectional images of L-PBF strut elements extracted nondestructively from micro-CT data. From these images the profile roughness R_a was extracted and presented as a function of rotation of the plane of the extracted profile about the central axis of the strut. The results highlight that for the cylinders inclined at 30 degrees to the build direction, there is increased roughness on the downward facing surface of the cylinder as expected (corresponding with the 180 degrees profile rotation).

In addition to the extraction of surface profile roughness, areal roughness measurements can be extracted from micro-CT data as described by Townsend et al. (2017a,b) and Du Plessis et al. (2018b). There are several factors to consider that may influence

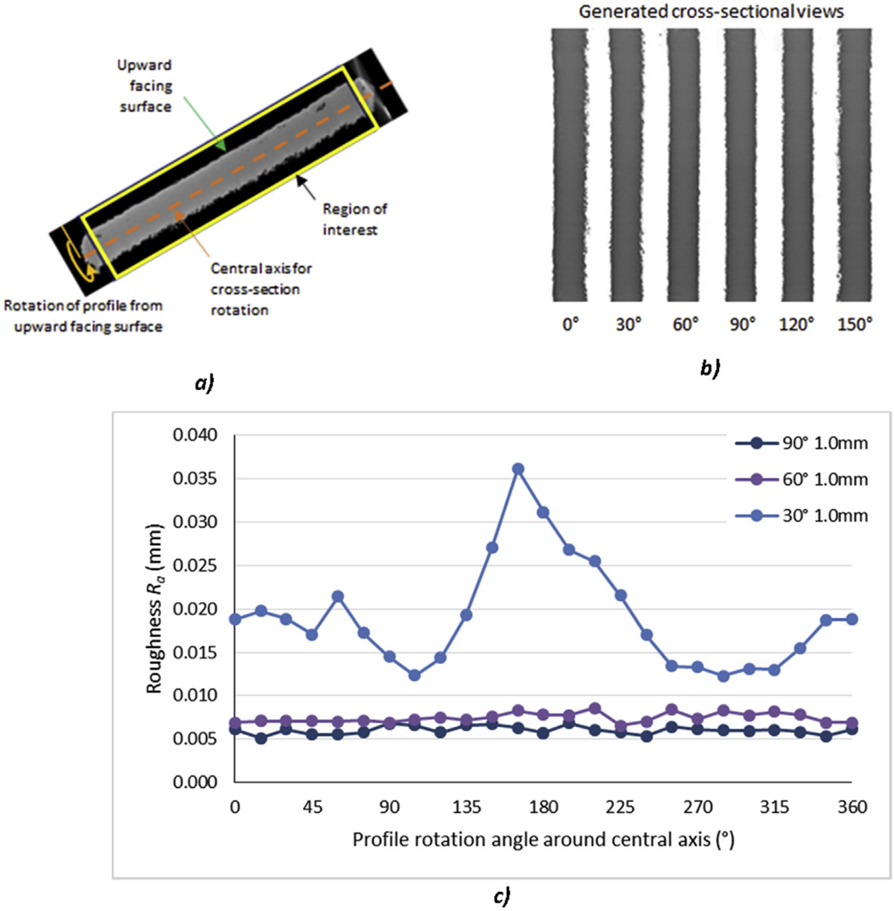

Figure 7.12 Profile roughness extracted from micro-CT data for lattice structure not accessible with contact or optical methods. (a) Identification of axis and region of interest selected from cross-section. (b) Profiles at different angles. (c) Roughness R_a with angle for different build inclinations.

the accuracy of the measurements, including (Townsend et al., 2017b) the method used for determination of the surface from relative gray scale values of the material and the background; the CT system performance which affects image quality (Du Plessis et al., 2020); and the location of the surface as either an internal or external surface. Furthermore, the resolution and spatial offset of the original micro-CT data affects the reconstructed surface and therefore the detail available for extracting surface information (Carmignato et al., 2017). The surface reconstruction process acts as a low pass filter that tends to reduce the sharpness of peaks and valleys, which needs to be considered when using micro-CT data.

7.6 Implications of surface roughness for technical applications

Commercial applications of L-PBF are emerging in a range of sectors that have roughness-critical functional requirements, including *medical* applications, where implant roughness impacts the biological integration of the implant with the patient; *dynamically loaded* applications, where the existence of roughness impacts fatigue failure; and *thermofluidic* applications, where the roughness of internal cooling channels is critically important to heat transfer efficiency and flow rates.

7.6.1 Medical L-PBF applications

Traditionally medical implants have been manufactured in discrete sizes using subtractive and formative methods. L-PBF technologies provide a pathway to innovative implant design including the opportunity to utilize as-manufactured surface roughness to enhance bone ingrowth and the opportunity for bespoke patient-specific implants (Yadroitsava et al., 2019), potentially allowing just-in-time implant manufacture, where the implant is manufactured on-demand with minimal delay between diagnostics, imaging, manufacture and surgery. These outcomes provide substantial clinical benefits for osteosarcoma (bone cancer) treatment by reducing surgical time, reducing unnecessary bone removal, and mitigating stress shielding and associated aseptic loosening.

L-PBF is a technology that by nature of the manufacturing technique provides for a rough surface. L-PBF technologies further allow for designed porosity, which, in addition to microroughness, aids in eliminating implant loosening through hard tissue ingrowth. Although post-processing can remove the larger accessible particles, complex geometries such as lattice structures may prevent all particles being removed. If these metallic particles remain on an implant and later dislodged in vivo, these can cause cell death and implant failure. Wear particles or wear debris is one of the key components in osteolysis whereby osteoclastic activity leads to bone resorption without repair. The presence of these particles causes a cascade of adverse cellular responses (Ollivere et al., 2012; Bitar and Parvizi, 2015). In particular, macrophages are drawn to the particles and attempt to rid the site of any dislodged particles, which begins an inflammatory process. In order to remove particles, the macrophages attempt to phagocytose the particle by engulfing it whole. If this does not occur, particles may enter the lymphatic system for removal, depending on size (Cobb and Schmalzreid, 2006). Further evidence suggests that metal debris can cause osteoblast cytotoxicity (Sansone et al., 2013). As particles are engulfed by macrophage activity, internalized particles have reportedly led to apoptosis (cell death) as the particles produce reactive oxygen species (Zhang et al., 2020).

The typical as-manufactured surface roughness of L-PBF components displays roughness in the micrometer scale: this scale of roughness can potentially enable enhanced cell attachment and bone ingrowth (osseointegration) (Rønold et al., 2003), but can also lead to an inflammatory response associated with wear and dislodged particles. Patient-specific L-PBF implants often include lattice structures which allow matching of elastic modulus of the implant with the surrounding bone and provides permeability for nutrient transport for long-term in-growth. Due to the surface quality and requirement for potential post-processing, which is challenging for lattice structures in particular, a better understanding of the biological implications of implant roughness is needed.

To understand the biological implications of surface roughness and attached (partially melted) particles, it is necessary to understand the fundamentals of cellular interaction with an implant. L-PBF implants are nonbiological metals (e.g., titanium alloys) that are not found in the human body. As a foreign material therefore, it is necessary to select materials and manufacturing processes that are biocompatible to prevent the biological attack known as foreign body response; a capsule formation of multinucleate giant cells that flood the area in response to a new material inside the body leading to inflammation. This foreign body response can be linked to the chemical, physical, and morphological characteristics of the implant and, as a result, the design and manufacture of the implant is paramount to its success.

L-PBF implants are exposed to a complex biological environment after implantation. Initial interaction between the implant and blood occurs with protein adsorption to the external surface of the implant and the formation of a blood-based matrix (i.e., whole blood, plasma, and serum) and later platelet adhesion (Anderson et al., 2008; Jäger et al., 2017). The bone remodeling process is a continual cycle of natural bone removal by osteoclasts and regrowth by osteoblast cells. For long-term implant success it is critical that the cell environment surrounding the implant returns to homeostasis (between bone formation and resorption); that osseointegration (connection between the underlying bone and the implant surface) of the implant occurs; and that inflammation is reduced over time. This process typically occurs over a period of around 6 months and can be lengthened by external processes such as inflammation and healing delays. The most common reasons for implant failure are infection and particle release during wear. As a result, researchers aim for a strong initial attachment and stability at the bone-implant interface. One method of doing so is to optimize the interface (the surface) by using bioactive coatings such as hydroxyapatite (a calcium phosphate material that resembles bone) or increasing the implant surface area by roughening the interface to gain better cell adhesion (Jäger et al., 2017).

Optimal values for L-PBF implant roughness remains an open research question. Many studies however point to a microscale roughness having better bone remodeling and osteointegrative properties (Fig. 7.13). This aligns with recent reports that suggest that a complex implant surface comprising both micro- and nano features is a suitable in vivo interface (Rønold et al., 2003; Lossdörfer et al., 2004; Jäger et al., 2017; Sarker et al., 2018; Saruta et al., 2019). Microstructured surfaces have an increased in vivo mechanical stability linked to the high implant-bone contact, and there is a strong link between the roughness and adhesion energy (Lossdörfer et al., 2004; Jäger et al., 2017). An emerging trend is for combinational micro-nano surfaces where implants can take advantage of the nano properties of the surface for cell attachment and spreading to enhance extracellular matrix protein activity and the microproperties for enhanced physical osteointegration (Gittens et al., 2014; Hasegawa et al., 2020).

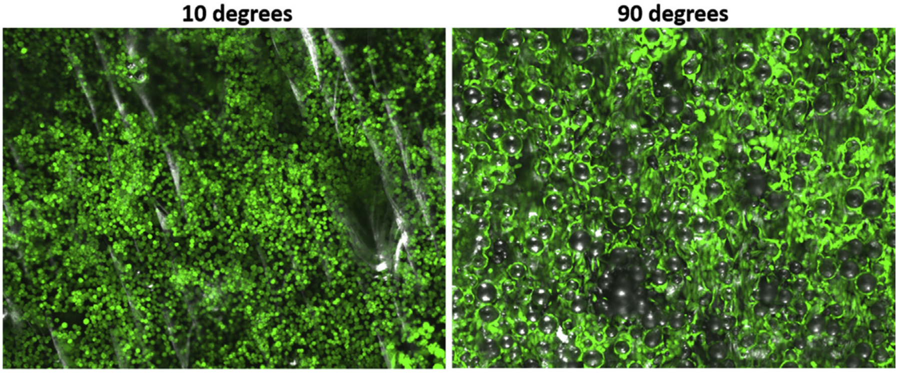

Figure 7.13 Chinese Hamster Ovarian cell attachment (green) on L-PBF Ti6Al4V samples manufactured with 10 and 90 degrees inclination, indicating that cells are mostly spherical in shape for 10 degrees whereas cells are elongated for 90 degrees inclination.

7.6.2 Dynamically loaded L-PBF applications

The fatigue response of dynamically loaded L-PBF structures is increasingly understood, and is highly dependant on surface quality in which the fatigue life is inversely proportional to the surface roughness (Yadollahi and Shamsaei, 2017; Günther et al., 2018; Pegues et al., 2018; Yadollahi et al., 2018; Shrestha et al., 2019; Yánez et al., 2020). Compared to conventional manufacture, L-PBF components in the as-manufactured condition show distinct surface roughness attributes Yadollahi and Shamsaei, 2017), Fig. 7.14. While surface roughness is potentially beneficial for certain applications, such as to promote osseointegration for medical implants (Shalabi et al., 2006); it is, however, potentially unfavorable for the fatigue response of components subject to dynamic loading.

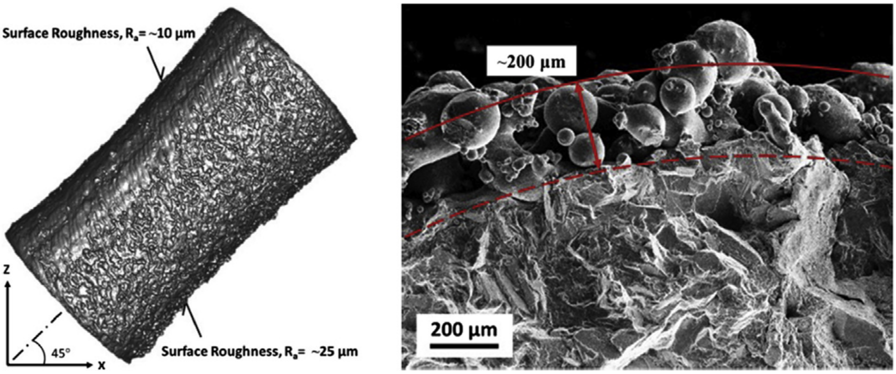
Surface Roughness, R$_a$= ~10 µm
z
45°
x
Surface Roughness, R$_a$= ~25 µm
~200 µm
200 µm

Figure 7.14 (left) X-ray CT image of a 45 degrees orientated Inconel 718 specimen, fabricated by L-PBF, showing a higher surface roughness for the overhanging side and (right) circumferential surface roughness (Yadollahi and Shamsaei, 2017).

Emerging studies in the literature have investigated the effect of post-manufacture surface condition on the fatigue response of L-PBF structures (Kahlin et al., 2017; Pegues et al., 2018; Yadollahi et al., 2018; Vayssette et al., 2019; Zhang and Fatemi, 2019; Lee et al., 2020). When investigating surface roughness and fatigue performance of AM alloy 718 using multiple surface roughness measurement techniques, Gockel et al. (2019) showed that the surface roughness is related to the processing parameters. Their results indicated that the mean areal roughness S_a (Eq. 7.8) (ISO 25178-2, 2012) decreases with the increase in laser power; however, increasing laser speed did not provide a clear trend. The maximum areal valley depth, S_v (Eq. 7.11), was observed to decrease with increasing laser power and increase with increasing laser speed. The study also showed the relationship between surface roughness metrics and fatigue life; specifically that the value of S_v, is inversely correlated to the fatigue life, while S_a does not show a correlation to fatigue life from either measurement method (wide area 3D measurement microscope or CT scan). In other investigations of fatigue behavior of as-built L-PBF Ti6Al4V fabricated at 45 degrees (Pegues et al., 2018), crack initiation was found to be highly sensitive to surface roughness, in which cracks preferentially initiate on the rougher downward-facing surface. In a recent study by Du Plessis and Beretta (2020), the individual surface "notches" in the as-built surface on various surface inclination angles were identified which initiate cracks, using X-ray CT before and after fatigue tests.

Various studies have investigated the influences of post-manufacturing surface treatment on the fatigue performance of various materials (see also Chapter 12 "Post Processing"). These surface treatments have been demonstrated to reduce the surface roughness of L-PBF specimens, and therefore enhance the associated fatigue life. For example, chemical etching has been demonstrated to increase both the yield strength and fatigue life of L-PBF Ti6Al4V (Sun et al., 2016 Van Hooreweder et al., 2017).

7.6.3 Hydraulic and thermofluidic L-PBF applications

Engineering systems that control fluid flow and thermal interactions include hydraulic control systems for power control; fluid manifolds for flow control; and heat exchangers, such as fluid-to-air radiators and active cooling of molding dies. These systems are industrially important but technically challenging for traditional manufacturing. For example, they often involve high geometric complexity and are not compatible with near-net manufacture, resulting in implementations that require multiple interacting components when fabricated with traditional manufacturing. The interaction of these components potentially compromises technical function (for example, by increased mass) and adds to the potential failure-modes of the technical system and therefore the cost and risk of certification. Furthermore, these systems are often manufactured for relatively low production volumes, for example, in custom system design and the maintenance of legacy systems. These low production volumes are often incompatible with the commercial requirements of traditional manufacturing but are matched to the economic capabilities of L-PBF systems (as discussed in Chapter 22 "Economic Feasibility and Cost-Benefit Analysis").

L-PBF technologies provide an emerging manufacturing capability for these hydraulic and thermofluidic systems due to their compatibility with high geometric complexity design and low-production volume (Fig. 7.15). Commercial success in these applications requires an understanding and accommodation of the effects of L-PBF surface roughness. Surface roughness is relevant to fluid applications for several reasons, including the as-manufactured cross-sectional area, powder removal, and thermal conduction.

The cross-sectional area of an L-PBF fluid channel is influenced by local surface roughness, which in turn is influenced by L-PBF process parameters including material type and local design variables including selection of channel geometry and inclination to powder bed. Empirical studies are emerging that quantify L-PBF manufacturability including cross-sections with enhanced manufacturability (Mazur et al., 2016) and internal structures that aid in L-PBF manufacturability as well as providing load bearing capability (Tan et al., 2020).

Powder removal from internal L-PBF conduits can be challenging due to the combination of local surface roughness and cross-sectional area, especially for scenarios with complex flow conduits. Post-processing options exist for the modification of roughness in as-manufactured internal flow conduits; in particular, abrasive flow machining is a robust commercial technology that is increasingly applied to remove residual powder and to reduce roughness (Han et al., 2020).

Thermal conduction is directly influenced by local roughness, which influences both the conductive heat transfer area as well as the turbulence of the flow state, where turbulent flow results in more effective fluid mixing and associated convective heat transfer. The turbulence induced by L-PBF surface roughness can result in a larger friction factor than for traditional design (Saltzman et al., 2018).

7.7 Conclusion

L-PBF enables significant design freedom in the manufacture of engineered products. Commercial applications of L-PBF are often associated with high-value applications where the functional performance is technically challenging; these applications are often associated with technical requirements that are inherrently dependant on surface roughness.

The L-PBF process is inherently associated with surface roughness. This roughness is due to various phenomena including the stair-step geometry inherent to the layer-wise manufacturing process; adhered particles, especially on the downward-facing surfaces that are supported during cooling by the powder bed; and local melt-pool geometry and thermofluidic interactions within the transient melt pool affecting spatter, attached satellite particles, track morphology, and the overlap and interaction of adjacent tracks and layers. An understanding of the fundamental basis for L-PBF roughness allows process and design variables to be optimized for the specific roughness requirements.

The available roughness characterization methods are presented and explained. Particular challenges of relevance to L-PBF include the roughness characterization

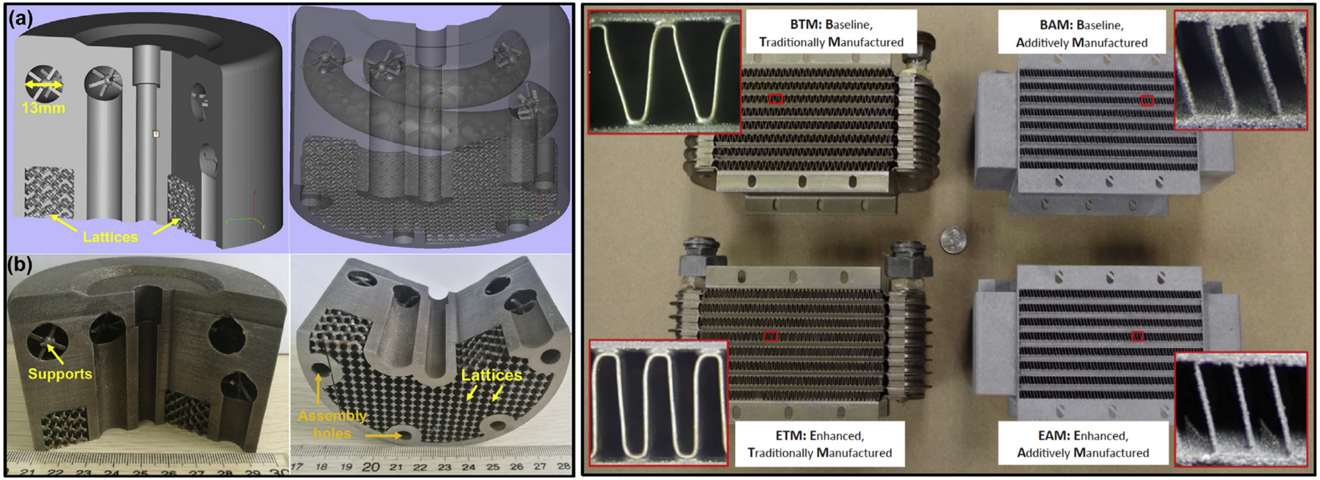
(a)
13mm
Lattices
(b)
Supports
Lattices
Assembly holes
BTM: Baseline, Traditionally Manufactured
BAM: Baseline, Additively Manufactured
ETM: Enhanced, Traditionally Manufactured
EAM: Enhanced, Additively Manufactured

Figure 7.15 Left: L-PBF conformal cooling die implemented with self-supporting cooling channels (Tan et al., 2020), Right: comparison of L-PBF and traditionally manufactured liquid-to-air heat exchangers (Saltzman et al., 2018).

of lattice structures and internal channels. For scenarios where L-PBF cannot be managed to within required tolerances, active methods of surface roughness management can be applied including methods such as erosion, corrosion, and fluid abrasion, which can accommodate surfaces that are not accessible with traditional machining processes.

The systematic accommodation of L-PBF roughness enables commercial advantages in a range of applications including medical implants where roughness impacts biological integration with the patient; dynamically loaded applications, where the impact of roughness on fatigue must be accommodated; and, hydraulic and thermofluidic applications, where cooling channel roughness is critical to efficiency and required fluid flow. Specific design opportunities and challenges of L-PBF surface roughness were presented for these commercial applications.

7.8 Questions

The following questions are provided to assist in review of the fundamental concepts associated with the surface roughness of components manufactured by L-PBF:

- The observed roughness of L-PBF components occurs due to a range of distinct phenomena. In broad terms identify these phenomena and describe their specific influence on surface roughness.
- L-PBF design variables can be categorized as either being either *pre-process* parameters, *process* parameters, or *post-process* parameters. Identify the specific design variables of relevance to each of these categories and consider how these design variables can influence the surface roughness of a manufactured L-PBF component.
- In simple terms explain the stair-step phenomenon. Why is this phenomenon inherently associated with L-PBF? How can a designer accommodate the stair-step phenomena without compromising the technical function of an L-PBF manufactured component?
- Why is the roughness of upward-facing L-PBF surfaces fundamentally distinct to the roughness of downward-facing L-PBF surfaces (Fig. 7.2)?
- Explain the *balling* and *necking* phenomena and explain how process parameters can be modified to achieve L-PBF track stability (Fig. 7.4).
- The recoil pressure equilibrates the pressure of metal vaporization. How does this recoil pressure influence the observed surface roughness (Fig. 7.5)?
- What are the fundamental assumptions associated with the idealized models of surface roughness (Fig. 7.7)?
- Estimated roughness $R_{a,est}$ is a function of layer thickness, L_t, and inclination angle, α (Eq. 7.2). For what values of inclination angle is the predicted roughness largest? Why does $R_{a,est}$ differ from the typical observation of L-PBF roughness at this inclination angle (Fig. 7.7)?
- What fundamental methods of surface roughness characterization exist (Table 7.1), and what are the specific attributes of these methods in terms of their ability to acquire data on internal and external surfaces, compatibility with Non-Destructive Testing (NDT), acquisition speed, and relative cost?
- What options for surface roughness management exist for scenarios where the as-manufactured L-PBF roughness does not match the associated technical requirements?

- When formally defining surface roughness, what is the distinction between *roughness*, *waviness*, and *form error*? Which of these distinctions would be appropriate for measuring irregularities at the scale of individual particles? For stair-step effects? For bulk thermal distortion?
- For an anticipated average roughness, R_a, of 5 μm, what roughness sampling length, l, is specified by ISO 4288 (1996) (Table 7.2)? If the measured average roughness is actually 12 μm, would the roughness measurement need to be repeated with a modified sampling length?
- What is the distinction between profile and areal roughness measurement? What are the relative advantages and disadvantages of these methods?
- The nondestructive acquisition of areal and profile roughness data is challenging for L-PBF lattice structures due to limited access for optical and tactile methods. How do virtual stylus methods provide an opportunity to overcome this challenge?
- The technical advantages of L-PBF are beneficial for a range of commercial scenarios including (Section 7.6): medical applications, dynamically loaded applications, and thermofluidic applications. Select one of these scenarios and summarize the challenges and opportunities associated with L-PBF roughness.

Acknowledgements

The authors acknowledge support from the facilities and technical staff of RMIT''s Advanced Manufacturing Precinct as well as the Australian Research Council Industrial Transformation Training Centre in Additive Biomanufacturing (IC160100026) www.additivebiomanufacturing.org. Dr. Khorasani acknowledges Deakin and RMIT Universities to provide the opportunity for research and experimental works. Dr. Khorasani also acknowledges Professor Rolfe and Professor Gibson, as well as his family, for support and help during the hours of working on this research. A. Du Plessis thanks the Collaborative Program for Additive Manufacturing for financial support.

References

Ali, U., Fayazfar, H., Ahmed, F., Toyserkani, E., 2020. Internal surface roughness enhancement of parts made by laser powder-bed fusion additive manufacturing. Vacuum 177, 109314.

Aboulkhair, N.T., Maskery, I., Tuck, C., Ashcroft, I., Everitt, N.M., 2016. On the formation of AlSi10Mg single tracks and layers in selective laser melting: microstructure and nano-mechanical properties. J. Mater. Process. Technol. 230, 88−98.

Alghamdi, A., Downing, D., McMillan, M., Brandt, M., Qian, M., Leary, M., 2019. Experimental and numerical assessment of surface roughness for Ti6Al4V lattice elements in selective laser melting. Int. J. Adv. Manuf. Technol. 105 (1−4), 1275−1293.

Anderson, J.M., Rodriguez, A., Chang, D.T., 2008. Foreign body reaction to biomaterials. Semin. Immunol. 20 (2), 86−100.

Ahn, I.H., Moon, S.K., Hwang, J., Bi, G., 2017. Characteristic length of the solidified melt pool in selective laser melting process. Rapid Prototyp. J. 23 (2).

Bitar, D., Parvizi, J., 2015. Biological response to prosthetic debris. World J. Ortho. 6 (2), 172−189.

Boschetto, A., Bottini, L., Veniali, F., 2013. Microremoval modeling of surface roughness in barrel finishing. Int. J. Adv. Manuf. Tech. 69 (9−12), 2343−2354.

Boschetto, A., Bottini, L., Veniali, F., 2017. Roughness modeling of AlSi10Mg parts fabricated by selective laser melting. J. Mater. Process. Technol. 241, 154−163.

Chan, K.S., Koike, M., Mason, R.L., Okabe, T., 2013. Fatigue life of titanium alloys fabricated by additive layer manufacturing techniques for dental implants. Metall. Mater. Trans. A 44 (2), 1010−1022.

Bourell, D., Stucker, B., Spierings, A.B., Herres, N., Levy, G., 2011. Influence of the particle size distribution on surface quality and mechanical properties in AM steel parts. Rapid Prototyp. J.

Cabanettes, F., Joubert, A., Chardon, G., Dumas, V., Rech, J., Grosjean, C., Dimkovski, Z., 2018. Topography of as built surfaces generated in metal additive manufacturing: a multi scale analysis from form to roughness. Precis. Eng. 52, 249−265.

Calignano, F., 2018. Investigation of the accuracy and roughness in the laser powder bed fusion process. Virtual Phys. Prototyp. 13 (2), 97−104.

Carmignato, S., Aloisi, V., Medeossi, F., Zanini, F., Savio, E., 2017. Influence of surface roughness on computed tomography dimensional measurements. CIRP Ann. 66 (1), 499−502.

Carmignato, S., Savio, E., 2011. Traceable volume measurements using coordinate measuring systems. CIRP Ann. 60 (1), 519−522.

Cobb, A.G., Schmalzreid, T.P., 2006. The clinical significance of metal ion release from cobalt-chromium metal-on-metal hip joint arthroplasty. Proc. Inst. Mech. Eng. H 220 (2), 385−398.

Du Plessis, A., Yadroitsev, I., Yadroitsava, I., Le Roux, S.G., 2018a. X-ray microcomputed tomography in additive manufacturing: a review of the current technology and applications. 3D Print. Addit. Manuf. 5 (3), 227−247.

Du Plessis, A., Sperling, P., Beerlink, A., Kruger, O., Tshabalala, L., Hoosain, S., Le Roux, S.G., 2018b. Standard method for microCT-based additive manufacturing quality control 3: surface roughness. MethodsX 5, 1111−1116.

Du Plessis, A., Tshibalanganda, M., Le Roux, S.G., 2020. Not all scans are equal: X-ray tomography image quality evaluation. Mater. Today Commun. 22, 100792.

Du Plessis, A., Beretta, S., 2020. Killer notches: the effect of as-built surface roughness on fatigue failure in AlSi10Mg produced by laser powder bed fusion. Addit. Manuf. 35, 101424.

Frazier, W.E., 2014. Metal additive manufacturing: a review. J. Mater. Eng. Perform. 23 (6), 1917−1928.

Gittens, R.A., Olivares-Navarrete, R., Schwartz, Z., Boyan, B.D., 2014. Implant osseointegration and the role of microroughness and nanostructures: lessons for spine implants. Acta Biomater. 10 (8), 3363−3371.

Greitemeier, D., Dalle Donne, C., Syassen, F., Eufinger, J., Melz, T., 2016. Effect of surface roughness on fatigue performance of additive manufactured Ti−6Al−4V. Mater. Sci. Technol. 32 (7), 629−634.

Günther, J., Leuders, S., Koppa, P., Tröster, T., Henkel, S., Biermann, H., Niendorf, T., 2018. On the effect of internal channels and surface roughness on the high-cycle fatigue performance of Ti-6Al-4V processed by SLM. Mater. Des. 143, 1−11.

Gladush, G.G., Smurov, I., 2011. Physics of Laser Materials Processing: Theory and Experiment, vol. 146. Springer Science & Business Media.

Gockel, J., Sheridan, L., Koerper, B., Whip, B., 2019. The influence of additive manufacturing processing parameters on surface roughness and fatigue life. Int. J. Fatig. 124, 380−388.

Han, S., Salvatore, F., Rech, J., Bajolet, J., 2020. Abrasive flow machining (AFM) finishing of conformal cooling channels created by selective laser melting (SLM). Precis. Eng. 64, 20−33.

Hasegawa, M., Saruta, J., Hirota, M., Taniyama, T., Sugita, Y., Kubo, K., Ishijima, M., Ikeda, T., Maeda, H., Ogawa, T., 2020. A newly created meso-, micro-, and nano-scale rough titanium surface promotes bone-implant integration. Int. J. Mol. Sci. 21 (3), 783.

ISO 4288, 1996. Geometric Product Specifications (GPS) − Surface Texture: Profile Method − Rules and Procedures for the Assessment of Surface Texture. International Organization for Standardization, Geneva, Switzerland.

ISO 25178 part 2, 2012. Geometrical Product Specification (GPS) − Surface Texture: Areal − Part 2: Terms, Definitions and Surface Texture Parameters. International Organization for Standardization, Geneva, Switzerland.

ISO 16610-1:2015, 2015a. Geometrical Product Specifications (GPS) − Filtration − Part 1: Overview and Basic Concepts. International Organization of Standardization, Geneva, Switzerland.

ISO/ASTM 52902, 2018. Additive Manufacturing − Test Artefacts − Standard Guideline for Geometric Capability Assessment of Additive Manufacturing Systems. International Organization for Standardization, Geneva, Switzerland.

ISO 4287, 1998. Geometrical Product Specifications (GPS) − Surface Texture: Profile Method − Terms, Definitions and Surface Texture Parameters.

ISO 16610-1, 2015b. Geometrical Product Specifications (GPS) - Filtration - Part 1: Overview and Basic Concepts, first ed. International Organization for Standardization.

Jäger, M., Jennissen, H.P., Dittrich, F., Fischer, A., Köhling, H.L., 2017. Antimicrobial and osseointegration properties of nanostructured titanium orthopaedic implants. Materials (Basel) 10 (11), 1302.

Kahlin, M., Ansell, H., Moverare, J.J., 2017. Fatigue behaviour of notched additive manufactured Ti6Al4V with as-built surfaces. Int. J. Fatig. 101, 51−60.

Khorasani, M., Gibson, I., Ghasemi, A., Brandt, M., Leary, M., 2020. On the role of wet abrasive centrifugal barrel finishing on surface enhancement and material removal rate of LPBF stainless steel 316L. J. Manuf. Process. 59, 523−534.

King, W.E., Anderson, A.T., Ferencz, R.M., Hodge, Neil E., Kamath, C., Khairallah, S.A., Rubenchik, A.M., 2015. Laser powder bed fusion additive manufacturing of metals; physics, computational, and materials challenges. Appl. Phys. Rev. 2 (4), 041304.

Leach, R. (Ed.), 2011. Optical Measurement of Surface Topography, vol. 14. Springer, Berlin, p. 326.

Leach, R.K., Bourell, D., Carmignato, S., Donmez, A., Senin, N., Dewulf, W., 2019. Geometrical metrology for metal additive manufacturing. CIRP Ann. 68 (2), 677−700.

Leary, M., 2017. Surface roughness optimisation for selective laser melting (SLM): accommodating relevant and irrelevant surfaces. In: Laser Additive Manufacturing. Woodhead Publishing, pp. 99−118.

Lee, S., Pegues, J.W., Shamsaei, N., 2020. Fatigue behavior and modeling for additive manufactured 304L stainless steel: the effect of surface roughness. Int. J. Fatig. 141, 105856.

Lossdörfer, S., Schwartz, Z., Wang, L., Lohmann, C.H., Turner, J.D., Wieland, M., Cochran, D.L., Boyan, B.D., 2004. Microrough implant surface topographies increase osteogenesis by reducing osteoclast formation and activity. J. Biomed. Mater. Res. Biomed. Mater. Res. A 70A (3), 361−369.

Martinez, R., Todd, I., Mumtaz, K., 2019. In situ alloying of elemental Al-Cu12 feedstock using selective laser melting. Virtual Phys. Prototyp. 14 (3), 242−252.

Mazur, M., Leary, M., McMillan, M., Elambasseril, J., Brandt, M., 2016. SLM additive manufacture of H13 tool steel with conformal cooling and structural lattices. Rapid Prototyp. J. 22 (3).

Nicoletto, G., Konečná, R., Frkáň, M., Riva, E., 2018. Surface roughness and directional fatigue behavior of as-built EBM and DMLS Ti6Al4V. Int. J. Fatig. 116, 140−148.

Ollivere, B., Wimhurst, J.A., Clark, I.M., Donell, S.T., 2012. Current concepts in osteolysis. J. Bone Joint Surg. Br. 94 (1), 10−15.

Peng, C., Fu, Y., Wei, H., Li, S., Wang, X., Gao, H., 2018. Study on improvement of surface roughness and induced residual stress for Additively Manufactured metal parts by Abrasive Flow Machining. Procedia CIRP 71, 386−389.

Pyka, G., Kerckhofs, G., Schrooten, J., Wevers, M., 2014. The effect of spatial micro-CT image resolution and surface complexity on the morphological 3D analysis of open porous structures. Mater. Char. 87, 104−115.

Pyka, G., Kerckhofs, G., Papantoniou, I., Speirs, M., Schrooten, J., Wevers, M., 2013. Surface roughness and morphology customization of additive manufactured open porous Ti6Al4V structures. Materials 6, 4737−4757.

Pyka, G., Burakowski, A., Kerckhofs, G., Moesen, M., Van Bael, S., Schrooten, J., Wevers, M., 2012. Surface modification of Ti6Al4V open porous structures produced by additive manufacturing. Adv. Eng. Mater. 14, 363−370.

Pegues, J., Roach, M., Scott Williamson, R., Shamsaei, N., 2018. Surface roughness effects on the fatigue strength of additively manufactured Ti-6Al-4V. Int. J. Fatig. 116, 543−552.

Reeves, P.E, Cobb, R.C., 1997. Reducing the surface deviation of stereolithography using in-process techniques. Rapid prototyp. J. 3 (1).

Reeves, P.E., Cobb, R.C., 1996. Surface deviation modelling of LMT processes - a comparative analysis. In: 5th European Conference on Rapid Prototyping & Manufacturing, Dipoli Conference Centre, Helsinki, Finland.

Rønold, H.J., Lyngstadaas, S.P., Ellingsen, J.E., 2003. Analysing the optimal value for titanium implant roughness in bone attachment using a tensile test. Biomaterials 24 (25), 4559−4564.

Saltzman, D., Bichnevicius, M., Lynch, S., Simpson, T.W., Reutzel, E.W., Dickman, C., Martukanitz, R., 2018. Design and evaluation of an additively manufactured aircraft heat exchanger. Appl. Therm. Eng. 138, 254−263.

Sato, H., O-hori, M., 1987. Surface roughness measurement using scanning electron microscope with digital processing. J. Eng. Ind. 109 (2), 106−111.

Sames, W.J., List, F.A., Pannala, S., Dehoff, R.R., Babu, S.S., 2016. The metallurgy and processing science of metal additive manufacturing. Int. Mater. Rev. 61 (5), 315−360.

Sansone, V., Pagani, D., Melato, M., 2013. The effects on bone cells of metal ions released from orthopaedic implants. A review. Clin. Cases Miner. Bone. Metab. 10 (1), 34−40.

Sarker, A., Tran, N., Rifai, A., Elambasseril, J., Brandt, M., Williams, R., Leary, M., Fox, K., 2018. Angle defines attachment: switching the biological response to titanium interfaces by modifying the inclination angle during selective laser melting. Mater. Des. 154, 326−339.

Saruta, J., Sato, N., Ishijima, M., Okubo, T., Hirota, M., Ogawa, T., 2019. Disproportionate effect of sub-micron topography on osteoconductive capability of titanium. Int. J. Mol. Sci. 20 (16), 4027.

Senin, N., Thompson, A., Leach, R.K., 2017. Characterisation of the topography of metal additive surface features with different measurement technologies. Meas. Sci. Technol. 28, 095003.

Shalabi, M.M., Gortemaker, A., Hof, M.A. V.t., Jansen, J.A., Creugers, N.H.J., 2006. Implant surface roughness and bone healing: a systematic review. J. Dent. Res. 85 (6), 496−500.

Sing, S.L., Yeong, W.Y., Wiria, F.E., 2016. Selective laser melting of titanium alloy with 50 wt% tantalum: microstructure and mechanical properties. J. Alloys Compd. 660, 461−470.

Strano, G., Hao, L., Everson, R.M., Evans, K.E., 2013. Surface roughness analysis, modelling and prediction in selective laser melting. J. Mater. Process. Technol. 213, 589−597.

Shrestha, R., Simsiriwong, J., Shamsaei, N., 2019. Fatigue behavior of additive manufactured 316L stainless steel parts: effects of layer orientation and surface roughness. Addit. Manuf. 28, 23−38.

Sun, Y.Y., Gulizia, S., Oh, C.H., Fraser, D., Leary, M., Yang, Y.F., Qian, M., 2016. The influence of as-built surface conditions on mechanical properties of Ti-6Al-4V additively manufactured by selective electron beam melting. J. Occup. Med. 68 (3), 791−798.

Tan, C., Wang, Di, Ma, W., Chen, Y., Chen, S., Yang, Y., Zhou, K., 2020. Design and additive manufacturing of novel conformal cooling molds. Mater. Des. 196, 109147.

Townsend, A., Pagani, l., Scott, P., Blunt, L., 2017a. Areal surface texture data extraction from X-ray computed tomography reconstructions of metal additively manufactured parts. Precis. Eng. 48, 254−264.

Townsend, A., Pagani, L., Blunt, L., Scott, P.J., Jiang, X., 2017b. Factors affecting the accuracy of areal surface texture data extraction from X-ray CT. CIRP Ann. 66, 547−550.

Van Hooreweder, B., Apers, Y., Lietaert, K., Kruth, J.-P., 2017. Improving the fatigue performance of porous metallic biomaterials produced by Selective Laser Melting. Acta Biomater. 47, 193−202.

Vayssette, B., Saintier, N., Brugger, C., El May, M., Pessard, E., 2019. Numerical modelling of surface roughness effect on the fatigue behavior of Ti-6Al-4V obtained by additive manufacturing. Int. J. Fatig. 123, 180−195.

Wang, X., Li, S., Fu, Y., Gao, H., 2016a. Finishing of additively manufactured metal parts by abrasive flow machining. In: Proc. 27th Annu. Int. Solid Free. Fabr. Symp., Austin, TX, pp. 2470−2472.

Whitehouse, D.J., 2002. Surfaces and Their Measurement. HPS, London.

Wang, P., Yang, Z., Hu, X., 2016b. An analysis of China's low-rent housing system based on the filtering model. In: ICCREM, pp. 1121−1125.

Yadroitsava, I., Du Plessis, A., Yadroitsev, I., 2019. Bone regeneration on implants of titanium alloys produced by laser powder bed fusion: a review. F. Froes, M. Qian and M. Niinomi, Elsevier Titanium Consum. Appl. 2019, 197−233.

Yadollahi, A., Mahtabi, M.J., Khalili, A., Doude, H.R., Newman, J.C., 2018. Fatigue life prediction of additively manufactured material: effects of surface roughness, defect size, and shape. Fatig. Fract. Eng. Mater. Struct. 41 (7), 1602−1614.

Yadollahi, A., Shamsaei, N., 2017. Additive manufacturing of fatigue resistant materials: challenges and opportunities. Int. J. Fatig. 98, 14−31.

Yuan, W., Chen, H., Tan, C., Wei, Q., 2020. Effects of laser scanning speeds on different states of the molten pool during selective laser melting: simulation and experiment. Mater. Des. 189, 108542.

Yánez, A., Fiorucci, M.P., Cuadrado, A., Martel, O., Monopoli, D., 2020. Surface roughness effects on the fatigue behaviour of gyroid cellular structures obtained by additive manufacturing. Int. J. Fatig. 138, 105702.

Zhang, J., Fatemi, A., 2019. Surface roughness effect on multiaxial fatigue behavior of additive manufactured metals and its modeling. Theor. Appl. Fract. Mech. 103, 102260.

Zhang, L., Haddouti, E.-M., Welle, K., Burger, C., Wirtz, D.C., Schildberg, F.A., Kabir, K., 2020. The effects of biomaterial implant wear debris on osteoblasts. Front. Cell Dev. Biol. 8 (352).

Microstructure of L-PBF alloys

8

Pavel Krakhmalev[1], *Nataliya Kazantseva*[2]
[1]Karlstad University, Department of Engineering and Physics, Karlstad, Sweden; [2]Institute of Metal Physics of the Ural Branch of the Russian Academy of Sciences (IMP UB RAS), Ekaterinburg, Russia

Chapter outline

8.1 Introduction 215
8.2 Basic principles of solidification of the melt pool in L-PBF 216
8.3 Microstructure of L-PBF materials that do not have solid-state transformation upon cooling 218
8.4 Influence of manufacturing strategy and process parameters on texture in L-PBF materials 221
8.5 Thermal cycling in L-PBF materials during manufacturing 221
8.6 Microstructure of L-PBF materials that have solid-state transformation upon cooling 224
8.7 Effect of post heat treatment on microstructure of key L-PBF materials 234
8.8 Conclusions 235
8.9 Questions 236
Acknowledgments 236
References 237

8.1 Introduction

Laser powder bed fusion (L-PBF) of metallic alloys results in the formation of solid metallic material with microstructure different from the conventional analogs. The differences are the result of high temperature of the melt pool, high cooling rates, steep temperature gradient, thermal cycling during manufacturing, and other factors. Since the microstructure affects the physical and mechanical properties of materials and influences the performance of L-PBF parts, microstructural analysis is crucial. Understanding of the formation of microstructure, therefore, is necessary to predict the final properties of the material, and it creates a strong basis for the microstructure control and manufacturing of components with tailored properties. This chapter outlines the main principles of the formation of microstructure in the L-PBF process and presents some examples of microstructures of the most common L-PBF alloys.

The L-PBF manufacturing process is a complex process involving physical and chemical phenomena. The moving laser beam heats up and melts the powder bed

Fundamentals of Laser Powder Bed Fusion of Metals. https://doi.org/10.1016/B978-0-12-824090-8.00018-4
Copyright © 2021 Elsevier Inc. All rights reserved.

locally, forming tracks, which in turn form layers. Temperatures of the melt pool are very high, which can result in volatilization of elements leading to the deviation of the chemical composition of the alloy from the nominal one (Aboulkhair et al., 2019; DebRoy et al., 2018; Krakhmalev et al., 2018b). Process parameters influence melt pool temperature gradients and solidification rates. Temperature gradients and solidification rates are the main parameters of the solidification, and in L-PBF high thermal gradients and high cooling rates commonly result in the characteristic cellular/dendritic microstructure.

Solidified material, due to the layer-by-layer manufacturing manner, is subjected to thermal cycles, which can initiate diffusional processes in solid state, leading to precipitation of nanoparticles. Since the complete thermal history of the manufactured component depends on process parameters, size and shape of the component, equipment used, manufacturing strategy, and other technological factors, a variety of possible microstructures can be observed even for one material grade. At the same time, proper control of the abovementioned factors may result in manufacturing of components with tailored microstructure and properties.

8.2 Basic principles of solidification of the melt pool in L-PBF

The basic principles of solidification and crystallization of the melt pool in L-PBF are quite similar to the ones in welding, with the difference that temperatures of the liquid are higher and the melt pool is smaller in L-PBF. The solidification process in L-PBF is governed by a balance between energy input and dissipation of the energy into already solidified solid phase. The type of the microstructure formed after solidification of the melt pool depends on the thermal gradient, G, and growth rate, R, Fig. 8.1.

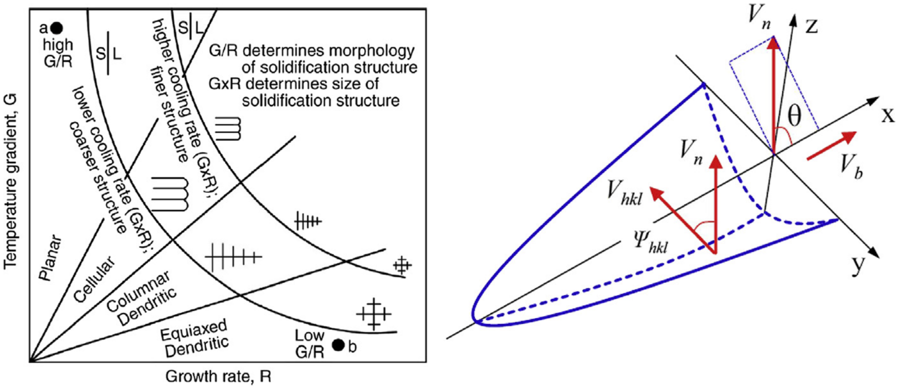
a●
high G/R
S|L
S|L
lower cooling rate (GxR); coarser structure
higher cooling rate (GxR); finer structure
G/R determines morphology of solidification structure
GxR determines size of solidification structure
Planar
Cellular
Columnar Dendritic
Equiaxed Dendritic
Low G/R ● b
Temperature gradient, G
Growth rate, R
V_n
Z
θ
X
V_b
V_n
V_{hkl}
Ψ_{hkl}
y

(a) (b)

Figure 8.1 (a) Influence of temperature gradient G and growth rate R on the morphology of solidification microstructure, (b) Schematic representation of the melt pool illustrating angular relationships between the scanning velocity V_b, the solidification interface normal V_n, and the dendrite growing direction V_{hkl} in Eq. (8.2).

(a) (Kou, 2003) with permission from Elsevier. (b) (DebRoy et al., 2018) with permission from Elsevier.

Experimentally, epitaxial nucleation (new grains nucleate at a polycrystalline substrate inheriting crystallographic orientation from parental grains) and cellular or cellular/dendritic crystallization are observed for different engineering alloys like austenitic steels, aluminum alloys, and nickel-base alloys manufactured by L-PBF. At high crystallization rates (also often named “growth rate”, Fig. 8.2) typical for the L-PBF process, a solute-rich boundary layer is built up in front of the

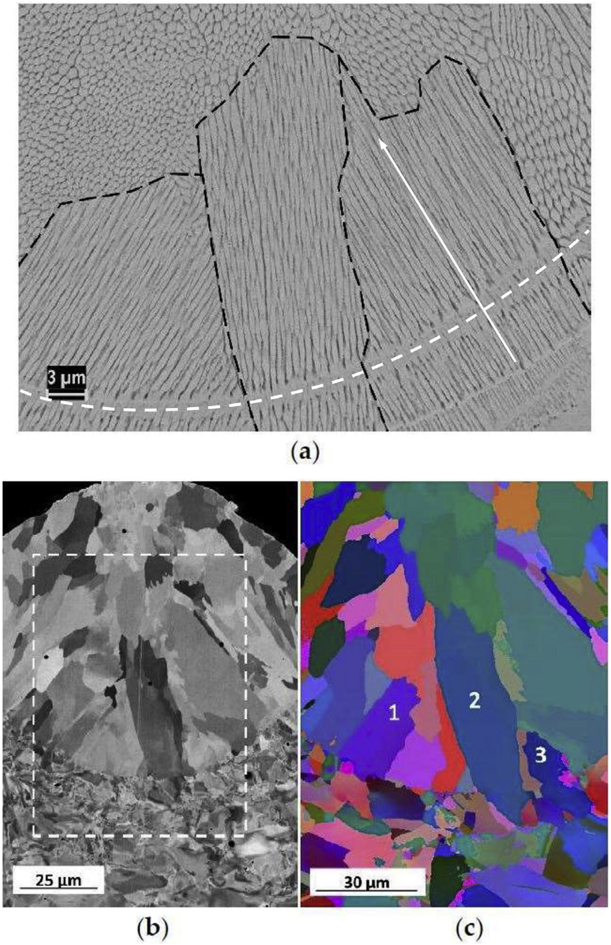

Figure 8.2 (a) Microstructure of L-PBF 316L stainless steel. Fusion boundary is marked as a *dashed line*, a *white arrow* indicates cells and colony growth direction; (b) cross-section of the L-PBF 316L single track; (c) an electron back-scattering diffraction (EBSD) orientation map of the marked region in (b). Colonies 1, 2, and 3 epitaxially nucleated from the substrate. Reproduced from (Yadroitsev et al., 2013), with permission from Elsevier, and (Krakhmalev et al., 2018a) under the Creative Commons Attribution License.

solid-liquid interface, thus approaching conditions for a constitutional supercooling. If conditions for the constitutional supercooling are obeyed, Eq. (8.1), a planar crystallization front becomes unstable and cellular/dendritic structure is formed.

$$\frac{G}{R} < \frac{\Delta T}{D_l} \tag{8.1}$$

where G is the thermal gradient, R is the growth rate, ΔT is the equilibrium freezing range, and D_l is the diffusion coefficient of the solute in the liquid. If the gradient G is steep, the material is crystallized in a directional cellular mode, Fig. 8.2. If the gradient G is sloping mildly, directly solidified dendrites with well-developed arms are formed. The latter microstructure is more typical for directed energy deposition or welding processes (Kou, 2003).

Thermal gradient is defined as a temperature change rate in a normal to the solid-liquid interface direction. Growth rate at a selected point of the solid-liquid interface is coupled with energy source movement velocity by the following expression (DebRoy et al., 2018; Kou, 2003; Kurz and Trivedi, 1994):

$$|\overrightarrow{V}_{hkl}| = |\overrightarrow{V}_b| \cdot \frac{\cos\theta}{\cos\psi} \tag{8.2}$$

where $\overrightarrow{V_{hkl}}$ is the local velocity of the solid-liquid interface, $\overrightarrow{V_b}$ is the laser beam velocity, θ is the misorientation angle between the source movement direction and the normal to the solid-liquid interface (highest thermal gradient), and ψ is the angle between the normal to the solid-liquid interface and the crystallographic orientation, along which preferable crystallization occurs. In a case of cubic crystals, both body-centered cubic (BCC) and face-centered cubic (FCC), this orientation is <100> (DebRoy et al., 2018; Kou, 2003).

From Eq. (8.2), one can also conclude that not all cells/dendrites which are nucleated epitaxially along curved solid-liquid interface in the melt pool at L-PBF satisfy conditions for the highest growth rate. Because of that some colonies will be outgrown by those that have better orientation with respect to thermal gradient and laser scanning direction, i.e., competitive crystal growth will take place.

8.3 Microstructure of L-PBF materials that do not have solid-state transformation upon cooling

A characteristic feature of L-PBF material is epitaxial nucleation on the underlying material (epitaxy is an oriented growth of one crystal on the surface of another crystal). Due to the epitaxial nucleation, newly growing cells/dendrites have the same crystallographic orientation as grains in the substrate or previously solidified layers, Fig. 8.2. This fact was many times confirmed by EBSD observations of materials solidified

without phase transformations in solid state, for example, stainless steels (Saeidi et al., 2015; Krakhmalev et al., 2018a), β-Ti alloys (Ishimoto et al., 2017), or Ni-Mo alloy (Sun S.H., et al., 2018a; Sun Y., et al., 2018b) .

The solid-liquid interface in the melt pool at L-PBF has a complex shape, see Fig. 8.1. The temperature gradient is continuously changed along the solid-liquid interface. It has the highest values at the bottom of melt pool, and decreases gradually along the interface toward the end and sides of the pool. Solidification rate, in contrast, is the lowest at the bottom but the highest at the end and side of the pool (Kou, 2003). In an intermediate location, the crystallization is defined by local thermal gradient and crystallization rate at the selected point and orientation of the preferred crystallization direction. This results in deviations of the cell size along the solidification interface within the melt pool.

The formation of cells and dendrites is a result of constitutional supercooling, which is related to diffusion of elements in liquid and solid phases. Often, enrichment of interdendritic space with selected alloying elements is observed. Which elements are found in the interdendritic space depends on the material chemical composition. In some materials that do not have phase transformation in the solid state upon cooling, and have solidification microstructure at room temperature, these segregations stay stable down to room temperature or lead to the formation of grain boundary phases. In some materials that have solid-state transformations upon cooling, for example, the formation of martensite in steels, the enrichment of interdendritic space with alloying elements can result in stabilization of a high amount of retained austenite phase at room temperatures. An additional feature of the intercellular boundaries in L-PBF materials is the high density of dislocations forming characteristic dislocation structures.

Austenitic stainless steel is a good example to present features of the microstructure obtained in L-PBF material solidified and cooled without phase transformations in solid state. The most investigated austenitic stainless steel grade manufactured by L-PBF is AISI 316L stainless steel. The microstructure of L-PBF 316L stainless steel substantially differs from the conventional material. Conventional cast alloy structure usually consists of different macroscopic zones: chill, columnar, and equiaxed zones. Usually, residual δ-ferrite in 316L steel is difficult to completely eliminate during thermomechanical processing, and it may be present in the structure of the alloy before the solution-annealing heat treatment (Padilha et al., 2007). In conventional manufacturing, the 316L steel ingot is quenched from 1000°C to avoid undesirable precipitations of carbides or intermetallic phases. Precipitations of the new phases on the grain boundary or changes of grain boundary properties result in loss of plasticity (temper embrittlement) or reduction of chemical resistance (corrosion cracking) (Lejcek, 2010). According to Barr et al. (2018), the large Cr-rich precipitates (carbides $M_{23}C_6$) and the subsequent Cr-depletion zone formed were the primary cause for the increased corrosion rates in austenitic steel 316L.

Typical microstructure formed in L-PBF 316L stainless steel is presented in Fig. 8.2. The high rate of cooling during laser melting of the powder and the presence of high thermal gradients result in the formation of cellular colonies (Krakhmalev et al., 2018a; Saeidi et al., 2015; Wang et al., 2018). Because of the epitaxial nucleation, cells within one colony have the same crystallographic orientation. It was pointed out in many studies that the L-PBF 316L steel as-built sample had single phase FCC structure. The structure of the FCC γ-phase of the as-built L-PBF 316L steel sample is presented in Fig. 8.3. As can be seen from Fig. 8.3, planar defects like twins and dislocations are seen in the structure. The presence of the planar defects in the structure of the FCC γ-phase was also reported in (Qiu et al., 2018).

The formation of cellular structure in L-PBF 316L austenitic steel during solidification in L-PBF is usually associated with microsegregation of Cr and Mo at cell walls (Krakhmalev et al., 2018a; Puichaud et al., 2019; Qiu et al., 2018; Saeidi et al., 2015; Zhong et al., 2016) . Additionally, specific dislocation structures associated with interdendritic segregations are formed in the L-PBF 316L steel. The formation mechanisms of the dislocation structures and the effect of these structures on the strength of L-PBF 316L stainless steel is under current investigations (Prashanth and Eckert 2017; Bertsch et al., 2020). Bertsch et al. (2020) suggested that "dendritic microsegregation, precipitates, or local misorientations influence how the dislocations *organize* during processing, but are not responsible for *producing* the organized cell structures." This work shows that AM dislocation structures originate due to thermal distortions during printing, which are primarily dictated by constraints surrounding the melt pool and thermal cycling.

Rounded oxide precipitations in as-built L-PBF sample 316L steel can also be observed in Fig. 8.3b (Krakhmalev et al., 2018a; Qiu et al., 2018; Saeidi et al., 2015). Qiu et al. (2018) found particles of (Si, Mn)O_2 oxides, which were observed within nanoscale cells and at the interfaces between cells. Spherical nanoscale oxides in as-built L-PBF 316L sample were also observed in Zhong et al. (2016), Krakhmalev et al. (2018a), and Saeidi et al. (2015). The origin of the particles is not fully proven: they can originate from the thin oxide layer at particles surfaces, form during L-PBF, or be the result of atomization process at powder manufacturing.

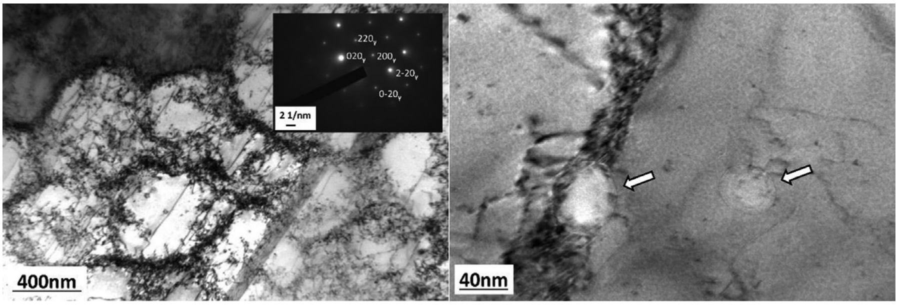

(a) (b)

Figure 8.3 Microstructure of as-built L-PBF sample 316L austenitic steel, TEM images: (a) the bright-field image of the cellular structure with high dislocation density structure; (b) round oxide particles indicated by *arrows*.

Reproduced from (Krakhmalev et al., 2018a) under the Creative Commons Attribution License.

8.4 Influence of manufacturing strategy and process parameters on texture in L-PBF materials

Due to epitaxial nucleation at the substrate or the previously melted and solidified layer, colonies of cells/dendrites having the same crystallographic orientation are formed. Those colonies that have favorable orientation and conditions of highest growth rate will dominate the microstructure, and this microstructure is inherited from layer to layer, developing a texture. The texture can be altered by change and control of process parameters, preheating temperature, and scanning strategy, Fig. 8.4.

In materials that do not have phase transformations in the solid state, solidification texture results in the crystallographic texture as well. The texture affects the physical and mechanical properties. One can either use texture features or try to reduce the acuity of the texture in the material, for example, changing the laser scanning strategy or using heat treatment. Crystallographic texture formation in L-PBF dependent on laser scanning strategy and process parameters is observed in stainless steel, β-Ti alloys, Ni-25% Mo alloys, and other materials (Köhnen et al., 2019; Ishimoto et al., 2017; Gu et al., 2020; Tian Z., et al., 2020a; Tian Y., et al., 2020b).

In materials like Ti6Al4V or martensitic steels, a martensitic transformation takes place in the solid state. Both these materials are crystallized forming cubic phase, and upon cooling, a martensitic phase transformation takes place. Low-temperature martensite phase is related to high-temperature cubic phase via Burgers crystallographic relationship. This means that there are a number of variants of orientation of martensite in one grain of parental high-temperature cubic phase. Because of that, weak crystallographic texture of martensite is commonly observed in, for example, L-PBF Ti6Al4V, although, reconstruction and analysis show the presence of the solidification texture in the parental high-temperature phase (Simonelli et al., 2014; Tian Z., et al., 2020a; Tian Y., et al., 2020b; Kazantseva et al., 2017). A weak HCP texture is retained in the sample even after incomplete relaxation annealing at 650°C for 3 h (Kazantseva et al., 2017). By variations of scanning strategies and change of scanning direction from layer to layer, the solidification texture can be minimized. Minimization of texture reduces anisotropy of properties in the L-PBF material in different directions. At the same time, solidification structure may be controlled by a selection of scanning strategy, and then, materials with tailored microstructure and texture in the desirable direction can be manufactured.

8.5 Thermal cycling in L-PBF materials during manufacturing

Because of the track-by-track and layer-by-layer manufacturing manner, at manufacturing of every track heat is dissipated into the previously manufactured solid material, so the interior of the L-PBF component is subjected to multiple heating and cooling cycles, Fig. 8.5. If the manufacturing component is high enough and has a constant cross-section, a steady state temperature dissipation condition in the component

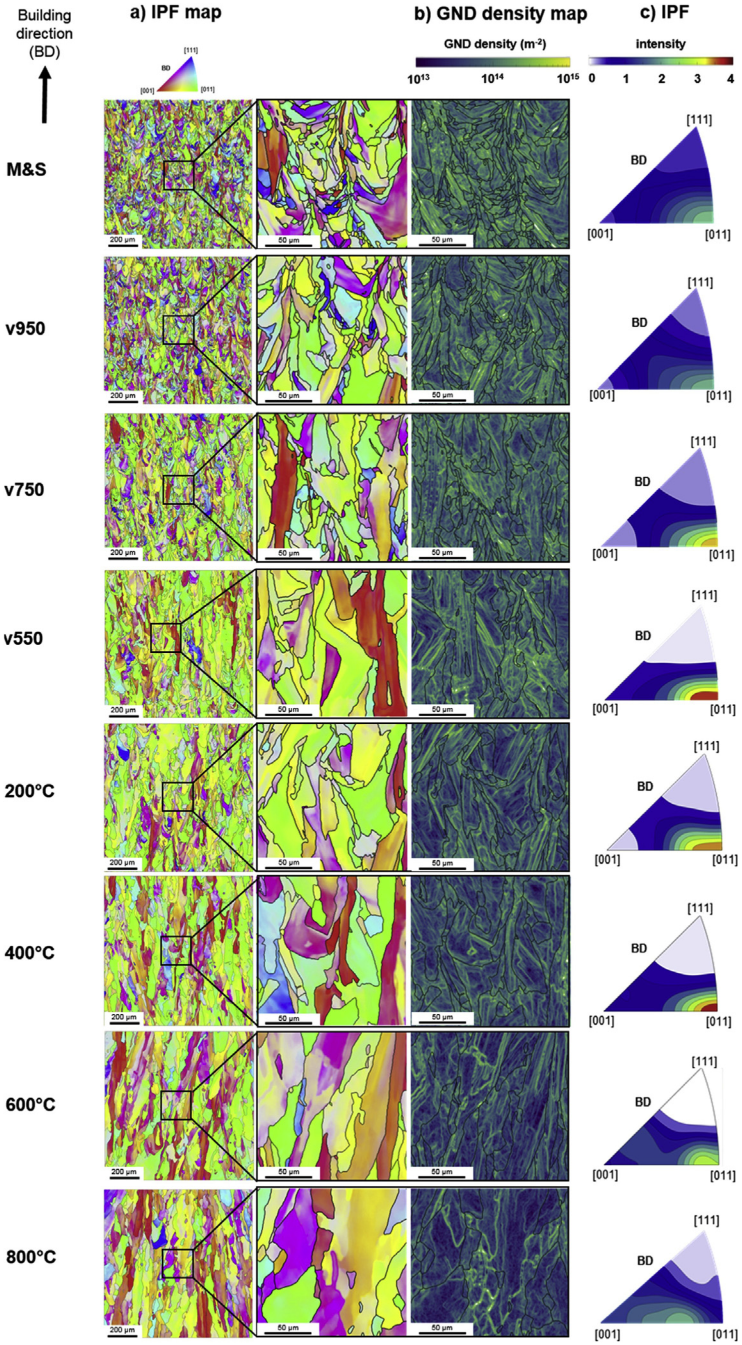
Building direction (BD)
a) IPF map
b) GND density map
c) IPF
GND density (m^{-2})
10^{13}
10^{14}
10^{15}
intensity
0
1
2
3
4
[111]
BD
[001]
[011]
M&S
v950
v750
v550
200°C
400°C
600°C
800°C
200 μm
50 μm

Figure 8.4 Grain structure and texture of the L-PBF X30Mn21 high manganese steel processed with varying laser speed (550−950 mm/s—indicated by "v"), preheating temperatures of the build platform (200−800°C), and an alternative mark and sleep (M&S, this is off-time of the laser between two laser hatch scans was 50 ms) scan strategy. A corresponding EBSD map with color-coding according to the inverse pole figure (IPF), Geometrically necessary dislocation (GND) density map, and the IPF plot parallel to the building direction is given for each condition, Köhnen et al. (2019), under the Creative Commons Attribution License.

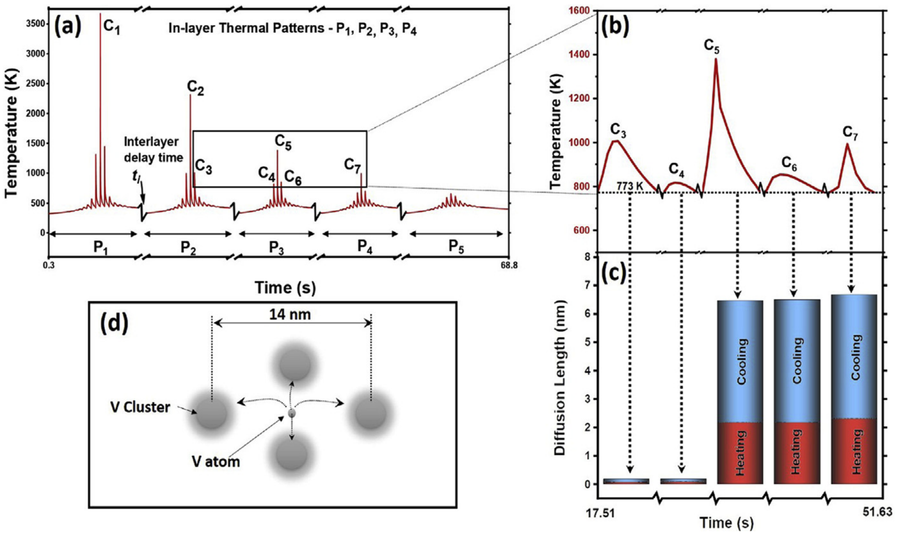

Figure 8.5 (a) Thermal history experienced by any given location during L-PBF printing of Ti6Al4V and (b) magnified view of the selected thermal cycles from (a), (c) cumulative diffusion length of vanadium corresponding to each heating-cooling cycle shown in (b). (d) Schematic showing probable diffusion distance of vanadium atoms based on their inter-cluster spacing. Thermal pattern P_1 consists of a collection of thermal cycles corresponding to sequential laser tracks during fabrication of a given build layer. When the laser moves to build another layer above the given layer, the same location in the previously built layer experiences the thermal pattern P_2 with reduced heat intensity. These thermal patterns are separated with the interlayer delay time (t_i), which is a time gap between building of two consecutive layers. As the instantaneous highest temperatures reached during thermal cycles in thermal patterns P_1, the first melting event at a given location in cycle C_1 occurs during fabrication of the first layer followed by remelting in C_2 during fabrication of the second layer, etc.
From (Pantawane et al., 2020) used under the terms of the Creative Commons CC BY license.

can be established. A real component, though, usually has a complex shape, can be built under different inclination angles and different kinds of supports, and because of that during L-PBF manufacturing, different parts of the component are subjected to different numbers of thermal cycles. Temperatures at the thermal cycling may be high enough to intensify diffusional processes in already solidified interior material (Bajaj et al., 2020; DebRoy et al., 2018; Jägle et al., 2016; Kazantseva et al., 2018a; Krakhmalev et al., 2015). These processes result in thermally activated solid-state phase transformations, changes in phase composition, and other microstructural changes that occur in-situ during manufacturing. In the other words, the L-PBF material is subjected to an in-situ heat treatment (also called intrinsic heat treatment) during the manufacturing process itself.

Cooling rates after the thermal cycles are nevertheless high, which results in the formation of metastable martensitic phases in some steels and titanium alloys manufactured by L-PBF. It is also clear that the upper layers are subjected to fewer thermal cycles compared to the interior of the component. For example, Krakhmalev et al. (2015), Šafka et al. (2016), Boes et al., (2018) showed that in steels the hardness of the top layer is higher than that of the interior of the build due to the in-situ heat treatment of martensite in the interior regions. In addition, in-situ heat treatment resulting in phase transformation was observed in maraging and precipitation hardening steels.

Eventually, accumulation of heat and in-situ heat treatment processes in L-PBF were used for the decomposition of martensite phase so that instead of α' hexagonal martensitic phase, $\alpha + \beta$ phases were obtained in as-built L-PBF Ti6Al4V alloy (Lui et al., 2017; Zafari et al., 2019; Barriobero-Vila et al., 2017; Xu et al., 2015, 2017). It clearly illustrates high potential of L-PBF to manufacture components with tailored microstructure, but often sets of parameters used to manufacture special desirable microstructure result in low manufacturing rates, which, to some extent, is contradictory to the industrial requirement of high manufacturing rate.

8.6 Microstructure of L-PBF materials that have solid-state transformation upon cooling

Heating and cooling cycles in L-PBF initiate phase transformations in solid state, namely martensitic transformation, decomposition of martensite, or the precipitation of carbides or intermetallic phases. In L-PBF materials, martensitic transformation can occur at cooling during manufacturing and is observed in many materials. Martensitic structure is a result of a specific type of phase transition. Martensitic transformation was first observed and described in steels and received its name from professor Adolf Martens who suggested a displacive diffusionless nature of this transformation that occurs without change in chemical composition (Christian, 1970). Different types of martensitic transformations are known, such as athermal and isothermal, which are divided with respect to their kinetics (temperature and time dependence of the amount of martensite) (Kakeshita et al., 2000). Athermal martensitic transformation occurs during cooling without the need for thermal activation. Isothermal martensitic transition occurs under external loads like uniaxial stress, magnetic field, and hydrostatic pressure. As was shown in (Kakeshita et al., 2000), these two transformation processes are closely related to each other. However, there is a difference in their driving force (i.e., a difference in the Gibbs free energy of the phases) and if the difference in driving force is supplemented by applying a magnetic field or a uniaxial stress, athermal martensitic transformation may occur in all alloys exhibiting isothermal martensitic transformation (Shimizu, 2002; Kajiwara et al., 1997). According to this definition, it can be considered that the L-PBF process can cause the formation of athermal martensite.

An example of a material that has the martensitic phase transformation during L-PBF is Ti6Al4V alloy. Ti6Al4V is a $\alpha + \beta$ titanium alloy and the most widespread of all titanium alloys, and because of that this alloy was the first under study in additive manufacturing. Many authors pointed out that because of fast cooling in the additive method using laser melting, α'- martensite formed in as-built Ti6Al4V samples

(Thijs et al., 2010; Yadroitsev et al., 2014, 2018; Simonelli et al., 2014; Yan and Yu, 2015; Kazantseva et al., 2017). Martensitic transformation is also observed in pure titanium and other Ti-alloys (Zwicker, 1979; Lütjering and Williams, 2007).

Pure titanium has a polymorphic transition at 882°C and may be in two polymorphic modifications: low-temperature modification α - Ti (HCP, a = 0.296 nm, c = 0.472 nm) and high-temperature β - Ti, (BCC, a = 0.332 nm) (Lütjering and Williams, 2007; Zwicker 1979). Upon rapid cooling from temperatures above beta-transus, a martensitic transformation $\beta \rightarrow \alpha'$ can occur. The α'-phase regions form an acicular structure. The type of alloying element and its quantity affect the temperatures of the beginning (M_s) and the end (M_f) of the martensitic transition. Moreover, in the titanium alloys, two martensitic phases (α', α'') with the different crystal structure can be observed— see Fig. 8.6 (Kim and Miyazaki, 2018).

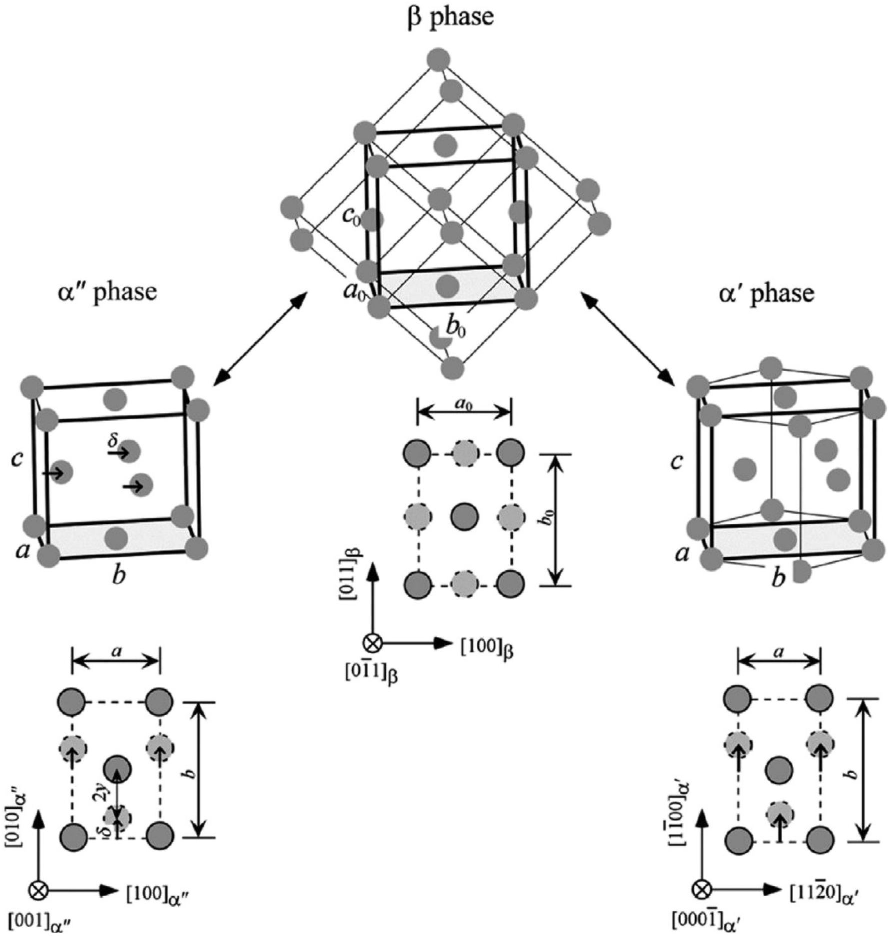

Figure 8.6 Crystal structures of α'', β, and α (α') phases and their lattice correspondences in titanium alloys ((Kim and Miyazaki, 2018) with permission from Elsevier).

The orthorhombic α'' martensite was found in conventional Ti-alloys with β stabilizers, transition metals Mo, Nb, Ta, W, Re and in Ti-alloys with Al + V (Lütjering and Williams, 2007). The morphology of the α''-phase regions depends on the level of stress in the material. α''-phase regions may be observed as small grains and/or plates with internal twins, in dependence on the content of alloying element or the level of the applied load (Castany et al., 2016). In titanium alloys α''-phase can be formed during quenching after aging in the intermediate $\alpha + \beta$ region (Welsch et al., 1993) or after cyclic deformation (Castany et al., 2016). Orthorhombic α''-phase has higher alloying element content than that in the hexagonal α' martensite (Lütjering and Williams, 2007).

One feature of the materials formed during the L-PBF process is a high level of internal stress in the structure of the as-built state. Because of that in L-PBF Ti6Al4V alloy, both $\beta \rightarrow \alpha'$ and $\beta \rightarrow \alpha''$ martensitic transformations show twinning structure, Fig. 8.7. Tensile twins of α'-martensite can form with {10—12} <-1011> twinning planes. Stacking faults can be found inside the twinned plates (Krakhmalev et al., 2016). α''-Martensite with an orthorhombic crystal lattice was also observed in as-built Ti6Al4V alloy (Kazantseva et al., 2018a; Pantawane et al., 2020; Simonelli et al., 2014). This type of martensite showed a lamellar morphology with internal transverse twins, and as it was suggested in (Kazantseva et al., 2018a) and (Pantawane et al., 2020), α''-martensite formed in the alloy under cyclic heating of the sample during L-PBF process. The temperature range of the cyclic heating is associated with the process parameters of the L-PBF system (Beese and Carroll 2016).

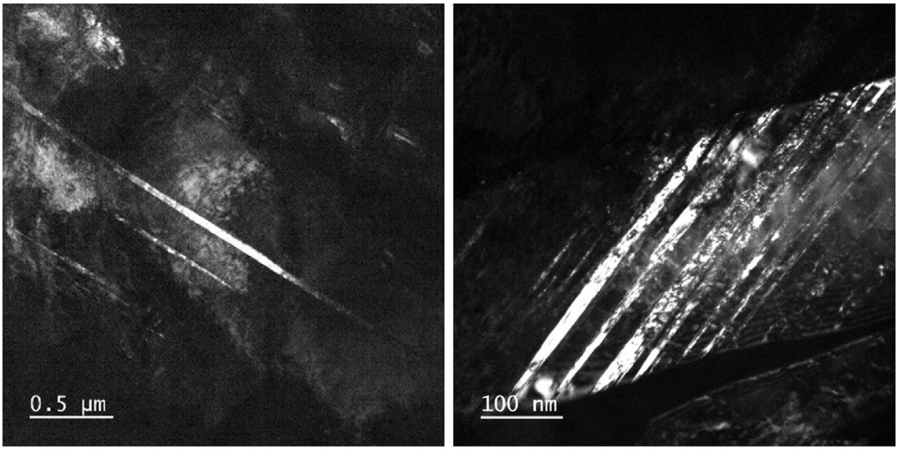

(a) (b)

Figure 8.7 Microstructure of the twins in martensitic phases in L-PBF Ti6Al4V alloy, TEM images: (a) α'-phase; (b) α''-phase.
(Kazantseva et al., 2018a) with permission from Elsevier.

The orientation relationships between the crystal lattices of the martensitic phases and the crystal lattice of parent BCC β-phase can be described as follows:

(110) β || (0001) α', <1−11> β || <11−20> α' (Wielewski et al., 2012)
{001} α'' || {110} β, <100>α'' || <001>β (Li et al., 2011).

In titanium alloys the appearance of α'-martensite leads to an increase in strength and a decrease in the plasticity of the alloy; the α''-martensite promotes a decrease in strength and an increase in plasticity (Kolachev et al., 2005; Welsch et al., 1993; Ivasishin et al., 1999). Both martensitic phases (α'- and α''-phase) are metastable and during aging they decompose with the formation of equilibrium α- and β-phases (Carreon et al., 2014).

Steel is another example of L-PBF material that has martensitic transformation during manufacturing. There are a number of steels that have martensitic transformation that were manufactured by L-PBF (Bajaj et al., 2020; DebRoy et al., 2018). Precipitation hardening and martensitic stainless steels, maraging steels and high-alloy tool steels are among them. In common, these steels manufactured in the conventional ways achieve required mechanical characteristics after heat treatment, austenitization/solution treatment, quenching to martensite and then tempering/aging to form fine carbide or intermetallic precipitates in tempered martensite structure. During the L-PBF manufacturing the solidified material is subjected to heating to high temperatures and rapid cooling cycles several times. Because of that the microstructure, phase morphology and constitution, physical and mechanical properties differ from the conventional grades.

Stainless precipitation hardening 17−4 PH and 15−5 PH and martensitic AISI 420 and 440 stainless steels have martensitic microstructure and show high corrosion resistance due to high Cr content. Both types of steels were manufactured by L-PBF during the last decades. Conventional 17−4 PH steel is solution treated and cooled down to form martensite, and then must be aged to achieve strengthening by Cu-rich precipitates. In the as-built L-PBF condition, this steel has cellular/dendritic microstructure, contains quite high amounts of austenite, and niobium carbides located in the interdendritic space. It has been shown that the microstructure of 17−4 PH steel is also dependent on the atmosphere used during manufacturing. The mixture of austenite and martensite is observed in steel built under nitrogen atmosphere, and mostly martensite (92 vol.%) is found in the steel built under argon atmosphere (Rafi et al., 2014; Murr et al., 2012). Martensitic stainless steels, like AISI 420, achieve the required combination of strength and toughness characteristics after quenching and tempering to form Cr-rich carbides. Similar to the precipitation hardening steels, high amounts of austenite are observed in L-PBF AISI 420 between martensite laths formed within the cells (Krakhmalev et al., 2015).

Among L-PBF tool steels, maraging and high-alloy tool steels are the most common. Maraging (martensitic + aging) tool steels are low carbon iron-based alloys that form martensite upon cooling. Aging results in the precipitation of intermetallic phases leading to high strength and hardness required by applications. 1.2709 steel (US classification ASTM A646 Grade 18% Ni (300) maraging steel, European

1.2709 and German X3NiCoMoTi 18-9-5) is the most widely investigated maraging tool steel manufactured by L-PBF, but some other maraging steels were also investigated. The as-built 1.2709 maraging steel has the microstructure of cellular/dendritic colonies, Fig. 8.8. The colonies formed at solidification of austenite are transformed to martensite upon cooling. Martensite laths are located within cells/dendrites formed at solidification. Some segregation of Ni in the interdendritic space leads to stabilization of austenite so that up to 15% retained austenite can be observed in the microstructure (Bajaj et al., 2020; Jägle et al., 2017).

In the case of L-PBF maraging steels, the in-situ heat treatment can initiate diffusional processes in the underlying solid and precipitates can form in the interior of the component. Nevertheless, experimental observations of precipitates in as-built maraging steels are not always in agreement with each other. Thus, no precipitates were observed by Bodziak et al. (2019) and Jägle et al. (2014), while Tan et al. (2017) and Kürnsteiner et al. (2017) reported the presence of nanoscale particles formed due to in-situ heat treatment during manufacturing. This disagreement can be related to different scanning strategies used in different equipment, and also to the fact that in dependence on the material, process parameters, and a different

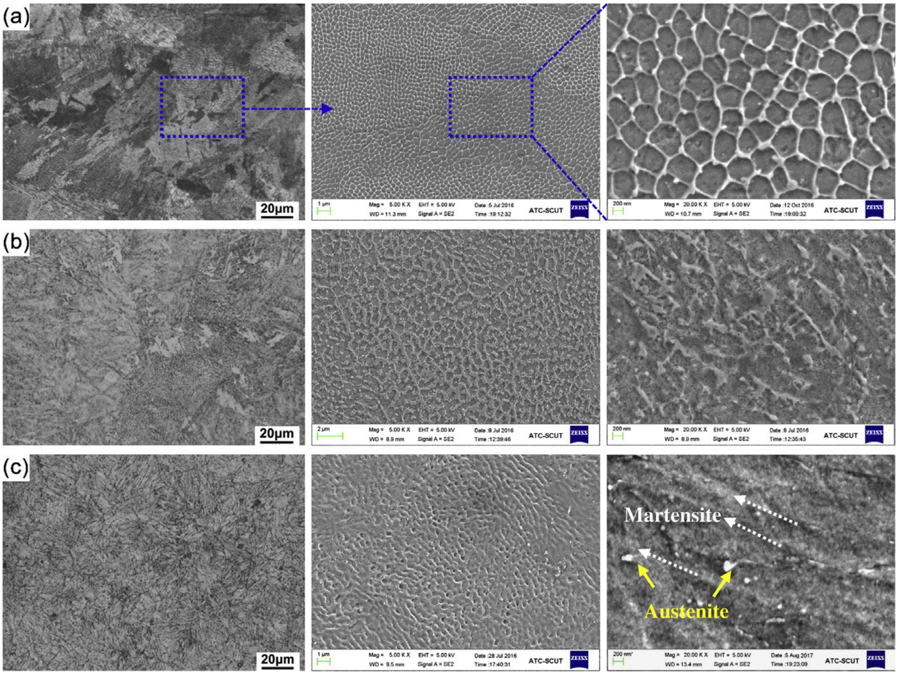

Figure 8.8 The OM and SEM images of L-PBF high-performance grade 300 maraging steel (a) as-built, (b) aging treated right after manufacturing at 490°C, 6 h and, (c) solution treated at 840°C for 1 h, followed by aging at 490°C for 6 h specimens.
(Tan et al., 2017) with permission from Elsevier.

geometry of the component, the in-situ heat treatment of the interior varies. Differences in the temperature and duration of thermal cycles, therefore, leads to different development of diffusional processes, i.e., precipitation in the material during L-PBF.

High-alloy tool steels are high-strength materials, and the strength of these alloys is achieved by the formation of fine carbides upon tempering after hardening to the martensite. Processing of these steels is quite challenging for L-PBF technology since high residual stresses are formed by cooling and thermal cycling, and may this result in cracking. Utilization of preheating of the base plate or powder to some extent solved this problem, and with preheating, a number of tool steel grades including H11, H13, and D2 were manufactured by L-PBF without thermal cracking to nearly full density (Boes et al., 2018; Casati et al., 2018; Sander et al., 2016; Geenen et al., 2019; Kempen et al., 2014). The most investigated steel is H13 hot work tool steel. The as-built L-PBF steels have cellular/dendritic microstructure with martensite formed within cells, and retained austenite located at cell boundaries. Because of high solidification rates, primary carbides are not often observed in L-PBF cold work tool steels, and because of the enrichment of the interdendritic regions with alloying elements, austenite is stabilized during manufacturing (Yan et al., 2017; Boes et al., 2018; Casati et al., 2018; Holzweissig et al., 2015; Mertens et al., 2016). Preheating may lead to initiation of the in-situ heat treatment, namely the formation of bainite or martensite with different morphology (Mertens et al., 2016; Boes et al., 2018).

As mentioned above, the strength of the precipitation hardening steels, martensitic stainless steels, maraging steels, and high-alloy tool steels is achieved after heat treatment resulting in the formation of nanoscale precipitates, carbides or intermetallics phases inside the martensitic matrix. In as-built L-PBF condition, all these steels have an increased content of austenite compared to conventionally manufactured analogs. Austenite may have a positive effect on mechanical characteristics causing a transformation-induced plasticity effect (Rafi et al., 2014), but also reduces the strengthening potential of L-PBF steels if aging/tempering heat treatment is further carried out. Additionally, possible segregation of elements and formation of phases at the colony boundary may reduce fracture toughness of steels in as-built condition. Conventional heat treatment including austenitizing/solution treatment applied to L-PBF steels eliminates cellular dendritic microstructure, Fig. 8.8. After heat treatment, the microstructure and properties may approach values which are typical for conventional materials, if manufacturing defects like pores do not deteriorate properties (Sun S.H., et al., 2018a; Sun Y., et al., 2018b; LeBrun et al., 2015; Cheruvathur et al., 2016; Åsberg et al., 2019).

Cobalt-chromium-molybdenum (CoCrMo) alloys are successfully used in medicine as orthopedic implants (Anusavice et al., 2012) or as a material for the manufacture of dentures (Lu et al., 2015) for many years. In CoCrMo alloys, the temperature of the FCC-HCP polymorphic transformation is 970°C. The athermal martensitic transition from the FCC to HCP phases in these alloys has the low value of the chemical driving force, because of that the metastable FCC γ-phase becomes the dominant phase at room temperature (Atamert and Bhadeshia, 1989). The martensitic transition in CoCrMo alloys can occur by the isothermal route, which is usually achieved by plastic deformation (Huang and Lopez, 1999) or by isothermal aging in the temperature range

800−850°C (Saldívar and Lopez, 2001). The orientation between crystal lattices of these FCC and HCP phases corresponds to the Shoji-Nishiyama orientation relationship (Balagna et al., 2012):

$$(111)_{FCC} \parallel (0001)_{HCP},\ <11-2>_{FCC} \parallel <011-10>_{HCP}$$

Widespread investigations of CoCrMo samples manufactured by additive technologies may be found now (Takaichi et al., 2013; Dikova, 2018; Zhang et al., 2018a,b; Kazantseva et al., 2019). Fig. 8.9 presents the difference between the structure of the conventional and L-PBF CoCrMo samples at the initial state and after standard

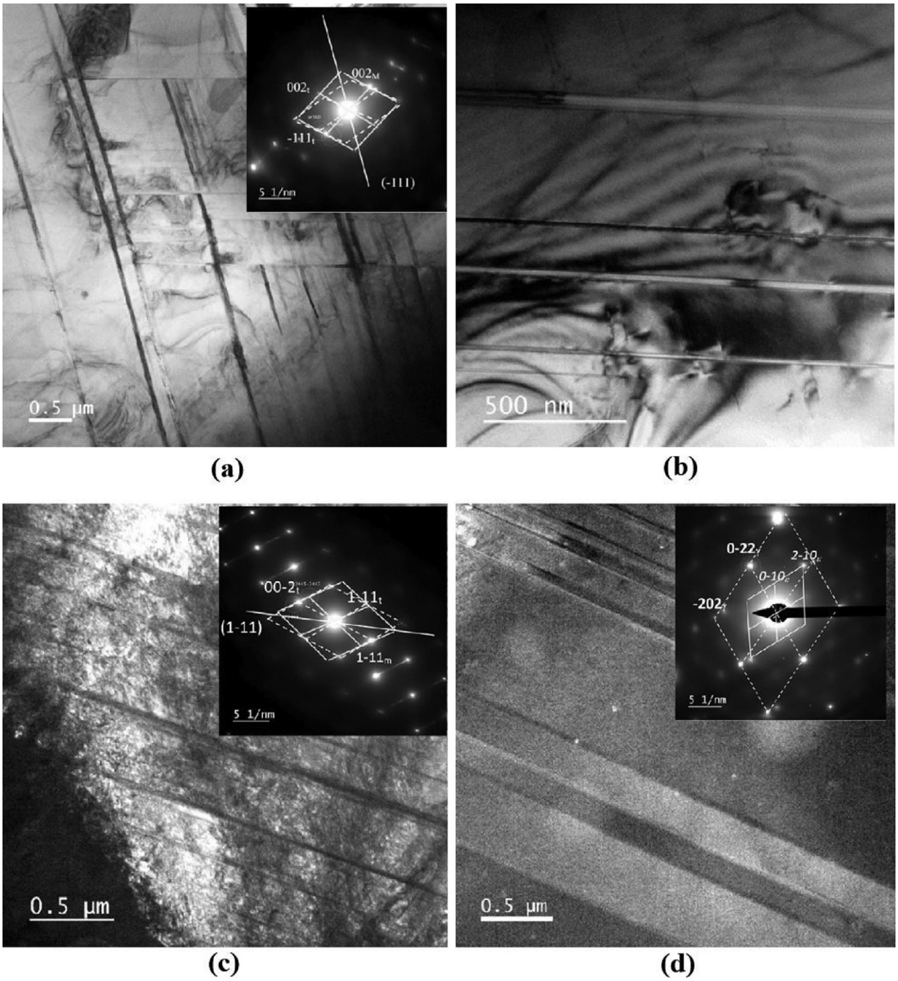
002$_M$
002$_t$
-111$_t$
(-111)
5 1/nm
0.5 μm
500 nm
00-2$_t$
1-11$_t$
(1-11)
1-11$_m$
5 1/nm
0.5 μm
0-22$_\gamma$
2-10$_\varepsilon$
0-10$_\varepsilon$
-202$_\gamma$
5 1/nm
0.5 μm

(a) (b) (c) (d)

Figure 8.9 Microstructure of the Co-28Cr-6Mo alloy in the different states, TEM images: (a) cast; (b) cast, solution treated (1150°C-30 min followed by water quenching); (c) L-PBF, as-built; (d) L-PBF, solution treated (1150°C-30 min followed by water quenching).

solution treatment recommended for this alloy. One can see from Fig. 8.9a and c that the sample at the initial state (cast or as-built L-PBF) has a single-phase state of FCC with twins. The same state was found after solution treatment in the cast alloy (Fig. 8.8b); however, solution-treated L-PBF sample showed two phase $\gamma + \varepsilon$ state. Explanation of the existence of athermal martensitic transformation in L-PBF CoCrMo alloys may be associated with increased density of planar defects in the structure formed during L-PBF. The twinning structure in the FCC state is a result of movement of the Shockley partial dislocations that leads to the formation of stacking faults. The same partial dislocations take part in crystallographic transition between FCC and HCP crystal lattices. As can be seen from Fig. 8.9c, the structure of L-PBF sample contains more stacking faults than in the solution-treated conventional sample, which makes the martensitic FCC to HCP transformation easier.

Precipitation hardening is another possible process, which occurs during in-situ heat treatment of the L-PBF aluminum- and nickel-base alloys. Precipitations of the different intermetallic hardening phases take place on the grain boundaries or inside the grains during heat treatment of the supersaturated solid solution (aging). The precipitates impede the movement of dislocations, or defects in a crystal lattice. Because of that, the process of the precipitation promotes an increasing yield strength of the materials. The number, size, and distribution of precipitates depend upon the temperature and time of heat treatment. In nickel superalloys, precipitation hardening is responsible for a yield strength anomaly (Gladman, 1999).

Conventional Ni-based superalloys contain several different alloying elements that allow one to get the desired mechanical properties like the high level for hot rupture strength, fatigue resistance, and creep strength controlled by the presence of the hardening intermetallic phases (γ'-Ni_3Al or γ''-Ni_3Nb, Ni_3V). The γ'-phase is Ni_3Al intermetallic compound, which possess special properties and has ordered $L1_2$-type superstructure. In nickel superalloys the γ'-phase may precipitate in the form of cuboids or rounded particles in dependence of the chemical composition and heat treatment of the alloy (Kazantseva et al., 2018b). The process of the formation of this phase in nickel superalloys is considered as a spinodal decomposition of the supersaturated solid solution, and is associated with the heterogeneity of the alloying element distribution (Tan et al., 2014). According to the literature data, the strengthening of grain boundaries in heat-resistant nickel superalloys is achieved due to the precipitation of MC carbides based on Nb, Ti, and W, as well as by selective microalloying with boron. To ensure high heat resistance, carbides should have a globular shape, a size of about 1 micron or less, be evenly distributed along the grain boundaries, and not form a continuous network. The probability of the formation of TCP (topologically close packed) brittle plate-like phases (σ-, μ-, or Laves phases), as well as carbides of M_6C or $M_{23}C_6$ type (where M denotes the metal), leading to the softening of the alloy, should be minimized (Chabina et al., 2012; Kazantseva et al., 2019). The μ-phase has a rhombohedral crystal structure and was found in nickel superalloys with excess percentage of Mo or W. The σ-phase with a tetragonal crystal lattice, and the hexagonal Laves phase may form due to high-temperature exposure. The type of carbide and TCP phases depends on the chemical composition of the alloy and its operating temperature

(Kazantseva et al., 2019). As an example, the main phases in conventional IN738 (IN738LC) are nickel solid solution (γ-phase, FCC), a hardening intermetallic compound Ni_3Al (γ'- phase, $L1_2$), carbide and boride phases (MC, Cr_3B_2, Cr_2B). IN738LC material has a high γ' volume fraction leading to a substantial hot cracking sensitivity.

A number of Ni-base superalloys were manufactured by L-PBF, among them IN718 (DebRoy et al., 2018; Kok et al., 2018; Zhang et al., 2018a,b), Inconel 625: Ni-22Cr-9Mo-3.5Nb-5Fe-1Co (Zhang et al., 2018a,b; Tian Z., et al., 2020a; Tian Y., et al., 2020b), Nimonic 263: Ni-20Cr-20Co-6Mo-2.5Al-2Ti-0.06C (Vilaro et al., 2012), Haynes 230: Ni-22Cr-14W-2Mo-0.3Al-0.02La-0.1C (Kok et al., 2018), Hastelloy X: Ni-22Cr-18Fe-9Mo-1.5Co-0.6W-0.1C (Han et al., 2019), and some others (Adegoke et al., 2020; Pourbabak et al., 2019; Marchese et al., 2020; Atabay et al., 2020; Divya et al., 2016). The microstructure of L-PBF Ni-base superalloys normally contains cellular/dendritic colonies with distinct texture along the building direction. The process of L-PBF of high-γ' nickel superalloys also has a number of challenges due to these alloys' complex chemistry. Pores (including nanoporosity between the dendritic arms), hot cracking, and interdendritic carbides were found in different nickel superalloys manufactured by L-PBF (Grange et al., 2020; Adegoke et al., 2020; Pourbabak et al., 2019; Marchese et al., 2020; Atabay et al., 2020; Divya et al., 2016). Grange et al. (2020) has shown that in IN 738, a change of process parameters to narrow melt pools and use of a large overlap results in grain refinement, which is a promising route to avoid hot cracking. A feature of L-PBF IN 738 and some other superalloy grades microstructure is the very small size of γ' particles, which are tens of nanometers in diameter and distributed densely in the γ matrix as reported in (Zhang et al., 2019). Many authors pointed out that they could not distinguish the γ' particles by SEM in the as-built state (Kunze et al., 2015; Rickenbacher et al., 2013; Pourbabak et al., 2019; Atabay et al., 2020). Others observed fine γ' in as-built L-PBF superalloys (Divya et al., 2016). Very fine carbides and/or oxides are also commonly observed at cell/dendrite boundaries in Ni-base superalloys, they usually have very small size, smaller than 200 nm (Grange et al., 2020; Adegoke et al., 2020; Pourbabak et al., 2019). Formation of precipitates in L-PBF Ni-base superalloys is controlled by thermal history that the material is subjected to during manufacturing. High cooling rates suppress the formation of precipitates, while in-situ heat treatment initiates diffusional processes and may lead to precipitations. In manufacturing practice, the chemical composition of the alloy, the L-PBF process parameters, the size and the shape of the manufactured component can all influence the thermal history and may control precipitation processes in L-PBF material.

Aluminum is an essential material to modern technologies because of its light weight, strength, and workability. Today there are a lot of applications of aluminum including fuel-efficient transportation vehicles, building construction, and food packaging. Pure aluminum is soft and has low strength; however, adding of a small amount of the alloying elements is able to increase the strength of the aluminum alloys substantially. Precipitation hardening is the main way to increase resistance to plastic deformation of the conventional aluminum alloys. Precipitation hardening in aluminum alloys occurs by a special mechanism, namely through Guinier-Preston (GP) zone formations. GP zones are nanoscaled (on the order of 3−10 nm in size) clusters enriched with the alloying elements. GP zones are absolutely coherent with the matrix, do not have the boundaries with the solid solution, are metastable, and precede the formation of equilibrium precipitates (Chen et al., 2006). GP zones form by diffusion during aging from the supersaturated solid solution with a high number of vacancies (Singh and Warner, 2010). In AlMgSi alloys, such Guinier-Preston zones are named as GP(I) and GP(II) zones which are metastable pre-β″ and β″ phases, or Si/Mg co-clusters (Chen et al., 2006). Along with GP zones, other coherent or semi-coherent precipitations may be found in aluminum alloys. Morphology and crystallographic orientation of GP zones, as well as intermediate and stable phases in various aluminum alloys were studied for example by Hosono et al. (2006), Wang and Starink (2005).

In comparison to conventional aluminum alloys, precipitation hardening in aluminum alloys manufactured by L-PBF has some specific features. Because of high cooling rates, microcrack formation is observed in aluminum alloys during L-PBF (Aboulkhair et al., 2019). However, it was also found that rapid cooling helped to retain the Al-rich supersaturated matrix as well as the Si-rich nanosized particles. It was found that AlSi10Mg, Al-Si alloys, and high strength Al2024 manufactured by laser powder bed fusion showed better mechanical properties and corrosion resistance than that obtained by conventional casting due to the unique microstructure features of the as-built L-PBF state (Zhang et al., 2016; Chen et al., 2020; Takata et al., 2017, 2020). The L-PBF aluminum alloys like AlSi10Mg and AA2024 showed strong texture and fine metastable cellular microstructure with a good dispersion of all the alloying elements. In L-PBF AlSi10Mg alloy, interdendritic precipitations enriched with silicon were observed on the boundaries of the columnar α-Al grains in as-built state as shown in Fig. 8.10. After aging, the alloy had a composite-like

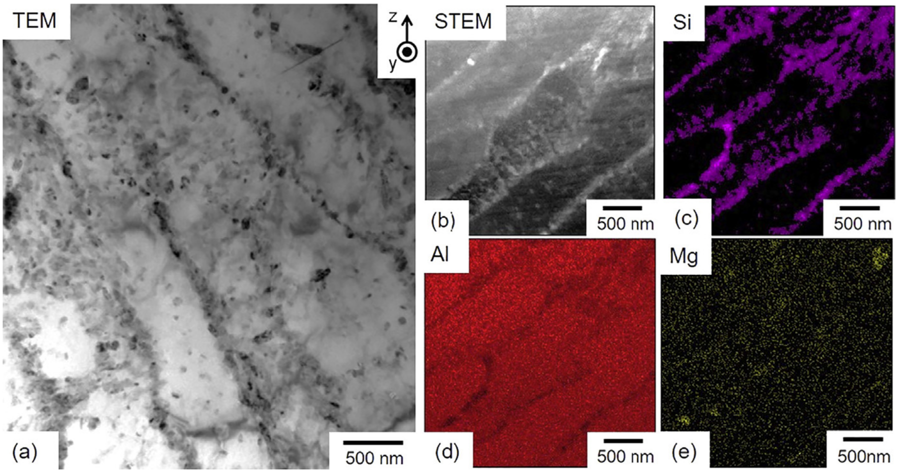

Figure 8.10 (a) Fine Si particles precipitated within the elongated α-Al phase in the intersection region, TEM bright-field image, (b) STEM-HAADF EDS element maps of Si, Al, and Mg. (Liu et al., 2018) with permission from Elsevier.

structure with an Al matrix reinforced by the uniformly distributed spherical Si particles (Aboulkhair et al., 2019; Chen et al., 2020). The absence of the S-phase (Al_2CuMg) and presence of θ-phase (Al_2Cu), Mg2Si, and Al-Cu-Mn-Fe(-Si) precipitations were observed in as-built AA2024 (Gharbi et al., 2018). Unlike AlSi10Mg alloy, AA2024 alloy was found not suitable to be produced by L-PBF because of hot crack formation. Tan et al. (2020) has suggested to add ∼0.7 wt.% Ti nanoparticles that promoted eliminating the hot-tearing cracks and columnar structure, and help in refining the grains. Nanoscale precipitates of the S-phase, S″-phase ($Al_{10}Cu_3Mg_3$), Al_3Ti, and Al_7Cu_2Fe were observed in the structure of the L-PBF sample with titanium after aging (Tan et al., 2020).

8.7 Effect of post heat treatment on microstructure of key L-PBF materials

A need for heat treatment after manufacturing is dictated by the required microstructure and properties of the final L-PBF manufactured component. As a rule of thumb, stress relief heat treatment is commonly carried out right after manufacturing before the component is cut off the building platform to relieve residual stresses, and to prevent distortion of the component. For example, in L-PBF Ti6Al4V alloy, stress relief heat treatment (usually carried out at about 650°C) itself can also initiate phase transformations and the formation of very small particles of β-phase (Vilardell et al., 2019; Sallica-Leva et al., 2016; DebRoy et al. 2018).

Another promising treatment of L-PBF materials is hot isostatic pressing (HIP) or HIP in combination with heat treatment, for example, quenching. This combination treatment results in the healing of defects and the modification of microstructure in one step. The positive effect of HIP was reported for many AM materials (DebRoy et al., 2018; Du Plessis and Macdonald, 2020; Åsberg et al., 2019; Vilardell et al., 2021), but an effect of high pressure on phase transformation may lead to some delays with, for example, the precipitation hardening effect (Krakhmalev et al., 2020).

Heat treatment of L-PBF materials depends on the type of materials and final requirements. Material solidifying without phase transformations, single-phase stainless steels, β-Ti alloys, etc., does not show strengthening effect after heat treatment. In stainless steel, at heating up to 950−1050°C, a cellular structure starts to disappear due to diffusion and annihilation of dislocations. Heat treatment at higher temperatures leads to grain growth, and generally softening of the L-PBF stainless steel (Krakhmalev et al., 2017; Riemer et al., 2014; Saeidi et al., 2015).

Heat treatment of alloys that have phase transformations in solid state may have different aims. For example, heat treatment of Ti6Al4V alloy may aim to form equilibrium α-β microstructure with higher ductility and lower strength. Regimes for these heat treatments may differ from the ones recommended for the conventionally manufactured materials. The reason is that in the conventional manufacturing route, hot/warm/cold work is used. Plastic deformation introduces dislocations, which intensify recrystallization processes and formation of globular α phase. In L-PBF Ti6Al4V, dislocation density is lower than in conventional material in deformed state and therefore recrystallization processes are slower. In some steels and Ni-base superalloys undesirable phases are formed at grain boundaries during L-PBF. Therefore, heat treatment is aiming to dissolve those phases. After heating to high temperature, when high-temperature phase is formed, the typical L-PBF material microstructure disappears, and microstructures and properties which are typical for conventional analogs can be achieved (Bajaj et al., 2020; DebRoy et al., 2018).

L-PBF materials such as maraging steels, Ni- and Al- alloys, in as-built state have rather a condition similar to the supersaturated solid solution (sometimes with some precipitates), which in conventional materials is achieved by solution heat treatment. After aging (the isothermal heat treatment initiating diffusional decomposition of supersaturated solid solution with a formation of precipitates), in these materials an increase in strength and a decrease in ductility can be observed due to the precipitation hardening effect. For example, in L-PBF maraging steel, solution treatment and aging heat treatment may completely change the microstructure, Fig. 8.8b and c. In Al alloys, the strength of the heat-treated L-PBF material exceeds the typical strength of conventional material of the same chemical composition (Takata et al., 2020; Hitzler et al., 2018; Fiocchi et al., 2020).

8.8 Conclusions

L-PBF manufacturing of metallic alloys leads to the formation of unique microstructures. Solidification processes result in the formation of cellular/dendritic colonial microstructure, segregation of elements, and solidification texture. These features of the microstructure are commonly observed in the L-PBF materials that do not have phase transformations upon cooling. In materials that do have phase transformation upon cooling, high cooling rates and in-situ heat treatment lead to the formation and partial decomposition of martensite, precipitates, and other thermally activated processes. The complete thermal history of the L-PBF material is complex and depends on manufacturing parameters, laser scanning strategy, size and orientation of the component in building chamber, and on preheating. Often because of the complexity of the solidification and thermal history, L-PBF materials show anisotropic properties and, therefore, require heat treatment after manufacturing. In conventional materials, plastic deformation at elevated temperatures is commonly used to homogenize the material and heal defects before the final forming, machining, and heat treatment. Deformation at room temperature is also often used to increase dislocation density and intensify recrystallization processes to control grain size. The L-PBF manufacturing process results in the manufacturing of near-net-shape components; therefore, hot- and cold-work operations are not applicable. Because of that, new heat treatment regimes that guarantee required microstructures and properties have to be developed. Existing examples show that in many cases, for example, in steels, suitable heat treatment of L-PBF materials may lead to the formation of the microstructure and properties similar to the conventional analogs.

8.9 Questions

- Explain, what is the difference between homogeneous and heterogeneous nucleation of solid from liquid in metallic alloy? To what type does the epitaxial nucleation belong?
- Where, in the melt pool, is the highest temperature gradient found, and the highest solidification rate? How does it influence final microstructure (use Fig. 8.1 to prove your conclusion)?
- Explain mechanisms of formation of interdendritic segregations in metallic alloys.
- Explain what the competitive grain growth is, and why this phenomenon is observed in L-PBF.
- What is crystallographic texture? Find in the literature, what crystallographic texture can often be observed in L-PBF β-Ti alloys? Suggest ways to manipulate texture in L-PBF materials.
- Explain why during L-PBF an interior of the manufactured component is subjected to thermal cycles. Suggest ways to control temperature and duration of those cycles.
- Explain the difference between diffusional and diffusionless phase transformations in solids.
- Present examples of diffusionless phase transformations that are activated in L-PBF materials due to in-situ heat treatment (for example in steels or Ti6Al4V alloy).
- Present examples of diffusional transformations that are activated in L-PBF materials due to in-situ heat treatment (for example in Ni-based superalloys or Al alloys).
- Describe the difference in microstructure of the conventional water quenched and as-built L-PBF Ti6Al4V alloy. How can these differences influence mechanical properties (refer to Chapter 13 of this book to answer)?
- Describe the difference in microstructure of the conventional water quenched and as-built L-PBF steel (select grade yourself). How do these differences influence mechanical properties (refer to Chapter 13 of this book to answer)?
- Describe the difference in microstructure of the conventional water quenched and as-built L-PBF Ni-based superalloy (if relevant, refer to select grade yourself). How do these differences influence mechanical properties (if relevant, refer to Chapter 13 of this book to answer)?
- Describe the difference in microstructure of the conventional water quenched and as-built L-PBF AlSi10Mg alloy. How do these differences influence mechanical properties (refer to Chapter 13 of this book to answer)?
- Explain needs and challenges in a selection of heat treatment regimes for L-PBF materials. Present properties of a selected L-PBF alloy in as-built and heat treated conditions. Present a correlation between changes in properties and changes in microstructure.

Acknowledgments

Professor Krakhmalev gratefully acknowledges the Swedish Agency for Economic and Regional Growth, project 20201144 “ATLAB—additive manufacturing laboratory at Karlstad University” and Region Värmland for support of this study. Professor Kazantseva thanks the Russian Science Foundation (project 21-79-20100) and the Government program of the M. N. Mikheev Institute of Metal Physics, Ural Branch, Russian Academy of Sciences (“Diagnostics” No. AAA-A18-118020690196-3) for financial support.

References

Aboulkhair, N.T., Simonelli, M., Parry, L., Ashcroft, I., Tuck, C., Hague, R., 2019. 3D printing of aluminium alloys: additive manufacturing of aluminium alloys using selective laser melting. Prog. Mater. Sci. 106, 100578.

Adegoke, O., Andersson, J., Brodin, H., Pederson, R., 2020. Review of laser powder bed fusion of gamma-prime-strengthened nickel-based superalloys. Metals 10 (8), 996.

Anusavice, K.J., Shen, C., Rawls, H.R. (Eds.), 2012. Phillips' Science of Dental Materials. Elsevier Health Sciences.

Åsberg, M., Fredriksson, G., Hatami, S., Fredriksson, W., Krakhmalev, P., 2019. Influence of post treatment on microstructure, porosity and mechanical properties of additive manufactured H13 tool steel. Mater. Sci. Eng. A 742, 584−589.

Atabay, S.E., Sanchez-Mata, O., Muñiz-Lerma, J.A., Gauvin, R., Brochu, M., 2020. Microstructure and mechanical properties of rene 41 alloy manufactured by laser powder bed fusion. Mater. Sci. Eng. A 773, 138849.

Atamert, S., Bhadeshia, H.K.D.H., 1989. Comparison of the microstructures and abrasive wear properties of stellite hardfacing alloys deposited by arc welding and laser cladding. Metall. Trans. A 20 (6), 1037−1054.

Bajaj, P., Hariharan, A., Kini, A., Kürnsteiner, P., Raabe, D., Jägle, E.A., 2020. Steels in additive manufacturing: a review of their microstructure and properties. Mater. Sci. Eng. A 772, 138633.

Balagna, C., Spriano, S., Faga, M.G., 2012. Characterization of Co−Cr−Mo alloys after a thermal treatment for high wear resistance. Mater. Sci. Eng. C 32 (7), 1868−1877.

Barr, C.M., Thomas, S., Hart, J.L., Harlow, W., Anber, E., Taheri, M.L., 2018. Tracking the evolution of intergranular corrosion through twin-related domains in grain boundary networks. npj Mater. Degrad. 2 (1), 1−10.

Barriobero-Vila, P., Gussone, J., Haubrich, J., Sandlöbes, S., Da Silva, J.C., Cloetens, P., Schell, N., Requena, G., 2017. Inducing stable $\alpha + \beta$ microstructures during selective laser melting of Ti-6Al-4V using intensified intrinsic heat treatments. Materials 10 (3), 268.

Beese, A.M., Carroll, B.E., 2016. Review of mechanical properties of Ti-6Al-4V made by laser-based additive manufacturing using powder feedstock. J. Occup. Med. 68 (3), 724−734.

Bertsch, K.M., de Bellefon, G.M., Kuehl, B., Thoma, D.J., 2020. Origin of dislocation structures in an additively manufactured austenitic stainless steel 316L. Acta Mater. 199, 19−33.

Bodziak, S., Al-Rubaie, K.S., Dalla Valentina, L., Lafratta, F.H., Santos, E.C., Zanatta, A.M., Chen, Y., 2019. Precipitation in 300 grade maraging steel built by selective laser melting: aging at 510 C for 2 h. Mater. Char. 151, 73−83.

Boes, J., Röttger, A., Mutke, C., Escher, C., Theisen, W., 2018. Microstructure and mechanical properties of X65MoCrWV3-2 cold-work tool steel produced by selective laser melting. Addit. Manuf. 23, 170−180.

Carreon, H., Ruiz, A., Santoveña, B., 2014, February. Study of aging effects in a Ti-6AL-4V alloy with Widmanstätten and equiaxed microstructures by non-destructive means. AIP Conf. Proc. 1581 (1), 739−745. American Institute of Physics.

Casati, R., Coduri, M., Lecis, N., Andrianopoli, C., Vedani, M., 2018. Microstructure and mechanical behavior of hot-work tool steels processed by Selective Laser Melting. Mater. Char. 137, 50−57.

Castany, P., Yang, Y., Bertrand, E., Gloriant, T., 2016. Reversion of a parent 130α" martensitic twinning system at the origin of 332β twins observed in metastable beta titanium alloys, physical review letters. Am. Phys. Soc. 117 (24), 245501.

Chabina, E.B., Filonova, E.V., Lomberg, B.S., Bakradze, M.M., 2012. The structure of modern wrought nickel alloys. Encyclopedic reference book, No. 6 All Mater. 1−11.

Chen, J.H., Costan, E., Van Huis, M.A., Xu, Q., Zandbergen, H.W., 2006. Atomic pillar-based nanoprecipitates strengthen AlMgSi alloys. Science 312 (5772), 416−419.

Chen, H., Zhang, C., Jia, D., Wellmann, D., Liu, W., 2020. Corrosion behaviors of selective laser melted aluminum alloys: a review. Metals 10 (1), 102.

Cheruvathur, S., Lass, E.A., Campbell, C.E., 2016. Additive manufacturing of 17-4 PH stainless steel: post-processing heat treatment to achieve uniform reproducible microstructure. J. Occup. Med. 68 (3), 930−942.

Christian, J.W., 1970. Basic crystallography and kinetics. In: Petty, E.R. (Ed.), Martensite: Fundamentals and Technology. Longman Ltda., London, United Kingdom.

DebRoy, T., Wei, H.L., Zuback, J.S., Mukherjee, T., Elmer, J.W., Milewski, J.O., Beese, A.M., Wilson-Heid, A.D., De, A., Zhang, W., 2018. Additive manufacturing of metallic components−process, structure and properties. Prog. Mater. Sci. 92, 112−224.

Dikova, T., 2018. Bending fracture of Co-Cr dental bridges, produced by additive technologies: experimental investigation. Procedia Struct. Integrity 13, 461−468.

Divya, V.D., Muñoz-Moreno, R., Messé, O.M.D.M., Barnard, J.S., Baker, S., Illston, T., Stone, H.J., 2016. Microstructure of selective laser melted CM247LC nickel-based superalloy and its evolution through heat treatment. Mater. Char. 114, 62−74.

Du Plessis, A., Macdonald, E., 2020. Hot isostatic pressing in metal additive manufacturing: X-ray tomography reveals details of pore closure. Addit. Manuf. 101191.

Fiocchi, J., Biffi, C.A., Tuissi, A., 2020. Selective laser melting of high-strength primary AlSi9Cu3 alloy: processability, microstructure, and mechanical properties. Mater. Des. 191, 108581.

Geenen, K., Roettger, A., Feld, F., Theisen, W., 2019. Microstructure, mechanical, and tribological properties of M3: 2 high-speed steel processed by selective laser melting, hot-isostatic pressing, and casting. Addit. Manuf. 28, 585−599.

Gharbi, O., Jiang, D., Feenstra, D.R., Kairy, S., Wu, Y., Hutchinson, C.R., Birbilis, N., 2018. Microstructure and corrosion properties of additively manufactured aluminum alloy AA2024. In: Proceedings of the 16th International Aluminum Alloys Conference (ICAA16), Canadian Institute of Mining, Metallurgy & Petroleum, Canada, pp. 17−21.

Gladman, T., 1999. Precipitation hardening in metals. Mater. Sci. Technol. 15 (1), 30−36.

Grange, D., Bartout, J.D., Macquaire, B., Colin, C., 2020. Processing a non-weldable Nickel-base superalloy by Selective Laser Melting: role of the shape and size of the melt pools on solidification cracking. Materialia 100686.

Gu, D., Guo, M., Zhang, H., Sun, Y., Wang, R., Zhang, L., 2020. Effects of laser scanning strategies on selective laser melting of pure tungsten. Int. J. Extreme Manuf. 2 (2), 025001.

Han, Q., Gu, Y., Setchi, R., Lacan, F., Johnston, R., Evans, S.L., Yang, S., 2019. Additive manufacturing of high-strength crack-free Ni-based Hastelloy X superalloy. Addit. Manuf. 30, 100919.

Hitzler, L., Merkel, M., Hall, W., Öchsner, A., 2018. A review of metal fabricated with laser-and powder-bed based additive manufacturing techniques: process, nomenclature, materials, achievable properties, and its utilization in the medical sector. Adv. Eng. Mater. 20 (5), 1700658.

Holzweissig, M.J., Taube, A., Brenne, F., Schaper, M., Niendorf, T., 2015. Microstructural characterization and mechanical performance of hot work tool steel processed by selective laser melting. Metall. Mater. Trans. B 46 (2), 545−549.

Hosono, H., Mishima, Y., Takezoe, H., MacKenzie, K.J. (Eds.), 2006. Nanomaterials: Research Towards Applications, vol. 161. Elsevier.

Huang, P., Lopez, H.F., 1999. Effects of grain size on development of athermal and strain induced ϵ martensite in Co—Cr—Mo implant alloy. Mater. Sci. Technol. 15 (2), 157—164.

Ishimoto, T., Hagihara, K., Hisamoto, K., Sun, S.H., Nakano, T., 2017. Crystallographic texture control of beta-type Ti—15Mo—5Zr—3Al alloy by selective laser melting for the development of novel implants with a biocompatible low Young's modulus. Scripta Mater. 132, 34—38.

Ivasishin, O.M., Flower, H.M., Lütjering, G., 1999. Mechanisms of martensite formation and tempering in titanium alloys and their relationship to mechanical property development, titanium'99. Sci. Technol. 77—84.

Jägle, E.A., Choi, P.P., Van Humbeeck, J., Raabe, D., 2014. Precipitation and austenite reversion behavior of a maraging steel produced by selective laser melting. J. Mater. Res. 29 (17), 2072.

Jägle, E.A., Sheng, Z., Wu, L., Lu, L., Risse, J., Weisheit, A., Raabe, D., 2016. Precipitation reactions in age-hardenable alloys during laser additive manufacturing. J. Occup. Med. 68 (3), 943—949.

Jägle, E.A., Sheng, Z., Kürnsteiner, P., Ocylok, S., Weisheit, A., Raabe, D., 2017. Comparison of maraging steel micro-and nanostructure produced conventionally and by laser additive manufacturing. Materials 10 (1), 8.

Kajiwara, S., Kikuchi, T., Pal, H., Asano, T., Kosuge, M., Yuyama, M., Inoue, K., Wada, H., 1997. Athermal and isothermal martensitic transformations induced at room temperature by ultra high magnetic field. J. Phys. IV 7 (C5), C5—C377.

Kakeshita, T., Saburi, T., Shimizu, K., 2000. Kinetics of martensitic transformations in some ferrous and non-ferrous alloys. Phil. Mag. B 80 (2), 171—181.

Kazantseva, N., Krakhmalev, P., Yadroitsev, I., Fefelov, A., Vinogradova, N., Ezhov, I., Kurennykh, T., 2017. Texture and twinning in selective laser melting Ti-6Al-4V alloys. Int. J. Mater. Metall. Eng. 11 (11), 769—772.

Kazantseva, N., Krakhmalev, P., Thuvander, M., Yadroitsev, I., Vinogradova, N., Ezhov, I., 2018a. Martensitic transformations in Ti-6Al-4V (ELI) alloy manufactured by 3D Printing. Mater. Char. 146, 101—112.

Kazantseva, N.V., Stepanova, N.N., Rigmant, M.B., 2018b. Superalloys: Analysis and Control of Failure Process. CRC Press.

Kazantseva, N.V., Ezhov, I.V., Davydov, D.I., Merkushev, A.G., 2019. Analysis of structure and mechanical properties of Co—Cr—Mo alloy obtained by 3D printing. Phys. Met. Metallogr. 120 (12), 1172—1179.

Kempen, K., Vrancken, B., Buls, S., Thijs, L., Van Humbeeck, J., Kruth, J.P., 2014. Selective laser melting of crack-free high density M2 high speed steel parts by baseplate preheating. J. Manuf. Sci. Eng. 136 (6).

Kim H.Y., Miyazaki S., Chapter 1 - Martensitic Transformation Characteristics, Editor(s): Hee Young Kim, Shuichi Miyazaki, Ni-Free Ti-Based Shape Memory Alloys, Butterworth-Heinemann, 2018, Pages 1-52, ISBN 9780128094013.

Köhnen, P., Letang, M., Voshage, M., Schleifenbaum, J.H., Haase, C., 2019. Understanding the process-microstructure correlations for tailoring the mechanical properties of L-PBF produced austenitic advanced high strength steel. Addit. Manuf. 30, 100914.

Kok, Y., Tan, X.P., Wang, P., Nai, M.L.S., Loh, N.H., Liu, E., Tor, S.B., 2018. Anisotropy and heterogeneity of microstructure and mechanical properties in metal additive manufacturing: a critical review. Mater. Des. 139, 565—586.

Kolachev, B.A., Elagin, V.I., Livanov, V.A., 2005. Metallurgy and Heat Treatment of Nonferrous Metals and Alloys. MISIS, Moscow, p. 416.

Kou, S., 2003. Welding metallurgy. New Jersey, USA, pp. 431—446.

Krakhmalev, P., Yadroitsava, I., Fredriksson, G., Yadroitsev, I., 2015. In situ heat treatment in selective laser melted martensitic AISI 420 stainless steels. Mater. Des. 87, 380−385.

Krakhmalev, P., Fredriksson, G., Yadroitsava, I., Kazantseva, N., Du Plessis, A., Yadroitsev, I., 2016. Deformation behavior and microstructure of Ti6Al4V manufactured by SLM. Phys. Procedia 83, 778−788.

Krakhmalev, P., Yadroitsava, I., Fredriksson, G., Yadroitsev, I., 2017. Microstructural and thermal stability of selective laser melted 316L stainless steel single tracks. S. Afr. J. Ind. Eng. 28 (1), 12−19.

Krakhmalev, P., Fredriksson, G., Svensson, K., Yadroitsev, I., Yadroitsava, I., Thuvander, M., Peng, R., 2018a. Microstructure, solidification texture, and thermal stability of 316 L stainless steel manufactured by laser powder bed fusion. Metals 8 (8), 643.

Krakhmalev, P., Yadroitsev, I., Baker, I., Yadroitsava, I., 2018b. Manufacturing of intermetallic Mn-46% Al by laser powder bed fusion. Procedia CIRP 74, 64−67.

Krakhmalev, P., Fredriksson, G., Thuvander, M., Åsberg, M., Vilardell, A.M., Oikonomou, C., Maistro, G., Medvedeva, A., Kazantseva, N., 2020. Influence of heat treatment under hot isostatic pressing (HIP) on microstructure of intermetallic-reinforced tool steel manufactured by laser powder bed fusion. Mater. Sci. Eng. A 772, 138699.

Kunze, K., Etter, T., Grässlin, J., Shklover, V., 2015. Texture, anisotropy in microstructure and mechanical properties of IN738LC alloy processed by selective laser melting (SLM). Mater. Sci. Eng. A 620, 213−222.

Kürnsteiner, P., Wilms, M.B., Weisheit, A., Barriobero-Vila, P., Jägle, E.A., Raabe, D., 2017. Massive nanoprecipitation in an Fe-19Ni-xAl maraging steel triggered by the intrinsic heat treatment during laser metal deposition. Acta Mater. 129, 52−60.

Kurz, W., Trivedi, R., 1994. Rapid solidification processing and microstructure formation. Mater. Sci. Eng. A 179, 46−51.

LeBrun, T., Nakamoto, T., Horikawa, K., Kobayashi, H., 2015. Effect of retained austenite on subsequent thermal processing and resultant mechanical properties of selective laser melted 17−4 PH stainless steel. Mater. Des. 81, 44−53.

Lejček, P., 2010. Grain Boundary Segregation in Metals. Springer-Verlag Berlin Heidelberg.

Li, C., Li, G., Yang, Y., Varlioglu, M., Yang, K., 2011. α''Martensitic twinning in Alpha + beta Ti-3.5 Al-4.5 Mo titanium alloy. J. Metall. 2011, 1−5.

Liu, M., Takata, N., Suzuki, A., Kobashi, M., 2018. Microstructural characterization of cellular AlSi10Mg alloy fabricated by selective laser melting. Mater. Des. 157, 478−491.

Lu, Y., Wu, S., Gan, Y., Li, J., Zhao, C., Zhuo, D., Lin, J., 2015. Investigation on the microstructure, mechanical property and corrosion behavior of the selective laser melted CoCrW alloy for dental application. Mater. Sci. Eng. C 49, 517−525.

Lui, E.W., Xu, W., Pateras, A., Qian, M., Brandt, M., 2017. New development in selective laser melting of Ti−6Al−4V: a wider processing window for the achievement of fully lamellar $\alpha + \beta$ microstructures. J. Occup. Med. 69 (12), 2679−2683.

Lütjering, G., Williams, J.C., 2007. Titanium. Springer Science & Business Media.

Marchese, G., Parizia, S., Saboori, A., Manfredi, D., Lombardi, M., Fino, P., Ugues, D., Biamino, S., 2020. The influence of the process parameters on the densification and microstructure development of laser powder bed fused inconel 939. Metals 10 (7), 882.

Mertens, R., Vrancken, B., Holmstock, N., Kinds, Y., Kruth, J.P., Van Humbeeck, J., 2016. Influence of powder bed preheating on microstructure and mechanical properties of H13 tool steel SLM parts. Phys. Procedia 83, 882−890.

Murr, L.E., Martinez, E., Hernandez, J., Collins, S., Amato, K.N., Gaytan, S.M., Shindo, P.W., 2012. Microstructures and properties of 17-4 PH stainless steel fabricated by selective laser melting. J. Mater. Res. Technol. 1 (3), 167−177.

Padilha, A.F., Escriba, D.M., Materna-Morris, E., Rieth, M., Klimenkov, M., 2007. Precipitation in AISI 316L (N) during creep tests at 550 and 600 C up to 10 years. J. Nucl. Mater. 362 (1), 132−138.

Pantawane, M.V., Dasari, S., Mantri, S.A., Banerjee, R., Dahotre, N.B., 2020. Rapid thermokinetics driven nanoscale vanadium clustering within martensite laths in laser powder bed fused additively manufactured Ti6Al4V. Mater. Res. Lett. 8 (10), 383−389.

Pourbabak, S., Montero-Sistiaga, M.L., Schryvers, D., Van Humbeeck, J., Vanmeensel, K., 2019. Microscopic investigation of as built and hot isostatic pressed Hastelloy X processed by Selective Laser Melting. Mater. Char. 153, 366−371.

Prashanth, K.G., Eckert, J., 2017. Formation of metastable cellular microstructures in selective laser melted alloys. J. Alloys Compd. 707, 27−34.

Puichaud, A.H., Flament, C., Chniouel, A., Lomello, F., Rouesne, E., Giroux, P.F., Maskrot, H., Schuster, F., Béchade, J.L., 2019. Microstructure and mechanical properties relationship of additively manufactured 316L stainless steel by selective laser melting. EPJ Nucl. Sci. Technol. 5, 23.

Qiu, C., Al Kindi, M., Aladawi, A.S., Al Hatmi, I., 2018. A comprehensive study on microstructure and tensile behaviour of a selectively laser melted stainless steel. Sci. Rep. 8 (1), 1−16.

Rafi, H.K., Pal, D., Patil, N., Starr, T.L., Stucker, B.E., 2014. Microstructure and mechanical behavior of 17-4 precipitation hardenable steel processed by selective laser melting. J. Mater. Eng. Perform. 23 (12), 4421−4428.

Rickenbacher, L., Etter, T., Hövel, S., Wegener, K., 2013. High temperature material properties of IN738LC processed by selective laser melting (SLM) technology. Rapid Prototyp. J. 282−290.

Riemer, A., Leuders, S., Thöne, M., Richard, H.A., Tröster, T., Niendorf, T., 2014. On the fatigue crack growth behavior in 316L stainless steel manufactured by selective laser melting. Eng. Fract. Mech. 120, 15−25.

Saeidi, K., Gao, X., Zhong, Y., Shen, Z.J., 2015. Hardened austenite steel with columnar subgrain structure formed by laser melting. Mater. Sci. Eng. A 625, 221−229.

Šafka, J., Ackermann, M., Volesky, L., 2016. April. Structural properties of H13 tool steel parts produced with use of selective laser melting technology. J. Phys. Conf. Ser. 709, 1−7. IOP Publishing.

Saldıvar, A.J., Lopez, H.F., 2001. Role of aging on the martensitic transformation in a cast cobalt alloy. Scr. Mater. 45 (4), 427−433.

Sallica-Leva, E., Caram, R., Jardini, A.L., Fogagnolo, J.B., 2016. Ductility improvement due to martensite α' decomposition in porous Ti−6Al−4V parts produced by selective laser melting for orthopedic implants. J. Mech. Behav. Biomed. Mater. 54, 149−158.

Sander, J., Hufenbach, J., Giebeler, L., Wendrock, H., Kühn, U., Eckert, J., 2016. Microstructure and properties of FeCrMoVC tool steel produced by selective laser melting. Mater. Des. 89, 335−341.

Shimizu, K.I., 2002. Martensitic transformations: microstructures and uniaxial stress, magnetic field and hydrostatic pressure effects. Mater. Trans. 43 (8), 2050−2057.

Simonelli, M., Tse, Y.Y., Tuck, C., 2014. Effect of the build orientation on the mechanical properties and fracture modes of SLM Ti−6Al−4V. Mater. Sci. Eng. A 616, 1−11.

Singh, C.V., Warner, D.H., 2010. Mechanisms of Guinier−Preston zone hardening in the athermal limit. Acta Mater. 58 (17), 5797−5805.

Sun, S.H., Hagihara, K., Nakano, T., 2018a. Effect of scanning strategy on texture formation in Ni-25 at.% Mo alloys fabricated by selective laser melting. Mater. Des. 140, 307−316.

Sun, Y., Hebert, R.J., Aindow, M., 2018b. Effect of heat treatments on microstructural evolution of additively manufactured and wrought 17-4PH stainless steel. Mater. Des. 156, 429–440.

Takaichi, A., Nakamoto, T., Joko, N., Nomura, N., Tsutsumi, Y., Migita, S., Doi, H., Kurosu, S., Chiba, A., Wakabayashi, N., Igarashi, Y., 2013. Microstructures and mechanical properties of Co–29Cr–6Mo alloy fabricated by selective laser melting process for dental applications. J. Mech. Behav. Biomed. Mater. 21, 67–76.

Takata, N., Kodaira, H., Sekizawa, K., Suzuki, A., Kobashi, M., 2017. Change in microstructure of selectively laser melted AlSi10Mg alloy with heat treatments. Mater. Sci. Eng. A 704, 218–228.

Takata, N., Liu, M., Kodaira, H., Suzuki, A., Kobashi, M., 2020. Anomalous strengthening by supersaturated solid solutions of selectively laser melted Al–Si-based alloys. Addit. Manuf. 101152.

Tan, X.P., Mangelinck, D., Perrin-Pellegrino, C., Rougier, L., Gandin, C.A., Jacot, A., Ponsen, D., Jaquet, V., 2014. Spinodal decomposition mechanism of γ' precipitation in a single crystal Ni-Based superalloy. Metall. Mater. Trans. A 45 (11), 4725–4730.

Tan, C., Zhou, K., Ma, W., Zhang, P., Liu, M., Kuang, T., 2017. Microstructural evolution, nanoprecipitation behavior and mechanical properties of selective laser melted high-performance grade 300 maraging steel. Mater. Des. 134, 23–34.

Tan, Q., Zhang, J., Sun, Q., Fan, Z., Li, G., Yin, Y., Liu, Y., Zhang, M.X., 2020. Inoculation treatment of an additively manufactured 2024 aluminium alloy with titanium nanoparticles. Acta Mater. 196, 1–16.

Thijs, L., Verhaeghe, F., Craeghs, T., Van Humbeeck, J., Kruth, J.P., 2010. A study of the microstructural evolution during selective laser melting of Ti–6Al–4V. Acta Mater. 58 (9), 3303–3312.

Tian, Z., Zhang, C., Wang, D., Liu, W., Fang, X., Wellmann, D., Zhao, Y., Tian, Y., 2020a. A review on laser powder bed fusion of inconel 625 nickel-based alloy. Appl. Sci. 10 (1), 81.

Tian, Y., Palad, R., Aranas Jr., C., 2020b. Microstructural evolution and mechanical properties of a newly designed steel fabricated by laser powder bed fusion. Addit. Manuf. 36, 101495.

Vilardell, A.M., Fredriksson, G., Yadroitsev, I., Krakhmalev, P., 2019. Fracture mechanisms in the as-built and stress-relieved laser powder bed fusion Ti6Al4V ELI alloy. Optic Laser. Technol. 109, 608–615.

Vilardell, A.M., Hosseini, S.B., Åsberg, M., Dahl-Jendelin, A., Krakhmalev, P., Oikonomou, C., Hatami, S., 2021. Evaluation of post-treatments of novel hot-work tool steel manufactured by laser powder bed fusion for aluminum die casting applications. Mater. Sci. Eng. A 800, 140305.

Vilaro, T., Colin, C., Bartout, J.D., Nazé, L., Sennour, M., 2012. Microstructural and mechanical approaches of the selective laser melting process applied to a nickel-base superalloy. Mater. Sci. Eng. A 534, 446–451.

Wang, S.C., Starink, M.J., 2005. Review of precipitation in Al-Cu-Mg (-Li) alloys. Int. Mater. Rev. 50, 193–215.

Wang, Y.M., Voisin, T., McKeown, J.T., Ye, J., Calta, N.P., Li, Z., Zeng, Z., Zhang, Y., Chen, W., Roehling, T.T., Ott, R.T., 2018. Additively manufactured hierarchical stainless steels with high strength and ductility. Nat. Mater. 17 (1), 63–71.

Welsch, G., Boyer, R., Collings, E.W., 1993. Materials Properties Handbook: Titanium Alloys. ASM International.

Wielewski, E., Siviour, C.R., Petrinic, N., 2012. On the correlation between macrozones and twinning in Ti–6Al–4V at very high strain rates. Scr. Mater. 67 (3), 229–232.

Xu, W., Brandt, M., Sun, S., Elambasseril, J., Liu, Q., Latham, K., Xia, K., Qian, M., 2015. Additive manufacturing of strong and ductile Ti–6Al–4V by selective laser melting via in situ martensite decomposition. Acta Mater. 85, 74–84.

Xu, W., Lui, E.W., Pateras, A., Qian, M., Brandt, M.J.A.M., 2017. In situ tailoring microstructure in additively manufactured Ti-6Al-4V for superior mechanical performance. Acta Mater. 125, 390–400.

Yadroitsev, I., Krakhmalev, P., Yadroitsava, I., 2014. Selective laser melting of Ti6Al4V alloy for biomedical applications: temperature monitoring and microstructural evolution. J. Alloys Compd. 583, 404–409.

Yadroitsev, I., Krakhmalev, P., Yadroitsava, I., Du Plessis, A., 2018. Qualification of Ti6Al4V ELI alloy produced by laser powder bed fusion for biomedical applications. J. Occup. Med. 70 (3), 372–377.

Yadroitsev, I., Krakhmalev, P., Yadroitsava, I., Johansson, S., Smurov, I., 2013. Energy input effect on morphology and microstructure of selective laser melting single track from metallic powder. J. Mater. Process. Technol. 213 (4), 606–613.

Yan, M., Yu, P., 2015. An Overview of Densification, Microstructure and Mechanical Property of Additively Manufactured Ti-6Al-4V — Comparison among Selective Laser Melting, Electron Beam Melting, Laser Metal Deposition and Selective Laser Sintering, and with Conventional Powder, Sintering Techniques of Materials, Arunachalam Lakshmanan, IntechOpen. https://doi.org/10.5772/59275. https://www.intechopen.com/books/sintering-techniques-of-materials/an-overview-of-densification-microstructure-and-mechanical-property-of-additively-manufactured-ti-6a.

Yan, J.J., Zheng, D.L., Li, H.X., Jia, X., Sun, J.F., Li, Y.L., Qian, M., Yan, M., 2017. Selective laser melting of H13: microstructure and residual stress. J. Mater. Sci. 52 (20), 12476–12485.

Zafari, A., Barati, M.R., Xia, K., 2019. Controlling martensitic decomposition during selective laser melting to achieve best ductility in high strength Ti-6Al-4V. Mater. Sci. Eng. A 744, 445–455.

Zhang, H., Zhu, H., Qi, T., Hu, Z., Zeng, X., 2016. Selective laser melting of high strength Al–Cu–Mg alloys: processing, microstructure and mechanical properties. Mater. Sci. Eng. A 656, 47–54.

Zhang, F., Levine, L.E., Allen, A.J., Stoudt, M.R., Lindwall, G., Lass, E.A., Williams, M.E., Idell, Y., Campbell, C.E., 2018a. Effect of heat treatment on the microstructural evolution of a nickel-based superalloy additive-manufactured by laser powder bed fusion. Acta Mater. 152, 200–214.

Zhang, M., Yang, Y., Song, C., Bai, Y., Xiao, Z., 2018b. An investigation into the aging behavior of CoCrMo alloys fabricated by selective laser melting. J. Alloys Compd. 750, 878–886.

Zhang, X., Chen, H., Xu, L., Xu, J., Ren, X., Chen, X., 2019. Cracking mechanism and susceptibility of laser melting deposited Inconel 738 superalloy. Mater. Des. 183, 108105.

Zhong, Y., Liu, L., Wikman, S., Cui, D., Shen, Z., 2016. Intragranular cellular segregation network structure strengthening 316L stainless steel prepared by selective laser melting. J. Nucl. Mater. 470, 170–178.

Zwicker, U., 1979. Titanium and its Alloys. [Russian Translation]. Metallurgiya, Moscow, p. 510. Zwicker, U., 1979.

Residual stress in laser powder bed fusion

9

Lameck Mugwagwa[1], *Ina Yadroitsava*[1], *Nkutwane Washington Makoana*[1,2], *Igor Yadroitsev*[1]
[1]Department of Mechanical and Mechatronic Engineering, Central University of Technology, Bloemfontein, Free State, South Africa; [2]Council for Scientific and Industrial Research, National Laser Centre, Pretoria, South Africa

Chapter outline

9.1 Introduction 245
9.2 Residual stress measurements 247
  9.2.1 Destructive methods 247
  9.2.2 Nondestructive techniques 249
9.3 Effects and origins of residual stress in L-PBF 251
9.4 Modeling of L-PBF process and residual stress evolution 258
9.5 Post-processing stress relieving 261
  9.5.1 Heat treatment 261
  9.5.2 Mechanical treatment 261
9.6 In situ stress relief 262
  9.6.1 Base plate and build chamber preheating 263
  9.6.2 Process parameter optimization 264
  9.6.3 Scanning strategy and in situ residual stress control 264
  9.6.4 Optimization of support structures 266
  9.6.5 Optimization of alloy composition 267
9.7 Conclusions 267
9.8 Questions 268
Acknowledgments 269
References 269

9.1 Introduction

Residual stresses in an object are those stresses that remain in the object when all external forces, apart from gravity, do not act on this object. Since residual stress is balanced in the object, the presence of tensile stress (positive in sign) in one part is compensated by compressive stress (negative) in other parts of this object. The primary reasons for residual stresses are nonuniform plastic deformations through the cross-section during mechanical processing, phase transformations, and thermal gradients, i.e., residual stresses have mechanical, chemical, and thermal origins.

Fundamentals of Laser Powder Bed Fusion of Metals. https://doi.org/10.1016/B978-0-12-824090-8.00014-7
Copyright © 2021 Elsevier Inc. All rights reserved.

Residual stresses can be introduced during manufacturing, during in-service repair or modification, during operation or even during part installation, assembly procedures, or occasional overloads. For example, residual stress in drilling is introduced by plastic deformation due to the removal of chips, thermal stress introduced by heating, and possible phase transformation if the temperature is sufficient. In practice, no component is entirely free of residual stress, which originates during processing.

Residual stresses can be divided into the following length scales: Type I, II, and III (Fig. 9.1). Type I are macro-stresses which equilibrate over large distances or dimensions (size of the part or structure). Macro-stresses may be introduced by nonuniform plastic deformation due to material processing such as shot peening, forging, milling, bending, welding, different surface treatments (plating, enameling, coatings, hardening), or by heating or cooling (for example, quenching heat treatment procedure). Residual stress can also be introduced by differing thermal expansion coefficients and mechanical mismatching of varying components of composites as multiphase materials, ceramic coatings, etc. Type I residual stress can also occur under material load: e.g., mechanical loading, thermal temperature fields, or chemical changes during operation.

Type II are micro-intergranular stresses that equilibrate over a length relating to the grain dimensions, usually 3–10 times that of the grain size (Totten et al., 2002). These stresses are caused by differences in microstructure of polycrystalline materials when phase transformation has taken place in a multiphase material or in a single-phase material when anisotropy of grains occurs. An example is thermal stresses in metal-matrix composites.

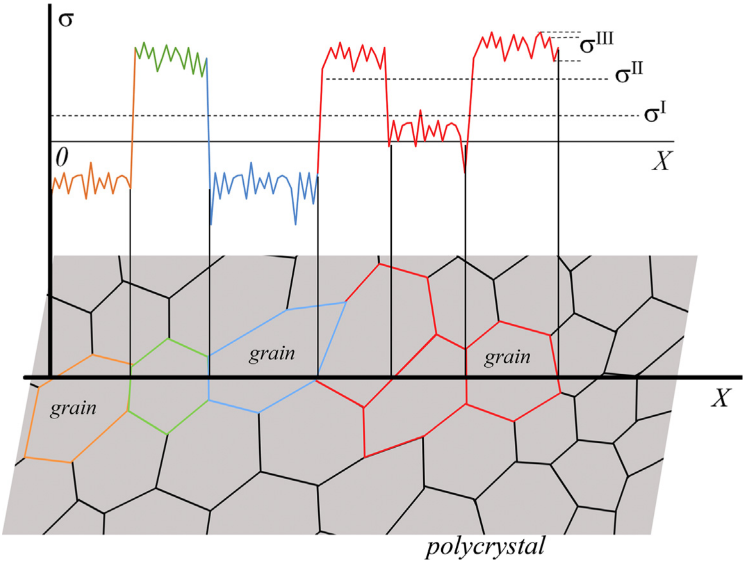

Figure 9.1 Residual stress in polycrystalline material categorized according to length scales.

Type III are stresses that are present within a grain and typically includes stresses due to coherency at interfaces and dislocation stress fields (Withers and Bhadeshia, 2001a).

The effects of residual stress may be either beneficial or detrimental, depending upon the magnitude, size, and distribution of the stress with respect to the load-induced stresses (Withers and Bhadeshia, 2001a,b). For example, tensile residual stress near the surface has a detrimental influence on fatigue and corrosive properties, especially if this part is also subjected to tensile load during operation. So, in parts with residual stresses, not only is loading magnitude critical but also direction.

All metal part manufacturing methods, such as die and investment castings, sintering, machining, metal injection molding, and additive manufacturing (AM), introduce residual stresses into the manufactured object. During welding or powder bed fusion, residual stress can be generated by shrinkage, deformations during processing, temperature variations, and phase transformations. This chapter provides metal AM researchers with important information regarding residual stress measurements, their origins, effects in L-PBF objects, the available residual stress mitigation methods and how such methods impact on the end-product quality characteristics. Furthermore, the implications of the various residual stress management approaches are discussed, bearing in mind the interdependent, competing or conflicting effects of the interventions on residual stress and other process outcomes such as density, surface quality, manufacturing time, and cost.

9.2 Residual stress measurements

The effective control of residual stress and qualification of the manufacturing process for various applications depend on accurate measurement of the residual stresses. Evaluation of residual stress is done by means of measuring strain using a variety of methods and using the measured strain to calculate stress based on variations of Hooke's laws. Alternatively, residual stress can be evaluated qualitatively by measuring distortions that emanate from them. Two broad approaches can be used to evaluate residual stress—nondestructive and destructive methods. Detailed explanation of measurement techniques of residual stress can be found in Withers and Bhadeshia (2001a). In this section, some frequently used methods are briefly described.

9.2.1 Destructive methods

All destructive and semi-destructive methods of measuring residual stress work on the same principle of inducing stress relaxation followed by strain or deflection measurements. Thus, destructive techniques are also called relaxation methods (Schajer, 2010). Stress relaxation can be achieved by cutting or removing some material from the specimen. Methods that rely on macro-deflection measurement are purely qualitative, although finite element (FE) methods can be used to calculate the actual stress responsible for the distortion. However, no standard geometries exist to allow universally acceptable and reliable evaluation. For this reason, deflection-based methods have largely remained qualitative.

The ***hole drilling method*** is one of the most common methods in which strain gages are used to measure the strain that results from stress relaxation after material removal from a specimen. This method has been used to evaluate residual stress in a range of L-PBF metal alloys including Ti6Al4V and AlSi10Mg (Knowles et al., 2012; Salmi et al., 2017). In this method, a small hole is drilled in the center of a strain gage rosette attached to the surface of the component to be measured. The action of drilling the hole relieves locked-up stress and this is accompanied by a change in the strain state, which can easily be measured using the strain gage (Fig. 9.2A). The strain change is then used to compute the equivalent stress state through a series of equations, as specified in ASTM E837-08. The accuracy of this method depends on surface roughness, levels of stress, correct alignment for drilling, selection of incremental hole depths, gage placements, etc. Similar to the hole drilling method, other relaxation techniques

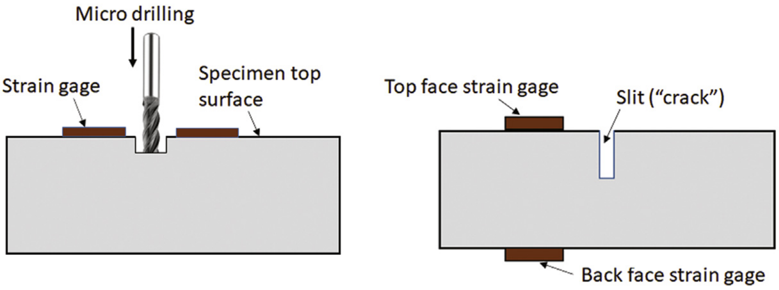
Micro drilling
Strain gage
Specimen top surface
Top face strain gage
Slit ("crack")
Back face strain gage

Hole drilling method

(A)

Crack compliance method

(B)

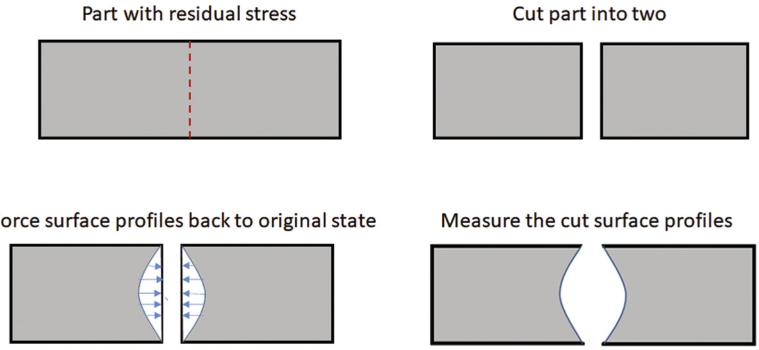
Part with residual stress
Cut part into two
Force surface profiles back to original state
Measure the cut surface profiles

Contour method

(C)

Figure 9.2 Measurements of residual stress by hole drilling (A), crack compliance method (B), and contour method (C).

such as indentation or cutting of a long slit (so-called "slitting method," or "***crack compliance method,***" Fig. 9.2B) are used for investigation of residual stress with strain gages (Schajer, 2013).

Digital image correlation (DIC) is a widely used method for measuring residual stress in L-PBF-manufactured components. DIC acquires strain data from images by comparing the location of a subset or block of pixels on a test piece before and after deformation (Lord et al., 2008). The image taken before deformation is the reference image, and several other images can be taken at different stages of the deformation. For example, when testing the hardness of a material which suffers from residual stress, the indentation may deform to a certain extent (or the residual stress may influence the hardness number). The magnitude of the deformity may be compared with that of a nonstressed part; the change in area of the indentation could be converted to strain which then can be converted to a stress value using Hooke's law (Totten et al., 2002; Song et al., 2014).

Residual stress can also be estimated using the ***contour method*** (Fig. 9.2C). The component under investigation is carefully cut in two using nonstress-inducing methods such as wire electric discharge machining. When the surface of the plane of interest is cut, residual stress is partially relieved, causing deformations or deviations of the cut surfaces from the expected surface profile. These distortions can be measured using a touch probe of a coordinate measurement machine or a laser profilometer. The stress state is determined with the aid of FE modeling by superimposing the partially relaxed stress state with the stress change, after forcing back the deformations to the original state before cutting (Ahmad et al., 2018; Robinson et al., 2018). The contour method only measures the stress component normal to the cut. A multi-axial contour method has been developed to determine 3D stress maps by introducing multiple cuts along different planes (or axes) of interest to measure the stresses normal to the cut planes (Pagliaro et al., 2010).

The ***curvature method*** is a technique in which deflection (curl-up angle) stemming from residual stress is measured for a bridge-like, thin plate or cantilever structure (Fig. 9.3). A specially shaped part is built on a base plate and later cut off. After removal from the base plate, the part can curl up through an angle which can be measured (Kruth et al., 2010, 2012; Vrancken et al., 2013; Buchbinder et al., 2014; Liang et al., 2020). Simulations are then used to calculate the actual residual stress corresponding to this measured curl-up angle. A major weakness of methods that rely on distortion and localized strain measurement to calculate residual stress is that the stress relaxation does not necessarily release all the stress from the component. As a result, the calculated stress is not necessarily representative of the actual state of stress in the part. Therefore, methods that can profile the residual stress for greater part volume are preferred.

9.2.2 Nondestructive techniques

Nondestructive techniques for residual stress measurement are largely based on diffraction and acoustic principles (see also Chapter 10). Common nondestructive residual stress measurement methods are neutron and X-ray diffraction (XRD). Less

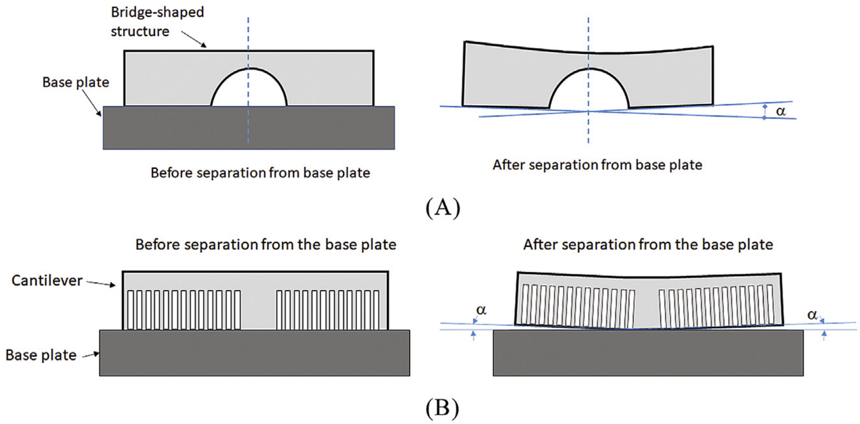
Bridge-shaped structure
Base plate
Before separation from base plate
α
After separation from base plate
(A)
Before separation from the base plate
After separation from the base plate
Cantilever
Base plate
α
α
(B)

Figure 9.3 Measurements of residual stress by curvature method: with bridges (A) and with cantilevers (B). Deformation after separation from the base plate and curl-up angle α are shown.

common methods include synchrotron radiation—based XRD, ultrasonic and electromagnetic techniques. A comprehensive review on ultrasonic testing of residual stress for AM parts was performed recently by Acevedo et al. (2020).

The diffraction methods basically make use of the inter-atomic *d*-spacing as a built-in strain gage. ***Neutron diffraction*** measurement of residual stress depends on strain evaluation through measurement of the change in crystallographic lattice spacing using Bragg's law of diffraction (Fig. 9.4) and utilizing Hooke's laws to calculate the subsurface residual stress. Due to the high penetration power of neutrons, neutron diffraction is capable of measuring volumetric residual stress in thick specimens. When a beam of neutrons impinges on the surface of a stressed material, the atomic planes will diffract the neutrons at a diffraction angle 2θ. The lattice plane spacing is then calculated from employing Bragg's law of constructive interference according to:

$$n\lambda = 2d\sin\theta \tag{9.1}$$

where n and λ represent the order and wavelength of the neutron radiation, respectively, and d is the lattice spacing (Fig. 9.4).

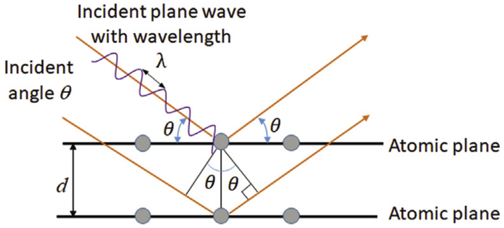
Incident plane wave with wavelength
λ
Incident angle θ
θ
θ
Atomic plane
d
θ
θ
Atomic plane

Figure 9.4 Bragg diffraction.

The residual strain ε can be calculated using Eq. (9.2) based on the change of lattice spacing from the normal spacing (d_0) to a new value (d) when the material is under stress.

$$\varepsilon = \frac{d - d_0}{d_0} \tag{9.2}$$

The strains are converted to stresses by applying Hooke's law with the incorporation of the appropriate constants, that is, the material's modulus of elasticity, Poisson's ratio and the diffraction elastic constants for the *hkl* family of lattice planes.

Unfortunately, neutron diffraction is expensive and time-consuming and facilities are limited. A cheaper, quicker, more accessible and more widely used option for residual stress measurement is the ***X-ray diffraction*** (XRD) method. XRD has a working principle similar to neutron diffraction, except that X-rays have less penetrating power than neutrons. Due to the lower penetration power of X-rays in metal, XRD is limited to surface and near surface stress measurement—for typical laboratory devices. The surfaces to be analyzed must be free from dirt and roughness, so light electropolishing is usually applied (Withers and Bhadeshia, 2001a). Great care must be taken to ensure that no residual stress or plastic deformation is induced during surface preparation.

9.3 Effects and origins of residual stress in L-PBF

The use of a fast-moving laser beam with high power leads to rapid heating, melting, solidifying, and cooling cycles during L-PBF. Large thermal gradients and layer-by-layer manufacturing using powder result in high anisotropic residual stress, specific microstructure (Chapter 8), random porosity (Chapter 6), and limited accuracy of fine structural units of L-PBF parts (Chapters 5, 7, 16). As-built L-PBF materials have anisotropic nonequilibrium microstructure that is a result of high cooling rates and the layer-wise nature of this process. In some materials, the resulting microstructure in combination with high residual stress can lead to cracking during processing (Qiu et al., 2019; Zhang et al., 2020). Some of the common defects associated with residual stress in L-PBF during processing are shown in Fig. 9.5: excessive residual stress leads to macro- and microcracking, deformation, and delamination from the base plate or supports during part manufacturing (Fig. 9.5A−C). When parts delaminate or deform during processing, the structures elevate above the powder bed top surface and come into contact with the recoater, which can cause damage to the parts and the entire deposition system. Even the slightest contact between the part and the recoater can cause the part to flex and then relax, causing the part to act as a spring which moves or shoots powder away from the contact area which leads to defects (Fig. 9.5D).

Where the distortion does not lead to process disruption, more defects are still likely to occur owing to the resultant uneven powder distribution and nonhomogenous powder layers that provoke porosity and dimensional errors (Du Plessis et al., 2018;

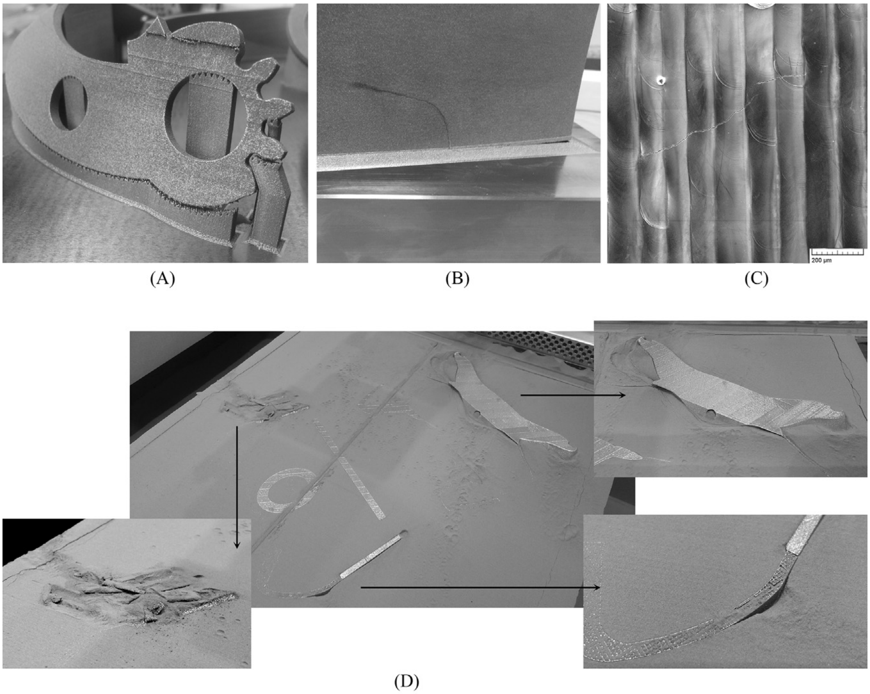

Figure 9.5 Defects in L-PBF parts during manufacturing: (A) delamination from the supports and deformation during processing Ti6Al4V alloy; (B) delamination from the base plate and macrocracking in massive Ti6Al4V solid sample; (C) cracks at the top surface of Ti-Al single layer; (D) general view of redistribution of powder bed during manufacturing: delamination from support and deformation resulting in contact with recoater: deformation of massive part (top image in D) and vibration of fine parts (bottom images).

Bartlett and Li, 2019). Furthermore, if delamination, cracking, or distortions do not occur during processing, as-built L-PBF parts have been known to deform after being removed from the base plate due to residual stress. Residual stress does not only impact the technical capabilities of the L-PBF processes but can severely offset the economic gains that could be associated with AM (see Chapter 22). L-PBF parts have to be heat-treated, machined, etc. in order to reduce residual stress. Inevitably, this additional post-processing results in loss of productive time and hampers the efficient use of manufacturing resources. When the effects of residual stress cause integrity problems such as cracks and these cannot be reversed by post-processing methods, the parts must be taken out of service. To qualify L-PBF as a process of choice for industrial applications that have stringent quality requirements, residual stress needs to be controlled.

The effect of residual stress on dimensional and form deviations has been widely demonstrated in Neugebauer et al. (2014), Yadroitsava and Yadroitsev (2015), and DebRoy et al. (2018). Stress-induced distortion by only a couple of micrometers could be detrimental to the possible industrial application. The fatigue and corrosion behaviors also depend on the nature and values of residual stress (Lu, 2002; Vrancken et al., 2014; Örnek, 2018; Cruz et al., 2020), see Chapters 14 and 15 on structural integrity and fatigue properties. As mentioned earlier, specific microstructure that develops during L-PBF, in cooperation with high stresses, can induce cracking and delamination in the final part (Kempen et al., 2013; DebRoy et al., 2018).

The development of residual stress in L-PBF in terms of heating/cooling cycles (“temperature gradient mechanism”) and shrinkage due to the thermal contraction and elastic-plastic behavior of the material at different temperatures (“cool-down phase model”) was described in (Shiomi et al., 2004; Mercelis and Kruth, 2006). First, the irradiated layers expand due to the heating effect of the laser beam (Fig. 9.6). However, the solid underlying substrate (or a previously processed layer) restricts this expansion resulting in an overall compressive stress-strain condition at the top surface. Then, after the removal of the laser beam, the material tends to cool down and to shrink. Again, this shrinkage is confined by the partial elastic-plastic deformation set up during the heating cycle, leading to an overall tensile stress state in the upper surface of the solidified material.

During L-PBF manufacturing, different process parameters and scanning strategies are used for different areas of the part and the geometry and the shape of the melt pool vary significantly. The temperature gradients and the amount of material involved also vary, which makes residual stress distribution quite complex: its values depend on many factors. Cooling down and solidification commences when the laser beam leaves the irradiated zone (Fig. 9.6). However, the contraction rates of different material areas are not uniform. This leads to nonuniform deformation along the tracks and between layers. The nonuniform contraction means that residual stress and deformations are dependent on the direction of scanning.

One of the first studies of residual stress in L-PBF was carried out by Shiomi et al. (2004) where the highest value of tensile residual stress was found at the top layer of the L-PBF part. Gusarov et al. (2011) showed that tensile stresses in AM depend on the shape of single tracks, and maximum tensile stresses are twice as great in the longitudinal direction than in the transversal direction. Residual stress can be redistributed by the formation of cracks and pores, making the understanding of stress distribution even more complex. Yadroitsev and Yadroitsava (2015) studied residual stress in SS 316L and Ti6Al4V alloys and the residual stress on the top surface of the L-PBF objects was shown to be tensile and the maximum stress was in the scanning direction for all specimens.

Simson et al. (2017) showed the dependence of residual stress on the selected process parameters; the value and orientation of the main stress component depended on the analyzed layer of 316L steel. On the top surface, higher residual stress values were also found in the scan direction. The lateral surface revealed the highest main stress component was parallel to the building direction. These findings support the processes described by the temperature gradient mechanism and cool-down phase model (Fig. 9.6). This study also showed that residual stress values depend on structural density. Fig. 9.7A illustrates FE simulations of the stress of rectangular Ti6Al4V solid blocks, fixed to the base plate, with initially high residual stress. Higher stresses are

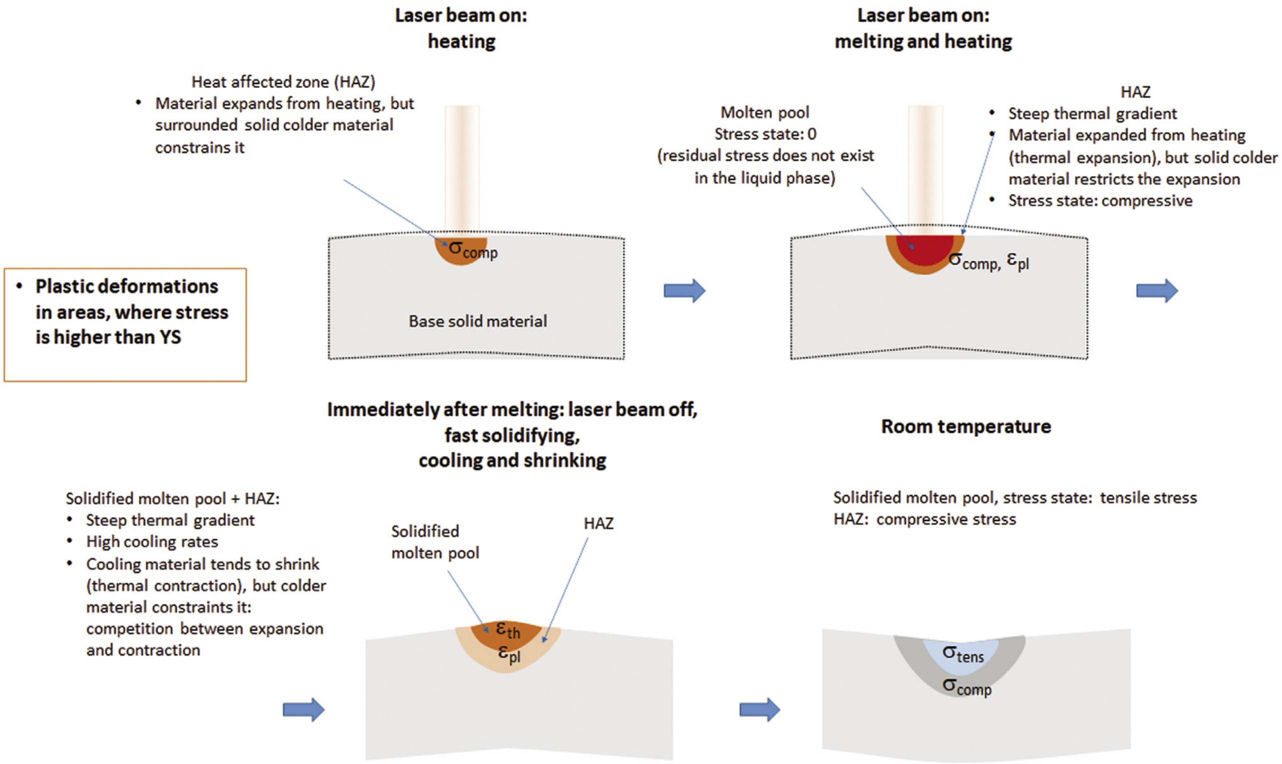
Laser beam on:
heating
Heat affected zone (HAZ)
• Material expands from heating, but surrounded solid colder material constrains it
σ_{comp}
Base solid material
• Plastic deformations in areas, where stress is higher than YS
Laser beam on:
melting and heating
Molten pool
Stress state: 0
(residual stress does not exist in the liquid phase)
HAZ
• Steep thermal gradient
• Material expanded from heating (thermal expansion), but solid colder material restricts the expansion
• Stress state: compressive
σ_{comp}, ε_{pl}
Immediately after melting: laser beam off,
fast solidifying,
cooling and shrinking
Solidified molten pool + HAZ:
• Steep thermal gradient
• High cooling rates
• Cooling material tends to shrink (thermal contraction), but colder material constraints it: competition between expansion and contraction
Solidified molten pool
HAZ
ε_{th}
ε_{pl}
Room temperature
Solidified molten pool, stress state: tensile stress
HAZ: compressive stress
σ_{tens}
σ_{comp}

Figure 9.6 Residual stress development during L-PBF.

found at the bottom, where samples are attached to the base plate. If samples are separated from the base plate during processing, the sample deforms and the residual stress changes from the original configuration. Overhanging parts that have no direct metallurgical contact with the base plate are deformed during processing, thereby redistributing stress significantly (Fig. 9.7B−E).

Numerical simulations have shown that residual stress is geometrically dependent on object shapes as well as building and scanning strategies applied (Nadammal et al., 2017; Parry et al., 2019). Parry et al. (2019) showed that longitudinal stresses (along the scanning direction) have a threshold depending on scan length: it increases linearly up to a critical length of scanning, then they are almost constant. Transverse stresses were more sensitive to the thermal history than longitudinal ones.

Experiments with different shapes of samples were performed in Yadroitsava et al. (2015). Surface residual stress in Ti6Al4V objects of simple geometries (Fig. 9.8) were measured by X-ray diffraction (XRD). Samples were scanned in a stripe pattern in

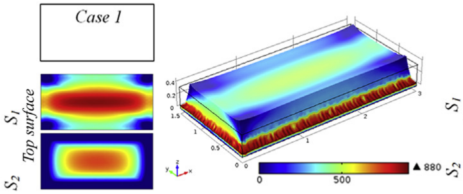

(A) block without defect attached to the substrate

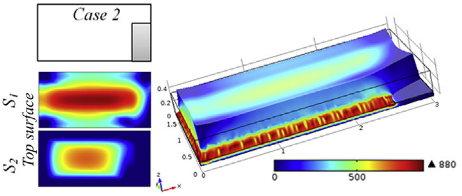

(B) defect along short side of the block

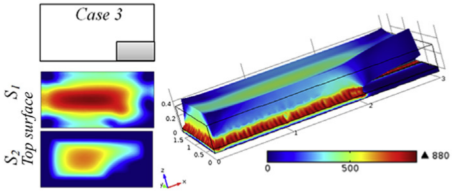

(C) defect along long side of the block

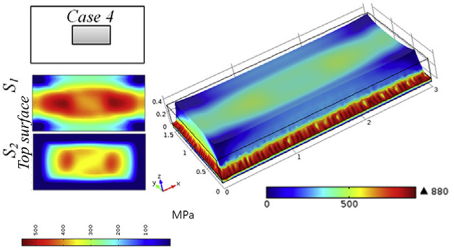

(D) defect in the middle part of the block

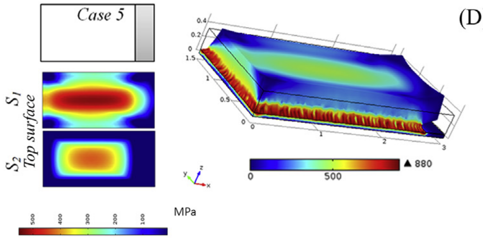

(E) defect along whole short side of the block

Figure 9.7 Residual stress in rectangular Ti6Al4V attached to base plate: solid blocks (A) and blocks with defects—planar regions causing loss of attachment to the baseplate 0.005 mm^3 in size (B−E). Dimensions of the block are 3 mm × 1.5 mm × 0.3 mm (x, y, z), initial stress of solid block are $\boldsymbol{\sigma}_{xx} = 600$ MPa, $\boldsymbol{\sigma}_{yy} = 900$ MPa, $\boldsymbol{\sigma}_{xy} = \boldsymbol{\sigma}_{xz} = 25$ MPa. Scale factor for the deformation is 50 (van Zyl et al., 2016).

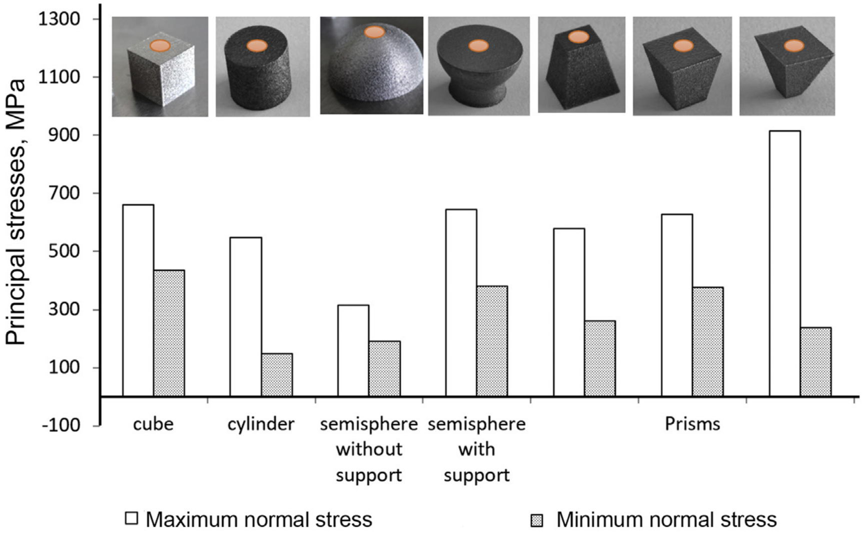

Figure 9.8 Principal stresses near the surface in 3D L-PBF Ti6Al4V objects attached to the substrate: cubes 10 mm × 10 mm × 10 mm without support; cylinder with diameter 10 mm and height 10 mm; semi-spheres without/with supports, diameter 10 mm; prisms: height 10 mm, bottom base 10 mm × 10 mm, top base 6 mm × 6 mm; height 10 mm, bottom base 6 mm × 6 mm, and top base 10 mm × 10 mm; height 10 mm, bottom base 3 mm × 3 mm, and top base 10 mm × 10 mm. Orange (light gray in printed version) points indicate where residual stress was measured.

back-and-forth directions with an EOSINT M280 system. For the semi-sphere without supports, the principal residual stress was lower in comparison with the inverted semi-sphere with supports. In prisms, the maximum residual stress near the top surface was 915 MPa, where the ratio of the top area to the base surface was 100:9. A prism with a lower ratio (100:36) had a lower residual stress of 628 MPa. It is possible that overheating led to higher values of residual stress for a prism with a small cross-section at the bottom, since local overheating is responsible for higher residual stress (Parry et al., 2019).

Salmi et al. (2017) showed that, in general, samples with supports had higher stress than specimens with direct contact with the base plate, mainly due to the different heat transmission modes along the building direction; thus, the thermal gradient was lower for samples without supports. Also, it was found that residual stress exhibited varying (oscillating) behavior with depth (Fig. 9.9A). These variations indicate the nonuniform heat distribution and transfer, and a possible effect of microstructural changes on residual stress distribution. Previously, similar oscillating behavior of residual stress with depth in L-PBF samples was shown in Yadroitsev and Yadroitsava (2015), Fig. 9.9B. Roughness has an influence on the residual stress value, as can be seen in Fig. 9.9B. In SS 316L samples, residual stress was measured at the center near the surface: residual stress was relatively low for the first approximately 100 μm. This correlates with as-built roughness on the top surface that was 70 ± 20 μm. Electrolytic removal of layers was done to measure normal stresses in-depth by XRD.

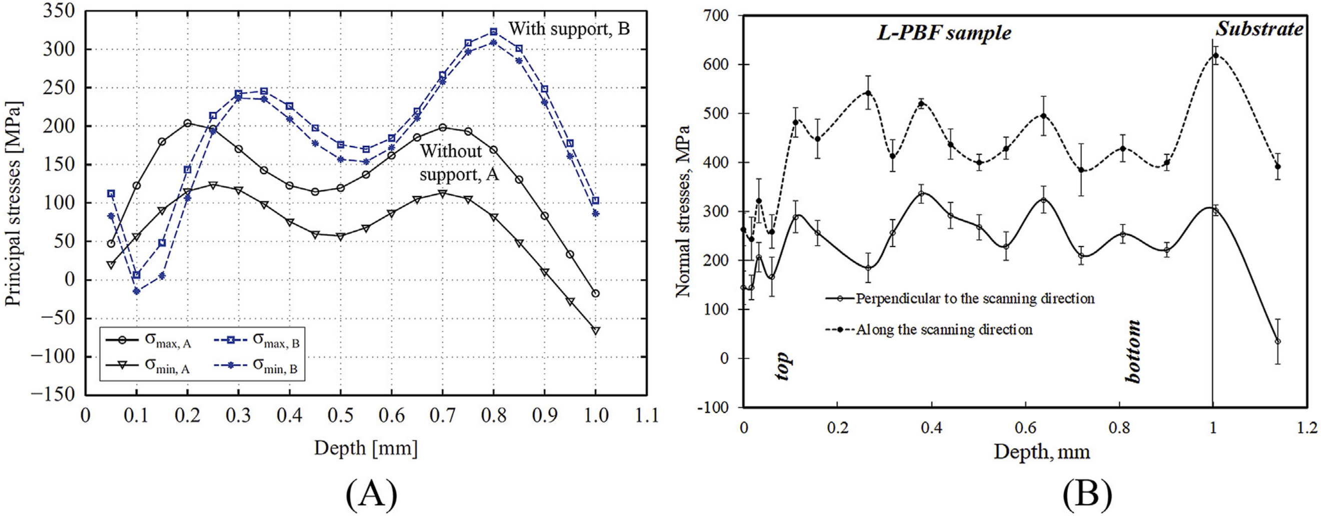

Figure 9.9 (A) Principal stresses in AlSi10Mg parallelepiped 30 mm × 20 mm × 10 mm samples manufactured with stripes scanning strategy with rotation of scanning direction in each layer of 67°; (B) the layer thickness is 30 μm (Salmi et al., 2017), and a profile of the residual stress in cuboid 30 mm × 30 mm × 1 mm SS 316L sample (50 μm layer thickness) produced in one scanning direction that did not change during the manufacturing process.

Based on data from Yadroitsev, I., Yadroitsava, I., 2015. Evaluation of residual stress in stainless steel 316L and Ti6Al4V samples produced by selective laser melting. Virtual Phys. Prototyp. Taylor and Francis Ltd 10 (2), 67−76. https://doi.org/10.1080/17452759.2015.1026045.

Cao et al. (2020) built inclined samples at angles (45°, 60°, and 75° to the horizontal) with and without supports from MS1 steel. It was found that samples without supports had slightly lower residual stress, but in these samples, residual stress was more unevenly distributed on the supporting surface. Generally, in inclined parts, support structures act as heat sinks, contributing to the conduction of heat away from the object, and leading to higher thermal stresses than when no supports are used.

Bayerlein et al. (2018) studied residual stress by performing neutron diffraction measurements for simple cuboid forms of Inconel 718 at different stages of the build-up (i.e., after one 20 μm-layer; at build heights of 4 and 20 mm; and for a fully built-up cuboid of 40 mm in height). High compressive and tensile stresses in three normal directions were found at the edges and around the middle part of the samples. Along the build direction, the stresses generally changed smoothly from tensile near the top surface to compressive stresses closer to the base plate. In addition, it should be noted that at later stages tensile stresses developed along the edges.

The distribution of residual stress is not straightforward and depends on many process conditions and the object's shape. Zhao et al. (2020) found tensile stress near the base plate in as-built L-PBF Ti6Al4V and AlSi10Mg blocks (X × Y × Z of 150 mm × 5 mm × 35 mm built along the Z direction). These blocks, manufactured with reticulated support, also exhibited compressive stress in the middle section and tensile stress at the top section.

Brown et al. (2016) showed differences in residual stress distribution and magnitudes in L-PBF 17-4 steel Charpy samples using neutron diffraction measurements before and after separation from the base plate (Fig. 9.10). It was found that the value of the residual stress was about two-thirds of the yield strength of the material. The largest residual stress in as-built samples was in the longitudinal direction (Fig. 9.10A and B). Sample A and C were built with similar process parameters, but sample A was suddenly separated from the support structure during processing (indicated as "Tear" in Fig. 9.10A, D, and F). The resulting asymmetric stress fields were found not only in the as-built sample A attached to the substrate but also in a separated sample as opposed to a sample C that was manufactured without any defects.

9.4 Modeling of L-PBF process and residual stress evolution

Process modeling and monitoring play important roles in detecting and predicting errors during AM. Modeling the L-PBF process from powder delivery, energy absorption, melting, solidification, and cooling of the melt material up to the initiation of residual stress and evolution of different microstructure is a challenge. Many factors must be considered: the absorption of laser radiation and melting of powder material with randomly distributed particles; thermal properties of the powder, liquid, and solid material; material properties at different temperatures; thermal gradient and cooling rates; microstructural and stress evolution; melt-pool size and geometry, etc. (King et al., 2015; Khairallah et al., 2016). These phenomena define the resulting porosity,

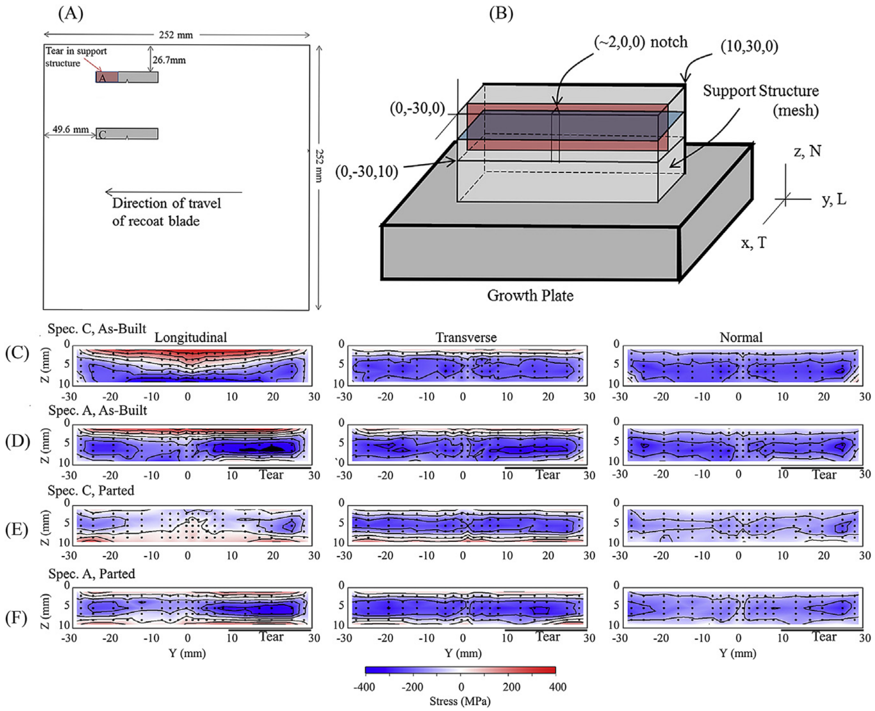

Figure 9.10 (A, B) Schematic of build of Charpy specimens; (C, D) contour plots of longitudinal, transverse, and normal direction stresses, respectively, on a y-z plane (at x = 3.8 mm) in sample C and A, respectively, while still attached to support and base plate; (E, F): similar contour plots after removal from support and base plate.
Modified from Brown, D.W., et al., 2016. Neutron diffraction measurements of residual stress in additively manufactured stainless steel. Mater. Sci. Eng. Elsevier Ltd 678, 291–298. https://doi.org/10.1016/j.msea.2016.09.086.

microstructure, the heat affected zone, and stresses in L-PBF parts. The challenge with microscale models is the effort required, cost, and long computational time. As indicated by DebRoy et al. (2018), residual stress in AM is highly variable in spatial and temporal domains, so high-quality experimental data and accurate numerical simulation are required.

Melt-pool geometry and temperature monitoring and control are essential in managing residual stress in situ. Unfortunately, it is difficult to execute experimental measurements of temperature during L-PBF (Krauss et al., 2012; Li and Gu, 2014), Chapter 11. Limitations of the resolution, lengthy image processing, and cost implications render monitoring of the melt pool very complex. Despite these challenges, machine learning is increasingly being used to study the vast data that can be gathered from camera-based melt-pool monitoring.

It is often convenient to simulate the behavior of manufacturing processes under various conditions, rather than conduct experiments that could be prohibitively expensive. Finite Element Analysis (FEA) is commonly used to predict residual stress and distortions during L-PBF. FEA makes use of mathematical models that incorporate laws of physics and boundary conditions such as material properties to study how processes respond to a set of parameters. In L-PBF, 3D finite element modeling is currently widely used, although 2D elements still find useful applications in residual stress prediction. Wu et al. (2017) used a 2D thermomechanical model to study the melt pool and residual stress characteristics of AlSi10Mg parts by means of FEA and experimental evaluation using X-ray diffraction. Their simulation and experimental results coincided showing compressive stress at the sample's mid-section and tensile stress at the edges.

Luo et al. (2018) introduced a 3D transient thermomechanically coupled finite element model to analyze the temperature and stress fields during L-PBF of SnTe. The predicted and experimental results showed concentration of thermal stress at the ends of the tracks and edges of the formed surface. Li et al. (2018c) showed with 3D thermal-mechanical modeling that the residual stress component in the building direction increases with the number of layers. Lu et al. (2019) combined computer vision and FEA to estimate the stress development within a layer from melt and solid-state surface displacement information.

Since L-PBF typically uses thin material layers, microscale modeling requires highly refined meshes. Researchers can overcome this challenge by simultaneously modeling a group of layers (Afazov et al., 2017).

Moser et al. (2019) developed a continuum thermomechanical model which approximates the powder as a continuous medium with effective material properties to avoid modeling powder particles individually. The results prove the viability of this approach for modeling residual stress. L-PBF specimens produced at similar process parameters can exhibit significant variation of measured residual stress (Georgilas et al., 2020). This can be mainly attributed to differences in specimen geometry, which can drastically change the heat transfer dynamics during manufacturing.

Developments in AM modeling have resulted in mesoscale modeling developed by Li et al. (2017), while Afazov et al. (2017) developed an approach for modeling at the component scale. The results showed that distortion can be successfully compensated for in L-PBF parts inverting the distortions and incorporating them into the target geometry's CAD model.

Jayanath and Achuthan (2019) developed an FEA model which hybridizes the conventional FEA and inherent strain tensor—based models. Boruah et al. (2018) presented an experimentally validated analytical model, which can be used for prediction of residual stress distribution in L-PBF parts. The model is based on the force and moment equilibrium of induced stresses by progressive deposition of material layers. Researchers are also increasingly utilizing machine learning methods such as deep learning (Francis and Bian, 2019) to predict residual stress and distortions from thermal images and local heat transfer information. Recently, Bertini et al. (2019) analyzed simulation strategies in residual stress prediction during L-PBF. This review clearly indicates that at the present stage of L-PBF, mesoscale modeling achieved a significant maturity while macroscale simulations require further efforts.

9.5 Post-processing stress relieving

9.5.1 Heat treatment

It is a common practice in L-PBF to perform stress-relief heat treatment to relieve stresses that have built up during the process. Heat treatment is usually implemented before detaching parts from the base plate to avoid distortion upon separation (Manfredi et al., 2013; Pupo et al., 2013; Sames et al., 2016). Appropriate heat treatment relieves up to 70%–90% of residual stress that is introduced by the L-PBF process (Shiomi et al., 2004; Schneller et al., 2019; Tong et al., 2019). Kreitcberg et al. (2017) indicated that the stress-relieving heat treatment procedure has to be chosen carefully, because for some alloys it can lead to undesirable phenomena, such as carbide precipitation and phase changes, as happens in nickel alloys at 650–870°C stress-relieving temperature, for example.

In some cases, despite the widespread use of heat treatment as a stress-relief technique, the process does not necessarily completely remove tensile residual stress. For example, Salmi et al. (2017) revealed the presence of high tensile stresses on the L-PBF AlSi10Mg, despite performing stress-relieving thermal treatment. A special heat treatment procedure for L-PBF parts must be found and approved, since the structures have a specific microstructure that is different from that of materials obtained by traditional methods. Moreover, this microstructure depends on specific process parameters, scanning and building strategies which make it challenging to find a generic solution (Chapters 12 and 13).

9.5.2 Mechanical treatment

Shot peening is the process of impacting the surface with high-speed shots (by metallic, ceramic or glass beads) to plastically deform the impacted surface and improve the fatigue performance. Maamoun et al. (2018) showed that shot peening of AlSi10Mg samples decreased surface defects, refined microstructure, and had a hardening effect while also introducing a relatively high compressive stress (−170 MPa) up to a 90 μm depth. This method was used also by Salmi and Atzeni (2017) for L-PBF AlSi10Mg samples after stress-relieving heat treatment. It was stated that a combination of optimal heat treatment with shot peening procedure allows the introduction of uniform compression stress into L-PBF samples.

Laser shock peening (LSP) can be applied in AM as a surface modification technique that alters the surface microstructure and mechanical properties (Guo et al., 2018). LSP is quite effective in reducing residual stress magnitudes, and even introducing desirable compressive stresses to the surface (Munther et al., 2020). Laser peening mimics the bulk deformation strengthening mechanisms such as rolling and shot peening. The effectiveness of LSP on surface modification and residual stress control depends on the selection of laser peening processing parameters such as laser energy, shot overlap, laser spot size, laser pulse duration, etc. Kalentics et al. (2017) used the hole drilling technique to investigate the effect of LSP parameters on surface residual stress. The value and depth of the compressive residual stress that was introduced was found to be dependent on the selected LSP parameters. In addition to the residual stress relief and compressive stress that is formed on the surface, the method was shown to close near-surface porosity in Du Plessis et al. (2019), all of which contributes to improved fatigue properties. The cost of LSP prohibits the wide use of this stress-relieving method, but it can be applied to localized high stress areas for critical applications in aerospace, power generation, and nuclear industries (Hackel et al., 2018).

The surface morphology of L-PBF parts is complex because it depends on many factors like powder size and particle shape, material, process parameters, scanning strategies, part orientation, etc. Industrial applications require high surface quality to prevent premature failure of the component that might arise from the initiation of cracks during use. Thus, many L-PBF parts inevitably demand ***machining***, and these machining operations also alter the stress state of the components. For example, surface tensile stress and a subsurface compressive stress induced by the milling operation were observed in L-PBF AlSi10Mg parts (Piscopo et al., 2019). In the research done by Sarkar et al. (2019), about −300 MPa compressive residual stress was found on the machined surface of L-PBF manufactured 15-5PH specimens. The compressive stress and reduced surface roughness induced by machining both led to improved fatigue life.

Ultrasonic impact treatment (UIT), whereby high-frequency ultrasonic oscillations are applied to the component, is used to eliminate tensile stress as well as to introduce compressive stress, to correct deformations and improve fatigue strength of welded structures. UIT is also known as high frequency mechanical impact. UIT was tested on L-PBF parts by Malaki and Ding (2015), Lesyk et al. (2019), and Walker et al. (2019). Lesyk et al. (2019) applied this technique on Inconel 718 turbine blade test parts manufactured by L-PBF. In that study, the tensile stress (+120 MPa) observed for the as-built condition was transformed into a compressive stress (about −430 MPa) after application of UIT. The surface roughness, microhardness, and near-surface porosity were also improved. Additionally, Walker et al. (2019) showed that UIT enhances the fatigue life of L-PBF-manufactured Ti6Al4V parts by 200%, while significantly improving the surface integrity and introducing compressive stress into the components. Zhang et al. (2016) showed that the application of UIT during L-PBF reduces defects and residual stress, and obtains fine equi-axed grains. However, ultrasound waves can lead to powder entrapment near edges, which leads to reduced accuracy and high defectiveness of the side surfaces of the final product. UIT-induced smoothness of the surface of the processed layer also leads to problems with powder delivery for the next layer.

Many of the post-process interventions for controlling residual stress are quite effective, but they are incapable of reversing stress-induced deformations. Furthermore, post-processing substantially increases both manufacturing time and cost (Jayanath and Achuthan, 2019).

9.6 In situ stress relief

The most popular in situ stress relief method is in situ thermal gradient management, which includes preheating of the substrate or powder bed, modification of scanning strategies and process parameters, i.e., control of temperature gradients and cooling rates. Another in situ stress relief method is in situ mechanical impact that introduces compressive stress (since L-PBF generates high tensile stresses) by LSP or machining during manufacturing, so called "hybrid AM."

9.6.1 Base plate and build chamber preheating

Residual stress is a function of thermal gradients brought about by the huge temperature difference between the melt pool and the "cold" surrounding material, i.e., powder and substrate (Fig. 9.6). Preheating reduces this temperature difference and thus reduces thermal stresses. A study conducted by Shiomi et al. (2004) on chrome molybdenum steel demonstrated a 40% reduction of residual stress with the application of base plate preheating. Kempen et al. (2013) applied base plate preheating during the manufacturing of parts from M2 medium alloyed steel and managed to progressively reduce stress-induced cracking and delamination. Furumoto et al. (2010) achieved 80% residual stress reduction for an in situ alloyed mixture of chromium molybdenum steel, copper and nickel alloys by preheating the base plate. Reduction in residual stress was also reported in the work done by Kemerling et al. (2018) with 304L stainless steel after raising the preheating temperature to 250°C. It was shown that *Z*-directional stresses are a function of the preheating temperature. Mertens et al. (2018) demonstrated that the effect of base plate preheating on residual stress and the stress-induced cracking does not follow the same trend for different materials (aluminum 7075 alloy, nickel alloy Hastelloy X, H13 tool steel, and cobalt-chrome).

Zhang et al. (2013) implemented powder bed preheating up to 150°C to prevent deformation and to improve the dimensional accuracy of 316L stainless steel tensile test specimens. The effectiveness of powder preheating on residual stress was demonstrated by Roberts (2012) who achieved up to 50% residual stress reduction in Ti6Al4V specimens by increasing the powder bed temperature from 40 to 300°C. In another study, Ali et al. (2017) reported a reduction of residual stress from 214 to 1 MPa by raising the powder bed temperature from 100 to 570°C for Ti6Al4V.

A study by Malý et al. (2019) revealed the possibility of increased oxidation and particle agglomeration as a result of powder preheating. These findings clearly indicate that when preheated to high temperatures, powder reuse may not be suitable for the manufacture of mechanically strong parts, since higher oxygen and nitrogen contents are known to promote embrittlement in Ti6Al4V alloy and could lead to part failure (Tal-Gutelmacher and Eliezer, 2005; Yan et al., 2014).

It must be noted that powder preheating can be achieved by keeping the build chamber at an elevated temperature, but this temperature must be lower than the powder sintering temperature, since it influences the L-PBF process (Yadroitsev et al., 2013). Preheating either the base plate or powder bed does not only affect the stress state of materials but can also influence the achievable density (Mertens et al., 2018), microstructure (Yadroitsev et al., 2013; Li et al., 2016b; Mertens et al., 2018), and mechanical properties (Li et al., 2016b). An important aspect is the presence of a module for preheating chamber/base plate with high temperatures in commercial L-PBF systems. Such solutions require special optics, materials, special machine design, special safety measures, etc. Basically, all studies with the preheating of the substrate and powder are carried out in unique systems and experimental setups.

9.6.2 Process parameter optimization

The effect of process parameters, such as laser power, layer thickness, scanning speed, and hatch distance, on residual stress in L-PBF parts has been studied in Levkulich et al. (2019), Mugwagwa et al. (2018), and Vrancken (2016). Levkulich et al. (2019) investigated the effect of laser power and scanning speed on residual stress in L-PBF Ti6Al4V parts by X-ray diffraction, hole drilling, and contour methods. The results showed that residual stress near the surface decreased with increasing laser power and decreasing scanning speed: larger melt pools promote slower cooling rates and, therefore, lead to reductions in residual stress in metals. Thus, selecting high laser power and low scanning speeds can achieve residual stress reduction while maintaining acceptable part density.

However, a blanket adjustment of process parameters throughout the component's geometry may not be ideal. Depending on part geometry, parameters such as the scanning strategy may need to be adjusted from layer to layer (Meier and Haberland, 2008). Ali et al. (2019) established that residual stress can be managed by in situ temporary adjustment of the powder layer thickness. In their study, residual stress was reduced by 8.5% by increasing the layer thickness in areas with the predetermined high-stress zones for a given geometry. From another perspective, in order to produce nonporous parts with thicker layers, more energy must be introduced to remelt the thicker powder layer and previously melted layer. The effect of layer thickness on residual stress was also investigated by measuring the deformation of bridge-shaped specimens (Kruth et al., 2012) and cantilever specimens (Zaeh and Branner, 2010; Mugwagwa et al., 2018). All these works indicate a decrease in deformation by increasing the layer thickness. Gao et al. (2018) also stated that increasing the layer thickness reduces the cooling rate and effectively lowers residual stress. Ali et al. (2018) showed that the decreased cooling rate of 40% caused by increasing the layer thickness from 25 to 75 μm was the primary reason for the reduction in deformation and residual stress. While increasing the layer thickness lowers residual stress, it was also shown that increasing the layer thickness has a tendency to increase interlayer defects and percentage porosity, thereby compromising the mechanical properties (Ali et al., 2018; Du Plessis, 2019).

In summary, there must be a reasonable "compromise" between reducing residual stress by increasing/decreasing power, scanning speed or hatch distance, or changing powder layer thickness or spot size to produce fully dense parts with the required accuracy, without cracks and distortions.

9.6.3 Scanning strategy and in situ residual stress control

Scanning strategies influence several process outcomes including residual stress, achievable density, microstructure, and surface finish. Wang et al. (2018) indicated that a combination of scanning strategy and preheating temperature influences the residual stress direction, values, and distribution; residual stress and grain microstructure are closely related and thus influence the performance of L-PBF parts. Thermal stresses can be partially overcome by scanning strategy adjustment to improve uniformity of heating and shrinkage (Beal et al., 2008; Jhabvala et al., 2010).

One of the specific methods proposed to decrease thermal gradients is the "chess board strategy." This scanning strategy uses short scan tracks by dividing the scanning area into smaller randomly scanned subsections (usually 5 mm × 5 mm) (Yasa et al., 2009; Kruth et al., 2010, 2012; Carter et al., 2014) and is similar to the island scanning strategy. Kruth et al. (2004) and Li et al., 2016a showed that the shorter scan track strategies yield lower stresses and distortions compared to strategies that employ longer tracks. However, Parry et al. (2016) demonstrated the geometric effect of scanning strategies on the build-up of residual stress, with indications of overheating where scan tracks become excessively short. Song et al. (2018) corroborated these results, both numerically and experimentally. Ganeriwala et al. (2019) measured residual stress with X-ray diffraction in Ti6Al4V bridges and revealed higher residual stress, especially near the boundaries of the bridges that were built using island strategies in comparison with parts built with continuous zig-zag scans. Chen et al. (2019) also studied the effect of overlap rate on residual stress in L-PBF of Ti6Al4V, and it was observed that overlap rates of 25%–50% between islands (by using the island scanning strategy) led to reduction of residual stress due to rescanning effects introduced during the overlap. However, with an increase in the overlap rate, there is an accompanying long scanning track and a weakened preheating effect on the next island, leading to higher thermal gradients and stresses. The paintbrush or stripe strategy was developed also with the aim of reducing thermal stresses by shortening the scan tracks. The common practice resulting in more isotropic stress distribution is to rotate the scanning direction between successive layers (Kempen, 2015; Li et al., 2018a).

Rescanning is an approach whereby the laser beam passes over the powder layer more than once on the same layer. Most of the studies on rescanning adopt the same process parameters as those used to melt the powder in the first pass. Wei et al. (2019) investigated rescanning in L-PBF of a Ti-5Al-2.5Sn alloy. In that study, rescanning once did not yield any reduction in residual stress. In fact, rescanning induced an increase in the maximum principal stress from 478 ± 33 to 562 ± 14 MPa. However, applying a second rescan lowered the maximum stress to 288 ± 47 MPa, representing a reduction of approximately 39%. In similar work on Ti6Al4V by Xiao et al. (2020), rescanning up to four times was performed to study the effect of rescanning cycles on density and residual stress. Small cuboid parts were manufactured with dimensions of 15 mm × 15 mm × 5 mm. Excessive heating resulted in slightly higher porosity of samples that were rescanned four times for each layer, but in general, all relative densities were near 99%. The residual stress in samples that were not rescanned was about 450 MPa. After one-cycle rescanning, it increased to about 620 MPa and then decreased on subsequent rescans, albeit nonuniformly, reaching approximately 400 MPa at the fourth rescan cycle. Effectively, this represents only about 11% stress reduction as a result of applying four rescans.

Shiomi et al. (2004) reported that rescanning every layer at the same process parameters reduced residual stress by up to 55%. Mercelis and Kruth (2006) observed a 30%

residual stress reduction in 316L stainless steel parts when implementing rescanning at 50% of the initial pass laser power. The application of rescanning does not only lower residual stress but also significantly reduces top surface roughness (Yu et al., 2019), refines/modifies the microstructure (Wei et al., 2019), and increases density (Yu et al., 2019) of L-PBF manufactured parts. A major setback with rescanning is the increase in manufacturing time and possible structural changes in material subjected to multiple heating/cooling cycles. Obviously, this increase in manufacturing time is directly proportional to the actual number of rescanning treatments performed.

Instead of using single or dual lasers, multiple-beam laser systems are becoming available for use in L-PBF. The multiple-beam strategies are a promising instrument for residual stress reduction during L-PBF processing, since multiple laser passes promote more uniform temperature distribution and reduce the cooling speeds within and around the melt pool (Heeling and Wegener, 2018). This can ultimately reduce thermal gradients and the associated stresses. Roehling et al. (2019) utilized multiple diodes to homogeneously illuminate the surface of the manufactured part, yielding a 90% reduction of residual stress magnitude. Their study also revealed that meaningful reduction in residual stress is only achievable when the diode power density generates sufficiently high temperature—called critical temperature—to achieve the annealing (in this case approximately 625°C, attained using 840 W diode power).

However, any scanning strategy adjustment must take into consideration the part geometry that is being processed. Scanning strategies that are suitable for wide areas (for example, chessboard strategies) may not be applicable for the fabrication of thin walls. Meier and Haberland (2008) pointed out that scanning strategies should be optimized for different geometries, and that they should even be altered layer by layer in order to accommodate changes in the geometry. The three-axis scanning systems in modern L-PBF machines allow manipulation of the scanning strategy parameters for every layer as needed. For example, it is possible to change the scanning strategy as well as the laser power, scanning speed, and spot size for a specific layer.

9.6.4 Optimization of support structures

During the manufacture of overhanging features, support structures are usually required. Designs and orientations that minimize the volume of supports are preferred, as they reduce residual stress magnitudes (Cheng and To, 2019). Töppel et al. (2016) showed that the type of support structure influences both heat dissipation and residual stress.

L-PBF has enabled freedom of design such that certain topological features of components can be optimized to not only reduce weight, but to enhance product performance through avoiding residual stress in pre-processing. On the one hand, optimization of support structures is used to avoid overheating; on the other hand, to prevent deformation of manufactured parts. Engineers can now design against distortion by utilizing the strengths of topology optimization and modeling. Allaire and Bogosel (2018) presented mathematical models in which supports were optimized to improve the stiffness of the supported structure, as well as optimizing the cooling during manufacturing. Cheng et al. (2019) used the topology optimization technique to design support structures with the aim of preventing residual stress-induced failure. The optimized lattice support structure resulted in approximately 70% less stress-induced distortion compared to uniform lattice and toothed supports.

9.6.5 Optimization of alloy composition

Microcracking in L-PBF requires special attention. Xu et al. (2020) recently studied L-PBF of 2xxx series Al—Cu—Mg—Li—Zr alloys and showed that cracks developed during cooling were linked with specific microstructure that was composed of long columnar grains. High cooling and solidification rates lead to high stress perpendicular to dendritic structure and hot cracking occurs.

The probability of solidification cracks increases with the range of solidification temperature of alloys because it is directly linked with solidification strain. To prevent the formation and propagation of hot cracks, modification in the chemical composition of the alloy by the addition of special elements that increase ductility and tensile strength in the solidification range as well as fine microstructure was used by Montero Sistiaga et al. (2016), Wang et al. (2019), and Xu et al. (2020).

To increase thermal shock resistance of AM nickel alloys, Harrison et al. (2015) proposed a minority increase in concentration of substitutional solid-solution-strengthening atoms within the lattice that increases ultimate tensile strength and yield stress at elevated temperature, thereby suppressing crack formation. Thus, there is need for the development of special alloys that take into account the specifics of high temperature gradients, cooling rates, and solidification, as well as internal stresses for L-PBF.

9.7 Conclusions

Recently, Schmeiser et al. (2020) studied stress formation in L-PBF by in situ X-ray diffraction. It was found that stress states in L-PBF specimens changed continuously up until the last laser beam exposure. Thus, different materials, process parameters, and building strategies, as well as geometry, are influencing factors on spatial distribution and values of residual stress in L-PBF objects. Analysis of studies in the field of residual stresses shows the multidirectional research and the lack of a unified approach. Outstanding capabilities of L-PBF allow working not only with different materials but also with different shapes and sizes of parts produced with different systems, which significantly complicates the task. L-PBF parts are produced with different process parameters, scanning strategies, and environmental parameters. For investigations, substrates with different geometries and initial stresses are used, as well as various support structures for parts. Comprehensive reviews on residual stress modeling and control and its effects on performance of L-PBF parts can be found in Bartlett and Li (2019), Azarmi and Sevostianov (2020), and Fang et al. (2020). Control of residual stress cannot be separated from the study of material properties, which have been shown to be closely related to the L-PBF microstructure (Li et al., 2018b) and porosity (Mugwagwa et al., 2018; Georgilas et al., 2020).

Residual stress in L-PBF is a result of nonuniform cooling and solidification and steep thermal gradients. Three main methods for residual stress control are evident—these are pre-process, in situ and post-processing techniques. Pre-process methods include careful process parameter selection and optimization, as well as predictive and corrective numerical modeling. During the process planning stage, it is vital to understand the thermomechanical behavior of the material being processed. The major in situ methods of managing residual stress are process parameter adjustment, scanning strategy optimization, feedback control, and preheating. Post-processing methods are either thermal (heat treatment) or mechanical (peening, machining, etc.) processing.

In this chapter, the residual stress arising in L-PBF, the reasons for its occurrence, and the methods for reducing it were presented. The choice of residual stress relief techniques does not only influence the final stress state of end products but also significantly affects manufacturing viability with regard to time and cost. The following conclusions can be made:

- Process parameters, such as laser power, scanning speed, layer thickness, preheating, scanning strategies, material, and geometry of the object, have an influence on the melt-pool geometry, cooling rates, and thermal gradients, as well as the resulting residual stress in L-PBF parts. Further analysis of the relationship between residual stress and these factors, as well as new materials developed specifically for L-PBF, are required.
- L-PBF is a complex thermal process, and, therefore, in situ monitoring and control is necessary. Melt-pool monitoring and temperature measurements during L-PBF generate big data that can be used for machine-learning-based residual stress control. However, it is also beneficial to couple process monitoring with feedback control in order to implement corrective action in situ.
- Numerical modeling for the prediction of residual stress remains a powerful tool during the process planning stage where suitable process parameters and scanning strategy can be selected based on predicted behavior of L-PBF parts during manufacturing.
- Control over homogeneity of heating and cooling is critical in managing residual stress. Careful selection and adjustment of scanning strategies can achieve uniform solidification and heat distribution, thereby reducing residual stress. Additionally, managing cooling rates is a major step toward residual stress control. Both scanning strategies and process parameters can be manipulated to achieve this.
- Currently, the most widely used residual stress management approach so far lies in base plate preheating and post-process heat treatment. Although powder preheating has been reported, limited studies have been performed on how this could affect surrounding powder.
- New approaches, such as exposing a processed layer to intense light and heat (rather than rescanning), have the potential to unlock new ways of in situ residual stress control. The use of laser diodes for this purpose has commenced.

9.8 Questions

- What is residual stress?
- How can residual stress in a polycrystalline material be categorized according to length scales?
- What methods of residual stress measurement exist? Explain main principles of these methods.

- How does residual stress influence mechanical properties of components?
- What defects are associated with residual stress in L-PBF?
- Explain the origin of residual stresses during L-PBF.
- Explain the development of residual stress in L-PBF in terms of heating/cooling cycles.
- Why does residual stress depend on process parameters?
- Why does residual stress depend on scanning strategy?
- How do support structures affect the development of residual stresses in L-PBF?
- How can one decrease/remove the residual stress in-situ?
- Why is preheating an effective method for reducing residual stresses?
- What mechanical methods exist to relieve residual stress in L-PBF parts?

Acknowledgments

The authors would like to thank the South African Research Chairs Initiative of the Department of Science and Technology and National Research Foundation of South Africa (Grant No. 97994).

References

Acevedo, R., et al., 2020. Residual stress analysis of additive manufacturing of metallic parts using ultrasonic waves: state of the art review. J. Mater. Res. Technol. 9 (7), 9457−9477. https://doi.org/10.1016/j.jmrt.2020.05.092.

Afazov, S., et al., 2017. Distortion prediction and compensation in selective laser melting. Addit. Manuf. 17, 15−22. https://doi.org/10.1016/j.addma.2017.07.005. Elsevier B.V.

Ahmad, B., et al., 2018. Residual stress evaluation in selective-laser-melting additively manufactured titanium (Ti-6Al-4V) and inconel 718 using the contour method and numerical simulation. Addit. Manuf. 22, 571−582. https://doi.org/10.1016/j.addma.2018.06.002. Elsevier B.V.

Ali, H., et al., 2017. In-situ residual stress reduction, martensitic decomposition and mechanical properties enhancement through high temperature powder bed pre-heating of selective laser melted Ti6Al4V. Mater. Sci. Eng. A 695, 211−220. https://doi.org/10.1016/j.msea.2017.04.033.

Ali, H., et al., 2019. Effect of pre-emptive in situ parameter modification on residual stress distributions within selective laser-melted Ti6Al4V components. Int. J. Adv. Manuf. Technol. 103 (9−12), 4467−4479. https://doi.org/10.1007/s00170-019-03860-6.

Ali, H., Ghadbeigi, H., Mumtaz, K., 2018. Processing parameter effects on residual stress and mechanical properties of selective laser melted Ti6Al4V. J. Mater. Eng. Perform. 27 (8), 4059−4068. https://doi.org/10.1007/s11665-018-3477-5. Springer US.

Allaire, G., Bogosel, B., 2018. Optimizing supports for additive manufacturing. Struct. Multidiscip. Optim. 58 (6), 2493−2515. https://doi.org/10.1007/s00158-018-2125-x.

Azarmi, F., Sevostianov, I., 2020. Evaluation of the residual stresses in metallic materials produced by additive manufacturing technology: effect of microstructure. Curr. Opin. Chem. Eng. 21−27. https://doi.org/10.1016/j.coche.2019.12.004. Elsevier Ltd.

Bartlett, J.L., Li, X., 2019. An overview of residual stresses in metal powder bed fusion. Addit. Manuf. 131−149. https://doi.org/10.1016/j.addma.2019.02.020. Elsevier B.V.

Bayerlein, F., et al., 2018. Transient development of residual stresses in laser beam melting − a neutron diffraction study. Addit. Manuf. 24, 587−594. https://doi.org/10.1016/j.addma.2018.10.024. Elsevier.

Beal, V.E., et al., 2008. Scanning strategies and spacing effect on laser fusion of H13 tool steel powder using high power Nd:YAG pulsed laser. Int. J. Prod. Res. 46 (1), 217−232. https://doi.org/10.1080/00207540500168279.

Bertini, L., et al., 2019. Residual stress prediction in selective laser melting: a critical review of simulation strategies. Int. J. Adv. Manuf. Technol. 105 (1−4), 609−636. https://doi.org/10.1007/s00170-019-04091-5. Springer London.

Boruah, D., Zhang, X., Doré, M., 2018. An analytical method for predicting residual stress distribution in selective laser melted/sintered alloys. In: Materials Research Proceedings. Materials Research Form LLC, Leuven, pp. 283−288. https://doi.org/10.21741/9781945291890-45.

Brown, D.W., et al., 2016. Neutron diffraction measurements of residual stress in additively manufactured stainless steel. Mater. Sci. Eng. A 678, 291−298. https://doi.org/10.1016/j.msea.2016.09.086. Elsevier Ltd.

Buchbinder, D., et al., 2014. Investigation on reducing distortion by preheating during manufacture of aluminum components using selective laser melting. J. Laser Appl. 26 (1), 012004. https://doi.org/10.2351/1.4828755. Laser Institute of America.

Cao, Q., et al., 2020. The effect of support structures on maraging steel MS1 parts fabricated by selective laser melting at different building angles. Rapid Prototyp. J. https://doi.org/10.1108/RPJ-11-2019-0287. Emerald Group Publishing Ltd.

Carter, L.N., et al., 2014. The influence of the laser scan strategy on grain structure and cracking behaviour in SLM powder-bed fabricated nickel superalloy. J. Alloys Compd. 615, 338−347. https://doi.org/10.1016/j.jallcom.2014.06.172.

Chen, C., et al., 2019. Effect of overlap rate and pattern on residual stress in selective laser melting. Int. J. Mach. Tool Manuf. 145, 103433. https://doi.org/10.1016/j.ijmachtools.2019.103433. Elsevier Ltd.

Cheng, L., et al., 2019. On utilizing topology optimization to design support structure to prevent residual stress induced build failure in laser powder bed metal additive manufacturing. Addit. Manuf. 27, 290−304. https://doi.org/10.1016/j.addma.2019.03.001. Elsevier.

Cheng, L., To, A., 2019. Part-scale build orientation optimization for minimizing residual stress and support volume for metal additive manufacturing: theory and experimental validation. Comput. Aided Des. 113, 1−23. https://doi.org/10.1016/j.cad.2019.03.004. Elsevier Ltd.

Cruz, V., et al., 2020. Electrochemical studies on the effect of residual stress on the corrosion of 316L manufactured by selective laser melting. Corros. Sci. 164, 108314. https://doi.org/10.1016/j.corsci.2019.108314. Elsevier Ltd.

DebRoy, T., et al., 2018. Additive manufacturing of metallic components − process, structure and properties. Prog. Mater. Sci. 112−224. https://doi.org/10.1016/j.pmatsci.2017.10.001. Elsevier Ltd.

Du Plessis, A., 2019. Effects of process parameters on porosity in laser powder bed fusion revealed by X-ray tomography. Addit. Manuf. 30, 100871. https://doi.org/10.1016/j.addma.2019.100871.

Du Plessis, A., et al., 2018. X-ray microcomputed tomography in additive manufacturing: a review of the current technology and applications. 3D Print. Addit. Manuf. 5 (3), 227−247. https://doi.org/10.1089/3dp.2018.0060. Mary Ann Liebert Inc.

Du Plessis, A., et al., 2019. Pore closure effect of laser shock peening of additively manufactured AlSi10Mg. 3D Print. Addit. Manuf. 6 (5), 245−252. https://doi.org/10.1089/3dp.2019.0064.

Fang, Z.C., et al., 2020. Review on residual stress in selective laser melting additive manufacturing of alloy parts. Optic Laser. Technol. 106283. https://doi.org/10.1016/j.optlastec.2020.106283. Elsevier Ltd.

Francis, J., Bian, L., 2019. Deep learning for distortion prediction in laser-based additive manufacturing using big data. Manuf. Lett. 20, 10−14. https://doi.org/10.1016/j.mfglet.2019.02.001. Society of Manufacturing Engineers (SME).

Furumoto, T., et al., 2010. Study on reduction of residual stress induced during rapid tooling process: influence of heating conditions on residual stress. Key Eng. Mater. 447−448, 785−789. https://doi.org/10.4028/www.scientific.net/KEM.447-448.785.

Ganeriwala, R.K., et al., 2019. Evaluation of a thermomechanical model for prediction of residual stress during laser powder bed fusion of Ti-6Al-4V. Addit. Manuf. 27, 489−502. https://doi.org/10.1016/j.addma.2019.03.034. Elsevier B.V.

Gao, P., et al., 2018. Influence of layer thickness on microstructure and mechanical properties of selective laser melted Ti-5Al-2.5Sn alloy. Jinshu Xuebao/Acta Metall. Sinica 54 (7), 999−1009. https://doi.org/10.11900/0412.1961.2017.00384.

Georgilas, K., Khan, R.H.U., Kartal, M.E., 2020. The influence of pulsed laser powder bed fusion process parameters on Inconel 718 material properties. Mater. Sci. Eng. A 769, 138527. https://doi.org/10.1016/j.msea.2019.138527. Elsevier B.V.

Guo, W., et al., 2018. Laser shock peening of laser additive manufactured Ti6Al4V titanium alloy. Surf. Coating. Technol. 349, 503−510. https://doi.org/10.1016/j.surfcoat.2018.06.020.

Gusarov, A.V., Pavlov, M., Smurov, I., 2011. Residual stresses at laser surface remelting and additive manufacturing. Phys. Procedia 12 (PART 1), 248−254. https://doi.org/10.1016/j.phpro.2011.03.032.

Hackel, L., et al., 2018. Laser peening: a tool for additive manufacturing post-processing. Addit. Manuf. 24, 67−75. https://doi.org/10.1016/j.addma.2018.09.013. Elsevier B.V.

Harrison, N.J., Todd, I., Mumtaz, K., 2015. Reduction of micro-cracking in nickel superalloys processed by Selective Laser Melting: a fundamental alloy design approach. Acta Mater. 94, 59−68. https://doi.org/10.1016/j.actamat.2015.04.035. Elsevier Ltd.

Heeling, T., Wegener, K., 2018. The effect of multi-beam strategies on selective laser melting of stainless steel 316L. Addit. Manuf. 22, 334−342. https://doi.org/10.1016/j.addma.2018.05.026. Elsevier.

Jayanath, S., Achuthan, A., 2019. A computationally efficient hybrid model for simulating the additive manufacturing process of metals. Int. J. Mech. Sci. 160, 255−269. https://doi.org/10.1016/j.ijmecsci.2019.06.007. Elsevier Ltd.

Jhabvala, J., et al., 2010. On the effect of scanning strategies in the selective laser melting process. Virtual Phys. Prototyp. 5 (2), 99−109. https://doi.org/10.1080/17452751003688368.

Kalentics, N., et al., 2017. Tailoring residual stress profile of selective laser melted parts by laser shock peening. Addit. Manuf. 16, 90−97. https://doi.org/10.1016/j.addma.2017.05.008.

Kemerling, B., et al., 2018. Residual stress evaluation of components produced via direct metal laser sintering. Weld. World 62 (3), 663−674. https://doi.org/10.1007/s40194-018-0572-z.

Kempen, K., et al., 2013. Lowering thermal gradients in selective laser melting by pre-heating the baseplate. In: Solid Freeform Fabrication Symposium. Austin.

Kempen, K., 2015. Expanding the Materials Palette for Selective Laser Melting of Metals. PhD thesis. KU Leuven.

Khairallah, S.A., et al., 2016. Laser powder-bed fusion additive manufacturing: physics of complex melt flow and formation mechanisms of pores, spatter, and denudation zones. Acta Mater. 108, 36−45. https://doi.org/10.1016/j.actamat.2016.02.014. Elsevier Ltd.

King, W.E., et al., 2015. Laser powder bed fusion additive manufacturing of metals; physics, computational, and materials challenges. Appl. Phys. Rev. 2 (4), 041304. https://doi.org/10.1063/1.4937809.

Knowles, C., Becker, T., Tait, R., 2012. Residual stress measurements and structural integrity implications for selective laser melted Ti-6Al-4V. S. Afr. J. Ind. Eng. 23 (3), 119−129. https://doi.org/10.7166/23-3-515.

Krauss, H., Eschey, C., Zaeh, M.F., 2012. Thermography for monitoring the selective laser melting process. In: Solid Freeform Fabrication Symposium. Austin, pp. 999−1014.

Kreitcberg, A., Brailovski, V., Turenne, S., 2017. Effect of heat treatment and hot isostatic pressing on the microstructure and mechanical properties of Inconel 625 alloy processed by laser powder bed fusion. Mater. Sci. Eng. A 689 (February), 1−10. https://doi.org/10.1016/j.msea.2017.02.038. Elsevier B.V.

Kruth, J.-P., et al., 2012. Assessing and comparing influencing factors of residual stresses in selective laser melting using a novel analysis method. Proc. Inst. Mech. Eng., B J. Eng. Manuf. 226 (6), 980−991. https://doi.org/10.1177/0954405412437085.

Kruth, J., et al., 2010. Part and material properties in selective laser melting of metals. In: 16th International Symposium on Electromachining, pp. 1−12.

Kruth, J.P., et al., 2004. Selective laser melting of iron-based powder. Journal of Materials Processing Technology 616−622. https://doi.org/10.1016/j.jmatprotec.2003.11.051. Elsevier.

Lesyk, D.A., et al., 2019. Post-processing of the Inconel 718 alloy parts fabricated by selective laser melting: effects of mechanical surface treatments on surface topography, porosity, hardness and residual stress. Surf. Coating. Technol. 381, 125136. https://doi.org/10.1016/J.SURFCOAT.2019.125136. Elsevier.

Levkulich, N.C., et al., 2019. The effect of process parameters on residual stress evolution and distortion in the laser powder bed fusion of Ti-6Al-4V. Addit. Manuf. 28 (May), 475−484. https://doi.org/10.1016/j.addma.2019.05.015. Elsevier.

Li, C., et al., 2016a. A multiscale modeling approach for fast prediction of part distortion in selective laser melting. J. Mater. Process. Technol. 229, 703−712. https://doi.org/10.1016/j.jmatprotec.2015.10.022.

Li, C., et al., 2017. Efficient predictive model of part distortion and residual stress in selective laser melting. Addit. Manuf. 17, 157−168. https://doi.org/10.1016/j.addma.2017.08.014.

Li, C., Guo, Y., et al., 2018a. A scalable predictive model and validation for residual stress and distortion in selective laser melting. CIRP Ann. Manuf. Technol. 67, 249−252. https://doi.org/10.1016/j.cirp.2018.04.105.

Li, C., Liu, Z.Y., et al., 2018b. Residual stress in metal additive manufacturing. Procedia CIRP 71, 348−353. https://doi.org/10.1016/j.procir.2018.05.039.

Li, W., et al., 2016b. Effect of substrate preheating on the texture, phase and nanohardness of a Ti-45Al-2Cr-5Nb alloy processed by selective laser melting. Scripta Mater. 118, 13−18. https://doi.org/10.1016/j.scriptamat.2016.02.022. Elsevier Ltd.

Li, Y., et al., 2018c. Modeling temperature and residual stress fields in selective laser melting. Int. J. Mech. Sci. 136, 24−35. https://doi.org/10.1016/j.ijmecsci.2017.12.001. Elsevier Ltd.

Li, Y., Gu, D., 2014. Thermal behavior during selective laser melting of commercially pure titanium powder: numerical simulation and experimental study. Addit. Manuf. 1 (4), 99−109. https://doi.org/10.1016/j.addma.2014.09.001.

Liang, X., et al., 2020. On incorporating scanning strategy effects into the modified inherent strain modeling framework for laser powder bed fusion. Addit. Manuf. 101648. https://doi.org/10.1016/j.addma.2020.101648. Elsevier BV.

Lord, J.D., Penn, D., Whitehead, P., 2008. The application of digital image correlation for measuring residual stress by incremental hole drilling. Appl. Mech. Mater. 13 (14), 65−73. https://doi.org/10.4028/www.scientific.net/AMM.13-14.65.

Lu, J., 2002. Prestress engineering of structural material: a global design approach to the residual stress problem. In: Totten, G., Howes, M., Inoue, T. (Eds.), Handbook of Residual Stress and Deformation of Steel. ASM International, Ohio, pp. 11−26.

Lu, Y., et al., 2019. Online stress measurement during laser-aided metallic additive manufacturing. Sci. Rep. 9, 7630. https://doi.org/10.1038/s41598-019-39849-0.

Luo, C., et al., 2018. Finite element analysis of temperature and stress fields during the selective laser melting process of thermoelectric SnTe. J. Mater. Process. Technol. 261, 74−85. https://doi.org/10.1016/j.jmatprotec.2018.06.001. Elsevier.

Maamoun, A., Elbestawi, M., Veldhuis, S., 2018. Influence of shot peening on AlSi10Mg parts fabricated by additive manufacturing. J. Manuf. Mater. Process. 2 (3), 40. https://doi.org/10.3390/jmmp2030040. MDPI AG.

Malaki, M., Ding, H., 2015. A review of ultrasonic peening treatment. Mater. Des. 87, 1072−1086. https://doi.org/10.1016/j.matdes.2015.08.102. Elsevier Ltd.

Malý, M., et al., 2019. Effect of process parameters and high-temperature preheating on residual stress and relative density of Ti6Al4V processed by selective laser melting. Materials 12, 930. https://doi.org/10.3390/ma12060930.

Manfredi, D., et al., 2013. From powders to dense metal parts: characterization of a commercial AlSiMg alloy processed through direct metal laser sintering. Materials 6 (3), 856−869. https://doi.org/10.3390/ma6030856.

Meier, H., Haberland, C., 2008. Experimental studies on selective laser melting of metallic parts. Mater. Werkst. 39 (9), 665−670. https://doi.org/10.1002/mawe.200800327.

Mercelis, P., Kruth, J., 2006. Residual stresses in selective laser sintering and selective laser melting. Rapid Prototyp. J. 12 (5), 254−265. https://doi.org/10.1108/13552540610707013.

Mertens, R., et al., 2018. Application of base plate preheating during selective laser melting. Procedia CIRP 5−11. https://doi.org/10.1016/j.procir.2018.08.002. Elsevier B.V.

Montero Sistiaga, M.L., et al., 2016. Changing the alloy composition of Al7075 for better processability by selective laser melting. J. Mater. Process. Technol. 238, 437−445. https://doi.org/10.1016/j.jmatprotec.2016.08.003. Elsevier Ltd.

Moser, D., Cullinan, M., Murthy, J., 2019. Multi-scale computational modeling of residual stress in selective laser melting with uncertainty quantification. Addit. Manuf. 29 (December 2018), 100770. https://doi.org/10.1016/j.addma.2019.06.021. Elsevier.

Mugwagwa, L., et al., 2018. Influence of process parameters on residual stress related distortions in selective laser melting. Procedia Manuf. 21 (2017), 92−99. https://doi.org/10.1016/j.promfg.2018.02.099. Elsevier B.V.

Munther, M., et al., 2020. Laser shock peening and its effects on microstructure and properties of additively manufactured metal alloys: a review. Eng. Res. Express 2 (2), 022001. https://doi.org/10.1088/2631-8695/ab9b16. IOP Publishing.

Nadammal, N., et al., 2017. Effect of hatch length on the development of microstructure, texture and residual stresses in selective laser melted superalloy Inconel 718. Mater. Des. 134, 139−150. https://doi.org/10.1016/j.matdes.2017.08.049. Elsevier Ltd.

Neugebauer, F., et al., 2014. Multi scale FEM simulation for distortion calculation in additive manufacturing of hardening stainless steel. In: International Workshop on Thermal Forming and Welding Distortion. Bremen, pp. 1−11.

Örnek, C., 2018. “Additive manufacturing−a general corrosion perspective. Corrosion Eng. Sci. Technol. 53 (7), 531−535. https://doi.org/10.1080/1478422X.2018.1511327. Taylor and Francis Ltd.

Pagliaro, P., et al., 2010. Measuring multiple residual-stress components using the contour method and multiple cuts. Exp. Mech. 50 (2), 187−194. https://doi.org/10.1007/s11340-009-9280-3.

Parry, L.A., Ashcroft, I.A., Wildman, R.D., 2019. Geometrical effects on residual stress in selective laser melting. Addit. Manuf. 25, 166−175. https://doi.org/10.1016/j.addma.2018.09.026. Elsevier.

Parry, L., Ashcroft, I.A., Wildman, R.D., 2016. Understanding the effect of laser scan strategy on residual stress in selective laser melting through thermo-mechanical simulation. Addit. Manuf. 12, 1−15. https://doi.org/10.1016/j.addma.2016.05.014. Elsevier B.V.

Piscopo, G., et al., 2019. Machining induced residual stresses in AlSi10Mg component produced by Laser Powder Bed Fusion (L-PBF). Procedia CIRP 79, 101−106. https://doi.org/10.1016/j.procir.2019.02.019. Elsevier B.V.

Pupo, Y., et al., 2013. Scanning space analysis in selective laser melting for CoCrMo powder. In: 5th Manufacturing Engineering Society International Conference. Zaragoza, pp. 370−378. https://doi.org/10.1016/j.proeng.2013.08.228.

Qiu, C., et al., 2019. On the solidification behaviour and cracking origin of a nickel-based superalloy during selective laser melting. Mater. Char. 148, 330−344. https://doi.org/10.1016/j.matchar.2018.12.032. Elsevier Inc.

Roberts, I.A., 2012. Investigation of Residual Stresses in the Laser Melting of Metal Powders in Additive Layer Manufacturing. PhD thesis. University of Wolverhampton.

Robinson, J., et al., 2018. Determination of the effect of scan strategy on residual stress in laser powder bed fusion additive manufacturing. Addit. Manuf. 23, 13−24. https://doi.org/10.1016/j.addma.2018.07.001. Elsevier B.V.

Roehling, J.D., et al., 2019. Reducing residual stress by selective large-area diode surface heating during laser powder bed fusion additive manufacturing. Addit. Manuf. 28 (May), 228−235. https://doi.org/10.1016/j.addma.2019.05.009. Elsevier.

Salmi, A., et al., 2017. Experimental analysis of residual stresses on AlSi10Mg parts produced by means of selective laser melting (SLM). Procedia CIRP 62, 458−463. https://doi.org/10.1016/j.procir.2016.06.030. The Author(s).

Salmi, A., Atzeni, E., 2017. History of residual stresses during the production phases of AlSi10Mg parts processed by powder bed additive manufacturing technology. Virtual Phys. Prototyp. 12 (2), 153−160. https://doi.org/10.1080/17452759.2017.1310439. Taylor and Francis Ltd.

Sames, W.J., et al., 2016. The metallurgy and processing science of metal additive manufacturing. Int. Mater. Rev. 1−46. https://doi.org/10.1080/09506608.2015.1116649.

Sarkar, S., Kumar, C.S., Nath, A.K., 2019. "Effects of different surface modifications on the fatigue life of selective laser melted 15−5PH stainless steel. Mater. Sci. Eng. A 762 (July), 138109. https://doi.org/10.1016/j.msea.2019.138109. Elsevier B.V.

Schajer, G.S., 2010. Relaxation methods for measuring residual stresses: techniques and opportunities. Exp. Mech. 50 (8), 1117−1127. https://doi.org/10.1007/s11340-010-9386-7. Springer.

Schajer, G.S., 2013. In: Schajer, G.S. (Ed.), Practical Residual Stress Measurement Methods, Practical Residual Stress Measurement Methods. John Wiley & Sons, Ltd, Chichester, UK. https://doi.org/10.1002/9781118402832.

Schmeiser, F., et al., 2020. Experimental observation of stress formation during selective laser melting using in situ X-ray diffraction. Addit. Manuf. 32, 101028. https://doi.org/10.1016/j.addma.2019.101028. Elsevier B.V.

Schneller, W., et al., 2019. Effect of post treatment on the microstructure, surface roughness and residual stress regarding the fatigue strength of selectively laser melted AlSi10Mg structures. J. Manuf. Mater. Process. 3 (4), 89. https://doi.org/10.3390/jmmp3040089.

Shiomi, M., et al., 2004. Residual stress within metallic model made by selective laser melting process. CIRP Ann. 53 (1), 195−198. https://doi.org/10.1016/S0007-8506(07)60677-5.

Simson, T., et al., 2017. Residual stress measurements on AISI 316L samples manufactured by selective laser melting. Addit. Manuf. 17, 183−189. https://doi.org/10.1016/j.addma.2017.07.007. Elsevier B.V.

Song, B., et al., 2014. Vacuum heat treatment of iron parts produced by selective laser melting: microstructure, residual stress and tensile behavior. Mater. Des. 54, 727−733. https://doi.org/10.1016/j.matdes.2013.08.085. Elsevier Ltd.

Song, J., et al., 2018. Role of scanning strategy on residual stress distribution in Ti-6Al-4V alloy prepared by selective laser melting. Optik 170, 342−352. https://doi.org/10.1016/j.ijleo.2018.05.128. Elsevier GmbH.

Tal-Gutelmacher, E., Eliezer, D., 2005. High fugacity hydrogen effects at room temperature in titanium based alloys. J. Alloys Compd. 404−406, 613−616. https://doi.org/10.1016/j.jallcom.2004.12.172.

Tong, Z., et al., 2019. Laser additive manufacturing of FeCrCoMnNi high-entropy alloy: effect of heat treatment on microstructure, residual stress and mechanical property. J. Alloys Compd. 785, 1144−1159. https://doi.org/10.1016/j.jallcom.2019.01.213. Elsevier B.V.

Töppel, T., et al., 2016. Eigenspannungen und verzug bei der additiven fertigung durch laserstrahlschmelzen. Schweissen Schneiden 68 (4), 176−186.

Totten, G., Howes, M., Inoue, T., 2002. Handbook of Residual Stress and Deformation of Steel. ASM International. Available at: https://www.asminternational.org/search/-/journal_content/56/10192/06700G/PUBLICATION (Accessed 11 September 2020).

Vrancken, B., et al., 2013. Study of the influence of material properties on residual stress in selective laser melting. In: Solid Freeform Fabrication Symposium. Austin, pp. 393−407.

Vrancken, B., et al., 2014. Residual stress via the contour method in compact tension specimens produced via selective laser melting. Scripta Mater. 87, 29−32. https://doi.org/10.1016/j.scriptamat.2014.05.016.

Vrancken, B., 2016. Study of Residual Stresses in Selective Laser Melting. PhD thesis. Katholieke Universiteit Leuven.

Walker, P., et al., 2019. Effects of ultrasonic impact treatment on the stress-controlled fatigue performance of additively manufactured DMLS Ti-6Al-4V alloy. Appl. Sci. 9 (22), 12−14. https://doi.org/10.3390/app9224787.

Wang, L., et al., 2018. Investigation of performance and residual stress generation of AlSi10Mg processed by selective laser melting. Adv. Mater. Sci. Eng. 2018, 1−12. https://doi.org/10.1155/2018/7814039. Research.

Wang, M., et al., 2019. Improved mechanical properties of AlSi7Mg/nano-SiCp composites fabricated by selective laser melting. J. Alloys Compd. 810, 151926. https://doi.org/10.1016/j.jallcom.2019.151926. Elsevier Ltd.

Wei, K., et al., 2019. Effect of laser remelting on deposition quality, residual stress, microstructure, and mechanical property of selective laser melting processed Ti-5Al-2.5Sn alloy. Mater. Char. 150, 67−77. https://doi.org/10.1016/j.matchar.2019.02.010. Elsevier.

Withers, P.J., Bhadeshia, H.K.D.H., 2001a. Residual stress part 1 - measurement techniques. Mater. Sci. Technol. 355−365. https://doi.org/10.1179/026708301101509980. IOM Communications Ltd.

Withers, P.J., Bhadeshia, H.K.D.H., 2001b. Residual stress part 2 - nature and origins. Mater. Sci. Technol. 366−375. https://doi.org/10.1179/026708301101510087. IOM Communications Ltd.

Wu, J., Wang, L., An, X., 2017. Numerical analysis of residual stress evolution of AlSi10Mg manufactured by selective laser melting. Optik 137, 65−78. https://doi.org/10.1016/j.ijleo.2017.02.060. Elsevier GmbH.

Xiao, Z., et al., 2020. Effect of rescanning cycles on the characteristics of selective laser melting of Ti6Al4V. Optic Laser. Technol. 122, 105890. https://doi.org/10.1016/j.optlastec.2019.105890. Elsevier Ltd.

Xu, R., et al., 2020. Microstructure, metallurgical defects and hardness of Al−Cu−Mg−Li−Zr alloy additively manufactured by selective laser melting. J. Alloys Compd. 835, 155372. https://doi.org/10.1016/j.jallcom.2020.155372. Elsevier Ltd.

Yadroitsava, I., et al., 2015. Residual stress in SLM Ti6Al4V alloy specimens. Mater. Sci. Forum. https://doi.org/10.4028/www.scientific.net/MSF.828-829.305.

Yadroitsava, I., Yadroitsev, I., 2015. Residual stress in metal specimens produced by direct metal laser sintering. In: Solid Freeform Fabrication Symposium. Austin, pp. 614−625. https://doi.org/10.1017/CBO9781107415324.004.

Yadroitsev, I., et al., 2013. Energy input effect on morphology and microstructure of selective laser melting single track from metallic powder. J. Mater. Process. Technol. 213 (4) https://doi.org/10.1016/j.jmatprotec.2012.11.014.

Yadroitsev, I., Yadroitsava, I., 2015. Evaluation of residual stress in stainless steel 316L and Ti6Al4V samples produced by selective laser melting. Virtual Phys. Prototyp. 10 (2), 67−76. https://doi.org/10.1080/17452759.2015.1026045. Taylor and Francis Ltd.

Yan, M., et al., 2014. A transmission electron microscopy and three-dimensional atom probe study of the oxygen-induced fine microstructural features in as-sintered Ti−6Al−4V and their impacts on ductility. Acta Mater. 68, 196−206. https://doi.org/10.1016/j.actamat.2014.01.015. Acta Materialia Inc.

Yasa, E., et al., 2009. Investigation on occurrence of elevated edges in selective laser melting. In: Solid Freeform Fabrication Symposium. Austin. https://doi.org/10.1017/CBO9781107415324.004.

Yu, W., et al., 2019. Influence of re-melting on surface roughness and porosity of AlSi10Mg parts fabricated by selective laser melting. J. Alloys Compd. 792, 574−581. https://doi.org/10.1016/j.jallcom.2019.04.017. Elsevier Ltd.

Zaeh, M.F., Branner, G., 2010. Investigations on residual stresses and deformations in selective laser melting. Prod. Eng. 4 (1), 35−45. https://doi.org/10.1007/s11740-009-0192-y.

Zhang, B., Dembinski, L., Coddet, C., 2013. The study of the laser parameters and environment variables effect on mechanical properties of high compact parts elaborated by selective laser melting 316L powder. Mater. Sci. Eng. A 584, 21−31. https://doi.org/10.1016/j.msea.2013.06.055.

Zhang, C., et al., 2020. Cracking mechanism and mechanical properties of selective laser melted CoCrFeMnNi high entropy alloy using different scanning strategies. Mater. Sci. Eng. A 789, 139672. https://doi.org/10.1016/j.msea.2020.139672. Elsevier Ltd.

Zhang, M., et al., 2016. Residual stress, defects and grain morphology of Ti-6Al-4V alloy produced by ultrasonic impact treatment assisted selective laser melting. Appl. Sci. 6 (11), 304. https://doi.org/10.3390/app6110304.

Zhao, L., et al., 2020. Comparison of residual stresses obtained by the crack compliance method for parts produced by different metal additive manufacturing techniques and after friction stir processing. Addit. Manuf. 36, 101499. https://doi.org/10.1016/j.addma.2020.101499. Elsevier B.V.

van Zyl, I., Yadroitsava, I., Yadroitsev, I., 2016. Residual stress in TI6AL4V objects produced by direct metal laser sintering. S. Afr. J. Ind. Eng. 27 (4) https://doi.org/10.7166/27-4-1468.

Non-destructive testing of parts produced by laser powder bed fusion

10

Anton Du Plessis[1,2], *Eric MacDonald*[3], *Jess M. Waller*[4], *Filippo Berto*[5]
[1]Research Group 3D Innovation, Stellenbosch University, Stellenbosch, Western Cape, South Africa; [2]Department of Mechanical Engineering, Nelson Mandela University, Port Elizabeth, Eastern Cape, South Africa; [3]W. M. Keck Center for 3D Innovation, University of Texas at El Paso, El Paso, TX, United States; [4]NASA-Johnson Space Center White Sands Test Facility, Las Cruces, NM, United States; [5]Department of Mechanical and Industrial Engineering, Norwegian University of Science and Technology (NTNU), Trondheim, Norway

Chapter outline

10.1 Introduction 278
  10.1.1 Traditional NDT 278
  10.1.2 NDT requirements for metal additive manufacturing 280
10.2 NDT for L-PBF 282
  10.2.1 X-ray and neutron radiography 282
  10.2.2 X-ray computed tomography 284
  10.2.3 Optical and tactile measurement 287
  10.2.4 Dye penetrant 289
  10.2.5 Ultrasonic testing 289
  10.2.6 Eddy current 291
  10.2.7 X-ray and neutron diffraction 292
  10.2.8 Archimedes bulk density measurement 292
  10.2.9 Optical and electron microscopy 292
  10.2.10 Process compensated resonance testing (PCRT) 293
  10.2.11 X-ray fluorescence 293
  10.2.12 Thermography 293
10.3 Quality control and NDT considerations 294
10.4 Emerging areas and outlook 298
10.5 Questions 298
Acknowledgments 298
References 299

Fundamentals of Laser Powder Bed Fusion of Metals. https://doi.org/10.1016/B978-0-12-824090-8.00016-0
Copyright © 2021 Elsevier Inc. All rights reserved.

10.1 Introduction

Nondestructive testing (NDT) is a broad discipline comprising of a range of technologies for the identification of flaws (cracks, pores, inclusions, etc.) in manufactured parts without damaging them. Traditionally, NDT is used to identify defects for a pass/reject decision, either for manufactured parts or for large industrial parts in use (e.g., pipelines, boilers, etc.). It is also used to inspect parts in use for service-related damage such as fatigue, corrosion, wear, etc. Laser powder bed fusion (L-PBF) has less defects than most additive manufacturing technologies but is also prone to possible defects associated with processing parameters or a range of errors which may occur during manufacturing. These defects are very different from those in typical castings, welded parts, or forgings. The L-PBF-specific defects are unique and hence some existing NDT tools are better suited to these particular defect types and sizes, and some might need modification for successful application to L-PBF. This chapter provides an overview of the most widely used NDT tools for additive manufacturing, focusing on L-PBF.

10.1.1 Traditional NDT

Nondestructive testing (NDT) is a broad category of techniques used to evaluate the integrity of a part or a component without damaging it. Nondestructive evaluation (NDE) and nondestructive inspection (NDI) are synonymous terms used to refer to the same category of techniques. In an overview of the topic by Mandache (2019), the distinction is explained such that NDT refers to tests of the as-manufactured part, NDI refers to parts that are in-service (checking for wear or damage of used parts), and NDE is a wider term incorporating all of these and also in-process monitoring, for example. In-process monitoring is not discussed in this chapter and is dealt with in Chapter 11 in some detail.

NDT is widely used in broader industry settings (often with portable equipment) for inspection of conventionally manufactured parts, welds, or critical areas of large parts. When these large parts are still in use, this is referred to as “in-service inspection.” NDT inspections are also used to improve manufacturing processes (these methods can therefore be non-portable) and this kind of inspection is focused at preventing early product failures by identifying structural integrity issues early on. The aim of NDT is to identify critical defects (pores, cracks, inclusions, etc.) which are termed “indications” in NDT terminology. The presence of indications (the number and size of indications, for example) allows a pass/fail decision to be made on the employment of a part for service, or to make an assessment of its predicted safe lifetime in continued operation. NDT may be used as a quality check or it may be used as a method to optimize the manufacturing process (e.g. by adjusting casting mold design or ingate locations). NDT may be used to ensure continued quality despite changing environmental conditions or feedstock material suppliers, for example. NDT is also useful to end-users to confirm that suppliers maintain required quality. NDT is a technical field with its own set of standards optimized for specific application fields such as oil and gas industries, automotive, aerospace, and more. The American Society of Nondestructive Testing (ASNT) is one large nonprofit organization supporting standardization and certification of NDT technicians and test methods (The American Society For Nondestructive Testing). Typically, NDT technicians are certified at different levels as outlined in the ASNT descriptions as level I, II, or III for each specific NDT method. Traditional NDT methods are summarized in Table 10.1 and more details of standard methods are described in ASTM standards (ASTM International, 2020).

Table 10.1 Traditional NDT methods summary.

Name	How it works	Different variations
Visual testing	Visual inspection with/without devices for surface flaws, deviations from design	Visual check/camera Optical microscopy Measurement by calipers Magnifiers, telescopes, endoscopes, scanning electron microscopy
Liquid penetrant testing	Dye liquid used to highlight surface cracks	Visible and fluorescent dyes
Magnetic particle testing	Magnetic field induced in sample, irregularities in field highlighted by magnetic particles on surface	Wet and dry magnetic particles
Eddy current testing	Uses an alternating electric current to induce a magnetic field, causing a small current in the material being tested. Changes in the induced field indicate defects altering the flow of the electric current	Eddy current testing Alternating current field measurement Remote field testing
Ultrasonic testing (UT)	Sound waves are sent through part, reflected waves detected with irregularities highlighting defects	A, B, and C scan methods, referring to different acquisition modes Phased array
Radiographic testing (RT)	Absorption of X-rays, differences in absorption relate to defects	2D radiography (film, digital, and computed radiography) X-ray CT and microCT
Infrared and thermal testing (IR)	Part is imaged with a thermal camera to look for irregularities in temperature or radiance while exposed to transient or passive heat	Active and passive thermography

10.1.2 NDT requirements for metal additive manufacturing

Metal additive manufacturing (AM) has very specific requirements and defect types which necessarily mean that traditional NDT tools and methods need to be adjusted or newly developed for their efficient application (Lu and Wong, 2017; Waller et al., 2014). AM enables complexity in parts which adds significant value to the end use, but challenges to NDT—there are hidden features, thin features, and varying wall thicknesses, which make it impossible to use the normal guidelines for NDT inspection except in simplest cases. Many of the traditional NDT methods are also focused on surface flaws only, as surface cracks are most detrimental to in-service operation of parts in industry. These methods typically require smooth surfaces for high sensitivity of crack detection in addition to direct access. Additively manufactured metal parts, however, have rough surfaces in the as-built state and often have complex internal features, which make it challenging to obtain the required sensitivity. Finally, many small defects are found inside additively manufactured parts and those of interest may be randomly distributed or clustered in specific locations, or irregular in shape or distribution (see Chapter 6 "Porosity in laser powder bed fusion"). The pores found in L-PBF are typically much smaller than those of interest in traditional NDT test scenarios on cast, wrought, and forged parts. A brief summary of specific types of defects of interest in laser powder bed fusion are listed in Table 10.2 with their extent and sizes. This table is meant as a summary highlighting the applicable NDT

Table 10.2 Summary of defects in L-PBF parts and the typical NDT methods used.

Defect type	Information	NDT techniques potentially suitable
Porosity	Different sizes and extents, typically from ~10 μm up to 1 mm, refer to Chapter 6 and keep in mind different forms of porosity, e.g., keyhole, lack of fusion, balling induced, etc.	Radiography, specifically X-ray microCT Archimedes and related methods Ultrasonic
Inclusions	Typically from powders, i.e., 50–100 μm	Radiography, specifically X-ray microCT Microscope visual inspection, chemical analysis
Surface cracks	Can be 50 μm deep or more	Liquid penetrant Magnetic particle inspection Ultrasonic surface wave for simple surfaces Eddy-current X-ray microCT

Table 10.2 Summary of defects in L-PBF parts and the typical NDT methods used.—cont'd

Defect type	**Information**	**NDT techniques potentially suitable**
Internal cracks	Can be 50 μm deep or more	X-ray microCT Magnetic particle up to a point Ultrasonic up to a point
Residual stress	Varies from surface to internal and especially in complex parts (differences in thin vs. thick regions, for example)	X-ray and neutron diffraction
Deviation from design	Actual parts may be up to 0.2 mm larger or smaller than design, either due to manufacturing error directly (scan tracks, shrinkage) or by warping due to residual stress. This depends strongly on dimensional calibration of the L-PBF scanner, spot size, layer thickness, and other system parameters	Visual inspection (3D scanning, calipers) Radiography, specifically X-ray microCT Metrology and 3D scanning
Surface roughness	Roughness R_a values from 5 to 50 μm depending on powder, process parameters, inclination angle, and orientation of surface	Visual inspection Dimensional measurement (tactile probe, noncontact probe, microscopy) X-ray microCT
Microstructure inhomogeneity or anisotropic texture	Not something usually required for NDT, usually done destructively using representative samples	Some information possible by neutron or X-ray diffraction
Reactions of oxygen, nitrogen, or hydrogen	Can cause surface films with different colors	Visual inspection

methods for each defect type. A detailed review covering the use of various NDT methods in additive manufacturing with examples of each is provided also in Sharratt (2015). Since aerospace applications require the highest quality parts, NDT has been investigated extensively in this area (Waller et al., 2014), with a new ASTM standard for NDT of additively manufactured parts for aerospace (ASTM E3166-20e1). These provide examples of the varied types of NDT applied to additively manufactured parts and discuss in detail the advantages and disadvantages of each. While application of conventional NDT techniques is possible for AM parts with simple geometries, topology optimized AM parts with more complex geometries and lattice structures require specialized NDT techniques (Todorov et al., 2014). In fact, geometric complexity was found to be a primary factor governing the ability to apply NDT to AM parts. Another review was carried out by Lu and Wong (2017) providing also detailed description of working methods of each NDT method applicable to additive manufactured parts. More recently, Dutton et al. (2020) classified and identified technologically important defects occurring in additively manufactured parts produced by PBF and directed energy deposition (DED). A breakdown of technologically important defects is presented in three sections: the cause, the defect, and detection by NDT. In general, reliable detection of defects by NDT does not depend on the process cause, but more on the size, geometry, and location (and, potentially, the morphology) of the defect, as well as the complexity, density, and surface finish of the part.

In the next section, NDT methods are described together with their potential capabilities and their limitations specifically in relation to L-PBF defect types. It should be noted that due to the unique nature of additively manufactured parts, some additional measurement tools are included which are not usually in the category of "traditional" NDT tools, but rather are measurement devices, used in nondestructive modes.

There are some key challenges to defects in metal AM. Firstly, one major advantage of AM is the complexity of design that is possible. This complexity however leads to many NDT tools becoming inadequate—some surfaces are hidden and cannot be accessed for inspection by surface tools, and volumetric methods are challenged by the varying thickness and curvatures leading to difficulty in flaw detection. In addition to complexity of the part, the key defect types may be extremely small—many pores <0.1 mm are present in metal AM parts and these may be particularly important. Some traditional NDT methods simply cannot reliably detect such small pores. Furthermore, the presence of defects (e.g., many small pores) does not necessarily imply poor performance of the part. Unlike well-known traditional manufacturing processes, the process-structure-performance characteristics in metal AM are still being researched. Some key points are emerging to identify which types of defects are most critical. This information is key to select appropriate NDT tools to ensure that the parts are free from critical defects. This is a requirement for process and part qualification, and NDT plays a key role in this field as discussed in Seifi et al. (2016, 2017).

10.2 NDT for L-PBF

10.2.1 X-ray and neutron radiography

Radiographic testing or radiography using X-ray or neutron sources (or gamma radiation) allows the inspection of the interior of an object of interest by absorption of radiation. An object is placed between a radiation source and a detector and the absorbed radiation is recorded in the form of a radiographic projection image or shadow image. The absorption is governed by the Beer-Lambert law:

$$I = I_0 e^{-\mu d} \tag{10.1}$$

Where I is the transmitted intensity, I_0 is the incident intensity, μ is the linear absorption coefficient of the material, and d is the distance of material through which the radiation passes. A defect such as a pore space would result in less X-ray absorption than the surrounding areas, creating a brighter region in the radiographic projection image. This is illustrated using a 2D X-ray radiography image of a test artifact containing two channels—one open channel and one latticed channel—as shown in Fig. 10.1. The different angles of viewing clearly identify the open channel and the lattice channel is also visible but less clearly, due to powder stuck in between the lattice struts. The original radiographic method used photographic film, but a digital format that uses reusable plate detectors that are read, called computed radiography (CR), provides a digital image and has a greater dynamic range.

Eq. (10.1) is strictly for monochromatic radiation; however, most laboratory X-ray sources are polychromatic. This means that the effective material absorption coefficient varies for low and high energy X-rays in the beam, creating differences in absorption across the sample. This absorption coefficient also depends on the material physical density as well as its atomic mass, with heavier atoms absorbing X-rays more strongly. For improved penetration of dense or large objects, a higher voltage of the X-ray source is needed, as the value of μ typically decreases with increased X-ray energy.

The use of digital X-ray imaging (using fast digital detectors), also known as radiographic testing (RT), allows to visualize the sample from different angles to determine the presence of an indication. The main challenge with this method for L-PBF is the combination of the complexity of parts (complex shadows in images) and the small pore sizes of interest (insufficient resolution).

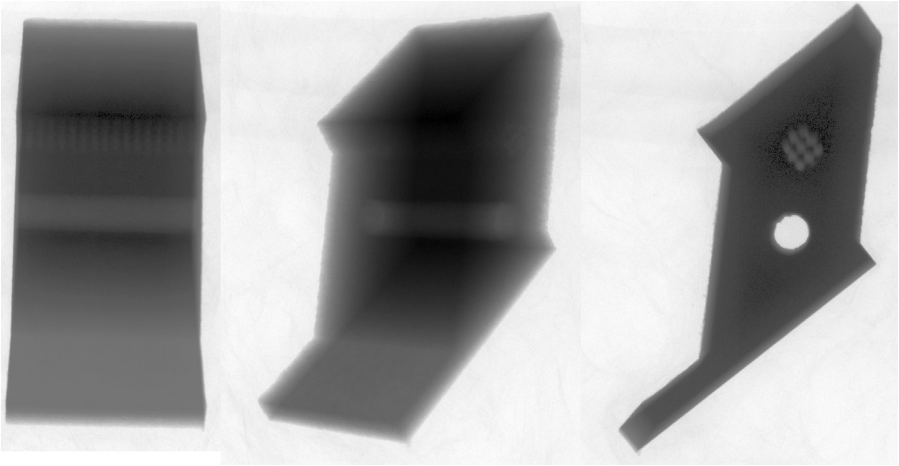

Figure 10.1 An example of a 2D X-ray radiographic images of a test artifact with empty channel and latticed channel in an L-PBF part—from left to right projection angles of 0, 45, and 90 degrees.

X-ray radiographic testing (RT) is widely used in laboratory or factory settings as well as with portable equipment for large objects. Some reference standards and image quality indicators (IQIs) are often used to prove the image quality is sufficient to identify a flaw of a particular size. These systems are optimized for inspection of welds and castings with typical associated large pores. Due to the unique nature of additive manufacturing, new image quality indicators would be needed. One possible solution is to use artificially designed flaws such as cracks, lack of fusion porosity, etc., in the same material as the tested material and use this as validation of the detection capability—an area of future development.

Neutron radiography is similar to X-ray but has advantages for some lighter elements including hydrogen. Hydrogen (e.g., from water) strongly absorbs neutrons but does not absorb X-rays. Neutron radiography is, however, not as readily available as X-ray radiography due to safety hazards and costs of such equipment.

10.2.2 X-ray computed tomography

X-ray computed tomography (CT) is technically a subsection of radiographic testing, but is highly important in the field of AM (Du Plessis et al., 2018e), so it is discussed separately here. The same physics as radiography hold for this technique (i.e., the Beer-Lambert law in Eq. 10.1). In a CT scan, a series of X-ray projection images are recorded as an object is rotated between an X-ray source and detector. All these angular projection images are subsequently used to reconstruct a 3D representation of the object based on the linear absorption coefficient in Eq. (10.1), using a back-projection algorithm. This 3D representation comprises of a stack of cross-sectional images with each pixel representing the X-ray density of that region of the object, with brighter pixels representing denser areas (and pore spaces darker areas). A typical CT schematic is shown in Fig. 10.2, showing the same test artifact as in Fig. 10.1 in a CT scan.

The use of X-ray CT in additive manufacturing has been widely used and was reviewed comprehensively in (Du Plessis et al., 2018e), where its use for porosity detection is discussed, among various other applications: dimensional measurements of hidden and complex structures, analysis of strut and pore sizes in lattice structures, volumetric measurements, deformation analysis and 4D CT, surface roughness evaluation, powder analysis, and more. The key benefit of CT is the ability to easily identify pores or cracks in any part of the sample, with much higher confidence than traditional radiography. This is true especially of pores in additively manufactured materials due to their small size and hence poor contrast in 2D radiography. A simple example of the same sample shown in Fig. 10.1 in radiography is shown in a CT cross-section in Fig. 10.3. The difference is striking—the CT image clearly shows powder inside the latticed channel.

X-ray CT is widely used in medical applications, which is optimized for imaging internal details of the human body, and typically generates images with voxel (voxel = volumetric pixel = 3D equivalent of a pixel) size of $\sim 0.5-1$ mm. MicroCT instruments (producing images as in Fig. 10.3) are increasingly available which have voxel sizes ranging from 0.005 to 0.5 mm. Despite drawbacks such as the time

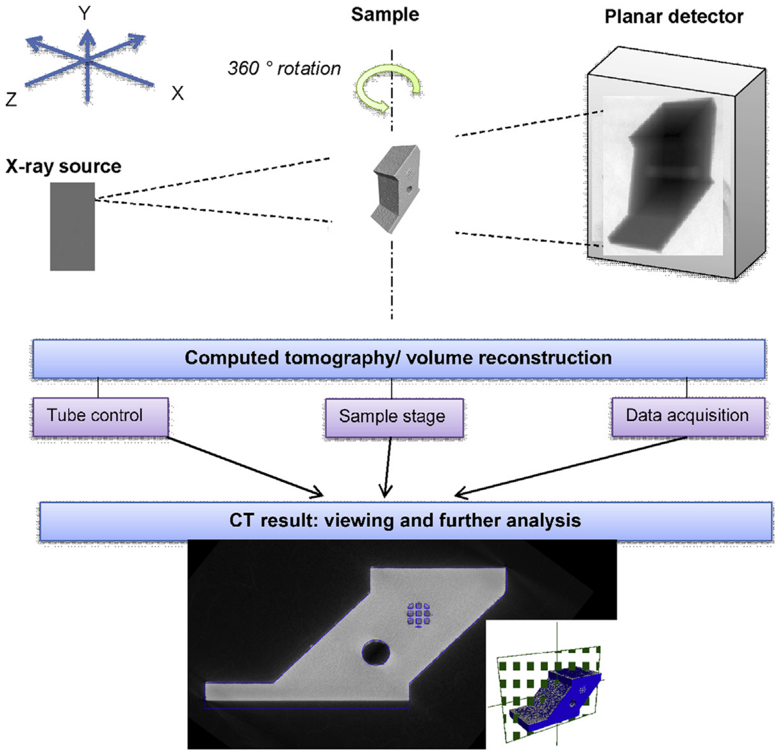
Y
Z
X
Sample
360 ° rotation
Planar detector
X-ray source
Computed tomography/ volume reconstruction
Tube control
Sample stage
Data acquisition
CT result: viewing and further analysis

Figure 10.2 Schematic of X-ray computed tomography of an additively manufactured test artifact.
Modified from (Du Plessis et al., 2018e).

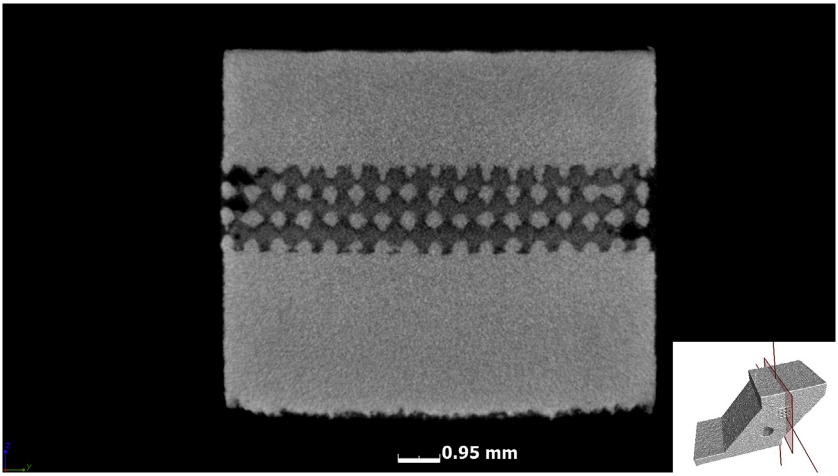

Figure 10.3 CT cross-sectional image (slice image) of the same test artifact in Fig. 10.1, showing powder stuck between lattice struts.

needed to obtain high resolution images of full size L-PBF parts, at least X-ray CT makes it possible to image all relevant pores and cracks in representative areas.

Higher resolution is also possible using nanoCT instruments, with voxel sizes down to hundreds of nanometers or even below. The utility of this kind of instrument is that even powder feedstock can be imaged for quality inspection, as shown in the example in Fig. 10.4; in this case porosity in powder particles are shown, some of which contain finer powders.

In addition to the ability to detect porosity, another relevant aspect of microCT is the ability to visualize internal details of complex parts such as lattice structures, and inspect the quality of the build inside these complex regions, for example, some lattice struts may have failed during the build, or powder may be trapped as shown in Fig. 10.3. In addition, the presence of high-density inclusions are detectable in microCT images as shown in two examples in (Du Plessis et al., 2018e; Du Plessis and le Roux, 2018). Depending on the surface quality and the scan resolution, the surface roughness can be evaluated as well. In addition to these applications, further measurements are possible such as individual feature thickness measurements or other complex dimensional evaluations. All of these however require good CT scan quality, as well as additional image processing, which is not yet widely appreciated and presents challenges to standardization efforts. Some efforts have been made toward creating simplified workflows, but this is still an area of development and presents challenges due to the wide variety of CT instruments, software types, and software

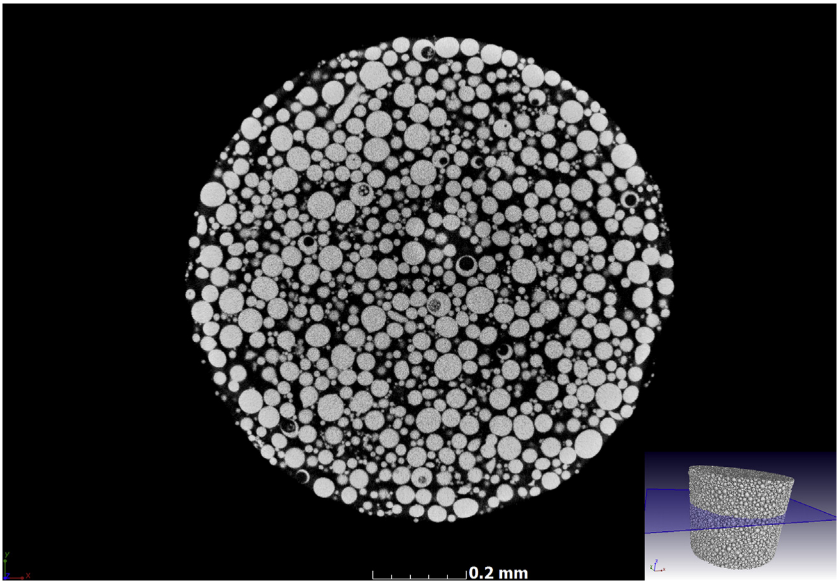

Figure 10.4 Gas atomized virgin Ti6Al4V powder: high resolution nanoCT cross-sectional image shows the presence of pores inside some particles and some pores contain fine powders (Du Plessis and le Roux 2018). Field of view approx. 1 mm, allowing voxel size 1.5 µm.

capabilities. Some examples are presented in methods papers and their application in an international round robin experiment in Du Plessis et al., 2018a, 2018b, 2018c, 2018d; Du Plessis et al., 2019.

Despite all the above-mentioned potential, CT has some drawbacks. As alluded to, resolution is limited by part size, which is the largest problem. In order to image an object, its width determines the field of view and hence the minimum voxel size, based on the magnification that can be achieved in the hardware (detector pixel size and number of pixels, distance from source to detector). Typically, a factor 1000 is a rough estimate for the relationship between part size and the achievable voxel size (for a typical detector with 1000 × 1000 pixels). This means that for a 100 mm part it is possible to obtain 100-μm voxel size (100 mm divided by factor 1000 = 100 μm voxel size). In special cases a smaller region of a large sample can be scanned but this results in image quality reduction—due to strong absorption of X-rays in different parts of the sample, reducing contrast—so is not usually recommended.

The second major limitation is on X-ray penetration which depends on both part size and density, limiting the image quality. For example, as steel absorbs X-rays strongly, only small steel samples can be scanned at high quality with typical laboratory CT devices. In theory, this can be overcome by employing high-voltage CT systems, which can increase substantially the penetration, but these systems are expensive and not widely available. Table 10.3 shows some guidelines about sample limits on size for different material types, for high quality CT scans allowing detailed analysis. For larger objects, scans are possible but image artifacts degrade the quality, restricting analysis to only inspection and not quantitative measurement.

10.2.3 Optical and tactile measurement

The simplest NDT test is visual inspection—it is easy to spot warping or cracks, especially when an experienced AM engineer or technician inspects the part. Manual measurements can be done using calipers and recorded. Alternatively, 3D scanners based on photogrammetry, laser scanning, and structured light are becoming widely available, making it possible to easily acquire a digital record of the geometry of the object, which can be compared to the CAD design. Such scanners are not all calibrated but some versions can be traceably calibrated and are meant for metrology

Table 10.3 Sample material thickness guide for best CT image quality (maximum total material penetrated by X-rays in one direction, assuming typical commercial microCT instrument with ~225 kV microfocus source).

Material	Thickness, mm
Steel	10
Titanium	40
Aluminum	70
Plastic	100

(see paragraph below). Generally these are used for identifying fidelity of the part geometry to design and to detect warping. It should be mentioned that during the L-PBF process, high residual stresses develop, which can cause warping; cutting a part from the base plate can also lead to subsequent warping. Measuring the part on the build plate or after cutting is therefore an important decision in the NDT workflow. The warping tends to reduce the stress, leaving the part with less stress after cutting from the base plate.

Tactile and optical scanners are also used for measuring surface roughness. The most widely used method is a simple handheld tactile probe according to (ASTM D7127-17, 2017), providing an R_a roughness value. Optical scanners with sufficient resolution allow for the generation of 2D roughness maps and determine S_a values which are equivalent to R_a for a 2D area. These require flat surfaces and additional measurements may also be used such as R_z. A discussion of roughness is provided in more detail in Chapter 7; the methods used—even tactile—are nondestructive.

Coordinate measurement machines (CMMs) make use of dimensionally calibrated tactile probes or optical scanners with traceable measurements to high accuracy, typically better than 5 μm. These systems are used for dimensional measurement of parts (also known as metrology) and require high accuracy. According to (ISO 5725-1:1994(En)), *accuracy* consists of trueness (proximity of measurement results to the true value) and precision (repeatability or reproducibility of the measurement)—see Fig. 10.5.

Dimensional metrology tools are limited to inspections of accessible surfaces and are therefore useful for tolerance measurements on exterior surfaces of parts, for example, for identifying warping of parts or inaccuracies in builds compared to intended CAD geometries. These systems are widely available and can measure larger parts than typical CT, with traceable measurement results. Metrological measurements can also be made by CT but special procedures and standards are required for their traceability. An example of a metrology measurement of a part compared to its CAD design is shown in Fig. 10.6 using the test artifact.

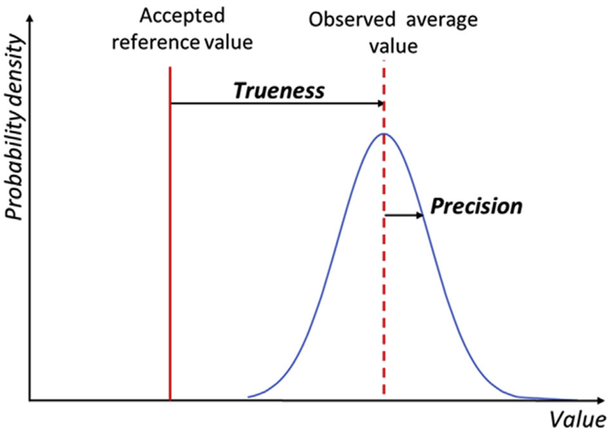

Figure 10.5 Accuracy involves both trueness of value compared to a reference and precision of values from multiple measurements.

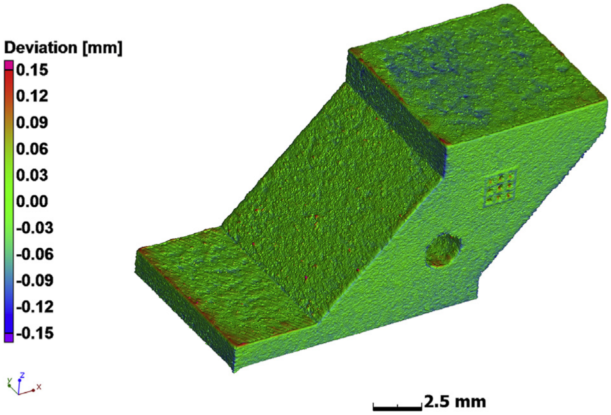

Figure 10.6 Color-coded deviation image showing deviation from CAD for complex part. Some upwards warping, or excess material, up to 0.15 mm is seen at the edges (red along left part of upwards facing surfaces). Surface data acquired by X-ray microCT in this example.

Since no internal information is possible with tactile CMMs and optical scanners, no hidden or internal features in complex parts or lattices can be measured (i.e., there are part complexity limitations). These systems can also be used to evaluate surface roughness, but undercuts and hidden features may be problematic as the systems measure structures from above. The design freedom provided by L-PBF can mean that reference planes and other easy to define datums may not exist, so it may be necessary to incorporate fiducial features onto the part that can be easily removed after inspection, if necessary.

10.2.4 Dye penetrant

Dye penetrant testing (PT) makes use of either visible or fluorescent dyes which are applied to the surface of a part. Due to capillary action, the liquid moves toward and into cracks or other narrow discontinuities on the surface. The excess liquid is wiped from the surface leaving mainly that which penetrated the crack. Using suitable lighting (UV or visible) the cracks are easily identified by visual means. This method is easy to use but requires smooth surfaces. The typical rough surface of as-built L-PBF parts makes the method challenging as dye is captured in many features on the surface. Dye penetrant testing after machining of the L-PBF part is therefore suggested, rather than in as-built state. This method is well suited for surface crack detection.

10.2.5 Ultrasonic testing

Ultrasonic testing (UT) involves the application of high frequency sound waves to a part and recording the reflected waves. In the simplest example, a wave is transmitted linearly from one flat surface toward an opposite parallel flat surface (Fig. 10.7, left).

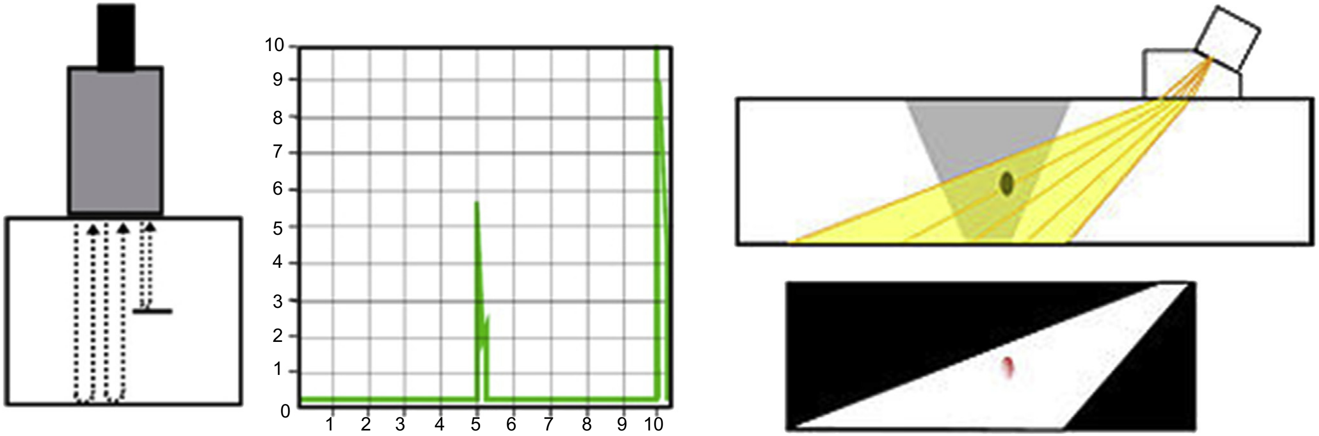

Figure 10.7 Schematic illustrations of (left) traditional linear ultrasonic testing, and (right) phased array ultrasonic testing. Pores or cracks reflect sound waves allowing detection.
Examples taken from American Society of Nondestructive Testing The American Society For Nondestructive Testing. https://asnt.org/. (Accessed 30 July 2020) and from Wikipedia Phased Array Ultrasonics - Wikipedia. n.d. https://en.wikipedia.org/wiki/Phased_array_ultrasonics. (Accessed 26 November 2020).

The reflected signal from the opposite surface may be attenuated by cracks and pores in the distance between the surfaces, and additional signals may be created directly from new (smaller) reflections from the cracks or pores. A single measurement of ultrasonic signal versus depth is called an A-scan. By moving the UT transducer linearly, a B scan is recorded. By moving in a continuous up-and-down hatch pattern to cover an area, sometimes with different probe angles, a C scan is recorded. UT has been used widely in industry and equipment is well developed, but like PT, requires smooth surfaces (rough as-built L-PBF surfaces are problematic, therefore testing by this method is better suited for machined L-PBF parts). Sensitivity variations may exist across an object, for example, the sensitivity may vary with frequency, depth, and sample geometry. This means that proper selection of the equipment, including the transducer size, frequency, and shape, entails tradeoffs with sensitivity and detection at different depths from the surface. The minimum feature sizes detectable are typically ~1 mm, with some recent work indicating improvements down to ~0.2 mm using phased array ultrasonic methods. The main advantages are that any metallic material can be analyzed, and the equipment and process can be relatively simple and low cost. It is also used for wall thickness measurement. The principle relies on sound waves transmitted into the material which are reflected from cracks and pores. Phased array ultrasonic testing makes use of an array of transmitters and receivers which are timed (phased) to allow digital variation of the wavefront interference (thereby focusing and sweeping through the material), shown in Fig. 10.7, right.

10.2.6 Eddy current

Eddy current testing (ET) makes use of Faraday's law of induction which states that a changing magnetic field induces an electric current and vice versa. The principle (Fig. 10.8) is that an alternating current is sent through a conducting coil held in close

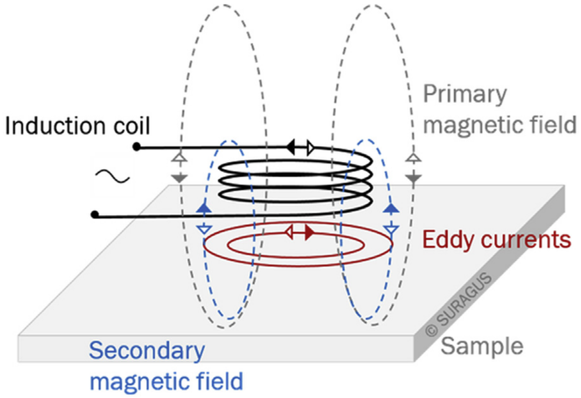

Figure 10.8 Eddy current testing principle—an induction coil creates a primary magnetic field, which induces a secondary magnetic field in the sample. This secondary magnetic field might be disturbed by pores and flaws in the material leading to eddy currents—these disturb the magnetic field allowing detection as the coil is moved over the sample.
With permission from Suragus.Com. n.d. https://www.suragus.com/en/technology/eddy-current/. (Accessed 26 November 2020).

proximity to the test object. This alternating current creates an alternating magnetic field around the coil, which induces small currents (eddy currents) in the test object. In the presence of defects in the test object, the eddy currents are disturbed from their normal flow, inducing small changes in the magnetic field which is detected by the ET coil. One advantage of the method is that it works even when a surface coating (e.g., nonconducting coating) is present. This method is well developed, low cost, and applicable to all conducting metals. However, it requires a smooth surface and is limited to near-surface inspection. The size of detectable defects is generally larger than 1 mm.

10.2.7 X-ray and neutron diffraction

X-ray diffraction (XRD) is a popular and widely available method to investigate the microstructure and residual stress. While this is discussed more in the chapter on residual stress (Chapter 9), it is important to note the method can be nondestructive if only surface measurements are made. However, internal residual stresses may vary significantly from that on the surface. Neutron diffraction works on the same principle but has a deeper penetration than typical X-ray sources, and synchrotron X-ray sources further enhance penetration depth of measurements. The latest synchrotron sources allow 3D XRD measurements, which is of interest for research applications, but not yet suitable for industrial NDT applications.

10.2.8 Archimedes bulk density measurement

A widely used test method for density determination (and hence porosity content) is the use of different variations of the Archimedes principle. While it is a simple method, it should be used correctly and interpreted with care. The most popular variation of the method uses an accurate scale to measure the mass of the test object in air and in water (or acetone). The bulk density (mean density) is then calculated according to (Spierings et al. 2011) and as outlined in Section 6.5.1 (Chapter 6 “Porosity in laser powder bed fusion”). This measurement takes into consideration bulk material density excluding open cavities to the surface. In the case of lattices, for example, the density of the bulk is measured, excluding the open cavities between struts. For measurement of the effective density of lattices and porous areas with open porosity, CT is better suited. A disadvantages of the Archimedes method is the assumption of material solid density values, making small porosity values unreliable. It is however a low cost and fast measurement method. An even simpler method is to use a scale and measure the mass and volume of the object for a rough estimate of bulk density, especially useful for cubes or simple geometries which can be measured by calipers.

10.2.9 Optical and electron microscopy

Microscopy tools allow detailed analyses of objects nondestructively, with some microscopes allowing pseudo-3D measurements for the measurement of surface topography or dimensional measurements of nonplanar feature sizes. Confocal microscopes can do the same, creating z-stacks and surface topographical maps. These tools are strongly dependent on appropriate software and reference measurements are recommended. Some are limited in their field of view, especially for nonplanar samples. Optical microscopy is suited to dimensional measurement while scanning electron microscopy (SEM) is suited to microscale and nanoscale investigations, also with energy dispersive X-ray fluorescence providing chemical analysis. This chemical analysis can be made in detail in individual selected point locations, or chemical maps can be generated by suitable scanning procedures (time consuming). SEM is mostly used as a destructive analysis tool due to sample sectioning and coating requirements. However, it is possible to use the method with small samples without sectioning—the disadvantage from the NDT perspective is that the non-ideal surface roughness makes focusing difficult and only small areas can be kept in focus, but some analysis is possible and in these (limited) cases can be considered nondestructive.

10.2.10 Process compensated resonance testing (PCRT)

This method is increasingly popular due to its simplicity and fast measurement times. The method is indirect and acts globally on the structure in which no information is provided on the flaws detected, such as pore sizes or locations. It works by exciting an entire part in the ultrasonic frequency range and measuring the resonant frequencies of the part. A model is built of typical resonant frequencies of good parts of the same geometry and material and possibly also some intentionally poorly manufactured parts. The frequency shifts measured in poor parts (differences of frequency compared to a good sample) are indicative of porosity, cracks, or other undesirable changes in the characteristic material state of the sample. These are then used to make a global pass/reject or pass/evaluate decision.

10.2.11 X-ray fluorescence

X-ray fluorescence (XRF) is a well-established analytical method allowing chemical analysis, typically used by grinding and pelletizing samples (destructive analysis). However, some forms of XRF such as handheld portable instruments allow a direct nondestructive chemical surface analysis. This is useful for investigating the alloy composition or for checking for inclusions, but is limited in its sensitivity due to the nature of the handheld instrument and low source brightness. The typically rough nonflat surface of AM parts produce additional noise. Some analytical instruments allow chemical mapping of flat surfaces using a focused XRF beam, which is a promising approach for more detailed information on chemical distribution or identification of inclusions, but requires a flat surface for best performance and is therefore affected by the surface roughness as well.

10.2.12 Thermography

Thermography in a popular tool for industrial NDT, as outlined in a review recently for aerospace part testing (Ciampa et al., 2018). Its application to metal additive manufacturing is mostly in the domain of process monitoring for detection of defects during manufacturing (Bartlett et al., 2018; Williams et al., 2019; Lu and Wong 2018). This is discussed in more detail in Chapter 11 "Process monitoring of laser powder bed fusion." It is not widely known in the AM community that the method can also be used offline for post-process part testing. By applying some heating or cooling to a part, the thermal signature and thermal changes may be used to infer the presence of a defect. The defect sensitivity varies with depth and the method is therefore limited to near-surface inspection.

10.3 Quality control and NDT considerations

The use of NDT for final AM parts is a topic of much debate. On the one hand, AM is costly and adding any further costs is always strongly opposed by AM enthusiasts and end-users alike. This might be due to the perception of NDT being nonessential, which relates to the perceived versus real added value brought to bear by the techniques. For example, NDT is most easily justified in high value fracture-critical or safety critical (e.g., aerospace and medical) applications, but is less justified in mass production quantity commodity applications. This reluctance might also be partly due to the historic high costs per part for additive manufacturing of metals and also due to the fact that most AM parts were one-off use cases in the early years of development. On the other hand, many reliability and reproducibility issues have been flagged, which requires strict quality control and NDT can play a key role. As L-PBF is becoming a mature manufacturing technology, with serial production and continued use cases in critical applications such as for medical and aerospace, the role of NDT is set to become more and more important. Quality control on all levels is required, from appropriate handling of powder feedstock and checking process quality regularly to hardware maintenance, online monitoring, and so forth. Post-build inspection is clearly needed, in combination with a well-understood and optimized process.

The need for inspection of final parts is clear, but the NDT of coupon or witness samples has not received much attention yet. Often coupon samples can be built alongside a complex part, which can be inspected at much higher resolution and at better quality than a complex part, or similarly, can be tested to failure more easily than a complex part. The role of coupon samples is twofold. First, coupon samples allow for potential optimization and standardization of the NDT inspection technique (identical NDT workflow despite differences in complex parts, the witness part stays the same and is much simpler in geometry). Second, coupon samples allow the material processes used (feedstock, processing equipment, and postprocessing considerations) to be qualified, ensuring NDT is used only on parts made by a qualified material process (QMP) known to produce the best possible parts (NASA MSFC-STD-3716, 2017). These witness parts might act as a "signature" for build quality, assisting in process and even production part qualification. Also, subscale mechanical test coupon samples can be manufactured with programmed defects and subjected to NDT and this information used to improve the "effect of defect" knowledge base. Fig. 10.9 shows an

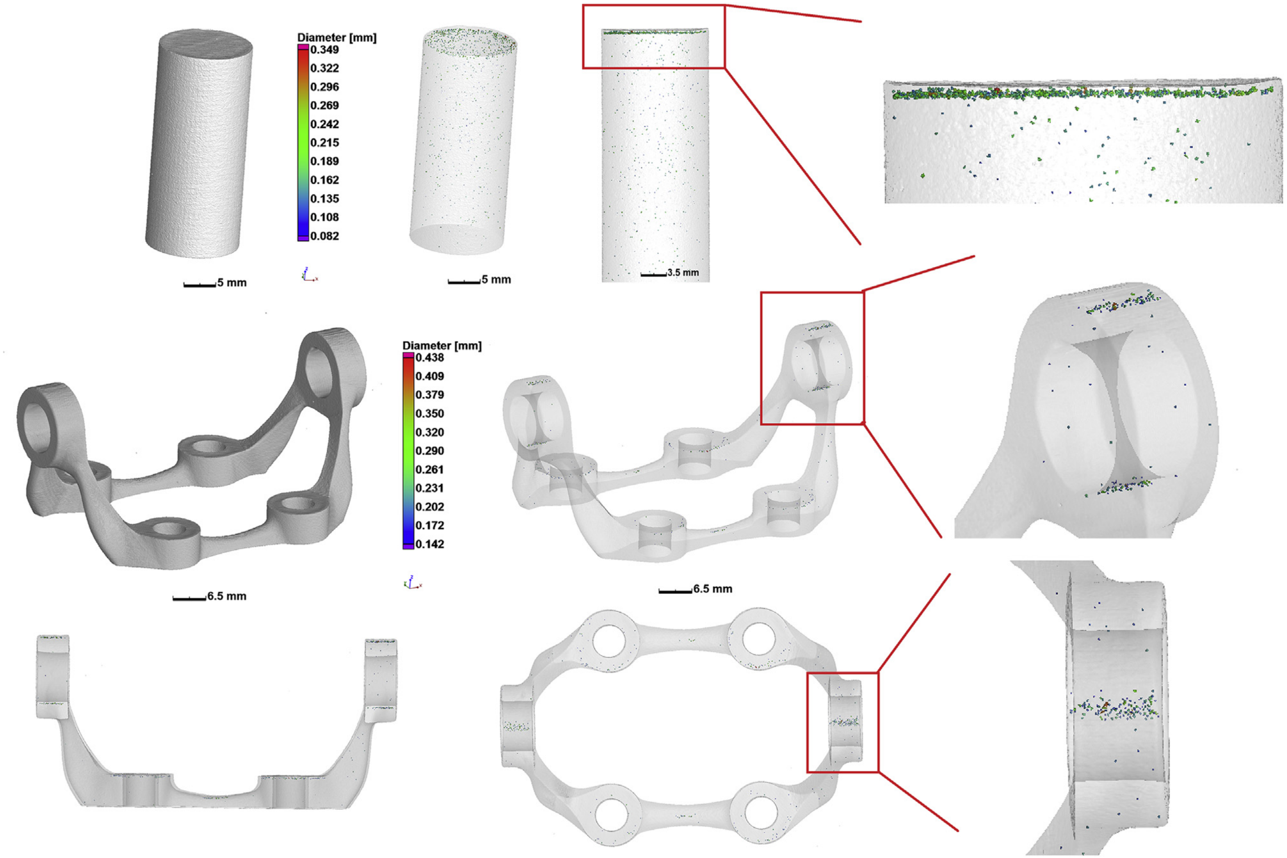
Diameter [mm]
0.349
0.322
0.296
0.269
0.242
0.215
0.189
0.162
0.135
0.108
0.082
5 mm
5 mm
3.5 mm
Diameter [mm]
0.438
0.409
0.379
0.350
0.320
0.290
0.261
0.231
0.202
0.172
0.142
6.5 mm
6.5 mm

Figure 10.9 Correlation of porosity signature (in this case subsurface porosity at top flat surfaces) in witness cylinder and in complex bracket. Example from (Du Plessis et al., 2020; Du Plessis and le Roux, 2018).

example of microCT of a witness cylinder build alongside a topology optimized bracket—in this case porosity is found underneath the top surface mainly, which is evident in both parts (viewed from various angles).

It should be kept in mind that, despite the description of advantages and disadvantages of each NDT method (summarized in Table 10.4), there does not necessarily have to be a single choice. For example, it is recognized that metallic spaceflight hardware L-PBF parts will require the use of multiple NDT techniques to achieve

Table 10.4 Summary of NDT techniques appropriate to L-PBF, with advantages and disadvantages.

Method	Advantages	Disadvantages
X-ray and neutron radiography	Widely available, easy and fast to detect internal flaws	Not well suited to complex geometries, and small pore sizes
X-ray computed tomography	Can detect very small pores, cracks, and almost all types of defects	Time-consuming and expensive, variability in quality depending on settings used, part size and geometry
Optical and tactile measurement	Simple and widely available, high accuracy	Only exterior surfaces accessible, rough surfaces not fully characterized
Dye penetrant	Low cost and simple to detect surface cracks	Only for surface and requires surface processing prior to use
Ultrasonic testing	Low cost and simple to detect large internal flaws	Not suited to small pores, sensitivity varies with frequency, depth, etc.
Eddy current	Low cost and simple to detect large internal flaws	Not suited to small pores, magnetic material only, sensitivity varies with depth and other part and system-specific parameters
X-ray and neutron diffraction	Widely available and suitable for residual stress measurement	Requires surface processing, interpretation is challenging and depends on material, only for surface measurements in typical instruments
Archimedes bulk density measurement	Low-cost method, simple to use	Not very accurate, assumes material density and mistakes can occur for surface-connected pore-spaces

Table 10.4 Summary of NDT techniques appropriate to L-PBF, with advantages and disadvantages.—cont'd

Method	Advantages	Disadvantages
Optical and electron microscopy	High resolution and good for porosity analysis in 2D, pseudo 3D images also possible	Often requires sectioning and polishing which is damaging to parts, 2D analysis is limited
Process compensated resonance testing (PCRT)	Very fast and simple to implement	Requires good training data and reliable instrument, no true information is provided as the measurement is indirect
X-ray fluorescence	Portable instruments allow spot measurements of chemical content—fast and low cost	Not widely available and chemical analysis is qualitative in this modality
Thermography	Can detect flaws near surface relatively easily	Not suitable for small pores or deep within a part, difficulty with complex geometries

full coverage (NASA MSFC-STD-3716, 2017). For such parts, a combination of ET, PT, RT, and UT may be common and should be considered. As noted earlier, surface inspection techniques may require the as-built surface be improved to render a successful inspection, depending upon the defect sizes of interest and the signal-to-noise ratio. Surfaces improved by methods such as machining or abrasion require etching prior to penetrant inspection to remove smeared metal. It is also noted that removal of the as-built AM surface merely to a level of visually smooth may be insufficient to reduce the NDT noise floor due to the propensity for L-PBF near-surface porosity and boundary artifacts. Therefore, a combination of techniques is likely the best solution for a particular inspection requirement and the combinations of methods may vary depending on the criticality of the defects, the application, the part size and geometry, the material and the availability of local facilities for the required NDT tests, among other factors. A good design for AM takes into consideration the ability to perform the necessary NDT.

In addition to round robin tests (various laboratories test the same parts according to the same procedures and compare results), the development of standards and guidelines, and refinement of NDT methods for additive manufacturing, it is envisaged that the manufacturing of artificially flawed test artifacts might be very useful in the near future. The ability to seed flaws and artificially induce different types of flaws is increasing, and this will lead to more reliable NDT despite the complexity in AM parts. Additionally, mechanical tests on seeded discontinuities will help develop valid NDT acceptance criteria, by determining their effects on performance.

10.4 Emerging areas and outlook

NDT in AM of metals, and in L-PBF in particular, is increasingly important. The number and variety of commercial L-PBF systems are increasing, powder feedstock suppliers vary and all these add to the possibility for unexpected errors or situations creating defects in parts. Overall, optimized processes are needed to ensure high quality. NDT plays a key role in the optimization process, but also in the continued quality control and approval of produced parts. As NDT takes an ever increasingly important role in the AM workflow, its incorporation into qualification of processes and parts is crucial.

Future development of NDT techniques for L-PBF will likely make use of machine learning to provide improved defect detection within the limitations of the given instruments and their detection capabilities. In addition, the ability to create test objects with known defect contents to be used as reference will assist in providing confidence in NDT measurements for this application. This type of reference specimen could be the subject of round robin tests to confirm the detection and quantification capabilities of various NDT methods, and they could be used in-house for reference checking of the NDT equipment.

With NDT techniques refined for L-PBF parts, the reliability of manufactured parts can be assured, which will help to drive L-PBF to new applications and wider industrial use.

10.5 Questions

- What is the goal of NDT?
- Name five traditional NDT techniques
- Which NDT methods work well for laser powder bed fusion?
- Which NDT methods allow porosity measurement?
- Which NDT methods allow crack detection?

Acknowledgments

A. Du Plessis thanks the Collaborative Program for Additive Manufacturing for financial support. J. Waller thanks the NASA Office of Safety and Mission Assurance NDE Program for its funding of additive manufacturing foundational efforts such as detecting and examining the effect-of-defect of unique L-PBF flaw types. E. MacDonald would like to thank the Murchison Endowment for support of this work at the University of Texas at El Paso, USA.

References

ASTM D7127-17, 2017. Standard Test Method for Measurement of Surface Roughness of Abrasive Blast Cleaned Metal Surfaces Using a Portable Stylus Instrument. ASTM International, West Conshohocken, PA. https://www.astm.org.

ASTM E3166-20e1, 2020. Standard Guide for Nondestructive Examination of Metal Additively Manufactured Aerospace Parts After Build. ASTM International, West Conshohocken, PA. www.astm.org.

ASTM International, 2020. List of nondestructive testing standards developed by ASTM. https://www.astm.org/Standards/nondestructive-testing-standards.html#E07.10. (Accessed 28 October 2020).

Bartlett, J.L., Heim, F.M., Murty, Y.V., Li, X., 2018. In situ defect detection in selective laser melting via full-field infrared thermography. Addit. Manuf. 24 (December), 595–605. https://doi.org/10.1016/j.addma.2018.10.045.

Ciampa, F., Mahmoodi, P., Pinto, F., Meo, M., 2018. Recent advances in active infrared thermography for non-destructive testing of aerospace components. Sensors 18 (2), 609. https://doi.org/10.3390/s18020609.

Du Plessis, A., Waller, J.M., le Roux, S.G., Yadroitsava, I., Yadroitsev, I., Els, J., Prinsloo, J., 2020. X-ray computed tomography inspection in metal additive manufacturing: the role of witness specimens. Struct. Integrity Addit. Manuf. Mater. Parts 17. https://doi.org/10.1520/STP163120190109.

Du Plessis, A., le Roux, S.G., 2018. Standardized X-ray tomography testing of additively manufactured parts: a round robin test. Addit. Manuf. 24 (September), 125–136. https://doi.org/10.1016/j.addma.2018.09.014.

Du Plessis, A., Sperling, P., Beerlink, A., Kruger, O., Tshabalala, L., Hoosain, S., le Roux, S.G., 2018a. Standard method for MicroCT-based additive manufacturing quality control 3: surface roughness. MethodsX 5 (May), 1111–1116. https://doi.org/10.1016/j.mex.2018.09.006.

Du Plessis, A., Sperling, P., Beerlink, A., du Preez, W., le Roux, S.G., 2018b. Standard method for MicroCT-based additive manufacturing quality control 4: metal powder analysis. MethodsX 5 (October), 1336–1345. https://doi.org/10.1016/j.mex.2018.09.006.

Du Plessis, A., Sperling, P., Beerlink, A., Tshabalala, L., Hoosain, S., Mathe, N., Stephan, G., 2018c. MethodsX standard method for MicroCT-based additive manufacturing quality control 1 : porosity analysis. MethodsX 5 (September), 1102–1110. https://doi.org/10.1016/j.mex.2018.09.005.

Du Plessis, A., Sperling, P., Beerlink, A., Tshabalala, L., Hoosain, S., Mathe, N., Stephan, G., 2018d. MethodsX standard method for MicroCT-based additive manufacturing quality control 2 : density measurement. MethodsX 5 (September), 1117–1123. https://doi.org/10.1016/j.mex.2018.09.006.

Du Plessis, A., Yadroitsev, I., Yadroitsava, I., le Roux, S.G., 2018e. X-ray microcomputed tomography in additive manufacturing: a review of the current technology and applications. 3D Print. Addit. Manuf. 5 (3), 227–247. https://doi.org/10.1089/3dp.2018.0060.

Du Plessis, A., le Roux, S.G., Waller, J., Sperling, P., et al., 2019. Laboratory x-ray tomography for metal additive manufacturing: round robin test. Addit. Manuf. 30 (December), 100837. https://doi:org/10.1016/j.addma.2019.100837.

Dutton, B., Vesga, W., Waller, J., James, S., Seifi, M., 2020. Metal additive manufacturing defect formation and nondestructive evaluation detectability. In: Shamsaei, N., Daniewicz, S., Hrabe, N., Beretta, S., Waller, J., Seifi, M. (Eds.), *Structural Integrity of Additive Manufactured Parts*. ASTM International, West Conshohocken, PA, pp. 1–50. https://doi.org/10.1520/STP162020180136.

ISO 5725-1:1994(En), 1994. Accuracy (trueness and precision) of measurement methods and results — Part 1: General principles and definitions. International Organization for Standardization, pp. 5725-1. (last review date 2018).

NASA MSFC-STD-3716, 2017. NASA Marshall Space Flight Center Technical Standard, Standard for Additively Manufactured Spaceflight Hardware by Laser Powder Bed Fusion in Metals, Section 6.2.2 Witness Testing Requirements, MSFC-STD-3716, Oct. 18, 2017.

Lu, Q.Y., Wong, C.H., 2017. Applications of non-destructive testing techniques for post-process control of additively manufactured parts. Virtual Phys. Prototyp. 12 (4), 301−321. https://doi.org/10.1080/17452759.2017.1357319.

Lu, Q.Y., Wong, C.H., 2018. Additive manufacturing process monitoring and control by non-destructive testing techniques: challenges and in-process monitoring. Virtual Phys. Prototyp. 13 (2), 39−48. https://doi.org/10.1080/17452759.2017.1351201.

Mandache, C., 2019. Overview of non-destructive evaluation techniques for metal-based additive manufacturing. Mater. Sci. Technol. 35 (9), 1007−1015. https://doi.org/10.1080/02670836.2019.1596370.

Phased Array Ultrasonics - Wikipedia. n.d. https://en.wikipedia.org/wiki/Phased_array_ultrasonics. (Accessed 26 November 2020).

Seifi, M., Gorelik, M., Waller, J., Hrabe, N., Shamsaei, N., Daniewicz, S., Lewandowski, J.J., 2017. Progress towards metal additive manufacturing standardization to support qualification and certification. J. Occup. Med. 69 (3), 439−455. https://doi.org/10.1007/s11837-017-2265-2.

Seifi, M., Salem, A., Beuth, J., Harrysson, O., Lewandowski, J.J., 2016. Overview of materials qualification needs for metal additive manufacturing. J. Occup. Med. 68 (3), 747−764. https://doi.org/10.1007/s11837-015-1810-0.

Sharratt, B.M., 2015. Non-destructive techniques and technologies for qualification of additive manufactured parts and processes. Lit. Rev. http://cradpdf.drdc-rddc.gc.ca/PDFS/unc186/p801800_A1b.pdf.

Spierings, A.B., Schneider, M., Eggenberger, R., 2011. Comparison of density measurement techniques for additive manufactured metallic parts. Rapid Prototyp. J. 17 (5), 380−386. https://doi.org/10.1108/13552541111156504.

Suragus.Com, n.d. https://www.suragus.com/en/technology/eddy-current/. (Accessed 26 November 2020).

The American Society For Nondestructive Testing. https://asnt.org/. (Accessed 30 July 2020).

Todorov, E., Spencer, R., Gleeson, S., Jamshidinia, M., Kelly, S.M., 2014. America makes: National additive manufacturing innovation institute (NAMII) project 1: Nondestructive evaluation (NDE) of complex metallic additive manufactured (AM) structures. https://apps.dtic.mil/sti/citations/ADA612775.

Waller, J.M., Parker, B.H., Hodges, K.L., Burke, E.R., Walker, J.L., Generazio, E.R., 2014. Nondestructive evaluation of additive manufacturing state-of-the-discipline report. Technical Memorandum, ID 20140016447. https://ntrs.nasa.gov/search.jsp?R=20140016447.

Williams, R.J., Alessandro, P., Tobias, R., Jones, C., Pham, M.S., Davies, C.M., Hooper, P.A., 2019. In situ thermography for laser powder bed fusion: effects of layer temperature on porosity, microstructure and mechanical properties. Addit. Manuf. 30 (December), 100880. https://doi.org/10.1016/j.addma.2019.100880.

Process monitoring of laser powder bed fusion

11

Marco Grasso[1], *Bianca Maria Colosimo*[1], *Kevin Slattery*[2], *Eric MacDonald*[3]
[1]Department of Mechanical Engineering, Polytechnic University of Milan, Milan, Italy; [2]The Barnes Global Advisors, Pittsburgh, PA, United States; [3]W. M. Keck Center for 3D Innovation, University of Texas at El Paso, El Paso, TX, United States

Chapter outline

11.1 Introduction 301
11.2 Machine and chamber condition monitoring 302
11.3 In-situ process sensing 304
11.4 In-situ process monitoring 309
11.5 In-situ NDT 315
11.6 Closed-loop control and repair 318
11.7 Challenges and future directions 319
11.8 Questions 323
Acknowledgments 323
References 323

11.1 Introduction

This chapter provides an overview of methods, tools, and approaches developed for Laser Powder Bed Fusion (L-PBF) process monitoring, with special attention to in-situ and in-line solutions. Process monitoring represents one of the most promising directions to reduce scrap and rework; and hence improve the process yield, which tends to be a crucial aspect in additive manufacturing (AM), where powders and equipment are rather expensive, and shape complexity and product variability are key important factors.

Process monitoring consists of gathering a significant amount of data (signals, images, and video) while the process is running with the aim of (i) improving the current knowledge of the basic mechanisms of selective melting and cooling; (ii) supporting/validating process modeling; (iii) defining appropriate solutions to detect or even predict the onset of flaws or job failure; (iv) suggesting corrective actions, or (v) guiding ex-situ inspection.

Compared with traditional processes, the layerwise paradigm of L-PBF allows gathering of a significant amount of information to be processed in real-time (Grasso and Colosimo, 2017). However, significant work still needs to be done to summarize

Fundamentals of Laser Powder Bed Fusion of Metals. https://doi.org/10.1016/B978-0-12-824090-8.00012-3
Copyright © 2021 Elsevier Inc. All rights reserved.

all the available data and translate it into reliable information on the process state at each location. This information should be eventually used to make appropriate decisions (i.e., stop the process, re-inspect the product at that layer, act on the process parameters, reprocess the layer to heal defects). This chapter will try to provide a systematic but comprehensive description of solutions that are currently under development in research laboratories or that are already implemented in production systems available on the market at this time. As process monitoring of L-PBF encompasses a broad range of technologies, analyses, and decisions, the structure of this chapter follows an increasing level of complexity. The first two sections present a framework of information available at machine/chamber and process levels, respectively. Then, data integration is discussed to detect unnatural/unstable process conditions or even product flaws (i.e., in-situ nondestructive testing, NDT), thus supporting in-line product acceptance. Eventually, solutions to move from process monitoring to process control via feedback/feedforward control loop or layerwise corrective actions are considered. A systematic description of the following sections is presented as follows, making analogies to driving an automobile.

> Machine and chamber data gathering—This section focuses on data acquired at the machine and chamber level, which are mainly acting as inputs of the process, such as laser power, scanning speed, chamber temperature, gas flow rate, etc. Driving comparisons are steering wheel turn, accelerator pedal depression, selected gear.
>
> In-situ process sensing—This section describes all the different sensing architectures and methods that can be used for in-situ monitoring of those process signatures. In this case, the attention is mainly focusing on the outputs of the process, such as melt-pool temperature, powder bed temperature, cooling dynamics, spattering, etc. Driving comparisons are revolutions per minute (RPM), speed, and direction.
>
> In-situ process monitoring—This section describes how process monitoring can provide information on the current state of the process and possibly linked to defects to be observed on the product.
>
> In-situ NDT—This is the same as in-situ process monitoring, except that conclusions are being made about the product (part), such as the part is free of discontinuities or there is a discontinuity of a certain size present. Driving comparison would be that the car is headed in the wrong direction.
>
> Closed-loop control—This activity employs the conclusions drawn in either in-situ process monitoring or in-situ NDT and renders modifications in the process to correct either the process or the product, such as reducing laser power to keep stable the size and temperature of the melt pool and to reduce spattering and evaporation. Driving comparison is automatically turning the wheel to avoid hitting the tree.

11.2 Machine and chamber condition monitoring

Similar to traditional manufacturing processes, the health conditions of the machine and of its components, together with the stability of operational settings over time, are fundamental to meet part quality and process repeatability requirements in L-PBF. The system conditions can be monitored by means of embedded sensors, whose purpose is to guarantee the normal functionalities of the machine and maintain stable operational parameters—within the target set points.

The **chamber environmental conditions** are particularly critical, and their continuous monitoring and control require a number of different sensors. Commonly measured and monitored quantities include the chamber ambient temperature and pressure, the oxygen concentration, the filter status affecting the inert gas flow, etc. The chamber atmosphere and the shielding gas flow have a direct influence on the quality of the L-PBF process and on the quality characteristics of the product. The shielding gas prevents chemical reactions (e.g., oxidation or nitridization) by shielding the process zone. The gas flow allows displacing process byproducts, i.e., spatters and plume emissions, from the process zone, reducing laser beam attenuation effects, powder bed contamination, and deposition of vaporized material on the laser window. Examples of detrimental effects caused by improper chamber ambient conditions were presented and discussed by various authors. Ladewig et al. (2016) showed that a reduced gas flow velocity causes an irregular surface pattern of the solidified layer and lack-of-fusion defects. Anwar and Pham (2017) showed that the inert gas flow influences the mechanical properties of the part, but a significant effect is related also to the location of the part with respect to the gas outlet and the scanning direction (e.g., more severe lack-of-fusion defects were observed when scanning in the direction of the flow and further from the gas outlet).

In addition to chamber ambient conditions, several other quantities are measured, ranging from laser power to absorbed currents of recoater and z-axis motors, from build plate temperature to powder level, etc. Most L-PBF system developers provide end-users with software suites that allow them to monitor and visualize all these data during the process and track alarms during the system life cycle. This data collection leads to a large amount of information and data that can be used not only for the normal control of the system but also to detect undesired variations or fluctuations that may have detrimental effects on the part quality and the process stability. Since data is available without the need of external sensors and additional monitoring equipment, they can be regarded as a “level 0” source of information for L-PBF process monitoring. The information enclosed by such embedded signals may not be sufficient to implement automated solutions for in-process defect detection, but this data can provide complementary knowledge that is also easily accessible.

This idea has been mainly explored in Electron Beam Powder Bed Fusion (EB-PBF), where hundreds of so-called “log signals” are freely available from embedded sensors. Many of these EB-PBF log signals are commonly used for troubleshooting because they are correlated with process errors and variations of process conditions. This correlation allows the data to be a relevant source of information for real-time process monitoring as well. Various studies demonstrated the potential of using these data during the process to detect anomalies that may directly affect the final quality of the part, like geometric warping caused by improper dosing of the powder during the recoating operation or lack-of-fusion defects caused by sudden beam interruptions (Grasso et al., 2018; Steed et al., 2017). A similar advanced use of machine and chamber condition signals in L-PBF process monitoring still represents a poorly explored path (Zhirnov et al., 2019). However, a reliable and robust sensing architecture for continuous monitoring of machine state degradation and chamber ambient conditions is necessary to ensure process repeatability and quality products. All other in-situ sensing and monitoring methods discussed in Section 11.3 represent additional tools aimed at "looking" at the process focusing on salient phenomena occurring during the laser-material interaction and their effects in each printed layer.

11.3 In-situ process sensing

One major distinction in terms of in-situ sensing configurations for the L-PBF process is between **co-axial** and **off-axis sensors**. A schematic representation of these two different configurations is shown in Fig. 11.1.

In-situ co-axial monitoring exploits the back-reflected radiation from the melt pool and a small surrounding area through the optical path of the laser to measure salient melt-pool signatures. The field of view is commonly small enough (e.g., less than 0.5 mm × 0.5 mm) to enhance the signal-to-noise ratio by focusing, as much as possible, on the melt pool only, regardless of its instantaneous location within the build area. Such co-axial monitoring approach enables the installation of multiple sensors due to beam splitters and partially reflective mirrors as shown in Fig. 11.1. Suitable sensors include both spatially integrated pyrometers, which integrate the total amount of radiation emitted by the melt pool, and spatially resolved sensors, i.e., high-speed cameras. The most common type of spatially integrated sensor for co-axial use is the **photodiode**, which converts the incoming electromagnetic radiation into an electrical current signal proportional to the radiation intensity. Thanks to the spatial integration, photodiodes allow very high sampling frequency (e.g., >10–50 kHz), which is needed to guarantee a continuous process monitoring, even at high scan speeds (in the order of meters per second), and to reduce information loss. **Co-axial cameras**, being spatially resolved sensors, provide richer information as these imaging sensors allow measuring the size and shape of the melt pool, but also spatial variations of brightness or temperature within the melt pool area. The richer information is usually achieved at the expense of the sampling frequency, although high-speed video imaging with a good compromise between field of view and spatial resolution (e.g., about

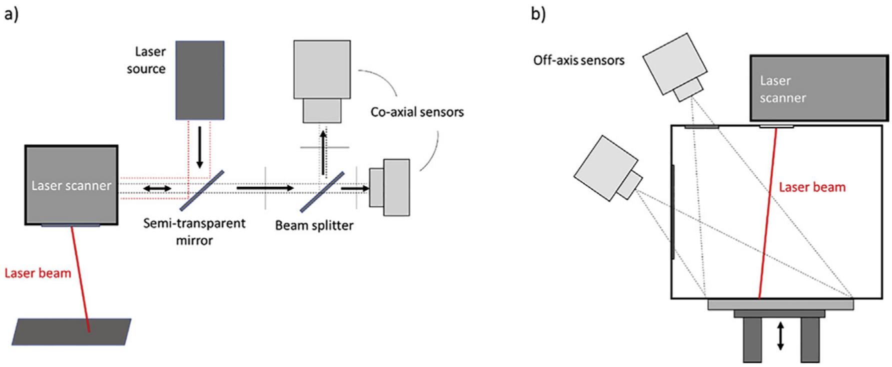

Figure 11.1 Examples of co-axial (a) and off-axis (b) in-situ sensing configurations in L-PBF.

5−20 μm/pixel over an area of 0.5 × 0.5 mm) allow achieving sampling frequencies in the order of tens of kHz. In this case, the primary drawback is the need to store and analyze a tremendous amount of data.

Some authors combined different co-axial sensors either to extend the amount of measurable quantities (e.g., by combining photodiodes and high-speed cameras) or to measure radiation emissions in different spectral ranges (Montazeri et al., 2020). Pyrometers capturing measurements at different wavelengths can also be used to achieve more accurate measurements of the absolute temperature without the need to know the surface emissivity of the melt pool. Indeed, passing from input irradiance measurement to absolute temperature estimation, the emissivity of the target must be known, but it depends on several factors, including phase transitions occurring during the L-PBF process. This makes a time-varying emissivity estimation quite difficult. Assuming that the emissivity of the target is constant at different wavelengths, measuring the ratio of signals at those wavelengths allows filtering out the emissivity term from the absolute temperature estimation.

Other co-axial measurement methods have been investigated, like the low-coherence interferometric technique, also known as **inline coherent imaging** (ICI) (DePond et al., 2018; Fleming et al., 2020). This method allows reconstructing the surface topology of the printed slice in terms of a height map exploiting a raster scanning of the area without the need for external scanning devices.

Co-axial monitoring in L-PBF entails a field of view that is always centered on the melt pool. This prevents gathering information on larger spatial scales and capturing defects that are not strictly related to the melt-pool behavior. Consequently, all other relevant process signatures can be measured via **off-axial sensors**. They mainly consist of spatially resolved sensors, which can be classified on the basis of their measurement wavelength range. On the one hand, standard cameras can be used to acquire image and video image data[1] in the visible range, with spatial and temporal resolutions that depend on the process signatures to be measured. On the other hand, near infrared (NIR) or infrared (IR) thermal cameras can be used to capture local and global temperature variations.

As far as **optical imaging** and **video imaging** are concerned, there are two major applications. The first consists of layerwise imaging before and after powder recoating. This application entails high-spatial resolution to properly detect small geometrical features and surface irregularities. Typically, spatial resolutions in the order to 20−250 μm/pixel can be achieved with off-axis cameras whose field of view includes the entire build area. Much higher spatial resolutions in the order of 5 μm/pixel were achieved by mounting a linear imaging sensor on the recoating system, to scan the build area like in common office scanners (Tan Phuc and Seita, 2019).

One relevant factor affecting the quality of layerwise measurements is **illumination**. Indeed, nonuniform illumination conditions within the build area may mask actual defects or introduce artifacts in the estimation of surface patterns and slice contours.

---

[1] The term “image data” refers to single images acquired once (or few times) per layer, whereas the term “video image data” refers to video streams acquired during the process.

One possible way to enhance the extraction of features of interest involves acquiring multiple images, each with a different lighting source, and then merging them with some image fusion technique (Gobert et al., 2018). When this is not possible, appropriate type and location of the lighting source can be selected with respect to the specific application, possibly in combination with robust image processing algorithms (Caltanissetta et al., 2018). A particular type of illumination suitable for the reconstruction of the surface topography of the layer is structured light for fringe projection. Stripe patterns are projected on the build area and recorded in a fast sequence by one camera or a stereo vision system. The aim is to reconstruct the 3D surface pattern by exploiting the gray level slopes at the stripe edges. This approach has been used in various studies to pass from traditional 2D pattern analysis to the actual height map measurement of surface irregularities in the layer (Kalms et al., 2019; Zhang et al., 2016).

Fig. 11.2 shows some examples of in-situ layerwise images acquired via off-axis high spatial resolution optical imaging.

The second application regards high-speed video imaging to capture fast transient phenomena like spatters, hot-spots, and variations in the solidified material. This application entails high-temporal resolutions to capture fast and transient patterns. Off-axis high-speed cameras enable sampling rates in the order of hundreds to thousands of frames per second, which are sufficient to capture most phenomena of interest with a reasonable trade-off in terms of spatial and temporal resolution for real-time use. In most applications, one high-speed camera is mounted outside the L-PBF system (exploiting the front viewport) or on the top of the chamber (exploiting additional viewports available on some industrial machines). Illumination settings may be critical for high speed imaging too. Synchronous strobe lighting is suitable for this application, whereas alternating current lighting sources shall be avoided due to flickering effects.

One use of high-speed setups adopted in various studies regards the monitoring and characterization of spatters ejected as byproducts of the laser-material interaction.

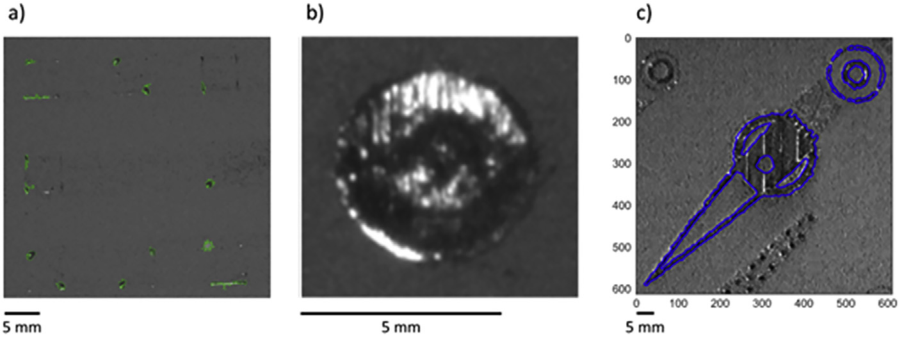

Figure 11.2 Examples of layerwise images in L-PBF: (a) post-recoating image with superelevated edges highlighted in green; (b) post-melting image (detail) for surface pattern characterization of the printed slice; (c) post-melting image with in-situ reconstructed contour for geometrical error detection (Pagani et al., 2020).

Despite the large amount of information that is potentially achievable with this approach, monocular vision is limited by the 2D characterization of spatter particles that move in a 3D space above the layer. To overcome these limitations, some studies showed the feasibility of high-speed stereo vision for spatter tracking and improved characterization of their speed, trajectory, and origination history (Barrett et al., 2019; Eschner et al., 2019).

Fig. 11.3 shows some examples of in-situ high-speed optical imaging applications.

As far as **thermal imaging** and **video imaging** are concerned, the main goal consists of determining the thermal history of the process through the reconstruction of spatial and temporal temperature variations. The electromagnetic spectrum can be divided into the following ranges of interest for in-situ sensing and monitoring applications: visible (0.4—0.8 μm), NIR (0.7 to ~1 μm), short wave IR (~0.9—1.7 μm, or ~0.9—2.5 μm), medium wave IR (2—5 μm), long wave IR (7.5—14 μm or more). The spectral sensitivity of standard cameras has a peak between 300 and 800 nm but the sensitivity in the NIR range can be still suitable to generate a signal. The use of NIR filters may provide different advantages in a number of applications with respect to monitoring the process in the entire visible spectral range. NIR video imaging may be suitable to filter out nuisance emissions at specific wavelengths (e.g., the laser wavelength or one of the plume emissions above the melted area) and to narrow the spectral range, reducing saturation effects in the presence of large temperature variations.

Cameras for in-situ thermography (or simply thermal cameras) enable measurements with better dynamic range performances than visible and NIR ranges, together with a very high sensitivity and a linear response over a wide range of temperatures. Although they enable accurate measurements of thermal gradients in space and time, the estimation of the absolute temperature is a troublesome task in L-PBF. Indeed, the fast phase transitions involved in the process (from powder to liquid to solidified material, in the order of 10^6 K/s), the consequent changes of surface properties and the presence of metal vaporization emissions limit the feasibility of accurate emissivity coefficient estimations. This limitation does not represent a critical issue when the

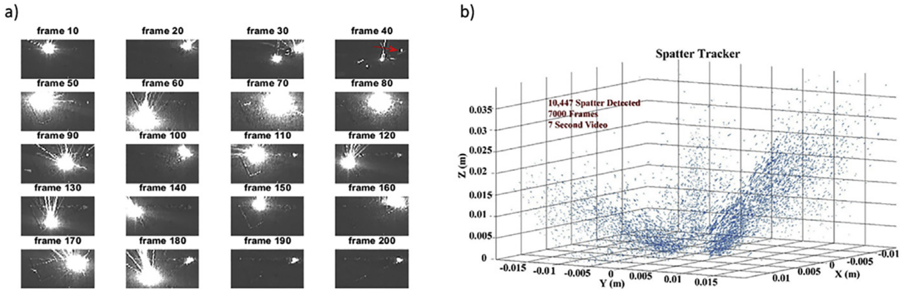

Figure 11.3 Examples of high-temporal resolution video imaging applications in L-PBF: (a) high-speed video frames for hot-spot detection (Colosimo and Grasso, 2018), (b) 3D spatter tracking via high-speed stereo vision (Barrett et al., 2019).

variation of the thermal signature over time is more relevant than the estimation of the absolute temperature. In those cases, data processing and monitoring algorithms can be directly applied on the measured irradiance (Grasso and Colosimo, 2019). For other applications, for example, when temperature gradients are studied to predict the microstructural properties of the part, an accurate estimate of the true temperature is needed. An example of an experimental calibration approach for the estimation of the emissivity coefficient of both solidified material and loose powder at different temperatures in L-PBF was presented by Williams et al. (2019).

Fig. 11.4 shows some examples of in-situ thermal video imaging applications.

Other sensing methods have been tested on L-PBF systems to measure process signatures for which machine vision is not applicable, e.g., recoating system vibration, acoustic emissions and deformations of the baseplate. Among them, in-situ acoustic emission measurement has attracted particular interest in industry, and some configurations have been patented by major L-PBF system developers too (Grasso and Colosimo, 2017).

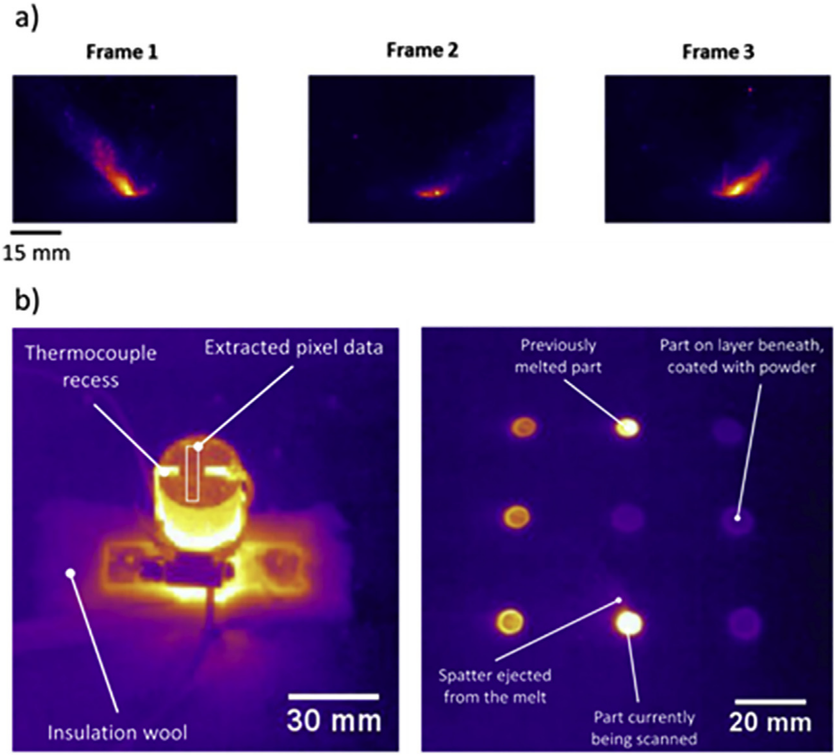
a)
Frame 1
Frame 2
Frame 3
15 mm
b)
Thermocouple recess
Extracted pixel data
Insulation wool
30 mm
Previously melted part
Part on layer beneath, coated with powder
Spatter ejected from the melt
Part currently being scanned
20 mm

Figure 11.4 Examples of thermal video imaging applications in L-PBF: (a) thermal video frames used to monitor the plume emission stability (Grasso and Colosimo, 2019), (b) apparatus used for thermal camera calibration (left) and in-situ thermal map for process monitoring (Williams et al., 2019).

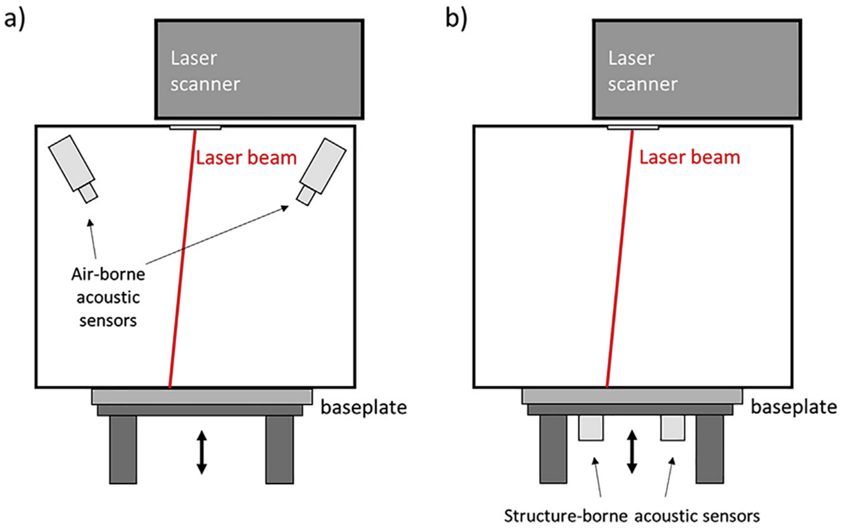

Figure 11.5 Examples of air-borne (a) and structure-borne (b) acoustic sensor mounting on L-PBF systems.

According to the nomenclature commonly used in laser welding (Ali and Farson, 2002), **acoustic emissions** can be divided into air-borne emissions (which can be captured by microphones in a wide range of frequencies) and structure-borne emissions (i.e., a release of elastic energy into the material, which requires contact sensors and high frequency bandwidth). Two examples of air-borne and structure-borne acoustic emission sensing configurations in L-PBF are shown in Fig. 11.5.

As a final remark, Table 11.1 shows a summary of the main sensing methods studied in the literature (which, in some cases, are also available in industrial systems) and the corresponding measurable process signatures.

11.4 In-situ process monitoring

Due to the layerwise production paradigm, a large amount of information can be gathered during the L-PBF process to determine the stability of the process itself and to detect the onset of defects while the part is being produced. The quantities, which can be measured in-situ and in-process, represent potential “signatures” of the process quality and can be classified into different categories depending on the spatial or temporal scale they belong to and on the nature of their enclosed information. This section briefly reviews the major types of process signatures that can be measured in the L-PBF process and their link to defects.

Among measurable process signatures in L-PBF, some quantities can be measured every layer, after the current layer has been recoated with powder and before starting the recoating of the next layer, to identify irregularities and deviations from expected patterns within the build area. Other quantities can be measured during the laser

Table 11.1 Mapping between in-situ measurable signatures and most common sensing methods.

		Co-axial sensing				**Off-axis sensing**				
Process signatures		**Spatially integrated pyrometry**	**Optical video imaging**	**NIR/IR video imaging**	**Inline coherent imaging**	**High spatial resolution optical imaging**	**High temporal resolution optical video imaging**	**Fringe projection**	**NIR/IR video imaging**	**Acoustic emissions**
Layer	Surface pattern and topography of the powder bed				X	X		X		
	Surface pattern and topography of the printed slice				X	X		X		
	Geometry of the printed slice					X				
Track	Heatmap and thermal gradients/ profiles								X	
	Hot and cold spots						X		X	
	Process byproducts						X		X	

(*continued*)

Table 11.1 Mapping between in-situ measurable signatures and most common sensing methods.—cont'd

Process signatures		Co-axial sensing				Off-axis sensing				
		Spatially integrated pyrometry	**Optical video imaging**	**NIR/IR video imaging**	**Inline coherent imaging**	**High spatial resolution optical imaging**	**High temporal resolution optical video imaging**	**Fringe projection**	**NIR/IR video imaging**	**Acoustic emissions**
Melt pool	Melt-pool size and shape		X							
	Melt-pool radiation intensity	X		X						
	Melt-pool temperature profile			X						
Other	Acoustic emissions intensity/ spectrum									X

scanning of the layer, to capture local and fast phenomena that can be proxies of anomalous melting and solidification conditions; with a third category measuring after scanning and before recoating.

In the framework of in-situ measurements gathered **before and after the powder recoating operation**, some quantities of interest are related to **surface pattern and topography of the powder bed**. The surface properties can be characterized through 2D machine vision (pixel intensity map) or 3D measurements (height map) and can be relevant to detect and localize flaws within the powder bed. As an example, the in-situ determination of the powder bed homogeneity is important to detect recoating errors, e.g., local lack of powder, rippling caused by recoater bouncing effects and/or rectilinear grooves generated either by particles dragging or other recoating system damage. In addition, **surface and geometrical irregularities of the printed layer** can be measured too, aiming at signaling possible departures from a natural expected pattern or from the nominal shape, respectively. Particular interest has been devoted in the scientific literature and in industrial studies to so-called "super-elevated edges" (zur Jacobsmühlen et al., 2015), i.e., elevated ridges of the solidified material that could not be fully recoated by the powder in next layers, inducing a potential propagation of defects within the build area and possible damage of the powder recoating system. Regarding the shape of the solidified layer (i.e., in-situ reconstructed contour in the layer), a major deviation from the nominal shape (sliced CAD model) may indicate a defect that cannot be recovered as the process goes on. This can be useful even if part dimensions and geometry measured in-situ may be not fully representative of the final dimensions and geometry of the as-built part as some deviations, including shrinkage and thermal stress-induced distortions, may not be captured on a layer-by-layer basis (Caltanissetta et al., 2018; Pagani et al., 2020).

The second major category of process signatures includes all quantities that can be measured **while the laser is scanning the area**. In this case, a distinction can be made considering the field of view of the measurement itself. If the field of view is sufficiently wide, phenomena occurring both within and outside the melt pool and the surrounding heat affected zone can be observed. This enables the measurement of **thermal gradients in time and space**, the detection of **anomalous heat accumulations or lack-of-fusion regions** (known as hot and cold spots, respectively), and the characterization of **process byproducts like spatters and plume emissions**.

Thermal gradients have a direct effect on the microstructural properties of the part, but in addition, local variations of the thermal history of the process affect pore formation and micro- or macro-geometrical distortions, as a consequence of either excessive or insufficient energy input. On the other hand, process byproducts have attracted an increasing interest in the recent years, as various studies showed that they can be proxies of process stability and melting state variations. Spatters can be caused by a vapor-driven entrainment of powder particles or by liquid material ejection from the melt pool as a result of unstable solid-liquid transitions. The plume is a partial material vaporization, which may also lead to plasma formation above the melting area. The **amount of spatters, their size, orientation,** and **speed** have been shown to be correlated to process parameters and scanning strategies causing either good (fully dense) or poor part quality (keyhole or lack-of-fusion porosity) (Barrett et al., 2019; Eschner et al., 2019; Bidare et al., 2018; Nassar et al., 2019; Repossini et al., 2017). Similarly, the **plume size, orientation,** and **temperature profile** have been shown to have an effect on the final quality of the part (internal porosity and geometrical accuracy) (Grasso and Colosimo, 2019; Bidare et al., 2018).

If the field of view is limited to the melt pool, most relevant process signatures include the **melt-pool size, shape, radiation intensity, and temperature profile** (Kolb et al., 2018; Okaro et al., 2019; Scime and Beuth, 2019). The melt pool represents the highest level of detail at which the L-PBF process can be observed and it is known to be a primary feature of interest, as its properties have a direct effect of melting and solidification mechanisms. Indeed, the stability, dimensions, and behavior of the melt pool determine to a great extent the quality of the part and stability of the process. Melt-pool signatures and their stability over time determine the geometrical accuracy of the track together with microstructural, physical, and mechanical properties of the final part.

All the above mentioned process signatures can be measured in the currently monitored layer, which prevents gathering additional information about what happens in previously melted and solidified layers as the process continues. However, some solutions are available to also capture phenomena occurring below the current layer. One example involves the measurement of **acoustic emissions** caused by cracks, delaminations, and detachments of supports (Shevchik et al., 2018; Ludwig, 2020). Some authors showed that acoustic emission signals can be correlated to the beam-material interaction (Eschner et al., 2020; Kouprianoff et al., 2017, 2018). Another example involves the measurement of deformations of the base plate as a consequence of thermal stresses originated during the process (Dunbar et al., 2016). Eventually, various studies have been devoted to the in-situ and in-process use of X-ray imaging techniques to look under the layer and investigate melt-pool depth variations and pore formation mechanisms (Samei et al., 2019; Martin et al., 2019). However, this latter approach requires ad-hoc L-PBF prototype systems, which relegates the application suitable for research studies but not for industrial implementation.

Table 11.2 summarizes the main types of process signatures that can be measured in-situ and the defects that can be potentially detected due to these measurements, according to the current state of the art.

Table 11.2 shows that porosity can be detected, at least in principle, by measuring several process signatures at different levels. However, it is worth specifying that in most studies, a global variation of internal porosity is forced by varying the laser power density and scanning speed. This allows showing that in-situ measured quantities are suitable to classify good (fully dense) parts from parts with either lack-of-fusion or keyhole porosity. The detection of single pores is a much more challenging task, and a much smaller number of studies have demonstrated reasonable agreement with post-process X-ray inspections. This is partially caused by the intrinsic limit of the layerwise paradigm, as pores may generate below the surface and/or remelting steps may close surface pores identified in previous layers. In-situ characterization of part porosity in terms of individual flaw identification still requires research efforts and novel advanced solutions.

Table 11.2 Mapping between in-situ measurable signatures and process defects in L-PBF. An "X" is shown in correspondence of known relationship demonstrated in the literature, while (X) is used to represent potential links.

Process signatures		Microstructural inhomogeneity	Porosity	Cracks and delamination	Geometrical distortions and warping	Surface defects
Layer	Surface pattern and topography of the powder bed		(X)		X	X
	Surface pattern and topography of the printed layer		(X)		(X)	X
	Geometry (shape) of the printed layer				X	
Track	Heat map and thermal gradients/ profiles	X	X		X	
	Hot and cold spots		X		X	
	Process byproducts	(X)	(X)			X
Melt pool	Melt-pool size and shape	(X)	X		(X)	X
	Melt-pool radiation intensity	(X)	X		(X)	X
	Melt-pool temperature profile	(X)	X		(X)	X
Other	Acoustic emissions intensity/ spectrum		(X)	X		

11.5 In-situ NDT

At first glance, in-situ NDT looks like in-situ process monitoring, in that it often uses the same sensors and data analysis tools. The difference comes in the conclusions that are made with the data. Whereas in in-situ process monitoring, a conclusion is made that the **process** of AM is either proceeding in the desired manner or not; in in-situ NDT, a conclusion is made that the **product** of AM (that is the actual part being produced) is acceptable or not, and to what degree it is not acceptable. To further understand this, refer back to Chapter 10 (Nondestructive Testing of parts produced by laser powder bed fusion), where the different NDT methods are used to detect and characterize physical discontinuities (porosity, lack of fusion, cracks, inclusions, etc.) that can compromise the ability of the part to meet requirements. Not only is NDT used to detect these discontinuities but also to help determine their size to make a determination if the part is acceptable.

In-situ NDT is performing the same role, except that instead of inspecting after part completion with radiography, penetrant liquids, ultrasonics, etc., the inspection is performed while the part is being built. The potential benefits of this are:

- Since the inspection is performed while the part is being built, particularly between layers, the challenges of complicated geometry are greatly mitigated, as the region of inspection is a flat layer versus a complex surface.
- Since the inspection is done for every layer or every few layers, the depth of material that needs to be inspected is a few hundred μm, versus mm or even cm. This can greatly enhance detection and characterization.
- Since inspection is completed shortly after the part is built, a determination can quickly be made if the part is acceptable. This will not only prevent adding post-processing value (~40% of final part cost) to something that may be scrapped in the end but can potentially prevent making another discrepant part if the cause can be determined.

Like in-situ process monitoring, in-situ NDT can also be used not only to make a decision to accept or reject but also to determine if additional evaluation is needed to make an accept/reject decision.

The current limitations to in-situ NDT in L-PBF are twofold. The first is that just because a part did not have any unacceptable discontinuities while it was being built, it doesn't mean that it is free of them when the part is completed. The most prevalent concern in L-PBF is cracking from residual stresses, but other forms of damage can also occur after build completion or during post-processing. Therefore, some industries and applications will still require a final inspection, such as penetrant liquid or resonance inspections, to ensure the acceptability of the part. The primary limitation at this time, however, is the lack of a standard methodology of the processing of data generated by in-situ NDT methods, their empirical relationship with actual defects available publicly, as well as the degree to which they have been validated for production use. While several industrial systems from L-PBF system developers or third-party companies are now available with in-situ NDT capabilities (e.g., QM meltpool 3D by Concept Laser, MPM by SLM Solutions, MeltView by Renishaw, Truprint Monitoring by Trumpf, PrintRide 3D by Sigma Labs, etc.), at this point, the only

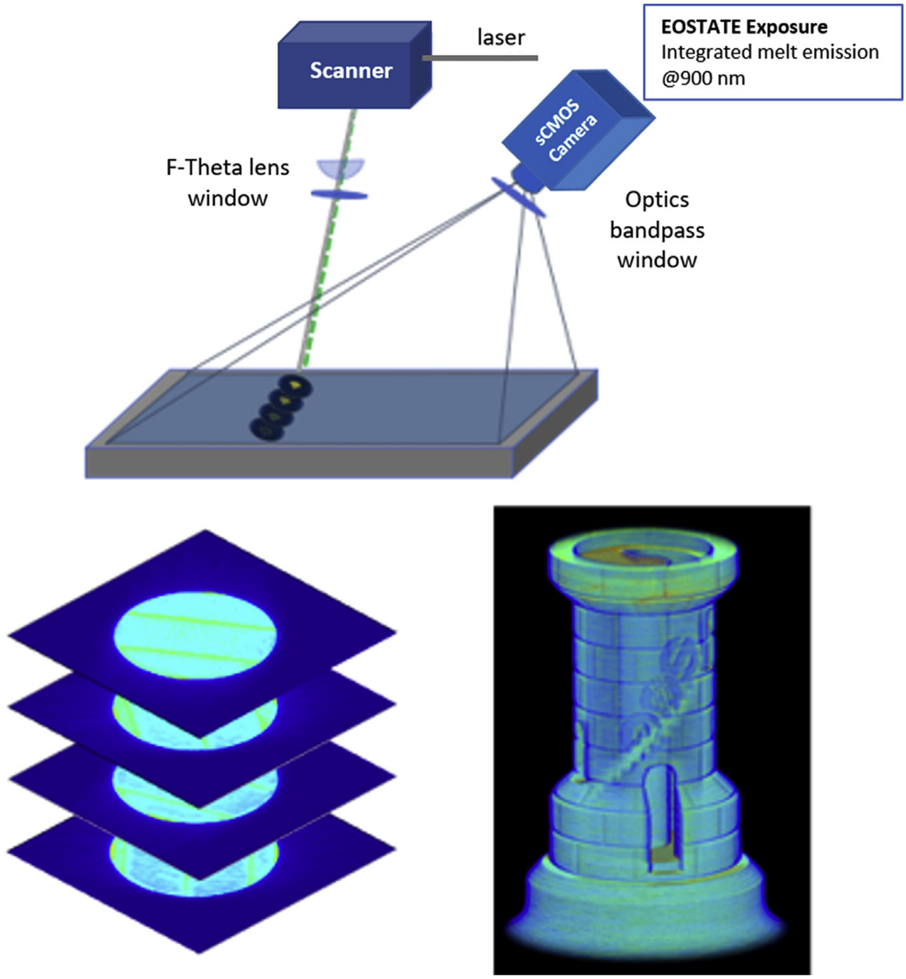
laser
Scanner
EOSTATE Exposure
Integrated melt emission
@900 nm
sCMOS Camera
F-Theta lens
window
Optics
bandpass
window

Figure 11.6 EOS exposure OT schematic (top) and reconstruction (bottom) (Ladewig et al., n.d.).

publicly announced usage of in-situ NDT on a production basis is by MTU Aero Engines of Munich, Germany, using EOSTATE Exposure OT on an EOS M290 (Ladewig et al., n.d.). This method, shown schematically in Fig. 11.6, takes near-infrared pictures of the top of the build after melting and before recoating. These images are then reconstructed after the build is complete, also shown in Fig. 11.6, and an assessment is made regarding the presence of discontinuities. In the case of the MTU application, significant effort was required to train the system to identify the discontinuities of interest.

One aspect that varies between in-situ NDT methods is when the analysis and conclusion are performed. In the above case, the analysis is performed post-build before any next step in the production chain. The results could prevent wasting value-added post-processing operations. However, automated alarm rules could be implemented in-process as well, enabling possible in-situ corrective actions, as discussed in the next section. In some cases, increases in computing power and/or more efficient analysis algorithms will enable post-build analyses to become real-time analysis. The difference in impact between post-build and real-time analysis also highlights the importance of having a robust and repeatable process. If the build process results in a 1% scrap rate, the benefit of real-time analysis is minimal. If the build process results in a 20% scrap rate, the benefit is substantially higher.

While Exposure OT uses still shots of each layer in the near-infrared range, the full range of sensors (still layer, melt-pool video, pyrometry, acoustic, etc.) and wavelengths (visible to infrared to ultraviolet) used for process monitoring may potentially also provide useful information. The key to all of this is determining the sensors that provide meaningful data and the analysis methods that will highlight the anomalies of interest without an excessive number of false-positives (concluding a discontinuity of concern is present when none exists). Finding this balance requires an interdisciplinary approach between those responsible for the reliability of the part, AM engineering, and NDT engineering, and often the customer or regulatory body. The subparts that need to be integrated are the following:

- Determining the size of each anomaly type that is of concern. Note that in many cases, multiple, smaller anomalies may have the same impact as a single, larger one.
- Developing the correlation between the sensor data and the presence of a discontinuity, along with the size of the discontinuity.
- Validating the ability of the in-situ NDT method to detect the discontinuities of concern. In most cases this will require running multiple tests to not only determine the limits of the in-situ NDT method but also the probability that it will find the discontinuity with a certain degree of confidence. In conventional post-process NDT, the goal is often to determine the size above which 90% of the discontinuities will be detected with a 95% level of confidence.
- Comparing the validated detection size with the part and system reliability criteria to ensure that the in-situ NDT method supports the desired level of reliability or life and finalizing the pass/fail criteria. In many cases, the pass/fail size will be set to something smaller than is absolutely necessary to detect in order to provide better monitoring of quality and to support future applications for more critical parts.

Like process monitoring, another difference in in-situ NDT methods is the final data that is archived. This can range from the final conclusion (acceptable, i.e., largest discontinuity smaller than a given threshold, or rejectable, discontinuity bigger than a given threshold) to intermediate analysis outputs, to storing everything including the raw data. The benefit of the final conclusion is reduced archiving costs, while the benefit of storing the raw data provides the potential to go back and reanalyze the data with an improved analysis method if some problem arises in service, or, if it is desired, to extend the life of the product by showing that discontinuities are compliant with acceptance criteria.

In summary, in-situ NDT has the potential to support a broader range of applications for L-PBF, provided that the build process and post-processing deliver parts that are reliably free of discontinuities that would prevent use in these applications. The development and validation of these methods will still require significant effort, however.

11.6 Closed-loop control and repair

The previous subsections pointed out the potential of in-situ sensing, measurement, and monitoring methods to detect process instability conditions and onsets of anomalies and defects. Nevertheless, in-situ monitoring is not sufficient by itself to guarantee defect-free additively manufactured products.

The common industrial practice to improve the final quality of parts produced via L-PBF and to reduce the defect rates consists of performing an experimental mapping between controllable process parameters and final quality and performance indicators. This is typically implemented during the so-called “material development” phase, where the processability window for a given material using a given L-PBF system is identified and optimal process parameters and scan strategies are set. Despite being a necessary step, **process mapping** does not guarantee that all parts produced with selected parameters will be defect-free. Indeed, optimal parameters are not only material-dependent but also geometry-dependent. This implies that using fixed process parameters and scan strategies may produce various kinds of defects and deviations from expected process behaviors in the presence of critical geometrical features like overhang areas, thin walls, acute corners, etc. In addition, stochastic variations in the beam-material interaction, powder recoating, process byproduct emissions, etc., may cause a wide range of undesired variations with potential impact on the final quality and acceptability of the part.

Some defects can be predicted, as they are related to the geometry of the part and the thermomechanical interactions occurring during the process. These defects can be at least partially avoided by setting locally varying process parameters and scan strategies in the build file transferred to the L-PBF system. Process modeling and simulations could be used to drive the selection of the within-layer and layer-by-layer variations of controllable parameters. This approach is also known as **model-based feedforward control** (Renken et al., 2019).

Unfortunately, not all defects can be predicted due to many sources of stochastic variability, nuisance factors related to the degradation of performance, system calibration, the prediction uncertainty of process simulation tools, etc. In this framework, in-situ sensor signals represent the information source to enable additional control and recovery actions aimed at mitigating or avoiding defects in the final part.

One way to exploit in-situ data to this aim consists of combining in-situ measurements and real-time adaptation of process parameters into a **closed-loop control** architecture. Some seminal studies demonstrated that it is possible to adapt the laser power based on the measured melt-pool emission, to keep the melt-pool properties stable over time (Kruth et al., 2007). In this seminal study of Kruth et al. (2007), the melt-pool emission was measured via a coaxial photodiode as a proxy of the melt-pool area, and the real-time adaptation of the laser power allowed improving the quality of bridges and overhang areas without supports. A more recent study explored the combination of feedback and feedforward control methods (Renken et al., 2019). Model-based feedforward control was used to locally adapt process parameters in the presence of critical geometrical features (e.g., overhang surfaces). The closed-loop control of laser power using as input information the melt-pool intensity enabled the additional reduction of fluctuations and deviations from a target set point that could not be avoided with the feedforward control method alone.

Generally speaking, feedback control methods can be implemented at different levels. The methods mentioned above focused on continuous variation of the laser power along the scan of each track. This implies a very fast reaction that is challenging to achieve on state-of-the-art L-PBF systems exploiting very high scan speed and, in many cases, multiple laser beams. Two alternative implementations involve a process parameter adaptation either on a track-by-track or a layer-by-layer basis. In these cases, the information gathered in previous tracks and/or in previous layers can be used to adapt the set point for tuning process parameters in the next track and/or in the next layer. An example of this approach was presented in a recent study (Vasileska et al., 2020), where a **layer-wise control** strategy based on coaxial melt-pool monitoring was proposed. Starting from a set point of the melt-pool area defined on a simple geometry, the melt-pool area was then monitored on more complex shapes, and the melt-pool area measured on each scan vector was used to compensate the energy density of the same scan vector in the next layer. The study showed that this approach was effective in reducing geometric errors.

When all previous control strategies are not applicable or not sufficient to guarantee actual defect-free components, one further type of intervention regards the **in-situ correction or removal of defects** after they have been detected. To this aim, layer remelting has been investigated as a repairing solution to reduce internal porosity, surface roughness, local stress concentration, and to improve microstructure characteristics (Heeling and Wegener, 2018; Demir and Previtali, 2017). Another defect repairing solution consists of combining additive and subtractive processes in the same machine to “cancel” defective areas or entire defective layers while the part is being produced. Some authors discussed the combination of L-PBF and selective laser erosion to improve the layerwise surface characteristics and, in principle, to remove defective layers before restarting the process (Yasa et al., 2011). Another concept was implemented and tested on an open-architecture L-PBF system called *Penelope* (Caltanissetta et al., 2018). A multisensor monitoring architecture was combined with a hybrid apparatus for in-situ defect removal. Such capability was achieved by using a surface grinding wheel mounted on a linear axis, which is activated as soon as an alarm is signaled by the in-situ monitoring system. The surface grinding operation allows getting rid of the last produced layers where the defects were identified. After the layer removal operation, the L-PBF process goes on with modified process parameters to avoid the re-occurrence of the same defect. In-situ defect correction or removal could be combined with previously mentioned control architectures to integrate different reaction and recovery capabilities suitable to maximize the avoidance of flaws and to enhance the final quality and performances of the product.

11.7 Challenges and future directions

The first seminal studies on in-situ monitoring in L-PBF date back to 2007 and 2008 and were mainly focused on the characterization of melt-pool properties via coaxial signals. The scientific literature devoted to this topic has quickly evolved and grown in recent years, and currently, many in-situ sensing and monitoring tools have been adopted by major L-PBF system developers. However, most of these tools are used to collect and visualize data during the process, without actual real-time analysis and autonomous anomaly detection capabilities. Collected data are provided to the user to support the investigation of specific problems and defects during post-processing qualification phases. Only in a few cases have automated alarm rules been implemented by machine vendors. Indeed, what is still missing in industrial systems is the availability of an embedded intelligence layer able to make sense of large and fast streams of in-situ gathered signals and automatically detect unstable conditions and defects within the part. As a matter of fact, several challenges and open issues need to be tackled to make prototype solutions developed in research studies reliable and robust enough for real industrial applications.

This section describes many of the challenges in which progress must be made to truly widen the adoption of L-PBF to a diversity of industries—beyond biomedical and aerospace for instance. Necessity is the mother of invention and these challenges may be central in the next generation of L-PBF research.

One of the main challenges for the effective use of in-situ monitoring in industrial settings concerns the cumbersome activity of **calibration and tuning** to be performed on algorithms in order to achieve good performances in terms of **false positive and false negative**. Calibration and tuning of the algorithms can consist of selecting a significant number of parameters (thresholding, filtering, image analysis) which can greatly influence the final ability to detect an out-of-control state. This can result in a complex task, especially in the presence of complex shapes that vary from one build to another. The natural sources of variation and nuisance factors in L-PBF render the achievement of these target performances a difficult task, which motivates the continuous investigation of novel data mining and statistical learning techniques. The task is made even more difficult by the lack of sufficient time or historical data to learn from. Indeed, the training dataset must be representative of in-control process conditions, but the underlying dynamics of the process may vary from one layer to another and from one part to another. Under these premises, novel training paradigms or novel adaptive and robust methods shall be explored.

The role played by false positives and false negatives on the economic viability of in-situ monitoring tools in L-PBF was explored by Colosimo et al. (2020). The authors presented a cost model suitable to determine the economic impact of defects in L-PBF and the extent to which in-situ monitoring tools are viable and economically convenient. Therefore, the proposed model can be used to define performance specifications of in-situ monitoring solutions that yield sustainable cost savings in specific industrial applications. Both technical and economic aspects shall be taken into account to assess the industrialization needs of in-situ monitoring solutions and to include them into L-PBF part and process qualification frameworks.

One additional challenge regards the efficient and effective **handling of big data**, where the term "big" refers not only to the size of data (tens to hundreds of gigabytes of data may be generated during the production of one single part) but also to the velocity of the data (e.g., high-speed videos and pyrometry signals acquired with sampling rate in order of thousands of hertz or more) and the variety of data types (signals, images, videos, thermal videos, etc.). This pushes the need for computationally efficient methodologies for real-time data analysis, data management, and storage. Due to the size and complexity of in-situ gathered data, a critical aspect regards the input data quality. The entire in-situ sensing and data collection architecture need to be selected and designed to maximize the signal-to-noise ratio and to enable the extraction and modeling of relevant process signatures, with a viable compromise in terms of equipment cost and measurement performances. Data reduction plays a primary role as well, since it allows extracting the actual information content from a large data stream. Thanks to this synthesis operation, it is possible to reduce the amount of data to be analyzed, transferred, and stored.

In particular, the sheer volume of data can be unbearable from a **data storage, disk drive,** and **networking perspective** for many types of sensor systems. On the low end of the spectrum, chemistry and temperature sensors may only require a handful of bytes every second or minute, but a mid-range, high-definition, high-speed camera can generate 10,000 frames a second and each frame can include 1920 columns and 1080 rows (approximately two million pixels total) with 8 bits for each of the three colors (RGB). Using this data bandwidth as a baseline, 60 GBs of data are generated every second. A minute of data would require 3.6 TB (an entire disk drive for a state-of-the-art desktop computer as of the end of 2020). An hour would require a quarter of petabyte of data and a petabyte of data storage with redundancy can cost over $1M USD at the time of this writing. Of course, the storage is an important consideration but this does not include dealing with the transport of the data through the network which must be capable of conveying the data at a rate of 60 GB per second or data loss could result. Generally, high speed and high frame rate cameras are the worst offenders in terms of network bandwidth and data storage, but other sensors that are used to map the powder surface in 3D including fringe projection techniques or laser line profilometry can also generate enormous amounts of data (Barrett et al., 2018).

The solution to this explosion in processing data is likely not to simply accommodate for the explosion in data by paying the IT department more as this could be **prohibitively expensive.** Manufacturers and researchers will certainly need to maintain awareness of advancements in ever improving computing and networking performance; however, there are other techniques that could be used to reduce the data, which could lead to many multiple orders of magnitude of reduction in data bandwidth and storage requirements. For instance, in a high speed spatter tracking project, two high speed cameras were synchronized at 1000 frames per second with a 500 μs exposure time. The raw data bandwidth for the dual cameras was 6 GB per second, but in fact, the true information locked in the images as features was only the start and stop point of 10—20 spatter arcs. The two points per spatter required the row and column to be identified simultaneously in both images thus requiring 8 bytes of data per arc. A three-dimensional coordinate can be calculated from this data to provide location in 3D space and requiring 6 bytes for each spatter arc. For 10 arcs in 1000 images, the total bandwidth is reduced from 6 GB to 100 KB (Barrett et al., 2019). By running the live data through a high performance computer and extracting these less storage-expensive features from the image, data can be dramatically reduced. The challenge with this approach is the requirement for a high performance computer reading the live “feed” of images and extracting and storing the features in real time. A potential inexpensive but highly technical solution includes using a high performance Field Programmable Gate Array (FPGA) to act on the data feed with hardware. Whereas a processor may have one multiplier (critical to almost all mathematical algorithms) which is generally accessed in a serial fashion with software, an FPGA can be programmed with a hard-wired computer vision algorithm that can parallelize the problem with 100,000 multipliers operating simultaneously on the same chip. With high performance interfaces, the high speed images can be fed to an FPGA system in close proximity and the important low byte-count features (like spatter location) can be extracted and stored. Storage is improved and the post-process or in-process analysis is dramatically simplified.

Finally, **data synchronization** is also crucial for the fusion of data so that the unassociated sensors can be "lined up" in time. A temperature spike during a given layer, as an example, requires recording accurately the start and stop time of the layer and recording an accurate timestamp for each temperature measurement to know which fall within the duration and are associated with the layer. In this fashion, the recorded temperatures of the given layer can be specifically analyzed over the course of minutes. Ambient temperature of course has one of the longest time scales of most of the commercially available sensors, but for shorter time scale sensors, such as high speed cameras, synchronization is even more of a challenge and more critical. To leverage stereovision to identify objects in 3D space, two 2D images must be recorded at as close to the same time as possible or the clocking skew will introduce spatial error. Generally, high speed cameras have a sync-in and sync-out port to allow for simultaneous image recording, but generally, the armada of sensors must be synchronized and automatic synchronization may not be available. Measurements of any sensors should be associated to the printing process in time: a layer, a track and even to a specific X-Y location of the laser on the top surface of the powder bed. Without this synchronization, data fusion is not possible and this severely limits the value of the sensor, which is most effective when analyzed in the context of the intended process and considered with data from other sensors.

An interesting direction for further study to reduce the amount of data to be stored and analyzed consists of combining process simulation to process monitoring. In this framework, numerical models of the process under study can be in principle augmented with real in-situ data to obtain a full **digital twin** of L-PBF. Virtual and real data fusion can eventually represent a key element to closed-loop control, as feedforward modeling can greatly reduce the needs of fast computing needed in feedback control.

As a final remark, in-situ process monitoring and control can represent a promising solution to prevent, control, and possibly correct many defects and flaws arising in printing. However, further efforts toward standardization of data formats, methods, and procedures are needed, to integrate in-situ measurements into industrial process and product qualification operations (Seifi et al., 2017). In this context, there is also the need to develop anomalies catalogs and manufacturing guidelines for seeding natural flaws in additively produced parts, to validate in-situ monitoring solutions and determine their compliance with industrial quality standards. Moreover, additional sources of defects due to the incoming material or to post-processing (thermal treatment, machining or finishing) cannot be captured with all the techniques described in this chapter. Thus, a more holistic cyber-physical framework should embrace data mining at all the steps of the process chain to move toward an industry 4.0 perspective.

11.8 Questions

- What is the difference between a spatially integrated and a spatially resolved measurement?
- For which kind of in-situ measurements the choice of an appropriate illumination is more relevant and why?
- What are the main advantages and drawbacks of a co-axial sensing method compared to an off-axis one?
- What is the spatial resolution of image data acquired by means of a 5 Mpixel camera equipped 1:1 aspect ratio sensor if the measurement field of view is 250 × 250 mm?
- What is the amount of data generated in 1 min with an off-axially mounted 1.5 Mpixel RGB sensor and a sampling rate of 800 Hz?
- What is the difference between feedforward and closed-loop control?

Acknowledgments

Professor Colosimo and Dr. Grasso acknowledge the Italian Ministry of Education, University and Research for the support provided through the Project “Department of Excellence LIS4.0—Lightweight and Smart Structures for Industry 4.0.” Professor MacDonald would like to thank the Murchison Endowment for support of this work at the University of Texas at El Paso, USA.

References

Ali, A., Farson, D., 2002. Statistical classification of spectral data for laser weld quality monitoring. J. Manuf. Sci. Eng. 124, 323—325.

Anwar, A.B., Pham, Q.-C., 2017. Selective laser melting of AlSi10Mg: effects of scan direction, part placement and inert gas flow velocity on tensile strength. J. Mater. Process. Technol. 240, 388—396.

Barrett, C., MacDonald, E., Conner, B., Persi, F., 2018. Micron-level layer-wise surface profilometry to detect porosity defects in powder bed fusion of inconel 718. JOM 1—9.

Barrett, C., Carradero, C., Harris, E., Rogers, K., MacDonald, E., Conner, B., 2019. Statistical analysis of spatter velocity with high-speed stereovision in Laser Powder Bed Fusion. Prog. Addit. Manuf. https://doi.org/10.1007/s40964-019-00094-6.

Bidare, P., Bitharas, I., Ward, R.M., Attallah, M.M., Moore, A.J., 2018. Fluid and particle dynamics in Laser Powder Bed Fusion. Acta Mater. 142, 107—120.

Caltanissetta, F., Grasso, M., Petrò, S., Colosimo, B.M., 2018. Characterization of in-situ measurements based on layerwise imaging in Laser Powder Bed Fusion. Addit. Manuf. 24, 183—199.

Colosimo, B.M., Grasso, M., 2018. Spatially weighted PCA for monitoring video image data with application to additive manufacturing. J. Qual. Technol. 50 (4), 391—417.

Colosimo, B.M., Cavalli, S., Grasso, M., 2020. A cost model for the economic evaluation of in-situ monitoring tools in metal additive manufacturing. Int. J. Prod. Econ. 223, 107532.

Demir, A.G., Previtali, B., 2017. Investigation of remelting and preheating in SLM of 18Ni300 maraging steel as corrective and preventive measures for porosity reduction. Int. J. Adv. Manuf. Technol. 93, 2697−2709.

DePond, P.J., Guss, G., Ly, S., Calta, N.P., Deane, D., Khairallah, S., et al., 2018. In situ measurements of layer roughness during Laser Powder Bed Fusion additive manufacturing using low coherence scanning interferometry. Mater. Des. 154, 347−359.

Dunbar, A.J., Denlinger, E.R., Heigel, J., Michaleris, P., Guerrier, P., Martukanitz, R., et al., 2016. Development of experimental method for in situ distortion and temperature measurements during the Laser Powder Bed Fusion additive manufacturing process. Addit. Manuf. 12, 25−30.

Eschner, E., Staudt, T., Schmidt, M., 2019. 3D particle tracking velocimetry for the determination of temporally resolved particle trajectories within Laser Powder Bed Fusion of metals. Int. J. Extrem. Manuf. 1, 035002.

Eschner, N., Weiser, L., Häfner, B., Lanza, G., 2020. Classification of specimen density in Laser Powder Bed Fusion (L-PBF) using in-process structure-borne acoustic process emissions. Addit. Manuf. 101324.

Fleming, T.G., Nestor, S.G.L., Allen, T.R., Boukhaled, M.A., Smith, N.J., Fraser, J.M., 2020. Tracking and controlling the morphology evolution of 3D powder-bed fusion in situ using inline coherent imaging. Addit. Manuf. 32, 100978.

Gobert, C., Reutzel, E.W., Petrich, J., Nassar, A.R., Phoha, S., 2018. Application of supervised machine learning for defect detection during metallic powder bed fusion additive manufacturing using high resolution imaging. Addit. Manuf. 21, 517−528.

Grasso, M., Colosimo, B.M., 2017. Process defects and in situ monitoring methods in metal powder bed fusion: a review. Meas. Sci. Technol. 28 (4), 044005.

Grasso, M., Colosimo, B.M., 2019. A statistical learning method for image-based monitoring of the plume signature in Laser Powder Bed Fusion. Robot. Comput. Integrated Manuf. 57, 103−115.

Grasso, M., Gallina, F., Colosimo, B.M., 2018. Data fusion methods for statistical process monitoring and quality characterization in metal additive manufacturing. Procedia CIRP 75, 103−107.

Heeling, T., Wegener, K., 2018. The effect of multi-beam strategies on selective laser melting of stainless steel 316L. Addit. Manuf. 22, 334−342.

Kalms, M., Narita, R., Thomy, C., Vollertsen, F., Bergmann, R.B., 2019. New approach to evaluate 3D laser printed parts in powder bed fusion-based additive manufacturing in-line within closed space. Addit. Manuf. 26, 161−165.

Kolb, T., Müller, L., Tremel, J., Schmidt, M., 2018. Melt pool monitoring for laser beam melting of metals: inline-evaluation and remelting of surfaces. Procedia CIRP 74, 111−115.

Kouprianoff, D., Luwes, N., Newby, E., Yadroitsava, I., Yadroitsev, I., 2017. On-line monitoring of Laser Powder Bed Fusion by acoustic emission: acoustic emission for inspection of single tracks under different powder layer thickness. In: Pattern Recognition Association of South Africa and Robotics and Mechatronics (PRASA-RobMech). IEEE, pp. 203−207.

Kouprianoff, D., Luwes, N., Yadroitsava, I., Yadroitsev, I., 2018. Acoustic emission technique for online detection of fusion defects for single tracks during metal Laser Powder Bed Fusion. Solid freeform fabrication. In: Proceedings of the 29th Annual International Solid Freeform Fabrication Symposium - an Additive Manufacturing Conference, SFF 2018, c, pp. 2087−2096.

Kruth, J.-P., Mercelis, P., Van Vaerenbergh, J., Craeghs, T., 2007. Feedback control of selective laser melting. In: Proceedings of the 3rd International Conference on Advanced Research in Virtual and Rapid Prototyping. Taylor & Francis Ltd, pp. 521−527.

Ladewig, A., Schlick, G., Fisser, M., Schulze, V., Glatzel, U., 2016. Influence of the shielding gas flow on the removal of process by-products in the selective laser melting process. Addit. Manuf. 10, 1−9.

Ladewig, A., Baron, H.U., Bamberg, J., Goegelein, A., Zenzinger, G., n.d. Quality Assessment during LPBF Process by Optical Tomography Inspection of Systematic and Local Deviations, Joint FAA − EASA Workshop on Qualification/Certification of Metal Additively Manufactured Parts August 21−23, 2018.

Ludwig, S., 2020. Instrumented Build Plate for In-Situ Stress Monitoring and Crack Detection during the Laser Powder Bed Fusion Additive Manufacturing Process. The University of North Carolina at Charlotte. Available. http://search.proquest.com/openview/31b87d5f737a53726d666622699b5c00/1?pq-origsite=gscholar&cbl=18750&diss=y.

Martin, A.A., Calta, N.P., Hammons, J.A., Khairallah, S.A., Nielsen, M.H., Shuttlesworth, R.M., et al., 2019. Ultrafast dynamics of laser-metal interactions in additive manufacturing alloys captured by in situ X-ray imaging. Mater. Today Adv. 1, 100002.

Montazeri, M., Nassar, A.R., Dunbar, A.J., Rao, P., 2020. In-process monitoring of porosity in additive manufacturing using optical emission spectroscopy. IISE Trans. 52 (5), 500−515.

Nassar, A.R., Gundermann, M.A., Reutzel, E.W., Guerrier, P., Krane, M.H., Weldon, M.J., 2019. Formation processes for large ejecta and interactions with melt pool formation in powder bed fusion additive manufacturing. Sci. Rep. 9, 5038.

Okaro, I.A., Jayasinghe, S., Sutcliffe, C., Black, K., Paoletti, P., Green, P.L., 2019. Automatic fault detection for laser powder-bed fusion using semi-supervised machine learning. Addit. Manuf. 27, 42−53.

Pagani, L., Grasso, M., Scott, P.J., Colosimo, B.M., 2020. Automated layerwise detection of geometrical distortions in Laser Powder Bed Fusion. Addit. Manuf. 36, 101435.

Renken, V., von Freyberg, A., Schünemann, K., Pastors, F., Fischer, A., 2019. In-process closed-loop control for stabilising the melt pool temperature in selective laser melting. Prog. Addit. Manuf. 4, 411−421.

Repossini, G., Laguzza, V., Grasso, M., Colosimo, B.M., 2017. On the use of spatter signature for in-situ monitoring of Laser Powder Bed Fusion. Addit. Manuf. Available https://www.sciencedirect.com/science/article/pii/S2214860416303402.

Samei, J., Amirmaleki, M., Dastgiri, M.S., Marinelli, C., Green, D.E., 2019. In-situ X-ray tomography analysis of the evolution of pores during deformation of AlSi10Mg fabricated by selective laser melting. Mater. Lett. 126512. https://doi.org/10.1016/j.matlet.2019.126512.

Scime, L., Beuth, J., 2019. Using machine learning to identify in-situ melt pool signatures indicative of flaw formation in a Laser Powder Bed Fusion additive manufacturing process. Addit. Manuf. 25, 151−165.

Seifi, M., Gorelik, M., Waller, J., Hrabe, N., Shamsaei, N., Daniewicz, S., Lewandowski, J.J., 2017. Progress towards metal additive manufacturing standardization to support qualification and certification. JOM 69 (3), 439−455.

Shevchik, S.A., Kenel, C., Leinenbach, C., Wasmer, K., 2018. Acoustic emission for in situ quality monitoring in additive manufacturing using spectral convolutional neural networks. Addit. Manuf. 21, 598−604.

Steed, C.A., Halsey, W., Dehoff, R., Yoder, S.L., Paquit, V., Powers, S., 2017. Falcon: visual analysis of large, irregularly sampled, and multivariate time series data in additive manufacturing. Comput. Graph. 63, 50−64.

Tan Phuc, L., Seita, M., 2019. A high-resolution and large field-of-view scanner for in-line characterization of powder bed defects during additive manufacturing. Mater. Des. 164, 107562.

Vasileska, E., Demir, A.G., Colosimo, B.M., Previtali, B., 2020. Layer-wise control of selective laser melting by means of inline melt pool area measurements. J. Laser Appl. 32, 022057.

Williams, R.J., Piglione, A., Rønneberg, T., Jones, C., Pham, M.-S., Davies, C.M., et al., 2019. In situ thermography for Laser Powder Bed Fusion: effects of layer temperature on porosity, microstructure and mechanical properties. Addit. Manuf. 30, 100880.

Yasa, E., Kruth, J.P., Deckers, J., 2011. Manufacturing by combining selective laser melting and selective laser erosion/laser re-melting CIRP Ann. Manuf. Technol. 60, 263−6.

Zhang, B., Ziegert, J., Farahi, F., Davies, A., 2016. In situ surface topography of Laser Powder Bed Fusion using fringe projection. Addit. Manufacturing 12 (Part A), 100−107.

Zhirnov, I., Yadroitsev, I., Lane, B., et al., 2019. Influence of optical operation on stability of single tracks in selective laser melting. NIST Adv. Manuf. Series 100−27. https://doi.org/10.6028/NIST.AMS.100-27.

zur Jacobsmühlen, J., Kleszczynski, S., Witt, G., Merhof, D., 2015. Elevated region area measurement for quantitative analysis of laser beam melting process stability. lfb.rwth-aachen.de. In: 26th International Solid Freeform Fabrication Symposium; Austin, TX, pp. 549−559.

Post-processing

12

Sara Bagherifard, Mario Guagliano
Department of Mechanical Engineering, Polytechnic University of Milan, Milan, Italy

Chapter outline

12.1 Introduction 327
12.2 Surface post-processing 330
  12.2.1 Mechanical surface post-processing 330
  12.2.2 Chemical and electrochemical surface post-processing 333
  12.2.3 Laser-based surface post-processing 335
  12.2.4 Surface coating 336
  12.2.5 Comparing surface post-processing techniques 337
12.3 Heat treatments 340
12.4 Hybrid post-processing 343
12.5 Conclusions 343
12.6 Questions 344
References 344

12.1 Introduction

One of the most important factors that is limiting the diffusion of additive manufacturing in many industrial sectors is the cost associated with the whole cycle, from powder to post-processing. A recent analysis shows that a relevant part (up to 40%) of the cost of additive manufacturing can be attributed to the need of pre- and post-manufacturing processes and not to the printing cost itself (Thomas and Gilbert, 2014). This justifies the increasing attention paid to the definition of efficient post-treatments and the rapid pace in development of (often customized) post-processing techniques for additive manufactured parts. The major characteristics of L-PBF technology that can be mitigated by post-processing are the irregular surface morphology, microstructural directionality, undesired residual stresses, and overall porosity.

L-PBF parts are often characterized with high surface roughness, irregular surface morphology, and randomly positioned undesired surface features. The major parameters recognized to contribute to this particular topography are the stair-case effect associated with the layer-by-layer deposition, partially melted powders, spatters, the balling effect, imprecise support removal, uncontrolled wetting, and instability of the melt pool (Yadollahi and Shamsaei, 2017; Stoffregen et al., 2014). Inaccurate

Fundamentals of Laser Powder Bed Fusion of Metals. https://doi.org/10.1016/B978-0-12-824090-8.00001-9
Copyright © 2021 Elsevier Inc. All rights reserved.

positioning of the energy source at the surface edges together with an inclined part orientation could emphasize the stair-case effect (Nicoletto et al., 2018). Surface roughness varies between different L-PBF systems and can be partially improved by using an optimized combination of powder size distribution and deposition parameters (Khorasani et al., 2020). The extent of supported area during fabrication and the precision of support removal process could also locally affect the surface state of the manufactured part. Fig. 12.1 represents typical surface morphologies of two types of PBF beams: laser and electron beam. The micrographs illustrate the distinction of the surface features, their scale and arrangement as a function of manufacturing technology, and the build direction. Perpendicular to the build direction, the L-PBF samples show an almost flat surface representing regular patterns of solidified raster tracks (Fig. 12.1a-i), while the surface parallel to the build direction (Fig. 12.1a-ii) right image exhibits a high density of partially melted powders attached to the surface that is characterized by features correlated with the layer thickness. The E-PBF samples, on the other hand, show a wavy surface perpendicular to the build direction (Fig. 12.1b-i) and a grainy surface with no directional preference parallel to the build direction (Fig. 12.1b-ii, Nicoletto et al., 2018). The factors contributing to the formation of irregular surface roughness are described in more detail in Chapter 7 of this book.

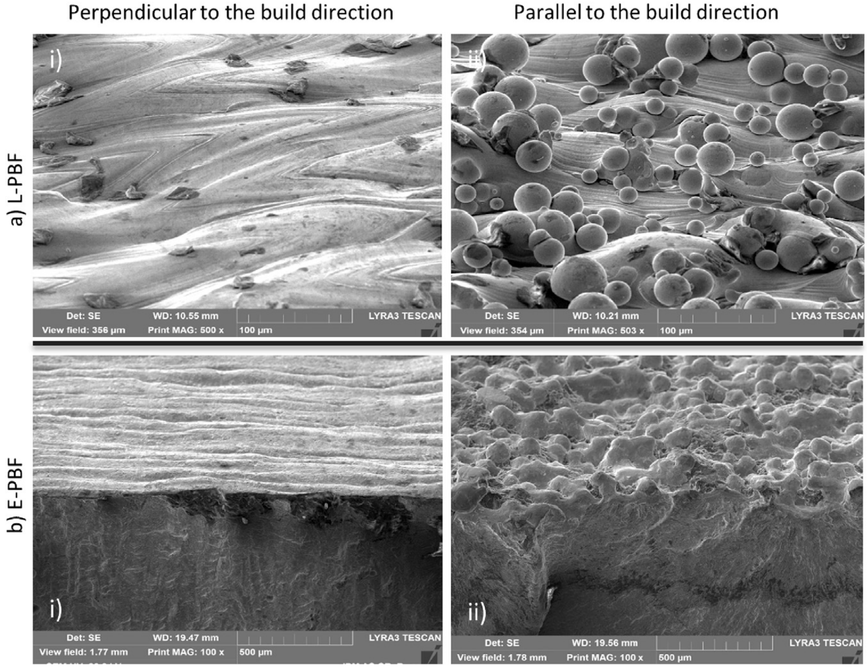
Perpendicular to the build direction
Parallel to the build direction
a) L-PBF
b) E-PBF
i)
ii)
Det: SE
WD: 10.55 mm
LYRA3 TESCAN
View field: 356 μm
Print MAG: 500 x
100 μm
Det: SE
WD: 10.21 mm
LYRA3 TESCAN
View field: 354 μm
Print MAG: 503 x
100 μm
i)
ii)
Det: SE
WD: 19.47 mm
LYRA3 TESCAN
View field: 1.77 mm
Print MAG: 100 x
500 μm
Det: SE
WD: 19.56 mm
LYRA3 TESCAN
View field: 1.78 mm
Print MAG: 100 x
500 μm

Figure 12.1 Variation of surface features as a function of manufacturing technology and build direction illustrated by SEM micrograph of as-built Ti6Al4V samples fabricated by (a) L-PBF and (b) electron beam powder bed fusion (E-PBF) for two directions of (i) perpendicular and (ii) parallel to the build direction (note that the images have different magnifications; dark bottom area for E-PBF images show the sample cross-section) (Nicoletto et al., 2018).

Considering the importance of surface morphology in directing material functionalities, these irregular surface features can highly restrict the performance of L-PBF as-built parts and their interaction with the surrounding environment. The high surface roughness of the as-built L-PBF parts can significantly reduce their scratch, wear, corrosion, and fatigue resistance. Surface roughness have been reported to be even able to overshadow the effect of notches on the fatigue strength of L-PBF parts by controlling the notch sensitivity factor (Razavi et al., 2020).

Although partial surface control can be achieved by adjusting the fabrication process parameters, irregular surface morphology remains a serious concern impeding the wide application of L-PBF parts in as-built configuration. Post-processing surface treatments have been found to be able to compensate the technological shortcomings and offer effective solutions for tuning the surface of L-PBF parts.

On the other hand, the intrinsic characteristics of the deposition process impose directionality to the microstructure of L-PBF materials. Columnar microstructure is reported for L-PBF parts representing elongated grains parallel to the build-up direction (Gorsse et al., 2017; Bagherifard et al., 2018b), see Chapter 8 of this book. A notable grain size inhomogeneity exists at molten-pool boundaries compared to the inside zones. This grain size difference is known to be induced by the cooling rate variation and different thermal gradients in neighboring zones (Siddique et al., 2017). The as-built parts are also characterized by high tensile residual stresses that are generally undesirable especially for structural components (Chapter 9). Moreover, post heat treatments have been developed to alleviate the effect of thermal history, release the tensile residual stresses, and promote microstructural homogenization through the bulk of the L-PBF material.

Additionally, L-PBF parts are known to be prone to internal defects and porosity. The internal defects and subsurface pores are known to compete with the surface defects in defining the limits for fatigue strength of L-PBF material (Romano et al., 2020). A directional distribution has been identified also in terms of internal porosity showing a higher density of pores perpendicular to the build-up direction between the individual layers (Zhang et al., 2017). This anisotropic distribution can further contribute to the uncontrolled adverse effect of internal pores on the mechanical performance of L-PBF material. Therefore, various post-processing techniques are being introduced as pore-closing strategies to moderate and minimize the internal pores that are typical for L-PBF material (Du Plessis and Macdonald, 2020).

This chapter provides an overview of the current post-processing technologies tuned to improve the properties and modulate the functionality of L-PBF parts. The first section focuses on post-surface treatments classifying them into major categories of mechanical, chemical, and electrochemical treatments followed by laser-based techniques and surface coatings. The advantages and limitations of these technologies are compared and briefly discussed, highlighting examples of the outcome and contribution of surface treatments to mechanical performance of L-PBF parts. The next section briefly describes the role and contribution of post-heat treatments to improve the bulk properties of as-built L-PBF parts, briefly discussing heat treatment's effects on microstructure, porosity, residual stresses, and mechanical strength. More details and examples about the choice and efficiency of heat treatments on modulating the microstructure and porosity aspects of as-built L-PBF parts are provided in the corresponding chapters of this book. The present chapter is concluded with a brief summary and a series of questions.

12.2 Surface post-processing

Surface post-processing techniques tackle the issues associated with the irregular morphology and the randomly positioned features on the surface of as-built L-PBF material, by either removing and smoothing the surface (to different extents based on the applied post-processing) or inducing a desired surface morphology (in line with the target application of the fabricated part), or reducing the tensile surface residual stresses or even substituting them with beneficial compressive stresses. Herein, the post-processing that has been developed and used to deal with the surface morphology of L-PBF parts is categorized based on their intrinsic characteristics in four major groups of mechanical surface treatments, chemical and electrochemical surface treatments, laser-based surface treatments, and coatings.

12.2.1 Mechanical surface post-processing

A diversity of mechanical surface treatments has been used for post-processing of additive manufactured surfaces. The conventional techniques that are applied to remove the surface irregularities by using abrasive tools include machining, milling, grinding, and polishing. These mechanical treatments are all based on subtracting a thin layer of material from the top surface to eliminate the geometrical imperfections. These methods can be used at industrial scale to substantially decrease the surface roughness of L-PBF parts leading to a smooth surface finish. As an example to provide an indication on the efficiency of these methods, the arithmetic mean roughness (R_a) parameter of Ti-6Al-4V as-built samples was reduced from 33.90 to 0.89 μm by machining (Edwards and Ramulu, 2014).

Vibratory grinding is an alternative method used to post-process and decrease the surface roughness of L-PBF parts. It consists of a grinding action promoted by the vibratory movements of abrasive media filled inside an oscillating or rotating barrel (Bagehorn et al., 2017). The choice of the media size, shape, and hardness, as well as vibration/rotation frequency and exposure time, should be tuned based on the material properties and surface state of the L-PBF part. Fig. 12.2 illustrates the surface morphology of L-PBF Ti-6Al-4V in the as-built configuration compared with the surface state after milling, and vibratory grinding. The vibratory grinding technology that is introduced under various commercial names of barrel/vibratory tumbling, vibratory finishing/polishing, or tribo-finishing tends to remove the high peaks of the surface without interfering with the valleys, as presented in Fig. 12.2c.

Polishing has been reported to be one of the most effective methods among those abovementioned, as the technique is able to remove surface imperfections of the additive manufactured part and does not leave artifacts that are typical of the machining or milling steps (Spierings et al., 2013).

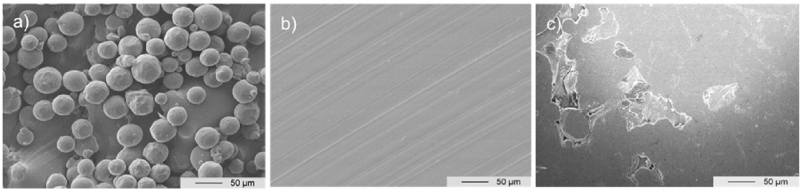

Figure 12.2 SEM micrographs of L-PBF Ti-6Al-4V surface (a) as-built (demonstrating a high density of partially melted powders attached to the surface; $R_a = 17.9 \pm 2.0$ µm and $R_z = 121.9 \pm 12.6$ µm), (b) after milling (representing smooth regular surface; $R_a = 0.3 \pm 0.1$ µm and $R_z = 1.9 \pm 0.8$ µm), and (c) after vibratory grinding (revealing the presence of the deep valleys that remained intact after post-processing; $R_a = 0.9 \pm 0.7$ µm and $R_z = 8.1 \pm 5.4$ µm) (Bagehorn et al., 2017).

Magnetically driven abrasive polishing (Karakurt et al., 2018), hydrodynamic cavitation abrasive finishing (Nagalingam and Yeo, 2018), and ultrasonic cavitation abrasive finishing (UCAF) (Tan and Yeo, 2017) are among the mechanical surface treatments that have been recently suggested by researchers to reduce the surface roughness of L-PBF materials; these technologies could offer the possibility of internal surface modification; however, they are often characterized by limitations imposed on the material and size of the part to be treated and thus have restricted applicability compared the other common subtractive mechanical treatments.

Another major category of mechanical surface treatment used for L-PBF materials consists of technologies that reduce the surface roughness by imposing severe plastic deformation on the top surface layer. These treatments do not necessarily remove any material from the surface and do not change the global dimensions, but leverage surface plastic deformation to induce a regular surface morphology; the obtained surface is not necessarily as smooth as that reached by methods based on material removal (see Fig. 12.3a–f, Bagherifard et al., 2018a). In addition to reducing the surface roughness, this category of surface treatments is able to improve the mechanical properties of the treated part and typically induce compressive residual stresses close to the surface. The technique can result in surface grain refinement depending on the selected parameters and can even lead to partial closure of near surface pores (Bagheri and Guagliano, 2009; Bagherifard et al., 2019).

Impact-based surface treatments including shot peening, sand/grit blasting, and ultrasonic impacts account for the most efficient techniques in this category. Shot peening and sand blasting consist in impacting the surface of the target material with a stream of peening media (metallic/ceramic shots with controlled shape and dimension for shot peening and sand/ceramic beads for sand blasting) that is accelerated by compressed air. The media used in sand blasting typically has an irregular shape and random size, while shot peening uses well-controlled media regarding size and geometry. Furthermore, the media in shot peening is accelerated at higher velocities compared to the mildly controlled sand blasting treatment. Shot peening also provides more flexibility and control on the kinetic energy transmitted to the target material and is more efficient in modulating the surface topography (Bagherifard, 2019).

In the L-PBF sector, sand blasting is a common practice on the as-built parts for the purpose of cleaning and removing the loose powder rather than necessarily reducing the surface roughness. However, studies have shown that, if finely tuned, sand blasting can be also very efficient in reducing the surface roughness of L-PBF material. Fig. 12.3e and f represent the variation of surface roughness data in terms of the most widely used standard parameters after different post-surface treatments. The results indicate that both applied treatments significantly reduced the surface roughness of L-PBF as-built AlSi10Mg samples; however, the subtler kinetic energy of the applied sand blasting treatment led to a lower surface roughness compared to the shot peened series. The heat-treated material that has higher ductility compared to the as-built series, showed higher surface roughness after shot peening compared to

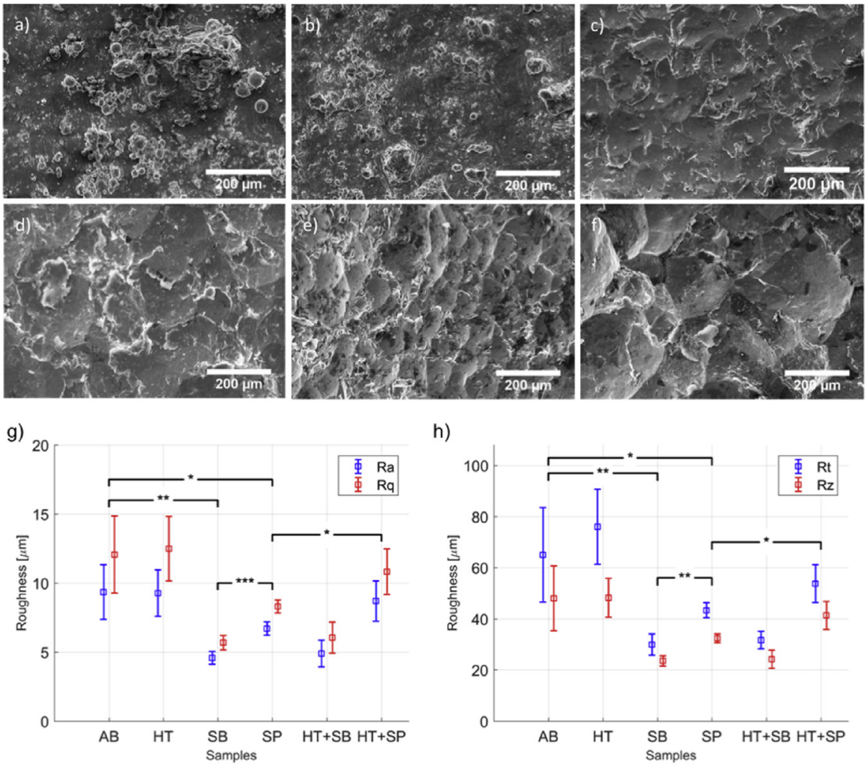

Figure 12.3 SEM micrographs of (a) as-built, (b) heat-treated (similar to as-built morphology), (c) sand blasted, (d) shot peened, (e) heat-treated and sand blasted, (f) heat-treated and shot peened L-PBF AlSi10Mg samples; comparison of surface roughness parameters after application of different post-processings highlighting the effect of impact-based surface treatments in reducing surface roughness (g) R_a and R_q (h) R_t and R_z; $*P < .05$, $**P < .01$ and $***P < .001$ (*AB*, as-built; *HT*, heat-treated; *HT* + *SB*, heat-treated and sand blasted; *HT* + *SP*, heat-treated and shot peened; *SB*, sand blasted; *SP*, shot peened) (Bagherifard et al., 2018a).

the as-built shot peened material; these results indicate that (besides geometry) the choice of blasting/peening parameters including media characteristics, the velocity of the media stream, and exposure time should be tuned based on the target material properties. It is interesting to note that despite the higher surface roughness of shot peened samples, the significantly deeper compressive residual stress field compared to the sand blasted series as well as near surface pore closure effect (due to the subsequent high energy impacts) led to a better mechanical performance for the as-built shot peened samples under cyclic loading compared to the sand blasted series (Bagherifard et al., 2018a). It is however to be noted that shot peening could potentially alter the geometry fine features due to the local plastic deformation; and this aspect should be accounted for when selecting the process parameters.

Ultrasonic nanocrystal surface modification is another impact-based mechanical surface treatment that can notably reduce surface roughness without removing material. Using simultaneous striking and burnishing effect induced by impacts of a tungsten carbide tip at ultrasonic frequencies, this treatment has been reported to decrease the surface roughness of as-built Nickel-titanium (NiTi) alloy L-PBF samples (from $R_a = 12.1\ \mu m$ to $R_a = 9.0\ \mu m$), while inducing over an order of magnitude of reduction in the subsurface porosity (Ma et al., 2017).

12.2.2 Chemical and electrochemical surface post-processing

Chemical treatments including etching, polishing, chemical brightening, and machining, as well as electrochemical polishing, have been leveraged to efficiently reduce the surface roughness of L-PBF parts. Unlike most mechanical surface treatments, chemical post-processing techniques can easily access the internal surfaces and thus are preferable for parts of intricate geometries such as cellular and lattice structures. They also can provide the possibility of working on the whole geometry, while offering still the option of local treatment through masking. The basis of these techniques is to submerge the L-PBF material in baths of chemical agents and control the extent of material removal by regulating the temperature of the solution and the exposure time. The mentioned parameters together with the aggressiveness of the chemical solution itself can be modulated in a way to obtain mirror-finish surfaces.

In some cases, chemical post-processing has been applied in multiple steps to decrease the surface roughness of L-PBF material. For example, AlSi10Mg samples were first chemically treated (immersed in the solution of HNO_3 and HF at 85°C for 75 min) for initial removal and dissolution of partially melted powder and more superficial defects, and were then subjected to chemical brightening (immersed in a solution of water, H_3PO_4, H_2SO_4, HNO_3, HF, and $CuSO_4$ at 95°C for 7.5 min) to further finish the treated surface. The surface roughness parameters of $S_a = 25\ \mu m$ and $S_z = 200\ \mu m$ for as built material were reduced to $S_a = 10\ \mu m$ and $S_z = 90\ \mu m$ after the first chemical treatment and eventually to $S_a = 7\ \mu m$ and $S_z = 55\ \mu m$ after chemical brightening (Scherillo, 2019). Detailed description of the roughness parameters is provided in the roughness chapter, Chapter 7, of this book.

Fig. 12.4 schematically represents the gradual surface flattening phases through electrochemical polishing of CP Ti parts, demonstrating the dissolution of protruding

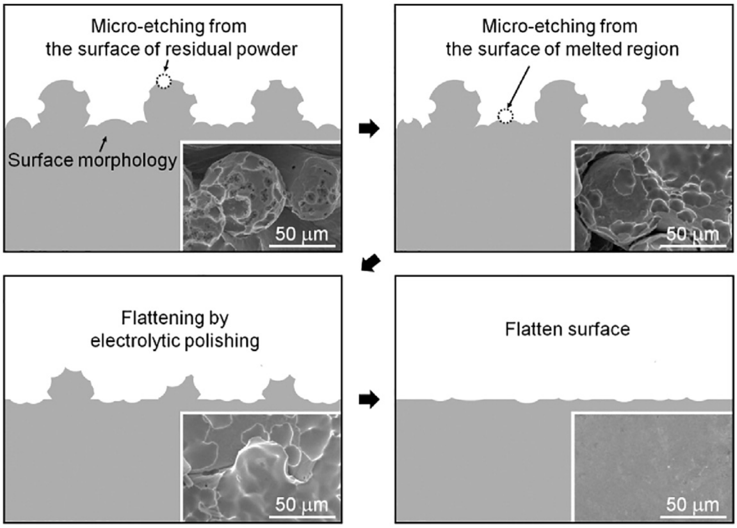

Figure 12.4 Schematic representation of surface flattening under electrochemical post-processing (Jung et al., 2017).

partially melted powder particles followed by the etching of the base surface. The process can lead to an entirely flattened surface at later stages.

Electrochemical etching has been also suggested for selective support removal in L-PBF parts. Using chemical etching to directly remove the supports without interfering with the geometrical accuracy of the part could be challenging; however, if before chemical etching the 100–200 μm thick outer layer is altered to become less chemically stable and more prone to chemical etching, a much higher control can be obtained on the support removal in a self-terminating electrochemical etching process (Lefky et al., 2017). The sensitizing step can be combined with the stress-relief process applied on the samples, by exposing them to a sensitizing agent during the heat treatment.

Despite the efficiency of the chemical and electrochemical methods in material removal, these methods could require long exposure times depending on the initial surface state. Lengthy processes can result in challenges in the control of the local dimensions of the part, unless a constant material removal rate is secured through optimizing the process parameters. Moreover, due to the complex kinetics of these processes and the local variations of dissolution rate as a function of the fluid dynamic conditions that depend on the part geometry, the flow condition shall be finely regulated to obtain homogeneous surfaces in case of more complicated geometries. Additionally, prolonged exposure to hazardous chemicals at elevated temperatures could bring in safety-health issues for working conditions.

Another interesting application of chemical post-processing for L-PBF surfaces is to induce particular surface patterns to direct specific surface functionalities rather than just reducing the surface roughness. Surface patterning and inducing controlled surface morphology can highly define the performance of the material in interaction with their immediate microenvironment, especially for biomedical applications, where the material will be in direct contact with cells and bacteria (Bagherifard et al., 2015). Chemical and electrochemical treatments have been widely used on inert biomedical metals to enhance their bioactivity by modulating surface topography. Acid-alkali treated L-PBF Ti6Al4V samples exhibited irregular nano-surface morphology with features of 100−200 nm, while the anodized surface presented a thin layer of relatively durable anodic oxide layer. The anodized layer was characterized by an ordered hierarchical pattern made of microscale features covered by nanotubes with diameters of 25−35 nm. These features were reported to be efficient in improving the bio-interface characteristics (Amin Yavari et al., 2014).

Abrasive Flow Machining (also known as Extrude Hone) is a valid solution for deburring unreachable internal passageways for elimination of partially melted powder and surface enhancement strategies. In this process the semi-solid abrasive media act as a deformable cutting tool and as it is extruded across the internal surfaces it removes the protruding features leading to a smoother surface (Peng et al., 2018).

12.2.3 Laser-based surface post-processing

Laser ablation has been used in different studies to improve the surface quality of L-PBF material. Femtosecond laser micromachining was used as an efficient single pass process to reduce the surface roughness of as-built Ti-6Al-4V material from 4.22 to 0.82 μm. The possibilities of using this technology to code the samples by engraving counterfeit proofing information as well as surface micropatterning were also demonstrated (Worts et al., 2019).

Laser polishing is another emerging technology that consists in using focused radiation of short laser pulses at a power density to induce melting at microscale; it has been reported to be efficient in improving surface quality of additive manufactured parts (see Fig. 12.5a) (Tian et al., 2018). As described in Fig. 12.5b, melting the highest peak of the surface profile, the laser polishing manages to fill the valleys leveraging the capillary pressure and surface tension effects in the melt pool in order to smoothen the surface roughness with no loss of material (Giorleo et al., 2015; Tian et al., 2018).

Laser remelting is also suggested to be performed either after the deposition of each single layer or as a final step on the part contour mainly aimed at densification and surface roughness reduction. Directional remelting within each layer in AlSi10Mg following same and opposite directions with respect to the first scanning track, resulted in notable roughness reduction on the top surface ($R_{a=}$20.67 μm decreased to 11.67 μm for same direction and 10.87 μm for opposite direction), whereas their application on side surfaces exhibited an opposing trend. Considering the peculiarities of surface state and pore distribution near the edges compared to the more central areas, application of directional remelting on edge areas was proved to be an efficient approach, as it could compensate for the distinct features at the head and wake of the laser tracks (Yu et al., 2019).

Using optimized process parameters, remelting can induce a surface roughness comparable with mechanical CNC machining. In comparison with the standard

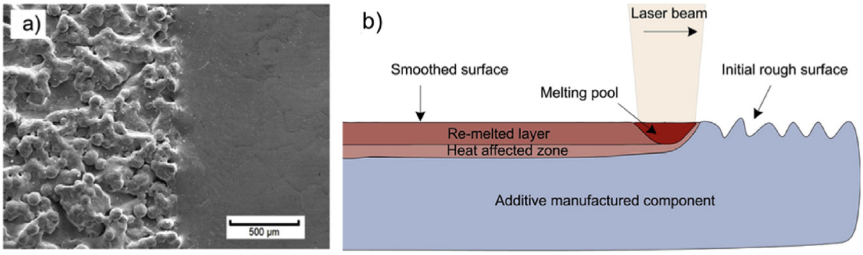

Figure 12.5 (a) SEM micrograph comparing the as-built (left zone) surface morphology with the laser-polished surface (right zone) (b) Schematic representation of laser polishing (Tian et al., 2018).

mechanical surface treatments, remelting has also the advantages of not leading to surface orientated patterns, and not involving tool wears or abrasion and debris; however, studies have shown that the repeated beam rastering during laser polishing can have adverse effects on the microstructure (change in the grain structure, texture and growth direction, phase transformation, and hardness increase), residual stresses (high tensile values that vanish swiftly with depth), and generating gas pores in the near surface region (Tian et al., 2018). Moreover, laser-based post-processing can cause considerably longer manufacturing times, thus the gain should be economically evaluated.

Laser shock peening is another efficient laser-based surface post-processing technique applied to L-PBF material mainly to modulate the distribution of residual stresses (Kalentics et al., 2017), as its effect on surface quality has been found to be trivial, i.e., the surface roughness of the polished samples increased from 0.4 to 0.7 μm after laser shock peening (Luo et al., 2018). The process consists of pulsed radiation of a focused laser beam used to vaporize a thin sacrificial layer of material (specific paints, thin metallic foils, or water); the ablation of the top sacrificial layer and the expansion of the generated hot plasma will induce high amplitude shock waves into the target material, causing surface plastic deformation and compressive residual stresses. Compared to mechanical shot peening, laser shock peening is more costly and has less effects on surface roughness, but can it induce a deeper field of compressive residual stresses (Bagherifard, 2019). Laser shock peening has been also reported to be able to entirely close the near-surface pores (Du Plessis et al., 2019).

12.2.4 Surface coating

The last group of surface post-processing to be included here are surface coatings that are applied to L-PBF materials to induce specific surface functions or controlled surface morphologies, rather than just decreasing surface roughness. A vast variety of L-PBF material functions have been targeted by coating deposition including tribological properties, corrosion resistance, fatigue, and crack propagation resistance, as well as biological performance.

As an emerging deposition technology with a high potential to be used also for additive manufacturing purposes, cold spray has been used to coat the surface of additive manufactured materials with the aim to enhance their performance

(Bagherifard et al., 2020; Bagherifard and Guagliano, 2020). Cold spray deposition of CrC-Ni on additive manufactured stainless steel reduced the equivalent substrate's residual stresses and surface roughness leading to significantly improved multi-axial fatigue performance of the coated samples compared to that of as-built material (Jafarlou et al., 2020).

Biointegration of additive manufactured material can be effectively modulated by deposition of bioactive coatings or inducing nanopatterns that can regulate the interface properties in contact with cells and bacteria. There are numerous studies on the application of various coating methods in this area reporting the efficiency of the coatings in promoting bone formation (Yadroitsava et al., 2019) (e.g., hydroxyapatite coatings (Yan et al., 2017)) and induced antibacterial properties (e.g., silver impregnated coatings (Croes et al., 2018)).

12.2.5 Comparing surface post-processing techniques

In the absence of a unique reference as-built surface, it is not possible to make a global comparison between various surface post-processing techniques and their efficiency in improving the performance of L-PBF material. Table 12.1, however, provides an overview of the efficiency of surface treatment for controlling surface roughness including the studies in which two or more surface treatments were directly compared. Based on the reported indications the following general reflections can be taken into account.

Mechanical surface treatments particularly those that are based on removing a thin surface layer seem to be the most commonly used category, also at industrial scale, probably due to the flexibility of their working tools and apparatus, as well as the wealth of information on how to tune their process parameters. This category of surface post-processes can also remove the pores within the topmost layer of material but at the same time they are prone to inducing undesired residual stresses in the near surface region; the latter can highly be avoided by using chemical surface treatments. Furthermore, mechanical methods based on material removal can have limited applicability where the material is of high hardness; they can be also challenging when access to internal surfaces is required or when strict tolerances are in place, especially for intricate geometries. Even for simpler geometries, if material removal is required on all surfaces, the design would be restricted by the traditional machining methods, undermining the benefits of additive manufacturing technology in the first place.

To address these challenges, chemical surface treatments could be preferred, especially as they can offer the possibility of performing surface post-processing in a global manner, by immersing the whole part in the chemical solution. Nevertheless, chemical surface treatments that are essentially based on material removal shall be well tuned to impart a regular global dissolution rate for parts other than those with simple geometries.

Peening-based surface treatments (sand blasting, shot peening, shock peening, cavitation peening, etc.) have been recognized among the most efficient post-processing techniques on L-PBF material. These treatments can simultaneously generate a more regular (although still rough) surface morphology, while imparting notable in-depth compressive residual stresses, with a notably positive impact on fatigue strength,

Table 12.1 Efficiency of surface post-processing in reducing surface roughness of L-PBF metallic materials.

Material	$R_a/S_a/P_a$* in as-built state (µm)	$R_a/S_a/P_a$* after surface post-processing (µm)			
SS316L (Spierings et al., 2013)	$R_a = 10.0$	Hand polishing	Machining	–	–
		$R_a = 0.40$	$R_a = 0.10$	–	–
Ti6Al4V (Bagehorn et al., 2017)	$R_a = 17.9$	Milling	Micro-machining	Vibratory grinding	Blasting
		$R_a = 0.30$	$R_a = 0.40$	$R_a = 0.90$	$R_a = 10.1$
Ti6Al4V (Benedetti et al., 2017)	$R_a = 6.83$	Electro polishing	Shot peening	Tribo-finishing	–
		$R_a = 0.54$	$R_a = 3.36$	$R_a = 4.96$	–
Ti6Al4V (Pyka et al., 2012)	$P_a = 7.11$ (strut top) $P_a = 12.40$ (strut bottom)	Chemical etching+electro chemical polishing	Electro chemical polishing	Chemical etching	–
		$P_a = 5.12$ (strut top) $P_a = 6.10$ (strut bottom)	$P_a = 5.74$ (strut top) $P_a = 7.10$ (strut bottom)	$P_a = 6.18$ (strut top) $P_a = 10.00$ (strut bottom)	–
AlSi10Mg (Scherillo, 2019)	$S_a = 24.00$	Chemical brightening	Chemical machining	–	–
		$S_a = 6.65$	$S_a = 11.19$	–	–
Stainless steel 316 (Tyagi et al., 2019)	$R_a = 20$	Electro chemical polishing	Chemical polishing	Blasting	–
		$S_a = 2.10$	$S_a = 5.22$	$S_a = 13.88$	–

(continued)

Table 12.1 Efficiency of surface post-processing in reducing surface roughness of L-PBF metallic materials.—cont'd

Material	**$R_a/S_a/P_a$* in as-built state (μm)**	**$R_a/S_a/P_a$* after surface post-processing (μm)**			
AlSi10Mg (Bagherifard et al., 2018a)	$R_a = 9.33$	Sand blasting	Heat treatment+ Sand blasting	Shot peening	Heat treatment+shot peening
		$R_a = 4.42$	$R_a = 4.88$	$R_a = 6.37$	$R_a = 8.45$
Ti6Al4V (Kahlin et al., 2020)	$S_a = 14.21$	Laser polishing	Linishing (abrasive finishing)	Shot peening	Laser shock peening
		$S_a = 1.77$	$S_a = 2.21$	$S_a = 3.56$	$S_a = 14.06$
AlSi10Mg (Hamidi Nasab et al., 2019)	$S_a = 15.4$	Machining+ Polishing	Vibro-finishing	Bead blasting	–
		$S_a = 0.50$	$S_a = 2.30$	$S_a = 8.30$	–

P_a, arithmetic mean height of primary (raw) profile; R_a, Arithmetic mean height of roughness profile; S_a, arithmetic mean height of 3D roughness.

and inducing near-surface pore closure. The synergistic effects of the aforementioned aspects can efficiently enhance the mechanical performance of L-PBF material under fatigue loading. Scalability is a point of strength for the peening surface treatments; however, their application can become challenging for internal surfaces of complex shapes, as they are limited by line of sight requirements.

After mechanical surface treatments, there seems to be a great interest in application of laser-based surface post-processing techniques, as they can provide an even smoother surface and can be directly integrated in the manufacturing phase. However, laser-based techniques can make the part preparation quite expensive in terms of time and costs. Furthermore, laser-based material removal or remelting techniques can locally induce adverse effects in the near-surface region including grain size variation, phase change, and pore formation, besides tensile residual stresses that can be even more precarious.

Generally, surface treatments have been aimed at surface roughness reduction, surface patterning, surface work hardening, inducing compressive residual stresses, and near-surface pore closure. Considering the importance of surface characteristics, these treatments have been reported to be able to tune the performance of L-PBF parts under fatigue loading, wear, corrosion, and also regarding their bioactivity. However, there are also numerous contradicting results concerning individual treatments and their application on different materials. These conflicting data point out the significance of the proper choice of process parameters and the necessity of careful process optimization based on the target material, part geometry and accessibility, the nature of the surface treatment and its limits, the sequence of post-processing techniques if more than one is planned (e.g., surface processing and heat treatment), and variations of surface state in different areas (e.g., side and top surfaces) of parts of complex geometries.

Regarding the costs, laser-based processes and coatings are generally more expensive compared to the mechanical and chemical surface processing techniques. Cost estimations, however, depend highly on the required time and efficiency of the process, complexity of the needed equipment, and also whether the processing cycle needs to be adjusted to the characteristics of individual L-PBF parts. A more detailed review on progress and challenges of surface post-processing for additive manufactured metallic parts is available in Maleki et al. (2020).

12.3 Heat treatments

Post-processing heat treatments can improve a long list of L-PBF material properties compared to the as-built condition; microstructural uniformity, and isotropic mechanical properties, as well as tensile residual stress relaxation are expected after application of suitable heat treatments to additive manufactured materials. The heat treatments typically considered for additive manufactured materials range from stress relief annealing, recrystallization annealing, low-temperature solution treatment, and aging. Initially the same heat treatments applied to materials manufactured using conventional methods were considered for additive manufactured parts; however, the intrinsic differences between additive manufactured and conventional bulk materials motivate the development of customized post-processing heat treatments. Subtle variations in temperature, duration, sequence of steps, and cooling rates have proved to considerably affect the microstructural properties and consequently the mechanical behavior of L-PBF materials, highlighting the need to regulate the heat treatments for achieving desirable microstructural, mechanical, and electrochemical characteristics (Alghamdi et al., 2020; Rafieazad et al., 2019).

High temperature gradients imposed during the fabrication process induce directional microstructural features and notable grain size irregularity in correspondence with the melting pools and their interfaces (see Fig. 12.6a-ii and c-ii). Fig. 12.6iii exhibits the apparent larger grain size at the interface between the neighboring melt pools and the smaller grains inside individual melt pool. Post-processing heat treatments have proved to efficiently address these issues by bringing in the opportunity to tune the mechanical response of the L-PBF parts and alleviate the build-direction effects (see Fig. 12.6b and d).

Besides homogenizing the microstructures and offering isotropy, heat treatments can also alleviate the undesirable tensile residual stresses induced during the fabrication process (Aboulkhair et al., 2016; Ma et al., 2014; Prashanth et al., 2014). The gain in bulk structure improvement obtained by proper heat treatments is reported to even

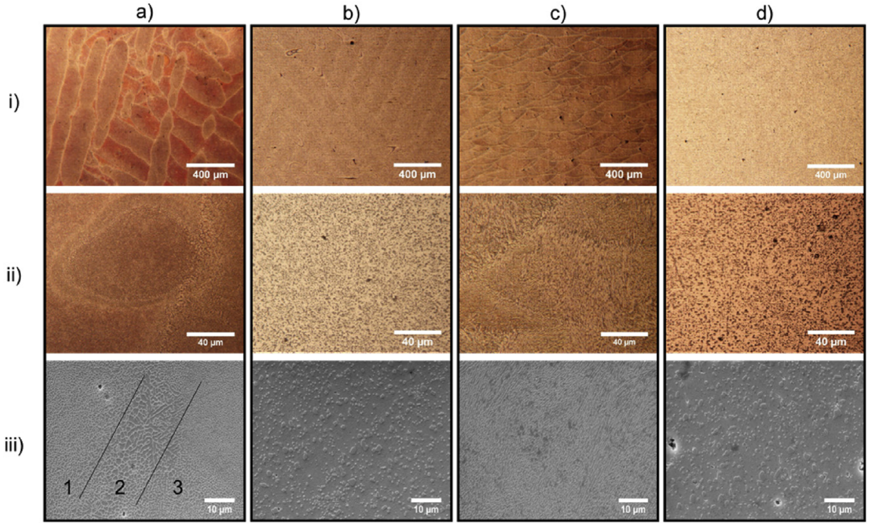

Figure 12.6 Microstructural features of L-PBF ALSi10 Mg at different enlargements. (a) As-built transversal section; (b) T6 heat-treated transversal section; (c) As-built longitudinal section; (d) T6 heat-treated longitudinal section; (i), (ii), refer to different enlargement of optical microscopy observations and (iii) exhibits scanning electron microscopy micrographs; in particular, (a-iii) exhibits the grain inhomogeneity between two adjacent melt pools (indicated as 1 and 3) and their interface (indicated as 2) (Bagherifard et al., 2018a).

mask to some extent the detrimental effect of surface roughness on fatigue performance of L-PBF material (Razavi et al., 2021).

Near surface and internal porosity are challenging issues for L-PBF materials; these include pores caused by the entrapped gases, those triggered by lack of fusion, as well as the keyhole pores that are caused by the movements of the laser source. These features can easily compete with surface irregularities in inducing detrimental effects on the structural integrity of the L-PBF parts. Some mechanical surface treatments that are based on plastic deformation were found to be effective in reducing near surface porosity in L-PBF materials, as discussed in the previous sections. However, the possibility of applying a post-processing technique that can potentially reduce also the bulk porosity would be quite intriguing. Hot isostatic pressure (HIP), an emerging heat treatment that has more recently found its way into the additive manufacturing sector, has been reported to bring in this opportunity. In addition to microstructural homogenization and stress relief, HIP can also induce pore closure in the bulk structures of complex geometries especially for applications that are demanding from structural performance point of view, e.g., aerospace applications. Simultaneous exposure to elevated temperature and isostatic gas pressure leads to pore consolidation and thus improves the L-PBF material's mechanical performance (Du Plessis et al., 2020). A recent study demonstrated that apart from some exceptions regarding the near surface or highly interconnected pores, HIP is able to fully consolidate various intentionally designed pores, as well as a wide range of the typical pores in L-PBF material (Du Plessis and Macdonald, 2020). Fig. 12.7 shows the efficiency of HIP in eliminating representative typical keyhole pores, while being less efficient on near-surface contour pores. The remaining surface pores can serve as stress raisers inducing adverse effects particularly on the fatigue performance of the part. To address the issue of surface pores, mechanical surface treatments could be paired with HIP to release the undesired residual stresses while substituting them with compressive stresses, finely tune the microstructural features and at the same time minimize the bulk and surface porosity of L-PBF parts. The next section provides more details on the hybrid post-processing.

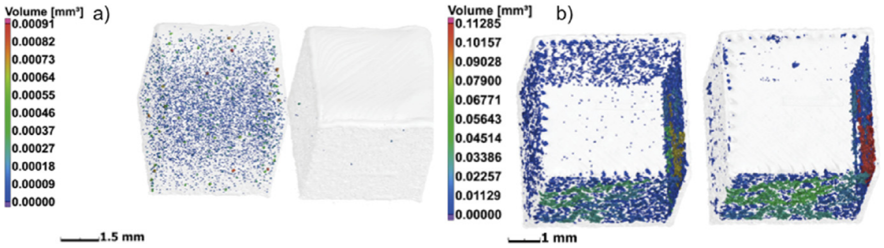

Figure 12.7 3D view of a cube comparing the distribution and size of intentionally induced pores before (left) and after (right) HIP for (a) keyhole pores that were fully closed after HIP except for some isolated near-surface pores and (b) connected near surface pores on which HIP was found to be ineffective (Du Plessis and Macdonald, 2020).

12.4 Hybrid post-processing

Combinations of different post-processing techniques, either multiple surface treatments or sequences of surface and heat treatments, can be carefully selected to overarch the limitations of individual treatments and induce significant improvement in multiple target properties of L-PBF materials.

An interesting option for structural components could be the combination of surface treatments that can first remove the larger irregular surface features followed by plastic deformation-based mechanical surface treatments that can induce compressive residual stresses and near-surface pore closure. Another worthwhile combination for applications that are more demanding in terms of surface smoothness could be the application of impact-based surface treatments that induce compressive residual stresses but do not necessarily lead to a low surface roughness, followed by a chemical or electrochemical material removal method to obtain smooth surface morphology. For example, sand blasting followed by chemical etching was used to first remove the loosely bonded powder particles by blasting and surface plastic deformation, followed by chemical etching to eliminate the tiny microcracks induced by the previous blasting step (Yan et al., 2017).

By combining proper heat treatment and mechanical impact-based surface treatments, one can take benefit from the synergistic effect of microstructural homogeneity, increased ductility, surface roughness reduction, and compressive residual stresses. Heat treatment followed by shot peening and sand blasting has been reported to successfully induce microstructural homogeneity and material ductility followed by reduced surface roughness and near-surface pore closure; this combination led to significant rotating bending fatigue strength enhancement compared to the as-built material (Bagherifard et al., 2018a).

The parameters and sequence of multiple post-processing techniques including chemical etching, plasma electrolytic oxidation (PEO) coating, and heat treatment were also reported to modulate the degradation behavior of L-PBF Mg alloy (WE43) (Kopp et al., 2019). Additionally, in the case of HIP, considering that HIP is unable to close surface pores, a mechanical surface treatment could be applied after HIP to eliminate the surface pores. Combined post-processing can offer a better chance to tune the output parameters; however, studies have shown that they can considerably increase the costs and fabrication time.

12.5 Conclusions

Post-processing can provide utility in order to tackle typical issues of L-PBF material regarding surface irregularity, microstructural inhomogeneity, tensile residual stresses, directionality of mechanical properties, and high porosity. As the additive manufacturing sector aims for mass production of load bearing and structurally valid parts, especially for critical and high risk environments, it is of great importance to develop new post-processing techniques or customize the currently available ones in a way to address the specific issues associated with the fabrication process of

L-PBF material and enhance the reliability and performance of the products. Developing customized or combined post-processing recipes can pave the way for a higher impact of L-PBF technology in critical applications.

To come to the point, the best results can be obtained when the L-PBF process parameters are optimized in the first place. Post-processing techniques can only be leveraged later to compensate for technological inadequacies. Thus, for enhanced functionality and optimized use of resources, it is essential to consider both the manufacturing and post-process parameters at the design stage. For example, the probability of distortion post heat-treatment should be envisioned based on the geometry of the part and the heat treatment cycle. Thereby, the original design and allowances should take into account the potential need of material removal for eventual geometrical adjustment after heat treatment.

It is unlikely to find a single post-processing technique as the optimal solution to all additive manufactured parts. Proper choice and successful application of post-processing would be ensured by an individual assessment of the manufacturing strategy, material, and geometry of the L-PBF part, its surface and bulk characteristics, its target application, in-service conditions, and of course, the costs. A full understanding of the role and relative importance of the key factors like surface finishing, porosity, residual stresses, etc. on the behaviour and performance of AM material is needed to allow for definition, customization and optimization of proper post-processing techniques.

12.6 Questions

- What issues of as-built L-PBF material can be mitigated by post-processing?
- What are the pros and cons of mechanical and chemical surface post-processing?
- Name three surface treatments that can simultaneously reduce surface roughness and porosity in the near-surface region of LPBF parts.
- Which post-processing method can concurrently release the undesired tensile residual stresses, homogenize the bulk microstructure, and induce pore closure?

References

Aboulkhair, N.T., Maskery, I., Tuck, C., Ashcroft, I., Everitt, N.M., 2016. Improving the fatigue behaviour of a selectively laser melted aluminium alloy: influence of heat treatment and surface quality. Mater. Des. 104, 174–182.

Alghamdi, F., Song, X., Hadadzadeh, A., Shalchi-Amirkhiz, B., Mohammadi, M., Haghshenas, M., 2020. Post heat treatment of additive manufactured AlSi10Mg: on silicon morphology, texture and small-scale properties. Mater. Sci. Eng. A 783, 139296.

Amin Yavari, S., van der Stok, J., Chai, Y.C., Wauthle, R., Tahmasebi Birgani, Z., Habibovic, P., Mulier, M., Schrooten, J., Weinans, H., Zadpoor, A.A., 2014. Bone regeneration performance of surface-treated porous titanium. Biomaterials 35 (24), 6172–6181.

Bagehorn, S., Wehr, J., Maier, H.J., 2017. Application of mechanical surface finishing processes for roughness reduction and fatigue improvement of additively manufactured Ti-6Al-4V parts. Int. J. Fatig. 102, 135−142.

Bagheri, S., Guagliano, M., 2009. Review of shot peening processes to obtain nanocrystalline surfaces in metal alloys. Surf. Eng. 25 (1), 3−14.

Bagherifard, S., 2019. Enhancing the structural performance of lightweight metals by shot peening. Adv. Eng. Mater. 21 (7), 1801140.

Bagherifard, S., Beretta, N., Monti, S., Riccio, M., Bandini, M., Guagliano, M., 2018a. On the fatigue strength enhancement of additive manufactured AlSi10Mg parts by mechanical and thermal post-processing. Mater. Des. 145, 28−41.

Bagherifard, S., Guagliano, M., 2020. Fatigue performance of cold spray deposits: coating, repair and additive manufacturing cases. Int. J. Fatig. 139, 105744.

Bagherifard, S., Heydari Astaraee, A., Locati, M., Nawaz, A., Monti, S., Kondás, J., Singh, R., Guagliano, M., 2020. Design and analysis of additive manufactured bimodal structures obtained by cold spray deposition. Addit. Manuf. 33, 101131.

Bagherifard, S., Hickey, D.J., de Luca, A.C., Malheiro, V.N., Markaki, A.E., Guagliano, M., Webster, T.J., 2015. The influence of nanostructured features on bacterial adhesion and bone cell functions on severely shot peened 316L stainless steel. Biomaterials 73, 185−197.

Bagherifard, S., Molla, M.F., Kajanek, D., Donnini, R., Hadzima, B., Guagliano, M., 2019. Accelerated biodegradation and improved mechanical performance of pure iron through surface grain refinement. Acta Biomater. 98, 88−102.

Bagherifard, S., Monti, S., Zuccoli, M.V., Riccio, M., Kondás, J., Guagliano, M., 2018b. Cold spray deposition for additive manufacturing of freeform structural components compared to selective laser melting. Mater. Sci. Eng. A 721, 339−350.

Benedetti, M., Torresani, E., Leoni, M., Fontanari, V., Bandini, M., Pederzolli, C., Potrich, C., 2017. The effect of post-sintering treatments on the fatigue and biological behavior of Ti-6Al-4V ELI parts made by selective laser melting. J. Mech. Behav. Biomed. Mater. 71, 295−306.

Croes, M., Bakhshandeh, S., van Hengel, I.A.J., Lietaert, K., van Kessel, K.P.M., Pouran, B., van der Wal, B.C.H., Vogely, H.C., Van Hecke, W., Fluit, A.C., Boel, C.H.E., Alblas, J., Zadpoor, A.A., Weinans, H., Amin Yavari, S., 2018. Antibacterial and immunogenic behavior of silver coatings on additively manufactured porous titanium. Acta Biomater. 81, 315−327.

Du Plessis, A., Glaser, D., Moller, H., Mathe, N., Tshabalala, L., Mfusi, B., Mostert, R., 2019. Pore closure effect of laser shock peening of additively manufactured AlSi10Mg. 3D Print. Addit. Manuf. 6 (5), 245−252.

Du Plessis, A., Macdonald, E., 2020. Hot isostatic pressing in metal additive manufacturing: X-ray tomography reveals details of pore closure. Addit. Manuf. 34, 101191.

Du Plessis, A., Razavi, S.M.J., Berto, F., 2020. The effects of microporosity in struts of gyroid lattice structures produced by laser powder bed fusion. Mater. Des. 194, 108899.

Edwards, P., Ramulu, M., 2014. Fatigue performance evaluation of selective laser melted Ti−6Al−4V. Mater. Sci. Eng. A 598, 327−337.

Giorleo, L., Ceretti, E., Giardini, C., 2015. Ti surface laser polishing: effect of laser path and assist gas. In: CIRP ICME'14-9th CIRP Conference on Intelligent Computation in Manufacturing Engineering. Elsevier, pp. 446−451.

Gorsse, S., Hutchinson, C., Gouné, M., Banerjee, R., 2017. Additive manufacturing of metals: a brief review of the characteristic microstructures and properties of steels, Ti-6Al-4V and high-entropy alloys. Sci. Technol. Adv. Mater. 18 (1), 584−610.

Hamidi Nasab, M., Giussani, A., Gastaldi, D., Tirelli, V., Vedani, M., 2019. Effect of surface and subsurface defects on fatigue behavior of AlSi10Mg alloy processed by laser powder bed fusion (L-PBF). Metals 9 (10), 1063.

Jafarlou, D.M., Ferguson, G., Tsaknopoulos, K.L., Chuang, A.C., Nardi, A., Cote, D., Champagne, V., Grosse, I.R., 2020. Structural integrity of additively manufactured stainless steel with cold sprayed barrier coating under combined cyclic loading. Addit. Manuf. 35, 101338.

Jung, J.-H., Park, H.-K., Lee, B.S., Choi, J., Seo, B., Kim, H.K., Kim, G.H., Kim, H.G., 2017. Study on surface shape control of pure Ti fabricated by electron beam melting using electrolytic polishing. Surf. Coating. Technol. 324, 106−110.

Kahlin, M., Ansell, H., Basu, D., Kerwin, A., Newton, L., Smith, B., Moverare, J.J., 2020. Improved fatigue strength of additively manufactured Ti6Al4V by surface post processing. Int. J. Fatig. 134, 105497.

Kalentics, N., Boillat, E., Peyre, P., Ćirić-Kostić, S., Bogojević, N., Logé, R.E., 2017. Tailoring residual stress profile of selective laser melted parts by laser shock peening. Addit. Manuf. 16, 90−97.

Karakurt, I., Ho, K.Y., Ledford, C., Gamzina, D., Horn, T., Luhmann, N.C., Lin, L., 2018. Development of a magnetically driven abrasive polishing process for additively manufactured copper structures. Procedia Manuf. 26, 798−805.

Khorasani, A.M., Gibson, I., Ghasemi, A., Ghaderi, A., 2020. Modelling of laser powder bed fusion process and analysing the effective parameters on surface characteristics of Ti-6Al-4V. Int. J. Mech. Sci. 168, 105299.

Kopp, A., Derra, T., Müther, M., Jauer, L., Schleifenbaum, J.H., Voshage, M., Jung, O., Smeets, R., Kröger, N., 2019. Influence of design and postprocessing parameters on the degradation behavior and mechanical properties of additively manufactured magnesium scaffolds. Acta Biomater. 98, 23−35.

Lefky, C.S., Zucker, B., Wright, D., Nassar, A.R., Simpson, T.W., Hildreth, O.J., 2017. Dissolvable supports in powder bed fusion-printed stainless steel. 3D Print. Addit. Manuf. 4 (1), 3−11.

Luo, S., He, W., Chen, K., Nie, X., Zhou, L., Li, Y., 2018. Regain the fatigue strength of laser additive manufactured Ti alloy via laser shock peening. J. Alloys Compd. 750, 626−635.

Ma, C., Andani, M.T., Qin, H., Moghaddam, N.S., Ibrahim, H., Jahadakbar, A., Amerinatanzi, A., Ren, Z., Zhang, H., Doll, G.L., Dong, Y., Elahinia, M., Ye, C., 2017. Improving surface finish and wear resistance of additive manufactured nickel-titanium by ultrasonic nano-crystal surface modification. J. Mater. Process. Technol. 249, 433−440.

Ma, P., Prashanth, K.G., Scudino, S., Jia, Y., Wang, H., Zou, C., Wei, Z., Eckert, J., 2014. Influence of annealing on mechanical properties of Al-20Si processed by selective laser melting. Metals 4 (1), 28−36.

Maleki, E., Bagherifard, S., Bandini, M., Guagliano, M., 2020. Surface post-treatments for metal additive manufacturing: progress, challenges, and opportunities. Addit. Manuf. 101619.

Nagalingam, A.P., Yeo, S., 2018. Controlled hydrodynamic cavitation erosion with abrasive particles for internal surface modification of additive manufactured components. Wear 414, 89−100.

Nicoletto, G., Konečná, R., Frkáň, M., Riva, E., 2018. Surface roughness and directional fatigue behavior of as-built EBM and DMLS Ti6Al4V. Int. J. Fatig. 116, 140−148.

Peng, C., Fu, Y., Wei, H., Li, S., Wang, X., Gao, H., 2018. Study on improvement of surface roughness and induced residual stress for additively manufactured metal parts by abrasive flow machining. Procedia CIRP 71, 386−389.

Prashanth, K.G., Scudino, S., Klauss, H.J., Surreddi, K.B., Löber, L., Wang, Z., Chaubey, A.K., Kühn, U., Eckert, J., 2014. Microstructure and mechanical properties of Al−12Si produced by selective laser melting: effect of heat treatment. Mater. Sci. Eng. A 590, 153−160.

Pyka, G., Burakowski, A., Kerckhofs, G., Moesen, M., Van Bael, S., Schrooten, J., Wevers, M., 2012. Surface modification of Ti6Al4V open porous structures produced by additive manufacturing. Adv. Eng. Mater. 14 (6), 363−370.

Rafieazad, M., Mohammadi, M., Nasiri, A.M., 2019. On microstructure and early stage corrosion performance of heat treated direct metal laser sintered AlSi10Mg. Addit. Manuf. 28, 107−119.

Razavi, S.M.J., Avanzini, A., Cornacchia, G., Giorleo, L., Berto, F., 2021. Effect of heat treatment on fatigue behavior of as-built notched Co-Cr-Mo parts produced by selective laser melting. Int. J. Fatig. 142, 105926.

Razavi, S.M.J., Van Hooreweder, B., Berto, F., 2020. Effect of build thickness and geometry on quasi-static and fatigue behavior of Ti-6Al-4V produced by electron beam melting. Addit. Manuf. 36, 101426.

Romano, S., Nezhadfar, P.D., Shamsaei, N., Seifi, M., Beretta, S., 2020. High cycle fatigue behavior and life prediction for additively manufactured 17-4 PH stainless steel: effect of sub-surface porosity and surface roughness. Theor. Appl. Fract. Mech. 106, 102477.

Scherillo, F., 2019. Chemical surface finishing of AlSi10Mg components made by additive manufacturing. Manuf. Lett. 19, 5−9.

Siddique, S., Imran, M., Walther, F., 2017. Very high cycle fatigue and fatigue crack propagation behavior of selective laser melted AlSi12 alloy. Int. J. Fatig. 94, 246−254.

Spierings, A.B., Starr, T.L., Wegener, K., 2013. Fatigue performance of additive manufactured metallic parts. Rapid Prototyp. J. 19 (2), 88−94.

Stoffregen, H.A., Butterweck, K., Abele, E., 2014. Fatigue analysis in selective laser melting: review and investigation of thin-walled actuator housings. In: 25th Solid Freeform Fabrication Symposium, pp. 635−650.

Tan, K.L., Yeo, S.H., 2017. Surface modification of additive manufactured components by ultrasonic cavitation abrasive finishing. Wear 378−379, 90−95.

Thomas, D.S., Gilbert, S.W., 2014. Costs and Cost Effectiveness of Additive Manufacturing, vol. 1176. NIST special publication, p. 12.

Tian, Y., Gora, W.S., Cabo, A.P., Parimi, L.L., Hand, D.P., Tammas-Williams, S., Prangnell, P.B., 2018. Material interactions in laser polishing powder bed additive manufactured Ti6Al4V components. Addit. Manuf. 20, 11−22.

Tyagi, P., Goulet, T., Riso, C., Stephenson, R., Chuenprateep, N., Schlitzer, J., Benton, C., Garcia-Moreno, F., 2019. Reducing the roughness of internal surface of an additive manufacturing produced 316 steel component by chempolishing and electropolishing. Addit. Manuf. 25, 32−38.

Worts, N., Jones, J., Squier, J., 2019. Surface structure modification of additively manufactured titanium components via femtosecond laser micromachining. Optic Commun. 430, 352−357.

Yadollahi, A., Shamsaei, N., 2017. Additive manufacturing of fatigue resistant materials: challenges and opportunities. Int. J. Fatig. 98, 14−31.

Yadroitsava, I., Du Plessis, A., Yadroitsev, I., 2019. Chapter 12 - bone regeneration on implants of titanium alloys produced by laser powder bed fusion: a review. In: Froes, F., Qian, M., Niinomi, M. (Eds.), Titanium for Consumer Applications. Elsevier, pp. 197−233.

Yan, C., Hao, L., Hussein, A., Wei, Q., Shi, Y., 2017. Microstructural and surface modifications and hydroxyapatite coating of Ti-6Al-4V triply periodic minimal surface lattices fabricated by selective laser melting. Mater. Sci. Eng. C 75, 1515−1524.

Yu, W., Sing, S.L., Chua, C.K., Tian, X., 2019. Influence of re-melting on surface roughness and porosity of AlSi10Mg parts fabricated by selective laser melting. J. Alloys Compd. 792, 574−581.

Zhang, B., Li, Y., Bai, Q., 2017. Defect formation mechanisms in selective laser melting: a review. Chin. J. Mech. Eng. 30 (3), 515−527.

Structural integrity I: static mechanical properties

13

Pavel Krakhmalev[1], *Anna Martin Vilardell*[2], *Naoki Takata*[2]
[1]Karlstad University, Department of Engineering and Physics, Karlstad, Sweden;
[2]Department of Materials Process Engineering, Graduate School of Engineering, Nagoya University, Nagoya, Aich, Japan

Chapter outline

13.1 Introduction to structural integrity and static mechanical properties 350
13.2 Correlation between mechanical properties and microstructure of the L-PBF materials 352
13.3 Mechanical properties of key L-PBF materials in as-built condition 353
  13.3.1 Mechanical properties of steels 353
    13.3.1.1 Stainless steels 353
    13.3.1.2 Precipitation hardening and martensitic stainless steels 354
    13.3.1.3 Maraging tool steels and high-alloy tool steels 355
  13.3.2 Mechanical properties of titanium-based alloys 356
  13.3.3 Mechanical properties of aluminum-based alloys 358
  13.3.4 Mechanical properties of nickel-based alloys 359
13.4 Influence of heat treatments on mechanical properties of key L-PBF materials 360
  13.4.1 Steels 360
  13.4.2 Titanium-based alloys 362
  13.4.3 Aluminum- and nickel-based alloys 363
13.5 Fracture analysis 364
  13.5.1 L-PBF steels 365
  13.5.2 High strength/low ductility materials — L-PBF titanium-based alloys 366
  13.5.3 Low strength/high ductility materials — L-PBF aluminum-based alloys 367
13.6 Conclusions 369
13.7 Questions 369
Acknowledgements 370
References 370

Fundamentals of Laser Powder Bed Fusion of Metals. https://doi.org/10.1016/B978-0-12-824090-8.00019-6
Copyright © 2021 Elsevier Inc. All rights reserved.

13.1 Introduction to structural integrity and static mechanical properties

Laser powder bed fusion (L-PBF) is one of the additive manufacturing (AM) methods to produce metallic parts. The layer-by-layer manufacturing nature results in the formation of specific microstructure, achieving different properties compared to conventional analogs. In this chapter, the mechanical properties of the main classes of materials such as steels, aluminum and titanium alloys, as well as nickel-base superalloys manufactured by L-PBF are overviewed. The focus is on the static mechanical properties obtained by tensile tests as the most common and standard method for the measurement of mechanical characteristics. A correlation between manufacturing, microstructure, and mechanical properties of these L-PBF materials is highlighted.

Mechanical properties are fundamental properties of materials that describe how a material performs under stress and strain conditions. Strength characteristics are used in engineering design and calculations of constructions, as these attributes indicate stresses that the material can withstand before plastic deformation and/or fracture occurs. Plasticity characteristics of materials are of importance in bulk and sheet forming processes and demonstrate how much the material can be deformed before fracture. Generally, mechanical properties are used for comparison and qualification of materials and for the materials selection process.

The most common ways to obtain mechanical properties of materials is by the performance of uniaxial tensile test (ASTM E8/E8M), compression test (ASTM E9) and hardness measurements (ASTM E384, ASTM E140). The test methods, size and shape of specimens, and data treatment are described in the standard specifications to ensure the reproducibility and comparability of the obtained results. For the performance of uniaxial tensile tests, a standard specimen is continuously tensed by a uniaxial force until fracture occurs. The results are represented in the form of a stress-strain diagram. The following properties (ASTM E6) are obtained from the engineering stress-strain diagram (Fig. 13.1):

- Modulus of elasticity E (elastic modulus, Young's modulus) is the measure that defines the stiffness of a material. It is defined as the ratio of tensile stress to its corresponding tensile strain below the proportionality limit. Stiffness is understood as the resistance of a material to elastic deformation.
- Yield tensile strength S_y or YS is the engineering stress at which a material exhibits occurrence of the permanent plastic deformation. In cases of yielding instability effects, YS is defined by the offset method as the stress at which the material exhibits a predefined permanent plastic deformation, usually 0.2%. The 0.2% value has been historically suggested as this magnitude is still close to the yield point, and at the same time is sufficiently large to be measured with conventional methods. The yield tensile strength obtained by this method is often called proof strength, and it is designed as $S_{y0.2}$.
- Ultimate tensile strength S_u or UTS is the maximum tensile stress which the specimen is capable of sustaining before the onset of nonuniform or localized plastic deformation.

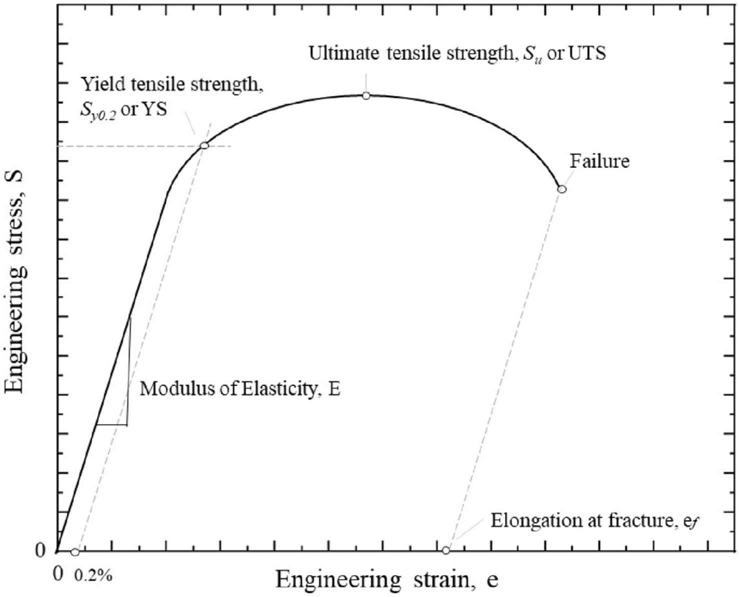

Figure 13.1 Generic schema of engineering tensile stress-strain curve.

- Ductility is the ability of a material to deform plastically before failure. In the tensile tests, ductility is measured as the elongation at fracture (true strain at fracture, %), or reduction in area (the difference between the area of the original cross-section of the specimen and the area of its smallest cross-section after test (*A*,%).
- Toughness is another way to measure material's resistance to fracture, and it is calculated as the area under the stress-strain curve. Toughness defines how much energy can be absorbed by a material before failure. The toughness values obtained by uniaxial tensile test should not be mistaken with fracture toughness.

Compression tests determine the material behavior under compression stresses and are important to measure the elastic properties and strength characteristics (compressive modulus, compressive yield strength, compressive strength) of brittle or low-ductility materials.

Hardness is defined as the resistance of a material to localized plastic deformation induced by either mechanical indentation or abrasion of a sharp object. Indentation hardness measurements are easy to perform and are commonly evaluated from measurements of the area or depth of the indentation made by an indenter of defined shape under specified static load. The most common hardness testing methods are Vickers hardness (HV), Rockwell hardness (HR) and Brinell hardness (HB). Those methods use indenters of different shape and different load ranges to perform hardness measurements. Conversion tables between hardness measured by different methods are available in ASTM E140.

Mechanical properties are structure-sensitive, which means that a material of the same chemical composition may have different properties in dependence of the manufacturing route, heat treatment, and microstructure. In engineering metallic alloys, solid solution strengthening, deformation hardening, precipitation and dispersion hardening, and grain boundary strengthening are the most common mechanisms responsible for improving the strength characteristics (Hertzberg et al., 2020).

13.2 Correlation between mechanical properties and microstructure of the L-PBF materials

In AM, a solid 3D object is formed in a unique way. During the laser powder bed fusion manufacturing, a laser beam melts powder locally forming a melt pool of a few hundred micrometers in size. Thermal gradients and solidification rates are high that results in the formation of very fine cellular or cellular-dendritic microstructure. The dendrites form colonies that grow following a preferable crystallographic direction, and the highest temperature gradient. Those that have the least misorientation angle with both, the preferable crystallographic direction and the highest temperature gradient have the best condition to keep growing. It results in the formation of a solidification texture, see Chapter 8 of this book for more details. This textured microstructure can cool down without phase transformation, like in some Al-alloy or stainless steels, or with martensitic transformation as observed in Ti-alloys or maraging steels. Nevertheless, because of the track-by-track and layer-by-layer manufacturing nature, the already solidified layers are subjected to additional thermal cycles and in-situ heat treatment in solid state. This in-situ heat treatment is a thermally activated diffusional process leading to bulk or grain boundary precipitations, in the case of maraging steels or Ni-based superalloys manufactured by L-PBF. All the above-mentioned features of the microstructure, along with molten-pool boundaries and possible defects, influence mechanical properties of L-PBF materials and result in substantial differences of mechanical properties of L-PBF materials from the same alloys manufactured and heat-treated by conventional processes.

Mechanical properties of the L-PBF materials, especially those that can be measured by tensile tests, are sensitive to the presence of defects in the material. There are several types of defects in AM materials that affect the final performance of a component under a load, see Chapters 3, 6, 7, and 9 of this book for more detail.

- Round pores can be the result of entrapped gas in the melt pool. The gas can originate from the powder or protection atmosphere, or be a result of not optimal process parameters.
- Elongated lack of fusion defects are usually located between layers, perpendicular to the building direction, and are the result of incomplete melting of the powder in the previous layer. These pores have sharp edges and act as stress concentration points under loading, which are very critical for static and dynamic mechanical properties.
- Residual stress is another feature of the manufacturing process that results in cracking and distortion of the part. Residual stresses may significantly deteriorate mechanical performance of the L-PBF component.

- Thermal cracks formed during manufacturing is another possible defect that negatively influence mechanical properties of the L-PBF materials. The control of laser scanning strategies and utilization of build chambers with preheating capacities may decrease residual stresses in L-PBF materials, thus reducing/avoiding residual stresses and thermal cracking.
- High surface roughness is the result of the track-by-track and layer-by-layer manufacturing manner in L-PBF. Surface roughness depends on many factors including scanning strategy, thickness of the layer, spattering, denudation effects, inclination angle of the printed surface, etc. Too high surface roughness may also negatively influence mechanical performance of L-PBF components.

The presence of defects results in a deterioration of tensile test properties decreasing the load-bearing cross-section under tension, and acting as stress concentrator points accelerating crack nucleation. In principle, the presence of defects in L-PBF materials explains a wide spread of mechanical properties in the currently available literature surveys, Fig. 13.2 (DebRoy et al., 2018; Vanmeensel et al., 2018; Zhang et al., 2019; Bajaj et al., 2020; Lewandowski and Seifi, 2016). The future progress in the development of process strategies, better control of the protective atmosphere, defects, and microstructure will lead to the manufacturing of defect-free L-PBF materials that demonstrate more consistent mechanical properties.

13.3 Mechanical properties of key L-PBF materials in as-built condition

13.3.1 *Mechanical properties of steels*

13.3.1.1 *Stainless steels*

AISI 316(L) and AISI 304(L) stainless steels are perhaps the most widely investigated grades of AM austenitic stainless steels, and are among the very first metallic alloys

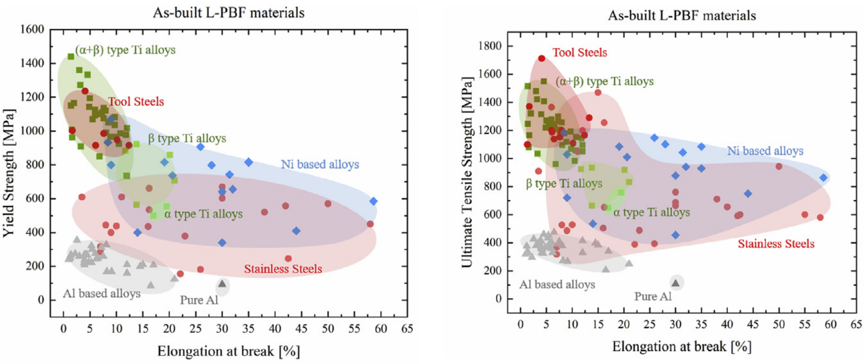

(a) (b)

Figure 13.2 Ashby plot style for (a) YS and (b) UTS against ductility of as-built L-PBF materials (Zhang et al., 2011, 2019; Attar et al., 2014; Vrancken et al., 2014; Lewandowski and Seifi, 2016; Sing et al., 2016; DebRoy et al., 2018; Liu and Shin, 2019; Qiu and Liu, 2019; Bajaj et al., 2020; Yap et al., 2014; Kok et al., 2018; Pellizzari et al., 2020).

evaluated for this manufacturing technology. Since these steels solidify without martensitic transformation, they are less prone to thermal cracking, and with a proper selection of process parameters can be manufactured pore-free. L-PBF manufactured austenitic stainless steels mostly have fully austenitic cellular dendritic microstructure. Strength characteristics of AM austenitic stainless steels vary in a broad range of 300−600 MPa and 350−760 MPa for YS and UTS, respectively (Bajaj et al., 2020; DebRoy et al., 2018). High strength values are the result of fine microstructure and high-density dislocation structure. Since cell size is sensitive to manufacturing parameters, a wide range of strength characteristics is experimentally observed. A dependence of strength on cell size is well described by the Hall-Petch relationship (Hertzberg et al., 2020). Additionally, it is suggested that nanoscale rounded inclusions also can contribute in material strength due to an interaction between dislocations and particles leading to the Orowan looping effect (Saeidi et al., 2015a,b; Zhang et al., 2019). Anisotropy in strength characteristics can be sometimes observed and is attributed to the directional solidification process and texture (DebRoy et al., 2018). Nevertheless, this effect is not very pronounced and can be eliminated by use of different laser scanning strategies resulting in almost anisotropic grain orientation within the L-PBF material. Ductility of L-PBF austenitic stainless steels varies in a broad range. Some authors have reported an elongation at fracture lower (12%) than in conventionally manufactured grades, while some report high elongation at fracture up to 67% (Carlton et al., 2016; Wang et al., 2018; Shamsujjoha et al., 2018). Such spread in ductility values may be related to internal pores, microcracks, inclusions, and lack of fusion defects which detrimentally influence elongation at fracture in tensile tests.

13.3.1.2 Precipitation hardening and martensitic stainless steels

L-PBF precipitation hardening 17-4 PH, 15-5 PH, and martensitic AISI 420 and 440 stainless steels have been intensively investigated over decades. Because of the high Cr content, these steels have a corrosion resistance comparable to austenitic stainless steels. Conventional 17-4 PH steel is solution treated and cooled down to form martensite, and subsequently, aged to achieve strengthening by Cu-rich precipitates. Martensitic stainless steels, like AISI 420, achieve the required combination of strength and fracture toughness characteristics after quenching and tempering to form Cr-rich carbides.

The strength of conventional 17-4 PH steel is higher than that of martensitic stainless steels. The microstructure of L-PBF manufacturing of these steels is not always fully martensitic and often contains substantial amounts of austenite. Microstructure, and therefore mechanical properties, of 17-4PH steel are also dependent on the atmosphere used during manufacturing. The mixture of austenite and martensite is observed in steel built under nitrogen atmosphere, and mostly martensite (92 vol.%) built under argon atmosphere (Rafi et al., 2014; Murr et al., 2012). In as-built 17-4 PH steel, a YS of 570−660 MPa, an UTS of 900−1250MPa and an elongation at fracture of 5%−50% is reported (DebRoy et al., 2018; Rafi et al., 2014). At the same time, as-built 17-4 PH exhibits higher elongation at fracture than conventionally heat-treated material (Facchini et al., 2010; Starr et al., 2012; Murr et al., 2012), which can be explained by the deformation-induced martensitic transformation of austenite.

Similarly, high amounts of austenite are observed in L-PBF AISI 420. Because of the microstructure, as-built conditions of these steels usually have lower strength characteristics than conventional heat-treated analogs. Nevertheless, L-PBF AISI420 steel has been reported to have YS of 600 MPa, UTS of 1670 MPa, elongation of 3.5% (Saeidi et al., 2019) and a hardness in a range of 550−650 HV (Krakhmalev et al., 2015; Zhao et al., 2015; Saeidi et al., 2019). Very broad scattering of the experimentally observed strength and ductility values are explained by differences in the content of soft austenitic phase in these L-PBF steels, which is a result of manufacturing parameters and protective atmosphere.

13.3.1.3 Maraging tool steels and high-alloy tool steels

In tooling applications, two main classes of steels are used. Maraging (martensitic + aging) tool steels are iron-based materials with low content of carbon. They normally form martensite upon cooling. After aging, the maraging steels obtain high strength and hardness required by demanding applications due to the precipitation of intermetallic phases. High-alloy tool steel, cold work and hot work, contains carbon and other alloying elements. The strength of these alloys is achieved by the formation of fine carbides upon tempering after hardening to the martensite. In conventional cold work tool steels, primary carbides are also desirable to provide wear resistance, but a high-volume fraction of them may negatively influence toughness of steel.

The most widely investigated maraging tool steel manufactured by L-PBF is 1.2709 steel (US classification ASTM A646 Grade 18% Ni (300) maraging steel, European 1.2709 and German X3NiCoMoTi 18-9-5), although a number of other maraging steels have been also investigated. This material is adopted for L-PBF and can be nearly full-dense manufactured. The L-PBF maraging steel, as other tool steel grades, has a cellular/dendritic colonies microstructure right after solidification. The colonies formed at solidification are transformed to martensite upon cooling. Martensite laths are located within cells/dendrites formed at solidification. As a result of Ni enrichment in the intercellular areas, up to 15% retained austenite can be observed in the microstructure (Bajaj et al., 2020; Jägle et al., 2017). The mechanical properties of as-built L-PBF maraging 1.2709 steel are comparable with conventional material in solution-treated condition. YS and UTS are slightly higher being 800−1100 MPa and 1000−1200 MPa, respectively. Hardness of the material in as-built condition is reported in a range of 350−400HV (Bai et al., 2017; Casati et al., 2016a,b), and elongation at fracture varied between 6%−12%. Variations in mechanical properties can be explained by the presence or absence of precipitates in the microstructure. In maraging steel, precipitation strengthening is the main strengthening mechanism, and formation of precipitates leads to higher strength characteristics. In as-built L-PBF maraging steels no precipitates were observed by Bodziak et al. (2019) and Jägle et al. (2014), while Tan et al. (2017) and Kürnsteiner et al. (2017) reported the presence of nanoscale particles formed due to in-situ heat treatment. This disagreement can be related to different process parameters used to manufacture maraging steel. If time and temperature of thermal cycles were high enough to initiate diffusional processes, precipitations can form during the L-PBF process.

Conventional high-alloy tool steels are quite challenging for L-PBF, because during manufacturing they develop a high level of residual stresses that often lead to cracks and delamination. Recent progress in crack-free L-PBF manufacturing of tool steels has been achieved by leveraging preheating of the build platform. Currently, a number of tool steel grades including H11, H13, and D2 can be manufactured by L-PBF with near full density without thermal cracking (Boes et al., 2018; Casati et al., 2018; Sander et al., 2016; Geenen et al., 2019; Kempen et al., 2014). The most common material is H13 hot work tool steel. Similarly to maraging tool steels, in as-built conditions, these steels have a structure of martensite located within cells/dendrites formed upon solidification. Primary carbides are not often observed in L-PBF cold work tool steels because of high solidification rates. The dissolution of carbides and enrichment of the interdendritic regions with alloying elements lead to the stabilization of austenite (Yan et al., 2017; Boes et al., 2018; Casati et al., 2018; Holzweissig et al., 2015; Mertens et al., 2016). YS and UTS of L-PBF H13 steel are usually lower than those of conventionally heat-treated material and vary in ranges of 830−1500 MPa and 1400−1900 MPa, respectively (Bajaj et al., 2020; Mazur et al., 2017; Ackermann et al., 2018; Dörfert et al., 2019). Variations in strength characteristics is due to a combination of several factors. First of all, differences in manufacturing parameters result in different thermal cycling of the build, which in turn results in variations in the stabilization of austenite and partial decomposition of martensite phase. For example, in several steels, the hardness of the top layer is higher than the interior of the built material due to the in-situ heat treatment of martensite in the interior regions (Krakhmalev et al., 2015; Šafka et al., 2016; Boes et al., 2018). Secondly, the additional effect of preheating may also intensify the in-situ heat treatment effect (Mertens et al., 2016; Boes et al., 2018). Thus, the formation of bainite or another type of martensite can be observed (Boes et al., 2018). Finally, often to avoid distortion and remove stresses, stress-relief treatment is performed. Stress-relief treatment can also initiate diffusional decomposition of martensite and, therefore, influence mechanical properties (Mazur et al., 2017; Åsberg et al., 2019). Low elongation at fracture, often below 2%, is typical for high-alloy tool steels in as-built conditions (Mazur et al., 2017; Ackermann et al., 2018; Dörfert et al., 2019; Boes et al., 2018; Holzweissig et al., 2015; Mertens et al., 2016; Šafka et al., 2016). Interestingly, low ductility is typical for L-PBF high-alloy tool steel in as-built and also in heat-treated conditions (Mazur et al., 2017; Ackermann et al., 2018; Åsberg et al., 2019), but it can be improved by HIP treatment, which can be associated with healing of some manufacturing defects (Åsberg et al., 2019).

13.3.2 Mechanical properties of titanium-based alloys

Titanium and titanium alloys can be classified into three main groups according to their crystallographic structure: α type (HCP: hexagonal-closed packed), (α+β) type, and β type (BCC: body-centered cubic). Compared to conventional technologies, the high cooling rates of the L-PBF process lead to the transformation from a high-temperature β phase to a nonequilibrium α′ (instead of α). It results in a high strength and hardness but low ductility of as-built L-PBF Ti6Al4V alloy, as α′ martensite phase has a high dislocation density, and contains stacking faults and twins. Protective atmosphere used at manufacturing can also influence mechanical properties. It is well known that interstitial elements like oxygen and nitrogen may be picked up during L-PBF process, which may result in an increase in strength, but at the same time in a decrease in ductility, promoting the initiation of brittle fracture (Velasco-Castro et al., 2019; Dietrich et al., 2020). Therefore, the possible impact of the contamination of Ti alloys by interstitials during manufacturing on final mechanical performance should not be underestimated.

The strength level of L-PBF commercial pure titanium Ti (CP-Ti) and Ti alloys in comparison with those fabricated by conventional cast process (as-cast materials) is displayed in Fig. 13.3. It can be observed that α-type (CP-Ti) and (α+β)-type alloys (e.g., Ti6Al4V and Ti6Al7Nb) obtained by L-PBF process exhibit higher tensile strengths compared to the same materials fabricated by cast process. However, β-type L-PBF alloys (for example, Ti15Mo) show similar strength compared to as-cast materials with the same composition.

- α-type refers to CP-Ti and α-type Ti alloys. As-built L-PBF CP-Ti has higher YS and UTS of 555 ±3 MPa and 757±12.5 MPa, respectively, compared to, for example, conventional sheet materials (280 and 345 MPa, respectively). However, no differences have been found for elongation at fracture (∼20%) (Attar et al., 2014).

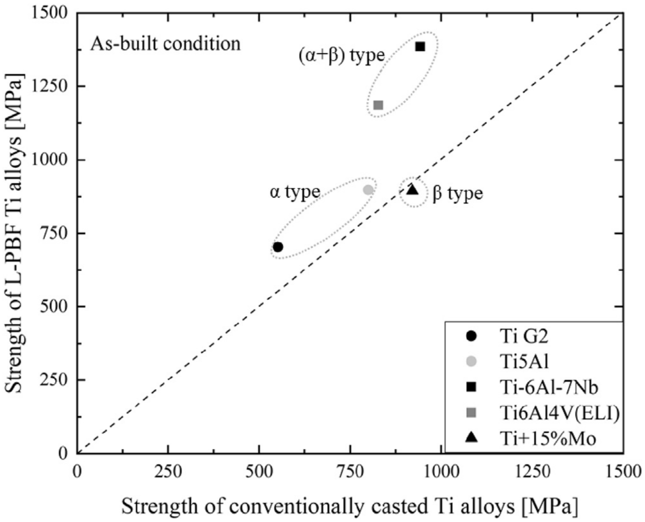

Figure 13.3 Tensile strength of various Ti alloys fabricated by L-PBF in comparison with conventionally cast alloys (Attar et al., 2014; Polozov et al., 2018; Yadroitsev, 2017; Koizumi et al., 2018; Xu et al., 2020; Zwilsky and Langer, 1990).

- (α+β)-type is the most common and widely used type of alloys. As-built L-PBF Ti6Al4V reaches YS and UTS values in a range between 910−1350 MPa and 1035−1407 MPa, respectively (see Ashby plot in Section 13.2), which are much higher compared to the 830−930 MPa and 870−995 MPa of wrought Ti6Al4V (Liu and Shin, 2019). Such wide differences in YS and UTS values in as-built condition are due to differences in process parameters, as well as scanning strategy, that lead to slightly different α′ microstructures with a low amount of β phase and different thickness of α′ needles. Due to the increase in strength, ductility of as-built L-PBF Ti6Al4V is often compromised by having elongation at fracture values below 10%, which might not be good for certain applications such as implant prosthesis (ASTM F136-13 and ASTM F1108-14) that require a minimum elongation at fracture at least of 8%. However, higher ductility is possible by choosing the suitable process parameters (Moletsane et al., 2016), or by the performance of post-processing treatments.
- β-type Ti alloys are known for their low elastic modulus. The addition of β-phase stabilizing elements, molybdenum (Mo), niobium (Nb), and tantalum (Ta) is required to retain β-phase after rapid cooling. For those cases, critical concentrations of 10, 36, and 45 (wt.%), respectively, are required to 100% retain the BCC for a binary Ti alloy (Kolli and Devaraj, 2018). An example of β-type binary alloy is the Ti15Mo alloy, for which UTS values obtained by as-cast and L-PBF processes are very similar (921 and 894 MPa, respectively) (Yadroitsev et al., 2017). Another β-type Ti alloy with more alloying elements obtained by L-PBF is Ti24Nb4Zr8Sn. It also reaches similar strength and ductility values as being manufactured with conventional technologies. As-built L-PBF Ti24Nb4Zr8Sn achieves YS of 563 MPa, and UTS of 665 MPa and an elongation at fracture of 13.8%. Similar values of 570 MPa (YS), 755 MPa (UTS), and 13% elongation at fracture have been obtained in hot forged material (Zhang et al., 2011).

13.3.3 Mechanical properties of aluminum-based alloys

Additive manufacturing of Al alloys by using the L-PBF process has been challenging due to the physical and chemical properties of Al alloy powders (light-weight, high reflectivity, and low absorptivity of fiber laser radiation with a wavelength near 1060 nm, which is often used in L-PBF). Nevertheless, a series of cast-type Al−Si alloys (e.g., AlSi10Mg, Al-12Si) is commonly applied for the L-PBF process (Aboulkhair et al., 2019). These alloys are relatively easy to process for manufacturing large-size samples and complex-shaped components. As-built L-PBF Al−Si alloys exhibit high hardness of approximately 130 HV.

It is generally known that heat-treatable (age-hardenable) Al alloys with high strength and adequate ductility (corresponding to alloy series of 2xxx: Al−Cu, 6xxx: Al−Mg−Si and 7xxx: Al−Mg−Zn) are being widely used in the automotive and aerospace industries. However, it is more difficult to find the process window for the L-PBF manufacturing of defect-free components of these 2xxx, 6xxx, and 7xxx heat-treatable alloys due to hot cracking (during solidification) propagated parallel to the building direction (Koutny et al., 2018; Stopyra et al., 2020). Recently, the processability of these alloys was developed to manufacture fully dense samples. For instance, as-built L-PBF Al−Mg−Zn alloy (AA7075) exhibits a high hardness of approximately 140 HV (Stopyra et al., 2020), although it can vary depending on laser parameters and baseplate temperature (Martin et al., 2017; Aboulkhair et al., 2019).

As mentioned above, the L-PBF process produces various Al alloys with superior strengths. In Fig. 13.4, the tensile strength levels of the as-built L-PBF Al—Si alloys on the vertical axis (Rao et al., 2017; Takata et al., 2017; Hitzler et al., 2018; Koutny et al., 2018; Yang et al., 2018; Aboulkhair et al., 2019; Kimura et al., 2019; Fiocchi et al., 2020) are plotted as a function of the strength of those produced by conventional gravity or die-cast processes (Kearney, 2000; Hitzler et al., 2018) on the horizontal axis. These data include a series of conventionally used Al—Si based alloys (e.g., AlSi10Mg, Al-12Si, A355, and A356). The as-built L-PBF alloy parts exhibit higher strength than the conventionally cast ones. It is intriguing that the difference in strength between as-built L-PBF and conventionally cast parts appear more significant in higher-strength materials. The summarized data suggest an interesting insight that higher-strength Al—Si-based alloys can be made much stronger by L-PBF processing. This unique strengthening by the L-PBF process could be due to the characteristic microstructures in the locally melted and rapidly solidified alloy parts produced via the L-PBF process. The supersaturated α-Al solid solutions matrix containing numerous nano-sized particles (metastable phases and/or atomic clusters) contribute to the strengthening of as-built L-PBF Al—Si alloys (Qin et al., 2020; Takata et al., 2020).

13.3.4 Mechanical properties of nickel-based alloys

Ni-based alloys are generally known as high-temperature materials. The commercial grades of their alloy series (Inconel, Nimonic, Rene, HAYNES, and Udimet) are

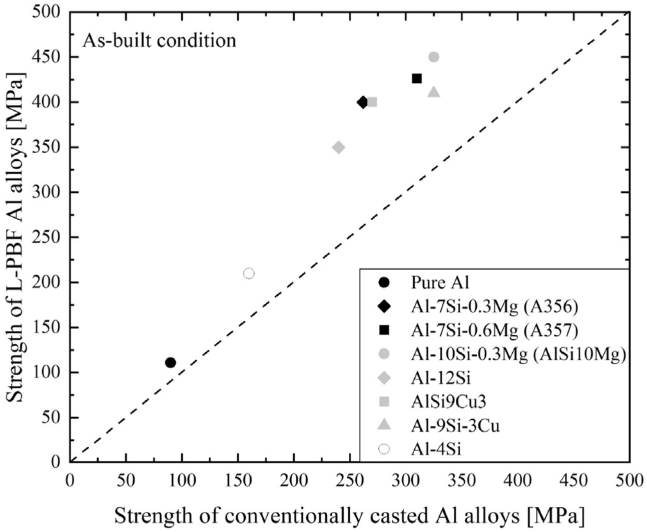

Figure 13.4 Tensile strength of various Al—Si based alloys fabricated by L-PBF in comparison with conventionally cast alloys (Kearney, 2000; Rao et al., 2017; Takata et al., 2017; Hitzler et al., 2018; Koutny et al., 2018; Yang et al., 2018; Aboulkhair et al., 2019; Kimura et al., 2019; Fiocchi et al., 2020).

widely used as superalloys (Reed, 2006). In particular, jet and gas turbine engines have benefited from the development of Ni-based alloys, which allowed increasing the engine operating temperature and led to an improved performance and thermal efficiency. Ni-based alloys are roughly classified into two grades of cast-type single-crystal superalloys for blade applications and wrought-type alloys for turbine disc applications (Reed, 2006). In general, the wrought-type alloys are in current use for L-PBF process.

One of the most commonly used wrought Ni-based alloy is Inconel 718 with a nominal composition of Ni-18Cr-5Nb-3Mo-1Ti-0.5Al-1Co (wt.%), which makes up 50% of the weight of a jet engine. L-PBF technologies allowes the manufacturing of various complex-shaped aerospace components for jet engines (e.g., engine cases, discs, combustors, blades, and seals). The L-PBF alloy 718 is the most extensively studied (DebRoy et al., 2018; Kok et al., 2018; Zhang D. et al., 2018a; Zhang F. et al., 2018b), and a number of the other L-PBF Ni-based alloys were investigated: Inconel 625: Ni-22Cr-9Mo-3.5Nb-5Fe-1Co (Zhang F. et al., 2018b), Nimonic 263: Ni-20Cr-20Co-6Mo-2.5Al-2Ti-0.06C (Vilaro et al., 2012), Haynes 230: Ni-22Cr-14W-2Mo-0.3Al-0.02La-0.1C (Kok et al., 2018), Hastelloy X: Ni-22Cr-18Fe-9Mo-1.5Co-0.6W-0.1C (Han et al., 2019). The L-PBF Ni-based alloys exhibit relatively high strengths (YS is 400−900 MPa and UTS is 750−1100 MPa) and quite high ductility in a range of 20%−40% at ambient temperature likely due to the formation of fine columnar grains including a number of nanoscale intermetallic phases in FCC γ-Ni matrix at rapid solidification during the L-PBF process (Jiang et al., 2020). The strength values are nevertheless lower than those for heat-treated wrought materials as after L-PBF precipitation hardening is not developed, instead, often precipitation of carbides and other compounds is observed at colony boundaries.

13.4 Influence of heat treatments on mechanical properties of key L-PBF materials

13.4.1 Steels

Annealing is the most common heat treatment of austenitic stainless steels. In conventional materials, it is commonly used after plastic deformation to remove residual stresses, initiate recrystallization and grain growth, and to dissolve undesirable precipitates. In L-PBF 316L steel, annealing leads to initiation of the recovery and recrystallization processes. Recovery takes place at temperatures below 900−950°C and results in the disappearance of cellular structure due to annihilation of dislocations. Annealing at higher temperatures leads to coarsening of colonies with a significant decrease in strength and an increase in ductility (Riemer et al., 2014; Saeidi et al., 2015a,b; Krakhmalev et al., 2017). After annealing of L-PBF 316L steel at temperatures above 1100°C, the strength and hardness are higher than those of wrought or cast 316L steel, which is attributed to the formation of a duplex austenite-ferrite structure (Saeidi et al., 2015a,b).

High strength in precipitation hardening steels is achieved after aging, an isothermal heat treatment that leads to precipitations of nanoparticles in martensite. Therefore, the response of L-PBF precipitation hardening steels on aging largely depends on the amount of retained austenite stabilized in the microstructure at manufacturing. The volume fraction of austenite depends on manufacturing parameters and protective atmosphere (Murr et al., 2012; Meredith et al., 2018). High amounts of austenite lower the effect of precipitation strengthening in as-built L-PBF 17-4 maraging steel (Rafi et al., 2014; LeBrun et al., 2015). Solution treatment at high temperatures can result in a decrease in austenite volume fraction thus increasing the strengthening effect after aging (Cheruvathur et al., 2016; Lass et al., 2019). Strengthening effect after aging is commonly accompanied with a decrease in ductility.

L-PBF maraging steels have good response to heat treatment, and gain strength by precipitation hardening after aging since after manufacturing, despite in-situ thermal cycling, they have mostly martensitic microstructure (Bodziak et al., 2019; Jägle et al., 2014). It was reported that aging of L-PBF 1.2709 maraging steel at 460−500°C directly from as-built condition results in an increase in YS up to 1800−1900 MPa and UTS up to 1900−2000 MPa, and a decrease in ductility of the material down to about 2%, Fig. 13.5 (Casati et al., 2016a,b; Tan et al., 2017). If aging is performed at higher temperatures (~600°C), reversion of austenite results in some decrease in strength of L-PBF 1.2709 maraging steel. Similar strength but slightly higher elongation at fracture was observed in the material that was solution treated and aged after manufacturing (Tan et al., 2017). Solution treatment above 800−850°C leads to disappearance of the fine cellular structure observed in L-PBF maraging steel (Bai et al., 2017; Tan et al., 2017).

L-PBF high alloy tool steels are usually heat-treated following the conventional procedure of austenitization and tempering. Austenitization and tempering heat treatment includes heating up the material into high-temperature regions to form austenite with subsequent rapid cooling to prevent diffusional decomposition of austenite and form martensite. It results in disappearance of cellular structure typical for the as-built condition (Boes et al., 2018; Åsberg et al., 2019; Mazur et al., 2017; Casati et al., 2018). The material is heated up to temperatures of 200−600°C to initiate

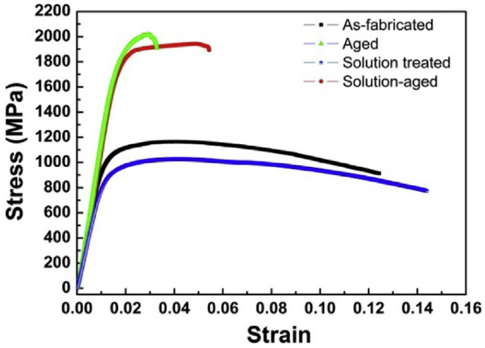

Figure 13.5 Stress-strain diagram for L-PBF maraging steel in as-built and heat-treated conditions (Tan et al., 2017).

formation of carbides in martensite. Tempering operation can be repeated two-three times to control amount of retained austenite. After austenitization and tempering, steels have more homogeneous microstructure and possess good combination of high strength and toughness required in applications. After this heat treatment, strength values of L-PBF high alloy steels approach levels typical for conventional materials (Åsberg et al., 2019; Mazur et al., 2017; Ackermann et al., 2018). Elongation at fracture after heat treatment though is lower than that in conventional materials, which can be a result of defects typical in L-PBF materials, but to some extent can be improved by hot isostatic pressing (HIP) (Åsberg et al., 2019). The improvement can be associated with healing of some defects after HIP.

13.4.2 Titanium-based alloys

Generally, post-processing treatments of L-PBF Ti and Ti alloys are performed to reduce residual stresses (stress-relief treatment) or produce an optimum combination of strength-ductility (heat treatment). The response of (α+β) Ti alloys to post-processing treatments depends on the alloy composition and the effect of heat treatment on the α-β phase volume fraction balance. Thus, among the main three Ti alloy types, the strength of L-PBF α- and β-alloys cannot be substantially raised by a post-processing treatment. Usually, a stress-relief treatment is applied to α- and β-alloys to relieve residual stresses. However, in the case of near β alloys, strengthening can happen due the precipitation of secondary α-phase. The (α+β)-type is the most heat-treatable one, and post-processing treatments overcome the low ductility of as-built L-PBF materials caused by the formation of α′ martensitic microstructure and residual stresses. Fig. 13.6 shows a schema of tensile stress-strain curve behavior of L-PBF Ti6Al4V in as-built, stress-relieved and heat-treated conditions.

- Stress-relief treatment (SR): SR results in the relaxation of residual stresses produced by the fast cooling of L-PBF process, which is beneficial to reduce/avoid geometrical distortion of the built part. For L-PBF Ti6Al4V alloy, SR treatment is usually performed around 650°C

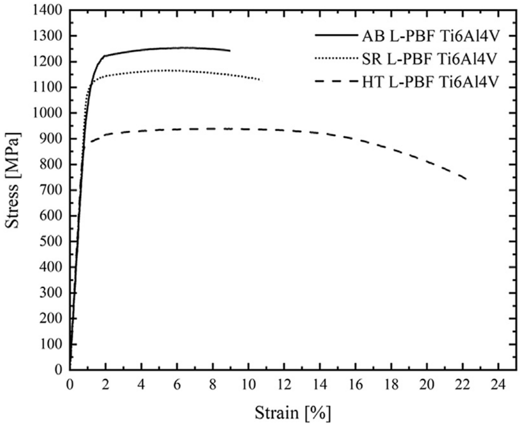

Figure 13.6 Schema of tensile stress-strain curves of as-built, SR (650°C for 3 h) and HT (950°C for 2 h) L-PBF Ti6Al4V (Yadroitsev et al., 2018).

with a duration between 2 and 4 h. Under such conditions, slight changes of as-built α′ martensite microstructure can be observed: (i) the formation of very fine α and α′ needles (Wycisk et al., 2015), (ii) partial decomposition of α′ toward acicular α (Wu and Lai, 2016), and (iii) the fine precipitation of β phase along the α′ needles (Vilardell et al., 2019) due to the early decomposition of α′ around 400°C (Xu et al., 2015). After SR treatment, it can be observed in Fig. 13.6 that UTS slightly decreases; meanwhile YS is maintained compared to as-built condition due to the relaxation of residual stresses, leading to a slight increase in ductility (Yadroitsev et al., 2018).

- Heat treatments (HT): HTs are usually performed slightly below β-transus temperature (between 800 and 980°C). The higher temperatures of HT compared to SR treatment lead to the decomposition of α′ martensite to (α+β)-phase. The dislocations and twin structures typical for α′ martensite disappear, leading to a significant decrease in strength and increase in ductility compared to SR treatment (Fig. 13.6, Yadroitsev et al., 2018). By increasing the HT temperature, YS and UTS decrease and the elongation at fracture rises due to the transformation of the fine α′ needles to a coarser (α+β) microstructure (Vrancken et al., 2012). At heat treatments above β-transus temperature, the cooling rate plays an important role, since it will determine the final morphology of α-phase at room temperature. Fully lamellar coarse Widmanstätten (α+β) microstructure is formed at furnace cooling, meanwhile finer microstructure of α platelets with an interplatelets β-phase is found at air cooling. However, faster cooling in water would lead to the formation of α′-phase, since the temperature of martensitic transition temperatures (M_s and M_f) were reported to be around 780 and 650°C (Liu and Shin, 2019), leading to the formation of dislocations within α′ plates and a decrease in ductility (Tsai et al., 2020).

13.4.3 Aluminum- and nickel-based alloys

In the case of Al alloys, various heat treatments are generally used to achieve high mechanical performance. A common heat treatment for commercially used Al alloys is T6 heat treatment. In general, conventional cast Al alloys are subjected to a T6 heat treatment in which solution treatment is carried out at elevated temperatures, above 450°C, for dissolving solute atoms into α-Al (FCC matrix) followed by aging treatment at lower temperatures ranging from 100 to 200°C (for precipitation in FCC α-Al matrix consuming solute atoms). The T6 treatment is used for the strengthening of Al alloys by fine precipitates in α-Al (FCC) matrix. The heat-treatment condition varies depending on the alloy series (alloy compositions), and it is often used for as-built L-PBF Al alloy parts (Aboulkhair et al., 2019).

Fig. 13.7 displays a comparison of strength levels of T6 heat-treated L-PBF fabricated Al alloys (Hitzler et al., 2018; Aboulkhair et al., 2019; Fiocchi et al., 2020) with those of T6 heat-treated ones produced by conventional cast process (Kearney, 2000). It is noteworthy that the general T6 heat treatment often reduces the strength of as-built L-PBF Al alloys, resulting in the same strength level to that of heat-treated conventionally cast alloys. These data show that the as-built L-PBF Al alloys experience a loss in strength on exposure to conventional heat treatments. This could be due to a change in the peculiar microstructure developed by the L-PBF process by the heat treatments. In L-PBF Ni-based superalloys, microstructure and mechanical properties are very sensitive to the in-situ thermal cycling during manufacturing and may vary in a broad

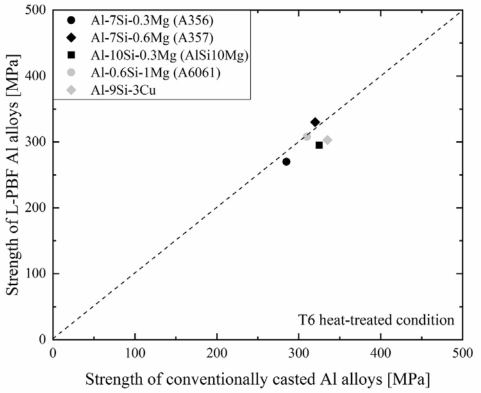

Figure 13.7 Tensile strength of various L-PBF heat-treated Al alloys in comparison with the conventionally cast heat-treated alloys (Kearney, 2000; Hitzler et al., 2018; Aboulkhair et al., 2019; Fiocchi et al., 2020).

range. Commonly, the in-situ thermal cycling leads to precipitation of carbide and intermetallic phases on cell/colony boundaries, but a strengthening effect of those precipitations is limited. Stress-relief of L-PBF Ni-based alloys may result in coarsening of undesirable phases and embrittlement. Homogenization heat treatment and aging heat treatment however lead to strength values comparable with the conventional analogs. The heat-treated conventional Ni-based alloys are being widely used in the practical applications (their heat treatment conditions are optimized for controlling the precipitation morphologies of intermetallic phases in γ-Ni(FCC) matrix (Reed, 2006)). These summarized data provide a suggestion that novel heat treatments would be required to achieve higher mechanical performance of the precipitation-hardening materials (Al- and Ni-based alloys) fabricated by L-PBF.

13.5 Fracture analysis

Fracture analysis reveals the potential failure causes of a tested part. It allows the observation of the origin of breakage as well as the failure modes. Fracture analysis can help to gather information that will aid preventing future failures. In general terms, the tensile failure mechanism can be described as the creation of crack nucleation, in which the coalescence of separate microcracks results in final failure. Fracture behavior can be mainly classified by ductile and brittle behavior, depending on the material's microstructure (e.g., composition, constituent phases, and structural integrity factors such as defects/inclusions).

Ductile fracture is the most common failure in metal alloys, and it relies on the mechanisms of plasticity (e.g., physics of dislocations, of hardening and strain-hardening mechanisms, crystal plasticity, and plastic anisotropy). In the case of ductile fracture, an extensive plastic deformation typically takes place before failure, and the deformation is characterized by the formation of cup and cone shapes, followed by the development of an irregular fibrous fracture, which corresponds to the pulled back edges from several microcracks. On the other hand, brittle fracture can occur in metals with high strength and low ductility, and in some cases at low temperature (for example, below the ductile-to-brittle transition temperature).

Brittle behavior occurs with very little deformation prior to failure. The formation of cracks takes place and propagates through the material by the process known as cleavage, which occurs through planar sectioning of the atomic bonds between the atoms at the crack tip showing a smoother fracture surface. As described by Danzer (1991), the statistical theory of a brittle fracture assumes that: (i) the material fails when the weakest structural element (most serious defect) fails, and (ii) the defect density is sufficiently low that the interaction between flaws can be neglected. However, ductile fracture also can start at an existing flaw, such as a brittle inclusion within a grain, a precipitate or a void (porosity).

Fracture behavior of as-built L-PBF manufactured materials can be divided in two groups according to their strength and ductility, showing different fracture modes and fracture surface morphologies.

13.5.1 L-PBF steels

Fracture behavior of as-built L-PBF steels is determined by microstructure and porosity (Ronneberg et al., 2020). The size and orientation of defects significantly depend on the process parameters and scanning strategy, thus influencing mechanical properties as well as fracture behavior. Fracture behavior of as-built L-PBF steels can vary depending on the type of steel by means of their strength and ductility. Among the different type of steels, stainless and tool steels made up the 91.6% of AM production in 2018 (SmarTech analysis, 2019).

As-built L-PBF tool steels consist of fine aggregates of multiple phases, martensitic microstructure often with precipitates, show a mixture of ductile and cleavage mode failures (quasi-cleavage). Cleavage features decrease with the increase in elongation at fracture. Manufactured conditions showing $>10\%$ elongation at fracture have less cleavage and more ductile failure (Kudzal et al., 2017). L-PBF austenitic stainless steels contain the ductile phase, FCC γ-Fe, and show a fibrous fracture surface typical for ductile fracture. As-built L-PBF stainless steels with lower strength and higher ductility than as-built L-PBF tool steels show fracture surfaces covered by small dimples typical of ductile materials. However, small crack propagations and premature debonding can be observed at low stress levels from microstructural defects such as oxide inclusions or lack of fusion (Casati et al., 2016a, 2016b). The phenomenon appears to occur only in the “ductile” materials fabricated by L-PBF.

13.5.2 High strength/low ductility materials — L-PBF titanium-based alloys

As-built L-PBF Ti alloys show cup-and-cone fracture morphology and obvious necking associated with ductile fracture. A periphery of shear lips is created followed by an irregular fibrous dimple-shape fractured surface in the central area (Fig. 13.8a). The fracture surface of as-built L-PBF Ti alloys is controlled by the pore coalescence mechanism which originates from the nucleation, growth, and coalescence of micro-voids during plastic deformation (Yadroitsev et al., 2018). Void nucleation occurs in the weakest part of the material, along the boundaries of prior β grains and also between α′ needles. After voids nucleate, they grow due to the further plastic deformation enlarging their size and distorting their shape along the direction of maximum tension stress leading, joining, and/or coalescing with adjacent voids until failure (Krakhmalev et al., 2016). Although dimple ductile fracture is the dominant one, quasi-cleavage features typical for brittle fracture are observed due to the α′ martensitic microstructure in as-built specimens (Fig. 13.8b). Crack propagation occurs through columnar prior β grains (along α′ platelets), as well as along the β grain boundaries. Quasi-cleavage fractures straight follow α′ needles, which can be observed on their facets. However, inherent defects such as pores have to be taken into account

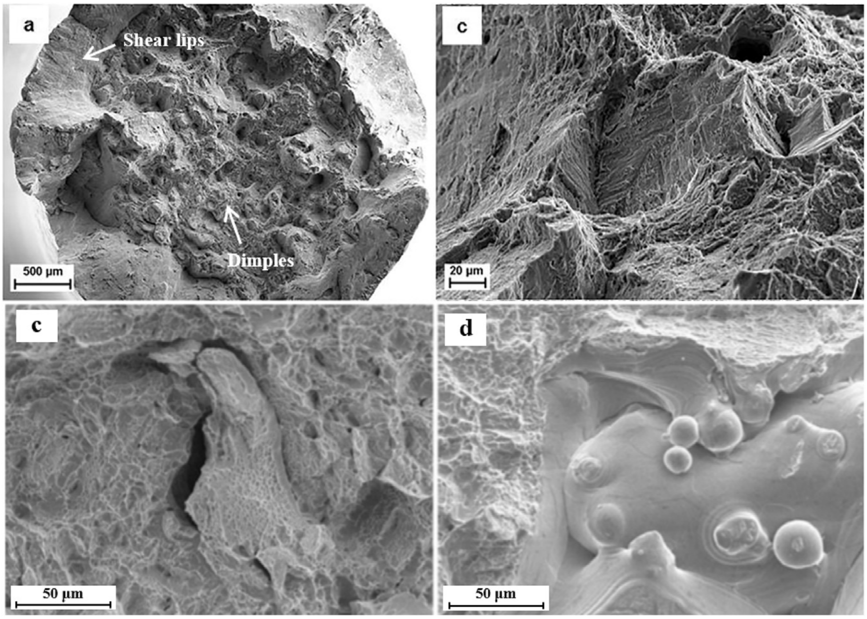

Figure 13.8 SEM micrographs of fracture surfaces of horizontal as-built L-PBF Ti6Al4V specimens deformed along the building direction (a) low and (b) higher magnification showing quasi-cleavage facets (Krakhmalev et al., 2016). (c—d) Lack of fusion defects observed on fracture surfaces after tensile test (Vilaro et al., 2011).

(Fig. 13.8c–d). On one hand, high inner porosity changes the failure mechanism from nucleation, growth, and coalescence of the microvoids to failure that initiated at incompletely melted particles and large pores within the material. Large number of defects does not allow the material to accommodate plastic strain, and failure occurs at the beginning of the plastic deformation stage (Attar et al., 2014). On the other hand, near fully dense as-built L-PBF Ti alloy parts (e.g., >99.9%) show fracture rather originated from the nucleation of new voids instead of growing the already present pores originated from the L-PBF process (Yadroitsev et al., 2018).

Additionally, the influence of microstructure on fracture behavior of as-built L-PBF Ti alloys should be taken into account. Intergranular fracture mode takes place when prior β grains are oriented along the applied tensile stress direction, but a combination of intergranular and transgranular fracture modes is observed when they are oriented perpendicular to it. The differences in fracture behavior are reflected in the mechanical behavior. A lower ductility is found for specimens where prior β grains are oriented perpendicular to the stress direction, probably due to grain boundaries acting as weak spots where cracks can propagate easily. Therefore, as-built L-PBF Ti alloys have shown less pronounced necking compared to stress-relieved and heat-treated conditions. The change in microstructure from α' martensitic to $(\alpha+\beta)$-phase after HT leads to an increase in ductility, leading to a ductile fracture fully governed by dimple-shaped surfaces. Quasi-cleavage brittle features in HT L-PBF Ti6Al4V cannot be observed anymore compared to as-built condition (Yadroitsev et al., 2018).

13.5.3 Low strength/high ductility materials – L-PBF aluminum-based alloys

As-built L-PBF Al alloys exhibit a unique tensile ductility and specific fracture surfaces. The representative case of AlSi10Mg alloy (a most commonly used Al alloy for L-PBF process) is shown in Fig. 13.9. The nominal stress-strain curves of the as-built L-PBF AlSi10Mg specimens (with a relative density above 99%) tensile-deformed parallel or perpendicular to the build direction (BD) indicate a direction-dependence of the tensile ductility (Fig. 13.9b). The tensile elongation at fracture of the specimen deformed parallel to the BD is approximately 5%, which is lower than that of the specimen deformed perpendicular to the BD (approximately 8%). The direction-dependence of the tensile ductility could be due to the characteristic microstructure consisting of a number of melt pools (in which the regions were locally melted and rapidly solidified). The morphology (Fig. 13.9a) corresponds to the scanning laser irradiation on powder-bed layers in the L-PBF process. Macroscopic fractographs of the tensile-tested specimens are shown in Fig. 13.9c and d. Numerous spherical dimples are found over the entire fracture surface of the specimens, which is indicative of ductile fracture mode. Several band-shaped surface areas with a width of approximately 200 μm are macroscopically observed on the fracture surface of the specimen deformed parallel to BD (Fig. 13.9c). These correspond to the melt-pool geometries observed in the as-built L-PBF AlSi10Mg alloy (Fig. 13.9a).

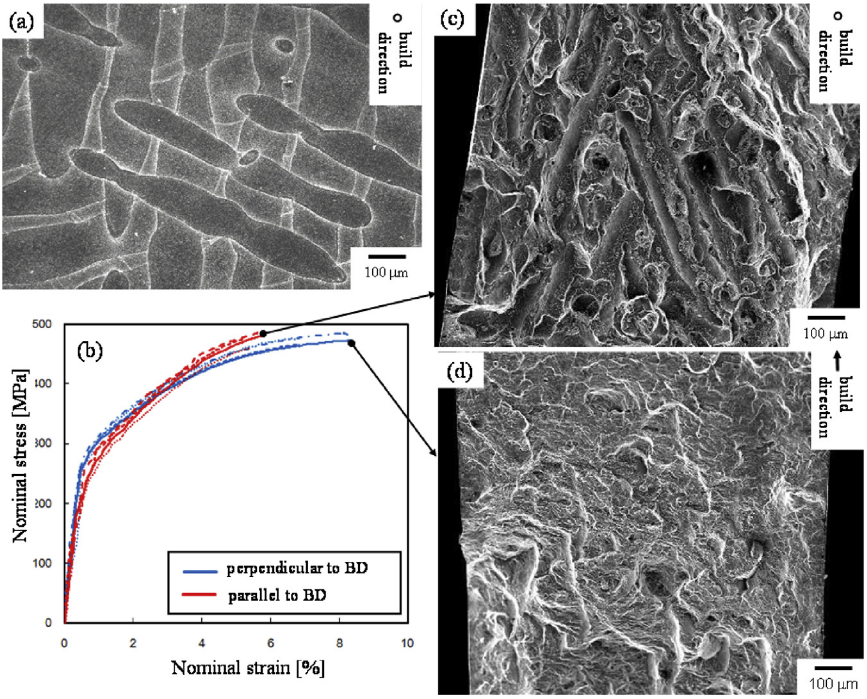

Figure 13.9 Representative direction-dependence tensile ductility of the L-PBF-built AlSi10Mg alloy specimens with a relative density above 99%: (a) optical micrographs showing microstructure, (b) nominal stress-strain curves, (c,d) fracture surface of tensile-tested specimens deformed (c) parallel or (d) perpendicular to the build direction (Takata et al., 2017).

The unique fracture surfaces demonstrate that fracture occurs around the boundaries between the melt pools, resulting in a relatively lower tensile ductility. The L-PBF process facilitates the formation of coarsened microstructures localized at boundaries between melt pools. The localized coarsened microstructure (with a relatively lower strength) might be preferentially deformed, resulting in microvoids to failure initiated at the melt-pool boundaries. The direction-dependence of the tensile ductility is one of unique mechanical properties of the L-PBF materials. The similar direction-dependence of the tensile ductility has been reported in the other Al-Si alloys (Rosenthal et al., 2017) or an austenitic stainless steel (316L) (corresponding to the ductile materials), whereas there is limited information on the direction-dependence of the tensile ductility of high-strengthened Ni-based alloys, Ti alloys and steels. Note that the direction-dependent tensile ductility has not been observed in the L-PBF-built Al alloy specimens after the solution treatment at elevated temperatures above 500°C (Takata et al., 2017), indicating that the formation of homogeneous microstructure (by heat treatments) can suppress the varied tensile ductility of the as-built L-PBF Al alloys.

13.6 Conclusions

Currently, many attempts to manufacture conventional materials by L-PBF were performed. Of course, the first issue was to manufacture defect-free material, which was achieved by development of manufacturing technology, quality of powder precursor, and optimization of manufacturing parameters and strategies. Nevertheless, mechanical properties of the L-PBF materials often differ from the conventional analogs. This difference is a result of another manufacturing route used in L-PBF. The very short process time including several steps of heating, melting, solidification, and in-situ heat treatment results in different microstructure and texture of L-PBF materials. In many materials, higher strengths are found for L-PBF compared to the same materials obtained by conventional technologies. Generally, finer microstructures, changes in phase composition, and the appearance of fine precipitates are responsible for the enhanced strength of L-PBF materials. However, in some cases, post-processing treatments are still required to compensate for the low ductility achieved by L-PBF materials. Additionally, typical for L-PBF, defects also contribute to the final properties and performance. Therefore, the understanding of the manufacturing— microstructure— properties relationship in L-PBF is vital for predictable manufacturing of components with required properties.

13.7 Questions

- List the main mechanical characteristics of metallic materials obtained by tensile test. Explain the importance of this test for engineering design.
- Shortly present mechanisms that may help to increase strength characteristics in metallic alloys.
- Find in the literature references to mechanical properties of conventional AISI 316L stainless steel, and compare this with values typical for L-PBF material. Explain differences referring to microstructure.
- In conventional tool, maraging and precipitation hardening steels, the material is austenitized and quenched to form martensitic structure. What is martensite and what are the properties of martensite compared to high-temperature austenitic phase or regular conventional ferrite phase? Are properties of martensite directly applicable to any industrial applications?
- Search in the literature and present the influence of the manufacturing atmosphere on the microstructure and properties of L-PBF materials, present examples of negative and positive influences of different protective atmospheres on mechanical properties of L-PBF alloys (choose Ti alloys and precipitation hardening steels as examples).
- In most cases, L-PBF materials have higher strength than the same ones obtained by conventional technologies. Does it happen for all L-PBF titanium alloys? Justify the answer.
- Find in the literature, references on the effect of post-processing treatments on mechanical properties of L-PBF titanium alloys. Mention and justify for which applications a stress relief or heat treatment is recommended.
- In general, solution heat treatment and subsequent aging treatment were subjected to Al alloys for strengthening by fine precipitates in α-Al FCC matrix. What are roles of the solution heat treatment and the subsequent aging treatment in strengthening Al alloys?

- Aging treatments can cause either strengthening or softening of L-PBF Al alloys. A role of the aging treatments change depending on their temperature. Discuss the mechanisms of strengthening or softening by aging treatments at different temperatures.
- Ni-based alloys are generally used in a hostile environment for extended periods of service at high temperatures. How dose strength of L-PBF Ni-based alloys change after long-term exposure at high temperatures? Discuss the change in strength in comparison with that of conventionally produced Ni-based alloys.
- Explain the fracture mechanism of high strength L-PBF materials. Compare them with the low strength L-PBF materials.
- Discuss the direction-dependence of the tensile ductility of ductile L-PBF materials (Al-Si alloys or austenitic stainless steels) in terms of microstructure around the boundaries between the melt pools.

Acknowledgements

Professor Krakhmalev thanks the Swedish Agency for Economic and Regional Growth, Grant No. 20201144, ATLAB—additive manufacturing laboratory at Karlstad University, Region Värmland for financial support. Dr. Vilardell thanks the Japan Society for the Promotion of Science (JSPS) for Postdoctoral Fellowships for Research in Japan (Grant No. P19754), as well as the support of JSPS KAKENHI (Grant No. 90225483). Associate Professor Takata gratefully acknowledges "Knowledge Hub Aichi" for the support provided through a Priority Research Project of the Aichi Prefectural Government in Japan (project leader: Professor Kobashi at Nagoya University).

References

Aboulkhair, N.T., Simonelli, M., Parry, L., Ashcroft, I., Tuck, C., Hague, R., 2019. 3D printing of aluminium alloys: additive manufacturing of aluminium alloys using selective laser melting. Prog. Mater. Sci. 106, 100578. https://doi.org/10.1016/j.pmatsci.2019.100578.

Ackermann, M., Šafka, J., Voleský, L., Bobek, J., Kondapally, J.R., 2018. Impact testing of H13 tool steel processed with use of selective laser melting technology. In: Materials Science Forum, vol. 919. Trans Tech Publications Ltd, pp. 43−51.

Åsberg, M., Fredriksson, G., Hatami, S., Fredriksson, W., Krakhmalev, P., 2019. Influence of post treatment on microstructure, porosity and mechanical properties of additive manufactured H13 tool steel. Mater. Sci. Eng. A 742, 584−589.

Attar, H., Calin, M., Zhang, L.C., Scudino, S., Eckert, J., 2014. Manufacture by selective laser melting and mechanical behavior of commercially pure titanium. Mater. Sci. Eng. A 593, 170−177.

Bai, Y., Yang, Y., Wang, D., Zhang, M., 2017. Influence mechanism of parameters process and mechanical properties evolution mechanism of maraging steel 300 by selective laser melting. Mater. Sci. Eng. A 703, 116−123.

Bajaj, P., Hariharan, A., Kini, A., Kürnsteiner, P., Raabe, D., Jägle, E.A., 2020. Steels in additive manufacturing: a review of their microstructure and properties. Mater. Sci. Eng. A 772, 138633.

Bodziak, S., Al-Rubaie, K.S., Dalla Valentina, L., Lafratta, F.H., Santos, E.C., Zanatta, A.M., Chen, Y., 2019. Precipitation in 300 grade maraging steel built by selective laser melting: aging at 510 C for 2 h. Mater. Char. 151, 73−83.

Boes, J., Röttger, A., Mutke, C., Escher, C., Theisen, W., 2018. Microstructure and mechanical properties of X65MoCrWV3-2 cold-work tool steel produced by selective laser melting. Addit. Manuf. 23, 170−180.

Carlton, H.D., Haboub, A., Gallegos, G.F., Parkinson, D.Y., MacDowell, A.A., 2016. Damage evolution and failure mechanisms in additively manufactured stainless steel. Mater. Sci. Eng. A 651, 406−414.

Casati, R., Coduri, M., Lecis, N., Andrianopoli, C., Vedani, M., 2018. Microstructure and mechanical behavior of hot-work tool steels processed by selective laser melting. Mater. Char. 137, 50−57.

Casati, R., Lemke, J.N., Tuissi, A., Vedani, M., 2016a. Aging behaviour and mechanical performance of 18-Ni 300 steel processed by selective laser melting. Metals 6 (9), 218.

Casati, R., Lemke, J., Vedani, M., 2016b. Microstructure and fracture behavior of 316L austenitic stainless steel produced by selective laser melting. J. Mater. Sci. Technol. 32 (8), 738−744.

Cheruvathur, S., Lass, E.A., Campbell, C.E., 2016. Additive manufacturing of 17-4 PH stainless steel: post-processing heat treatment to achieve uniform reproducible microstructure. JOM 68 (3), 930−942.

Danzer, R., 1991. Mechanical performance and lifetime prediction. In: Concise Encyclopedia of Advanced Ceramic Materials. Elsevier, pp. 286−299.

DebRoy, T., Wei, H.L., Zuback, J.S., Mukherjee, T., Elmer, J.W., Milewski, J.O., Beese, A.M., Wilson-Heid, A.D., De, A., Zhang, W., 2018. Additive manufacturing of metallic components−process, structure and properties. Prog. Mater. Sci. 92, 112−224.

Dietrich, K., Diller, J., Dubiez-Le Goff, S., Bauer, D., Forêt, P., Witt, G., 2020. The influence of oxygen on the chemical composition and mechanical properties of Ti-6Al-4V during laser powder bed fusion (L-PBF). Addit. Manuf. 32, 100980.

Dörfert, R., Zhang, J., Clausen, B., Freiße, H., Schumacher, J., Vollertsen, F., 2019. Comparison of the fatigue strength between additively and conventionally fabricated tool steel 1.2344. Addit. Manuf. 27, 217−223.

Facchini, L., Vicente Jr., N., Lonardelli, I., Magalini, E., Robotti, P., Molinari, A., 2010. Metastable austenite in 17−4 precipitation-hardening stainless steel produced by selective laser melting. Adv. Eng. Mater. 12 (3), 184−188.

Fiocchi, J., Biffi, C.A., Tuissi, A., 2020. Selective laser melting of high-strength primary AlSi9Cu3 alloy: processability, microstructure, and mechanical properties. Mater. Des. 191, 108581. https://doi.org/10.1016/j.matdes.2020.108581.

Geenen, K., Roettger, A., Feld, F., Theisen, W., 2019. Microstructure, mechanical, and tribological properties of M3: 2 high-speed steel processed by selective laser melting, hot-isostatic pressing, and casting. Addit. Manuf. 28, 585−599.

Han, Q., Gu, Y., Setchi, R., Lacan, F., Johnston, R., Evans, S.L., Yang, S., 2019. Additive manufacturing of high-strength crack-free Ni-based Hastelloy X superalloy. Addit. Manuf. 30, 100919. https://doi.org/10.1016/j.addma.2019.100919.

Hertzberg, R.W., Vinci, R.P., Hertzberg, J.L., 2020. Deformation and Fracture Mechanics of Engineering Materials. John Wiley & Sons.

Hitzler, L., Merkel, M., Hall, W., Öchsner, A., 2018. A review of metal fabricated with laser- and powder-bed based additive manufacturing techniques: process, nomenclature, materials, achievable properties, and its utilization in the medical sector. Adv. Eng. Mater. 20, 1700658. https://doi.org/10.1002/adem.201700658.

Holzweissig, M.J., Taube, A., Brenne, F., Schaper, M., Niendorf, T., 2015. Microstructural characterization and mechanical performance of hot work tool steel processed by selective laser melting. Metall. Mater. Trans. B 46 (2), 545−549.

Jägle, E.A., Choi, P.P., Van Humbeeck, J., Raabe, D., 2014. Precipitation and austenite reversion behavior of a maraging steel produced by selective laser melting. J. Mater. Res. 29 (17), 2072.

Jägle, E.A., Sheng, Z., Kürnsteiner, P., Ocylok, S., Weisheit, A., Raabe, D., 2017. Comparison of maraging steel micro-and nanostructure produced conventionally and by laser additive manufacturing. Materials 10 (1), 8.

Jiang, R., Mostafaei, A., Wu, Z., Choi, A., Guan, P.-W., Chmielus, M., Rollett, A.D., 2020. Effect of heat treatment on microstructural evolution and hardness homogeneity in laser powder bed fusion of alloy 718. Addit. Manuf. 35, 101282. https://doi.org/10.1016/j.addma.2020.101282.

Kearney, A.L., 2000. Chapter: Properties of Cast Aluminum Alloys, Properties and Selection: Nonferrous Alloys and Special-Purpose Materials. ASM International, Materials Park, Ohio, pp. 152−177. https://doi.org/10.31399/asm.hb.v02.9781627081627.

Kempen, K., Vrancken, B., Buls, S., Thijs, L., Van Humbeeck, J., Kruth, J.P., 2014. Selective laser melting of crack-free high density M2 high speed steel parts by baseplate preheating. J. Manuf. Sci. Eng. 136 (6).

Kimura, T., Nakamoto, T., Ozaki, T., Sugita, K., Mizuno, M., Araki, H., 2019. Microstructural formation and characterization mechanisms of selective laser melted Al−Si−Mg alloys with increasing magnesium content. Mater. Sci. Eng. A 754, 786−798. https://doi.org/10.1016/j.msea.2019.02.015.

Koizumi, H., Ishii, T., Okazaki, T., Kaketani, M., Matsumura, H., 2018. Castability and mechanical properties of Ti-15Mo-5Zr-3Al alloy in dental casting. J. Oral Sci. 60 (2), 285−292. https://doi.org/10.2334/josnusd.17-0280.

Kok, Y., Tan, X.P., Wang, P., Nai, M.L.S., Loh, N.H., Liu, E., Tor, S.B., 2018. Anisotropy and heterogeneity of microstructure and mechanical properties in metal additive manufacturing: a critical review. Mater. Des. 139, 565−586. https://doi.org/10.1016/j.matdes.2017.11.021.

Koutny, D., Palousek, D., Pantelejev, L., Hoeller, C., Pichler, R., Tesicky, L., Kaiser, J., 2018. Influence of scanning strategies on processing of aluminum alloy EN AW 2618 using selective laser melting. Materials 11, 298. https://doi.org/10.3390/ma11020298.

Kolli, R., Devaraj, A., 2018. A review of metastable beta titanium alloys. Metals 8, 506.

Krakhmalev, P., Yadroitsava, I., Fredriksson, G., Yadroitsev, I., 2015. In situ heat treatment in selective laser melted martensitic AISI 420 stainless steels. Mater. Des. 87, 380−385.

Krakhmalev, P., Fredriksson, G., Yadroitsava, I., Kazantseva, N., Du Plessis, A., Yadroitsev, I., 2016. Deformation behavior and microstructure of Ti6Al4V manufactured by SLM. Phys. Procedia 83, 778−788.

Krakhmalev, P., Yadroitsava, I., Fredriksson, G., Yadroitsev, I., 2017. Microstructural and thermal stability of selective laser melted 316L stainless steel single tracks. S. Afr. J. Ind. Eng. 28 (1), 12−19.

Kudzal, A., McWilliams, B., Hofmeister, C., Kellogg, F., Yu, J., Taggart-Scarff, J., Liang, J., 2017. Effect of scan pattern on the microstructure and mechanical properties of powder bed fusion additive manufactured 17-4 stainless steel. Mater. Des. 133, 205−215.

Kürnsteiner, P., Wilms, M.B., Weisheit, A., Barriobero-Vila, P., Jägle, E.A., Raabe, D., 2017. Massive nanoprecipitation in an Fe-19Ni-xAl maraging steel triggered by the intrinsic heat treatment during laser metal deposition. Acta Mater. 129, 52−60.

Lass, E.A., Stoudt, M.R., Williams, M.E., 2019. Additively manufactured nitrogen-atomized 17-4 PH stainless steel with mechanical properties comparable to wrought. Metall. Mater. Trans. 50 (4), 1619−1624.

LeBrun, T., Nakamoto, T., Horikawa, K., Kobayashi, H., 2015. Effect of retained austenite on subsequent thermal processing and resultant mechanical properties of selective laser melted 17−4 PH stainless steel. Mater. Des. 81, 44−53.

Lewandowski, J.J., Seifi, M., 2016. Metal additive manufacturing: a review of mechanical properties. Annu. Rev. Mater. Res. 46.

Liu, S., Shin, Y.C., 2019. Additive manufacturing of Ti6Al4V alloy: a review. Mater. Des. 164, 107552.

Martin, J.H., Yahata, B.D., Hundley, J.M., Mayer, J.A., Schaedler, T.A., Pollock, T.M., 2017. 3D printing of high-strength aluminium alloys. Nature 549, 365−369. https://doi.org/10.1038/nature23894.

Mazur, M., Brincat, P., Leary, M., Brandt, M., 2017. Numerical and experimental evaluation of a conformally cooled H13 steel injection mould manufactured with selective laser melting. Int. J. Adv. Manuf. Technol. 93 (1−4), 881−900.

Meredith, S.D., Zuback, J.S., Keist, J.S., Palmer, A.T., 2018. Impact of composition on the heat treatment response of additively manufactured 17−4 PH grade stainless steel. Mater. Sci. Eng. A 738, 44−56.

Mertens, R., Vrancken, B., Holmstock, N., Kinds, Y., Kruth, J.P., Van Humbeeck, J., 2016. Influence of powder bed preheating on microstructure and mechanical properties of H13 tool steel SLM parts. Phys. Procedia 83, 882−890.

Moletsane, M.G., Krakhmalev, P., Kazantseva, N., Du Plessis, A., Yadroitsava, I., Yadroitsev, I., 2016. Tensile properties and microstructure of direct metal laser-sintered Ti6Al4V(ELI) alloy. S. Afr. J. Ind. Eng. 27 https://doi.org/10.7166/27-3-1667.

Murr, L.E., Martinez, E., Hernandez, J., Collins, S., Amato, K.N., Gaytan, S.M., Shindo, P.W., 2012. Microstructures and properties of 17-4 PH stainless steel fabricated by selective laser melting. J. Mater. Res. & Technol. 1 (3), 167−177.

Pellizzari, M., Jam, A., Tschon, M., Fini, M., Lora, C., Benedetti, M., 2020. A 3D-printed ultra-low Young's modulus β-Ti alloy for biomedical applications. Materials 13 (12), 2792. https://doi.org/10.3390/ma13122792.

Polozov, I., Sufiiarov, V., Popovich, A., Masaylo, D., Grigoriev, A., 2018. Synthesis of Ti-5Al, Ti-6Al-7Nb, and Ti-22Al-25Nb alloys from elemental powders using powder-bed fusion additive manufacturing. J. Alloys Compd. 763, 436−445. https://doi.org/10.1016/j.jallcom.2018.05.325.

Qin, H., Dong, Q., Fallah, V., Daymond, M.R., 2020. Rapid solidification and non-equilibrium phase constitution in laser powder bed fusion (LPBF) of AlSi10Mg alloy: analysis of nano-precipitates, eutectic phases, and hardness evolution. Metall. Mater. Trans. 51, 448−466. https://doi.org/10.1007/s11661-019-05505-5.

Qiu, C., Liu, Q., 2019. Multi-scale microstructural development and mechanical properties of a selectively laser melted beta titanium alloy. Addit. Manuf. 30, 100893. https://doi.org/10.1016/j.addma.2019.100893.

Rafi, H.K., Pal, D., Patil, N., Starr, T.L., Stucker, B.E., 2014. Microstructure and mechanical behavior of 17-4 precipitation hardenable steel processed by selective laser melting. J. Mater. Eng. Perform. 23 (12), 4421−4428.

Rao, J.H., Zhang, Y., Fang, X., Chen, Y., Wu, X., Davies, C.H.J., 2017. The origins for tensile properties of selective laser melted aluminium alloy A357. Addit. Manuf. 17, 113−122. https://doi.org/10.1016/j.addma.2017.08.007.

Reed, R.C., 2006. The Superalloys: Fundamentals and Applications. Cambridge University Press, Cambridge. https://doi.org/10.1017/CBO9780511541285.

Riemer, A., Leuders, S., Thöne, M., Richard, H.A., Tröster, T., Niendorf, T., 2014. On the fatigue crack growth behavior in 316L stainless steel manufactured by selective laser melting. Eng. Fract. Mech. 120, 15–25.

Ronneberg, T., Davies, C.M., Hooper, P.A., 2020. Revealing relationships between porosity, microstructure and mechanical properties of laser powder bed fusion 316L stainless steel through heat treatment. Mater. Des. 189, 108481.

Rosenthal, I., Stern, A., Frage, N., 2017. Strain rate sensitivity and fracture mechanism of AlSi10Mg parts produced by selective laser melting. Mater. Sci. Eng. A 682, 509–517. https://doi.org/10.1016/j.msea.2016.11.070.

Saeidi, K., Gao, X., Zhong, Y., Shen, Z.J., 2015a. Hardened austenite steel with columnar sub-grain structure formed by laser melting. Mater. Sci. Eng. A 625, 221–229.

Saeidi, K., Gao, X., Lofaj, F., Kvetková, L., Shen, Z.J., 2015b. Transformation of austenite to duplex austenite-ferrite assembly in annealed stainless steel 316L consolidated by laser melting. J. Alloys Compd. 633, 463–469.

Saeidi, K., Zapata, D.L., Lofaj, F., Kvetkova, L., Olsen, J., Shen, Z., Akhtar, F., 2019. Ultra-high strength martensitic 420 stainless steel with high ductility. Addit. Manuf. 29, 100803.

Šafka, J., Ackermann, M., Volesky, L., April 2016. Structural properties of H13 tool steel parts produced with use of selective laser melting technology. In: J. Phys. Conf. Ser, vol. 709. IOP Publishing, pp. 1–7.

Sander, J., Hufenbach, J., Giebeler, L., Wendrock, H., Kühn, U., Eckert, J., 2016. Microstructure and properties of FeCrMoVC tool steel produced by selective laser melting. Mater. Des. 89, 335–341.

Shamsujjoha, M., Agnew, S.R., Fitz-Gerald, J.M., Moore, W.R., Newman, T.A., 2018. High strength and ductility of additively manufactured 316L stainless steel explained. Metall. Mater. Trans. 49 (7), 3011–3027.

Sing, S.L., Yeong, W.Y., Wiria, F.E., 2016. Selective laser melting of titanium alloy with 50 wt% tantalum: microstructure and mechanical properties. J. Alloys Compd. 660, 461–470. https://doi.org/10.1016/j.jallcom.2015.11.141.

SmarTech analysis, 2019. Additive Manufacturing with Steels 2019. Available at: https://www.smartechanalysis.com/reports/additive-manufacturing-steels-2019/. Accessed 4 November 2020.

Starr, T.L., Rafi, K., Stucker, B., Scherzer, C.M., 2012. Controlling phase composition in selective laser melted stainless steels. Power 195 (195), 1.

Stopyra, W., Gruber, K., Smolina, I., Kurzynowski, T., Kuźnicka, B., 2020. Laser powder bed fusion of AA7075 alloy: influence of process parameters on porosity and hot cracking. Addit. Manuf. 35, 101270. https://doi.org/10.1016/j.addma.2020.101270.

Takata, N., Kodaira, H., Sekizawa, K., Suzuki, A., Kobashi, M., 2017. Change in microstructure of selectively laser melted AlSi10Mg alloy with heat treatments. Mater. Sci. Eng. A 704, 218–228. https://doi.org/10.1016/j.msea.2017.08.029.

Takata, N., Liu, M., Kodaira, H., Suzuki, A., Kobashi, M., 2020. Anomalous strengthening by supersaturated solid solutions of selectively laser melted Al–Si-based alloys. Addit. Manuf. 33, 101152. https://doi.org/10.1016/j.addma.2020.101152.

Tan, C., Zhou, K., Ma, W., Zhang, P., Liu, M., Kuang, T., 2017. Microstructural evolution, nanoprecipitation behavior and mechanical properties of selective laser melted high-performance grade 300 maraging steel. Mater. Des. 134, 23–34.

Tsai, M.-T., Chen, Y.-W., Chao, C.-Y., Jang, J.S.C., Tsai, C.-C., Su, Y.-L., Kuo, C.-N., 2020. Heat-treatment effects on mechanical properties and microstructure evolution of Ti-6Al-4V alloy fabricated by laser powder bed fusion. J. Alloys Compd. 816, 152615.

Vanmeensel, K., Lietaert, K., Vrancken, B., Dadbakhsh, S., Li, X., Kruth, J.P., Krakhmalev, P., Yadroitsev, I., Van Humbeeck, J., 2018. Additively manufactured metals for medical applications. Addit. Manuf. 261−309. Butterworth-Heinemann.

Velasco-Castro, M., Hernández-Nava, E., Figueroa, I.A., Todd, I., Goodall, R., 2019. The effect of oxygen pickup during selective laser melting on the microstructure and mechanical properties of Ti−6Al−4V lattices. Heliyon 5 (12), e02813.

Vilardell, A.M., Takezawa, A., Du Plessis, A., Takata, N., Krakhmalev, P., Kobashi, M., Yadroitsava, I., Yadroitsev, I., 2019. Topology optimization and characterization of Ti6Al4V ELI cellular lattice structures by laser powder bed fusion for biomedical applications. Mater. Sci. Eng. A 766, 138330.

Vilaro, T., Colin, C., Bartout, J.D., 2011. As-Fabricated and Heat-Treated Microstructures of the Ti-6Al-4V Alloy Processed by Selective Laser Melting. Metall. Mater. Trans. A 42 (10), 3190−3199.

Vilaro, T., Colin, C., Bartout, J.D., Nazé, L., Sennour, M., 2012. Microstructural and mechanical approaches of the selective laser melting process applied to a nickel-base superalloy. Mater. Sci. Eng. A 534, 446−451. https://doi.org/10.1016/j.msea.2011.11.092.

Vrancken, B., Thijs, L., Kruth, J.-P., Van Humbeeck, J., 2012. Heat treatment of Ti6Al4V produced by selective laser melting: microstructure and mechanical properties. J. Alloys Compd. 541, 177−185.

Vrancken, B., Thijs, L., Kruth, J.-P., Van Humbeeck, J., 2014. Microstructure and mechanical properties of a novel β titanium metallic composite by selective laser melting. Acta Mater. 68, 150−158. https://doi.org/10.1016/j.actamat.2014.01.018.

Wang, Y.M., Voisin, T., McKeown, J.T., Ye, J., Calta, N.P., Li, Z., Zeng, Z., Zhang, Y., Chen, W., Roehling, T.T., Ott, R.T., 2018. Additively manufactured hierarchical stainless steels with high strength and ductility. Nat. Mater. 63−71.

Wu, M.-W., Lai, P.-H., 2016. The positive effect of hot isostatic pressing on improving the anisotropies of bending and impact properties in selective laser melted Ti-6Al-4V alloy. Mater. Sci. Eng. A 658, 429−438.

Wycisk, E., Siddique, S., Herzog, D., Walther, F., Emmelmann, C., 2015. Fatigue performance of laser additive manufactured Ti−6Al−4V in very high cycle fatigue regime up to 109 cycles. Front. Mater. 2.

Xu, W., Brandt, M., Sun, S., Elambasseril, J., Liu, Q., Latham, K., Xia, K., Qian, M., 2015. Additive manufacturing of strong and ductile Ti−6Al−4V by selective laser melting via in situ martensite decomposition. Acta Mater. 85, 74−84.

Xu, C., Sikan, F., Atabay, S.E., Muñiz-Lerma, J.A., Sanchez-Mata, O., Wang, X., Brochu, M., 2020. Microstructure and mechanical behavior of as-built and heat-treated Ti−6Al−7Nb produced by laser powder bed fusion. Mater. Sci. Eng. A 793, 139978. https://doi.org/10.1016/j.msea.2020.139978.

Yadroitsev, I., Krakhmalev, P., Yadroitsava, I., 2017. Titanium alloys manufactured by in situ alloying during laser powder bed fusion. JOM 69, 2725−2730.

Yadroitsev, I., Krakhmalev, P., Yadroitsava, I., Du Plessis, A., 2018. Qualification of Ti6Al4V ELI alloy produced by laser powder bed fusion for biomedical applications. JOM 70, 372−377.

Yan, J.J., Zheng, D.L., Li, H.X., Jia, X., Sun, J.F., Li, Y.L., Qian, M., Yan, M., 2017. Selective laser melting of H13: microstructure and residual stress. J. Mater. Sci. 52 (20), 12476−12485.

Yang, K.V., Rometsch, P., Davies, C.H.J., Huang, A., Wu, X., 2018. Effect of heat treatment on the microstructure and anisotropy in mechanical properties of A357 alloy produced lby selective laser melting. Mater. Des. 154, 275−290. https://doi.org/10.1016/j.matdes.2018.05.026.

Yap, C.Y., Chua, C.K., Dong, Z.L., Liu, Z.H., Zhang, D.Q., 2014. State-of-the-art review on selective laser melting of non-ferrous metals. In: Proceedings of the 1st International Conference on Progress in Additive Manufacturing. Research Publishing Services, pp. 193−201. https://doi.org/10.3850/978-981-09-0446-3_035.

Zhang, D., Sun, S., Qiu, D., Gibson, M.A., Dargusch, M.S., Brandt, M., Qian, M., Easton, M., 2018a. Metal alloys for fusion-based additive manufacturing. Adv. Eng. Mater. 20 (5), 1700952.

Zhang, L.C., Klemm, D., Eckert, J., Hao, Y.L., Sercombe, T.B., 2011. Manufacture by selective laser melting and mechanical behavior of a biomedical Ti−24Nb−4Zr−8Sn alloy. Scripta Mater. 65, 21−24.

Zhang, F., Levine, L.E., Allen, A.J., Stoudt, M.R., Lindwall, G., Lass, E.A., Williams, M.E., Idell, Y., Campbell, C.E., 2018b. Effect of heat treatment on the microstructural evolution of a nickel-based superalloy additive-manufactured by laser powder bed fusion. Acta Mater. 152, 200−214. https://doi.org/10.1016/j.actamat.2018.03.017.

Zhang, J., Song, B., Wei, Q., Bourell, D., Shi, Y., 2019. A review of selective laser melting of aluminum alloys: processing, microstructure, property and developing trends. J. Mater. Sci. Technol. 35 (2), 270−284. https://doi.org/10.1016/j.jmst.2018.09.004.

Zhao, X., Wei, Q., Song, B., Liu, Y., Luo, X., Wen, S., Shi, Y., 2015. Fabrication and characterization of AISI 420 stainless steel using selective laser melting. Mater. Manuf. Process. 30 (11), 1283−1289.

Zwilsky, K.M., Langer, E.L., 1990. ASM handbook volume 2, properties and selection: nonferrous alloys and special purpose materials. ASM Int. 2. https://www.asminternational.org/handbooks/-/journal_content/56/10192/06182G/PUBLICATION.

Structural integrity II: fatigue properties

14

Uwe Zerbst, Mauro Madia
Federal Institute for Materials Research and Testing (BAM), Berlin, Germany

Chapter outline

14.1 Introduction 377
14.2 Short fatigue crack propagation 380
14.3 The Kitagawa-Takahashi (KT) approach 383
14.4 Murakami's $\sqrt{\texttt{area}}$ approach 385
14.5 The cyclic R-curve concept 387
14.6 Open questions 389
14.7 Conclusions 392
14.8 Questions 392
References 392

14.1 Introduction

The term "fatigue" derives from the Latin word "fatigare" which means the weakening of resistance (in relation to the static strength under monotonic loads) of a material under cyclic loading due to progressive material damage. The common concept for describing the fatigue resistance and lifetime is provided by the stress versus the number of loading cycles (S-N) curve concept developed in the 19th century by August Wöhler. Fig. 14.1 illustrates the concept for constant and variable amplitude loading.

Depending on the number of loading cycles N that the component must perform unscathed, it is distinguished between low cycle fatigue (LCF) up to $N = 10^3 - 10^4$, high cycle fatigue (HCF) up to $N = 10^6 - 10^7$ and very high cycle fatigue (VHCF) beyond that value. The concept of a fatigue limit below which failure can be excluded regardless of the time and number of loading cycles is today in question. This is illustrated by the dashed line in Fig. 14.1a. In the case of variable amplitude loading it has never been used but was replaced by the concept of damage accumulation such as shown in Fig. 14.1b. A component is considered to be safe if: (a) the applied cyclic stress is less than the fatigue limit; a finite-life fatigue strength (constant amplitude loading); (b) if the linear sum of the damage from each level of the loading spectrum is less than a critical value (variable amplitude loading). In the latter case a simple

Fundamentals of Laser Powder Bed Fusion of Metals. https://doi.org/10.1016/B978-0-12-824090-8.00015-9
Copyright © 2021 Elsevier Inc. All rights reserved.

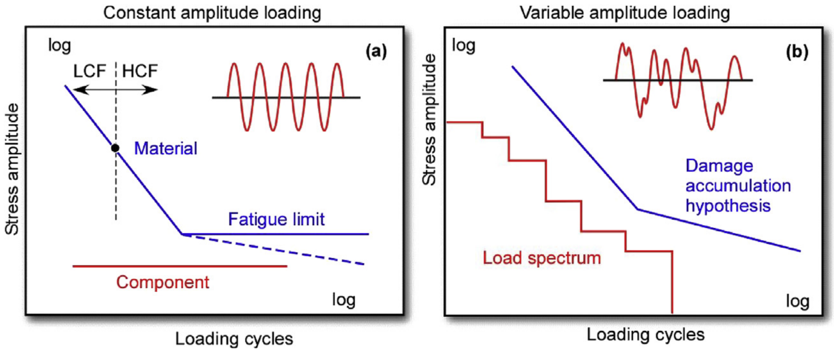

Figure 14.1 S-N curve concept for (a) constant and (b) variable amplitude loading.

criterion for predicting the extent of fatigue damage is provided by the so-called Palmgren-Miner cumulative damage rule (Suresh, 2003). The most important problem for the application of the conventional S-N curve concept to L-PBF parts is the generation of the relevant input information. Due to the pronounced inhomogeneity of the material in the component, it is difficult to produce companion specimens that represent the component at its critical points. We will come back to this in Section 14.6. Further problems are the (frequently occurring) large scatter and the effect of residual stresses.

In common metal fatigue there exists a simple relationship between the ultimate tensile strength or hardness and the fatigue limit σ_w (for a stress ratio $R = \sigma_{\min}/\sigma_{\max} = -1$). The latter is illustrated in Fig. 14.2 (Murakami, 2002). For steels, this relation

$$\sigma_w[MPa] = 1.6\, HV \pm 0.1\, HV \tag{14.1}$$

loses its validity for hardness values $HV > 400$. The reason is that microcracks that are initiated at defects such as inclusions or pores arrest after some limited growth, e.g., at grain boundaries. However, if the size of the defects exceeds a certain value usually in the order of 10–25 μm in the case of structural steel grades, there will be no crack arrest (Zerbst et al., 2019a). The defect size becomes immediately fatigue-relevant in that it controls the fatigue limit. This is illustrated by the downward turning curves in Fig. 14.2.

A number of points are added in Fig. 14.2, which represent L-PBF samples. It is easy to see that they do not fit into the usual paradigm of metal fatigue and the reason for the discrepancy is the size of the defects in the order of 20–180 μm (average: 85 μm, batch A) and even 50–260 μm (average: 149 μm, batch B). In other words: they are significantly larger than the expected nonpropagating crack size. This in turn means that the fatigue strength is controlled by the defects which, therefore, must be explicitly taken into account in any fatigue analysis. Murakami et al. (2019) implemented a comparable study and concluded that the relationship of Eq. (14.1) and Fig. 14.2 can be used for additively manufactured materials only if a combination of hot isostatic pressing and surface polishing are performed to reduce the detrimental effect of pores and surface irregularities.

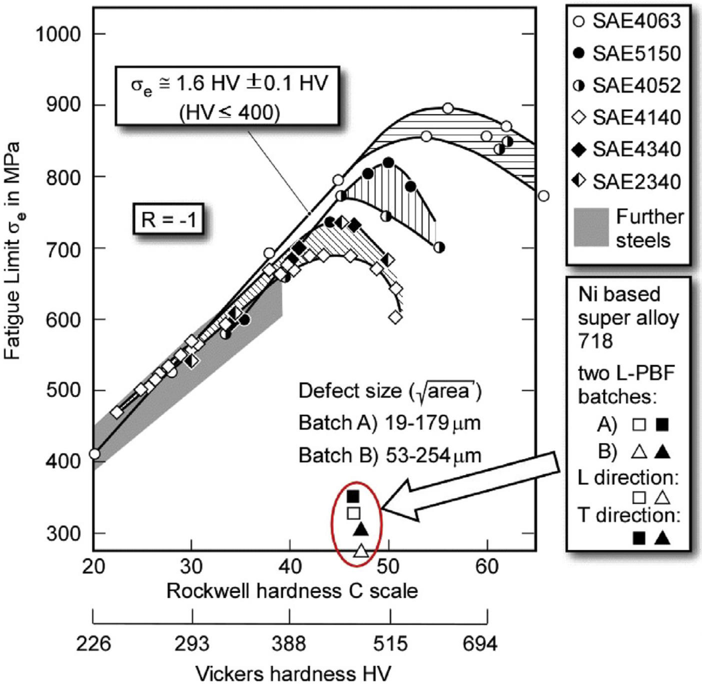

Figure 14.2 Relationship between hardness and fatigue limit (Murakami, 2002). Additional points: L-PBF manufactured superalloy (Yamashita et al., 2018). The materials denoted by Batch A and Batch B were exposed to heat treatments for stress relief, solution heat treatments, and precipitation heat treatments in accordance with Inconel 718 basically. Therefore, residual stress was reduced sufficiently and major residual stress states could be avoided.

The adequate consideration of defects, which in the case of L-PBF usually also includes surface roughness, requires the inclusion of fracture mechanics—based approaches in the fatigue assessment. In contrast to a conventional fatigue analysis, fracture mechanics assumes the pre-existence of defects and determines a residual lifetime, i.e., the time or number of loading cycles these defects (assumed as cracks) need to grow to their critical sizes. The basic tool of a fracture mechanics fatigue crack growth analysis is the $da/dN - \Delta K$ diagram ($a =$ crack depth; cyclic stress intensity factor $\Delta K = K_{\max} - K_{\min}$ with $K_{\max}$ being the upper and $K_{\min}$ the lower value in the loading cycle) which is schematically shown in Fig. 14.3. The crack driving force ΔK in a component is determined by finite element calculations or by the application of analytical solutions available in compendia. It depends on the load, the geometry of the component, and the crack size. If it is known, the $da/dN - \Delta K$-curve can be used to determine the crack propagation rate da/dN as the basis for the residual lifetime.

However, the conventional fracture mechanics concept has two limitations: (a) it is restricted to long cracks and (b) the initial crack size is usually provided by means of nondestructive testing (NDT), e.g., it is defined by the detection limits of NDT which is in the order of millimeters. As a consequence, the remaining lifetime is much shorter than the total lifetime. Modern short-crack concepts are able to overcome this limitation.

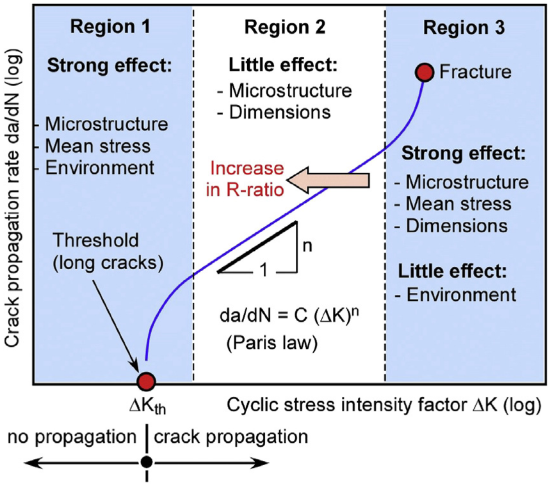
Region 1
Strong effect:
- Microstructure
- Mean stress
- Environment
Threshold
(long cracks)
Region 2
Little effect:
- Microstructure
- Dimensions
Increase
in R-ratio
n
1
da/dN = C (ΔK)^n
(Paris law)
Region 3
Fracture
Strong effect:
- Microstructure
- Mean stress
- Dimensions
Little effect:
- Environment
Crack propagation rate da/dN (log)
ΔK_th
Cyclic stress intensity factor ΔK (log)
no propagation
crack propagation

Figure 14.3 Crack propagation diagram $da/dN - \Delta K$ for long fatigue crack propagation; schematic view. The R-ratio is given as $R = K_{\min}/K_{\max}$.

The following sections will provide a brief introduction into the nature of short fatigue crack propagation. Light will be shed on the most important approaches for the fracture mechanics—based determination of the fatigue limit and lifetime and its potential application to L-PBF components. Finally, insufficiently resolved problems will be highlighted, which still limit the application to additively manufactured parts. For a more in-depth discussion, the reader is referred to Zerbst et al. (2020).

14.2 Short fatigue crack propagation

Fig. 14.4 illustrates the subsequent states of fatigue crack propagation of a crack which initiated at a defect such as a pore, an unmelted area or at a surface notch (roughness).

(a) Crack nucleation or initiation: The initiation stage of a fatigue crack is usually very short even in conventional metallic materials (Polak, 2003) and is triggered by defects such as pores, shrink holes, lack of fusion or micro-geometrical defects such as scratches, indents, etc. (Zerbst et al., 2019a). A defect type which can be assigned either to the material or the geometry side is surface roughness which is often very pronounced in L-PBF components without post-treatment. Kahlin et al. (2017) report a roughness-induced stress concentration of $K_t = 2.5$ and in combination with the designed notch even of $K_t = 6.64$. Note that there is a competitive situation between the individual defect types. As a rule, defects are more harmful when they are larger, when they are closer to the surface, when their stress concentration (with respect to the loading direction) is high, and when they are clustered or occur somehow preferably orientated. In as-built L-PBF the fatigue behavior is usually controlled by the surface roughness (e.g., Günther et al., 2017; Kahlin et al., 2017; Molaei and Fatemi, 2019). If the surface is mechanically smoothed, porosity and lack of fusion regions come into play wherein in particular those near the surface are significant. Greitemeier et al. (2017), investigating electron beam melted TiAl6V4, found that voids dominated the fatigue properties in the absence of surface roughness.

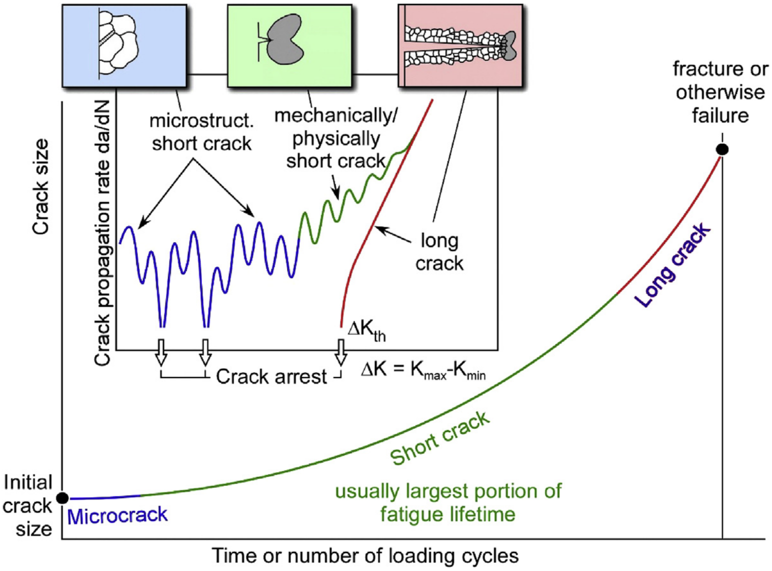
microstruct. short crack
mechanically/ physically short crack
long crack
fracture or otherwise failure
Crack size
Crack propagation rate da/dN
ΔK_{th}
Crack arrest
$\Delta K = K_{max}-K_{min}$
Long crack
Short crack
Initial crack size
Microcrack
usually largest portion of fatigue lifetime
Time or number of loading cycles

Figure 14.4 Subsequent fatigue crack propagation stages in conventional materials, schematic view.

(b) A fatigue crack will first grow as a microstructurally short crack, the size of which is in the order of microstructure parameters, such as the grain size. The local stress-strain field is strongly influenced by the surrounding microstructure with the consequence that the acceleration and deceleration phases of crack growth follow one another. Many cracks are arrested at that stage. The stress level at which the largest microstructurally short crack is just arrested refers to the plain fatigue strength (of the material) (Murakami, 2002). This will disappear if a mechanism, e.g., corrosion, exists for overcoming the barrier (Miller, 1993).

(c) When a microstructurally short crack is capable of propagating beyond the microstructural barriers, the crack reaches the size of a mechanically short crack. It is embedded in the plastic zone ahead of its tip, because of which elastic-plastic crack driving force parameters such as the cyclic J integral have to be applied (Madia et al., 2017; Tchoffo Ngoula et al., 2018). The characteristics of physically short cracks is that the so-called crack closure phenomenon is not fully built up at that stage. Crack closure means that a crack will prematurely close in the loading cycle. This is important because the crack will grow only while it is open. Consequently, the crack propagation analysis needs to be based on the effective crack driving force $\Delta K_{eff} = K_{\max} - K_{op}$ instead of $\Delta K = K_{\max} - K_{\min}$ such as illustrated in Fig. 14.5a. K_{op} is the value of the stress intensity factor above which the crack is open in a loading cycle.

Crack closure can be caused by various mechanisms (Suresh, 2003), which are all based on geometrical mismatch between the corresponding crack faces. For the plasticity-induced mechanism (Fig. 14.5b) this is due to the remaining plastic zone at the crack wake when the crack propagates. The roughness-induced mechanism (Fig. 14.5c) is caused by the asperities on the crack faces and can be enhanced by crack kinking or branching. The oxide-debris-induced mechanism (Fig. 14.5d) is based on a thin oxide layer at the crack faces in materials prone to oxidation

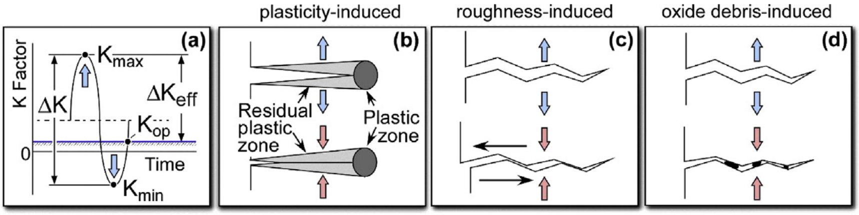
plasticity-induced
roughness-induced
oxide debris-induced
(a)
K Factor
K_{max}
ΔK
ΔK_{eff}
K_{op}
0
Time
K_{min}
(b)
Residual plastic zone
Plastic zone
(c)
(d)

Figure 14.5 Important crack closure mechanisms. (a) Nomenclature for defining the cyclic crack driving force for crack closure; (b) plasticity-induced mechanism; (c) roughness-induced mechanism; (d) oxide debris-induced mechanism.

(such as structural steels with martensitic and bainitic microstructures). At low *R* ratios the crack faces are partially furbished, the blank metal corrodes again and an oxide-debris layer is generated which is much thicker than the original one. The degree of crack closure generally depends on the stress ratio, it is higher at low *R* (and mean stresses) and decreases and finally disappears at high *R*. Note that besides the closure mechanisms mentioned previously, further ones exist, such as the strain-induced martensitic transformation occurring in some austenitic steels which build up compressive stresses at the tip due to the change in volume happening during the phase transformation. This has also been observed in L-PBF material (Ganesh et al., 2014; Suryawanshi et al., 2017).

As mentioned above, at the physically short crack stage, the crack closure effects gradually build up. At the beginning no closure effect exists, since the latter needs a certain amount of crack extension. Fig. 14.6 illustrates this concept based on the crack closure parameter $U = \Delta K_{eff}/\Delta K$. When plotted against the crack extension, it starts with a value of $U = 1$, then it decreases during a transition phase and finally reaches a plateau on which U is independent of the crack depth. To overlook this transition would lead to a (sometimes significant) underestimation of the crack propagation rate and to an overestimation of the remaining lifetime of the component. When the crack depth independent plateau of U is reached, the crack has reached its long crack stage.

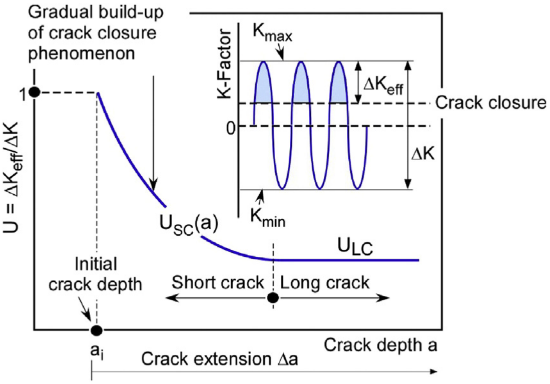
Gradual build-up of crack closure phenomenon
1
$U = \Delta K_{eff}/\Delta K$
K-Factor
K_{max}
ΔK_{eff}
Crack closure
0
ΔK
K_{min}
$U_{SC}(a)$
U_{LC}
Initial crack depth
Short crack
Long crack
a_i
Crack extension Δa
Crack depth a

Figure 14.6 Gradual build-up of the crack closure phenomenon, schematic view.

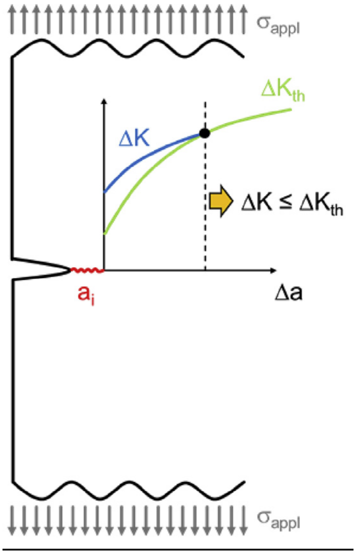

Figure 14.7 Mechanism of short crack arrest at notches: the combined effect of local stress gradient and increasing resistance to crack growth leads to $\Delta K < \Delta K_{th}$.

The standard case is fatigue crack propagation from a designed notch (e.g., shoulders, grooves, or threads), where the phenomenon of "anomalous" crack growth (e.g., Ding et al., 2007) can be observed. First, the crack grows at a high rate due to the stress concentration at the notch root, then its propagation slows down, and eventually it either accelerates again or the crack arrests. The latter is typical for very sharp notches. The reason for the crack arrest is a combination of two effects: (a) the decreasing stress in wall thickness direction away from the notch root (effect of the stress gradient) and (b) the gradual build-up of the crack closure phenomenon. In other words, the rate of increase in the crack driving force with crack growth ($\Delta K / \Delta a$) is lower than the rate of increase in resistance against crack propagation ($\Delta K_{th} / \Delta a$), so that the crack might arrest if $\Delta K < \Delta K_{th}$ (see Fig. 14.7). In contrast to the plain fatigue limit of the microstructurally short crack stage, this crack arrest is associated with the fatigue limit of the component.

14.3 The Kitagawa-Takahashi (KT) approach

A common approach for describing the effect of defects on the fatigue limit is provided by the Kitagawa-Takahashi (KT) diagram which is shown in Fig. 14.8 (Kitagawa and Takahashi, 1976). The threshold stress, i.e., the fatigue limit is plotted against the crack size in double-logarithmic scale. The diagram combines the stages of microstructurally short crack propagation (Region I) and that of long crack propagation (Region III) by means of an empirical transition function (Region II) which describes the stage of the mechanically/physically short crack. KT diagrams can be obtained purely empirically

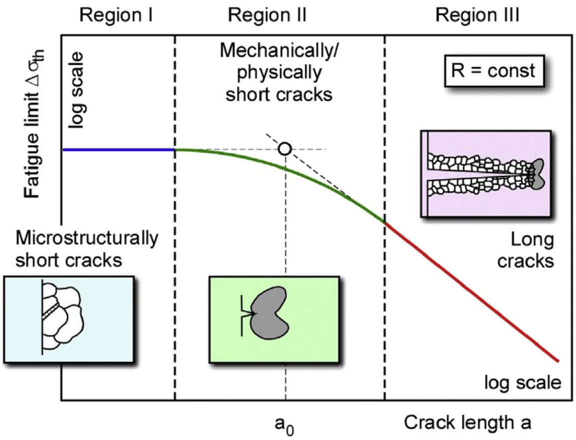
Region I
Region II
Region III
Fatigue limit Δσth
log scale
Mechanically/ physically short cracks
R = const
Microstructurally short cracks
Long cracks
log scale
a0
Crack length a

Figure 14.8 Kitagawa-Takahashi (KT) diagram.

by fatigue experiments with very sharp artificial notches or they can be constructed by means of the so-called El Haddad approach (El Haddad et al., 1979):

$$\Delta\sigma_{th}(a)\,/\,\Delta\sigma_e = \sqrt{a/(a+a_0)} \tag{14.2}$$

In Eq. (14.2) a_0 is a reference length resulting from the intersection of the straight lines of Regions I and III in double-logarithmic scale. Other way round, it can be determined if the fatigue strength $\Delta\sigma_{th} = \Delta\sigma_e$, i.e., the fatigue limit, and the long crack threshold $\Delta K_{th,LC}$ are known:

$$a_0 = \frac{1}{\pi}\left(\Delta K_{th,LC}/\Delta\sigma_e\right)^2 \tag{14.3}$$

Note that this approach is faced with a number of problems:

(a) In the presence of the corrosion-induced crack closure effect, the determination of the long crack threshold at lower R ratios might provide different values depending on the experimental method used (Zerbst et al., 2016). Since a_0 is proportional to the square of $\Delta K_{th,LC}$ (see Eq. 14.3), the effect can be considerable.

(b) Eq. (14.3) is a shortening of

$$a_0 = \frac{1}{\pi}\left(\Delta K_{th,LC}/(Y\cdot\Delta\sigma_e)\right)^2 \tag{14.4}$$

which additionally includes the boundary correction function Y. In Eq. (14.3) this is implicitly set to a value of 1, which corresponds to the infinite plate with a through crack under tension. The problem is that this is not always the case and sometimes it is not reported which Y is used. For instance, for a semi-elliptic surface crack in a plate subjected to tension the value is $Y = 0.728$ (Tanaka and Akinawa, 2003).

(c) The shape of the KT curve in range II is determined by Eq. (14.2). However, the theoretical prediction using the cyclic R-curve method presented in Section 14.5 gives a slightly different curve and up to 25% lower $\Delta\sigma_{th}$values in this range. The discrepancy is the subject of ongoing investigations.

The KT diagram can also be represented as a function of the fatigue crack propagation threshold ΔK_{th} against crack extension Δa

$$\Delta K_{th}(\Delta a) = \Delta K_{th,LC} \cdot \sqrt{\Delta a/(\Delta a + a_0)} \tag{14.5}$$

This, however, requires a slight modification since it gives $\Delta K_{th}(\Delta a = 0) = 0$. This is physically incorrect, because there is a lower bound ΔK_{th} designated as the intrinsic threshold $\Delta K_{th,eff}$ in the order of 2.4–2.6 MPa$\sqrt{\text{m}}$ for steel (excluding duplex), 0.9–1.9 MPa$\sqrt{\text{m}}$ for aluminum alloys, 1.4–1.9 MPa$\sqrt{\text{m}}$ for copper alloys, 0.8–1.0 MPa$\sqrt{\text{m}}$ for magnesium alloys, 1.7–2.5 MPa$\sqrt{\text{m}}$ for titanium alloys, and 5.1–6.7 MPa$\sqrt{\text{m}}$ for nickel-based superalloys (Hardboletz et al., 1994). Therefore, a correction to Eq. (14.5) is provided by an additional term a^*, such that

$$\Delta K_{th}(\Delta a) = \Delta K_{th,LC} \cdot \sqrt{(\Delta a + a^*)/(\Delta a + a_0 + a^*)} \tag{14.6}$$

with a^* being determined by

$$a^*/a_0 = \left(\Delta K_{th,eff}/\Delta K_{th,LC}\right)^2 / \left[1 - \left(\Delta K_{th,eff}/\Delta K_{th,LC}\right)^2\right] \tag{14.7}$$

Fig. 14.9 shows an example of a KT diagram for an L-PBF material based on Eq. (14.2) in conjunction with Eq. (14.4). On its abscissa it makes use of a parameter $\sqrt{area}$ borrowed from the approach described in Section 14.4.

14.4 Murakami's $\sqrt{area}$ approach

Murakami has demonstrated that the maximum K factor along the front of small surface cracks can roughly be correlated with the square root of their projected areas, $\sqrt{area}$, perpendicular to the loading axis (Murakami, 2002).

$$K_{I,\max} \approx \sqrt{\pi\sqrt{area}} \tag{14.8}$$

This is the case regardless of the individual shapes of these cracks. The accuracy in K is in the order of 10%. He also found a general correlation of the fatigue crack propagation threshold ΔK_{th} with $\sqrt{area}$:

$$\Delta K_{th} \sim \left(\sqrt{area}\right)^{1/3} \tag{14.9}$$

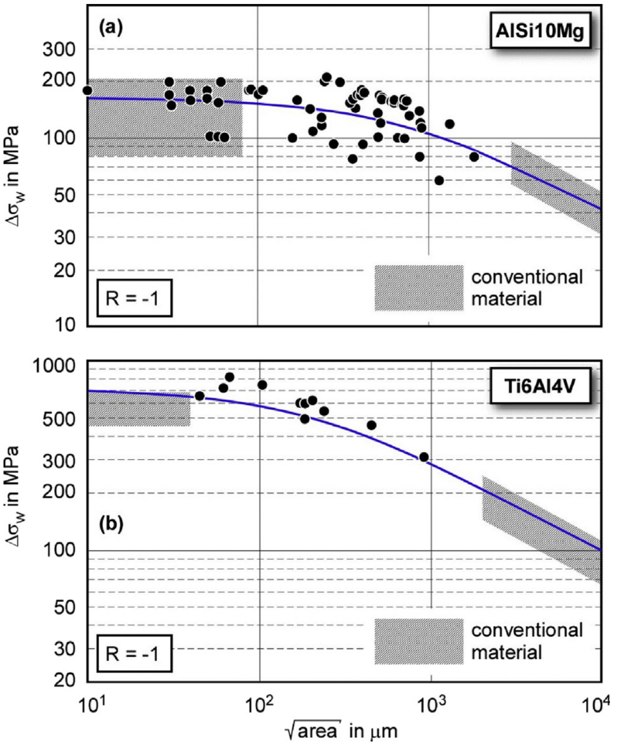

Figure 14.9 KT diagrams obtained from literature data of (a) L-PBF manufactured AlSi10Mg and (b) AM manufactured Ti6Al4V (Beretta and Romano, 2017).

while the parameter $\sqrt{area}$ is obtained for cracks, it can also be used for defects such as inclusions or pores or surface roughness. There are two reasons for this. First, below a certain notch root radius, a notch will behave mechanically like a crack. This is usually the case for micropores (see, e.g., Xu et al., 1997) but also with respect to surface roughness (Taylor and Clancy, 1991; Madia and Zerbst, 2016). Second, cracks can rapidly develop from defects. Since these are too small to be detectable under realistic conditions they should be assumed as existent at least as a conservative option. Eq. (14.9) was demonstrated to be valid within 20 $\mu m < \sqrt{area} < 1$ mm for a range of metallic materials (Murakami, 2002) which roughly refers to Region II of the KT diagram.

As in the case of the fatigue strength (Fig. 14.2), the threshold ΔK_{th} can be correlated with the hardness

$$\Delta K_{th} = 3.3 \cdot 10^{-3} \cdot (HV + 120) \cdot \left(\sqrt{area}\right)^{1/3} \cdot [(1 - R) / 2]^{\alpha} \qquad (14.10)$$

with the exponent α being given as $a = 0.226 + HV \cdot 10^{-4} 0.226 + HV \cdot 10^{-4}$. The error band of this equation is ±20% (Murakami, 2002).

The $\sqrt{area}$ concept is also used in conjunction with the fatigue limit:

$$\Delta\sigma_{th} = 2.86 \cdot (HV + 120) \cdot \left(\sqrt{area}\right)^{-1/6} \cdot [(1 - R)/2]^{\alpha} \tag{14.11}$$

for surface defects. For embedded defects, the factor 2.86 is replaced by 3.12.

14.5 The cyclic R-curve concept

The cyclic R-curve is the dependency of the resistance against fatigue crack propagation on the crack growth, $\Delta K_{th}(\Delta a)$, as it has already been mentioned briefly in Eqs. (14.6) and (14.10). In principle, the threshold consists of two components, the intrinsic one, $\Delta K_{th,eff}$, and the extrinsic one due to the crack closure phenomenon, $\Delta K_{th,op}$ (see also Fig. 14.10).

$$\Delta K_{th} = \Delta K_{th,eff} + \Delta K_{th,op} \tag{14.12}$$

$\Delta K_{th,eff}$ is a real material parameter in that it only depends on the elastic properties of the material, i.e., the modulus of elasticity (E modulus) and the lattice type (in terms of the magnitude of the Burger's vector $\| b \|$, Pokluda et al., 2014). In contrast, $\Delta K_{th,op}$ is affected by material properties such as the grain size (which may have an influence on the roughness-induced crack closure effect, Fig. 14.5c) and also (by its effect on the yield strength) on the crack tip plastic zone size and thus on the plasticity-induced crack closure mechanism. Furthermore, $\Delta K_{th,op}$ depends on the stress ratio R and, at the physically short crack stage, on the amount of crack propagation Δa. Environmental effects (e.g., oxidation) and phase transformation (if present) also play a major role in the development of $\Delta K_{th,op}$.

This is illustrated schematically in Fig. 14.10 along with an example of a curve for an L-PBF material. Note that the latter has been obtained within the frame of ongoing research and still needs further validation.

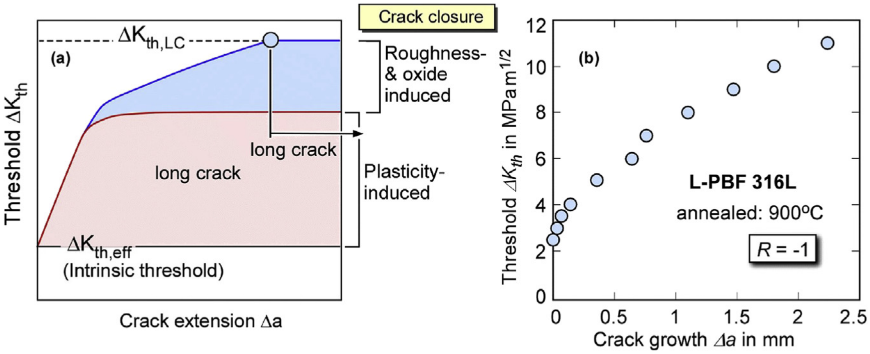

Figure 14.10 Cyclic R curve. (a) schematic view; (b) example for annealed L-PBF 316L (Werner, 2020), BAM Berlin.

For the experimental determination of the cyclic R-curve a closure-free initial crack is needed. This may, e.g., be realized by compression precracking starting from a very sharp notch. Compression pre-cracking means that the upper and the lower stress levels are compressive. That a crack grows at all under these conditions is due to the finite width of the notch. At the first loading step, the notch is compressed and a monotonic plastic zone is generated at the notch root. During subsequent unloading a cyclic plastic zone forms within the monotonic one. This is also known as reversed plastic zone, and it is characterized by tensile residual stresses. Both this tensile stress and the applied cyclic stress promote a ΔK which drives the growth of the crack through the monotonic plastic zone. When the crack grows, the effective driving force progressively decreases and the crack stops when its tip reaches the border of the monotonic plastic zone from the first loading step. At the point of crack arrest it can be argued that the damage at the crack tip is very small (the plastic zone is vanishingly small) and that the precrack is almost closure-free as both maximum and minimum load remain in compression during precracking (Suresh, 1985).

The further procedure follows a proposal in Tabernig and Pippan (2002), see also Maierhofer et al. (2018). The cyclic load is stepwise increased. Above $\Delta K = \Delta K_{th,eff}$ the crack propagates for a certain amount until it arrests due to the build-up of the crack closure phenomenon. By connecting the arrest points one obtains the cyclic R-curve. Further results of this test are the intrinsic threshold and the long crack threshold $\Delta K_{th,LC}$ above which the crack no longer arrests. This curve can be used as part of a cyclic R-curve analysis such as illustrated in Fig. 14.11.

Fig. 14.11 contains cyclic crack driving force curves for different stress levels. These are designated by ΔK_p, where the index p stands for "plasticity-corrected." This is because the crack is also a mechanically short one (Section 14.2), which requires the description of the crack driving force in terms of elastic-plastic fracture mechanics concepts. The cyclic R-curve starts from the closure-free initial crack size a_i $\left(a_i, \Delta K_{th,eff}\right)$. This can refer to a defect size but can also be obtained by crack arrest considerations or other approaches (Zerbst et al., 2019b).

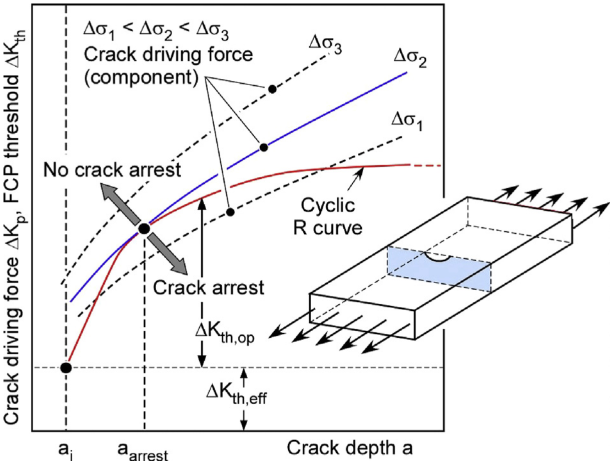

Figure 14.11 Principle of a cyclic R-curve analysis.

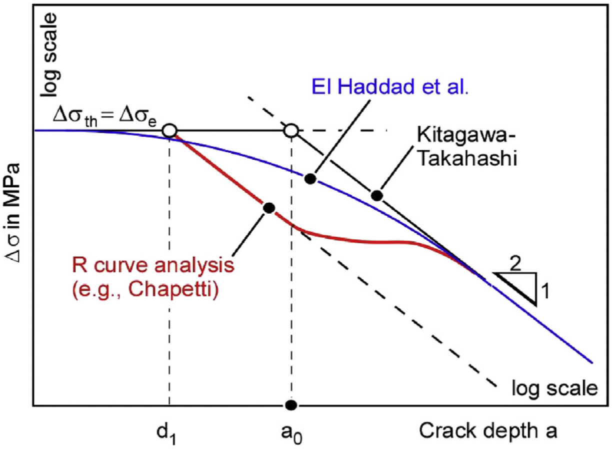

Figure 14.12 Schematic view of the KT diagram based on the original approach of Kitagawa and Takahashi, on El Haddad's method (Eq. 14.2) and on a cyclic R-curve analysis. Here d_1 is meant to be the microstructural barrier defining the boundary between microstructural short crack and physically mechanically short crack regimes.

The point of tangency between the crack driving force curve and the cyclic R-curve defines the transition from crack arrest to crack propagation. In other words, it determines the fatigue limit. In Fig. 14.11, the tension loaded plate with the semi-elliptical surface crack stands for components in general.

This approach allows the determination of the fatigue strength (and the S-N curve) if the initial crack size is known. For L-PBF applications the latter can be taken, e.g., from CT scan data (Chapter 10) in conjunction with extreme value statistics (Romano et al., 2017). It can also be applied to the generation of KT diagrams. This is illustrated in Fig. 14.12 which schematically shows that there is a systematic offset in Region II in that the R-curve-based KT gives up to 25% lower stress values. As mentioned above, this discrepancy is still a topic of ongoing investigations.

14.6 Open questions

In Sections 14.1 and 14.3—14.5 methods were presented which can be applied to the description of the fatigue behavior of L-PBF components. Particularly 14.3—14.5 integrated the size of defects, which is extremely important for these applications. Note, however, that in addition, a number of further requirements have to be fulfilled. This is not in any case state-of-the-art today.

The first requirement refers to representative material parameters. As a result of the different local thermal conditions in the powder bed fusion process, the microstructure can be extremely inhomogeneous, and this also applies to the distribution of defects. In principle, this problem could be solved in two ways: (a) one possibility would be to determine material properties that cover all regions in the component conservatively;

or (b) the second, more realistic option is to first identify the potentially critical sites in the component and then to determine material properties for these sites. This principle is known in the additive manufacturing literature as "critical location" or "zone-based approach" (Yadollahi and Shamsaei, 2017; Gorelik, 2017). The critical sites in the component are defined by the stress hotspots (note that it is not just the stress concentration at surface, but also the stress gradient in wall thickness direction) plus by other features such as the local building direction (in relation to the loading direction) and residual stress aspects. Following Leutenecker-Twelsiek et al. (2016), it makes sense to consider these aspects before the final design is fixed.

When the positions of interest are defined, the local thermal conditions in the manufacturing process must be evaluated such that it is possible to produce companion specimens that represent the material properties at these critical positions. This philosophy can be compared with the thermomechanical simulation of HAZ microstructures in welds, but the situation with L-PBF is even more complex due to the many different process parameters.

Which material parameters are needed depends on which of the above listed methods are used to evaluate the structure. In the simplest case this can be the S-N curve. If a cyclic R-curve analysis is to be carried out, the long crack $da/\,dN-\,\Delta K$ data including the threshold ΔK_{th} and the cyclic R-curve are needed. The El Haddad-based KT method needs the (reliable) long crack threshold $\Delta K_{th,LC}$ along with the endurance limit. The estimation of the latter is a major issue as an additively manufactured material is inherently flawed. Note that a further problem is the application to different R ratios and components, which is solved implicitly by the R-curve approach. Finally, hardness values are needed for Murakami's method.

Another, widely open question is that of the critical defect size. Although defect distributions can be obtained with comparatively high effort and on comparatively small samples, e.g., by CT scans, a more robust procedure will be necessary for engineering applications. For example, a categorization of defect sizes is conceivable such that this kind of fixed information is available for the component assessment. The effect of post-treatments must be included. Special problems are defect clusters and the preferential orientations of nonwelded regions (with respect to the direction of loading).

If a KT-type assessment is performed, no prior information about the defect situation is needed. Conversely, the analysis provides information about the permissible defect size. The problems mentioned above are nevertheless retained, although this time on the side of the NDT. How is the information on the maximum allowable size of one surface defect transferred to a defect cluster, what maximum defect size is really expected on the critical site, etc.?

A last major problem area that is still waiting for a solution is that of residual stresses that arise in the manufacturing process. Perhaps this is the weakest link in component assessment as it currently stands. The main problem is to gather the information on the magnitude and distribution across the section, which depend on a number of geometrical and process parameters (Chapter 9). An open question is also the potential relaxation of residual stresses under cyclic loading.

An example for the consideration of residual stresses (σ_r) in component assessment, although in a simplified way, is presented in Beretta et al. (2020) for AM processed

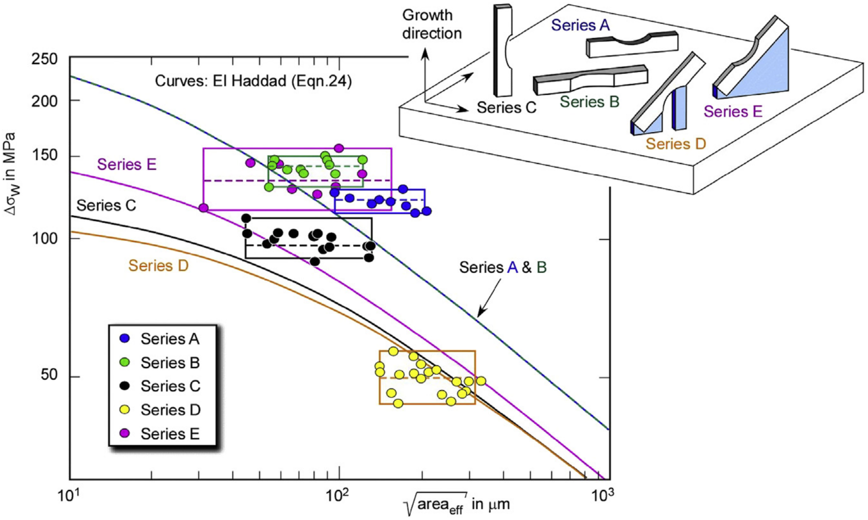

Figure 14.13 Analysis of the fatigue strength for as-built specimens made of AlSi10Mg printed in different orientations and tested at $R = 0.1$ (series C: residual stresses: 140 MPa, series D residual stresses: 72 MPa). The residual stresses were measured at the surface. For series C, a simplified limit condition for elastic shakedown was considered (Beretta et al., 2020).

AlSi10Mg. Fig. 14.13 shows KT diagrams for different building directions. The differences in the curves were attributed to the defects detected at the crack origin for the different orientations as well as to the residual stresses (series C: $\sigma_r = 140$ MPa; series D: $\sigma_r = 72$ MPa) that made the effective R ratio $R_{eff} = 0.55 - 0.6$ for series C and D. The nominal R ratio was $R = 0.1$. In case of series C, the sum $\sigma_r + \Delta\sigma_{appl}$ would have exceeded the yield strength of the material, so the estimation of stress relaxation based on the limit of elastic shakedown was a conservative assumption.

The fact that real defects are not centered on the estimated KT diagram can be due to different reasons: (a) the simple estimation of stress relaxation together with scatter of residual stress measurements; (b) a too simplistic description of the KT diagram with the El-Haddad model especially at different R ratios; and/or (c) the "shielding" effect due to the roughness profile and surface texture that makes the effect of a sequence of surface depressions less detrimental (in terms of the K factor at the prospective cracks) than the effect of a single notch.

There are many cases in the literature where residual stress fields have been evaluated by FEM simulations (for an overview see Zerbst et al., 2020). However, much effort is still required in the determination of the material parameters needed for the models. Additionally, some metrological problems need still to be solved when dealing with the experimental determination of residual stresses in additively manufactured parts. Standards such as ISO 21432 (2019) and EN 15305 (2009) do currently not encompass AM materials and components.

14.7 Conclusions

The well-established methods of fatigue assessment cannot be transferred to L-PBF without modifications due to the following principal reasons:

- Pronounced inhomogeneity of material properties across the components;
- Unavoidable material defects such as pores and unmelted regions;
- A complex and difficult to reproduce pattern of residual stresses that is influenced by the component geometry and several technological parameters.

Starting from a very brief introduction to the classic S-N curve concept, this chapter concentrated on methods which take into account the effect of defects on fatigue strength and life. These concepts are the Kitagawa-Takahashi diagram, Murakami's $\sqrt{area}$ method, and the cyclic R-curve approach. In a final section, open points were discussed which still hinder the application of these methods to real L-PBF applications. These comprise the acquisition of representative material parameters, the treatment of critical defect sizes by NDT, and the consideration of the residual stresses.

14.8 Questions

- Why have the classic fatigue concepts to be modified for its use on L-PBF?
- What are the main parameters that affect the fatigue behavior of L-PBF components?
- How can a Kitagawa-Takahashi (KT) diagram be determined?
- What is the basic approach of Murakami's $\sqrt{area}$ method?
- Explain the two components of the threshold against fatigue crack propagation $\Delta K_{th}\Delta K_{th}$.
- Describe a cyclic R-curve.
- How is the fatigue limit determined by a cyclic R-curve analysis?
- What are the main problems that make fatigue assessment of L-PBF parts difficult?
- Which strategies are conceivable to solve the inhomogeneity problem of material parameters?

References

Beretta, S., Gargourimotlagh, M., Folletti, S., Du Plessies, A., Riccio, M., 2020. Fatigue strength assessment of "as built" $AlSi_{10}Mg$ manufactured by SLM with different build directions. Int. J. Fatig. 139, 105737.

Beretta, S., Romano, S., 2017. A comparison of fatigue strength sensitivity to defects for materials manufactured by AM or traditional processes. Int. J. Fatig. 94, 178−191.

Ding, F., Feng, M., Jiang, Y., 2007. Modeling of fatigue crack growth from a notch. Int. J. Plast. 23, 1167−1188.

El Haddad, M.H., Smith, K.N., Topper, T.H., 1979. 'Fatigue crack propagation of short cracks' transactions of the American Society for Mechanical Engineering (ASME). J. Eng. Mater. Technol. 101, 42−46.

EN 15305-2009-1, 2009. Non-destructive Testing - Test Method for Residual Stress Analysis by X-Ray Diffraction. European Standard.

Ganesh, P., Kaul, R., Sasikala, G., Kumar, H., Venugopal, S., Tiwari, P., Rai, S., Prasad, R., Kukreja, L., 2014. Fatigue crack propagation and fracture toughness of laser rapid manufactured structures of AISI 316L stainless steel. Metall. Microstruct. Anal. 1, 36−45.

Gorelik, M., 2017. Additive manufacturing in the context of structural integrity. Int. J. Fatig. 94, 168−177.

Greitemeier, D., Palm, F., Syassen, F., Melz, T., 2017. Fatigue performance of additive manufactured $TiAl_6V_4$ using electron and laser beam melting. Int. J. Fatig. 94, 211−217.

Günther, J., Krewerth, D., Lippmann, T., Leuders, S., Tröster, T., Weidner, A., Biermann, H., Niendorf, T., 2017. Fatigue life of additively manufactured Ti-6Al-4V in the very high cycle fatigue regime. Int. J. Fatig. 94, 236−245.

Hardboletz, A., Weiss, B., Stickler, R., 1994. Fatigue thresholds of metallic materials. In: Carpenteri, A. (Ed.), Handbook of Fatigue Crack Propagation in Metallic Structures. Elsevier, pp. 847−882.

ISO 21432, 2019. Non-destructive Testing - Standard Test Method for Determining Residual Stresses by Neutron Diffraction. International Organization for Standardization (ISO), Geneva, Switzerland.

Kahlin, M., Ansell, H., Moverare, J.J., 2017. Fatigue behaviour of notched additive manufactured Ti6Al4V with as-build surfaces. Int. J. Fatig. 101, 51−60.

Kitagawa, H., Takahashi, S., 1976. Applicability of fracture mechanics to very small cracks or the cracks in the early stage. In: Proc 2nd International Conference on the Mechanical Behavior of Materials, Boston, ASM, Cleveland, Ohio, pp. 627−631.

Leutenecker-Twelsiek, B., Klahn, C., Meboldt, M., 2016. Considering part orientation in design for additive manufacturing. Procedia CIPR 50, 408−413.

Madia, M., Thoffo Ngoula, D., Zerbst, U., Beier, H.T., 2017. Approximation of the crack driving force for cracks at notches under static and cyclic loading. Procedia Struct. Integrity 5, 875−882.

Madia, M., Zerbst, U., 2016. Application of the cyclic R-curve method to notch fatigue analysis. Int. J. Fatig. 82, 71−79.

Maierhofer, J., Kolitsch, S., Pippan, R., Gänser, H.-P., Madia, M., Zerbst, U., 2018. The cyclic R-curve − determination, problems, limitations and application. Eng. Fract. Mech. 198, 45−64.

Miller, K.J., 1993. The two thresholds of fatigue behavior. Fatig. Fract. Eng. Mater. Struct. 16, 931−939.

Molaei, R., Fatemi, A., 2019. Crack paths in additive manufactured materials subjected to multiaxial cyclic loads including surface roughness, HIP, and notch effects. Int. J. Fatig. 124, 558−570.

Murakami, Y., 2002. Metal Fatigue. Effects of Small Defects and Nonmetallic Inclusions. Elsevier, Oxford.

Murakami, Y., Masuo, H., Tanaka, Y., Nakatani, M., 2019. Defect analysis for additively manufactured materials in fatigue from a viewpoint of quality control and statistics of extremes. Procedia Struct. Integrity 19, 113−122.

Pokluda, J., Pippan, R., Vojtek, T., Hohenwarter, A., 2014. Near-threshold behavior of shear-mode fatigue cracks in metallic materials. Fatig. Fract. Eng. Mater. Struct. 37, 232−254.

Polak, J., 2003. Cyclic deformation, crack initiation, and low-cycle fatigue. In: Ritchie, R.O., Murakami, Y. (Eds.), Comprehensive Structural Integrity, Cyclic Loading and Fracture, Vol. 4. Elsevier, pp. 1−39.

Romano, S., Beretta, S., Brandão, A., Gumpinger, J., Ghidini, T., 2017. HCF resistance of $AlSi_{10}Mg$ produced by SLM in relation to the presence of defects. Procedia Struct. Integrity 7, 101−108.

Suresh, S., 1985. Crack initiation in cyclic compression and its implications. Eng. Fract. Mech. 21 (3), 453–463.

Suresh, S., 2003. Fatigue of Materials, second ed. Cambridge University Press.

Suryawanshi, J., Prashanth, K.G., Ramamurty, U., 2017. Mechanical behavior of selective laser melted 316L stainless steel. Mater. Sci. Eng. A 696, 113–121.

Tabernig, B., Pippan, R., 2002. Determination of the length dependence of the threshold for fatigue crack propagation. Eng. Fract. Mech. 69, 899–907.

Tanaka, K., Akinawa, Y., 2003. Modelling of fatigue crack growth: mechanistic models. In: Ritchie, R.O., Murakami, Y. (Eds.), Comprehensive Structural Integrity, Cyclic Loading and Fracture, vol. 4. Elsevier, pp. 165–189.

Taylor, D., Clancy, O.M., 1991. The fatigue performance of machined surfaces. Fatig. Fract. Eng. Mater. Struct. 14, 329–336.

Tchoffo Ngoula, D., Madia, M., Beier, H.T., Vormwald, M., Zerbst, U., 2018. Cyclic J-integral: numerical and analytical investigations for surface cracks in weldments. Eng. Fract. Mech. 198, 24–44.

Werner, T., 2020. Internal Report. BAM, Berlin.

Xu, R.X., Topper, T.H., Thompson, J.C., 1997. Mode I stress intensity factor equations for cracks at notches and cavities. Fatig. Fract. Eng. Mater. Struct. 20, 1351–1361.

Yadollahi, A., Shamsaei, N., 2017. Additive manufacturing of fatigue resistant materials: challenges and opportunities. Int. J. Fatig. 98, 14–31.

Yamashita, Y., Murakami, T., Mihara, R., Okada, M., Murakami, Y., 2018. Defect analysis and fatigue design basis for Ni-based superalloy 718 manufactured by selective laser melting. Int. J. Fatig. 117, 485–495.

Zerbst, U., Bruno, G., Buffiere, J.-Y., Wegener, T., Niendorf, T., Wu, T., Zhang, X., Kashaev, N., Meneghetti, G., Hrabe, N., Madia, M., Werner, T., Hilgenberg, K., Koukolíková, M., Procházka, R., Džugan, J., Möller, B., Beretta, S., Evans, A., Wagener, R., Schnabel, K., 2020. Damage tolerant design and assessment of additively manufactured metallic components subjected to cyclic loading. State-of-the-art, problems, challenges. In: Submitted to Progress in Materials Science.

Zerbst, U., Madia, M., Klinger, C., Bettge, D., Murakami, Y., 2019a. Defects as the root cause of fatigue failure of metallic components. Part I: basic aspects. Elsevier Eng. Fail. Anal. 97, 777–792. Part II: non-metallic inclusions. Eng. Fail. Anal. Elsevier, 98, 228–239; Part III: cavities, dents, corrosion pits, scratches. Eng. Fail. Anal. 97, 759–776.

Zerbst, U., Vormwald, M., Pippan, R., Gänser, H.-P., Sarrazin-Baudoux, C., Madia, M., 2016. About the fatigue crack propagation threshold of metals as a design criterion – a review. Eng. Fract. Mech. 153, 190–243.

Zerbst, U., Madia, M., Vormwald, M., 2019b. Applying fracture mechanics to fatigue strength determination – some basic considerations. Int. J. Fatig. 126, 188–201.

Structural integrity III: energy-based fatigue prediction for complex parts

15

Seyed Mohammad Javad Razavi[1], *Anton Du Plessis*[2,3], *Filippo Berto*[1]
[1]Department of Mechanical and Industrial Engineering, Norwegian University of Science and Technology (NTNU), Trondheim, Norway; [2]Department of Mechanical Engineering, Nelson Mandela University, Port Elizabeth, Eastern Cape, South Africa; [3]Research Group 3D Innovation, Stellenbosch University, Stellenbosch, Western Cape, South Africa

Chapter outline

15.1 Introduction 395
15.2 Fatigue of AM components 398
  15.2.1 Microstructure 398
  15.2.2 Internal porosity 401
  15.2.3 Surface condition 403
  15.2.4 Residual stress 405
15.3 Theoretical framework for strain energy density approach 405
  15.3.1 Local approaches for failure assessment 406
  15.3.2 Strain energy density 406
  15.3.3 Numerical method 410
15.4 Energy-based fatigue prediction of complex AM components 412
15.5 Conclusions 417
15.6 Questions 418
References 418

15.1 Introduction

One of the major hurdles of laser powder bed fusion (L-PBF) is the inconsistent fatigue performance, depending on many possible defect types, microstructural differences, surface roughness effects, residual stresses, and more, as described in other chapters in this book. Many improvements have been made in material properties by L-PBF process optimization, quality control efforts, nondestructive testing in-process and inspection of final parts, and post-processing of the parts to remove and mitigate many of the defects causing detrimental failures. In this chapter the concepts of fatigue prediction are applied to complex part design and discussed in particular in relation to

Fundamentals of Laser Powder Bed Fusion of Metals. https://doi.org/10.1016/B978-0-12-824090-8.00005-6
Copyright © 2021 Elsevier Inc. All rights reserved.

designed notches, which allows to inform the design process and allows incorporating the effects of defects into the design process. This is one promising approach to improve the outcomes and performance of critical complex-shaped components produced by L-PBF, working toward fatigue-tolerant design for additive manufacturing.

The knowledge and prediction of the overall mechanical and especially fatigue performance of components produced by additive manufacturing (AM) still encounter many open questions and depend on various factors such as the microstructure of the printed material, the surface condition, and statistics of the internal defects. In the design of complex industrial components (see Fig. 15.1), the presence of nonuniform section areas and geometrical discontinuities such as notches is unavoidable. This geometrical variation results in a part that has different microstructural features, surface roughness, and internal defects.

The material properties of AM parts are dependent on the process parameters and the geometry of the part, and therefore can evolve during the fabrication process.

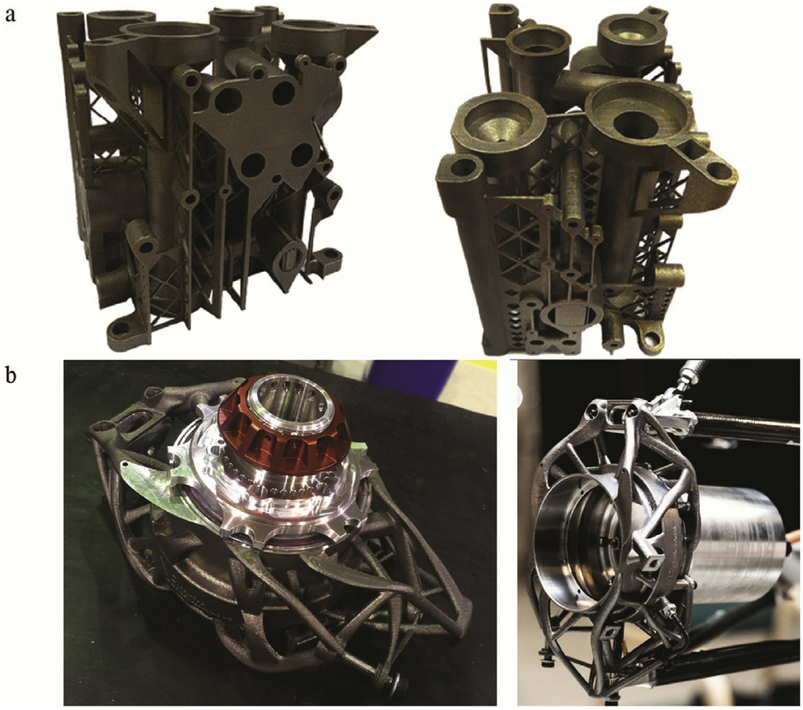

Figure 15.1 Complex components manufactured by L-PBF process; (a) steel manifold block produced using AM with 50% weight reduction and improved fluid flow compared to traditional equivalent part, (b) Ti6Al4V upright of a race car (Berto et al., 2018).
(a) © Copyright Renishaw plc. All rights reserved. Images reproduced with the permission of Renishaw. Saunders, M., 2015. Minimal Manifolds - How to Shed Weight and Boost Performance. Available at: https://www.linkedin.com/pulse/minimal-manifolds-how-shed-weight-boost-performance-marc-saunders/.

Due to specific AM fabrication routines, the fabricated parts are commonly not isotropic, and the surface morphology reflects the layerwise nature of the produced part. The intensity of the mentioned characteristics highly depends on the underlying manufacturing strategy, which in turn, depends on the input geometry of the part (Herzog et al., 2016; Liu and Shin, 2019).

Examination of the state-of-the-art reveals that quality assurance and fatigue assessment of complex-shaped AM components cannot yet be accurately performed due to a lack of advanced methodologies incorporating the specific microstructural features, defects, as well as the specific mechanical behavior of AM materials to be modeled effectively. Therefore, considering the growing importance of AM technologies including laser powder bed fusion, a fundamental theoretical understanding of fatigue behavior of AM metallic alloys is an essential step that must be taken into the design process as a matter of necessity. To date, the assessment and the quality assurance of AM components have been the topic of numerous research studies evaluating the effect of process parameters on the microstructure of the resulting material, the geometrical accuracy, and the mechanical behavior of the AM parts. Limited attempts have been performed to evaluate the mechanical behavior of geometrically complex AM parts using the available theoretical models for mechanical parts produced by conventional techniques. Further, very limited fatigue data generated by testing such geometrical discontinuous complex-shaped metal AM parts can be found in the technical literature.

Considering all the mentioned challenges regarding AM components, a mechanistic knowledge of mechanical strength and failure modes of these parts under specific loading conditions is of great importance for developing a design and failure prediction tool which are expected to be highly demanded in the near future.

In this context, this chapter aims to review the applicability of an energy-based fatigue failure prediction methodology suitable for designing complex AM components. The key feature of this unifying approach is that the adopted linear-elastic effective strain energy density is calculated via a control volume whose size is related to the microstructural and surface features (such as porosity, grain size and shape, surface roughness, etc.) of the material in the vicinity of the crack initiation locations. In this chapter, several important factors that influence the fatigue behavior of AM parts including microstructure, internal defects, surface condition, and residual stresses are first presented. Then, the ability of an energy-based criterion, namely the Average Strain Energy Density (ASED), to predict the fatigue failure of AM components is discussed by referring to the experimental and theoretical results taken from literature. Although the discussed points in this chapter can be valid for a wide range of metallic alloys, the majority of the discussed information here are related to a common Ti alloy (Ti6Al4V) produced with different AM techniques; examples are shown here for Directed Energy Deposition (DED) in comparison to L-PBF. Lastly, a summary of the chapter and future perspectives are provided.

15.2 Fatigue of AM components

The main challenge against the wider adoption and application of metal AM by industries is the uncertainty in structural properties of the components produced by AM techniques. This uncertainty can be either due to production conditions such as variation in as-received powder, and process parameters (e.g., laser power, scanning speed, hatching distance, layer thickness, etc.), microstructural heterogeneities, randomly dispersed defects, surface roughness, and residual stresses, which are all partially related to the input geometry of the component.

Generally speaking, the mechanical properties of L-PBF parts under static loading (e.g., tensile, compressive, hardness, etc., see Chapter 13) are on par with their wrought counterparts, often even exceeding them. This characteristic of the L-PBF parts arises from fairly high cooling rates during fabrication, leading to finer microstructural features compared to their wrought counterparts. Unlike the strength of the L-PBF parts, as a result of possible presence of internal defects or brittle phases, they can experience lower ductility compared to the wrought material, in the as-built state (Du Plessis et al., 2020). Dealing with the mechanical performance of L-PBF components, a major concern arises when they are subjected to cyclic loading (see Chapter 14 also). Due to the local nature of fatigue failure, the presence of any geometrical discontinuities can significantly reduce the overall performance of the structural part. Hence, a thorough understanding of the fatigue failure mechanisms and their relation to the microstructure of the material, internal defects, and surface condition is an essential task to improve the durability of engineering components produced with the L-PBF process. The key parameters in the majority of the research on fatigue of AM parts in general are described as follows, using examples from DED and L-PBF in comparison.

15.2.1 Microstructure

The microstructure of AM parts strongly depends on the thermal histories experienced during fabrication, which itself is dependent on the AM system, process parameters, geometry of the part, and interlayer time (i.e., the amount of time taken for the heat source to start melting new layers after finishing the previous layer). The Ti6Al4V alloy solidifies in the β phase, and as the temperature decreases, the β phase transforms to martensitic or α phases. The microstructures of AM parts are oriented along the heat transfer path, resulting in columnar morphology of prior β grains following the build direction and consequently anisotropic behavior of the parts is found. Fig. 15.2 illustrates the columnar microstructure of Ti6Al4V produced by different AM techniques (and therefore different cooling rates due to different processes).

As an important factor, the cooling rate during the AM process affects the grain size and phase fraction. Considering the L-PBF process in particular, the induced heat in the deposited layer mainly transfers through the powder bed surrounding the part and the previous deposited layers to the build platform. Owing to the high cooling rate during the L-PBF process ($>10^6$ K/s), the microstructure of as-built Ti6Al4V

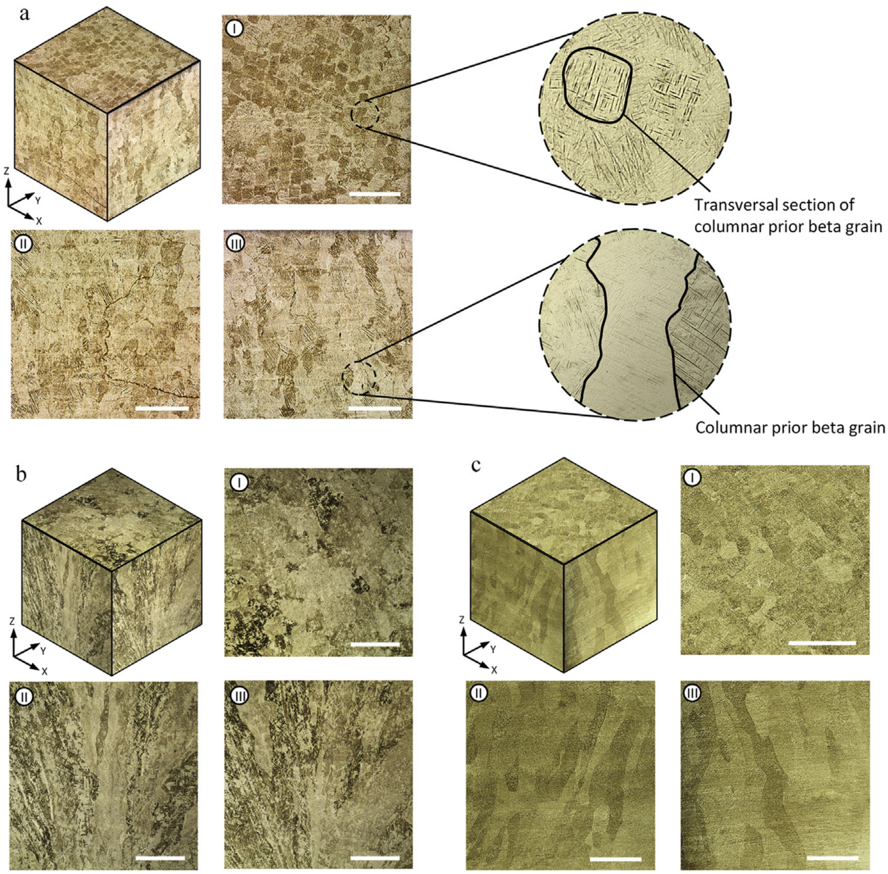

Figure 15.2 Comparison of Ti6Al4V microstructures for different AM technologies (build direction: Z): (a) L-PBF based on the fabricated material in (Razavi et al., 2017; Razavi et al., 2018); (b) EB-PBF (Razavi et al., 2020), (c) DED (Razavi and Berto, 2019). (I) lateral view (normal to build direction) (II,III) longitudinal view (along build direction, Z axis). (Scale bar: 500 μm).
(a) Taken from (Razavi, 2019).

parts mainly consists of martensitic phase (Liu and Shin, 2019) (see Figs. 15.2a and 15.3a). It is worth mentioning that by varying the process parameters, different ratios of phases can be obtained for the L-PBF materials resulting in improved fatigue properties of these parts (Xu et al., 2015).

Preheating at 570°C has been recommended to eliminate the martensitic phases during the L-PBF process (Ali et al., 2017) (see also Chapter 8). In this treatment, the martensitic phases are deposited into a microstructure consisting of α phases (Xu et al., 2015). As a matter of fact, longer heat treatments at higher temperatures results in coarser microstructures and appearance of β phase (Leuders et al., 2013; Kasperovich and Hausmann, 2015). Similar observations were also reported in other

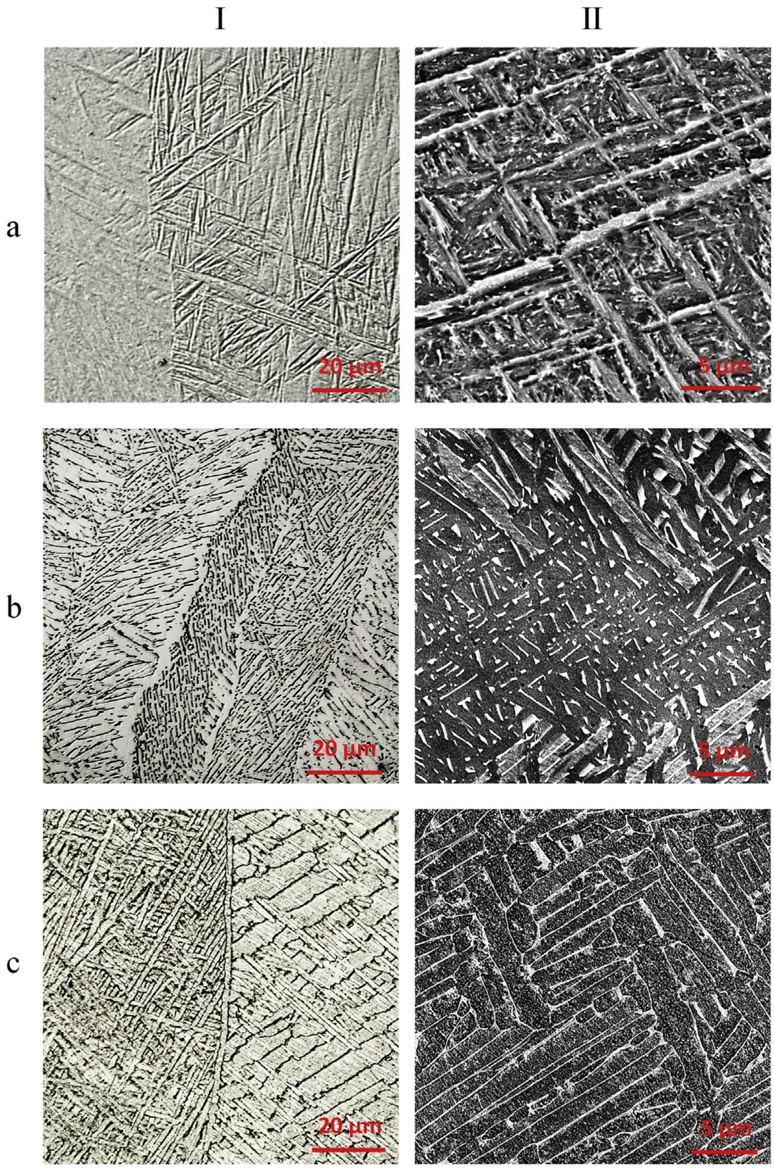

Figure 15.3 Comparative microstructures of Ti6Al4V produced by (a) L-PBF based on the fabricated material in (Razavi et al., 2017; Razavi et al., 2018), (b) EB-PBF (Razavi et al., 2020), and (c) DED (Razavi and Berto, 2019). Optical microscopy and SEM results of the samples are indicated by (I) and (II), respectively.
(a, b) Taken from (Razavi, 2019).

research studies on the microstructure of L-PBF specimens (Thijs et al., 2010; Puebla et al., 2012; Chan et al., 2013; Rafi et al., 2013b; Khorasani et al., 2019).

Electron beam PBF (EB-PBF) has a relatively similar heat transfer mechanism to the L-PBF process with the exception that the powder bed in EB-PBF machines is heated with controlled temperature to eliminate the presence of any residual stresses during and after the process. Slow cooling rates from the elevated build chamber temperature in EB-PBF results in fine basketweave and lamellar $\alpha+\beta$ microstructure (see Figs. 15.2b and 15.3b) (Murr et al., 2009; Antonysamy et al., 2013; Chan et al., 2013; Galarraga et al., 2016).

The heat transfer during Directed Energy Deposition (DED) occurs due to a combination of conduction through the previously deposited layers and convection induced by argon flow, which is different than the L-PBF process where the heat transfer is mainly through conduction. In this case the high energy input and the slow scan speed in the DED process results in more severe cyclic reheating of the previous layers and causes phase transformation in the material resulting in basketweave and lamellar $\alpha+\beta$ structure and possible martensitic structure (see Figs. 15.2c and 15.3c) (Bontha et al., 2006, 2009; Zheng et al., 2008; Zhai et al., 2015; Sandgren et al., 2016; Zhai et al., 2016a).

Dealing with the fatigue resistance of AM parts, the as-built DED and L-PBF Ti6Al4V parts have shown higher fatigue strength but lower fatigue toughness (ΔK_{th}) compared to the equivalent parts fabricated by the EB-PBF process (Rafi et al., 2013a; Zhai et al., 2016b; Liu and Shin, 2019). This superior fatigue resistance was thought to be related to the presence of fine martensitic phases containing a high density of dislocations. This fine microstructure results in further impeding of dislocation motion and enhances the dislocation strengthening effect by sacrificing the plastic strain (Rafi et al., 2013a). Performing annealing treatment enhances the fatigue toughness of L-PBF specimens to the same level of EB-PBF parts. This enhancement was reported to be related to the decomposition of martensite phase and elimination of residual stresses (Zhai et al., 2016b).

15.2.2 Internal porosity

Internal porosity can be classified into two main categories: keyhole pores and lack of fusion pores (which implies weak metallurgical bonding between layers or adjacent tracks, see Chapter 6) (see Fig. 15.4). Pore formation during solidification of metals in L-PBF is discussed in more detail in Chapter 6. The lack of fusion forms due to the low power density of the laser radiation which can lead to insufficient bonding between layers. Besides, incorrect selection of hatch distance can lead to formation of gaps between the scanning tracks leaving this type of defect in the fabricated part (Sterling et al., 2016; Yadollahi et al., 2017; Du Plessis, 2019). Unlike keyhole or gas entrapment pores which have a more spherical shape and are typically small in size, lack of fusion defects are elongated and if the process parameters are not set properly, they can be significantly larger in size. In wrought material, slip bands and microstructural defects are typically known as the sources of local plastic deformation and consequently fatigue crack initiation. However, research studies on fatigue failure of AM

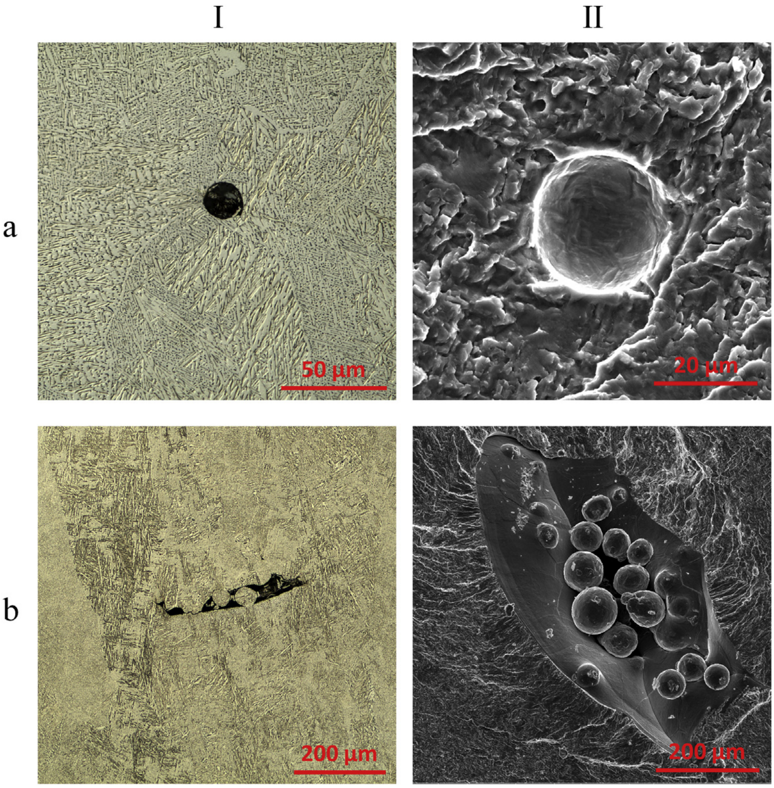

Figure 15.4 Typical internal defects in AM parts, (a) small pore resulting from irregularities in the melting process, (b) lack-of-fusion defect due to insufficient melting between the layers, leaving a powder-filled cavity. Optical microscopy of polished samples and SEM of the fracture surface of AM Ti6Al4V specimens tested under fatigue loading are indicated by (I) and (II), respectively (Razavi, 2019).

components have revealed that fatigue crack initiation occurs from surface roughness (for as-built parts) and/or the pores close to the free surface of component (for machined parts). By acting as a stress raiser, internal pores close to the surface locally increase the stress level and initiate the fatigue cracks at lower number of fatigue cycles (Stephens et al., 2000; Sterling et al., 2016; Yadollahi and Shamsaei, 2017; Yadollahi et al., 2017).

Even though the fatigue crack initiation mechanisms depend on the material and applied load level (i.e., Low Cycle Fatigue (LCF) versus High Cycle Fatigue (HCF)), larger pores, with more irregular shapes, close to the surface are reported to be more detrimental to fatigue strength due to their higher stress concentrations (Yadollahi et al., 2017). Owing to the dominance of fatigue crack initiation in the overall life of components under HCF, the geometry and location of defects in this loading regime have a major role in the fatigue resistance of the part (Sanaei and Fatemi, 2020).

On the other hand, the sensitivity to the defects is less pronounced in the LCF regime, where the fatigue crack initiation life is shorter, and the overall fatigue life of the component is dominated by fatigue crack propagation (Stephens et al., 2000).

Hot Isostatic Pressing (HIP) is a post-processing method used widely for improving the fatigue performance of AM parts. The HIP process can close the internal defects by applying uniform pressure to the surface of the part at high temperature, which improves the fatigue resistance and ductility of the part. Nevertheless, since HIP does not affect the surface defects (open porosities), its highest efficiency can be obtained for machined AM parts (Kobryn and Semiatin, 2001; Leuders et al., 2014; Popov et al., 2018).

15.2.3 Surface condition

As a result of various reasons including partially melted powder on the surface of powder-based AM components, they commonly possess high surface roughness in as-built condition (see Chapter 7 for more information). The relatively high surface roughness of AM parts can be beneficial for some biomedical applications such as implants. They have been proven to be beneficial for bone fixation and bone cell attachment and subsequent bone in-growth resulting in faster and more effective osseointegration providing a stronger bond between the living bone and the surface of the load-carrying implant (Shalabi et al., 2006; Anil et al., 2011; Gittens et al., 2014; Yadollahi and Shamsaei, 2017). However, the fatigue resistance of engineering components is strongly affected by surface roughness (Bagherifard et al., 2018). Hence, numerous research studies have been recently performed on post-processing of AM parts to reduce the surface roughness (Maleki et al., 2020). Although a large number of research studies on AM have been performed on machined specimens, many AM parts are desired to be used in their as-built condition, at least in terms of their surface condition. One of the advantages of AM has always been the possibility of producing net-shaped components with complex geometries. In this case machining the surface or performance of post-processing treatments on the surface would still be a big challenge, diminishing the benefits of AM. In very complex parts this type of surface processing is not possible at all, leading to the need to accept the as-built surface condition or perform surface finishing only in critical areas of the component.

The surface condition of AM parts is a function of the powder size, type of AM system, process parameters, building strategy, and the input geometry of the part. Considering the three mentioned AM processes, L-PBF and DED have the lowest and highest surface roughness, respectively. The higher surface roughness of DED parts is due to larger powder size and larger layer height, laser spot size, and hatch distance. The build rate has been reported to directly affect the surface quality, in a way that the surface quality decreases by an increase in the build rate (Frazier, 2014).

Dealing with components with complex geometries, anisotropic surface roughness can be obtained. Fig. 15.5 shows a schematic illustration of the overhang effect on surface roughness of AM bridge-shaped parts. Considering a specimen with a V-notch, the downward surface of the notch (also named as overhang) is found to possess higher

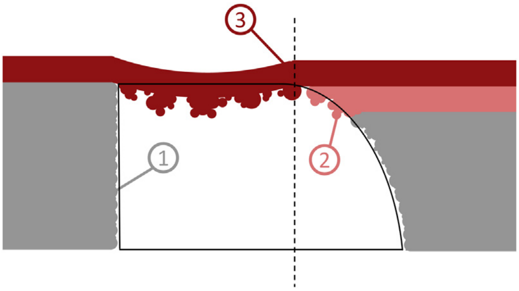

Figure 15.5 Schematic illustration of anisotropic surface roughness in an AM bridge-shaped part. (1) surface perpendicular to the build platform—the layers in this region are supported by the layer below. (2) The layers in the overhang region would be built but they may suffer from poorer surface quality. (3) The layers which have greater angles to the vertical axis may distort during AM production and have the worst surface quality. According to the rule of thumb in AM the overhang angles larger than ~45° to the vertical axis should be avoided. Overhang angles greater than 45° require support structures.
Redrawn from (Saunders, 2016).

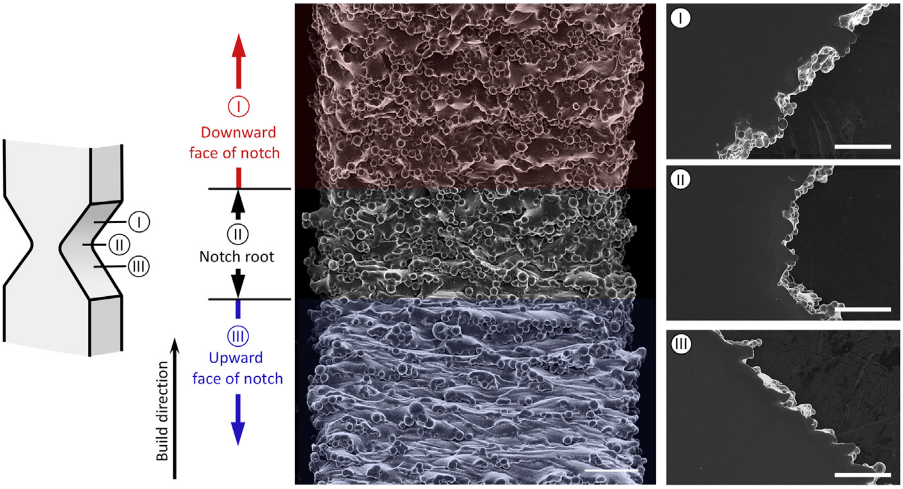

Figure 15.6 Surface condition in a V notched specimen with an opening angle of 90 degrees produced via EB-PBF. Surface morphologies of the downward, notch root, and upward surfaces are represented. A clear difference in the number of partially melted powder particles and surface morphology can be observed (Razavi et al., 2020). (Scale bar: 500 μm).

surface roughness compared to the upward surface (see Fig. 15.6). This can be attributed to the lower cooling rate of the overhang region and consequently attachment of more partially melted powder particles to this surface (Fox et al., 2016; Shrestha et al., 2016).

15.2.4 Residual stress

During AM processing, the development of large thermal gradients around the melt pool, rapid cooling, uneven cooling of the metal on the substrate material, and repetition of this process results in localized compressive and tensile residual stresses in the AM parts (see Chapter 9 for more information). The presence of these residual stresses in the built parts leads to reduced mechanical properties, possible warping or cracking, and lower geometrical accuracy of the AM part. Accordingly, a wide range of characterization and modeling work has been performed to model and evaluate the effect of residual stresses (Mercelis and Kruth, 2006; Pal et al., 2014; Denlinger et al., 2015; Heigel et al., 2015; Ali et al., 2018). For instance Edwards and Ramulu (2014) measured residual stresses in two as-built L-PBF Ti6Al4V specimens with different build orientations. Dependent on the build orientation of the specimens, tensile residual stresses of ~410 and ~550 MPa at the surface and ~0 and ~200 MPa at 200 μm below the surface were measured and reported. The level of residual stresses was reported to be dependent on the geometry of the part and also the location on the specimens (i.e., top or bottom of the specimen). As mentioned earlier, EB-PBF parts are reported to have lower or even negligible levels of residual stresses compared to the parts produced by L-PBF due to high preheating temperature during manufacturing (Hrabe et al., 2017). As a solution for this issue in L-PBF, stress relief heat treatments and proper programming of the build orientation have been studied by researchers in the past and is nowadays a standard part of the production cycle (Leuders et al., 2013; Li et al., 2018).

It is worth noting that the orientation in which AM parts are fabricated may significantly affect the thermal histories (and consequently the microstructures), the distribution of internal defects, surface roughness, and residual stresses. This variation dictates the anisotropic structural response of AM parts in strength, elongation at failure, and fatigue strength (Yadollahi and Shamsaei, 2017).

15.3 Theoretical framework for strain energy density approach

Very limited data are available to date from notched components fabricated by additive manufacturing, and no design criteria based on fatigue prediction have been proposed and validated so far. Since post-processing local stress fields near a notch is never an easy task, the empirical design methods commonly employed in situations of practical interest make use of nominal stresses based on the available fatigue data. In contrast to the philosophy on which this empirical approach is based, an examination of the state-of-the-art shows that the most advanced design methods assess engineering materials' fatigue strength by post-processing the local stress fields in the vicinity of crack initiation sites. Among the different local approaches that have been formalized so far, much experimental evidence suggests that the highest level of accuracy in designing against fatigue loading components containing geometrical features of all kinds is reached, irrespective of the type of material, by using the Strain Energy Density (SED) approach. In particular, it has been demonstrated that the SED is successful in addressing a variety of structural integrity problems which include, amongst others, the assessment of ductile notched/cracked metals subjected to static, dynamic, and fatigue loading. Stepwise description of this approach is provided in the following subsections.

15.3.1 Local approaches for failure assessment

In asserting structural safety, it is of paramount importance to be able to evaluate the loading capacity of notched components, where stresses concentrate and can trigger cracks leading to catastrophic failure or leading to a shortening of the assessed life of the structure. The phenomenon of brittle fracture is encountered in many aspects of everyday life and many catastrophic structural failures involving loss of life have occurred because of a sudden, unexpected failure. The fields of fracture mechanics and the fatigue behavior of structural materials are focused on the prevention of brittle fracture and, as a scientific discipline, are not old (Berto et al., 2018). However, the concern over brittle fracture is not new and the origin of the design to ensure the safety of structures against sudden collapse is well established. This topic has involved many researchers in different engineering fields from ancient times to nowadays. As an attempt by these researchers, numerous failure prediction methods have been proposed for materials produced by conventional methods in several published articles in the open literature. Fatigue failure has a localized nature, meaning that the failure initiation commonly occurs at a small volume of the material around the geometrical discontinuities of the structural parts. Due to this local nature of fatigue failure, the majority of the proposed criteria in the literature are focused on the local failure approaches.

According to the fundamentals of local failure approaches, material failure occurs when the key parameter (e.g., stress, strain, SED, etc.) at a critical distance from the geometrical discontinuity reaches a given critical value (Santecchia et al., 2016). These local approaches commonly follow three different methodologies namely, point method, line method, and volumetric method, performing the failure assessment in a single point, on a line, or in a control volume, respectively (Taylor, 2008; Berto and Lazzarin, 2009). SED has been widely used as one of the common key parameters for failure assessment of components made of various brittle, quasi-brittle, and ductile materials in the presence of geometrical discontinuities under static and fatigue loads (Berto and Lazzarin, 2009, 2014).

15.3.2 Strain energy density

To the best of the authors' knowledge, Beltrami proposed the application of strain energy density for failure assessment under pure tension and pure compression for the first time in 1885 (Beltrami, 1885). Later on, a point method failure criterion based on SED was proposed by Sih (1973). Lazzarin and Zambardi (2001) formulated a volumetric SED method, namely the Average Strain Energy Density (ASED) criterion. According to the ASED criterion, failure occurs when the averaged SED in a control volume around the notch or crack, reaches a critical value that is material dependent. This concept was later employed by Lazzarin and Zambardi (2001) and Lazzarin et al. (2003) to synthesize the fatigue data obtained by testing different geometries of welded joints. It was reported that the average SED in a control volume around the geometrical discontinuities can provide a fatigue master curve independent of the geometry of the notch. Having this master curve for each material, one can simply predict the fatigue life of different notch geometries without the necessity to perform new sets of experiments.

The evaluation of the local strain energy density needs precise information about the control volume size. From a theoretical point of view, the material properties in the vicinity of the notch root depend on a number of parameters such as residual stresses and distortions, heterogeneous metallurgical microstructures, thermal cycles, heat source characteristics, load histories, internal defects, surface roughness, and so on. To devise a model capable of predicting the size of the control volume and fatigue life of AM components based on all these parameters is a complicated task. Thus, the spirit of the approach is to give a simplified method able to summarize the fatigue life of components only on the basis of geometrical information, treating all the other effects only in statistical terms, with reference to a well-defined group of AM materials and, for the time being in this discussion, limited to as-built L-PBF and machined DED components.

According to the formulation of the ASED criterion, the critical radius around the notch tip can be calculated using the fatigue strengths of two sets of reference specimens, namely smooth (rounded) and V-notch specimens. In this way, the influence of defects and surface roughness in the material, in the absence of any global stress concentration effect would be captured in the fatigue data obtained from testing smooth specimens (Lazzarin and Zambardi, 2001). Fig. 15.7 illustrates the representative control volumes for different notch geometries in plane problems, in which 2α is the notch opening angle, ρ is the notch root radius, R_0 is the size of control volume (critical radius), and r_0 is the distance between the notch root and the center of the control volume in blunt notch defined as $r_0 = \rho \times (\pi - 2\alpha)/(2\pi - 2\alpha)$. In case of cracks ($2\alpha = 0$, $\rho = 0$) and sharp notches ($\rho = 0$), the control volume is considered as a circle with a radius of R_0 centered at crack/notch tip, while for blunt notches under mode I

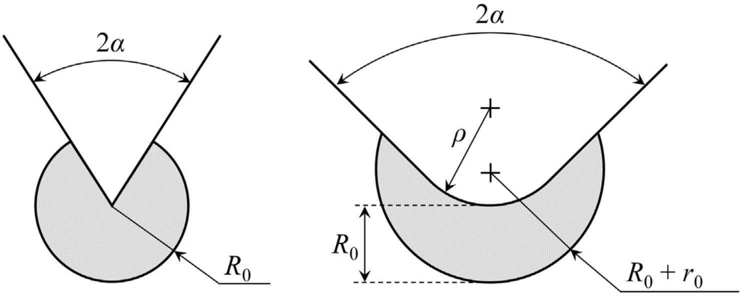

Figure 15.7 Schematic illustration of control volume around sharp V-notch and blunt V-notch under mode I loading condition (Berto and Lazzarin, 2009).

loading (tension mode), the control volume is a crescent with an external radius of ($R_0 + r_0$) and a maximum width of R_0 measured along the notch bisector line. In plane-strain condition, the critical radius R_0 can be calculated using the following equation (Lazzarin and Zambardi, 2001):

$$R_0 = \left(\frac{\sqrt{2e_1}\Delta K_{1A}^{V}}{\Delta\sigma_A} \right)^{\frac{1}{1-\lambda_1}} \tag{15.1}$$

in which e_1 is dependent on the notch opening angle 2α, ΔK_{1A}^{V} is the mode I Notch Stress Intensity Factor (NSIF) range of notched specimen at fatigue limit, $\Delta\sigma_A$ is the fatigue strength of smooth specimens (calculated in the net section), and λ_1 is the Williams' series eigenvalue (Williams, 1952).

The ASED range for smooth specimens is defined as

$$\Delta\overline{W_1} = (\Delta\sigma)^2 / 2E \tag{15.2}$$

in which $\Delta\sigma$ is the stress range (calculated in the net section) and E is the elastic modulus of material. For sharp notches under mode I loading, the average SED value in the control volume can be theoretically calculated using the following equation (Lazzarin et al., 2003):

$$\Delta\overline{W}_1 = \frac{e_1}{E} \left(\frac{\Delta K_1^V}{R_0^{1-\lambda_1}} \right)^2 \tag{15.3}$$

The average SED for blunt notches can be analytically expressed as a function of tensile stress range at the notch tip under mode I loading (Lazzarin and Berto, 2005)

$$\Delta\overline{W}_1 = F(2\alpha) \times H\left(2\alpha, \frac{R_0}{\rho}\right) \times \frac{\Delta\sigma_{tip}^2}{E} \tag{15.4}$$

where F is a function dependent on notch opening angle, 2α, H is a function dependent on notch opening angle, 2α and the ratio of critical radius to notch root radius, R_0/ρ, and $\Delta\sigma_{tip}$ is the tensile stress range at the notch tip.

Lazzarin et al. (2003, 2004, 2008) and Livieri and Lazzarin (2005) investigated the applicability of the ASED criterion for fatigue failure prediction of welded joints with different geometries. The weldment geometries exhibited a strong variability of the main plate thickness (6—100 mm), the transverse plate (3—200 mm), and the bead flank (0—150 degrees). By re-analyzing the experimental results taken from the literature on pulsating fatigue (zero loading ratio, $R = 0$), they reported a mean value of $\Delta K_{1A}^{N} = 211$ MPa mm$^{0.326}$ at $N_A = 5 \times 10^6$ cycles, whereas a mean fatigue strength value of $\Delta\sigma_A = 155$ MPa (at $N_A = 5 \times 10^6$ cycles, with $R = 0$) obtained from butt ground ferritic steel welds was employed for setting the ASED method. Then, by introducing the above-mentioned value into Eq. (15.1), a critical radius of $R_0 = 0.28$ mm was obtained for steel welded joints with failures from the weld toe.

Using only the simplified geometry of the weld toe as sharp V-notches, more than 900 fatigue data from welded joints with weld toe and weld root failures were analyzed using ASED criterion (Berto and Lazzarin, 2009). Fig. 15.8 illustrates a synthesis of all those data where fatigue life is given as a function of $\Delta\overline{W}_1$. The master curve in Fig. 15.8 includes fatigue data obtained both under tension and bending loads for "as-welded" and "stress-relieved" welds. The scatter index T_W (the ratio between the stress level corresponding to $P_S = 2.3\%$ and 97.7% probabilities of survival) of the obtained master curve is 3.3, to be compared with the variation of the strain energy density range, from about 4 to about 0.1 MJ/m^3. The ASED scatter band of 3.3 becomes equal to 1.50 when reconverted to an equivalent local stress range with probabilities of survival $P_S = 10\%$ and 90% ($T_W = \sqrt{3.3}/1.21 = 1.5$). Considering the relatively small scatter index, a good agreement is found, giving a sound, robust basis to the approach.

According to the numerous research studies on the application of ASED criterion for failure prediction of different materials, various advantages have been reported for this criterion, from which the simplicity of the method, in addition to its ability to take into account the effect of load ratio, multiple crack initiation, T-stress, and higher-order terms of stress, mode mixity, and capability of the criterion to consider the scale effect and three-dimensional effects can be pointed out.

To summarize the ASED criterion for fatigue design, by performing fatigue experiments on two sets of specimens, i.e., smooth and sharp notched specimens, the critical radius can be calculated using Eq. (15.1) and the fitting constants of the ASED-life

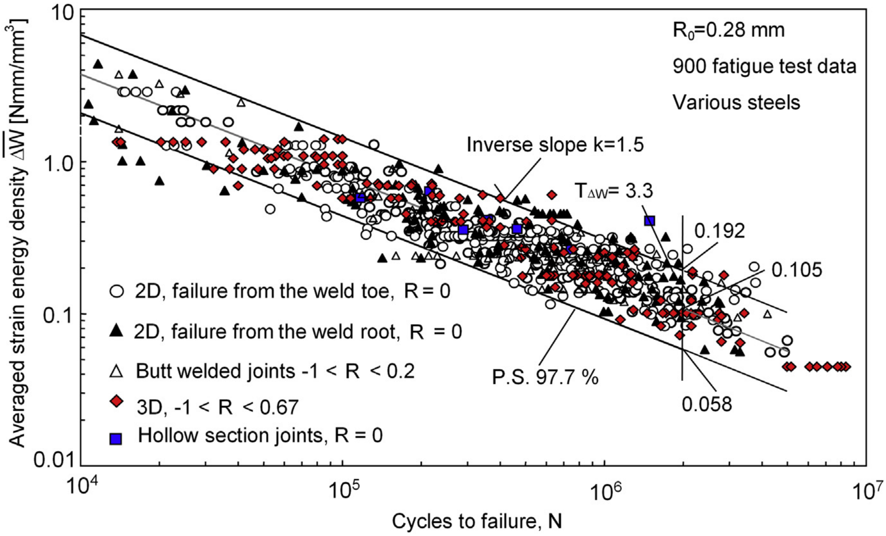

Figure 15.8 Fatigue strength of welded joints as a function of the averaged local strain energy density; R is the nominal load ratio (Berto and Lazzarin, 2009).

formula can be derived $\overline{W} = AN_f^B$. This equation can then be used to predict the fatigue behavior of other notched components with different geometries made by the same material and fabrication process.

15.3.3 Numerical method

As an alternative for theoretical ASED calculation, one may use finite element (FE) analysis to directly obtain this value by performing linear elastic finite element analysis on the notched models. In order to calculate the NSIF range in Eqs. (15.1) and (15.3), linear elastic stress analysis should be performed. In this case, due to the dependency of the accuracy of stress results to mesh size, mesh convergence analysis is required to obtain the proper element size. By obtaining the critical radius using Eq. (15.1), the control volume can be introduced in the FE model by partitioning the model. The averaged SED value can then be obtained from FE results by simply dividing the strain energy value in the control volume to the volume of the control volume. As reported by Lazzarin et al. (2008), the ASED value is independent of the mesh size. Therefore, the FE analysis to obtain ASED can be performed using models meshed with coarser elements compared to the first set of stress analysis. It is worth mentioning that due to the linear elastic nature of ASED criterion for HCF, and according to Eqs. (15.2)−(15.4), SED is proportional to the square of the applied nominal stress. Therefore, to plot ASED-life data for a notch geometry, only one FE analysis under a known applied stress should be performed and the rest of fatigue data can be expressed in the form of ASED using the relation given below:

$$\Delta\overline{W}|_{EXP} = \Delta\overline{W}|_{FEM} \times \left(\frac{\Delta\sigma|_{EXP}}{\Delta\sigma|_{FEM}}\right)^2 \tag{15.5}$$

where $\Delta\overline{W}|_{EXP}$ is the ASED range for the notched specimen with fatigue strength of $\Delta\sigma|_{EXP}$ and $\Delta\overline{W}|_{FEM}$ is the numerical ASED range for the FE model loaded under the nominal applied stress range of $\Delta\sigma|_{FEM}$. The flowchart of ASED calculation is given in Fig. 15.9.

Since one of the biggest advantages of the ASED method compared to stress-based methodologies is its independency to the mesh size, structural components with very complex geometries can be analyzed using this method with considerably lower run time compared to stress analysis of notched components. In this regard, to overcome the first set of stress analysis for obtaining the NSIF, an alternative method can be used. According to the basic concept of ASED criterion, regardless of the geometry of the tested parts, their fatigue data should follow a single master curve when plotted in the form of ASED versus fatigue life (see Fig. 15.8). In this scenario, all geometries are expected to have similar ASED values at the fatigue limit. Therefore, by referring to the fatigue strength of the smooth and double V-notched samples at the fatigue limit,

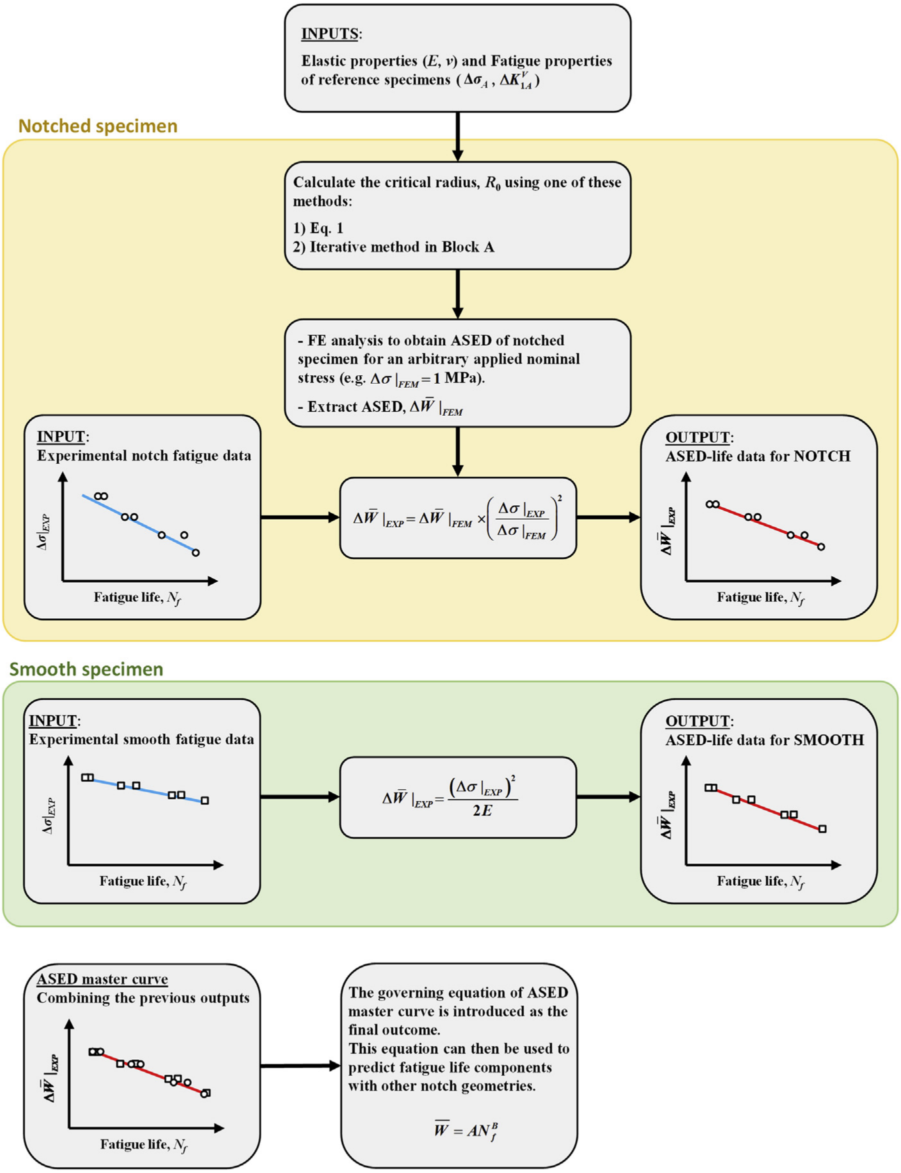
INPUTS:
Elastic properties (E, ν) and Fatigue properties of reference specimens ($\Delta\sigma_A$, ΔK^V_{1A})
Notched specimen
Calculate the critical radius, R_0 using one of these methods:
1) Eq. 1
2) Iterative method in Block A
- FE analysis to obtain ASED of notched specimen for an arbitrary applied nominal stress (e.g. $\Delta\sigma|_{FEM} = 1$ MPa).
- Extract ASED, $\Delta\overline{W}|_{FEM}$
INPUT:
Experimental notch fatigue data
$\Delta\sigma|_{EXP}$
Fatigue life, N_f
$\Delta\overline{W}|_{EXP} = \Delta\overline{W}|_{FEM} \times \left(\frac{\Delta\sigma|_{EXP}}{\Delta\sigma|_{FEM}}\right)^2$
OUTPUT:
ASED-life data for NOTCH
$\Delta\overline{W}|_{EXP}$
Fatigue life, N_f
Smooth specimen
INPUT:
Experimental smooth fatigue data
$\Delta\sigma|_{EXP}$
Fatigue life, N_f
$\Delta\overline{W}|_{EXP} = \frac{(\Delta\sigma|_{EXP})^2}{2E}$
OUTPUT:
ASED-life data for SMOOTH
$\Delta\overline{W}|_{EXP}$
Fatigue life, N_f
ASED master curve
Combining the previous outputs
$\Delta\overline{W}|_{EXP}$
Fatigue life, N_f
The governing equation of ASED master curve is introduced as the final outcome.
This equation can then be used to predict fatigue life components with other notch geometries.
$\overline{W} = AN_f^B$

Figure 15.9 Flowchart of fatigue analysis based on ASED criterion.

the R_0 value can be obtained by equating the ASED value of the smooth and notched specimen according to the following equation:

$$\Delta\overline{W}_A^{smooth} = \frac{(\Delta\sigma_A)^2}{2E} = \Delta\overline{W}_A^{V-notch}(R_0) \tag{15.6}$$

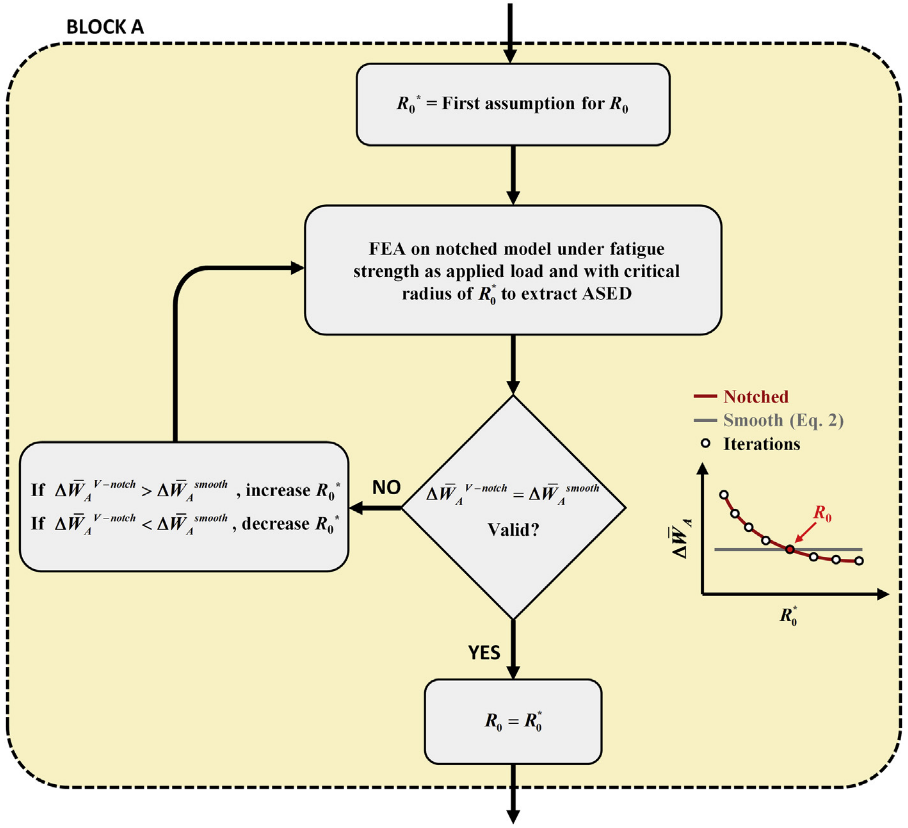
BLOCK A
R_0^* = First assumption for R_0
FEA on notched model under fatigue strength as applied load and with critical radius of R_0^* to extract ASED
If $\Delta\overline{W}_A^{V-notch} > \Delta\overline{W}_A^{smooth}$, increase R_0^*
If $\Delta\overline{W}_A^{V-notch} < \Delta\overline{W}_A^{smooth}$, decrease R_0^*
NO
$\Delta\overline{W}_A^{V-notch} = \Delta\overline{W}_A^{smooth}$
Valid?
YES
$R_0 = R_0^*$
Notched
Smooth (Eq. 2)
Iterations
$\Delta\overline{W}_A$
R_0
R_0^*

Figure 15.9 cont'd.

where $\Delta\overline{W}_A^{smooth}$ is the ASED value of smooth specimen calculated using fatigue strength of the smooth sample, $\Delta\sigma_A$, E is elastic modulus, and $\Delta\overline{W}_A^{V-notch}(R_0)$ is the ASED value obtained from the reference notch model (i.e., V-notch) with a control radius of R_0 loaded under experimental fatigue strength of the notched specimens. Eq. (15.6) should then be calculated numerically by varying the critical radius value until the ASED over the sector of radius R_0 is equal to $\Delta\overline{W}_A^{smooth}$. Doing so, the control radius can be calculated without the need for stress analysis (see block A in Fig. 15.9).

15.4 Energy-based fatigue prediction of complex AM components

The investigation of the overall fatigue strength of AM components is still challenging because it depends not only on the local geometry but also on the microstructural features of the material in the vicinity of the critical zones. In these regions, characteristics of the fusion zone, defects, alternation of coarse and fine grains, and residual stresses play primary roles. The volumetric local approaches such as ASED are thought to account for the mentioned factors by the help of averaging all material inhomogeneities, resulting in the criterion to be valid for the multiscale design of components. The key challenge and novelty of future research studies on this topic would be creating a rigorous link between R_0 and the microstructural features/properties of additively manufactured materials in the notch regions in order to devise an efficient numerical tool capable of accurately assessing fatigue strength and quality of complex components weakened by geometrical discontinuities of all kinds.

Initial studies on the application of ASED for fatigue prediction of AM specimens in the presence of geometrical discontinuities have revealed its capability in fulfilling this aim. In this context, the ASED criterion was applied to assess the fatigue behavior of three different test specimens namely smooth, semicircular, and blunt V- notch made by the L-PBF process (Razavi et al., 2017; Razavi et al., 2018; Razavi, 2019). The schematic geometries of the test specimens are given in Fig. 15.10. The reported Wöhler curves of the tested specimens are illustrated in Fig. 15.11a and the detailed fatigue properties are reported in Table 15.1. It is worth mentioning that the test specimens were all sandblasted and subjected to stress-relieving heat treatment to eliminate the residual stresses. As expected, the presence of notches in the test specimens resulted in a reduction of fatigue strength due to intensified stress levels in the vicinity of the notch tip.

The critical radius of $R_0 = 0.329$ mm was calculated for L-PBF materials using the formulation given in Section 15.3. The results of ASED analysis with confidence bands of 10%, 50%, and 90% are presented in Fig. 15.11b. By using the fatigue data in a range from 10^4 to 10^6 and considering the probabilities of survival $Ps = 10\%$ and 90%, energy-based scatter indexes, T_W of 1.46 was obtained for L-PBF specimens. The obtained scatter bands have reasonably small values compared

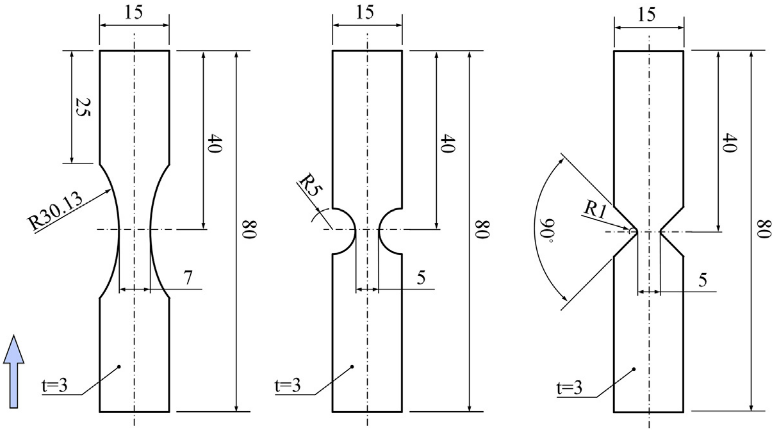

Figure 15.10 Geometrical dimensions of the fatigue test specimens (the build direction is shown with *arrow*).

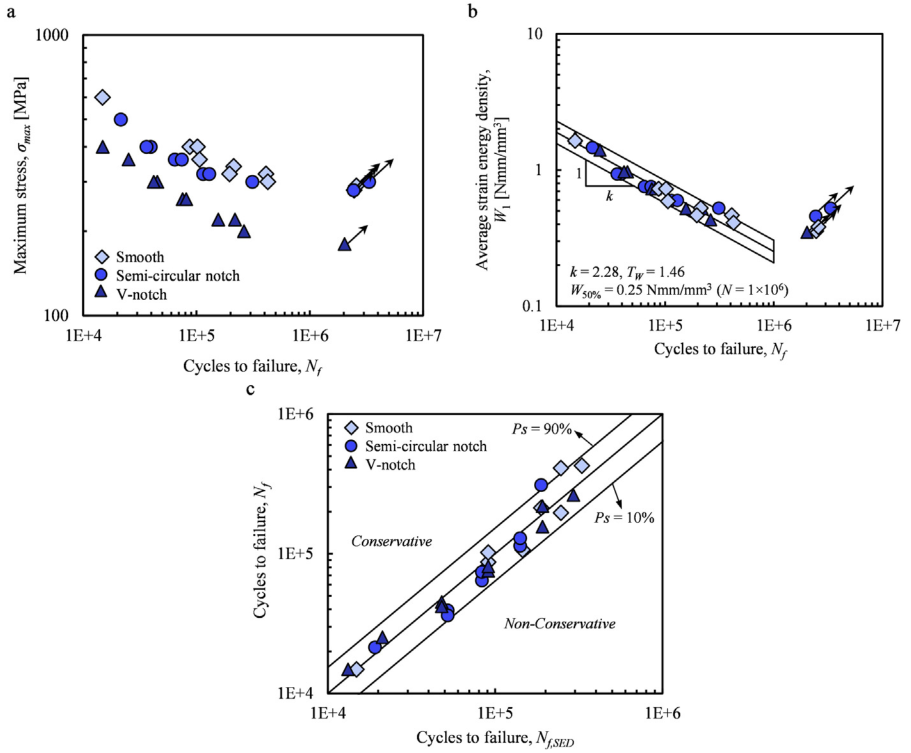

Figure 15.11 (a) Experimental fatigue data from different Ti6Al4V specimen geometries made by L-PBF process ($R = 0.01$) (Razavi et al., 2017; Razavi et al., 2018), (b) Synthesis of fatigue data based on ASED; (c) the accuracy of ASED criterion in predicting the fatigue life of the tested specimens (Razavi, 2019). In (c), the scatter bands with 10%, 50%, and 90% probability of survival were obtained from the test results of reference specimens (here smooth and V-notch specimens).

Table 15.1 Detailed fatigue properties of stress-relieved L-PBF Ti6Al4V specimens with sandblasted surface (Razavi et al., 2017; Razavi et al., 2018).

	K_t[a]	$\Delta\sigma_{50\%}$[b] [MPa]	T_σ[c]	k[d]
Smooth	1.073	243	1.38	4.74
Semicircular notch	1.308	213	1.39	4.88
V-notch	2.279	144	1.18	4.15

[a] Stress concentration factor considering the stress in the net section of the specimens.

[b] Fatigue strength: stress amplitude related to a survival probability of 50% at one million cycles.

[c] Ratio between the stress amplitudes corresponding to 10% and 90% of survival probability.

[d] Inverse slope of the Wöhler curve.

to the values reported in the open literature for steel notched components (Berto and Lazzarin, 2009). This scatter index becomes equal to 1.21 when reconverted to an equivalent local stress range with the same probability of survival ($T_\sigma = \sqrt{T_W}$), which is a reasonably small value compared to the stress-based curves in Fig. 15.11a.

By performing ASED analysis on the reference specimens, i.e., smooth and V-notched specimens, the constants of the ASED-life formula (i.e., $\overline{W} = AN_f^B$) were obtained and found to be $A = 119.73$ and $B = -0.447$. These data can then be used to predict the fatigue behavior of other notched components made by the same material and process parameters. The obtained theoretical results for different geometries of test specimens are summarized in the experimental, N_f, versus estimated, $N_{f,SED}$ fatigue life plots illustrated in Fig. 15.11c. The fatigue predictions are seen to fall always within the parent scatter band obtained from the reference specimens.

Despite the presence of surface roughness and possible internal defects in the specimens, the volumetric ASED criterion provided very good fatigue life predictions for notched specimens by considering the mentioned factors as an input for analyses. As stated earlier, the effect of surface roughness and internal defects was incorporated in the model by use of the fatigue data from smooth specimens.

In a separate research, the fatigue behavior of Ti6Al4V specimens produced by the DED process was evaluated by Razavi and Berto (2019). For this aim, they produced vertical prisms of 81 mm × 16 mm × 4 mm dimension, and the test specimens with similar geometries as the previous research (see Fig. 15.10) were machined out of the prisms. All test specimens, in this case, were subjected to stress-relieving treatment. The difference between the DED research and the former research on L-PBF specimens is the surface condition of the specimens and the process-related microstructure of the fabricated material (see Figs. 15.2 and 15.3). The fatigue tests were performed on machined DED specimens and specimens fabricated from wrought Ti6Al4V, and the results are presented in Fig. 15.12a and b. Table 15.2 represents the detailed fatigue properties of the tested specimens. Based on the fatigue data, critical radii of $R_0 = 0.366$ mm and 0.538 mm were reported, respectively, for DED and wrought materials. The resulting master curves using the mentioned critical radii are presented in Fig. 15.12c and d. All fatigue data were presented in scatter bands of $T_W = 2.07$ and 1.63 for DED and wrought specimens, respectively. Once again, converting the SED scatter indexes to an equivalent local stress range results gives $T_\sigma = 1.44$ and 1.28 which are reasonably small values in comparison with the scatters of stress-based curves in Fig. 15.12a and b. The ASED-life formulae for the DED and wrought materials are $\overline{W} = 67.02N_f^{-0.308}$ and $\overline{W} = 181.04N_f^{-0.419}$, respectively. The fatigue life predictions are then presented in Fig. 15.12e and f. The fatigue life predictions for wrought specimens always fall within the parent scatter band of the reference specimens. However, more conservative predictions were observed for semicircular specimens made by DED. Since the AM parts in this research have shown a negligible amount of internal porosity, we basically do not face the challenges related to the presence of defects. In this case, by considering AM material as a new input material for theoretical analysis, an engineering prediction of fatigue life can be obtained by the use of the ASED method.

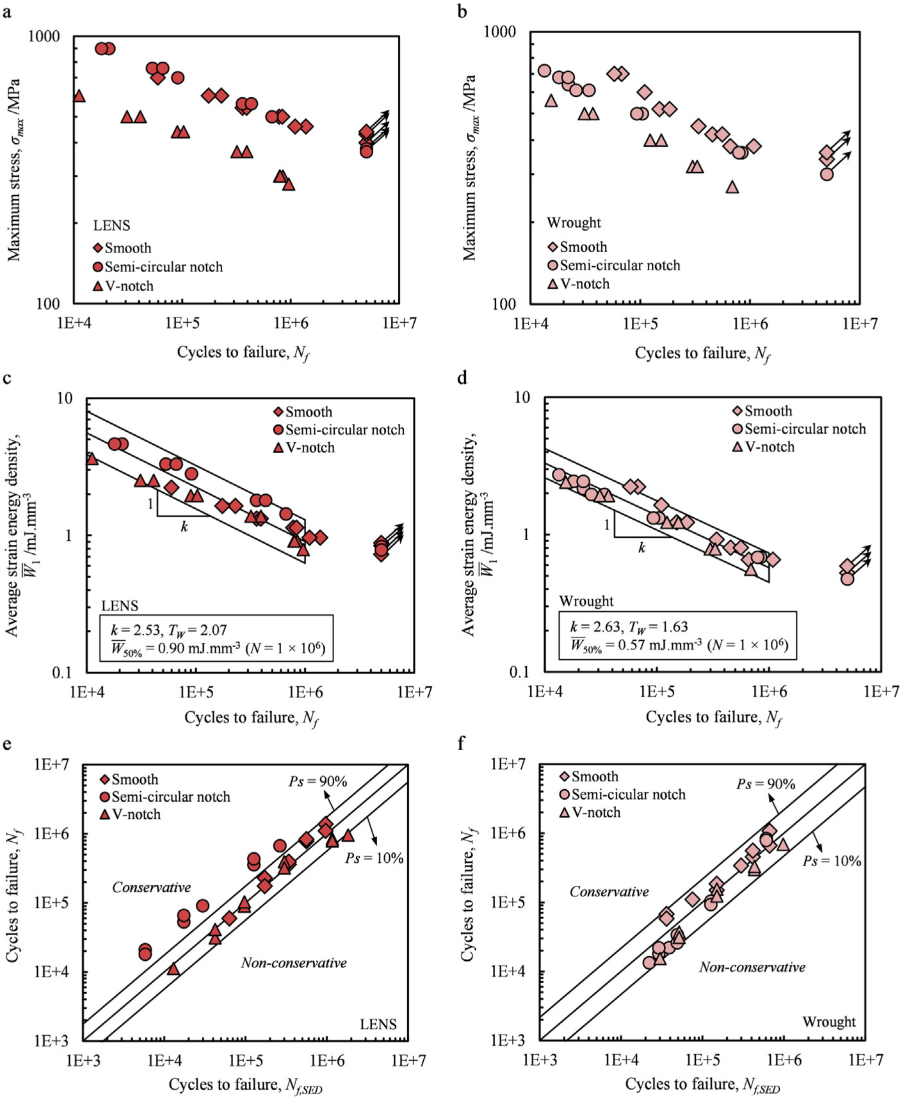

Figure 15.12 Fatigue data from different specimen geometries made by (a) DED process and (b) wrought material ($R = 0.01$). Synthesis of fatigue data based on ASED; (c) DED specimens, (d) wrought specimens. The accuracy of ASED criterion in predicting the fatigue life of the tested specimens; (e) DED, (f) wrought. In (e) and (f) the scatter bands with 10%, 50%, and 90% probability of survival were obtained from the test results of smooth and V-notch specimens (Razavi and Berto, 2019).

It is worth mentioning that the size of the control volume is dependent on the material microstructure, surface condition, and internal porosity (Razavi et al., 2021). In this scenario, a direct comparison of R_0 values in the reported studies cannot be performed due to the variation of more than one influencing factor. Generally

Table 15.2 Detailed fatigue properties of stress-relieved DED and wrought Ti6Al4V specimens with machined surface (Razavi and Berto, 2019).

Material	Geometry	K_t	$\Delta\sigma_{50\%}$ [MPa]	T_σ	k
DED	Smooth	1.073	482	1.11	7.54
	Semicircular notch	1.308	477	1.11	6.15
	V-notch	2.279	293	1.20	6.05
Wrought	Smooth	1.073	345	1.19	3.99
	Semicircular notch	1.308	344	1.13	5.94
	V-notch	2.279	258	1.25	5.10

speaking, for each fabrication condition (i.e., AM process, process parameters, heat treatment, surface post-treatment, etc.) fatigue life analysis can be performed by having limited experimental data as input. The direct relation of each of the influencing factors on the fatigue properties (here R_0) requires further experimental and theoretical analyses in which the effect of each individual parameter is studied. To achieve this goal, machine learning is expected to be a feasible tool to construct a bridge between the fatigue data obtained from various conditions of processing and post-processing of AM components and R_0 as the key parameter for ASED analysis. Up to now, limited efforts have been made on the use of machine learning for prediction of fatigue behavior of metallic materials using miniature specimens without the presence of geometrical discontinuities (Abendroth and Kuna, 2006; Liao et al., 2008; Partheepan et al., 2011; Wan et al., 2019). In this scenario, a combination of simple theoretical tools such as ASED criterion and machine learning can extend the possibilities of design of AM components against fatigue.

15.5 Conclusions

Several key factors such as global geometrical discontinuities (i.e., notch and crack), local geometrical discontinuities (i.e., surface roughness and internal defects), microstructure, and residual stress govern the fatigue failure of different mechanical structures. Hence, a practical way for fatigue assessment of these components would be to employ a general failure criterion that can take into account all these factors by use of limited experimental information as input.

In this chapter, the applicability of a local approach based on the strain energy density for the fatigue assessment of AM components has been discussed showing the potential of the approach and also the logic flow for its systematic application. The key feature of this unifying approach has been described in detail with reference to additively manufactured materials and structures. Some interesting points have been also mentioned as possible future developments. The approach can be further improved considering realistic materials, constitutive laws, as well as a real distribution of defects characterizing a representative volume element for the material.

15.6 Questions

- Name four factors that contribute to the inconsistency in fatigue behavior of L-PBF parts.
- What are the main reasons for geometrical-dependent properties of AM components?
- Which is the proper logic flow for an efficient application of the strain energy density criterion for the fatigue assessment of notched components?
- Describe the advantages and drawbacks of using strain energy density criterion for fatigue evaluation of L-PBF parts.
- What are the pros and cons of using data-driven approaches combined with strain energy density for the fatigue design of L-PBF parts?

References

Abendroth, M., Kuna, M., 2006. Identification of ductile damage and fracture parameters from the small punch test using neural networks. Eng. Fract. Mech. https://doi.org/10.1016/j.engfracmech.2005.10.007.

Ali, H., et al., 2017. In-situ residual stress reduction, martensitic decomposition and mechanical properties enhancement through high temperature powder bed pre-heating of selective laser melted Ti6Al4V. Mater. Sci. Eng. A. https://doi.org/10.1016/j.msea.2017.04.033.

Ali, H., Ghadbeigi, H., Mumtaz, K., 2018. Residual stress development in selective laser-melted Ti6Al4V: a parametric thermal modelling approach. Int. J. Adv. Manuf. Technol. https://doi.org/10.1007/s00170-018-2104-9.

Anil, S., et al., 2011. Dental implant surface enhancement and osseointegration. In: Implant Dentistry - A Rapidly Evolving Practice. https://doi.org/10.5772/16475.

Antonysamy, A.A., Meyer, J., Prangnell, P.B., 2013. Effect of build geometry on the β-grain structure and texture in additive manufacture of Ti6Al4V by selective electron beam melting. Mater. Char. https://doi.org/10.1016/j.matchar.2013.07.012.

Bagherifard, S., et al., 2018. On the fatigue strength enhancement of additive manufactured AlSi10Mg parts by mechanical and thermal post-processing. Mater. Des. 145, 28–41. https://doi.org/10.1016/j.matdes.2018.02.055.

Beltrami, E., 1885. Sulle condizioni di resistenza dei corpi elastici. Il Nuovo Cimento. https://doi.org/10.1007/BF02824697.

Berto, F., Lazzarin, P., 2009. A review of the volume-based strain energy density approach applied to V-notches and welded structures. Theor. Appl. Fract. Mech. https://doi.org/10.1016/j.tafmec.2009.10.001.

Berto, F., Lazzarin, P., 2014. Recent developments in brittle and quasi-brittle failure assessment of engineering materials by means of local approaches. Mater. Sci. Eng. R Rep. https://doi.org/10.1016/j.mser.2013.11.001.

Berto, F., Razavi, S.M.J., Torgersen, J., 2018. Frontiers of fracture and fatigue: some recent applications of the local strain energy density. Frat. Ed. Integrità Strutt. 12 (43). https://doi.org/10.3221/IGF-ESIS.43.01.

Bontha, S., et al., 2006. Thermal process maps for predicting solidification microstructure in laser fabrication of thin-wall structures. J. Mater. Process. Technol. https://doi.org/10.1016/j.jmatprotec.2006.03.155.

Bontha, S., et al., 2009. Effects of process variables and size-scale on solidification microstructure in beam-based fabrication of bulky 3D structures. Mater. Sci. Eng. A. https://doi.org/10.1016/j.msea.2009.02.019.

Chan, K.S., et al., 2013. Fatigue life of titanium alloys fabricated by additive layer manufacturing techniques for dental implants. Metall. Mater. Trans. A Phys. Metall. Mater. Sci. https://doi.org/10.1007/s11661-012-1470-4.

Denlinger, E.R., et al., 2015. Effect of inter-layer dwell time on distortion and residual stress in additive manufacturing of titanium and nickel alloys. J. Mater. Process. Technol. https://doi.org/10.1016/j.jmatprotec.2014.07.030.

Du Plessis, A., 2019. Effects of process parameters on porosity in laser powder bed fusion revealed by X-ray tomography. Addit. Manuf. https://doi.org/10.1016/j.addma.2019.100871.

Du Plessis, A., Yadroitsava, I., Yadroitsev, I., 2020. Effects of defects on mechanical properties in metal additive manufacturing: a review focusing on X-ray tomography insights. Mater. Des. https://doi.org/10.1016/j.matdes.2019.108385.

Edwards, P., Ramulu, M., 2014. Fatigue performance evaluation of selective laser melted Ti-6Al-4V. Mater. Sci. Eng. A. https://doi.org/10.1016/j.msea.2014.01.041.

Fox, J.C., Moylan, S.P., Lane, B.M., 2016. Effect of process parameters on the surface roughness of overhanging structures in laser powder bed fusion additive manufacturing. Procedia CIRP. https://doi.org/10.1016/j.procir.2016.02.347.

Frazier, W.E., 2014. Metal additive manufacturing: a review. J. Mater. Eng. Perform. https://doi.org/10.1007/s11665-014-0958-z.

Galarraga, H., et al., 2016. 'Effects of the microstructure and porosity on properties of Ti-6Al-4V ELI alloy fabricated by electron beam melting (EBM)'. Addit. Manuf. https://doi.org/10.1016/j.addma.2016.02.003.

Gittens, R.A., et al., 2014. Implant osseointegration and the role of microroughness and nanostructures: lessons for spine implants. Acta Biomater. https://doi.org/10.1016/j.actbio.2014.03.037.

Heigel, J.C., Michaleris, P., Reutzel, E.W., 2015. Thermo-mechanical model development and validation of directed energy deposition additive manufacturing of Ti-6Al-4V. Addit. Manuf. https://doi.org/10.1016/j.addma.2014.10.003.

Herzog, D., et al., 2016. Additive manufacturing of metals. Acta Mater. https://doi.org/10.1016/j.actamat.2016.07.019.

Hrabe, N., Gnäupel-Herold, T., Quinn, T., 2017. 'Fatigue properties of a titanium alloy (Ti–6 Al–4V) fabricated via electron beam melting (EBM): effects of internal defects and residual stress. Int. J. Fatig. 94, 202–210. https://doi.org/10.1016/j.ijfatigue.2016.04.022.

Kasperovich, G., Hausmann, J., 2015. Improvement of fatigue resistance and ductility of TiAl6V4 processed by selective laser melting. J. Mater. Process. Technol. https://doi.org/10.1016/j.jmatprotec.2015.01.025.

Khorasani, A.M., et al., 2019. Investigation on the effect of heat treatment and process parameters on the tensile behaviour of SLM Ti-6Al-4V parts. Int. J. Adv. Manuf. Technol. https://doi.org/10.1007/s00170-018-3162-8.

Kobryn, P.A., Semiatin, S.L., 2001. Mechanical properties of laser-deposited Ti-6Al-4V. Solid Freeform Fab. Proc. 179–186. https://doi.org/10.26153/tsw/3261.

Lazzarin, P., et al., 2008. Some advantages derived from the use of the strain energy density over a control volume in fatigue strength assessments of welded joints. Int. J. Fatig. https://doi.org/10.1016/j.ijfatigue.2007.10.012.

Lazzarin, P., Berto, F., 2005. Some expressions for the strain energy in a finite volume surrounding the root of blunt V-notches. Int. J. Fract. https://doi.org/10.1007/s10704-005-3943-6.

Lazzarin, P., Lassen, T., Livieri, P., 2003. A notch stress intensity approach applied to fatigue life predictions of welded joints with different local toe geometry. Fatig. Fract. Eng. Mater. Struct. https://doi.org/10.1046/j.1460-2695.2003.00586.x.

Lazzarin, P., Sonsino, C.M., Zambardi, R., 2004. A notch stress intensity approach to assess the multiaxial fatigue strength of welded tube-to-flange joints subjected to combined loadings. Fatig. Fract. Eng. Mater. Struct. https://doi.org/10.1111/j.1460-2695.2004.00733.x.

Lazzarin, P., Zambardi, R., 2001. A finite-volume-energy based approach to predict the static and fatigue behavior of components with sharp V-shaped notches. Int. J. Fract. 112 (3), 275−298. https://doi.org/10.1023/A:1013595930617.

Leuders, S., et al., 2013. On the mechanical behaviour of titanium alloy TiAl6V4 manufactured by selective laser melting: fatigue resistance and crack growth performance. Int. J. Fatig. https://doi.org/10.1016/j.ijfatigue.2012.11.011.

Leuders, S., et al., 2014. On the fatigue properties of metals manufactured by selective laser melting - the role of ductility. J. Mater. Res. https://doi.org/10.1557/jmr.2014.157.

Li, C., et al., 2018. Residual stress in metal additive manufacturing. Procedia CIRP. https://doi.org/10.1016/j.procir.2018.05.039.

Liao, X.L., Xu, W.F., Gao, Z.Q., 2008. Application of artificial neural network to forecast the tensile fatigue life of carbon material. Key Eng. Mater. https://doi.org/10.4028/www.scientific.net/kem.385-387.533.

Liu, S., Shin, Y.C., 2019. Additive manufacturing of Ti6Al4V alloy: a review. Mater. Des. https://doi.org/10.1016/j.matdes.2018.107552.

Livieri, P., Lazzarin, P., 2005. Fatigue strength of steel and aluminium welded joints based on generalised stress intensity factors and local strain energy values. Int. J. Fract. https://doi.org/10.1007/s10704-005-4043-3.

Maleki, E., et al., 2020. Surface post-treatments for metal additive manufacturing: progress, challenges, and opportunities. Addit. Manuf. https://doi.org/10.1016/j.addma.2020.101619.

Mercelis, P., Kruth, J.P., 2006. Residual stresses in selective laser sintering and selective laser melting. Rapid Prototyp. J. https://doi.org/10.1108/13552540610707013.

Murr, L.E., et al., 2009. Microstructures and mechanical properties of electron beam-rapid manufactured Ti-6Al-4V biomedical prototypes compared to wrought Ti-6Al-4V. Mater. Char. https://doi.org/10.1016/j.matchar.2008.07.006.

Pal, D., et al., 2014. An integrated approach to additive manufacturing simulations using physics based, coupled multiscale process modeling. J. Manuf. Sci. Eng. Trans. ASME. https://doi.org/10.1115/1.4028580.

Partheepan, G., Sehgal, D.K., Pandey, R.K., 2011. Quasi-non-destructive evaluation of yield strength using neural networks. Adv. Artif. Neural Syst. https://doi.org/10.1155/2011/607374.

Popov, V., et al., 2018. Effect of hot isostatic pressure treatment on the electron-beam melted Ti-6Al-4V specimens. Procedia Manuf. https://doi.org/10.1016/j.promfg.2018.02.102.

Puebla, K., et al., 2012. Effect of melt scan rate on microstructure and macrostructure for electron beam melting of Ti-6Al-4V. Mater. Sci. Appl. https://doi.org/10.4236/msa.2012.35038.

Rafi, H.K., et al., 2013a. Microstructures and mechanical properties of Ti6Al4V parts fabricated by selective laser melting and electron beam melting. J. Mater. Eng. Perform. https://doi.org/10.1007/s11665-013-0658-0.

Rafi, H.K., Starr, T.L., Stucker, B.E., 2013b. A comparison of the tensile, fatigue, and fracture behavior of Ti-6Al-4V and 15-5 PH stainless steel parts made by selective laser melting. Int. J. Adv. Manuf. Technol. https://doi.org/10.1007/s00170-013-5106-7.

Razavi, S.M.J., Ferro, P., Berto, F., 2017. Fatigue assessment of Ti−6Al−4V circular notched specimens produced by selective laser melting. Metals 7 (8). https://doi.org/10.3390/met7080291.

Razavi, S.M.J., et al., 2018. Fatigue strength of blunt V-notched specimens produced by selective laser melting of Ti-6Al-4V. Theor. Appl. Fract. Mech. 97, 376−384. https://doi.org/10.1016/j.tafmec.2017.06.021.

Razavi, S.M.J., 2019. Structural Integrity of Additively Manufactured Metallic Components under Fatigue Loading. Norwegian University of Science and Technology (NTNU).

Razavi, S.M.J., et al., 2021. Effect of heat treatment on fatigue behavior of as-built notched Co-Cr-Mo parts produced by selective laser melting. Int. J. Fatig. 142, 105926. https://doi.org/10.1016/j.ijfatigue.2020.105926.

Razavi, S.M.J., Berto, F., 2019. Directed energy deposition versus wrought Ti-6Al-4V: a comparison of microstructure, fatigue behavior, and notch sensitivity. Adv. Eng. Mater. https://doi.org/10.1002/adem.201900220.

Razavi, S.M.J., Van Hooreweder, B., Berto, F., 2020. Effect of build thickness and geometry on quasi-static and fatigue behavior of Ti-6Al-4V produced by Electron Beam Melting. Addit. Manuf. https://doi.org/10.1016/j.addma.2020.101426.

Sanaei, N., Fatemi, A., 2020. Defects in additive manufactured metals and their effect on fatigue performance: a state-of-the-art review. Prog. Mater. Sci. https://doi.org/10.1016/j.pmatsci.2020.100724.

Sandgren, H.R., et al., 2016. Characterization of fatigue crack growth behavior in LENS fabricated Ti-6Al-4V using high-energy synchrotron x-ray microtomography. Addit. Manuf. 12, 132−141. https://doi.org/10.1016/j.addma.2016.09.002.

Santecchia, E., et al., 2016. A review on fatigue life prediction methods for metals. Adv. Mater. Sci. Eng. 2016 https://doi.org/10.1155/2016/9573524.

Saunders, M., 2015. Minimal Manifolds - How to Shed Weight and Boost Performance. Available at: https://www.linkedin.com/pulse/minimal-manifolds-how-shed-weight-boost-performance-marc-saunders/.

Saunders, M., 2016. DfAM Essentials - Print Parts Efficiently and Effectively. Available at: https://www.linkedin.com/pulse/dfam-essentials-print-parts-efficiently-effectively-marc-saunders/.

Shalabi, M.M., et al., 2006. Implant surface roughness and bone healing: a systematic review. J. Dent. Res. https://doi.org/10.1177/154405910608500603.

Shrestha, R., et al., 2016. Effect of build orientation on the fatigue behavior of stainless steel 316L manufactured via a laser-powder bed fusion process. In: Solid Freeform Fabrication 2016: Proceedings of the 27th Annual International Solid Freeform Fabrication Symposium - An Additive Manufacturing Conference, SFF 2016.

Sih, G.C., 1973. A special theory of crack propagation: methods of analysis and solutions of crack problems. In: Sih, G.C. (Ed.), Mechanics of Fracture I. Noordhoff International Publishing, Leyden, pp. 21−45.

Stephens, R.I., et al., 2000. Metal Fatigue in Engineering, second ed. Engineering Computations.

Sterling, A.J., et al., 2016. Fatigue behavior and failure mechanisms of direct laser deposited Ti-6Al-4V. Mater. Sci. Eng. A 655, 100−112. https://doi.org/10.1016/j.msea.2015.12.026.

Taylor, D., 2008. The theory of critical distances. Eng. Fract. Mech. 75 (7), 1696−1705. https://doi.org/10.1016/j.engfracmech.2007.04.007.

Thijs, L., et al., 2010. A study of the microstructural evolution during selective laser melting of Ti-6Al-4V. Acta Mater. https://doi.org/10.1016/j.actamat.2010.02.004.

Wan, H.Y., et al., 2019. Data-driven evaluation of fatigue performance of additive manufactured parts using miniature specimens. J. Mater. Sci. Technol. 35 (6), 1137−1146. https://doi.org/10.1016/j.jmst.2018.12.011.

Williams, M., 1952. Stress singularities resulting from various boundary conditions in angular corners of plates in extension. J. Appl. Mech. 19 (4), 526−528.

Xu, W., et al., 2015. Ti-6Al-4V additively manufactured by selective laser melting with superior mechanical properties. J. Occup. Med. https://doi.org/10.1007/s11837-015-1297-8.

Yadollahi, A., et al., 2017. Effects of building orientation and heat treatment on fatigue behavior of selective laser melted 17-4 PH stainless steel. Int. J. Fatig. https://doi.org/10.1016/j.ijfatigue.2016.03.014.

Yadollahi, A., Shamsaei, N., 2017. Additive manufacturing of fatigue resistant materials: challenges and opportunities. Int. J. Fatig. https://doi.org/10.1016/j.ijfatigue.2017.01.001.

Zhai, Y., et al., 2016a. Fatigue crack growth behavior and microstructural mechanisms in Ti-6Al-4V manufactured by laser engineered net shaping. Int. J. Fatig. https://doi.org/10.1016/j.ijfatigue.2016.08.009.

Zhai, Y., Galarraga, H., Lados, D.A., 2015. Microstructure evolution, tensile properties, and fatigue damage mechanisms in Ti-6Al-4V alloys fabricated by two additive manufacturing techniques. Procedia Eng. 114, 658−666. https://doi.org/10.1016/j.proeng.2015.08.007.

Zhai, Y., Galarraga, H., Lados, D.A., 2016b. Microstructure, static properties, and fatigue crack growth mechanisms in Ti-6Al-4V fabricated by additive manufacturing: LENS and EBM’. Eng. Fail. Anal. https://doi.org/10.1016/j.engfailanal.2016.05.036.

Zheng, B., et al., 2008. Thermal behavior and microstructural evolution during laser deposition with laser-engineered net shaping: part I. Numerical calculations’. Metall. Mater. Trans. A 39 (9), 2228−2236. https://doi.org/10.1007/s11661-008-9557-7.

Lattice structures made by laser powder bed fusion

16

Mohammad J. Mirzaali[1], *Abolfazl Azarniya*[2], *Saeed Sovizi*[3], *Jie Zhou*[1],
Amir A. Zadpoor[1]
[1]Department of Biomechanical Engineering, Faculty of Mechanical, Maritime, and Materials Engineering, Delft University of Technology (TU Delft), Delft, the Netherlands; [2]Department of Mechanical Engineering, National University of Singapore, Singapore, Singapore; [3]Independent Researcher, Tehran, Iran

Chapter outline

16.1 Introduction 424
16.2 Geometrical design 425
  16.2.1 Library-based designs 425
    16.2.1.1 Strut-based unit cells 425
    16.2.1.2 Sheet-based unit cells 427
    16.2.1.3 Nonuniform designs 427
    16.2.1.4 Isotropy/anisotropy 428
  16.2.2 Topology optimization 428
  16.2.3 Metamaterials 429
  16.2.4 Bio-inspired design 429
16.3 Materials 430
  16.3.1 Biomedical metals and alloys 430
  16.3.2 Biodegradable metals 431
  16.3.3 Shape memory alloys 432
  16.3.4 Superalloys 433
  16.3.5 *In-situ* alloying and composites 433
16.4 Process-related effects 434
  16.4.1 Effects of processing parameters on internal porosity and microstructure 434
  16.4.2 Effects of strut orientation 436
  16.4.3 Chemical composition 436
16.5 Morphological properties 437
  16.5.1 Porosity 437
  16.5.2 Pore characteristics 438
16.6 Post-processing 438
  16.6.1 Residual stress relieving 438
  16.6.2 Heat treatments 439
  16.6.3 Hot isostatic pressing (HIP) 439
  16.6.4 Surface treatments 439
16.7 Physical properties 440
  16.7.1 Density 440

Fundamentals of Laser Powder Bed Fusion of Metals. https://doi.org/10.1016/B978-0-12-824090-8.00020-2
Copyright © 2021 Elsevier Inc. All rights reserved.

  16.7.2 Surface roughness 440

16.8 Mechanical properties 441
  16.8.1 Quasi-static mechanical properties 441
  16.8.2 Fatigue life 444

16.9 Computational modeling and analytical solutions 445

16.10 Applications 447
  16.10.1 Light-weight and load-bearing structures 447
  16.10.2 Biomedical 448

16.11 Conclusions 449

16.12 Questions 449

References 450

16.1 Introduction

Foam-like porous structures have been widely used in the past to design load-bearing cellular materials (both open- and closed-cell). These foam-like materials have been traditionally fabricated using conventional manufacturing techniques, including liquid-state processes (e.g., direct forming, spray forming) and solid-state processes (e.g., powder metallurgy, sintering of powders and fibers), or through electro- or vapor-deposition (Ryan et al., 2006; Banhart, 2001; Mirzaali et al., 2016a, 2017c). Although the statistical distribution of the sizes and the shape of the pores can be adjusted to some extent by changing the processing parameters of conventional techniques, such fabrication techniques suffer from multiple inherent limitations, the most important of which is the lack of form-freedom. Additive manufacturing (AM) processes, on the other hand, offer the freedom to precisely control the sizes and architecture of pores at the microscale (Bose et al., 2013; Murr et al., 2010; Zadpoor, 2017). AM processes also provide the opportunity to design organic geometries with complex internal architectures and passages that are otherwise impossible to create or control by using conventional manufacturing techniques, such as casting or molding (Gokuldoss et al., 2017).

In this chapter, we are primarily concerned with metallic lattice structures. Powder bed fusion processes are perhaps the most widely used AM techniques for the fabrication of such structures. Even though the energy source may be either an electron beam or a laser beam, we will focus on the laser beam—based powder bed fusion (L-PBF) process. The L-PBF technique allows for creating porous structures made of metals, polymers, or ceramics with complex microarchitectures at high resolutions (Frazier, 2014; Mirzaali et al., 2019a).

Although the L-PBF technique is generally considered to offer form-freedom, there are still some design constraints that need to be taken into account. Several guidelines (Kranz et al., 2015) have been proposed in the past to deal with the limitations of the L-PBF process and to define the processibility windows. The relevant topics in this regard include the minimum feature size (e.g., wall thickness, edges, and corners), the orientation of the lattice with respect to the build direction, the sizes of the overhangs, and the requirements regarding the design of support structures and their removal (Wang et al., 2016). Overhangs are one of the most important aspects that need to be carefully considered, as they can create undesired defects in lattices (Su et al., 2012; Calignano, 2014). In this context, overhangs refer to the parts of lattice structures that are not self-supporting. As the manufacturing process progresses, there are no solidified sections from the previous layers that support overhangs, making them susceptible to defect formation. Successful fabrication of overhangs is, therefore, often dependent on the proper choice of the fabrication angle (Su et al., 2012). For overhangs exceeding a specific size and having a smaller angle with the power bed than a specific threshold, support structures need to be used. These support structures need to be removed during post-processing, which can damage the AM parts.

16.2 Geometrical design

The development of lattice structures starts with geometrical design. Lattice structures can be categorized as being either open-cell or closed-cell. Only open-cell lattices can be fabricated using AM techniques, as it is impossible to remove the entrapped powder particles in fully closed-cell lattices. Several principles have been proposed for the geometrical design of lattice structures, which we will briefly review hereafter.

16.2.1 Library-based designs

Traditional design strategies include computer-aided design (CAD), implicit surfaces, and image-based design (Giannitelli et al., 2014). CAD-based design can be obtained using open-source or commercial CAD software. The CAD design may be transformed into the standard tessellation language (STL) format to facilitate the manufacturing processes. In addition to STL files, a vector-based approach (Ahmadi et al., 2017) can also be implemented to create laser scanning lines for 3D printing. There are several advantages to the vector-based approach as compared to STL files, including the easier manipulation of the files due to a smaller size of the geometry file, which may facilitate the design of more complex structures (see Chapter 5 for more information).

The final lattice structure may have either a regular or an irregular microarchitecture. Regular lattices are usually made by repeating one or more types of unit cells in different spatial directions. Several types of unit cells have been proposed in the past, such as cubic or prismatic unit cells. The unit cells can be categorized into two main types, namely strut-based (beam-based) or sheet-based. In irregular or random lattices, no specific repeating unit cells can be found.

16.2.1.1 Strut-based unit cells

Most metallic lattices studied to date are the beam-based ones, where beam-like structural elements (i.e., struts) are spatially arranged to create the basic unit cell

(Fig. 16.1a,b,e,f). The dimensions and spatial arrangement of the struts determine the geometry and topology (e.g., connectivity) of the repeating unit cell, the morphological parameters of the lattice structures (e.g., pore size, relative density), and the overall physical properties of the resulting porous materials (Maconachie et al., 2019). Some examples of strut-based unit cells are body centered cubic (BCC), face centered cubic (FCC) (Maskery et al., 2017; Zadpoor, 2019), cubic, diamond, and octet-truss (Yavari et al., 2015).

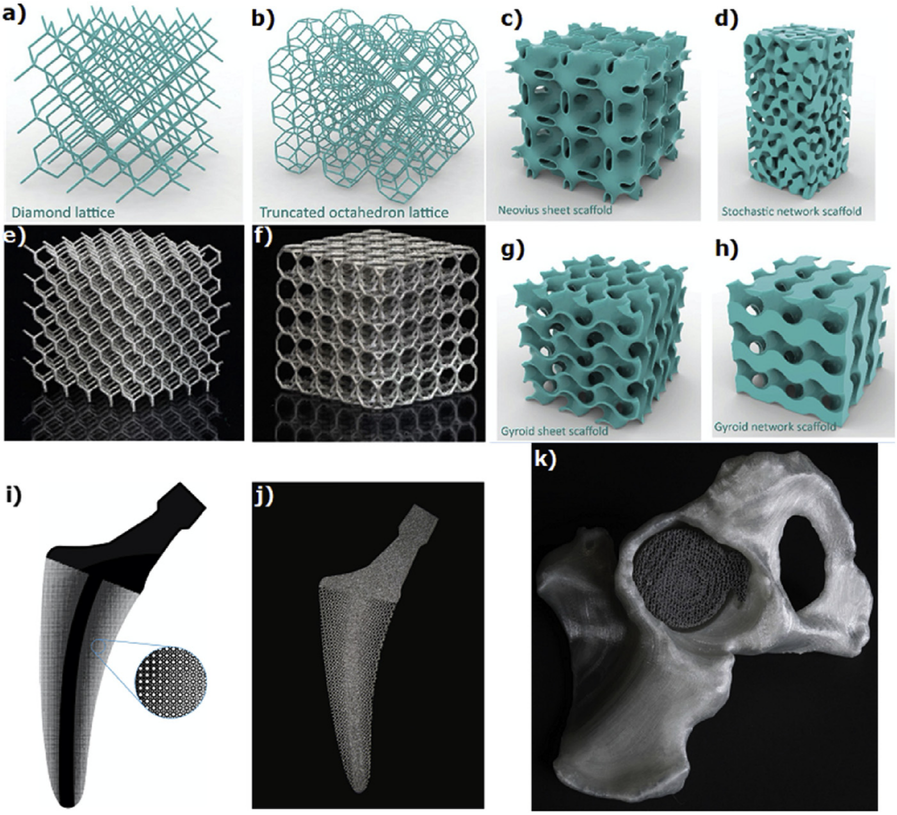
a)
Diamond lattice
b)
Truncated octahedron lattice
c)
Neovius sheet scaffold
d)
Stochastic network scaffold
e)
f)
g)
Gyroid sheet scaffold
h)
Gyroid network scaffold
i)
j)
k)

Figure 16.1 There are several strategies for the design of the microarchitectures of AM lattices. Examples include strut-based (a, b) and sheet-based (c, d, and g, h) CAD designs (Callens et al., 2020). These strut-based lattices can be fabricated by the L-PBF technique, for example, using Ti-alloys (e.g., Ti6Al4V (de Jonge et al., 2019) (e, f)). Another approach to the design of the microarchitecture of AM lattices is to apply optimization methods, which can result in functionally graded porous structures (i, j). The geometry of lattices can also be based on computed tomography (CT) images of spongy bone which allow for the fabrication of patient-specific implants (Zadpoor, 2017) (k).
(i, j) Reprinted from Garner et al., 2019. Copyright (2020), with permission from Elsevier.

From a mechanical viewpoint, lattice structures may be classified as being either bending-dominated or stretch-dominated. The elastic properties of stretch-dominated unit cells are higher than bending-dominated unit cells (Deshpande et al., 2001b). However, pure stretching or pure bending lattices can hardly be achieved, as there is usually a combination of bending and stretching in a unit cell. For a beam-based unit cell with s struts and n joints (i.e., strut intersections), the Maxwell number (i.e., $M = s - 3n + 6$) can be used to determine whether the unit cell is bending-dominated ($M < 0$) or stretch-dominated ($M \geq 0$) (Deshpande et al., 2001a).

16.2.1.2 Sheet-based unit cells

The structural elements constituting sheet-based unit cells are the surfaces (shells) that may be defined using mathematical equations. One class of sheet-based unit cells is the triply periodic minimal surfaces (TPMS) that offer a high level of flexibility in the design of lattice structures. In TPMS, pores are fully interconnected, making them suitable for tissue engineering applications (Kapfer et al., 2011; Yoo, 2011a,b; Bobbert et al., 2017). Another unique property of TPMS-based porous structures is that they exhibit a mean surface curvature of zero (Zadpoor, 2015; Bobbert et al., 2017). AM of high-quality TPMS geometries may be challenging due to the difficulties in achieving parts with high surface quality. Some examples of TPMS are primitive, I-WP, gyroid, Neovius, and diamond (Fig. 16.1c,g, and h).

16.2.1.3 Nonuniform designs

Both the type and dimensions of unit cells can be changed to create nonuniform lattice structures, such as those incorporating functional gradients. AM of porous structures with functional gradients has recently gained much attention (Choy et al., 2017; Loh et al., 2018), particularly for biomedical applications (Han et al., 2018; Monzón et al., 2018). Such graded designs can reduce stress concentrations and make it possible to satisfy contradictory design requirements. AM of functionally graded lattice structures is, however, challenging due to their geometrical complexity, particularly if stochastic or disordered design features are included.

Disordered lattice structures (Fig. 16.1d) may have some advantages over ordered lattices. First, random lattices offer a broader range of properties than the ordered ones, making it possible to change the properties more smoothly. For example, independent tuning of the elastic modulus and Poisson’s ratio can be more easily achieved using random networks (Mirzaali et al., 2017b). Second, due to their inherently irregular design, random networks are less susceptible to local defects resulting from the AM process. Finally, the design of random networks is simpler than ordered networks, particularly when several types of unit cells (e.g., stretch-dominated and bending-dominated) need to be combined.

16.2.1.4 Isotropy/anisotropy

The theoretical upper and lower bounds (i.e., C_1 and C_2) of isotropic porous structure in 3D can be defined in terms of their elastic modulus (E) and Poisson's ratio (ν) as $0 < \frac{E(\nu)}{3(1-2\nu)} < C_1, 0 < \frac{E(\nu)}{2(1+\nu)} < C_2$ (Hashin and Shtrikman, 1963), where,

$$C_1 = E_b\left(\frac{1}{3(1-2\nu_b)} + \frac{1-\phi}{\frac{(1-2\nu_b)(1+\nu_b)\phi}{(1-\nu_b)} - 3(1-2\nu_b)}\right),$$

$$C_2 = E_b\left(\frac{1}{2(1+\nu_b)} + \frac{1-\phi}{\frac{4(4-5\nu_b)(1+\nu_b)\phi}{15(1-\nu_b)} - 2(1+\nu_b)}\right)$$

E_b and ν_b are, respectively, the elastic modulus and Poisson's ratio of the base material, and ϕ is defined as the volume fraction of the lattice structure.

Anisotropic lattices may, however, be used to increase the load transfer efficiency of the lattice structures in specific directions. Such anisotropic lattices can exceed those limits in selected directions (Berger et al., 2017).

16.2.2 Topology optimization

Topology optimization can be used to computationally design optimal lattices. Several optimization approaches have been developed (Bendsoe and Sigmund, 2013), particularly using "inverse homogenization" techniques (Sánchez-Palencia, 1980; Bensoussan et al., 2011) that allow for finding a spatial arrangement of unit cells and material distribution, thereby giving rise to the desired (unusual) properties, such as a negative thermal expansion coefficient (Sigmund and Torquato, 1997).

Different objective functions can be used for the design of AM lattices. One such objective function is maximizing the specific stiffness (stiffness to mass ratio), which may result in lattices with trabecular bone-like microarchitectures (Garner et al., 2019; Wu et al., 2017a). There are optimization models based on bone tissue adaptation processes (Zadpoor et al., 2013; Zadpoor, 2013, 2017), which are useful for the design of bone substitutes (Fraldi et al., 2010; Chuah et al., 2010; Hollister et al., 2002) (Fig. 16.1i,j). Other objective functions, such as strain energy, can be used as well. Multi-physics topology optimization algorithms can optimize multiple objective functions simultaneously (Zhou et al., 2009), for example, to combine maximum bulk modulus or elastic modulus with specific values of permeability (Guest and Prévost, 2006; Ryan et al., 2006). There are several optimization techniques involved in finding the optimized topology of lattice structures with multifunctional properties, including evolutionary structural optimization (ESO) (Xie and Steven, 1993, 1997), solid isotropic material with penalization (SIMP) (Zhou and Rozvany, 1991; Bendsøe, 1989), bidirectional evolutionary structural optimization (BESO) (Huang et al., 2009;

Huang and Xie, 2007), and level-set algorithms (Wang et al. 2003). An increasing number of optimization tools (e.g., TOSCA, Pareto works, and PLATO (Blacker et al., 2015)) and freely available codes (Blacker et al., 2015) can be used for such design purposes. Integrating the specific requirements of AM processes into (topology) optimization algorithms is an active area of research (Challis et al., 2010; Xiao et al., 2013). An example of such integrations is the algorithms that deal with optimizing the arrangements of support materials during AM processes (e.g., see Langelaar (2018) and Krol et al. (2012)).

16.2.3 Metamaterials

"Batch-size-indifference" and "complexity-for-free" are the two essential features offered by AM that could be exploited to develop novel types of "designer" materials (Zadpoor, 2017, 2018). Such types of designer materials, which are also referred to as metamaterials, are architected and often lattice-based structures that may exhibit unusual properties originating from their small-scale shape (Zadpoor, 2016). One of these remarkable properties is the possibility for a negative Poisson's ratio (auxeticity) (Kolken and Zadpoor, 2017), which leads to lateral expansion upon longitudinal stretching. A wide range of other properties can be also achieved through the rational design of metamaterials, such as shape morphing (Mirzaali et al., 2018a; van Manen et al., 2018; Janbaz et al., 2016), strain rate dependency (Janbaz et al., 2019, 2020), crumpling (Mirzaali et al., 2017a), and action-at-a-distance (Hedayati et al., 2018c).

Metamaterials may also be useful for biomedical applications, in which case they are referred to as "meta-biomaterials." For example, auxetic behavior has been reported in skeletal tissues, such as tendons (Gatt et al., 2015) and trabecular bone. Evidence shows that scaffolds with auxetic behavior may promote neural differentiation by providing mechanical cues to pluripotent stem cells (Yan et al., 2017). Although there is not much evidence as to the advantages of auxetic behavior for improving bone tissue regeneration, a hybrid design of meta-biomaterials (i.e., the rational combination of unit cells with positive and negative values of the Poisson's ratio) may enhance the longevity of orthopedic implants (Kolken et al., 2018). Meta-biomaterials need to have fully open and interconnected pores to ensure the transportation of nutrients and oxygen to the cells (Bobbert and Zadpoor, 2017; Karageorgiou and Kaplan, 2005; Zadpoor, 2015). Lattice structures exhibit lower elastic moduli than the bulk material they are made of, which allows them to match the properties of native tissues, even if they are made from metals. Meta-biomaterials can also be designed using TPMS-based geometries (Bobbert et al., 2017; Al-Ketan et al., 2018; Ataee et al., 2018; Mohammed and Gibson, 2018; Yánez et al., 2018). AM strut-based and sheet-based meta-biomaterials are currently being intensively researched and are believed to hold great promise.

16.2.4 Bio-inspired design

Bio-inspired design is another approach in the design of lattice structures (see Chapter 17 for more information on Bio-inspired Design). Natural cellular materials, such as bone, cork, and wood enrich the scaffold design libraries (Nam et al., 2004; Bucklen et al., 2008). There are several key design elements in the structures of natural materials. These design elements can be translated into bio-inspired porous materials. An example of natural cellular materials is the cancellous (or trabecular) bone, which is a porous biological material made of hydroxyapatite crystals and collagen molecules formed at several hierarchical levels. The cellular structure of the cancellous bone consists of a connected network of trabeculae in the form of rods and plates (Ding et al., 2018). Trabecular bone can be also seen as a functionally graded material because its porosity distribution exhibits clear spatial patterns. These features can be used for the design of bio-inspired lattice structures.

The bio-inspired aspect is important, particularly in the design of orthopedic implants. When bone defects exceed a critical size, external intervention is necessary to facilitate the healing processes (Bose et al., 2013). The repair of such a critical-size bone defect can be challenging. The current treatment options are the use of either an autograft (patient's own tissue) or an allograft (donated tissue) (Parthasarathy, 2014). However, the application of autografts and allografts is associated with limited availability and medical challenges. The alternative solution is to design biomimetic materials and structures, such as AM lattices. One way to create the geometry of biomimetic lattice structures is to use imaging modalities, such as computed tomography (CT) and magnetic resonance imaging (MRI). Such image-based designs have been widely used for the design of biomaterials aimed for tissue reconstructions (Hollister et al., 2000; Van Eijnatten et al., 2018). Patient-specific implants (Fig. 16.1k), where the implant geometry and dimensions are matched to the anatomy of the patient are also relevant in this regard (Dérand et al., 2012; Jardini et al., 2014; Mohammed et al., 2016).

16.3 Materials

An ever-increasing list of metals can nowadays be processed using the L-PBF technique. In this section, we will review some key categories of materials relevant for the fabrication of metallic lattices.

16.3.1 Biomedical metals and alloys

To be used in biomedical applications, materials need to exhibit good biocompatibility (Gepreel and Niinomi, 2013). Examples of biocompatible metals are titanium (Ti) and its alloys, stainless steels, cobalt-based alloys (e.g., CoCrMo), zirconium (Zr), niobium (Nb), and tantalum (Ta). These materials exhibit good biocompatibility as well as high corrosion resistance and good mechanical properties (Long and Rack, 1998).

Ti and its alloys (e.g., Ti6Al4V) are perhaps the most commonly used biomaterials. Ti6Al4V is very strong and relatively inexpensive, but it exhibits lower ductility than pure Ti (Wauthle et al., 2015a). Ti6Al4V has been widely applied and is approved for medical use. However, there are concerns regarding its biocompatibility because of the presence of Al and V (Gepreel and Niinomi, 2013). Pure Ti, on the other hand, has lower mechanical properties but higher ductility and is very biocompatible. Stainless steel is also biocompatible, has a lower price than others, and can be easily fabricated by the L-PBF process, but its elastic modulus is higher than Ti6Al4V (Zadpoor, 2019). Ti6Al4V exhibits sufficiently high fatigue strength. However, its fatigue strength is, for example, lower than that of some CoCr alloys (Ahmadi et al., 2018).

The elastic moduli of solid metals are significantly higher than those of bone. To put this into perspective, the range of elastic moduli of cortical and trabecular bones vary between 3 and 30 GPa (Mirzaali et al., 2016b; Rho et al., 1998) and between 0.02 and 2 GPa (Mirzaali et al., 2018b; Goldstein, 1987), respectively. The elastic moduli of Ti6Al6V and CoCrMo are 110 and 210 GPa, respectively (Niinomi, 2003; Long and Rack, 1998). The elastic moduli of metallic biomaterials need to be adjusted to prevent stress-shielding at the bone-implant interface. Introducing porosity and using lattice structures is an effective approach to creating metallic biomaterials with bone-mimicking elastic moduli. Another approach to reducing the elastic modulus of porous structures is the addition of certain elements to the alloys. For example, β-type Ti alloys can be developed by adding β-stabilizing elements (e.g., Ta, Nb, Zr, and Mo), which offer lower elastic moduli. Examples of such alloys are Ti13Nb13Zr (elastic modulus = 79 GPa) (Davidson et al., 1994) and Ti29Nb13Ta4.6Zr (elastic modulus = 55—65 GPa) (Kuroda et al., 1998).

16.3.2 Biodegradable metals

Biodegradable metals are intended to be present in the body only temporarily to support the healing process. AM lattice structures made of biodegradable metals have been recently developed (Li et al., 2020b), including L-PBF porous iron (Li et al., 2018a), L-PBF porous magnesium (WE43) (Li et al., 2018b), and L-PBF porous zinc (Li et al., 2020a). Different types of medical devices can be fabricated from these biodegradable metals. Mg alloys, as an example, have been used in cardiovascular stents (Erbel et al., 2007), bone fixation, and bone screws (Windhagen et al., 2013).

The in vitro rates of biodegradation of pure zinc and its alloys are around 20—300 μm/year (Wen et al., 2018; Hou et al., 2018; Vojtěch et al., 2011; Katarivas Levy et al., 2017). For Fe- and Mg-based biomaterials, the rates may be, respectively, lower than 50 μm/year and higher than 300 μm/year (Li et al. 2014a; Zheng et al. 2014), which are either too low (Fe) or too high (Mg). Mg-based biomaterials may also produce hydrogen gas at a higher rate than can be dealt with inside the host body. Alloying may be used to adjust the rate of biodegradation of biodegradable metals. For instance, Mg-based alloys with elements, such as Y, Sr, Zn, Zr, and Ca have significantly lower biodegradation rates, as compared to pure Mg (Wang et al., 2016). These alloys also exhibit higher strengths, making them suitable for the fabrication of load-bearing parts (Yuan et al., 2019a). Increasing the surface area can tune the biodegradation rate as well. Given that lattice structures have a much larger surface area than corresponding solid parts, they could be used to increase the biodegradation rates of slow-degrading metals, such as iron. AM of biodegradable metals is quite challenging, particularly in the case of magnesium and its alloys, because they are extremely inflammable and require special safety measures. The biodegradation process may cause cytotoxicity (Li et al., 2015) against human cells, which is why the cytocompatibility of all biodegradable metals should be thoroughly investigated (Zadpoor, 2019).

16.3.3 Shape memory alloys

Shape memory alloys (SMAs) can switch between two permanent shapes when stimulated by external stimuli (Andani et al., 2014). The shape memory effects originate from the temperature-driven phase transformation of SMAs. SMAs have recently made their way to biomedical applications. Typical SMAs include nitinol (NiTi), which contains approximately 50% Ni and 50% Ti by atomic composition. The shape memory behavior of NiTi originates from the change from the austenite phase to the martensite phase in high and low temperatures, respectively (Buehler et al. 1963; Elahinia et al., 2012). The austenitic elastic modulus of bulk nitinol is $\approx$ 48 GPa, which is significantly lower than that of Ti alloys. Nitinol can also recover relatively large deformations of up to 8%. NiTi SMAs can undergo large strains while maintaining constant stress (Haberland et al., 2014; Morgan, 2004). These characteristics make nitinol an appropriate candidate for medical devices, including surgical guides, stents, orthodontic wires, plates, and staples for bone fracture.

The lattice structures of near equiatomic Ni-Ti alloys are also promising materials for application in the development of bio-implants and biological microelectromechanical systems (bio-MEMS) due to their unique combination of thermal and mechanical shape memories, high corrosion resistance, superelasticity, and biocompatibility (Elahinia et al., 2012; Mitchell et al., 2018). The presence of Ni in NiTi SMAs, however, may raise concerns in biomedical applications, as Ni ranks high in metallic allergy tests (Biesiekierski et al., 2012; Köster et al., 2000). Therefore, surface modification techniques and alternative alloying elements have been proposed (Obbard et al., 2010). For example, TiNb and related alloys (i.e., TiNbX, where X = Zr, Ta, Hf) have been developed, which exhibit recoverable strains of up to $\approx$ 4.2% (Miyazaki et al., 2006). Ti(C, N) barrier coatings have been applied to NiCr alloys by means of magnetron sputtering to reduce the amounts of nickel and chromium ions released to biologically relevant environments (Banaszek and Klimek, 2019).

Due to high reactivity, low workability, and the strong dependence of their properties on microstructure (Bormann et al., 2014; Van Humbeeck, 2018), manufacturing of parts from SMAs could be quite difficult. AM in general and the L-PBF technique in particular are the promising approaches for the fabrication of lattice structures of SMAs (Speirs et al., 2017; Wang et al., 2018a). The L-PBF technique has been recently used to fabricate lattice structures of NiTi SMAs, particularly for biomedical applications (Hoffmann et al., 2014; Habijan et al., 2013; Haberland et al., 2014; Bernard et al., 2012; Gorgin Karaji et al., 2017). The mechanical properties of L-PBF NiTi SMA parts have been shown to be similar to cast NiTi SMA counterparts (Haberland et al., 2014).

16.3.4 Superalloys

Superalloys are the specific types of alloys, including Co-, Fe-, and Ni-based alloys, that have superior resistance against surface degradation and are able to maintain their mechanical properties at high temperatures and are, thus, attractive options for aerospace, automotive, and energy industries (Kataria et al., 2020). Similar to SMAs, superalloys may also exhibit unusual properties, such as superelasticity (i.e., recover large deformations). Inconel alloys, such as Inconel 100, 625, 718, and 825, are the typical examples of Ni-based superalloys that show superior creep and oxidation resistance, as well as retained mechanical properties at elevated temperatures (Han et al., 2019; Juillet et al., 2018). The L-PBF process provides the opportunity to build lattice structures of superalloys with complex geometries to offer a combination of tailored mechanical properties, light weight, and heat resistance (Leary et al., 2018).

16.3.5 In-situ *alloying and composites*

In-situ alloying refers to the processes that combine several feedstocks with various compositions and simultaneously feed them into the melt pool. Such a compositional mixture can achieve tailored properties and functionalities (Bourell et al., 2017). Examples of such materials include the L-PBF-processed in-situ Ti-26Nb alloys for biomedical applications (Fischer et al., 2016), biofunctionalized Cu-containing titanium alloys (Krakhmalev et al., 2017; Vilardell et al., 2020), and the anchorless L-PBF AlSi12 in-situ alloy that has been developed to mitigate the residual stresses developed during the L-PBF process (Vora et al., 2015).

Generally, reinforcing particles (mostly ceramics) or *in-situ* alloying elements can be added to metal matrices to enhance the mechanical properties of the processed materials including their hardness, stiffness, and strength, while benefiting from the intrinsic properties of the matrix materials, such as high toughness and/or electrical/thermal conductivity. Reinforcing particles can be added through *ex-situ* mixing methods, such as ball milling, or be formed in-situ during the AM processes by combining the metal matrix with the alloying elements. The processing parameters used in the L-PBF processes, such as laser power, must be adjusted to ensure the complete melting of the metal matrix and the alloying elements, to improve the interaction with the surrounding *ex-situ* added particles, or to achieve the maximum reaction between the matrix and the alloying elements. For instance, Ti-TiB porous composites have been fabricated through *in-situ* reaction between the Ti matrix and TiB2 reinforcing particles (Attar et al., 2015). The concept of porous metal-matrix composites is not restricted to *ex-situ* or *in-situ* metal-ceramic composites. It is also possible to fabricate porous metallic glass composites through the L-PBF process. The reinforcing agents in such composites are the crystalline phases distributed in the porous amorphous matrix (Liang et al., 2020). The capabilities of the L-PBF process to fabricate various metal matrix composites has been demonstrated in the literature (Zhang and Attar, 2016; Zhao et al., 2019; Mandal et al., 2020; Attar et al., 2014), indicating the excellent opportunity to take advantage of both abilities of these processes (i.e., compositing and lattice structure formation) to build lattice structures that are reinforced by composite elements. Functionally graded lattice structures with a gradient of chemical composition can be also created.

16.4 Process-related effects

While AM processes, particularly the L-PBF process, are capable of fabricating lattices with complex geometries, the quality of the resulting structures significantly depends on the processing parameters (Wang et al., 2013). Some of the important processing parameters include laser beam power density, laser spot size, laser scanning speed, focal offset distance, scanning strategy, and build-plate preheat temperature (Gokuldoss et al., 2017; Wang et al., 2016) (see Chapter 3 for more information). In order to manufacture uniform, reproducible, and reliable AM lattices, these parameters should be controlled and adjusted. Therefore, several design maps have been proposed in the past to help in the proper identification and selection of AM-related processing parameters (Beuth et al., 2013; Beuth and Klingbeil, 2001; Gockel and Beuth, 2013).

16.4.1 Effects of processing parameters on internal porosity and microstructure

Inappropriate selection of the processing parameters can create defects, such as microporosities, during the AM processes (Fig. 16.2a–e). The formation of microporosities highly depends on the density of the energy transferred to the melting material, because it directly affects gas/flow interactions and temperature evolution during the AM process (see Chapter 6 for more information). It should, however, be noted that the energy density alone cannot explain all the effects of the processing parameters and the processing parameters should be individually optimized. When using the L-PBF process, there are multiple processing windows within which a minimum number of pores can be achieved in lattice structures (Cosma et al., 2020; Du Plessis et al., 2020; Salem et al., 2019; Sing et al., 2018), see Chapter 3. As a rule of thumb, low power densities increase the microporosities due to insufficient melting. On the other hand, at high laser power densities keyhole pore formation happens, and it may make the melt pool more turbulent, with intensive spattering, evaporate alloying elements, entrap inert gas, and form gas bubbles that become entrapped as the material resolidifies. Moreover, increasing the hatch spacing and thickening the powder layer result in unwanted porosities, especially in the case of thick struts (due to insufficient melting and bonding) (Zhang et al., 2019). Such undesired porosities influence the functionality of the struts and may adversely affect their mechanical performance. Moreover, unmolten particles and spatter melts increase the surface roughness of struts, which may also deteriorate their mechanical performance, particularly their fatigue life.

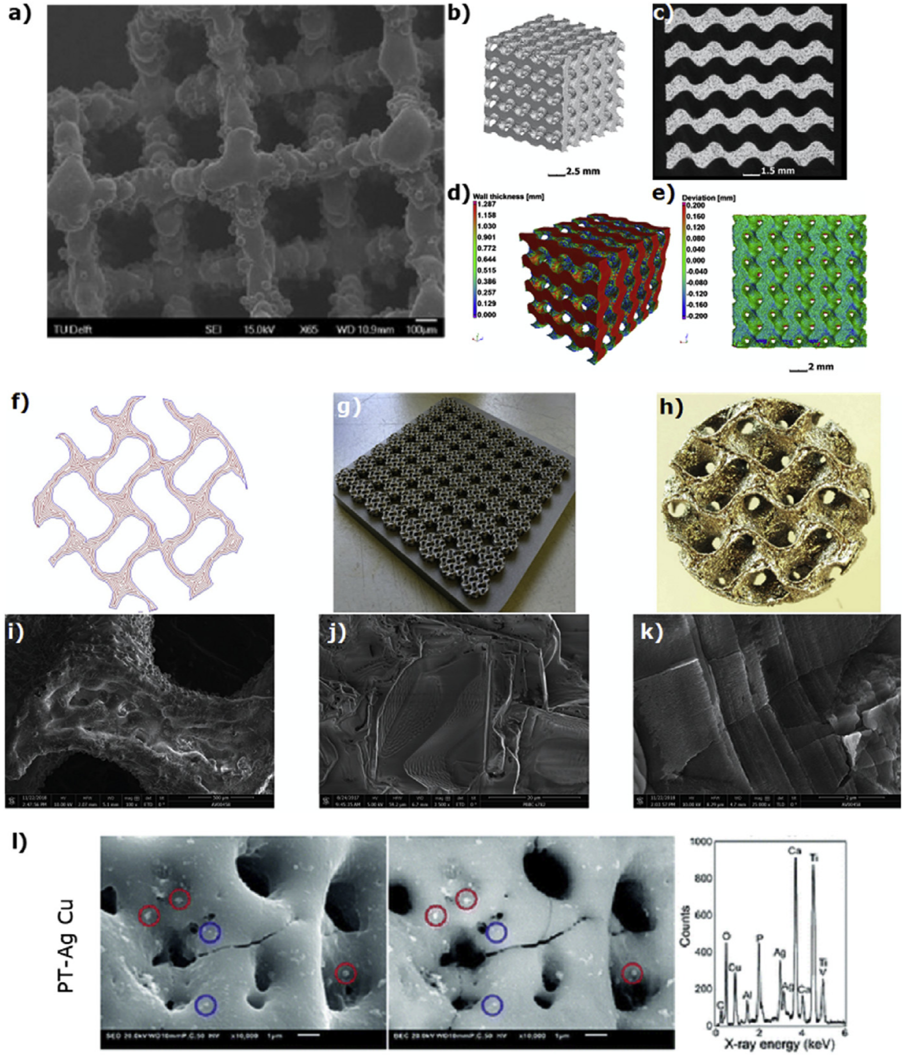
a)
TUDelft SEI 15.0kV X65 WD 10.9mm 100μm
b)
2.5 mm
c)
1.5 mm
d)
Wall thickness [mm]
1.287
1.158
1.030
0.901
0.772
0.644
0.515
0.386
0.257
0.129
0.000
e)
Deviation [mm]
0.200
0.160
0.120
0.080
0.040
0.000
-0.040
-0.080
-0.120
-0.160
-0.200
2 mm
f)
g)
h)
i)
j)
k)
l)
PT-Ag Cu
Counts
X-ray energy (keV)
1000
800
600
400
200
0
2
4
6
O
Cu
Al
P
Ag
Ca
Ti
Ti
V

Figure 16.2 AM processing parameters affect the formation of geometrical irregularities (a) or the micro-porosities present in the struts of lattice structures (b, c). Nondestructive imaging techniques, such as CT can be used to quantify the morphological variations (d, e). Various post-AM surface treatments can be used to introduce additional functionalities to lattice structures (e.g., biofunctionalities). The post-AM treatments can be through layer-by-layer approaches (Yavari et al., 2020) (f−k) or adding specific agents (e.g., silver and copper nanoparticles) to activate self-defending abilities of AM lattice-structured biomaterials (van Hengel et al., 2020) (l).
(a) Reprinted from Campoli et al., 2013. Copyright (2020), with permission from Elsevier.
(b−e) Reprinted from Du Plessis et al., 2020. Copyright (2020), with permission from Elsevier.

For instance, it has been observed that for laser powers between 170 and 350 W, energy densities higher than 8 J/mm^2 worsen the surface quality of struts in AlSi10Mg lattice structures while energy densities below 2 J/mm^2 bring about unmolten particles and internal porosities to the extent that they prevent the successful manufacturing of such structures (Großmann et al., 2019). Even for a constant value of the energy density, changes in other individual processing parameters can influence the print quality (Ghouse et al., 2017). That is why energy densities alone without specifying other process parameters cannot be a process indicator and are unable to capture the complex physics of the melt pool (see Chapters 3 and 4).

The actual strut thickness depends on the processing parameters too. Moreover, any changes in the processing parameters affect the thermal history of the melt pools, and, thus, the microstructure of lattice structures. The volume fraction of each phase highly depends on the processing routes and process parameters (Chapter 8). Since microstructure is one of the most important factors determining the mechanical properties of lattice structures, the specification of the applied L-PBF process strongly affects the microstructure and functional properties of lattice structures (Ghouse et al., 2017).

16.4.2 Effects of strut orientation

The manufacturing quality of the struts within a lattice structure is dependent on their orientation with respect to the building direction. Horizontal or near horizontal struts may be associated with some difficulties, including uneven distribution of material during layer deposition, overhang of accumulated molten material, and, thus, localized waviness within the struts (Wauthle et al., 2015c; Campoli et al., 2013). Such an inhomogeneous distribution of material can generate sharp notches on the struts, which are prone to failure and decrease the fatigue life of the lattice structures (Dallago et al., 2019). The orientation of struts can also introduce anisotropy into the mechanical behavior of metallic lattices (Kok et al., 2018).

The orientation of struts or unit cells with respect to the direction, along which the mechanical load is applied (defined by the parameter θ) influences the fatigue properties of the porous structures, because the apparent relative density of such structures is determined by this structural parameter. This influence has been studied in the case of Ti6Al4V octahedral structures. In these structures, the optimized fatigue life per unit density is obtained when $\theta = 43°$ (Bai et al., 2020). The mechanical properties of the lattice structure can, therefore, be adjusted by changing the orientation of unit cells.

16.4.3 Chemical composition

The chemical composition of the powder material governs the possible phase transformations during the AM process as well as the final microstructure and mechanical properties of the resulting lattices. The presence or absence of any alloying elements may also influence the outcome. For instance, the addition of Nb or V to Ti enhances the stability of the β phase and restricts the β to α' (martensite) transformation (Wang et al., 2017a). As a result, the final lattice structure may show better ductility. Moreover, adding large amounts of interstitial atoms, such as O, N, and C, causes some titanium-based cellular structures to behave like brittle materials with no plateau regions in their stress-strain curves. Such impurities may arise from the initial powder bed or be due to oxygen pickup during the AM process. As a result, it is necessary to control the amounts of such impurities, for example, by using an inert atmosphere with high purity. The addition of pore-inducing agents to the chemical composition of raw powders can also enhance the pore formation during the AM processes and lead to lighter porous parts. Therefore, this effect should also be kept in mind in the design process. To date, most of the research on the chemical compositions of the materials fabricated by the L-PBF process has been restricted to bulk specimens.

16.5 Morphological properties

One of the requirements of a successful AM process is that the geometry of the 3D printed part should match the CAD design (geometrical fidelity). Geometrical imperfections can drastically reduce the mechanical properties (e.g., fatigue properties) of AM lattice structures. Statistical quantification of the discrepancies between the as-designed and as-built geometries is of critical importance (Brajlih et al., 2011). There are (at least) two types of defects in AM parts, including irregularities on the cross-section of the struts (Fig. 16.2a) and the formation of microdefects (Campoli et al., 2013) (Fig. 16.2b and c). The factors that influence the morphological variations are: (a) the complexity of the geometry, (b) the processing parameters, and (c) the local variations of the thermal properties of the system (El Elmi et al., 2020; Li et al., 2017). There are several methods that can be used for nondestructive measurement of the morphological properties of lattices, including optical and confocal microscopies, scanning electron microscopy (SEM), and microcomputed tomography (μCT) (Fig. 16.2d and e).

In order to quantify the morphological characteristics of lattice structures, nondestructive imaging techniques can be used. The spatial resolution of the images (i.e., voxel size) should be equal or better than the minimum feature size that the imaging technique needs to capture. Several steps, including image reconstruction, image filtering (noise removal), and image segmentation, are necessary for image analysis. There are various tools and software (e.g., ImageJ (Abràmoff et al. 2004) and BoneJ plugin (Doube et al., 2010)) that can be used to extract this morphological information from images.

16.5.1 Porosity

There are two types of porosities in AM lattice structures. The first type (microporosities) refers to the microporosities formed within the material. The second type refers to the porosity of the lattice structure (porous structure) as a whole. Microporosities may be in the range of 10−50 μm (Vilaro et al. 2011), while the pores of AM lattices are usually >100 μm. Microporosities can act as stress concentration zones and can promote crack propagation, thereby reducing the mechanical properties of AM lattices (Azarniya et al., 2019; Ahmed et al., 2019).

16.5.2 Pore characteristics

Pores are some of the most important morphological features of lattice structures and are described using a host of qualitative and quantitative factors, including pore shape, pore size, strut thickness, pore spacing, connectivity of the unit cell, and the connectivity of the overall lattice structure. The pore size and distribution are among the main indices describing the geometry of lattice structures. The morphology and microstructural characteristics of pores can be measured using optical microscope, SEM, transmission electron microscope (TEM), and atomic force microscopy (AFM) (see Chapter 6 for more details). The 3D shape of pores can be measured using μCT (in addition to the above-mentioned characteristics). Controlling the geometrical features of lattice structures allows one to achieve specific mechanical and physical properties. For example, by controlling the shape, distribution, and interconnectivity of the pores of a lattice structure (or other porous materials), it is possible to adjust the mass transport properties (e.g., permeability) of tissue engineering scaffolds (Bobbert and Zadpoor, 2017; Bobbert et al., 2017; Van Bael et al., 2012; Zadpoor, 2015) and increase their surface area-to-volume ratio (Ahmadi et al., 2014).

16.6 Post-processing

The as-built AM lattice structures often contain defects in the form of microcavities in individual struts, for example, due to lack of fusion (LOF) or other pore types (see Chapter 6 for more details). The presence of these process-induced defects may introduce considerable variations into the mechanical properties of AM lattices structures. Several post-processing treatments, such as heat treatments at high temperatures combined with increased pressures, can be used to eliminate or modify such (microstructural) imperfections. Post-processing can also reduce the residual stresses present in the as-built L-PBF parts (see Chapters 9 and 12).

16.6.1 Residual stress relieving

Due to the thermal gradients experienced during AM, residual stresses develop in lattice structures (Hussein et al., 2013). The amount of residual stresses depends on the thermal history experienced during the AM process. These residual stresses can adversely affect the mechanical performance and geometrical fidelity of AM (Maconachie et al., 2019). Post-processing can reduce the thermal stresses in AM parts. For example, stress relief treatments may be used to transform the microstructure of AM Ti6Al4V lattice structures from acicular martensite α' to the alpha phase (Huang et al., 2020). This phenomenon is concurrent with the elimination of printing-induced residual stresses and a reduction in the cracking tendency, resulting in a significant improvement in the fatigue behavior of post-processed AM materials (Huang et al., 2020).

16.6.2 Heat treatments

Heat treatments are used for improving the microstructures resulting from the L-PBF process (Chapter 8). These treatments can influence the grain size and precipitates (Brandl and Greitemeier, 2012; Song et al., 2014). As an example, post-AM heat treatment of Ti6Al4V parts at temperatures higher than the β transus temperature (i.e., $T_{ß} = 995\ °C$) can thoroughly dissolve the α-phase while coarsening the prior-β grains (Vrancken et al., 2012). A successful heat-treatment process can also improve the mechanical properties of AM lattice structures, such as L-PBF Ti6Al4V (Thöne et al., 2012). Such improvements in the mechanical properties are a direct consequence of microstructural changes and the elimination of thermal stresses.

16.6.3 Hot isostatic pressing (HIP)

HIP is a common post-processing treatment that combines high temperatures with high pressures to decrease or eliminate the internal pores present inside AM parts (Ahmadi et al., 2019; Tammas-Williams et al., 2016; Van Hooreweder et al., 2017). Implementing the HIP process can improve the ductility of AM materials (Zadpoor, 2019), increase the quasi-static mechanical properties of AM meta-biomaterials (Ahmadi et al., 2019), and decrease the degree of anisotropy present in metallic lattices (Wu and Lai, 2016).

However, the role of the HIP treatment in influencing the fatigue behavior of AM lattice structures remains controversial. Some studies have reported no improvement of the fatigue life for AM lattice structures made of Ti6Al4V (Dallago et al., 2018) and CoCr alloy (Cutolo et al., 2018). This can be explained by the fact that HIP treatment cannot fix the defects (e.g., strut thickness variations, strut waviness) presented on top surfaces (Dallago et al., 2018). These defects are the preferred zones for crack initiation. In the case of Ti6Al4V lattice structure, it is shown that HIP at 1000°C/150 MPa decreases the microhardness by 20%, the yield strength by 30%, and increases the fatigue endurance ratio at 10^6 cycles by 83% through removing the pores present in the struts and the phase transformation of brittle α'-martensite to tough $\alpha + \beta$ mixed phases. The coarser $\alpha + \beta$ mixture can blunt the fatigue cracks, thereby decelerating their propagation and improving the fatigue performance of the material (Wu et al., 2017b; Huang et al., 2020).

16.6.4 Surface treatments

Several types of surface treatment processes have been proposed for (metallic) lattice structures. One approach to smoothen the external surface of struts is physical erosion by using abrasive materials. An example of such techniques is sandblasting, which can remove the excess powder particles adhered to the surface of struts, introduce compressive residual stresses to their superficial regions, and form a nanocrystalline thin film covering the outer regions of the struts. These changes can enhance the endurance limit of AM lattices (Yang et al., 2019). However, the abrasive materials may not reach the internal struts of lattice structures. Another method to modify the surface roughness of struts is chemical etching, which can better reach the internal struts.

However, chemical etching may not always improve the fatigue performance of lattice structures. For example, while chemical etching is reported to improve the fatigue behavior of Ti6Al4V lattices, the opposite has been reported for CoCr (Van Hooreweder and Kruth, 2017). One of the reasons is that too much material may be removed during such a process.

Chemical surface treatments can have different influences on the fatigue properties of AM lattices. In general, there are two types of chemical surface treatments: light chemical surface treatments that are used to remove the unmolten powders from the strut surfaces, and chemical surface treatments for inducing specific (bio-)functionalities (Fig. 16.2f–l). Some chemical surface treatments applied for biofunctionalization (Fig. 16.2f–l) have been shown to improve the fatigue properties of the materials as well (Cutolo et al., 2018). There is also some evidence that certain biofunctionalizing surface treatments, such as alkali-acid heat treatment (Yavari et al., 2014a) and plasma electrolytic oxidation (Karaji et al., 2017), do not affect the fatigue lives of AM lattices. Combining HIP with surface treatments, such as sandblasting and chemical etching, however, has been shown to further improve the fatigue lives of AM lattices (Ahmadi et al., 2019).

In the case of AM meta-biomaterials, those include surface bio-functionalization processes that enhance the tissue regeneration performance of such materials (Yavari et al., 2014b; Nune et al., 2018; Van Der Stok et al., 2015b; Nouri-Goushki et al., 2019) and prevent implant-associated infections (Geng et al., 2017; Amin Yavari et al., 2016; van Hengel et al., 2017; Ganjian et al., 2020). This can be achieved through chemical and electrochemical surface treatments and coatings. Some of those surface treatment processes may, however, decrease the mechanical properties of AM lattices as they erode struts and make them rougher.

16.7 Physical properties

16.7.1 Density

The relative density (ρ) of AM lattice structures refers to the amount of solid constituent that fills the nominal volume of the porous body. The relative density or porosity ($= 1 - \rho$) is among the key parameters determining the mechanical and physical properties of lattice structures. The relative density of a porous structure can be measured using the Archimedes' principle or through the analysis of microscopic or µCT images (see Chapter 10 for more details). The relative density of a designed object can also be calculated from the CAD design. The mismatches between the "designed" and "measured" densities can be due to the formation of (geometrical) defects and the irregularities caused by the AM process.

16.7.2 Surface roughness

Surface roughness is one of the most important features affecting the quality of AM lattices. Several factors can influence the surface roughness of AM lattice structures, including the quality of the feedstock material (Tang et al., 2015a). Moreover, unmolten powder particles and the occurrence of the balling effect during the L-PBF process can increase the surface roughness (Gu and Shen, 2009; Niu and Chang, 1999). Unmolten particles, which may result from an inadequate level of energy input, stick to the surface of the struts of lattice structures and roughen the surface. The third parameter influencing the surface quality is the build rate, with higher build rates leading to poorer surface quality, which may necessitate post-AM treatments, such as chemical polishing, shot peening, or HIP (Łyczkowska et al., 2014; Alghamdi et al., 2019). Nondestructive imaging techniques, such as SEM and surface profilometry, can be used to assess the surface roughness (Strano et al., 2013).

16.8 Mechanical properties

A wide variety of materials, process type, process parameters, and design factors significantly influence the quasi-static mechanical properties and fatigue properties of the lattice structures made through L-PBF. Whether the microstructure of the material constituting the struts is isotropic or anisotropic may also considerably affect the mechanical properties. In order to establish a reliable relationship between the design of the repeating unit cell and the "effective" mechanical properties of a lattice structure, the lattice structure should contain a minimum number of unit cells (i.e., the minimum number of unit cells is 10 unit cells, as proposed in ISO13314). The mechanical properties of functionally graded porous structures are, as expected, strongly size-dependent. Comparing the mechanical properties of graded designs with those of uniform structures has shown higher elastic moduli (Wang et al., 2018b) and energy absorption capacities (Choy et al., 2017) of functionally graded lattice structures.

16.8.1 Quasi-static mechanical properties

The mechanical properties of lattices (i.e., the elastic modulus, E, and yield strength, σ_y) depend on their geometrical and physical features and follow a power-law relationship $E = a\rho^b$, where ρ is the relative density (Ashby, 2006; Gibson and Ashby, 1999) (Fig. 16.3a and b). The coefficients of the power-law (i.e., a and b) depend on the geometry of lattice structures (Hedayati et al., 2016c, d). For example, b is close to 1 for stretch-dominated unit cells, while it tends to be closer to 2 for bending-dominated unit cells (Ashby, 2006; Deshpande et al., 2001b).

The differences between the estimated mechanical properties (i.e., using computational modeling) and those predicted by the power-law relationship often originate from the presence of the residual stresses created during the L-PBF process (Wang et al., 2017b; Yan et al., 2014), uncertainties in the exact geometry of the struts (Zhang et al., 2018), and the overestimation of the relative density when using the Archimedes technique (Yakout et al. 2019). One of the possible reasons for such an overestimation is the presence of unmolten powder particles on the surface of the struts.

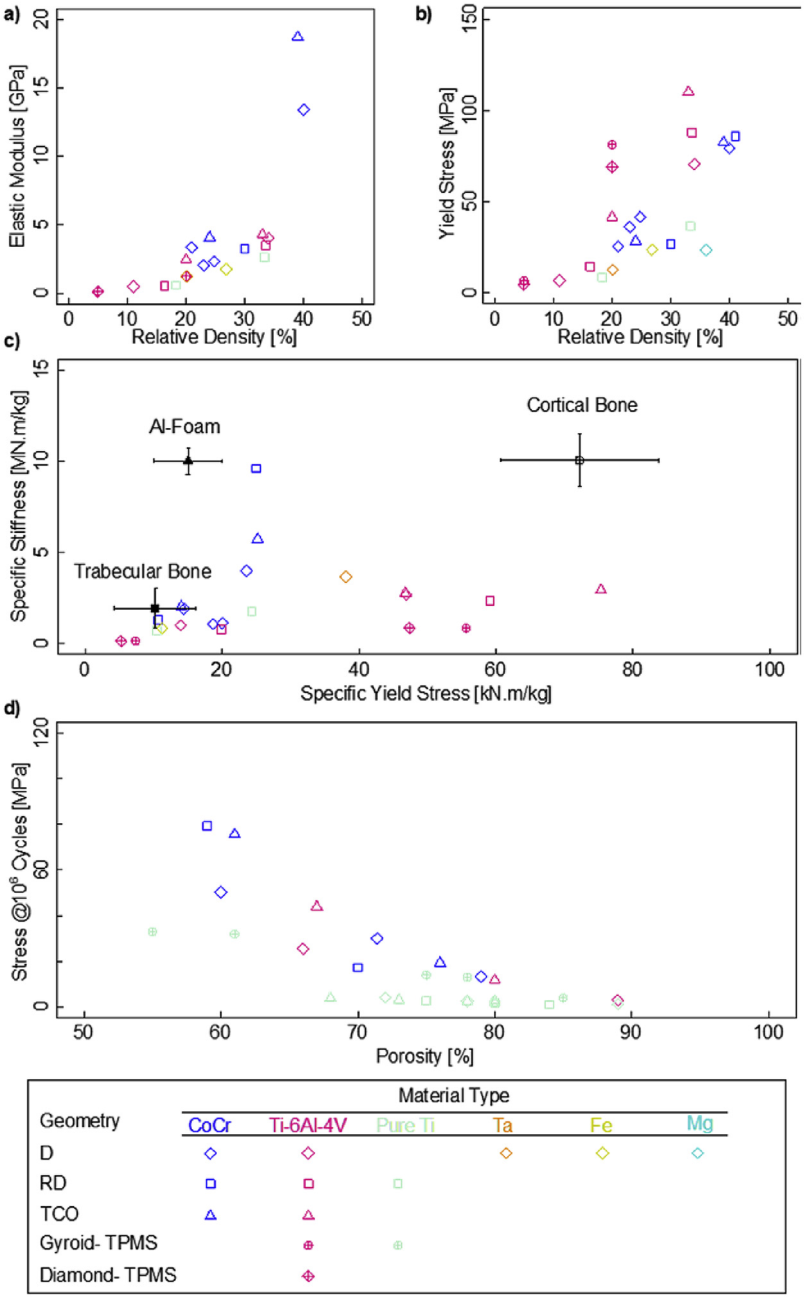

Figure 16.3 The mechanical properties (elastic modulus (a) and compressive strength (b)) of L-PBF lattice structures as a function of their relative densities. The data were collected for CoCr (Hedayati et al., 2018a; Cutolo et al., 2018), Ti-6Al-4V (Ahmadi et al., 2014; Ge et al., 2020; Yan et al., 2015), pure titanium (Ti) (Wauthle et al., 2015a), tantalum (Ta) (Wauthle et al., 2015b), iron (Fe) (Li et al., 2018a), and magnesium (Mg) (Li et al., 2018b). The specific mechanical properties (i.e., the ratio of the elastic properties to the density of porous structures) are compared with those of natural materials (e.g., cortical (Carter and Spengler 1978; Mirzaali et al., 2016b; Mirzaali et al., 2015) and trabecular (Goldstein 1987; Mirzaali et al., 2018b; Mirzaali et al., 2017c; Mirzaali et al., 2020) bone) and aluminum foams (Andrews et al. 1999; Miyoshi et al., 2000; Mirzaali et al., 2016a). The endurance limit values at 10^6 cycles versus

To exclude the effects of the material type, the mechanical properties can be normalized with respect to the mechanical properties of the bulk material from which the struts are made. However, it has been recently shown that these normalized values of the elastic modulus and yield stress can significantly change with the type of the material (Hedayati et al., 2018a) (Fig. 16.3a and b). Moreover, different metals have different ductility levels and, thus, different post-yield behaviors. For example, changing the bulk material may influence the plateau stress and densification behavior at the start of the self-contact of struts in lattice structures (Hedayati et al., 2018a). Despite the presence of such effects, the normalized values of the quasi-static mechanical properties of AM lattices are more strongly affected by the geometrical design of the lattice structures than the material type (Hedayati et al., 2018a; Zadpoor, 2019).

Microscale measurements of the full field strain during the mechanical testing of AM lattices have shown that the failure of AM lattices is caused by strain concentrations in the weak spots formed during the AM process (Genovese et al., 2017). The strain concentrations intensify as the loading progresses and lead to premature failure. While the microscale failure mechanism of AM metallic lattices seems to be independent of their geometrical design (Genovese et al., 2017), the geometrical design significantly influences the macroscale failure mechanisms of AM lattices (Kadkhodapour et al., 2015; Ahmadi et al., 2014). In particular, the failure mechanisms of stretch-dominated unit cells differ from those of bending-dominated unit cells (Kadkhodapour et al., 2015). In stretch-dominated unit cells, entire rows of unit cells collapse as the struts and joints in stretch-dominated structures are highly stiff and do not bend under axial loads (Deshpande et al., 2001b). In contrast, the struts of bending-dominated structures can easily rotate at their joints under macroscopically applied loads, leading to their overall collapse (Bauer et al., 2014). Therefore, in bending-dominated unit cells, 45° shearing bands and the consequent propagation of cracks are responsible for the failure of lattice structures (Kadkhodapour et al., 2015). The local buckling of individual struts is another failure mechanism involved in the overall failure of AM lattices, and may lead to a more brittle mechanical behavior (Li et al., 2014b).

There are some distinct differences between the typical stress-strain curves of bending-dominated and stretch-dominated lattice structures. Bending-dominated cellular structures exhibit a linear elastic behavior up until the end of their elastic region, where the walls or edges of the unit cells start to yield, buckle, or fracture, after which the integrity of the lattice structure is compromised around the plateau stress, σ_{pl}, and densification strain, ε_d. In contrast, stretch-dominated lattice structures

◀

the porosities of the LPBF-lattice structures made of Ti-6Al-4V (Yavari et al., 2015) and CoCr (Ahmadi et al., 2018; Van Hooreweder and Kruth, 2017) and Ti (Zargarian et al., 2016; Kelly et al., 2019) (D). Wherever possible, the data for different beam-based unit cells types, such as diamond (D), rhombic dodecahedron (RD), and truncated cuboctahedron (TCO) and sheet-based unit cells, including TPMS-gyroid and TPMS-diamond, were added.

benefit from a higher strength and elastic modulus, but undergo post-yield softening. As expected, the biodegradation process can reduce the mechanical properties of AM lattice structures in the case of biodegradable metals. This effect has been observed to be more severe for the yield stress than for the elastic modulus (Li et al., 2018a, b).

16.8.2 Fatigue life

The fatigue life of AM lattices is an important consideration for most of load-bearing applications, including orthopedic implants that are often subjected to repetitive loading due to the physical activities of the human body. Given the importance of the biomedical applications of AM lattices, compression-compression fatigue is one of the most well-studied types of the fatigue loading modes applied to AM lattices. However, the other types of fatigue loading, such as tension and bending, are also highly consequential. A macroscopically applied compression-compression load may lead to the development of tensile stresses in the struts of AM lattice structures, thereby promoting crack initiation and eventual strut failure. Several studies on the compression-compression fatigue behavior of AM lattices made from different metals have in recent years appeared in the literature (Ahmadi et al., 2018; Van Hooreweder et al., 2017; Yavari et al., 2013, 2015; Speirs et al., 2017). The S-N curves determined in such studies show the number of cycles to failure for different levels of the applied stress. The endurance limit or fatigue strength is defined as the stress at which the number of loading cycles exceeds a specific threshold (e.g., 10^6 cycles). The fatigue strengths of lattice structures increase with the fatigue strength of the bulk materials of the same composition (Zargarian et al., 2019) (Fig. 16.3d).

Geometrical variables, such as the relative density and unit cell type, are also important in this regard (Fig. 16.3d). The fatigue strength of lattice structures decreases as the porosity increases (Yavari et al. 2013, 2015). Several normalization approaches have been proposed in the past to eliminate the effects of the quasi-static mechanical properties from the dynamic properties and define the so-called "normalized S-N curves." One of those approaches is to divide the stress levels by the yield or plateau stress of the lattice structure. For Ti6Al4V, the S-N curves of lattice structures with different values of the relative density but the same type of unit cell tend to collapse into one curve once they are normalized with respect to the their quasi-static mechanical properties (Yavari et al., 2013). This observation seems to be approximately (but not exactly) valid for some other alloys as well (Ahmadi et al., 2018). The use of a single normalized S-N curve is a powerful idea that has a huge time- and cost-saving potential. That is because to apply a normalized S-N curve to a new lattice structure (of the same unit cell type), one only needs to determine the plateau or yield stress by conducting a limited number of quasi-static mechanical tests.

The tensile fatigue behavior of AM lattice structures has been also studied (Dallago et al., 2018; Lietaert et al., 2018). The fatigue performance of AM lattices decreases under tension-tension as compared to compression-compression loading (Lietaert et al., 2018). The tension-compression loading, however, tends to increase the fatigue lives of AM lattices because, as opposed to tension-tension and compression-compression loading modes, a smaller number of struts experience local tensile stresses.

The geometrical design of AM lattice structures (i.e., unit cell types) significantly influences their fatigue behavior (Yavari et al., 2015; Zhao et al., 2016) (see Fig. 16.3d for comparison). In compression-compression fatigue, the geometry of the unit cell determines how much of the macroscopically applied compressive loading is experienced as tensile stresses by the struts. Sheet-based lattice structures tend to outperform strut-based lattices in terms of their fatigue resistance (Bobbert et al., 2017). This is due to two reasons. First, sheet-based lattices are less sensitive to the defects and irregularities caused by the AM process. Second, due to the continuity of their unit cells, no stress concentration points exist in sheet-based lattice structures (Lietaert et al., 2018). The fatigue behavior of AM lattices with disordered geometries needs to be further investigated. As for functionally graded lattice structures, they have been found to cause a continuous redistribution of stresses due to their inhomogeneous microstructural arrangements (Zhao et al., 2018).

In addition to geometrical design, the material type plays an important role in determining the fatigue life of AM lattices, particularly in the high cycle regime (see Fig. 16.3d for comparison). Depending on the geometrical design and material type, the fatigue strengths of most (strut-based) AM metallic lattices range between 20% and 60% of their yield strengths (Ahmadi et al., 2018). Examples of the related properties that could improve the fatigue strength of AM lattices are ductile mechanical properties (e.g., the relatively high ductility of pure titanium (Wauthle et al., 2015a) and superelasticity (e.g., of β-type titanium alloys (Liu et al., 2017)). The L-PBF process can also create anisotropy in the fatigue behavior and other mechanical properties of lattice structures (Kajima et al., 2016). Further studies are, therefore, needed to determine the relationship between the fatigue behavior and build orientation of AM lattice structures. A recent review of fatigue performance of lattice structures is found in (Benedetti et al., 2021).

16.9 Computational modeling and analytical solutions

Predictive models in the form of computational models (Campoli et al., 2013; Hedayati et al., 2016c; Du Plessis et al., 2018a) and analytical solutions (Zadpoor and Hedayati, 2016; Hedayati et al., 2017; Hedayati et al., 2016d) can be used to better understand the roles of geometrical design, microstructure, and manufacturing defects in determining the effective properties of lattice structures. Such models can also be used in heuristic algorithms that determine the optimal design of lattices to achieve the desired properties under a specific loading scenario.

The analytical solutions for strut-based unit cells are usually based on the Euler-Bernoulli or Timoshenko beam theories. The relationships between the geometrical design and mechanical properties for various unit cell types have been established. One of the limitations of the analytical solutions based on the Euler-Bernoulli beam theory is that they are only valid for unit cells with slender struts (i.e., low relative densities) and deviate from experimental results and the results obtained from computational models for the higher values of the relative density (Zadpoor and Hedayati, 2016). The Timoshenko beam theory offers a better performance for thick struts. However, exact solutions based on the Timoshenko theory are only available for a few geometries. One of the limitations of analytical solutions is that they cannot take the geometrical imperfections of the strut shapes into account. To improve the accuracy of analytical solutions, the relative density of the lattice structures should be accurately calculated taking account of the 3D shape of the struts at the junctions (Lozanovski et al., 2020). Ignoring the 3D shapes of the struts and junctions leads to mass multiple counting in the traditional models of lattice structures that model the struts as two-dimensional (2D) lines (Hedayati et al., 2016b; Zadpoor and Hedayati, 2016). Despite their lack of accuracy, analytical solutions offer unique insights into the mechanical behavior of AM lattices and the effects of various design parameters on mechanical properties.

Computational models can also be used to predict the geometry-property relationships of AM lattices. Computational models based on high-fidelity finite element (FE) models can offer more accurate results than analytical models (Campoli et al., 2013). Different elements, such as solid, shell, and beam (based on the Euler-Bernoulli or Timoshenko formulations) elements can be employed in the FE modeling of lattice structures. The idealized geometry, as well as the actual geometry that includes the imperfection and defects imposed during the AM processes, can be used in such FE models. An example of the actual geometry can be constructed from the segmented μCT images (Cho et al., 2015; Youssef et al., 2005; Du Plessis et al., 2017). Computational models can be combined with optimization algorithms to optimize the design of lattice structures for specific applications (e.g., patient-specific implants) under a specific set of loading conditions. One example of such optimization algorithms is the models based on bone tissue adaptation (Arabnejad Khanoki and Pasini, 2012; Lin et al., 2007; Wang et al., 2016).

Computational models could also predict the fatigue behavior of AM lattices. This is important as collecting the data required for establishing experimental S-N curves of lattice structures is extremely expensive and time-consuming. The computational models proposed to date usually use the S-N curves of the base materials, damage evolution laws, and iterative solutions to predict the fatigue lives of lattice structures (Hedayati et al., 2016a, 2018b; Zargarian et al., 2016). These models can be combined with other characterization techniques, such as digital image correlation (DIC) (de Krijger et al., 2017) or *in-situ* imaging (Du Plessis et al., 2018b), to validate the predicted strain distributions and to explore the mechanisms responsible for the local or global failure of lattice structures.

16.10 Applications

16.10.1 Light-weight and load-bearing structures

The high porosity and tailored mechanical properties of AM lattice structures make them attractive options for the design of light-weight and load-bearing structures in various industries, including the automotive, civil, energy, and aerospace industries (Fig. 16.4a). Some examples are fairings, payload adapters, and space telescopes in aerospace engineering, submarine bodies in maritime engineering, and sandwich composites in civil engineering (Nagesha et al., 2020). A more specific example is the lattice sandwich structures fabricated by L-PBF, whose application as light-weight thermal controllers has been shown to increase the thermal capacity by up to 50%. Such controllers are used in spacecraft to control the temperature of various electronics (Zhou et al., 2004).

In the automotive industry, light-weight lattice structures are used for noise reduction, better recyclability, and reduced fuel consumption. A 10% decrease in the weight of the structural parts of an automobile delivers a 6%−8% of saving in fuel consumption (Nagesha et al., 2020) (partially due to the snowball effect). Moreover, the natural frequencies of lattice structures increase with their stiffnesses, making them suitable for application in fast motors and vibratory components. Moreover, due to the low weight and good mechanical properties of strut-based lattice structures, they can be

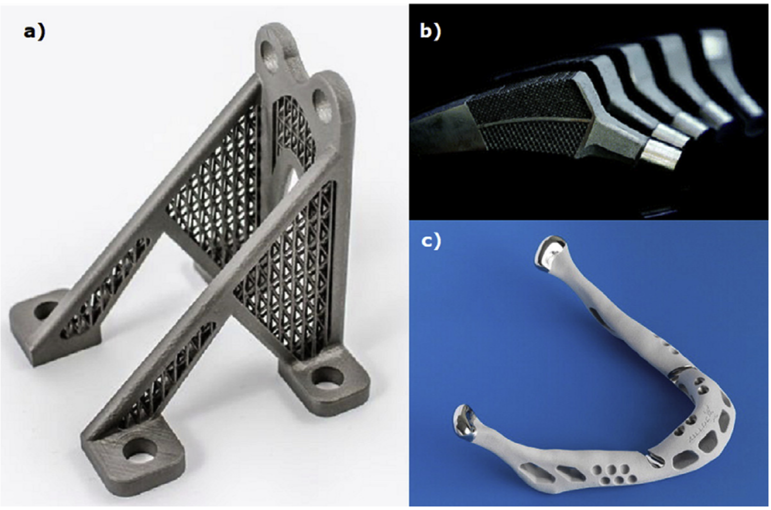

Figure 16.4 AM lattices have several applications in load-bearing lightweight structures particularly for aerospace engineering. This example is an optimized bracket designed by Materialise 3-Matic (reprinted with permission) which exhibits 63% weight reduction (a). Other examples of AM lattice structures include hybrid meta-implants (Kolken et al., 2018) (b) and a patient-specific mandible implant (c).
Reprinted from Nickels, L., 2012. World's first patient-specific jaw implant. Met. Powder Rep. 67, 12−14, Copyright (2020), with permission from Elsevier.

used for the construction of structures located in earthquake-prone areas to prevent subsequent damages, such as fracture, support failure, and local and global buckling (Nagesha et al., 2020).

The relatively high specific stiffness as well as the extended stress plateau of AM lattice structures make them attractive candidates for energy absorption, load-bearing, and impact alleviation applications. The form-freedom offered by the L-PBF process means that it is possible to use novel geometries and periodic patterns that considerably enhance the energy absorption capacity of AM lattices as compared to traditionally fabricated cellular materials (e.g., foams). It has been shown, for example, that auxetic metamaterials offer superior energy absorption capabilities (Yuan et al., 2019b). Moreover, stretch-dominated lattices are known for being able to store more energy than their bending-dominated counterparts (Sun et al., 2020). Using the AM technologies, it is also possible to optimize the internal geometry of parts at several length scales to further enhance their load-bearing capacity (Wang et al., 2018a,b).

In addition to the abovementioned applications, lattice structures can be used in many other areas, such as the design of heat exchangers for chemical processing, waste treatment, thermal management (Maloney et al., 2012), digital signal processing (DSP), digital filtering, spectral estimation, and adaptive signal processing (Roy, 2014).

16.10.2 Biomedical

AM parts in general and AM lattices in particular have found many biomedical applications, particularly in orthopedic (Fig. 16.4b), maxillofacial, and trauma surgeries. Examples include the AM patient-specific mandible implants coated with hydroxyapatite and implanted in a patient in 2012 (Nickels, 2012) (Fig. 16.4c). AM parts have been also applied for the reconstruction of class III cranial defects (Mertens et al., 2013). In addition to porous implants, the L-PBF process can be used to fabricate multifunctional porous medical devices (Bártolo and Bidanda, 2008), controlled drug delivery systems (Burton et al., 2019), and engineered tissues (Putra et al., 2020; Stevens et al., 2008; Gibson et al. 2014).

As extensively discussed elsewhere (Bejarano et al., 2017; Zadpoor, 2019, 2020), there are four main advantages to the use of AM lattice structures as porous biomaterials. First, it is possible to adjust the elastic properties, yield stress, fatigue strength, permeability, diffusivity, and the rate of biodegradation of lattice structures through rational design of their geometries. All these properties of porous biomaterials play important roles in determining the *in vivo* performance of the relevant medical devices. Second, the macroscale shape and microscale architecture of AM lattices can be designed to match the specific anatomy and loading conditions of a specific patient. Third, the surface area of AM lattice structures is much larger than that of a corresponding solid material. The increased surface area of such porous biomaterials could be used for amplifying the effects of surface bio-functionalization treatments, such as those aimed at inducing antibacterial (van Hengel et al., 2017) and osteogenic (Zadpoor, 2019) properties. Finally, the pore space of AM lattices not only allows for unhindered bony ingrowth but can also be used to accommodate drug delivery vehicles (e.g., those loaded with growth factors (van der Stok et al., 2013, 2015a) and/or antibiotics (Bakhshandeh et al., 2017; Croes et al., 2018; Yavari et al., 2020)) to further enhance the performance of the resulting implants. In addition to these four advantages, researchers continue to develop other innovative ways to exploit the benefits of AM processes.

16.11 Conclusions

To summarize, we reviewed the fundamental aspects of applying the L-PBF process for the fabrication of (metallic) lattice structures as a reference for students and researchers who intend to use this technique. In order to have reliable and reproducible AM lattice structures, special attention must be paid to choosing proper parameters starting from the design steps to the fabrication process and during the post-processing actions.

The design of the geometry of lattice structures is the first step, which determines their overall physical (e.g., permeability) and mechanical properties. There are several classes of geometries that can help designers to make a proper selection. Each of these design classes can provide specific properties.

The L-PBF process parameters have a great influence on the quality of the final parts (e.g., surface roughness, anisotropy, and geometrical fidelity) as well as the formation of defects, all of which can subsequently influence the mechanical performance of AM lattices. The proper selection and adjustment of such processing parameters can minimize unwanted microstructural defects at macro and micro levels.

Several post-processing methods, such as HIP, heat, surface, and chemical treatments can be used to reduce or eliminate some of those defects created during the L-PBF process. Those post-treatments can also introduce multifunctionalities to AM lattice structures (e.g., biofunctionalization) and may strongly influence their (quasi-static or fatigue) mechanical properties. The proper selection of the processing and post-processing parameters highly depend on the material type.

L-PBF lattice structures have found their ways to high-tech industries, such as automotive, aerospace, and biomedical. The research into the development of processing windows and the use of various kinds of materials are some of the active fields expected to grow in the near future.

16.12 Questions

- What are the differences in geometrical and mechanical properties between bending-dominated and stretch-dominated lattice structures?
- What are the important morphological parameters of AM lattice structures?
- What are the most common defects formed during the L-PBF process to fabricate lattice structures?

- How do the L-PBF process parameters influence the morphological and mechanical properties of AM lattice structures?
- How can the post-AM treatment processes (i.e., HIP, heat treatments, surface treatments, chemical treatments) affect the quasi-static and fatigue properties of AM lattice structures?
- What are the main benefits of using disordered AM lattice structures over ordered AM lattice structures?
- What are the main advantages of in-situ alloying in the fabrication of AM lattice structures?

References

Abràmoff, M.D., Magalhães, P.J., Ram, S.J., 2004. Image processing with ImageJ. Biophot. Int. 11, 36−42.

Ahmadi, S.M., Campoli, G., Amin Yavari, S., Sajadi, B., Wauthlé, R., Jan, S., Weinans, H., Zadpoor, A.A., 2014. Mechanical behavior of regular open-cell porous biomaterials made of diamond lattice unit cells. J. Mech. Behav. Biomed. Mater. 34, 106−115.

Ahmadi, S.M., Hedayati, R., Ashok Kumar Jain, R.K., Li, Y., Leeflang, S., Zadpoor, A.A., 2017. Effects of laser processing parameters on the mechanical properties, topology, and microstructure of additively manufactured porous metallic biomaterials: a vector-based approach. Mater. Des. 134, 234−243.

Ahmadi, S.M., Hedayati, R., Li, Y., Lietaert, K., Tümer, N., Fatemi, A., Rans, C.D., Pouran, B., Weinans, H., Zadpoor, A.A., 2018. Fatigue performance of additively manufactured meta-biomaterials: the effects of topology and material type. Acta Biomater. 65, 292−304.

Ahmadi, S.M., Kumar, R., Borisov, E.V., Petrov, R., Leeflang, S., Li, Y., Tümer, N., Huizenga, R., Ayas, C., Zadpoor, A.A., 2019. From microstructural design to surface engineering: a tailored approach for improving fatigue life of additively manufactured meta-biomaterials. Acta Biomater. 83, 153−166.

Ahmed, A.B., Mohamed, I.H., Fathallah, R., Sidhom, H., 2019. The effect of interacting defects on the HCF behavior of Al-Si-Mg aluminum alloys. J. Alloys Compd. 779, 618−629.

Al-Ketan, O., Rowshan, R., Al-Rub, R.K.A., 2018. Topology-mechanical property relationship of 3D printed strut, skeletal, and sheet based periodic metallic cellular materials. Addit. Manuf. 19, 167−183.

Alghamdi, A., Downing, D., McMillan, M., Brandt, M., Qian, M., Leary, M., 2019. Experimental and numerical assessment of surface roughness for Ti6Al4V lattice elements in selective laser melting. Int. J. Adv. Manuf. Technol. 105, 1275−1293.

Amin Yavari, S., Loozen, L., Paganelli, F.L., Bakhshandeh, S., Lietaert, K., Groot, J.A., Fluit, A.C., Boel, C.H.E., Alblas, J., Vogely, H.C., 2016. Antibacterial behavior of additively manufactured porous titanium with nanotubular surfaces releasing silver ions. ACS Appl. Mater. Interfaces 8, 17080−17089.

Andani, M.T., Moghaddam, N.S., Haberland, C., Dean, D., Miller, M.J., Elahinia, M., 2014. Metals for bone implants. Part 1. Powder metallurgy and implant rendering. Acta Biomater. 10, 4058−4070.

Andrews, E., Sanders, W., Gibson, L.J., 1999. Compressive and tensile behaviour of aluminum foams. Mater. Sci. Eng. A 270, 113−124.

Arabnejad Khanoki, S., Pasini, D., 2012. Multiscale design and multiobjective optimization of orthopedic hip implants with functionally graded cellular material. J. Biomech. Eng. 134.

Ashby, M.F., 2006. The properties of foams and lattices. Phil. Trans. R. Soc. A Math. Phys. Eng. Sci. 364, 15−30.

Ataee, A., Li, Y., Fraser, D., Song, G., Wen, C., 2018. Anisotropic Ti-6Al-4V gyroid scaffolds manufactured by electron beam melting (EBM) for bone implant applications. Mater. Des. 137, 345−354.

Attar, H., Bönisch, M., Calin, M., Zhang, L.C., Zhuravleva, K., Funk, A., Scudino, S., Yang, C., Eckert, J., 2014. Comparative study of microstructures and mechanical properties of in situ Ti−TiB composites produced by selective laser melting, powder metallurgy, and casting technologies. J. Mater. Res. 29, 1941−1950.

Attar, H., Löber, L., Funk, A., Calin, M., Zhang, L.C., Prashanth, K.G., Scudino, S., Zhang, Y.S., Eckert, J., 2015. Mechanical behavior of porous commercially pure Ti and Ti−TiB composite materials manufactured by selective laser melting. Mater. Sci. Eng. A 625, 350−356.

Azarniya, A., Garmendia Colera, X., Mirzaali, M.J., Sovizi, S., Bartolomeu, F., Wits, W.W., Yap, C.Y., Ahn, J., Miranda, G., Silva, F.S., 2019. Additive manufacturing of Ti−6Al−4V parts through laser metal deposition (LMD): process, microstructure, and mechanical properties. J. Alloys Compd. 804, 163−191.

Bai, L., Zhang, J., Xiong, Y., Chen, X., Sun, Y., Gong, C., Pu, H., Wu, X., Luo, J., 2020. Influence of unit cell pose on the mechanical properties of Ti6Al4V lattice structures manufactured by selective laser melting. Addit. Manuf. 34, 101222.

Bakhshandeh, S., Gorgin Karaji, Z., Lietaert, K., Fluit, A.C., CHE, B., Charles Vogely, H., Vermonden, T., Hennink, W.E., Weinans, H., Zadpoor, A.A., 2017. Simultaneous delivery of multiple antibacterial agents from additively manufactured porous biomaterials to fully eradicate planktonic and adherent *Staphylococcus aureus*. ACS Appl. Mater. Interfaces 9, 25691−25699.

Banaszek, K., Klimek, L., 2019. Ti (C, N) as barrier coatings. Coatings 9, 432.

Banhart, J., 2001. Manufacture, characterisation and application of cellular metals and metal foams. Prog. Mater. Sci. 46, 559−632.

Bártolo, P., Bidanda, B., 2008. Bio-Materials and Prototyping Applications in Medicine. Springer.

Bauer, J., Hengsbach, S., Tesari, I., Schwaiger, R., Kraft, O., 2014. High-strength cellular ceramic composites with 3D microarchitecture. Proc. Natl. Acad. Sci. 111, 2453−2458.

Bejarano, N.C., Pedrocchi, A., Nardone, A., Schieppati, M., Walter, B., Monticone, M., Ferrigno, G., Ferrante, S., 2017. Tuning of muscle synergies during walking along rectilinear and curvilinear trajectories in humans. Ann. Biomed. Eng. 45, 1204−1218.

Bendsøe, M.P., 1989. Optimal shape design as a material distribution problem. Struct. Optim. 1, 193−202.

Bendsoe, M.P., Sigmund, O., 2013. Topology Optimization: Theory, Methods, and Applications. Springer Science & Business Media.

Benedetti, M., du Plessis, A., Ritchie, R.O., Dallago, M., Razavi, S.M.J., Berto, F., 2021. Architected cellular materials: a review on their mechanical properties towards fatigue-tolerant design and fabrication. Mater. Sci. Eng. R Rep. 144, 100606.

Bensoussan, A., Lions, J.-L., Papanicolaou, G., 2011. Asymptotic Analysis for Periodic Structures. American Mathematical Society.

Berger, J.B., Wadley, H.N.G., McMeeking, R.M., 2017. Mechanical metamaterials at the theoretical limit of isotropic elastic stiffness. Nature 543, 533−537.

Bernard, S., Krishna Balla, V., Bose, S., Bandyopadhyay, A., 2012. Compression fatigue behavior of laser processed porous NiTi alloy. J. Mech. Behav. Biomed. Mater. 13, 62−68.

Beuth, J., Klingbeil, N., 2001. The role of process variables in laser-based direct metal solid freeform fabrication. J. Occup. Med. 53, 36−39.

Beuth, J., Fox, J., Gockel, J., Montgomery, C., Yang, R., Qiao, H., Soylemez, E., Reeseewatt, P., Amin, A., Narra, S., 2013. Process mapping for qualification across multiple direct metal additive manufacturing processes. In: Solid Freeform Fabrication Proceedings. University of Texas, Austin, pp. 655−665.

Biesiekierski, A., Wang, J., Gepreel, M.A.-H., Wen, C., 2012. A new look at biomedical Ti-based shape memory alloys. Acta Biomater. 8, 1661−1669.

Blacker, T.D., Robbins, J., Owen, S.J., Aguilovalentin, M.A., Clark, B.W., Voth, T.E., 2015. PLATO platinum topology optimization. In: Sandia National Lab. SNL-NM), Albuquerque, NM (United States).

Bobbert, F.S.L., Zadpoor, A.A., 2017. Effects of bone substitute architecture and surface properties on cell response, angiogenesis, and structure of new bone. J. Mater. Chem. B 5, 6175−6192.

Bobbert, F.S.L., Lietaert, K., Eftekhari, A.A., Pouran, B., Ahmadi, S.M., Weinans, H., Zadpoor, A.A., 2017. Additively manufactured metallic porous biomaterials based on minimal surfaces: a unique combination of topological, mechanical, and mass transport properties. Acta Biomater. 53, 572−584.

Bormann, T., Müller, B., Schinhammer, M., Kessler, A., Peter, T., de Wild, M., 2014. Microstructure of selective laser melted nickel−titanium. Mater. Char. 94, 189−202.

Bose, S., Vahabzadeh, S., Bandyopadhyay, A., 2013. Bone tissue engineering using 3D printing. Mater. Today 16, 496−504.

Bourell, D., Kruth, J.P., Ming, L., Levy, G., Rosen, D., Beese, A.M., Adam, C., 2017. Materials for additive manufacturing. CIRP Ann. 66, 659−681.

Brajlih, T., Valentan, B., Balic, J., Drstvensek, I., 2011. Speed and accuracy evaluation of additive manufacturing machines. Rapid Prototyp. J. 17 (1), 64−75.

Brandl, E., Greitemeier, D., 2012. Microstructure of additive layer manufactured Ti−6Al−4V after exceptional post heat treatments. Mater. Lett. 81, 84−87.

Bucklen, B.S., Wettergreen, W.A., Yuksel, E., Liebschner, M.A.K., 2008. Bone-derived CAD library for assembly of scaffolds in computer-aided tissue engineering. Virtual Phys. Prototyp. 3, 13−23.

Buehler, W.J., Gilfrich, J.V., Wiley, R.C., 1963. Effect of low-temperature phase changes on the mechanical properties of alloys near composition TiNi. J. Appl. Phys. 34, 1475−1477.

Burton, H.E., Eisenstein, N.M., Lawless, B.M., Jamshidi, P., Segarra, M.A., Owen, A., Shepherd, D.E.T., Attallah, M.M., Grover, L.M., Cox, S.C., 2019. The design of additively manufactured lattices to increase the functionality of medical implants. Mater. Sci. Eng. C 94, 901−908.

Calignano, F., 2014. Design optimization of supports for overhanging structures in aluminum and titanium alloys by selective laser melting. Mater. Des. 64, 203−213.

Callens, S.J.P., Uyttendaele, R.J.C., Fratila-Apachitei, L.E., Zadpoor, A.A., 2020. Substrate curvature as a cue to guide spatiotemporal cell and tissue organization. Biomaterials 232, 119739.

Campoli, G., Borleffs, M.S., Yavari, S.A., Wauthle, R., Weinans, H., Zadpoor, A.A., 2013. Mechanical properties of open-cell metallic biomaterials manufactured using additive manufacturing. Mater. Des. 49, 957−965.

Carter, D.R., Spengler, D.M., 1978. Mechanical properties and composition of cortical bone. Clin. Orthop. Relat. Res. (1976−2007) 135, 192−217.

Challis, V.J., Roberts, A.P., Grotowski, J.F., Zhang, L.-C., Sercombe, T.B., 2010. Prototypes for bone implant scaffolds designed via topology optimization and manufactured by solid freeform fabrication. Adv. Eng. Mater. 12, 1106−1110.

Cho, H.-H., Cho, Y., Han, H.N., 2015. Finite element analysis for mechanical response of Ti foams with regular structure obtained by selective laser melting. Acta Mater. 97, 199−206.

Choy, S.Y., Sun, C.-N., Leong, K.F., Wei, J., 2017. Compressive properties of functionally graded lattice structures manufactured by selective laser melting. Mater. Des. 131, 112−120.

Chuah, H.G., Abd Rahim, I., Imran Yusof, M., 2010. Topology optimisation of spinal interbody cage for reducing stress shielding effect. Comput. Methods Biomech. Biomed. Eng. 13, 319−326.

Cosma, C., Kessler, J., Gebhardt, A., Campbell, I., Balc, N., 2020. Improving the mechanical strength of dental applications and lattice structures SLM processed. Materials 13, 905.

Croes, M., Bakhshandeh, S., van Hengel, I.A.J., Lietaert, K., van Kessel, K.P.M., Pouran, B., van der Wal, B.C.H., Vogely, H.C., Van Hecke, W., Fluit, A.C., 2018. Antibacterial and immunogenic behavior of silver coatings on additively manufactured porous titanium. Acta Biomater. 81, 315−327.

Cutolo, A., Neirinck, B., Lietaert, K., de Formanoir, C., Van Hooreweder, B., 2018. Influence of layer thickness and post-process treatments on the fatigue properties of CoCr scaffolds produced by laser powder bed fusion. Addit. Manuf. 23, 498−504.

Dallago, M., Fontanari, V., Torresani, E., Leoni, M., Pederzolli, C., Potrich, C., Benedetti, M., 2018. Fatigue and biological properties of Ti-6Al-4V ELI cellular structures with variously arranged cubic cells made by selective laser melting. J. Mech. Behav. Biomed. Mater. 78, 381−394.

Dallago, M., Winiarski, B., Zanini, F., Carmignato, S., Benedetti, M., 2019. On the effect of geometrical imperfections and defects on the fatigue strength of cellular lattice structures additively manufactured via selective laser melting. Int. J. Fatig. 124, 348−360.

Davidson, J.A., Mishra, A.K., Kovacs, P., Poggie, R.A., 1994. New surface-hardened, low-modulus, corrosion-resistant Ti-13Nb-13Zr alloy for total hip arthroplasty. Bio Med. Mater. Eng. 4, 231−243.

de Jonge, C.P., Kolken, H., Zadpoor, A.A., 2019. Non-auxetic mechanical metamaterials. Materials 12, 635.

de Krijger, J., Rans, C., Van Hooreweder, B., Lietaert, K., Pouran, B., Zadpoor, A.A., 2017. Effects of applied stress ratio on the fatigue behavior of additively manufactured porous biomaterials under compressive loading. J. Mech. Behav. Biomed. Mater. 70, 7−16.

Dérand III, P., Rännar, L.-E., Hirsch, J.-M., 2012. Imaging, virtual planning, design, and production of patient-specific implants and clinical validation in craniomaxillofacial surgery. Craniomaxillofacial Trauma Reconstr. 5, 137−143.

Deshpande, V.S., Fleck, N.A., Ashby, M.F., 2001a. Effective properties of the octet-truss lattice material. J. Mech. Phys. Solid. 49, 1747−1769.

Deshpande, V.S., Ashby, M.F., Fleck, N.A., 2001b. Foam topology: bending versus stretching dominated architectures. Acta Mater. 49, 1035−1040.

Ding, M., Lin, X., Liu, W., 2018. Three-dimensional morphometric properties of rod-and plate-like trabeculae in adolescent cancellous bone. J. Orthop. Trans. 12, 26−35.

Doube, M., Kłosowski, M.M., Arganda-Carreras, I., Cordelières, F.P., Dougherty, R.P., Jackson, J.S., Schmid, B., Hutchinson, J.R., Shefelbine, S.J., 2010. BoneJ: free and extensible bone image analysis in ImageJ. Bone 47, 1076−1079.

Du Plessis, A., Yadroitsava, I., Le Roux, S.G., Yadroitsev, I., Fieres, J., Reinhart, C., Rossouw, P., 2017. Prediction of mechanical performance of Ti6Al4V cast alloy based on microCT-based load simulation. J. Alloys Compd. 724, 267−274.

Du Plessis, A., Yadroitsava, I., Yadroitsev, I., le Roux, S.G., Blaine, D.C., 2018a. Numerical comparison of lattice unit cell designs for medical implants by additive manufacturing. Virtual Phys. Prototyp. 13, 266−281.

Du Plessis, A., Kouprianoff, D.-P., Yadroitsava, I., Yadroitsev, I., 2018b. Mechanical properties and in situ deformation imaging of microlattices manufactured by laser based powder bed fusion. Materials 11, 1663.

Du Plessis, A., Razavi, S.M.J., Berto, F., 2020. The effects of microporosity in struts of gyroid lattice structures produced by laser powder bed fusion. Mater. Des. 194, 108899.

El Elmi, A., Melancon, D., Asgari, M., Liu, L., Pasini, D., 2020. Experimental and numerical investigation of selective laser melting−induced defects in Ti−6Al−4V octet truss lattice material: the role of material microstructure and morphological variations. J. Mater. Res. 35, 1900−1912.

Elahinia, M.H., Hashemi, M., Tabesh, M., Bhaduri, S.B., 2012. Manufacturing and processing of NiTi implants: a review. Prog. Mater. Sci. 57, 911−946.

Erbel, R., Di Mario, C., Bartunek, J., Bonnier, J., de Bruyne, B., Eberli, F.R., Paul, E., Haude, M., Heublein, B., Horrigan, M., 2007. Temporary scaffolding of coronary arteries with bioabsorbable magnesium stents: a prospective, non-randomised multicentre trial. Lancet 369, 1869−1875.

Fischer, M., Joguet, D., Robin, G., Peltier, L., Laheurte, P., 2016. In situ elaboration of a binary Ti−26Nb alloy by selective laser melting of elemental titanium and niobium mixed powders. Mater. Sci. Eng. C 62, 852−859.

Fraldi, M., Esposito, L., Perrella, G., Cutolo, A., Cowin, S.C., 2010. Topological optimization in hip prosthesis design. Biomech. Model. Mechanobiol. 9, 389−402.

Frazier, W.E., 2014. Metal additive manufacturing: a review. J. Mater. Eng. Perform. 23, 1917−1928.

Ganjian, M., Angeloni, L., Mirzaali, M.J., Modaresifar, K., Hagen, C.W., Ghatkesar, M.K., Leon Hagedoorn, P., Fratila-Apachitei, L., Zadpoor, A.A., 2020. Quantitative mechanics of 3D printed nanopillars interacting with bacterial cells. Nanoscale 12, 21988−22001. https://doi.org/10.1039/D0NR05984F (Communication).

Garner, E., Kolken, H.M.A., Wang, C.C.L., Zadpoor, A.A., Wu, J., 2019. Compatibility in microstructural optimization for additive manufacturing. Addit. Manuf. 26, 65−75.

Gatt, R., Wood, M.V., Gatt, A., Zarb, F., Formosa, C., Azzopardi, K.M., Casha, A., Agius, T.P., Schembri-Wismayer, P., Attard, L., 2015. Negative poisson's ratios in tendons: an unexpected mechanical response. Acta Biomater. 24, 201−208.

Ge, J., Huang, J., Lei, Y., O'Reilly, P., Ahmed, M., Zhang, C., Yan, X., Yin, S., 2020. Microstructural features and compressive properties of SLM Ti6Al4V lattice structures. Surf. Coat. Technol. 403, 126419.

Geng, H., Poologasundarampillai, G., Todd, N., Devlin-Mullin, A., Moore, K.L., Golrokhi, Z., Gilchrist, J.B., Jones, E., Potter, R.J., Sutcliffe, C., 2017. Biotransformation of silver released from nanoparticle coated titanium implants revealed in regenerating bone. ACS Appl. Mater. Interfaces 9, 21169−21180.

Genovese, K., Sander, L., Zadpoor, A.A., 2017. Microscopic full-field three-dimensional strain measurement during the mechanical testing of additively manufactured porous biomaterials. J. Mech. Behav. Biomed. Mater. 69, 327−341.

Gepreel, M.A.-H., Niinomi, M., 2013. Biocompatibility of Ti-alloys for long-term implantation. J. Mech. Behav. Biomed. Mater. 20, 407−415.

Ghouse, S., Babu, S., Van Arkel, R.J., Nai, K., Hooper, P.A., Jeffers, J.R.T., 2017. The influence of laser parameters and scanning strategies on the mechanical properties of a stochastic porous material. Mater. Des. 131, 498−508.

Giannitelli, S.M., Accoto, D., Trombetta, M., Rainer, A., 2014. Current trends in the design of scaffolds for computer-aided tissue engineering. Acta Biomater. 10, 580−594.

Gibson, L.J., Ashby, M.F., 1999. Cellular Solids: Structure and Properties. Cambridge University Press.

Gibson, I., Rosen, D.W., Stucker, B., 2014. Additive Manufacturing Technologies. Springer.

Gockel, J., Beuth, J., 2013. Understanding Ti-6Al-4V microstructure control in additive manufacturing via process maps. In: Solid Freeform Fabrication Proceedings. University of Texas, Austin, pp. 666−674.

Gokuldoss, P.K., Kolla, S., Eckert, J., 2017. Additive manufacturing processes: selective laser melting, electron beam melting and binder jetting—selection guidelines. Materials 10, 672.

Goldstein, S.A., 1987. The mechanical properties of trabecular bone: dependence on anatomic location and function. J Biomech 20 (11−12), 1055−1061.

Gorgin Karaji, Z., Speirs, M., Dadbakhsh, S., Kruth, J.-P., Weinans, H., Zadpoor, A.A., Amin Yavari, S., 2017. Additively manufactured and surface biofunctionalized porous nitinol. ACS Appl. Mater. Interfaces 9, 1293−1304.

Großmann, A., Gosmann, J., Mittelstedt, C., 2019. Lightweight lattice structures in selective laser melting: design, fabrication and mechanical properties. Mater. Sci. Eng. A 766, 138356.

Gu, D., Shen, Y., 2009. Balling phenomena in direct laser sintering of stainless steel powder: metallurgical mechanisms and control methods. Mater. Des. 30, 2903−2910.

Guest, J.K., Prévost, J.H., 2006. Optimizing multifunctional materials: design of microstructures for maximized stiffness and fluid permeability. Int. J. Solid Struct. 43, 7028−7047.

Haberland, C., Elahinia, M., Walker, J.M., Meier, H., Frenzel, J., 2014. On the development of high quality NiTi shape memory and pseudoelastic parts by additive manufacturing. Smart Mater. Struct. 23, 104002.

Habijan, T., Haberland, C., Meier, H., Frenzel, J., Wittsiepe, J., Wuwer, C., Greulich, C., Schildhauer, T.A., Köller, M., 2013. The biocompatibility of dense and porous nickel−titanium produced by selective laser melting. Mater. Sci. Eng. C 33, 419−426.

Han, C., Li, Y., Wang, Q., Wen, S., Wei, Q., Yan, C., Liang, H., Liu, J., Shi, Y., 2018. Continuous functionally graded porous titanium scaffolds manufactured by selective laser melting for bone implants. J. Mech. Behav. Biomed. Mater. 80, 119−127.

Han, Q., Gu, Y., Setchi, R., Lacan, F., Johnston, R., Evans, S.L., Yang, S., 2019. Additive manufacturing of high-strength crack-free Ni-based hastelloy X superalloy. Addit. Manuf. 30, 100919.

Hashin, Z., Shtrikman, S., 1963. A variational approach to the theory of the elastic behaviour of multiphase materials. J. Mech. Phys. Solid. 11, 127−140.

Hedayati, R., Hosseini-Toudeshky, H., Sadighi, M., Mohammadi-Aghdam, M., Zadpoor, A.A., 2016a. Computational prediction of the fatigue behavior of additively manufactured porous metallic biomaterials. Int. J. Fatig. 84, 67−79.

Hedayati, R., Sadighi, M., Mohammadi-Aghdam, M., Zadpoor, A.A., 2016b. Effect of mass multiple counting on the elastic properties of open-cell regular porous biomaterials. Mater. Des. 89, 9−20.

Hedayati, R., Sadighi, M., Mohammadi-Aghdam, M., Zadpoor, A.A., 2016c. Mechanical properties of regular porous biomaterials made from truncated cube repeating unit cells: analytical solutions and computational models. Mater. Sci. Eng. C 60, 163−183.

Hedayati, R., Sadighi, M., Mohammadi-Aghdam, M., Zadpoor, A.A., 2016d. Mechanics of additively manufactured porous biomaterials based on the rhombicuboctahedron unit cell. J. Mech. Behav. Biomed. Mater. 53, 272−294.

Hedayati, R., Sadighi, M., Mohammadi-Aghdam, M., Zadpoor, A.A., 2017. Analytical relationships for the mechanical properties of additively manufactured porous biomaterials based on octahedral unit cells. Appl. Math. Model. 46, 408−422.

Hedayati, R., Ahmadi, S.M., Lietaert, K., Pouran, B., Li, Y., Weinans, H., Rans, C.D., Zadpoor, A.A., 2018a. Isolated and modulated effects of topology and material type on the mechanical properties of additively manufactured porous biomaterials. J. Mech. Behav. Biomed. Mater. 79, 254−263.

Hedayati, R., Hosseini-Toudeshky, H., Sadighi, M., Mohammadi-Aghdam, M., Zadpoor, A.A., 2018b. Multiscale modeling of fatigue crack propagation in additively manufactured porous biomaterials. Int. J. Fatig. 113, 416−427.

Hedayati, R., Mirzaali, M.J., Vergani, L., Zadpoor, A.A., 2018c. Action-at-a-distance metamaterials: distributed local actuation through far-field global forces. APL Mater. 6, 036101.

Hoffmann, W., Bormann, T., Rossi, A., Müller, B., Schumacher, R., Martin, I., de Wild, M., Wendt, D., 2014. Rapid prototyped porous nickel−titanium scaffolds as bone substitutes. J. Tissue Eng. 5, 2041731414540674.

Hollister, S.J., Levy, R.A., Chu, T.-M., Halloran, J.W., Feinberg, S.E., 2000. An image-based approach for designing and manufacturing craniofacial scaffolds. Int. J. Oral Maxillofac. Surg. 29, 67−71.

Hollister, S.J., Maddox, R.D., Taboas, J.M., 2002. Optimal design and fabrication of scaffolds to mimic tissue properties and satisfy biological constraints. Biomaterials 23, 4095−4103.

Hou, Y., Jia, G., Yue, R., Chen, C., Jia, P., Zhang, H., Huang, H., Xiong, M., Yuan, G., 2018. Synthesis of biodegradable Zn-based scaffolds using NaCl templates: relationship between porosity, compressive properties and degradation behavior. Mater. Char. 137, 162−169.

Huang, X., Xie, Y.M., 2007. Bidirectional evolutionary topology optimization for structures with geometrical and material nonlinearities. AIAA J. 45, 308−313.

Huang, X., Xie, Y.M., 2009. Bi-directional evolutionary topology optimization of continuum structures with one or multiple materials. Comput. Mech. 43, 393.

Huang, X., Lang, L., Gong, S., Zhao, M., 2020. Effect of post-treatment on the microstructure and mechanical properties of selective laser melted Ti6Al4V lattice structures. Rapid Prototyp. J. 26.

Hussein, A., Liang, H., Yan, C., Everson, R., Young, P., 2013. Advanced lattice support structures for metal additive manufacturing. J. Mater. Process. Technol. 213, 1019−1026.

Janbaz, S., Hedayati, R., Zadpoor, A.A., 2016. Programming the shape-shifting of flat soft matter: from self-rolling/self-twisting materials to self-folding origami. Mater. Horiz. 3, 536−547.

Janbaz, S., Bobbert, F.S.L., Mirzaali, M.J., Zadpoor, A.A., 2019. Ultra-programmable buckling-driven soft cellular mechanisms. Mater. Horiz. 6, 1138−1147.

Janbaz, S., Narooei, K., van Manen, T., Zadpoor, A.A., 2020. Strain rate−dependent mechanical metamaterials. Sci. Adv. 6, eaba0616.

Jardini, A.L., Aparecida Larosa, M., Maciel Filho, R., de Carvalho Zavaglia, C.A., Bernardes, L.F., Lambert, C.S., Reis Calderoni, D., Kharmandayan, P., 2014. Cranial reconstruction: 3D biomodel and custom-built implant created using additive manufacturing. J. Cranio-Maxillofacial Surg. 42, 1877−1884.

Juillet, C., Oudriss, A., Balmain, J., Feaugas, X., Pedraza, F., 2018. Characterization and oxidation resistance of additive manufactured and forged IN718 Ni-based superalloys. Corrosion Sci. 142, 266−276.

Kadkhodapour, J., Montazerian, H., Darabi, A.C., Anaraki, A.P., Ahmadi, S.M., Zadpoor, A.A., Schmauder, S., 2015. Failure mechanisms of additively manufactured porous biomaterials: effects of porosity and type of unit cell. J. Mech. Behav. Biomed. Mater. 50, 180−191.

Kajima, Y., Takaichi, A., Nakamoto, T., Kimura, T., Yogo, Y., Ashida, M., Doi, H., Nomura, N., Takahashi, H., Takao, H., 2016. Fatigue strength of Co−Cr−Mo alloy clasps prepared by selective laser melting. J. Mech. Behav. Biomed. Mater. 59, 446−458.

Kapfer, S.C., Hyde, S.T., Mecke, K., Arns, C.H., Schröder-Turk, G.E., 2011. Minimal surface scaffold designs for tissue engineering. Biomaterials 32, 6875−6882.

Karageorgiou, V., Kaplan, D., 2005. Porosity of 3D biomaterial scaffolds and osteogenesis. Biomaterials 26, 5474−5491.

Karaji, Z.G., Hedayati, R., Pouran, B., Apachitei, I., Zadpoor, A.A., 2017. Effects of plasma electrolytic oxidation process on the mechanical properties of additively manufactured porous biomaterials. Mater. Sci. Eng. C 76, 406−416.

Kataria, R., Singh, R.P., Sharma, P., Phanden, R.K., 2020. Welding of super alloys: a review. Mater. Today Proc. https://doi.org/10.1016/j.matpr.2020.07.198.

Katarivas Levy, G., Goldman, J., Aghion, E., 2017. The prospects of zinc as a structural material for biodegradable implants—a review paper. Metals 7, 402.

Kelly, C.N., Francovich, J., Julmi, S., Safranski, D., Guldberg, R.E., Maier, H.J., Gall, K., 2019. Fatigue behavior of as-built selective laser melted titanium scaffolds with sheet-based gyroid microarchitecture for bone tissue engineering. Acta Biomater. 94, 610−626.

Kok, Y., Tan, X.P., Wang, P., Nai, M.L.S., Loh, N.H., Liu, E., Tor, S.B., 2018. Anisotropy and heterogeneity of microstructure and mechanical properties in metal additive manufacturing: a critical review. Mater. Des. 139, 565−586.

Kolken, H.M.A., Zadpoor, A.A., 2017. Auxetic mechanical metamaterials. RSC Adv. 7, 5111−5129.

Kolken, H.M.A., Janbaz, S., Leeflang, S.M.A., Lietaert, K., Weinans, H.H., Zadpoor, A.A., 2018. Rationally designed meta-implants: a combination of auxetic and conventional meta-biomaterials. Mater. Horiz. 5, 28−35.

Köster, R., Vieluf, D., Kiehn, M., Sommerauer, M., Jan, K., Baldus, S., Meinertz, T., Hamm, C.W., 2000. Nickel and molybdenum contact allergies in patients with coronary in-stent restenosis. Lancet 356, 1895−1897.

Krakhmalev, P., Yadroitsev, I., Yadroitsava, I., De Smidt, O., 2017. Functionalization of biomedical Ti6Al4V via in situ alloying by cu during laser powder bed fusion manufacturing. Materials 10, 1154.

Kranz, J., Herzog, D., Emmelmann, C., 2015. Design guidelines for laser additive manufacturing of lightweight structures in TiAl6V4. J. Laser Appl. 27, S14001.

Krol, T.A., Zaeh, M.F., Seidel, C., 2012. Optimization of Supports in Metal-Based Additive Manufacturing by Means of Finite Element Models. Bourell DL.

Kuroda, D., Niinomi, M., Morinaga, M., Kato, Y., Yashiro, T., 1998. Design and mechanical properties of new β type titanium alloys for implant materials. Mater. Sci. Eng. A 243, 244−249.

Langelaar, M., 2018. Combined optimization of part topology, support structure layout and build orientation for additive manufacturing. Struct. Multidiscip. Optim. 57, 1985−2004.

Leary, M., Mazur, M., Williams, H., Yang, E., Ahmad, A., Lozanovski, B., Zhang, X., Shidid, D., Farahbod-Sternahl, L., Witt, G., 2018. Inconel 625 lattice structures manufactured by selective laser melting (SLM): mechanical properties, deformation and failure modes. Mater. Des. 157, 179−199.

Li, H., Zheng, Y., Qin, L., 2014a. Progress of biodegradable metals. Prog. Nat. Sci. Mater. Int. 24, 414−422.

Li, S.J., Xu, Q.S., Wang, Z., Hou, W.T., Hao, Y.L., Yang, R., Murr, L.E., 2014b. Influence of cell shape on mechanical properties of Ti−6Al−4V meshes fabricated by electron beam melting method. Acta Biomater. 10, 4537−4547.

Li, W., Zhou, J., Xu, Y., 2015. Study of the in vitro cytotoxicity testing of medical devices. Biomed. Rep. 3, 617–620.

Li, S., Xiao, H., Liu, K., Xiao, W., Li, Y., Han, X., Mazumder, J., Song, L., 2017. Melt-pool motion, temperature variation and dendritic morphology of inconel 718 during pulsed- and continuous-wave laser additive manufacturing: a comparative study. Mater. Des. 119, 351–360.

Li, Y., Jahr, H., Lietaert, K., Pavanram, P., Yilmaz, A., Fockaert, L.I., Leeflang, M.A., Pouran, B., Gonzalez-Garcia, Y., Weinans, H., 2018a. Additively manufactured biodegradable porous iron. Acta Biomater. 77, 380–393.

Li, Y., Zhou, J., Pavanram, P., MA, L., LI, F., Pouran, B., Tümer, N., Schröder, K.-U., Mol, J.M.C., Weinans, H., 2018b. Additively manufactured biodegradable porous magnesium. Acta Biomater. 67, 378–392.

Li, Y., Pavanram, P., Zhou, J., Lietaert, K., Taheri, P., Li, W., San, H., Leeflang, M.A., Mol, J.M.C., Jahr, H., 2020a. Additively manufactured biodegradable porous zinc. Acta Biomater. 101, 609–623.

Li, Y., Jahr, H., Zhou, J., Zadpoor, A.A., 2020b. Additively manufactured biodegradable porous metals. Acta Biomater. 115, 29–50.

Liang, S.-X., Wang, X., Zhang, W., Liu, Y.-J., Wang, W., Zhang, L.-C., 2020. Selective laser melting manufactured porous Fe-based metallic glass matrix composite with remarkable catalytic activity and reusability. Appl. Mater. Today 19, 100543.

Lietaert, K., Cutolo, A., Boey, D., Van Hooreweder, B., 2018. Fatigue life of additively manufactured Ti6Al4V scaffolds under tension-tension, tension-compression and compression-compression fatigue load. Sci. Rep. 8, 1–9.

Lin, C.-Y., Wirtz, T., Frank, L.M., Hollister, S.J., 2007. Structural and mechanical evaluations of a topology optimized titanium interbody fusion cage fabricated by selective laser melting process. J. Biomed. Mater. Res. A 83, 272–279.

Liu, Y.J., Wang, H.L., Li, S.J., Wang, S.G., Wang, W.J., Hou, W.T., Hao, Y.L., Yang, R., Zhang, L.C., 2017. Compressive and fatigue behavior of beta-type titanium porous structures fabricated by electron beam melting. Acta Mater. 126, 58–66.

Loh, G.H., Pei, E., Harrison, D., Monzon, M.D., 2018. An overview of functionally graded additive manufacturing. Addit. Manuf. 23, 34–44.

Long, M., Rack, H.J., 1998. Titanium alloys in total joint replacement—a materials science perspective. Biomaterials 19, 1621–1639.

Lozanovski, B., Downing, D., Tino, R., Du Plessis, A., Tran, P., Jakeman, J., Shidid, D., Emmelmann, C., Qian, M., Peter, C., 2020. Non-destructive simulation of node defects in additively manufactured lattice structures. Addit. Manuf. 36, 101593.

Łyczkowska, E., Szymczyk, P., Dybała, B., Chlebus, E., 2014. Chemical polishing of scaffolds made of Ti-6Al-7Nb alloy by additive manufacturing. Arch. Civil Mech. Eng. 14, 586–594.

Maconachie, T., Leary, M., Lozanovski, B., Zhang, X., Qian, M., Faruque, O., Brandt, M., 2019. SLM lattice structures: properties, performance, applications and challenges. Mater. Des. 183, 108137.

Maloney, K.J., Fink, K.D., Schaedler, T.A., Kolodziejska, J.A., Jacobsen, A.J., Roper, C.S., 2012. Multifunctional heat exchangers derived from three-dimensional micro-lattice structures. Int. J. Heat Mass Tran. 55, 2486–2493.

Mandal, A., Tiwari, J.K., AlMangour, B., Sathish, N., Kumar, S., Kamaraj, M., Ashiq, M., Srivastava, A.K., 2020. Tribological behavior of graphene-reinforced 316L stainless-steel composite prepared via selective laser melting. Tribol. Int. 151, 106525.

Maskery, I., Aboulkhair, N.T., Aremu, A.O., Tuck, C.J., Ashcroft, I.A., 2017. Compressive failure modes and energy absorption in additively manufactured double gyroid lattices. Addit. Manuf. 16, 24−29.

Mertens, C., Hubert, L., Hoffmann, J., 2013. Image data based reconstruction of the midface using a patient-specific implant in combination with a vascularized osteomyocutaneous scapular flap. J. Cranio-Maxillofacial Surg. 41, 219−225.

Mirzaali, M.J., Alexander, B., Schwiedrzik, J., Zysset, P.K., Wolfram, U., 2015. Continuum damage interactions between tension and compression in osteonal bone. J. Mech. Behav. Biomed. Mater. 49, 355−369.

Mirzaali, M.J., Libonati, F., Vena, P., Mussi, V., Vergani, L., Strano, M., 2016a. Investigation of the effect of internal pores distribution on the elastic properties of closed-cell aluminum foam: a comparison with cancellous bone. Procedia Struct. Integrity 2, 1285−1294.

Mirzaali, M.J., Schwiedrzik, J.J., Thaiwichai, S., Best, J.P., Michler, J., Zysset, P.K., Wolfram, U., 2016b. Mechanical properties of cortical bone and their relationships with age, gender, composition and microindentation properties in the elderly. Bone 93, 196−211.

Mirzaali, M.J., Habibi, M., Janbaz, S., Vergani, L., Zadpoor, A.A., 2017a. Crumpling-based soft metamaterials: the effects of sheet pore size and porosity. Sci. Rep. 7, 1−7.

Mirzaali, M.J., Hedayati, R., Vena, P., Vergani, L.A.U.R.A., Strano, M., Zadpoor, A.A., 2017b. Rational design of soft mechanical metamaterials: independent tailoring of elastic properties with randomness. Appl. Phys. Lett. 111, 051903.

Mirzaali, M.J., Mussi, V., Vena, P., Libonati, F., Vergani, L., Strano, M., 2017c. Mimicking the loading adaptation of bone microstructure with aluminum foams. Mater. Des. 126, 207−218.

Mirzaali, M.J., Janbaz, S., Strano, M., Vergani, L., Zadpoor, A.A., 2018a. Shape-matching soft mechanical metamaterials. Sci. Rep. 8, 1−7.

Mirzaali, M.J., Libonati, F., Ferrario, D., Rinaudo, L., Messina, C., Ulivieri, F.M., Cesana, B.M., Strano, M., Vergani, L., 2018b. Determinants of bone damage: an ex-vivo study on porcine vertebrae. PLoS One 13, e0202210.

Mirzaali, M.J., Bobbert, F.S.L., Li, Y., Zadpoor, A.A., 2019a. 4 additive manufacturing of metals using powder bed-based technologies. Addit. Manuf. 93.

Mirzaali, M.J., Libonati, F., Böhm, C., Rinaudo, L., Cesana, B.M., Ulivieri, F.M., Vergani, L., 2020. Fatigue-caused damage in trabecular bone from clinical, morphological and mechanical perspectives. Int. J. Fatig. 133, 105451.

Mitchell, A., Lafont, U., Hołyńska, M., Semprimoschnig, C.J.A.M., 2018. Additive manufacturing—a review of 4D printing and future applications. Addit. Manuf. 24, 606−626.

Miyazaki, S., Kim, H.Y., Hosoda, H., 2006. Development and characterization of Ni-free Ti-base shape memory and superelastic alloys. Mater. Sci. Eng. A 438, 18−24.

Miyoshi, T., Itoh, M., Akiyama, S., Kitahara, A., 2000. ALPORAS aluminum foam: production process, properties, and applications. Adv. Eng. Mater. 2, 179−183.

Mohammed, M.I., Gibson, I., 2018. Design of three-dimensional, triply periodic unit cell scaffold structures for additive manufacturing. J. Mech. Des. 140.

Mohammed, M., Fitzpatrick, A., Malyala, S., Gibson, I., 2016. Customised design and development of patient specific 3D printed whole mandible implant. In: Proceedings of the 27th Annual International Solid Freeform Fabrication Symposium, pp. 1708−1717.

Monzón, M., Liu, C., Ajami, S., Oliveira, M., Donate, R., Ribeiro, V., Reis, R.L., 2018. Functionally graded additive manufacturing to achieve functionality specifications of osteochondral scaffolds. Bio-Des. Manuf. 1, 69−75.

Morgan, N.B., 2004. Medical shape memory alloy applications—the market and its products. Mater. Sci. Eng. A 378, 16–23.

Murr, L.E., Gaytan, S.M., Medina, F., Lopez, H., Martinez, E., Machado, B.I., Hernandez, D.H., Martinez, L., Lopez, M.I., Wicker, R.B., 2010. Next-generation biomedical implants using additive manufacturing of complex, cellular and functional mesh arrays. Phil. Trans. R. Soc. A Math. Phys. Eng. Sci. 368, 1999–2032.

Nagesha, B.K., Dhinakaran, V., Varsha Shree, M., Manoj Kumar, K.P., Chalawadi, D., Sathish, T., 2020. Review on characterization and impacts of the lattice structure in additive manufacturing. Mater. Today Proc. 21, 916–919.

Nam, J., Starly, B., Darling, A., Sun, W., 2004. Computer aided tissue engineering for modeling and design of novel tissue scaffolds. Comput.-Aided Des. Appl. 1, 633–640.

Nickels, L., 2012. World's first patient-specific jaw implant. Met. Powder Rep. 67, 12–14.

Niinomi, M., 2003. Recent research and development in titanium alloys for biomedical applications and healthcare goods. Sci. Technol. Adv. Mater. 4, 445.

Niu, H.J., Chang, I.T.H., 1999. Instability of scan tracks of selective laser sintering of high speed steel powder. Scripta Mater. 41, 1229–1234.

Nouri-Goushki, M., Mirzaali, M.J., Angeloni, L., Fan, D., Minneboo, M., Ghatkesar, M.K., Staufer, U., Fratila-Apachitei, L.E., Zadpoor, A.A., 2019. 3D printing of large areas of highly ordered submicron patterns for modulating cell behavior. ACS Appl. Mater. Interfaces 12, 200–208.

Nune, K.C., Misra, R.D.K., Gai, X., Li, S.J., Hao, Y.L., 2018. Surface nanotopography-induced favorable modulation of bioactivity and osteoconductive potential of anodized 3D printed Ti-6Al-4V alloy mesh structure. J. Biomater. Appl. 32, 1032–1048.

Obbard, E.G., Hao, Y.L., Akahori, T., Talling, R.J., Niinomi, M., Dye, D., Yang, R., 2010. Mechanics of superelasticity in Ti–30Nb–(8–10) Ta–5Zr alloy. Acta Mater. 58, 3557–3567.

Parthasarathy, J., 2014. 3D modeling, custom implants and its future perspectives in craniofacial surgery. Ann. Maxillofacial Surg. 4, 9.

Putra, N.E., Mirzaali, M.J., Apachitei, I., Zhou, J., Zadpoor, A.A., 2020. Multi-material additive manufacturing technologies for Ti-, Mg-, and Fe-based biomaterials for bone substitution. Acta Biomater. 109, 1–20.

Rho, J.-Y., Kuhn-Spearing, L., Zioupos, P., 1998. Mechanical properties and the hierarchical structure of bone. Med. Eng. Phys. 20, 92–102.

Roy, S.C.D., 2014. Some recent work on lattice structures for digital signal processing. Sadhana 39, 1271–1294.

Ryan, G., Pandit, A., Apatsidis, D.P., 2006. Fabrication methods of porous metals for use in orthopaedic applications. Biomaterials 27, 2651–2670.

Salem, H., Carter, L.N., Attallah, M.M., Salem, H.G., 2019. Influence of processing parameters on internal porosity and types of defects formed in Ti6Al4V lattice structure fabricated by selective laser melting. Mater. Sci. Eng. A 767, 138387.

Sánchez-Palencia, E., 1980. Non-homogeneous media and vibration theory. Lect. Notes Phys. 127.

Sigmund, O., Torquato, S., 1997. Design of materials with extreme thermal expansion using a three-phase topology optimization method. J. Mech. Phys. Solid. 45, 1037–1067.

Sing, S.L., Wiria, F.E., Yeong, W.Y., 2018. Selective laser melting of lattice structures: a statistical approach to manufacturability and mechanical behavior. Robot. Comput. Integrated Manuf. 49, 170–180.

Song, B., Dong, S., Qi, L., Liao, H., Coddet, C., 2014. Vacuum heat treatment of iron parts produced by selective laser melting: microstructure, residual stress and tensile behavior. Mater. Des. (1980–2015) 54, 727–733.

Speirs, M., Van Hooreweder, B., Van Humbeeck, J., Kruth, J.-P., 2017. Fatigue behaviour of NiTi shape memory alloy scaffolds produced by SLM, a unit cell design comparison. J. Mech. Behav. Biomed. Mater. 70, 53–59.

Stevens, B., Yang, Y., Mohandas, A., Stucker, B., Nguyen, K.T., 2008. A review of materials, fabrication methods, and strategies used to enhance bone regeneration in engineered bone tissues. J. Biomed. Mater. Res. B 85, 573–582.

Strano, G., Liang, H., Everson, R.M., Evans, K.E., 2013. Surface roughness analysis, modelling and prediction in selective laser melting. J. Mater. Process. Technol. 213, 589–597.

Su, X.-bin, Yang, Y., Peng, Y.U., Sun, J.-feng, 2012. Development of porous medical implant scaffolds via laser additive manufacturing. Trans. Nonferrous Metals Soc. China 22, s181–s187.

Sun, Z.P., Guo, Y.B., Shim, V.P.W., 2020. Characterisation and modeling of additively-manufactured polymeric hybrid lattice structures for energy absorption. Int. J. Mech. Sci. 191, 106101.

Tammas-Williams, S., Withers, P.J., Todd, I., Prangnell, P.B., 2016. The effectiveness of hot isostatic pressing for closing porosity in titanium parts manufactured by selective electron beam melting. Metall. Mater. Trans. A 47, 1939–1946.

Tang, H.P., Qian, M., Liu, N., Zhang, X.Z., Yang, G.Y., Wang, J., 2015a. Effect of powder reuse times on additive manufacturing of Ti-6Al-4V by selective electron beam melting. J. Occup. Med. 67, 555–563.

Thöne, M., Leuders, S., Riemer, A., Tröster, T., HA, R., 2012. Influence of heat-treatment on selective laser melting products–eg Ti6Al4V. In: Solid Freeform Fabrication Symposium SFF, Austin Texas.

Van Bael, S., Chai, Y.C., Truscello, S., Moesen, M., Kerckhofs, G., Van Oosterwyck, H., Kruth, J.-P., Schrooten, J.J.A.B., 2012. The effect of pore geometry on the in vitro biological behavior of human periosteum-derived cells seeded on selective laser-melted Ti6Al4V bone scaffolds. Acta Biomater. 8, 2824–2834.

van der Stok, J., Wang, H., Yavari, S.A., Siebelt, M., Sandker, M., Waarsing, J.H., Verhaar, J.A.N., Jahr, H., Zadpoor, A.A., Leeuwenburgh, S.C.G., 2013. Enhanced bone regeneration of cortical segmental bone defects using porous titanium scaffolds incorporated with colloidal gelatin gels for time-and dose-controlled delivery of dual growth factors. Tissue Eng. A 19, 2605–2614.

van der Stok, J., Koolen, M.K.E., de Maat, M., Yavari, S.A., Alblas, J., Peter, P., Verhaar, J.A.N., van Lieshout, E., Zadpoor, A.A., Weinans, H., 2015a. Full regeneration of segmental bone defects using porous titanium implants loaded with BMP-2 containing fibrin gels. Eur. Cell. Mater. 141–154.

Van Der Stok, J., Lozano, D., Chai, Y.C., Yavari, S.A., Bastidas Coral, A.P., Verhaar, J.A.N., Gómez-Barrena, E., Jan, S., Jahr, H., Zadpoor, A.A., 2015b. Osteostatin-coated porous titanium can improve early bone regeneration of cortical bone defects in rats. Tissue Eng. A 21, 1495–1506.

Van Eijnatten, M., van Dijk, R., Dobbe, J., Streekstra, G., Koivisto, J., Wolff, J., 2018. CT image segmentation methods for bone used in medical additive manufacturing. Med. Eng. Phys. 51, 6–16.

van Hengel, I.A.J., Riool, M., Fratila-Apachitei, L.E., Witte-Bouma, J., Farrell, E., Zadpoor, A.A., Zaat, S.A.J., Apachitei, I., 2017. Selective laser melting porous metallic implants with immobilized silver nanoparticles kill and prevent biofilm formation by methicillin-resistant *Staphylococcus aureus*. Biomaterials 140, 1–15.

van Hengel, I.A.J., Tierolf, M.W.A.M., Valerio, V.P.M., Minneboo, M., Fluit, A.C., Fratila-Apachitei, L.E., Apachitei, I., Zadpoor, A.A., 2020. Self-defending additively manufactured bone implants bearing silver and copper nanoparticles. J. Mater. Chem. B 8, 1589−1602.

Van Hooreweder, B., Kruth, J.-P., 2017. Advanced fatigue analysis of metal lattice structures produced by selective laser melting. CIRP Ann. 66, 221−224.

Van Hooreweder, B., Apers, Y., Lietaert, K., Kruth, J.-P., 2017. Improving the fatigue performance of porous metallic biomaterials produced by selective laser melting. Acta Biomater. 47, 193−202.

Van Humbeeck, J., 2018. Additive manufacturing of shape memory alloys. Shape Mem. Superelasticity 4, 309−312.

van Manen, T., Janbaz, S., Zadpoor, A.A., 2018. Programming the shape-shifting of flat soft matter. Mater. Today 21, 144−163.

Vilardell, A.M., Takezawa, A., Du Plessis, A., Takata, N., Krakhmalev, P., Kobashi, M., Albu, M., Kothleitner, G., Yadroitsava, I., Yadroitsev, I., 2020. Mechanical behavior of in-situ alloyed Ti6Al4V (ELI)-3 at.% Cu lattice structures manufactured by laser powder bed fusion and designed for implant applications. J. Mech. Behav. Biomed. Mater. 104130.

Vilaro, T., Colin, C., Bartout, J.-D., 2011. As-fabricated and heat-treated microstructures of the Ti-6Al-4V alloy processed by selective laser melting. Metall. Mater. Trans. A 42, 3190−3199.

Vojtěch, D., Kubásek, J., Šerák, J., Novák, P., 2011. Mechanical and corrosion properties of newly developed biodegradable Zn-based alloys for bone fixation. Acta Biomater. 7, 3515−3522.

Vora, P., Mumtaz, K., Todd, I., Hopkinson, N., 2015. AlSi12 in-situ alloy formation and residual stress reduction using anchorless selective laser melting. Addit. Manuf. 7, 12−19.

Vrancken, B., Thijs, L., Kruth, J.-P., Van Humbeeck, J., 2012. Heat treatment of Ti6Al4V produced by selective laser melting: microstructure and mechanical properties. J. Alloys Compd. 541, 177−185.

Wang, M.Y., Wang, X., Guo, D., 2003. A level set method for structural topology optimization. Comput. Methods Appl. Mech. Eng. 192, 227−246.

Wang, Di, Yang, Y., Liu, R., Xiao, D., Sun, J., 2013. Study on the designing rules and processability of porous structure based on selective laser melting (SLM). J. Mater. Process. Technol. 213, 1734−1742.

Wang, X., Xu, S., Zhou, S., Xu, W., Leary, M., Peter, C., Qian, M., Brandt, M., Xie, Y.M., 2016. Topological design and additive manufacturing of porous metals for bone scaffolds and orthopaedic implants: a review. Biomaterials 83, 127−141.

Wang, Q., Han, C., Choma, T., Wei, Q., Yan, C., Song, B., Shi, Y., 2017a. Effect of Nb content on microstructure, property and in vitro apatite-forming capability of Ti-Nb alloys fabricated via selective laser melting. Mater. Des. 126, 268−277.

Wang, Z., Denlinger, E., Michaleris, P., Stoica, A.D., Dong, M., Beese, A.M., 2017b. Residual stress mapping in inconel 625 fabricated through additive manufacturing: method for neutron diffraction measurements to validate thermomechanical model predictions. Mater. Des. 113, 169−177.

Wang, X., Kustov, S., Van Humbeeck, J., 2018a. A short review on the microstructure, transformation behavior and functional properties of NiTi shape memory alloys fabricated by selective laser melting. Materials 11, 1683.

Wang, Y., Zhang, L., Daynes, S., Zhang, H., Feih, S., Wang, M.Y., 2018b. Design of graded lattice structure with optimized mesostructures for additive manufacturing. Mater. Des. 142, 114−123.

Wauthle, R., Ahmadi, S.M., Yavari, S.A., Mulier, M., Zadpoor, A.A., Weinans, H., Van Humbeeck, J., Kruth, J.-P., Schrooten, J., 2015a. Revival of pure titanium for dynamically loaded porous implants using additive manufacturing. Mater. Sci. Eng. C 54, 94−100.

Wauthle, R., Van Der Stok, J., Yavari, S.A., Van Humbeeck, J., Kruth, J.-P., Zadpoor, A.A., Weinans, H., Mulier, M., Schrooten, J., 2015b. Additively manufactured porous tantalum implants. Acta Biomater. 14, 217−225.

Wauthle, R., Vrancken, B., Beynaerts, B., Jorissen, K., Jan, S., Kruth, J.-P., Van Humbeeck, J., 2015c. Effects of build orientation and heat treatment on the microstructure and mechanical properties of selective laser melted Ti6Al4V lattice structures. Addit. Manuf. 5, 77−84.

Wen, P., Jauer, L., Voshage, M., Chen, Y., Poprawe, R., Schleifenbaum, J.H., 2018. Densification behavior of pure Zn metal parts produced by selective laser melting for manufacturing biodegradable implants. J. Mater. Process. Technol. 258, 128−137.

Windhagen, H., Radtke, K., Weizbauer, A., Diekmann, J., Noll, Y., Kreimeyer, U., Schavan, R., Stukenborg-Colsman, C., Waizy, H., 2013. Biodegradable magnesium-based screw clinically equivalent to titanium screw in hallux valgus surgery: short term results of the first prospective, randomized, controlled clinical pilot study. Biomed. Eng. Online 12, 62.

Wu, M.-W., Lai, P.-H., 2016. The positive effect of hot isostatic pressing on improving the anisotropies of bending and impact properties in selective laser melted Ti-6Al-4V alloy. Mater. Sci. Eng. A 658, 429−438.

Wu, J., Aage, N., Westermann, R., Sigmund, O., 2017a. Infill optimization for additive manufacturing—approaching bone-like porous structures. IEEE Trans. Visualization Comput. Graph. 24, 1127−1140.

Wu, M.-W., Chen, J.-K., Lin, B.-H., Chiang, P.-H., 2017b. Improved fatigue endurance ratio of additive manufactured Ti-6Al-4V lattice by hot isostatic pressing. Mater. Des. 134, 163−170.

Xiao, D., Yang, Y., Su, X., Wang, Di, Sun, J., 2013. An integrated approach of topology optimized design and selective laser melting process for titanium implants materials. Bio Med. Mater. Eng. 23, 433−445.

Xie, Y.M., Steven, G.P., 1993. A simple evolutionary procedure for structural optimization. Comput. Struct. 49, 885−896.

Xie, Y.M., Steven, G.P., 1997. Basic evolutionary structural optimization. In: Evolutionary Structural Optimization. Springer.

Yakout, M., Elbestawi, M.A., Veldhuis, S.C., 2019. Density and mechanical properties in selective laser melting of Invar 36 and stainless steel 316L. J. Mater. Process. Technol. 266, 397−420.

Yan, C., Liang, H., Ahmed, H., Young, P., Raymont, D., 2014. Advanced lightweight 316L stainless steel cellular lattice structures fabricated via selective laser melting. Mater. Des. 55, 533−541.

Yan, C., Liang, H., Ahmed, H., Young, P., 2015. Ti−6Al−4V triply periodic minimal surface structures for bone implants fabricated via selective laser melting. J. Mech. Behav. Biomed. Mater. 51, 61−73.

Yan, Y., Li, Y., Song, L., Zeng, C., 2017. Pluripotent stem cell expansion and neural differentiation in 3-D scaffolds of tunable Poisson's ratio. Acta Biomater. 49, 192−203.

Yánez, A., Cuadrado, A., Martel, O., Afonso, H., Monopoli, D., 2018. Gyroid porous titanium structures: a versatile solution to be used as scaffolds in bone defect reconstruction. Mater. Des. 140, 21−29.

Yang, L., Yan, C., Cao, W., Liu, Z., Song, B., Wen, S., Zhang, C., Shi, Y., Yang, S., 2019. Compression−compression fatigue behaviour of gyroid-type triply periodic minimal surface porous structures fabricated by selective laser melting. Acta Mater. 181, 49−66.

Yavari, S.A., Wauthlé, R., van der Stok, J., Riemslag, A.C., Janssen, M., Mulier, M., Kruth, J.-P., Jan, S., Weinans, H., Zadpoor, A.A., 2013. Fatigue behavior of porous biomaterials manufactured using selective laser melting. Mater. Sci. Eng. C 33, 4849−4858.

Yavari, S.A., Ahmadi, S.M., van der Stok, J., Wauthlé, R., Riemslag, A.C., Janssen, M., Jan, S., Weinans, H., Zadpoor, A.A., 2014a. Effects of bio-functionalizing surface treatments on the mechanical behavior of open porous titanium biomaterials. J. Mech. Behav. Biomed. Mater. 36, 109−119.

Yavari, S.A., Wauthlé, R., Böttger, A.J., Jan, S., Weinans, H., Zadpoor, A.A., 2014b. Crystal structure and nanotopographical features on the surface of heat-treated and anodized porous titanium biomaterials produced using selective laser melting. Appl. Surf. Sci. 290, 287−294.

Yavari, S.A., Ahmadi, S.M., Wauthle, R., Pouran, B., Schrooten, J., Weinans, H., Zadpoor, A.A., 2015. Relationship between unit cell type and porosity and the fatigue behavior of selective laser melted meta-biomaterials. J. Mech. Behav. Biomed. Mater. 43, 91−100.

Yavari, S.A., Croes, M., Akhavan, B., Jahanmard, F., Eigenhuis, C.C., Dadbakhsh, S., Vogely, H.C., Bilek, M.M., Fluit, A.C., CHE, B., 2020. Layer by layer coating for bio-functionalization of additively manufactured meta-biomaterials. Addit. Manuf. 32, 100991.

Yoo, D.J., 2011a. Porous scaffold design using the distance field and triply periodic minimal surface models. Biomaterials 32, 7741−7754.

Yoo, D.-J., 2011b. Computer-aided porous scaffold design for tissue engineering using triply periodic minimal surfaces. Int. J. Precis. Eng. Manuf. 12, 61−71.

Youssef, S., Maire, E., Gaertner, R., 2005. Finite element modelling of the actual structure of cellular materials determined by X-ray tomography. Acta Mater. 53, 719−730.

Yuan, L., Ding, S., Wen, C., 2019a. Additive manufacturing technology for porous metal implant applications and triple minimal surface structures: a review. Bioact. Mater. 4, 56−70.

Yuan, S., Chua, C.K., Zhou, K., 2019b. 3D-Printed mechanical metamaterials with high energy absorption. Adv. Mater. Technol. 4, 1800419.

Zadpoor, A.A., 2013. Open forward and inverse problems in theoretical modeling of bone tissue adaptation. J. Mech. Behav. Biomed. Mater. 27, 249−261.

Zadpoor, A.A., 2015. Bone tissue regeneration: the role of scaffold geometry. Biomater. Sci. 3, 231−245.

Zadpoor, A.A., 2016. Mechanical meta-materials. Mater. Horiz. 3, 371−381.

Zadpoor, A.A., 2017. Design for additive bio-manufacturing: from patient-specific medical devices to rationally designed meta-biomaterials. Int. J. Mol. Sci. 18, 1607.

Zadpoor, A.A., 2018. Frontiers of additively manufactured metallic materials. In: Multidisciplinary Digital. Publishing Institute.

Zadpoor, A.A., 2019. Additively manufactured porous metallic biomaterials. J. Mater. Chem. B 7, 4088−4117.

Zadpoor, A.A., 2020. Meta-biomaterials. Biomater. Sci. 8, 18−38.

Zadpoor, A.A., Hedayati, R., 2016. Analytical relationships for prediction of the mechanical properties of additively manufactured porous biomaterials. J. Biomed. Mater. Res. A 104, 3164−3174.

Zadpoor, A.A., Campoli, G., Weinans, H., 2013. Neural network prediction of load from the morphology of trabecular bone. Appl. Math. Model. 37, 5260−5276.

Zargarian, A., Esfahanian, M., Kadkhodapour, J., Ziaei-Rad, S., 2016. Numerical simulation of the fatigue behavior of additive manufactured titanium porous lattice structures. Mater. Sci. Eng. C 60, 339−347.

Zargarian, A., Esfahanian, M., Kadkhodapour, J., Ziaei-Rad, S., Zamani, D., 2019. On the fatigue behavior of additive manufactured lattice structures. Theor. Appl. Fract. Mech. 100, 225−232.

Zhang, L.-C., Attar, H., 2016. Selective laser melting of titanium alloys and titanium matrix composites for biomedical applications: a review. Adv. Eng. Mater. 18, 463−475.

Zhang, X.Z., Leary, M., Tang, H.P., Song, T., Qian, M., 2018. Selective electron beam manufactured Ti-6Al-4V lattice structures for orthopedic implant applications: current status and outstanding challenges. Curr. Opin. Solid State Mater. Sci. 22, 75−99.

Zhang, X., Yocom, C.J., Mao, B., Liao, Y., 2019. Microstructure evolution during selective laser melting of metallic materials: a review. J. Laser Appl. 31, 031201.

Zhao, S., Li, S.J., Hou, W.T., Hao, Y.L., Yang, R., Misra, R.D.K., 2016. The influence of cell morphology on the compressive fatigue behavior of Ti-6Al-4V meshes fabricated by electron beam melting. J. Mech. Behav. Biomed. Mater. 59, 251−264.

Zhao, S., Li, S.J., Wang, S.G., Hou, W.T., Li, Y., Zhang, L.C., Hao, Y.L., Yang, R., Misra, R.D.K., Murr, L.E., 2018. Compressive and fatigue behavior of functionally graded Ti-6Al-4V meshes fabricated by electron beam melting. Acta Mater. 150, 1−15.

Zhao, Z., Li, J., Bai, P., Qu, H., Liang, M., Liao, H., Wu, L., Huo, P., Liu, H., Zhang, J., 2019. Microstructure and mechanical properties of TiC-reinforced 316L stainless steel composites fabricated using selective laser melting. Metals 9, 267.

Zheng, Y.F., Gu, X.N., Witte, F., 2014. Biodegradable metals. Mater. Sci. Eng. R Rep. 77, 1−34.

Zhou, M., Rozvany, G.I.N., 1991. The COC algorithm, Part II: topological, geometrical and generalized shape optimization. Comput. Methods Appl. Mech. Eng. 89, 309−336.

Zhou, J., Shrotriya, P., Soboyejo, W.O., 2004. On the deformation of aluminum lattice block structures: from struts to structures. Mech. Mater. 36, 723−737.

Zhou, J., Dong, J., Wang, B., Koschny, T., Kafesaki, M., Soukoulis, C.M., 2009. Negative refractive index due to chirality. Phys. Rev. B 79, 121104.

Bio-inspired design

17

Yash Mistry, Daniel Anderson, Dhruv Bhate
3DX Research Group, The Polytechnic School, Arizona State University, Mesa, AZ, United States

Chapter outline

17.1 Introduction 467
17.1.1 Innovation inspired by nature 467
17.1.2 Bio-inspired design and laser powder bed fusion 468
17.2 Types of bio-inspired design 469
17.2.1 Simulation-driven biomimetic design 469
17.2.2 Explicit biomimicry 472
17.2.3 Abstracted bio-inspired design 472
17.3 Concepts 475
17.3.1 Discretization 475
17.3.2 Symmetry 478
17.3.3 Gradients 478
17.3.4 Structural hierarchy 480
17.4 Applications 480
17.4.1 Structural components 481
17.4.2 Thermal management 483
17.4.3 Energy absorption 483
17.4.4 Optics 484
17.5 Manufacturing considerations 484
17.6 Discussion 485
17.7 Conclusion 486
17.8 Questions 486
Acknowledgements 487
References 487

17.1 Introduction

17.1.1 Innovation inspired by nature

John Muir, the influential naturalist and author, once wrote in a letter to a contemporary, “in every walk with nature one receives far more than he seeks.” Designers and engineers have occasionally made a similar, if figurative, walk with nature in their

Fundamentals of Laser Powder Bed Fusion of Metals. https://doi.org/10.1016/B978-0-12-824090-8.00010-X
Copyright © 2021 Elsevier Inc. All rights reserved.

continuous pursuit of design ideas that make our world better, and have often discovered ideas in the most unexpected of places. Advances in additive manufacturing (AM), computational design tools, and digitization techniques are converging in an exciting new era of engineering design, as humanity has never experienced before. Within this convergent domain, Bio-Inspired Design (BID) is a particularly promising area of research since the potential space for establishing structure-function correlation is vast, and the majority of it is untapped. In this chapter, this field is studied specifically in the context of Laser Powder Bed Fusion (L-PBF). At the outset however, some definitions are necessary.

The 21st century has elevated this notion of drawing inspiration from nature to inform engineering design to a discipline in its own right, called biomimicry. Bio-Inspired Design, or BID, is a subset of the wider field of biomimicry, which itself is perhaps best defined most generally as "innovation inspired by nature" (Benyus, 1997). When this innovation mimics form or structure, as opposed to processes or systems, one arrives at BID. BID may typically be implemented in one of two ways, posing a design challenge to nature (such as how to minimize mass in structures), or translating a biological observation in nature to an engineering application (such as plant burrs leading to Velcro).

17.1.2 Bio-inspired design and laser powder bed fusion

A challenge with interpreting and mimicking biological structure is in handling and realizing the sheer complexity of its designs. Recent advances in digitization methods, computational design tools, and Additive Manufacturing (AM) have now made it possible to study, design, and make structures that leverage biological design principles (Du Plessis et al., 2018, 2019). Additive manufacturing, in particular, is well known for its ability to realize complex designs—the first argument for using AM for realizing BID is therefore a somewhat trivial one: there is no other way to realize the structures at the level of design freedom being sought. But there is another, more subtle reason why the focus on AM makes sense: BID is widely recognized as a field with great potential and demonstrated successes, but BID in engineering design largely remains empirical in its implementation (Vincent et al., 2006). For example, whereas the application of the TRIZ (a Russian acronym that may be translated as the "theory of the resolution of invention-related tasks") (Altshuller, 1984) methodology to BID (Vincent et al., 2005) has yielded powerful insights, in particular the greater use of information, structure, and space in nature to address problems (Vincent et al., 2006), it is still not an integral part of an aerospace or automotive engineering designer's toolkit. A key observation of relevance is the prescient recommendation by Vincent et al. (2006) to "concentrate on those materials synthesis systems with least energy requirement and the greatest initial variability, and generate the required functionality by closer control of the information content." It may be thus argued that the key to the greater implementation of BID in engineering applications is the use of AM technologies, due to their ability to operate on a fine discretization of space, and allocate material with a higher degree of control than hitherto possible (Kamps et al., 2017; Bhate et al., 2019).

Within the domain of metal AM, L-PBF has emerged as the dominant technology—while there are several reasons for this, one of the factors in favor of L-PBF that make it a strong candidate for realizing bio-inspired designs is the range of scales that it operates over. With L-PBF, generally speaking, one can realize part geometries in sizes approaching 1 m in the largest machines being developed, and yet resolve features on the order of tens of microns, as shown in Fig. 17.1. The specific dimensions that are achievable are dependent on the machine and material under consideration, but this control of dimensions over six orders of magnitude is remarkable, and arguably unmatched in any other metals manufacturing process. Somewhat conveniently, this range of structural dimensions overlaps with a significant extent of biological structures, which of course do extend beyond this range as well. One does not expect to be manufacturing metals with the dimensions of amino acids or a blue whale on an L-PBF machine anytime soon.

L-PBF is thus a manufacturing process that is not only already finding increasing application in the aerospace and biomedical industries particularly, with other sectors following suit, but also well suited for realizing BID in applications where such a design approach can be impactful. Authors have suggested that BID and L-PBF may represent the perfect "symbiosis" (Gralow et al., 2020), or "synergy" (Du Plessis and Broeckhoven, 2021).

17.2 Types of bio-inspired design

Over the past two decades, several high-level methodologies have been developed for BID, and biomimicry more generally (Vincent, 2009; Baumeister and Smith, 2014; Cohen et al., 2014; Mcnulty et al., 2017; Vincent et al., 2006, 2005). In the context of BID for L-PBF, specific practical approaches have emerged (Du Plessis et al., 2019), which may be classified in three areas, depending on the design intent and the application in question, as simulation-driven, explicit biomimicry, and abstracted BID, shown together in Fig. 17.2.

17.2.1 Simulation-driven biomimetic design

Most simulation-driven designs attempt to optimize a functional benefit of some sort, such as minimizing thermal expansion or maximizing stiffness. One may argue that evolution by natural selection, with some exceptions, is also an optimization process. This holds true even beyond the abstract—consider, for example, the long bones in the legs of mammals, which have, it may be supposed, evolved to resist forces which tend to bend them. These long bones are hollow and filled with marrow. Solving the bending equation for hollow tubes, and applying methods of calculus, yields an optimum ratio of inner diameter to outer diameter of 0.63. In mammals, this ratio is found to be in the range 0.4−0.7 (Alexander, 1996).

Over the past three decades, design and analysis have increasingly moved toward reliance on computational tools, and the present era of design is one in which

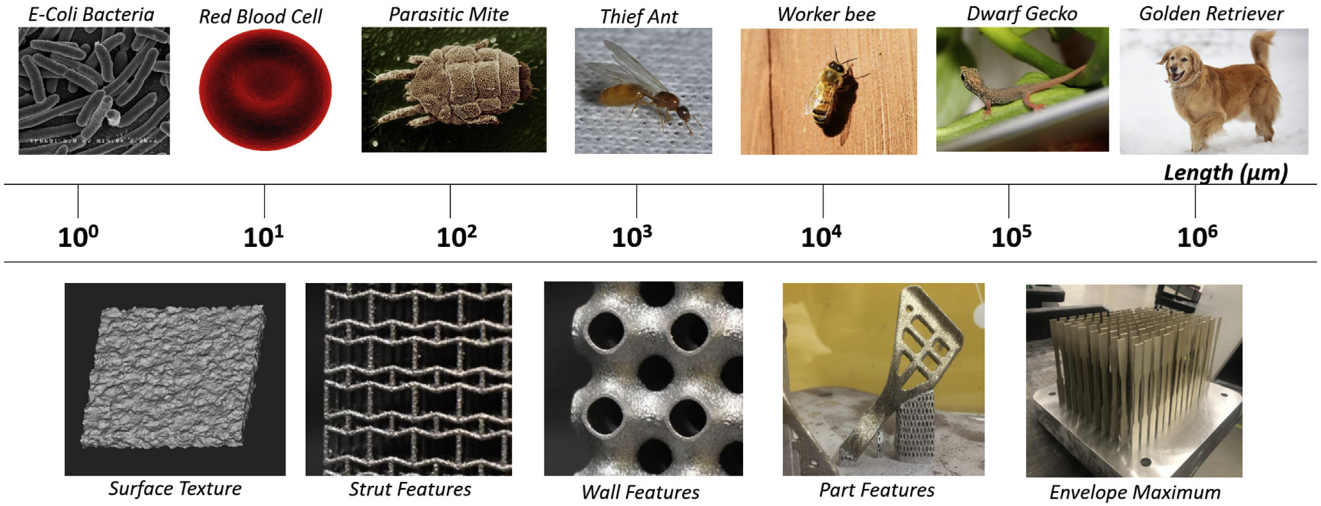
E-Coli Bacteria
Red Blood Cell
Parasitic Mite
Thief Ant
Worker bee
Dwarf Gecko
Golden Retriever
Length (μm)
10^0
10^1
10^2
10^3
10^4
10^5
10^6
Surface Texture
Strut Features
Wall Features
Part Features
Envelope Maximum

Figure 17.1 Length scales of organisms in nature (top) and achievable with L-PBF (bottom) show remarkable, if not complete, overlap.

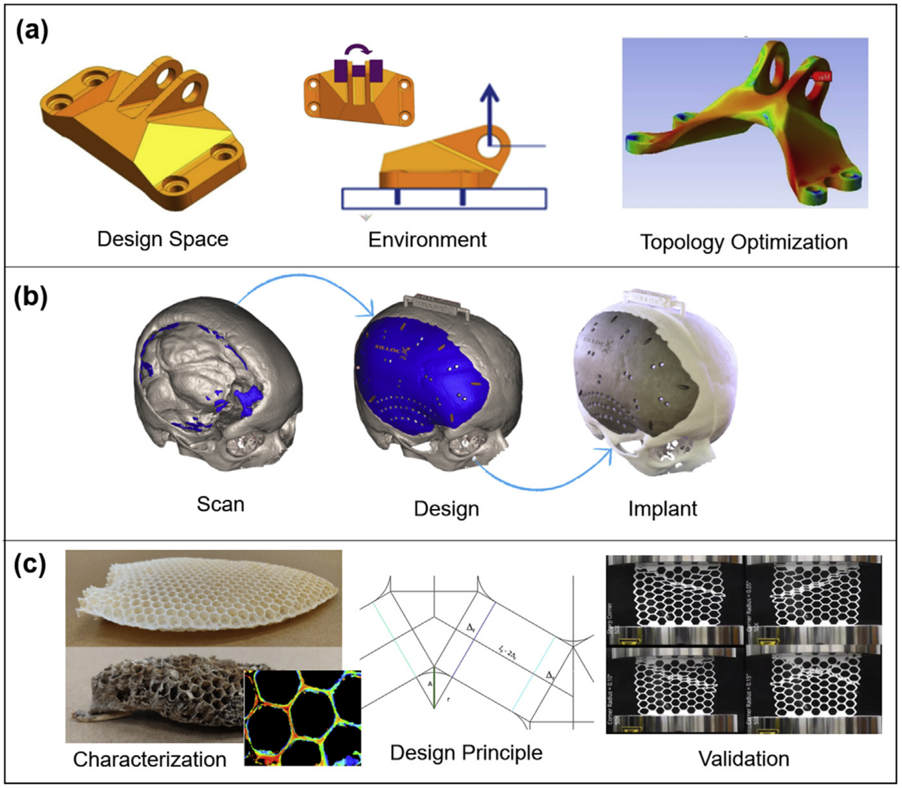

Figure 17.2 Three approaches to bio-inspired design: (a) Simulation-driven design, demonstrated here for topology optimization of a bracket; (b) Explicit biomimicry, shown here for a cranial implant; and (c) Abstracted design, shown here for a study of the nature of the corner radius in a honeycomb.
(b) Image credits: Maikel Beerens, Xilloc, licensed under Creative Commons Attribution-Share Alike 4.0 International.

simulation is driving the design process, integrating the previously separate realms of design and analysis into "Computer Aided Engineering" tools that can do both. Design for AM has emerged at a particularly interesting realm of study, with several commercial software packages offering simulation-driven design tools specifically aimed at manufacturing with AM, including L-PBF. The main idea behind this approach is to begin with a design space, specify boundary conditions and loads in the environment, and then leverage optimization techniques such as Solid Isotropic Material with Penalization (SIMP) or the level set method to arrive at a topology (Plocher and Panesar, 2019), as shown in Fig. 17.2a. Simulation-driven design is thus often referred to as topology optimization or generative design, both of which are synonymous concepts.

While the process of simulation-driven design may result in organic shapes that appear bio-inspired, there is no explicit requirement of any inputs from the designer that is derived from a study of natural structure. There are, however, at least two ways simulation-driven design may be coupled to BID. The first is the use of bio-inspired design constraints—for example, optimization may be performed over the entire design space, or discretized into smaller regions, prescribed by bio-inspired observations to yield bonelike structures (Wu et al., 2017). Alternatively, the design process may leverage genetic algorithms to select among a range of solutions, which does derive inspiration from biological evolution.

17.2.2 Explicit biomimicry

Whereas simulation-driven design is implicitly coupled to biological inspiration, there are areas where a more direct replication of biological structure is the goal. The immediate example of this use of biomimicry is in the design of engineering materials and structures with the intent of replacing a biological structure in its natural environment, as is the case for patient-specific biomedical implants, as shown in Fig. 17.2b. The biological structure of interest is first digitized, often using X-ray tomography or magnetic resonance imaging. This digital replica is used as a foundation to design a structure that will serve as the implant, which is finally manufactured with AM techniques. This is a critical application where L-PBF has proved to be a leading manufacturing technology due to its ability to resolve fine features and manufacture parts from biocompatible materials like titanium and cobalt-chrome alloys (Yuan et al., 2019).

17.2.3 Abstracted bio-inspired design

Perhaps the most appropriate use of the term BID is when it is applied to the abstraction of design principles (Fig. 17.2c) (Baumeister, 2014). A design principle in this context is a relationship between structure and function that has been distilled down to a form where it may be abstracted from its biological context and implemented in an engineering application. This approach straddles the space between the two previous approaches where BID is either implicit or at best has a limited interaction with the design process, as in the case of simulation-driven design, and the more explicit form of replicating biological structure and operating within the identical context. The abstracted BID approach is a more involved one, often requiring a deeper study of the biological structure and its functional context, coupled with analytical, computational, and/or experimental methods that enable a validation of the design principle in the engineering context.

The abstracted BID approach may be broken down into four main steps, each with two substeps within it, as shown in Fig. 17.3, where it is demonstrated for the development of honeycomb core used in aircraft panels (Goss et al., 2020). All these steps are not always necessary, and the depth of study undertaken within each step may be different based on the application in question. These four steps, adapted from a

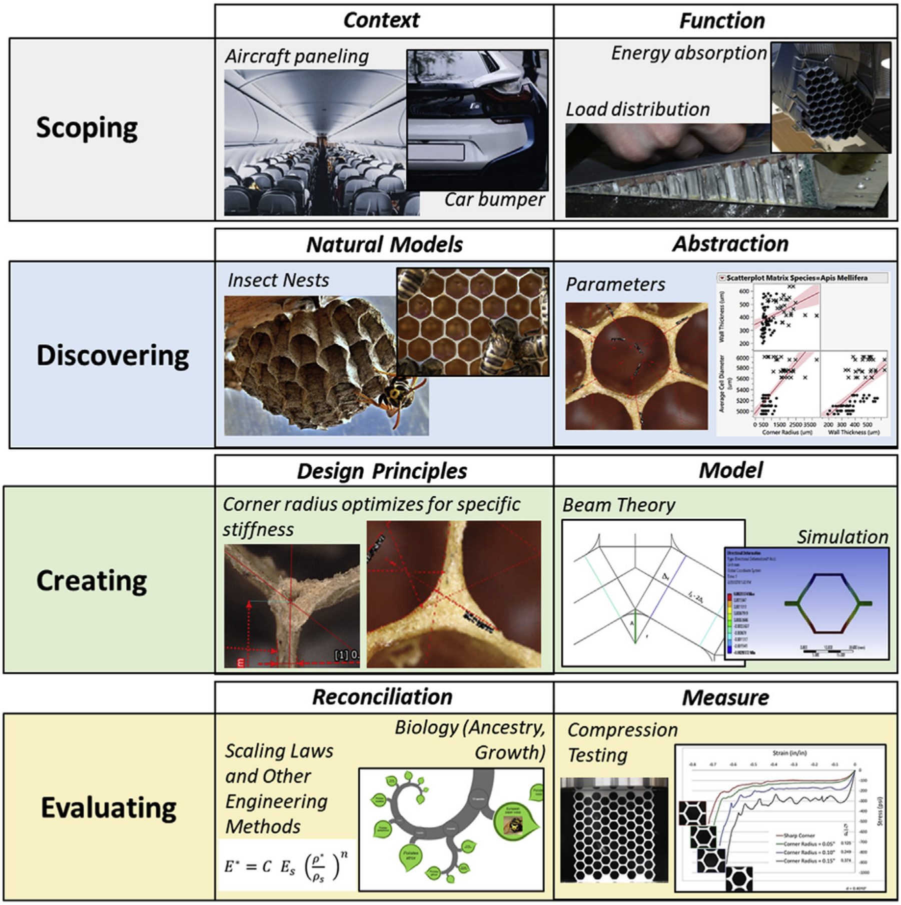
Context
Function
Scoping
Aircraft paneling
Car bumper
Energy absorption
Load distribution
Natural Models
Abstraction
Discovering
Insect Nests
Parameters
Scatterplot Matrix Species=Apis Mellifera
Wall Thickness (um)
Average Cell Diameter (um)
Corner Radius (um)
Wall Thickness (um)
Design Principles
Model
Creating
Corner radius optimizes for specific stiffness
Beam Theory
Simulation
Reconciliation
Measure
Evaluating
Biology (Ancestry, Growth)
Scaling Laws and Other Engineering Methods
$E^* = C\ E_s \left(\frac{\rho^*}{\rho_s}\right)^n$
Compression Testing
Strain (in/in)
Stress (psi)
Sharp Corner
Corner Radius = 0.05"
Corner Radius = 0.10"
Corner Radius = 0.15"

Figure 17.3 Four steps in the process of abstracting a design principle from nature for implementation in engineering application with additive manufacturing (Goss et al., 2020).

previously developed biomimicry methodology (Baumeister and Smith, 2014), are as follows:

i. Scoping: the first step involves definition of the scope of the engineering application of interest. In this case, the scope may be defined as being specific to the application (context) of aircraft interior paneling. This then provides an expectation of the functions this structure needs to serve in this context, viz., to distribute loads over large planar regions without local failures, but also to absorb energy from impacts such as when an overhead compartment door is slammed against the wheels of protruding carry-on baggage, and doing so while minimizing mass.

ii. Discovering: in the second step, biological structures that thrive in similar environments as the ones scoped above are sought out. In this instance, insect nests are one candidate that may be studied. In this phase, key design features are abstracted, such as the thickness or corner radius parameters.

iii. Creating: in the third stage the abstracted design feature is studied for its functional benefit in the engineering context, typically leveraging analytical or computational methods. This step is vital for establishing a relationship between function and a structural parameter.

iv. Evaluating: finally, the relationship established is evaluated both in the biological context, to ascertain if there is evidence of the relationship in the species studied and/or in related species. Corroborating evidence may also be sought in traditional engineering approaches relevant to the application in question. Additionally, experimental validation can be performed using parts made with AM and translated into final application.

Abstracting design principles in the manner discussed above helps the user of a BID approach sidestep some of the potential pitfalls of the method. For example, it must be remembered that nature constructs structure from organic matter, not the alloys commonly used in the L-PBF process. Additionally, natural structures are arrived through specific growth and development processes that are not relevant in AM, and further, may be operating in a constrained design space for evolutionary reasons. Finally, natural structures may have evolved for reasons beyond just the one or more functional benefits the designer is interested in. As a result, it is helpful to perform these steps as described above, or at least address the questions they raise.

A key question in the use of BID with L-PBF is: *When does it make sense to take a BID approach to designing for L-PBF?* With replication of biological designs as in the case of designing and fabricating biomedical implants, this is an obvious path to take. However, in nonbiomedical applications, more consideration needs to be given to the value proposition of using BID. After all, one may counter, humans have made it to the moon and back using a wide range of metal components, without relying on BID and L-PBF. There are, however, at least four practical reasons to consider BID, in addition to the fact that a BID approach almost always uncovers some form of previously unknown insight. The four reasons below, if prevalent in the design problem under consideration, increase the likelihood that this insight can be impactful.

i. Multifunctionality: Most studies of biological structure quickly reveal that the structure in question has almost always evolved for more than one specific function. An inverse argument thus can be made that biological structures are particularly useful for study when a multi-objective problem is being addressed. To consider one example, the honeybee's nest is not just a structural framework that sustains self-weight, wind loads, and other abuses placed by virtue of being in an open environment but also enables the storage of materials, gaseous exchange, thermal management, vibration transmission to aid in communication, and more (Hepburn et al., 2014).

ii. Design uncertainty: Natural structures have to thrive in fairly uncertain loading conditions, in comparison to the more well-defined engineering environment that designers tailor to. Nature achieves remarkable structural performance even in presence of this uncertainty. A particularly interesting application on the horizon is the design of extraterrestrial structures with materials of large variance or uncertainty in mechanical properties (Meurisse et al., 2017), or the design of engineering structures with low-quality, recycled or bio-derived materials (Ormondroyd and Morris, 2019).

iii. Large deformation: Several natural structures handle large deformation with ease—consider the pomelo fruit that impacts the ground with minimum damage, or the swaying of palm tree fronds in the wind. Design optimization in the presence of large deformation, and often accompanying nonlinear material behavior common in metals, is currently a significant computational hurdle—one where a BID approach can enable rapid identification of design strategies for exploration. A specific example of this is in irreversible energy absorption, where the structure in question experiences large deformations and highly nonlinear behavior (Ha and Lu 2020).

iv. Damage tolerance: Finally, natural structures tend to have remarkable damage tolerance, and have a far smaller dependence on the purity and performance of the base materials involved, instead relying on geometry and repair to make robust structures (Vincent et al., 2006). The wings of insects are a particular example, where it has been argued that the venation pattern aids in limiting damage propagation (Dirks and Taylor, 2012). This also has implications in L-PBF from a process standpoint, since as-printed L-PBF parts have nonnegligible porosity and surface roughness that can have significant impact on part performance.

17.3 Concepts

Each biological species embodies a wealth of information for study and potential abstraction into engineering application using the previously described methods. A case may be made, however, for some general cross-cutting concepts observed in biological structures that translate well into design for L-PBF. This builds on the notion that any natural structure is essentially some combination of form (i.e., shape and size) and pattern (i.e., texture, or infill) (Ball, 2009). The form is often what is visible at a superficial level, like the wing of a bird. The pattern, in this case the overlay of feathers, themselves constituted of smaller elements, is revealed on closer examination.

An explicit BID approach would, for example, perform a 3D scan or X-ray tomography analysis and directly replicate that design in a computer and use AM to realize the part in question. The key however is in the *abstraction* of the design principle, the comprehension of the relationship between the observed form and/or pattern, and the postulated functional benefit. To arrive at the design principle, it helps to examine the biological structure in question by asking four design questions: (i) How is the overall form discretized? (ii) What symmetry does it exhibit—both globally, as well as locally? (iii) Does the structure demonstrate any gradients? (iv) Does it demonstrate any hierarchy? While these four questions are not comprehensive, they do allow the designer to focus on ideas that are quantifiable, and amenable for implementation in design software, and by extension, realizable with L-PBF, as long as the resulting geometry lies within process constraints.

17.3.1 Discretization

Natural structures such as the examples shown in Fig. 17.4 tend to be discretized at several length scales, all the way to the individual cells that constitute the tissue in question. A homogeneous material can be considered as an instance of a discretized structure taken to its volume-filling limit. This approach of thinking of engineering design mirrors the local symmetry breaking mechanisms that underlie morphogenesis (Li and Bowerman, 2010), i.e., the formation of biological structure, which while fascinating in its own right, is not of immediate relevance for the current discussion,

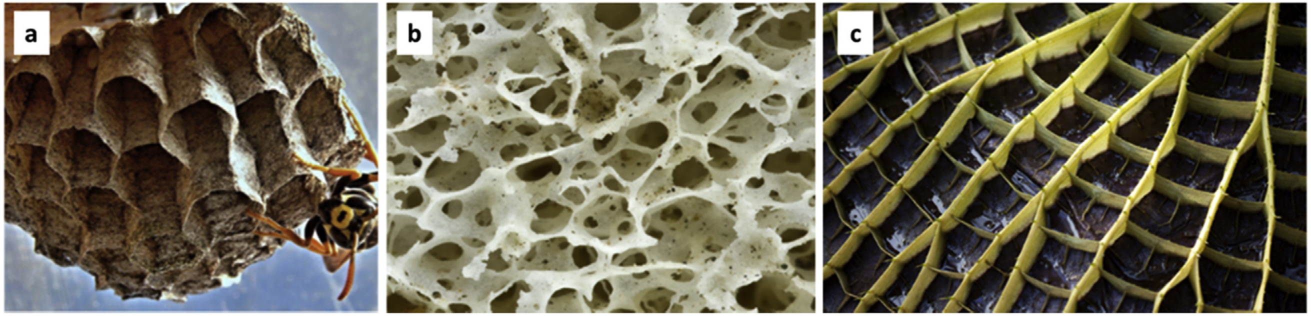

Figure 17.4 Natural structures exhibit discretized, or cellular design: (a) wasp nest, (b) cancellous bone, and (c) venation of a water lily leaf. Photo Credits: Wikimedia Commons, (b) Neon, (c) Laitr Keiows.

where the aim is not to mimic nature's manufacturing process but the structure that results from it. Beyond the developmental aspects of natural structure however there are clear functional benefits of discretized structure, be these scales on a snakeskin or the foam-like cellularity of bone (Gibson et al., 2010; Mcnulty et al., 2017). Discretization also enables the local refinement of design, and enables the subsequent concepts of gradients and hierarchy. The key design decisions that need to be made are (Bhate, 2019):

i. Cell shape: nature of tessellation, constituent elements of unit cell (e.g., strut vs. surface), and nodal connectivity.
ii. Cell size distribution: how large a cell should be, and how this size should vary across the structure.
iii. Optimization of cell parameters: how thick members should be, and how this should evolve spatially.
iv. Integration: termination of cellular materials at external boundaries.

Discretization, from a design standpoint, need not be limited to infilling of three-dimensional space; it can also be applied to a surface, as shown in Fig. 17.5, to generate textures that mitigate dust accumulation and erosion, enhance self-cleaning, reduce drag, or minimize biofouling, to cite a few examples, which mirror the surfaces of insect exoskeletons, reptile scales, and mussels found in nature. With the aid of 3D scanning and similar techniques, biological specimens can be scanned, and using imaging software (Du Plessis and Broeckhoven, 2019) can be translated into a field that can be imported into design software for evaluating its use. A mathematical

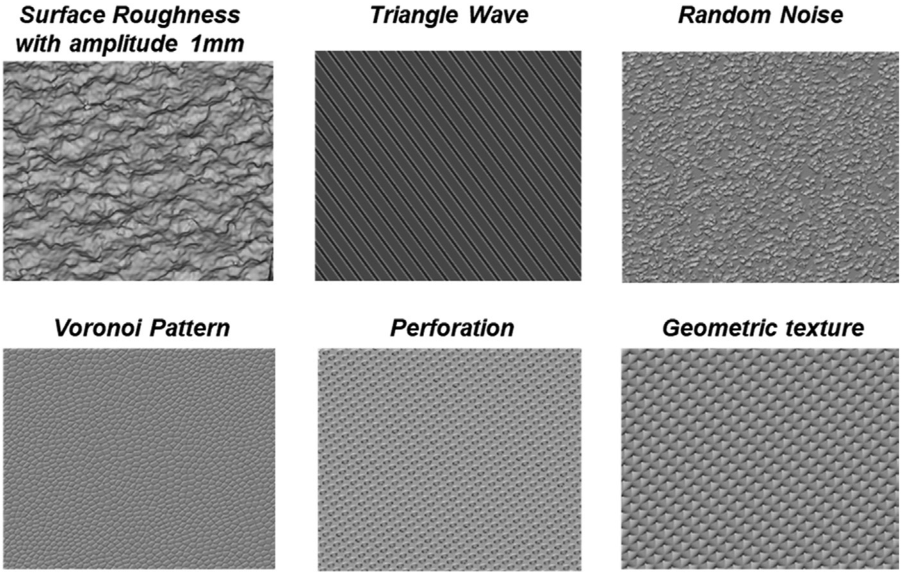

Figure 17.5 A range of designs for surface texturing developed in nTopology Platform (NTopology, 2020) design software.

description of the surface is useful, not only since it enables implementation in design software as shown in Fig. 17.5 but also since it allows the evaluation of performance by changing specific variables that constitute the underlying mathematical formulation.

17.3.2 Symmetry

Symmetry and its breaking are a common theme in biological structure (Du Sautoy, 2008; Li and Bowerman, 2010; Ball, 2009). In its most correct sense, developed in physics, symmetry refers to invariance, under translation or rotation about a defined axis—leading to the perhaps counterintuitive result that a sphere has greater symmetry than the bilateral symmetry of a house fly. Transitioning from a spherical structure to a complex entity such as a fly requires symmetry breaking at multiple levels. It has been argued that increasing levels of broken symmetry correlates with increasing complexity and functional specialization, and that this is especially evident in biology, where symmetry breaking is closely associated with the diversity of functional specialization on multiple scales, from molecular assemblies to body axes that generate bilateral symmetry, for example. It has also been demonstrated that asymmetry at larger scales owes its origins to asymmetries at smaller scales (Li and Bowerman, 2010). From a design standpoint, symmetry is a useful concept to work with since it can be represented mathematically, and then leveraged to influence structural design, as shown for two examples in Fig. 17.6, where a Voronoi perturbation is applied to two initially periodic lattice structures, gradually making them increasingly more aperiodic, specified only by a single sigma variable. The designer would therefore seek to characterize and, where possible, quantify symmetry and then translate that into the design code being used to develop geometry for further study and validation.

17.3.3 Gradients

Gradients are commonly observed in natural structures, and have been classified into six categories: gradients in composition, arrangement, distribution, dimension, orientation, and interface (Liu et al., 2017). While true compositional gradients are challenging to develop with most commercial L-PBF platforms (see Chapter 22), it is easier to achieve other forms of gradients by leveraging structure, and these designs can also be realized using commercial design software, as shown in Fig. 17.7a for a surface- and beam-based cellular material. Gradient designs have been demonstrated to possess improved structural properties—they aid in stress management, strengthening, and fracture resistance and are also useful when transitioning an interface between two different materials or property domains (Dunlop et al., 2011). Gradients have also been leveraged to improve elongation and serve as wetting surfaces for water collection. The designer employing a BID approach would therefore look for gradients in the structure(s) under study —these gradients can typically be measured and quantified, after which they can be validated in the engineering context computationally or with experiments.

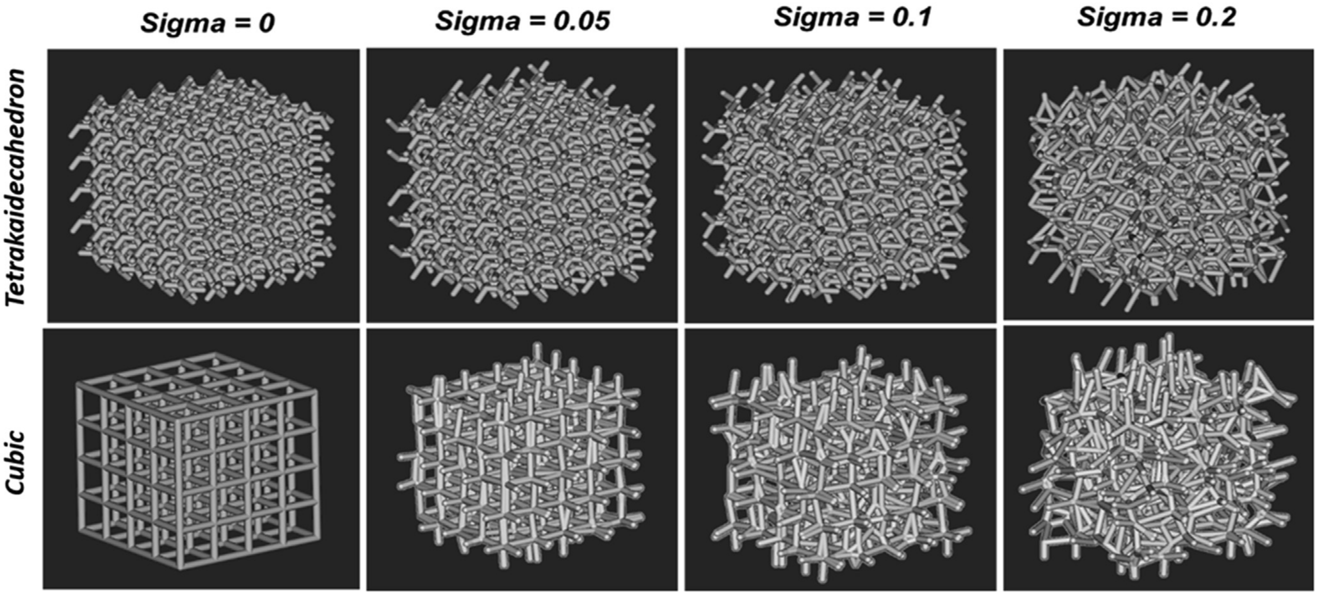
Sigma = 0
Sigma = 0.05
Sigma = 0.1
Sigma = 0.2
Tetrakaidecahedron
Cubic

Figure 17.6 Use of nTopology Platform (NTopology, 2020) design software to develop cellular material designs with varying degrees of aperiodicity (sigma values).

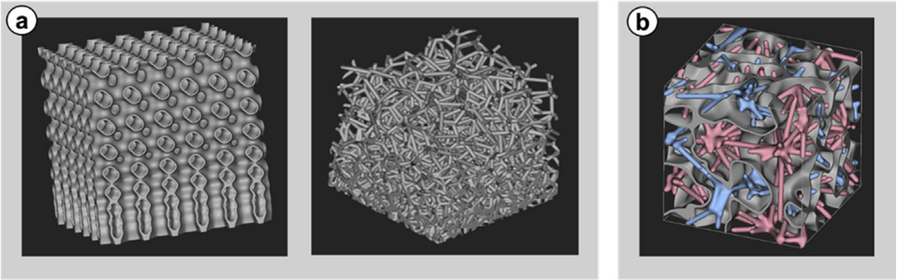

Figure 17.7 A range of cellular designs developed in nTopology Platform (NTopology, 2020) design software: (a) graded surface- and strut-based cellular materials; (b) hierarchical structure combining strut-based and surface elements.

17.3.4 Structural hierarchy

Hierarchy is a term with many context-specific interpretations. In the context of BID, however, the notion of hierarchy can be either explicitly structural, where there are clearly distinguishable levels of design or construction; or it can represent abstract design levels where the transition from one level to the other has clear structural markers that can be identified. Structural hierarchy may be said to be found in solids containing structural elements which themselves have structure (Lakes, 1993)—this is akin to the classic Matryoshka (or Russian) nesting doll example. In nature, these level-within-level structures can span several scales. Bone is a classic biological example, where structure spans several orders of length scale, from collagen molecules (nanometers) to the external boundary of the bone structure (centimeters). Several examples in nature combine hierarchy of structure with two or more compositions (such as collagen and mineral in the case of bone, for example) (Fratzl and Weinkamer, 2007), though in the context of L-PBF, the interest is more on structural hierarchy, since composition is fixed by material selection, though it is conceivable this will change over time as some companies are already demonstrating with multimaterial prints. Infilling volumes with cellular materials is one example of structural hierarchy that is realizable with L-PBF. Another interpretation of hierarchy can be within the context of cellular design itself—as shown in Fig. 17.7b, for example, where strut-based lattices are combined with surface-based cellular materials. In this case, the composition is the same, but property differences are created with geometry. Another interpretation of hierarchy in the context of BID is the presence of levels defined by branching nodes, as seen in venation patterns in leaves (Fig. 17.4c) and dragonfly wings, for example.

17.4 Applications

Companies that adopt AM invariably find themselves asking the “should-could” duo of questions—viz., should a part be made with AM, and if so, could it be successfully fabricated (Bhate, 2018)? A similar question may be asked of BID for L-PBF: Should a designer even consider a BID approach for a particular part or application? As discussed previously, the applications most likely to benefit from the confluence of BID and L-PBF tend to involve one or more of the following: weight reduction, multifunctionality, large deformation, and/or damage tolerance. For metallic structures, this combination of requirements has typically, if not exclusively, been addressed by metal foams. It is therefore noteworthy to examine the kinds of applications metal foams are used for, since this suggests areas of exploration for BID with L-PBF as well, and would give the designer a more useable framework for considering a BID approach. Table 17.1 is adapted from a design guide on metal foams (Ashby et al., 2000), with additional applications called out for surface-based applications. For each of these applications there are one or more examples of model biological organisms listed that may serve as model organisms, extracted from the webpage AskNature.org (2018), indicative of the wealth of information contained in the biodiversity on our planet. The designer assigned with the task of developing solutions for the applications specified would do well to consider a BID approach.

The conjunction of AM and BID is increasingly receiving attention in the commercial and academic sectors (Du Plessis et al., 2019). Many applications leverage topology optimization without any explicit connection to bioinspiration, and are not included here but are discussed elsewhere in the literature (Plocher and Panesar, 2019), as is the case for the use of L-PBF and BID for biomedical implants (Sing et al., 2016). The following discussion instead focuses on application examples where BID has been realized specifically with L-PBF by a direct consideration of, and extraction of, BID principles.

17.4.1 Structural components

Since nature always seeks to minimize material in the construction of biological structures, the underlying design principles are often extendable to light-weighting applications commonly seen in the aerospace and transportation industries. This is perhaps nowhere truer than in the use of honeycomb panels, one of the many applications that have leveraged the hexagonal cell design motif (Zhang et al., 2015). To cite a specific example of BID with L-PBF, Autodesk and Airbus developed a 3D printed airplane cabin partition to separate the passenger cabin from the galley. The design mimicked the organic cellular structure and bone growth found in living organisms. The complete partition was broken down into 116 pieces fabricated with L-PBF, which were then assembled. Scalmalloy, a second-generation aluminum-magnesium-scandium alloy was the material of choice, and the resulting component was found to be 45% lighter than current designs, saving up to 465,000 metric tons of CO_2 emissions per year (Micallef, 2019; Gralow et al., 2020). Airbus also leveraged the Amazonian water lily venation pattern as a stiffening strategy for an aircraft spoiler to minimize weight (Gralow et al., 2020). This approach is particularly appealing for isogrid design for stiffening plates, which is a key requirement in several aerospace applications.

Table 17.1 Selected applications at the intersection of L-PBF and BID along with the relevant desired properties.

	Application	Desired properties	Model biological organism(s)
Space-filling structures	Lightweight structures	- High specific stiffness - High specific strength	- Bee's honeycomb - Bone
	Vibration control	- High mechanical loss/damping coefficient - High specific natural flexural vibration frequencies	- Woodpecker beak - Elephant feet
	Shock absorption	- High energy absorption at high strain rates	- Pomelo peel - Mantis shrimp club
	Thermal insulation	- Low thermal conductivity - Low specific heat	- Polar bear skin - Grass-cutting ant colonies
	Heat exchanger	- High thermal diffusivity - Low differential thermal expansion (expansion limited) - High failure stress (pressure limited)	- Blood vessel network in Thomson's gazelle - Toucan bill
	Buoyancy	- Low density - Good corrosion resistance	- Nautilus siphuncle - Cuttlefish cuttlebone
	Filtration	- High pore size control - Adequate pore connectivity	- Giant manta ray - Whale baleen
	Electrodes, carriers	- High surface/volume ratio	- Nanowires in sediment bacteria
	Acoustic absorption	- High sound-absorption coefficient	- Reed grass - Bee's honeycomb

Table 17.1 Selected applications at the intersection of L-PBF and BID along with the relevant desired properties.—cont'd

	Application	Desired properties	Model biological organism(s)
Surface texture	Anti-biofouling	- Texture discouraging biological accumulation	- Ridged surface of mussel - Cicada wings
	Aero- and hydrodynamics	- Drag reduction	- Shark skin - Bull kelp blades
	Self-cleaning	- Protect from dust accumulation, or excess liquid accumulation	- Gecko and tree frog toe pads - Sacred lotus leaves
	Erosion	- Withstand wear from impinging dust and particulate matter	- Desert scorpion exoskeleton

Adapted from Ashby, M.F., Evans, A.G., Fleck, N.A., Gibson, L.J., Hutchinson, J.W., Wadley, H.N.G., 2000. Metal Foams: A Design Guide. Butterworth Heinemann, with organisms identified using AskNature AskNature.org. 2018. Ask Nature, The Biomimicry Institute. https://asknature.org/

17.4.2 Thermal management

A key area where metal structures with L-PBF are relevant is in thermal management, and the use of L-PBF for heat exchanger manufacturing, to cite one example, is receiving a lot of attention. This is also an area where biological organisms have developed some very interesting thermal management strategies that may be adopted for L-PBF. One example of a BID approach for design of L-PBF structures is the work done to replicate the microstructure of the Norway spruce stem for Thermal Protection Systems (TPS) (Lin et al., 2019). The authors in this paper took the inspiration from microstructure of Norway spruce stem to design a good TPS. In particular, the authors studied the effect of gradients and demonstrated improved performance with reduced thermal resistivity in certain types of gradients. The Triply Periodic Minimal Surface (TPMS) geometries commonly found in sea urchin spicules and butterfly wings have also been leveraged for heat exchanger designs due to their high surface area density (Al-Ketan et al., 2018; Han and Che, 2018).

17.4.3 Energy absorption

As discussed previously, large deformation problems such as typically encountered in energy absorption applications are particularly attractive for BID approaches, as well as for manufacturing with the L-PBF process. Several biological structures such as deer antlers, fruit skins, and spongy bone have to manage impact energies without structural failure and achieve this through a wide range of strategies, such as multimateriality, open cell foam structures and gradients (Ha and Lu, 2020).

17.4.4 Optics

A somewhat less intuitive application for BID with L-PBF is in the domain of optics. The lobster eye design has inspired the design of the Wide Field Imager in the Hubble telescope, and this concept was also realized more recently with L-PBF (Lin et al., 2018). The eye of lobster is composed of numerous small square channels arranged over a spherical surface. Each channel is long and narrow, with its central axis going toward to the center of the spherical surface; light enters the channel array from different angles, which is focused through grazing-incident reflection and forms a single image on the curved retina of lobster, and this was fabricated with L-PBF from the AlSi10Mg aluminum alloy.

17.5 Manufacturing considerations

Despite greatly expanding the available design space, the L-PBF process does impose some design constraints on what can be manufactured. The designer of BID with the intent of manufacturing with L-PBF should be aware of these constraints, and account for them in the design process. While challenges associated with supports, trapped powder, and orientation dependence are universal challenges in this process and discussed elsewhere, there are two specific concerns relevant to BID, and both arise from the need to manipulate features across several orders of magnitude.

First of these, and perhaps the most significant challenge to realizing BID with L-PBF is the ability of the process to accurately resolve features of interest. As has been discussed previously, a key part of realizing BID is the ability to span multiple length scales within the part of interest. Structures designed with a BID approach tend to have fine feature sizes internally, or on the surface, and therefore a key consideration is whether the L-PBF process can actually resolve these features, and if so, do so with high fidelity such that the geometric intent and subsequent performance benefits are realized. While every machine and material combination typically has independent design thresholds that can be fabricated, such as minimum wall thicknesses and strut diameters, the interactions of these with adjacent material may shift these thresholds in either direction, depending on, for example, the available solid material to conduct heat away from the region being melted. Even when features are printable, dimensional inaccuracies can impact the response desired. These deviations may appear small numerically, but can be quite substantial for structures such as lattices and foams where the original dimension of interest itself is very small (Le et al., 2017). Further, fine geometries tend to create internal cavities and channels, which even if well-connected, must be large enough to allow for powder evacuation.

A second complication associated with fabricating designs that often push the L-PBF process to its limits is that it can result in behaviors (for example: material properties like yield strength or elastic modulus) that are not the same as one would expect at the bulk scale; that properties are typically measured at Roach et al. (2020). Laser scan strategies, particularly at the extremes of the process window, have the effect of impacting the dimensional accuracy and porosity in these walls, which in turn affects mechanical and other properties.

Finally, each of the above constraints varies as a function of orientation of the part—for example, down-facing surfaces typically tend to be rougher than up-facing surfaces or vertical walls. This can be particularly challenging for cellular materials due to the large variances in surface orientation due to the complex geometries of most cellular materials. Orientation can impact feature manufacturability, where some of the thinnest walls that can be fabricated vertically cannot be realized at low angles relative to the build platform, for example, without support structures or specialized scanning strategies. This also applies to the fidelity of the geometry and surface roughness.

17.6 Discussion

If the preceding sections give the impression that BID with L-PBF is a nascent field of study, it is because the field is indeed fairly new. While some industries and academics have embraced the potential of BID, the field has not yet scaled as a legitimate design technique, the way concepts in topology optimization and cellular material design have in recent years, for example. The reason for this is perhaps twofold: on the one hand, successes in BID tend to be highly specific to a single application or product, with the marketing of said product often putting the real science and engineering in the shade. On the other hand, there is a lot of academic work in BID, if one is to judge by the growing quantity of papers published in this area (Du Plessis et al., 2019); but the design ideas developed have not yet translated into design tools for general use. For BID to truly become a regular part of a designer's toolkit, we may need a convergence of bio-inspired and simulation-driven design, and a methodology to couple big datasets of natural structure (Shyam et al., 2019) to independent physics-based computational or experimental sandboxes that examine BID principles in different contexts to extract valid structure-function relationships. The need for the latter is driven by the sheer complexity of structure-function relationships in nature, where isolating these for engineering application can prove to be very challenging.

In the interim, a BID approach coupled to L-PBF is likely to be most impactful when it is targeted to domains that are just beyond the reach of traditional analytical or computational techniques, particularly in the context of complex geometry, and typically involves multifunctional design, large deformation behaviors, or damage and uncertainty tolerance. In this sense, BID actually serves to constrain the design space and accelerate the time to a working design of improved performance.

Finally, this chapter is focused, quite narrowly, on the BID of structures. Bio-inspiration is, however, also applicable to processes and systems (Baumeister and Smith, 2014). With regard to L-PBF, it is hard to imagine a process that is more different from natural ones, with its reliance on lasers, melting powders, themselves derived from atomization processes, in inert atmospheres. Nonetheless, there are opportunities to be found if one seeks to employ biomimicry thinking to the L-PBF process and surrounding systems. One such example is to reduce the temperatures at which powders in L-PBF melt and make the process more energetically favorable—for which there may be ideas in nature to be found. Similar opportunities exist in applying bio-inspiration to the complementary processes in L-PBF such as disposal of fugitive powder from the machine, and other ancillary equipment, and other sources of waste in the process. A true holistic approach of biomimicry as it applies to L-PBF would address all these opportunities but is beyond scope of the present discussion.

17.7 Conclusion

The convergence of simulation-driven design and AM has resulted in perhaps the most exciting developments in both the design and manufacturing domains in the past two decades. This intersection has also reinvigorated several ideas that lay dormant for the preceding decade or more, such as topology optimization and BID. The promise of BID is that it opens up entirely new design spaces to improve performance, reduce material and fuel costs, and enable entirely new products and solutions. Additionally, BID may prove to be a key driver for the adoption of the L-PBF process, since it is arguably true that the best utilization of the L-PBF process is when it is coupled with design that significantly improves on performance objectives that the engineer is seeking. And if that is the case, it is hard to find a better source of inspiration than nature, where, with apologies to Darwin, "endless forms most high performing have been, and are being, evolved" (Darwin, 1859).

17.8 Questions

- Why is additive manufacturing, and specifically laser powder bed fusion, a key factor in realizing bio-inspired design?
- What are the three main approaches to realizing bio-inspired design for laser powder bed fusion? How are these approaches different from each other?
- List five examples of applications where a bio-inspired design approach coupled to the laser powder bed fusion for manufacturing may be impactful.
- Using AskNature.org or other sources, identify a biological model organism that may be studied for each of the following applications:
  - **a.** Water collection from fog
  - **b.** Low drag airfoil surface
  - **c.** Energy absorbing crumple structure
- Explain the differences between discretization, symmetry, gradients, and hierarchy. Identify a structure in nature that exemplifies each of these concepts.
- Cite two manufacturing constraints in laser powder bed fusion that could impact the ability to manufacture bio-inspired designs.

Acknowledgements

The authors acknowledge nTopology, Inc. for providing educational licenses for using their Platform design tools that were used to create several images in this chapter as well as support a wide exploration of the bio-inspired design landscape.

References

Al-Ketan, O., Ahmad, S., AlQubaisi, A.M., Abu Al-Rub, R.K., 2018. Nature-inspired lightweight cellular co-continuous composites with architected periodic gyroidal structures. Adv. Eng. Mater. 20, 1700549.

Alexander, R.M.N., 1996. Optima for Animals. Revised. Princeton University Press.

Altshuller, G.S., 1984. Creativity as an Exact Science: The Theory of the Solution of Inventive Problems, first ed. CRC Press.

Ashby, M.F., Evans, A.G., Fleck, N.A., Gibson, L.J., Hutchinson, J.W., Wadley, H.N.G., 2000. Metal Foams: A Design Guide. Butterworth Heinemann.

AskNature.org, 2018. Ask Nature. The Biomimicry Institute. https://asknature.org/.

Ball, P., 2009. Shapes. Nature's Patterns.

Baumeister, D., 2014. Biomimicry Resource Handbook: A Seed Bank of Best Practices. Biomimicry, Missoula, MT, 3.8.

Baumeister, D., Smith, J., 2014. Biomimicry Resource Handbook: A Seed Bank of Best Practices. CreateSpace Independent Publishing Platform.

Benyus, J.M., 1997. Biomimicry: Innovation Inspired by Nature. Morrow, New York.

Bhate, D., 2018. Design for Additive Manufacturing: Concepts and Considerations for the Aerospace Industry. SAE International.

Bhate, D., 2019. Four questions in cellular material design. MDPI Mater. 12 (7), 1−12.

Bhate, D., Penick, C., Ferry, L., Lee, C., 2019. Classification and selection of cellular materials in mechanical design: engineering and biomimetic approaches. MDPI Des. 3 (1), 1−27.

Yael, H.C., Reich, Y., Greenberg, S., 2014. Biomimetics: structure−function patterns approach. J. Mech. Des. 136 (11), 111108. https://doi.org/10.1115/1.4028169.

Darwin, C., 1859. On the Origin of Species by Means of Natural Selection, or Preservation of Favoured Races in the Struggle for Life, First edn. John Murray, London.

Dirks, J.H., Taylor, D., 2012. Veins improve fracture toughness of insect wings. PLoS One 7 (8). https://doi.org/10.1371/journal.pone.0043411.

Dunlop, J.W.C., Weinkamer, R., Fratzl, P., 2011. Artful interfaces within biological materials. Mater. Today 14 (3), 70−78.

Du Plessis, A., Broeckhoven, C., 2019. Looking deep into nature: a review of micro-computed tomography in biomimicry. Acta Biomater. 85 (February), 27−40. https://doi.org/10.1016/j.actbio.2018.12.014.

Du Plessis, A., Broeckhoven, C., 2021. Functional synergy of biomimicry and additive manufacturing: towards a bio-enhanced engineering approach. In: Biomimicry for Materials, Design and Habitats: Innovations and Applications, first ed. Elsevier (in press).

Du Plessis, A., Yadroitsev, I., Yadroitsava, I., le Roux, S., 2018. X-ray micro computed tomography in additive manufacturing: a review of the current technology and applications. 3D Print Addit. Manuf. 5 (3), 227−247. https://doi.org/10.1089/3dp.2018.0060.

Du Plessis, A., Broeckhoven, C., Yadroitsava, I., Yadroitsev, I., Hands, C.H., Kunju, R., Bhate, D., 2019. Beautiful and functional: a review of biomimetic design in additive manufacturing. Addit. Manuf. 27 (March), 408–427. https://doi.org/10.1016/j.addma.2019.03.033.

Du Sautoy, M., 2008. Symmetry: A Journey into the Patterns of Nature. http://www.citeulike.org/user/robertoalamino/article/2641546.

Fratzl, P., Weinkamer, R., 2007. Nature's hierarchical materials. Prog. Mater. Sci. 52 (8), 1263–1334. https://doi.org/10.1016/j.pmatsci.2007.06.001.

Gibson, L.J., Ashby, M.F., Harley, B.A., 2010. Cellular Materials in Nature and Medicine, first ed. Cambridge University Press.

Goss, D., Mistry, Y., Santhanam, B., Noe, C., Sridhar, N., Ozturk, C., Penick, C.A., et al., 2020. Bio-inspired honeycomb core Design: an experimental study of the role of corner radius, coping and interface. MDPI Biomi. 5 (4), 1–24. https://doi.org/10.3390/biomimetics5040059, 59.

Gralow, M., Weigand, F., Herzog, D., Wischeropp, T., Emmelmann, C., 2020. Biomimetic design and laser additive manufacturing—a perfect symbiosis? J. Laser Appl. 32 (2), 021201. https://doi.org/10.2351/1.5131642.

Ha, N.S., Lu, G., 2020. A review of recent research on bio-inspired structures and materials for energy absorption applications. Compos. B Eng. 181. https://doi.org/10.1016/j.compositesb.2019.107496. Elsevier Ltd.

Han, L., Che, S., 2018. An overview of materials with triply periodic minimal surfaces and related geometry: from biological structures to self-assembled systems. Adv. Mater. 1705708, 1–22. https://doi.org/10.1002/adma.201705708.

Hepburn, H.R., Pirk, C.W.W., Duangphakdee, O., 2014. Honeybee Nests. Springer Science & Business Media. https://doi.org/10.1007/978-3-642-54328-9.

Kamps, T., Gralow, M., Schlick, G., Reinhart, G., 2017. Systematic biomimetic part design for additive manufacturing. Procedia CIRP 65, 259–266. https://doi.org/10.1016/j.procir.2017.04.054.

Lakes, R.S., February 1993. Materials with structural hierarchy. Nature 361, 511–515. https://www.nature.com/articles/361511a0.pdf.

Le, T., Bhate, D., Parsey, J.M., Hsu, K.H., 2017. Determination of a shape and size independent material modulus for honeycomb structures in additive manufacturing. In: Solid Freeform Fabrication Symposium.

Li, R., Bowerman, B., 2010. Symmetry breaking in biology. Cold Spring Harbor Perspect. Biol. 2 (3), 1–5. https://doi.org/10.1101/cshperspect.a003475.

Lin, K., Yuan, L., Gu, D., 2018. Influence of laser parameters and complex structural features on the bio-inspired complex thin-wall structures fabricated by selective laser melting. J. Mater. Process. Technol. 267 (May), 34–43. https://doi.org/10.1016/j.jmatprotec.2018.12.004.

Lin, K., Hu, K., Gu, D., 2019. Metallic integrated thermal protection structures inspired by the Norway spruce stem: design, numerical simulation and selective laser melting fabrication. Optic Laser. Technol. 115 (July), 9–19. https://doi.org/10.1016/j.optlastec.2019.02.003.

Liu, Z., Meyers, M.A., Zhang, Z., Ritchie, R.O., 2017. Functional gradients and heterogeneities in biological materials: design principles, functions, and bioinspired applications. Prog. Mater. Sci. 88, 467–498. https://doi.org/10.1016/j.pmatsci.2017.04.013.

Mcnulty, T., Bhate, D., Zhang, A., Kiser, M.A., Ferry, L., Suder, A., Bhattacharya, S., 2017. A framework for the design of biomimetic cellular materials for additive manufacturing. In: Solid Freeform Fabrication Symposium, pp. 2188–2200.

Meurisse, A., Sperl, M., Makaya, A., 2017. 3D printing of a model building block for a lunar base outer shell. Space Eng. Technol. Final Present. Days. https://www.esa.int/Our_Activities/Space_Engineering_Technology/Shaping_the_Future/3D_printing_of_a_model_building_block_for_a_lunar_base_outer_shell.

Micallef, K., 2019. Airbus Continues to Innovate Bionic Design for Future Sustainable Flights. https://redshift.autodesk.com/bionic-design/.

NTopology, 2020. Platform. New York.

Ormondroyd, G.A., Morris, A.F., 2019. Designing with Natural Materials. CRC Press, Taylor & Francis Group.

Plocher, J., Panesar, A., August 2019. Review on design and structural optimisation in additive manufacturing: towards next-generation lightweight structures. Mater. Des. 183, 108164. https://doi.org/10.1016/j.matdes.2019.108164.

Roach, A.M., White, B.C., Garland, A., Jared, B.H., Carroll, J.D., Boyce, B.L., 2020. Size-dependent stochastic tensile properties in additively manufactured 316L stainless steel. Addit. Manuf. 32 (January), 101090. https://doi.org/10.1016/j.addma.2020.101090.

Shyam, V., Friend, L., Whiteaker, B., Bense, N., Dowdall, J., Boktor, B., Johny, M., et al., 2019. PeTaL (periodic table of life) and physiomimetics. Designs 3 (3), 43.

Swee Leong, S., Jia, A., Yeong, W.Y., Edith Wiria, F., 2016. Laser and electron-beam powder-bed additive manufacturing of metallic implants: a review on processes, materials and designs. J. Orthop. Res. 34 (3), 369−385.

Vincent, J.F.V., 2009. Biomimetics - a review. Proc. IME H J. Eng. Med. 223 (8), 919−939. https://doi.org/10.1243/09544119JEIM561.

Vincent, J.F.V., Bogatyreva, O., Karina Pahl, A., Bogatyrev, N., Bowyer, A., 2005. Putting biology into TRIZ: a database of biological effects. Creativ. Innovat. Manag. 14 (1), 66−72. https://doi.org/10.1111/j.1476-8691.2005.00326.x.

Vincent, J.F.V., Bogatyreva, O.A., Bogatyrev, N.R., Bowyer, A., Pahl, A.-K., 2006. Biomimetics: its practice and theory. J. R. Soc. Interface 3 (9), 471−482. https://doi.org/10.1098/rsif.2006.0127.

Wu, J., Aage, N., Sigmund, O., 2017. Infill optimization for additive manufacturing − approaching bone-like porous structures. IEEE Trans. Visual. Comput. Graph. 24 (2), 1127−1140.

Yuan, L., Ding, S., Wen, C., 2019. Additive manufacturing technology for porous metal implant applications and triple minimal surface structures: a review. Bioact. Mater. 4 (1), 56−70. https://doi.org/10.1016/J.BIOACTMAT.2018.12.003.

Zhang, Q., Yang, X., Peng, L., Huang, G., Feng, S., Shen, C., Han, B., et al., 2015. Bioinspired engineering of honeycomb structure - using nature to inspire human innovation. Prog. Mater. Sci. 74, 332−400. https://doi.org/10.1016/j.pmatsci.2015.05.001.

Powder characterization—methods, standards, and state of the art

18

Robert Groarke[1,2], *Rajani K. Vijayaraghavan*[2,3], *Daniel Powell*[4,5], *Allan Rennie*[5], *Dermot Brabazon*[1,2]
[1]School of Mechanical Engineering, Dublin City University, Dublin, Ireland; [2]I-Form, Advanced Manufacturing Research Centre, Dublin City University, Dublin, Ireland; [3]School of Electronic Engineering, Dublin City University, Dublin, Ireland; [4]Centre for Defense Engineering, Cranfield University, Shrivenham, United Kingdom; [5]Engineering Department, Lancaster University, Lancaster, United Kingdom

Chapter outline

18.1 Introduction 492
18.2 Powder rheology 494
  18.2.1 Methods 494
    18.2.1.1 Hall flowmeter 495
    18.2.1.2 Dynamic testing flow regime 1 497
    18.2.1.3 Dynamic flow testing regime 2 499
  18.2.2 Applications of powder rheology measurement in additive manufacturing 500
  18.2.3 Powder rheology standards 501
18.3 Powder shape, size, and morphology 501
  18.3.1 Methods 501
  18.3.2 Applications of powder, shape, size, and morphology measurement in additive manufacturing 503
  18.3.3 Powder size and morphology standards 504
18.4 Chemical composition of powders 504
  18.4.1 Methods 505
    18.4.1.1 X-ray photoelectron spectroscopy 505
    18.4.1.2 Auger electron spectroscopy 506
    18.4.1.3 SEM—energy dispersive X-ray spectroscopy (micro-analysis) 506
    18.4.1.4 Inductively coupled plasma optical emission spectroscopy (bulk) 508
    18.4.1.5 X-ray fluorescence spectroscopy 508
    18.4.1.6 X-ray diffraction (bulk) 508
    18.4.1.7 Inert gas fusion (bulk) 509
  18.4.2 Applications of composition measurement in additive manufacturing 509
  18.4.3 Powder material composition measurement standards 510
18.5 Thermal, mechanical, and humidity properties 510
  18.5.1 Methods 510
    18.5.1.1 Thermal conductivity 510

Fundamentals of Laser Powder Bed Fusion of Metals. https://doi.org/10.1016/B978-0-12-824090-8.00006-8
Copyright © 2021 Elsevier Inc. All rights reserved.

    18.5.1.2 Nano-indentation 512
    18.5.1.3 Porosity 512
    18.5.1.4 Humidity 513
    18.5.1.5 Phase transition temperature and type 513
  18.5.2 Application of thermal, mechanical, and humidity measurements in additive manufacturing 513
  18.5.3 Powder thermal conductivity and porosity assessment standards 514
18.6 Powder life cycle and sustainability analysis 514
  18.6.1 Powder reuse methods 516
  18.6.2 Effect of powder recycling on additive manufacturing 517
18.7 Powder safety 519
  18.7.1 Health and safety standards 520
18.8 Questions 521
18.9 List of abbreviations 521
18.10 List of terms 521
Acknowledgements 522
References 522

18.1 Introduction

A “powder” is a generic term that encapsulates a wide range of properties. If even small changes are made to just one of these properties, a different powder is formed. This can be seen in Fig. 18.1; the Particle Size Distribution (PSD)[1] of powders can vary greatly within a relatively small size range, forming a potentially infinite number of powders. Two powders with different PSDs are unlikely to produce the exact same component properties from the L-PBF process. However, other properties also make up any one powder, such as particle morphology, chemical composition, and

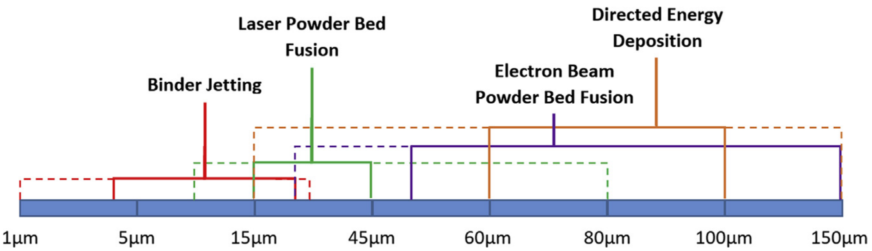

Figure 18.1 Typical particle size ranges used by the different metal powder—based additive manufacturing techniques. *Thick lines* indicate the desirable particle sizes for each process, while *dashed lines* indicate usable but less acceptable particle sizes.

---

[1] For detailed lists of terms and abbreviations see the end of this chapter.

flowability. If many of these properties change simultaneously, as is typical when powder is recycled (Powell et al., 2020), it can become very difficult to determine whether a powder is suitable for use in additive manufacturing (AM). Controlling powder quality and being aware of powder degradation is therefore paramount in L-PBF.

A powder is a complex material form, composed of solid (the powder particles), liquid (moisture or solvent on the particle surface), and gas (usually air, however, as we will see later, this can also be inert gases such as argon or nitrogen) entrained between the particles. Therefore, we can expect a complex interplay of properties such as shape, size, and flow as well as humidity, thermal conductivity, and mechanical strength, all of which will be affected by the process in which the powder is utilized. The focus of this chapter is to give an understanding of how powder properties are investigated and quantified, and how these are relevant to additive manufacturing. For the scope of this chapter, additive manufacturing will be taken to mean L-PBF; however, other processes such as Direct Energy Deposition (DED) and Electron Beam Melting (EBM) also use a powder feedstock. In earlier chapters, the process and parameters of the L-PBF operation were discussed and will not be repeated here. Fig. 18.2 shows the interior of an Aconity MINI L-PBF machine during part production and a Scanning Electron Microscope (SEM) image of a 316L stainless steel particle, magnified 10,960 times.

Metallic powders can be produced from a number of different methods, yet they all involve atomization of a solid metallic feedstock, for example, an ingot. The methods differ in the medium of atomization, namely water, gas, or plasma. In our experience, powder produced from water atomization are less spherical and have a wider size distribution. Gas and plasma atomization methods both yield more spherical and uniform powder particles. The powder production methods are discussed in detail in Section 18.6.1 below. Given that L-PBF has over 100 parameters which can affect the quality of the parts fabricated, it is widely agreed that it is a very complicated process (Oliveira et al., 2020). Therefore, it is essential that a thorough understanding and quantification of numerous powder properties be obtained, prior to a powder feedstock being used in the process. It is still however a matter of some debate as to the “ideal” powder properties; this is likely due to the number of available materials (pure metals and alloys), variability between suppliers, batch-to-batch variability, variability in how the same powder from the same batch will behave in different L-PBF machines, and also how different machine operators store, handle, and use the powders. This makes the characterization of the powder properties all the more important, since, if they can be quantified, then one source of variability can be, if not controlled, then at least limited and understood within the process. In this chapter, the following powder properties will be discussed; rheology or flow; size, shape, and morphology (shape, circularity, and aspect ratio of individual particles); elemental composition; and thermal, mechanical, and hygroscopic characteristics. In each section, a discussion of the relevant international standards of analytical methods is presented along with a consideration of how these powder properties pertain to additive manufacturing. Important industrial and academic contributions to these methods and to the overall powder life cycle and sustainability of the L-PBF process will be highlighted and discussed. This chapter is not intended to be an exhaustive review of these areas, but a high-level snapshot of the current best practices and standards.

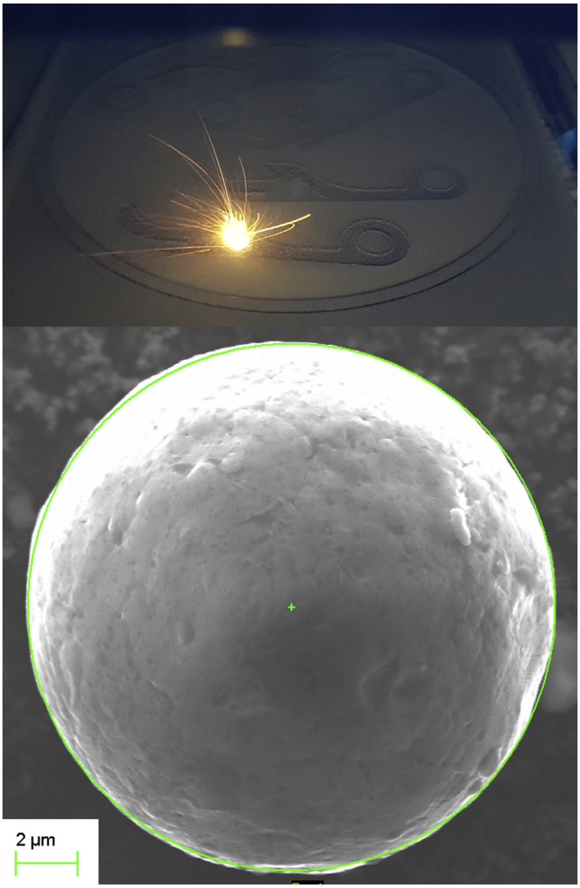

Figure 18.2 Interior of an Aconity MINI L-PBF machine during a build operation, and a microscope image of a single 316L stainless steel powder particle.

The standards noted are from the ASTM International, Metal Powder Industries Federation (MPIF), International Organization for Standardization (ISO), and DIN (German national organization for standardization) standard databases, where appropriate and available for each analytical technique.

18.2 Powder rheology

18.2.1 Methods

Powder flow and powder deposition are complex multivariate phenomena. The former has been investigated over the past decades, and a number of standard methods exist to quantify and compare powders of similar materials or batches. Powder flow methods can be static or dynamic. For example, the angle of repose is a static measurement, since the powder is allowed to stabilize prior to the measurement whereas the application of a moving blade within the powder while recording torque is a dynamic measurement. Angle of repose is the largest angle that the powder can make with the horizontal surface it is on without the powder falling. Powder cohesion is a measure of how the powder particles interact with each other, via a number of forces such as friction, van der Waals forces, etc. It is still a matter of discussion as to the relevance of each method for a particular process. Some testing methods yield a quantity and a unit, while others provide a unitless quantity or empirical value, which on comparison with that of another powder can be used to evaluate the one more suitable for a given process.

18.2.1.1 Hall flowmeter

This method was first developed in 1945 and is documented in the MPIF and ASTM standards (ASTM B213-20 (2020); MPIF, 2019). The procedure involves passing 50 g of powder through a funnel of specific geometry and size, the hole in the funnel is of 2.5 mm diameter. The time required for the powder to pass through the funnel is measured, and from this, the flow rate is determined. The test may be run in static (where the flow of the powder is initially blocked) or dynamic (where the powder is poured into the funnel and allowed to flow right through it) into an empty weighing dish. The apparent density of a powder can also be determined using a Hall apparatus (ASTM B964-16, 2016) and an Arnold Meter (ASTM B855-17, 2017; MPIF, 2019). The Carney method is a similar procedure and is used when the powder does not pass through the Hall funnel orifice and is therefore not considered free-flowing (ASTM B964-16, 2016). Additionally, there are a number of other standardized methods of evaluating tapped and bulk densities of powders. Tap density is defined as the density of a powder when the receptacle of known volume is tapped or vibrated under specified conditions. Tapping or vibrating a loose powder induces movement and separation and lowers the friction between the powder particles. This short-term lowering in friction results in powder packing and in a higher calculated density of the powder mass. Tap density is a function of particle shape, particle porosity, and particle size distribution.

A number of standards are available, collected in the MPIF standard publication (MPIF, 2019); for tapped density, consult standard 46, and for apparent density measurements, standards 4 (using Hall apparatus) and 28 (using a Carney funnel) are most relevant. Their ASTM counterparts for powders typically used within metal AM are (ASTM B213-20, 2020; ASTM B527-20, 2020). ISO standards for this measurement are codified in ISO 3953 ISO 3953 (2011).

The tapping mechanism is important, and a calibrated mechanical tapping machine should be used. A graduated cylinder should be used to measure the volume of the powder under investigation.

In the initial test, the number of taps, N, should be that required such that no further decrease in the volume of the powder is observed. In practice, once N is established, a tap number value of 2N should be used, or a value based on experience with the particular powder. However, for reproducibility purposes, the value should be documented and periodically rechecked.

For apparent density measurements using a Carney funnel (of 5 mm orifice), a test sample of powder is loaded into the funnel and allowed to flow through and fill the density cup container, see Fig. 18.3. The volume of the density cup is accurately known. The mass of the powder in the density cup after leveling of the powder on the top of the density cup is then determined. Replicates can be carried out and an average obtained. The experimental setup is shown in Fig. 18.3 (MPIF, 2019).

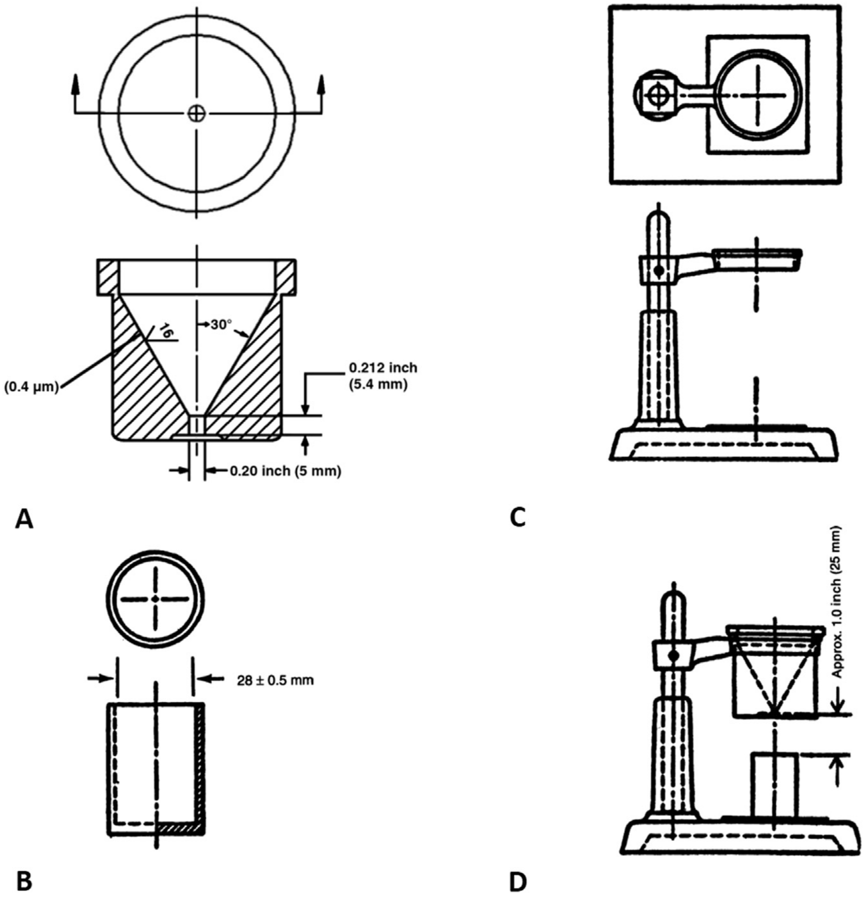

Figure 18.3 (A) The schematic drawing of the Carney Funnel, (B) schematic drawing of the density cup, (C) stand required for the funnel and cup, maintaining the correct distance between both, and (D) the complete setup.
Adapted from MPIF, 2019. A Collection of Powder Characterization Standards for Metal Additive Manufacturing. Available at: https://www.techstreet.com/mpif/standards/a-collection-of-powder-characterization-standards-for-metal-additive-manufacturing?product_id=2085958.

A method known as Carr Indices (ASTM D6393-14, 2014) is used to quantify a number of bulk powder properties such as cohesion, angle of repose, bulk densities, and powder dispersibility (Eq. 18.1):

$$C = 100(\rho_T - \rho_B / \rho_T) \tag{18.1}$$

where ρ_T is the tapped density and ρ_B is the bulk density.

Hausner Ratio is a similar metric for flowability, and is defined in Eq. (18.2):

$$H = \frac{\rho_T}{\rho_B} \tag{18.2}$$

This standard method is suitable for free flowing and moderately cohesive powders, and granular materials of up to 2 mm diameter, and must be able to flow through a nozzle of 6 −8 mm in diameter. Angle of repose is defined as the maximum angle a mound of powder makes with the surface it is deposited on, at which it is stable and does not fall (no powder movement on slope) (ASTM D6393-14, 2014). There are a number of other methods which can be used for determining the angle of repose of a powder, which can lead to confusion among researchers; however, since this method is mainly for powders of larger particle size (sands), it is not as widely used in L-PBF powder research as the other methods described here. Powders are cohesive if they clump or aggregate during flow. In general, metal powders are not considered cohesive under a flow regime, given their high density and aeration behavior.

The Arnold meter is a technique which requires a higher degree of operator training, as the powder deposition method and filling method of the stainless-steel die is difficult and as such is more prone to variability and error.

In recent years, a number of other techniques have been developed to analyze powder in both static and dynamic regimes and are applicable to a wide range of material types and particle sizes. Two will be discussed in detail here and are considered the current best practices in additive manufacturing labs around the world for powder flow analysis. They use different methods to induce a flow in the powder sample, and yield different, yet somewhat complementary, results.

18.2.1.2 Dynamic testing flow regime 1

The Freeman Technology FT4 (Freeman Technology, 2016) instrument uses a precisely machined 23.5 mm stainless steel blade to measure a number of properties (dynamic flow, shear, and bulk properties) of a powder sample (see Fig. 18.4). These include basic flowability energy (BFE), specific energy (SE), flow rate index (FRI), minimum aeration velocity, as well as bulk and tapped densities. These tests are conducted on precise masses of powder, and the blade is rotated and lowered through the powder at a defined rotational and vertical velocity. The blade experiences a torque as it passes through the powder. Bulk, dynamic, wall friction, and shear force tests can be performed. The wall friction test is in accordance with ASTM Standard D7891 (ASTM D7891, 2015).

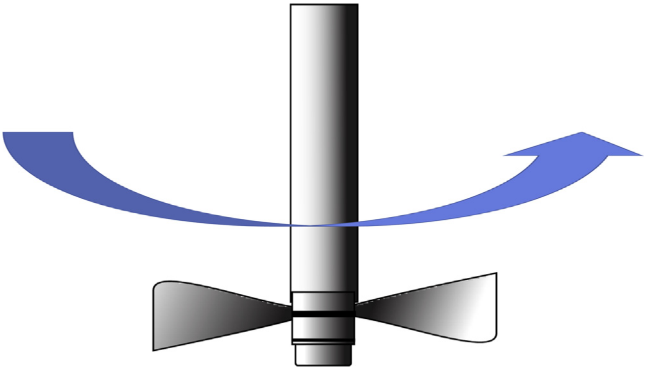

Figure 18.4 Illustration of the geometry of the 23.5 mm blade used in Freeman Technology FT4.

The stability of a powder can be measured with the procedure as follows. In passing through the powder, the blade measures the resistance to flow exhibited by the powder over several repetitions (tests 1−7) and the velocity of the blade is varied to discrete values for each remaining test (tests 8−11). This variation in torque as a function of powder height and blade velocity is calculated as the BFE while the blade is moving downwards, known as the confined regime. When the blade moves back up through the powder it is in the unconfined regime, and in this test the SE is calculated. These can be expressed as mJ/g of powder (Freeman Technology W7013, 2007; Freeman Technology W7030, 2008; Freeman Technology W7031, 2008).

During the aeration test, compressed air is allowed to flow upwards through the vessel and the powder through the mesh at the base of the vessel. The velocity of the air is precisely controlled and the variation in the BFE is plotted as a function of the air velocity. The velocity of the air at which the BFE is at or near zero is taken to be the minimum fluidization velocity. This is therefore a measure of how easy the powder is to fluidize and therefore of how free flowing it is.

The compressibility, or extent a powder will compress under an applied load, of the powder can also be calculated using the FT4, using a vented piston in place of the blade. The height of the piston is measured precisely as incrementally increasing kinematic forces are applied to the powder. The compressibility percentage of the powder is thereby calculated. This is influenced by packing efficiency, hardness, chemistry, particle shape, and size. If a powder possesses a large number of satellite particles, the breaking of these particles from the larger ones can potentially be seen in the variation of the compressibility, if a large nonlinear shift is observed, particularly at higher applied forces.

Interpretation of the results is based on the values of the various calculated parameters, and in which range of values they fall. Powders can be identified as cohesive or noncohesive, free flowing or aggregating, stable or unstable. However, it should be pointed out that reliance on just one test or calculated value for the determination of the powder properties is not recommended. Values should not be considered in isolation, and may in fact provide conflicting interpretations of the properties. The interpretation of rheological properties is a complex science, and additional characterization tools should also be employed to better understand the results.

18.2.1.3 Dynamic flow testing regime 2

An alternative and complementary measurement device to the FT4 is the Revolution device (Mercury Scientific, 2020) which utilizes a rotating drum in which the powder is placed. Fig. 18.5 illustrates the experimental setup. A camera is placed at one end of the drum and the drum is rotated at a defined rpm. As the powder rotates, it undergoes what is termed as an "avalanche event." The precise surface of the powder as each avalanche occurs is imaged and a number of parameters such as surface fractal, avalanche energy, as well as rest and avalanche angles are measured and averaged over a series of such events. This is a different flow regime to that of the Freeman device, yet is also appropriate for powder in an additive manufacturing application. Again, interpretation of the results is difficult and requires operator experience. The flowability of the powder is interpreted as a function of the avalanche angle. The lower the angle, the higher the flowability, i.e., the better the powder flows. The rest angle is comparable to the angle of repose of a powder sample. The rotation speed can be varied to account for different flow regimes under investigation. The Revolution device can also be used to investigate the packing efficiency of the powder after it has been subjected to a vibrational energy from the rotating drum (Mercury Scientific, 2020).

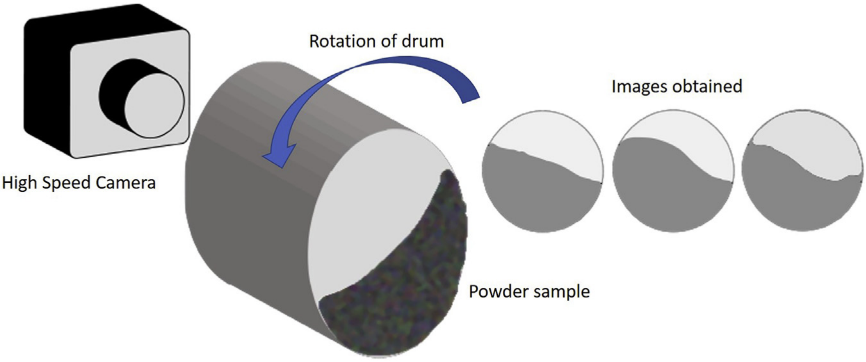

Figure 18.5 Experimental setup of the Revolution powder rheology analyzer. A high-speed camera captures images of the rotating powder, and the avalanche events it undergoes. On the right-hand side, a set of typical images of the avalanche event from the camera point of view are shown.

18.2.2 Applications of powder rheology measurement in additive manufacturing

The understanding of how a powder flows and is deposited and spread is of critical importance in many AM techniques, but in particular in L-PBF. Part density, microstructure, and surface finish are some of the part properties that rely on the formation of a well-packed, evenly distributed layer of powder, and necessitate layers to be consistently formed in this way. Powder flow is affected by particle size and shape, as well as by cohesivity, density, packing efficiency, permeability. Various research groups have investigated the influence of powder properties on resultant part properties in L-PBF processes, as well as the interplays of various powder parameters on each other. Much of the research has been focused on 316L stainless steel, which is one of the most commonly used materials in metallic additive manufacturing; however other materials have also been studied (Klausner et al., 2000; Clayton et al., 2015; Strondl et al., 2015; Hausnerova et al., 2017; Liverani et al., 2017; Kurzynowski et al., 2018). Increasingly, a different interpretation of flow is being proposed as an area of study, particularly for AM, but also as a regime which may be suitable for certain other powder applications. It focusses on how a powder is delivered across a flat surface, mimicking a build plate in an L-PBF machine. The effect of powder rheology and powder delivery dynamics on the AM process, and in terms of the basic science, has been increasingly a source of interest (Lyckfeldt, 2013; Spierings et al., 2016; Hausnerova et al., 2017; Escano et al., 2018; Chen et al., 2019; Snow et al., 2019). The two rheological devices discussed in the Section 18.2.1 that are the most relevant to L-PBF processes are the FT4 and the Revolution devices, though in differing ways. We must consider how the powder spreads and flows, upon its interaction with itself, the surrounding boundaries, and the recoating mechanism in the AM device. It may be argued that the FT4 blade rotating through the powder is one way of simulating the flow of the powder under the applied force of the moving recoater mechanism, on a quasi-bulk scale. The Revolution may be considered to yield important information regarding the nature of the "leading edge" of the powder, investigating as it does the formation of an avalanche event, and the angle at which the powder starts to move downward and become less stable (beyond the rest angle). This may be important in order to understand why powders may not form stable layers of consistent height, depending on recoating velocity, recoater height, and particularly for larger layer heights. The Revolution sample drum can also be filled with an inert gas for powders which are hygroscopic or air-sensitive. The FT4 can give information about how resistant a powder is to flow, how likely aggregation is to occur, how compressible a powder is, which will inform how well a powder will pack. Therefore, it is readily seen that both techniques have a place in the characterization of powder behavior in an additive manufacturing process. However, powder rheology should not be studied in isolation. There are many other properties of powders which must also be understood in the context of their relevance and application to L-PBF, which will be addressed in the following sections.

18.2.3 Powder rheology standards

Table 18.1 lists the important international standards for powder rheology and flow. It is important to note that two other standards are being developed which are related to the characterization of powder rheology. These pertain specifically to additive manufacturing and are given the working designations ASTM WK55610 and ASTM/ISO DIS 52907 (America Makes and AMSC, 2018). While there is no specific standard for powder delivery, a shear cell test can be used to approximate this effect but a quantitative standard is still required (America Makes and AMSC, 2018).

18.3 Powder shape, size, and morphology

18.3.1 Methods

As discussed in the preceding section, the flow behavior of powder is a complex phenomenon, and is very relevant to the success and reproducibility of an L-PBF process. This flow behavior can be influenced by the shape, size, and morphology of the powder particles. In this section we will discuss how such characteristics are analyzed and quantified. The basis of most techniques is a microscope and image analysis software. The difference between techniques is generally a case of throughput, how many individual particles can be analyzed in a reasonable amount of time, while still allowing for statistically relevant deductions to be concluded about the bulk sample. A sample of powder which has sampled correctly can be considered a

Table 18.1 International standards used for powder rheology assessment.

Test/method	ASTM	ISO	MPIF
Flow rate by Hall Flowmeter	ASTM B213-20 (2020)	ISO 4490	MPIF (2019), Page 17
Apparent density	ASTM B964-16 ASTM B855-17 ASTM B212-17	ISO 3923/1	MPIF (2019), Page 21
Tapped density	ASTM - B213 (2014) ASTM B527-20 (2020)	ISO 3953	
Flow rate by Carr Indices	ASTM D6393-14		
Shear test by angle of repose	ASTM D6393-14	ISO 902 (1976)	
Shear cell tests	ASTM D6128-16 ASTM D6773-16 ASTM D7891-15		

representative sample of the whole. The sampling techniques which are considered best practice as well as appropriate tools required are codified in international standards such as (ASTM B215-20, 2020). In this section, several standards and somewhat novel methods for characterization of powder shape, dimensions, and morphology are considered.

There are a number of methods by which the average dimensions of the particles in a powder sample may be measured. The simplest means of measuring the particle size distribution of a sample is by using a series of sieves of calibrated mesh sizes (pore sizes) and passing the powder through the sieves using a vibratory motion. The amount of material remaining in each sieve plate at the end of the test is tabulated relative to the total mass of the sample. This approach is codified in the MPIF standard number 5 (MPIF, 2019) and is also dealt with in an ASTM standard (ASTM B214-16, 2016). For additional guidance, ASTM F3049-14 can also be used (ASTM F3049-14, 2014). For this method, the powder is measured as a solid; however, the measurement can also be carried out in a solvent matrix. The conventional wisdom is that the powder should be measured in the form in which it is utilized in the process. In the case of additive manufacturing, therefore, the particle size measurement should be carried out on the powder in the solid form. The type of technique employed is somewhat dictated by the expected size range of the particles, for example, Dynamic Light Scattering (DLS) would be ideal for nanoparticles, but less suited to powder particle size ranges typically found in L-PBF processes, which are generally of the order of 10−100 μm. For particles in the latter range, Laser Diffraction (LD) is more appropriate. According to the definition from Malvern Panalytical, DLS is recommended for particles and dispersions in the range of 1 nm−10 μm, whereas LD has a broader particle size range of application (sub-micron to mm) (Malvern Panalytical, 2020). This technique also has the advantages of rapid measurement time, large particle sampling, ease of interpretation, and can be integrated at or online to the process. In terms of standards it is codified in ISO 13320 (2020). It is suited to both spherical and nonspherical particles. The results are reported as either a volume-based distribution or a number-based distribution. The results are summarized as D_{10}, D_{50}, and D_{90}, which is the particle size below which 10%, 50%, and 90% of the total volume (so-called diameters "weighted by volume") or total number of particles (weighted by number) lies. Usually, D_{10}, D_{50}, and D_{90} weighted by volume are used in AM. Modern LD systems will give an indication of the reliability of the result or results, and can be configured to report the values in accordance with various standards or industrial settings for statistical analysis, and to ensure compliance for regulatory testing environments. Care must be taken during the experiment that the powder feed is controlled and constant, to ensure a consistent occlusion of the beam by the particles.

A third approach is to examine the particles using a Scanning Electron Microscope (SEM), along with image analysis software such as ImageJ. The analyst then selects individual particles and adjusts the contrast of the image within the software to yield a grayscale (for example a 16-bit scale version of the image) where the selected particles are seen. The software then calculates the dimensions of the particles based on scaling data provided by the analyst. This approach is not designed for high-throughput applications, as it is a time-consuming process and is not designed to allow a large number of particles to be analyzed, not least because the SEM image itself even at low magnification will show perhaps a few hundred particles. However, with the advent of AI, this technique may see a resurgence, as it may allow a vast number of images and particles to be analyzed, but these images must still be acquired; therefore, it is still only ideal for small-scale samples. This technique is similar to the basis of operation of the Malvern Morphologi G4 instrument (https://www.malvernpanalytical.com/en/products/product-range/morphologi-range/morphologi-4). This uses compressed air to deposit a precise volume of particles on to a glass plate. This is then imaged using an optical microscope. Vertical "stacking" of images can be performed to clarify if a particle is indeed a single, mis-shaped particle or in fact two particles fused or touching. The proprietary software allows for upwards of 400,000 particles to be individually imaged per sample, and their dimensions to be calculated. Specific analysis criteria for the size and shape of the particles can be set, to remove certain unwanted particles (or dust) from the calculation. This instrument reports particle shape data in the form of a large number of parameters. Circularity refers to how spherical a particle is, as viewed from above, aspect ratio is the ratio of the particles largest dimension with its shortest dimension. Convexity is a measure of the roughness of the edge of the particle. As with all microscopic-based methods, care must be taken to ensure that particles are not touching each other, which is why the SEM approach is more prone to errors. The data allows for detailed quantitative comparisons to be made between powder samples and can be correlated with SEM images.

18.3.2 Applications of powder, shape, size, and morphology measurement in additive manufacturing

As with other powder processing methods, knowledge of particle size and shape is important process information for L-PBF. The lower limit of layer height chosen for a build is often determined by the D_{50} of the powder sample with the layer thickness selected not being lower than this. This will in turn dictate the laser power parameters, in order to ensure melting and partial remelting of previous layers. Particle shape is important as this is a key factor in how a powder will pack within the layer or layers and will affect the contact between powder particles, both in the plane of the build plate, but also vertically through the build. This in turn determines the heat affected zone and the thermal conductivity through the powder. Taken together, these factors will influence the level of powder melting, defect formation, and porosity. The powder particles can also be analyzed post-build, to see if their shape or size has been changed; invariably there are fused particles which have been ejected from the build layer by the laser energy. This spatter phenomenon has recently been examined and shown to be more significant for altering particle shape and size though agglomeration and coalescence than change of the bulk particle crystal structure (Obeidi et al., 2020). The effect of powder shape on packing and flow, and subsequent part properties using micro-CT has also recently been examined (Brika et al., 2020). In this work it was found that spherical particles resulted in parts with better mechanical properties. Interestingly, they also found that samples manufactured from powders with differing morphologies and rheological characteristics, within the range examined, did not have measurably different mechanical properties. This illustrates how complex the L-PBF process is, and while certain characteristics may not lead to significantly different part properties, a quantitative analysis of the feedstock is still an important research topic to allow for improved process control and sustainability.

18.3.3 Powder size and morphology standards

The international standards for powder morphology assessment are shown in Table 18.2. Further progress in these methods is required to improve repeatability and reproducibility of results (America Makes and AMSC, 2018).

18.4 Chemical composition of powders

The chemical composition of the powder samples (powder chemistry) is critical in determining properties of final L-PBF produced parts. Impurities may be introduced during the manufacture and handling of the powder feedstock and thus will be incorporated into the melt pool during processing. These impurities can remain as discrete particulates or nonfused interfaces in the produced parts which then can act as stress

Table 18.2 International standards in particle size and shape analysis.

Name/test	ASTM	ISO	MPIF
Standard Test Method for Sieve Analysis of Metal Powders	ASTM B214-16		
Standard Practices for Sampling Metal Powders	ASTM B215-20		
Estimating Average Particle Size of Metal Powders Using Air Permeability			Standard 32
Particle Sizing Using Light Scattering	ASTM B822-20		
Particle Sizing Using Laser Diffraction		ISO13320 - 2009	
Particle Size Result Presentation		ISO 9276, Parts 1–6	
Standard Guide for Characterizing Properties of Metal Powders Used in Additive Manufacturing Processes	ASTM F3049-14		

concentrators and may reduce fatigue life by increasing the probability of fatigue crack initiation. Similarly, the presence of elements such as carbon, oxygen, nitrogen, sulfur, and hydrogen can influence the physical properties of the final product. Methods used for the powder chemistry analysis can be divided into three types, surface, micro, and bulk analysis techniques. Bulk chemistry analysis and validation are particularly important to ensure that recycled, as well as virgin alloy powders, meet their purity standards and alloy designation. Many techniques are available for powder chemistry analysis and suitable methods can be used depending on the elements of interest and level of accuracy needed for the final applications (Samal and Newkirk, 2015).

18.4.1 Methods

18.4.1.1 X-ray photoelectron spectroscopy

The X-ray photoelectron spectroscopy (XPS) technique is an extensively used method for surface chemical composition analysis. It can be used to measure both the presence and bonding state of elements near the surface (typically <10 nm for lab based XPS; and <100 nm High Energy XPS) of the powder particles. This technique is based on the photoelectric effect, in which the material is irradiated/bombarded with X-rays and the kinetic energy of the ejected core-level electrons are measured. The binding energy of the ejected photoelectrons from the powder samples can be calculated using the knowledge of the kinetic energy of the ejected electrons (using electron analyzer), energy of the X-rays, and the work function of the spectrometer. XPS analysis will provide information on the elemental composition as well as the chemical state of the powder surfaces, as the core-electron binding energy represents the characteristics of an element in a particular chemical environment. Thus, it is possible to determine quantitative information of the elements present as well as their oxidation states on the surface layers of the powder particles. XPS can detect all elements except hydrogen and helium with a detection limit of <0.1 atomic percentage (Slotwinski et al., 2014); however, it depends on the elements and the matrix in which it is present (Shard, 2014). It requires the use of ultrahigh vacuum for the sample analysis and the measurement area can range from 70 μm^2 to 1 cm^2 and the lateral resolution of commercial XPS instruments is typically about 10 μm.

The XPS technique can also be utilized to extract elemental analysis at a particular depth from the surface by combining it with an ion sputtering capability. Thus a depth profile of elemental composition versus sputtering time can be obtained, in which the sputtering time can be correlated to the depth (Gruber et al., 2019). For example, this technique has been used to determine oxide layer thickness in powder samples, however, the elemental composition analysis may not be very accurate due to the possible effects of (i) ion beam damage, (ii) preferential elemental sputtering, and (iii) the curved nature of the powder particle surface. ASTM E1829-14 (2020) represents Standard Guide for Handling Specimens Prior to Surface Analysis (ASTM E1829-14, 2020).

18.4.1.2 Auger electron spectroscopy

Auger Electron Spectroscopy (AES) is a surface-sensitive quantitative elemental analysis technique, in which L-level (auger electrons) electrons will be ejected after a series of electron transitions, from the material, by the irradiation of an electron beam. Similar to XPS, this technique can be used for the quantitative detection of all elements except hydrogen and helium, along with some information on the chemical state, within a depth of 2 nm. While both AES and XPS are surface analysis techniques, changes in the electron escape depth results in differences in the sample volume analyzed using the two methods. AES has an advantage of higher spatial resolution (compared to the XPS). Similar to XPS, AES also can be used for depth profile analysis of elements and to determine oxide layer thickness on the powder particles (Gruber et al., 2019). AES has a depth resolution of 5−25 Å. AES also require the use of ultra-high vacuum for the analysis as in the case of XPS. ASTM E1127 represents a Guide for Depth Profiling in Auger Electron Spectroscopy (ASTM E1127-08, 2015).

18.4.1.3 SEM—energy dispersive X-ray spectroscopy (microanalysis)

Energy dispersive X-ray spectroscopy (EDS or EDX) is a widely used analytical technique, generally performed in combination with SEM or TEM, to carry out semi-quantitative elemental or compositional analysis of the powder particles. EDS utilizes the X-ray signals produced due to the interaction of the SEM's electron beam with the powder samples. Primary electrons when incident on the powder sample surface eject inner shell electrons, and X-rays are produced by the transition of outer shell electrons to fill up the vacancy in the inner shell. Each element produces a characteristic X-ray emission pattern due to its unique atomic structure, and hence can be used to perform chemical/compositional analysis with an energy dispersive spectrometer. The analysis of these peaks provides qualitative as well as semi-quantitative information on the material. The position of the peaks in the resulting spectrum gives information on the type of elements present in the sample and area/peak height measurement provide semi-quantitative information on the concentration of the element in the sample. A more refined quantitative result can be obtained by measuring a standard of known chemistry. The area under the peaks can be generally correlated to the weight percentage of the elements and this semi-quantitative information is very useful to make a comparison between different particles (Mussatto et al., 2019; Obeidi et al., 2020), see a particle EDS result example in Fig. 18.6. Nevertheless, more accurate compositional analysis on spherical powder particle can be difficult to perform as the EDS technique has been found to work better on flat surfaces (Sutton et al., 2016).

Chemical composition analysis in a microscopic area is possible using EDS due to the capability to focus electron beam to an area of this size. The interaction volume of the EDS X-ray microanalysis can be varied by changing the accelerating voltage used for imaging the sample. The interaction volume is approximately 1 μm in steel at 15 kV accelerating voltage (Slotwinski et al., 2014). Since EDS is a semi-

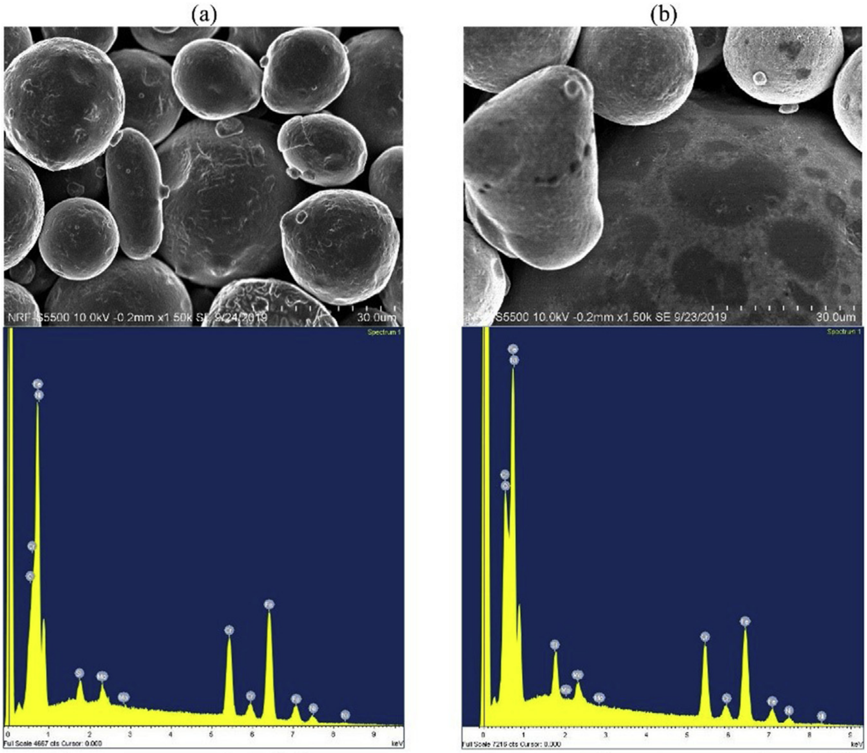

Element	Atomic%
Fe	55.37
Ni	17.55
Cr	13.15
O	4.20
Si	1.51
Mo	1.12

Element	Atomic%
Fe	52.30
Ni	13.82
Cr	16.27
O	14.17
Si	2.48
Mo	0.96

Figure 18.6 EDX comparison between the surface chemical composition of a (a) virgin stainless steel powder particle, and (b) spattered particles (Obeidi et al., 2020).

quantitative composition analysis technique, appropriate reference standards should ideally be used for the system calibration in order to extract more accurate quantitative information from the sample.

EDS suffers from difficulties such as overlapping peaks (poor energy resolution) and inability to detect light elements. The use of wavelength dispersive spectroscopy (WDS) can improve the energy resolution and increase the accuracy of elemental quantification compared to EDS. ASTM E1508-12a (2019) is the “Standard Guide for Quantitative Analysis by Energy-Dispersive Spectroscopy” (ASTM E1508 - 12a, 2019). ASTM E 1078-14 (2020) is the standard guide for “Specimen Preparation and Mounting in Surface Analysis.”

18.4.1.4 Inductively coupled plasma optical emission spectroscopy (bulk)

Inductively coupled plasma optical emission spectroscopy (ICP-OES) or atomic emission spectroscopy (ICP-AES) is used for the identification and quantitative determination of elements present in the powder samples. In this technique the sample in the liquid form, for example, metal powder dissolved in acid solutions, is injected into the plasma, which is used as the excitation source. The plasma excites electrons in the elements and their de-excitation results in the emission of characteristic wavelengths, which can be used for the composition analysis. The emitted wavelengths are measured using a spectrometer. This technique can be used to measure major as well as trace elements simultaneously. ICP-OES produces qualitative elemental information by measuring the intensity of the emission peaks, which correspond to the various elements. Since the elements generally have numerous emission peaks, specific emission lines will be used for different elements in order to avoid any peak overlapping (Sutton et al., 2016). The concentration detection accuracy of this technique can be improved (up to three decimal places) by using an internal standard.

18.4.1.5 X-ray fluorescence spectroscopy

The X-ray fluorescence (XRF) spectroscopy technique is used for the qualitative and quantitative analysis of powder samples. XRF identifies elements in the sample by detecting characteristic X-rays emitted from the respective elements after the irradiation with high energy primary X-rays. XRF generally detects elements with accuracy at the ppm (parts per million) level.

18.4.1.6 X-ray diffraction (bulk)

X-ray Diffraction (XRD) is an analytical technique used to characterize phase, crystal structure, and composition of the bulk powder particles. A beam of X-rays is directed on the crystalline powder materials, in which atomic planes are arranged in a regular manner, thereby scattering the X-rays in a regulated manner. The interatomic distances in crystalline solids (few angstroms) are of the same order as that of the X-rays and the scattered X-rays produce the diffraction pattern where the Bragg's Law condition ($n\lambda = 2d\,\mathrm{Sin}\theta$) is satisfied (see Chapter 9 Residual Stress). Thus, the X-ray diffraction patterns, which consist of diffracted X-ray intensity as function of diffraction angle, observed from a material will be the "fingerprint" of that material. These XRD patterns are used to identify crystal structure and phases, and can be used to measure micro strain, grain size, crystal orientation, etc. Powder sample chemistry can be measured by comparing with diffraction patterns from materials of the same chemistry, which are available for many materials in the powder diffraction data base (ICDD). ASTM E975-13 is a standard practice for the X-ray determination of austenite in steel (ASTM E975-13, 2013). Rietveld refinement analysis of the XRD data can provide a quantitative estimation of different phases, if more than one crystalline phases are present in the powder samples (Rietveld, 1967, 1969; Slotwinski et al., 2014).

18.4.1.7 Inert gas fusion (bulk)

Inert Gas Fusion (IGF) is a quantitative analytical technique used to determine the amount of hydrogen, oxygen, and nitrogen in the metal powders. The presence of H, O, and N has a significant influence in determining the mechanical properties, shelf life, and quality of the metallic parts/materials. Hence their identification and quantification in the metal powder samples are important for the quality control process. To meet specification for a given application, the determination of these impurity levels is essential.

In this technique, the powder sample is melted in a graphite crucible at very high temperature over which an inert carrier gas is flowed. As the powder sample melts, the hydrogen present in the sample is released as molecular hydrogen, nitrogen as molecular nitrogen, and oxygen present in the sample can react with the carbon in the graphite crucible and produce carbon monoxide (CO) and carbon dioxide (CO_2). The gases produced are swept by the inert gas flow onto a detector where they are analyzed separately to yield a weight percentage of the elements present. This technique is described by ASTM E1409-08 (ASTM E1409-13, 2013), ASTM E1447-09 (ASTM E1447-09, 2016), and E2792-11 (ASTM-E2792, 2016).

18.4.2 Applications of composition measurement in additive manufacturing

Quality and chemistry of powder feedstock play a crucial role in determining the properties of the parts and are key to the additive manufacturing quality control process. The quality of the powder feedstock influences features such as (i) manufacture of defect-free parts, (ii) build-to-build consistency, (iii) manufacturing defects on surfaces, and (iv) reproducibility between additive manufacturing machines (EPMA, 2019). The chemical composition of the powder can change the melting and solidification behavior during the PBF process and affect parts properties. The nonmetallic elements like oxygen, nitrogen, carbon, sulfur, and hydrogen, which may be present in the powder feedstock or introduced during the manufacturing process, will significantly influence the physical properties of the additive manufactured parts.

Some powder surfaces are more susceptible to oxidation, moisture adsorption, and hydroxide layer growth. The powder properties may also change with re-use due to the repeated exposure to the build chamber conditions. In all the above situations, powder composition analysis is crucial for the quality control of the final product.

Studies show that oxidation of the powder particles are detrimental due to their ability to maintain a low level of porosity in the parts produced. For example, Simchi (2004) found an increase in the porosity of steel manufactured parts with an increase in the initial oxygen content in the powder. Similarly, Leung et al. (2019) investigated the effect of powder oxidation on the molten-pool dynamics and defect formation during laser additive manufacturing of Invar 36 powder. In a different EBM study, (Tang et al. (2015)) observed an increase in the oxygen content of Ti6Al4V due to powder re-use, which eventually exceeds the maximum specification for oxygen content in the material, indicating that the powder may not be suitable for use after more than four recycles.

It is important to recognize that, depending on the analytical method used for the chemical analysis of additive manufacturing powders and the element of interest, each method has its own limitations to perform accurate elemental analysis. For example, EDS cannot detect the lightest elements and has poor energy resolution. More reliable quantitative information can be extracted using destructive bulk chemical analysis.

18.4.3 Powder material composition measurement standards

The international standards for powder composition measurement are shown in Table 18.3.

18.5 Thermal, mechanical, and humidity properties

18.5.1 Methods

18.5.1.1 Thermal conductivity

Thermal conductivity of powder feedstock is a key parameter affecting the consolidation characteristics of powder particles in PBF, which are very important in determining the L-PBF produced part quality (Cooke and Slotwinski, 2012).

There are a number of techniques used for the measurement of thermal conductivity of powder samples, and they are generally classified into two groups: steady state and transient (Sih and Barlow, 1992). The steady state approaches include (i) plate (or disk) method, (ii) cylindrical method, and (iii) spherical and ellipsoidal methods. The Guarded-Hot-Plate Method, which is described in ASTM C177-19, is an example of the plate method. In this approach, two sample test specimens are sandwiched between a guarded-hot-plate and two isothermal cold plates. The thermal conductivities are calculated using measurement of various surface temperatures, area, and thickness of the sample. In the cylindrical method a heater is located along the axis of the cylindrical sample specimen, while in the spherical and ellipsoidal method, a spherical heater is placed in the center of the spherical or ellipsoidal sample. In both the cylindrical and spherical/ellipsoidal methods, thermal conductivities are calculated using heat transfer principles and the measured temperature values at different radii (Sih and Barlow, 1992; Cooke and Slotwinski, 2012).

Examples for the transient thermal conductivity measurements include techniques such as the transient hot wire method, thermal probe method, transient hot strip method, and the flash method. In the transient hotwire method, a long thin heater wire is embedded in a large powder sample specimen. The heater is turned on and the temperature at a point in the specimen is recorded as a function of time, and thermal conductivity can be calculated using heat transfer principles. The thermal probe works similar to the transient hot wire method, but the heat source is enclosed inside a probe

Table 18.3 International standards, specifications, and methods in material characterization of powders.

Name/test	ASTM	M PIF
Chemical analysis of stainless, heat-resisting, maraging, and other similar chromium-nickel-iron alloys	ASTM E353-19	
Determination of C, S, N, and O in steel, iron, nickel, and cobalt alloys by various combustion and fusion techniques	ASTM E1019-18	
Analysis of low-alloy and stainless steels, cast irons, and nickel-base alloys by wavelength dispersive XRF	ASTM E322-12 ASTM E572-13 ASTM E1085-16 ASTM E2465-19	
Guide for minimizing unwanted electron beam effects in AES	ASTM E983-19	
Analysis of nickel alloys by ICP-AES	ASTM E2594-20 ASTM E2823-17	
Analysis of titanium alloys by XRF	ASTM E539-19	
Analysis of titanium and titanium alloys by ICP-AES	ASTM E2371-13	
Determination of O and N in titanium and titanium alloys by inert gas fusion	ASTM E1409-13	
Chemical analysis of aluminum and aluminum-base alloys	ASTM E3061-17	
Guide for depth profiling in Auger Electron Spectroscopy	ASTM E1127-08(2015)	
Method for determination of acid insoluble matter in iron and copper powders		MPIF Standard Test Method 06
Method for sample preparation for the determination of the total carbon content of powder metallurgy (pm) materials		MPIF Standard Test Method 66
Guide to charge control and charge referencing techniques in XPS	ASTM E1523-15	
Guide for handling specimens prior to surface analysis	ASTM E1829-14(2020)	

for easy insertion into the sample. In the transient hot strip method, a thin metal strip with a known temperature coefficient of resistance, which acts as the heat source as well as a resistance thermometer, is placed within the sample specimen. Resistance as well as the output voltage of the strip varies as a function of temperature. When a constant current is applied to the strip, the temperature of the strip and the surroundings increases. The thermal conductivity of the surrounding material is calculated by monitoring the output voltage of the strip (Gustafsson et al., 1979; Sih and Barlow, 1992; Cooke and Slotwinski, 2012). In another transient approach called the flash method, a high intensity light pulse is focused onto the surface of the powder specimen (powder bed) and the temperatures on the sample surfaces are determined, from which the heat capacity can be calculated. The thermal conductivity of the powder sample can be calculated by multiplying the heat capacity, thermal diffusivity, and the density (Parker et al., 1961; ASTM E1461-13, 2013).

18.5.1.2 Nano-indentation

Nano-indentation is a technique used for assessing metal powders in which a diamond tip of precise geometry is pressed into a sample surface under a controlled known constant or varying load or force. Based on the deformation of the sample, the modulus and hardness of the surface can be determined. For powder, this experiment is very challenging, in terms of sample preparation and addressing the powder particle with the indenter tip. Care must be taken to use the correct type of material in which to embed the powder particles, it should not deform itself under the applied load. Particle concentration must be such that powder particles are present at the surface, but are not densely packed such that the packing of the particles would affect the reaction of the powder particle to the applied indenter load.

18.5.1.3 Porosity

Porosity within the powder particle is an important characteristic which can negatively affect the final produced part properties (Du Plessis et al., 2018). Porosity within the particles can lead to porosity within the final L-PFB produced part. A high level of porosity can lead to poor melting, gas entrainment, and outgassing during the L-PBF process. Porosity can also lead to lower part density, cracks, and lower part strength. Powder porosity can be measured using Micro-Computed Tomography (μCT), however this can be a relatively time-consuming and costly technique, with significant expertise required for its application and significant data post-processing is required. It does however have the capability of providing porosity data for a large number of particles. μCT hardware and software have also progressed significantly in recent times providing higher accuracy measurements in shorter periods (Du Plessis et al., 2018). A simpler and faster approach is pycnometry, where a powder sample is placed in a sample holder, and an inert gas is introduced into the sample, filling the voids and surface pores. Based on the volume of gas introduced, a measure of porosity can be obtained. It can be used for micropore and mesopore analysis. However, fully closed pores within the part will not be measured by this approach. The reader is directed to Chapter 6 for more details on porosity measurement techniques. The ASTM standard for pycnometry for skeletal density of metal powders is codified in ASTM B923-20 (ASTM B923-20, 2020). Specific surface area, related to porosity, can be measured using ASTM standard B922-20 (ASTM B922-20, 2020).

18.5.1.4 Humidity

Humidity in a powder sample can play a very important role in safety, stability, reliability, and fluidity of the powder (Matthes et al., 2020). One method used to quantitatively measure the moisture content utilizes the Relequa MP-1000 moisture analyzer (http://www.relequa.com/). This instrument uses a sealed chamber which contains a small amount of powder to calculate the amount of moisture present in the powder sample. The specific starting relative humidity (RH) % is set as a baseline, and the amount of moisture lost per unit time is then calculated. In practice, a number of different starting %RH values are chosen, one for each new sample of powder. The correct %RH value to begin with is the one where the final Water Vapor Equilibrium Point (WVEP) value is the same as the starting %RH. A second approach is to choose the same starting %RH for every sample and material and compare the moisture loss under similar conditions.

18.5.1.5 Phase transition temperature and type

Differential thermal analysis (DTA) and thermal gravimetric analysis (TGA) measure respectively the temperature difference between a sample and an inert reference sample as a function of temperature, and the weight change of a sample as a function of temperature, while subjected to a controlled heating program. These methods are used to determine the phase change temperatures and can also be used to help confirm the composition of the solid material. DTA and TGA are detailed in the ASTM standards (ASTM E2160-04, 2018 and ASTM E1131-20, 2020).

18.5.2 Application of thermal, mechanical, and humidity measurements in additive manufacturing

Due to the presence of weak conduction through the gas voids between the powder particles, thermal conductivity of powder will be significantly lower than that of the bulk material. The packing density of the powder can influence the contact area between the particles and the thermal conduction path. Thus, the thermal conductivity of the powder samples are found to increase with packing density (Field et al., 2020). Similarly, Alkahari et al. (2012) found that the thermal conductivity of 316L metal powder increases with increase in the bulk density and particle diameter, while the thermal conductivity of the consolidated metal decreases with increased porosity. In general, thermal properties of the powder, especially their reduced effective thermal conductivity compared to the bulk, influence the melt-pool characteristics and hence the mechanical properties of the parts produced using PBF additive manufacturing.

Understanding the mechanical properties of metal powders on the other hand allows for a greater appreciation of powder flow, packing, and for more accurate predictions of the interactions between powders and the recoater blade, roller, or other powder distribution mechanism employed in the L-PBF tool. Density and hardness are also important when mixtures of powders are used, such as when a metal powder is mixed with a reinforcing agent such as silicon carbide or tungsten carbide. Hardness and mechanical properties obtained via indentation methods such as nano-indentation may also inform the operator about density and porosity, and the presence of defects with the powder particle.

One potential way of integrating the moisture testing into the additive manufacturing workflow is shown in Fig. 18.7 below. In this concept, the powder would be tested upon receipt from supplier. This powder sample is then stored (Sample A). After each build or at monthly/weekly intervals, the virgin powder is tested and compared with Sample A (*red arrows*: gray arrows in printed version). After each build, the used and sieved powder is tested and compared with the original Sample A (*yellow arrows*: light gray arrows in printed version).

18.5.3 Powder thermal conductivity and porosity assessment standards

The international standards for powder conductivity and porosity assessment are shown in Table 18.4.

18.6 Powder life cycle and sustainability analysis

In order to ensure the economic feasibility of powder-based additive manufacturing, powder is almost always used multiple times in L-PBF processes. Sartin et al. (2017)

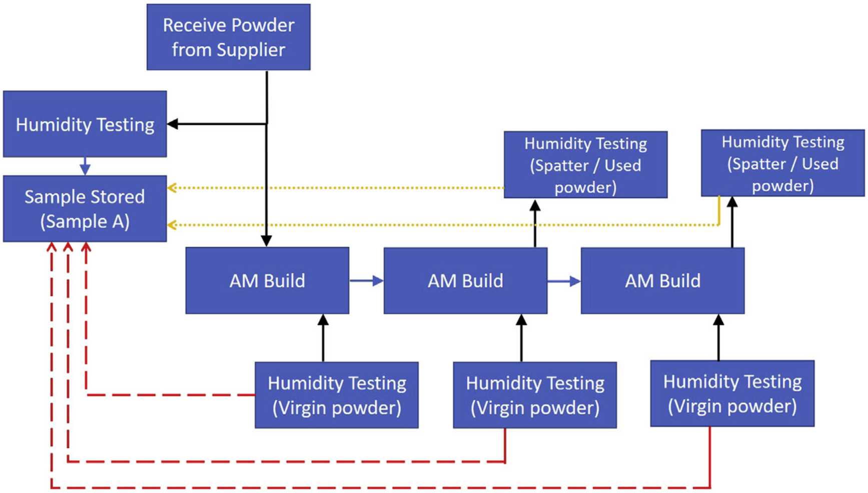
Receive Powder from Supplier
Humidity Testing
Sample Stored (Sample A)
Humidity Testing (Spatter / Used powder)
Humidity Testing (Spatter / Used powder)
AM Build
AM Build
AM Build
Humidity Testing (Virgin powder)
Humidity Testing (Virgin powder)
Humidity Testing (Virgin powder)

Figure 18.7 Schematic illustration of the integration of humidity testing into AM quality control workflow.

Table 18.4 International standards, specification, and methods in powder thermal conductivity and porosity.

Name/test	ASTM
Standard Test Method for Steady-State Heat Flux Measurements and Thermal Transmission Properties by means of the Guarded-Hot-Plate Apparatus	ASTM C177-19
Standard Test Method for Thermal Diffusivity by the Flash Method	ASTM E1461-13
Standard Test Method for Metal Powder—Specific Surface Area by Physical Adsorption	ASTM B922-20
Standard Test Method for Metal Powder Skeletal Density by Helium or Nitrogen Pycnometry	ASTM B923-20
Standard Test Method for Compositional Analysis by Thermogravimetry	ASTM E1131-20

found that only 6.7% of powder fed into the L-PBF process was consumed; the remaining 93.3% was recovered and could be reused in future builds. A case study by LPW Technology Ltd.˙ (Rushton, 2019) showed that a 92% reduction in material costs could be achieved if powder was reused up to 15 times versus just one use as virgin powder. However, some or all of the reclaimed powder will have been subjected to high-temperature melt pools, spatter particles, partial melting of adjacent particles, suboptimal atmospheric environments, and human handling (introducing oxygen and humidity contamination and contamination from powders in the build chamber from previous builds). These factors can contribute to powder degradation through debris contamination, changes in particle morphology/size, and changes in the chemical composition of the powder.

The recycling process should be strictly controlled to minimize the risk of powder degradation, attempting to keep the properties as similar to the virgin powder as possible. While standards exist to characterize metal powders (ASTM F3049-14, 2014), there is no standard methodology for powder reclamation or powder recycling. This leads to a wide variation in the rate of powder degradation when recycling metal powders across the industry. Equipment such as the AMPro Sieve Station by Russell Finex (https://www.russellfinex.com/) offers fully automated and closed-loop recycling of powders under inert atmospheric conditions. After automatically extracting powder from the build chamber, it sieves out unsuitable particles and returns the remaining powder back into the feed hopper. This reduces degradation by eliminating manual handling of powders and minimizing exposure to the atmosphere. However, many additive manufacturing users still manually remove loose powder from the completed build (either by hand or the use of a vacuum cleaner) and sieve the powder in a separate machine, reintroducing the sieved powder to the material feed hopper. This results in increased exposure to the atmosphere and the potential inclusion of contaminants such as dust or other powder particles, accelerating powder degradation.

18.6.1 Powder reuse methods

An important question is raised: “What can be done with the remaining End-of-Life (EoL) powder?” Powell et al. (2020) investigated methods to improve the resource efficiency of powders in additive manufacturing, identifying several potential solutions. The suggested approach to achieving this was to both reduce the need for new virgin powder to be created and increase the longevity of metal powders. Several potential solutions were investigated, with a technique called “plasma spheroidization” showing the most promise.

A rudimentary understanding of powder creation is necessary to appreciate potential powder upcycling methods. Powder is typically generated through “atomization” (shown schematically in Fig. 18.8). Metal is melted, allowing it to flow through a nozzle. High-pressure jets of fluid are aimed at the end of this nozzle, rapidly dispersing the metal upon contact and creating tens of thousands of small particles. The fluid chosen greatly influences the powder properties. For example, using a jet of water rapidly cools the metal, resulting in less spherical particles, while using a jet of inert gas creates highly spherical particles and minimizes the risk of changes in the chemical composition (Dawes et al., 2015). The metal flow rate and jet velocity can be altered to tailor the size of particles created, allowing many different specifications of powder to be produced.

Plasma spheroidization uses a similar principle to gas and water atomization, however, rather than atomizing molten metal, the feedstock material is heated rapidly inside the nozzle. This has two distinct advantages over gas or water atomization. The first is that the metal spends less time at high temperatures, reducing the likelihood of chemical reactions with the surrounding atmosphere (even an “inert” atmosphere contains small quantities of oxygen and other reagents). The second advantage is that the feedstock material can be small in volume, such as a wire or powder, which will melt faster than an ingot, bar, or similar.

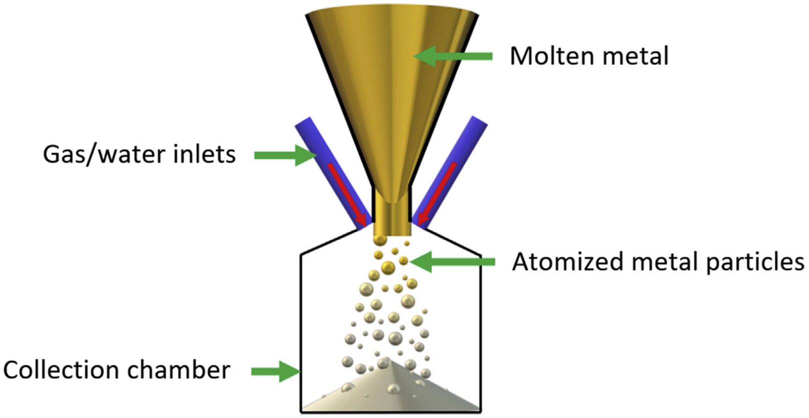

Figure 18.8 Schematic showing the material and processing elements within the atomization process.

The latter advantage makes plasma spheroidization a viable technique to upcycle poor-quality powders that have been reused numerous times and are no longer suitable for use in L-PBF. This principle has been demonstrated by Kelkar (2019), where low-quality oversized nonspherical water-atomized powder particles were converted to smaller high-quality spherical powder particles through plasma spheroidization. Perhaps more impressive was the ability of the plasma spheroidizer to alter the chemical composition of the particles through introducing reducing agents to the gas inlets, reducing the oxygen content by 97%. Oxygen is considered to be a likely contributor to the formation of pores (Pal et al., 2020), so coupling the improvement in chemical composition with the superior morphology suggests that plasma spheroidization could sufficiently upcycle EoL powders. This would both reduce the waste output in the form of EoL powders from L-PBF while reducing the necessity to create virgin powders from raw materials, greatly improving the sustainability of L-PBF. Powell (2020). conservatively estimated that powder production through plasma spheroidization could reduce energy consumption by 18.3%, if not more, when compared with gas atomization to create high-quality powders.

An alternative and simpler (albeit less effective) solution to improve powder longevity is to blend recycled powders with virgin powders. While this is common practice within industry and can be empirically demonstrated to work, there is little research into this technique. Vock et al. (2019) found that mixing equal quantities of virgin and recycled powders resulted in no changes being observed in the powder properties, suggesting that the components produced from blended powder may also be unchanged. Jacob et al. (2017) used another blending technique that introduced virgin powder at regular intervals to a number of consecutive builds, finding that both the powder properties and properties of the produced components remained relatively constant, further demonstrating the viability of blended powders. It should be noted that blending powders does not remove the contamination that may result from the existence of spatter particles. While it does dilute their concentration in the powder mixture, a single heavily oxidized spatter particle could still cause porosity in a fabricated component.

18.6.2 Effect of powder recycling on additive manufacturing

Research has been undertaken into the impact of recycling powders in various powder-based additive manufacturing techniques. This is well summarized by Powell et al. (2020) and Vock et al. (2019), offering an overview of the trends that are witnessed as powder is repeatedly reused. Different powder recycling techniques were applied, emphasizing the lack of standardization in powder recycling in additive manufacturing. Changes observed when comparing the properties of virgin and recycled powder tended to be small, indicating that powder can be recycled effectively. However, the changes were also found to be gradual; the magnitude of these changes increased as the powder was continuously reused/processed. As powder properties can have a considerable influence on component properties in L-PBF, it has been found that recycled powders often influence the component properties such as surface roughness, strength/hardness, chemical composition, and porosity (Renderos et al., 2016; Seyda et al., 2012; Tang et al., 2015).

One of the biggest problems found in recycled powders was "spatter." Spatter particles can be seen as "sparks" flying off in the build chamber of the AM machine. An example of a spatter particle can be seen in Fig. 18.9. These particles have a higher oxygen content than the virgin powder (Liu et al., 2015) and can vary in morphology and oxide coverage (Gasper et al., 2018; Obeidi et al., 2020). After sparking off, the spatter particles often fall back into the build chamber powder bed, either becoming incorporated into the build or are extracted through the recycling process. LPW Technology Ltd. (2018) state that a "significant amount" of contaminated spatter particles are small enough to pass through sieves in the recycling process, resulting in them being present in future builds, a clear explanation of how this can negatively impact future builds through the creation of pores, in turn creating regions of weakness in fabricated components, is offered by Pal (2020).

Spatter is not currently measured in ASTM F3049-14 as it is not present in virgin powders. It would be incredibly difficult to measure the presence of spatter particles quantitatively. Their effect is unlikely to be detected through standard powder quality measurements such as PSD or bulk chemical composition, as oversized spatter particles will be sieved out and the quantity of spatter particles will be small in comparison to normal particles. However, it is reasonable to assume that spatter forms at a constant rate per minute of "laser on" time (provided build parameters are unchanged). Therefore, as powder is reused repeatedly over time, the quantity of spatter particles present in a powder will inevitably increase. This leads to an increased probability of spatter particles being incorporated into components and potentially forming pores, as demonstrated by Pal (2020).

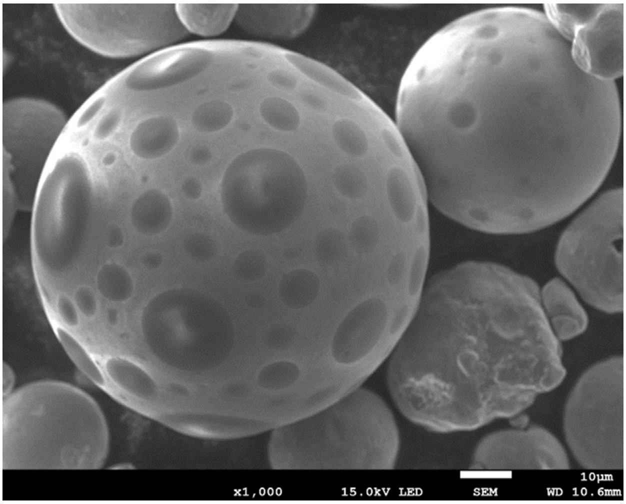

Figure 18.9 A partially oxidized spatter particle. The *darker spots* are heavily oxidized.

As the powder degrades gradually, it is difficult to confidently determine an EoL point where it is no longer suitable for use in L-PBF AM processes. Due to the numerous L-PBF systems on the market, there is no minimum standard for powder quality; it is up to both the machine user and manufacturer to decide what powder is suitable for use, and more importantly, when powder is no longer suitable. Some materials used in high-end industries are highly reactive, notably Al- and Ti-based materials, resulting in them being recycled fewer times before falling out of specification (Daraban et al., 2019). In industries using less reactive materials, the powder is likely to have a considerably longer lifespan. Either way, there is eventually going to be a quantity of powder that is no longer useful as a material feedstock for additive manufacturing.

18.7 Powder safety

It would be remiss to discuss the analysis of powder for L-PBF processing without addressing safety and the potential risks and hazards associated with the powder feedstock and its use within the L-PBF chamber. This is not intended to be an exhaustive discussion, and the reader is encouraged to seek out the Safety Data Sheet for the particular powder feedstock they are using, including from their preferred supplier for the most up-to-date information.

Briefly however, the risks include those arising from the chemical nature of the metals or alloys, their reaction with water, oxygen, the laser (hence the necessity of an inert environment in the L-PBF process chamber), itself (is it self-igniting), and the presence of static charges (operator, tools). Many of the most commonly used alloys such as stainless steel and Inconels (nickel superalloys) contain carcinogenic or suspected carcinogenic materials. Therefore, when working with such materials, it is important to plan how much of the material is to be used, how to contain this material (for example, by using a glove box), transfer steps, how to avoid the formation of a dust cloud, choosing the correct personal and respiratory protective equipment (PPE and RPE), and using engineering controls (O_2 sensors, Class D powder fire extinguisher, and antistatic mats) to limit the risks associated with working with these materials. Appropriate risk assessments need to be completed for an L-PBF process tool prior to installation and commissioning.

As mentioned above, certain powders will react violently with water; therefore, isopropyl alcohol wipes (70% or 100%) should be used to clean up powder spills and for general housekeeping and cleaning.

One important aspect of working with metal powders is the concept of ATEX compliance. For powder usage, there are three zone (20, 21, and 22) classifications. These are defined as below:

- Zone 20—A place in which an explosive atmosphere in the form of a cloud of combustible dust in air is present continuously, or for long periods or frequently.
- Zone 21—A place in which an explosive atmosphere in the form of a cloud of combustible dust in air is likely to occur in normal operation occasionally.

- Zone 22—A place in which an explosive atmosphere in the form of a cloud of combustible dust in air is not likely to occur in normal operation but, if it does occur, will persist for a short period only.

This allows for an understanding of the risks involved in each element of the process; for example, in the absence of the inert atmosphere, the L-PBF process chamber would be considered Zone 20, the vacuum cleaner for removal of powder from the process chamber needs to be ATEX rated, as it is considered a Zone 22. It is important to understand the air flow of the laboratory in which powder is manipulated, to avoid strong air currents in the area where powder is open, for example, in the process chamber during loading. A dust explosion requires five contributing factors: turbulence, confinement, heat, material or fuel, and oxygen. Hence it is described as the explosion pentagon. If any of these factors are removed, the explosion is not possible, or the risk is greatly diminished. When planning an installation, it is important to consider the room volume, the number of air changes per hour, the flow of inert gas required for the safe operation of the L-PBF tool, and the maximum inert gas outflow rate in the event of a leak.

Metallic powders should be stored in cabinets which are rated as fire resistant for 90 min (EN 14470-1). Powder should be stored in a laboratory with low relative humidity, and should be handled/poured in an isolation cabinet or glove box. An inert atmosphere should be considered but is usually not required. Powder that has already been processed via L-PBF should be sieved prior to being used again and can be mixed with virgin powder, though standards-based part-quality controls should be implemented. Isolation cabinets for pouring, handling, and sieving; fire-proof storage cabinets; and robust procedures for spill management, L-PBF machine cleaning and appropriate training for staff are elements that can be used for the safe handling of L-PBF feedstocks. The formation of a dust cloud, which is possible for lighter metallic powders and nanoparticles is to be avoided, as are heat sources and sparking sources. Working in a well-ventilated space or isolating the operator from large quantities of the feedstock using engineering controls is more important than relying on PPE alone. Experience with specific materials suppliers and batches is required in order to develop a robust workflow for use and recycling of powder in L-PBF, as discussed above.

18.7.1 Health and safety standards

Some standards related to powder combustibility include ASTM E2019-03 (2019), ASTM E1515-14 (2014), and ASTM E1226-19 (2019). The reader is also directed to the local regulations of the country they are working, as these can be different between regions. Beyond the potential combustibility of metallic powder feedstocks, they are potential carcinogens (as mentioned above) and can also cause irritation in the respiratory tract, while nanoparticles can penetrate further into the lungs and alveoli, potentially causing long-term damage depending on the level and duration of exposure. There are studies on the effect of such particles, captured well in a recent contribution by Arrizubieta et al. (2020), which also discusses the waste disposal of such feedstocks. Nanoparticles are now being investigated in L-PBF processes as additives to potentially improve the thermal conductivity and flow properties of the feedstock and melt pool, as well as the mechanical properties of the finished parts. Therefore, additional care should be taken in their storage, handling, and processing.

18.8 Questions

- What is the typical size range for powders used in L-PBF?
- Name three methods of analyzing powder flow properties.
- What is the difference between tapped and bulk/apparent density of a powder?
- List three methods of powder size analysis.
- Name a method for characterizing the oxidation state of powder surfaces.
- Name three common methods for analyzing the chemical composition of powders.
- What effects on the physical properties can porosity lead to in a part produced by L-PBF?
- List three changes that may be seen in reused powder.
- List three types of powder production process.

18.9 List of abbreviations

AES	Auger Electron Spectroscopy
BFE	Basic Flowability Energy: resistance a powder exhibits to flow in a confined environment.
DLS	Dynamic Light Scattering
EoL	End of Life
FRI	Flow Rate Index: metric of how sensitive a powder is to changes in flow rate.
ICP-OES	Inductively Coupled Plasma-Optical Emission Spectroscopy
IGF	Inert Gas Fusion
L-PBF	Laser-Powder Bed Fusion
LD	Laser Diffraction
MPIF	Metal Powder Industries Federation
PPE	Personal Protective Equipment
PSD	Particle Size Distribution
RH%	Relative Humidity
RPE	Respiratory Protective Equipment
SE	Specific Energy: metric of powder flow in an unconfined environment.
SI	Stability Index: metric of how the stability of a powder varies with being made to flow.
TGA	Thermogravimetric Analysis
WVEP	Water Vapor Equivalence Point
XPS	X-ray Photo-electron Spectroscopy
XRF	X-ray Fluorescence

18.10 List of terms

Angle of repose	Angle that a pile of powder makes with the horizontal without slumping.

Apparent density	Bulk density of a loosely packed powder.
Bulk density	Ratio of powder mass to the volume occupied under normal conditions (at rest).
Compressibility percentage	The amount a powder will be compressed under an applied normal load.
Equivalent diameter of powder particles	The diameter of a circle possessing the same area as the projected area of the imaged particle.
Minimum aeration velocity	The minimum velocity of compressed air at which the flow energy of a powder approaches zero.
Morphology	The shape of a powder; metrics such as circularity, sphericity, aspect ratio, and convexity.
Satellites	Smaller particles physically attached to a larger particle.
Sphericity	This refers to how spherical a particle is, based on the projected image of the particle.
Tapped (tap) density	Tap density is defined as the density of a powder when the receptacle is tapped or vibrated under specified conditions.

Acknowledgements

This work is supported by a research grant from Science Foundation Ireland (SFI) under Grant No. 16/RC/3872 and is co-funded under the European Regional Development Fund and by I-Form industry partners.

References

Alkahari, M.R., et al., 2012. Thermal conductivity of metal powder and consolidated material fabricated via selective laser melting. Key Engineering Materials 244–249. https://doi.org/10.4028/www.scientific.net/KEM.523-524.244.

America Makes and AMSC, June 2018. Standardization Roadmap for Additive Manufacturing - Version 2.0, vol. 2. America Makes & ANSI Additive Manufacturing Standardization Collaborative (AMSC), pp. 1–269.

Arrizubieta, J.I., Ukar, O., Ostolaza, M., Mugica, A., 2020. Study of the environmental implications of using its handling. Metals 10, 261. https://doi.org/10.3390/met10020261.

ASTM B214-16, 2016. Standard Test Method for Sieve Analysis of Fine, p. 571. https://doi.org/10.1520/B0214-16.

ASTM B215-20, 2020. Standard Practices for Sampling Metal Powders. West Conshohocken, PA. www.astm.org.

ASTM - B855-17, 2017. Standard Test Method for Volumetric Flow Rate of Metal Powders Using Arnold Meter. ASTM B855 - 17, 94(Reapproved), pp. 1–3. https://doi.org/10.1520/B0855-17.

ASTM B964-16, 2016. Standard Test Methods for Flow Rate of Metal Powders Using the Carney Funnel, pp. 213–216. https://doi.org/10.1520/B0213-13.2 (i).

ASTM D7891, 2015. Standard Test Method for Shear Testing of Powders Using the Freeman Technology. ASTM International, pp. 1−11. https://doi.org/10.1520/D7891-15.1.5.

ASTM B213-20, 2020. Standard Test Methods for Flow Rate of Metal Powders Using the Hall Flowmeter Funnel. ASTM International, West Conshohocken, PA. www.astm.org.

ASTM B527-20, 2020. ASTM B527-20 Standard Test Method for Tap Density of Metal Powders and Compounds. ASTM International. https://doi.org/10.1520/B0527-20.

ASTM B922-20, 2020. ASTM B922: Standard Test Method for Metal Powder Specific Surface Area by Physical Adsorption. https://doi.org/10.1520/B0922-10.2.

ASTM B923-20, 2020. ASTM B923: Standard Test Method for Metal Powder Skeletal Density by Helium or Nitrogen. https://doi.org/10.1520/B0923-10.2.

ASTM D6393-14, 2014. D6393: Standard Test Method for Bulk Solids Characterization by Carr Indices. ASTM International, pp. 1−7. https://doi.org/10.1520/D6393-14, 04.09(D).

ASTM E1078-14, 2020. Standard Guide for Specimen Preparation and Mounting in Surface Analysis. ASTM International, West Conshohocken, PA.

ASTM E1127, 2015. E1127: Standard Guide for Depth Profiling in Auger Electron Spectroscopy 1. https://doi.org/10.1520/E1127-08R15.2.

ASTM E1131-20, 2020. ASTM E1131-20, Standard Test Method for Compositional Analysis by Thermogravimetry. ASTM International. https://doi.org/10.1520/E1131-20.

ASTM E1226-19, 2019. Standard Test Method for Explosibility of Dust Clouds 1, vol. 2, pp. 1−13. https://doi.org/10.1520/E1226-12A.Copyright.

ASTM E1409, 2008. E1409-13: Standard Test Method for Determination of Oxygen and Nitrogen in Titanium and Titanium Alloys by Inert Gas Fusion. https://doi.org/10.1520/E1409.

ASTM E1447-09, 2016. Standard Test Method for Determination of Hydrogen in Titanium and Titanium Alloys by Inert Gas Fusion Thermal Conductivity/Infrared Detection Method. ASTM International, West Conshohocken, PA. www.astm.org.

ASTM E1461-13, 2013. ASTM E1461-13: Standard Test Method for Thermal Diffusivity by the Flash Method 1. https://doi.org/10.1520/E1461-13.

ASTM E1508-12a(2019), 2019. Standard Guide for Quantitative Analysis by Energy-Dispersive Spectroscopy. ASTM International, West Conshohocken, PA. www.astm.org.

ASTM E1515-14, 2014. Standard Test Method for Minimum Explosible Concentration of Combustible Dusts, vol. 05. American Society Testing Materials, pp. 1−9. https://doi.org/10.1520/E1515-07.2.

ASTM E1829, 2014. ASTM 1829: Standard Guide for Handling Specimens Prior to Surface Analysis 1. https://doi.org/10.1520/E1829-09.2.

ASTM E2019-03, 2019. Standard Test Method for Minimum Ignition Energy of a Dust Cloud in Air. ASTM International, West Conshohocken, PA. www.astm.org.

ASTM E2160-04, 2018. Standard Test Method for Heat of Reaction of Thermally Reactive Materials by Differential Scanning Calorimetry. https://doi.org/10.1520/E2160-04R18.

ASTM E975-13, 2013. Standard Practice for X-Ray Determination of Retained Austenite in Steel with Near Random Crystallographic Orientation. ASTM International, West Conshohocken, PA. www.astm.org.

ASTM F3049-14, 2014. Standard Guide for Characterizing Properties of Metal Powders Used for Additive Manufacturing Processes. ASTM International, pp. 1−3. https://doi.org/10.1520/F3049-14.

ASTM E1409-13, 2013. Standard Test Method for Determination of Oxygen and Nitrogen in Titanium and Titanium Alloys by Inert Gas Fusion. ASTM International, West Conshohocken, PA. www.astm.org.

Brika, S.E., et al., 2020. Influence of particle morphology and size distribution on the powder flowability and laser powder bed fusion manufacturability of Ti-6Al-4V alloy. Addit. Manuf. 31. https://doi.org/10.1016/j.addma.2019.100929 (October 2019).

Chen, H., et al., 2019. Powder-spreading mechanisms in powder-bed-based additive manufacturing: experiments and computational modeling. Acta Mater. 179, 158−171. https://doi.org/10.1016/j.actamat.2019.08.030.

Clayton, J., Millington-Smith, D., Armstrong, B., 2015. The application of powder rheology in additive manufacturing. JOM 67 (3), 544−548. https://doi.org/10.1007/s11837-015-1293-z.

Cooke, A., Slotwinski, J., 2012. NIST report 7873: properties of metal powders for additive manufacturing: a review of the state of the art of metal powder property testing. Addit. Manuf. Mater. Stand. Test. & Appl. 21−48. https://doi.org/10.6028/NIST.IR.7873.

Daraban, A.E.O., et al., 2019. A deep look at metal additive manufacturing recycling and use tools for sustainability performance. Sustainability 11 (19). https://doi.org/10.3390/su11195494.

Dawes, J., Bowerman, R., Trepleton, R., 2015. Introduction to the Additive Manufacturing Powder Metallurgy Supply Chain. Johnson Matthey Technol. Rev. 59 (3), 243. https://doi.org/10.1595/205651315x688686.

Du Plessis, A., et al., 2018. X-ray microcomputed tomography in additive manufacturing: a review of the current technology and applications. 3D Print. Addit. Manuf. 5 (3), 227−247. https://doi.org/10.1089/3dp.2018.0060.

EPMA, 2019. Introduction to Additive Manufacturing Technology, a Guide for Designers and Engineers. European Powder Metallurgy Association, pp. 28−34. Available at: http://www.sf2m.asso.fr/CommissionsThematiques/DocComThematiques/EPMA_Additive_Manufacturing.pdf.

Escano, L.I., et al., 2018. Revealing particle-scale powder spreading dynamics in powder-bed-based additive manufacturing process by high-speed x-ray imaging. Sci. Rep. 8 (1), 1−11. https://doi.org/10.1038/s41598-018-33376-0. Springer US.

Field, A.C., et al., 2020. The effect of powder characteristics on build quality of high-purity tungsten produced via laser powder bed fusion (LPBF). Metall. Mater. Trans. Phys. Metall. & Mater. Sci. 51 (3), 1367−1378. https://doi.org/10.1007/s11661-019-05601-6. Springer US.

Freeman Technology, 2016. Measuring and Understanding the Flow Properties of Powders with the FT4 Powder Rheometer®.

Freeman Technology W7030, 2008. The Basic Flowability Energy.

Freeman Technology W7013, 2007. Stability & Variable Flow Rate Method.

Freeman Technology W7031, 2008. Specific Energy. https://doi.org/10.1016/B978-0-8155-2018-4.50022-7.

Gasper, A., et al., 2018. Spatter and oxide formation in laser powder bed fusion of Inconel 718. Addit. Manuf. 24, 446−456. https://doi.org/10.1016/j.addma.2018.09.032.

Gruber, H., et al., 2019. Effect of powder recycling in electron beam melting on the surface chemistry of alloy 718 powder. Metall. Mater. Trans. Phys. Metall. & Mater. Sci. 50 (9), 4410−4422. https://doi.org/10.1007/s11661-019-05333-7. Springer US.

Gustafsson, S.E., Karawacki, E., Khan, M.N., 1979. Transient hot-strip method for simultaneously measuring thermal conductivity and thermal diffusivity of solids and fluids. J. Phys. Appl. Phys. 12 (9), 1411−1421. https://doi.org/10.1088/0022-3727/12/9/003.

Hausnerova, B., Mukund, B.N., Sanetrnik, D., 2017. Rheological properties of gas and water atomized 17-4PH stainless steel MIM feedstocks: effect of powder shape and size. Powder Technol. 312, 152−158. https://doi.org/10.1016/j.powtec.2017.02.023.

ISO 3953, 2011. Metallic Powders—Determination of Tap Density. Technical Committee ISO, Geneva, Switzerland.

ISO 13320, 2020. Particle size analysis — Laser diffraction methods. https://www.iso.org/standard/69111.html.

Jacob, G., et al., 2017. Effects of Powder Recycling on Stainless Steel Powder and Built Material Properties in Metal Powder Bed Fusion Processes. NIST Advanced Manufacturing Series, Series 100, p. 59.

Kelkar, R.M., 2019. US Patent US 2019/0061005: High Quality Spherical Powders for Additive Manufacturing Processes along with Methods of Their Formation. US Patent Office, USA.

Klausner, J.F., Chen, D., Mei, R., 2000. Experimental investigation of cohesive powder rheology. Powder Technol. 112 (1–2), 94–101. https://doi.org/10.1016/S0032-5910(99)00310-1.

Kurzynowski, T., et al., 2018. Correlation between process parameters, microstructure and properties of 316 L stainless steel processed by selective laser melting. Mater. Sci. Eng. 718, 64–73. https://doi.org/10.1016/j.msea.2018.01.103 (December 2017).

Leung, C.L.A., et al., 2019. The effect of powder oxidation on defect formation in laser additive manufacturing. Acta Mater. 166, 294–305. https://doi.org/10.1016/j.actamat.2018.12.027.

Liu, Y., et al., 2015. Investigation into spatter behavior during selective laser melting of AISI 316L stainless steel powder. Mater. Des. 87, 797–806. https://doi.org/10.1016/j.matdes.2015.08.086. Elsevier B.V.

Liverani, E., et al., 2017. Effect of selective laser melting (SLM) process parameters on microstructure and mechanical properties of 316L austenitic stainless steel. Elsevier J. Mater. Process. Technol. 249, 255–263. https://doi.org/10.1016/j.jmatprotec.2017.05.042 (November 2016).

Lyckfeldt, O., 2013. Powder rheology of steel powders for additive manufacturing. In: International Powder Metallurgy Congress and Exhibition, Euro PM 2013.

LPW Technology Ltd, 2018. Metal powder reuse regimes and impact on part reproducibility e Part I. http://maschinetech.com/ wp-content/uploads/2018/06/Powder-Degradation-in-Serial-Production-Pt-I. pdf. (Accessed 23 August 2019).

Matthes, S., et al., 2020. Factors influencing powder-properties of TiAl6V4 along the L-PBF process chain. Prog. Addit. Manuf. 5 (1), 33–39. https://doi.org/10.1007/s40964-020-00120-y. Springer International Publishing.

Mercury Scientific, 2020. Fluidization Analysis with the Revolution. Available at: http://www.mercuryscientific.com/instruments/fluidization-analysis-revolution. (Accessed 5 June 2020).

MPIF, 2019. A Collection of Powder Characterization Standards for Metal Additive Manufacturing. Available at: https://www.techstreet.com/mpif/standards/a-collection-of-powder-characterization-standards-for-metal-additive-manufacturing?product_id=2085958.

Mussatto, A., et al., 2019. Evaluation via powder metallurgy of nano-reinforced iron powders developed for selective laser melting applications. The Authors Mater. & Design 182, 108046. https://doi.org/10.1016/j.matdes.2019.108046.

Obeidi, M.A., et al., 2020. Comprehensive assessment of spatter material generated during selective laser melting of stainless steel. Mater. Today Commun. 25, 101294. https://doi.org/10.1016/j.mtcomm.2020.101294. Elsevier.

Oliveira, J.P., LaLonde, A.D., Ma, J., 2020. Processing parameters in laser powder bed fusion metal additive manufacturing. Mater. Des. 193, 1–12. https://doi.org/10.1016/j.matdes.2020.108762.

Pal, S., et al., 2020. As-fabricated surface morphologies of Ti-6Al-4V samples fabricated by different laser processing parameters in selective laser melting. Additive Manufacturing 33, 101147. https://doi.org/10.1016/j.addma.2020.101147.

Pal, S., 2020. Melting, fusion and solidification behaviors of Ti-6Al-4V alloy in selective laser melting at different scanning speeds. Rapid Prototyp. J. 26 (7), 1209−1215. https://doi.org/10.1108/RPJ-07-2019-0206.

Parker, W.J., et al., 1961. Flash method of determining thermal diffusivity, heat capacity, and thermal conductivity. J. Appl. Phys. 32 (9), 1679−1684. https://doi.org/10.1063/1.1728417.

Powell, D., 2020. Recycling and Reuse of Metal Powders for Various Applications in Additively Manufactured Products. MSc. Thesis. Lancaster University.

Powell, D., et al., 2020. Understanding powder degradation in metal additive manufacturing to allow the upcycling of recycled powders. J. Clean. Prod. 268, 122077. https://doi.org/10.1016/j.jclepro.2020.122077. Elsevier Ltd.

Renderos, M., et al., 2016. Ni based powder reconditioning and reuse for LMD process. Phys. Procedia 83, 769−777. https://doi.org/10.1016/j.phpro.2016.08.079.

Rietveld, H.M., 1967. Line profiles of neutron powder-diffraction peaks for structure refinement. Acta Crystallogr. 22 (1), 151−152. https://doi.org/10.1107/s0365110x67000234. International Union of Crystallography.

Rietveld, H.M., 1969. A profile refinement method for nuclear and magnetic structures. J. Appl. Crystallogr. 2 (2), 65−71. https://doi.org/10.1107/s0021889869006558. International Union of Crystallography.

Rushton, J., 2019. Powder management in additive manufacturing. In: Mastering AM: Sharing User Experience. Coventry, UK.

Samal, P.K., Newkirk, J.W., 2015. ASM Handbook - Vol 7: Powder Metallurgy, Metal Powder Characterization and Bulk Properties of Powders.

Seyda, V., et al., 2012. Investigation of Aging Processes of Ti-6Al-4 V Powder Material in Laser Melting. Phys. Procedia 39, 425−431. https://doi.org/10.1016/j.phpro.2012.10.057.

Sartin, B. Powder reuse for metal additive manufacturing. In: Proceedings of the 28th Annual International Solid Freeform Fabrication Symposium − An Additive Manufacturing Conference, Austin, Texas, USA, pp. 351−364. https://doi.org/10.1016/j.phpro.2012.10.057.

Shard, A.G., 2014. Detection limits in XPS for more than 6000 binary systems using Al and Mg Kα X-rays. Surf. Interface Anal. 46 (3), 175−185. https://doi.org/10.1002/sia.5406.

Sih, S.S., Barlow, J.W., 1992. The measurement of the thermal properties and absorptances of powders near their melting temperatures. Chem. Eng. (1), 131−140.

Simchi, A., 2004. The role of particle size on the laser sintering of iron powder. Metall. Mater. Trans. B 35, 937−948. https://doi.org/10.1007/s11663-004-0088-3.

Slotwinski, J.A., et al., 2014. Characterization of metal powders used for additive manufacturing. J. Res. Natl. Inst. Stand. & Technol. 119, 460−493. https://doi.org/10.6028/jres.119.018.

Snow, Z., Martukanitz, R., Joshi, S., 2019. On the development of powder spreadability metrics and feedstock requirements for powder bed fusion additive manufacturing. Elsevier Addit. Manuf. 28, 78−86. https://doi.org/10.1016/j.addma.2019.04.017 (November 2018).

Spierings, A.B., et al., 2016. Powder flowability characterisation methodology for powder-bed-based metal additive manufacturing. Prog. Addit. Manuf. 1 (1−2), 9−20. https://doi.org/10.1007/s40964-015-0001-4. Springer International Publishing.

Strondl, A., et al., 2015. Characterization and control of powder properties for additive manufacturing. JOM 67 (3), 549−554. https://doi.org/10.1007/s11837-015-1304-0.

Sutton, A.T., et al., 2016. Powder characterisation techniques and effects of powder characteristics on part properties in powder-bed fusion processes. Virtual Phys. Prototyp. 12 (1), 3–29. https://doi.org/10.1080/17452759.2016.1250605.

Tang, H.P., et al., 2015. Effect of Powder Reuse Times on Additive Manufacturing of Ti-6Al-4V by Selective Electron Beam Melting. JOM 67, 555–653. https://doi.org/10.1007/s11837-015-1300-4.

Vock, S., et al., 2019. Powders for powder bed fusion: a review. Prog. Addit. Manuf. 4 (4), 383–397. https://doi.org/10.1007/s40964-019-00078-6. Springer International Publishing.

New materials development

19

Bonnie Attard[1,2], *Abd El-Moez A. Mohamed*[1], *Moataz M. Attallah*[1]
[1]School of Metallurgy and Materials, University of Birmingham, Birmingham, United Kingdom; [2]Department of Metallurgy and Materials Engineering, Faculty of Engineering, University of Malta, Msida, Malta

Chapter outline

19.1 Introduction 529
19.2 L-PBF of functionally graded materials (FGMs) 530
19.3 Microstructural grading in L-PBF 531
  19.3.1 Microstructural grading through laser parameters and motion 532
  19.3.2 Microstructural features through in-situ temperature variations 538
  19.3.3 Effect of powder additives and process parameters on microstructure 539
19.4 Compositional grading 542
  19.4.1 Use of alloying to modify microstructure 543
  19.4.2 Hybrid manufacturing 544
19.5 L-PBF of functional materials 545
19.6 Magnets 546
  19.6.1 Soft magnets 547
  19.6.2 Hard magnets 548
  19.6.3 Magnetic refrigerants 549
19.7 Shape memory alloys 551
19.8 Conclusion 552
19.9 Questions 553
Acknowledgements 553
References 554

19.1 Introduction

The majority of literature on laser powder bed fusion (L-PBF) focuses on a limited number of engineering alloys due to their combination of printability and diverse applications, namely:

- Ti6Al4V; extensively used for biomedical implants and aero-engine compressors,
- Inconel 718 (IN718); a staple of the aero-engine turbine, with other applications in the oil and gas and automotive industries,
- 316L stainless steel; the most commonly used corrosion resistant alloy, and

Fundamentals of Laser Powder Bed Fusion of Metals. https://doi.org/10.1016/B978-0-12-824090-8.00025-1
Copyright © 2021 Elsevier Inc. All rights reserved.

- AlSi10Mg; the standard cast Al-alloy, with multiple applications in the aerospace and automotive sector.

Additional engineering alloys have attracted significant attention due to the potential benefits that can be achieved if fabricated using L-PBF. For instance, high-temperature Ni-superalloys (e.g., CM247LC, Hastelloy-X, and IN738LC) have been investigated in a number of studies, due to the potential in aero-engine applications. Similarly, a growing interest in β-Ti-alloys is due to the lower elastic modulus compared with Ti6Al4V, which renders the material ideal for medical implants due to a reduction in stress shielding. More recently, a proliferation in studies investigating high entropy alloys (alloys containing equal amounts of five or more elements) has flourished due to their unique combination of mechanical and physical properties, although the focus has not moved significantly from process optimization and assessment of mechanical behavior. Further information about high entropy alloys can be found elsewhere (Cantor, 2014, 2020).

In this chapter, we aim to explore a number of approaches to develop new materials using L-PBF, through solidification control and the process environment. In addition, we look into some of the novel materials that are currently being investigated and garnering significant attention, especially the metallic functional materials (e.g., shape memory alloys, magnetic materials, superconductors, etc.).

19.2 L-PBF of functionally graded materials (FGMs)

A functionally graded material (FGM) incorporates a variation of a structural element or material element throughout the volume of the component. The focus of such a variation is to incorporate incompatible functions (such as a high ductility and a high hardness) into the volume of a single component (Chen et al., 1999). The concept was introduced by Japanese scientists in the Sendai area in Japan in the 1980s as a means to produce a material having a sufficient high temperature strength, but also, to function as a thermal barrier for space applications (Koizumi, 1997). The central theme of FGMs is to eliminate problems associated with delamination, often observed in composite materials and coatings, associated with sharp interfaces, and to reduce the lengthy process of forming a new, complex and often expensive alloy (Koizumi, 1997; Mahamood et al., 2012; Bohidar et al., 2014). FGMs were considered well suited to relax the thermal stresses over the part volume while still providing a thermal barrier functionality (Sasaki and Hirai, 1991). Furthermore, the sharp transition between properties of two dissimilar materials present in composites can be eliminated to relieve stress concentrations while the incorporation of different properties in a component can be used to tailor a component to a specific application (Bohidar et al., 2014; Chen and Liou, 2018).

Functionally graded materials can be divided into two broad groups namely thin and bulk FGMs. Thin FGMs incorporate thin coatings with some form of variation between the coating and substrate while bulk FGMs have a variation in properties occurring over the entirety of the component (Mahamood et al., 2012). Functional gradients can be used to create site-specific properties distributed in a material, resulting from variations in features like chemical composition, microstructure, and geometry or a combination of these. Spatially, the variation in elements can vary through a wide zone (i.e. over the entire component) or within a limited zone such as at an interface, while properties may change discontinuously or in a gradual manner (Liu et al., 2017). Functional grading can also be categorized depending on the element being graded including grading in the chemical composition, microstructural grading, or structural grading. Structural grading is described in more detail in Chapter 16. A combination of elements (e.g. chemical grading combined with graded porosity or a graded microstructure combined with graded porosity) may also be used in more complex systems.

Due to the layer-by-layer building nature inherent to additive manufacturing (AM), bulk FGM geometries and compositions are relatively accessible. AM provides a high degree of control over the spatial resolution of the component and offers the opportunity to locally control the composition and microstructure in multiple dimensions (Zhang et al., 2019a). In the L-PBF methodology, the laser beam will selectively scan a layer in a predetermined path, melting the powder. Through this method, a change in composition along the building direction can be readily achieved but directions other than the build direction provide operational challenges. Changing the laser heat input parameters and scanning strategy will also modify the temperature gradient of the melt pool (*G*) and the solidification rate of the melt pool (*R*), which can be used to vary the microstructural morphology. Component design itself can be used to implement complex structural grading such as graded porosity in lattices.

19.3 Microstructural grading in L-PBF

Microstructural grading is a relatively recent application being investigated in L-PBF. The concept is to change laser parameters such as laser heat input parameters (power, speed, hatch distance) or scanning strategy parameters (e.g. laser scanning direction, rescanning, and track length) to tailor the microstructure and in turn to obtain specifically designed mechanical properties. By modifying the temperature gradient and solidification rate of the melt pool, unique three-dimensional properties can be achieved. The temperature gradient (*G*) at the solid/liquid interface is the difference in temperature in the melt pool moving from the liquid into the solid and is strongly dependent on the convective flow in the melt pool, material properties, and heating time (David and Vitek, 1989; Thijs et al., 2013; Wang et al., 2016). The solidification rate (*R*) is the rate at which the solid/liquid interface of the melt pool advances and is directly related to the laser scanning speed (David and Vitek, 1989).

By modifying parameters affecting *G* and *R*, the microstructure growth will transition from columnar to equiaxed. This is called the columnar-equiaxed transition (CET). Columnar and cellular growth is driven by steep temperature gradients from the high resulting heat flow toward the build plate typical to AM (Nadammal et al., 2017). The directional heat flow tends to result in a grain morphology aligned parallel with the building direction i.e. in parallel with the direction of maximum heat flow (Kurz et al., 2001). Cellular and columnar substructures are commonly observed for L-PBF processes due to the steep temperature gradient and the very high cooling rates present during the process, so there is insufficient time for secondary dendrite arms to form (Casati et al., 2016; Wang et al., 2016, 2018). A low ratio of G/R (i.e. low temperature gradient and high solidification rate) favors the formation of equiaxed dendrites while a high G/R ratio (high temperature gradient and low solidification rate) favors the formation of columnar/cellular dendrites (David and Vitek, 1989; Wei et al., 2016; Nadammal et al., 2017; Zhang et al., 2017). These microstructural transformations are dependent on the material and processing maps for these transformations can be found in literature for different alloys and processes (Dehoff et al., 2015; Gorsse et al., 2017).

The alignment of the unit cell axes with the build direction usually introduces anisotropic properties along the build axis in comparison to the transverse axis—this may affect both room temperature and high temperature mechanical behavior (Kunze et al., 2015; DebRoy et al., 2018; Bean et al., 2019; Im et al., 2020). Thus, it is beneficial to be able to control the microstructure along the loading axis to optimize the performance. The cooling rate which is also equivalent to the product of $G \cdot R$ plays a role. A faster cooling rate leads to a smaller cell size or a finer dendrite spacing (AlMangour et al., 2017; DebRoy et al., 2018). L-PBF has some of the highest cooling rates among AM processes with cooling rates measured in the range of 5×10^5 to 6×10^6 K (Roberts et al., 2009; Li and Gu, 2014; Wang et al., 2016; DebRoy et al., 2018). A finer cell spacing can be beneficial for steels to improve their mechanical performance (Krakhmalev et al., 2018).

19.3.1 Microstructural grading through laser parameters and motion

The modification of the melt pool and consequently the microstructure through laser parameters such as power, speed, hatch distance, and layer thickness is widely known to be possible (Yadroitsev et al., 2013; Suder and Williams, 2012; Sadowski et al., 2016; Yang et al., 2017; Dong et al., 2018; Metelkova et al., 2018). These parameters will directly affect subgrain features such as the cell size.

The use of a dual laser system in L-PBF has been used to form a single component with a graded structure through the use of two separate laser sources with different laser beam profiles (e.g., gaussian vs. flat-top beam profiles) and separate laser heat input parameters. Through these variations, the microstructures obtained are drastically different, varying from highly textured columnar to randomly textured "quasi-equiaxed" structures (Popovich et al., 2017). Thus, distinct areas in the structure such as coarse columnar grains in a matrix of fine grains have been produced (Niendorf et al., 2013, 2014; Popovich et al., 2017). It has also been shown that these zones have varying mechanical properties as shown in Figs. 19.1 and 19.2. From digital image correlation (DIC) results by Niendorf et al. (2014), it can be observed that columnar coarse grained regions feature higher regions of strain under monotonic tensile loading from the very early stages of deformation due to a difference in stiffness of the differing regions. This is similar to behavior also observed by Popovich et al. (2017) for Inconel 718.

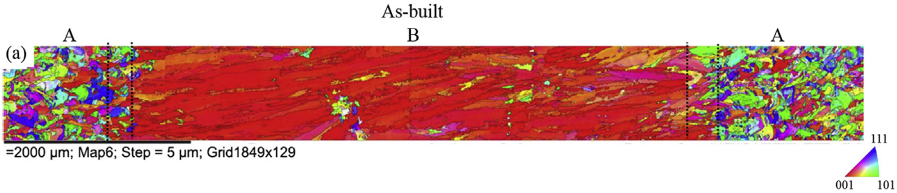

Zone	Laser Power (W)	Scanning speed (mm/s)	Hatch spacing (mm)	Layer thickness (μm)	Beam diameter (μm)	Beam profile	Yield strength (MPa)	Ultimate tensile strength (MPa)	Young's modulus (GPa)
A	250	700	0.12	50	80	Gaussian	668	1011	173
B	950	320	0.5	100	100	Flat top	531	866	113

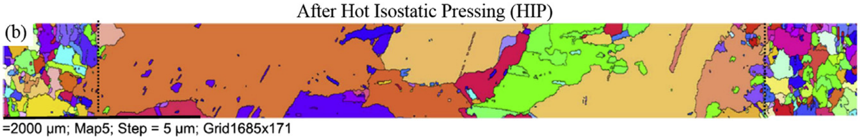
After Hot Isostatic Pressing (HIP)
(b)
=2000 μm; Map5; Step = 5 μm; Grid1685x171

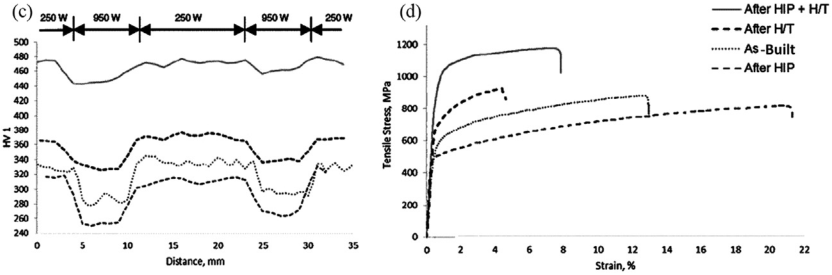

Figure 19.1 Graded Inconel 718 showing an inverse pole figure (IPF) map for (a) a coarse columnar microstructure alternating with a fine-grained matrix together with beam heat input parameters used and mechanical properties for each area, (b) the same structure after hot isostatic pressing together with (c) the hardness variation in each area and (d) mechanical property variation with different heat treatments (Popovich et al., 2017).

The scanning strategy, i.e. the path the heat source traverses during AM processing, has also been used to functionally grade the microstructure. The scanning strategy affects the heat flow direction and heat build-up in parts and thus the microstructure generated. The laser can rescan over already solidified areas to refine the solidification microstructure by remelting material and inducing recrystallization effects or effectively performing in-situ heat treatments (AlMangour et al., 2017; Barriobero-Vila et al., 2017).

The grain growth direction will follow laser beam scanning direction, where a simple left-to-right motion will yield grains slanted from left to right (Thijs et al., 2010; AlMangour et al., 2017). A more complex strategy has been implemented for CoNiCrFeMn using a consecutive 67° rotation in an island chessboard methodology (Fig. 19.3A) resulting in a spiral-like grain structure as shown in Fig. 19.3B with a

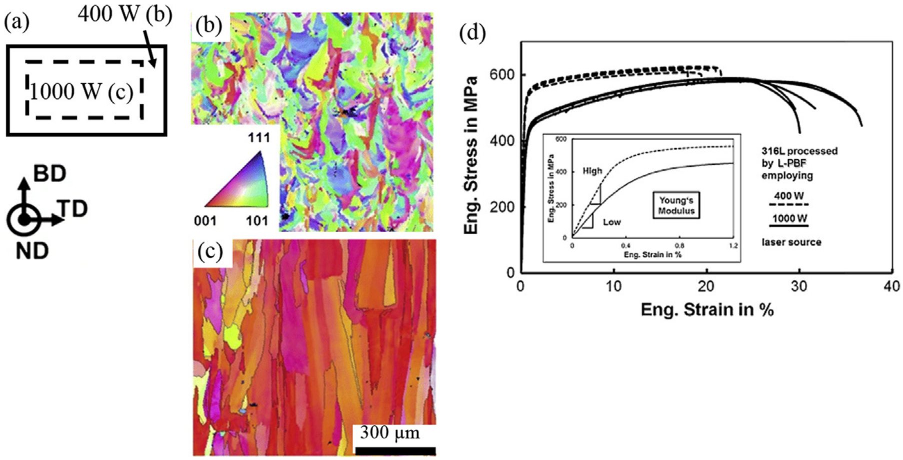

Figure 19.2 (a) Schematic for functionally graded as-built 316L stainless steel specimens showing (b) an inverse pole figure (IPF) map for a fine-grained matrix together with (c) a coarse columnar microstructure and (d) mechanical properties for each area (Niendorf et al., 2013).

[011] alignment to the build direction rather than the usually observed [001] alignment for cubic materials. Due to the rotations applied between layers and between the islands themselves, the heat flow direction is changed consecutively (Wei et al., 2015; Wang et al., 2018). Thus the grain angle to the heat flow direction is minimized by a 45° angle of the <001> axis to the build direction which means that the <011> axis will now be parallel to the building direction (Wei et al., 2015; Wang et al., 2018). The movement of grains with the motion of the laser can be harnessed to modify the texture in the transverse direction (XY) plane. Geiger et al. (2016), Thijs et al. (2013),

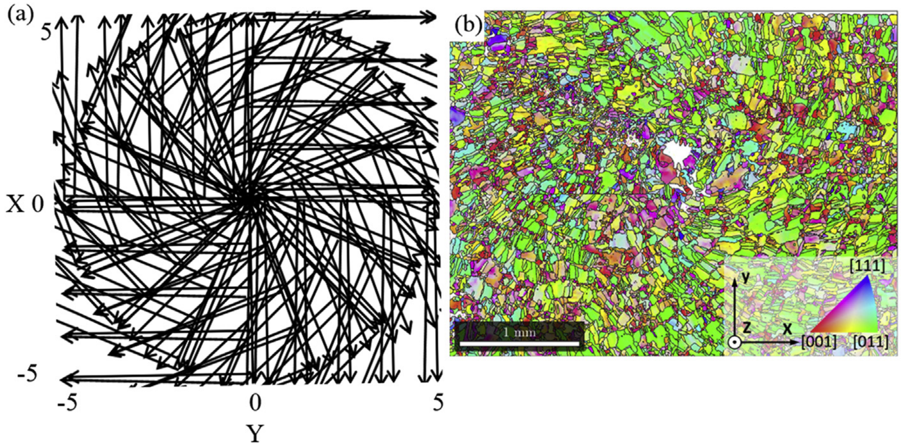

Figure 19.3 (a) Laser motion path and (b) IPF map for obtained grain structure (Dovgyy et al., 2020).

and Kunze et al. (2015) observe that a bidirectional strategy with a 90° angle rotation between layers results in a texture where all the <001> crystal axes are aligned with the x, y, and z scanning axes within a certain degree. Rotating the entire strategy by 45° results in a 45° rotation of the cube texture which means that when directional loading along the transverse axis is applied, a different slip system will be active which will influence the mechanical behavior (Geiger et al., 2016).

Track length will also affect the microstructure generated, with longer track lengths associated with the increased formation of stray grains as shown in Fig. 19.4A and the formation of tilted "quasi-equiaxed" morphologies as shown in Fig. 19.4C (Nadammal et al., 2017; Attard et al., 2020). Shorter track lengths are associated with the formation of aligned highly columnar structures as shown in Fig. 19.4B and D with a consequent steep increase in alignment of the <001> unit cell direction to the build direction

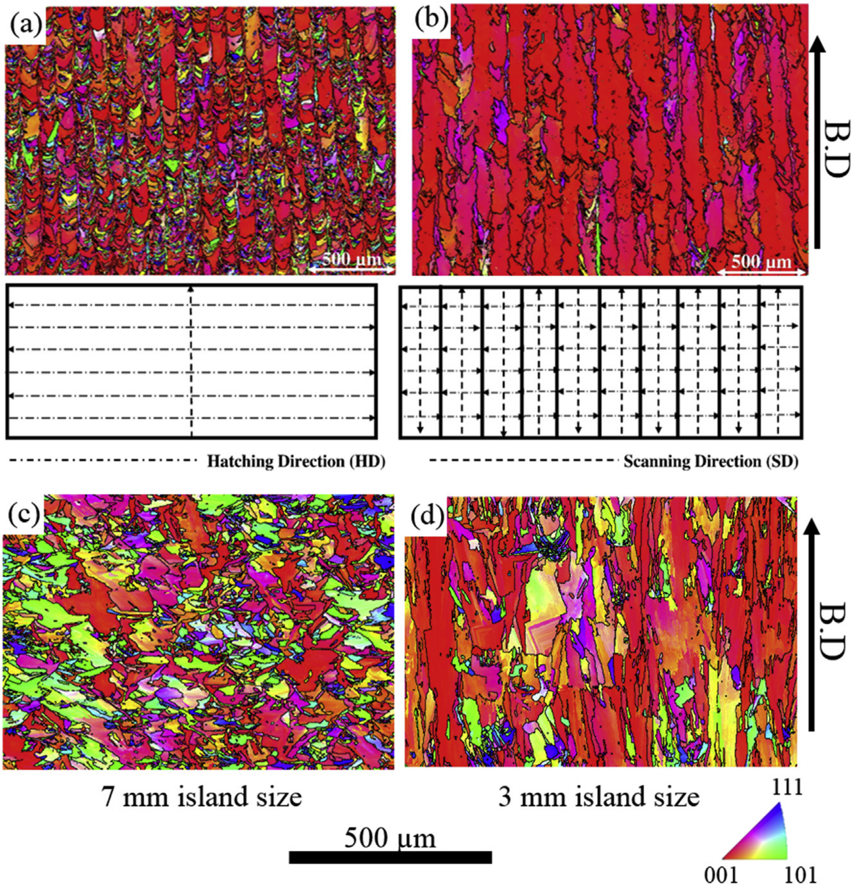

Figure 19.4 IPF grain maps obtained with different track lengths for Inconel 718 (a) long and (b) short track length together with (c) 7 mm chessboard island and (d) 3 mm chessboard island strategies (Nadammal et al., 2017; Attard et al., 2020).

(Nadammal et al., 2017; Attard et al., 2020). Small randomly oriented (stray) grains can develop in between columnar grains attributed to regions of very steep temperature gradients and faster cooling (Nadammal et al., 2017). The shorter track lengths would be expected to heat up the material more as the laser requires less time to arrive at the adjacent melt pool (Rai et al., 2017; Attard et al., 2020). This would lead to a lower solidification rate, and also an increased time where the parts are at elevated temperature resulting in more grain growth (Petch, 1953; Stevens et al., 2017; DebRoy et al., 2018). With a longer track length, there will be a longer time between the laser arriving at adjacent points compared to a shorter track length. This means that the adjacent and underlying material will have more time to cool before the laser arrives at the adjacent point. In turn the material will be at a lower temperature and melt pools tend to not melt through as many previously solidified layers (shallower melt pool depth) in turn reducing the epitaxial growth occurring (Nadammal et al., 2017). This would result in overall finer microstructural and submicrostructural features and lower texture intensity (Nadammal et al., 2017; Attard et al., 2020). A lower texture intensity is beneficial as it means the material is less anisotropic and therefore the mechanical performance will be more uniform for isotropic loading. Furthermore, a smaller grain size and more refined submicrostructural features such as a smaller cell size are beneficial to resist dislocation motion and thus lead to an increased strength (Petch, 1953; Wu et al., 2016; Zhong et al., 2016; Liu et al., 2018; Wang et al., 2020b).

Different laser scanning strategies have been combined in order to produce a graded concept of a hollow Inconel 718 turbine blade, shown in Fig. 19.5A. In this case a chessboard island strategy was used to manufacture the entire component. In chessboard strategies, the cross-sectional area being scanned is partitioned into smaller areas called islands and each island is scanned in a random order to ensure better heat distribution. Neighboring islands are typically rotated by 90° within the layer and between layers the pattern is shifted by a certain amount to avoid overlapping of defects in between layers. This shifting is called the island shift parameter. For the image shown in Fig. 19.5A a number of these parameters were altered to generate different grain sizes along the build direction, different texture along the build direction, and a different grain morphology. For the top section—the hollow turbine blade, a small island size (3 mm) was used coupled with a small island shift between layers (1 mm). For the bottom section, the fir root is in general at a lower temperature than the turbine blade as it is attached to the turbine disc; different parameters were used namely a larger island size (5 mm) and a higher island shift in between layers (4 mm) (Attard et al., 2020). The fir root section connects a turbine blade to a turbine disc and needs to have a more isotropic structure to cater for the isotropic loading while the blade region will be at a higher temperature and will need a better creep performance along the blade axis. This is taken into consideration by designing the blade section to have a fiber texture with a strong alignment of the one of the <001> crystallographic directions to the direction of thermal flux with the other two directions not aligned with either X or Y axes of the laser traversing direction as shown in Fig. 19.5B and E. The alignment of the <001> crystallographic direction with the build direction is beneficial in scenarios where creep loading is present, as the <001> directions perform better in creep loading scenarios (Caron et al., 1986).

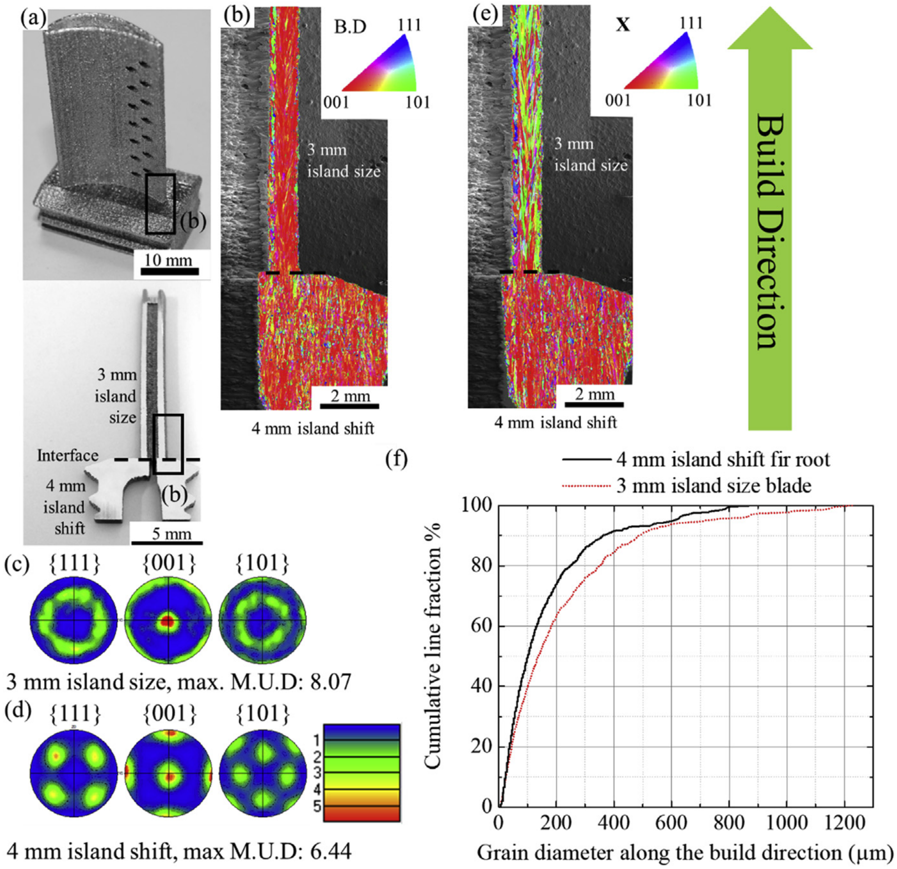

Figure 19.5 (a) As-built functionally graded Inconel 718 microstructure turbine blade built without supports with (b) corresponding XZ cross-section IPF map along build direction and pole figures for (c) blade, (d) fir root, and (e) XZ cross-section IPF map along the transverse direction together with (f) corresponding variation in cumulative line fraction distribution against grain diameters (Attard et al., 2020).

The fir-tree root has a cube texture, commonly observed in AM where all three <001> axes are aligned with the X, Y, and Z axes corresponding to the laser scanning directions and the build direction, respectively, as shown in Fig. 19.5B and E. The pole figure intensity given through the M.U.D (multiples of uniform distribution) also varies between sections of the component as shown in Fig. 19.5C and D. There is a difference in the grain length along the build direction with the blade section having grains which are much more elongated than the fir-tree root section as can be seen from the cumulative area distribution versus line intercept curves shown in Fig. 19.5F. A solution treatment below the recrystallization temperature of Inconel 718 was applied coupled with aging specifically to retain this microstructural grading and allow such components to obtain the strength and hardness required for use.

19.3.2 Microstructural features through in-situ temperature variations

The thermal gradient is affected by the rate of heat flow through the base plate. By heating or cooling the base plate, a change in heat flow can occur, affecting the microstructure. Base plate heating can also be used to perform in-situ heat-treatments during or after a building process. The L-PBF process is performed under a controlled atmosphere; however using base plate heating, this requirement becomes much more stringent to prevent oxygen dissolution from occurring into the parts and the powder a higher degree of control is required to keep any oxygen present in the chamber as low as possible. Furthermore, the powder would also have been exposed to a heat treatment which, depending on the temperature, could sinter the powder to the base plate and components (Sames et al., 2017). This needs to be taken into account, as the powder may not be reusable and may also present issues with powder removal especially in the case of complex geometries and internal cavities in the part (Sames et al., 2017).

Base plate heating has been used for L-PBF of a number of alloys including Ti-Fe eutectics and Al alloys (Rao et al., 2019; Gussone et al., 2020). Eutectic systems benefit greatly from the high cooling rates evident during L-PBF, as this results in the formation of a very fine eutectic microstructure resulting in an excellent mechanical performance. The use of a high temperature (~600°C) heated bed in this case acted to prevent solidification cracking through a reduction in the residual stresses, and the L-PBF process was used to successfully generate a nanometrically fine lamellar structure (Gussone et al., 2020). More information about solidification cracking mechanisms can be found elsewhere (Coniglio and Cross, 2009). Base-plate heating also acts to reduce the residual stresses in a build (Rao et al., 2019). For instance, for the Al alloy A357, it was found that a 90°C preheated base plate was enough to reduce the residual stresses present in the as-printed condition and promote the formation of nanometric Si particles along the grain boundaries of the Al alloy, resulting in a much higher strength compared to conditions fabricated without base-plate heating or fully heat-treated conditions (Rao et al., 2019).

Alternatively, laser movement may be used to change the thermal cycles the component is subjected to, for instance, by rescanning areas of a component multiple times. This is known as an intrinsic or in-situ heat treatment. Rescanning an already solidified area will lead to some remelting (depending on the laser parameters selected) and additional heat input into the underlying material layers which can result in microstructural phase changes. For instance, intrinsic heat treatments applied to Ti6Al4V alloys were found to provoke martensite decomposition resulting in a uniform, fine lamellar $\alpha+\beta$ microstructure (Barriobero-Vila et al., 2017). A double laser pass on 316L stainless steel has been reported to also refine the microstructure (AlMangour et al., 2018). Other studies reported the formation of austenite in a martensitic AISI 420 stainless steel through the application of rescanning and the associated reheating applied to the material (Krakhmalev et al., 2015). Accurate temperature control using such a method is still problematic and can result in unexpected phase formation. Furthermore in L-PBF due to the high cooling rates typical of the process and very short laser interaction times the application of an in-situ heat treatment becomes more challenging (Yang et al., 2019a). Some authors have also reported a possibility of in-situ aging Inconel 718, with an increase in hardness observed for single pass vertical thin walls from the precipitation of nanometric γ' and γ'' (Yang et al., 2019a). This single pass vertical build functioned similarly to a case of rescanning where the same track is rescanned after solidification to induce heating. In this case, the build consisted only of a single track built vertically. Heat would be conducted from the newly scanned track mainly downwards to the build plate. Thus, the underlying tracks would remain at a higher temperature when compared to a wider build. In fact, the increase in hardness was not observed when the components consisted of horizontal thermal cycles, i.e. scan tracks overlapping each other as the flow of heat is mostly downwards toward the build plate; thus the adjacent tracks would not heat up to degrees required to induce precipitation (Yang et al., 2019a). To obtain a similar effect for wider builds one would have to employ rescanning of the entire surface area as has been discussed.

19.3.3 Effect of powder additives and process parameters on microstructure

Powder additives such as nanoparticle nucleation agents and secondary phase ceramic powders combined with powder variables such as layer thickness can be used to modify the microstructure generated through L-PBF. Producing equiaxed structures in AM requires large amounts of undercooling to the melt to promote homogenous nucleation. The addition of fine nanoparticles to the powder acts as a grain refinement mechanism promoting homogenous nucleation from the refining particles in the melt ahead of the solidification front (Martin et al., 2017). Fine particle reinforcement to metal matrix through powder additives is also applied to improve the wear resistance of the parent material (Gu et al., 2011). Furthermore, the powder layer thickness itself can be modified to change the melt pool size and thus alter the thermal gradient and move from columnar toward more equiaxed growth as will be subsequently discussed. Further discussion about the addition of powder additives and nanoparticles in grain refinement can be found in Zhang et al. (2020).

Smaller sized ceramic particles have been used as additives in order to modify the solidification structure. For instance, Zhang et al. (2018) applied molybdenum satellite particles (satellite particles are smaller particles attached to the surface of larger particles). Slotwinski et al. (2014) attached Mo particles to larger Ti particles, where the laser parameters are chosen in such a way as not to melt the Mo particles. The unmelted Mo particles are retained in the melt and act as cold source nucleation points thus reducing the energy barrier required for homogenous nucleation rather than epitaxial growth (Zhang et al., 2018). Unmelted particles however can be a source of mechanical failure if they are not remelted in the subsequent laser passes due to the generation of stress concentrations (Zhang et al., 2018). AlMangour et al. (2018) applied L-PBF to 316L stainless steel together with 2−12 μm sized TiC reinforcement particles. The use of smaller TiC particles resulted in the formation of a bimodal grain structure potentially due to TiC particles acting as nucleation agents for the smaller equiaxed structure (AlMangour et al., 2017). For titanium alloys which have a low wear resistance the addition of TiC, SiC, TiB, and WC particles is often also used to improve their mechanical and tribological properties. Due to the poor wettability of these oxide particles with the melted metal, in conventional processing, the interfacial bonding capability between the particles and matrix is limited and can lead to the formation of stress concentrations, cracking of the ceramic particles, and premature failure (Gu et al., 2011). Nanocrystalline ceramic dispersed particles can be used to limit this undesirable behavior (Gu et al., 2011). By proper parameter selection the high melting point ceramics can be melted which in turn results in a better bonding mechanism (Gu et al., 2011). TiC particles also act as grain nucleation sites and result in the formation of an equiaxed microstructure (Gu et al., 2011). The addition of TiB particles to a cp-Ti matrix has also been reported to change the typical acicular cp-Ti L-PBF microstructure to a microstructure containing needle-like TiB particles in an α-Ti matrix (Attar et al., 2015).

The addition of nucleation agents to powder allows the L-PBF of previously non-weldable high-performance Al alloys such as grades 7075 or 6061 (Martin et al., 2017; Carluccio et al., 2018). Nanoparticles having a low lattice mismatch with the parent material tend to provide very good results. For instance, hydrogen-stabilized Zr particles have been used in conjunction with Al 7075 to form the Al_3Zr nucleant phase upon melting and provide a high mixing and high density of nucleation sites (Martin et al., 2017). Al_3Zr has more than 20 matching interfaces with the primary fcc aluminum phase with a very low lattice mismatch (0.52%) and a 1% variation in atomic density (Martin et al., 2017). This results in the formation of equiaxed grains, having a very fine grain size ($\sim 5\ \mu m$) with the Al_3Zr particles uniformly distributed in the matrix which can also help with dislocation movement and grain pinning (Martin et al., 2017). Solidification cracking and hot tearing typically observed after L-PBF is absent as the connected interdendritic zones prone to solidification cracking are much smaller and not favorably oriented (Martin et al., 2017). Si particles have also been added to Al in an attempt to reduce the coefficient of thermal expansion for thermal management applications in space (Hanemann et al., 2019). The addition of Si to Al7075 was used as a grain refining agent and to increase the fluidity of the alloy leading to the prevention of crack formation and propagation (Montero Sistiaga et al., 2016). Grain refiners based on titanium-boron and scandium used in casting have also been successfully used in L-PBF of Al-Si alloys and Al 6061 (Carluccio et al., 2018; Xi et al., 2019). Inoculants have also been added to Inconel 718 during L-PBF, where the addition of eutectic WC-W_2C particles acted to generate nucleation on the surface of the inoculants resulting in more surfaces in the melt available to generate heterogenous nucleation (Ho et al., 2018). The mechanical properties obtained through such powder additions are shown in Table 19.1.

Powder layer thickness can also be used as a variable to control the microstructure. Layer thickness has been used successfully by Popovich et al. (2018) to create a graded microstructure over the length of an Inconel 718 turbine blade, keeping laser heat input parameters constant. With increasing layer thickness, the cell size was observed to increase and the microstructure transitioned from a curved “quasi-equiaxed” morphology with a quasi-random distribution toward a fully columnar morphology

Table 19.1 Mechanical properties before and after particle additions.

Material	Young's modulus (GPa)	Hardness		Wear rate (mm^3/Nm)	Yield strength (MPa)	UTS (MPa)	% ε	
		Nano hardness (GPa)	Micro hardness					
Ti	107 113	4.0	–	2.8×10^{-6}	–	–	–	Gu et al. (2011), Attar et al. (2015)
Ti-TiC	256	90.9	–	1.8×10^{-7}	–	–	–	Gu et al. (2011)
Ti-TiB	145	–	–		–	–	17.8	Attar et al. (2015)
Al7075 (T6)	–	–	–	–	–	25.5	0.4	Martin et al. (2017)
Al7075 + Zr (T6)	63–66	–	–	–	325–373	383–417	3.8–5.4	Martin et al. (2017)
Al7075 + Si	–	–	160 (HV 0.5)	–	–	–	–	Montero Sistiaga et al. (2016)
AlSi10Mg	69.4	–	–	–	209	315	7.3	Martin et al. (2017)
Al-12Si (cast)	–	–	62 (HV0.01)	–	95 (compressive)	–	–	Xi et al. (2019)
Al-12Si	–	–	119 (HV0.01)	–	211 (compressive)	–	–	Xi et al. (2019)
Al-12Si+ TiB_2	–	–	142 (HV0.01)	–	225 (compressive)	–	–	Xi et al. (2019)
Al-15Si	–	–	154 (HV1)	–	–	398	2.6	Y. Zhou et al. (2019b)
Al-15Si+ TiC (1%)	–	–	146 (HV1)	–	–	578	7.86	Y. Zhou et al. (2019b)

T6: Heat treatment condition

aligned with the build direction (Popovich et al., 2018). The differences in mechanical performance between different powder layer thicknesses are most evident prior to any form of heat treatment, with a smaller powder layer resulting in a better mechanical performance (Popovich et al., 2018). Powder layer thickness was also successfully applied by Thijs et al. (2013) to reduce the crystal texture and obtain fine grained Al parts. Porosity using such methods is a problem, as increasing powder layer thickness beyond a certain threshold will result in insufficient consolidation and melt pool instability. Conversely, other variables related to powder quality have been shown to directly affect the laser absorptivity and thus improve consolidation for challenging AM materials such as tungsten (Field et al., 2020).

19.4 Compositional grading

In compositional grading, a gradual variation in chemical composition occurs over the component (Chen and Liou, 2018). AM manufacture of gradually varying components comes with the added benefit that delamination and the need for bond coats will be drastically reduced (Mumtaz and Hopkinson, 2007). A gradual variation in composition can be used to reduce residual stresses (Beal et al., 2006; Mumtaz and Hopkinson, 2007). Compositional grading has been applied to both metal-metal systems and metal-ceramic systems.

One such application for metal to metal grading is the improvement of the thermal conductivity of molds through the gradual increase of Cu in tool steels (Beal et al., 2006). Molds are typically manufactured out of tool steels to provide a high dimensional stability and high toughness at elevated temperatures. However, a high thermal conductivity is beneficial to enable low molding times. Cooling channels and inserts are not always viable and thus by grading the tool steel with a more conductive metal such as Cu, the thermal conductivity of the mold is improved. A similar approach has been applied for 316L stainless steel and copper where elemental diffusion at the interface resulted in a very good bond strength at the interface of the two materials (Yadroitsev, 2009; Liu et al., 2014).

Metal-ceramic combinations have been investigated for applications such as thermal barriers, for instance, grading from a Waspaloy toward a zirconia outer layer through L-PBF (Mumtaz and Hopkinson, 2007). Despite the stepwise grading applied in the powder reservoir, the composition in the component gradually varies without distinct boundaries in between layers. Other applications of metal-ceramic grading include the biomedical field, where titanium has been graded with hydroxyapatite through L-PBF to tailor the mechanical properties to be close to that of bone (Han et al., 2018). A variation in laser heat source properties such as power can be beneficial in such cases to melt the increasing amounts of ceramic in the melt and result in homogenous mixing within layers.

L-PBF is a powder bed—based process and therefore accurately performing real-time control of the chemical composition is very challenging (Chen and Liou, 2018). The major drawback of chemically grading from one powder composition to another in L-PBF is the incorporation of contaminants in the remaining powder from the different powder compositions (Lin et al., 2006). This effectively limits the viability of powder recycling after a build thus limiting the scope of application of chemical grading in L-PBF and increases the costs (Lin et al., 2006). When applying compositional grading, laser heat input parameters also need to be selected in such a way as to be suitable and provide adequate melting for both compositions and must avoid cracking and balling (Beal et al., 2006; Mumtaz and Hopkinson, 2007; Wei et al., 2019). Some form of laser heat input variation and optimization needs to occur over the gradation of the component for the different chemical compositions which, depending on the system in question, may make manufacturing of components slightly more challenging. Due to the horizontal powder delivery occurring during L-PBF, horizontal grading in L-PBF is quite challenging, requiring some form of a powder dispensing array to build horizontally graded components (Wei et al., 2019). Such powder delivery systems may be additionally added to L-PBF setups to enable accurate powder alloying and mixing using vibration or gravity to deliver the powder (Kumar et al., 2004; Yang and Evans, 2004). The addition of a powder dispensing system to an L-PBF system moves toward a hybrid system borrowing some aspects from directed energy deposition.

19.4.1 Use of alloying to modify microstructure

Most work in AM focuses on the generation of structures using established alloys which may not have been designed with additive manufacturing in mind. A more promising path forward in AM would be the design of alloys tailored toward being additively manufactured and thus being less sensitive to variations in processing conditions (Johnson et al., 2019; Karlsson et al., 2019). Two factors affect an alloy's printability: intrinsic factors such as the alloy's solidification range and secondary solidification phases and extrinsic factors related to the processing parameters. In-situ alloying is a very promising recent development in L-PBF where the approach takes two forms or a combination of them as follows:

- **i.** Either small amounts of alloying elements are blended with the main powder material and processed;
- **ii.** Or gases in the protective atmosphere in the build chamber are used to chemically react with the molten material to obtain different phases, e.g., oxides, nitrides, or carbides;
- **iii.** Or a combination of (i) and (ii).

For instance, adding Cu as an alloying element in L-PBF of titanium has been demonstrated by Zhang et al. (2019b) to be a feasible method to obtain fine-grained alloys. Copper has a high solubility in Ti and the eutectoid reaction occurring upon cooling coupled with its rapid diffusivity in Ti results in the formation of a very fine eutectoid lamellar microstructure, which improves strength of the alloy considerably compared to cp-Ti. The addition of Cu will convert the typically columnar microstructure of Ti into an equiaxed grain morphology. Cu increases the constitutional supercooled zone in front of the solidification front by segregating around the first β-phase dendritic grains forming which in turn results in an amount of homogenous nucleation occurring early ahead of the solidification front in the undercooled melt. Additions of Cu to Ti alloys have potential for biomedical applications due to the antibacterial properties of Cu (Vilardell et al., 2020).

Recently, small percentages of carbon have been added to high entropy alloys such as CoCrFeNi, where C additions were found to form $M_{23}C_6$ type carbides at subgrain boundaries (Wu et al., 2018; Zhou et al., 2019a). These carbides together with dislocation networks due to AM manufacturing, resulted in the strengthening of the alloys (Wu et al., 2018). In-situ alloying of CoCrFeNi through the addition of Mn and the reaction of Mn to residual oxygen in-situ during the process have also been reported (Chen et al., 2020). The Mn oxide particles increase the yield strength and tensile strength of the alloy over nonoxide dispersion strengthened conditions. A similar occurrence was observed to occur when printing Ti-Fe alloys, where fine η-Ti_4Fe_2Ox oxides were observed to have formed in the matrix as a result of oxygen pick up during processing (Gussone et al., 2020). These oxides were observed to be thermodynamically stable at temperatures of up to 600°C and contributed significantly to the high temperature mechanical properties of the Ti-Fe alloy. In-situ oxide dispersion strengthening (ODS) was also performed by Mirzababaei et al. (2020) using an FeCrAl alloy with small additions of yttrium (0.5 wt.%). The Al and Y bonds with oxygen are more thermodynamically favorable and hence both elements reacted preferentially with the residual oxygen in the processing chamber forming small spherical oxide nanoparticles evenly distributed in the FeCrAl alloy.

19.4.2 Hybrid manufacturing

Hybrid manufacturing in the context of additive manufacturing with compositional grading is the use of different manufacturing processes to collate different part sections to fabricate a single component. For instance, L-PBF may be used in conjunction with hot isostatic pressing, where L-PBF is employed to manufacture complex-shaped cans which are then consolidated using hot isostatic pressing (HIP). These cans may be of the same material or different than the powder they are filled with. One such example is the manufacturing of blisks, which are a combination of turbine discs with built-in turbine blades rather than the blades being a separate assembly (Wang et al., 2020c). The outer sacrificial low carbon steel can is built using L-PBF, then CM247LC powder was used to fill the can with a solid interior Inconel 718 disc to produce a hybrid multimaterial component.

Machining in conjunction with L-PBF has also been applied where the machined section would be used as the base for the part being deposited onto it using L-PBF, effectively fusing the two parts together. Tungsten-copper FGMs are commonly used as plasma-facing components in fusion reactors (Tan et al., 2019). Tan et al. (2019) attempted to manufacture W-Cu FGMs using L-PBF to manufacture the tungsten sections to the premachined copper parts. A similar approach was applied to steels where a machined stainless-steel base was used to deposit a strongly bonded maraging steel part on to it, with applications for hybrid tooling (Tan et al., 2020).

Hybrid manufacturing has also been used to form FGMs of non-weldable materials, for instance, L-PBF Ti6Al4V with a cold sprayed Al-Al_2O_3 section of significant thickness for tribological applications in the automotive or aerospace sectors (Yin et al., 2018). The use of cold spraying avoided the formation of brittle Ti-Al intermetallic phases at the junction and allowed a good interfacial bonding (Yin et al., 2018).

19.5 L-PBF of functional materials

Functional materials play an important role in fields such as engineering, medicine, and space applications where they are used to actively provide a function through the material's intrinsic properties. These materials include semiconductors, dielectrics, superconductors, and magnetic composites and are used in several fields. For example, Bi-Te-Se is a topological insulator with high thermoelectric performance, which is compatible for energy conversion devices (Pesin and MacDonald, 2012), NiTi shape memory alloys are outstanding in the medical field for orthodontic arch wires, heart stents and laparoscopic applications (Van Humbeeck, 2001; Tarniţă et al., 2009; Fuster, 2014) and rare earth based alloys are suitable for magnetic-spin applications (Moore et al., 2013). Some functional materials can perform the required function directly without any external stimulation such as carbon nanotubes used in drug delivery (Mohamed and Mohamed, 2019). Meanwhile, there are functional materials where the properties are responsive to external stimuli such as electrical, thermal, magnetic, optical, mechanical stimuli etc. Functional materials have been produced in various bulk forms including powder, thin films, nanoparticles, bulk and ribbons. Nevertheless, none of these traditional methods have the ability to produce a complex shaped part as required for specific applications. Even casting has shape limits, restricting almost all of the associated potential phenomena to the lab. Furthermore, a number of these materials have a propensity toward brittleness such as the fragile shape memory Heusler ribbons (Wang et al., 2020a) and the rare earth-based magnetocaloric alloys (Moore et al., 2013), which makes machining problematic as induced cracking may occur. L-PBF provides geometrical capabilities for manufacturing complex-shaped structures, where several functional materials have been processed via L-PBF such as Ni-Fe-Mo (Zou et al., 2018), NiTi (Haberland et al., 2014) and Ni-Mn-Ga (Nilsén et al., 2019), and have shown functionality shape tuning. However, L-PBF manufactured components are usually associated with metallurgical processing effects during processing such as microstructural defects and anisotropic effects (Mohamed et al., 2020). Microstructural defects such as porosity and cracks result from the mismatch between process parameters (laser power, scanning speed and hatch space, scanning strategy, etc.) and material properties, leading to a weak mechanical strength. Meanwhile, anisotropic effects occur due to the layer-by-layer build technique itself that result in a preferred crystallographic texture/grain orientation that may affect the functionality of some processed materials (Detavernier et al., 2003). In the next sections some of the properties of L-PBF processed functional materials in comparison with traditional synthesis methods will be highlighted.

19.6 Magnets

Ferromagnetic materials are classified according to their soft and hard magnetic characteristics (Jiles, 2003). Electron spins in a ferromagnet are entirely arranged in domains as presented in Fig. 19.6A, whose free motion controls the magnetic properties (Lu et al., 1999).

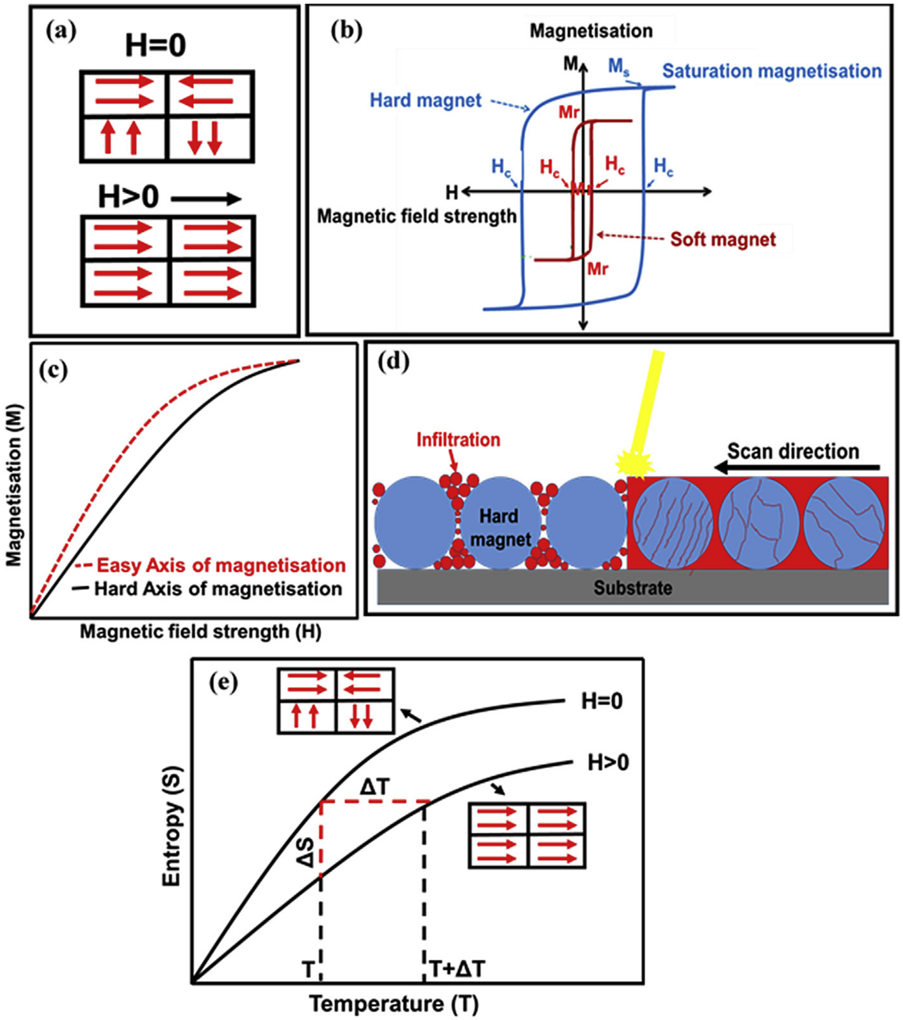
(a)
H=0
H>0
(b)
Magnetisation
M
M_s
Saturation magnetisation
Hard magnet
Mr
H_c
H_c
H_c
H_c
H
Magnetic field strength
Mr
Soft magnet
Mr
(c)
Magnetisation (M)
Easy Axis of magnetisation
Hard Axis of magnetisation
Magnetic field strength (H)
(d)
Infiltration
Hard magnet
Scan direction
Substrate
(e)
H=0
H>0
ΔT
ΔS
Entropy (S)
T
T+ΔT
Temperature (T)

Figure 19.6 (a) Spin order in a ferromagnet at H = 0 T and H > 0 T, (b) full magnetic hysteresis loop of a ferromagnet, (c) magnetic anisotropy, (d) L-PBF process of infiltrated Nd-Fe-B hard magnets, and (e) adiabatic change in ΔS and ΔT and spin orientation of magnetic material after magnetic field application.

Exposing a ferromagnet to an externally applied magnetic field aligns the magnetic domains in parallel with the magnetic field direction. After removing the external magnetic field, the domains rotate back to the initial random position, leaving a residual magnetism state of aligned domains M_r in the hysteresis loop in Fig. 19.6B. These residual magnetization (M_r) states are too low in soft magnetic materials and too high in hard magnetic materials (see Fig. 19.6B), and an opposite low/high coercive magnetic field (H_c), respectively, is required to randomize these aligned domains, getting back the material to the initial unmagnetized states as seen in Fig. 19.6B. Soft and hard magnets have been successfully 3D printed by L-PBF with low eddy current effect (controlled via topological structure (Goll et al., 2019)), overcoming the induced heat during operation (Volegov et al., 2020).

19.6.1 Soft magnets

Soft magnetic materials can be easily magnetized and demagnetized and have a low coercivity. Coercivity is a magnet's ability to withstand an external magnetic field without becoming demagnetized. Soft magnets based on Ni-Fe-Mo (permalloy) and Fe-Ni-Si are widely used as magnetic shields for highly sensitive quantum gravity sensors (Vovrosh et al., 2018) and in motor cores (Jhong et al., 2019). The potential functionality of soft magnets refers to the characteristic high permeability (the ability to absorb magnetic field lines) and the low H_c (Chikazumi, 1997) where a high magnetic permeability could be accomplished via the reduction of domain pinning (decreasing H_c) and magnetic anisotropy (Jiles, 2003). In the L-PBF process, domain pinning and magnetic anisotropy can be easily controlled by optimizing the component density (i.e., minimizing porosity and lack of consolidation) and the directional grain growth (Zou et al., 2018; Mohamed et al., 2020). First, to understand the relationship between the magnetic domain pinning and the microstructural defects, it is worth mentioning the ability of microstructure optimization, in L-PBF process, via tuning the laser parameters (laser power, hatch space, and scanning speed) (Carter et al., 2016). Several studies reported the microstructure-magnetic properties correlation in L-PBF processed soft magnets, and permalloy has received the most attention (Zhang et al., 2012; Mikler et al., 2017; Zou et al., 2018; Mohamed et al., 2020) due to the highest reported magnetic permeability (Jiles, 2003). Mikler et al. (2017) observed a decrease in the H_c value with the improvement in the microstructure of L-PBF processed permalloy, where the H_c value decreases from 2337 to 1511 A/m with the decrease in porosity fraction. The same observation was also reported by Zhang et al. (2012); meanwhile, Kang et al. (2018) got a constant H_c value of L-PBF Fe-Ni-Si (2148 A/m) when the change in laser scanning speed was too small. Furthermore, Zou et al. (2018) and Mohamed et al. (2020) reported a detailed study about the influence of laser parameters on the component density of L-PBF processed permalloy and the relevant magnetic properties. They found an improvement in the component density with the increase in E, reaching a maximum constant relative density value of 98.9% at a threshold, and then slightly decrease beyond. The improvement in the component density below the threshold refers to the decrease in the porosity fraction and the lack of fusion defects within the builds; however, above the threshold, the high E leads to keyholing and cracks (Carter et al., 2016). Simultaneously, the measured H_c shows a monotonic decrease with the improvement in the density, showing a minimum of 76 A/m at the same component density threshold (Zou et al., 2018). All previous findings reveal that the presence of microstructural defects (pores, cracks, lack of fusion, etc.) damp the soft magnetic properties by pinning the magnetic domains and hindering their free motion after removing the applied magnetic field, increasing the residual magnetization states and hence the H_c value (Lu et al., 1999).

The second factor that affects the permeability of a soft magnet is the magnetic anisotropy. Magnetic anisotropy occurs when the magnetic material shows directional dependent magnetic properties under the same applied magnetic field (see Fig. 19.6C), where the direction with the highest magnetic properties is called the easy axis of magnetization and the direction with the lower properties is called the hard axis of magnetization (Mohamed et al., 2020). The control of magnetic anisotropy occurs when the entire spins within a part are aligned in a specific direction during the solidification or sintering process (Zhang et al., 2005). The L-PBF processed alloys usually show a strong texture/spin orientation in the build direction due to the directional cooling and solidification (preferred orientation); however, the preferred orientation may change according to the laser processing parameters (Zhou et al., 2015; Li et al., 2020). Nevertheless, if the preferred texture/spin orientation within the L-PBF processed builds coincides with the hard axis of magnetization for the processed magnet, the magnetic properties are expected to be very poor, which is the case for Ni-based alloys (Mohamed et al., 2020). For example, the magnetic properties of the L-PBF permalloy are lower than powder processed and cast alloys (Zou et al., 2018), as it shows a strong texture in the <100> build direction, which is the hard axis of magnetization of this alloy (Zou et al., 2018). To overcome the compulsory spin/grain population in the [100], Zou et al. (2018) and Mohamed et al. (2020) managed to control the grain growth along the easy axes of magnetization [111] and [110] with respect to the build direction. Their suggestion was based on achieving a strong (100) texture along the build direction, and then the texture of the tilted sample along the cube principal geometrical directions will be tilted texture in the easy magnetization axes; [110] and [111] (45° and 35°, respectively). According to the published results, the H_c changed from 230 A/m for the [100] crystallographic orientation to 221 and 209 A/m for the [110] and [111] orientations, respectively. Based on the microstructure optimization and the magnetic anisotropy control, the first L-PBF 3D printed permalloy prototype achieved a shielding factor value of 1048, which exceeds the shielding factor of permalloy sheets (600).

19.6.2 Hard magnets

Hard magnetic materials are materials which tend to have a high coercivity (i.e. tend to stay magnetized when exposed to an external magnetic field). Magnets made from hard magnetic materials tend to generate strong magnetic fields. Some alloys have superior hard magnetic characteristics such as Nd-Fe-B and are ideal for use in permanent magnets (Lu et al., 1999; Jaćimović et al., 2017). These alloys are of great interest for several applications such as alternatives to the expensive superconductor magnets in magnetic resonance devices and data storage and sensing (Sugimoto, 2011). Therefore, a netshape magnet with high performance stability at elevated temperatures (nearly up to 200°C) should be considered (Gutfleisch et al., 2011). The bonding magnet method was proposed previously to manufacture complex net shape Nd-Fe-B magnets, however there were some operational limits due to the polymer thermal stability and the low magnet density (Slusarek and Zakrzewski, 2012). Recently, Nd-Fe-B permanent magnets have been successfully 3D printed using several additive manufacturing techniques such as binder jetting (Li et al., 2017) and L-PBF (Jaćimović et al., 2017; Huber et al., 2019) The binder-jetted magnets are not too promising as the polymer thermal stability limits the operating temperature (Li et al., 2017). Even when introducing binder with metallic material, it was found that the formed porosity suppresses the magnetic properties (Paranthaman et al., 2016). In contrast, the L-PBF is found more promising in producing highly dense Nd-Fe-B magnets (Volegov et al., 2020). Jaćimović et al. (2017) were the first to produce highly dense L-PBF (melted) Nd-Fe-B magnets, where they used a commercial spherical pre-alloyed powder (Nd7.5-Pr0.7-Zr2.6-Ti2.5-Co2.5-Fe75-B8.8). The results showed the improvement in the magnetic properties with the increase in E and the highest achieved H_c value was 695 kA/m with 92% relative density (Jaćimović et al., 2017). Nevertheless, this H_c value is still lower than that in sintered Nd-Fe-B magnets (1000 kA/m) (Zeng et al., 2019). This could be due to the formation of non-magnetic oxides during the L-PBF process that suppresses the magnetic properties (Woodcock et al., 2012) and iron segregation that reduces the H_c due to the total decrease of the hard magnet volume and its soft magnetic nature. Generally, it has been concluded that the full melting of the Nd-Fe-B MQP-S powder via L-PBF process drains the associated crystalline microstructure that is responsible for the hard magnetic properties as this kind of powder is originally designed for bonded magnets (Jaćimović et al., 2017). Recent studies have reported that the L-PBF partial melting is more effective than full melting all components in increasing the H_c of the spherical MQP-S powder, especially, with using grain boundaries infiltration (Huber et al., 2019; Volegov et al., 2020). This method includes the incomplete melt of Nd-Fe-B with the infiltration of lower melting temperature alloy such as PrCu that increases the H_c value (see Fig. 19.6D) (Huber et al., 2019). For example, the infiltration of Nd-Fe-B MQP-S pre-alloyed powder with $(Pr_{0.5}Nd_{0.5})_3(Cu_{0.25}Co_{0.75})$, NdCuCo and PrCuCo alloys increased the H_c value to 1273, 1345, and 1233 kA/m, respectively (Huber et al., 2019; Volegov et al., 2020). Recently, a development has been made in additive manufacturing of a Mn-Al-based permanent magnet through electron beam melting which is out of the scope of this work. Further information can be found elsewhere (Radulov et al., 2019).

19.6.3 Magnetic refrigerants

The spin order/disorder in a ferromagnetic material due to switching an external magnetic field on/off is normally associated with a temperature change which is known as the magnetocaloric effect (MCE). The MCE is used in magnetic refrigeration technology, an environmentally friendly cooling technology that can be an alternative to the traditional gas compression-cooling mode (Gschneidner and Pecharsky, 2008). The MCE occurs in magnetic materials due to a change in the magnetic entropy (ΔS) that is associated with a temperature change (see Fig. 19.6E), in other words, the total entropy of an isolated system is a sum of spin and lattice entropies. The externally applied magnetic field decreases the spin entropy because of the spin order, however, in an adiabatic process, the decrease in the spin entropy is simultaneously compensated for by an increase in the lattice entropy (lattice vibration) that leads to heat release, being maximum at the phase transition temperature (Mohamed et al., 2016). Consequently, high ΔS is favorable for applications that are a character of first order phase transition (FOPT) magnetic materials, where large structural changes are associated around the transition temperature such as $Gd_5(Si_xGe_{1-x})_4$ (Pecharsky and Gschneidner, 1997), $La(Fe,Si)_{13}$ (Ouyang et al., 2020), and Ni-Mn-based Huseluer alloys (Louidi et al., 2018). Other features are required in a promising magnetic refrigerant such as low-cost synthesis, near room temperature magnetic phase transition, tailored corrosion resistance, and high thermal conductivity (Liu et al., 2012). In a real magnetic refrigerator, the induced heat is transferred to the whole system via a fluid, so, the key question now is how to maximize the heat transfer between the exchangers in a short time. The answer is by increasing the surface area of the magnetic refrigerant by shaping into porous structure, parallel thin plates, and sphere packed beds (Moore et al., 2013; Kitanovski et al., 2015), which can be done through AM technology.

The L-PBF 3D printing of several magnetocaloric materials is a challenge due to the brittleness of the material and the narrow processing window (Moore et al., 2013), but some trials were performed on $La(Fe,Si)_{13}$ and $(Mn,Fe)_2(Pi,Si)$ alloys (Moore et al., 2013; Miao et al., 2020). Miao et al. (2020) L-PBF processed the $(Mn,Fe)_2(Pi,Si)$ magnetocaloric alloy using different laser parameters and they reported the change in the microstructure with different laser parameters, where they reported that porosity and cracks can be found at low laser power and high scanning speed. Also, it is observed that the magnetic phase Curie temperature (T_c) is shifted toward higher temperatures with the increase in E and the same behavior for ΔS that achieves a maximum value of 10.8 J/kgK at 1 T applied magnetic field for the highest component density sample. The importance of laser heat input parameters and powder particle morphology should not be overlooked here—in cases where incomplete consolidation occurred from insufficient energy input, cracks were observed originating from irregularly shaped powder particles acting as stress concentration sites.

$La(Fe,Si)_{13}$-based alloy is another magnetic refrigerant that is successfully processed via L-PBF; this alloy has the $NaZn_{13}$-type (1:13) structure that is responsible for the MCE properties (Liu et al., 2011). The $La(Fe,Co,Si)_{13}$ alloy has been shaped into complex porous structures of blocks with (I) an array of internal wavy-channels and (II) internal transverse fins (Moore et al., 2013). The MCE properties of the as-built parts disappeared due to the decomposition of the (1:13) phase during the L-PBF process and instead, the parts were rich in α-Fe and La-rich phases. This results from the α-Fe dendritic growth during the L-PBF process, confining the La phases in the interdendritic regions, which are frozen due to the rapid cooling rate (Zhang et al., 2008). As a result, the parts had to be heat-treated at 1323 K in an argon atmosphere for 7 days before being subsequently quenched. This heat treatment protocol increases the

1:13 phase volume and the quenching process is required for freezing, avoiding the thermal decomposition that occurs between 876 and 1173 K (Liu et al., 2011). The as-quenched parts show ΔS value of ≈3.2 J/kgK with adiabatic temperature change (ΔT) of 1.5 K. These values are quite promising in comparison with the high cost pure Gd (≈3 J/kgK, $\mu_0H = 1$ T) (Gutfleisch et al., 2016), and the La-Fe-Si spark plasma sintered (1.8 J/kgK, $\mu_0H = 1$ T) (Shamba et al., 2016), however lower than the sintered ($\Delta T = 2.8$ K at $\mu_0H = 1$ T) (Liu et al., 2012) and cast ($\Delta S = 4$ J/kgK, $\mu_0H = 1$ T) (Ouyang et al., 2020) alloys. Despite the interesting MCE properties of the 3D printed parts, the corrosion resistance was not sufficient. The quenched parts disintegrated within 24 h in air and within 1 h in distilled water due to the induced strains by the large temperature gradient during the quenching process and the formation of La_2O_3 hydrides, causing pits that act as a cracking source. Despite the observed challenges in the above two magnetocaloric materials to get a dense magnetic refrigerant, the results point to the optimistic role of L-PBF AM in magnetic refrigeration technology.

19.7 Shape memory alloys

The shape memory effect (SME) is an outstanding property that enables recovery of the original shape after deformation, the shape recovery occurs under the effect of an external stimuli such as magnetic field or heat (Ullakko et al., 1966). Recently, there is a growing interest in AM of several shape memory alloys (SMAs) due to the high demand of SME in several fields. NiTi (nitinol) alloy has generated significant research focus in biomedical implants (Dadbakhsh et al., 2016). NiTi is a ductile intermetallic that can restore the original shape via a reversible martensitic transformation (Otsuka and Kakeshita, 2002). This reversible shape character is used in vascular stents manufacturing for vascular trauma diseases (Fuster, 2014), where the stents, after expansion, can support blood vessels making sure of the lumen unobstructed. All vascular stents produced by traditional methods are standard in size; however, sometimes there are individual differences in real blood vessel shapes that may require custom sizes or even shapes, which can be done by AM (Yang et al., 2019b). However, the formation of intermetallic phases in the L-PBF NiTi processed stents and porous structures such as Ni_4Ti_3 and Ti_2Ni or oxides (TiO_2 and Ti_4Ni_2) is a challenge, where they inhibit the phase transformation and deteriorate the SME (Ou et al., 2018). The microstructure of the NiTi, in particular the secondary phases, is highly dependent on processing parameters (Ou et al., 2018). The transformation temperature of NiTi increases with the increase in energy input, for instance, through a combination of an increased laser power and reduced laser speed (Haberland et al., 2014). The increased heat input will lead to the formation of a large melt pool, leading to the preferential evaporation of Ni due to its lower melting point compared to Ti. Ni depletion will modify the chemical composition of the alloy resulting in an enrichment of Ti, increasing the transformation temperature (Halani et al., 2013; Haberland et al., 2014). Secondary phase formation at high heat input will reduce the transformation temperature somewhat but the Ni evaporation will greatly offset this effect resulting in a net increase in transformation temperature (Haberland et al., 2014). The SME of the L-PBF NiTi alloy was compared to that prepared by conventional methods under stress value of 400 MPa. After deformation, the samples were heated to 120°C, and the L-PBF samples showed a promising irreversible strain of 2.5% in comparison with the conventional material (3.9%) (Ou et al., 2018).

Similarly, several attempts have been made in the AM of magnetic shape memory (MSM) alloys, in which these alloys produce reversible magnetic field–induced strains (MFIS) once exposed to an external magnetic field (Ullakko, 1996). The MFIS effect is highly sensitive to microstructural defects and chemical composition, where the chemical composition defines the crystal structure and the transformation temperature, and defects determine the twin boundary movement during straining (Pons et al., 2000). In contrast, with the magnetostrictive materials that show a maximum strain of 0.1, MSM alloys show outstanding strains that can reach 12% (Sozinov et al., 2013). Such characteristic suggest MSM could be an alternative to piezoelectric materials in sensors and micro-actuators (Hobza et al., 2018). The non-modulated Ni-Mn-Ga shows the most promising magnetic effect due to the largest deformation that results from the twin boundary movement and the highest twinning stress (17–25 MPa) (Sozinov et al., 2013), in which several works reported the L-PBF processing of Ni-Mn-Ga (Laitinen et al., 2019a,b; Nilsén et al., 2019). The first trial of Ni-Mn-Ga L-PBF processing indicated the good processability of such alloy in acceptable density. Nilsén et al. (2019) obtained a bulk relative density of 91.4%; such low density may be through incomplete consolidation resulting from improper processing parameters selection (Tammas-Williams et al., 2016). Additionally, Laitinen et al. (2019b) showed a cracked microstructure; the induced microcracks were longitudinal and parallel to the build direction and this has been attributed to the rapid cooling rate. Both studies recommended further investigation of processing parameters for a denser microstructure, and they also reported the possible evaporation of Mn and Ga from the builds at high E, which will affect the MSM effect. Laitinen et al. (2019a) showed that the as-built sample had a ferromagnetic behavior and the phase transformation and Curie temperatures located at the paramagnetic state. However, these values were lower than the raw pre-alloyed powder due to the uncontrollable Mn loss (Laitinen et al., 2019a). These magnetic results are different from Nilsén et al. (2019) where they found that the as-built parts are paramagnetic without any detected phase transformation or Curie temperatures. Nevertheless, after heat treatment, the transformation temperatures became clearer, where the heat treatment process increases the homogeneity and the atomic ordering in the L21 structure.

19.8 Conclusion

The need for high performance and geometrically complex structures is driving the development of novel materials to be used for AM allowing customization and optimization with regards to functionality and performance. L-PBF allows a degree of flexibility previously unavailable for conventional techniques such as casting or forging where materials can be customized down to the basic unit cell orientation, grain shape and morphology, and minute features, which may be incorporated into the structure. The technique can be used to control the heat input into the created parts and therefore modify the thermal gradient and solidification rate to locally change the microstructure. This can be used to tailor mechanical properties to further optimize component properties such as mechanical performance or functional behavior. The processing conditions of the technique itself can be harnessed further to develop stronger materials, for instance, through in-situ micro-oxide formation. Technologies applied to conventional processes such as casting can be crossed over to L-PBF such as the use of nucleation agents to allow the AM of previously unprintable alloys such as Al7075. Functional materials play an important role in several applications such as NiTi vascular stents in heart diseases, soft magnets in magnetic shielding, and rare earth—based alloys in magnetic refrigeration. Conventional synthesis methods lack the ability to produce complex shapes possible with AM. Furthermore, the application of machining may cause surface damage and residual stresses at the surface. The L-PBF of functional materials enables the manufacture of high precision complex shapes with the potential enhanced functionality, comparable in quality to that fabricated by conventional methods. Optimization of laser parameters such as heat input and scanning strategy is key to achieve a maximized performance in L-PBF manufactured components while keeping defect generation to a minimum.

19.9 Questions

- Why is additive manufacturing a feasible production method to generate functionally graded materials?
- How can the anisotropy of the unit cell be harnessed to generate functional or mechanical grading?
- How can additives to the base powder be used to modify the microstructure? Are there any parallels to casting technology?
- What are some challenges when manufacturing functional materials (e.g., shape memory alloys or magnetic materials) through traditional methods? How are these overcome in L-PBF?
- Why are processing parameters so important in L-PBF of NiTi alloys?
- A relatively recent idea is to harness traces of oxygen present in the build chamber to modify the material properties. Discuss some of the examples where this has been applied.

Acknowledgements

Moataz M. Attallah would like to acknowledge the financial support of the Engineering and Physical Sciences Research Council (EPSRC) for the PhD Scholarship of BA, as well as funding through the grants EP/M013294/1 and EP/R002789/1, which supported the postdoctoral research of AAM on magnetic materials.

References

AlMangour, B., et al., 2018. Strengthening of stainless steel by titanium carbide addition and grain refinement during selective laser melting. Mater. Sci. Eng. Elsevier B.V 712 (November 2017), 812–818. doi:10.1016/j.msea.2017.11.126.

AlMangour, B., Grzesiak, D., Yang, J.-M., 2017. Scanning strategies for texture and anisotropy tailoring during selective laser melting of TiC/316L stainless steel nanocomposites. J. Alloys Compd. 728, 424–435. https://doi.org/10.1016/j.jallcom.2017.08.022. Elsevier B.V.

Attar, H., et al., 2015. Mechanical behavior of porous commercially pure Ti and Ti − TiB composite materials manufactured by selective laser melting. Mater. Sci. Eng. A 625, 350–356. https://doi.org/10.1016/j.msea.2014.12.036. Elsevier.

Attard, B., et al., July 2020. Microstructural control during laser powder fusion to create graded microstructure Ni-superalloy components. Addit. Manuf. 36, 101432. https://doi.org/10.1016/j.addma.2020.101432. Elsevier.

Barriobero-Vila, P., et al., 2017. Inducing stable $\alpha + \beta$ microstructures during selective laser melting of Ti-6Al-4V using intensified intrinsic heat treatments. Materials 10 (268), 1–14. https://doi.org/10.3390/ma10030268.

Beal, V.E., et al., 2006. The effect of scanning strategy on laser fusion of functionally graded H13/Cu materials. Int. J. Adv. Manuf. Technol. 30 (9–10), 844–852. https://doi.org/10.1007/s00170-005-0130-x.

Bean, G.E., et al., 2019. Build orientation effects on texture and mechanical properties of selective laser melting Inconel 718. J. Mater. Eng. Perform. 28 (4), 1942–1949. https://doi.org/10.1007/s11665-019-03980-w. Springer US.

Bohidar, S.K., Sharma, R., Mishra, P.R., 2014. Functionally graded materials: a critical review. Int. J. Res. 1 (7), 289–301. Available at: https://journals.pen2print.org/index.php/ijr/article/view/378#.XO0ZqXktAjs.mendeley.

Cantor, B., 2014. Multicomponent and high entropy alloys. Entropy 16 (9), 4749–4768. https://doi.org/10.3390/e16094749.

Cantor, B., September 2020. Multicomponent high-entropy Cantor alloys. Progr. Mater. Sci. 100754. https://doi.org/10.1016/j.pmatsci.2020.100754. Elsevier.

Carluccio, D., et al., August 2018. Grain refinement of laser remelted Al-7Si and 6061 aluminium alloys with Tibor® and scandium additions. J. Manuf. Process. 35, 715–720. https://doi.org/10.1016/j.jmapro.2018.08.030.

Caron, P., Kan, T., Nakagawa, Y.G., 1986. Effect of orientation on the intermediate temperature creep behaviour of Ni-base single crystal superalloys. Scripta Metall. 20, 499–502.

Carter, L.N., et al., 2016. Process optimisation of selective laser melting using energy density model for nickel based superalloys. Mater. Sci. Technol. 0836, 1–5. https://doi.org/10.1179/1743284715Y.0000000108.

Casati, R., et al., 2016. Aging behaviour and mechanical performance of 18-Ni 300 steel processed by selective laser melting. Metals 6, 1–13. https://doi.org/10.3390/met6090218.

Chen, L., et al., 1999. Introduction. In: Miyamoto, Y., et al. (Eds.), Functionally Graded Materials: Design, Processing and Applications, first ed. Springer Science+Business Media, LLC, pp. 1–6.

Chen, P., et al., 2020. In-situ alloyed, oxide-dispersion-strengthened CoCrFeMnNi high entropy alloy fabricated via laser powder bed fusion. Mater. Des. 194, 108966. https://doi.org/10.1016/j.matdes.2020.108966. Elsevier Ltd.

Chen, Y., Liou, F., 2018. Additive manufacturing of metal functionally graded materials: a review. In: Solid Freeform Fabrication 2018: Proceedings of the 29th Annual International Solid Freeform Fabrication Symposium - an Additive Manufacturing Conference, SFF 2018, pp. 1215−1231.

Chikazumi, S., 1997. Physics of Ferromagnetism, second ed. Oxford Science Publications, Tokyo.

Coniglio, N., Cross, C.E., 2009. Mechanisms for solidification crack initiation and growth in aluminum welding. Metall. Mater. Trans. Phys. Metall. & Mater. Sci. 40 (11), 2718−2728. https://doi.org/10.1007/s11661-009-9964-4.

Dadbakhsh, S., et al., 2016. Laser additive manufacturing of bulk and porous shape-memory NiTi alloys: from processes to potential biomedical applications. MRS Bull. 41 (10), 765−774. https://doi.org/10.1557/mrs.2016.209.

David, S.A., Vitek, J.M., 1989. Correlation between solidification parameters and weld microstructures. Int. Mater. Rev. 34 (1), 213−245. https://doi.org/10.1179/imr.1989.34.1.213.

DebRoy, T., et al., 2018. Additive manufacturing of metallic components − process, structure and properties. Prog. Mater. Sci. 92, 112−224. https://doi.org/10.1016/j.pmatsci.2017.10.001.

Dehoff, R.R., et al., 2015. Site specific control of crystallographic grain orientation through electron beam additive manufacturing. Mater. Sci. Technol. 31 (8), 931−938. https://doi.org/10.1179/1743284714Y.0000000734.

Detavernier, C., et al., 2003. An off-normal fibre-like texture in thin films on single-crystal substrates. Nature 426 (6967), 641−645. https://doi.org/10.1038/nature02198.

Dong, Z., et al., 2018. Effect of hatch spacing on melt pool and as-built quality during selective laser melting of stainless steel: modeling and experimental approaches. Materials 12 (1). https://doi.org/10.3390/ma12010050.

Dovgyy, B., et al., 2020. Comprehensive assessment of the printability of CoNiCrFeMn in laser powder bed fusion. Mater. Des. 194, 108845. https://doi.org/10.1016/j.matdes.2020.108845. Elsevier Ltd.

Field, A.C., et al., 2020. The effect of powder characteristics on build quality of high-purity tungsten produced via laser powder bed fusion (LPBF). Metall. Mater. Trans. Phys. Metall. & Mater. Sci. 51 (3), 1367−1378. https://doi.org/10.1007/s11661-019-05601-6. Springer US.

Fuster, V., 2014. Top 10 cardiovascular therapies and interventions for the next decade. Nat. Rev. Cardiol. 11 (11), 671−683. https://doi.org/10.1038/nrcardio.2014.137. Nature Publishing Group.

Geiger, F., Kunze, K., Etter, T., 2016. Tailoring the texture of IN738LC processed by selective laser melting (SLM) by specific scanning strategies. Mater. Sci. Eng. 661, 240−246. https://doi.org/10.1016/j.msea.2016.03.036. Elsevier.

Goll, D., et al., 2019. Additive manufacturing of soft magnetic materials and components. Addit. Manuf. Elsevier 27 (December 2018), 428−439. doi:10.1016/j.addma.2019.02.021.

Gorsse, S., et al., 2017. Additive manufacturing of metals: a brief review of the characteristic microstructures and properties of steels, Ti-6Al-4V and high-entropy alloys. Sci. Technol. Adv. Mater. 18 (1), 584−610. https://doi.org/10.1080/14686996.2017.1361305. Taylor & Francis.

Gschneidner, K.A., Pecharsky, V.K., 2008. Thirty years of near room temperature magnetic cooling: where we are today and future prospects. Int. J. Refrig. 31 (6), 945−961. https://doi.org/10.1016/j.ijrefrig.2008.01.004.

Gu, D., et al., 2011. Nanocrystalline TiC reinforced Ti matrix bulk-form nanocomposites by Selective Laser Melting (SLM): densification, growth mechanism and wear behavior.

Compos. Sci. Technol. 71 (13), 1612−1620. https://doi.org/10.1016/j.compscitech.2011.07.010. Elsevier Ltd.

Gussone, J., et al., 2020. Ultrafine eutectic Ti-Fe-based alloys processed by additive manufacturing − a new candidate for high temperature applications. Appl. Mater. Today 20, 1−11. https://doi.org/10.1016/j.apmt.2020.100767. Elsevier Ltd.

Gutfleisch, O., et al., 2011. Magnetic materials and devices for the 21st century: stronger, lighter, and more energy efficient. Adv. Mater. 23 (7), 821−842. https://doi.org/10.1002/adma.201002180.

Gutfleisch, O., et al., 2016. Mastering hysteresis in magnetocaloric materials. Phil. Trans. Math. Phys. Eng. Sci. 374 (2074) https://doi.org/10.1098/rsta.2015.0308.

Haberland, C., et al., 2014. On the development of high quality NiTi shape memory and pseudoelastic parts by additive manufacturing. Smart Mater. Struct. 23 (10) https://doi.org/10.1088/0964-1726/23/10/104002. IOP Publishing.

Halani, P.R., et al., 2013. Phase transformation characteristics and mechanical characterization of nitinol synthesized by laser direct deposition. Mater. Sci. Eng. 559, 836−843. https://doi.org/10.1016/j.msea.2012.09.031. Elsevier.

Han, C., et al., 2018. Titanium/hydroxyapatite (Ti/HA) gradient materials with quasi-continuous ratios fabricated by SLM: material interface and fracture toughness. Mater. Des. 141, 256−266. https://doi.org/10.1016/j.matdes.2017.12.037. Elsevier Ltd.

Hanemann, T., et al., 2019. In-situ alloying of AlSi10Mg+Si using Selective Laser Melting to control the coefficient of thermal expansion. J. Alloys Compd. 795, 8−18. https://doi.org/10.1016/j.jallcom.2019.04.260. Elsevier B.V.

Ho, I.T., et al., April 2018. Microstructure evolution induced by inoculants during the selective laser melting of IN718. Addit. Manuf. 21, 465−471. https://doi.org/10.1016/j.addma.2018.02.018. Elsevier.

Hobza, A., et al., 2018. Sensing strain with Ni-Mn-Ga. Sens. Actuators A 269, 137−144. https://doi.org/10.1016/j.sna.2017.11.002. Elsevier B.V.

Huber, C., et al., 2019. Coercivity enhancement of selective laser sintered NdFeB magnets by grain boundary infiltration. Acta Mater. 172, 66−71. https://doi.org/10.1016/j.actamat.2019.04.037. Elsevier Ltd.

Van Humbeeck, J., 2001. Shape memory alloys: a material and a technology. Adv. Eng. Mater. 3 (11), 837−850. https://doi.org/10.1002/1527-2648(200111)3:11<837::AID-ADEM837>3.0.CO;2-0.

Im, S.Y., et al., 2020. Unidirectional columnar microstructure and its effect on the enhanced creep resistance of selective electron beam melted Inconel 718. J. Alloys Compd. https://doi.org/10.1016/j.jallcom.2019.153320.

Jaćimović, J., et al., 2017. Net shape 3D printed NdFeB permanent magnet. Adv. Eng. Mater. 19 (8), 1−7. https://doi.org/10.1002/adem.201700098.

Jhong, K.J., et al., 2019. Characteristic of high frequency Fe-Si-Cr material for motor application by selective laser melting. AIP Adv. 9 (3) https://doi.org/10.1063/1.5080134.

Jiles, D.C., 2003. Recent advances and future directions in magnetic materials. Acta Mater. 51 (19), 5907−5939. https://doi.org/10.1016/j.actamat.2003.08.011.

Johnson, L., et al., 2019. Assessing printability maps in additive manufacturing of metal alloys. Acta Mater. 176, 199−210. https://doi.org/10.1016/j.actamat.2019.07.005.

Kang, N., et al., May 2018. Controllable mesostructure, magnetic properties of soft magnetic Fe-Ni-Si by using selective laser melting from nickel coated high silicon steel powder. Appl. Surf. Sci. 455, 736−741. https://doi.org/10.1016/j.apsusc.2018.06.045.

Karlsson, D., et al., 2019. Elemental segregation in an AlCoCrFeNi high-entropy alloy – a comparison between selective laser melting and induction melting. J. Alloys Compd. 784, 195–203. https://doi.org/10.1016/j.jallcom.2018.12.267. Elsevier B.V.

Kitanovski, A., et al., 2015. Magnetocaloric Energy Conversion: From Theory to Applications, first ed. Springer, New York.

Koizumi, M., 1997. FGM activities in Japan. Compos. B Eng. 28B (1–2), 1–4. https://doi.org/10.1016/s1359-8368(96)00016-9.

Krakhmalev, P., et al., 2015. In situ heat treatment in selective laser melted martensitic AISI 420 stainless steels. Mater. Des. 87, 380–385. https://doi.org/10.1016/j.matdes.2015.08.045. Elsevier Ltd.

Krakhmalev, P., et al., 2018. Microstructure, solidification texture, and thermal stability of 316 L stainless steel manufactured by laser powder bed fusion. Metals 8 (8). https://doi.org/10.3390/met8080643.

Kumar, P., et al., 2004. Direct-write deposition of fine powders through miniature hopper-nozzles for multi-material solid freeform fabrication. Rapid Prototyp. J. 10 (1), 14–23. https://doi.org/10.1108/13552540410512499.

Kunze, K., et al., 2015. Texture, anisotropy in microstructure and mechanical properties of IN738LC alloy processed by selective laser melting (SLM). Mater. Sci. Eng. 620, 213–222. https://doi.org/10.1016/j.msea.2014.10.003. Elsevier.

Kurz, W., Bezençon, C., Gäumann, M., 2001. Columnar to equiaxed transition in solidification processing. Sci. Technol. Adv. Mater. 2 (1), 185–191. https://doi.org/10.1016/S1468-6996(01)00047-X.

Laitinen, V., et al., July 2019a. Laser powder bed fusion of Ni-Mn-Ga magnetic shape memory alloy. Addit. Manuf. 30, 100891. https://doi.org/10.1016/j.addma.2019.100891. Elsevier.

Laitinen, V., Salminen, A., Ullakko, K., 2019b. First investigation on processing parameters for laser powder bed fusion of Ni-Mn-Ga magnetic shape memory alloy. J. Laser Appl. 31 (2), 022303. https://doi.org/10.2351/1.5096108.

Li, B., et al., 2020. Additively manufactured Ni-15Fe-5Mo permalloy via selective laser melting and subsequent annealing for magnetic-shielding structures: process, micro-structural and soft-magnetic characteristics. J. Magn. Magn Mater. 494. https://doi.org/10.1016/j.jmmm.2019.165754 (June 2019).

Li, L., et al., 2017. A novel method combining additive manufacturing and alloy infiltration for NdFeB bonded magnet fabrication. J. Magn. Magn Mater. 438, 163–167. https://doi.org/10.1016/j.jmmm.2017.04.066.

Li, Y., Gu, D., 2014. Parametric analysis of thermal behavior during selective laser melting additive manufacturing of aluminum alloy powder. Mater. Des. 63, 856–867. https://doi.org/10.1016/j.matdes.2014.07.006.

Lin, L., Syed, W.U.H., Pinkerton, A.J., 2006. Rapid additive manufacturing of functionally graded structures using simultaneous wire and powder laser deposition. Virtual Phys. Prototyp. 1 (4), 217–225. https://doi.org/10.1080/17452750601141523.

Liu, J., et al., 2011. Systematic study of the microstructure, entropy change and adiabatic temperature change in optimized La-Fe-Si alloys. Acta Mater. 59 (9), 3602–3611. https://doi.org/10.1016/j.actamat.2011.02.033. Acta Materialia Inc.

Liu, J., et al., 2012. Exploring La(Fe,Si)13-based magnetic refrigerants towards application. Scripta Mater. 67 (6), 584–589. https://doi.org/10.1016/j.scriptamat.2012.05.039.

Liu, L., et al., 2018. Dislocation network in additive manufactured steel breaks strength–ductility trade-off. Mater. Today 21 (4), 354–361. https://doi.org/10.1016/j.mattod.2017.11.004. Elsevier Ltd.

Liu, Z., et al., 2017. Functional gradients and heterogeneities in biological materials: design principles, functions, and bioinspired applications. Prog. Mater. Sci. 88, 467−498. https://doi.org/10.1016/j.pmatsci.2017.04.013. Elsevier Ltd.

Liu, Z.H., et al., 2014. Interfacial characterization of SLM parts in multi-material processing: metallurgical diffusion between 316L stainless steel and C18400 copper alloy. Mater. Char. 94, 116−125. https://doi.org/10.1016/j.matchar.2014.05.001. Elsevier Inc.

Louidi, S., et al., 2018. Effect of cobalt doping on martensitic transformations and the magnetic properties of $Ni_{50-x}Co_xMn_{37}Sn_{13}$ ($x = 1, 2, 3$) Heusler ribbons. J. Alloys Compd. 739, 305−310. https://doi.org/10.1016/j.jallcom.2017.12.280. Elsevier B.V.

Lu, B., et al., 1999. Microstructure and magnetic domain structure of boron-enriched $Nd_2(Fe\text{-}Co)_{14}B$ melt-spun ribbons. J. Magn. Magn Mater. 195 (3), 611−619. https://doi.org/10.1016/S0304-8853(99)00291-7.

Mahamood, R.M., Akinlabi, E.T., Shukla, M., Pityana, S., 2012. Functionally graded material: an overview. In: Proceedings of the World Congress on Engineering, Vol III. London, UK, 4−6 July 2012.

Martin, J.H., et al., 2017. 3D printing of high-strength aluminium alloys. Nature 549, 365−369. https://doi.org/10.1038/nature23894. Nature Publishing Group.

Metelkova, J., et al., April 2018. On the influence of laser defocusing in selective laser melting of 316L. Addit. Manuf. 23, 161−169. https://doi.org/10.1016/j.addma.2018.08.006. Elsevier.

Miao, X., et al., 2020. Printing $(Mn,Fe)_2(P,Si)$ magnetocaloric alloys for magnetic refrigeration applications. J. Mater. Sci. 55 (15), 6660−6668. https://doi.org/10.1007/s10853-020-04488-8. Springer US.

Mikler, C.V., et al., 2017. Tuning the phase stability and magnetic properties of laser additively processed Fe-30at%Ni soft magnetic alloys. Mater. Lett. 199, 88−92. https://doi.org/10.1016/j.matlet.2017.04.054. Elsevier B.V.

Mohamed, A.A., Mohamed, M.A., 2019. Carbon nanotubes: synthesis, characterization, and applications. In: Abd-Elsalam, K. (Ed.), Carbon Nanomaterials for Agri-Food and Environmental Applications, first ed. Elsevier, pp. 21−32.

Mirzababaei, S., et al., 2020. In-situ manufacturing of ODS FeCrAlY alloy via laser powder bed fusion. Mater. Lett. 284 (2), 129046, 1 February 2021.

Mohamed, A.E.M.A., et al., 2016. Magnetoresistive and magnetocaloric response of manganite/insulator system. J. Alloys Compd. 657, 495−505. https://doi.org/10.1016/j.jallcom.2015.10.095. Elsevier B.V.

Mohamed, A.E.M.A., et al., 2020. Magnetic shielding promotion via the control of magnetic anisotropy and thermal post processing in laser powder bed fusion processed NiFeMo-based soft magnet. Addit. Manuf. Elsevier 32 (October 2019), 101079. doi:10.1016/j.addma.2020.101079.

Montero Sistiaga, M.L., et al., 2016. Changing the alloy composition of Al7075 for better processability by selective laser melting. J. Mater. Process. Technol. 238, 437−445. https://doi.org/10.1016/j.jmatprotec.2016.08.003. Elsevier B.V.

Moore, J.D., et al., 2013. Selective laser melting of La(Fe,Co,Si)13 geometries for magnetic refrigeration. J. Appl. Phys. 114 (4), 0−8. https://doi.org/10.1063/1.4816465.

Mumtaz, K.A., Hopkinson, N., 2007. Laser melting functionally graded composition of Waspaloy® and Zirconia powders. J. Mater. Sci. 42 (18), 7647−7656. https://doi.org/10.1007/s10853-007-1661-3.

Nadammal, N., et al., 2017. Effect of hatch length on the development of microstructure, texture and residual stresses in selective laser melted superalloy Inconel 718. Mater. Des. 134, 139−150. https://doi.org/10.1016/j.matdes.2017.08.049. Elsevier Ltd.

Niendorf, T., et al., 2013. Highly anisotropic steel processed by selective laser melting. Metall. Mater. Trans. B Process Metall. Mater. Process. Sci. 44 (4), 794—796. https://doi.org/10.1007/s11663-013-9875-z.

Niendorf, T., et al., 2014. Functionally graded alloys obtained by additive manufacturing. Adv. Eng. Mater. 16 (7), 857—861. https://doi.org/10.1002/adem.201300579.

Nilsén, F., et al., 2019. Effect of process parameters on non-modulated Ni-Mn-Ga alloy manufactured using powder bed fusion. Addit. Manuf. Elsevier 28 (November 2018), 464—474. doi:10.1016/j.addma.2019.05.029.

Otsuka, K., Kakeshita, T., 2002. Science and technology of shape-memory alloys: new developments. MRS Bull. 27 (2), 91—98. https://doi.org/10.1557/mrs2002.43.

Ou, S.F., et al., 2018. Manufacturing and characterization of NiTi alloy with functional properties by selective laser melting. Metals 8 (5). https://doi.org/10.3390/met8050342.

Ouyang, Y., et al., 2020. Plastically deformed La—Fe—Si: microstructural evolution, magnetocaloric effect and anisotropic thermal conductivity. Acta Mater. 187, 1—11. https://doi.org/10.1016/j.actamat.2020.01.030. Elsevier Ltd.

Paranthaman, M.P., et al., 2016. Binder jetting: a novel NdFeB bonded magnet fabrication process. JOM 68 (7), 1978—1982. https://doi.org/10.1007/s11837-016-1883-4.

Pecharsky, V.K., Gschneidner, K.A., 1997. Giant magnetocaloric effect in Gd5 (Si2 Ge2). Phys. Rev. Lett. 78 (23), 4494—4497. https://doi.org/10.1103/PhysRevLett.78.4494.

Pesin, D., MacDonald, A.H., 2012. Spintronics and pseudospintronics in graphene and topological insulators. Nat. Mater. 11 (5), 409—416. https://doi.org/10.1038/nmat3305. Nature Publishing Group.

Petch, N.J., 1953. The cleavage strength of polycrystals. J. Iron Steel Inst. 25—28. https://doi.org/10.1007/BF01972547.

Pons, J., et al., 2000. Crystal structure of martensitic phases in Ni-Mn-Ga shape memory alloys. Acta Mater. 48 (12), 3027—3038. https://doi.org/10.1016/S1359-6454(00)00130-0.

Popovich, A.A., et al., 2018. Design and manufacturing of tailored microstructure with selective laser melting. Mater. Phys. Mech. 38 (1), 1—10. https://doi.org/10.18720/MPM.3812018_1.

Popovich, V.A., et al., 2017. Functionally graded Inconel 718 processed by additive manufacturing: crystallographic texture, anisotropy of microstructure and mechanical properties. Mater. Des. 114, 441—449. https://doi.org/10.1016/j.matdes.2016.10.075.

Radulov, I.A., et al., February 2019. Production of net-shape Mn-Al permanent magnets by electron beam melting. Addit. Manuf. 30, 100787. https://doi.org/10.1016/j.addma.2019.100787. Elsevier.

Rai, A., Helmer, H., Körner, C., 2017. Simulation of grain structure evolution during powder bed based additive manufacturing. Addit. Manuf. 13, 124—134. https://doi.org/10.1016/j.addma.2016.10.007. Elsevier B.V.

Rao, J.H., et al., 2019. Selective laser melted Al-7Si-0.6 Mg alloy with in-situ precipitation via platform heating for residual strain removal. Mater. & Design 182, 108005. https://doi.org/10.1016/j.matdes.2019.108005. The Authors.

Roberts, I.A., et al., 2009. A three-dimensional finite element analysis of the temperature field during laser melting of metal powders in additive layer manufacturing. Int. J. Mach. Tool Manufact. 49 (12—13), 916—923. https://doi.org/10.1016/j.ijmachtools.2009.07.004. Elsevier.

Sadowski, M., et al., 2016. Optimizing quality of additively manufactured Inconel 718 using powder bed laser melting process. Addit. Manuf. 11, 60—70. https://doi.org/10.1016/j.addma.2016.03.006. Elsevier B.V.

Sames, W.J., et al., 2017. Feasibility of in situ controlled heat treatment (ISHT) of Inconel 718 during electron beam melting additive manufacturing. Addit. Manuf. 13, 156–165. https://doi.org/10.1016/j.addma.2016.09.001. Elsevier B.V.

Sasaki, M., Hirai, T., 1991. Fabrication and properties of functionally gradient materials. Centen. Meml. Issue Ceram. Soc. Jpn. 99 (10), 1002–1013.

Shamba, P., et al., 2016. Optimization of magnetocaloric properties of arc-melted and spark plasma-sintered LaFe11.6Si1.4. Appl. Phys. Mater. Sci. Process 122 (8), 1–9. https://doi.org/10.1007/s00339-016-0253-y. Springer Berlin Heidelberg.

Slotwinski, J.A., et al., 2014. Characterization of metal powders used for additive manufacturing. J. Res. Natl. Inst. Stand. & Technol. 119, 460. https://doi.org/10.6028/jres.119.018.

Slusarek, B., Zakrzewski, K., 2012. Magnetic properties of permanent magnets for magnetic sensors working in wide range of temperature. Prz. Elektrotech. 88 (7 B), 123–126.

Sozinov, A., et al., 2013. 12% magnetic field-induced strain in Ni-Mn-Ga-based non-modulated martensite. Appl. Phys. Lett. 102 (2), 1–6. https://doi.org/10.1063/1.4775677.

Stevens, E.L., et al., 2017. Variation of hardness, microstructure, and laves phase distribution in direct laser deposited alloy 718 cuboids. Mater. Des. 119, 188–198. https://doi.org/10.1016/j.matdes.2017.01.031. Elsevier Ltd.

Suder, W.J., Williams, S.W., 2012. Investigation of the effects of basic laser material interaction parameters in laser welding. J. Laser Appl. 24 (3), 032009. https://doi.org/10.2351/1.4728136.

Sugimoto, S., 2011. Current status and recent topics of rare-earth permanent magnets. J. Phys. Appl. Phys. 44 (6) https://doi.org/10.1088/0022-3727/44/6/064001.

Tammas-Williams, S., et al., 2016. Porosity regrowth during heat treatment of hot isostatically pressed additively manufactured titanium components. Scripta Mater. 122, 72–76. https://doi.org/10.1016/j.scriptamat.2016.05.002. Elsevier B.V.

Tan, C., et al., April 2020. In-situ synthesised interlayer enhances bonding strength in additively manufactured multi-material hybrid tooling. Int. J. Mach. Tool Manufact. 155, 103592. https://doi.org/10.1016/j.ijmachtools.2020.103592. Elsevier Ltd.

Tan, C., Zhou, K., Kuang, T., 2019. Selective laser melting of tungsten-copper functionally graded material. Mater. Lett. 237, 328–331. https://doi.org/10.1016/j.matlet.2018.11.127. Elsevier B.V.

Tarniţă, D., et al., 2009. Review: properties and medical applications of shape memory alloys. Rom. J. Morphol. Embryol. 50 (1), 15–21.

Thijs, L., et al., 2010. A study of the microstructural evolution during selective laser melting of Ti-6Al-4V. Acta Mater. 58 (9), 3303–3312. https://doi.org/10.1016/j.actamat.2010.02.004. Acta Materialia Inc.

Thijs, L., et al., 2013. Fine-structured aluminium products with controllable texture by selective laser melting of pre-alloyed AlSi10Mg powder. Acta Mater. 61 (5), 1809–1819. https://doi.org/10.1016/j.actamat.2012.11.052.

Ullakko, K., et al., 1966. Large magnetic-field-induced strains in Ni2MnGa single crystals. Appl. Phys. Lett. 69.

Ullakko, K., 1996. Magnetically controlled shape memory alloys: a new class of actuator materials. J. Mater. Eng. Perform. 5 (3), 405–409. https://doi.org/10.1007/BF02649344.

Vilardell, A.M., et al., January 2020. Manufacturing and characterization of in-situ alloyed Ti6Al4V(ELI)-3 at.% Cu by laser powder bed fusion. Addit. Manuf. 36 https://doi.org/10.1016/j.addma.2020.101436.

Volegov, A.S., et al., 2020. Additive manufacturing of heavy rare earth free high-coercivity permanent magnets. Acta Mater. 188, 733−739. https://doi.org/10.1016/j.actamat.2020.02.058.

Vovrosh, J., et al., 2018. Additive manufacturing of magnetic shielding and ultra-high vacuum flange for cold atom sensors. Sci. Rep. 8 (1), 1−10. https://doi.org/10.1038/s41598-018-20352-x. Springer US.

Wang, D., et al., 2016. Investigation of crystal growth mechanism during selective laser melting and mechanical property characterization of 316L stainless steel parts. Mater. Des. 100, 291−299. https://doi.org/10.1016/j.matdes.2016.03.111. Elsevier Ltd.

Wang, L., et al., 2020a. Enhanced elastocaloric effect and mechanical properties of Gd-doped Ni−Mn−Sn-Gd ferromagnetic shape memory alloys. J. Alloys Compd. 846, 156313. https://doi.org/10.1016/j.jallcom.2020.156313. Elsevier B.V.

Wang, M., et al., 2020b. Effect of cellular dislocation structure on the strength of additively manufactured 316L stainless steel. In: International Conference on Processing & Manufacturing of Advanced Materials Processing, Fabrication, Properties, Applications. Trans Tech Publications Ltd, pp. 1−9.

Wang, X., et al., 2018. Microstructure and mechanical properties of stainless steel 316L vertical struts manufactured by laser powder bed fusion process. Mater. Sci. Eng. 736, 27−40. https://doi.org/10.1016/j.msea.2018.08.069.

Wang, X., et al., 2020c. Novel hybrid manufacturing process of CM247LC and multi-material blisks. Micromachines 11 (5). https://doi.org/10.3390/MI11050492.

Wei, C., et al., 2019. Additive manufacturing of horizontal and 3D functionally graded 316L/Cu10Sn components via multiple material selective laser melting. J. Manuf. Sci. & Eng. Trans. ASME 141 (8), 1−8. https://doi.org/10.1115/1.4043983.

Wei, H.L., Elmer, J.W., Debroy, T., 2016. Origin of grain orientation during solidification of an aluminum alloy. Acta Mater. 115, 123−131. https://doi.org/10.1016/j.actamat.2016.05.057. Elsevier Ltd.

Wei, H.L., Mazumder, J., DebRoy, T., 2015. Evolution of solidification texture during additive manufacturing. In: Scientific Reports, vol. 5. Nature Publishing Group, pp. 1−7. https://doi.org/10.1038/srep16446.

Woodcock, T.G., et al., 2012. Understanding the microstructure and coercivity of high performance NdFeB-based magnets. Scripta Mater. 67 (6), 536−541. https://doi.org/10.1016/j.scriptamat.2012.05.038. Acta Materialia Inc.

Wu, J., et al., 2016. Microstructure and strength of selectively laser melted AlSi10Mg. Acta Mater. 117, 311−320. https://doi.org/10.1016/j.actamat.2016.07.012.

Wu, W., et al., August 2018. Nanosized precipitates and dislocation networks reinforced C-containing CoCrFeNi high-entropy alloy fabricated by selective laser melting. Mater. Char. 144, 605−610. https://doi.org/10.1016/j.matchar.2018.08.019. Elsevier.

Xi, L., et al., 2019. Effect of TiB2 particles on microstructure and crystallographic texture of Al-12Si fabricated by selective laser melting. J. Alloys Compd. 786, 551−556. https://doi.org/10.1016/j.jallcom.2019.01.327.

Yadroitsev, I., 2009. Selective laser melting: direct manufacturing of 3D-objects by selective laser melting of metal powders. In: LAP Lambert Academic Publishing, pp. 233−234.

Yadroitsev, I., et al., 2013. Energy input effect on morphology and microstructure of selective laser melting single track from metallic powder. J. Mater. Process. Technol. 213 (4), 606−613. https://doi.org/10.1016/j.jmatprotec.2012.11.014. Elsevier B.V.

Yang, H., et al., 2019a. Controllable in-situ aging during selective laser melting: stepwise precipitation of multiple strengthening phases in Inconel 718 alloy. Edit. Off. J. Mater. Sci. & Technol. 35 (9), 1925−1930. https://doi.org/10.1016/j.jmst.2019.05.024.

Yang, L., et al., 2019b. Additive manufacturing in vascular stent fabrication. In: MATEC Web of Conferences, 253, p. 03003. https://doi.org/10.1051/matecconf/201925303003.

Yang, S., Evans, J.R.G., 2004. Acoustic control of powder dispensing in open tubes. Powder Technol. 139 (1), 55−60. https://doi.org/10.1016/j.powtec.2003.10.008.

Yang, Y., et al., 2017. Effect of scan line spacing on texture, phase and nanohardness of TiAl/TiB 2 metal matrix composites fabricated by selective laser melting. J. Alloys Compd. 728, 803−814. https://doi.org/10.1016/j.jallcom.2017.09.053. Elsevier B.V.

Yin, S., et al., 2018. Hybrid additive manufacturing of Al-Ti6Al4V functionally graded materials with selective laser melting and cold spraying. J. Mater. Process. Technol. Elsevier 255 (April 2017), 650−655. doi:10.1016/j.jmatprotec.2018.01.015.

Zeng, H., et al., 2019. Significantly enhancing the coercivity of NdFeB magnets by ternary Pr-Al-Cu alloys diffusion and understanding the elements diffusion behavior. J. Magn. Magn Mater. 471, 97−104. https://doi.org/10.1016/j.jmmm.2018.09.080 (June 2018).

Zhang, B., et al., 2012. Studies of magnetic properties of permalloy (Fe30%Ni) prepared by SLM technology. J. Magn. Magn Mater. 324 (4), 495−500. https://doi.org/10.1016/j.jmmm.2011.08.030. Elsevier.

Zhang, C., et al., May 2019a. Additive manufacturing of functionally graded materials: a review. Mater. Sci. Eng. 764, 138209. https://doi.org/10.1016/j.msea.2019.138209. Elsevier B.V.

Zhang, C.H., et al., 2017. Multi-layer functional graded stainless steel fabricated by laser melting deposition. Vacuum 141, 181−187. https://doi.org/10.1016/j.vacuum.2017.04.020.

Zhang, D., et al., 2019b. Additive manufacturing of ultrafine-grained high-strength titanium alloys. Nature 576 (7785), 91−95. https://doi.org/10.1038/s41586-019-1783-1. Springer US.

Zhang, D., et al., 2020. Grain refinement of alloys in fusion-based additive manufacturing processes. Metall. Mater. Trans. Phys. Metall. & Mater. Sci. 51 (9), 4341−4359. https://doi.org/10.1007/s11661-020-05880-4. Springer US.

Zhang, F., et al., 2018. Novel nucleation mechanisms through satelliting in direct metal deposition of Ti-15Mo. Mater. Lett. 213, 197−200. https://doi.org/10.1016/j.matlet.2017.11.036. Elsevier B.V.

Zhang, H., et al., 2008. Phase formation with $NaZn_{13}$ structure in metamagnetic $La(Fe_{1-x}Co_x)_{11.9}Si_{1.1}$ compounds. J. Rare Earths 26 (5), 727−730. https://doi.org/10.1016/S1002-0721(08)60171-4. The Chinese Society of Rare Earths.

Zhang, Y.D., et al., 2005. Grain boundary characteristics and texture formation in a medium carbon steel during its austenitic decomposition in a high magnetic field. Acta Mater. 53 (19), 5213−5221. https://doi.org/10.1016/j.actamat.2005.08.007.

Zhong, Y., et al., 2016. Intragranular cellular segregation network structure strengthening 316L stainless steel prepared by selective laser melting. J. Nucl. Mater. 470, 170−178. https://doi.org/10.1016/j.jnucmat.2015.12.034. Elsevier B.V.

Zhou, R. et al., 2019a. Precipitation behavior of selective laser melted FeCoCrNiC0.05 high entropy alloy. Intermetallics Elsevier 106 (July 2018), 20−25. doi:10.1016/j.intermet.2018.12.001.

Zhou, X., et al., 2015. Textures formed in a CoCrMo alloy by selective laser melting. J. Alloys Compd. 631, 153−164. https://doi.org/10.1016/j.jallcom.2015.01.096. Elsevier B.V.

Zhou, Y., et al., April 2019b. Effect of TiC content on the Al-15Si alloy processed by selective laser melting: microstructure and mechanical properties. Optic Laser. Technol. 120 https://doi.org/10.1016/j.optlastec.2019.105719.

Zou, J., et al., 2018. Controlling the grain orientation during laser powder bed fusion to tailor the magnetic characteristics in a Ni-Fe based soft magnet. Acta Mater. 158, 230−238. https://doi.org/10.1016/j.actamat.2018.07.064.

Recent progress on global standardization

20

Johannes Gumpinger[1], *Mohsen Seifi*[2,3], *Nima Shamsaei*[4,5], *Christian Seidel*[6,7], *Richard W. Russell*[8]
[1]ESA/ESTEC, European Space Research and Technology Center, Noordwijk, the Netherlands; [2]ASTM International, Washington, DC, United States; [3]Case Western Reserve University, Cleveland, OH, United States; [4]National Center for Additive Manufacturing Excellence (NCAME), Auburn University, Auburn, AL, United States; [5]Department of Mechanical Engineering, Auburn University, Auburn, AL, United States; [6]Munich University of Applied Sciences Munich, Germany; [7]Fraunhofer IGCV, Augsburg, Germany; [8]NASA Engineering and Safety Center (NESC), Langley Research Center, Hampton, VA, United States

Chapter outline

20.1 Introduction to standardization 563
  20.1.1 Background 563
  20.1.2 Terminology ISO/ASTM 52900 564
  20.1.3 Why standards are important 564
  20.1.4 Role of standards 565
20.2 Worldwide standardization activities 566
  20.2.1 Introduction of ISO/ASTM collaboration 566
  20.2.2 ISO technical committee 261 567
  20.2.3 ASTM F42 committee 568
  20.2.4 Introduction to ASTM AM Center of Excellence 572
    20.2.4.1 Background 572
    20.2.4.2 Mission, vision, function 572
    20.2.4.3 Research and development 573
  20.2.5 Standardization for European and North American space industry 576
  20.2.6 Spotlight on other standardization activities 581
20.3 Questions 582
References 582

20.1 Introduction to standardization

20.1.1 Background

This chapter describes recent progress and some fundamental aspects of standards, their importance, and which role they play in adoption of the technology. The very first

Fundamentals of Laser Powder Bed Fusion of Metals. https://doi.org/10.1016/B978-0-12-824090-8.00021-4
Copyright © 2021 Elsevier Inc. All rights reserved.

dual logo standard in Additive Manufacturing (AM), ISO/ASTM 52900 2015, on terminology is introduced. This standard distinguishes between seven different process categories for AM technologies. While general standardization activities are described, some deeper insights are given into standardization for space applications, covering the latest North American (NASA) and European (ECSS) approaches. The added value through a collaboration between ASTM International and ISO (International Organization for Standardization) for the AM industry is described. The aim of this chapter is not to give a comprehensive list of all AM standards which are published worldwide, but to present a concise overview.

20.1.2 Terminology ISO/ASTM 52900

When a new technology emerges, the first topic to which technical regulations are devoted is always terminology. This is established practice, since without a common terminology, i.e., language, no in-depth technical exchange is possible. For this reason, terminology was addressed by the first standardization project in the field of AM as well. In 2015, the result was published as ISO/ASTM 52900 "Additive manufacturing − General principles − Terminology" ISO/ASTM 52900:2015. ISO/ASTM 52900:2015 establishes and defines terms used in additive manufacturing (AM) technology, which applies the additive shaping principle and thereby builds physical 3D geometries by successive addition of material. Within ISO/ASTM 52900:2015, the terms have been classified into specific fields of application (Fig. 20.1). Furthermore, new terms emerging from the further work in the field of AM will be included in upcoming amendments, such as the Draft International Standard update as of 2020, and overviews of this International Standard.

20.1.3 Why standards are important

The AM industry as a whole is rather a niche industry and is still "in its infancy". However, this niche market has recorded high growth rates in recent years and has therefore received a lot of attention. For this to remain so, a comprehensive set of industry standards is a prerequisite.

AM technologies have gained significance as production technologies during the past years. According to recent industry reports, total AM market volume has exceeded the 10 billion US$ mark in the year 2019. As a result, total market volume has increased tenfold within 10 years, referred to about one billion US$ in the year 2009. Originally, the only field of application for AM was the time-efficient production of prototypes—also known as Rapid Prototyping. During the last 5 years, a significant increase in applications for direct part production can be observed, especially in the aerospace industry, medical industry, and in general engineering. This extension in application from prototyping to manufacturing is crucial to continue the growth rates known from the last years, because prototyping does often not require the production of more than 1 to 10 parts. However, for realizing a double-digit compound annual growth rate over the next years, it is necessary to identify and exploit business cases within small- and medium-scale series (Chapter 22 on economic viability). As a result, machine and material sales will increase and additive manufacturing technologies will further establish themselves as production technologies.

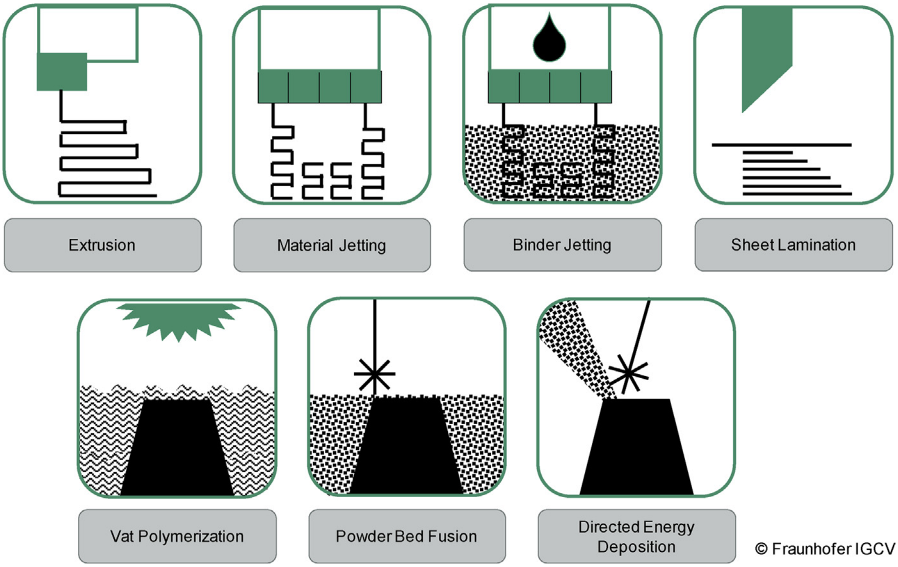

Figure 20.1 Additive manufacturing categories defined by ISO/ASTM 52900:2015. Courtesy of Fraunhofer IGCV.

In order to enable the use of AM technologies for the manufacture of end products in series production, industry standards are needed to provide the framework. This makes it possible, for example, to design global and local supply chains efficiently, ensure quality cost-effectively, and design additive manufacturing machines robustly. In summary, standards enable cost-efficient additive manufacturing.

20.1.4 Role of standards

The foremost aim of international standardization is to facilitate the exchange of goods and services through the elimination of technical barriers to trade. Standards serve as a common language that promote the flow of goods between buyer and seller and protect the general welfare. Typically, standards are used for (among others):

- specifying requirements;
- communicating guidance and possibly course of actions;
- documenting best practices;
- defining test methods and protocols;
- documenting technical data;
- classifying materials, products, systems, or services into groups;
- providing terms, definitions, etc.

Thereby, standards can help in accelerating the adoption of new technologies and ease international collaboration. In the field of AM, standards are a key enabler for the upscaling of the industry. However, in contrast to laws and regulations, compliance is not compulsory for standards and guidelines, Fig. 20.2.

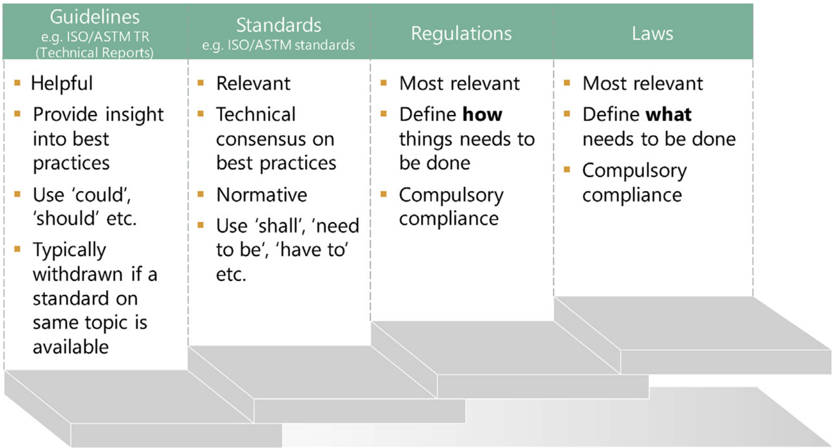
Guidelines
e.g. ISO/ASTM TR (Technical Reports)
Helpful
Provide insight into best practices
Use 'could', 'should' etc.
Typically withdrawn if a standard on same topic is available
Standards
e.g. ISO/ASTM standards
Relevant
Technical consensus on best practices
Normative
Use 'shall', 'need to be', 'have to' etc.
Regulations
Most relevant
Define **how** things needs to be done
Compulsory compliance
Laws
Most relevant
Define **what** needs to be done
Compulsory compliance

Figure 20.2 Simplified ranking between laws, regulations, standards, and guidelines.

Typical benefits of standardization in the field of AM comprise:

- systematic development, modification, and use of processes of joining materials from 3D model data resulting in innovative products;
- assistance to users within the assessment of different additive processes resulting in using the appropriate technology for the specified product demands;
- specification of quality parameters of different processes needed for standardized test procedures;
- specification of appropriate test procedures, thereby ensuring uniform interpretation and evaluation of quality parameters;
- standardization of process chains of AM technologies securing functionality and compatibility;
- standardization of data formats, data structures, and metrics for AM models;
- standardization of vocabulary required to define the product and to find a common speech.

20.2 Worldwide standardization activities

20.2.1 Introduction of ISO/ASTM collaboration

In September 2011, ISO and ASTM signed a cooperative agreement to govern the ongoing collaborative efforts between the two organizations to adopt and jointly develop international standards that serve the global marketplace in the field of AM. The purpose of this so-called Partner Standards Developing Organization (PSDO) cooperative agreement is to eliminate duplication of effort while maximizing resource allocation within the AM industry.

ISO Technical Committee 261 (ISO/TC 261) and ASTM Committee F42 are striving for so called dual logo standards, "ISO/ASTM"-standards, that reflect a strong international consensus. Therefore, these standards can be used by companies worldwide. In 2020, the TC261/ASTMF42-joint steering committee decided to focus its business development activities on meeting further industry-specific requirements. Ongoing standardization activities are focused, for example, on the aerospace and medical industries. For 2021, projects will increasingly address standardization requirements of the automotive and space industries, as well as other sectors such as oil/gas, etc. The objectives of this collaboration can be summarized:

- deliver ISO/ASTM-standards needed for industry;
- consider worldwide standard needs;
- deliver comprehensive sets of industry-specific standards;
- cooperate and collaborate with relevant players in the AM industry;
- serve as a melting pot for the international AM community.

As of June 2020, there are now 10 published joint ISO/ASTM AM standards (Table 20.2, items 16–25) and 50+ joint standards under development.

ASTM International is a Standards Development Organization (SDO) and has been developing standards for more than 90 industry sectors since 1898. ASTM provides a platform for experts from across the world to develop voluntary consensus-based standards that are often used as a basis for commercial and regulatory action. Consensus is developed by representatives of all sectors that have an interest in the use of the standard (producers, users, and those having a general interest, consumers). Consensus standards, with their broad input, are considered by many as the most technically sound and credible documents. Currently, there are more than 140 technical committees with a total 30,000+ volunteer members representing some 140+ countries. In summary, there are more than 12,800 ASTM standards operating globally. Defined by ASTM, they improve the lives of millions every day. Combined with the innovative business services, they enhance performance and help everyone have confidence in the things they make, buy, and use. ASTM staff do not write standards and continue to remain neutral.

ISO, the International Organization for Standardization, is a legal association, the members of which are the National Standards Bodies (NSBs) of some 140 countries (organizations representing social and economic interests at the international level), supported by a Central Secretariat based in Geneva, Switzerland. In total, 23,413 international standards were published by ISO (10/2020) covering almost all aspects of technology and manufacturing. In 2020, a total of 792 technical committees (TC) and subcommittees took care of standards development.

20.2.2 ISO technical committee 261

ISO TC261 is the technical committee within ISO on “Additive Manufacturing.” The scope of ISO TC261 is

> *Standardization in the field of Additive Manufacturing (AM) concerning their processes, terms and definitions, process chains (Hard- and Software), test procedures, quality parameters, supply agreements and all kind of fundamentals.*

In the year 2020, ISO TC261 had 25 participating and 8 observing members. Moreover, 17 ISO standards were published and an additional 29 are under development, most of which are joint ISO/ASTM standards. Most recent information on published documents and ongoing work can be found here: https://committee.iso.org/home/tc261. For questions or comments, the Chairperson of TC261, is always available via secretariat or directly, cf. website.

The structure of the TC261 is characterized by working groups. In 2020, five working groups (WG) were:

- WG1 "Terminology"
- WG2 "Processes, systems and materials"
- WG3 "Test methods and quality specifications"
- WG4 "Data and Design"
- WG6 "Environment, health and safety"

Currently, there is no WG5. This gap is a result of a renumbering of Joint Working Groups (JWG). Cooperation with other ISO TC has always been "in the DNA" of ISO TC261 in order to meet highly application-specific AM needs. For that reason, the following JWG were established:

- JWG10 "Joint ISO/TC 261 - ISO/TC 44/SC 14 WG: Additive manufacturing in aerospace applications"
- JWG11 "Joint ISO/TC 261 - ISO/TC 61/SC 9 WG: Additive manufacturing for plastics"
- TC 150/JWG 1 "Joint ISO/TC 150 - ISO/TC 261 WG: Additive manufacturing in surgical implant applications"

Besides, about 20 formal liaisons were established to other ISO TC and relevant organizations in order to ensure exchange of information and a foundation for collaboration.

20.2.3 ASTM F42 committee

The ASTM F42 Technical Committee on AM technologies was formed in 2009. F42 is one of the 140+ technical committees within ASTM. The F42 has close to 900 members from over 28 countries who contribute actively to AM standards development. Today, 25 standards on AM have been published and more than 65 are in development.

The F42 committee meets in person twice a year and there have been 22 meetings since 2009, with 10 meetings outside of the United States. To date, F42 meetings continue to attract large industry interest and participation from the AM community including representatives from government agencies, industries, academia, and trade associations. Besides the biannual meeting, members within each working group attend conference calls at least once every month. This practice has worked well in ASTM's standards development processes. ASTM F42 frequently receives requests from members to hold meetings at various locations and Fig. 20.3 shows the locations of F42 meetings since 2009.

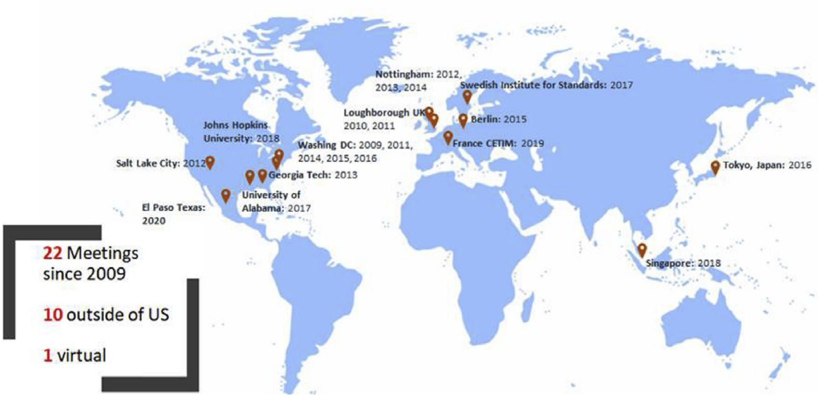
Nottingham: 2012, 2013, 2014
Swedish Institute for Standards: 2017
Loughborough UK 2010, 2011
Berlin: 2015
Johns Hopkins University: 2018
France CETIM: 2019
Washing DC: 2009, 2011, 2014, 2015, 2016
Salt Lake City: 2012
Georgia Tech: 2013
Tokyo, Japan: 2016
University of Alabama: 2017
El Paso Texas: 2020
Singapore: 2018
22 Meetings since 2009
10 outside of US
1 virtual

Figure 20.3 F42 meeting locations since inception in 2009.

Generally, each main committee in ASTM is composed of subcommittees that address specific segments within the general subject area covered by the technical committee. F42 follows the same structure and is composed of the subcommittees listed in Table 20.1.

There are now 25 published AM standards, as summarized in Table 20.2, showing each standard's designation and title.

Table 20.1 F42 additive manufacturing subcommittees.

F42 subcommittee	Area
F42.01	Test methods
F42.04	Design
F42.05	**Materials and processes**
F42.05.01	Metals
F42.05.02	Polymers
F42.05.05	Ceramics
F42.06	Environment, health, and safety
F42.07	**Applications**
F42.07.01	Aviation
F42.07.02	Spaceflight
F42.07.03	Medical/Biological
F42.07.04	Transportation/Heavy machinery
F42.07.05	Maritime
F42.07.06	Electronics

Continued

Table 20.1 F42 additive manufacturing subcommittees.—cont'd

F42 subcommittee	Area
F42.07.07	Construction
F42.07.08	Oil/Gas
F42.07.09	Consumer
F42.08	Data
F42.90	**Executive**
F42.90.01	
F42.90.02	
F42.90.05	
	Strategic planning
	Awards
	Research and innovation
F42.91	Terminology
F42.95	US TAG[a] to ISO TC 261

[a] Committee that represents ASTM balloting to ISO documents.

Table 20.2 Summary of published standards.

S/N	Designation	Title
1	ASTM F2971-13	Standard practice for reporting data for test specimens prepared by additive manufacturing
2	ASTM F3049-14	Standard guide for characterizing properties of metal powders used for additive manufacturing processes
3	ASTM F3001-14	Standard specification for additive manufacturing titanium-6 aluminum-4 vanadium ELI (extra low interstitial) with powder bed fusion
4	ASTM F3091/F3091M-14	Standard specification for powder bed fusion of plastic materials
5	ASTM F3122-14	Standard guide for evaluating mechanical properties of metal materials made via additive manufacturing processes
6	ASTM F2924-14	Standard specification for additive manufacturing titanium-6 aluminum-4 vanadium with powder bed fusion

Table 20.2 Summary of published standards.—cont'd

S/N	Designation	Title
7	ASTM F3056-14e1	Standard specification for additive manufacturing nickel alloy (UNS N06625) with powder bed fusion
8	ASTM F3055-14a	Standard specification for additive manufacturing nickel alloy (UNS N07718) with powder bed fusion
9	ASTM F3184-16	Standard specification for additive manufacturing stainlesss steel alloy (UNS S31603) with powder bed fusion
10	ASTM F3187-16	Standard guide for directed energy deposition of metals
11	ASTM F3213-17	Standard for additive manufacturing—finished part properties — standard specification for cobalt-28 chromium-6 molybdenum via powder bed fusion
12	ASTM F3302-18	Standard for additive manufacturing—finished part properties—standard specification for titanium alloys via powder bed fusion
13	ASTM F3318-18	Standard for additive manufacturing—finished part properties—specification for AlSi10Mg with powder bed fusion—laser beam
14	ASTM F3301-18a	Standard for additive manufacturing—post-processing methods—standard specification for thermal post-processing metal parts made via powder bed Fusion1, 2
15	ASTM F3335-20	Standard guide for assessing the removal of additive manufacturing Residues in medical devices fabricated by powder bed fusion
16	ISO/ASTM52900-15	Standard terminology for additive manufacturing—general principles—terminology1, 2
17	ISO/ASTM52901-16	Standard guide for additive manufacturing—general principles—requirements for purchased AM parts
18	ISO/ASTM52915-16	Standard specification for additive manufacturing file format (AMF) version 1.
19	ISO/ASTM52910-18	Additive manufacturing—design—requirements, guidelines, and recommendations
20	ISO/ASTM52902-19	Additive manufacturing—test artifacts—geometric capability assessment of additive manufacturing systems

Continued

Table 20.2 Summary of published standards.—cont'd

S/N	Designation	Title
21	ISO/ASTM52921-13(2019)	Standard terminology for additive manufacturing—coordinate systems and test methodologies
22	ISO/ASTM52907-19	Additive manufacturing— feedstock materials—methods to characterize metallic powders
23	ISO/ASTM52911-1-19	Additive manufacturing—design—part 1: laser-based powder bed fusion of metals
24	ISO/ASTM52911-2-19	Additive manufacturing—design—part 2: laser-based powder bed fusion of polymers
25	ISO/ASTM52904-19	Additive manufacturing—process characteristics and performance: practice for metal powder bed fusion process to meet critical applications

20.2.4 Introduction to ASTM AM Center of Excellence

20.2.4.1 Background

The Additive Manufacturing Center of Excellence (AM CoE) was officially launched in July 2018 with founding partners: Auburn University, Edison Welding Institute (EWI), the Manufacturing Technology Center (MTC), and National Aeronautical and Space Agency (NASA). Following huge interest from the global community, National Institute of Aviation Research (NIAR) and National Additive Manufacturing Innovation Cluster (NAMIC) subsequently joined the AM CoE as strategic partners. The AM CoE is a global activity with more than 100 people involved across the partnership. It serves as a platform that F42 members can tap into to conduct research to fill gaps in the AM standards. Furthermore, it is also open for other ASTM technical committees to utilize resources.

20.2.4.2 Mission, vision, function

The mission of AM CoE is to bridge standards development with Research and Development (R&D) to better enable efficient development of standards, Education and Training, as well as certification and proficiency testing programs. The vision is to facilitate collaboration and coordination among government, academia, and industry to advance AM standardization for a faster adoption of the AM technologies. There are four functions within the AM CoE: (1) R&D, (2) Education and Workforce Development, (3) Standards and Certification, and (4) Industry Consortia. As shown in Fig. 20.4 each function plays a critical role toward AM standards development.

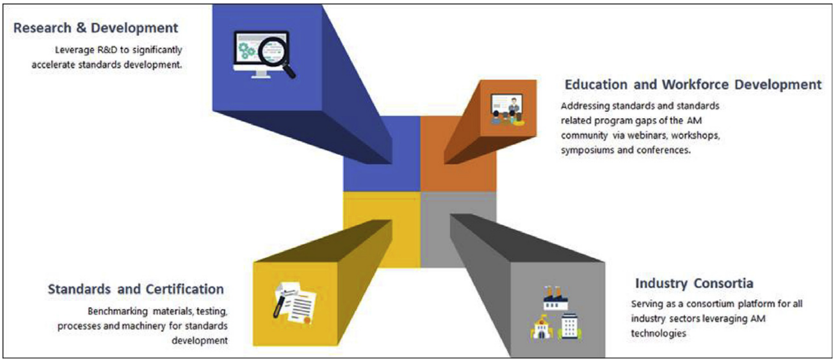
Research & Development
Leverage R&D to significantly accelerate standards development.
Education and Workforce Development
Addressing standards and standards related program gaps of the AM community via webinars, workshops, symposiums and conferences.
Standards and Certification
Benchmarking materials, testing, processes and machinery for standards development
Industry Consortia
Serving as a consortium platform for all industry sectors leveraging AM technologies

Figure 20.4 AM CoE functions.

20.2.4.3 Research and development

20.2.4.3.1 Themes

R&D function plays a key role to standards development, by generating high-quality data. These data together with an initial draft of a work item are transferred to ASTM committees for further development, revisions, and finally approval through the consensus-based approach. R&D topics are commonly cross-linked to create synergy with different subcommittees. The five main R&D themes are:

i. Design, Data, and Modeling
ii. Feedstock Materials (testing, reuse)
iii. Processes/Post-Process
iv. Mechanical Testing
v. Qualification (NDT, etc.)

These themes are defined based on the input of the CoE R&D Team where high priority areas have been identified. One resource utilized was the Standardization Roadmap for AM (AMSC roadmap), jointly published by America Makes and America National Standards Institute (ANSI, 2016). Another source that is leveraged was published in 2017 and addressed some of the critical areas in the field (Seifi et al., 2017). In this document, a total of 93 gaps were identified, from which 65 gaps were determined to require R&D. This reaffirmed the need for R&D to close AM standards gaps and meet standard's needs.

AM CoE's R&D activities started in 2018 with five projects and were continued in 2019 with additional 9 projects. As a benefit to ASTM members, all ASTM members are invited to identify AM standardization gaps and propose their R&D ideas through an online survey. All ideas are evaluated against a set of requirements such as project duration and cost, readiness for standardization (Technology Readiness Level—TRL 6 and above), industry needs, and impact. AM CoE will then solicit Scope of Works (SOWs) from the CoE partners, finalize and allocate projects to appropriate partners to conduct research.

Table 20.3 R&D round 1.

	Project title	Standards gaps addressed	Existing standards impacted
Auburn University	Metallic AM mechanical testing	3	4
EWI	AM Post-processing	2	2
MTC	AM feedstock	5	4
NASA/ Auburn Univ.	LB-PBF process qualification— Phase 1	9	6
NIAR	Polymer	3	9

R&D round 1 was called in 2018 with a total of 18 submissions. Five submissions were selected where these projects demonstrated success in addressing at least 13 standards gaps and impacting at least 16 standards. Four of the projects have been since completed successfully and one is close to completion, with contribution to the associated work items shown in Table 20.3.

The second round of funding continued in 2019. A total of 33 ideas were received, from which 9 ideas were selected after the evaluation process (Table 20.4).

Table 20.4 R&D round 2.

	Project title	Standards gaps addressed	Existing standards impacted
Auburn University	Rapid quality inspection specimen	7	6
EWI	AM data pedigree	1	9
MTC	AM powder spreadability	1	5
MTC	Design guides for post-processing	1	7
NAMIC	Design guides for AM processes	1	5
NAMIC	In-process monitoring	2	8
NASA/ Auburn Univ.	LB-PBF process qualification—phase II	9	6
NIAR	Polymer AM design values tests	2	4
NIAR	Dynamic testing of polymer AM	2	4

To achieve our “Research to Standardization” goal, each R&D project directly contributes to one or more existing or new standards. Fig. 20.5 shows the projects funded by the AM CoE and the status of their respective standard drafts (as of May 2020). For more information, see the Strategic Roadmap for Research and Development at https://amcoe.org/rd-publications.

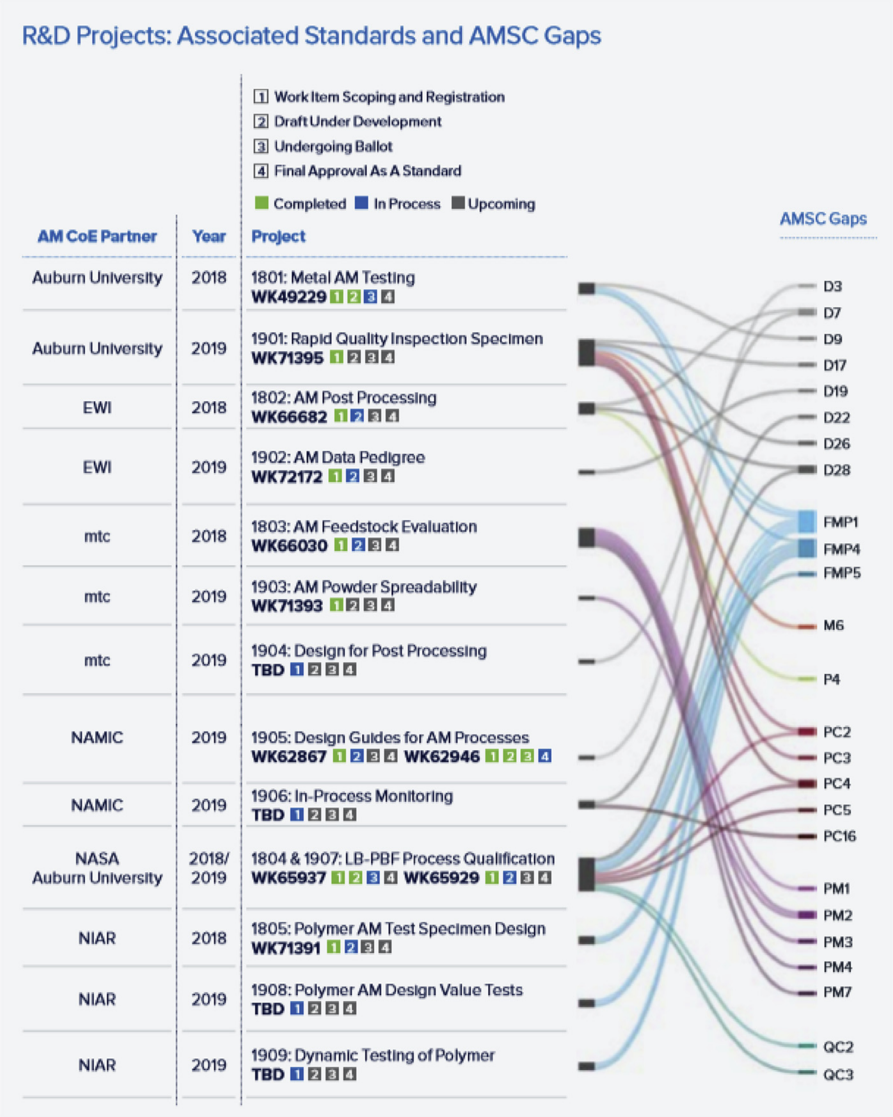

R&D Projects: Associated Standards and AMSC Gaps

1 Work Item Scoping and Registration
2 Draft Under Development
3 Undergoing Ballot
4 Final Approval As A Standard

🟩 Completed 🟦 In Process ⬛ Upcoming

AM CoE Partner	Year	Project
Auburn University	2018	1801: Metal AM Testing **WK49229** 🟩1 🟩2 🟦3 ⬛4
Auburn University	2019	1901: Rapid Quality Inspection Specimen **WK71395** 🟩1 ⬛2 ⬛3 ⬛4
EWI	2018	1802: AM Post Processing **WK66682** 🟩1 🟦2 ⬛3 ⬛4
EWI	2019	1902: AM Data Pedigree **WK72172** 🟩1 🟦2 ⬛3 ⬛4
mtc	2018	1803: AM Feedstock Evaluation **WK66030** 🟩1 🟦2 ⬛3 ⬛4
mtc	2019	1903: AM Powder Spreadability **WK71393** 🟩1 ⬛2 ⬛3 ⬛4
mtc	2019	1904: Design for Post Processing **TBD** 🟦1 ⬛2 ⬛3 ⬛4
NAMIC	2019	1905: Design Guides for AM Processes **WK62867** 🟩1 🟦2 ⬛3 ⬛4 **WK62946** 🟩1 🟩2 🟩3 🟦4
NAMIC	2019	1906: In-Process Monitoring **TBD** 🟦1 ⬛2 ⬛3 ⬛4
NASA Auburn University	2018/ 2019	1804 & 1907: LB-PBF Process Qualification **WK65937** 🟩1 🟩2 🟦3 ⬛4 **WK65929** 🟩1 🟦2 ⬛3 ⬛4
NIAR	2018	1805: Polymer AM Test Specimen Design **WK71391** 🟩1 🟦2 ⬛3 ⬛4
NIAR	2019	1908: Polymer AM Design Value Tests **TBD** 🟦1 ⬛2 ⬛3 ⬛4
NIAR	2019	1909: Dynamic Testing of Polymer **TBD** 🟦1 ⬛2 ⬛3 ⬛4

Figure 20.5 Overview of AM CoE projects and their relations with gaps, specified by the America Makes & ANSI Additive Manufacturing Standardization Collaborative (AMSC).

20.2.5 Standardization for European and North American space industry

In the majority of cases, the space industry doesn't have the luxury to learn from a serial production. If, for example, several hundreds of thousands of parts of the same design are fabricated, the manufacturing processes can be fine-tuned, and influencing factors be identified at the early stages of production. Opposed to this, for space products, high efforts need to be made to qualify processes such that they will produce fit-for-purpose flight hardware in low sample numbers.

For this reason, space-industry standards are put in place to describe how qualification for different processes needs to be approached.

Examples in this chapter contain US-American (NASA) and European (ECSS) qualification approaches.

At the time of publication, NASA had recently released two technical standards; NASA-STD-6030 "Additive Manufacturing Requirements for Crew Spacecraft Systems" and NASA-STD-6033 "Additive Manufacturing Requirements for Equipment and Facilities Control". These documents together provide the Agency with the framework for advanced AM programs and for the development and manufacture of hardware produced using AM technologies.

NASA-STD-6030 begins with the general requirements for an Additive Manufacturing Control Plan (AMCP) which, along with a Quality Management System (QMS), forms the backbone that defines and guides the engineering and production practices. As shown in Fig. 20.6 below, the requirements of NASA-STD-6030

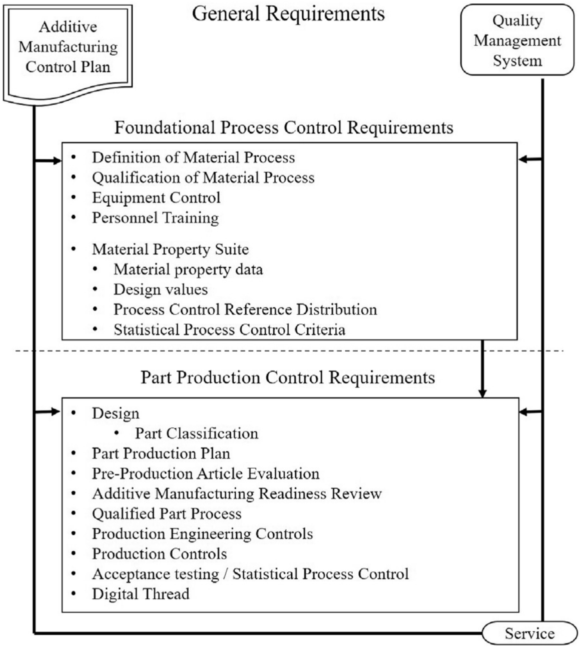
Additive Manufacturing Control Plan
General Requirements
Quality Management System
Foundational Process Control Requirements
• Definition of Material Process
• Qualification of Material Process
• Equipment Control
• Personnel Training
• Material Property Suite
• Material property data
• Design values
• Process Control Reference Distribution
• Statistical Process Control Criteria
Part Production Control Requirements
• Design
• Part Classification
• Part Production Plan
• Pre-Production Article Evaluation
• Additive Manufacturing Readiness Review
• Qualified Part Process
• Production Engineering Controls
• Production Controls
• Acceptance testing / Statistical Process Control
• Digital Thread
Service

Figure 20.6 Topical outline for NASA-STD-6030.

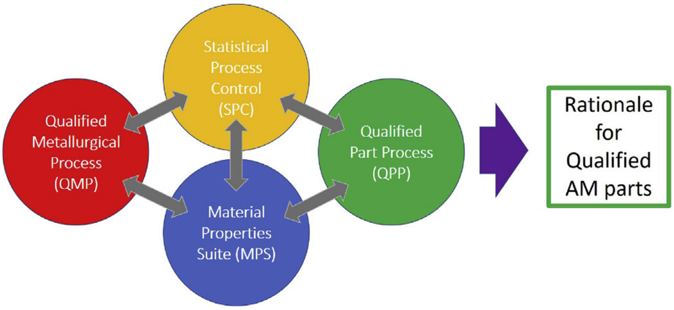
Statistical Process Control (SPC)
Qualified Metallurgical Process (QMP)
Qualified Part Process (QPP)
Material Properties Suite (MPS)
Rationale for Qualified AM parts

Figure 20.7 AM certification governing principles.

fall into two categories. The first, foundational process control includes the requirements for AM processes that provide the basis for reliable part design and production. These include qualification of material processes, equipment controls, personnel training, and material property development. The second category, part production control, consists of requirements typical of many aerospace operations and includes design and assessment controls, part production plans (PPP), preproduction article processes, and AM production controls.

The interaction of the key aspects of an AM plan is shown in Fig. 20.7. At the far left of this figure one can see one of the initial key steps which is the establishment of a Qualified Material Process (QMP). The QMP will ensure a consistent process using specified controls of the raw material feedstock and an evaluation of the process capability for each AM machine, all of which are documented in a configuration controlled QMP record. The QMP uses data from machine qualification, monitored by process control metrics and Statistical Process Control (SPC), which all feed into the creation of design values. The Materials Properties Suite (MPS) concept includes three entities: a material property database; a subset of that database used to derive and implement a Process Control Reference Distribution (PCRD), which provides SPC criteria for witness test evaluation; and a maintained set of material allowables and design values for part design. Integrating simple SPC concepts to monitor the process and substantiate the integrity of material allowables is a unique aspect of NASA-STD-6030 and is necessary given the process-sensitive nature of AM. Fig. 20.8 below outlines how the QMP becomes the foundation for the establishment of the MPS, which along with SPC, leads to part qualification.

The Part Production Plans (PPP) document the rationale for, and the implementation of, the production methodology, including such items as the part build orientation, associated QMP, witness test requirements, inspection methods and limitations, and proof-testing methodology. The PPP is a deliverable product requiring NASA approval prior to proceeding into production; the PPP needs to convey succinctly the full design and production intent of the part. Once approved, the combination of drawing and PPP serve as the basis for establishing the complete engineering production controls. Once a first article is manufactured and found to meet requirements, the Qualified Part Process is established, and production of flight parts can begin.

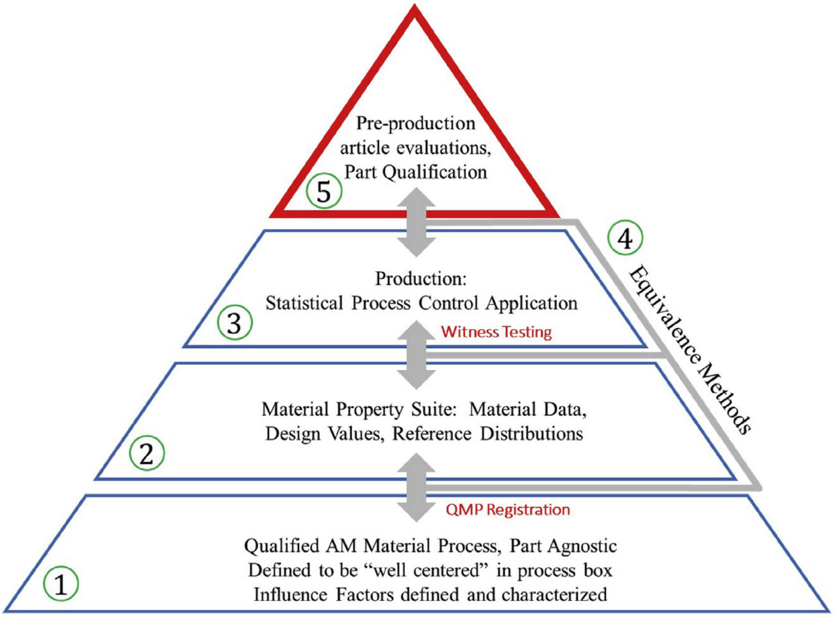
Pre-production
article evaluations,
Part Qualification
⑤
④
Equivalence Methods
Production:
Statistical Process Control Application
③
Witness Testing
Material Property Suite: Material Data,
Design Values, Reference Distributions
②
QMP Registration
Qualified AM Material Process, Part Agnostic
Defined to be "well centered" in process box
Influence Factors defined and characterized
①

Figure 20.8 Material properties building blocks for qualification.

AM has been investigated at the European Space Agency since the early 2000s. The first projects dealt with the question if this novel technique could be successfully applied for ESA's space missions and which benefits it would bring. It became clear quite quickly that both the benefits and associated challenges were significant. For this reason, this intriguing manufacturing process was further investigated through a series of R&D projects. At the same time, the European space industry developed an ever-increasing interest to use this technique for flight applications. Increasing the performance of space products is always a key topic. Within ESA's Advanced Manufacturing cross-cutting initiative (Norman and Rohr, 2019), the goal is to increase performance and design freedom while reducing cost and lead time. AM is one of the technologies that can bring these benefits. Typical examples of performance increase include mass reduction, or embedded functionality, often making use of topology optimization tools. At the same time, AM can often reduce costs by reducing the part count number, which leads to lower labor costs associated to assembly and integration.

However, the variation of quality levels of various suppliers was significant and the existing European Cooperation for Space Standardisation (ECSS) standards related to materials and processes did not provide the necessary requirements for the specifics of AM. It was then decided to assemble a preliminary working group composed of key stakeholders of the European space industry to assess whether or not the manufacturing technology would be mature enough so that an ECSS standard could be meaningfully applied. Shortly after, the development of a dedicated ECSS standard for AM titled “Processing and quality assurance requirements for metallic powder bed fusion technologies for space applications” was kicked off.

The working group is composed of representatives of European space companies, national space agencies, and ESA. In this way, industry best practices could be merged with agencies’ nonconfidential lessons learned, intending to provide a practical, yet firm standard.

Developing a “one size fits all” standard proved to be challenging, as various companies dealing with AM are on different levels of maturity. The principal idea of the standard is to walk the reader through a typical development phase of an AM product, see Fig. 20.9. This includes the AM definition phase, the verification phase, and the hardware production phase. Within the definition phase, the part requirements are compared with the AM constraints. Basic considerations like the parts sizes and the available build envelope or cleanliness requirements and ability for cleaning besides many others need to be made. Different parts on a spacecraft or a launch vehicle have different consequences of failure. For example, a tertiary structure is generally less critical as an injector head of a launcher engine. Therefore, four different safety classes were defined to account for this:

- Class 1.1 parts are considered critical and structural. Failure of a Class 1.1 part results in loss of spacecraft, major components, loss of life, or loss of control of the spacecraft.
- Class 1.2 parts are critical, but nonstructural. Failure of a Class 1.2 part results in loss of spacecraft, major components, loss of life, or loss of control of the spacecraft.
- Class 2 parts are noncritical but structural. Their failure can reduce the efficiency of the system but not cause the loss of the spacecraft.
- Class 3 parts are noncritical and nonstructural and are contained so that failure does not affect other flight elements. These parts require minimal integrity verification, the controls are mainly visual.

This classification is an important step, as it drives the test envelope within the verification phase.

At the definition phase, it is also established, if an existing Additive Manufacturing Procedure (AMP) can be re-used. An AMP intends to describe all non-geometry-dependent parameters of all processes along the AM end-to-end process.

The verification is done on specimen and part level. The former intends to show that a set of parameters is capable of producing acceptable mechanical and physical properties, whereas the latter should demonstrate that a specific geometry can be built without unacceptable imperfections. In this way, preliminary procedures (pAMP) and preliminary Hardware Fabrication Procedure (pHFP) are verified through testing to become the actual procedures (AMP and HFP).

After having successfully performed the verification phase, the (flight) hardware is produced according to the previously developed procedures.

Metal Powder Bed Fusion (mPBF) techniques are also known to be sensitive to variations of environmental conditions in the used facilities or the used powder feedstock. The machines need to be well maintained and qualified personnel are required to produce high-quality parts. Therefore, requirements for these topics were also included in the standard.

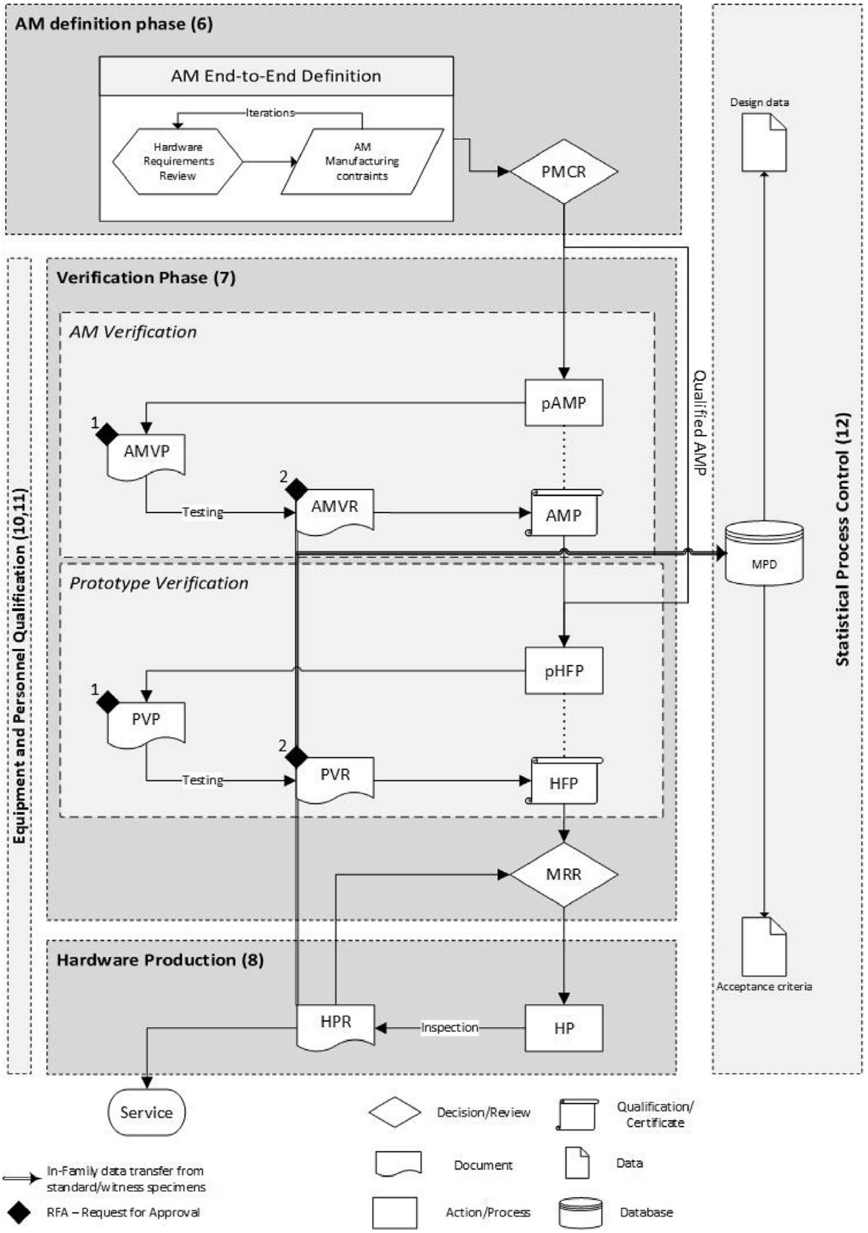
AM definition phase (6)
AM End-to-End Definition
Iterations
Hardware Requirements Review
AM Manufacturing contraints
PMCR
Design data
Verification Phase (7)
AM Verification
pAMP
1
AMVP
2
Testing
AMVR
AMP
Qualified AMP
MPD
Statistical Process Control (12)
Equipment and Personnel Qualification (10,11)
Prototype Verification
pHFP
1
PVP
2
Testing
PVR
HFP
MRR
Hardware Production (8)
HPR
Inspection
HP
Acceptance criteria
Service
Decision/Review
Qualification/ Certificate
Document
Data
Action/Process
Database
In-Family data transfer from standard/witness specimens
RFA – Request for Approval

Figure 20.9 Development of AM hardware according to ECSS.
Reproduced from ECSS-Q-ST-70-80C, 2020. Processing and Quality Assurance Requirements for Metallic Powder Bed Fusion Technologies for Space Applications with permission of ESA as copyright owner for the members of ECSS.

The current ECSS standard ECSS-Q-ST-70-80C is applicable for metal powder bed fusion—based processes, including both electron- and laser-beams as energy sources. This limitation in scope was a result of the preliminary working group, as these material and process combinations were considered mature enough to be covered by ECSS standards. In the near future though, it is planned to extend the standardization efforts to other processes for metals, but also for polymers, ceramics, and composite materials.

20.2.6 Spotlight on other standardization activities

Nowadays, we see a lot of standardization activities. Hence, various Standards Development Organizations (SDOs), Certification bodies and Associations are active in the field of AM. Fig. 20.10 is intended to provide an overview of this, but nevertheless only contains an extract of the worldwide activities. In general, a distinction can be made between standardization activities that are rather intended to bring national added value (e.g., for Germany DVS—German Welding Society) and those that are intended to gain international recognition (e.g., ISO TC 261 and ASTM F42 on AM). Furthermore, it makes sense to picture SDOs, certification bodies, and associations within one illustration, as there is a close link between these organizations. SDOs intend to develop technical regulations which are then used by certification bodies to develop their certification procedures. Associations, as another important player, serve as the voice of the industry and provide both SDOs and certification bodies with information on the needs of its members. In addition, standards only become of value when applied in industry. For that reason, associations also serve as information and marketing channel for SDOs as part of a win-win situation.

In Fig. 20.10, the text fields are marked with logos or flags in the background that indicate the origin of the above-mentioned groupings. The upper row shows the

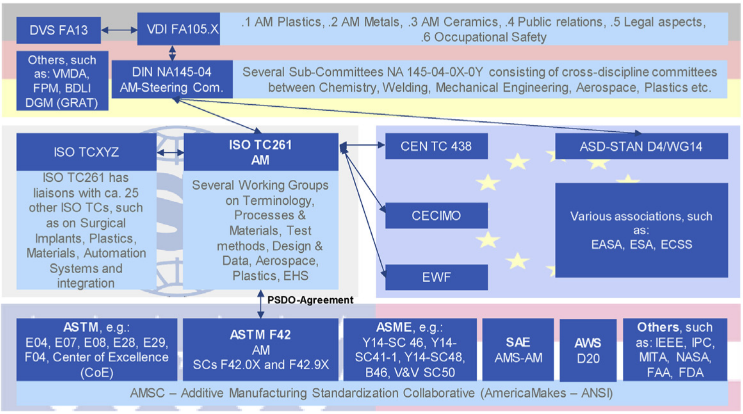
DVS FA13
VDI FA105.X
.1 AM Plastics, .2 AM Metals, .3 AM Ceramics, .4 Public relations, .5 Legal aspects, .6 Occupational Safety
Others, such as: VMDA, FPM, BDLI DGM (GRAT)
DIN NA145-04 AM-Steering Com.
Several Sub-Committees NA 145-04-0X-0Y consisting of cross-discipline committees between Chemistry, Welding, Mechanical Engineering, Aerospace, Plastics etc.
ISO TCXYZ
ISO TC261 has liaisons with ca. 25 other ISO TCs, such as on Surgical Implants, Plastics, Materials, Automation Systems and integration
ISO TC261 AM
Several Working Groups on Terminology, Processes & Materials, Test methods, Design & Data, Aerospace, Plastics, EHS
CEN TC 438
ASD-STAN D4/WG14
CECIMO
EWF
Various associations, such as: EASA, ESA, ECSS
PSDO-Agreement
ASTM, e.g.: E04, E07, E08, E28, E29, F04, Center of Excellence (CoE)
ASTM F42 AM SCs F42.0X and F42.9X
ASME, e.g.: Y14-SC 46, Y14-SC41-1, Y14-SC48, B46, V&V SC50
SAE AMS-AM
AWS D20
Others, such as: IEEE, IPC, MITA, NASA, FAA, FDA
AMSC – Additive Manufacturing Standardization Collaborative (AmericaMakes – ANSI)

Arrows indicate formal cooperation
TC =Technical Committee
FA & NA = German for Committee
AM = Additive Manufacturing
EHS = Environment, Health and Safety
PSDO = Partner Standards Developing Organization
SDO = standards development organizations
Source USA: AMSC – Standardization Roadmap for Additive Manufacturing, Version 2.0, June 2018

Figure 20.10 Excerpt of worldwide standardization activities covering selected associations, certification bodies, and SDOs.
The original layout of this graphic was developed by Joerg Lenz, former chairman of ISO TC261.

situation for Germany, where mainly the DIN and VDI are promoting standardization in the area of AM. The middle row contains information on AM-relevant committees within the ISO organization and the European Union. The bottom row gives an insight into the standardization landscape in the USA.

20.3 Questions

- Which AM categories are defined by ISO/ASTM?
- Why are standards important for AM?
- Which ASTM committee was formed for AM?
- Which two fundamental areas of AM for space are typically qualified?
- Which five main R&D topics were defined in the ASTM Center of Excellence?

References

ANSI, 2016. https://www.ansi.org/standards-coordination/collaboratives-activities/additive-manufacturing-collaborative.

ECSS-Q-ST-70-80C, 2020. Processing and Quality Assurance Requirements for Metallic Powder Bed Fusion. Technologies for Space Applications.

ISO/ASTM_52900:2015, 2015, Additive Manufacturing — General principles — Terminology. Extended preview available online. https://www.iso.org/obp/ui/#iso:std:iso-astm:52900:dis:ed-2:v1:en. (Access 2 November 2020).

NASA-STD-6030, n.d. Additive Manufacturing Requirements for Crew Spacecraft Systems.

NASA-STD-6033, n.d. Additive Manufacturing Requirements for Equipment and Facilities Control.

Norman, A., Rohr, T., 2019. Advanced Manufacturing for Space Applications. ESA/ESTEC, European Space Research and Technology Center, Noordwijk, The Netherlands.

Seifi, M., Gorelik, M., Waller, J., et al., 2017. Progress towards metal additive manufacturing standardization to support qualification and certification. JOM 69, 439–455. https://doi.org/10.1007/s11837-017-2265-2.

Industrial applications

21

Elena Lopez, Frank Brueckner, Samira Gruber
Fraunhofer IWS, Dresden, Germany

Chapter outline

21.1 Introduction 583
21.2 Case studies on Laser Powder Bed Fusion 584
  21.2.1 Aerospace industry 584
  21.2.2 Automotive and transport industry 588
  21.2.3 Energy sector 589
  21.2.4 Medical industry 590
21.3 Hybrid manufacturing with Laser Powder Bed Fusion 592
21.4 Future potential industrial applications of L-PBF and applied research trends 592
21.5 Questions 594
Acknowledgements 594
References 594

21.1 Introduction

One of the earliest Laser Powder Bed Fusion (L-PBF) processes was developed in 1995 at Fraunhofer ILT and the ILT SLM patent DE 19649865 “Shaped body especially prototype or replacement part production” was issued in 1996. L-PBF has since then found its way as a new production process into many industrial applications (for more on the historical development of L-PBF and various other patents see Chapter 1). The Fraunhofer Society with its more than 70 institutions widespread throughout Germany has since this time been deeply involved in further developing Additive Manufacturing (AM) and transferring knowledge of processing different materials for various applications in several branches. This chapter will give some examples of industrial applications in the field and latest research projects of the Fraunhofer Institute for Material and Beam Technology (from now on mentioned as Fraunhofer IWS) using L-PBF in which the authors of this chapter are directly involved. AM accelerates the development process because calculations, simulations, and prototype production no longer have to follow one another in time. Due to the cost-effective and flexible production of a prototype, test results are available much faster and can be incorporated directly into development. This leads to increased implementation in

Fundamentals of Laser Powder Bed Fusion of Metals. https://doi.org/10.1016/B978-0-12-824090-8.00027-5
Copyright © 2021 Elsevier Inc. All rights reserved.

industrial applications. The sales of metal printing machines have significantly increased from 2013 to 2018 from under 500 machines to over 2200 machines per year (see Fig. 21.1). These sale numbers are a good indication of increased final part production in the next couple of years and increased industrialization.

A survey conducted by Wohlers Report (2020) asked service providers, machine manufacturers, and producers of materials and desktop 3D printers which industry they serve and the approximate revenues in percent they receive. The result shows that the main four industry branches for AM are automotive (16.4%), consumer products/electronics (15.4%), aerospace (14.7%), and medical/dental (13.9%). For these industry branches, several applications have been selected for this chapter, including industrial examples from GE Aviation, Siemens, Audi, and Bugatti, and latest research projects with participation of Fraunhofer IWS.

21.2 Case studies on Laser Powder Bed Fusion

21.2.1 Aerospace industry

This section will give an overview of current industrial applications and applied industrial research projects of L-PBF in the aerospace sector.

GE Aviation is producing fuel nozzles for its LEAP engine since 2013, reducing the part numbers from 20 to 1, increasing the life of the fuel delivery system due to greater design freedom by factor 5, and reducing the weight by 25% compared to its predecessor version (https://www.industrial-lasers.com/welding/article/16485564/additive-manufacturing-at-ge-aviation) and expects to manufacture more than 120,000 parts using L-PBF for their engines by the end of 2020 (Wohlers Report, 2020). Another industry example is an additively manufactured combustion chamber by ArianeGroup which was hot-fired in June 2020 on the P8 test bench of the DLR German Aerospace Center's Lampoldshausen testing facility. The tests were

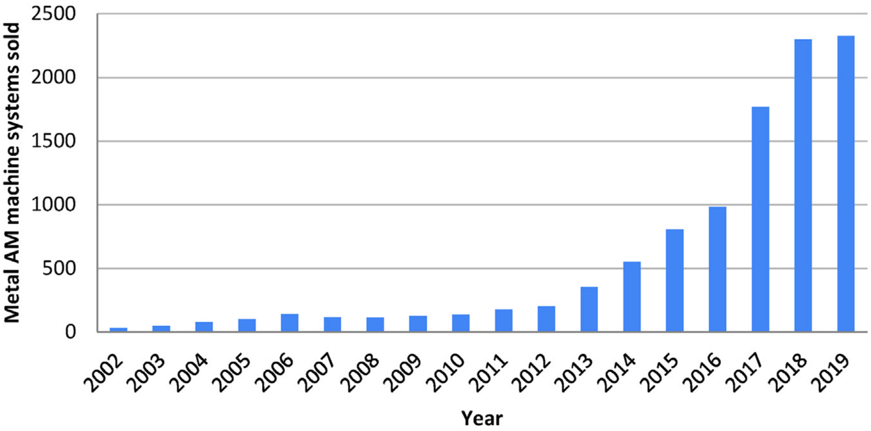

Figure 21.1 Metal AM machine systems sold from 2002 to 2019 (Wohlers Report, 2020).

conducted jointly by ArianeGroup and DLR and followed on from the hot-fire test campaign conducted last year, which validated 14 technological building blocks for future liquid propellant rocket engines. The results are believed to represent a key step in the preparations for the future development of very-low-cost rocket engines. The additively manufactured combustion chamber was produced and tested under ESA's Expander-Cycle Technology Integrated Demonstrator (ETID) project, part of ESA's Future Launchers Preparatory Program (FLPP). It is a full-scale demonstrator for a launcher upper stage engine, which incorporates the latest propulsion technologies and is designed to validate innovative manufacturing technologies, materials, and processes, such as AM, laser ignition, and the use of low-cost materials. The combustion chamber features numerous innovations, such as low-cost copper alloy cooling channels and an outer jacket made by cold gas spraying. Additionally, the combustion chamber includes a single-piece injection head produced by L-PBF (Fuhrmann et al., 2019).

HPS GmbH—a specialist for space subsystems—designed and built an antenna with a diameter of 400 mm using L-PBF and Ti6Al4V within an ESA (European Space Agency) project together with Fraunhofer IWS (Fig. 21.2). The required geometric accuracy could only be achieved in combination with suitable finishing processes. By optimized positioning and orientation, production time could be reduced by 50% in the project phase. The topology-optimized design took advantage of process-specific geometric freedom and reduced both weight and the number of individual components compared to the original design.

In the ESA project "AAM2ISH— Assessing the use of advanced manufacturing to improve and extend space hardware capabilities," the redesign, manufacturing, and qualification of a metallic space bracket was successfully conducted (Fig. 21.3). A preceding selection process was established and lessons learned for topology optimization

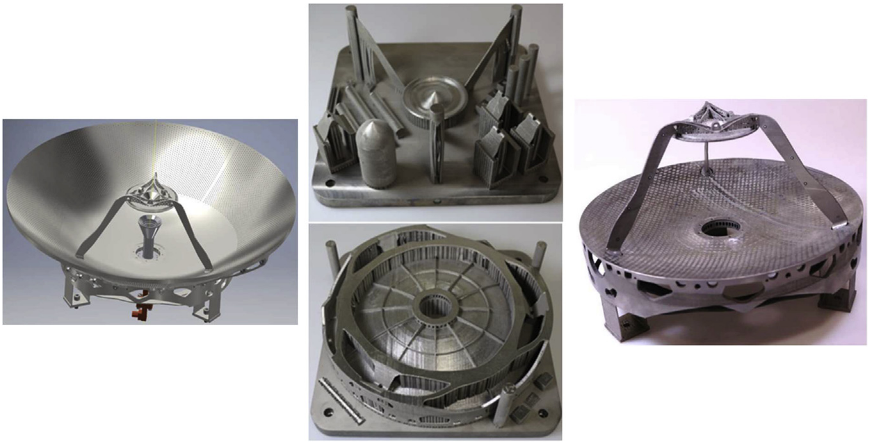

Figure 21.2 Left: Design of the antenna consisting of subreflector and main reflector, center: additive manufacturing of the components using L-PBF, right: assembled antenna (without outer segments), Fraunhofer IWS and HPS GmbH.

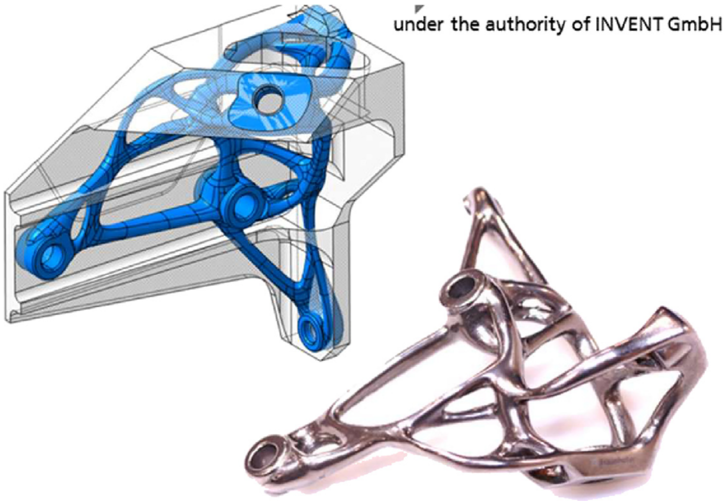

Figure 21.3 Topology optimized bracket, Fraunhofer IWS and INVENT GmbH.

additionally gave feedback and was documented in INVENT's internal work instruction for topology optimization (TO) and AM that is an outcome of the project. In the redesign evaluation and later in the qualification campaign the demonstrators yielded massive improvements like reduced displacement by 55%, and overachieved design and performance goals such as reduced mass by 68% and increased minimum factor of safety by 72% (Willner et al., 2020). Thus, the initially stated goals are achieved, and the demonstrator was qualified up to Technology readiness level 5 (TRL 5).

Furthermore, again within an ESA project "Development of an AM mirror demonstrator for space applications", a set of process parameters for L-PBF for the aluminum alloy AlSi40 was optimized by an extensive process development campaign. A large amount of material data for additive manufactured AlSi40 was determined by an in-depth characterization campaign for different heat treatments. Very specific post-machining strategies and supports are required for L-PBF of AlSi40 to prevent cracking. A custom topology optimization code was developed for multimaterial build-ups with objective functions and constraints specific to optical components. A mirror demonstrator was designed that is ~40% lighter and has >20% better optical performance than the reference part (Fig. 21.4). Experiments showed that a preheating temperature of 400°C is required to build a crack-free component (Eberle et al., 2019; Müller et al., 2019).

Microlaunchers are an alternative to conventional launch vehicles. Able to carry payloads of up to 350 kg, these midsized transport systems are designed to launch small satellites into space. Researchers at the Fraunhofer IWS in Dresden and TU Dresden's aerospace experts developed an additively manufactured rocket engine with an aerospike nozzle for microlaunchers. The scaled metal prototype is expected to consume 30% less fuel than conventional engines. What sets this aerospike engine apart from others is that its fuel injector, combustion chamber, and nozzle are more

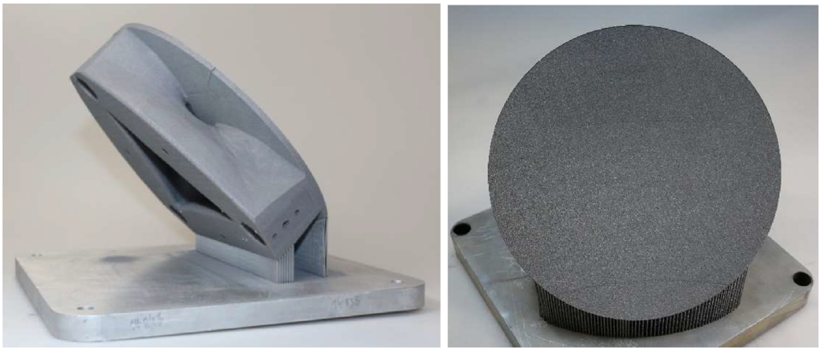

Figure 21.4 Demonstrator manufacturing of AM (L-PBF) mirror assembly by AlSi40, Fraunhofer IWS and crack-free with preheating the platform to 400°C.

complex than traditionally manufactured designs due to the L-PBF manufacturing process, allowing enhanced performance. The nozzle consists of a spikelike center-body designed to accelerate combustion gases and the outer combustion chamber (Fig. 21.5). Internal cooling channels for the spike and combustion chamber are needed to cool the combustion walls during firing. The suitable material in this project for the functional aerospike is Inconel 718 due to its high temperature strength. The hot fire tests using the bi-liquid propelled engine without thrust vector control (TVC) have been conducted at the Institute of Aerospace Engineering (ILR) of the Technische Universität Dresden's own liquid oxygen and ethanol engine test bench.

Another recent application suitable for L-PBF is the production of compliant systems or compliant mechanisms (abbreviation CM), which was assessed in the ESA project "Development of a Compliant Mechanism Based on Additive Manufacturing"

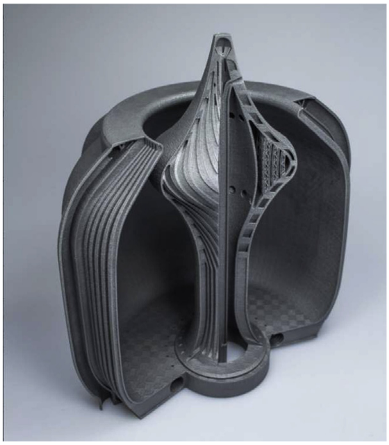

Figure 21.5 A design demonstrator for an additively manufactured aerospike nozzle with a height of 200 mm by Fraunhofer IWS and ILR, TU Dresden (Buchholz et al., 2020).

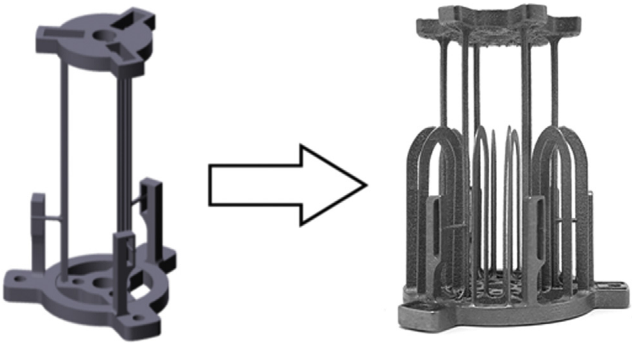

Figure 21.6 Compliant Mechanism of early development stage and final AM part, Fraunhofer IWS and RUAG Space.

with HTS GmbH and Fraunhofer IWS. These can perform a joint, spring, damping, or compensator function achieving the force and motion transmission through elastic body deformation, without the need for hinges or separate components. A variant for such a mechanism is shown in Fig. 21.6, a so-called Compliant Rotation Reduction Mechanism (CRRM). Compared to conventional motion systems, CM offer a number of advantages such as lower weight and lower maintenance due to the absence of lubricants because of lack of frictional wear. In general, compliant mechanisms are conventionally manufactured by eroding (Howell et al., 2017) or milling and turning with fine tools (Lateş et al., 2017). The geometric degrees of freedom opened up by L-PBF can allow completely new possibilities for the design of such CM (Fig. 21.6). A completely three-dimensional system can be produced with a corresponding increase in functionality and weight savings. For the functionality and lightweight design of a compliant mechanism, knowledge of the mechanical properties, contour accuracy, and the quality of the additively manufactured components play a decisive role. Mechanical properties such as fatigue strength due to systematic cyclical operating stress must be considered separately.

21.2.2 Automotive and transport industry

With the newly developed 3D-printed titanium (Ti6Al4V) brake caliper, Bugatti has designed and built one of the largest topology optimized titanium parts with L-PBF worldwide collaborating with the Fraunhofer Research Institution for Additive Manufacturing Technologies (Fraunhofer IAPT, Fig. 21.7). The new titanium brake caliper is 41 cm long, 21 cm wide, 13.6 cm high, and weighs just 2.9 kg resulting in a weight saving over 40% compared to a conventional brake caliper out of aluminum (Wischeropp et al., 2019) and (Du Plessis et al., 2019).

Another interesting example for additively manufactured automotive applications are LED headlight components by Betatype (Fig. 21.8). They require comparatively large heatsinks which are often actively cooled. Using the geometrical freedom with L-PBF, multiple manufacturing processes can be reduced to a single build job for manufacturing 384 qualified metal automotive parts. This reduces the part cost to £3

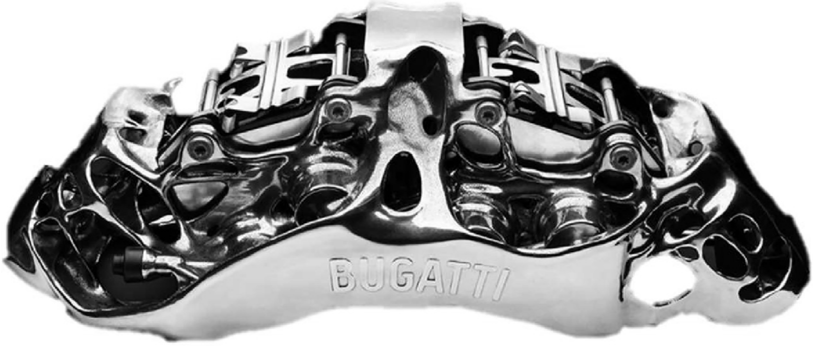

Figure 21.7 Bugatti AM brake caliper, Fraunhofer IAPT, and Bugatti.

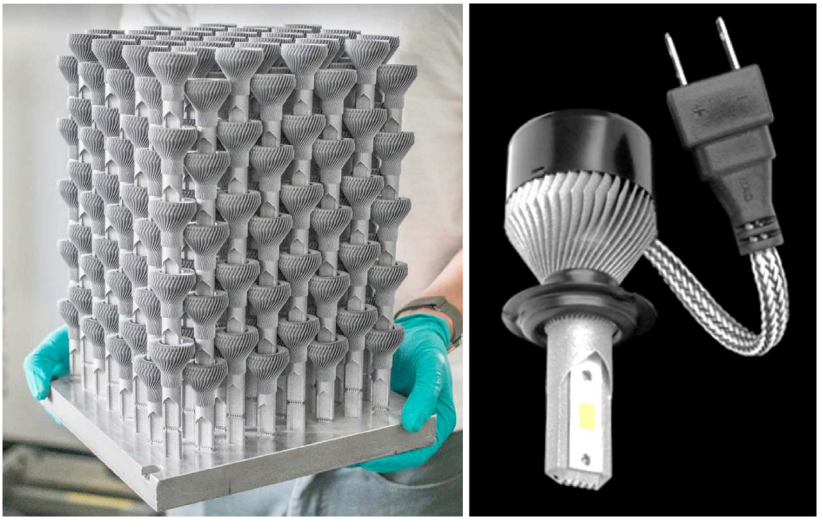

Figure 21.8 Production build of 384 heatsinks (left), LED headlight with L-PBF heatsink (right), Betatype (https://www.betaty.pe/case-studies/automotive-headlights/).

from £30 and reduces build times from 444 to 30 h. Newer machines with multiple lasers further decrease the build time to 19 h (https://www.betaty.pe/case-studies/automotive-headlights/).

21.2.3 Energy sector

One example in the energy sector developed by the company Siemens is the 3D printing of turbine vanes. DREWAG AG, a municipal utility in the German town of Dresden, operates a 25-year-old combined-cycle power plant with three Siemens V64.3 gas turbines. As part of a comprehensive lifetime extension and modernization upgrade, Siemens Energy replaced conventional turbine vanes with 3D-printed ones.

The project consists of two stages: phase 1 focused on the reproduction of the vanes in the original design, while in phase 2 improved, redesigned vanes will be installed. The initial phase has already brought remarkable results: The vanes—produced by Materials Solutions, a Siemens company—are characterized by high accuracy and show an excellent operational behavior after nearly 8000 operating hours. The new generation of vanes, that will be installed in June 2021, have an advanced air cooling design, that can contribute to increased efficiency and decreased emissions (https://www.siemens-energy.com/global/en/news/key-topics/additive-manufacturing.html).

Another impressive example this time provided by Materials Solutions is the additively manufactured turbine blade of the SGT-400 gas turbine reducing costs by 70% and cutting lead times by 75% (Siebold, 2019). Since 2016, burner components for gas turbines of the SGT-1000F type have been manufactured on a commercial scale in additive production. In 2013 burner tips for SGT-700 (Fig. 21.9) and SGT-800 gas turbines were repaired on a commercial scale using AM. Only the damaged area of the torch tip is cut off and then reprinted. This reduces repair time by around 60%. Since 2017, the burner rigs have been redesigned for AM reducing the parts from 13 to 1, eliminating 18 welding operations and increasing functionality by including the gas supply as part of the burner head, resulting in longer service life. Another application is the supply of spare parts. Components of various turbines were conventionally manufactured in an investment casting process. However, the annual spare parts requirement for these components is rather low and varies greatly. Furthermore, even small improvements would require new casting molds. It proved to be more economical to switch production to AM offering maximum supply security without expensive warehousing.

21.2.4 Medical industry

L-PBF offers economic advantages for individualized patient-specific and low-cost production of medical device products, and BEGO is one industrial example for dental implants made by L-PBF. BEGO GmbH is a German company specialized in dental products for over 100 years and now operating worldwide. The conventional method for the manufacturing of dental implants is the lost wax process. With L-PBF, customers send BEGO an STL file of the mouth scan of their patient and after examination

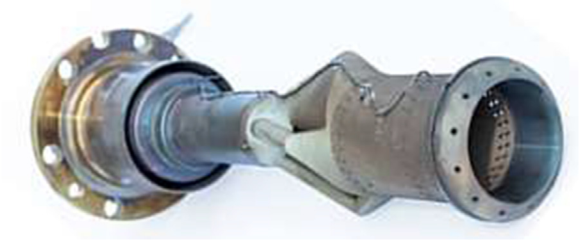

Figure 21.9 3D Gas burner from Siemens for the SGT-700 gas turbine in the E.ON-GuD power plant Philippsthal (Siebold, 2019).

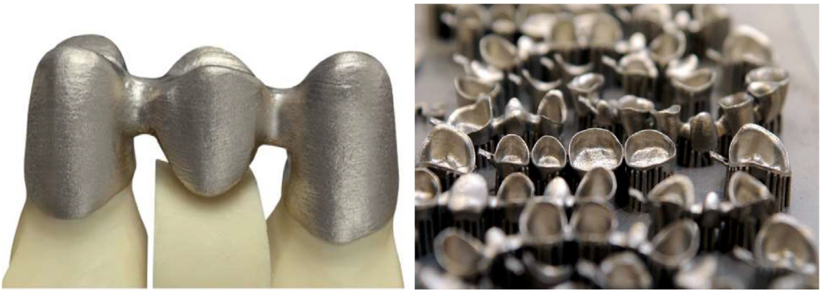

Figure 21.10 Three-unit bridge manufactured by BEGO USA using the material "Wirobond C+" (left) and 3D-printed dental implants still attached to the build plate with support structures (right) (https://www.eos.info/01_parts-and-applications/case_studies_applications_parts/_case_studies_pdf/de_cases/cs_m_medical_begousa_de.pdf).

of the data the crown is manufactured by L-PBF and delivered within 48 h. The precision of the dental implants is between ±20 μm and the dentures are durable, efficient, and of consistently high quality (Fig. 21.10).

Another medical industrial example is the American company DePuy Synthes Spine which is printing cellular titanium implants featuring 80% porous macro-, micro-, and nanostructures and 500−700 μm pore size range to mimic the cortical and cancellous bone (Fig. 21.11).

Leading research institutions, industrial players, and small and medium enterprises (SMEs) form the consortium AGENT-3D as a strategic alliance for research, innovation, and growth in Germany with over 100 partners. The AGENT-3D "Osseo-Distrakt" project addresses the Additive Manufacturing of fully individualized mandibular distraction systems. Based on a digital workflow, starting with 3D diagnostics of the existing anatomical structures followed by software-supported 3D

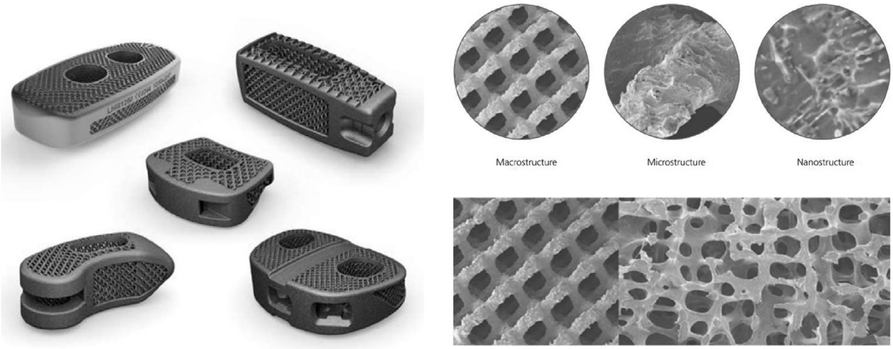

Figure 21.11 Bone-mimicking cellular titanium implants by DePuy Synthes spine (left) and pore structures on different scales (right) (https://www.jnjmedicaldevices.com/sites/default/files/user_uploaded_assets/pdf_assets/2019-05/Conduit%20Interbody-%20EIT%20Sales%20Sheet.pdf).

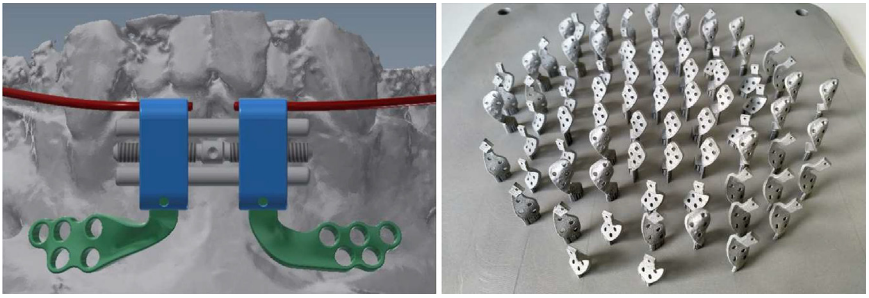

Figure 21.12 Model of the mandibular distraction system with AM part (left), mandibular distraction parts manufactured by L-PBF (right).

therapy planning, patient-specific distractor models were designed and manufactured using L-PBF in Ti6Al4V ELI. A two-stage post-treatment route consisting of vibratory grinding followed by vibratory polishing, electro polishing, or plasma polishing was suitable for achieving a requested surface quality. Biocompatibility tests showed an increased vanadium concentration with toxic effect in the samples post-treated by plasma polishing, characterized by a lower cell adhesion and a lower cell growth (Bernhardt et al., 2021) (Fig. 21.12).

21.3 Hybrid manufacturing with Laser Powder Bed Fusion

Hybrid manufacturing represents the combination of multiple manufacturing processes to build a final part. One example of implementing hybrid manufacturing in AM is addressed in the Agent3D project "Improve." In that project a functional injection mold insert was manufactured whose heat dissipation from the corner areas is considerably improved and homogenized over the entire surface by means of the inserted copper cores (manufactured by Laser Metal Deposition with a 515 nm green laser source) and near-shape cooling channels (manufactured by L-PBF) and additional conventional processes such as milling and hardening (Fig. 21.13).

21.4 Future potential industrial applications of L-PBF and applied research trends

Some materials have been challenging in processing with commercial laser systems. Pure copper is one of them, since the absorptivity is very low in the infrared wavelength. The Fraunhofer IWS is conducting research using a green laser system at 515 nm enabling the processing of pure copper almost defect-free (Fig. 21.14) due to higher absorptivity in shorter wavelength ranges. The resulting electrical conductivity is close to 58 MS/m and therefore close to 100% of the International Annealed

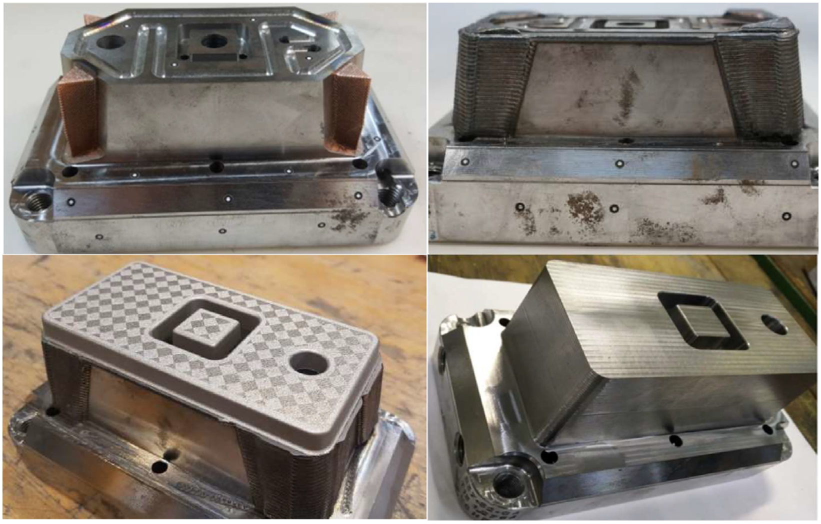

Figure 21.13 Demonstrator with copper cores (upper left) and with steel cladding and leading edge for L-PBF (upper right), L-PBF of the steel top cover with cooling channels (bottom left) and finishing of the demonstrator surface with machining allowance (bottom right).

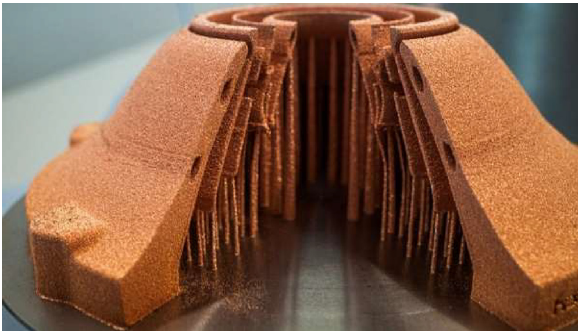

Figure 21.14 COAXshield nozzle manufactured from pure copper with L-PBF using a green laser source.

Copper Standard (IACS). It enables designing complex components made of pure copper and copper alloys for the aerospace and automotive industry and increases the efficiency of electric motors and heat exchangers. It can also be seen that companies form alliances to increase market shares on this topic.

Siemens and HP have partnered in one of those alliances. The solution from Siemens and HP integrates hardware, software, data intelligence, and services, making the entire manufacturing process more efficient. Combining the digital twin of product, production and performance with the MindSphere cloud solution enables automotive and industrial customers to produce high-quality 3D printed parts in medium volumes faster, with unique product designs, new applications, and in digital factories (https://new.siemens.com/global/en/company/stories/industry/hp-3d-printer-additive-manufacturing.html).

Another network is "Mobility Goes Additive" acting as a central platform bundling the value creation potentials along the process chain and promoting the mutual development of its members' competencies. More than 100 international member companies from all parts of industry are working in various working groups to develop appropriate solutions. The main challenges in the future will be increasing productivity through integrating more laser sources, smart positioning and orientating, increasing the productivity, and increasing the build space.

21.5 Questions

- Name industrial applications of L-PBF in aerospace.
- What is the largest topology optimized part manufactured and used in a final commercial application?
- Why is heatsink development for LED lights better using L-PBF—what is the advantage?
- Why are certain materials hard to process and how can the integration of other laser sources in other wavelength ranges improve the part quality?
- Name further sectors which you think will be producing industrial AM parts in the next 5−10 years.

Acknowledgements

The authors acknowledge German federal ministry of education and research for funding within the program "Zwanzig20—AGENT-3D," the European Space Agency for support during all related projects, and the Fraunhofer Society.

References

Bernhardt, A., Schneider, J., Schroeder, A., Papadopoulous, K., Lopez, E., Frank, B., Botzenhart, U., 2021. Surface conditioning of additively manufactured titanium implants and its influence on materials properties and in vitro biocompatibility. Mater. Sci. Eng. C 119, 111631. https://doi.org/10.1016/j.msec.2020.111631. ISSN 0928-4931.

Buchholz, M., Gloder, A., Gruber, S., Marquardt, A., Meier, L., Müller, M., Propst, M., Riede, M., Selbmann, A., Sieder-Katzmann, J., Tajmar, M., Bach, C., October 12−14, 2020. Developing a roadmap for the post-processing of additively manufactured aerospike engines. In: 71st International Astronautical Congress (IAC) − The CyberSpace Edition.

Du Plessis, A., Broeckhoven, C., Yadroitsava, I., Yadroitsev, I., Hands, C.H., Kunju, R., Bhate, D., 2019. Beautiful and functional: a review of biomimetic design in additive manufacturing. Addit. Manuf. 27, 408−427. https://doi.org/10.1016/j.addma.2019.03.033. ISSN 2214-8604.

Eberle, S., Reutlinger, A., Bailey, C., Mueller, M., Riede, M., Wilsnack, C., Brandão, A., Laurent, P., Seidel, A., López, E., Frank, B., Beyer, E., Leyens, C., July 12, 2019. Additive manufacturing of an AlSi40 mirror coated with electroless nickel for cryogenic space applications. In: Proc. SPIE 11180, International Conference on Space Optics — ICSO 2018, p. 1118015.

Fuhrmann, T., Mewes, B., Kroupa, G., Lindblad, K., Dorsa, A., Matthijssen, R., Underhill, K., 2019. FLPP ETID: TRL6 Reached for Enabling Technologies for Future European Upper Stage Engines.

Howell, L.L., Magleby, S.P., Olsen, B.M., 2017. Fabrication methods of compliant mechanisms. Procedia Eng. Bd. 181, 221–225. https://doi.org/10.1016/j.proeng.2017.02.377 [Handbook of Compliant Mechanisms. John Wiley & Sons, 2013] or milling and turning with fine tools [D. Lateş, M. Căşvean, und S. Moica].

Lateş, D., Căşvean, M., Moica, S., 2017. Fabrication methods of compliant mechanisms. Procedia Eng. 181, 221–225. https://doi.org/10.1016/j.proeng.2017.02.377. ISSN 1877-7058.

Müller, M., Riede, M., Eberle, S., Reutlinger, A., Brandão, A.D., Pambaguian, L., et al., 2019. Microstructural, mechanical, and thermo-physical characterization of hypereutectic AlSi40 fabricated by selective laser melting. J. Laser Appl. 31 (2), 22321. https://doi.org/10.2351/1.5096131.

Siebold, M., May 1, 2019. Additive manufacturing for serial production of high-performance metal parts. ASME. Mech. Eng. 141 (05), 49–50. https://doi.org/10.1115/1.2019-MAY5.

Willner, R., Lender, S., Ihl, A., Wilsnack, C., Gruber, S., Brandão, A., et al., 2020. Potential and challenges of additive manufacturing for topology optimized spacecraft structures. J. Laser Appl. 32 (3), 32012. https://doi.org/10.2351/7.0000111.

Wischeropp, T.M., Hoch, H., Beckmann, F., Emmelmann, C., 2019. Opportunities for braking technology due to additive manufacturing through the example of a Bugatti brake caliper. In: Mayer, R. (Ed.), XXXVII. Internationales μ-Symposium 2018 Bremsen-Fachtagung. Proceedings. Springer Vieweg, Berlin, Heidelberg. https://doi.org/10.1007/978-3-662-58024-0_12.

Wohlers Report, 2020. 3D Printing and Additive Manufacturing State of the Industry. ISBN 978-0-9913332-6-4.

Economic feasibility and cost-benefit analysis

22

Martin Leary
Centre for Additive Manufacturing, School of Engineering, RMIT University, Melbourne, VIC, Australia

Chapter outline

22.1 Introduction 598
22.2 Technology fundamentals 599
  22.2.1 Effective design processes 599
  22.2.2 The paradox of design flexibility and understanding 599
  22.2.3 Evolutionary and revolutionary design scenarios 600
  22.2.4 Defining system quality with process capability indices 600
  22.2.5 Net-shape and near-net-shape manufacturing 601
  22.2.6 Topology optimization and generative design 601
  22.2.7 The management of technical risk by parts consolidation 602
22.3 Cost-benefit fundamentals 602
  22.3.1 Cost versus production volume 602
  22.3.2 Cost versus complexity 604
  22.3.3 Cost-price-value 604
22.4 Commercial opportunities for assumed cost-independence of L-PBF 605
  22.4.1 Batch-enabled scenarios 605
  22.4.2 Complexity-enabled scenarios 607
  22.4.3 Ultra-high-complexity scenarios 607
  22.4.4 Integrated cost and volume opportunities 607
22.5 L-PBF disruption to classical engineering economics 608
  22.5.1 Flexibility of traditional methods 608
  22.5.2 Cost-independence of AM—low-volume influence 609
  22.5.3 Cost-independence of AM—high-volume influence 609
22.6 Nuanced view of L-PBF economics 611
  22.6.1 Aerospace components for high-complexity, medium-volume applications 612
    22.6.1.1 Project implementation 612
  22.6.2 Bespoke medical implants 613
    22.6.2.1 Clinical implementation of patient-specific implant 614
    22.6.2.2 Generative design system 614
  22.6.3 Bespoke medical fasteners 615
  22.6.4 High-value, low-volume product design evolution 616
22.7 Concluding remarks 617
22.8 Questions 618
Acknowledgements 619
References 619

Fundamentals of Laser Powder Bed Fusion of Metals. https://doi.org/10.1016/B978-0-12-824090-8.00022-6
Copyright © 2021 Elsevier Inc. All rights reserved.

22.1 Introduction

Laser Powder Bed Fusion (L-PBF) technology is technically mature, and represents an opportunity for radical change in the quality and affordability of high-value commercial products. This opportunity is increasingly demonstrated by innovative design outcomes within a range of technological domains, including aerospace and medical (Fig. 22.1); this includes application scenarios that are technically challenging or economically prohibitive for traditional manufacturing methods.

It is evident that these L-PBF production opportunities provide the potential for significant competitive advantage, both by enabling increased functional performance and by the potential to reduce overall product cost. Despite this opportunity, uncertainties exist as to the specific technical and economic characteristics that determine commercial success in a production environment. This uncertainty results in either a limited confidence to invest in commercial L-PBF product development (potentially resulting in missed or overlooked commercial opportunities) or investment in poorly conceived projects (resulting in commercial loss and mistrust in future L-PBF investment).

This chapter provides strategic insight into the economic feasibility of commercial L-PBF applications. This insight enables technology developers and commercially focused research engineers to confidently make investment decisions that are technically and commercially sound, thereby allowing for commercially sound technology application. To achieve this objective of a technically aware cost-benefit analysis for L-PBF technology, a fundamental understanding of both the technical and economic aspects of relevance to successful L-PBF applications is presented.

It is intended that, by stating the fundamental truths relevant for both engineering and economic analyses, a harmonized common understanding will be developed.[1]

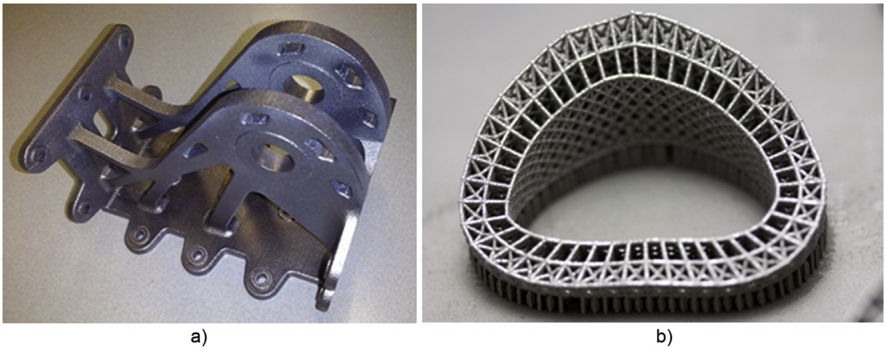

Figure 22.1 L-PBF applied to the manufacture of high-value products in (a) aerospace brackетry (Section 22.6.1) and (b) patient-specific medical applications (Section 22.6.2).

---

[1] Engineering designers may find the technology summary to be somewhat redundant, and will likely skip to the economic analysis, vice-versa for economic analysts.

Based on these areas of commonality, contemporary methods of L-PBF economic analysis are presented, including the typically asserted but somewhat simplified regions of positive cost-benefit. These simplified economic analyses are then further assessed to identify potential flaws and to propose more robust approaches of economic cost-benefit analysis for L-PBF applications.

22.2 Technology fundamentals

The commercial development of high technology products has been the focus of extensive research in both technical and commercial domains. See, for example, Dodgson et al. (2008), Rodgers and Milton (2013), Pahl and Beitz (2013). Of this available research, the following key topics have been selected to educate economic analysts as to the pertinent technical aspects of L-PBF production: fundamentals of effective design processes; the paradox of design flexibility and understanding; evolutionary and revolutionary design scenarios; defining system accuracy by process capability indices; adding value by net- and near-net-shape manufacturing; topology optimization and generative design; and the management of technical risk by parts consolidation.

22.2.1 Effective design processes

The engineering design process refers to decision-making strategies that enable efficient implementation of customer requirements in an engineered product. Although proposed models of engineering design vary in their specific implementation, they typically include some sequential phases of embodiment design, detail design, and manufacture (Pahl and Beitz, 2013; Wu et al., 1988).

22.2.2 The paradox of design flexibility and understanding

A common observation of engineering design is that the decisions of the early design phase accrue relatively little cost; however, these decisions commit costs of manufacture and therefore reduce flexibility (Fig. 22.2, left). As the design progresses, the design team increases their understanding of the design problem, but, paradoxically, the flexibility to act on this increased understanding is diminished, thereby introducing risks to successful product deployment (Fig. 22.2, right). Compared with traditional manufacturing methods (which require custom tooling and input material) L-PBF allows flexibility to be retained for longer in the project timeline, thereby allowing the design team greater opportunity to respond to design opportunities and challenges as they arise.

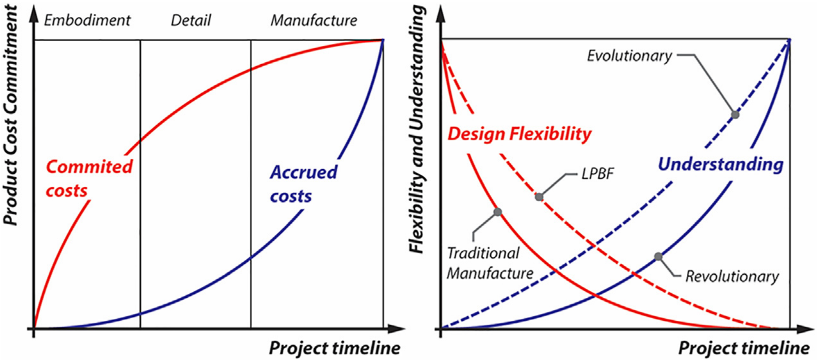

Figure 22.2 Product cost commitment (left) and design flexibility and understanding (right) as a function of project timeline. Axes shown in normalized not absolute scale.

22.2.3 Evolutionary and revolutionary design scenarios

Design scenarios may be categorized as either *evolutionary* or *revolutionary* according to whether the design involves relatively well-understood methods and processes or involves aspects that are novel or previously untested. This categorization assists in managing commercial risks, where both revolutionary and evolutionary designs exhibit a specific risk profile. Revolutionary designs are associated with higher risk of commercial success, but, if successful, enable a valuable commercial monopoly. Conversely, evolutionary products involve less risk to successful product deployment, but are subject to the commercial risk associated with significant competition and relatively low-profit margin. In terms of the paradox of design flexibility and understanding, revolutionary design scenarios may be expected to present a lower level of design certainty in comparison to evolutionary scenarios (Fig. 22.2).

22.2.4 Defining system quality with process capability indices

Product quality can be defined as the "degree to which a set of inherent characteristics fulfills requirements" (ISO 9000:2005). Measurable characteristics of relevance to product quality are formally defined as Key Product Characteristics (KPC) (Mathieu and Marguet, 2001). Quality engineered products are therefore associated with an allowable KPC range, specified in terms of Upper and Lower Specification Limits (USL, LSL). The ability for a manufacturing process to satisfy a defined process limit is statistically characterized by a Process Capability Index (PCI) (Montgomery, 2001). This PCI formally defines the relevant capabilities of the manufacturing process, for example, L-PBF, and is used to estimate the production *yield*, or expected percentage of manufactured product that satisfies the associated KPC (Fig. 22.3).

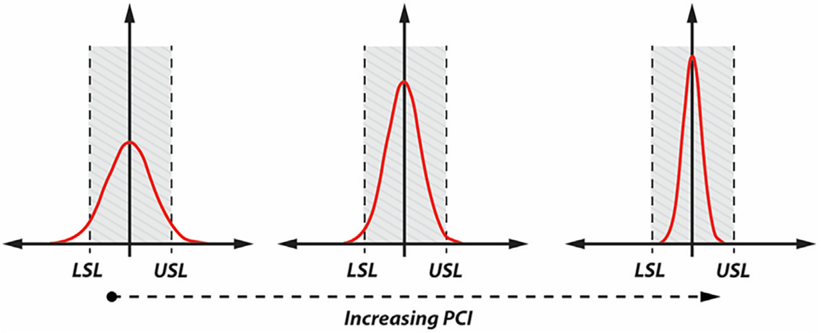

Figure 22.3 Process Capability Index (PCI) defines the ability of a manufacturing process to satisfy the associated upper and lower specification limits (USL, LSL).

22.2.5 Net-shape and near-net-shape manufacturing

Net-shape manufacture refers to a manufacturing process that is entirely capable of satisfying the production KPC without the need for secondary processing, for example, surface finishing or the machining of interacting surfaces. Net-shape manufacture is commercially valuable as cost overheads are reduced; both in terms of the reduced direct costs of secondary processing and the costs associated with managing and certifying these additional processing stages. The complexity enabled by L-PBF provides an opportunity to enable net-shape manufacturing, even for geometrically complex designs. However, technical challenges may necessitate minor secondary processing, resulting in *near-net-shape* outcomes.

22.2.6 Topology optimization and generative design

Engineering design procedures seek to identify the combination of material selection, manufacturing processes, and component geometry that optimizes functional outcomes within the available design time and budget. As design complexity increases, so does the effort required to implement this optimization due to the substantial increase in the number of possible design solutions, an attribute known formally as *dimensionality*. In fact, the challenge of optimizing complex problems is referred to as the "curse of dimensionality." This "curse" is particularly debilitating for revolutionary design scenarios and can readily compromise the ability for a design team to successfully implement high-complexity design. Technical design tools have evolved in response to these challenges, and of particular interest are methods of topology optimization and generative design.

Topology optimization refers to algorithmic methods that seek to identify a topology[2] that optimizes functional requirements—a capability that is invaluable for identifying effective geometry in the presence of high dimensionality. Generative design refers to “the rules for generating form, rather than the forms themselves” (Frazer, 2002). Generative design systems are deployed to provide algorithmic solutions to complex design problems. Generative design can be challenging to implement, especially for revolutionary design scenarios; and are economically feasible only for scenarios where the production volume is sufficient to adequately offset the costs of developing and commissioning the generative design system (Leary, 2019).

---

[2] *Topology* refers to the connectivity between locations of a physical object as distinct to the *geometry* of local features within this topology.

22.2.7 The management of technical risk by parts consolidation

Formal philosophies of technical risk management are accommodated by strategies such as Failure Modes and Effects Analysis (FMEA) that seek to identify and mitigate technical risks of product failure. These risk management tools place a priority on failure that incurs a safety consequence, followed by economic consequences according to their associated magnitude. The failure modes associated with part interactions include a failure to initiate and maintain fastener tension, leakage of fluid connections, and galvanic corrosion due to the chemistry of dissimilar material interactions. These failure modes can be eliminated by *parts consolidation*, whereby multiple distinct components are fabricated concurrently. This technical design strategy enables enhanced commercial advantage by enabling further mass reduction due to the mechanical efficiency of integrated structural connections as well as being subject to fewer spatial constraints due to the reduced need for assembly access and tooling. The geometric complexity enabled by L-PBF provides an important commercial opportunity for reducing technical risk by the consolidation of multiple components.

22.3 Cost-benefit fundamentals

Classical engineering economics provides a systematic and approachable basis for the assessment of the economic feasibility of a proposed design in terms of the relevant economic attributes. The following aspects of engineering economics are especially useful in classifying the commercial performance of L-PBF systems (Yates, 2016; Marnell, 2016; Whitman and Terry, 2012): cost-volume modeling and the influence of fixed and variable costs; cost-complexity modeling; concepts of cost, price, and value; and the assumed cost-independence of AM technologies. These concepts are briefly introduced to assist AM design engineers to become familiar with the fundamental economic concepts of relevance to commercially successful L-PBF applications.

22.3.1 Cost versus production volume

Cost-Volume-Profit (CVP) methods formally quantify the effect of variation in production volume on the profitability of a specific manufacturing scenario. Typical cost-volume representation implies that costs decrease asymptotically as production volume increases. This cost reduction occurs as the fixed production costs (for example, associated with product design, tooling, and commissioning) are assumed to be constant and are then amortized over an increasing number of manufactured units. Overall part cost then asymptotes toward the *defrayed variable cost* that is essentially the variable production costs (energy, labor, and material input) per unit of production.

$$P(n) = pn - (bn + a) = (p - b)n - a$$

$$\frac{P(n)}{n} = C(n) = \frac{(p - b)n - a}{n} = (p - b) - \frac{a}{n}$$

$$C(n) \rightarrow (p - b),\ \text{for}\ n \rightarrow \infty$$

where:
$P(n)$ = total profit [\$]
$C(n)$ = unit-cost [\$]
p = unit price [\$]
n = quantity sold
b = unit-cost [\$]
a = fixed costs [\$]

The deterministic CVP approach is based on assumptions that are appropriate to provide insight into the fundamental interactions between production volume and unit-cost, resulting in an *economy of scale* with increasing production volume (Fig. 22.4). In practice it may be observed in production environments that some disruption of this relationship occurs. This disruption may be due to a number of effects that are in practice nonlinear, thereby resulting in some "diseconomy of scale." These effects include the technical challenges associated with accommodating product complexity—a highly relevant L-PBF design attribute that is often challenging to incorporate in traditional CVP modeling.

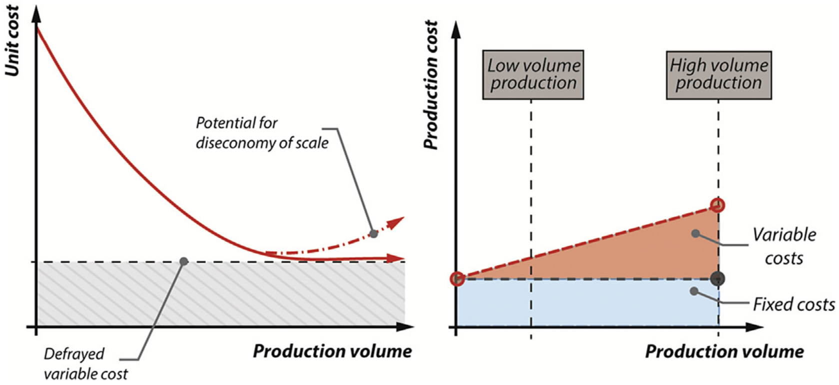
Unit cost
Potential for diseconomy of scale
Defrayed variable cost
Production volume
Production cost
Low volume production
High volume production
Variable costs
Fixed costs
Production volume

Figure 22.4 Schematic representation of deterministic CVP relationship, including the potential for diseconomy of scale (left). As production volume increases, fixed costs are amortized over an increasing number of products (right) and costs tend to the defrayed variable cost.

22.3.2 Cost versus complexity

Product complexity directly influences the effort and time required to reliably manufacture and certify the intended product. As product complexity increases, design effort and other fixed costs increase, as do variable costs due to increased scrap rates and inspection challenges. These increased costs directly result in higher unit-cost with increasing product complexity. Characterization of the impact of complexity on product cost is challenging due to the elusive nature of a definition of complexity.

In order to provide clear economic guidance, models for cost-complexity relationships can be implied from established economic models of the cost incurred by a required precision tolerance; where geometric precision is considered to be analogous to complexity. These models provide an exponential relationship that can be fit to observed (or predicted) data for a specific design application (Fig. 22.5), and can be truncated to accommodate the allowable technical limits of complexity inherent in a specific manufacturing process (ISO 9000:2005; Mathieu and Marguet, 2001):

$$g(X) = Ze^{-\phi(X-X_0)} + g_0,$$

Where $g(X)$ = unit-cost associated with specific complexity [$];
X = product complexity;
$X_{\min} \leq X \leq X_{\max}$, limits of complexity;
g_0 = minimum threshold cost [$];
X_0 = minimum threshold tolerance;
Z, ϕ = curve fitting parameters.

22.3.3 Cost-price-value

A fundamental economic balance must be satisfied for a product to be economically successful. This balance requires specifically that the product *cost*, C, must be less

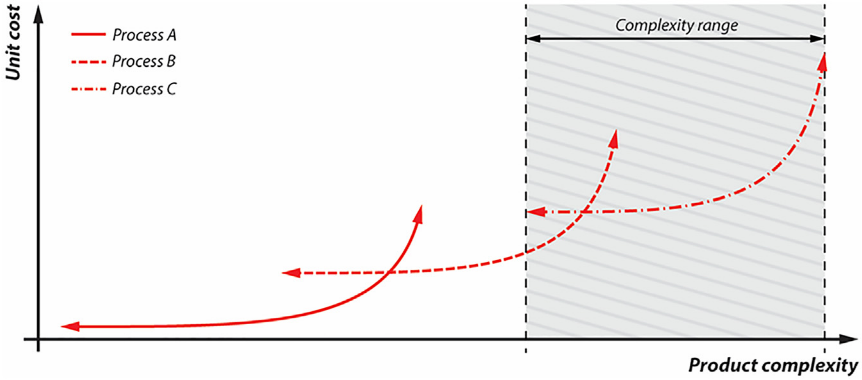

Figure 22.5 Proposed cost-complexity model representing the exponential cost increase associated with increased product complexity. Various production processes shown, each of which is associated with an allowable complexity range and with a specific unit-cost for a given complexity.

than the *price*, P_r, at which the product is made available to the customer, implying that the operation is economically sustainable. Concurrently, the price at which the product is made available must always be lower than the *value*, V, of the product to the customer, implying that the customer is willing to purchase the product: $C < P_r < V$.

This simple inequality for economically sustainable product design provides the design engineers and production economists with a common language to strategically assess the influence of design decisions on economic sustainability. Costs to be considered are all expenses incurred in the deployment of the product to the customer. Value includes all aspects that are relevant to the customer requirements, including the primary functional requirements, time of delivery, reliability, and influence on associated costs. Economic flexibility is greatest when the product value is maximized and product cost is minimized. L-PBF technologies provide an opportunity to achieve both of these outcomes. For example, reduced costs for low-volume production of specialized product (Section 22.6.3), and enhanced value for medical implants by reducing surgical time and increasing the compatibility of the implant to the patient (Section 22.6.2).

22.4 Commercial opportunities for assumed cost-independence of L-PBF

The economic response modeled thus far is based on observations that are appropriate for traditional manufacturing methods. AM processes are fundamentally distinct to traditional manufacturing (Petrick and Simpson, 2013). In particular, the *digital* nature of AM design, coupled with the use of a *common source material*, is often reported to fundamentally affect the observed economic response, specifically that costs are observed to be independent of both complexity and volume (DebRoy et al., 2019; Serena et al., 2017). This simplified representation can provide misleading guidance (as presented in Section 22.5) but is valuable in demonstrating the fundamentally distinct nature of L-BPF, allowing zones of economic opportunity to be systematically identified, including batch-enabled, complexity-enabled, and ultra-high-complexity enabled scenarios (Fig. 22.6).

22.4.1 Batch-enabled scenarios

Batch-enabled scenarios occur for relatively low production volumes where the unit-costs associated with AM are less than for traditional manufacture. This zone is primarily due to the cost-differential associated with the fabrication of fixtures and forms required for traditional manufacturing methods. Conversely L-PBF methods enable rapid production of high-value products directly from the associated digital design data. For example, L-PBF provides a cost optimal manufacturing method for custom sports equipment that are of high-complexity and with relatively low-production volume (Fig. 22.7).

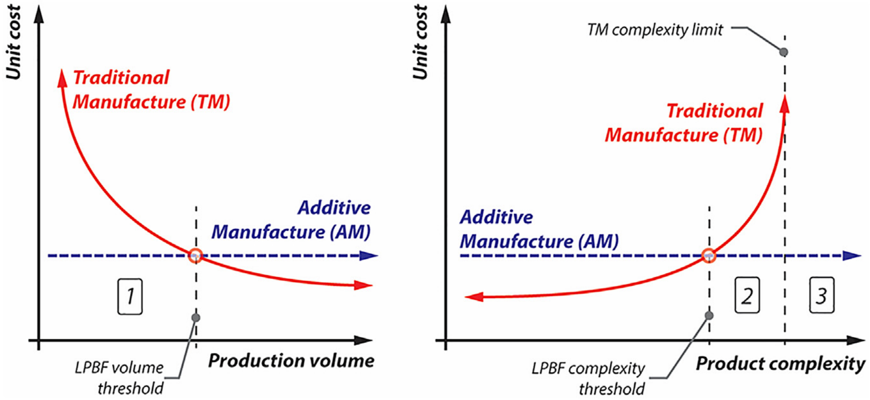

Figure 22.6 Schematic curves of unit-cost versus production volume and product complexity. AM process costs are based on the assumption of AM cost-independence. Zones of economic opportunity: (1) batch-enabled, (2) complexity-enabled, and (3) ultra-high-complexity enabled.

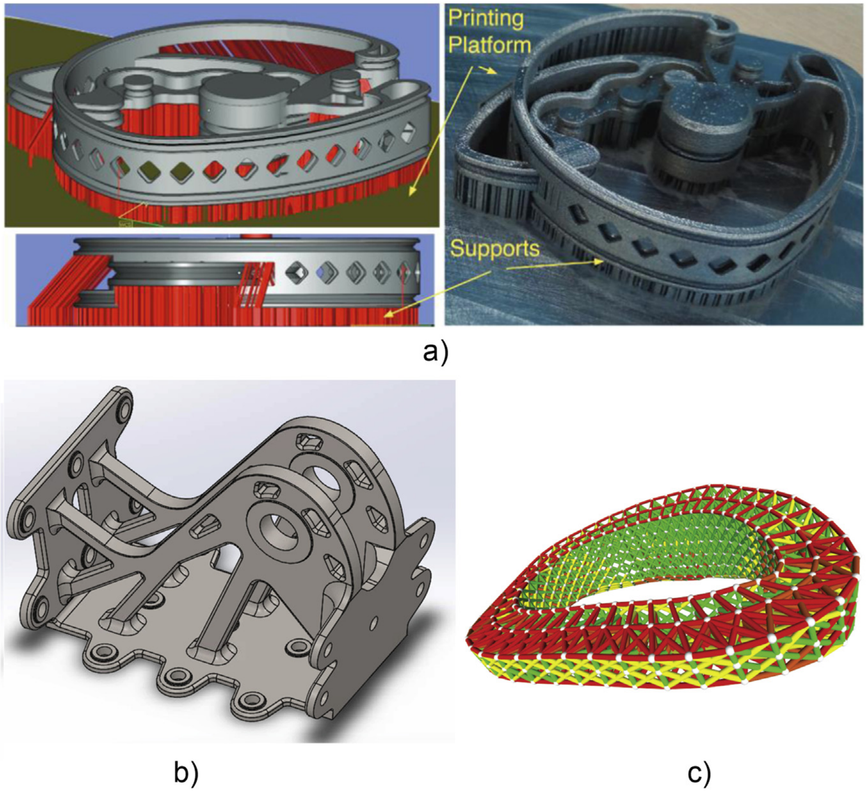

Figure 22.7 Laser powder bed fusion applied to cost optimal scenarios (a) batch-enabled application (niche consumer products for archery applications) (DebRoy et al., 2019; Serena et al., 2017), (b) complexity-enabled (aerospace bracket), (c) ultra-high-complexity-enabled application (patient-specific medical implant).

22.4.2 Complexity-enabled scenarios

L-PBF technology accommodates high-complexity with lower unit-cost than traditional manufacture (Section 22.3). This economic assessment may be made directly from an understanding of the cost-complexity relationships associated with the L-PBF technology and the incumbent traditional manufacturing method. This opportunity enables commercially competitive design applications for which the complexity required for correct product function is economically challenging for traditional manufacture. As an example, the fabrication of high-complexity aviation hinge bracketry can be challenging for traditional manufacturing methods and provides a commercial opportunity for L-PBF production (Fig. 22.7a and b).

The high level of achievable complexity associated with L-PBF technologies can be utilized to enable commercial opportunities that are not technically feasible with traditional manufacturing processes. Particular commercial opportunities include parts consolidation, whereby an initially complex assembly of components is simplified to a single L-PBF component. This parts consolidation opportunity can add value to an engineered product in several ways—firstly by reducing the overall costs associated with the individual components; secondly, by reducing the necessity for parts assembly; and thirdly by adding value by reducing the risk of failure modes associated with assembly; for example, leakage of assembled fittings or stress concentration of mechanical joints.

22.4.3 Ultra-high-complexity scenarios

Laser powder bed fusion technology can fabricate structures with sufficient complexity as to be entirely impossible with traditional manufacturing methods. These scenarios are commercially important, as they are potentially solvable by L-PBF methods only, thereby providing a commercial monopoly. These emerging commercial opportunities are gradually becoming established in the marketplace, with examples including high-complexity medical implants and thermal systems (Fig.22.7c).

These ultra-high-complexity scenarios are often associated with a substantial commercial risk associated with product failure. These risks can be, for example, associated with blockage of complex heat exchangers, such as when applied to safety-critical aviation applications, and the design of patient-specific medical implants subject to dynamic loading and in-vivo environmental conditions. The costs associated with the systematic design, quality control, and certification of high-complexity products should not be underestimated, and must be accounted for. Advanced design methodologies such as generative design and topology optimization provide an opportunity to manage the challenges of high-complexity L-PBF design.

22.4.4 Integrated cost and volume opportunities

The commercial opportunities discussed in the previous section do not accommodate the economic advantage of satisfying both cost-volume and cost-complexity opportunities simultaneously. L-PBF applications that are economically optimal due to complexity considerations are potentially associated with relatively small production volumes. These high-complexity, low-volume production scenarios receive an amplified commercial benefit and are potentially lucrative; however, the required design effort can readily exceed the allowable cost budget, resulting in economically failed design. This risk can be mitigated by algorithmic design methods; for example, generative design is applied for the mass-customization of L-PBF medical implant devices in Section 22.6.2.

22.5 L-PBF disruption to classical engineering economics

The L-PBF process potentially disrupts classical concepts of engineering economics, enabling commercial opportunities that may be unexpected from a classical perspective. Although the simplified representation of Fig. 22.6 is valuable in demonstrating the fundamentally distinct nature of L-PBF, it can provide misleading guidance on the economic cost-benefit, thereby compromising the commercial success of a proposed project. The following arguments illustrate these nuanced behaviors in order to provide robust L-PBF cost-benefit prediction and to protect commercial design teams from the associated pitfalls of the simplified AM cost model, as well as to identify commercial opportunities that may be overlooked by less experienced design teams. Specific economic opportunities enabled by these outcomes are described below, including the opportunity for continual product development and generative design.

22.5.1 Flexibility of traditional methods

The assumption of cost-independence of AM systems is prevalent. The associated rationale is based on the relatively high fixed costs incurred by the tooling necessary for traditional forging and casting methods of manufacture. Conversely, AM systems obviate the need for custom tooling[3]. This assumption enables rapid insight into the primary differences between traditional manufacturing operations and L-PBF technologies. However, the contribution of capital tooling costs to unit-cost varies according to the classification of manufacturing processes, even for traditional manufacturing (Fig. 22.8).

Formative processes, such as casting and forging, enable high production rate by the use of custom tooling to impose a standard geometry on input materials. Formative processes are typically associated with low complexity and large production volumes in order to offset high tooling costs, meaning that these methods are not appropriate for low-volume production. While AM technologies are not competitive with formative methods in term of production rate, AM does not require custom tooling—thereby enabling low unit-costs at low production volume. However, it is important to note that *subtractive* methods, such as machining and sheet cutting, enable an economic

---

[3] L-PBF tooling costs are associated with the initial cost and refurbishment of consumable materials, specifically the build platen which may require resurfacing between production batches.

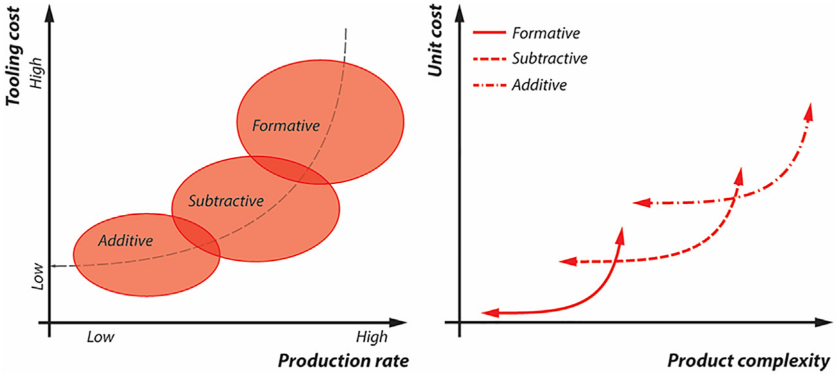

Figure 22.8 Left: A continuum of manufacturing processes rated schematically according to tooling cost and production rate. Right: Schematic representation of unit-costs and achievable production complexity.

compromise between formative and additive processes, whereby standard material stock (bar, plate, or billet) is numerically processed using standard machining tools. Subtractive processes enable production variability with relatively low tooling costs and can therefore provide a robust challenge to L-PBF for low-production volumes. For these scenarios it is necessary to also consider the technical feasibility of the process to identify optimal manufacturing process (Fig. 22.8).

22.5.2 Cost-independence of AM—low-volume influence

The assumption of cost-independence is useful to clarify the commercial benefit associated with AM technologies. However, caveats must be applied to uphold this assumption, primarily that none of the cost contributors be significantly influenced by reduced production volume. This assumption is appropriate for evolutionary scenarios where costs of design, machine use, and certification are relatively stable and predictable. The uncertainties associated with revolutionary design are more likely to result in variation in costs, resulting in a cost-volume relationship that is more closely approximated by the exponential relationship typically associated with traditional manufacture, although potentially with smaller variation (Fig. 22.9).

22.5.3 Cost-independence of AM—high-volume influence

Peak production volume is limited by the achievable production rate of the manufacturing process. L-PBF systems are subject to a lower production rate than equivalent formative processes, resulting in a lower achievable production volume (Fig. 22.10). A rational analysis of L-PBF production mode may therefore conclude that such processes are feasible only for relatively low production volumes.

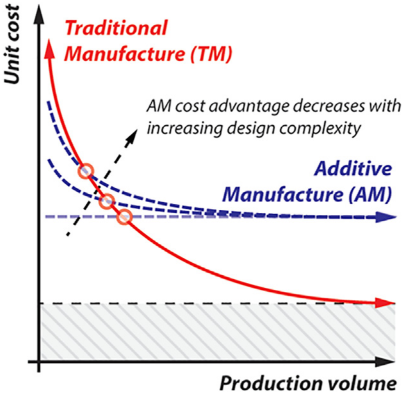

Figure 22.9 For low production volumes, the cost-independence assumption of AM is potentially flawed, leading to a potential decrease in the L-PBF cost advantage, especially for revolutionary design activities due to their increased design complexity.

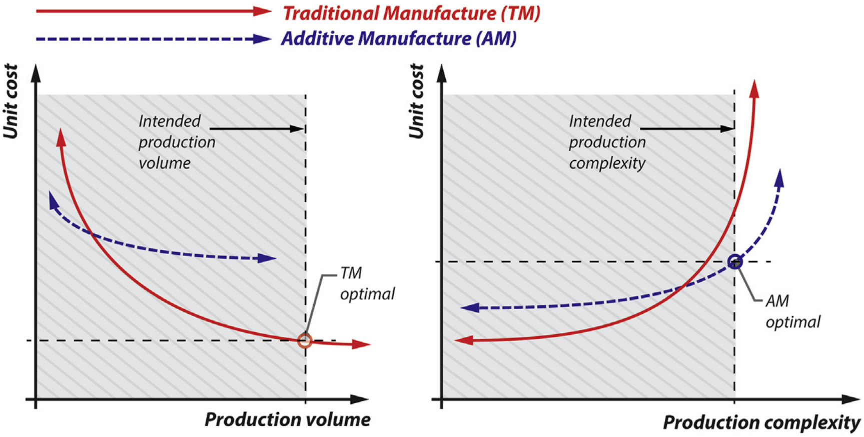

Figure 22.10 Schematic representation of a scenario where the intended product complexity is optimized by L-PBF processes, but the production volume appears to exceed the available resource.

An alternative economic analysis is also valuable: L-PBF systems are digitally controlled and can therefore be implemented as a *parallel batch system* (Fig. 22.11). This system utilizes individual L-PBF stations to amplify the overall production rate with the following complimentary advantages:

- The ability to allow *in-situ design evolution*, whereby the product design can be iteratively enhanced during production without requiring tooling modification.
- The ability to accommodate *serial-production*, whereby L-PBF is used to fabricate medium to large production runs of a single product.

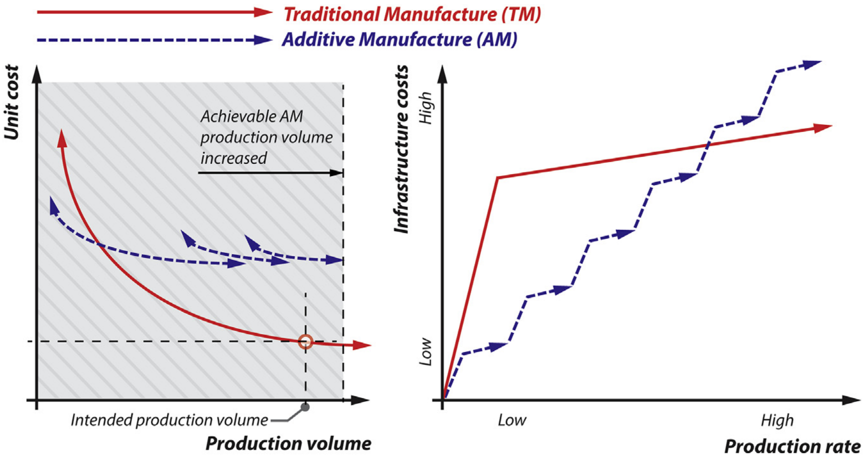

Figure 22.11 Parallel batch implementation of L-PBF systems enables the increased production rates required for increased production volume. Capital costs are incurred in a stepwise manner which reduces the capital investment required to initiate production.

- *Delayed cost of infrastructure*, whereby the additional infrastructure costs associated with parallel batch system may be borne incrementally, thereby managing costs for products with uncertain production volume.
- *Distributed manufacture*, whereby the physical location of the L-PBF hardware is located concurrently with the end-user to reduce lead-time and transportation costs.

22.6 Nuanced view of L-PBF economics

The nuanced economic response of L-PBF presented here identifies distinct commercial opportunities. These enhanced opportunities are potentially valuable, as they may have been overlooked by commercial analysts who apply only the simplified concepts of commercial AM economics. The following case studies provide examples of these enhanced commercial opportunities, specifically:

1. *High-complexity, medium-volume series production*. Whereby the complexity and material efficiency enabled by LBPF is utilized to compete with subtractive and formative methods for the design of low- to medium-volume production. For example, in the manufacture of aviation components with a high-value assigned to structural efficiency (Section 22.6.1).
2. *Ultra-high-complexity, mass-customization*. Whereby the ultra-high complexity enabled by L-PBF is combined with generative design methods to allow fabrication of implant structures that are automatically customized to specific patient requirements (Section 22.6.2).
3. *High-value, low-volume product design*. Whereby L-PBF technologies are applied to enable production of custom products. For example, the manufacture of high-value niche products fabricated at low volume (Section 22.6.3).

4. *High-value, bespoke product design*. Whereby L-PBF components are designed algorithmically according to predefined constraints and objectives. For example, in the design of patient-specific medical hardware either for prototyping or for clinical application in specialist surgical scenarios (Section 22.6.4).

22.6.1 Aerospace components for high-complexity, medium-volume applications

Aerospace components are subject to stringent weight limits, and substantial financial value is assigned to commercial technologies that can reduce component mass. Concurrently, production volumes for specialist structural components are relatively low. Furthermore, aerospace structural components are typically subject to a dynamic (fatigue) loading and are potentially safety-critical (structural failure implies a risk to safety).

This design scenario is typically satisfied by either subtractive or formative methods; however, these processes are commercially challenged for this scenario. Specifically, the high fixed costs inherent to formative tooling are challenging for formative methods, as is the low material utilization and high processing time associated with subtractive methods[4]. L-PBF provides an emerging opportunity for the design of high-value aerospace components manufactured at low to moderate production volume, specifically:

1. The additive nature of L-PBF utilizes a *common source material* that is additively deposited as required, enabling high-efficiency material utilization as is required for the design of cost-effective structures. This process attribute is a valuable differentiator between L-PBF and subtractive manufacturing processes, which typically have poor buy-to-fly ratios.
2. The high geometric complexity enabled by L-PBF is compatible with aerospace requirements for *high structural efficiency* (Whitman and Terry, 2012). Specifically, L-PBF processes can be used to fabricate high-efficiency components that would be technically challenging with formative or subtractive methods, including: hollow-section structural elements, parts consolidation, and near-net manufacture.

22.6.1.1 Project implementation

To demonstrate the opportunities for L-PBF in providing a commercial solution to the fabrication of high-value structural aviation componentry for low- to medium-volume applications the following L-PBF technology demonstration was developed (Fig. 22.12). Topology optimization methods were used to provide insight into the optimal distribution of material for the defined structural loading. This optimized geometry was then converted to a parametric representation that enabled local refinement of the geometry for both structural and manufacturability requirements. For example,

---

[4] Subtractive manufacture of aviation brackets is typically associated with a high *buy-to-fly ratio*, implying that extensive material removal is required from a high-value billet material, resulting in lost material value and high processing costs (Yates, 2016).

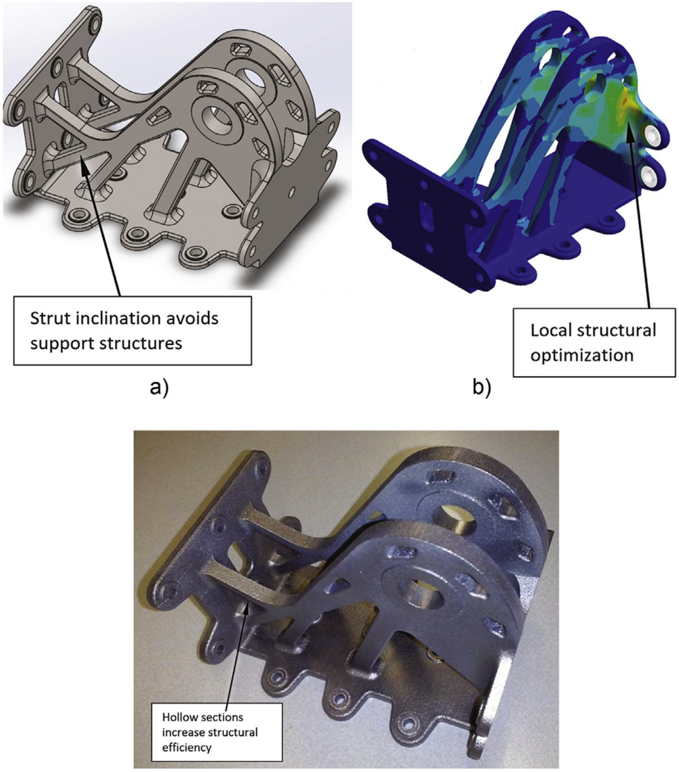
Strut inclination avoids support structures
a)
Local structural optimization
b)
Hollow sections increase structural efficiency
c)

Figure 22.12 High-value aerospace bracketry: (a) topologically optimized design, (b) parametric optimization of the component details, (c) implementation of AlSi10Mg L-PBF component.

connected sections are hollow to increase efficiency while providing buckling resistance. Near-net design philosophies enable value to be added to the design by, for example, allowing clearance for fastener assembly and inclining structural sections to avoid the cost and post-processing required by the use of supporting structures.

22.6.2 Bespoke medical implants

Orthopedic implants are an important high-technology application that are predominantly manufactured to standard sizes using traditional manufacturing technologies. Many clinical scenarios are not entirely suited to these mass-produced products and would benefit from customized geometry; however, the associated costs and production lead-time are prohibitive for traditional manufacture.

The design flexibility and manufacturing readiness of L-PBF systems is entirely compatible with the clinical requirements of bespoke medical implants. Furthermore, L-PBF manufacture enables an implant structure that mitigates stress-shielding by mimicking the structural response of the resected bone (Sumner and Galante, 1992) and provides an implant surface that promotes bone attachment (Yang et al., 2019). Despite these technical opportunities, commercial and technical risks must be accommodated to enable bespoke L-PBF production of medical implants in a clinical scenario, as is described in the following commercial application.

22.6.2.1 Clinical implementation of patient-specific implant

The structural design of an interbody fusion implant requires that the structure be conformal to the patient-specific geometry; accommodate structural loads; allow a central zone for bone graft delivery and containment; enable the correction of abnormal spinal curvature; retain the as-manufactured L-PBF surface to encourage bone ingrowth; and consist of internal structural elements that are self-supporting during manufacture to reduce post-processing. These technical design requirements can be met with a space frame lattice structure that is custom-sized to meet the identified geometric, structural, and clinical requirements; however, the manual design of such a structure is challenging due to the high dimensionality of this complex structure. This complexity imposes a relatively high cost of design on the commercial application of L-PBF implants, thereby restricting its clinical deployment. Generative design provides a mechanism to accommodate the complexities of patient-specific implant design while allowing reduction in production costs and associated lead-time and providing a design protocol that aids in certification.

22.6.2.2 Generative design system

A generative design system was developed to define the structural deployment of lattice elements within the patient-specific interbody fusion implant (Fig. 22.13). Boundary conditions to the geometric design were defined by patient-specific CT data and modified to accommodate the required change in spinal curvature. Predefined manufacturability data was used to allow the generative design system to algorithmically satisfy manufacturability limits (Mazur et al., 2016). To accommodate the requirement for bone ingrowth and avoid thermal overloads due to excessive lattice density, the generative design system was defined to automatically modify the number of row structures (Downing et al., 2020). Consequently, the manufactured lattice structure has five rows at the larger thickness and two rows in the thinner section. Based on interactions with the surgical team, a variable cell structure was selected to accommodate manufacturability, structural stability, and bone ingrowth requirements; specifically, the outer circumference includes diagonal strut elements within the cubic structure (McMillan et al., 2017; Alghamdi et al., 2019). Based on these outcomes, L-PBF was applied to successfully deploy the bespoke implant. Surgical procedures were routine, and the 12-month radiological follow-up demonstrated solid mature fusion with no failure of fixation and no subsidence (Mobbs et al., 2017).

The successful deployment of the patient-specific interbody fusion implant demonstrates the clinical opportunities for L-PBF systems in concert with generative design algorithms. These opportunities are being increasingly applied commercially to

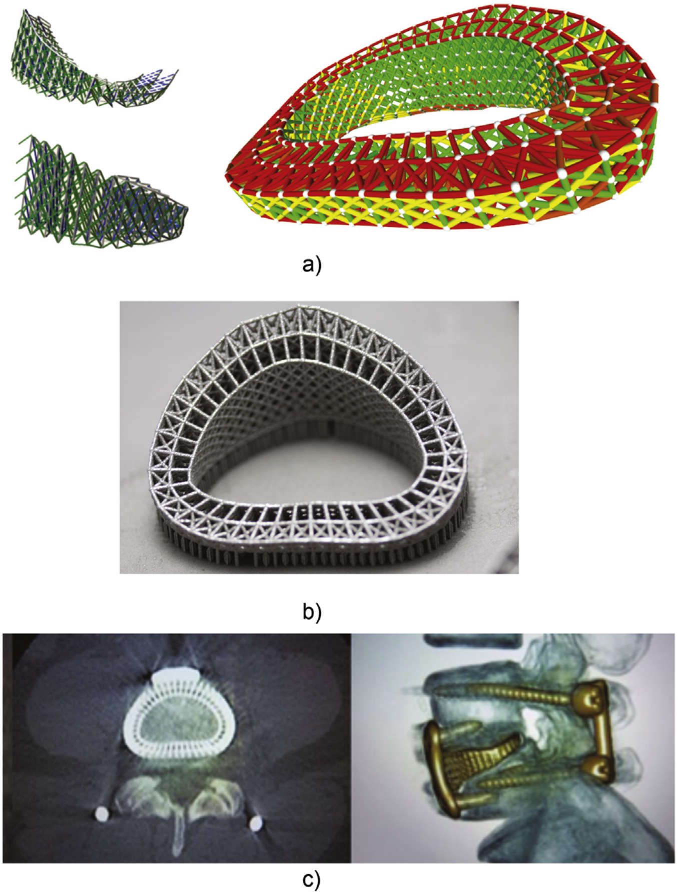

Figure 22.13 Patient-specific L-PBF interbody fusion implant: (a) fundamental model implemented by generative design methods, including final design and (inset) initial prototypes, (b) L-PBF implant production, (c) 12-month post-implant radiographic follow-up (Mobbs et al., 2017).

address the complexity and lead-time challenges associated with manual design (Shidid et al., 2016, 2020). Furthermore, L-PBF enables robust control and documentation of engineering design decisions, as is required for medical certification.

22.6.3 Bespoke medical fasteners

Similarly, custom implants may benefit from custom fastener hardware. These fastener systems typically have low geometric complexity and are therefore highly compatible with generative design methods. For example, the custom fastener hardware of Fig. 22.14 was algorithmically specified by generative methods to accommodate implant-specific geometric requirements while being constrained by standard methods

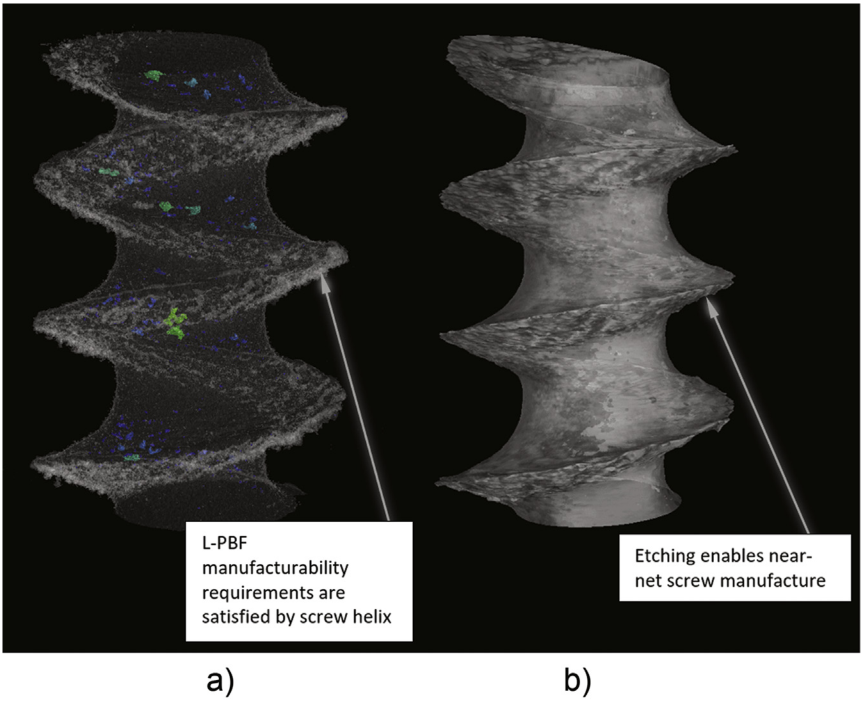
L-PBF manufacturability requirements are satisfied by screw helix
Etching enables near-net screw manufacture
a)
b)

Figure 22.14 L-PBF fabrication of custom titanium Ti6Al4V medical fastener: (a) as-manufactured system indicating adhered powder, (b) acid etched screw indicating powder removal and sharpening effect.

for screw thread design. As-manufactured L-PBF processes display attached particles, especially on downward facing surfaces. These attached particles are removed by an etchant prior to use (Sun et al., 2016).

Furthermore, this technique can be used to provide a rapid-prototyping function whereby the L-PBF system is used to enable the rapid experimental assessment of the mechanical response of a range of proposed fastener designs. Once finalized the optimal design can then be implemented by either L-PBF or traditional methods.

22.6.4 High-value, low-volume product design evolution

The manufacture of high-complexity products can be prohibitively expensive for niche consumer products that cannot accommodate a high production cost. L-PBF can provide a commercial opportunity to decouple production cost from design complexity and production volume, which can be valuable for the production of niche consumer products.

For example, high technology archery bows use complex cam elements to allow variable string tension such that arrow velocity and accuracy are optimized. The cost of traditional manufacturing processes may be prohibitive for high-complexity

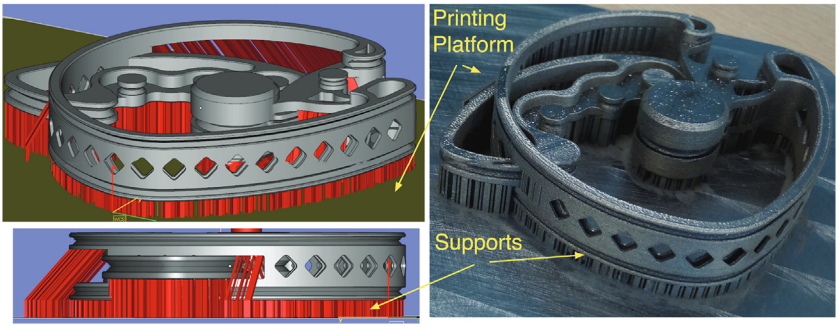

Figure 22.15 Application of L-PBF to enable low-volume production of consumer goods. In this case the design of niche consumer products for archery applications (DebRoy et al., 2019; Serena et al., 2017).

product design, especially during the product development phases where design iteration is required. By utilizing L-PBF processes, inexpensive production can be achieved even at low production volumes (Fig. 22.15).

This approach is particularly valuable in the rapid-prototyping mode, as it allows confirmation of the technical function of the product as well as the rapid evaluation of proposed production variants. Once confirmed to be successful, the product can then be deployed either using L-PBF methods or where appropriate with traditional methods.

22.7 Concluding remarks

L-PBF is a commercially robust AM technology implementation that enables commercial innovation in product development. To commercialize these opportunities requires that both design engineers and production economists engage with L-PBF technology such that both technical and economic aspects are optimized in harmony. This research monograph provides a basis for fostering this common understanding.

L-PBF potentially disrupts classical concepts of engineering economics, enabling commercial opportunities that may be unexpected from a classical economics perspective. By assessing these unexpected opportunities in detail, a systematic approach to economic feasibility may be applied to AM production. Specific economic opportunities enabled by these outcomes are described based on the fundamental understanding of technical and economic attributes. These opportunities include: product design for high-value products, continual product development of high-value, low-volume products, low-volume production and generative design to enable mass-customization of high-complexity designs.

22.8 Questions

The following questions are provided to assist in review of the fundamental concepts associated with the economic feasibility and cost-benefit analysis of L-PBF systems:

- What is the fundamental difference between an evolutionary design and a revolutionary design? Note that this distinction is entirely dependent on the experience of the design team and a design that may be revolutionary for one team may be evolutionary for a team with greater experience.
- How can L-PBF allow increased flexibility in product design when compared with traditional methods? What commercial opportunities does this flexibility enable?
- How does the Process Capability Index (PCI) of a manufacturing process (such as L-PBF) determine the production yield for a set of required Key Product Characteristics (KPC)?
- Net-shape and near-net-shape manufacture provide an important commercial opportunity for L-PBF technologies. Explain how L-PBF can potentially enable near-net-shape outcomes that would be technically infeasible for traditional manufacturing methods.
- Parts consolidation refers to the fabrication of a single component that was previously an assemblage of multiple components. L-PBF provides a strategic opportunity for parts consolidation due to its ability to accommodate geometric complexity in comparison with traditional manufacture. How can parts consolidation enable increased product reliability by the elimination of failure modes?
- Would the design effort required to specify and validate an L-PBF product be considered as a fixed cost or a variable cost? Can you consider a scenario where design effort is both a fixed and a variable cost?
- Fig. 22.4 is a schematic representation of cost versus production volume. We can see that for increasing production volume ($n \rightarrow \infty$) the unit-cost asymptotes to the defrayed variable cost. How can the defrayed variable cost be independent of the fixed-costs?
- In simple terms explain why cost increases as complexity increases. Explain why there is a technical upper limit to the complexity that can be achieved by a specific manufacturing technology (see Fig. 22.5).
- It is often reported that the unit-cost for AM processes such as L-PBF are independent of both complexity and production volume. What attributes of AM processes in general (and L-PBF specifically) are used to justify the assumption of cost-independence of L-PBF?
- Based on the assumption of cost-independence of L-PBF, what three zones of economic opportunity exist? Provide a hypothetical L-PBF product for each of these optimal economic zones.
- In practice, the assumption of cost-independence of L-PBF is not always justifiable and can provide misleading guidance on the economic cost-benefit of L-PBF. Put yourself in the role of an L-PBF production manager and, in simple terms, explain to a junior colleague why the assumption of cost-independence of L-PBF is not always justifiable. Illustrate this discussion with reference to potential economic pitfalls of the simplified AM cost model, as well as commercial opportunities that are not identified by the simplified AM cost model.

Acknowledgements

The author acknowledges the enabling support of the RMIT University Advanced Manufacturing Precinct as well as the ARC Training Centre for Lightweight Automotive Structures and from the Australian Research Council (IC160100032).

References

Alghamdi, A., Lozanovski, B., McMillan, M., Tino, R., Downing, D., Zhang, X., Kelbassa, I., Choong, P., Qian, M., Brandt, M., Leary, M., 2019. Effect of polygon order on additively manufactured lattice structures: a method for defining the threshold resolution for lattice geometry. Int. J. Adv. Manuf. Technol. 105 (5−6), 2501−2511.

DebRoy, T., Mukherjee, T., Milewski, J.O., Elmer, J.W., Ribic, B., Blecher, J.J., Zhang, W., 2019. Scientific, technological and economic issues in metal printing and their solutions. Nat. Mater. 18 (10), 1026−1032.

Dodgson, M., Gann, D.M., Salter, A., 2008. The Management of Technological Innovation: Strategy and Practice. Oxford University Press on Demand.

Downing, D., Leary, M., McMillan, M., Alghamdi, A., Brandt, M., 2020. Heat transfer in lattice structures during metal additive manufacturing: numerical exploration of temperature field evolution. Rapid Prototyp. J. 26 (5), 911−928.

Frazer, J., 2002. Creative design and the generative evolutionary paradigm. In: Creative Evolutionary Systems. Morgan Kaufmann, pp. 253−274.

ISO 9000:2005. International standard “Quality management systems -. Fundamentals and vocabulary”. I.S. EN (ISO 9000:2005), pp. 1-12.

Leary, M., 2019. Design for Additive Manufacturing. Elsevier.

Marnell, P., 2016. Engineering Economics for the 21st Century. John Wiley & Sons.

Mathieu, L., Marguet, B., 2001. Integrated design method to improve producibility based on product key characteristics and assembly sequences. CIRP Ann. 50 (1), 85−88.

Mazur, M., Leary, M., Sun, S., Vcelka, M., Shidid, D., Brandt, M., 2016. Deformation and failure behaviour of Ti-6Al-4V lattice structures manufactured by selective laser melting (SLM). Int. J. Adv. Manuf. Technol. 84 (5−8), 1391−1411.

McMillan, M.L., Jurg, M., Leary, M., Brandt, M., 2017. Programmatic generation of computationally efficient lattice structures for additive manufacture. Rapid Prototyp. J. 23.

Mobbs, R.J., Coughlan, M., Thompson, R., Sutterlin, C.E., Phan, K., 2017. The utility of 3D printing for surgical planning and patient-specific implant design for complex spinal pathologies: case report. J. Neurosurg. Spine 26 (4), 513−518.

Montgomery, D.C., 2001. Introduction to Statistical Quality Control, fourth ed. John Wiley & Sons, New York.

Pahl, G., Beitz, W., 2013. Engineering Design: A Systematic Approach. Springer Science & Business Media.

Petrick, I.J., Simpson, T.W., 2013. 3D printing disrupts manufacturing: how economies of one create new rules of competition. Res. Technol. Manag. 56 (6), 12−16.

Rodgers, P.A., Milton, A., 2013. Research Methods for Product Design. Laurence King.

Serena, G., Rosa, F., Casati, R., Solarino, P., Vedani, M., Bordegoni, M., 2017. Designing for metal additive manufacturing: a case study in the professional sports equipment field. Procedia Manufac. 11, 1544−1551.

Shidid, D., Leary, M., Choong, P., Brandt, M., 2016. Just-in-time design and additive manufacture of patient-specific medical implants. Phys. Procedia 83, 4−14.

Shidid, D., Leary, M., Brandt, M., Choong, P., Royal Melbourne Institute of Technology Ltd, 2020. Method for Producing a Customised Orthopaedic Implant. U.S. Patent 10,688,726.

Sumner, D.R., Galante, J.O., 1992. Determinants of stress shielding. Clin. Orthop. Relat. Res. 274, 203−212.

Sun, Y.Y., Gulizia, S., Oh, C.H., Fraser, D., Leary, M., Yang, Y.F., Qian, M., 2016. The influence of as-built surface conditions on mechanical properties of Ti-6Al-4V additively manufactured by selective electron beam melting. J. Occup. Med. 68 (3), 791−798.

Whitman, D.L., Terry, R.E., 2012. Fundamentals of engineering economics and decision analysis. Synth. Lect. Eng. 7 (1), 1−219.

Wu, Z., El Maraghy, W.H., El Maraghy, H.A., 1988. Evaluation of cost-tolerance algorithms for design tolerance analysis and synthesis. Manufac. Rev. ASME 1 (3), 168−179.

Yang, Y., Wang, G., Liang, H., Gao, C., Peng, S., Shen, L., Shuai, C., 2019. Additive manufacturing of bone scaffolds. Int. J. Bioprint. 5, 1.

Yates, J.K., 2016. Engineering Economics. CRC Press.

Current state and future trends in laser powder bed fusion technology

23

Andrey Molotnikov, Alex Kingsbury, Milan Brandt
Centre for Additive Manufacturing, School of Engineering, RMIT University, Melbourne, VIC, Australia

Chapter outline

23.1 Introduction 621
23.2 Current state of L-PBF technology 622
  23.2.1 Brief historical background 622
  23.2.2 L-PBF systems and materials 622
23.3 Future trends 626
  23.3.1 Innovations in laser system technology 626
  23.3.2 Metal powder manufacture 628
  23.3.3 New alloys 628
  23.3.4 Post-processing 630
  23.3.5 Automatization and quality control 630
23.4 Summary 632
References 632

23.1 Introduction

Today additive manufacturing (AM) is shaping the future of global manufacturing and is influencing how many of today's components will be manufactured in the future. With Laser Powder Bed Fusion (L-PBF), parts can be built directly from computer models or from measurements of existing components to be re-engineered, and therefore bypass traditional manufacturing processes such as cutting, milling, and grinding. L-PBF builds up finished components from metal powders layer by layer through laser melting and solidification. Benefits include (1) new designs not possible using conventional subtractive technology, (2) substantial savings in time, materials, wastage, energy, and other costs in producing new components, (3) significant reduction in environmental impact, (4) faster time to market, and (5) production of parts on-demand from a digital inventory. L-PBF removes many of the shape restrictions that limit design, thereby allowing computationally optimized, high-performance

Fundamentals of Laser Powder Bed Fusion of Metals. https://doi.org/10.1016/B978-0-12-824090-8.00011-1
Copyright © 2021 Elsevier Inc. All rights reserved.

structures to be manufactured and tested. Functional engineering prototypes and actual components can then be built in their final shape with minimal material wastage. Samples and small product runs can be produced quickly at comparatively low cost to test and build market acceptance without major investment.

23.2 Current state of L-PBF technology

23.2.1 Brief historical background

The discovery of the laser in 1960 has changed the landscape of manufacturing and contributed to the increase in productivity and reduction in cost for many industries including automotive, aerospace, biomedical (Advanced information, 2018). The laser has become an integral part in many instruments performing cutting, drilling, welding, or surface treatments. The continuing research and development of laser applications has significantly contributed to the creation of a new manufacturing branch known as additive manufacturing (AM) which is at the core of this book. While lasers are one of the fundamental technological pieces in laser-based metal printers, many other technology sub-systems such as optics, material delivery systems, electronics, software, etc., needed to be developed to create a functional metal 3D printer. The historical background and basic principles of this process are summarized in Chapters 1−3. The first commercial L-PBF systems became available in early 2000. Since then, the technology matured greatly and has overcome many technological hurdles. In the last 5 years several companies succeeded with their efforts to qualify parts for serial production and commercial operation and continue to invest and build manufacturing facilities. Notably, it includes applications in energy (Siemens Energy), aerospace (GE, MTU), automotive (BMW), medical (Stryker), space (SpaceX), to name a few, see Fig. 23.1 and Chapter 21 “Industrial applications.” This trend is also reflected in the growth of the metal AM sector with reported growth of 29.9% and with over 2300 L-PBF machines sold alone in 2018 (Wohler, 2019).

As it is shown in this book, the L-PBF process has many advantages over conventional manufacturing including the elimination of tooling, increased freedom of design to enable manufacturing of complex parts, efficient use of raw materials, part consolidation and lightweighting, decentralized production, and support of digital inventory. However, the industry still faces many challenges including limited productivity of the existing AM machines, lack of specialized software linking conventional CAD and FEA models to AM production software enabling better control and monitoring of the AM equipment, process-induced defects and reliability of the AM systems, limited size of the build chambers, significant efforts to introduce and qualify new materials, to name a few.

23.2.2 L-PBF systems and materials

This section briefly outlines the current state of L-PBF technology, setting the scene for discussion of future trends. As it was shown in Chapter 2, the L-PBF equipment consists of two main components: (1) laser and scanner system and (2) build chamber

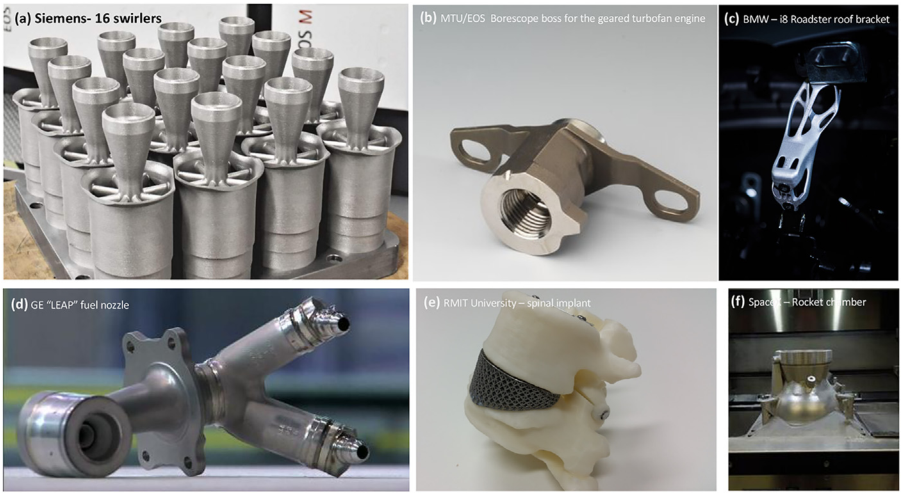
(a) Siemens- 16 swirlers
(b) MTU/EOS Borescope boss for the geared turbofan engine
(c) BMW – i8 Roadster roof bracket
(d) GE "LEAP" fuel nozzle
(e) RMIT University – spinal implant
(f) Spac – Rocket c mber

Figure 23.1 Examples of serial production parts manufactured using laser powder bed fusion process. (a) Siemens combustor swirlers for a gas turbine, (b) MTU borescope boss for the geared turbofan engine, (c) BMW roof bracket, (d) GE "LEAP" fuel nozzle, (e) Ti6Al4V spinal disc designed and manufactured at the RMIT University, and (f) SpaceX Inconel rocket chamber.

including powder delivery system. The working principle is based on depositing/spreading a thin layer of metal powder on the build platform, followed by selective melting of prescribed regions using laser, lowering the build platform by a specified height (layer thickness), and repeating the process until the final geometry of the part is produced. The laser and scanner system are core components of L-PBF printers.

The first commercial L-PBF systems utilized low-power CO_2 lasers (typically between 50 and 100 W) which were developed for efficient processing of thermoplastic materials. However, the characteristic wavelength of this laser (around 10 μm) and its low power meant that the processing of metallic alloys was inefficient and resulted in parts with low densities, below 95%. Today the laser of choice is the fiber laser which can provide higher output power (ranging between 100 W and 1 kW) and smaller laser spot size (30–200 μm) while simultaneously increasing the absorptivity of metallic powders by operating at a wavelength around 1 μm (see Chapters 2 and 4). These lasers can operate either in continuous or pulsed mode and the aforementioned improvements allowed a greater control of melt-pool formation. Furthermore, the laser beam profile is an important factor which influences the energy delivered to the material with the majority of the commercial systems using a Gaussian laser beam intensity distribution to obtain maximum intensity at the center of the melt pool (Brandt, 2017; Metel et al., 2019). A laser beam is controlled using high-speed galvanometers and focusing optics allowing the beam to scan across the powder bed platform following the computer-generated path. The laser beam is capable of moving several meters per second and a number of commercial systems are reported today to reach speeds up to 10 m/s (Khorasani et al., 2020). The scanning path/strategy is critical for controlling the thermal history of the manufactured parts and influences its material properties, such as density, residual stress, and formation of the microstructure (Kruth et al., 2015; DebRoy et al., 2018) (see Chapters 3,6,8,9).

The laser and scanning system are operating in the build chamber which hosts the powder delivery system, build platform/plate and integrated gas flow system to assist with the removal of process byproducts such as spatter and metal vapor (Ladewig et al., 2016) and to prevent/reduce the oxidation of materials. Currently nitrogen and argon are two primarily used gasses in the commercial systems and systems with integrated vacuum build chamber are emerging. The build plate size and build volume have gradually increased from small size 50 mm × 50 mm × 80 mm to medium size 250 mm × 250 mm × 250 mm and large size approaching 800 mm × 400 mm × 500 mm. Progressively, the medium and large size printers started integrating multiple lasers with twin laser systems introduced in 2013 and up until early 2020 several manufacturers (SLM Solutions, GE, EOS) offered commercial systems with quad lasers up to 1 kW power. These developments are mainly driven by the desire to improve the productivity of the L-PBF systems by increasing the build rate. The earlier L-PBF systems were capable of achieving build rates of 25 cm^3/h for a single 400 W system, and this rate increased in the last few years to 105 cm^3/h for a quad 400 W system.

All L-PBF systems utilize metal powders which are typically spherical, dense, and of a size distribution of 15−45 μm (see Chapter 18). Ideally, powder for L-PBF should be of a narrow size distribution, fully dense with no internal porosity, have an even packing density, and have no irregularities in shape or attached satellites. The powder is spread over the build plate using a spreader bar or recoater which distributes the powder across the powder bed evenly. A uniformly packed, flat layer of powder is essential for ease of processability by the laser, and a uniform, quality deposit.

The layer thickness used for the build and the particle size distribution (PSD) of the powder being processed are interlinked. As a general rule, the D50 of the metal powder being processed should be half that of the layer height, and the maximum particle size should be less than the layer height. Following this guide minimizes the chance of lack of fusion defects due to incomplete melting, and also reduces the surface roughness of the part (see Chapter 7).

The initial development phase of L-PBF technology saw the use of the finer fractions of thermal spray metal powders. Since this time, the AM market has grown and material producers established dedicated atomization capacity for AM. To an extent, this has enabled runs of specialty alloys, with chemistry, size distribution, and morphology tailored for L-PBF.

In the L-PBF process, powder can be reused a number of times in order to minimize waste and lower the cost of production. The unfused metal powder is sieved to remove oversized particles and then reused in the printer. Each reuse however can degrade the powder quality in a number of ways. Firstly, the powder reacts with oxygen and other impurities such as nitrogen or water in the atmosphere; trace amounts of these impurities can also be found in the inert gas stream in the L-PBF system. Reused metal powder particles can also partially fuse with other particles in the melting process, which changes their shape, and hence reduces their flowability. This partial fusing can occur at the part boundary, or more likely, is caused by spatter—partially melted particles that are emitted from the melt pool into unfused powder. The powder can also undergo chemistry changes as elements within the alloy may be preferentially reactive, or vaporize in unequal amounts under melting conditions (see Chapter 18).

When reusing metal powders, the user may opt for a number of different reuse strategies. These are:

1. No reuse—in highly regulated, critical industries, the powder is used on a once-through basis only, and then disposed.
2. Reuse only—a batch of virgin (i.e., previously unused) powder is used consecutively until there is either insufficient powder for another build, or the powder has been used up to a specified number of times.
3. Top-up—unfused powder from a build is sieved and topped up with virgin powder from the same batch to keep the starting volume of powder consistent for every build. This is repeated until there is insufficient powder for a build, or the powder has been used up to a specified number of times.
4. Top-up and blending—unfused powder from a build is sieved and topped with virgin powder from another batch of powder, or previously used powder from another build.

Each of the above options presents trade-offs in cost, traceability, consistency of chemistry, and flowability of the powder. The reuse strategy depends entirely on operator choices and is governed by the industry, the criticality of the parts being built, and the economic of part manufacture (Chapter 22).

Metal powders are currently available in a range of standard weldable alloys such as aluminum, stainless steels, nickel-based alloys, titanium, and cobalt-chrome alloys. Special alloys with bespoke chemistry are available as a customized order.

Overall, the L-PBF process is a very complex solidification process. The high scanning speed of laser and short interaction time between the laser beam and powder lead to rapid solidification with cooling rate between 10^4 and 10^6 K/s (DebRoy et al., 2018) depending on the material properties and processing parameters. The operators are required to carefully select many processing parameters in order to produce fully dense parts with the required microstructure and surface finish. These include *laser-related, scan-related, powder and temperature-related parameters* (Sun et al., 2017) such as:

- laser power, wavelength, spot size, laser profile distribution,
- scanning speed, scanning spacing, and scan strategy,
- powder particle size and distribution and shape, layer thickness,
- powder bed preheating temperature.

These processing parameters determine the stability of the L-PBF process as well as dictate the mechanical properties, surface characteristics (surface roughness), and build-up of residual stresses in the produced parts. After the printing is completed, the part is removed and typically undergoes several post-processing steps including stress relieving, support structure removal, surface treatment to improve the surface roughness, and potentially heat-treatment to improve the mechanical properties.

23.3 Future trends

The L-PBF process continues to be a dominant technology for metal AM due to its unique advantages to aerospace, tooling, energy, medical, space, and other industries. Over the past decade the number of academic publications with keywords selective laser melting or laser powder bed fusion increased by eight-fold and close to 1600 publications were published in 2018 (Dowling et al., 2020). This is a large testament to the importance of this technology, but also highlights that the technology is still undergoing major developments. This section of the chapter provides a short summary of recent and future trends in the field.

23.3.1 Innovations in laser system technology

Future trends focus on the speed and productivity of L-PBF systems, and the ability to process new materials. The race to incorporate more lasers than ever before is on, with announcements on this in 2020 by Additive Industries, 3DSystems, Velo3D, and SLM Solutions; all are using multi-laser systems in their latest systems with 8, 9, 10, and 12 lasers up to 1 kW each, respectively (Fig. 23.2). All multi-laser systems have also increased build volumes (up to 1 m × 1 m × 0.6 m) that are either rectangular in shape in the case of Additive Industries, 3DSystems, and SLM Solutions, or cylindrical in the case of Velo3D. This need is being driven by customers in defense, aerospace, energy, and high performance automotive industries who have been articulating the need for large-scale platforms to manufacture larger-sized parts.

With an increased number of lasers comes a more sophisticated approach to build planning that accounts for laser interaction and optimized thermal management. Rather than have lasers dedicated to specific areas of the build, the focus is heading toward all lasers working in concert, with a counter-current gas flow removing smoke plume and spatter away from the direction of the laser path. Multiple research performed on the formation of spatter and the laser plume (Yang et al., 2020; Shen et al., 2020), provides

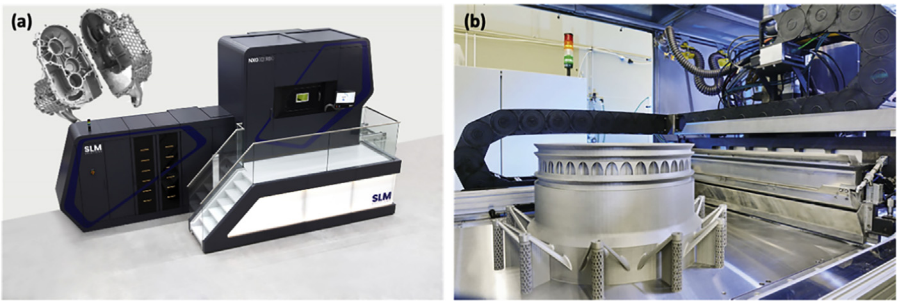

Figure 23.2 Examples of emerging industrial-scale L-PBF printers: (a) SLM Solutions NXG XII 600 printer and printed large engine housing made out of AlSi10Mg, (b) a view of a large demonstrator part build for the future Rolls-Royce engine on Fraunhofer XXL L-PBF system with a mobile optical system.

an input for redesign and optimization of the L-PBF system. These studies utilized sophisticated in-situ X-ray imaging techniques to reveal the formation of the melt tracks, possible defects, processing parameters, and influences of the gas flow during the L-PBF process (Cunningham et al., 2017; Zhao et al., 2017; Leung et al., 2018). It however remains to be seen whether these new multiple laser machines will provide the desired cost advantages or continue to be serving niche applications for high-value industries.

Recoaters have been reconsidered in many new systems, as the traditional recoating mechanisms would spread powder from one end of the build chamber to the other, which for a small build volume is generally acceptable. However, for a large build volume where the recoating surface area can be orders of magnitude greater than the smaller systems, the process requires much more powder. It can unevenly distribute the powder across the bed, leading to a higher packing density at the beginning of the spreading process, and a much lower packing density toward the end. This leads to uneven distribution that has serious implications for build quality. Strategies to address this challenge have been implemented on these larger machines, and may likely be deployed to smaller and mid-sized machines in the future.

One notable example is the development of L-PBF printer utilizing a "mobile optical system" with multiple lasers by Fraunhofer ILT shown in Fig. 23.2b. It is anticipated that this approach can simultaneously increase the build volume, as well as improve the productivity. The system is capable of producing parts with dimensions up to 1000 mm × 800 mm × 400 mm and a large demonstrator part built for the future Rolls-Royce engine can be seen on the build platform. It is reported that this approach can lead to a tenfold increase in productivity. However, it should be noted that the quoted productivity is only applicable for a specific geometry of components and new types of scanning strategies and gas flow are under development to obtain high-quality parts.

Further possibilities exist in making better use of modulated or pulsed lasers. For instance, it was shown that this type of laser can be effective in manufacturing lattice structures and could avoid the use of contour and hatch scanning strategies (Onal et al., 2019). The other important trend is the development of variable shaping beam profiles in combination with new types of optics. For instance, changes from a Gaussian laser beam intensity profile to a flat-top or donut-like profile can change the energy delivered locally to the melt pool and positively influence its solidification behavior (Metel et al., 2019). These results indicate that a new generation of programmable fiber laser which can change their profile on demand might be integrated in the future L-PBF machines to allow for even broader possibilities of controlling the process of melting and solidification. One example includes a recently announced single-mode fiber laser with the beam shaping function by nLIGHT, Inc. (nLIGHT, 2020).

Another example is the new laser sources used in these systems. For instance, a disk green laser was introduced in late 2017 by Fraunhofer ILT and Trumpf. This laser is capable of operating with wavelength of 515 nm instead of the commonly used infrared light laser (1064 nm) and therefore can significantly boost the absorptivity of material such as pure copper, silver, or gold and create fully dense parts. This development will affect applications in space, electronics, automotive, and jewellery industries.

Furthermore, the development of diode bars which can cover the entire build plate is underway with a number of patents submitted in the last few years. Each individual diode laser should possess sufficient intensity to melt the powder and be addressable on demand allowing to further improve the productivity of L-PBF systems. A similar approach is also reported by Graz University of Technology where the investigators are utilizing an array of high-power LEDs (Brillinger and Haas, 2020).

23.3.2 Metal powder manufacture

Innovation in metal powders continues to develop, as metal powder manufacturers and new, start-up businesses look to address some of the barriers to the industrialization of AM, in terms of cost, productivity, and product consistency.

Conventional gas atomization (GA) and plasma atomization (PA) powder manufacturing technologies work within a set of process boundaries that require a level of inert gas flow and produce a size distribution that does not correspond well to L-PBF requirements. As a result, a number of new powder manufacturing technologies are being developed. These technologies produce powder in a narrower size distribution and can require less gas flow. Combining the benefits of both a tailored PSD and lower gas flow corresponds to a lower unit operating cost, making metal powders more affordable.

Other powder producers are working on differing feedstocks, accessing a recycled metals stream for use as an input material. Extractive metallurgy methods have also been employed to produce materials that are particulate-like, but as yet, none have done so at commercial-scale rates. Spheroidization technologies have been used to make irregular-shaped particles more spherical, dense, and chemically pure. Currently there is a small commercial quantity supply of metal powders suitable for L-PBF that is made with spheroidization.

There is a growing trend in L-PBF to increase the layer thickness and therefore raise the productivity of the L-PBF system, and hence reduce the cost of the build. Likewise, there is a trend to use cheaper, coarser powders to reduce cost. This comes at the expense of surface finish, an increase in lack of fusion defects, and a decrease in mechanical properties in the built part.

23.3.3 New alloys

L-PBF has largely worked within the existing framework of commercially available alloys. Using commercially available alloys facilitates an easier transition to acceptance of the technology by industry. However current alloys have been designed for the existing metal technologies of casting and welding. Many alloys do not perform as well in an L-PBF system as they do with other technologies.

With the unique nature of the L-PBF process, in particular, a very high cooling rate, there is much interest and speculation in designing alloys that are more compatible with the L-PBF process. There are two trends afoot, the first is a microalloying approach that adds alloying additions to a certified alloy without compromising its chemistry specification; the second is design of completely novel alloys formulated specifically for the L-PBF process (see Chapter 19 for more).

A good example of microalloying is Elementum3D that offer an aluminum alloy A6061-RAM2 which meets the standard specification of the certified AA6061 alloy, but contains additional grain refining elements that enable it to perform well in an L-PBF process. Scalmalloy is a patented aluminum-magnesium-scandium alloy that has been designed for use in L-PBF systems and is a good example of an alloy designed specifically for L-PBF. Scalmalloy takes advantage of the high cooling rates to create a grain refining effect within the solidified deposit.

Currently, a number of interesting alloys are under development including aluminum alloys (Aboulkhair et al., 2019; Bayoumy et al., 2021), magnetic materials (Chaudhary et al., 2020), Ti-alloys (Qian et al., 2016; Brodie et al., 2020; Brodie et al., 2020), new steels (Kies et al., 2018; Allam et al., 2020), and nickel-based alloys (Tang et al., 2021; Panwisawas et al., 2020). The L-PBF process has triggered a renaissance in metallurgy and many groups are exploring new compositions using computational tools across different scales (Wei et al., 2020; Kundin et al., 2019; Zinovieva et al., 2018; Motaman et al., 2020; DebRoy et al., 2020) combined with high-throughput testing using on the fly in-situ alloying (Brodie et al., 2020; Simonelli et al., 2018). For instance, it was shown that the L-PBF process is a viable tool to produce high entropy alloys (HEA) (George et al., 2019; Lin et al., 2020; Chen et al., 2020), which can increase the applications space and make it more viable compared to traditional manufacturing techniques. Furthermore, it should be noted that the L-PBF process provides unique opportunities to *architecture* a desired microstructure (Xu et al., 2017, 2015) using in-situ heat treatments or other special processing techniques, and this area will continue to grow.

Recently, a number of studies also attempted to expand the L-PBF process to integrate more than one material. Fig. 23.3 shows two examples of multimaterial printed parts (Girnth et al., 2019; Koopmann et al., 2019) combining stainless steel and copper alloys and a sandwich structure consisting of a ceramic core and steel skins. Multimaterial parts can further boost the performance of components and make use of vast design opportunities to create a new type of functional parts targeting areas such as heat exchangers, wear-resisting coatings, aerospace engine parts, etc. While the current

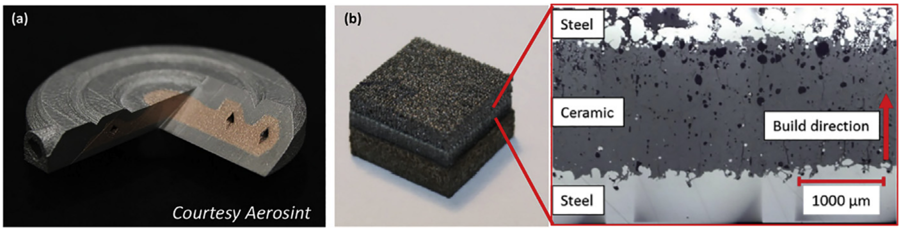

Figure 23.3 Examples of multimaterial printing parts obtained using modified L-PBF equipment: (a) Stainless steel 316L and CuCrZr part manufactured using Aerosint powder deposition system, (b) sandwich structure consisting of a ceramic core and steel skins (Koopmann et al., 2019).

examples only utilize two different materials and have discrete material boundaries, it is anticipated that continuous material transitions and even voxel type L-PBF printing could be developed in the next 5—10 years using new concepts of powder delivery and patterning.

In summary, novel alloy formulations are an obvious pathway to better alloy performance for L-PBF; however, the time horizon for broad-scale certification, acceptance, and adoption remains lengthy.

23.3.4 Post-processing

Increasingly attention is being dedicated to the post-processing of L-PBF parts, and the trend shows that this area will become more important as more parts are used in critical applications (Chapter 12). Automating the post-processing step is seen as the key to industrializing L-PBF and viably operating at scale, particularly in high labor-cost economies. Automated post-processing relies on a robust digital thread, so that powder removal and support structure removal regimes can be automatically generated and optimized. Cleaning is becoming increasingly important, as many parts made on L-PBF systems are being deployed into critical applications where stray metal powder cannot be tolerated, for example, in applications of petrochemical or food handling. As parts become more complex, cleaning and ensuring complete powder removal becomes more challenging, and this is where mechanized powder removal that is guided by a removal regime dictated by part geometry starts to become the only option for powder removal.

Heat treatment and hot isostatic pressing are thermal treatments often required to stress relieve parts, and for more comprehensive treatments, enhance mechanical properties. Critical parts will often have a thermal post-build treatment mandated for certified parts; however, thermal post-build treatments are expensive, and often need to be outsourced. Further, as L-PBF parts grow larger in size, thermal treatments become harder to access. An emerging field is opening up in in-situ heat treatments, where the L-PBF process can be exploited to provide heat treatments in-situ, or during the build. Removal of the need for thermal treatments post-build will save significantly on the cost of L-PBF parts, and the time needed to finish them. The introduction of heated build chambers seen on systems such as Renishaw and EOS has enabled this in-situ heat treatment to some extent, and increasingly a heated build chamber is becoming a more standard offering.

23.3.5 Automatization and quality control

As AM relies heavily on a digital thread, the technology has the ability to fit seamlessly with the Factory of the Future, or Industry 4.0 concept, where every manufactured part has a digital twin, and all manufacturing processes and steps are tracked digitally. Several OEMs such as EOS, Additive Industries, and Trumpf have proposed concepts of digital factories. They include interconnection of multiple printers with other workstations focusing on job preparation stations, automated delivery of modular build platform followed by automated post-processing including powder and part removal, heat treatment, and surface treatment, see Fig. 23.4.

The AM industry is increasingly focusing on the development of process monitoring solutions and even closed loop control (Zhao et al., 2017; Freeman et al., 2020; Egan and Dowling, 2019; Grasso et al., 2018; Grasso et al., 2016; Everton et al., 2016; Scipioni Bertoli et al., 2017), to improve the traceability of the manufacturing process, ensure the quality of the parts, and improve the yield. While the productivity improvements are driven by business consideration, the quality of the parts and its traceability are regulatory requirements of different regulatory bodies such as FAA or FDA for aerospace and medical sectors, respectively. The existing solutions for in-process monitoring have reached a commercial implementation for monitoring of powder bed morphology. This can be achieved by integrating visual camera(s) and using different types of illumination linked to computer vision techniques to reveal irregularities in spreading of the powder or problems linked to support failures. The real-time assessment of the quality of the build is significantly harder and still remains in the research stage. The current monitoring systems are focusing on integrating photodiodes, infrared cameras, or acoustic sensors in order to monitor melt-pool formation and interpreting these data. A detailed discussion of this topic is presented in Chapter 11. While the inherent nature of the layer-by-layer manufacturing provides unique possibilities to study the process, the current solutions are still in the R&D phase suffering mainly from low spatial and temporal resolution as well as from high data volumes due to fast acquisition rates. Advances in machine learning (DebRoy et al., 2020; Huang et al., 2020; Johnson et al., 2020) and multiscale modeling (Wei et al., 2020; Kundin et al., 2019; Zinovieva et al., 2018; Motaman et al., 2020; DebRoy et al., 2020) will provide in the future important input for improving the

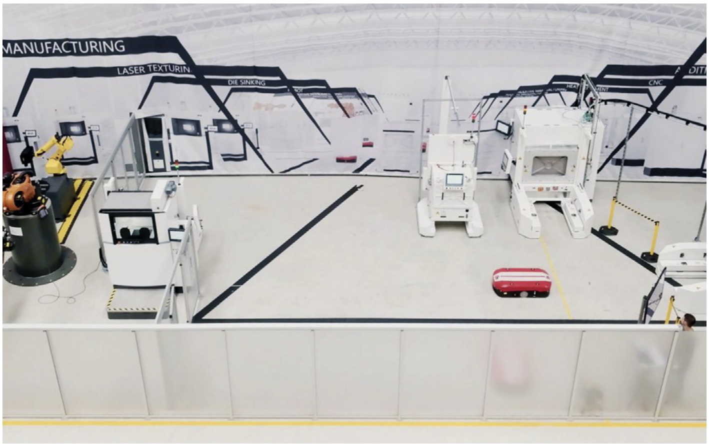

Figure 23.4 Pilot plant setup of automated additive manufacturing including L-PBF equipment and post-processing facilities.
Courtesy of the NextGenAM project by Daimler, Premium AEROTEC, and EOS.

software algorithms for real-time detection of defects, process parameter optimization, and lead to implementation of closed loop control systems. This should further decrease the cost of manufacturing and quality assurance for L-PBF process and manifest it as a viable advanced manufacturing technique for multiple industries.

23.4 Summary

This chapter presents current status and future trends in L-PBF technology including machine architecture, process monitoring, and powder materials. The changes and growth in the technology since its inception have been spectacular because of the close link between the many advantages it offers compared to traditional manufacturing and industry pull. Increasingly, L-PBF systems are becoming and will continue to become more productive and cost-efficient, and produce functional parts of a quality acceptable for some of our most safety critical industries. The trends outlined in this chapter will continue into the future as more industrial applications emerge.

References

Aboulkhair, N.T., et al., 2019. 3D printing of aluminium alloys: additive manufacturing of aluminium alloys using selective laser melting. Prog. Mater. Sci. 106, 100578.

Advanced information, 2018. NobelPrize.org. Nobel Media AB 2020.

Allam, T., et al., 2020. Tailoring the nanostructure of laser powder bed fusion additively manufactured maraging steel. Addit. Manuf. 36, 101561.

Bayoumy, D., et al., 2021. Intensive processing optimization for achieving strong and ductile Al-Mn-Mg-Sc-Zr alloy produced by selective laser melting. Mater. Des. 198, 109317.

Brandt, M., 2017. The role of lasers in additive manufacturing. In: Laser Additive Manufacturing. Woodhead Publishing, pp. 1−18.

Brillinger, M., Haas, F., 2020. Vorrichtung Zur Additiven Fertigung. Austria.

Brodie, E.G., et al., 2020a. Remelt processing and microstructure of selective laser melted Ti25Ta. J. Alloys Compd. 820, 153082.

Brodie, E.G., et al., 2020b. Low-cycle fatigue performance of remelted laser powder bed fusion (L-PBF) biomedical Ti25Ta. Mater. Sci. Eng. A 798, 140228.

Chaudhary, V., et al., 2020. Additive manufacturing of magnetic materials. Prog. Mater. Sci. 114, 100688.

Chen, P., et al., 2020. In-situ alloyed, oxide-dispersion-strengthened CoCrFeMnNi high entropy alloy fabricated via laser powder bed fusion. Mater. Des. 194, 108966.

Cunningham, R., et al., 2017. Synchrotron-based X-ray microtomography characterization of the effect of processing variables on porosity formation in laser power-bed additive manufacturing of Ti-6Al-4V. J. Occup. Med. 69 (3), 479−484.

DebRoy, T., et al., 2018. Additive manufacturing of metallic components − process, structure and properties. Prog. Mater. Sci. 92, 112−224.

DebRoy, T., et al., 2020. Metallurgy, mechanistic models and machine learning in metal printing. Nat. Rev. Mater. 6.

Dowling, L., et al., 2020. A review of critical repeatability and reproducibility issues in powder bed fusion. Mater. Des. 186, 108346.

Egan, D.S., Dowling, D.P., 2019. Influence of process parameters on the correlation between in-situ process monitoring data and the mechanical properties of Ti-6Al-4V non-stochastic cellular structures. Addit. Manuf. 30, 100890.

Everton, S.K., et al., 2016. Review of in-situ process monitoring and in-situ metrology for metal additive manufacturing. Mater. Des. 95 (Suppl. C), 431−445.

Freeman, F.S.H.B., Chechik, L., Todd, I., 2020. Beat the machine (learning): metal additive manufacturing and closed loop control. Phys. Educ. 55 (5), 055012.

George, E.P., Raabe, D., Ritchie, R.O., 2019. High-entropy alloys. Nat. Rev. Mater. 4, 515−534.

Girnth, S., et al., 2019. 3D hybrid-material processing in selective laser melting: implementation of a selective coating system. Prog. Addit. Manuf. 4 (4), 399−409.

Grasso, M., et al., 2016. In-process monitoring of selective laser melting: spatial detection of defects via image data analysis. J. Manuf. Sci. Eng. 139 (5), 051001-051001-16.

Grasso, M., et al., 2018. In situ monitoring of selective laser melting of zinc powder via infrared imaging of the process plume. Robot. Comput. Integrated Manuf. 49 (Suppl. C), 229−239.

Huang, S., et al., 2020. Laser powder bed fusion of titanium-tantalum alloys: compositions and designs for biomedical applications. J. Mech. Behav. Biomed. Mater. 108, 103775.

Johnson, N.S., et al., 2020. Invited review: machine learning for materials developments in metals additive manufacturing. Addit. Manuf. 36, 101641.

Khorasani, A., et al., 2020. A review of technological improvements in laser-based powder bed fusion of metal printers. Int. J. Adv. Manuf. Technol. 108 (1), 191−209.

Kies, F., et al., 2018. Design of high-manganese steels for additive manufacturing applications with energy-absorption functionality. Mater. Des. 160, 1250−1264.

Koopmann, J., Voigt, J., Niendorf, T., 2019. Additive manufacturing of a steel−ceramic multi-material by selective laser melting. Metall. Mater. Trans. B 50 (2), 1042−1051.

Kruth, J.-P., et al., 2015. Additive manufacturing of metals via selective laser melting: process aspects and material developments. In: Additive Manufacturing. CRC Press, pp. 69−99.

Kundin, J., et al., 2019. Microstructure evolution of binary and multicomponent manganese steels during selective laser melting: phase-field modeling and experimental validation. Metall. Mater. Trans. A 50, 2022−2040.

Ladewig, A., et al., 2016. Influence of the shielding gas flow on the removal of process by-products in the selective laser melting process. Addit. Manuf. 10, 1−9.

Leung, C.L.A., et al., 2018. In situ X-ray imaging of defect and molten pool dynamics in laser additive manufacturing. Nat. Commun. 9 (1), 1355.

Lin, W.-C., et al., 2020. Microstructure and tensile property of a precipitation strengthened high entropy alloy processed by selective laser melting and post heat treatment. Addit. Manuf. 36, 101601.

Metel, A.S., et al., 2019. Power density distribution for laser additive manufacturing (SLM): potential, fundamentals and advanced applications. Technologies 7 (1), 5.

Motaman, S.A.H., et al., 2020. Optimal design for metal additive manufacturing: an integrated computational materials engineering (ICME) approach. J. Occup. Med. 72 (3), 1092−1104.

nLIGHT, 2020. nLIGHT Launches Programmable Laser for Metal Additive Manufacturing. Available from: https://www.nlight.net/press-releases-content/nlight-launches-programmable-laser-for-metal-additive-manufacturing.

Onal, E., et al., 2019. Novel microstructural features of selective laser melted lattice struts fabricated with single point exposure scanning. Addit. Manuf. 29, 100785.

Panwisawas, C., Tang, Y.T., Reed, R.C., 2020. Metal 3D printing as a disruptive technology for superalloys. Nat. Commun. 11 (1), 2327.

Qian, M., et al., 2016. Additive manufacturing and postprocessing of Ti-6Al-4V for superior mechanical properties. MRS Bull. 41 (10), 775−784.

Scipioni Bertoli, U., et al., 2017. In-situ characterization of laser-powder interaction and cooling rates through high-speed imaging of powder bed fusion additive manufacturing. Mater. Des. 135, 385−396.

Shen, H., et al., 2020. Influence of gas flow speed on laser plume attenuation and powder bed particle pickup in laser powder bed fusion. J. Occup. Med. 72 (3), 1039−1051.

Simonelli, M., et al., 2018. A comparison of Ti-6Al-4V in-situ alloying in selective laser melting using simply-mixed and satellited powder blend feedstocks. Mater. Char. 143, 118−126.

Sun, S., Brandt, M., Easton, M., 2017. 2 - powder bed fusion processes: an overview. In: Laser Additive Manufacturing. Woodhead Publishing, pp. 55−77.

Tang, Y.T., et al., 2021. Alloys-by-design: application to new superalloys for additive manufacturing. Acta Mater. 202, 417−436.

Wei, H.L., et al., 2020. Mechanistic models for additive manufacturing of metallic components. Prog. Mater. Sci. 100703.

Wohler, T., 2019. Additive Manufacturing and 3D Printing State of the Industry - Annual Worldwide Progress Report.

Xu, W., et al., 2015. Ti-6Al-4V additively manufactured by selective laser melting with superior mechanical properties. J. Occup. Med. 67, 668−673.

Xu, W., et al., 2017. In situ tailoring microstructure in additively manufactured Ti-6Al-4V for superior mechanical performance. Acta Mater. 125, 390−400.

Yang, L., et al., 2020. Monitoring and detection of meltpool and spatter regions in laser powder bed fusion of super alloy Inconel 625. Prog. Addit. Manuf. 5 (4), 367−378.

Zhao, C., et al., 2017. Real-time monitoring of laser powder bed fusion process using high-speed X-ray imaging and diffraction. Sci. Rep. 7 (1), 3602.

Zinovieva, O., Zinoviev, A., Ploshikhin, V., 2018. Three-dimensional modeling of the microstructure evolution during metal additive manufacturing. Comput. Mater. Sci. 141, 207−220.

Case study

24

Anton Du Plessis[1,2], *Igor Yadroitsev*[3], *Ina Yadroitsava*[3], *Johan Els*[4], *Eric MacDonald*[5]

[1]Research Group 3D Innovation, Stellenbosch University, Stellenbosch, Western Cape, South Africa; [2]Department of Mechanical Engineering, Nelson Mandela University, Port Elizabeth, Eastern Cape, South Africa; [3]Department of Mechanical and Mechatronic Engineering, Central University of Technology, Bloemfontein, Free State, South Africa; [4]Centre for Rapid Prototyping and Manufacturing, Central University of Technology, Bloemfontein, Free State, South Africa; [5]W. M. Keck Center for 3D Innovation, University of Texas at El Paso, El Paso, TX, United States

Chapter outline

24.1 Introduction 635
24.2 The test artifact design 636
24.3 Build preparation 638
24.4 Manufacturing the part 640
24.5 Part removal 640
24.6 Post-processing 641
24.7 Part inspection 641
24.8 Concluding remarks 643
Acknowledgements 643
References 643

24.1 Introduction

This short chapter provides a practical case study which can be followed step by step by reading the chapter or by designing and manufacturing the same part. It provides a practical test case to demonstrate some of the concepts presented in the book, aiming at students and new users. This is meant primarily as a simple low-cost exercise for building confidence, yet readers are also urged to share their experiences of this process and their results to the benefit of the community. This is therefore also simultaneously a round robin test, and it is envisaged that results obtained will be shared in a future publication. There is a clear need and interest to continue to improve the quality of laser powder bed fusion (L-PBF) parts, eliminate problems, and enhance the quality-control processes. In the interests of these goals, sharing of results of this

Fundamentals of Laser Powder Bed Fusion of Metals. https://doi.org/10.1016/B978-0-12-824090-8.00017-2
Copyright © 2021 Elsevier Inc. All rights reserved.

test case is encouraged, including negative results and suggested modifications or improvements suited to specific systems or situations encountered.

As L-PBF is now increasingly used in high-tech industry, the focus has shifted from proof-of-concept to end-use—here specifically quality control helps to ensure reliable and accurate part production. In this global effort at improving and refining the quality, it is useful to be cognizant of variability and their sources from a holistic viewpoint. To this end, round robin tests[1] are useful to improve our understanding of possible sources of quality reduction and to further refine the technology. This refers to the same parts manufactured in different laboratories, and compared with one another. These are also sometimes termed inter-laboratory comparisons and are used especially in standardization communities, such as in ISO/ASTM working groups. This case study chapter presents an opportunity for a highly simplified round robin test.

This case study is limited in that, for simplicity of measurements, it only proposes manufacturing a small-size part that contains vertical, horizontal, and inclined planes, upskin and downskin features, and also includes a round straight empty channel and a round channel filled with a lattice structure, to add some complexity. Testing involves only limited dimensional evaluation, surface roughness measurement, recording the mass of the part and if possible microCT scanning, physical cross-sectioning, and optical microscopy, whichever is more readily available. Important aspects such as residual stress, microstructure, and mechanical properties are omitted from this evaluation, for simplicity. More detailed round robin tests may delve deeper and some suggestions are made in this regard; for more information, readers can refer to Moylan et al. (2016), Townsend et al. (2018), and Du Plessis and le Roux (2018).

24.2 The test artifact design

The test artifact was designed according to the guidelines and measurements provided below and the STL file is available for download at Mendeley data "Artifact manufactured by laser powder bed fusion".

The part dimensions are provided in Table 24.1 and Fig. 24.1. The proposed material is Ti6Al4V, due to its widespread use and optimized process parameters available for this alloy on most commercial L-PBF systems. In case of optimized process parameters not being available, the reader is encouraged to use the guidelines presented in Chapter 3 for process parameter optimization.

The design was done in this case using Autodesk Fusion360 with basic model design tools and the part was saved in .stl format, but any appropriate software can be used as preferred by the user. We invite software vendors to submit videos of the design process for this model in their software, to the dedicated information

---

[1] A round robin test is a study in which a number of suppliers manufacture and/or test identical samples and materials in order to compare repeatability and reproducibility of some parameters/methods.

Table 24.1 Basic design dimensions for the test artifact.

Design feature	Design value
Total height	11 mm
Total thickness (depth)	10 mm
Length along top	10 mm
Top section height	2 mm
Length along bottom	15 mm
Bottom section height	2 mm
Angle of middle section	135 degrees
Channel diameter	2 mm

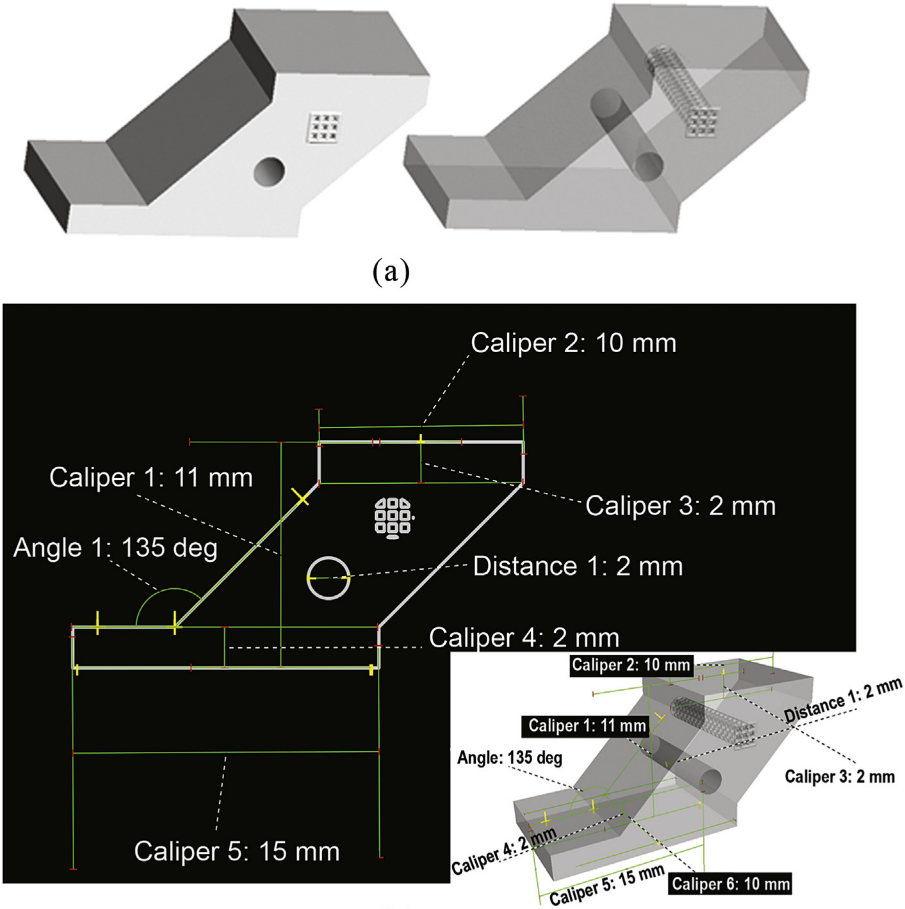
Caliper 2: 10 mm
Caliper 1: 11 mm
Caliper 3: 2 mm
Angle 1: 135 deg
Distance 1: 2 mm
Caliper 4: 2 mm
Caliper 5: 15 mm
Caliper 2: 10 mm
Distance 1: 2 mm
Caliper 1: 11 mm
Angle: 135 deg
Caliper 3: 2 mm
Caliper 4: 2 mm
Caliper 5: 15 mm
Caliper 6: 10 mm

(a)

(b)

Figure 24.1 CAD design showing semi-transparent and solid views of the 3D model (a) and dimensions of the sample (b).

page for this book, located at "Fundamentals of L-PBF of Metals | Research Group 3D Innovation". While designing the part, the original design file from this website can be used as reference.

24.3 Build preparation

Once the part is designed (or taking the completed design file from the website link or Mendeley Data), the model is submitted to the L-PBF system software for planned placement on the base plate (see Figs. 24.2–24.4). At the next stage, in special software (see Chapter 2), the part is sliced into layers, the build time, the need for supports, and the support structures are checked. Possible build simulation can be done at this stage to check hotspots and change build orientation to minimize the effects of residual stress.

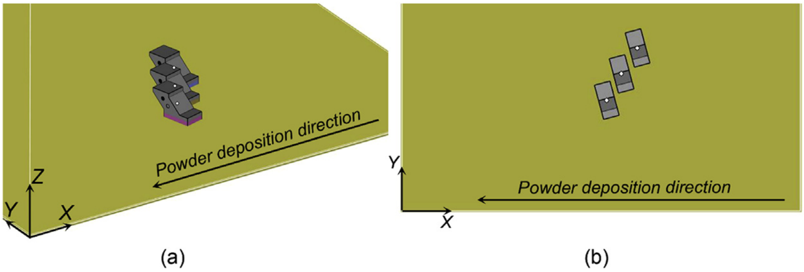

Figure 24.2 Isometric (a) and top view (b) relative to the powder deposition direction from MAGICS software of part placement on the base plate prior to printing. Three test artifacts were produced in this case as shown.

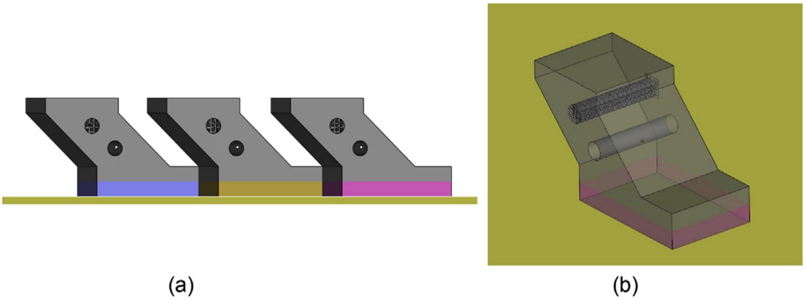

Figure 24.3 Side view (a) of three artifacts showing that the angles of the parts are self-supporting, that does not require any additional support structures in order to print the artifacts. Transparent view (b) showing the hole and lattice structure. A thickness of 2 mm solid was added to the bottom of the artifact to allow for wire EDM cutting to remove the part from the building plate.

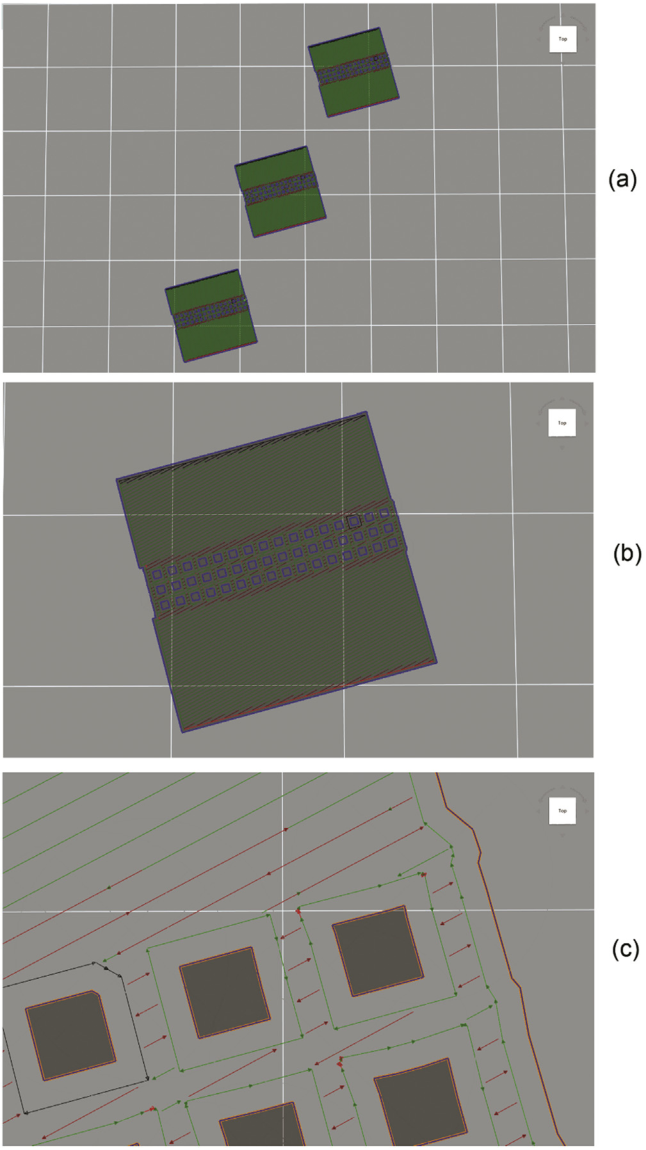

Figure 24.4 Scanning strategy for the layer, where the lattice feature is located, at a distance of 8.6 mm from the base plate: general view (a), closer view for single part (b), and detailed scanning strategy is shown in (c) where hatch tracks are shown in red and green, contour tracks in pink. Red and black indicate upskin and downskin regions; part boundary is in blue color.

24.4 Manufacturing the part

The physical manufacturing takes place according to guidelines for each system, adhering to all safety aspects as needed (including personal protective equipment). The example of steps involved shown in Fig. 24.5 is for an EOS M290 system located at the Center for Rapid Prototyping and Manufacturing (CRPM), Central University of Technology, Bloemfontein, South Africa.

24.5 Part removal

When printing is complete, powder is removed from the building platform, the platform with parts is physically removed, and the machine is cleaned, which may include recycling the unused powder (Fig. 24.6).

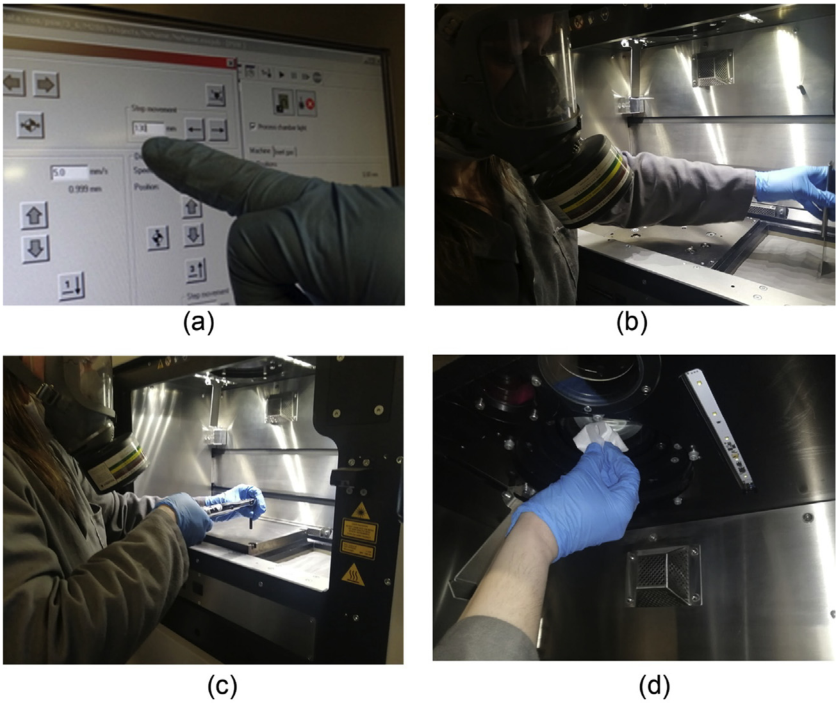

Figure 24.5 Steps in order showing: homing recoater and all other platforms in software interface (a), filling dispenser duct with powder and level powder (b), fitting and adjusting building platform (c), cleaning window of the F-Theta lens (d), close chamber and fill building chamber with argon until <0.1% oxygen concentration is reached (takes around 30 min), then start building process.

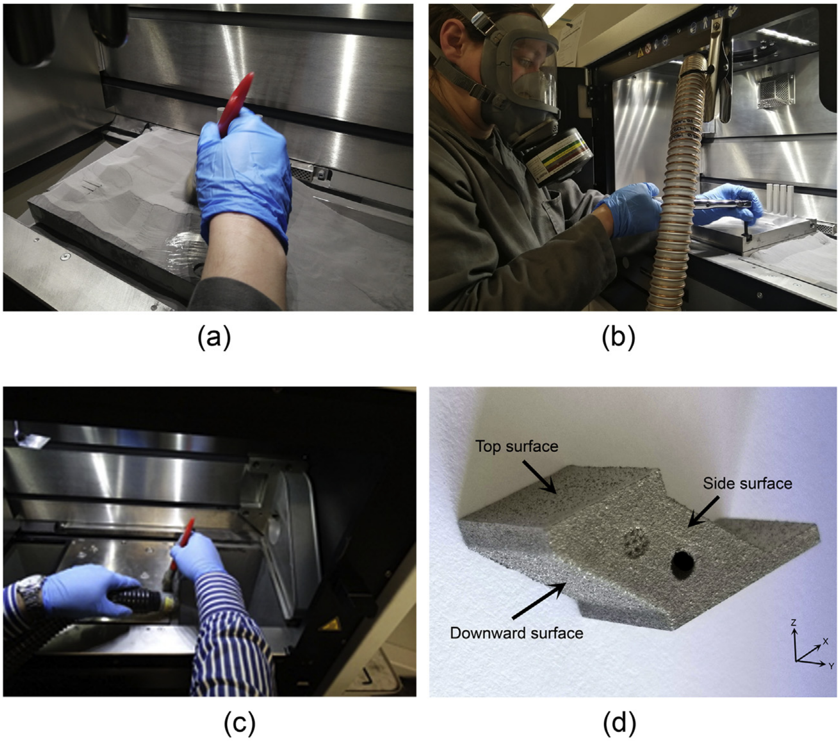

Figure 24.6 Powder is removed from the building platform (a), the platform with parts is physically removed (b) and the machine is cleaned (c). Manufactured L-PBF sample, arrrows indicate the surfaces where roughness was studied (d).

The parts on the base plate are then subjected to stress-relieving heat treatment (e.g., 650°C for 3 h in argon atmosphere or vacuum for Ti6Al4V alloy), after which they are physically removed from the base plate by means of wire EDM or other forms of cutting technology.

24.6 Post-processing

After above steps, support removal must be done if supports are attached (which is not the case with the test artifact). Other processing steps may be incorporated at this stage but in the case of the test artifact these are omitted.

24.7 Part inspection

Optical inspection of parts is often done and measurements made of critical feature sizes which are physically accessible. Various nondestructive testing methods are

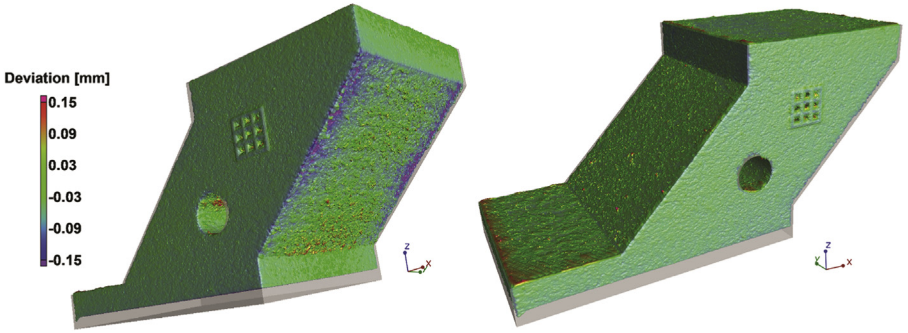

Figure 24.7 CT scan of part (or 3D scan by other method) showing comparison with CAD design (optional result). Deviations from designed values are shown with color.

available as described in Chapter 10. In the case shown here a microCT scan and analysis was performed as in previous round robin tests described in more detail in (Du Plessis et al., 2019; Du Plessis and le Roux, 2018). Basically, the dimensional measurements are compared to the CAD design as shown in Fig. 24.7. As the part was cut off the base plate too close to the part, the bottom surface is 0.6 mm under the design geometry all over the bottom surface. Ignoring the bottom surface, the rest of the surface conforms to the design with a cumulative value for 90% of the surface points being within 0.08 mm of design. No internal porosity was detected by CT scans.

Roughness measurements were done on the top surface, downward-facing inclined surface, and vertical side surface of the sample by a SurfTest profilometer from Mitutoyo (see Table 24.2). Measurements were done in parallel and perpendicular to edges at different surfaces as indicated in Fig. 24.6 five times in each set (Table 24.3).

Chapter 7 "Surface roughness" recommended that a sampling length of 8 mm is preferable for roughness measurements $10\ \mu m < Ra \leq 80\ \mu m$ or $50\ \mu m < Rz \leq 200\ \mu m$ on nonperiodic profiles. Measuring surface roughness on small objects with holes and thin details is difficult, and sometimes impossible. Therefore, these results obtained using a profilometer with a sampling length of 2.5 mm are very evaluative and will be checked in the future using other methods of roughness analysis.

Table 24.2 Parameters for roughness measurements.

Standard	**ISO 1997**
Profile	R
λs	8 μm
Cut-off:	2.5 mm
N	2
Filter	GAUSS

Table 24.3 Average roughness values for tested surfaces.

Value	Top surface	Downward surface	Side surface (along edges)
Ra, µm	9.5 ± 2.56	16.2 ± 4.06	12.0 ± 1.49
Rq, µm	12.4 ± 3.57	20.4 ± 4.22	14.6 ± 1.96
Rz, µm	66.7 ± 17.97	101.3 ± 15.68	72.3 ± 6.28
Rp, µm	39 ± 13.73	43.9 ± 10.59	37.7 ± 7.08
Rv, µm	27.7 ± 7.37	57.4 ± 9.6	34.7 ± 2.25

24.8 Concluding remarks

This case study can be used to improve confidence in practically using L-PBF. Any results can be submitted for recording of experiences and future publication —simple photos, manual measurements, and a description are acceptable. Submitting results are encouraged especially from new users and students, even in case of negative results, in which case this can be treated confidentially if so desired. More advanced analyses are of course also welcome. Sharing of experiences and results, and solving these problems in a transparent way is the best way to overcome the hurdles toward wider adoption and acceptance of L-PBF and thereby gaining the advantages of using this technology.

Acknowledgements

The authors acknowledge the Collaborative Program in Additive Manufacturing.

References

Du Plessis, A., le Roux, S.G., 2018. Standardized X-ray tomography testing of additively manufactured parts: a round robin test. Addit. Manuf. 24 (September), 125–136. https://doi.org/10.1016/j.addma.2018.09.014.

Du Plessis, A., Stephan, G., le Roux, Waller, J., Sperling, P., Achilles, N., Andre, B., Jean, F.M., et al., 2019. Laboratory X-ray tomography for metal additive manufacturing: round robin test. Addit. Manuf. 30 (December), 100837. https://doi.org/10.1016/j.addma.2019.100837.

n.d., Fundamentals of L-PBF of Metals | Research Group 3D Innovation. https://blogs.sun.ac.za/duplessis/fundamentals-of-l-pbf-of-metals/

Moylan, S., Brown, C.U., Slotwinski, J., 2016. Recommended protocol for round-robin studies in additive manufacturing. J. Test. Eval. 44 (2), 20150317. https://doi.org/10.1520/JTE20150317.

Townsend, A., Racasan, R., Leach, R., Nicola Senin, Thompson, A., Ramsey, A., Bate, D., Peter, W., Brown, S., Blunt, L., 2018. An interlaboratory comparison of X-ray computed tomography measurement for texture and dimensional characterisation of additively manufactured parts. Addit. Manuf. 23 (October), 422–432. https://doi.org/10.1016/J.ADDMA.2018.08.013.

Index

Note: ‘Page numbers followed by “f” indicate figures and “t” indicate tables.’

A

Absorptance, 83, 85–86
Absorption of laser radiation, 83, 87–88, 258–259
Abstracted bio-inspired design, 472–475, 473f
Acoustic emissions, 309
Additive manufacturing (AM), 1–2, 2f, 15–17, 39–40, 120, 156, 350
Additive Manufacturing Center of Excellence (AM CoE), 572–575
Additive Manufacturing Standardization Collaborative (AMSC), 575, 575f
  function, 572, 573f
  mission, 572
  themes, 573–575, 574t
  vision, 572
Additive Manufacturing Format (AMF), 134–135
Alloy composition, optimization of, 267
Altair Inspire Print3D, 32
Aluminum-based alloys, 358–359, 367–368, 368f
Anisotropy, 428
ASTM, 278–282, 495, 502, 512–513, 568
Artifact design, 636–638
Athermal martensitic transformation, 224
Auger Electron Spectroscopy (AES), 506
Austenitic stainless steel, 219
Automotive industry, 588–589, 589f
Average Strain Energy Density (ASED), 406–409, 415

B

Balling effect, 106, 122, 183
Bambi-second-generation L-PBF system, 6, 7f
Base plate
Batch-enabled scenarios, 605, 606f
Bidirectional Evolutionary Structural Optimization (BESO), 138–139
Binder jetting, 16–17
Biodegradable metals, 431–432
Bio-inspired design, 429–430
  applications, 480–484, 482t–483t
    energy absorption, 483–484
    optics, 484
    structural components, 481
    thermal management, 483
  concepts, 475–480
Biointegration, 337
Biomedical alloys, 430–431
Boltzmann equation, 87–88
Boundary representation (B-Rep), 134–135
  CAD models, 135
Bragg’s law of diffraction, 250
Brittle behavior, 365
Build chamber, 263
Build platform, 28
Build orientation, 67
Build preparation, 638

C

Calibration and tuning, 320
Carr indices, 497
Chamber environmental conditions, 303
Chemical surface post-processing, 333–335, 334f
“Chess board strategy”, 265
Clausius-Clapeyron relation, 87
Closed-loop control, 302, 318
Co-axial cameras, 304–305
Co-axial/off-axis sensors, 304
Cobalt-Chromium-Molybdenum (CoCrMo) alloys, 229–230
Columnar equiaxed transition (CET), 531–532

Commercial L-PBF systems, 3, 3f, 149
Commercial materials (powders), 30, 31t
Complexity-enabled scenarios, 607
Component orientation, 128–130
Compositional grading
  hybrid manufacturing, 544–545
  modify microstructure alloying, 543–544
Computational fluid dynamics (CFD), 89–90
Computational modeling, 445–446
Computed Tomography (CT), 170
Computer Aided Design (CAD) software, 30–31
Computer numerical control (CNC), 17
Condensed phase, heat transfer in, 100–106
Constant amplitude loading, 377, 378f
Continuous wave laser, 23–24
Contour method, 249
Contour scanning, 162–163
Conventional cast alloy structure, 219
Conventional Ni-based superalloys, 231–232
Coordinate descent, 140–141
Corrosion, 171–172, 384
Cost-benefit fundamentals complexity *vs.*, 604, 604f
  cost-price-value, 604–605
  production volume *vs.*, 602–603, 603f
Cost-independence assumed, commercial opportunities for
  batch-enabled scenarios, 605, 606f
  complexity-enabled scenarios, 607
  integrated cost, 607–608
  ultra-high-complexity scenarios, 607
  volume opportunities, 607–608
Crack closure, 381–382
"Crack compliance method", 248–249
Crack nucleation or initiation, 380–381
Curvature method, 249
Cyclic R-curve concept, 387–389, 387f–388f

D
Damage tolerance, 475
Data synchronization, 322
"Denudation zone", 81
Density measurements, 292
Archimedes method, 169–170
Design flexibility and understanding
effective design processes, 599
  evolutionary design scenarios, 600, 600f
  generative design, 601–602
  net-shape and near-net-shape manufacturing, 601
  parts consolidation, risk management by, 602
  revolutionary design scenarios, 600, 600f
Design for additive manufacture (DFAM), 30–31, 120, 148–149
Design of Experiments (DoE), 141
Design principles, 120
  boundary representation, 134–135
  digital data optimization, 130–133
  digital geometry formats
  emerging opportunities for L-PBF design, 147–148
  generative design, 137
  metadata analysis, 132
  resolution restriction, 132–133
  support structures, 125
  volumetric representation, 136–137
Design uncertainty, 474
Digital data management, 130
Digital data optimization
  metadata analysis, 132
  resolution restriction, 132–133
Digital data overload, 122
Digital geometry formats
  boundary representation, 134–135
  volumetric representation, 136–137
Digital image correlation (DIC), 249
Directed energy deposition (DED), 16–17, 493
Direct Monte Carlo methods, 144
Discretization, 475–478, 476f
3D Manufacturing Format (3MF), 134–135
Dross, 57
DTM SinterStation 2000, 11, 11f
Ductile fracture, 364–365
Dye penetrant testing (PT), 289
Dynamically loaded applications, 201
Dynamically loaded L-PBF applications, 203–204
Dynamic flow testing regime 2, 499, 499f
Dynamic focusing module (DFM), 25–26

E
Early L-PBF system, 5
Eddy current testing (ET), 291–292
Effect of defects, 143, 156, 170–172, 294–296, 383–384
Electrochemical surface post-processing, 333–335, 334f
Electron beam melting (EBM), 493
Electron-beam powder bed fusion, 12
“Electron gas”, 24–25
Engineering economics
  AM-high-volume influence, 609–611
  AM-low-volume influence, 609
Energy absorption, 483–484
Energy sector, 589–590, 590f
Energy transfers, 83–88
Enhanced support structures, 148
European and North American space industry, 576–581, 576f–577f
European Cooperation for Space Standardisation (ECSS) standards, 578–579
Explicit biomimicry, 472

F
False negative, 320
False positive, 320
Fatigue properties, 171
  constant amplitude loading, 377, 378f
  cyclic R-curve concept, 387–389, 387f–388f
  high cycle fatigue (HCF), 377–378
  Kitagawa-Takahashi (KT) approach, 383–385
  long fatigue crack propagation, 380f
  low cycle fatigue(LCF), 377–378
  Murakami’s approach, 385–387
  short fatigue crack propagation, 380–383
  variable amplitude loading, 377, 378f
Fiber Bragg Grating (FBR), 23–24
Field Programmable Gate Array (FPGA), 321–322
Filtration systems, 29
Finite Element Analysis (FEA), 259–260
First commercial system DTM 125, 10–11, 10f
Form error, 195–196
Fracture analysis
  brittle, 365
  ductile, 364–365
  high strength/low ductility materials, 366–367, 366f
  low strength/high ductility materials, 367–368, 368f
Fresnel equations, 84–85
Functionally graded materials (FGMs), 530–531
Functional materials, 545
Functional optimization, 130, 149
Fused deposition modeling (FDM), 17
Fused filament fabrication (FFF), 17

G
Gas phase flow, 89–95
  Gas porosity, 122–123
  Gas supply module, 29
Generative design, 137
Genetic algorithms, 141
Geometry optimization, 122
Geometrical design, 425–430
Gradients, 140–141, 478, 480f
Granulo-morphometric properties, 30

H
Hall flowmeter, 495–497, 496f
Hard blade recoaters, 27
Hard magnets, 548–549
Hardness, 351
Hardware, L-PBF for, 21–29
  build platform and base plate, 28
  lasers, 23–25
  powder delivery system, 26
  powder deposition system, 26–28
  powder removal, gas supply, and filtration systems, 29
  scanning systems, 25–26
Hatch distance, 44–45, 50–52, 62–63
Hatching, 50–51
Heat affected zone (HAZ), 79–80, 82–83, 109–110
Heat transfer in condensed phase, 100–106
Heat treatment, 261, 340–342, 341f–342f, 360–364
  aluminum- and nickel-based alloys, 363–364, 364f
  steels, 360–362, 361f
  titanium-based alloys, 362–363, 362f
Heuristic optimization methods, 141

Hierarchical design principles, 59f
High-alloy tool steels, 229
High cycle fatigue (HCF), 377−378
High speed X-ray imaging experiments, 161
Hole drilling method, 248−249, 248f
Hooke's laws, 111, 247
Hot isostatic pressure (HIP), 342, 439
Humidity measurements, 513−514
Hybrid manufacturing, 544−545
Hybrid post-processing, 343

I

Impact-based surface treatments, 331
Inductively coupled plasma optical emission spectroscopy (ICP-OES), 508
Industrial applications
  case studies
    automotive industry, 588−589, 589f
    energy sector, 589−590, 590f
    medical industry, 590−592, 591f
    space industry, 584−588, 585f−587f
    transport industry, 588−589, 589f
  future potential industrial applications, 592−594
  hybrid manufacturing, 592
Inert gas fusion (IGF), 509
Infrared (IR) absorption, 24−25
Inline coherent imaging (ICI), 305
Innovation inspired by nature, 467−468
Inside-out design approach, 128
In-situ alloying, 433−434
In-situ co-axial monitoring, 304−305
In situ stress relief, 262−267
  base plate and build chamber preheating, 263
  optimization of alloy composition, 267
  optimization of support structures, 266−267
  process parameter optimization, 264
Internal porosity, 401−403, 434−436
International Organization for Standardization (ISO), 563−564
Intra-layer porosity, 122−123
Island shift parameter, 536−537
ISO/ASTM collaboration, 566−567
ISO/ASTM 52900 terminology, 564
Isotropy/anisotropy, 428

K

Keyhole mode in L-PBF, 47−49
Keyhole porosity, 122−123
Kitagawa-Takahashi (KT) approach, 383−385

L

Lack of fusion (LoF) defects (porosity), 122−123, 158
Laser-based powder bed fusion process (L-PBF), 16
Laser-based surface post-processing, 335−336, 336f
Laser beam-matter interaction zone, 42
Laser beam spatial profile, 24f
Laser-interaction zone, 79−83
Laser Powder Bed Fusion (L-PBF), 1−2, 4, 15−18, 21−22, 39−40, 79, 120, 148−149, 156, 180−190, 215−216
  conception of, 4−6
  current state and historical background, 622
  future trends, 626−632
  materials, 622−625
  mechanical properties, 171
  modeling for, 183−185
  post-processing, 630
  quality control, 630−632
  safety aspects, 35
Laser scanning path optimization, 128
Laser shock peening (LSP), 261−262, 336
Latent heat, 87, 98−99
Lattice simulation
  component level, 144
  node level, 147
  strut level, 144−147
Lattice structures
  applications, 447−449
  biomedical, 448−449
  lattice simulation
    analytical solutions, 445−446
    component level, 144
    node level, 147
    strut level, 144−147
Layer thickness, 61, 540−542, 624
the relationship with build platform movement, 52f
Layer-wise control strategy, 319
Layer-wise manufacture, 123
Level-set method, 138−139

Library-based designs, 425–428
Light-weight and load-bearing structures, 447–448, 447f
Local approaches for failure assessment, 406
Long fatigue crack propagation, 380f
Low cycle fatigue(LCF), 377–378
Low-volume product design evolution, 616–617, 617f

M
Magnetic field-induced strains (MFIS), 552
Magnetic refrigerants, 549–551
Magnetocaloric effect (MCE), 549–551
Magnets, 546f
  hard magnets, 548–549
  soft magnets, 547–548
Materials
  addition, optimization for, 128
  composition measurement standards, 510, 511t
Materials Properties Suite (MPS), 577
Maxwell equations, 83–85
Mechanical properties, 171
  aluminum-based alloys, 358–359
    nickel-based alloys, 363–364, 364f
    steels, 360–362, 361f
    titanium-based alloys, 362–363, 362f
Microstructure, 352–353
  nickel-based alloys, 359–360
  high-alloy tool steels, 355–356
  maraging tool steels, 355–356
  martensitic stainless steels, 354–355
  steels precipitation hardening, 354–355
  stainless steels, 353–354
  titanium-based alloys, 362–363, 362f
  thermal cracks, 353
  treatment, 261–262
Mechanical surface post-processing, 330–333, 331f–332f
Medical L-PBF applications, 201–202
Medical implants, 180, 192, 201, 207, 472, 530, 607, 613–615
Melt pool dynamics, 95–100
Melt-pool
  phenomena, 180
  simulations, 142
  single track formation, 40–49, 82, 106
  solidification, 122–123
  stability, 183
Mesh models, 134–135
Metadata analysis, 132
Metal 3D printing systems, 21–22, 21f
Metallic powders, 493
Metal Powder Bed Fusion (mPBF) techniques, 579
Metamaterials, 429
Micro-computed tomography (microCT), 143
Microstructural grading columnar equiaxed transition (CET), 531–532
Mirror-based laser scanning system, 51
Model-based feedforward control, 318
Monte Carlo method, 145
Multifunctionality, 474
Multiscale modeling methods, 145
Murakami’s approach, 385–387

N
Nano-indentation, 512
National Standards Bodies (NSBs), 567
Navier-Stokes approach, 90
Necking, 183
Netfabb software, 32
Net-shape manufacture, 128
Neutron diffraction measurement, 250
Neutron radiography, 282–284
Newton’s method, 140–141
Nickel-based alloys, 359–360
Nickel-titanium (NiTi) alloys, 333
“Non-contact” deposition system, 26
Nondestructive pore detection methods, 169
Nondestructive testing (NDT), 34–35, 249–251, 379
  considerations, quality control, 294–297
  requirements for metal additive manufacturing, 280–282
  traditional, 278–279
  in-situ NDT, 302, 315–317
Nonintrusive SFEM, 144
Nonuniform designs, 427
Notch Stress Intensity Factor (NSIF), 407–408
Numerical simulations of single tracks, 58–60

O

Offset, 51, 120, 136−137, 199−200, 251−252, 350, 389, 434, 551−552, 601−602
Optical imaging, 305
Optical microscopy, 170
Optics, 484
Optimal component orientation, 148
Optimal process parameters
  for 3D parts, 64−67
  for single layers, 62−64
  for single tracks, 61−62
Optimized process parameters, 335−336
Orientation, 312−313
Overhang components and bridges, 57
Overlapping rate, 62−63, 63f
Oxide-debris-induced mechanism, 381−382

P

Parameters in L-PBF
  machine-based, 18−19
  material-based, 18−19
  process-parameters, 18−19
  post-treatment parameters, 18−19
Parametric optimization, 140−141
Particle attachment, 122
Particle size distribution (PSD), 27, 492−493
Part Production Plans (PPP), 577
Part inspection, 641−642
Part manufacturing, 247, 251
Part removal, 640−641
Post-processing, 33−35, 40, 57, 128, 156, 180−181, 201, 205, 261−262, 315−316, 327−348, 358, 362−363, 405−406, 438−440, 512−513, 612−614, 630, 641
Phase transition temperature, 498f, 501−503
Photodiode, 304−305
Physics and modeling, 79−83
  energy transfers, 83−88
  gas phase flow, 89−95
  heat transfer in condensed phase, 100−106
  melt pool dynamics, 95−100
  nomenclature, 113−114
  process stability, 106−109
  thermomechanics, 109−112
Plasma electrolytic oxidation (PEO) coating, 343
Plasticity, 388
Plateau-Rayleigh instability of circular cylinder, 108
Plume size, 312−313
Polynomial Chaos Expansions, 144
Pore closure and mitigation
  hot isostatic pressing, 173
  peening and surface processing, 173−174
  porosity minimization, 172
  remelting, 173
Pore characteristics, 438
Pore formation mechanisms, 163
  porosity types, 166t−168t
    multiple layers, 163−165
    single layers, 162−163
    single track without powder, 160
    single track with powder, 160−162
    summary of pore types, 165
Porosity, 122−123, 156, 437−438
  assessment standards, 514
  in cast metals, 157−158
  in L-PBF, 158−159
  measurement
    Archimedes method, 169−170
    computed tomography, 170
    optical microscopy, 170
Positioning of the part on the base plate, 28f
Post-processing, 33−35, 181
  heat treatment, 261
  mechanical treatment, 261−262
  stress relieving, 261−262
  surface post-processing. *See* Surface post-processing
Powder additives, 539−542, 541t
Powder bed fusion (PBF), 16, 120
Powder characterization
  additive manufacturing, 503−504
  applications, 503−504
  Auger Electron Spectroscopy (AES), 506
  chemical composition, 504−510
  composition measurement in, 509−510
  definition, 492−493
  humidity measurements, 513−514
  inductively coupled plasma optical emission spectroscopy (ICP-OES), 508
  inert gas fusion (IGF), 509

  - life cycle, 514–519
  - material composition measurement standards, 510, 511t
  - mechanical measurements, 513–514
  - metallic powders, 493
  - morphology, 501–504
  - particle size distribution (PSD), 492–493
  - phase transition temperature, 513
  - porosity, 512–513
  - powder recycling, 517–519, 518f
  - powder thermal conductivity, 514
  - reuse methods, 516–517
  - thermal measurements, 513–514
  - rheology, 494–501
    - applications, 500
    - Carr indices, 497
    - dynamic flow testing regimes, 497–499, 498f–499f
    - Hall flowmeter, 495–497, 496f
    - safety, 519–521
    - health standards, 520–521
    - shape, 501–504
    - size, 501–504
    - standards, 504
    - sustainability analysis, 514–519
    - X-ray diffraction, 508
    - X-ray fluorescence (XRF) spectroscopy, 508
    - X-ray photoelectron spectroscopy (XPS), 505

Powder delivery system, 3, 26
Powder deposition system, 26–28
Powder recycling, 517–519, 518f
Powder removal, 29
Powder thermal conductivity, 514
Predefined parameters, 18–19
Pre-process parameters, 181
Preheating, 4, 28–29, 49, 66–67, 112, 125, 181, 235, 263–265, 405, 586, 625
Process compensated resonance testing (PCRT), 293
Process Control Reference Distribution (PCRD), 577
Process parameters, 181, 539–542, 541t
  - optimization, 264

Process stability, 106–109
Process monitoring
in-situ process monitoring, 309–313, 314t
in-situ process sensing, 304–309, 304f, 306f–309f
machine/chamber condition monitoring, 302–304
Processing map, 61–62, 62f, 531–532
Profile roughness parameters, 197–198
Project implementation, 612–613

Q

Qualified Material Process (QMP), 577
Quasi-equiaxed morphologies, 535–536
Quasi-static mechanical properties, 441–444

R

Radiative laser energy, 95
Rapid Prototyping, 13–14
Recoater
  - hard recoater, 27
  - soft recoater, 27
  - trajectory, 124

Recoil pressure, 183–185
Reduced-order models, 143
Reflectivity, 24–25, 54, 358
Reflectance, 85–86
Rescanning, 54, 56, 265–266, 538–539
Residual stress, 245–247, 352, 405
  - destructive methods, 247–249
  - effects and origins of, 251–258
  - evolution, 258–260
  - heat treatment, 261
  - measurements, 247–251
  - mechanical treatment, 261–262
  - nondestructive techniques, 249–251
  - post-processing stress relieving, 261–262
  - relieving, 438
    - base plate and build chamber preheating, 263
    - in situ stress relief, 262–267
    - optimization of alloy composition, 267
    - optimization of support structures, 266–267
    - process parameter optimization, 264
    - scanning strategy and in situ residual stress control, 264–266

Reynolds number, 90, 92, 100
Roughness parameters, 197–199, 333

S
Scalability, 337–340
Scanning speed, 18–19, 35, 42–43, 45, 50–51, 55, 61, 64–65, 162, 181, 264, 266, 531, 547–548, 625
  dwell time, 45
Scanning strategy, 533
  stripes, 50f, 62, 163, 257f
  islands, 265
  chess-board, 50–51
Scanning systems, 25–26
  with active optics, 25–26, 26f
  with passive optics, 25–26
Second law of thermodynamics, 95
Selective Laser Melting (SLM), 2
Selective Laser Sintering (SLS), 2
SEM-energy dispersive X-ray spectroscopy, 506–507, 507f
Shape memory alloys (SMAs), 432
Shape memory effect (SME), 551–552
Sheet-based unit cells, 427
Sheet lamination, 17
Short fatigue crack propagation, 380–383
Shot peening, 261
Signed-distance functions (SDF), 136–137
Simulated annealing, 141
Simulation driven design, 137–141, 148, 469–472
  parametric optimization, 140–141
  topology optimization, 138–140
Single layer formation, 142
  characterization of, 51–54
  contouring, 51
  delivery of powder layer, 45–47
  hatching pattern, 50–51
  offset, 51
  scanning strategies, 50–51
  skywriting, 51
Single track formation
  beginning-end effect, 45, 51
  droplets, 17, 42, 53–54, 106, 108
  geometry of single tracks, 47–49
  humping effect, 44–45, 44f, 162
  melt-pool dynamics and track formation, 40–42
  morphology of single track, 42–43, 52, 61
  necking, 183, 352, 366–367
  process parameters on, 45–49
  process stability, 42–45
  ripples, 42–43
  satellites, 41–42, 586–587
  spattering, 41–42, 81, 122, 162, 180, 183, 302, 353, 434–436
Size optimization, 141
Shielding inert gas, 29
Skywriting, 51
Slumping, 122
Soft magnets, 547–548
Soft recoater, 27
Software, L-PBF, 30–33
Solid freeform fabrication (SFF), 1–2
Solidified laser track, 180
Solid-isotropic material with penalization (SIMP), 138–139
Solid-state transformation, 218–220, 224–234
Spot size, of laser beam, 25–26, 41–42, 102, 160, 261–262, 623–624
Space industry, 55, 183, 434, 584–588, 585f–587f
Spattering, 183
Satellites, 41–42, 586–587
Stair-step effects, 121, 182–183
Standardization
  additive manufacturing, 565f
  background, 563–564
  International Organization for Standardization (ISO), 563–564
  ISO/ASTM 52900 terminology, 564
  worldwide standardization activities, 566–582
Standards Development Organizations (SDOs), 581, 581f
Statistical Process Control (SPC), 577
Steels, 365
  high-alloy tool steels, 355–356
  maraging tool steels, 355–356
  martensitic stainless steels, 354–355
  precipitation hardening, 354–355
  stainless steels, 353–354
Stefan-Boltzmann constant, 86
Stereolithography (STL), 31, 134–135
Stochastic Finite Element Method (SFEM), 144
Stochastic uncertainties, management of, 130
Strain energy density, 405–412, 407f
Strut orientation effects, 436

Stress-induced distortion, 252–253
Structural hierarchy
  symmetry, 478
  types of, 480
Structural lightweighting, 139–140
Strut-based unit cells, 425–427, 426f
Strut orientation effects, 436
Subsequent fatigue crack propagation stages, 381f
Subtractive manufacturing methodologies, 17
Substrate (base plate), 19–21, 27–28, 42, 45–46, 64, 81–83, 93, 100, 109, 122, 160, 218–219, 253, 267, 405, 530–531
Superalloys, 433
Support structures, optimization of, 266–267
Surface condition, 403–404, 404f
Surface post-processing, 330–340
  chemical/electrochemical surface post-processing, 333–335, 334f
  comparing techniques, 337–340, 338t–339t
  heat treatments, 340–342, 341f–342f
  hybrid post-processing, 343
  impact-based surface treatments, 331
  laser-based surface post-processing, 335–336, 336f
  mechanical surface post-processing, 330–333, 331f–332f
  plasma electrolytic oxidation (PEO) coating, 343
  surface coating, 336–337
  ultrasonic cavitation abrasive finishing (UCAF), 331
Surface orientation
  upward (upskin) surfaces, 57, 181, 183, 190, 403–404
  downward (downskin) surfaces, 123, 126f, 182f, 187, 187f, 193f, 403–404, 498, 538–539, 615–616, 642
Surface roughness, 195–196, 440–441
  characterization, 190–194
  methods
    areal roughness parameters, 198–199
    profile roughness parameters, 197–198
    virtual stylus methods, 199–200
  models, 188–190
  objective, 190–191
  spattering and satellite particles, 183
  stair-step phenomena, 182–183
  surface orientation on residual attached particles, 185–187
Sustainability analysis, 514–519
Swarm optimization, 141

T
Tactile methods, 191
Taguchi method, 65–66
Temperature profile, 312–313
Texture, 31, 137, 195–200, 196f, 221, 232, 335–336, 352, 391
Thermal conductivity, 510–512
Thermal cracks, 353
Thermal cycling, 221–224, 356, 361, 363–364
Thermal gradients, 218
Thermal imaging, 307
Thermal management, 130, 483
Thermal measurements, 513–514
Thermal systems, 125
Thermocapillary force vector, 95
Thermocapillary convection, 95, 96f, 99–100
Thermography, 293–294
Thermomechanics, 109–112
Thin wall formation, 54–55
Three-dimensional part nesting, 148
Titanium-based alloys, 356–358, 357f, 366–367, 366f
Topology optimization, 128, 133, 138–140
Traditional manufacturing methods, 128
Transient thermal energy, 125
Transport industry, 588–589, 589f

U
Ultra-high-complexity scenarios, 607
Uncertainty quantification methods, 143–144
Ultrasonic cavitation abrasive finishing (UCAF), 331
Ultrasonic impact treatment (UIT), 262
Ultrasonic nanocrystal surface modification, 333
Ultrasonic testing (UT), 289–291
Uncertainty quantification, 142–147
  experimental methods, 143

Uncertainty quantification (*Continued*)
  lattice simulation
    component level, 144
    node level, 147
    strut level, 144–147
  methods, 143–144
  numerical prediction, 142–143

V
Vapor jet, 42, 80–81, 80f, 89–92
Variable amplitude loading, 377, 378f
Vat photopolymerization, 17
Vibratory grinding, 330
Video imaging, 305, 307
Virtual stylus methods, 199–200
Volumetric energy density, 64–65
Volumetric representation, 136–137

W
Waviness, 195–196
Workflow of part creation, 19f
Worldwide standardization activities
  Additive Manufacturing Center of Excellence (AM CoE), 572–575
  Additive Manufacturing Standardization Collaborative (AMSC), 575, 575f
  Additive Manufacturing Procedure (AMP), 579
  ASTM F42 Technical Committee, 568–569, 569f, 569t–570t
  European and North American space industry, 576–581, 576f–577f
  European Cooperation for Space Standardisation (ECSS) standards, 578–579
  ISO/ASTM collaboration, 566–567
  ISO Technical Committee 261, 567–568
    materials properties suite (MPS), 577
    metal powder bed fusion (mPBF) techniques, 579
  National Standards Bodies (NSBs), 567
    part production plans (PPP), 577
    process control reference distribution (PCRD), 577
    published standards, 570t–572t
    qualified material process (QMP), 577
    Standards Development Organizations (SDOs), 581, 581f
    statistical process control (SPC), 577

X
X-ray computed tomography, 284–287
X-ray diffraction (XRD), 251, 255–256, 508
X-ray fluorescence (XRF) spectroscopy, 293, 508
X-ray photoelectron spectroscopy (XPS), 505